



AD-A286 734



Ocean Optics XII

Jules S. Jaffe
Chair/Editor

13-15 June 1994
Bergen, Norway

DTIC
ELECTE
DEC 20 1994

D

95-01100



95

2

21

005

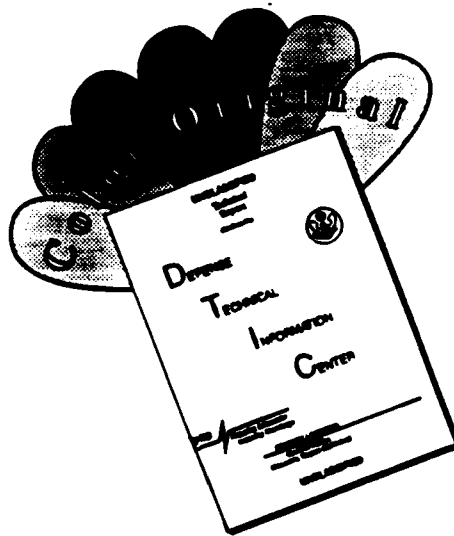


Volume 2258

DTIC QUALITY INSPECTED 1

1	2	3	4	5	6	7	8	9	10	11	12
A. [unclear] the release;											
Distribution Unlimited											

DISCLAIMER NOTICE



THIS DOCUMENT IS BEST QUALITY AVAILABLE. THE COPY FURNISHED TO DTIC CONTAINED A SIGNIFICANT NUMBER OF COLOR PAGES WHICH DO NOT REPRODUCE LEGIBLY ON BLACK AND WHITE MICROFICHE.



SPIE—The International Society for Optical Engineering

PROCEEDINGS

Ocean Optics XII

Jules S. Jaffe
Chair/Editor

13–15 June 1994
Bergen, Norway

Sponsored and Published by
SPIE—The International Society for Optical Engineering

In cooperation with
Bergen High-Technology Centre, Ltd. (Norway)
**Nansen Environmental and Remote Sensing Centre/
University of Bergen (Norway)**
**Institute of Marine Research/Norwegian Ministry
of Fisheries**
**Norwegian Institute of Technology/
University of Trondheim**
**Scripps Institution of Oceanography/
University of California/San Diego (USA)**
U.S. Office of Naval Research (USA)

Accession For		
NTIS	CRA&I	<input checked="" type="checkbox"/>
DTIC	TAB	<input type="checkbox"/>
Unannounced		<input type="checkbox"/>
Justification		
By		
Distribution /		
Availability Codes		
Dist	Avail and/or Special	
A-1		



Volume 2258

SPIE (The Society of Photo-Optical Instrumentation Engineers) is a nonprofit society dedicated to the advancement of optical and optoelectronic applied science and technology.

DISTRIBUTION STATEMENT A

**Approved for public release;
Distribution Unlimited**



The papers appearing in this book comprise the proceedings of the meeting mentioned on the cover and title page. They reflect the authors' opinions and are published as presented and without change, in the interests of timely dissemination. Their inclusion in this publication does not necessarily constitute endorsement by the editors or by SPIE.

This work relates to Department of Navy Grant N00014-93-1-1000 issued by the Office of Naval Research. The United States Government has a royalty-free license throughout the world in all copyrightable material contained herein.

Please use the following format to cite material from this book:

Author(s), "Title of paper," in *Ocean Optics XII*, Jules S. Jaffe, Editor, Proc. SPIE 2258, page numbers (1994).

Library of Congress Catalog Card No. 94-65774
ISBN 0-8194-1574-X

Published by
SPIE—The International Society for Optical Engineering
P.O. Box 10, Bellingham, Washington 98227-0010 USA
Telephone 206/676-3290 (Pacific Time) • Fax 206/647-1445

Copyright ©1994, The Society of Photo-Optical Instrumentation Engineers.

Copying of material in this book for internal or personal use, or for the internal or personal use of specific clients, beyond the fair use provisions granted by the U.S. Copyright Law is authorized by SPIE subject to payment of copying fees. The Transactional Reporting Service base fee for this volume is \$6.00 per article (or portion thereof), which should be paid directly to the Copyright Clearance Center (CCC), 222 Rosewood Drive, Danvers, MA 01923. Other copying for republication, resale, advertising or promotion, or any form of systematic or multiple reproduction of any material in this book is prohibited except with permission in writing from the publisher. The CCC fee code is 0-8194-1574-X/94/\$6.00.

Printed in the United States of America.

Contents

xi	<i>Conference Committee</i>
xiii	<i>Introduction</i>

SESSION 1 INSTRUMENTATION

- 2 **Inherent optical property estimation in ocean water using the Zaneveld-Wells algorithm [2258-01]**
L. J. Holl, N. J. McCormick, Univ. of Washington

- 12 **Estimation of ozone concentrations based on measurements of solar ultraviolet radiation in the Antarctic using the BSI PUV-510 instrument [2258-02]**
E. J. Bruce, P. L. Handley, Z. Wan, R. C. Smith, Univ. of California/Santa Barbara

- 21 **New instrumentation and platforms for subsurface optical measurements [2258-04]**
D. K. Costello, K. L. Carder, Univ. of South Florida

- 33 **Multisensor in-situ fiber optic fluorometer [2258-05]**
E. J. D'Sa, S. E. Lohrenz, V. L. Asper, Univ. of Southern Mississippi; R. A. Walters, M. J. Morris, Ocean Optics; C. Rathbun, Univ. of Southern Mississippi

- 44 **Scattering error correction of reflecting-tube absorption meters [2258-06]**
J. R. V. Zaneveld, J. C. Kitchen, Oregon State Univ.; C. C. Moore, Western Environmental Technology Labs. Inc.

- 56 **Three-dimensional reconstruction of ocean chlorophyll distributions from underwater serial sectioned fluorescence images [2258-07]**
A. W. Palowitch, J. S. Jaffe, Scripps Institution of Oceanography

- 67 **In-situ spectral absorption profiler using optical fibers [2258-08]**
T. Saito, A. Nishimoto, Y. Kakui, M. Nanjo, Life Electronics Research Ctr. (Japan); R. Tsuda, Kinki Univ. (Japan)

- 77 **Instrument to measure in situ visible light absorption in natural waters [2258-09]**
J. H. M. Hakvoort, A. E. R. Beeker, J. Krijgsman, Delft Univ. of Technology (Netherlands)

SESSION 2 BIO-OPTICAL VARIABILITY

- 90 **Maintaining a phytoplankton bloom in low mixed layer illumination in the Bellinghausen Sea in the Austral Spring, 1992 [2258-10]**
A. R. Weeks, I. S. Robinson, Univ. of Southampton (UK); J. Aiken, G. F. Moore, Plymouth Marine Lab. (UK)

- 105 **Observing biologically induced optical variability in coastal waters [2258-11]**
J. J. Cullen, Dalhousie Univ. and Bigelow Lab. for Ocean Sciences (Canada); A. M. Ciotti, M. R. Lewis, Dalhousie Univ. (Canada)

- 116 **Optical backscattering measurements off the coast of Hawaii [2258-12]**
J. M. Voss, SRI International; J. H. Smart, Johns Hopkins Univ.

- 123 **Instrumental considerations for deriving spectral photosynthetic absorption coefficients from total phytoplankton absorption [2258-13]**
M. E. Culver, Univ. of Washington; R. F. Davis, Oregon State Univ.; M. J. Perry, Univ. of Washington
- 134 **Light attenuation on unicellular marine phytoplankton [2258-14]**
T. Król, M. Łotocka, Institute of Oceanology (Poland)
- 140 **Diel variability of in vivo chlorophyll fluorescence in near-surface water layer [2258-16]**
A. M. Chekalyuk, M. Yu. Gorbunov, Moscow State Univ. (Russia)
- 152 **Question of a nutrient effect on the bio-optical properties of phytoplankton [2258-17]**
J. Marra, Columbia Univ.; R. R. Bidigare, Univ. of Hawaii/Manoa
- 163 **Bio-optical mapping procedure for the North Atlantic Ocean [2258-18]**
D. A. Kiefer, Univ. of Southern California; C. A. Atkinson, Systems Science Applications; D. Ondercin, Johns Hopkins Univ.

SESSION 3 CLOSURE

- 174 **Optical properties of pure water [2258-19]**
H. Buiteveld, Institute for Inland Water Management and Waste Water Treatment (Netherlands); J. H. M. Hakvoort, M. Donze, Delft Univ. of Technology (Netherlands)
- 184 **Influences of microbial particles on oceanic optics [2258-20]**
C. D. Mobley, SRI International; D. Stramski, Univ. of Southern California
- 194 **Analytic phase function for ocean water [2258-21]**
G. R. Fournier, J. L. Forand, Defence Research Establishment Valcartier (Canada)
- 202 **Geometrical light field parameters for improving remote sensing estimates of the backscattering coefficient for the marine hydrosol [2258-22]**
R. H. Stavn, Univ. of North Carolina/Greensboro; A. D. Weidemann, Naval Research Lab.
- 210 **Comparison between different spectral models of the diffuse attenuation and absorption coefficients of seawater [2258-23]**
O. V. Kopelevich, P.P. Shirshov Institute of Oceanology (Russia); Y. V. Filippov, Moscow Institute of Physics and Technology (Russia)
- 222 **Detecting Raman scattering in the ocean by use of polarimetry [2258-24]**
G. W. Kattawar, X. Xu, Texas A&M Univ.
- 234 **Multiple scattering metamorphosis of a non-Gaussian single-scatter phase function [2258-25]**
B. D. Joelson, G. W. Kattawar, Texas A&M Univ.; H. C. van de Hulst, Sterrewacht Rijkuniv. Leiden (Netherlands)
- 247 **Light scattering induced by turbulent flow [2258-26]**
D. Bogucki, A. Domaradzki, Univ. of Southern California; J. R. V. Zaneveld, Oregon State Univ.; T. D. Dickey, Univ. of Southern California
- 256 **Estimate of the average cosine for the radiance distribution resulting from a point source in the ocean [2258-27]**
K. J. Voss, Univ. of Miami; R. A. Maffione, SRI International

SESSION 4 COASTAL WATERS I

- 266 **Variations in bio-optical properties in the Greenland/Iceland/Norwegian seas [2258-28]**
R. Dalløkken, R. Sandvik, E. Sakshaug, Univ. of Trondheim (Norway)
- 277 **Chlorophyll sounding data in the bio-optical model of the Gulf of Gdansk spring bloom [2258-29]**
S. V. Semovski, B. Woźniak, R. Hapter, Institute of Oceanology (Poland)
- 288 **Solar ultraviolet radiation penetration and photochemical effect on colored dissolved organic matter in coastal waters [2258-30]**
A. P. Vasilkov, P.P. Shirshov Institute of Oceanology (Russia)
- 300 **Effects of surface waves and sea bottom on self-shading of in-water optical instruments [2258-31]**
J. Piskozub, Institute of Oceanology (Poland)
- 309 **High-resolution vertical profiles of spectral absorption, attenuation, and scattering coefficients in highly stratified waters [2258-33]**
C. S. Roesler, J. R. V. Zaneveld, Oregon State Univ.

SESSION 5 COASTAL WATERS II

- 322 **Effects of vertical chlorophyll structure and solar irradiance on remote sensing ocean color spectrum [2258-34]**
R. A. Arnone, Naval Research Lab.; R. W. Gould, Sverdrup Technology, Inc.; R. A. Oriol, Planning Systems Inc.; G. E. Terrie, Naval Research Lab.
- 332 **Remote sensing of coastal water quality [2258-35]**
K. Sørensen, Norwegian Institute for Water Research; E. Aas, Univ. of Oslo (Norway)
- 342 **Extending Coastal Zone Color Scanner estimates of the diffuse attenuation coefficient into Case II waters [2258-36]**
R. W. Gould, Sverdrup Technology, Inc.; R. A. Arnone, Naval Research Lab.
- 357 **Origin of the Kattegat water [2258-37]**
N. K. Højerslev, Univ. of Copenhagen (Denmark)
- 366 **Use of ERS-1 and Landsat imagery for monitoring coastal water properties and current circulation [2258-38]**
M. Necsoiu, C. Braescu, Institute of Optoelectronics (Romania); N. Oprescu, Technical Univ. of Civil Engineering (Romania); V. Diaconu, Institute of Marine Research (Romania); M. Burca, Maritime Hydrographic Directorate of the Navy (Romania)
- 377 **Investigation of the geochemistry of dissolved organic matter in coastal waters using optical properties [2258-39]**
P. G. Coble, M. M. Brophy, Univ. of South Florida

SESSION 6 LIDAR

- 392 **Airborne laser depth sounding: system aspects and performance [2258-40]**
O. K. Steinvall, K. R. Koppari, U. C. Karlsson, Swedish Defence Research Establishment/FOA

- 413 **Underwater laser imaging system with large field of view [2258-41]**
G. R. Fournier, D. Bonnier, J. L. Forand, Defence Research Establishment Valcartier (Canada)
- 422 **Multiple surface channels in Scanning Hydrographic Operational Airborne Lidar Survey (SHOALS) airborne lidar [2258-43]**
G. C. Guenther, NOAA; P. E. LaRocque, Optech, Inc. (Canada); W. J. Lillycrop, U.S. Army Corps of Engineers
- 431 **Optical properties of seawater for a short pulse [2258-46]**
K. S. Shifrin, I. G. Zolotov, Oregon State Univ.
- 438 **Interferometric analysis of the spatial coherence of a laser beam propagating in seawater and through the wavy air-water interface [2258-48]**
A. Perennou, J. Cariou, J. Lotrian, Univ. de Bretagne Occidentale (France)
- 449 **Applicability of lidar remote sensing methods for vertical structure investigation of ocean optical properties distribution [2258-49]**
V. I. Feigels, St. Petersburg Institute of Fine Mechanics and Optics (Russia); Yu. I. Kopilevich, S.I. Vavilov State Optical Institute (Russia)
- 458 **Theoretical model for backscattered pulse kinetics and interpretation of some anomalies in lidar remote sensing data [2258-50]**
Yu. I. Kopilevich, S.I. Vavilov State Optical Institute (Russia); V. I. Feigels, St. Petersburg Institute of Fine Mechanics and Optics (Russia)
- 472 **Studies of optical ringing in seawater [2258-51]**
G. D. Gilbert, M. H. North, Naval Research and Development Div.
- 480 **Some aspects of wide-beam imaging lidar performance [2258-52]**
R. N. Keeler, B. L. Ulich, Kaman Aerospace Corp.

SESSION 7 INSTRUMENTATION

- 502 **Analysis of Sea Tech absorption meter characteristics and comparisons to K_d measurements [2258-56]**
J. H. Smart, Johns Hopkins Univ.
- 512 **Photometer for the continuous measurement of calcite-dependent light scatter in seawater [2258-57]**
K. A. Kilpatrick, W. M. Balch, Y. Ge, K. J. Voss, Univ. of Miami
- 522 **New instrument for measuring the scattering coefficient and the concentration of suspended particles in turbid water [2258-59]**
L. S. Dolin, Institute of Applied Physics (Russia); I. M. Levin, T. M. Radomysl'skaya, P.P. Shirshov Institute of Oceanology (Russia)
- 529 **Monte Carlo modeling of the light field in reflective-tube-type absorption meters [2258-60]**
J. H. M. Hakvoort, Delft Univ. of Technology (Netherlands); R. R. Wouts, Netherlands Institute of Ecological Research
- 539 **Bermuda Bio-Optics Project (BBOP) data processing system [2258-61]**
J. C. Sorensen, M. C. O'Brien, D. Konhoff, D. A. Siegel, Univ. of California/Santa Barbara

- 547 **Use of a laser stripe illuminator for enhanced underwater viewing [2258-62]**
S. Tetlow, R. L. Allwood, Cranfield Univ. (UK)
- 556 **New type of scatterometer for measuring the small-angle volume scattering function of seawater and the experiments in the East China Sea [2258-66]**
X. Huang, J. Zhang, W. Chen, T. Zhang, M. He, Z. Liu, Ocean Univ. of Qingdao (China)
- 560 **Image transmission method for measuring the small-angle scattering function of seawater [2258-67]**
T. Zhang, X. Huang, Z. Liu, Ocean Univ. of Qingdao (China)
- 564 **Deblurring the underwater image using the Monte Carlo method [2258-68]**
T. Zhang, H. Liu, Ocean Univ. of Qingdao (China)
- 568 **Spectral fluorescence and scattering of cyanobacteria and diatoms held by optical tweezers [2258-116]**
G. J. Sonek, Y. Liu, Univ. of California/Irvine; R. H. Iturriaga, Univ. of Southern California

SESSION 8 ENVIRONMENTAL

- 576 **Database of oceanic optical properties [2258-69]**
G. R. Fournier, Defence Research Establishment Valcartier (Canada); M. Jonasz, M. Jonasz Consultants (Canada)
- 588 **Theory of satellite observation of the sea bottom in coastal waters: maximal sighting range and resolution [2258-72]**
L. S. Dolin, Institute of Applied Physics (Russia); I. M. Levin, P.P. Shirshov Institute of Oceanology (Russia)
- 597 **Temperature dependence of the absorption coefficient of pure water in the visible portion of the spectrum [2258-70]**
W. S. Pegau, J. R. V. Zaneveld, Oregon State Univ.
- 605 **Method for detection of jump-like change points in optical data using approximations with distribution functions [2258-71]**
A. K. Yasakov, Byelorussian Univ.
- 613 **Comparison of analytical calculations with experimental measurements for polarized light scattering by microorganisms [2258-73]**
P. G. Hull, F. G. Shaw, Tennessee State Univ.; M. S. Quinby-Hunt, D. B. Shapiro, A. J. Hunt, Lawrence Berkeley Lab.; T. Leighton, Univ. of California/Berkeley
- 623 **Assessment of seawater optical characteristics in the upper 200 m of ocean on their subsurface values [2258-75]**
O. V. Kopelevich, O. V. Prokhorenko, P.P. Shirshov Institute of Oceanology (Russia)
- 634 **Statistical analysis of vertical profiles of beam attenuation coefficient and temperature in the North Atlantic [2258-77]**
V. I. Burenkov, P.P. Shirshov Institute of Oceanology (Russia)
- 644 **Optical properties of the northwest African upwelling region [2258-78]**
V. I. Burenkov, O. V. Kopelevich, A. I. Sud'bin, P.P. Shirshov Institute of Oceanology (Russia)

- 654 **Errors in the reporting of solar spectral irradiance using moderate bandwidth radiometers: an experimental investigation [2258-79]**
C. R. Booth, T. Mestechkina, J. H. Morrow, Biospherical Instruments Inc.
- 664 **Spatial distribution of radiation near the sea line in the mid-infrared region [2258-80]**
M. Matsui, Fukuyama Univ. (Japan); S. Tamashige, Okayama Polytechnic College (Japan); S. Matsui, Nara Saho-Jogakuin Junior College (Japan)
- 671 **Remote sensing investigations of dissolved organic matter and chlorophyll fluorescence fields [2258-81]**
V. I. Repin, E. G. Goncharov, O. I. Repina, S.I. Vavilov State Optical Institute (Russia)
- 682 **Photometry of optical fields of the upper layers of seawater [2258-82]**
I. V. Aleshin, E. A. Tsvetkov, S.I. Vavilov State Optical Institute (Russia); V. N. Ryabova, St. Petersburg Univ. (Russia)
- 685 **Numerical model for prediction of sublittoral optical visibility [2258-83]**
J. S. Schoonmaker, Naval Command, Control and Ocean Surveillance Ctr.; R. R. Hammond, A. L. Heath, Science Applications International Corp.; J. S. Cleveland, San Diego State Univ.

SESSION 9 GENERAL

- 704 **Gas microbubbles: an assessment of their significance to light scattering in quiescent seas [2258-84]**
D. Stramski, Univ. of Southern California
- 711 **Ocean source estimation using irradiance measurements at only one depth [2258-85]**
N. J. McCormick, Univ. of Washington
- 723 **Pose estimation and representation of cylinders from single two-dimensional images in modeling remotely operated vehicle (ROV) environments [2258-86]**
R. Volden, Norwegian Institute of Technology (Norway)
- 735 **Predicting polarization properties of marine aerosols [2258-87]**
M. S. Quinby-Hunt, Lawrence Berkeley Lab.; P. G. Hull, Tennessee State Univ.; A. J. Hunt, Lawrence Berkeley Lab.
- 747 **Remote sensing and measurement of the thickness of oil films on the sea surface using reflectivity contrast [2258-88]**
V. U. Osadchy, P.P. Shirshov Institute of Oceanology (Russia); K. S. Shifrin, Oregon State Univ.; I. Y. Gurevich, P.P. Shirshov Institute of Oceanology (Russia)
- 759 **Spectral contrast of oil films on the sea surface: influence of water type, wind velocity, and solar altitude [2258-89]**
I. M. Levin, P.P. Shirshov Institute of Oceanology (Russia)
- 768 **Some effects of the sensitivity threshold and spatial resolution of a particle imaging system on the shape of the measured particle size distribution [2258-90]**
D. K. Costello, W. Hou, K. L. Carder, Univ. of South Florida
- 784 **Scattering by cylindrically symmetric particles [2258-94]**
A. Y. Perelman, St. Petersburg Forestry Academy (Russia)

- 793 **Intensity of the water fluorescence variation caused by organic matter transition from suspended state into the solution [2258-95]**
V. M. Sidorenko, S. A. Pakkonen, S.I. Vavilov State Optical Institute (Russia)
- 797 **Oil spreading in the deep sea and search for methods of discovering oil pollution under the sea surface [2258-96]**
V. K. Goncharov, A. N. Krylov Shipbuilding Research Institute (Russia); V. G. Lyskov, S.I. Vavilov State Optical Institute (Russia)
- 806 **Vertical stratification of the fluorescence intensity dissolved in seawater organic matter [2258-97]**
V. M. Sidorenko, S. A. Pakkonen, S.I. Vavilov State Optical Institute (Russia)
- 811 **Ocean hydrophysical parameters evaluation from multispectral optical sensing data [2258-98]**
A. G. Zhurenkov, V. A. Yakovlev, S.I. Vavilov State Optical Institute (Russia)
- 815 **In-situ evaluation of a ship's shadow [2258-99]**
C. T. Weir, D. A. Siegel, Univ. of California/Santa Barbara; A. F. Michaels, Bermuda Biological Station for Research; D. W. Menzies, Univ. of California/Santa Barbara
- 822 **Diagnostics of seawater turbulence by small-angle light scattering [2258-118]**
Yu. I. Kopilevich, N. V. Alekseyev, B. V. Kurasov, V. A. Yakovlev, S.I. Vavilov State Optical Institute (Russia)
- 831 **Moored optical particle flux instrument [2258-119]**
E. Chang, R. J. Patton, R. L. Gran, Dynamics Technology, Inc.

SESSION 10 REMOTE SENSING AND ALGORITHM DEVELOPMENT

- 850 **Scalar irradiance estimation from downward and upward plane irradiance measurements [2258-100]**
Z. Tao, N. J. McCormick, Univ. of Washington
- 861 **Method of experimental design for optical remote sensing of chlorophyll concentration in ocean waters [2258-101]**
I. M. Levin, I. V. Zolotukhin, P.P. Shirshov Institute of Oceanology (Russia)
- 870 **Accounting for the marine reflectance bidirectionality when processing remotely sensed ocean color data [2258-105]**
C. Myrmehl, Lab. de Physique et Chimie Marines (France) and Nansen Environmental and Remote Sensing Ctr.; A. Morel, Lab. de Physique et Chimie Marines (France)
- 879 **Design and evaluation of a cosine collector for a SeaWiFS-compatible marine reflectance radiometer [2258-106]**
J. H. Morrow, M. S. Duhig, C. R. Booth, Biospherical Instruments Inc.
- 887 **Inverse modeling for retrieval of ocean color parameters in Case II coastal waters: an analysis of the minimum error [2258-107]**
R. Dörffer, H. Schiller, GKSS Forschungszentrum GmbH (FRG)
- 894 **Variation of optical properties in the Baltic Sea and algorithms for the application of remote sensing data [2258-108]**
H. Siegel, M. Gerth, M. Beckert, Univ. Rostock (FRG)

SESSION 11 SEA ICE

- 908 **Polarization-dependent measurements of light scattering in sea ice [2258-110]**
D. Miller, M. S. Quinby-Hunt, A. J. Hunt, Lawrence Berkeley Lab.
- 920 **Fluorometric characterization of dissolved and particulate matter in Arctic sea ice [2258-111]**
R. H. Iturriaga, Naval Research Lab.; C. S. Roesler, Oregon State Univ.
- 933 **Absorption properties of marine-derived material in Arctic sea ice [2258-112]**
C. S. Roesler, Oregon State Univ.; R. H. Iturriaga, Univ. of Southern California
- 944 **In-situ measurements of optical scattering from the water-ice interface of sea ice [2258-113]**
J. R. Longacre, M. A. Landry, Naval Undersea Warfare Ctr.
- 954 **Transport of photosynthetically active radiation in sea ice and the ocean [2258-114]**
Z. Jin, K. H. Stamnes, W. F. Weeks, Univ. of Alaska
- 965 **Use of beam spreading measurements to estimate volume-scattering properties in sea ice [2258-115]**
F. J. Tanis, Environmental Research Institute of Michigan

SESSION 12 ADDITIONAL PAPERS

- 976 **Relationship between spectral reflected irradiance at the sea surface and optical properties of marine phytoplankton [2258-103]**
B. Woźniak, Institute of Oceanology (Poland); W. von Smekot-Wensierksi, Max-Planck-Institut für Meteorologie (FRG); R. Dörffer, GKSS Forschungszentrum GmbH (FRG); H. Graßl, Max-Planck-Institut für Meteorologie (FRG)
- 994 **Remote sensing of natural water quality parameters: retrieval algorithm development and optimization analysis [2258-104]**
K. Ya. Kondratyev, Scientific Research Ctr. for Ecological Safety (Russia); D. V. Pozdnyakov, Nansen International Environmental and Remote Sensing Ctr. (Russia); L. H. Pettersson, Nansen Environmental and Remote Sensing Ctr. (Norway)
- 1005 *Addendum*
- 1007 *Author Index*

Conference Committee

Conference Chair

Jules S. Jaffe, Scripps Institution of Oceanography/University of California/San Diego

Program Committee

Steven G. Ackleson, Office of Naval Research
Roland Dörffer, GKSS Forschungszentrum GmbH (FRG)
Niels K. Højerslev, University of Copenhagen (Denmark)
Robert A. Maffione, SRI International and Oregon State University
Oliverio D. Soares, Centro de Ciencias e Tecnologias Opticas/
Universidade do Porto (Portugal)
J. Ronald V. Zaneveld, Oregon State University

Session Chairs

- 1 Instrumentation I
 Jules S. Jaffe, Scripps Institution of Oceanography/University of California/San Diego
- 2 Bio-Optical Variability
 Steven G. Ackleson, Office of Naval Research
- 3 Closure
 J. Ronald V. Zaneveld, Oregon State University
- 5 Coastal Waters II
 Niels K. Højerslev, University of Copenhagen (Denmark)
- 10 Remote Sensing and Algorithm Development
 Roland Dörffer, GKSS Forschungszentrum GmbH (FRG)
- 11 Sea Ice
 Robert A. Maffione, SRI International and Oregon State University

Introduction

I am very pleased to write this introduction to our collected papers from the Ocean Optics XII conference. As one can see from the large number of high-quality papers, the meeting was a great success. First, I want to thank Steven G. Ackleson, Roland Dörffer, Niels K. Højerslev, Robert A. Maffione, and J. Ronald V. Zaneveld for contributing their efforts in leading sessions. As can be seen from this large volume and the various subject areas that have been addressed here, ocean optics is certainly a vibrant area.

Special sessions were held on instrumentation, basic physics, remote sensing for biology and geology, laser techniques, and the propagation of light in sea ice. The conference was held at the Bergen High-Technology Centre, a state-of-the-art facility, where the approximately 100 scientists and engineers spent three days. I believe that the meeting was noteworthy in many aspects. As can be seen from the proceedings, we had a truly international meeting. This accomplished one of the major goals that led to having the meeting in Europe and resulted in the attendance of many European scientists as well as scientists from former Eastern Bloc countries including the Soviet Union. I believe that this meeting was noteworthy in that this "thaw" in the cold war was extended to our ocean optics community in a very productive way. It was indeed my personal pleasure, and I'm sure that this enjoyment extended to all at the meeting, to learn about the activities of many of our international colleagues. In this sense, Ocean Optics XII, the first ocean optics meeting held in Europe, was truly successful.

One of the most delightful events of the meeting was the banquet on the first evening at which we were treated to a very entertaining lecture by Niels Højerslev on the history of ocean optics. Another significant event of the meeting was the student paper competition. Andrew Palowitch of the Scripps Institution of Oceanography/Univ. of California/San Diego was the winner of the competition that included many excellent presentations.

As Ocean Optics moves forward toward the end of the century, I am hopeful that the degree of activity in the field will both continue and increase. Certainly the capability of collecting nearly quantum-limited multispectral data in concert with our increased awareness of the change in the world ecosystem, which has been influenced by man, will continue to encourage the utilization of optical techniques. After all, most of the surface of the earth is covered by the oceans, and photons power the whole thing!

Finally, I want to extend my great thanks to SPIE for making this conference a success and to my peers for providing me with the opportunity to create a forum for the exchange of information on a topic that I consider important, interdisciplinary, and on the cutting edge of modern environmental science: ocean optics.

Jules S. Jaffe

SESSION 1

Instrumentation I

Inherent optical property estimation in ocean water using the Zaneveld-Wells algorithm

Lydia J. Holl and N.J. McCormick

Department of Mechanical Engineering
University of Washington, Seattle, WA 98195

ABSTRACT

The Zaneveld-Wells technique for determining the inherent optical properties of ocean water is based on calculating the angle-integrated moments of the radiant light field at various depths by an inversion algorithm based on the radiative transfer equation. The hypothesis is that $N+1$ sensors can be used to obtain N "inherent optical expansion coefficients", A_n , from which the single scattering albedo and $N-1$ expansion coefficients of the volume scattering function can be calculated. We have evaluated the performance and limitations of the proposed algorithm.

An error analysis has shown that the algorithm will be most sensitive to the condition of the response matrix and the error in the spatial derivatives of the moments of the radiant field. For the Doss-Wells instrument, the algorithm is stable and well-conditioned, but very sensitive to error in the spatial derivatives. The vertical spacing of measurements in optically dense waters necessary to minimize the error associated with the spatial derivative is prohibitively small. Results from numerical testing indicate that this technique is a promising way to estimate optical properties of some ocean waters, but attempts to estimate too many expansion coefficients give spurious results for the higher-order coefficients in other cases. Recommendations are given for improving the implementation of the algorithm.

1. INTRODUCTION

Zaneveld¹ and Wells² proposed an algorithm and an instrument for determining the inherent optical properties of ocean water using directionally-integrated angular moments of the ambient light field measured at varying depths. Doss and Wells^{3,4} have presented a further description of the experimental technique along with preliminary results from data collected with the special radiometer they built for such measurements.

The algorithm was devised to estimate the coefficients A_n in the Legendre polynomial expansion of the volume scattering function defined by

$$\beta(\eta) = \sum_{n=0}^{\infty} \frac{2n+1}{2} (c - A_n) P_n(\eta) \quad , \quad (1)$$

where η is the cosine of the scattering angle. With this notation A_{∞} would equal the total attenuation coefficient, c , and A_0 equals the absorption coefficient, $a = c - b$, where b is the scattering coefficient. The coefficients can be related to the more-traditional expansion of the scattering phase function in terms of the coefficients $f_n = (c - A_n)/b$, where $f_0 = 1$ and $f_n \rightarrow 0$ as $n \rightarrow \infty$.

In principle the entire set of standard attenuation coefficients could be extracted from a complete set of A_n coefficients. The basic hypothesis of the Zaneveld-Wells algorithm^{1,2} is that N inherent optical expansion coefficients can be obtained from measurements with $N+1$ sensors. These sensors must measure integrated moments of the radiant light field at various depths. The integrated moments and derivatives of these moments, obtained from measurements at adjacent depths, are used to calculate the inherent optical expansion coefficients A_n from an algorithm based on the radiative transfer equation.

The algorithm is discussed in section 2 and the models for the waters used to test the algorithm are given in section 3. The numerical methods used to test the algorithm are presented in section 4, with the results of the tests given in section 5. Conclusions and recommendations for improvements in the algorithm and instrument are discussed in section 6.

2. THE ZANEVELD-WELLS ALGORITHM

The algorithm is developed from the radiative transfer equation for a homogeneous, isotropic, plane-parallel medium for which the radiation is azimuthally-independent (or averaged),

$$\mu \frac{\partial}{\partial z} L(\mu, z) + cL(\mu, z) = \int_{-1}^1 \beta(\mu' \rightarrow \mu) L(\mu', z) d\mu' , \quad (2)$$

where $L(\mu, z)$ is the azimuthally-averaged radiance, μ is the cosine of the zenith angle, z is the depth, c is the total attenuation coefficient, and internal sources have been neglected. After multiplying Eq. (2) by $P_n(\mu)$, using the spherical harmonics addition theorem and the recursion relation for Legendre polynomials, and integrating the result over the range $-1 \leq \mu \leq 1$, Zaneveld¹ obtained the algorithm

$$A_n = -\frac{(n+1)L'_{n+1}(z) + nL'_{n-1}(z)}{(2n+1)L_n(z)} , \quad n = 0, 1, 2, \dots, \quad (3)$$

where L' denotes the derivative of L with respect to depth and the angle-integrated radiance moments are

$$L_n(z) = \int_{-1}^1 L(\mu, z) P_n(\mu) d\mu . \quad (4)$$

To implement the algorithm, Wells² recognized that a set of sensors could be designed to measure a different set of moments,

$$\Lambda_j(z) = \int L(\mu, z) R_j(\mu) d\mu , \quad (5)$$

where $R_j(\mu)$ is the angular response function of the j th sensor, $j = 1$ to $N+1$. If the radiance is expanded in terms of spherical harmonics as

$$L(\mu, z) = \sum_n \frac{2n+1}{2} L_n(z) P_n(\mu) \quad (6)$$

then the measured data can be expressed as a truncated series of the form

$$\Lambda_j(z) = \sum_{n=0}^N R_{jn} L_n(z) + X_j(z) , \quad (7)$$

where the response matrix elements R_{jn} are defined to be

$$R_{jn} \equiv \frac{2n+1}{2} \int_{-1}^1 R_j(\mu) P_n(\mu) d\mu , \quad (8)$$

and where the truncation error term, $X_j(z)$, is defined by

$$X_j(z) \equiv \sum_{n=N+1}^{\infty} R_{jn} L_n(z) . \quad (9)$$

The inversion in this algorithm consists of calculating the moments of the radiance from the data and then using those moments in equation (3). The inversion of equation (7) for $N+1$ sensors is

$$L_n(z) = \sum_{j=1}^{N+1} \left[\mathbf{R}^{-1} \right]_{nj} \left[\Lambda_j(z) - X_j(z) \right] . \quad (10)$$

The response functions for the sensors on the Doss-Wells instrument were optimized for use with this algorithm. For their instrument, the response function for the j th detector was selected to be

$$R_j(\mu) = \begin{cases} \prod_{i \neq j} \frac{(\mu - \mu_i)}{(\mu_j - \mu_i)} & \mu_{j-1} \leq \mu \leq \mu_{j+1} \\ 0 & \text{otherwise} \end{cases} , \quad (11)$$

where μ_j is the j th root of the Legendre polynomial of order $N+1$. Equation (11) is Lagrange's formula for polynomial interpolation⁵ truncated at adjacent roots. The truncation implied in Eq. (11) is necessary because the response function for any real instrument must be nonnegative everywhere.

A sensitivity analysis of the coefficients computed from Eq. (3) yields, to first order,

$$\frac{\delta A_n}{A_n} = -\frac{\delta L_n}{L_n} + \frac{(n+1)\delta L'_{n+1} + n\delta L'_{n-1}}{(n+1)L'_{n+1} + nL'_{n-1}} . \quad (12)$$

Therefore the relative error $\delta A_n/A_n$ in the calculated inherent properties is proportional to the relative error in the moments of the radiance, L_n , and the errors in the derivatives of L_n . The errors in the derivatives result from not knowing the value of L_n precisely and from approximating the spatial derivatives with a finite-difference scheme. Doss and Wells used a first-order backward difference scheme in their analyses.

3. MODELS FOR NUMERICAL TESTING

To test the algorithm numerically, analyses were performed on a variety of radiant light fields. For the cases studied here, the properties of the medium (b, c, f_n) are assumed to be known with good accuracy so that the errors inherent in only the inversion algorithm can be assessed under the best-possible conditions.

In the test cases presented here, for both convenience and generality, the problem is non-dimensionalized by the use of $\tau = cz$, the optical depth, instead of z . Thus, in the non-dimensionalized form,

$$A_n = 1 - w_0 f_n \quad (13)$$

where w_0 is the albedo of single scattering, defined as b/c . The non-dimensionalized form is not dependent on the total attenuation coefficient, which would have to be either estimated from A_∞ or measured separately but an error in the estimation of w_0 , as obtained from the calculation of A_0 , will propagate through all the f_n coefficients.

Of the different models for the optical properties of ocean water, pure water is the simplest. The expansion coefficients for the volume scattering function of pure water⁶ are given by $f_0 = 1, f_2 = 0.1504$, and $f_n = 0$ for all other n . Over the wavelengths of interest to most oceanographers (400-700 nm) the albedo of single scattering is less than 0.3. The total attenuation coefficient and albedo of single scattering for pure water were calculated by Smith and Baker.⁷

A more realistic model for ocean water is pure water with chlorophyll added. Chlorophyll provides additional scattering and absorption centers for radiation. The model for the absorption and scattering properties of the chlorophyll-pure water mixtures that are used for these tests have also been used by Mobley et. al.⁸ and others.⁹ The absorption coefficients for the model waters is calculated using the model proposed by Prieur and Sathyendranath.¹⁰ Their model is an empirical correlation from data for many different water types from seven different cruises. Neglecting absorption effects of gelbstoff and nonchlorophyllous particles, the Prieur-Sathyendranath absorption model applied to a mixture of pure water and chlorophyll can be written as

$$a_{mix}(\lambda) = a_{water}(\lambda) + 0.06C^{0.602} \frac{a_C(\lambda)}{a_C(440nm)} \quad (14)$$

for a chlorophyll concentration C in mg/m^3 . The ratio $a_C(\lambda)/a_C(440\text{nm})$ has been tabulated by Prieur and Sathyendranath. Similarly, the scattering coefficients for chlorophyll particles were calculated using a model developed by Morel.^{11,12} The model can be written as

$$b_{mix}(\lambda) = b_{water}(\lambda) + C^{0.62} b_C(550nm) \left(\frac{550}{\lambda} \right)^n, \quad (15)$$

where $b_C(550)$ is taken to be its average value of 0.3 m^{-1} for the low chlorophyll concentrations to be studied here.

The Delta-Eddington approximation is applied to the expansion coefficients of the volume scattering function when simulating the radiance distribution. In the Delta-Eddington approximation the volume scattering function is written as a combination of a dirac-delta function in the forwardmost direction and a smoothly varying function that requires fewer expansion coefficients to describe it (than the original function). A cut-off angle can be chosen to specify how much of the forward peak is included in dirac-delta function. Table 1 lists the values of the cut-off angle and fraction of scattering allocated to the forwardmost direction for the waters considered here.

For testing the algorithm with numerical data, two wavelengths (470 and 570nm) and three chlorophyll concentrations (0.0, 0.1, 1.0 mg/m^3) are considered, giving a total of six combinations of wavelengths-optical properties. These six combinations are evaluated at four optical depths and for two increments in depth for calculating the spatial derivatives, either 1m or 2m spacing. The optical depths are selected to represent different regimes of the radiant field: near-surface (0.5 optical depths), mid-water (2.0 optical depths), deep (10 optical depths), and asymptotically deep (true for these test cases at 20 optical depths). Table 1 contains the optical properties used to generate the simulated data for the test cases.

Table 1: Theoretical optical properties for numerical tests

Description	$c \text{ [m}^{-1}\text{]}$	w_0	Cutoff Angle (deg)	Forward fraction	N of f_n
470nm, Pure	0.0193	0.1917	NA	NA	2
470nm, [chl]=0.1	0.1166	0.7542	2.5119	0.1215	85
470nm, [chl]=1.0	0.4226	0.8395	1.9953	0.1987	90
570nm, Pure	0.0816	0.0208	NA	NA	2
570 nm, [chl]=0.1	0.1552	0.4584	1.9953	0.1448	90
570 nm, [chl]=1.0	0.3876	0.7512	2.5119	0.2099	80

4. NUMERICAL METHODS

To obtain simulated data the radiative transfer equation was solved to obtain the radiance as a function of depth. For these tests the code package ONEDANT (ONE-dimensional, Diffusion-Accelerated, Neutral-Particle Transport) using the Discrete Ordinates (S_n) method was employed. ONEDANT¹³ has been in use for decades by researchers working with neutron transport theory but is rarely used for ocean optics work. An S_{200} scheme was used, hence the continuum of zenith angles was approximated with 200 discrete angular directions, μ_k for $k = 1$ to 200. The discrete directions and corresponding weights were determined with a Gauss-Legendre quadrature routine from $P_{200}(\mu_k) = 0$ and are symmetric about $\mu = 0$. It should be emphasized

that the simulated radiances were computed for idealized detectors -- no statistically-generated noise has been added.

The two boundary conditions used for testing are shown in Fig. 1. The boundary conditions are prescribed for the forward directions only ($0 \leq \mu \leq 1$). The values shown for the upwelling radiance at the surface are calculated during the numerical testing, resulting in a discontinuity at $\mu = 0$. Most of the testing was done for an isotropic incident boundary illumination just below the surface. For this boundary condition, the algorithm was tested to determine the sensitivity to wavelength, chlorophyll concentration, depth, and the increment in depth between adjacent measurements.

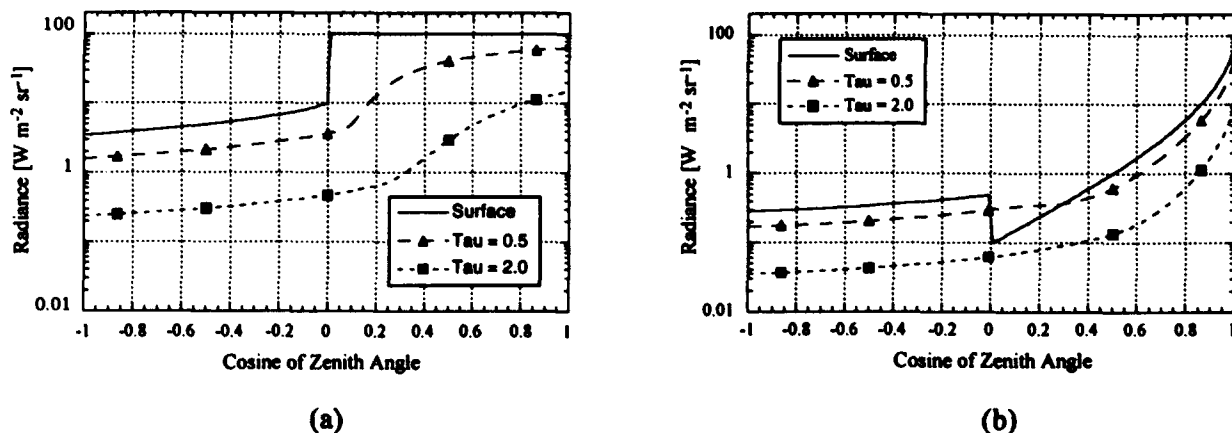


Figure 1: Angular distribution of the radiant field with non-dimensional depth for two surface boundary conditions, $C=0.0 \text{ gm/m}^3$, 470 nm : (a) Isotropic illumination of $100 \text{ W m}^{-2} \text{ sr}^{-1}$, (b) Logarithmic illumination with $L(\mu=0)=0.1$ and $L(\mu=1)=100 \text{ W m}^{-2} \text{ sr}^{-1}$

Some additional testing was performed with a second boundary condition to test the sensitivity of the results to the type of surface illumination. The second surface boundary condition was designed so that across the forward directions, the \log_{10} of the incident radiance will be linear when plotted against the index for the discrete directions, k , for $k = 101$ to 200 . The value of the radiance impinging just below the surface is 0.1 at the discrete angle nearest to $\mu = 0$ and 100 at the discrete angle nearest to $\mu = 1.0$ and can be approximated by $\log_{10}(L(\mu_k)) = 0.0303k - 4.06$. This incident radiance can be thought of as a smeared-out delta function and represents direct normal solar illumination with some "smearing". It is a cross between a downward-directed delta function and the isotropic boundary conditions first tested.

5: NUMERICAL RESULTS

Tables 2 and 3 provide some sample results for the percent error in the A_n coefficients with the isotropic surface illumination shown in Fig. 1a. The results are for two chlorophyll concentrations (0.0 and 0.1 mg/m^3) and 1 m and 2 m spacing between adjacent measurements. Table 2 contains the percent error results for pure water at 470 nm . Table 3 contains results for 470 nm and a chlorophyll concentration of 0.1 mg/m^3 .

Table 2: Percent error in estimated A_n coefficients at 470 nm with isotropic incident illumination at various depths and increments, dz , between adjacent measurements: $C=0.0$ mg/m^3 , $c=0.0193 \text{ m}^{-1}$.

n of A_n	$dz = 1.0$ meters			$dz = 2.0$ meters		
	0.5 Optical Depths	2 Optical Depths	20 Optical Depths	0.5 Optical Depths	2 Optical Depths	20 Optical Depths
0	-1.806	-1.404	-1.233	-3.360	-2.621	-2.249
1	-1.409	-1.163	-1.057	-2.757	-2.330	-2.070
2	-0.226	-0.768	-0.747	-0.769	-1.797	-1.753
3	-----	-0.640	-1.074	-----	-1.335	2.079
4	-----	-0.679	-0.842	-----	0.721	-1.836
5	-----	-----	-1.153	-----	-----	-2.141
6	-----	-----	0.012	-----	-----	-0.952
7	-----	-----	-0.866	-----	-----	-1.824
8	-----	-----	3.913	-----	-----	3.017

* A dash indicates that the moment of the radiance was negative.

For Table 2, a one meter depth increment in pure water at 470nm is equivalent to 0.0193 optical depths. However, when the chlorophyll concentration is raised to 0.10 mg/m^3 as in Table 3, one meter is equivalent to 0.1166 optical depths, a difference of a factor of 6. The results in Table 3 are approximately a factor of 10 worse than those in Table 2. The results for water with a chlorophyll concentration of 1.0 mg/m^3 (not shown here) at 470nm ($c = 0.4226 \text{ m}^{-1}$) are about a factor of three worse than the results given in Table 3. The results indicate that the percent error of the algorithm is more sensitive to errors in the calculation of the derivatives than to the value of the albedo or the composition of the medium.

Table 3: Percent error in estimated A_n coefficients at 470 nm with isotropic incident illumination at various depths and increments, dz , between adjacent measurements: $C = 0.1$ mg/m^3 , $c=0.1166 \text{ m}^{-1}$.

n of A_n	$dz = 1$ meter			$dz = 2$ meters		
	0.5 Optical Depths	2 Optical Depths	20 Optical Depths	0.5 Optical Depths	2 Optical Depths	20 Optical Depths
0	-16.132	-15.007	-14.600	-21.685	-19.494	-18.595
1	-6.490	-6.008	-5.796	-10.819	-9.954	-9.482
2	5.247	-3.395	-4.755	5.329	-6.358	-8.402
3	-----	2.014	-4.997	-----	3.055	-8.645
4	-----	-----	-7.320	-----	-----	-11.032
5	-----	-----	-5.032	-----	-----	-8.637
6	-----	-----	8.183	-----	-----	5.052
7	-----	-----	2.069	-----	-----	-1.207
8	-----	-----	-26.957	-----	-----	-----

* A dash indicates that the moment of the radiance was negative.

When a higher-order moment changed sign (compared to the lower-order moments), catastrophic cancellation in Eq. (5) resulted in highly erroneous calculated values for the corresponding, higher-order A_n coefficients. Truncation errors dominate the near-zero higher moments causing this problem. No results for $A_{n>J}$ are given if the calculated $L_J(z)$ was found to be negative. Strictly speaking, from equation (3) only the first $(j-1)$ coefficients will be unaffected by $L_{j+1}(z)$. However, the results presented here show that if $L_{j+1}(z)$ becomes negative, the error in A_n will usually remain small if $L_n(z)$ is set equal to zero. This allows j inherent optical expansion coefficients to be preserved when $L_{j+1}(z)$ becomes negative.

The angular shape of the radiance can be strongly influenced by the shape of the surface illumination except at asymptotically deep depths. Near the surface, little light has been scattered into the backward direction and the calculation of the higher moments of the radiance became swamped by the truncation error of the response matrix. As the sensor is moved deeper, the effects of the surface boundary condition diminish and more radiance moments are recoverable. The shape of the radiance plays a role in determining the error in the higher-order optical expansion coefficients. Figure 1 shows how the radiant field changes with depth for pure water, given the two different boundary conditions at the surface.

The effects of the surface illumination on results from the algorithm can be quantified by testing with a different boundary condition. The percent errors in the A_n coefficients for 470 nm with the logarithmic surface illumination shown in Fig. 1b are presented in Table 4. The marked decrease in the percent errors near the surface in Table 4 compared to those in Table 2 shows that the estimated coefficients significantly dependent on the boundary condition. As expected, the discrepancy between the errors decreases with depth as the radiance approaches the same asymptotic angular shape. What is very interesting about the results in Table 4, however, is that no optical expansion coefficients had to be discarded because the moments of the radiance calculated by the inversion of Eq. (10) never flipped signs (they were always positive). Thus, the number of optical expansion coefficients that are recoverable by the algorithm is dependent on both the inherent optical properties of the water and the shape of the incident illumination at the surface.

Table 4: Percent error in estimated A_n coefficients for water pure at 470 nm with logarithmic interpolated incident illumination, $dz=1$ meter.

n	$C = 0.0 \text{ mg/m}^3$			$C = 0.1 \text{ mg/m}^3$		
	0.5 Optical Depths	2 Optical Depths	20 Optical Depths	0.5 Optical Depths	2 Optical Depths	20 Optical Depths
0	-1.371	-1.395	-1.541	-14.726	-14.871	-14.605
1	-1.064	-1.069	-1.112	-5.725	-5.781	-5.796
2	-0.757	-0.740	-0.622	-6.411	-5.565	-4.773
3	-1.051	-1.049	-1.108	-6.685	-6.110	-5.043
4	-0.737	-0.725	-0.476	-6.174	-6.401	-7.238
5	-0.927	-0.958	-0.963	-5.449	-5.853	-5.191
6	0.757	0.609	0.932	-2.787	-2.585	5.837
7	0.153	0.030	0.264	-3.519	-3.779	-0.086
8	5.750	5.897	6.730	1.720	1.924	-12.804

6. CONCLUSIONS AND RECOMMENDATIONS

The numerical testing showed that the Zaneveld-Wells algorithm of Eqs. (3) and (10) performed well when the incremental distance between measurements in depth was small so that the spatial derivative could be calculated with little error. Also, the sensitivity of A_0 to errors is especially important for anyone wishing to estimate the more traditionally-used f_n coefficients since the error in A_0 will propagate throughout all the f_n results.

As the higher moments of the radiant field approach zero, some became negative. Fields of physical interest should have angular moments with consistent signs. Flipping signs can produce catastrophically large errors in the calculated A_n coefficients. Anytime the algorithm is used, the moments returned by the inversion of equation (10) must be routinely checked to verify that the signs are consistent. Once an angular moment (at a given depth) is found to have a sign different than the moment of next lower-order, no higher order A_n 's should be reported.

The boundary conditions were found to have a significant impact on the number of coefficients that could be calculated at any given depth. Boundary conditions that produce weakly angle-dependent radiances (such as isotropic illumination) are more likely to induce negative moments because inversion algorithms are generally more sensitive to error sources (such as truncation) with only weakly-variant data.

In the original formulation of the algorithm the total attenuation coefficient, c , is not measured directly but is instead inferred from estimates of A_∞ . The results for ten sensors and the waters considered here show that the A_n 's have not decayed sufficiently to c (i.e., unity in the non-dimensional form of the analysis) for a good estimation of c to be made. Since c , which defines the optical thickness of a meter of water, is so important in determining how much error the spatial derivative will introduce, not having a good estimate can undermine the results. Fortunately, c is one of the easiest inherent optical properties to measure with traditional instrumentation. By attaching a separate instrument to the array to get an independent measurement of c , the extrapolation to A_∞ can be avoided. This has the additional benefit that since the A_n 's approach c with increasing n , by knowing c , one gets a qualitative measure of how completely the properties of the water can be estimated with a finite number of expansion coefficients. If an independent measurement of c is not made, one is probably better off using the non-dimensional form of the algorithm.

Since the error in the spatial derivative is dominant, one might consider using a different, higher-order finite difference scheme to approximate the derivatives of $L_n(z)$. The difficulty, of course, is that the water properties must then be assumed to be homogeneous over a greater range of depth since higher-order approximations of the derivative require the use of measurements at more depths.

Another concern is that the light is attenuated significantly in productive waters over fairly short distances. The Doss-Wells instrument which used the Zaneveld-Wells algorithm has a length of 1.6 meters for ten sensors. The algorithm of Eq. (3) uses data for all sensors in the array and assumes that measurements of adjoining sensors are at the same depth. For a chlorophyll concentration of 1 gm/m³ at 470 nm there would be a difference of 0.68 optical depths from the top to the bottom of the array. This means that just over 50% of the downwelling light can be attenuated between the top and bottom sensors, which makes it very difficult to justify that all measurements are at the same depth!

One solution to this problem might be to arrange the sensors into a rosette which would allow all the sensors to be located in the same horizontal plane. This design, however, would require additional modifications to reduce the effect of tipping (i.e., non-horizontal positioning of the instrument in the water due to drag and current effects). Alternately, the algorithm could be applied to data from instruments such as RADS¹⁴ which takes a hemispherical radiance measurement, in which case one would generate the integrated moments from Eq. (4) by applying different Legendre polynomials as weighting functions to the data.

7. ACKNOWLEDGEMENTS

This work was supported by grants from the U.S. Office of Naval Research and the San Diego Supercomputer Center, as well as an Augmentation Award for Science and Engineering Research Training grant.

8. REFERENCES

1. J. R. V. Zaneveld, "New Development of the Theory of Radiative Transfer in the Oceans", in Optical Aspects of oceanography, N.G. Jerlov and E.S. Nielsen, eds. Academic Press, New York, 121-134, 1974.
2. W.H. Wells, "Techniques for measuring radiance in sea and air", *Applied Optics*, **22**, 2313-21, 1983.
3. W. Doss and W. Wells, "Undersea compound radiometer", *Applied Optics*, **31**, 4268-74, 1992.
4. W. Doss and W. Wells, "Radiometer for light in the sea", SPIE, **1302**, *Ocean Opt. X*, 363-372, 1990.
5. S. Chandrasehkar, Radiative transfer, pp. 54-61, Dover, New York, 1960.
6. H.R. Gordon, "Bio-optical model describing the distribution of irradiance at the sea surface resulting from a point source embedded in the ocean", *Applied Optics*, **26**, 4133-48, 1987.
7. R.C. Smith and K. S. Baker, "Optical Properties of the clearest natural waters (200-800nm)", *Applied Optics*, **20**, 177-184, 1981.
8. C.D. Mobley, et. al., "Comparison of numerical methods for solving the radiative transfer equation", *Applied Optics*, **32**, 7484-7504 1993.
9. P. Francisco and N.J. McCormick, "Chlorophyll concentration effects on asymptotic optical attenuation", *Limnol. Oceanogr.*, (in press).
10. L. Prieur and S. Sathyendranath, "An optical classification of coastal and oceanic waters based on the specific spectral absorption curves of phytoplankton pigments, dissolved organic matter, and other particulate materials", *Limnol. Oceanogr.*, **26**, 671-689, 1981.
11. C. D. Mobley, "The optical properties of water" in Handbook of Optics, Second Ed., Michael Bass editor, Optical Society of America, New York, 1993.
12. H. Gordon and A. Morel, Remote assesment of ocean color for interpretation of satellite visible imagery, in Lecture Notes on Coastal and Estuarine Studies, **4**, Sringer-Verlag, New York, 1983.
13. R. D. O'Dell, "Revised user's manual for ONEDANT: a code package for ONE-dimensional, Diffusion-Accelerated, Neutral-partical Transport", Los Alamos National Laboratory LA-9184-M, 1989.
14. K. Voss, "An underwater electro-optic radiance distribution camera system", *Opt. Eng.*, **28**, 241-247, 1989.

ESTIMATION OF OZONE CONCENTRATIONS BASED ON MEASUREMENTS OF SOLAR ULTRAVIOLET RADIATION IN THE ANTARCTIC USING THE BSI PUV-510 INSTRUMENT

Elizabeth J. Bruce, Philip L. Handley, Zhengming Wan & Raymond C. Smith

University of California Santa Barbara
CSL/Center for Remote Sensing and Environmental Optics
and Geography Department
Santa Barbara, California 93106

ABSTRACT

The greatly reduced stratospheric ozone concentrations over the Antarctic continent (popularly known as the Antarctic Ozone Hole), the consequent increase in short wavelength ultraviolet radiation (UVB) and the influence of this increased UVB on the Antarctic ecosystem has led to the development of new instruments for the measurement of these effects. One objective of research in this area is to estimate column ozone concentrations based upon surface UV measurements. Current commercial instruments vary in their characteristics from full spectral narrow-band to single broad-band so the nature, quality and usefulness of data from these instruments for linking surface UV measurements to column ozone concentrations also varies. One instrument, arguably a compromise between a more complex and expensive full spectral narrow-band instrument and a simpler broad-band instrument, is manufactured by Biospherical Instruments (BSI) for the measurement of surface and in-water UV radiation. Here we present preliminary results of direct observations of springtime UVB, using the BSI PUV-510, under the Antarctic ozone hole and provide an algorithm, using the radiative transfer code of Wan, for the accurate estimation of column ozone based upon these measurements. We show that data from the PUV-510 can be used to estimate column ozone, given a rough estimate of surface albedo, to within an accuracy of ± 10 DU and that this algorithm is robust, working well for both clear and cloudy skies.

1. INTRODUCTION

There is undisputed observational evidence that human activities are influencing the concentration of stratospheric ozone¹⁻⁴ and will continue to reduce the average global stratospheric ozone over the next century despite international efforts to mitigate the problem⁵. There is also evidence showing reduced atmospheric ozone concentrations will result in increased ultraviolet radiation (UVR) reaching the earth's surface⁶⁻⁹. Ultraviolet radiation has been divided into several spectral regions: UVA (320-400nm) radiation; UVB (280-320nm); and UVC (200-280nm). UVC is absorbed strongly by the atmosphere so that negligible amounts reach the earth's surface. Stratospheric ozone strongly absorbs extraterrestrial solar radiation in the UVB. This is the spectral region where proteins and nucleic acids, which are key components of living plants and animals, show strong absorption. Consequently, UVB wavelengths are those most influenced by anthropogenic changes to atmospheric chemistry and the ensuing ozone depletion. UVA wavelengths are known to induce both photodamage and photoreactivation processes in living cells and this radiation is relatively unaffected by variations in stratospheric O₃ depletion.

Concern that depletion of the ozone layer may cause harmful increases of ultraviolet radiation to both natural and manmade components of the biosphere has prompted the development of new instruments and the establishment of UV monitoring networks^{10,11}. Instruments for the measurement of incident UVR range from those that have high spectral resolution, which are relatively complex, bulky and expensive to operate, to simpler moderate to broad-band instruments with limited spectral information. A family of new instruments, Biospherical Instruments (BSI) PUV and GUV 500 series, have been specifically designed as ground-based UV radiometers to measure the flux of terrestrial and in-water UVR. These instruments measure UVR with moderate-bandwidths (roughly 10nm full width at half maximum, FWHM) centered at 305, 320, 340 and 380nm plus a broad-band channel for photosynthetic available radiation (PAR, 400-700nm).

An important objective is to estimate column ozone concentrations based upon surface UVR measurements. Total column ozone has traditionally been measured using ground-based Dobson spectrophotometers^{6,12-14} and, for the past few decades, by means of satellite observations^{7,15}. High resolution surface observations of UVR and radiative transfer computations have also been used to estimate total column ozone concentrations¹⁶. In addition to the more complex ozone monitoring methods, there is a need for simple field observation of ozone concentration to accompany biological effects research¹⁷. Variables important for the estimation of ozone concentration from surface UVR include: solar elevation,

surface albedo, atmospheric aerosols, stratospheric temperature and the distribution of cloud cover. Here we present preliminary results of direct observations of springtime UVR, using the PUV-510 instrument under the Antarctic ozone hole, compare these data with simulations using an atmospheric radiative transfer model, and provide simple graphics for the estimation of column ozone using data from the PUV instrument. In section 2 we describe the instrument and methods, results are given in section 3 and a discussion follows in section 4.

2. INSTRUMENT & METHODS

2.1. Measurement of ultraviolet radiation

The BSI PUV-500 family of spectroradiometers have been designed specifically as a simple, portable, and relatively inexpensive method of monitoring changes in solar ultraviolet radiation¹¹. The instrument includes sensors to measure UVR, with nominal sensor wavelengths at 308nm, 320nm, 340nm, and 380nm. Kirk et.al.¹⁸ and Booth (personal communication) have indicated that the naming of the 308 nm channel for this family of instruments may not be accurate. Results of intercomparison of the PUV with a high-resolution scanning spectroradiometer show that the actual center wavelength for this channel is between 304 and 305 nm. These authors suggest naming this lowest PUV channel 305 nm, which we do. The in-water PUV instrument also includes a sensor which, along with the channels mentioned, measures natural solar stimulated fluorescence. The downward irradiance is collected using a Teflon and quartz flat plate diffuser. This provides a geometric cosine response and the sensor is calibrated in units of $\mu\text{watts}/\text{cm}^2/\text{nm}$. The spectral responsivity of the sensor is a function of the detector, filters, and the diffuser. Figure 1 shows BSI's published response curve of the PUV instrument for the solar spectrum. We have not yet independently measured either the spectral response or the cosine response of this instrument.

In our testing of an algorithm for the estimation of total column ozone we use only data collected using the 305nm and 340nm channels. The detector for the 305nm channel uses an ultraviolet Cs-Te vacuum tube diode with ultraviolet glass, allowing maximum sensitivity for the relatively small irradiance values expected in this region of the solar spectrum as well as blocking irradiance at wavelengths above 320nm. The low wavelength side of this channel makes use of the naturally occurring, and very sharp, atmospheric (or in-water) cutoff which permits some variability in bandwidth as environmental conditions change. The sharp cutoff results from the fact that the absorption cross section for ozone at wavelength 280 nm exceeds that at 320 nm by more than two orders of magnitude. This leads to a sharp decrease in transmission from long to short wavelengths¹⁹. Figure 2 shows a plot of $E_d(305\text{nm})$, weighted for the PUV spectral response for this channel, vs ozone concentration for a range of solar zenith angles. The strong variability of $E_d(305\text{nm})$ with ozone is obvious from this figure.

The 340 nm channel uses a silicon photodiode that is optimized for use in this particular region of the spectrum and is chosen to minimize spectral leakage from longer wavelengths. In contrast to the 305 nm channel, the 340 nm channel is relatively insensitive to changes in column ozone concentration (Fig. 3). Also, it has been shown¹⁶ that the irradiance ratio we use to estimate ozone concentration is relatively insensitive to the influence of aerosols. As a consequence, we can assume that variations in the irradiance in this region of the spectrum which are due to atmospheric conditions and cloud cover are wavelength independent. That is, to first order, the variations in the irradiance ratio of 305 to 340 nm are primarily ozone related.

2.2. Ozone estimates

For comparison with our PUV-model results we independently determined ozone concentrations using data from the NSF/OPP UV monitoring station and an ozone estimation code developed by Wan as described by Smith et al.¹⁶. These independent ozone estimates were also compared with independently determined satellite estimates of total ozone from the Total Ozone Mapping Spectroradiometer (TOMS)²⁰ and found to be in agreement within about ± 15 DU, a variability consistent with our uncertainty associated with a space/time intercomparison of surface and satellite derived ozone values. A sensitivity analysis using this code¹⁶ showed that the relative uncertainty in ozone was only a few DU as the surface albedo varied by 0.1. Thus we would anticipate an albedo effect on our PUV-derived ozone estimates only for relatively large changes in albedo, say from ocean water to ice/snow cover. The wavelength-dependence for aerosol loadings were also shown by these workers to be relatively weak. High resolution, narrow band UV data were obtained from the NSF/OPP UV spectroradiometer monitoring system located at Palmer Station on Anvers Island off the Antarctic Peninsula ($64^\circ 46'S$ $64^\circ 03'W$). For this monitoring system, measurements are collected hourly during a 10 to 15 minute scanning interval consisting of 3 data blocks which include: 280-315nm at 0.2nm resolution, 280-380nm at 0.5nm resolution, and 280-620nm

at 1.0nm resolution. Our high resolution model uses a ratio of 308.26 nm to 337.28 nm to estimate column ozone concentration. Previous simulations with this model¹⁶, based upon comparison with dobson, ballonsond and satellite data, demonstrated that the model permits total column ozone and surface albedo to be estimated from ground-based UV spectroradiometer data with an accuracy of ± 5 DU for ozone and 0.1 for surface albedo.

2.3. Field area and data collection

Using the PUV spectroradiometer, moderate-band measurements of 305, 320, 340, 380 nm, and broadband PAR data were collected for a ten day period. During this period the ozone hole moved with respect to our location creating ozone values ranging from a low of 150 to a high of over 350 DU. The data were collected while stationed in Dallman Bay, on the north side of Anvers Island, during the November 1993 Icecolors cruise. Conditions during the ten day period were relatively calm and consistent. The environment was mainly open water with minimal ice cover and with none to relatively little (for the Antarctic) cloud cover. We logged PUV downward irradiance values every 15 seconds and these data were subsequently selected and binned by solar zenith angle for further analysis. The solar zenith angle was calculated based on time, latitude and longitude, which were recorded along with the PUV data.

3. RESULTS

3.1. PUV ozone algorithm

Figures 4 & 5 present results of our atmospheric radiative transfer code showing the ratio of $E_d(305nm) / E_d(340nm)$, where each waveband has been weighted by the appropriate PUV response function, versus ozone concentration and with solar zenith angle as a parameter. Figure 4 gives results for a surface albedo of 0.1, roughly the value of ocean water with some whitecapping and sea ice, which is our best guess of the albedo during our Dallman Bay station. Figure 5 shows the ratio $E_d(305nm) / E_d(340nm)$ versus ozone for selected solar zenith angles with the albedo varied in steps of 0.1 from 0.0 to 1.0 and provides an indication of how variation in surface albedo affects the relationship between the irradiance ratio and ozone. These figures can be used to estimate ozone concentration by making use of the $E_d(305nm) / E_d(340nm)$ ratio from PUV data.

3.2. Comparison of PUV vs high spectral resolution ozone estimates

Using the absolute moderate-band measurements of UVR from the PUV-510, we calculated the 305 to 340 nm irradiance ratio to examine how ozone fluctuated as a function of time and solar zenith angle. Figure 6 shows a plot of these ratios from PUV data, binned in 5° solar zenith angle bins, plotted along with curves computed using our radiative transfer model for several sun angles. The actual measurements compare well with the computed curves.

Figure 7 shows TOMS ozone data for the Dallman bay area²⁰ over the ten day period we were on station at this location along with ozone estimates using our PUV-ozone algorithm. Our data agree well with the satellite data, recognizing that there are space/time differences between the point shipboard measurements and the 30km resolution satellite data, and show that the PUV algorithm (Figs. 4 & 5) permit realtime tracking of the ozone variability associated with the Antarctic ozone hole.

4. DISCUSSION

There is now overwhelming evidence that UVB can be an important environmental stress in aquatic ecosystems^{21,22}. The BSI PUV family of instruments have been developed to permit the direct measurement of selected wavebands of UVR both incident on the surface and in-water²³. We estimate that the error involved in estimating column ozone concentrations using the PUV instrument and our model (Figs. 4 & 5), given a rough estimate of surface albedo, is approximately ± 10 DU. There are circumstances when this is acceptable accuracy, particularly when high resolution spectral irradiance and/or TOMS data are unavailable. This is especially true for Antarctic regions where relatively large changes in column ozone occur on space/time scales that require near realtime ozone estimates for both the science and logistics of UV-effects research.

A more rigorous assessment of the PUV model results could be made by comparing ozone estimated using this model with ozone estimates made using high resolution spectral data matched in time and space. The current comparison of our model results with independent ozone data suggest that the precision of the model is relatively high, say \pm a few DU, but that the absolute accuracy has yet to be determined. This is planned for future work.

Our PUV model (Figs. 4 & 5) is not linear, so an error estimate requires judgment and depends upon solar zenith angle and ozone concentration. We have optimized the model presented here for the Antarctic, where solar zenith angles are greater than 45° and where springtime ozone now routinely varies between 150 to 300 DU. The accuracy suggested above holds for ozone values around 275 DU, with the accuracy decreasing with higher ozone and increasing with lower ozone for a fixed accuracy in determining the irradiance ratio.

The surface albedo can contribute variations in the measurement of UVR, impacting the resulting irradiance ratios. Uncertainty in albedo, as shown in Fig. 5, contributes to additional uncertainty in estimating ozone. During the Antarctic spring, September to November 1993, we were able to obtain crude estimates of surface albedo over a range of conditions. We found UVR albedos varied from 0.10, for open water, to 0.85, for pack ice covered with snow. It has been shown, based on theoretical simulations, that the surface albedo is wavelength independent in the ultraviolet region²⁴. We can quantitatively predict the absolute effects of the variations in albedo on our PUV model. However, due to the relative lack of accurate surface albedo measurements in the Antarctic, we have few data to check these predictions.

Future work associated with using a simple, widely available UVR instrument for column ozone estimation will include: more accurate estimates of surface albedo, examination of the space/time variations in ozone so as to more accurately compare high resolution and satellite estimates, working to increase the accuracy of the model and extending it to lower latitude situations.

5. ACKNOWLEDGEMENT

Support for this research was from the National Science Foundation Office of Polar Programs Grants DPP90-11927 (RCS) and DPP92-20962 (RCS & BBP) and the National Aeronautics and Space Administration Grant NSGW 290-3 (to RCS).

6. REFERENCES

1. R. Watson "Ozone Trends Panel," (Executive Summary. NASA, Washington, D.C., 1988)
2. M. P. McCormick, R. E. Veiga, and W. P. Chu, "Stratospheric ozone profile and total ozone trends derived from the Sage I and Sage II data," *Geophys. Res. Let.*, **19**, 269-272 (1992).
3. R. Stolarski, R. Bojkov, L. Bishop, C. Zerefos, J. Stachelin, and J. Zawodny, "Measured trends in stratospheric ozone," *Science*, **256**, 342-349 (1992).
4. WMO "Scientific assessment of ozone depletion: 1991," (World Meteorological Organization, Geneva, 1991) Global Ozone Research and Monitoring Project - Report No. 25.
5. M. Crawford, "Landmark ozone treaty negotiated," *Science*, **237**, 1557 (1987).
6. J. C. Farman, B. G. Gardiner, and J. D. Shanklin, "Larger losses of total ozone in Antarctica reveal seasonal ClO_x/NO_x interaction," *Nature*, **315**, 207-210 (1985).
7. R. S. Stolarski, A. J. Krueger, M. R. Schoeberl, R. D. McPeters, P. A. Newman, and J. C. Alpert, "Nimbus 7 satellite measurements of the springtime Antarctic ozone decrease," *Nature*, **322**, 808-811 (1986).
8. R. S. Stolarski, M. R. Schoeberl, P. A. Newman, R. D. McPeters, and A. J. Krueger, "The 1989 Antarctic Ozone Hole as observed by TOMS," *Geophys. Res. Let.*, **17**, 1267-1270 (1990).
9. P. Newman, R. Stolarski, M. Schoeberl, R. McPeters, and A. Krueger, "The 1990 Antarctic Ozone Hole as Observed by TOMS," *Geophys. Res. Let.*, **18**, 661-664 (1991).
10. C. R. Booth, T. B. Lucas, T. Mestechkina, J. Tusson, D. Neuschuler, and J. H. Morrow "NSF Polar Programs UV Spectroradiometer Network 1991-1993 Operations Report," (1993)
11. C. R. Booth, T. B. Lucas, H. J. Morrow, C. S. Weiler, and P. A. Penhale, "The United States National Science Foundation's Polar Network for monitoring ultraviolet radiation," in: *Ultraviolet radiation in Antarctica: Measurements and biological effects*, C. S. Weiler and P. A. Penhale, Eds., (American Geophysical Union, Washington, D.C., 1994) p. 17-37. Antarctic Research Series, Volume 62.
12. S. Chubachi and R. Kajiwara, "Total ozone variations at Syowa, Antarctica," *Geophys. Res. Let.*, **13**, 1197-1198 (1986).

13. W. D. Komhyr, R. D. Grass, and R. K. Leonard, "Total ozone decrease at South Pole, Antarctica," *Geophys. Res. Let.*, **13**, 1248-1251 (1986).
14. W. D. Komhyr, S. J. Oltmans, and R. D. Grass, "Atmospheric ozone at South Pole, Antarctica, in 1986," *J. Geophys. Res.*, **93**, 5167-5184 (1988).
15. A. J. Krueger, M. R. Schoebert, and R. S. Stolarski, "TOMS observations of total ozone in the 1986 Antarctica spring," *Geophys. Res. Let.*, **14**, 527-530 (1987).
16. R. C. Smith, Z. Wan, and K. S. Baker, "Ozone depletion in Antarctica: modeling its effect on solar uv irradiance under clear-sky conditions," *J. Geophys. Res.*, **97**, 7383-7397 (1992).
17. R. C. Smith, B. B. Prézelin, K. S. Baker, R. R. Bidigare, N. P. Boucher, T. Coley, D. Karentz, S. MacIntyre, H. A. Matlick, D. Menzies, M. Ondrusek, Z. Wan, and K. J. Waters, "Ozone depletion: Ultraviolet radiation and phytoplankton biology in Antarctic waters," *Science*, **255**, 952-959 (1992).
18. J. T. O. Kirk, B. R. Hargreaves, D. P. Morris, R. Coffin, B. David, D. Fredrickson, D. Karentz, D. Lean, M. Lesser, S. Madronich, J. H. Morrow, N. Nelson, and N. Scully, "Measurement of uv-b radiation in freshwater ecosystems," in: *The Impact of uv-b radiation on pelagic freshwater ecosystems*, C. E. Williamson and H. E. Zagarese, Eds., (1994) In press.
19. L. T. Molina and M. J. Molina, "Absolute Absorption Cross Sections of Ozone in the 185- to 350-nm Wavelength Range," *J. Geophys. Res.*, **91**, 14,501-14,508 (1986).
20. J. Herman and A. Krueger "Meteor-3/TOMS and Nimbus-7/TOMS data, archive version #1," (NASA, GSFC, Greenbelt, MD 20771, 1994)
21. D. P. Hader, R. C. Worrest, H. D. Kumar, and R. C. Smith, "Effects of increased solar UVB irradiation on aquatic ecosystems," *Environmental Effects of Ozone Depletion: 1994 Update*, (United Nations Environmental Programme (UNEP) 1994, 1994) In Press.
22. C. E. Williamson and H. E. Zagarese, Eds., *The Impact of uv-b radiation on pelagic freshwater ecosystems*, (1994) In press.
23. PUV-500 profiling ultraviolet radiometer user's manual," (Biospherical Instruments, Inc., San Diego, CA 92117, 1994) (68 pages)
24. W. J. Wiscombe and S. G. Warren, "A model for the spectral albedo of snow. I: Pure snow," *J. Atmos. Sci.*, **37**, 2712-2733 (1980).

Figure Legends

1. Normalized spectral response of the PUV & GUV 500 series of instruments from Biospherical Instruments Inc.
2. Incident downwelling spectral irradiance at 305nm, $E_d(305)$, ($Wm^{-2} \mu^{-1}$) versus column ozone concentration (DU) for a surface albedo of 0.1 and for various solar zenith angles. Curves computed using an atmospheric radiative transfer model with input parameters as described by Smith et al.
3. $E_d(340)$ vs ozone concentration as described for Fig. 2.
4. Computed PUV irradiance ratio, $E_d(305) / E_d(340)$, versus ozone (DU) for surface albedo of 0.1 and for various solar zenith angles. Each waveband has been weighted with the appropriate PUV response function as shown in Fig. 1.
5. Same as for Fig. 4, but with the albedo varied in steps of 0.1 from 0 (lower curves) to 1 (upper curves).
6. PUV irradiance ratio vs ozone for several solar zenith angles. Curves computed using radiative transfer model. Points data from PUV instrument binned into 5° solar zenith angle bins.
7. Comparison of ozone values obtained using the PUV-model vs ozone values obtained by making use of high resolution spectral data from the Palmer NSF/OPP UV monitoring station and our radiative transfer model.

Figure 1: PUV 510 Normalized Spectral Response Curve

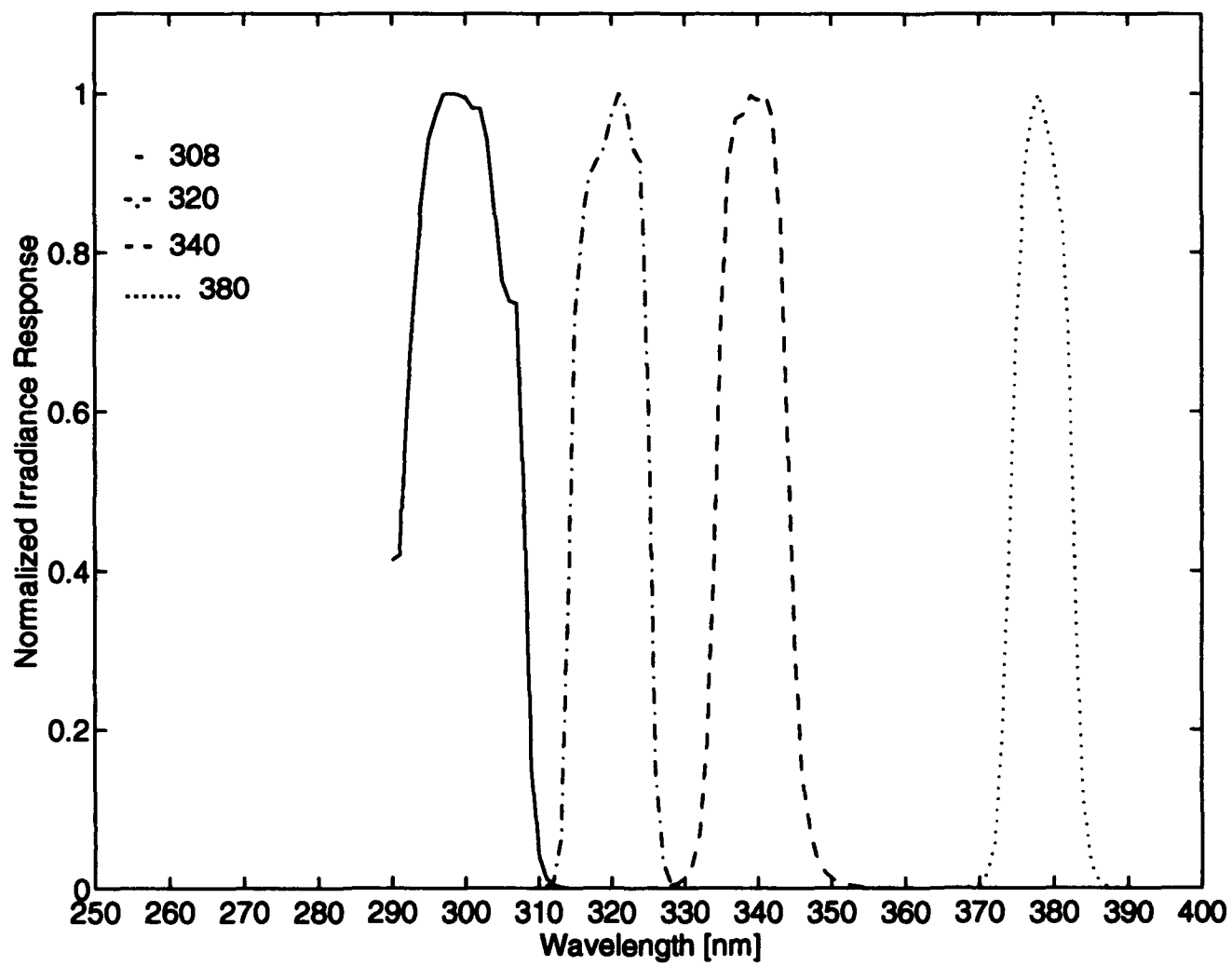


Figure 2: Modeled $E_d(305)$ vs. Ozone (albedo = 0.1)

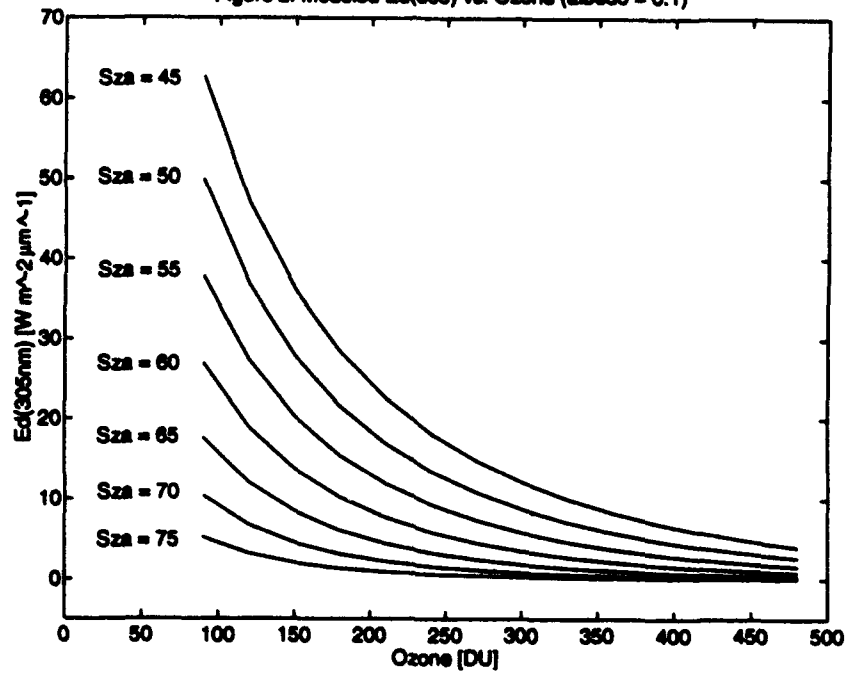


Figure 3: Modeled $E_d(340)$ vs. Ozone (albedo = 0.1)

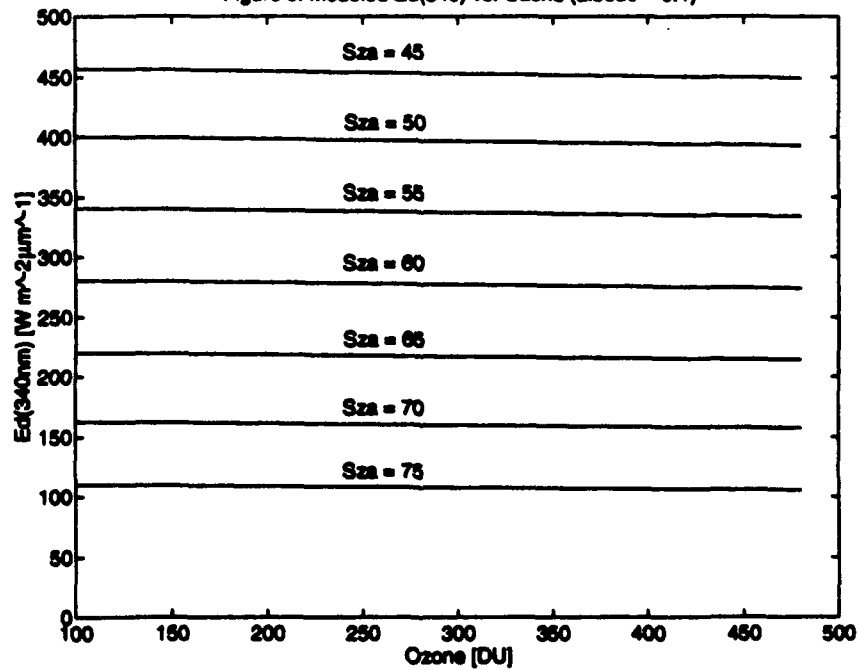


Figure 4: Modeled $Ed(305)/Ed(340nm)$ vs. Ozone (albedo = 0.1)

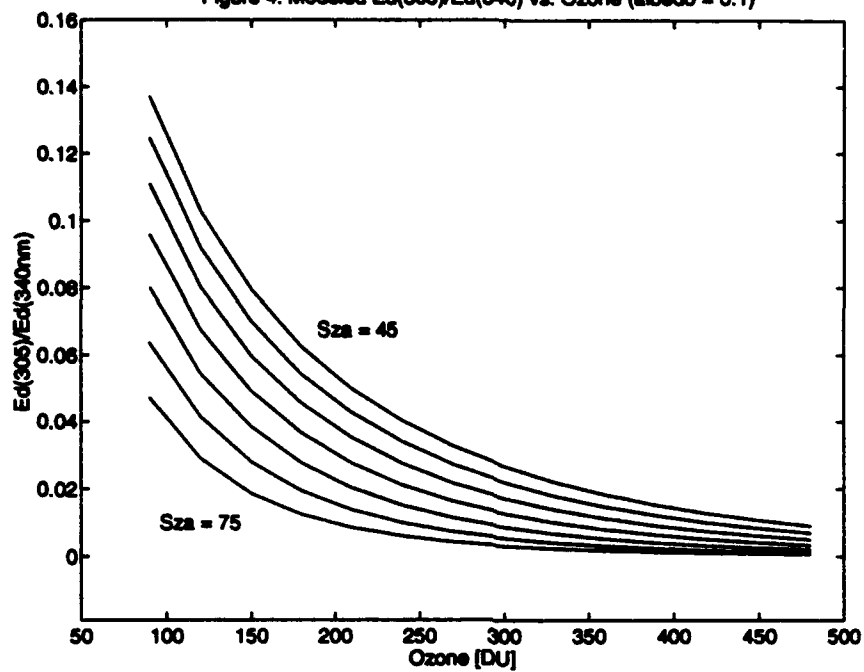


Figure 5: Modeled $Ed(305)/Ed(340nm)$ vs. Ozone (albedo = 0.0 to 1.0)

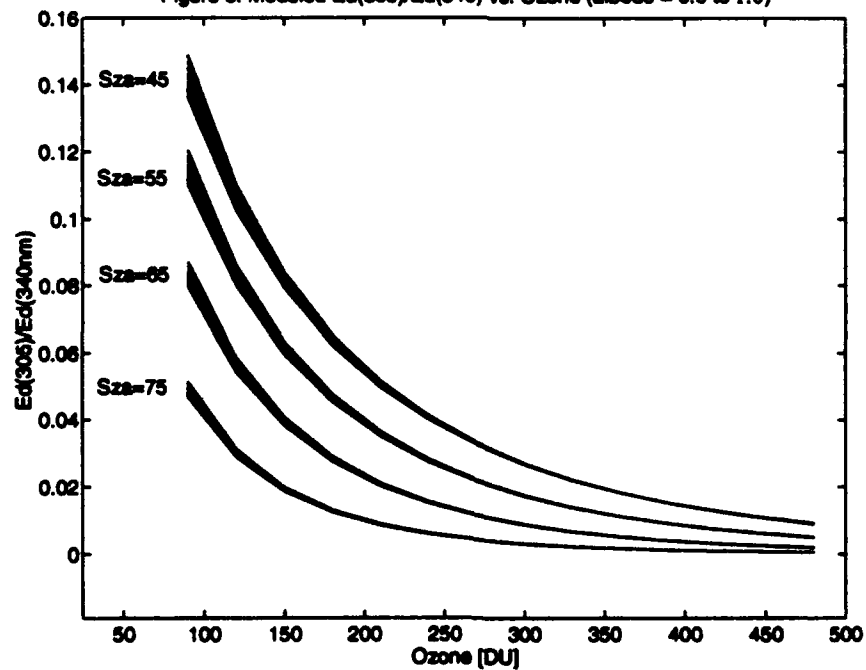


Figure 6: Modeled and Empirical PUV Irradiance Ratio vs. Ozone

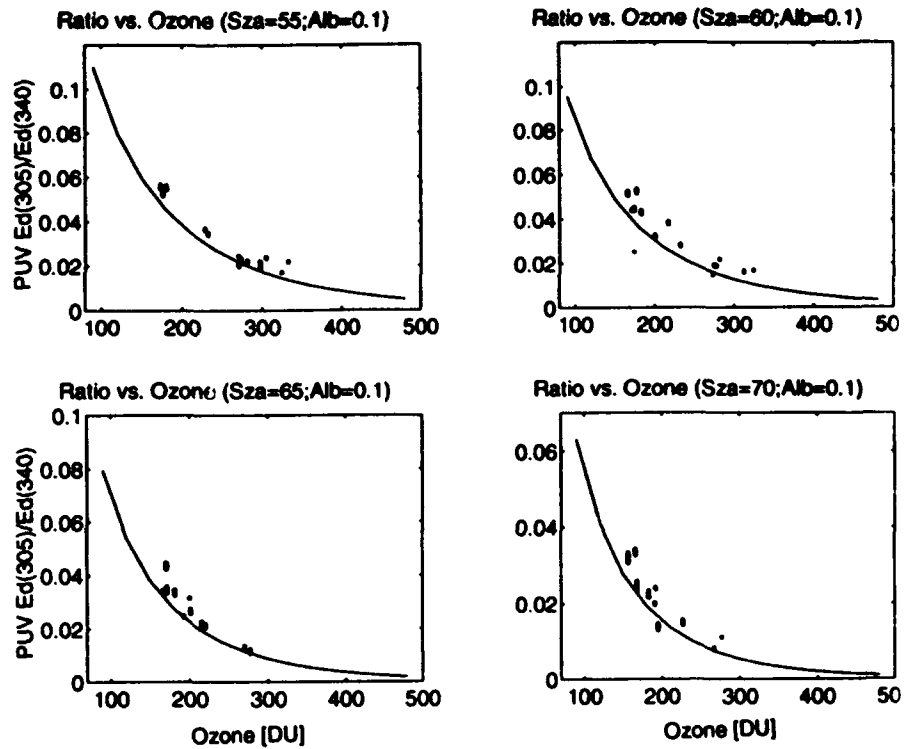
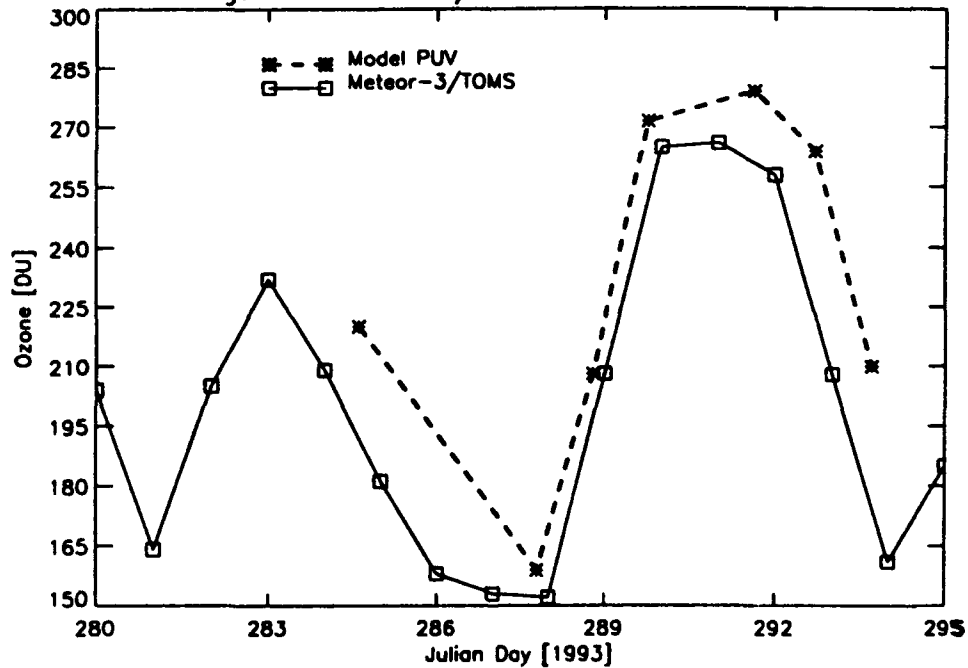


Figure 7: Meteor-3/TOMS and Model PUV Ozone



New Instrumentation and Platforms for Subsurface Optical Measurements

David K. Costello* and Kendall L. Carder*

**Department of Marine Science, University of South Florida, 140 7th Avenue South
St. Petersburg, FL 33701-5016, U.S.A.*

ABSTRACT

The underwater light field is affected by the geometry of the incident radiance, the sea-surface state, the inherent optical properties of the water-column constituents, the distribution of these constituents, and, in shallow areas, the bottom albedo. New instrumentation and platforms designed to assist in the quantification of the above are herein described. The new instrumentation includes the Marine Aggregated Particle Profiling and Enumerating Rover (MAPPER), the next-generation MAPPER II system, and the Bottom Classification and Albedo Package (BCAP). The new platforms include a custom-manufactured Remotely Operated Vehicle (ROV) designed to deploy the MAPPER II module, the BCAP module, and a vertical-profiling instrument suite, and an Autonomous Underwater Vehicle (AUV) designed for optical measurements in coastal waters. These include the deployment of the BCAP module on long-range, bottom-mapping missions.

1.0 INTRODUCTION

In the new millenia, our planet will be encircled with a host of orbiting machines. These satellites will enable a truly global, instantaneous information network serving communications, commerce, entertainment, security, and both theoretical and applied scientific research. While some of these research platforms will be looking outward, in search of information from the rest of our solar system and beyond, most will be looking inward with a solitary purpose, to monitor the planet from which they were launched. These space-based, inward-looking machines will be built and launched not out of curiosity but out of the necessity to acquire global data in order to address global questions arising from an ecosystem under stress. Many of these global questions involve, either directly or subtly, the coastal oceans, the areas where most of our populations live and where manifestations of man's affects on the oceans are most likely to appear. Among many others, these global questions include agriculture, mariculture and fisheries production, deforestation, desertification, ozone depletion, air and water quality, international security, global warming, and complex chemical and heat exchanges among the air, land, and sea. As with any instrument system, however, this space-based, remote sensing network will require calibration, algorithm validation, and the interpretation of the remotely sensed data.

This contribution focuses on new instrumentation and platforms designed for underwater optical measurements for the calibration of algorithms and the validation of satellite data regarding a significant part of our planet's surface, the coastal ocean. The instrumentation discussed includes the Marine Aggregated Particle Profiling and Enumerating Rover (MAPPER) and the next-generation MAPPER II system, both of which use structured, diode laser illumination for particle imaging, and the Bottom Classification and Albedo Package (BCAP), a suite of instrumentation which includes hyperspectral radiometers, a multi-channel intensified bottom imager, and commercial instrumentation. The platforms discussed are two Unmanned Underwater Vehicle systems (UUVs), a Remotely Operated Vehicle (ROV) custom-manufactured for the deployment of optical instrumentation and a state-of-the-art Autonomous Underwater Vehicle (AUV).

2.0 INSTRUMENTATION

2.1 BOTTOM CLASSIFICATION AND ALBEDO PACKAGE (BCAP)

Bottom-reflected radiance is quite apparent at depths to 30 m in hyperspectral, water-leaving radiance (AVIRIS data) off Florida when bottom albedos exceed 0.3 even when pigment levels exceed 0.4 mg/m^3 . This perturbation can be exploited to estimate bottom depth and to locate bottom features with contrasting albedos if measurements of the submarine light field and the water-column and bottom constituents that affect it can be obtained for calibration and validation purposes. This not only includes measuring the traditional water-column constituents and their absorption, scattering, and fluorescence properties, but also the reflectance and fluorescence properties of the bottom plants and sediments. This information will facilitate the development of models and algorithms for the remote determination of nearshore bottom sediment types, flora concentration/characteristics, water column constituents (dissolved and particulate), and bottom features (eg. foreign objects) incompatible with the natural spectral/spatial setting.

The Bottom Classification/Albedo Package (BCAP) is an ensemble of optical sensors under development at USF. BCAP principle components are hyperspectral (512 channel) upwelling radiance/reflectance and downwelling irradiance meters, a dual-laser range finder/chlorophyll probe, and a 6-wavelength, image-intensified, CCD bottom camera for bottom classification and object identification purposes. The prototype radiometer has a nominal resolution of 3 nm from 350-900 nm^2 . The two diode lasers (Melles Griot Electro-Optics) can function as near-bottom range finders providing the high-resolution altitude determination necessary for light propagation modelling. They will also be utilized in an attempt to quantify the chlorophyll *a* content of the bottom sediment, exploiting the differential absorption of the pigment at the two different laser wavelengths. One laser emits at 675 nm, a major peak of the chl *a* absorption spectra, while the other laser emits at 650 nm, a local minima of the chl *a* absorption spectra (see Figure 1). The 650 nm wavelength choice also minimizes potential crosstalk with the absorption spectra of chl *c*, a pigment often present with chl *a*.

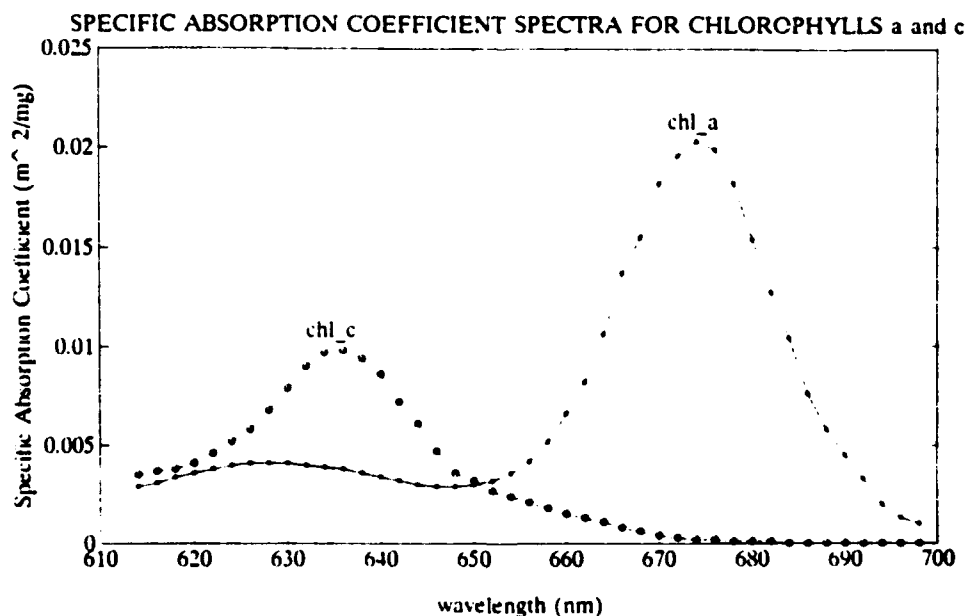


Figure 1. Specific absorption spectra for chlorophylls *a* and *c* (from Bidigare, et. al. 1990, see text for discussion).

The 6-channel (see Table 1 for filter specifications), Xybion IMC-301 imager utilizes a recently developed, Generation-III, micro-channel plate image intensifier with an extended blue photocathode (GEN-III-Blue) which has a dynamic range of over ten orders of magnitude. Tests in our laboratory showed that a less sensitive, GEN-II-RED was capable of imaging fluorescence from macrophytes, seagrasses, and benthic diatoms, and would, therefore, be capable of imaging albedo and/or fluorescence variations of the bottom. The increase in instrument response afforded by a GEN-III-Blue vs. a GEN-II-RED at an important chl *a* fluorescence band (685 nm), for example, is a factor of three. The calibration consistency of the IMC-301 GEN-III-Blue imager is, however, currently unknown. To provide unambiguous data, the calibrated 512-channel spectral reflectometer/radiometer will obtain spectra from a known (as a function of altitude) segment of the IMC-301 image, thus providing calibration constants for the imager. Another 512-channel spectral radiometer, equipped with a cosine collector, will obtain the spectra of the downwelling light field illuminating the bottom. Calibrated reflectance panels (Spectralon) will be used to calibrate bottom reflectance (albedo) measurements.

Center wavelength	FWHM bandwidth	Comments
460	20	Chl <i>c</i> absorption maxima
520	20	Co-pigment absorption maxima, coral fluorescence
575	30	Phycoerythrin fluorescence maxima coral fluorescence
620	20	Pigment absorption minima
685	30	Chl <i>a</i> fluorescence maxima
730	40	Fluorescence band

Table 1. Filter specifications for the Xybion IMC-301 Instrument.

For active bottom-mapping missions utilizing spectral albedo and stimulated fluorescence, a high-pressure, rare-earth-doped light source (Deep-Sea Power and Light) provides a relatively smooth illumination spectra for spectral albedo measurements and sufficient blue intensity to investigate stimulated fluorescence. A short-pass filtered, metal hallide arc lamp will be utilized for multi-channel fluorescence investigation during night deployments. In both scenarios, calibration is provided by the downward-looking spectroradiometer and calibrated reflectance panels.

Ancillary, commercially available instrumentation will measure the water inherent optical properties (IOP's) and physical properties and dissolved and particulate matter concentrations. These sensors include a nine-channel absorption/attenuation meter (ac-9, WET Labs), a multi-channel volume scattering meter (WET Labs, available FY 1995), an optical backscattering meter (OBS, Seatech), and a CTD (Falmouth).

2.2 MAPPER AND MAPPER II

Another potentially significant factor affecting the underwater light field in coastal waters is the changing suite of particulates. This includes sediment introduced by riverine or coastal erosional processes, dust flux, as well as biological production and the accompanying detritus. In oceanic Case I waters, the water-leaving radiance is primarily backscatter from water molecules and the small ($< 10 \mu\text{m}$ equivalent spherical diameter, ESD) particles present³. In coastal waters, however, much larger particles can be present and can have a significant effect on the light field^{4,5}. Costello et al.⁶ calculated that attenuation in Monterey Bay (July 1993) by particles larger than $70 \mu\text{m}$ diameter exceeded the attenuation by the numerically dominant, smaller-particle fraction. Their calculations were based on data from a 25 cm pathlength, SeaTech transmissometer and the conversion of the imaged geometrical cross-sections of the particles to effective optical cross-sections using an attenuation efficiency factor⁷, $Q_e = 2$, for optically large particles. It should be noted, however, that the transmissometer sample volume was much less than the imagery volume and, therefore, biased data toward the smaller particle fraction⁴.

The particle imagery was obtained using the Marine Aggregated Particle Profiling and Enumerating Rover (MAPPER), an instrument system developed during the ONR Accelerated Research Initiative Significant Interactions Governing Marine Aggregation (SIGMA). The MAPPER system (see Figure 2) and the type of data acquired are described elsewhere^{8,9,10,11}. Succinctly, MAPPER is a free-fall, vertical profiling system which utilizes structured, visible diode laser illumination to produce a thin sheet of light at the image planes of three, synchronized CCD video cameras of differing magnifications. This unique, synchronous imagery from the three independent cameras allowed an investigation (see Costello et al.¹², this volume) of imaging artifacts which would not be noticed nor quantifiable in a system with a single camera.

MAPPER realizes 50 μm resolution in the horizontal dimensions and sub-centimeter vertical resolution. The density of the MAPPER database is illustrated in Figure 3 which shows the 3-dimensional spatial distribution of large particles ($\text{ESD} > 215 \mu\text{m}$) in a randomly-chosen water volume from Monterey Bay of dimensions 29 mm x 58 mm x 100 mm (0.67 l). These data allow not only the 3-dimensional reconstruction of the particle distribution but also the classification of particles by shape and by reflectivity (eg. zooplankton vs. phytoplankton aggregates). This type of data is available for the entire database. For most purposes, however, the data are most often displayed in bins as a function of depth. Figure 4 shows particle size distribution data from the Monterey Bay deployments presented in one-meter depth bins.

Although the MAPPER system dependably (119 data tapes secured out of 120 attempted) captures unprecedented high-resolution imagery, the size of the present system (0.66 m³, 100 kg) precludes incorporation into other platforms capable of other deployment modes. Hence, a second-generation MAPPER II is under development. MAPPER II will be configured as a small (0.016 m³, and 10 kg), modular package capable of incorporation into the platforms discussed below.

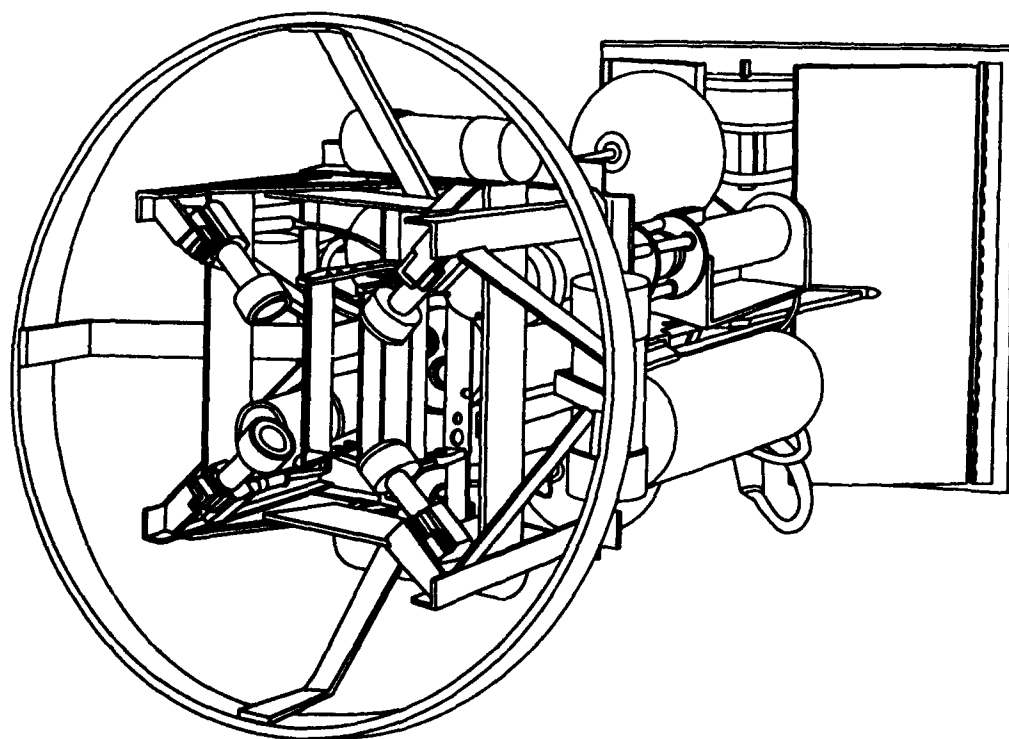


Figure 2. MAPPER. The normal vector out of this page describes the fall direction of MAPPER. The laser sheet is at the leading edge of the sensor. See Costello et al.^{8,9} for more details.

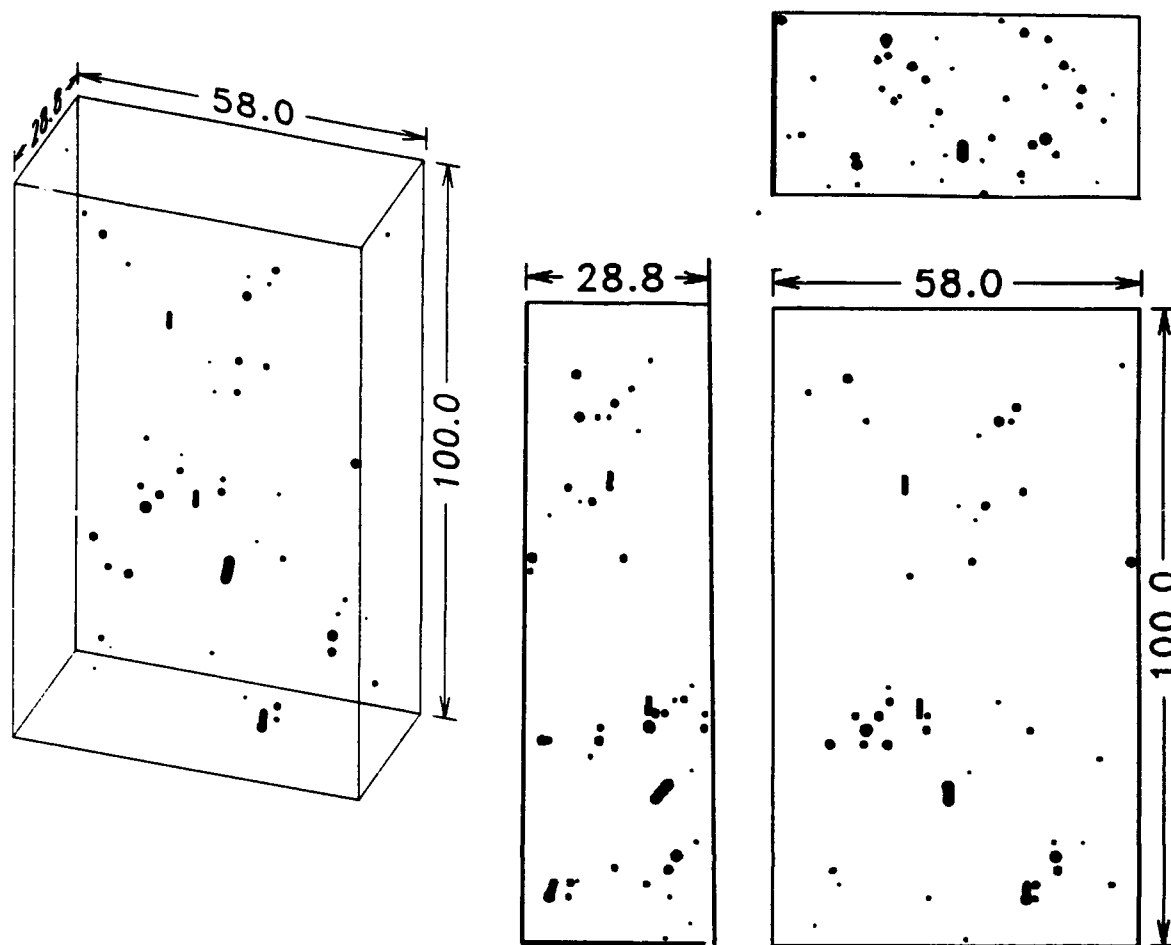


Figure 3. 3-dimensional reconstruction of particles (diameter $> 210 \mu\text{m}$) in a water volume at 10 m depth in Monterey Bay. Particle patchiness is evident by examination of the three orthogonal views on the left.

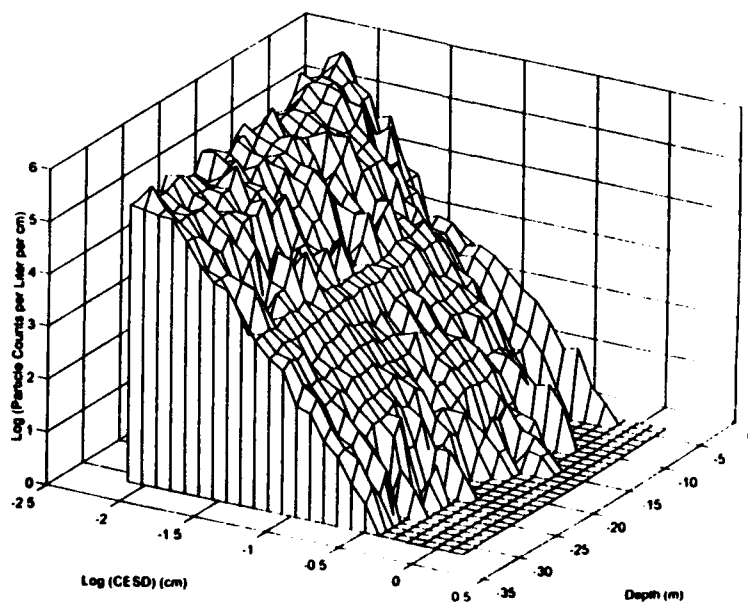


Figure 4. Particle size distribution spectra from Monterey Bay in one-meter depth bins (MAPPER data).

3.0 PLATFORMS

3.1 Remotely Operated System Equipped for Bio-optical Underwater Deployment (ROSEBUD)

The land-analog to the ROSEBUD ROV is a pickup truck with variable load configurations. A concept drawing for the system is shown in Figure 5. The ROV has a low optical-profile to minimize instrument shadows. Four horizontal thrusters developing up to 120 lbs. of thrust will help alleviate common ROV control problems associated with umbilical drag, surface and sub-surface currents, and mothership drift. The primary ROSEBUD design objective is to enable incorporation of a diverse set of instrumentation on a "plug-and-play" basis. An open, central cargo bay lined with instrument mount racks, for example, will accommodate approximately 0.25 m^3 of instrumentation.

The fiscal philosophy behind the design is the minimization of the costs of sophisticated ROV technology which is not applicable to ROSEBUD's envisioned missions. The result of this approach will be a robust vehicle at a fraction of the cost of the acquisition (and modification) of many more sophisticated systems. The sophistication of ROSEBUD will lie in more flexible payload configurations and deployment parameters and in an artificial-intelligence approach to data acquisition and integration. The digital and analog data from the instruments, for example, will be integrated in a VXWorks LON network using Motorola neural network hardware and protocol (see AUV section below) where data from any of the instruments are available to any other instrument node as required without interruption of the high-level system controller. In this operating system, the instrumentation plugged into the system is automatically recognized and the power and data stream requirements are automatically accommodated. Other planned enhancements include a four-channel, fiber-optic video multiplexer, an articulated instrument rack, moveable vertical thrusters (to accommodate hydrodynamically different instrument configurations), and a passively articulated instrument tray to accommodate instrumentation requiring constant orientation relative to the water flow.

ROSEBUD will be used for concept- and sensor-development activities prior to sensor transitions to an AUV. It will also be used for very-near-bottom ($< 2 \text{ m}$) studies.

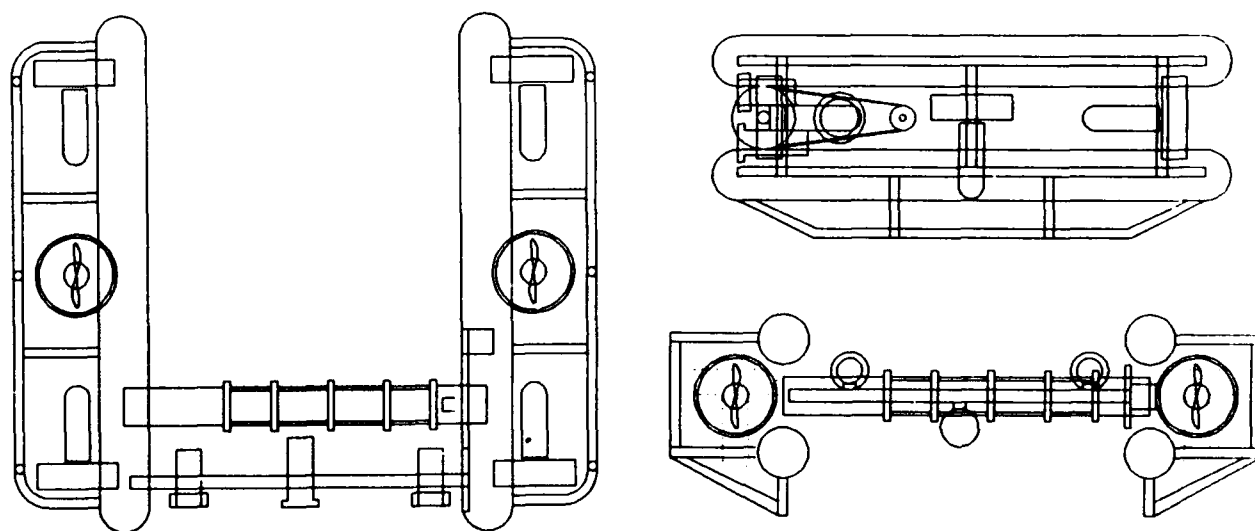


Figure 5. Concept drawing for the ROSEBUD ROV. Three orthogonal views are shown, see text for discussion.

3.2 Autonomous Underwater Vehicle Ocean Voyager II (OVII AUV)

The Ocean Voyager II (OVII) is an autonomous, untethered, underwater vehicle under development for USF/DMS by the Department of Ocean Engineering, Florida Atlantic University. In contrast to MIT's ODESSEY vehicle which is designed for deep-water, long-range missions, and WHOI's ABE vehicle which is optimized for deep-water, short-range, long duration deployments, the OVII (Figure 6) is a small vehicle optimized for coastal applications including long-range, bottom-following missions. The OVII is 2.4 m in length, has a maximum diameter of 0.6 m, a depth rating of 600 m, a maximum speed of 5 knots, and a theoretical range of 480 km (@ 3 knots). In sea trials at FAU and at USF, the prototype vehicle successfully performed missions following 3-dimensional waypoints on a completely autonomous basis. The payload bay of this prototype vehicle is currently being modified for integration of the BCAP system and, to our knowledge, will be the first Autonomous Underwater Vehicle dedicated to optical oceanography. The next-generation OVII has a three-piece modular design in order to accommodate several sensor suites under developed at USF Department of Marine Science. All modular-vehicle configurations share the aft propulsion section, most configurations share the forward control section, and multiple, interchangeable, central sections are under development. For some deployment configurations (using the MAPPER II module, for example) modified forward sections will be utilized.

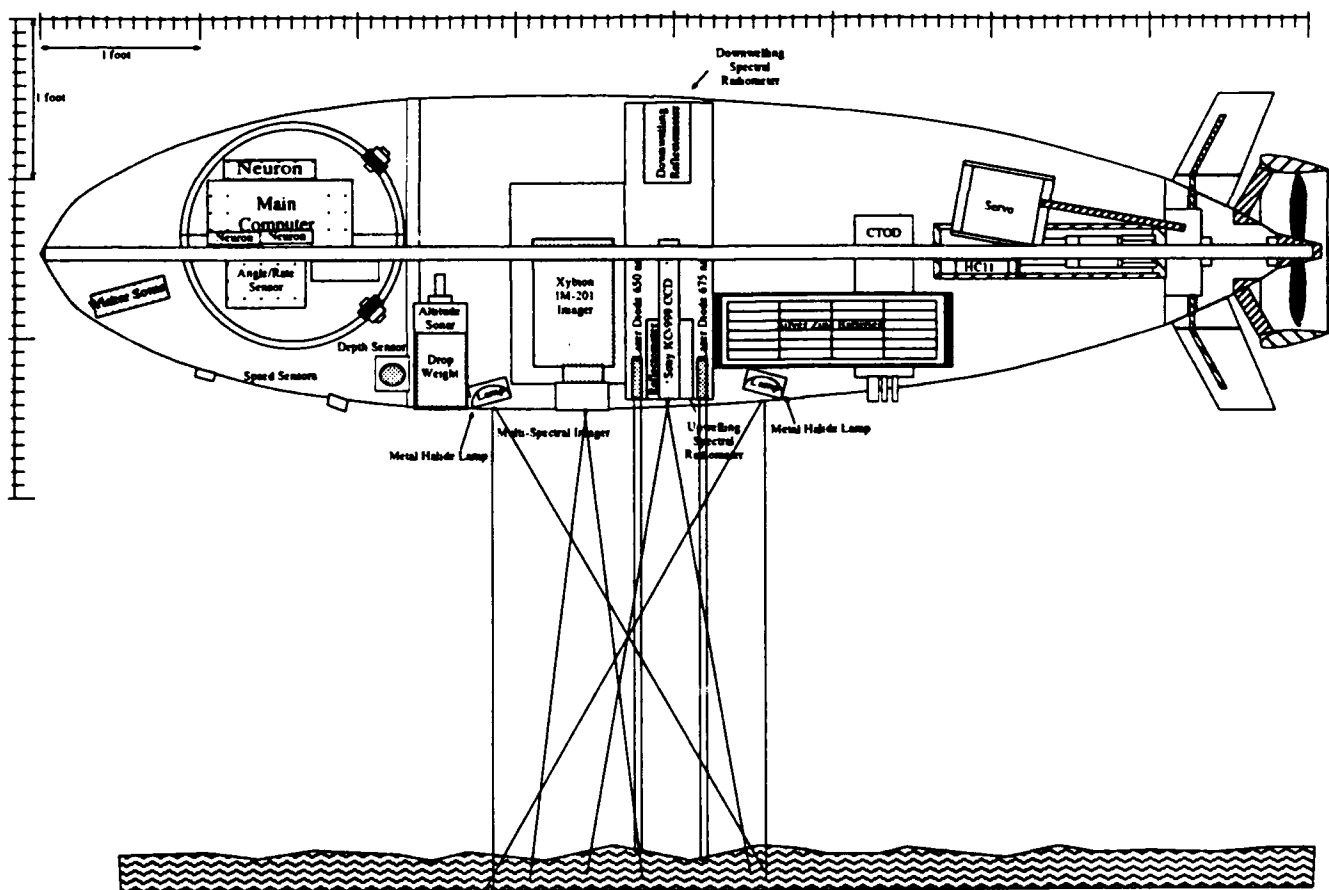


Figure 6. Depiction of the Ocean Voyager II AUV equipped with the BCAP module, see text for discussion (Figure courtesy of Sam Smith, Ocean Engineering, Florida Atlantic University).

The modularity of the OVII is unique among non-defense UUVs and arose out of the diversity of the planned instrument packages. In large part, the modularity is possible because of the utilization of an Intelligent Distribution Control System (IDCS)¹³. In essence, the IDCS consists of a main controller which is responsible for high level scheduling and for monitoring numerous (up to 32K) microcontrolled subsystems called "nodes". Each node consists of sensor(s), actuator(s) and a microcontroller. The node microcontroller (the "Neuron Chip", Motorola) is actually three, integrated microcontrollers with built-in communications firmware. These follow LONwork protocols where nodes are addressed as network variables and multi-tasking and event-driven scheduling are supported. The IDCS allows all network data to be addressed by any node, for node actuators to respond to information from other nodes independent of the main controller, and for essentially an unlimited number of sensor system configurations/permutations to be deployed without reprogramming the main controller.

4.0 MISSION SCENARIO

Coastal areas are complicated environments where most of our population lives. The difficulties described above are magnified near-shore because of complex and often rapidly changing physical processes. Tidal processes, inertial currents, upwelling, buoyant plumes, and internal waves are but a few mechanisms that change rapidly and require synoptic sampling. Satellites provide synoptic data, but calibration/validation of each image requires rapid, multiple-vessel coverage of the optical features (e.g. fronts, plumes, etc.) of interest. The more we learn about coastal areas, the more significant they become in terms of our understanding of global processes.

4.1 Coastal Ocean Color, the Primary Mission

The complexity of coastal waters demands that a wide variety of data be acquired in order to interpret satellite ocean color data. Water molecules, for example, affect light profoundly but in a manner that has been relatively well researched and documented^{14,15}. In natural waters, plant pigments (eg. chlorophylls, carotenoids, etc.) can also play a significant role in water color. The efficiency of the different absorption and fluorescence bands for these pigments has been recently an area of intense research and is becoming increasingly understood^{16,17,18}. In many coastal areas, one significant agent affecting light is Colored Dissolved Organic Matter (CDOM or "gelbstoff"), a biogenic degradation product of terrestrial or marine primary production. Carder et al.¹⁹ found that terrestrial and marine CDOM had differing spectral signatures. For a given river plume, however, CDOM images can be mapped into salinity images from AVIRIS²⁰.

Other factors that can affect the underwater light field and, hence, remotely sensed water color in coastal areas are suspended sediments (associated with riverine input or resuspended from the bottom by currents), the magnitude and shape of the particle size distribution (phytoplankton blooms and/or aggregation can have significant effects on water clarity^{4,6}) and bottom albedo. For an optically thick, homogenous ocean (e.g., well-mixed, deep water), the following equation^{14,21} describing remote sensing reflectance, R_{rs} , can be applied:

$$R_{rs}(\lambda) = L_w(\lambda)/E_d(\lambda) = \{0.33b_b(\lambda)/[a(\lambda) + b_b(\lambda)]\}(t/n)^2/Q, \quad (1)$$

where the parameters which are functions of the wavelength λ are noted. Here L_w is the water-leaving radiance measured from space, E_d is the downwelling irradiance, b_b and a are the backscattering and absorption coefficients of water and its suspended particles, and $Q = E_u(\lambda)/L_u(\lambda)$ (the ratio of the upwelling irradiance to the upwelling radiance), is only weakly dependent upon λ (Gordon and Morel²²). The squared term provides for the radiance divergence and air transmittance, t , of radiance leaving the water. The index of refraction of seawater, n , is about 1.334. This equation contains no provision for transpectral phenomena such as water-Raman scattering (considered negligible for near-shore environments) or fluorescence due to CDOM and chlorophyll a (not necessarily negligible for certain wavelengths). Provision for these can be made by adding an additional term^{21,23,24,25}.

For an optically shallow environment (e.g. depths shallower than about 2.0 optical thicknesses), bottom reflectance needs to be considered. Equation 1 can be expanded as follows:

$$R_{rs}(\lambda)_s = R_{rs}(\lambda)_d(1 - \exp\{-[k_d(\lambda) + k_u(\lambda)]D\}) + (t/n)^2(\alpha/\pi)\exp\{-[k_d(\lambda) + k_u(\lambda)]D\}, \quad (2)$$

where the subscripts *s* and *d* depict shallow- and deep-water conditions, α is the bottom albedo, the bottom reflectance is considered to be Lambertian [e.g. $E_u(\lambda) \approx \pi L_u(\lambda)$ at the bottom], and *D* is the water-column depth. The term $(1 - \exp\{-[k_d(\lambda) + k_u(\lambda)]D\})$ only becomes important when the depth *D* is smaller than about 0.5 optical depth. The diffuse attenuation coefficients k_d and k_u are for downwelling and upwelling light, respectively, and are largely a function of $a(\lambda) + b_b(\lambda)$ multiplied by the average slant-path enhancement of the rays relative to the vertical^{1,26}.

Satellite- or aircraft-derived ocean color data can be used to extrapolate from the data acquired on ship or AUV transects across or along the coastal transition zone of the ocean. Alternatively, *in situ* data can be used to validate algorithms used with remotely sensed data.

Once the atmospheric effects have been removed from remotely sensed data, Eqs. 1 and 2 can be validated by comparing remote-sensing reflection ($R_{rs}(\lambda)$) values to *in situ* measures of $R_{rs}(\lambda)$ and the combined terms found on the right sides of the equations. Of these, the bottom albedo, $\alpha(\lambda)$, is the most stable, with short-term temporal variability expected to be relatively low. This argues that α could be mapped before or after a major field validation effort. This mapping, however, would be prohibitively time consuming from a surface vessel using instrumentation hung over the side. A properly instrumented tow-body could provide the required areal coverage but altitude control and obstacle avoidance near the bottom would be problematic, especially in rough weather. Bottom mapping, however, is an ideal mission for an AUV.

The primary remaining validation variables that require measurement are $R_{rs}(\lambda)$, $a(\lambda)$, and $b_b(\lambda)$ from Eq. 1 and $k_d(\lambda)$ and $k_u(\lambda)$ from Eq. 2. The water depth *D* can also be determined, often after the fact, using depth charts and tidal models. This information is, however, readily available in an AUV deployment.

$R_{rs}(\lambda)$ can be measured near the surface from an AUV measuring the downwelling irradiance $E_d(\lambda, z)$ and upwelling radiance $L_u(\lambda, z)$, where *z* indicates sensor depth. By programming vehicle depth changes (Fig. 7), these values can be obtained for different depths, and diffuse attenuation coefficients are obtained through

$$E_d(\lambda, z + \Delta z) = E_d(\lambda, z) \exp[-k_d(\lambda, z) \Delta z], \quad (3)$$

and a similar expression for $k_u(\lambda, z)$ involving L_u instead of E_d . Instruments have been developed to provide direct measurements of beam attenuation, *c*, and absorption, *a*, at 9 wavelengths and also yield the total scattering coefficient *b* since $b = c - a$. Backscattering sensors are also available for several wavelengths and multi-channel volume scattering $\beta(\theta)$ instruments are under development.

All of these instruments can be incorporated into the sensor suite of a UUV (that is, an ROV or an AUV) that also includes temperature, salinity, beam attenuation, pressure (depth), height above bottom, water and bottom velocity relative to the AUV, and six-color bottom imagery for albedo/fluorescence.

4.11 AUV Deployment Scenario

Ocean color measurements require a solar zenith angle which allows adequate light penetration into the water column. For the purpose of illustration, we will use a six-hour sampling window, from 1000 to 1600 hours. An ideal mission scenario would utilize multiple OVII vehicles to maximize areal coverage during the

sample window. Even a single OVII, however provides coverage not available with a surface vessel. For water depth of 30 m, for example, it is desirable to obtain bottom albedo as well as optical vertical profiles and the AUV would cruise at 25-28 m depth obtaining down-welling irradiance and upwelling radiance spectra. The upwelling radiance would include any contribution from the bottom. If optical profiles were desired at one-kilometer intervals, for example, the AUV could, every kilometer, rise to 20 m, level off, cruise for 10 seconds acquiring data, perform the same tasks at 15, 10, and 5 m, and then dive back to 25 m (see Figure 7). Assuming an OVII cruise speed of 4 knots, a vertical ascent rate of 0.5 m/sec and descent rate of 1.0 m/sec, 10-second cruises at intermediate depths, and vertical profiling stations at one kilometer intervals, the OVII could complete 43 sample stations (that is, acquire 43 vertical profiles underway), and map 90% of the bottom along the transect.

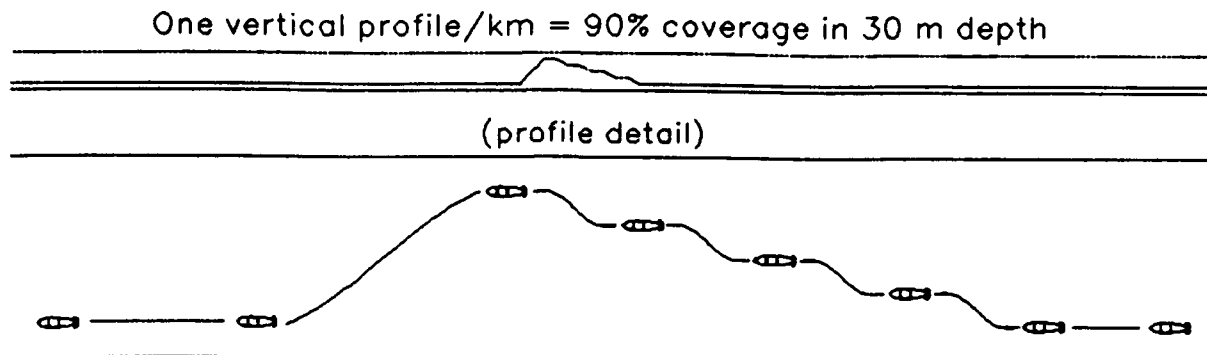
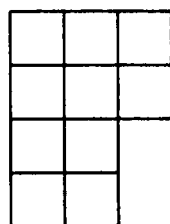
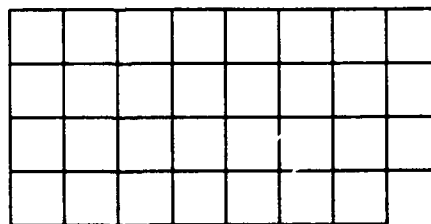


Figure 7. Vertical profiling scenario for an AUV which minimizes measurement perturbations which can be induced by vehicle pitch-angle. The neural node containing the 3-axis tilt sensor communicates with the optical instrumentation node and measurements are taken during level flight.

For an $n \times m$ grid, $(n+1) \times (m+1)$ stations are required



10 km²

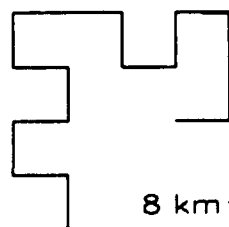


31 km²

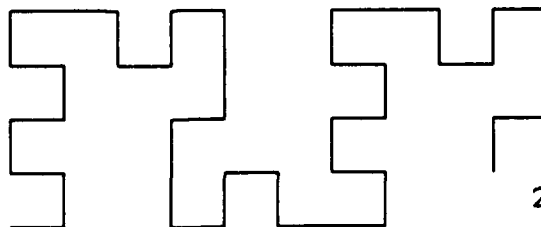
Surface Vessel

AUV

For a transect bracketing 1 km, $(n-1)/2$ stations are required



8 km²



20 km²

Figure 8. Areal coverage provided by a surface vessel and by an AUV both performing vertical optical profiles within a 6-hour sample window. See text for discussion.

For contrast, a surface vessel with an experienced crew able to perform a vertical optical profile in only 15 minutes, and allowing an additional 5 minutes to steam to the next station, could only complete 18 stations and would have albedo measurements of a very small percentage of the bottom. Figure 8 shows the areal coverage provided in this scenario by a surface vessel and an AUV for a grid with a station spacing of 1 km and for a mapping mission with the transect stations bracketing a 1 km swath. In the grid mission, the AUV is 210% more efficient in obtaining vertical profiles than the surface vessel and is 150% more efficient in the transect mission. Additionally, the bottom albedo data is easily obtained with an AUV but is essentially not available from a surface vessel.

5.0 SUMMARY

The technology enabling the use of air- and space-borne optical sensors to study coastal waters is rapidly advancing in response to our growing awareness of the importance of these areas to global concerns. The calibration, algorithm validation, and interpretation of the remotely sensed data, however, requires the collateral development of instrumentation and platforms capable of providing ground-truth in the complicated coastal environment.

The instrumentation described herein provides high-resolution particle size distributions, hyperspectral measurements of the underwater light field, and spectral bottom albedo. These when combined with other commercially available instruments, will allow us to approach optical model closure in coastal waters, and calibrate/validate algorithms for remote-sensing platforms.

Finally, we feel the UUV platforms described herein are requisite components in this endeavor. The ROV allows precise vertical positioning of optical instrumentation away from ship shadow. It also allows for sensor package integration and testing prior to its incorporation into an AUV, the weather-independent, cost-effective, underwater platform of the future.

ACKNOWLEDGEMENTS

The authors recognize Drs. Stanley Dunn and Sam Smith, Ocean Engineering Department, Florida Atlantic University and Drs. Peter Betzer and Tom Hopkins, Department of Marine Science, University of South Florida for their significant efforts in the FAU/USF AUV/sensor development project. Financial support was provided by the Office of Naval Research to the University of South Florida through Grant N00014-88-J-1017, by the National Oceanic and Atmospheric Administration through Grant NA360A0292, and by the National Aeronautics and Space Administration through Grant NAGW-465 and GSFC Contract NAS5-30779.

REFERENCES CITED

1. Lee, Z. P., K.L. Carder, S.K. Hawes, R.G. Steward, T.G. Peacock, and C.O. Davis (1994) A model for interpretation of hyperspectral remote sensing reflectance, Appl. Opt. (in press).
2. Steward, R. G., K. L. Carder, and T. G. Peacock (1994) High resolution, in water optical spectrometry using the Submersible Upwelling and Downwelling Spectrometer (SUDS). EOS AGU/ASLO (75) 3, 102.
3. Stramski, D. and D. A. Kiefer (1991) Light scattering by microorganisms in the open ocean. Prog. Oceanog. 28,343-383.
4. Carder, K. L. and D. K. Costello (1994) Optical effects of Large Particles. In: Ocean Optics. Spinrad, Carder, and Perry, editors, Oxford University Press, New York, N.Y.
5. Baker, E.T. and J.W. Lavelle (1984) The effect of particle size on the light attenuation coefficient of natural suspensions. J. Geophys. Res. 89, 8197-8203.

6. Costello, D.K., K.L. Carder, R.G. Steward and A. Alldredge (1994) The Distribution and Optical Properties of Large Marine Particles: Data From a Culture Tank and Field Experiments. EOS AGU/ASLO (75), 3, 35.
7. Van de Hulst, H. C. (1957) Light Scattering by Small Particles. John Wiley, New York.
8. Costello, D.K., K.L. Carder and R.G. Steward. (1991) Development of the Marine Aggregated Particle Profiling and Enumerating Rover (MAPPER). Underwater Imaging, Photography, and Visibility, Richard W. Spinrad, Editor, Proc. SPIE 1537, 161-172.
9. Costello, D.K., K.L. Carder and W. Hou (1992) Structured visible diode laser illumination for quantitative underwater imaging. Ocean Optics XI. Gary D. Gilbert, Editor, Proc. SPIE 1750, 95-103.
10. Costello, D.K., K.L. Carder, W. Hou and R.G. Steward (1994) 3-dimensional particle size spectra, transmissometry and temperature profiles, and filter pad absorption data. In: Monterey Bay Field Experiment Data Report to the Office of Naval Research under the Accelerated Research Initiative, Significant Interactions Governing Marine Aggregation (SIGMA). 24 pp.
11. Hou, W., D.K. Costello, K.L. Carder and R.G. Steward (1994) High-resolution Marine Particle data from MAPPER, a new, in situ optical ocean instrument. EOS AGU/ASLO (75), 3, 21.
12. Costello, D.K., W. Hou and K.L. Carder (1994) Some effects of the sensitivity threshold and spatial resolution of a particle imaging system on the shape of the measured particle size distribution. Ocean Optics XII, Bergen, Norway.
13. Smith, S.M. (1994) Implications of low cost distributed control systems in UUV design. AUVS '94 - Intelligent Vehicle Systems and Technology, Detroit, MI.
14. Morel, A. and Prieur, L. (1977) Analysis of variations in ocean color Limnol. Oceanogr. 22:709-722.
15. Smith, R.C. and K. S. Baker (1981) Optical properties of the clearest natural waters (200-800 nm). Appl. Opt. (20), 2, 117-184.
16. Kishino, M., C. R. Booth and N. Okami (1984) Underwater radiant energy absorbed by phytoplankton, detritus, dissolved organic matter, and pure water. Limnol. Oceanogr. 29(2), 340-349.
17. Mitchell, B.G. and D.A. Kiefer (1988) Chlorophyll *a* specific absorption and fluorescence excitation spectra for light-limited phytoplankton. Deep-Sea Res. 35(5), 639-663.
18. Sathyendranath, S., L. Lazzara and L. Prieur (1987) Variations in the spectral values of specific absorption of phytoplankton. Limnol. Oceanogr. 32(2), 403-415.
19. Carder, K. L., R. G. Steward, G. Harvey, and P. Ortner (1989) Marine humic and fulvic acids: Their effects on remote sensing of ocean chlorophyll. Limnol. Oceanogr. 34(1): 68-81.
20. Carder, K.L., R.G. Steward, R.F. Chen, S. Hawes, Z. Lee and C.O. Davis (1993) AVIRIS calibration and application in coastal oceanic environments: tracers of soluble and particulate constituents of the Tampa Bay Coastal Plume. Photogram. Engr. & Remote Sensing. Special Issue on Imaging Spectrometry. 487-500.
21. Carder, K.L. and R.G. Steward (1985) A remote-sensing reflectance model of a red tide dinoflagellate off west Florida. Limnol. Oceanogr. 30:286-298.
22. Gordon, H.R. and A. Morel (1983) Remote Assessment of Ocean Color for Interpretation of Satellite Visible Imagery: A Review. Springer-Verlag, New York.
23. Gordon, H.R. (1979) Diffuse reflectance of the ocean: The theory of its augmentation by chlorophyll *a* fluorescence at 685 nm. Appl. Opt. 18(8):1161-1166.
24. Stavn, R.H. (1990) Raman scattering effects at the shorter visible wavelengths in clear ocean waters. In: Ocean Optics X, Proc. SPIE 1302, 94-100.
25. Marshall, B.R. and R.C. Smith (1990) Raman scattering and in-water ocean optical properties. Appl. Opt. 29:71-84.
26. Kirk, J.T.O. (1983) Light and Photosynthesis in Aquatic Ecosystems, Cambridge University Press, Cambridge.

A multi-sensor *in situ* fiber optic fluorometer

Eurico J. D'Sa¹, Steven E. Lohrenz¹, Vernon L. Asper¹,
Roy A. Walters², Michael J. Morris² and Catherine Rathbun¹

¹Center for Marine Sciences, Univ. of Southern Mississippi
Stennis Space Center, MS 39529

²Ocean Optics, 1104 Pinehurst Rd., Dunedin, FL 34698

ABSTRACT

A prototype *in situ* multi-sensor fiber optic fluorometer is described which was designed to acquire long term time-series fluorescence measurements. The multi-sensor system uses dual detectors with four excitation sources, thereby providing for independent measurements at eight sensor locations. Strobe excitation light of wavelength < 500 nm is passed through one of each pair of optical fibers and stimulated chlorophyll fluorescence is carried back to a photomultiplier tube. The excitation and detection hardware are enclosed in a pressure case along with a battery operated 500 kHz data acquisition/storage system. Aspects of the design of the fiber optic sensor are described which were intended to optimize detection of fluorescence signals and minimize interference by ambient light.

An illustration of the utility of fiber optics for fluorescence measurements was made by comparing a prototype fiber optic profiling fluorometer with a commercial fluorometer. Time series fluorescence measurements were made with the multi-sensor fluorometer in the Gulf of Mexico, and revealed chlorophyll variability in the benthic boundary layer. The results demonstrated that the newly developed *in situ* fluorometer is well suited for remote and high resolution fluorescence measurements.

1. INTRODUCTION

The measurement of chlorophyll fluorescence is becoming increasingly important in studying biological processes in the ocean and *in situ* fluorometry is widely used to provide estimates of chlorophyll concentrations or phytoplankton biomass in both spatial and temporal scales of distribution¹⁻⁶. Moored fluorometers provide information on the temporal variability of phytoplankton biomass, whereas profiling instruments are used to give both horizontal and vertical distributions of phytoplankton variability. Fluorescence measurements have an advantage over other optical measurement techniques due to their sensitivity and ease of measurement, although fluorescence yield (the ratio of fluorescence signal to chlorophyll concentration within the fluorescence detection volume) can be influenced by various physiological factors^{7,8,9}.

The property of optical fibers to efficiently transmit a variety of optical signals due to their large bandwidth makes them ideally suited for applications to measure fluorescence signals remotely in oceanographic environments. Use of fiber optics to make *in situ* measurements of environmental

variables, including fluorescence measurements have been reported¹⁰. Here, we describe a novel multi-sensor fiber optic based fluorometer that was developed to measure chlorophyllous pigment concentrations primarily in the benthic boundary layer. Measurements made with a single sensor fiber optic fluorometer were used to evaluate performance of different system components that were later incorporated into a multi-sensor system. The prototype system was tested and evaluated during two cruises undertaken in the Gulf of Mexico, and their results are presented.

2. MATERIALS AND METHODS

In general, chlorophyll fluorescence is characterized by a broad excitation spectrum centered around 435 nm (blue) and a narrow emission spectrum at 685 nm (red)¹. The basic optical configuration of a single sensor system used to evaluate the system components of a multi-sensor fiber optic fluorometer is shown in Fig. 1. It uses a strobe (EG&G) to generate the excitation light, dual optical fibers (3M) to guide the light to or from the sampling volume, and a photomultiplier (Hamamatsu HC-125) to detect the fluorescence emission signal. The strobe excitation light is filtered by a broad band blue filter (Schott BG28) and is focused by a lens onto the end of a 600 μm optical fiber, which guides the light to the sampling volume. The fluorescence emission light from the sampling volume is guided by another 600 μm optical fiber to a detection system made up of a photomultiplier tube (PMT) fitted with a front end narrow bandpass interference filter (Edmond G43140) centered at 675 nm.

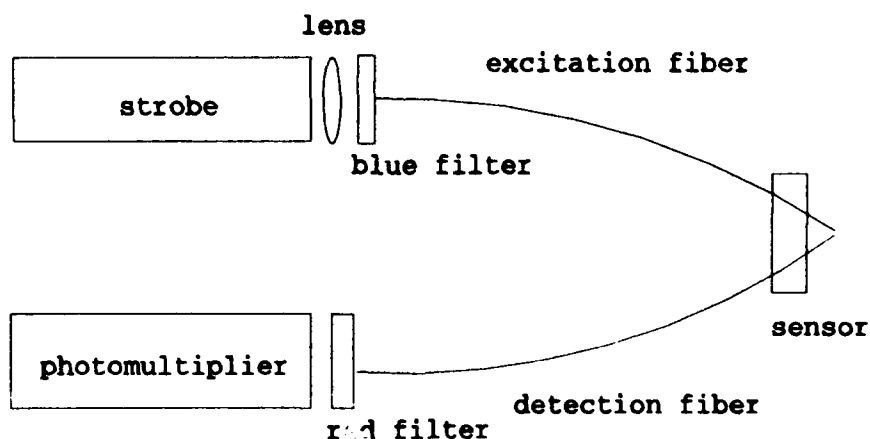


Figure 1. Basic optical configuration of a single sensor system.

2.1 The Optical fibers

The optical fiber used in the fluorometer is a 600 μm plastic clad silica core step-index fiber (3M) with broad spectral transmission characteristics. As the OH radical is the only impurity known to cause absorption in high silica fibers¹¹, fiber with low OH material was selected, having good spectral characteristics in the range of interest. The plastic clad silica core fibers, additionally have a kevlar reinforced PVC jacket for protection from external forces. Studies have shown that the light coupling efficiency is proportional to a first approximation to the fiber optic numerical aperture (NA) and the core diameter¹², which defines a cone of emission or acceptance volume. Fig. 2 shows geometrically

the regions of spatial dependence¹³ that describe the excitation and detection fields. The active region of illumination can be found from the following equations:

$$NA = \sin(\Phi) \quad (1)$$

$$\text{and } z_0 = a/\tan(\Phi) \quad (2)$$

where a is the fiber optic core radius. For the optical fiber chosen, the NA in water is 0.31, $\Phi (=18^\circ)$ defines the total cone angle of 36° , and the length of the conical region adjacent to the fiber face where the illumination intensity is constant, z_0 , is equal to 0.93 mm. For region B, the spatial dependence of the illumination intensity approaches an inverse square law. The conical sections defined by A and C contain the largest signal, whereas it is much reduced in regions B and D.

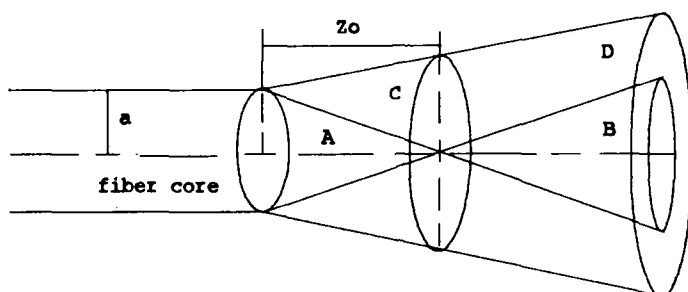


Figure 2. Cross sectional view of the illumination and collection fields of an optical fiber; a = radius of fiber; regions A, B, C and D define cones of different illumination intensity.

Selection of the optical fibers involved considerations of cost, performance and ease of use in the ocean environment. From above, it is seen that the light detection efficiency of an optical fiber depends on the numerical aperture and the fiber core diameter, with the active sampling volume increasing with larger values of both the parameters. However, large core optical fibers are susceptible to breakage and difficult to handle in the harsh oceanic environment. A trade off is therefore involved in the selection of the core size for the optical fibers.

2.2 The optical sensor

The optical sensor for the fluorometer is made up of a pair of bare polished fiber ends of the excitation and emission fibers that are oriented at an angle to each other. The active sampling volume is a cone defined by the numerical aperture and the fiber core diameter. The overlap between the excitation and collection cones is the region of sampling volume from which fluorescence is measured. Different optical probe configurations were tested in laboratory experiments. The polished fiber sensor ends were held together at different angles and distances by a holder. The fluorescence response of the sensor was evaluated in a solution of coproporphyrin (Aldrich Chem. Co.), a substance with fluorescence properties similar to chlorophyll. The use of this solution enabled fluorescence response of the optical fibers to be evaluated without the variability due to chemical degradation of chlorophyll. For the double fiber configuration, an approximate angle of 30° between the axis of the two fibers gave

the best fluorescence response (Fig. 3). The total fluorescence flux collection will originate from the volume of interaction of the cones subtended by the two fibers. Although theoretically, the common area could be infinite there is a trade off between attenuation of light over distance and volume of interaction.

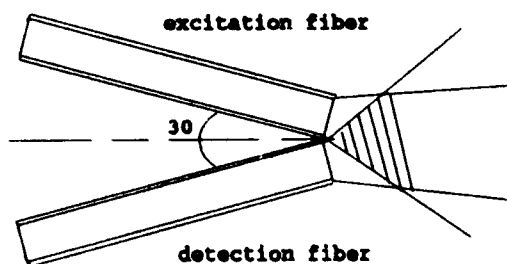


Figure 3. The dual fiber sensor configuration set to 30° interfiber angle.

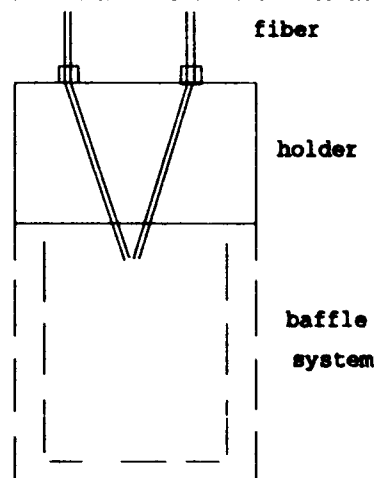


Figure 4. The fiber optic sensor with baffles reduce ambient light effects.

Fluorometers have been found to be sensitive to extraneous light¹⁴, that may cause interference in fluorescence measurements during daylight operations. We addressed this problem by designing and testing a series of sensors with different light baffle configurations. Fig. 4 shows the conceptual design of a fiber optic sensor with a baffle system to reduce ambient light effects. We are currently examining different baffle designs in an effort to introduce minimal ambient light with maximal water flow.

2.3 The multi-sensor fiber optic fluorometer

The multi-sensor fiber optic fluorometer is designed to obtain chlorophyll fluorescence at multiple depths for estimating the distribution and abundance of particulate pigment biomass. It is a battery operated system with capability for long term deployment, autonomous operation, and high sampling frequencies (1 Hz). The large number of sensors provides capability for increased vertical resolution, the present system designed to measure fluorescence at eight different locations in a water column. A schematic of the *in situ* multi-sensor fluorometer is shown in Fig. 5, and consists primarily of an optical, an electronic and a mechanical system. The optical system is comprised of 4 strobes, 2 photomultipliers and 8 optical sensors. Each strobe (EG&G) has a front end lens and filter assembly, that is coupled to a connector with a pair of excitation fibers that leads to the optical sensors. The detection fibers convey the fluorescence emission light from the optical sensors to one of the two detectors (Hamamatsu HC-125 photomultiplier) having a front end interference filter (Edmond G43140) with a peak at 675 nm and a bandwidth of 10 nm [full width at half-maximum (FWHM) intensity]. The intensity of the strobe is monitored with a phototransistor. Fiber lengths from the sensors to the instrument casing ranged from 2 to 5 meters.

The system operation is controlled by a Tattletale 7 microcomputer with 120 Mb hard disk drive for data storage. The data acquisition system has a 500 kHz analog-to-digital converter (Ocean Optics

PC1000) that digitizes the fluorescence signal from the 2 PMTs. Control software for initiating the strobes, multiplexing the PMTs and the data stream, signal pre-processing, and data recording was developed in 'Aztec-C' language. During field operation, system control and data offloading is via a serial RS-232 link through an underwater connector.

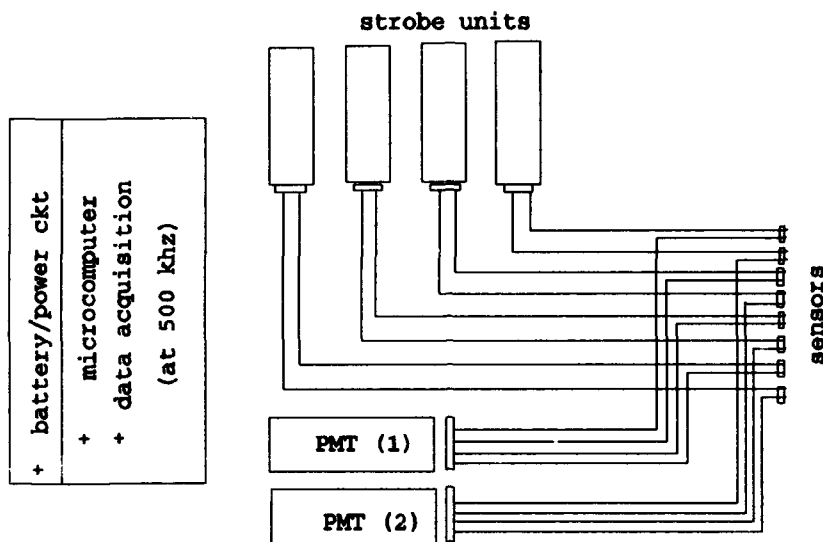


Figure 5. A schematic of the *in situ* multi-sensor fiber optic fluorometer.

Fiber optic penetrators were designed specifically for this application to provide an optical path between the inside of the pressure casing and the external environment (i.e., from the sensors to the strobes and the PMTs). The penetrators use a 600 μm optical fiber as an integral waveguide within a metal housing¹⁵. Interior and exterior SMA fiber optic couplings provide mounting capability to the fibers. Laboratory tests have shown optical coupling losses of the penetrator. These have been reduced by using index matching liquid (Norland P/N 9000) to fill the gap between the fiber tips and the penetrator optics. An O-ring sealed connector and receptacle was used to make the penetrator optics watertight. The instrument pressure housing is constructed of standard 6061 Al alloy cylindrical tubing (dimensions: 40 inches length and 6 inches diameter) and has flat end plates fitted with pressure rated double 'O' ring type seals.

2.4 Calibration

The single and multi-sensor fiber optic fluorometer were calibrated at different concentrations with laboratory grown pure phytoplankton cultures (*Nannochloris atomis* Butcher, clone GSB *Nanno* from the Bigelow Laboratories Culture Collection of Marine Phytoplankton). The calibration was performed for different cell concentrations in artificial seawater¹⁶ (ASW). The culture samples were filtered onto glass fiber (Whatman GF/F) filters, ground and extracted in 10 mL of 90% acetone. The extracts were re-filtered through GF/F filters and the concentrations of chlorophyll *a* and phaeopigments determined fluorometrically¹⁷ using a Turner Designs (10-005R) fluorometer.

3. RESULTS AND DISCUSSIONS

Laboratory evaluation of the optical fiber sensor design involved experiments to determine the optimum interfiber angle and distance. The optimum configuration was found to be 30° angle, with the fiber sensor ends separated by a distance of ≤ 0.1 mm. Fig. 6 shows a plot of fluorescence intensity as a function of interfiber angle for the 600 μm and 1000 μm plastic clad silica core optical fibers. Experiments with the 400 μm and 200 μm silica core fibers gave correspondingly lower fluorescence response, whereas plastic core fibers showed high levels of background emission. Though the 1000 μm fiber gave slightly higher fluorescence signal, it was not selected due to difficulty in handling this core size fiber. Therefore, 600 μm core glass fiber was selected. A typical fluorescence time scan of phytoplankton in seawater (Fig. 7) displays a steep increase in fluorescence signal corresponding to increasing intensity of strobe illumination. The peak fluorescence intensity corresponded to peak in strobe intensity at the temporal resolution shown.

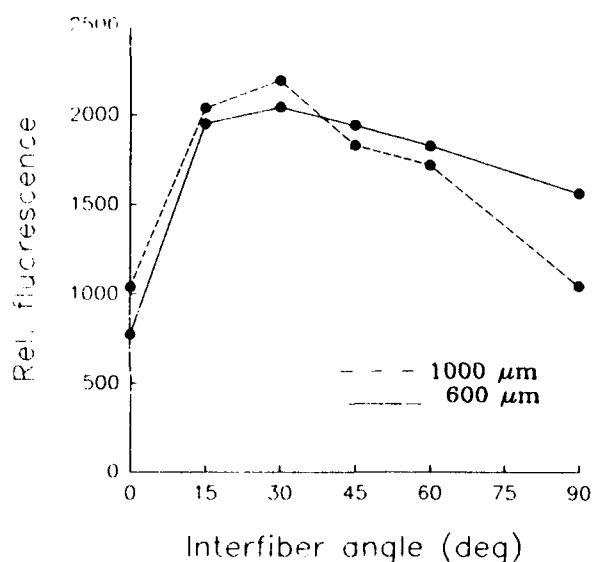


Figure 6. Interfiber angle vs relative fluorescence: 600 μm (solid line), 1000 μm (dashes).

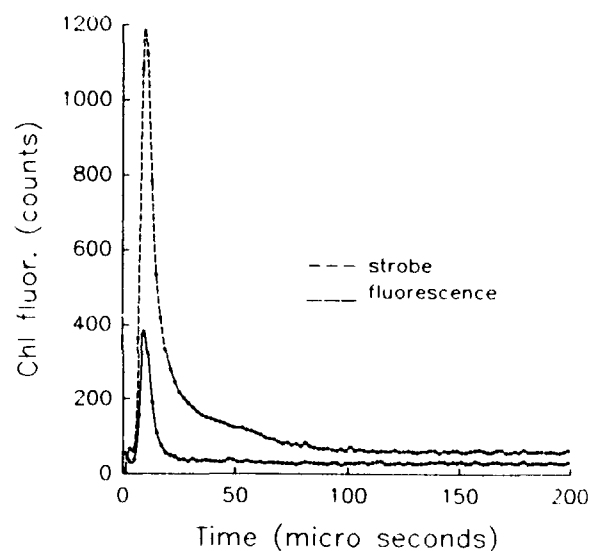


Figure 7. A typical fluorescence scan of phytoplankton plotted against time.

Laboratory calibration of the single sensor prototype profiling fluorometer and the multisensor system in different concentrations of phytoplankton cultures (*Nannochloris atomis* Butcher) are shown in Fig. 8A and 8B. There exists a high degree of correlation between the chlorophyll concentrations and *in vivo* fluorescence ($r^2 = 0.995$ and 0.996 for the single sensor and the multi-sensor fluorometers respectively). The fluorometers were calibrated from 0.05 to approximately 25 $\mu\text{g/l}$ chlorophyll. The sensitivity of the instrument can be adjusted by controlling the gain voltage of the photomultiplier tubes.

Field tests were carried out during two cruises undertaken in the slope waters of Gulf of Mexico in October 1993 and May 1994 on the R/V *Pelican*. The vessel was equipped with a CTD (Seabird), fluorometer, and transmissometer (SeaTech) profiling package. A rosette bottle sampler was used to collect water samples for fluorometric chlorophyll determination¹⁷. During the first field trial of the single sensor fiber optic fluorometer, fluorescence profiles were obtained using an optical fiber length of 70 m. Phytoplankton pigment concentrations showed variability with depth (Fig. 9A), with a

chlorophyll maximum located at approximately 45 m depth. *In vivo* fluorescence measured with the fiber optic fluorometer showed good agreement with a SeaTech fluorometer profile. Fig. 9B shows a profile obtained during a second cruise in May 1994 in shallower waters of the Mississippi River plume in the Gulf of Mexico. Peak fluorescence due to chlorophyll was recorded by the fiber optic and the SeaTech fluorometer at similar depths of approximately 4 meters. Profiles of chlorophyll concentrations measured from water samples obtained from a CTD cast showed similar vertical distribution patterns. However, there was no evidence of a decrease in chlorophyll concentration at the surface, while both fluorometers showed lower fluorescence in surface waters. This may have been due to photoinhibition in the near surface populations.

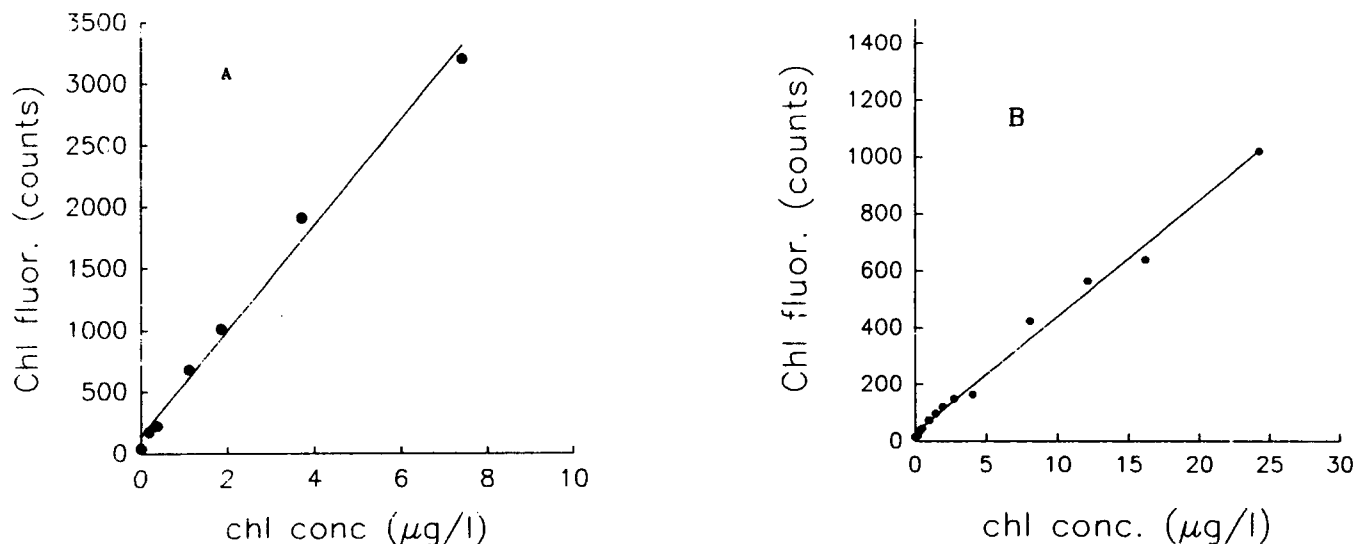


Figure 8. (A) Chl *a* fluorescence calibration of the single sensor fiber optic fluorometer ($r^2=0.995$; $N=7$). (B) system calibration of the multi-sensor fiber optic fluorometer ($r^2=0.996$; $N=11$). Samples for calibration are laboratory cultures of *Nannochloris*.

The multi-sensor fiber optic fluorometer was deployed on the May 1994 cruise to investigate temporal variability in near bottom pigment gradients. The fluorometer was attached to a frame and lowered to the sea bottom in shallow waters off the Louisiana shelf, near the Mississippi River plume. The sensors were mounted at different depths from the sea bottom and fluorescence was recorded at 5 minute intervals over a period of six hours. Fig. 10 shows a time series contour of chlorophyll/phaeopigment concentrations from one deployment. Chlorophyll concentrations were plotted as a function of depth from the sea bottom. The instrument was calibrated before and during the cruise and found to be stable. Fig. 11 shows vertical profiles of density (σ_t), fluorescence and beam attenuation (SeaTech fluorometer and transmissometer).

The time series revealed unusually high levels of chlorophyllous pigment concentrations reaching 100 mg/m^3 as recorded by one of the fiber optic sensors at about 1.6 meters above the sea bottom. The high chlorophyll levels were recorded 3 hours after deployment and lasted until recovery. Instrument retrieval began at about 18.5 hours at which time the chlorophyll levels decreased due to displacement of the sensor. The high levels did not appear in other deployments during the same cruise. Though water sample analyses were made at approximate depths corresponding to the fiber optic sensors, no

evidence of high pigment concentration were found. Hence, it was not possible to corroborate the high chlorophyll concentrations recorded by the *in situ* fluorometer. Chlorophyll concentrations of water samples taken at depths corresponding to the other fiber sensors agreed with those sensor measurements. For instance, at 7 m depth the fiber optic sensor measured around 6 mg/m³, and was also measured from water samples. At 8 m depth the fluorometer measured about 6-10 mg/m³, whereas water sample measurements gave 5 mg/m³ of chl *a*. The possibility of the signal being due to an artifact of high turbidity was investigated in the laboratory. Tests indicated only a marginal effect on the instrument response.

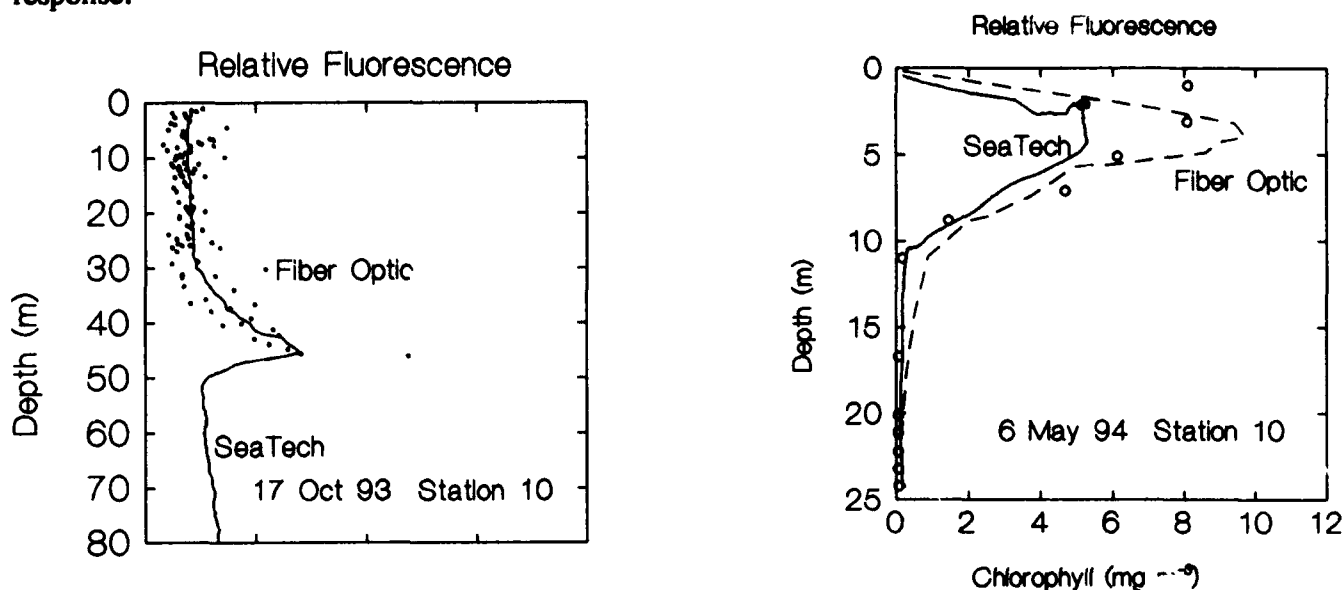


Figure 9. Fluorescence profiles obtained during two cruises in the Gulf of Mexico using the fiber optic fluorometer in October 93 (A) and May 94 (B). Profiles at the same locations with a SeaTech fluorometer are shown for comparison. Hollow circles indicate chlorophyll concentrations.

Analysis of the beam attenuation profile (Fig. 11) from a cast near the multi-sensor fluorometer deployment area indicated high levels of turbidity near the sea bottom and approximately near the sensor recording high chlorophyll concentrations. High fluorescence was not indicated here by the SeaTech fluorometer. Why the feature was not evident in the SeaTech fluorometer profile is unclear. There was a slight fluorescence increase recorded by the profiling SeaTech fluorometer, just above the high beam attenuation recorded by the transmissometer. The fluorescence levels then decreased, which may be related to increased water turbidity. Sigma-t also showed a large increase at the approximate depth of high chlorophyll measured by the *in situ* fluorometer.

A variety of reasons may be attributed to the high levels of chlorophyll signal recorded by one of the sensors of the fluorometer. High chlorophyll concentrations of up to 50 mg/m³ have been measured in the Mississippi River plume¹⁸, though not reaching the levels measured by the fiber optic fluorometer. It is possible that a layer of high turbidity waters containing high concentrations of chlorophyll/phaeopigments was present, perhaps associated with the high density gradient at the salt/freshwater interface. The ability of a fiber optic sensor to measure fine structure of the water column may have been required to resolve such a feature. More deployments of the instrument are required to validate such measurements.

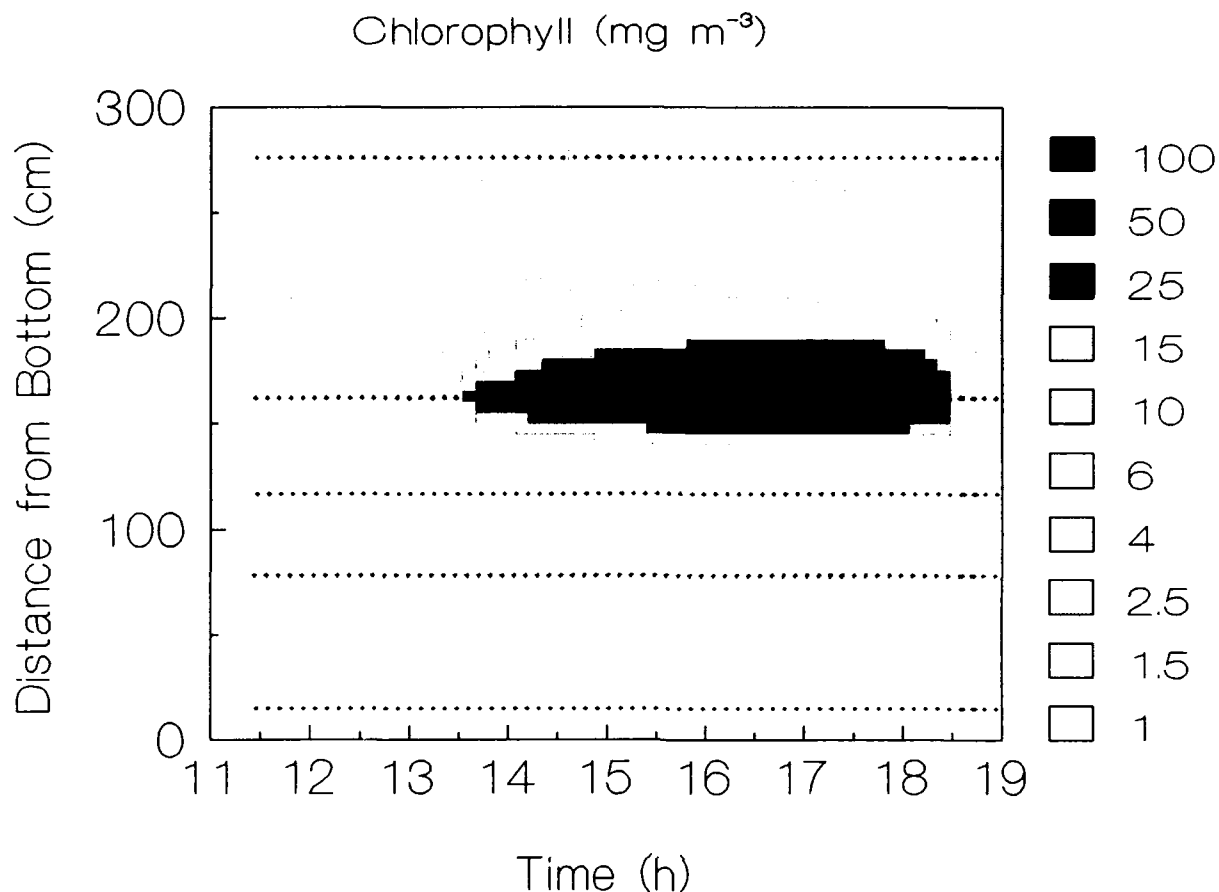
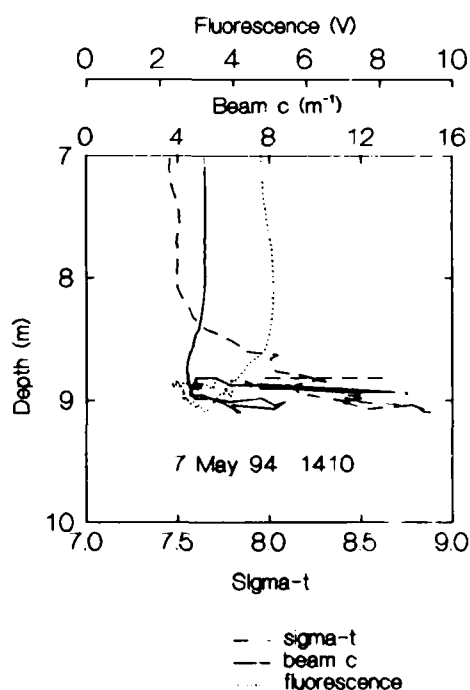


Figure 10. Time series contour of the benthic boundary layer chlorophyll concentrations obtained with the *in situ* multi-sensor fiber optic fluorometer on 7 May 1994 in the Mississippi River plume, at a depth of approximately 10 m.

Figure 11. Vertical profiles of density (σ_t), fluorescence and beam attenuation (SeaTech fluorometer and transmissometer) taken on 7 May in the vicinity of the *in situ* fluorometer deployment site. Bottom depth was 10 m.



4. CONCLUSIONS

Preliminary results obtained from field tests indicate that reliable fluorescence data are obtainable with the fiber optic fluorometer. The instrument is unique as it provides the capability to obtain fluorescence time series profiles at different depths simultaneously. Thus far, vertical resolution in moored applications of *in vivo* fluorometers has been achieved through deployment of multiple instruments. Our system expands the effectiveness of individual strobe and detector packages by use of multiple optical fibers to allow increased vertical resolution. The instrument is capable of yielding distinct information about the biological processes in the ocean as illustrated by observations of chlorophyllous particulate matter in the benthic boundary layer. Based on preliminary results the single sensor profiling fluorometer is able to provide fluorescence measurements at high vertical resolution. The detection volume of the fiber optic sensor is about 1 mm³ thus allowing the possibility of studying the fine scale structure of the water column in pigment distributions. The flexible design of the multi-sensor *in situ* fiber optic fluorometer using 4 strobes and 2 photomultipliers facilitates future modifications to give more detailed information about the natural phytoplankton populations. For example, using different filters on the strobe or on the photomultipliers, it would be possible to look at chlorophyllous emission spectra due to different fluorescing components in the water column such as chlorophyll *a* (685 nm) and phycoerythrin (between 570 and 590 nm)¹⁹.

The multi-sensor fiber optic fluorometer is particularly suited to measurements conducted in the benthic boundary layer because of the ability to place fiber optic sensors in close proximity to one another and other instruments (e.g., current meters) with minimal interference to the current regime. Future deployments of the instrument will examine the relationship between current regime and fine-scale gradients in benthic boundary layer fluorescence.

5. ACKNOWLEDGEMENT

This work was supported by the Department of Energy through contract DE-FG02-92ER61443. We are grateful to crew and captain of R/V *Pelican* for their efforts.

6. REFERENCES

1. C.J. Lorenzen, "A method for the continuous measurement of *in vivo* chlorophyll concentration", *Deep-Sea Res.* 13, 223-227, (1966).
2. V. Strass, "On the calibration of large-scale fluorometric chlorophyll measurements from towed undulating vehicles," *Deep-Sea Res.* 37, 525-540, (1990).
3. A.W. Herman and K.L. Denman, "Rapid underway profiling of chlorophyll with an *in situ* fluorometer mounted on a 'Batfish' vehicle," *Deep-Sea Res.* 24, 385-397, (1977).
4. J. Aiken, "A chlorophyll sensor for automatic remote operation in the marine environment," *Mar. Ecol. Prog. Ser.* 4, 235-239, (1981).

5. T.E. Whitledge and C.D. Wirick, "Observations of chlorophyll concentrations off Long Island from a moored *in situ* fluorometer," *Deep-Sea Res.* 30, 297-309, (1983).
6. R. Bartz and R.W. Spinrad, "Low power, high resolution, *in situ* fluorometer for profiling and moored applications," *Proc. SPIE* 925, 157-170, (1988).
7. D.A. Kiefer, "Chlorophyll *a* fluorescence in marine centric diatoms: response of chloroplasts to light and nutrient stress," *Mar. Biol.* 23, 39-46, (1973a).
8. D.A. Kiefer, "Fluorescence properties of natural phytoplankton populations," *Mar. Biol.* 22, 263-269, (1973b).
9. P. Falkowski and D.A. Kiefer, "Chlorophyll *a* fluorescence in phytoplankton: relationship to photosynthesis and biomass," *J. Plank. Res.* 7, 715-731, (1985).
10. T.J. Cowles, J.N. Moum, R.A. Desiderio and S.M. Angel, "*In situ* monitoring of ocean chlorophyll via laser-induced fluorescence backscattering through an optical fiber," *Appl. Opt.* 28, 595-600, (1989).
11. D.B. Keck and R.E. Love, "Fiber optics for communications", in *Applied Optics and Optical Engineering*, vol. VI, R. Kingslake and B.J. Thompson, ed., Academic Press, (1980).
12. P. Plaza, N.Q. Dao, M. Jouan, H. Fevrier and H. Saisse, "Simulation et optimisation des capteurs a fibres optiques adjacentes," *Appl. Opt.* 25, 3448-3454, (1986).
13. R.A. Desiderio, T.J. Cowles and J.N. Moum, "Microstructure profiles of Laser-induced chlorophyll fluorescence spectra: Evaluation of backscatter and forward-scatter fiber-optic sensors, *J. Atmosph. Ocean Tech.* 10, 209-224, (1993).
14. G.L. Hitchcock, E.J. Lessard, D. Dorson, J. Fontaine and T. Rossby, "The IFF: the isopycnal float fluorometer," *J. Atmosph. Ocean Tech.* 6, 19-25, (1989).
15. G.C. Burke, "Hermetic optical fiber penetrators for aquatic environments", *Proc. SPIE* 1750, 319-329, (1992).
16. S.E. Lohrenz and C.D. Taylor, "Inorganic ^{14}C as a probe of growth rate-dependent variations in intracellular free amino acid and protein composition of NH_4^+ -limited continuous cultures of *Nannochloris atomis* Butcher", *J. Exp. Mar. Biol. Ecol.* 106, 31-55, (1987).
17. T.R. Parsons, Y. Maita and C.M. Lalli, "*A manual of chemical and biological methods for seawater analysis*," Pergamon Press, New York, (1984).
18. S.E. Lohrenz, M.J. Dagg, and T.E. Whitledge, "Enhanced primary production at the plume/oceanic interface of the Mississippi River," *Cont. Shelf Res.* 10, 639-664, (1990).
19. C.S. Yentsch and D.A. Phinney, "Spectral fluorescence: an ataxonomic tool for studying the structure of phytoplankton populations", *J. Plank. Res.* 7, 617-632, (1985).

The Scattering Error Correction of Reflecting-Tube Absorption Meters

J. Ronald V. Zaneveld, James C. Kitchen

College of Oceanic and Atmospheric Sciences, Oregon State University
Corvallis, Oregon 97331-5503

Casey Moore

Western Environmental Technology Laboratories, Inc.
PO Box 518, Philomath, Oregon 97370

ABSTRACT

In this paper we examine correction methods for the scattering error of reflecting tube absorption meters and spectrophotometers. We model the scattering error of reflecting tube absorption meters for different tube parameters and different inherent optical properties. We show that the only reasonable correction method for an absorption meter without attenuation measurements or a spectrophotometer is the method in which the measured absorption at a wavelength in the near infrared is subtracted. A better correction is obtained if attenuation is measured simultaneously and the absorption at the reference wavelength is multiplied by the ratio of the measured scattering at the measurement wavelength divided by the measured scattering coefficient at the reference wavelength. This is the proportional method. We showed that the important geometrical parameters of the reflecting tube can be obtained by a comparison of measurements and models of polystyrene beads. Finally we examine the improvements that could be obtained if a direct scattering measurement were made simultaneously with the absorption and attenuation measurements.

1. INTRODUCTION

The question of optical closure cannot be addressed scientifically until the instrumental problems are understood and accounted for. Even if the instruments that measure the inherent optical properties are perfectly calibrated to some standard, there remain design limitations that will cause variable errors depending on the volume scattering function of the particulate constituents of the water. These errors need to be accounted for and their uncertainty established to get correct readings and error estimates. On the whole, these errors are relatively small and traditionally have been ignored in absorption meters and spectrophotometers.

The reader should not conclude that the *in situ* devices are less accurate than spectrophotometers, simply because we analyze the errors. In fact the reverse is true. Some models of spectrophotometer developed for analytic chemistry are designed for measuring the absorption of solutions only. These models make minimal attempts at collecting the scattered light and are poor choices for measuring the absorption of suspended particulates. Even the best models do not collect all the scattered light and the method of analysis used below would apply to them also.

We will explore the interaction of changes in the volume scattering function ($\beta(\theta)$) with design criteria and calibration methods for an *in situ* absorption meter and a good spectrophotometer setup. First we will consider the reflective-tube absorption (a) meter^{1,2} which is designed to collect all of the transmitted light plus most of the scattered light. Errors are introduced since the absorption meter misses scattered light within a certain angular range, losses at the reflective surfaces and increased pathlength of the scattered light. Spectrophotometer errors using a cylindrical glass cuvette are quite similar to reflecting tube errors as nearly the same geometry is used, so that this analysis is also applicable for the measurement that is considered standard. The 1 cm square glass cuvette is limited by critical reflection off the front face at around 50° but increasing reflection losses as this critical angle is reached limits the marginal advantage over the longer tubes. The magnitude of this error depends strongly on the magnitude and angular shape of the volume scattering function. This necessitates obtaining an estimate of the scattering error if the absorption coefficient is to be determined correctly.

2. SCATTERING ERROR

Four approaches can be used to estimate the scattering error: 1) the error can be assumed to be a certain percentage of the total scattering coefficient (b) and thus can be calculated if the beam attenuation coefficient (c) is measured simultaneously with the absorption coefficient (average correction); 2) scattering can be measured over some angular range and a relationship assumed between the measured scattering and the scattering error (scattering meter correction); 3) assuming that at some wavelength there is no particulate absorption and very little absorption by dissolved substances, the absorption measurement at that wavelength will be the absorption of pure water plus the scattering error (constant IR correction); and 4) a combination of any of the above approaches. A combination of 1) and 3) is the proportional method in which the proportion of b that is the scattering error is constant, but b itself is known to first order and its wavelength dependence is taken into account.

Attenuation meters also have a scattering error which is caused by the finite reception angle of the receiver and in cylindrically limited instruments by the collimation of the light source. This results in scattered light being accepted by the receiver up to a well defined angle³ (for well-collimated attenuation meters). However, we have come to question whether the total scattering coefficient is ever really finite in nature⁴. Mie scattering calculations show that, even for relatively steeply sloped size distributions, the large particles continue to add significantly to near forward scattering. In addition, inhomogeneities in the density and temperature of the water itself add to the near forward scattering⁵. For the purpose of this paper, however, we will assume that there is some true b (either actual or by definition of some standard acceptance angle) and that the scattering error of both the absorption and attenuation meters can be defined as a fraction of this true b .

A correction algorithm using simultaneous measurements from c and a meters (c_m and a_m) results from simultaneously solving the following equations for nonwater absorption and scattering a_n and b_n :

$$c_m = c_w + a_n + (1 - e_c)b_n, \quad a_m = a_w + a_n + e_a b_n, \quad (1)$$

where c_w and a_w are known⁶ and e_c and e_a are the estimated scattering errors of the c and a meters. This results in the following solutions which are starred to denote that an estimated scattering error is used:

$$a_n^* = (a_m - a_w) + \left(\frac{e_a}{1 - e_c - e_a} \right) (a_m - a_w) - \left(\frac{e_a}{1 - e_c - e_a} \right) (c_m - c_w) \quad (2)$$

$$b_n^* = \frac{(c_m - c_w) - (a_m - a_w)}{1 - e_c - e_w} \quad (3)$$

$$c_n^* = (c_m - c_w) + \left(\frac{e_c}{1 - e_c - e_a} \right) (c_m - c_w) - \left(\frac{e_c}{1 - e_c - e_a} \right) (a_m - a_w) \quad (4)$$

The problem to be resolved, is how to arrive at these estimates of $e_c(\lambda)$ and $e_a(\lambda)$ or $a_n(\lambda)$ $b_n(\lambda)$, and what are the magnitude of errors involved in the various methods of making these estimates. The problem is that the percentage errors of both instruments can (depending on instrument design) vary widely from location to location as the nature of the particles changes. They also vary spectrally.

3. MODELING THE REFLECTIVE TUBE ABSORPTION METER

Assuming single scattering, we can estimate the efficiency, $D(\theta)$, with which scattering at each angle is collected by numerically integrating along the path of the tube (Figure 1).

$$D(\theta, a) = \frac{\sum_n R^{m_n} e^{-a \left(x_n + \frac{L - x_n}{\cos(\theta)} \right)}}{e^{-La}} \quad (5)$$

where a is the absorption coefficient, L is the optical pathlength of the tube, R is the reflectivity of the tube, x_n is the distance from the entrance window of the tube to the n th point, and m_n is the number of times light scattered at that point and angle would reflect off the wall of the tube. We must then multiply this factor by any chosen volume scattering function $\beta(\theta)$, normalize by

the total scattering coefficient and integrate over θ to obtain the scattering error, $e_s(\theta_a)$, relative to the total scattering coefficient as a function of acceptance angle, θ_a , of the detector.

$$e_s(\theta_a, a) = 1 - \frac{2\pi}{b} \int_0^{\theta_a} \beta(\theta) D(\theta, a) \sin(\theta) d\theta \quad (6)$$

This equation was numerically integrated. It applies to the reflective tube absorption meter and to spectrophotometers using the 10 cm cylindrical sample cell and a large area diffuser in front of the detector.

The best spectrophotometers for measuring particulate absorption use an integrating cavity which collects all light passing out of the exit face of the sample cell. If the 10 cm cell is used this is still the same as the previous example. If a 1 cm cell is used then the light collected is limited only by the Fresnel reflection of light off the exit face of the sample cell. Thus scattered light is collected up to about 51° . However, 1 cm is generally too short a pathlength to get a significant signal from natural samples. So this method is usually used only with laboratory cultures or by artificially concentrating the sample. To examine the errors of this method, the Fresnel reflection equations were applied to the water/glass and glass/air interfaces to yield the transmittance of the exit window as a function of scattering angle. This function was then convolved with the volume scattering function and integrated as in the previous analysis.

Many spectrophotometers designed only for absorption of dissolved substances use a cylindrically limited light beam and then focus the transmitted light on the detector or diode array with no effort directed specifically at collecting scattered light. The angular efficiency of these systems depend on the geometry of the light stops, lenses and detectors, but can be no better than the reflecting tube design. In general, they are much worse, perhaps collecting scattered light out to only 10° . Thus they have a large scattering error and, with no method of measuring the scattering itself, are useless for measuring particulate absorption.

A prototype of the modern reflective-tube absorption meter had an acceptance angle of 30° and a tube reflectivity of $95\%^2$. Recent improvements⁷ have increased the acceptance angle to 41° . Theoretically, 100% reflectivity can be accomplished by using a reflecting tube consisting of glass with an air pocket behind it as in the new absorption meters⁷ or with the 10 cm sample cell in a spectrophotometer with a large diffusive collector. Fresnel reflection then gives 100% reflection to about 41° . All designs considered here are for 25 cm pathlength instruments. A 10 cm instrument would yield slightly lower scattering errors, but with a loss of sensitivity. A combination of these geometry considerations and a volume scattering function model allow us to calculate errors via equation (2).

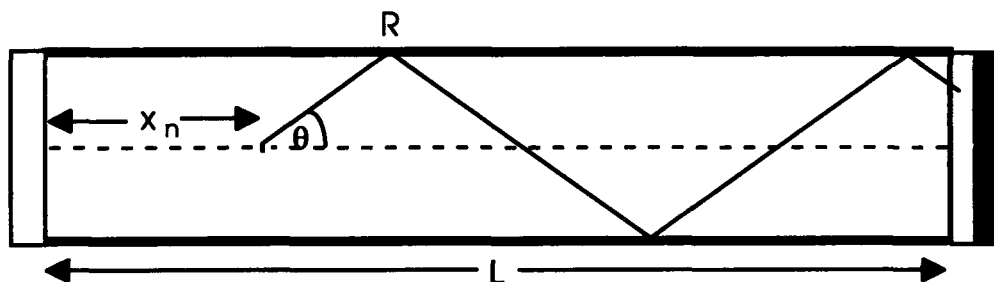


Figure 1. Principle of the reflective-tube absorption meter

4. VARIATIONS IN VOLUME SCATTERING FUNCTIONS

Six models of inherent optical properties based on power law size distributions ($dN = N_0 D^{-s} dD$) have been examined. The parameter s is the exponent (or slope) of the size distribution. The first three models come from size distributions observed during the ODEX cruise⁸ in the Pacific Central Gyre. The "Chl Max" was observed⁹ at the chlorophyll maximum near 100 m depth and the exponents of its size distribution were 3.63 from 2 to $6.6 \mu\text{m}$ diameter and 4.96 from 6.6 to $16 \mu\text{m}$ diameter. Slopes for the "Mixed Layer" (0-50 m) were similarly 2.97 and 5.41 and for the "Deep" water (125 m) were 3.92 and 4.96. The Mie scattering was computed for three layered spheres¹⁰ with an outer layer with thickness 10% of the radius and an index of refraction equal to 1.09 with no absorption. The core radius was 80% of the radius of the inside of the shell. The core had an

index of refraction of 1.02. The layer between the core and the shell had an index of refraction of approximately 1.09 (adjusted to reflect the anomalous dispersion effect) and had an imaginary component as well to model an absorbing chloroplast layer. The real part of the index of refraction for the chloroplast layer used here is different from that used by Kitchen and Zaneveld¹⁰ because the higher index appears to be more reasonable^{11,12}. The Mie scattering was computed on the above size distributions extrapolated from 0.5 to 30 μm diameter.

The particles in the bottom nepheloid layer (BNL) are assumed to be detrital particles. Therefore, we modeled the BNL using a homogeneous sphere with an index of refraction of $1.09 - 0.005i$ and a particle size distribution exponent (as defined above) of 5. In order to bracket the possible volume scattering function shapes we calculated the errors for two extreme cases. We also used uniform slopes of 3.0 and 5.0 with our 3-layered sphere Mie model. The former might represent a diatom bloom in coastal upwelling areas, while the other might represent a population dominated by bacteria and small phytoplankton.

5. RESULTS

5.1 Calculation of θ_a and θ_c for various reflecting tube characteristics and scattering functions.

The scattering errors for a collimated beam c meter as a percentage of the total scattering coefficient are computed (Table I) by integrating the volume scattering function for particles out to the acceptance angle (modeled at 0.4° or 0.9°) of the detector divided by the total scattering. Table II displays the results of our calculations as described in the first paragraph for various absorption meter designs with varying reflectivities of the reflecting tube and assuming no detection of scattered light beyond the angle given. Again the percentages given are percentages of the total scattering coefficient that are erroneously included in the absorption measurement for the design with the reflection coefficient and maximum acceptance angle as given. Calculations for a total absorption coefficient of 0.400 m^{-1} were carried out for all designs. The absolute value of the absorption coefficient only contributes to the error via the correction for increased pathlength of the scattered photons which appears to be minimal for $a = 0.400 \text{ m}^{-1}$ and is seen (Figure 2) to be only a weak influence on the error, since the error only increases slowly with increasing absorption coefficient.

Table I Scattering errors for attenuation meters for the six models of particle size distribution

	c Meter Errors (θ_c)	
	$\theta_c = 0.4^\circ$	$\theta_c = 0.9^\circ$
"BNL"	0.24%	1.12%
"Chl Max"	1.18%	5.28%
"Mixed Layer"	1.36%	6.24%
"Deep"	1.02%	4.90%
SL=3	4.80%	16.90%
SL=5	0.42%	1.97%
Median	1.10%	5.09%

5.2 Dependence of θ_a and θ_c on b/a using an average correction.

Values of a_m were computed for the various designs and water types assuming $c_w = a_w = 0.364$ and $a_n = 0.036$. b_n was assigned values of 1,2,4,8 and 16 times a_n . Then a_n^* was computed using equation (2) assuming the median scattering corrections for each design as displayed in tables I and II yielding the following algorithms:

$$a_n^* = 1.1379(a_m - 0.364) - 0.1379(c_m - 0.364) \quad \text{for } R = 95\%, \theta_{\max} = 30^\circ, \theta_c = 0.9^\circ \quad (7)$$

$$a_n^* = 1.1063(a_m - 0.364) - 0.1063(c_m - 0.364) \quad \text{for } R = 95\%, \theta_{\max} = 41^\circ, \theta_c = 0.4^\circ \quad (8)$$

$$a_n^* = 1.0416(a_m - 0.364) - 0.0416(c_m - 0.364) \quad \text{for } R = 100\%, \theta_{\max} = 41^\circ, \theta_c = 0.4^\circ \quad (9)$$

Table II. Scattering errors for absorption meters for the six models of particle size distribution.

	a Meter Errors (θ_a)				
	$a_n + a_{\pi} = 0.400$				
	R=95%, $\theta_{\max} = 30^\circ$	R=95%, $\theta_{\max} = 41^\circ$	R=100%, $\theta_{\max} = 30^\circ$	R=100%, $\theta_{\max} = 41^\circ$	Best Spectro-
"BNL"	18.0%	14.0%	9.9%	4.1%	3.2%
"Chl Max"	10.8%	8.9%	6.6%	3.8%	3.0%
"Mixed Layer"	8.9%	7.3%	5.3%	3.0%	2.3%
"Deep"	12.2%	10.1%	7.6%	4.4%	3.4%
SL=3	8.9%	7.3%	5.9%	3.6%	2.9%
SL=5	18.6%	15.2%	12.0%	7.0%	5.6%
Median	11.50%	9.50%	7.10%	3.95%	3.10%
from Petzold					
Gyre deep	16.6%	13.5%	13.5%	8.4%	6.1%
Coastal mixed	12.2%	10.0%	9.3%	5.7%	4.2%
Harbor	17.0%	14.2%	13.8%	9.2%	6.9%
Average	15.3%	12.6%	12.2%	7.8%	5.7%

The resulting relative percent errors in absorption coefficients (Figure 3) as a function of b_p/a_p show the relative importance of angular acceptance and tube reflectivity on the accuracy of the absorption computed in this manner. The error for uncorrected absorption measurements from the spectrophotometer with integrating cavity and the 1 cm cell (Figure 3d) is similar to that for the poorer designs of reflecting tube. We show the uncorrected error for the spectrophotometer since attenuation measurements are not usually available for spectrophotometric measurements. Also shown are similar calculations using volume scattering functions from Petzold¹³. Values from the first degree were not included in b since there are known diffraction errors in Petzold's instrument. The errors using these measured volume scattering functions are higher than our modeled values indicating that we may not have included small enough particles in our model or that we don't have the distribution of particle structures close enough. However, the relative behavior of the errors with water type and the size of the variation are quite similar between our models and Petzold's data.

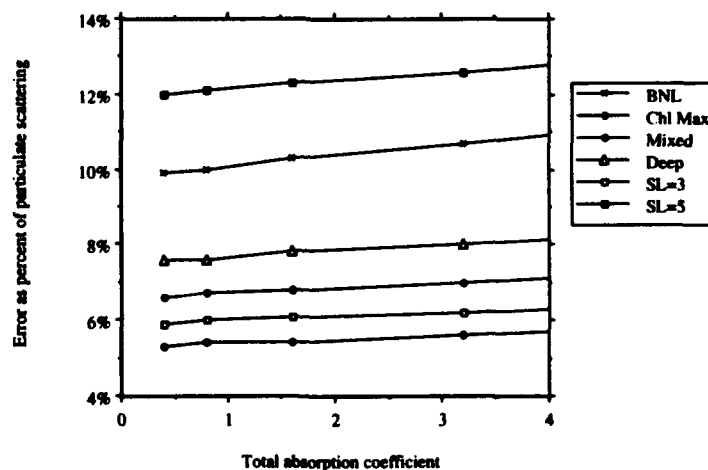


Figure 2. Effect of the total absorption coefficient on the scattering error.

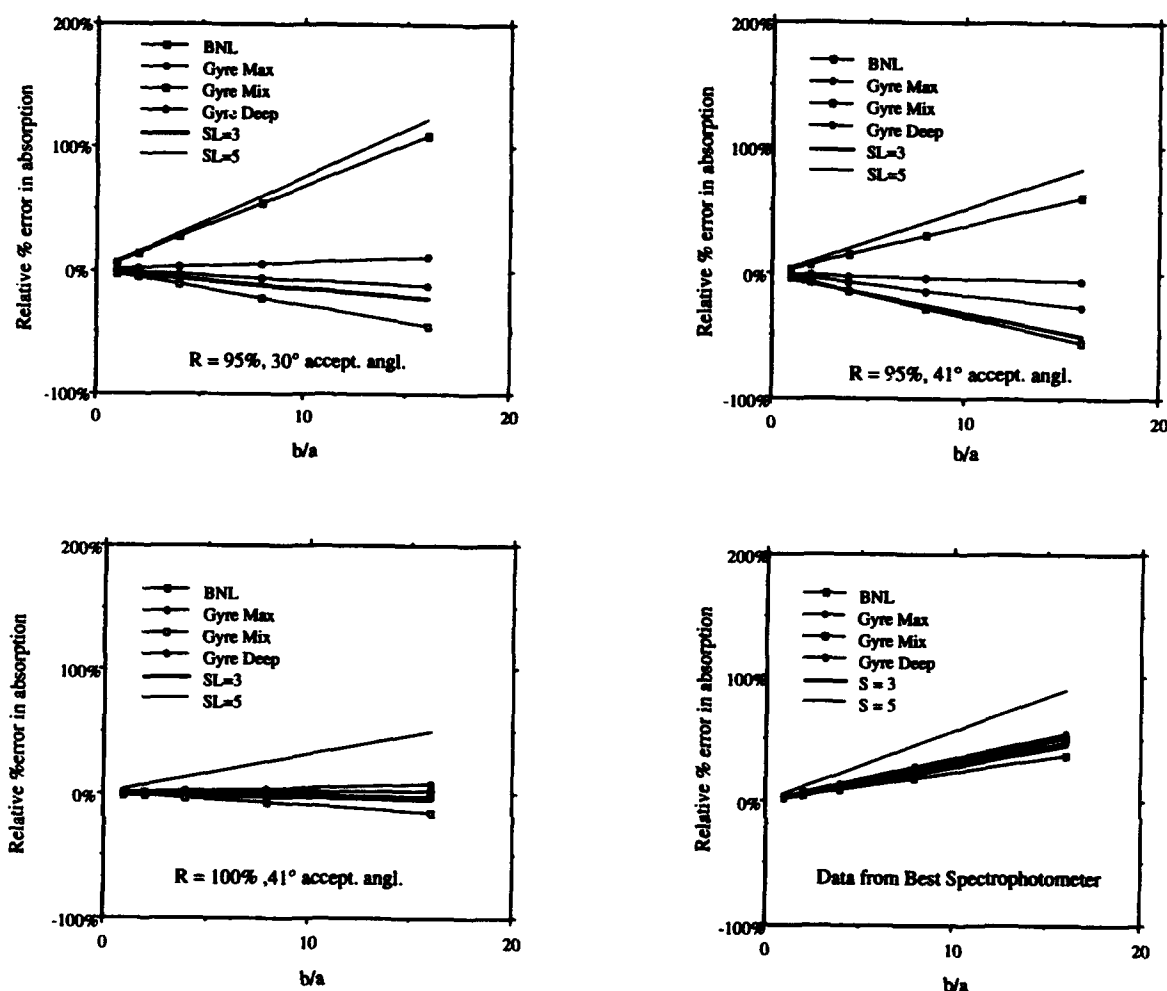


Figure 3. Errors in the corrected absorption after correcting for the scattering error using the median correction (see Tables I and II) except for (d) which is not corrected since attenuation data is not normally available for spectrophotometers.

5.3 A correction scheme using measured absorption in the near-infrared.

For what follows we assume that pure water absorption and attenuation have been subtracted. For a given wavelength, λ , the absorption tube overestimates the absorption coefficient as it does not measure all of the scattered light. Designate the proportion of the total scattering coefficient that the device does not receive by $e_a(\lambda)$. If the shape of the scattering function does not change much, we may assume that $e_a(\lambda)$ is not a function of λ .

We assume that the fraction of the scattered light not received by the absorption meter is independent of wavelength. We designate the *true* absorption coefficient at a wavelength by $a_t(\lambda)$, and the *measured* absorption coefficient by $a_m(\lambda)$. Similarly $c_t(\lambda)$ and $c_m(\lambda)$ are the true and measured attenuation coefficients, respectively. We define the scattering coefficients similarly:

$$b_t(\lambda) = c_t(\lambda) - a_t(\lambda) \quad (10)$$

$$b_m(\lambda) = c_m(\lambda) - a_m(\lambda) \quad (11)$$

Assuming that e_a and e_c are not functions of λ , we then set:

$$a_t(\lambda) = a_m(\lambda) - e_a b_t(\lambda), \text{ and} \quad (12)$$

$$c_t(\lambda) = a_t(\lambda) + b_t(\lambda) = c_m(\lambda) + e_c b_t(\lambda). \quad (13)$$

We now subtract equation (12) from (13):

$$b_t(\lambda) = b_m(\lambda) + b_t(\lambda)[e_c + e_a], \quad (14)$$

so that:

$$b_t(\lambda) = b_m(\lambda)/(1 - e_c - e_a) \quad (15)$$

We see that the measured scattering coefficient spectrum, $b_m(\lambda)$, is proportional by a constant $[1/(1 - e_c - e_a)]$ to the true scattering spectrum. We may then conclude that:

$$b_t(\lambda_1)/b_t(\lambda_2) = b_m(\lambda_1)/b_m(\lambda_2) \quad (16)$$

We thus see that the acceptance angle of the attenuation meter is immaterial, given the assumptions above.

We now assume that there is some reference wavelength, λ_r , at which the absorption coefficient (excluding the already subtracted water component) is zero. For the present we set $\lambda_r = 712$ nm, although there may be better choices further in the infrared.

Thus,

$$a_t(\lambda_r) = 0 \quad (17)$$

Substitution of equation (17) into (12) gives: $a_m(\lambda_r) = e_a b_t(\lambda_r)$. (18)

Hence,

$$e_a = a_m(\lambda_r)/b_t(\lambda_r). \quad (19)$$

Substitution of equation (19) into (12) gives:

$$a_t(\lambda) = a_m(\lambda) - a_m(\lambda_r) \frac{b_t(\lambda)}{b_t(\lambda_r)} \quad (20)$$

Substitution of equation (16) into the above gives:

$$a_t(\lambda) = a_m(\lambda) - a_m(\lambda_r) \frac{b_m(\lambda)}{b_m(\lambda_r)} \quad (21)$$

Note that we can thus determine the true absorption coefficient at any wavelength, assuming that the ratios of the absorption and attenuation scattering errors to total scattering are not a function of wavelength. We do not need to know the fraction of scattered light not received by the attenuation meter, i.e. we need not know e_c . This correction scheme will be designated as the "proportional" correction scheme in the remainder of the paper.

For spectrophotometric work one normally cannot take into account the spectral variations in $b(\lambda)$. One simply subtracts the absorption at the reference wavelength. This then would imply that $b_m(\lambda_r) = b_m(\lambda)$ from equation (12), an unnecessary assumption in our case. This standard spectrophotometric correction scheme will be designated as the "constant" correction scheme in the remainder of the paper.

A source of spectral change in the shape of the volume scattering function is the presence of absorption bands¹². Anomalous dispersion near absorption bands cause changes in the real part of the index of refraction and thus the volume scattering function. To model this, we used the particle size distribution and chloropigment content of particles from the chlorophyll maximum in Central Gyre of the Pacific Ocean⁹. This should be a good estimate of the maximum influence of anomalous dispersion on the correction of absorption meters. The optical model used was a three-layered sphere¹⁰ with a high-index of refraction outer shell, a middle layer containing the absorbing pigments and an inner layer with low-index of refraction cytoplasm. For the volume scattering functions produced by this model, the proportional correction method still produces smaller errors on average than the constant correction method. This is especially true for the fine detail of the spectral structure (Figure 4).

Figure 4 indicates that the blue part of the spectrum may be better matched by the constant correction method. Thinking that this may be due to the larger relative optical size at shorter wavelengths reducing the effective scattering error, we carried out a test for homogeneous non-absorbing spheres with two different size distributions. The results (Table III) still show the proportional correction scheme outperforming the constant subtraction scheme. We conclude that the low error in the constant subtraction method at 412 nm for the phytoplankton model was due to the reduced index of refraction caused by being on the short wavelength side of the 443 nm absorption peak.

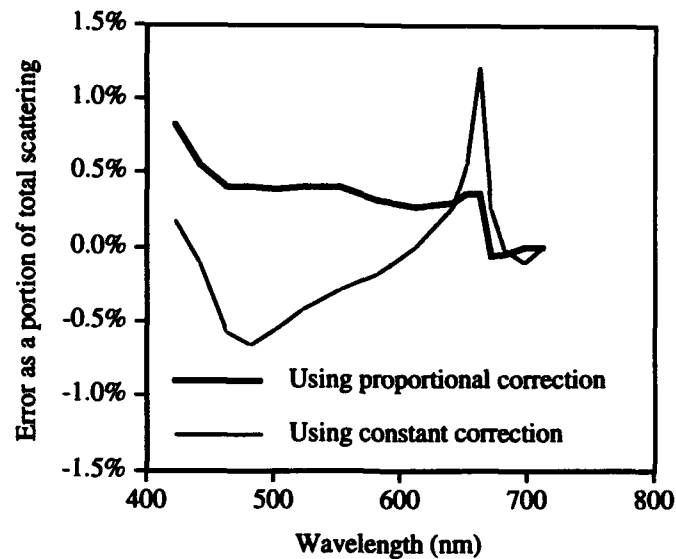


Figure 4. Errors produced by the proportional and constant correction schemes for a volume scattering function derived from an anomalous dispersion model of the phytoplankton maximum in the central gyre.

Table III. Residual scattering errors after correcting by a constant $a(715)$ and by the proportion $a(715)/c(715) \times b(\lambda)$ for homogeneous spheres with indices of refraction of 1.1875 and 1.05 relative to water.

wavelength	412 nm		560 nm	
method	constant	proportional	constant	proportional
index of refraction				
	Slope = 3			
1.1875	0.60%	-0.07%	0.32%	0.04%
1.05	0.23%	0.10%	0.12%	0.06%
	Slope = 5			
1.1875	16.23%	-4.04%	10.43%	-1.32%
1.05	9.47%	-3.19%	6.25%	-1.07%
	Kneed, Slopes = 3,5			
1.1875	1.04%	-0.26%	0.53%	-0.11%
1.05	0.26%	0.02%	0.12%	-0.01%

5.4 The effect of temperature on the scattering error correction of a reflecting tube absorption meter.

In the derivations of section 5.3, it was assumed that the measurements were carried out at the same temperature at which the calibration was carried out. Pegau and Zaneveld¹⁴ showed that the absorption of light by pure water in the near infrared is strongly temperature dependent. Maximum temperature dependence was found at 745 nm. A commonly used reference wavelength for reflective tube absorption meters is 715 nm. The absorption coefficient of water at that wavelength is also temperature dependent. The temperature dependence was found to be linear in the temperature range encountered in the ocean¹⁵. This temperature dependence at 715 nm was measured to be $0.0035 \text{ m}^{-1}/^{\circ}\text{C} = S(715)$. We need to derive the effect of this temperature dependence on the correction factor.

Let $a_i(\lambda_r)$ be the instrumental output at the reference wavelength $\lambda_r = 715$ nm for the calibration temperature T_{cal} . The value measured at a different temperature will be designated by $a_i(\lambda_r, T)$. We then find that for the absorption of pure water we may set:

$$a_w(\lambda_r, T) = a_w(\lambda_r, T_{cal}) + S(715)(T - T_{cal}). \quad (22)$$

The value determined by the instrument at a temperature T is due to the true absorption coefficient $a_t(\lambda, T)$ from which the absorption due to water at the calibration wavelength was subtracted and to which the scattering error must be added, so that

$$a_i(\lambda, T) = a_t(\lambda, T) - a_w(\lambda, T_{cal}) + e_a b_t(\lambda, T). \quad (23)$$

Eq. 23 is also true at the calibration temperature, so that

$$a_i(\lambda, T_{cal}) = a_t(\lambda, T_{cal}) - a_w(\lambda, T_{cal}) + e_a b_t(\lambda, T_{cal}). \quad (24)$$

We will assume that light scattering is not a function of temperature, so that $b_t(\lambda, T) = b_t(\lambda, T_{cal})$. Subtracting equations 23 and 24 then gives:

$$a_i(\lambda, T) - a_i(\lambda, T_{cal}) = a_t(\lambda, T) - a_t(\lambda, T_{cal}). \quad (25)$$

Equation 1 showed that the true absorption coefficient is equal to the water absorption plus the non-water absorption. We will assume that the non-water absorption is not a function of temperature, although nothing is known about the temperature dependent absorption of yellow matter or pigments. Subtracting equation 10 for T_{cal} from equation 10 for T then gives:

$$a_t(\lambda, T) - a_t(\lambda, T_{cal}) = a_w(\lambda, T) - a_w(\lambda, T_{cal}), \quad (26)$$

so that

$$a_t(\lambda, T) - a_t(\lambda, T_{cal}) = S(\lambda)(T - T_{cal}), \quad (27)$$

from equation 22. Using equation 25 then gives:

$$a_i(\lambda, T_{cal}) = a_i(\lambda, T) - S(\lambda)(T - T_{cal}). \quad (28)$$

We are now ready to return to our earlier final result, equation 21, which is valid at the calibration temperature.

$$a_n(\lambda, T_{cal}) = a_i(\lambda, T_{cal}) - a_i(\lambda_r, T_{cal}) [b_i(\lambda, T_{cal}) / b_i(\lambda_r, T_{cal})]. \quad (29)$$

We note once again that light scattering is assumed to be not a function of temperature, so that the temperature designation can be deleted for the scattering coefficients as the values are the same for any temperature. Similarly we assumed that the non-water absorption is not a function of temperature. Using these assumptions and equation 28, equation 29 can be transformed into:

$$a_n(\lambda) = a_i(\lambda, T) - S(\lambda)(T - T_{cal}) - [a_i(\lambda_r, T) - S(\lambda_r)(T - T_{cal})] [b_i(\lambda) / b_i(\lambda_r)]. \quad (30)$$

Under most circumstances $S(\lambda)$ will be considered to be zero except at the reference wavelength, although this is strictly speaking not correct. Pegau and Zaneveld¹⁵ found that at 600nm, for instance $S(\lambda) = 0.0015 \text{ m}^{-1} \text{ }^\circ\text{C}^{-1}$.

As an example we see that if $\lambda_r = 715$ nm and hence $S(\lambda_r) = 0.0035 \text{ m}^{-1} \text{ }^\circ\text{C}^{-1}$ and if the instrument was calibrated with water at 15°C and the measurement was made at 25°C, equation 30 becomes:

$$a_n(\lambda) = a_i(\lambda, T) - [a_i(\lambda_r, T) - 0.035] [b_i(\lambda) / b_i(\lambda_r)]. \quad (31)$$

The non-water absorption so determined thus is larger by $0.035 [b_i(\lambda) / b_i(\lambda_r)]$ (or approximately 0.035 m^{-1}) than if the original equation 12b had been applied without concern for the temperature effect on the absorption of pure water. The temperature effect can be very large in spectrophotometers if the reference water is at room temperature and the sample water is much colder. Pegau and Zaneveld¹⁴ showed that for $\lambda_r = 750$ nm, this can lead to large apparently negative absorption coefficients.

5.5 Use of a scattering sensor to correct a reflecting-tube absorption meter

It may be possible to incorporate a simple scattering sensor into a reflective-tube absorption meter. Any scattering sensor would measure a weighted integral of the volume scattering function between a lower limit and an upper limit. Here we will consider the weighting function to be unity and will study the effect of varying upper and lower limits only. The signal from such a sensor would correlate to a greater or lesser degree with the scattering error depending on how well it matched the angular distribution of the error. To study this, we revert to our six models of the volume scattering function and introduce five different angular ranges that a scattering meter could conceptually measure. For each combination of angular range and volume scattering function we compute the portion of b that is included in that range. Then, for each reflective tube design and angular range of the scattering sensor, we can correlate the scattering error with the scattering signal for the six volume scattering functions. The

resulting regressions are shown in Table IV. The output of the scattering sensor is given by "B" and the absolute magnitude of the scattering error is given by b_e .

TABLE IV Regression equations, squared correlation coefficients and maximum residual errors for prediction of b_e/b for various instrument designs.

a-Meter Design	Scat. Sensor Range	Regression Equation for 6 models of $\beta(\theta)$	r^2	<u>max err</u> b
$\theta_a = 30^\circ$, R=95%	10-30°	$\frac{b_e}{b} = 0.0407 + 0.250 B/b$	0.868	0.023
	20-60°	$= 0.0300 + 0.736 B/b$	0.949	0.016
	41-90°	$= 0.0199 + 3.135 B/b$	0.627	0.054
	90-180°	$= 0.0752 + 7.258 B/b$	0.250	0.065
	120-160°	$= 0.0869 + 18.24 B/b$	0.173	0.064
$\theta_a = 41^\circ$, R=95%	10-30°	$= 0.0446 + 0.331 B/b$	0.912	0.021
	20-60°	$= 0.0293 + 0.559 B/b$	0.912	0.016
	41-90°	$= 0.0155 + 2.555 B/b$	0.695	0.038
	90-180°	$= 0.0585 + 6.199 B/b$	0.304	0.048
	120-160°	$= 0.0679 + 15.84 B/b$	0.218	0.047
$\theta_a = 30^\circ$, R=100%	10-30°	$= 0.0339 + 0.176 B/b$	0.746	0.022
	20-60°	$= 0.0249 + 0.401 B/b$	0.813	0.018
	41-90°	$= 0.0055 + 2.103 B/b$	0.816	0.022
	90-180°	$= 0.0356 + 5.812 B/b$	0.463	0.032
	120-160°	$= 0.0427 + 15.62 B/b$	0.367	0.032
$\theta_a = 41^\circ$, R=100%	10-30°	$= 0.0282 + 0.059 B/b$	0.285	0.020
	20-60°	$= 0.0238 + 0.145 B/b$	0.358	0.019
	41-90°	$= -0.0007 + 1.263 B/b$	0.993	0.003
	90-180°	$= 0.0116 + 4.267 B/b$	0.842	0.010
	120-160°	$= 0.0153 + 12.11 B/b$	0.744	0.013

The most significant finding in Table IV is that almost all of the regression intercepts are significant. This indicates that a change in scattering sensor signal due to a change in shape of the VSF will mean a different a-meter error than the same change in scattering sensor signal due to a change in total scattering coefficient. We see this from:

$$e_a = \frac{b_e}{b} = A_1 + A_2 \frac{B}{b} \quad \text{yields} \quad b_e = A_1 b + A_2 B \quad (32)$$

which means that we need to know b in order to apply the above regressions. We remind the reader that e_a is the proportion of scattered light not detected by the absorption meter. Thus by using a poorly matched scattering sensor we are no better off than by using a simultaneous measurement of c and the proportional correction scheme. If we are using all three instruments, we now have three equations in three unknowns and can arrive at a better estimate of a . However, a well matched scattering sensor such as the 41-90° sensor for the 100% reflective tube a-meters does give a negligible intercept (so that $A_1 = 0$) and a small residual error, indicating that it would provide a very good estimation of the correction, b_e , without a c measurement. For combinations with a significant intercept, the residual column probably represents the uncertainty using both the scattering sensor and a c -meter to correct a .

To apply the above, it would be necessary to document the actual performance of the absorption meter and then design a scattering sensor to match the scattered light not detected. Neither of these tasks are necessarily easy. Finally, the actual regression between the signal from the scattering sensor and scattering error would have to be determined experimentally. In the end though, it would correct much of the variation due to changes in the shape of the volume scattering function that the simultaneous measurement of a and c and application of the proportional correction scheme does not address.

6. LABORATORY CONFIRMATION

In order to verify the above error analysis we compared the attenuation and apparent absorption of polystyrene spheres with the results of Mie theory calculations of their volume scattering functions in our model of instrument performance. Assuming a 100% reflectance resulted in agreement only at rather low acceptance angles for the absorption meter (Figure 5). However, decreasing the reflectance of the tube to 95% results in agreement at angles very close to the design criterion of 41° . For the $0.5\ \mu\text{m}$ particles the 95% reflectance also results in a much closer agreement in the spectral shape of the measured and predicted results. The improvement in spectral shape at the other two sizes is not appreciable. The $0.5\ \mu\text{m}$ particles provide the best test of the angular inclusion of the absorption meter since the small particles have the highest proportion of large angle scattering. The reduced reflection could be due to imperfections on the outside of the glass tube or by some of the scattered light being intercepted by the O-rings between the end of the glass tube and the receiver window.

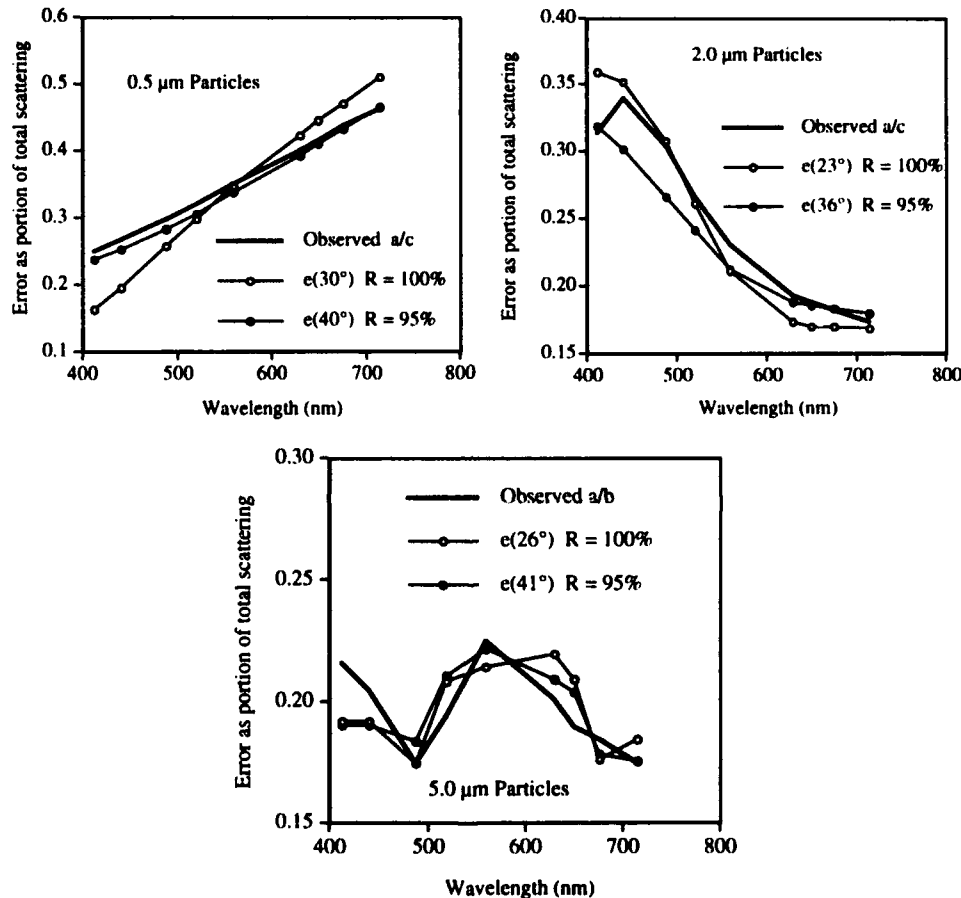


Figure 5. Measured a/c and computed portion of scattering in various angular ranges for three different calibration particles.

7. SUMMARY.

In situ reflecting tube absorption meters have allowed us for the first time to obtain continuous vertical profiles of the absorption coefficient in natural waters. The reflecting tube absorption meter has almost the same geometry as a spectrophotometer with a cuvette. The main difference is that the absorption meter uses a collimated beam whereas most spectrophotometers do not. In addition, reflecting tube absorption meters are usually combined with beam attenuation meters.

The geometry of the reflecting tube results in some of the scattered light not being collected by the detector. This undetected light is the scattering error. The scattering error can be estimated in a number of ways, which we examine. We show that the only available correction method for an absorption meter without attenuation measurements or a spectrophotometer is the

constant correction method in which the measured absorption at a wavelength in the near infrared is subtracted. A better correction is obtained if attenuation is measured simultaneously and the absorption at the reference wavelength is multiplied by the ratio of the measured scattering at a given wavelength divided by the measured scattering coefficient at the reference wavelength. This is called the proportional correction method as it takes into account variations in the scattering coefficient as a function of wavelength.

We showed that the important geometrical parameters of the reflecting tube can be obtained by a comparison of measurements and models of polystyrene beads. Finally we examine the improvements that could be obtained if a direct scattering measurement was made simultaneously with the absorption and attenuation measurements. Obviously, if a measurement could be made that nearly exactly matches the light that is not measured by the absorption meter, the absorption coefficient could be measured nearly exactly. The scattering measurement then could also be corrected to be nearly perfect from the collimation angle onward.

8. ACKNOWLEDGEMENTS

The support of the Ocean Optics division of the Office of Naval Research (Grant No. N00014-93-1-0649) is gratefully acknowledged.

9. REFERENCES

1. C. S. Yentsch "Measurement of visible light absorption by particulate matter in the ocean," *Limnol. Oceanogr.*, 7, 207-217; 1962; J. R. V. Zaneveld and R. Bartz. "Beam attenuation and absorption meters," *Ocean Optics VII*, Proc. Soc. Photo Opt. Instrum. Eng., 489, 318-324, 1984; J. R. V. Zaneveld, J. C. Kitchen, A. Bricaud and C. Moore. "Analysis of *in situ* spectral absorption meter data," *Ocean Optics XI*, G. D. Gilbert, Ed., Proc. Soc. Photo Opt. Instrum. Eng., 1750, 187-200, 1992.
2. J. R. V. Zaneveld, R. Bartz and J. C. Kitchen, "Reflective-tube absorption meter," *Ocean Optics X*, Proc. Soc. Photo Opt. Instrum. Eng., 1302, 124-136, 1990.
3. K. J. Voss and R. W. Austin, "Beam-attenuation measurement error due to small-angle scattering acceptance," *J. Atmos. Ocean. Tech.*, 10, 113-121, 1993.
4. W. S. Pegau, J. R. V. Zaneveld and K. J. Voss, "Towards closure of the inherent optical properties," Submitted to *J. Geophys. Res.*
5. D. Bogucki, T. D. Dickey, A. Domaradzki and J. R. V. Zaneveld, "Light scattering induced by turbulent flow," *Ocean Optics XII*, Proc. SPIE, this issue.
6. e.g. A.C. Tam. and C. K. N. Patel, "Optical absorptions of light and heavy water by laser optoacoustic spectroscopy," *Appl. Opt.*, 18, 3348-3358, 1979.
7. C. Moore, J. R. V. Zaneveld and J. C. Kitchen "Preliminary results from an *in situ* spectral absorption meter data," *Ocean Optics XI*, Proc. SPIE 1750, 330-337, 1992.
8. H. Pak, D. W. Menzies and J. C. Kitchen, *Optical Dynamics Experiment (ODEX) data report, R/V Acania expedition 10 October-17 November 1982*, Ref. 86-10, College of Oceanography, Oregon State University, Corvallis, 1986.
9. J. C. Kitchen and J. R. V. Zaneveld, "On the non-correlation of the vertical structure of light scattering and chlorophyll *a* in Case I waters," *J. Geophys. Res.*, 95, 20237-20246, 1990.
10. J. C. Kitchen and J. R. V. Zaneveld, "A Three-Layered Sphere Model of the Optical Properties of Phytoplankton," *Limnol. Oceanogr.*, 37, 1680-1690, 1992.
11. E. Aas, "The refractive index of phytoplankton," Univ. Oslo Rep. Ser. 46 61 p., 1981.
12. J. R. V. Zaneveld and J. C. Kitchen. "The effects of anomalous dispersion and diffraction on the inherent optical properties near an absorption peak as determined by various models of phytoplankton structure". Submitted to *J. Geophys. Res.*
13. T. J. Petzold, *Volume scattering functions for selected ocean waters*. SIO Ref. 72-28, 79 pp., 1972.
14. W. S. Pegau and J. R. V. Zaneveld "Temperature dependent absorption of water in the red and near infrared portions of the spectrum," *Limnol. Oceanogr.* 38, 188-192, 1993.
15. W. S. Pegau and J. R. V. Zaneveld, "Temperature dependence of the absorption coefficient of pure water in their visible portion of the spectrum," *Ocean Optics XII*, Proc. SPIE, this issue.

Three-dimensional reconstruction of ocean chlorophyll distributions from underwater serial sectioned fluorescence images

Andrew W. Palowitch and Jules S. Jaffe

Marine Physical Laboratory
Scripps Institution of Oceanography, La Jolla, CA 92093-0205

ABSTRACT

An underwater optical serial sectioning system has been developed to measure in-situ three-dimensional distributions of biological particles. The technique involves scanning a thin plane of laser light sequentially through a range of distances parallel to the imaging plane of a digital CCD camera. Images of induced fluorescence in the sequentially illuminated planes are recorded. A computer based inverse program is then used to reconstruct three-dimensional chlorophyll *a* distributions from the plane images. The inverse method compensates for attenuation of the fluorescence excitation and emission throughout the volume and converts camera image plane intensity values to mg Chl *a*/m³. Graphic display of the composite data set with spatial resolution of 1 cm³ in a 20 x 20 x 20 cm volume is presented in a three-dimensional rendered volume. Chl *a* concentration discrimination of 0.1 mg Chl *a*/m³ over the range of 0.1 to 2.0 mg Chl *a*/m³ has been demonstrated in the laboratory with the optical serial sectioning system. The combination of high spatial and intensity resolution indicates future potential for in-situ phytoplankton microstructure analysis and further application to the study of ocean inherent water properties.

1. INTRODUCTION

The in-situ evaluation of three-dimensional biological microstructures requires sampling techniques with fine resolution which do not disturb the distributions during sampling as do conventional water bottle and fluorometer techniques. An underwater optical serial sectioning system, conceptually depicted in Figure 1, images induced 685 nm Chl *a* fluorescence emission in sequential two dimensional planes to develop a three-dimensional Chl *a* distribution data set. The serial sectioning data acquisition and three-dimensional reconstruction process is based upon an imaging model of the underwater optical process and has been shown to accurately account for spatial variability in optical properties through mathematical volumetric reconstruction steps.¹

2. 3D RECONSTRUCTION THEORY

A three step process model serves as the foundation for the three-dimensional reconstruction algorithm. The first step is fluorescence excitation which describes the propagation of excitation light through the underwater medium. The second step is the intercellular Chl *a* fluorescence process which includes excitation light absorption and fluorescence emission. The third step is fluorescence emission which describes the propagation of the fluoresced light back to the imaging system. In the development of the fundamental equation, an arbitrarily selected differential volume, dV , located in plane k , receives fluorescence excitation irradiance along path $R1$ from the light source. Conversion of the excitation light to fluoresced light takes place in the Chl *a* contained within this small differential volume. Fluoresced light travels to the camera image plane along path $R2$. Each differential volume within plane k contributes to the

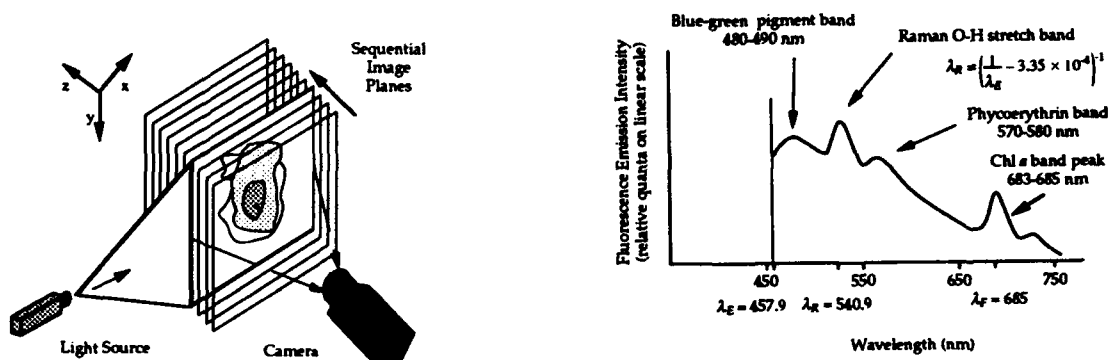


Figure 1. Serial sectioning configuration and emission spectrum from 457.9 nm excitation.

image only that amount of fluoresced light that is accepted by the small solid angle formed by the camera lens along path $R2$. The full image of plane k that is recorded by the camera is the sum of the fluorescence contributions of all differential volumes that compose plane k . An expression for the fluorescence generation process that begins the development of the reconstruction algorithm expresses the radiance imaged by the camera at the fluorescence wavelength in terms of the original radiance at the excitation wavelength, the intercellular conversion factors and the light path attenuation

$$E_{I\lambda_F} = L E_{0\lambda_E} \exp \left(- \int_{R1} \{ a_\phi(r, \lambda_E) + c_i(r, \lambda_E) \} dr \right) C(dV) a_{c\lambda_E} \Delta x \Phi_f P \times \exp \left(- \int_{R2} \{ a_\phi(r, \lambda_F) + c_i(r, \lambda_F) \} dr \right) \quad (1)$$

$E_{I\lambda_F}$ represents the excitation irradiance received at the camera from dV in terms of the source irradiance $E_{0\lambda_E}$. The total loss factor, L , combines the excitation and fluorescence path losses. The attenuation associated with the fluorescence excitation and emission are represented in the exponential integrals over path lengths $R1$ and $R2$ respectively. The attenuation terms in the exponents of Eq. (1) are presented as a non-chlorophyll dependent spectral attenuation coefficient subtotal, $c_i(\lambda)$, and a phytoplankton absorption term, $a_\phi(\lambda)$ divided as follows from the absorption contributions of the water, a_W , dissolved organic matter, a_D , and detritus, a_X .

$$a(\lambda) + b(\lambda) = a_W(\lambda) + a_D(\lambda) + a_\phi(\lambda) + a_X(\lambda) + b(\lambda) = a_\phi(\lambda) + c_i(\lambda) \quad (2)$$

Linking the two attenuation path expressions together are terms that convert the excitation irradiance, E_{λ_E} , to the fluorescence emission, E_{λ_F} . The conversion process includes the absorption of the incident irradiance, the fluorescence yield, and the fractional amount of fluoresced light emitted along path $R2$ in the solid angle accepted by the camera lens,

$$E_{\Delta\lambda_F} = E_{\lambda_E} C_{(dV)} a_{c\lambda_E} \Delta x \Phi_f P \quad (3)$$

where the absorption of the incident irradiance, over the dimension, Δx , of the differential volume, dV , is given by the concentration of Chl a , $C_{(dV)}$ (mg Chl a/m^3), times the specific absorption coefficient, $a_{c\lambda_E}$ (m^2/mg Chl a).^{2,3} The quantum yield of fluorescence, ϕ_f , represents the ratio of the quanta of photons fluoresced to the quanta of photons absorbed. The factor P incorporates the structure of the volume fluorescence function, β_ϕ , and geometric spreading of the fluoresced light.

Equation (1) is solved for implementation into a Chl a calculation and volumetric reconstruction program by substituting in discrete voxel dimensions, completing an approximation to transition from the integral to a summation representation, rearranging terms, and evaluating the natural logarithm of both sides of the equation to yield

$$\ln \left[\frac{\iint_{[\cdot]} \Psi(x_n, z_m) dx dz}{\kappa} \right] = \ln (C(x_n, z_m) \Delta x \Delta z) - a_{c\lambda_E} \sum_{i=1}^{n-1} C(x_i, z_m) \Delta x - c_{i\lambda_E} (n-1) \Delta x \\ - a_{c\lambda_F} \sum_{j=1}^{m-1} C(x_n, z_j) \Delta z - c_{i\lambda_F} (m-1) \Delta z \quad (4)$$

where κ , a conversion constant, is defined as

$$\kappa = L E_{0\lambda_E} a_{c\lambda_E} \Delta x \Phi_f P \quad (5)$$

The attenuation terms previously expressed exponentially are now separated into Chl a dependent and independent components in a linear format. In a simple expression, Eq. (4) can be presented as

$$\mathbf{i} = \ln \mathbf{c} + \mathbf{A} \mathbf{c} + \mathbf{x} \quad (6)$$

The attenuation matrix, \mathbf{A} , contains terms composed of specific absorption values. When \mathbf{A} is multiplied by the Chl a column vector, \mathbf{c} , the term $\mathbf{A} \mathbf{c}$ contains a Chl a dependent absorption coefficient term for every voxel in the volume. The attenuation column vector, \mathbf{x} , is composed of non-Chl a dependent attenuation coefficient terms. With known or assumed Chl a levels, attenuation coefficient values, and volume dimensions, \mathbf{i} can be readily computed from Eq. (6). The inverse solution of Eq. (6) however with only image values, \mathbf{i} , known (as with serial section image acquisition), is difficult to solve explicitly due to the incorporation of the logarithmic term. In general, the equation format does not lend itself to solution for the Chlorophyll column vector \mathbf{c} except through iterative means. The attenuation matrix, \mathbf{A} , though, for this imaging scenario has a zero diagonal providing a method for solution. With a lower triangular form of the attenuation matrix \mathbf{A} coupled with a backsubstitution solution method, \mathbf{c} can be calculated voxel by voxel starting with voxel (1,1). This iterative solution method establishes a mechanism to analyze the inverse solution analytically. When divided by a system calibration constant, X , a compensated image intensity value, K , is defined from Eq. (6) image column vector components as

$$K = \frac{\iint_{[.]} \Psi(x_n, z_m) dx dz}{\kappa \cdot X} \quad (7)$$

The Chl *a* level in the voxel that is located at any arbitrary *x-z* plane origin, voxel (1,1), can be solved for by using the first elements in the associated vectors and matrices rewritten as

$$K_{(1,1)} = C_{(1,1)} \exp(A_1 C_{(1,1)} + x_1) \quad (8)$$

For voxel (1,1) the attenuation path lengths are zero leading to the solution for voxel (1,1) of

$$K_{(1,1)} = C_{(1,1)} \quad (9)$$

For voxel (1,2) located one attenuation voxel back in the *z* direction the solution for $C_{(1,2)}$ is

$$C_{(1,2)} = \frac{K_{(1,2)}}{\exp(A_2 K_{(1,1)} + x_2)} \quad (10)$$

In a similar manner, the Chl *a* concentration in any voxel throughout the *x-z* plane can be calculated in terms of the previous attenuation path voxels as

$$C_{(x_n, z_m)} = \frac{K_{(x_n, z_m)}}{\exp - \left(\sum_{i=1}^n a_{c\lambda_E}(K_{(x_i, z_m)}) + \sum_{j=1}^m a_{c\lambda_F}(K_{(x_n, z_j)}) + (n-1) c_{l\lambda_E} \Delta x + (m-1) c_{l\lambda_F} \Delta z \right)} \quad (11)$$

3. SERIAL SECTIONING EXPERIMENTS

A general diagram of the volumetric imaging system designed for laboratory verification of the serial sectioning method is depicted in Figure 2. The two main components of the system are the illumination source, a Spectra Physics Model 164 Argon Ion Laser, and the imaging sensor, a Photometrics Series 200 camera with a 1024 x 1024 Thompson CCD chip. Testing was conducted in a glass tank as shown with prepared water samples of varying Chl *a* concentrations. The laser beam was expanded into a thin vertical plane and positioned along the length of the glass tank by means of a lead screw driven linear positioner. The water samples containing various phytoplankton and prepared Chl *a* concentrations used for system testing were analyzed by using standard fluorometer methods for Chl *a* levels.

The Spectra Physics Model 164 laser used in the system produced a 506 mW output at 457.9 nm which was selected to coincide with the peak of the Chl *a* absorption spectrum. A series of lenses was used on the linear positioner table to transform the round laser spot into the thin sectioning illumination plane. Lens combinations varied during the optical serial sectioning experiments depending on the size of the sample volume, the desired illumination plane thickness, and the distance between the linear positioner and the sample tank. Adjustments in lens configuration were made to maintain the uniform intensity distribution across the plane. Prior to commencing testing in each new configuration, a radiometric quality digitally acquired beam profile was produced to document the variation of excitation illumination for the reconstruction process. Beam profile analysis showed that across the width of the illumination plane 97.4% of the laser power was contained within the desired 1 cm thick central plane. Along the vertical axis

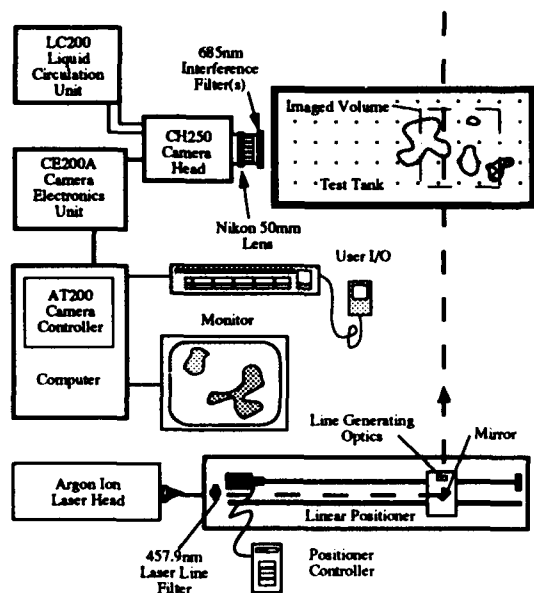


Figure 2. Serial Sectioning System Layout

Although dark current noise is minimized through the use of -35°C thermoelectric cooling, it is still significant when at levels comparable to electronic preamplifier or photon shot noise when long integration times are used for low light levels. Since the dark current noise can not be isolated during the imaging event, it was measured prior to and subtracted digitally pixel-by-pixel from each acquired image.

The overall objective for laboratory tests of the optical serial sectioning system was to validate the serial sectioning imaging technique by comparing acquired three dimensional Chl *a* distribution images with actual measured values. An initial progression of tests was completed verifying the following imaging capabilities of the serial sectioning system which were initially established as goals for system performance

- | | |
|-----------------------------|--|
| 1. Chl <i>a</i> range | 0.1 to 2.0 mg Chl <i>a</i> /m ³ |
| 2. Chl <i>a</i> sensitivity | 0.1 mg Chl <i>a</i> /m ³ |
| 3. Spatial resolution | 1 cm x 1 cm x 1 cm |
| 4. Sample volume size | 1m x 1m x 1m |

4. PERFORMANCE CHARACTERIZATION

Additional tests were designed to characterize the performance of the system with respect to the interdependent parameters of effective volume, spatial resolution, and temporal resolution. With the sensitivity and noise levels of the camera directly limiting overall performance, techniques such as pixel binning and increasing integration time were both used to improve image SNR and extend the effective range of the imaging system and consequently the maximum volumetric capability for three-dimensional phytoplankton distribution evaluation.

A divided tank configuration was established to allow the creation of a variable attenuation path with a fixed image plane concentration. In one set of tests, pure water filled the attenuation section of the tank creating a

in the 1 cm central plane, a 4.6% variation in peak energy was measured.

The Photometrics Series 200 camera used in the serial sectioning system maximized the capability for low light level imaging with a three stage thermoelectric (Peltier) cooler, a fixed 200K readout speed, 14 bit resolution, and a 0.04% response linearity over the camera's full dynamic range. An image focused on the CCD parallel register produces a pattern of electron charge in proportion to the total integrated flux incident on each photosite.

Each $19\text{ }\mu\text{m} \times 19\text{ }\mu\text{m}$ photosite (pixel) in the array performed as a separate photometer recording, digitally, the number of imaging events during the open shutter integration time. Dark field subtraction was used during image capture to improve the quality of the image data and overcome inherent camera hardware noise sources. Dark field subtraction compensates for thermally generated charge developed by interface states at the silicon-silicon dioxide interface just below the parallel gate structure.

uniform attenuation path of $c = 0.534 \text{ m}^{-1}$. Various uniform Chl a concentrations from 0.1 to 2.0 mg Chl $a \text{ m}^3$ were then imaged in the adjacent tank section. A 1 cm wide laser illumination plane and a fixed camera and filter configuration were used for all of the tests. Since initial results indicated that low concentration level detection was the limiting imaging condition and that CCD potential well saturation would not be a problem, a 4x camera gain was selected. Single plane images were taken for these experiments. Each plane image was dark field image compensated. In the first set of tests, 4 x 4 binning was established which provided a data set for resolution capability better than 1 cm^3 at a range of 1 meter and an SNR improvement over single pixel image recording. With spatial resolution held constant, integration (exposure) time was varied from 10 to 4000 msec with Chl a image plane concentrations of 0.16, 0.68, 1.25, and 2.13 mg Chl $a \text{ m}^3$. The median from the histogram of pixel ADU values for each plane image was plotted versus exposure time.

The resulting plots all possessed highly linear relationships. Deviations in linearity were only seen at short exposure times where very low SNRs were registered. The linear quality of the plots permitted the extrapolation and prediction of minimum image exposure times. Based upon acquired signal and noise data, an SNR level of 5.0 was selected as minimum acceptable for verifiable image detection. A review of the data sets shows that as the concentration level decreased, the minimum acceptable single image exposure time increased from 100 msec (2.13 mg Chl $a \text{ m}^3$) to 1000 msec (0.16 mg Chl $a \text{ m}^3$). This minimum time can be multiplied by the number of planes to determine the total time to image a complete volume. Applicability to in-situ analysis can be judged from the overall volume image time compared to the expected vertical and horizontal phytoplankton migration times, internal wave speeds, and currents.

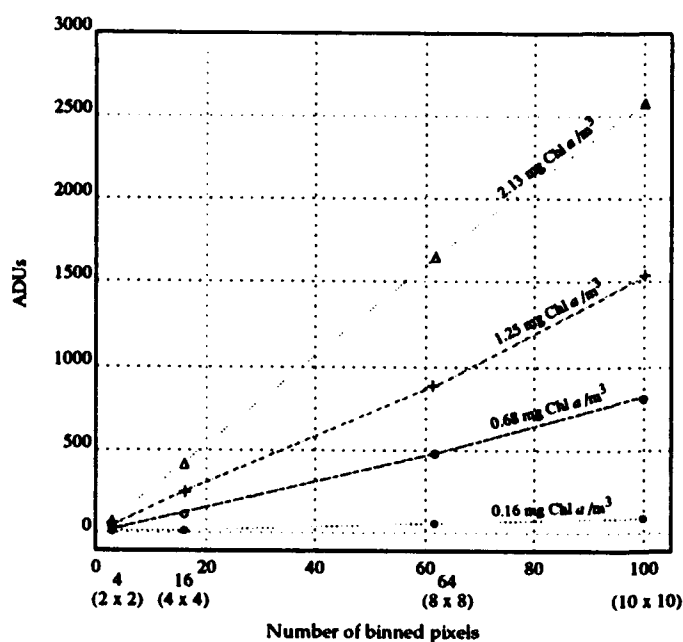
Further testing was conducted with the same configuration as the variable exposure set except that exposure time now was held constant while binning was varied from 2 x 2 through 4 x 4 and 8 x 8 to 10 x 10. Results from this set of tests for the same range of Chl a concentrations are shown in Figure 3. ADUs are plotted versus variation in binning. For the 1 meter x 1 meter image plane geometry with a 1024 x 1024 pixel CCD, 10 x 10 binning yields the 1 cm x 1 cm pixel size identified as the spatial resolution objective. SNRs for all concentrations at this binning level are significantly above the minimum 5.0 level. The data from Figure 3 further indicate that for the attenuation paths used in these tests, resolution to 0.4 cm x 0.4 cm is possible with a 4 x 4 binning at 0.16 mg Chl $a \text{ m}^3$ and the specified attenuation path.

The determination of a minimum imaging speed at the spatial resolution and Chl a concentration goals was conducted using 10 x 10 binning and a 0.09 mg Chl $a \text{ m}^3$ sample. Exposure times were varied from 10 to 4000 msec. Results are displayed in Figure 4. Using linear interpolation, an exposure time of 220 msec correlates with the minimum acceptable 5.0 SNR. This result shows that the use of 10 x 10 binning provides an improvement of over four times in volume imaging speed from the previous 4 x 4 binning configuration while maintaining the imaging objective 1 cm x 1 cm resolution at less than or equal to 0.1 mg Chl $a \text{ m}^3$.

A non-dimensional parameter, the optical depth, for the system which can be used for defining the system's imaging application to the range of naturally occurring seawater conditions was then determined using a similar laboratory test configuration. Since the performance limiting process is the fluorescence attenuation from the illuminated plane to the camera focal plane due to the large value of $c_w(685)$ a system optical depth, ξ , is defined as

$$\xi = c(685) z \quad (12)$$

where c is the beam attenuation coefficient at 685 nm and z is the distance from the illumination plane to the



BIN	PIXEL SIZE (cm)	SNR / (ADU)			
		0.16	0.68	1.25	2.13
2 x 2	0.2	3.4 (18)	8.1 (43)	11.7 (68)	16.7 (110)
4 x 4	0.4	5.1 (26)	19.2 (135)	28.6 (251)	38.4 (423)
8 x 8	0.8	10.9 (62)	41.9 (495)	58.6 (924)	81.0 (1705)
10 x 10	1.0	15.4 (98)	55.5 (830)	77.0 (1535)	160.3 (2583)

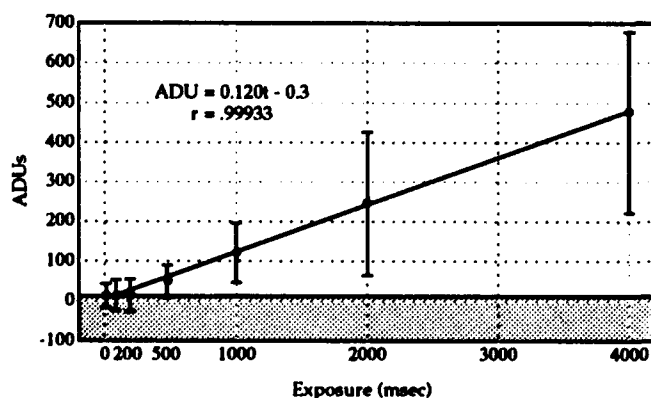
Figure 3. Evaluation of minimum acceptable images at various concentrations and spatial resolutions. With a 5.0 minimum acceptable SNR, 0.4 cm resolution was achieved at a concentration as low as 0.16 mg Chl a/m^3 .

camera image plane. Applied to the general equation

$$E(z) = E(o) e^{-\xi} \quad (13)$$

the optical depth defines the system's ability to image in waters of various attenuation properties.

An experimental determination of the minimum ξ for the system was accomplished by varying the attenuation properties and distances in an attenuation portion of a divided tank to get the minimum acceptable image SNR level of 5.0 for an image of 0.1 mg Chl a/m^3 in the imaging section of the tank. Several distances and concentrations were used to confirm the measurement. The value of $\xi = 0.97$ was determined as the effective optical depth for the system in the configuration of 4x gain, 10 x 10 binning, 35



Performance Characterization 0.09 mg Chl a/m^3 15 June 1993			
200 x 200 PIXELS		Gain 4x	Bin 10 x 10
Exposure Time (msec)	Range (ADU's)	Median	SNR
10	-21 to 43	12	2.1
100	-26 to 45	12	2.1
200	-28 to 51	17	3.2
500	11 to 95	53	9.6
1000	40 to 193	118	17.5
2000	63 to 431	245	28.0
4000	220 to 680	480	41.2
4000 Background	-22 to 44	12	

Figure 4. Minimum exposure time determination for 1cm³ resolution at 0.1 mg Chl a/m^3 concentration

A laser power, and $f = 1.8$. The overall system optical depth increases with the minimum Chl a level desired for imaging. The optical depth value can be used to determine application of the system for in-situ distribution analysis. For a coastal water mass with an average $c_{(685)} = 1.1 \text{ m}^{-1}$ the effective imaging range of the would be 0.88 m. Images with $0.1 \text{ mg Chl } a/\text{m}^3$ would have to be acquired at distances closer than 0.88 m for adequate SNR. Images for greater Chl a levels could be acquired at longer distances. For open ocean conditions with a representative average value of $c_{(685)} = 0.7 \text{ m}^{-1}$, the optical depth of 0.97 equates to an effective range of 1.4 meters.

5. VOLUMETRIC VISUALIZATION

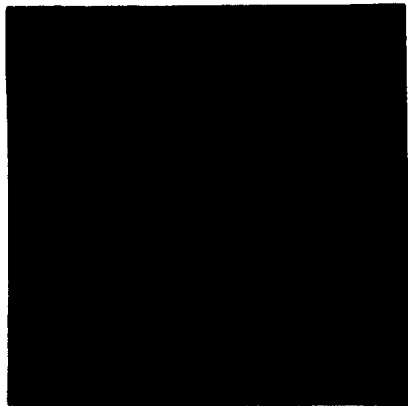
As a test of the application of serial sectioning on random phytoplankton distributions, various strains of phytoplankton with measured Chl a concentrations were injected into laboratory tank sample volumes to simulate phytoplankton patches. Serial sectioning was performed on the sample volume while maximizing the system operating parameters to achieve 1 cm spatial resolution and the highest temporal resolution. The volume samples were made of various concentrations of cultured phytoplankton, unfiltered seawater, and distilled water. After a sample volume was prepared in the test tank, 20 one centimeter wide images, each $20 \text{ cm} \times 20 \text{ cm}$ with a full image 1024×1024 pixels, were taken sequentially through the volume to generate a volumetric data set. Camera gain was $4\times$, $f = 1.8$, and 35 A laser power was used for illumination. Either a 4×4 or a 10×10 camera binning was used to experiment with spatial resolution. Exposure times were varied between 100 msec and 2000 msec to evaluate volume imaging speed and resultant SNRs. The reconstruction algorithm was verified by correlation of the imaged patch concentrations to sample fluorometer readings.

The data from one imaged volume is presented as an example of the process. A sample volume, see Figure 5, was prepared from a test tank of unfiltered seawater drawn from the SIO pier. The seawater had a $1.06 \text{ mg Chl } a/\text{m}^3$ concentration. A volume of a *Gonyaulax polyedra* culture measured at $2.18 \text{ mg Chl } a/\text{m}^3$ was injected with a pipette into the lower portion of the tank. A volume of warm distilled water was floated on top of the seawater. Differential temperatures were used to slow the mixing process and maintain the highest possible concentration differences. A $12 \text{ cm} \times 12 \text{ cm} \times 12 \text{ cm}$ volume in the center of the larger test volume was selected for analysis with 1 cm spatial resolution as the goal. Camera binning was set at 4×4 . Exposure time was 2000 msec per image. Twenty image planes were acquired and saved as sets of camera ADU values. Binning reduced the data sets to 256×256 each.

Three-dimensional reconstruction of the volumetric data set was first accomplished by increasing the data set to 260×260 data points with the addition of four rows and four columns. The data set was then reduced by averaging 13×13 sets of pixels to get a data set of 20×20 . A 12×12 section of the 20×20 data set was then isolated for analysis. Each data point in the reduced data set now represented 2704 original pixels as the product of 4×4 binning and 13×13 averaging. Each data point represented a 1 cm^3 voxel in the sample volume. The 12 data sets were then combined and processed with the Chlorophyll Computer Program which converted the intensity values to mg Chl a concentrations. Two points were used in the sample volume to determine the calibration coefficient for the volume reconstruction. The first was a $1.06 \text{ mg Chl } a/\text{m}^3$ value in the lower right hand corner of image plane 2. The second was a check point of $0.00 \text{ mg Chl } a/\text{m}^3$ from the top center of image plane 3. After reconstruction, the resultant data sets contained attenuation compensated mg Chl a/m^3 values. As a check on the reconstructed Chl a levels, comparison was made between post image fluorometer sample values and the calculated values. After the imaging experiment three 25 ml samples were drawn from specific areas in the sample volume and measured for Chl a level. Fluorometer readings taken prior to mixing and after imaging are compared to calculated voxel values near the sample point. A set of nine voxels adjacent to the sample point are

represented in the range of calculated values presented in Figure 5 data. The differences between measured and calculated values are attributed to mixing of the sample volume over time and to the inaccuracies associated with disturbing the distribution while drawing the post-imaging samples for fluorometer analysis.

The Sunvision program: voxvu was then used to take the 12 data sets and convert them into a three-dimensional graphic display of the reconstructed volume. Figure 5 shows image plane 9 as discrete voxels shaded to represent absolute levels of Chl *a* concentrations and illustrates an interpolation of the data used prior to volumetric reconstruction. The three dimensional reconstruction presents the correct spatial arrangement of the variation in Chl *a* concentration.



Chl <i>a</i> Concentrations (mg Chl <i>a</i> / m ³) Fluorometer Values				Calculated Voxel Values Near Sample Point (mg Chl <i>a</i> / m ³)
Sample	Before	Sample Point	After	
S	1.06	10,10,1	1.85	0.85 - 1.75
D	0.00	5,1,4	0.08	0.01 - 0.03
F	2.18	5,11,11	1.67	1.53 - 3.60

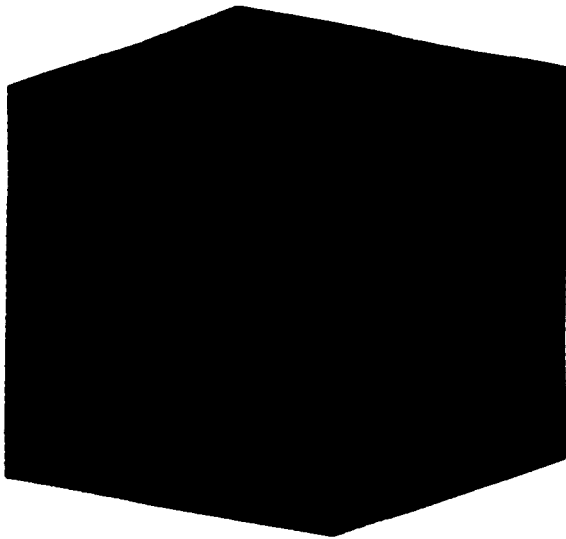
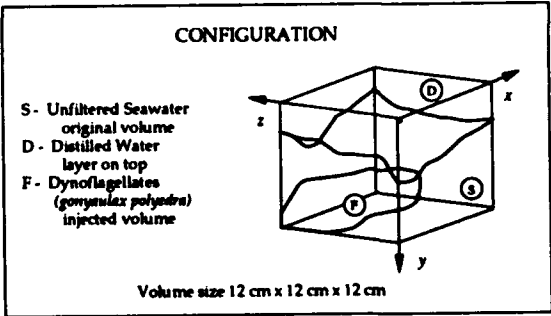


Figure 5. Volumetric visualization. Upper left: Image Plane 9 as discrete voxels. Middle left: Image Plane 9 as interpolated data. Lower left: Comparison of imaged/calculated values vs. measured values. Upper right: Test configuration. Lower Right: Three-dimensional visualization of Chl *a* distribution.

6. IN-SITU APPLICATIONS

The three-dimensional Chl *a* presentation shown in Figure 5 indicates that a spatially accurate reconstruction of Chl *a* variations is possible with the underwater serial sectioning system potentially leading to use as a Chl *a* microscale mapping tool. The remote sensing aspect permits in-situ Chl *a* microstructure information to be obtained without disturbing the naturally occurring phytoplankton distributions. The next significant biological step is to begin the evaluation of the correlation between Chl *a* concentration variations and phytoplankton distributions. As documented in many phytoplankton biomass studies, there are many problems with a one-to-one correlation between Chl *a* and biomass since there are numerous variable parameters involved with the Chl *a* fluorescence generation.

The performance characterization presented in Section 4 showed that performance improvements can be made individually to different system parameters. However, due to the interrelation of all system parameters they are at the expense of each other. For example, increasing the number of binned pixels to increase SNR and reduce exposure time is accomplished at a loss of spatial resolution. The minimum effective system optical depth of $\xi = 0.97$ determined at $0.1 \text{ mg Chl } a/\text{m}^3$ provides the capability to image one cubic meter distributions at one centimeter resolution. An important point about the optical depth determination conducted is that the value indicated is configuration specific. With an improvement in the 685 nm interference filter transmission, for example, ξ will improve due to the ability to get more imaging photons to the image plane. Reducing the spatial resolution with pixel binning also will improve ξ . On the contrary, an increase in the spatial resolution for small volumes would help reduce the boxy voxel representation during volumetric visualization. The final justification for resolution changes must be based though on the scientific requirements for verifying theoretically derived patch sizes.

A key consideration for applying optical serial sectioning in the ocean is the timing of image acquisition to meet expected biological and physical time scales. The rates of independent phytoplankton motion are relatively slow. Dinoflagellate movement has been placed at 1 cm/min. The sinking rate of phytoplankton is approximately 1 mm/min. Gas-filled vacuole algae vertical motion is about 5 mm/min. In relatively calm bodies of water, each of these motions could be adequately isolated with sectioned imaging at the 220 msec frame acquisition time at the ξ and design spatial resolution. Internal wave and current velocities have a much more serious effect on phytoplankton distributions. Vertical upwelling is characterized at 6 mm/min, but internal waves, for a $\Delta\rho$ of 1.4 kg/m^3 , travel at 60 m/min. Horizontal waves by comparison travel at 70 m/min. For open ocean near surface imaging, correct spatial arrangement may be more difficult to maintain due to these rapid water mass movements. Improvements in image frame time can be accomplished working at a system point less than ξ (by reducing the effective ranges and spatial resolution). Binning and closer ranges could improve acquisition time significantly if the loss of resolution and effective volume imaged did not impact the achievement of the biological survey objectives.

Other possible biological and physical oceanographic applications also exist. As currently configured, predator prey interactions could be studied and models verified. Localized phenomena such as red tides could be mapped over time. With some implementation modifications and using Chl *a* as a natural tracer, under-ice fresh water / salt water boundaries could be evaluated. A similar approach could be used for analyzing the effects of random fluctuations of turbulently generated shear on phytoplankton dispersion. Wind induced surface currents could possibly be tracked.

In the future, the system could be easily modified for multispectral analysis. In a preliminary laboratory analysis, scattered excitation illumination was correlated with the fluorescence illumination. An unfiltered image was acquired which showed a scattered light distribution. A sequential fluorescence image was acquired in the same plane with interference filters. Comparison between the two images showed the relative distributions of the amount of scattering (non-Chl *a* containing) material and the amount of

fluorescing (Chl *a* live biological) material in the plane. In addition to studying biological and physical processes, possibilities such as these exist for gaining insight into spatially varying inherent optical water properties with future multispectral scattering and absorption system modifications.

7. ACKNOWLEDGMENT

This work was supported by the Office of Naval Research (Ocean Optics) under grant N00014-93-1-0121 and N00014-89-J-141.

8. REFERENCES

1. Palowitch, A.W. and J.S. Jaffe, "Three dimensional ocean chlorophyll distributions from underwater serial-sectioned fluorescence images," *Appl. Opt.* **33**: 3023-3033, 1994.
2. Kirk, J.T.O., Light and photosynthesis in aquatic ecosystems, Cambridge University Press, Cambridge, 1983.
3. Morel, A., "Light and marine photosynthesis: A spectral model with geochemical and climatological implications," *Prog. Oceanogr* **26**: 263-303, 1991.

In situ spectral absorption profiler using optical fibers

T. Saito, A. Nishimoto, Y. Kakui, M. Nanjo

Life Electronics Research Center, Electrotechnical Laboratory
3- 11- 46, Nakoji, Amagasaki, Hyogo, 661, Japan

R. Tsuda

Department of Fisheries, Faculty of Agriculture, Kinki University
Nakamachi, Nara, 631, Japan

ABSTRACT

Phytoplankton spectral absorption of light energy is one of the important factors to estimate primary production of the ocean. We have developed a system which measures *in situ* spectral absorption of suspended matter mainly phytoplankton by a modified opal glass technique. The system was designed to provide sub meter-scale profile of phytoplankton distribution without water sampling. The system consists of halogen lamp as a white light source, a multi-channel spectrometer and submersible optical sensor unit. The collimating lens and diffuser constitute this unit. The optical fiber cables are employed to transmit the light between the sensor unit and the equipments on shipboard. The received light was measured by spectrometer which ranges from 400 nm to 800 nm with 1024-channel temperature stabilized linear photodiode array.

Our preliminary experiment with the cultured phytoplankton (diatoms, flagellate and green algae) has shown that minimum detectable absorption coefficient is 0.01 m^{-1} .

1. INTRODUCTION

The optical method plays important roles to obtain the continuous data of the temporal and the spatial distributions of the phytoplankton in terms of its species and concentration in the water environments. Since the phytoplankton has the specific absorption spectra according to the pigment constituent and concentration, it is useful for classifying the phytoplankton based on the photosynthesis pigment constituent. The conventional method measures absorption spectra of the phytoplankton collected on the filter after sampling and filtering water. Recently, the several methods for *in situ* measurement were reported to obtain reliable spectral absorption data; (1) a reflective tube absorption meter¹⁾, (2) an integrating cavity absorption meter²⁾, (3) a fiber-optic scanning spectrophotometer for measurement of aquatic light fields³⁾. The first two methods have difficulties in reducing the size of the measurement volume which contains the suspended phytoplankton in the water sample and therefore, can not give the fine spatial structure of the spectral absorption in the measurement. The third one has difficulties in reducing the measurement time because of the mechanism to scan the wavelength of the spectrometer. It is necessary to devise a method which reduces the measurement volume and time to obtain the spatial and temporal distribution of the spectral absorption

data in situ manner.

We have developed a new method that reduces the volume size and the time by adopting the configuration of the opal glass which catches effectively the absorption spectra in the radiation scattered by suspended phytoplankton particles, and of a multichannel photodiode array detector on which the spectral radiation is irradiated through a spectrometer. Moreover, adoption of optical fiber bundles enables the *in situ* measurement configuration. The errors in the absorption measurement are analyzed and estimated.

2. PRINCIPLE OF THE METHOD

The absorption is usually obtained to measure the transmittance of the parallel beam flux attenuated in the specified optical path length. This configuration gives the data of the absorption due to the medium such as water, and does not give the one to the suspended particles, because the absorption data is hidden in the radiation scattered by the particles. Fig.1 shows the principle of the opal glass transmission method described originally by Shibata⁵⁾, where the radiation scattered informs of the absorption by the particles. The data of the absorption by particles is extracted in the following, if an opal glass is ideally lambertian for whole wavelength range concerned, both the parallel transmitted flux and the forward scattered radiation are captured after passing through the opal glass.

The incident parallel flux $I_0(\lambda)$ is expressed by the sum of the absorbed flux in the sample $I_a(\lambda)$, the scattered total flux $I_d(\lambda)$, and the transmitted parallel flux $I_t(\lambda)$, as shown in eq.(1),

$$I_0(\lambda) = I_a(\lambda) + I_t(\lambda) + I_d(\lambda) \quad (1).$$

The incident flux suffers the absorption and scattering processes caused by the suspended particles, the water media, and the dissolved matter like so called yellow substances, so that the absorption coefficient $a(\lambda)$, and the scattering coefficient $b(\lambda)$ are expressed by

$$a(\lambda) = a_p(\lambda) + a_w(\lambda) + a_y(\lambda), \text{ and } b(\lambda) = b_p(\lambda) + b_w(\lambda) \quad (2)$$

where subscripts p, w, y are used to denote the contribution by particles, pure water and dissolved substance respectively.

When the incident flux travels the distance l , the absorbed flux I_a is approximated by

$$I_a(\lambda) = I_0(\lambda) (1 - e^{-a(\lambda)l}) \quad (3).$$

The incident flux on the opal glass $I(\lambda)$ consists of the transmitted flux $I_t(\lambda)$, and a fraction of the flux scattered into all direction as shown in eq.(4),

$$I(\lambda) = I_t(\lambda) + f I_d(\lambda) \quad (4)$$

where f denotes the ratio of the flux into the solid angle of the opal glass to the scattered flux into all direction. We denote these quantities corresponding to the reference water sample by attaching ' mark. If we assume that the opal glass diffuses nearly perfectly both I and I' , namely I_t , $f I_d$, I'_t , and $f' I'_d$, the ratio of

the flux into the solid angle of the sensing system to the whole flux transmitting the opal glass is approximately the same value x for the reference water and the sample water containing suspended particles. If we measure this flux by the spectral sensing system in terms of the sample water and the reference water respectively, the attenuation coefficient is obtained from the logarithm of the quotient of the detector's output for the reference $P'(\lambda)$ by that for the sample as shown $P(\lambda)$ in eq. (5) and eq. (6):

$$P(\lambda) = S(\lambda) \cdot \xi \cdot I(\lambda), \text{ and } P'(\lambda) = S(\lambda) \cdot \xi \cdot I'(\lambda) \quad (5),$$

$$A(\lambda) = \frac{1}{l} \ln \left(\frac{P'(\lambda)}{P(\lambda)} \right) = \frac{1}{l} \ln \left(\frac{S(\lambda) \cdot \xi (I_t(\lambda) + f I_d(\lambda))}{S(\lambda) \cdot \xi (I_t(\lambda) + f I_d(\lambda))} \right) \\ = \{a_s(\lambda) + a_p(\lambda)\} + \frac{1}{l} \ln \left\{ \frac{(1-f)e^{-b_w(\lambda)l} + f}{(1-f)e^{-(b_w(\lambda) + b_p(\lambda))l} + f} \right\} \quad (6),$$

where $S(\lambda)$ is the spectral sensitivity of the sensing system. Based on the reasonable assumption that the second term do not change with wavelength, the spectral absorption coefficient of the particles is obtained from the attenuation coefficient by subtracting the value independent of the wavelength.

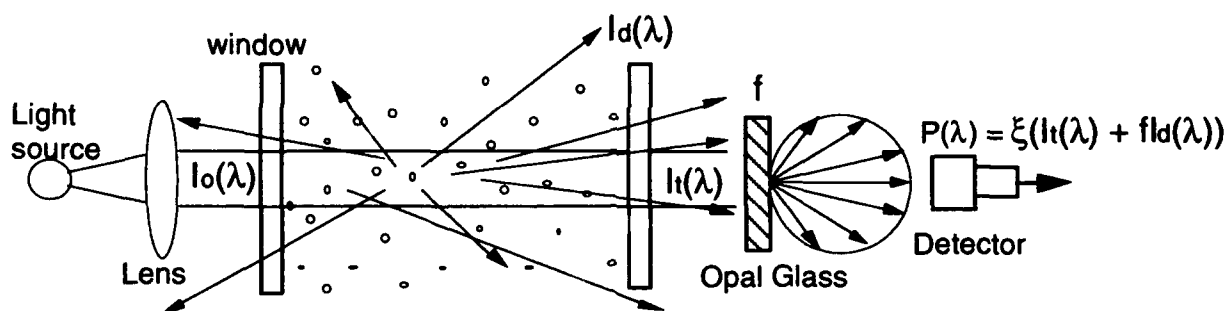


Fig.1. Optical design of opal glass transmission method.

3. INSTRUMENTAL SYSTEM

An optical fiber-coupled spectrometer of absorption was designed by considering advantages in ocean optics to obtain vertical profiles of spectral data with high spatial resolution. The measurement system located underwater is desirable to have relatively inexpensive and potentially passive components, while the system on a ship or a stationary platform is allowed to have relatively expensive and delicate components. Fig.2 shows a diagram of a prototype system for laboratory experiment. The system is composed of a light source, fiber optical cables, a sample cell, and a spectrometer with multichannel diode array detector, where the sample cell is intended to be submersed.

3.1. Light source and optical fiber cable

A tungsten halogen cycle lamp (24V, 150W) was used as a light source whose color temperature is changed by color filter so that the system has spectrally flat characteristics. Two optical bundled fiber cables

(200- μm silica core, polymer cladding, 0.22 N. A. Diaguide, Mitsubishi Cable Industries, Ltd.) in 1 m length were used to couple optically the sample cell with the light source and with the spectrometer unit. The fiber cable consisting of 16 fibers was shaped in circle type end and in slit type end for effective coupling to spectrometer, and the other cable was shaped in 8mm diameter for both ends.

3.2. Sample cell

The sample cell to be submersed *in situ* measurement should have simple structure screened from useless illumination without giving disturbances to surroundings. The sample cell used in the experiment was a methyl metacrylate cylinder of 50mm in diameter, 86mm in length, and 80ml in volume. The collimated beam from a bundle fiber illuminated the cell with the silica windows of 30mm in diameter, one of which was attached with the opal glass 30mm in diameter, and 2.3mm thick.

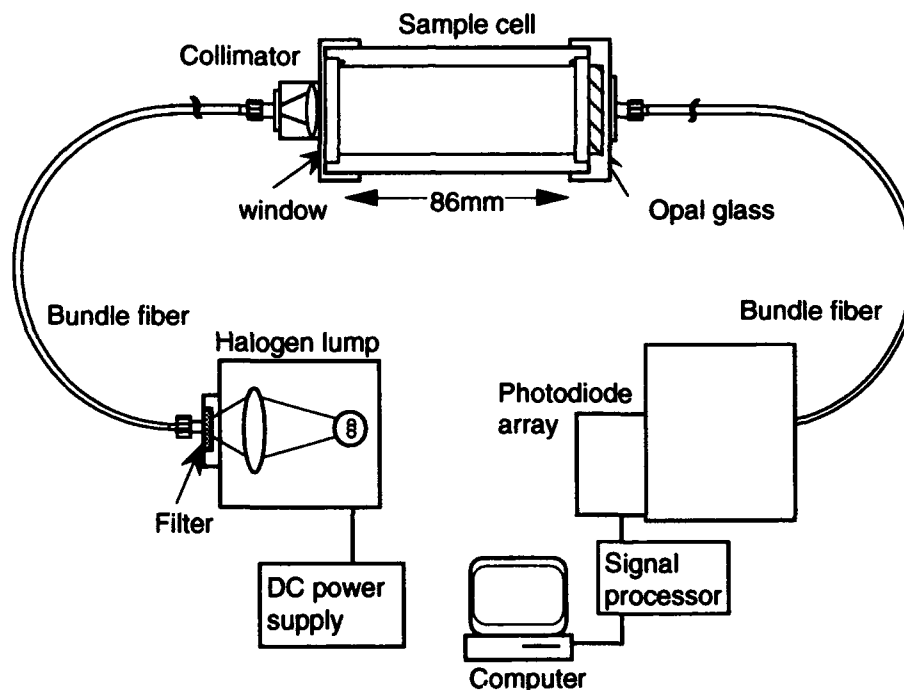


Fig. 2. Diagram of a prototype system for laboratory experiment.

3.3. Spectrometer and detector unit

This unit was composed of a polychromator, a linear photodiode array (PDA), and electronic processor, where the polychromator dispersed the light and focused a spectrum on the plane of the detector array surface. The polychromator of 16nm/mm in linear dispersion with 3nm in half width was calibrated with line spectra of a low pressure mercury lamp regarding the wavelength. The PDA has 1024 elements where each size is 25mm x 2mm in length. A scanning time of the diode array was 10ms to cover the whole wavelength range of 400 to 800nm and sampled at the interval of 0.25nm. The temperature of the photodiode detector was stabilized and cooled down to about 15 °C by a thermoelectric element to reduce thermal noise of the diode array. The photocurrent from the detector was digitized by a 16 bits analog to

the digitized output of which was accumulated to improve the signal to noise ratio. The spectral characteristic of the system made flat by using the color conversion filter.

4. EXPERIMENTAL RESULT AND ITS ANALYSIS

4.1. Measured output of the photodetector array

In case of the experimental system shown in Fig.2, the output from the detector is expressed by eq.(7) modified from eq. (5), by considering spectral characteristics of each subunit constructing the whole measurement system and also by taking account of the detector's offset $P_{\text{off}}(\lambda)$ measured in the absence of light.

$$P(\lambda) = S(\lambda) \cdot \xi \cdot I(\lambda) + P_{\text{off}}(\lambda) \quad (7),$$

where

$$S(\lambda) = D(\lambda) \cdot T(\lambda) \cdot J(\lambda)$$

$D(\lambda)$: Spectral sensitivity of photo diode array detector

$T(\lambda)$: Spectral transmittance of optical system, including optical fiber, polychromator and opal glass

$J(\lambda)$: Spectral irradiance of light source with color conversion filter.

The attenuation coefficient $A(\lambda)$ is obtained from

$$A(\lambda) = \frac{1}{l} \ln \left(\frac{P(\lambda) - P'_{\text{off}}(\lambda)}{P(\lambda) - P_{\text{off}}(\lambda)} \right) \quad (8).$$

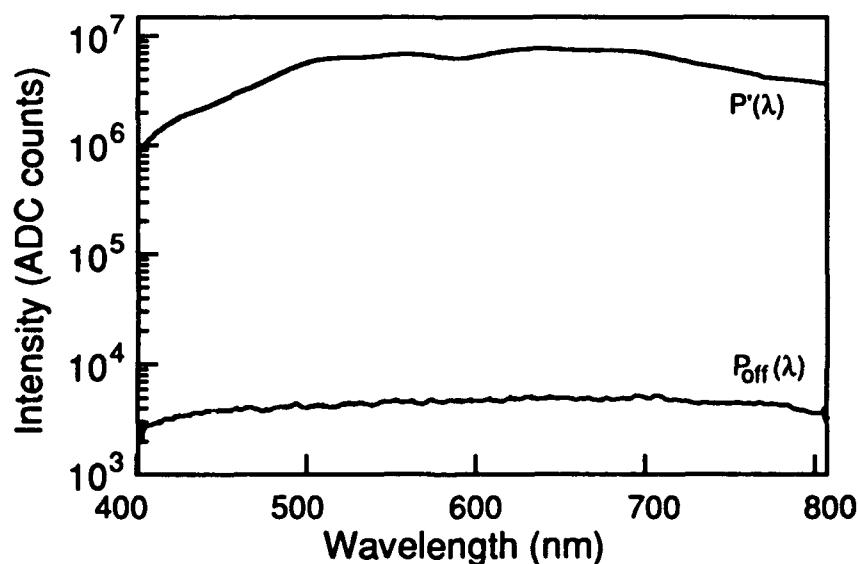


Fig.3. Photo diode array output (ADC output counts) of measuring the reference water $P'(\lambda)$ and the offset $P_{\text{off}}(\lambda)$.

Fig.3 shows a typical example of the output measuring the reference water $P'(\lambda)$ under the exposure time of 0.25 seconds corresponding to 256 accumulations at 15°C. Since the sample output $P(\lambda)$ was nearly equal to $P'(\lambda)$, and the difference between them was only less than 1% on this scale, it was too difficult to be shown in the same figure. $P_{\text{off}}(\lambda)$ is also shown in Fig. 3.

Fig. 4 shows a result of $A(\lambda)$ obtained where the cultured phytoplankton *Prorocentrum minimum* was suspended at different level of concentration. The vertical axis was scaled by absorption coefficient $a_p(\lambda) + a_y(\lambda)$ where the average value between 750nm and 800nm was subtracted from $A(\lambda)$.

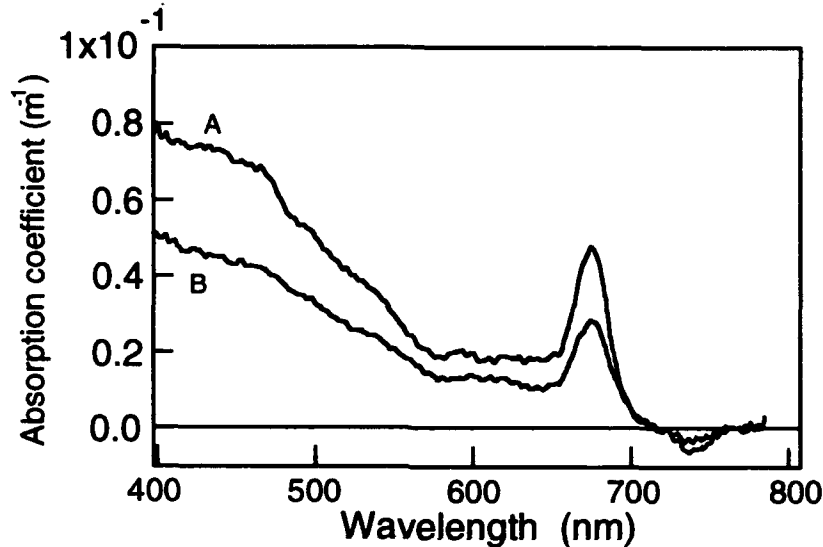


Fig. 4. Spectral absorption coefficient measured by the prototype system with the cultured phytoplankton *Prorocentrum minimum*, A:1000cell/ml, B:500cell/ml.

4.2. Estimation of the errors in the spectral absorption coefficient

From eq.(8), the errors are estimated by

$$|\Delta A(\lambda)| = \frac{1}{I} \left(\left| \frac{\Delta P(\lambda)}{P(\lambda)} \right| + \left| \frac{\Delta P_{\text{off}}(\lambda)}{P(\lambda)} \right| + \left| \frac{\Delta P'(\lambda)}{P'(\lambda)} \right| + \left| \frac{\Delta P_{\text{off}}'(\lambda)}{P'(\lambda)} \right| \right)$$

where

$$\left| \frac{\Delta P(\lambda)}{P(\lambda)} \right| = \left| \frac{\Delta P_{\text{off}}(\lambda)}{P(\lambda)} \right| + \left| \frac{\Delta J(\lambda)}{J(\lambda)} \right| + \left| \frac{\Delta T(\lambda)}{T(\lambda)} \right| + |\Delta a(\lambda)| \quad (9).$$

Consider that $P(\lambda)$ nearly equals to $P'(\lambda)$, eq.(9) is simply reduced to eq.(10).

$$|\Delta A(\lambda)| = \frac{1}{I} \left(4 \left| \frac{\Delta P_{\text{off}}(\lambda)}{P(\lambda)} \right| + 2 \left| \frac{\Delta J(\lambda)}{J(\lambda)} \right| + 2 |\Delta a(\lambda)| \right) \quad (10),$$

where the first term gives the error due to the offset, the second to the fluctuation of the light source and the third to the fluctuation of the absorption of the reference or the water itself.

(a) Effect of the offset

The main component of the offset generally results from the accumulation of thermally generated current. We estimated the error due to offset by taking the fluctuation of the photo diode outputs obtained in the series of measurements under dark condition. The error $\Delta P_{\text{off}}(\lambda)$ was evaluated by the standard deviation of the offset. Fig.5 shows the measurable minimum value of the absorption coefficient limited by this offset noise. The magnitude of the absorption coefficient is estimated about $4 \times 10^{-4} \text{m}^{-1}$ from 500nm to 700nm and is higher in shorter and longer wavelength.

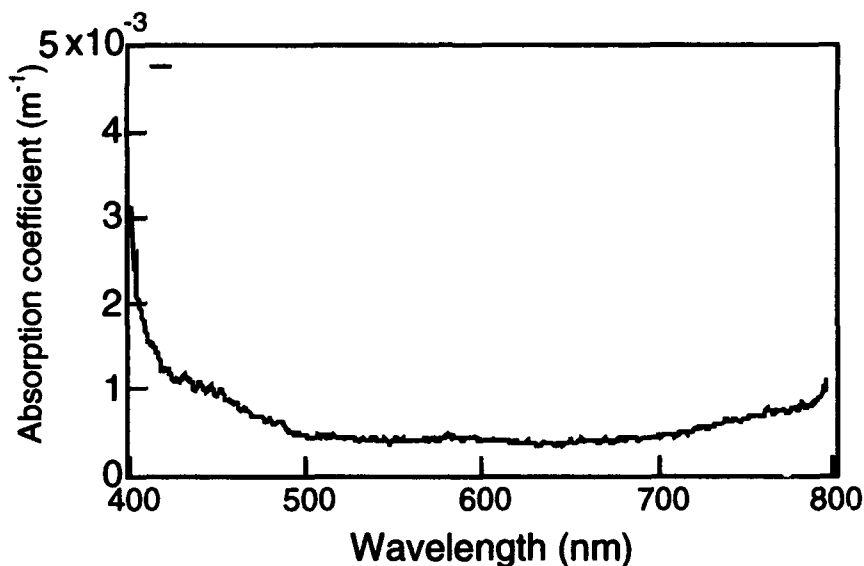


Fig. 5. Measurable minimum value of the absorption coefficient limited by the offset noise of the system.

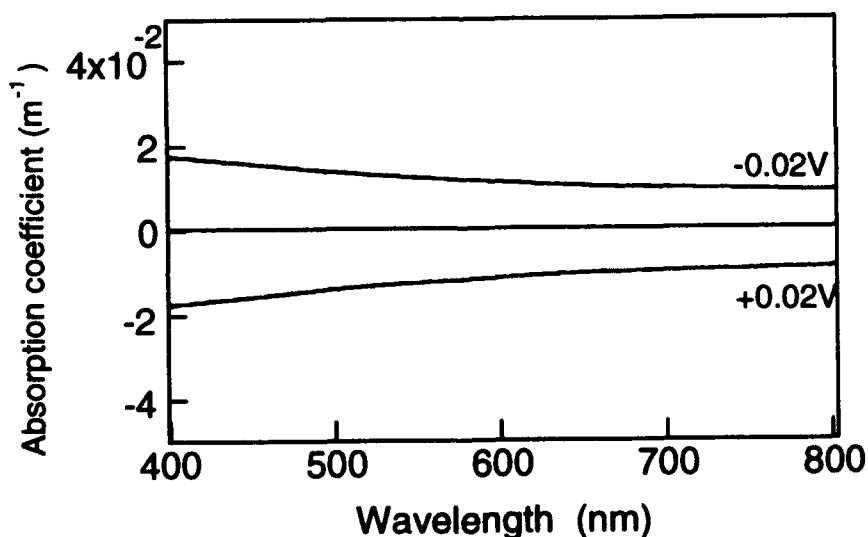


Fig. 6. The apparent absorption coefficient due to the variation of input voltage $\pm 0.02\text{V}$ ($\pm 0.1\%$ of 21.00V) to tungsten halogen lamp

(b) Effect of the fluctuation of the light source

This error was estimated by taking the difference of the photo diode outputs obtained in a series of the measurements, where the voltages supplied to the lamp have a difference of ± 0.02 volt amounting to 0.1% at normally used voltage of 21.00V. Fig.5 shows the equivalent absorption coefficient induced by this amount of illuminating light source change. The ± 0.005 volt stability in the prototype system is estimated to give much better results.

(c) Effect of the absorption change caused by the water temperature

The absorption coefficient of the water is known to change with the temperature in the red and near-infrared region⁶⁾. The spectral absorption coefficient of water was measured at several conditions from 21°C to 23°C water temperature. The temperature effect of the spectral absorption coefficient was shown in Fig. 7, where the vertical axis shows the difference of the spectral absorption coefficient in case of the water temperature change of 1°C.

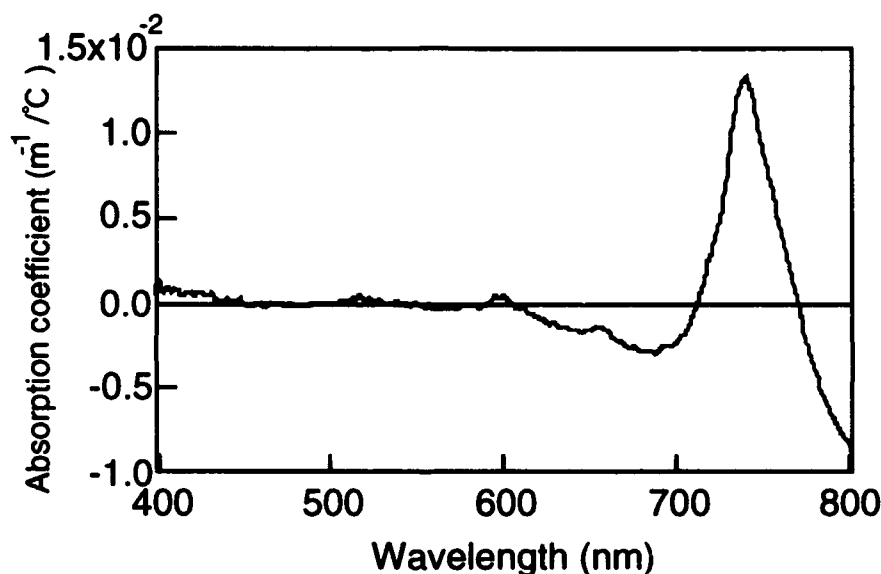


Fig.7. Spectral absorption coefficient change of the water induced by temperature difference

4.3. Analysis

(a) Correction of the results

According to the experimental results given in the above section, the water temperature affects much more the absorption coefficients not only in the magnitude but also in the wavelength concerned than the other factors affect mainly only in magnitude by small values. The spectral absorption coefficient given in Fig. 4 was corrected by monitoring the water temperature during the experiments to exclude the temperature effect, and the corrected data were shown in Fig. 8. The base line was determined as described in the previous section.

(b) Linearity test

The linearity of this opal glass method was checked by a series of spectral absorption measurements, where the concentration of the phytoplankton cell was changed systematically. The absorption coefficient at the wavelength of 674nm was plotted in Fig. 9, where the concentration of the phytoplankton cell was evaluated

by the scale of the concentration of chlorophyll pigment in the cells. The results assured that this system was linear in absorption coefficient down to 10^{-2}m^{-1} , which was equivalent to the concentration of about $0.4\mu\text{g/l}$. This value is much higher than the magnitude of $4 \times 10^{-4}\text{m}^{-1}$, which is critical value inherent to this prototype system.

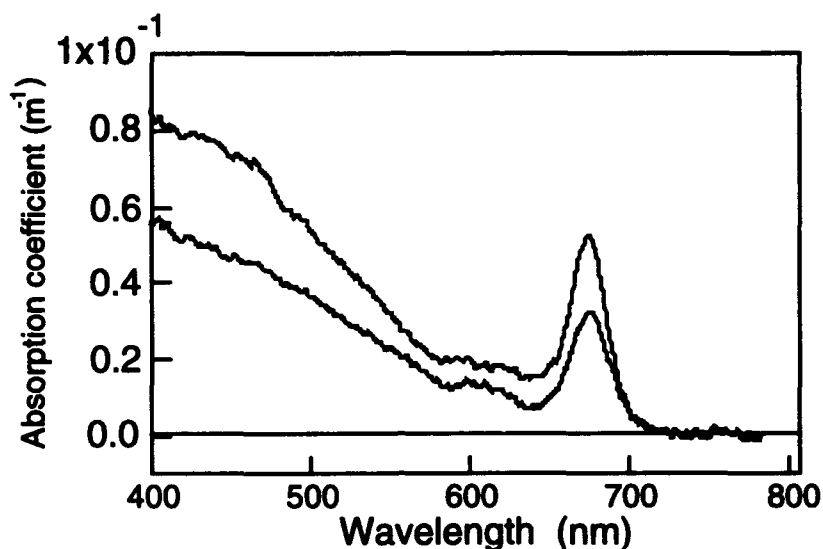


Fig. 8. Spectral absorption coefficient with temperature correction

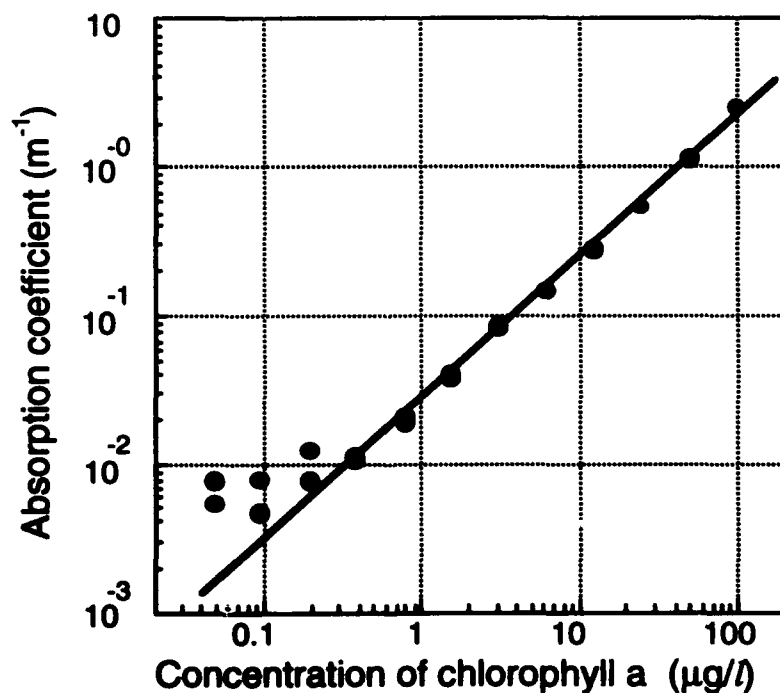


Fig.9. Absorption coefficient vs. chlorophyll concentration

For the measurement of lower concentration, it is necessary to consider the slight effect of the absorption coefficient of dissolved substance on the wavelength, and the slight difference of the scattering mode by the particles.

5. SUMMARY

The spectral absorption measurement based in the opal glass method was shown to be reliable and linear down to 10^{-2}m^{-1} by the preliminary small size prototype system, high spectral resolution and potentially rapid response. The analysis was made on the magnitude of the errors concerned by the some factors such as the water temperature variation, the detector noise and the fluctuation of light source. The critical limit of the absorption coefficient is estimated to be $4 \times 10^{-4}\text{m}^{-1}$ inherent to the detection system.

6. ACKNOWLEDGMENTS

The authors would like to thank Dr. T. Akiba for useful discussions and advice, and Mitsubishi Cable Industries, Ltd. for technical supports of optical fiber cables.

7. REFERENCES

- 1) J. R. V. Zaneveld, R. Bartz and J. C. Kitchen, "A reflective-tube absorption meter," *Ocean Optics X*, Proc. SPIE, **1302**, 124-136, 1990.
- 2) R. M. Pope, E. S. Fry, R. L. Montgomery and F. Sogandares, "Integrating cavity absorption meter, measurement results," *Ocean Optics X*, Proc. SPIE, **1302**, 165-175, 1990.
- 3) M. Aizaki, K. Kohata and H. Tanaka, "Direct measurement of phytoplankton biomass in aquatic fields using the fiber-optic scanning spectrophotometer," *Jpn. J. Limnol.*, **53**, 99-101, 1992.
- 4) D. A. Neuschuler, C. R. Booth and J. H. Morrow, "Innovative applications of optical fibers in the measurement of *in-situ* spectra," *Ocean Optics X*, Proc. SPIE, **1750**, 338-353, 1992.
- 5) K. Sibata, "Spectrophotometry of intact biological materials," *J. Biochem*, **45**, 599-623, 1958.
- 6) W. S. Pegau and J. R. V. Zaneveld, "Temperature-dependent absorption of water in the red and near-infrared portions of spectrum," *Limnol. Oceanogr*, **38**, 188-192, 1992.

An instrument to measure *in situ* visible light absorption in natural waters.

J.H.M. Hakvoort, A.E.R. Beeker and J. Krijgsman.

Faculty of Civil Engineering, Delft University of Technology, PO Box 5048, 2600 GA Delft, The Netherlands.

ABSTRACT

A submersible absorption meter was built to measure the light absorption plus backscattering coefficients of natural waters in one term. The instrument is based on close correspondence between the radiance attenuation and the sum of absorption and backscattering under the following conditions. The radiance attenuation is measured close to the surface of a Lambertian light source and it is measured along the direction of the net vector irradiance. Photons scattered out of this normal direction are replaced by photons initially travelling at a deviating direction being scattered into the normal direction. Photons scattered in the backward direction are lost.

The instrument can replace laborious sample handling used to determine the optical characteristics of particulate matter. The performance of the absorption meter was tested in the laboratory working with several simple test suspensions and in the field in estuarine and in marine water. Radiance attenuation spectra of clear water and absorption spectra of clear water matched closely. The radiance attenuation of algae increased linearly with concentration of chlorophyll *a* in the measured range of 0-70 mg m⁻³, while the radiance attenuation spectrum was very close to the absorption spectrum of the algal sample as measured with a semi-integrating sphere. An offset between these spectra remained. This was not observed when field data from estuarine and marine water were compared to laboratory measurements.

1. INTRODUCTION

Two inherent optical properties are usually sufficient to describe a volume of surface water: the absorption coefficient and the volume scattering function. These are called inherent optical properties because they are independent on incident radiance¹. The absorption coefficient *a* is the fraction of energy absorbed from a collimated beam per unit distance; the volume scattering function describes the angular distribution of radiant intensity scattered out of a beam. Integration of the volume scattering function gives the scattering coefficient *b*, the fraction of energy scattered out of a collimated beam per unit distance. The total radiance attenuation due to absorption and scattering is the beam attenuation coefficient *c* ($c = a + b$). The scattering coefficient and the beam attenuation coefficient also are inherent optical properties.

Inherent optical properties of surface water are used to estimate concentration of aquatic humus, algae and silt in the water. The inherent properties also are used in models of primary production when combined with radiative transfer equations and the distribution of incident light intensity². Absorption is caused by molecules that absorb light and so mainly contains chemical information; scattering is mainly caused by inhomogeneity of the physical properties of the volume of water and so contains information about particle characteristics. Here scattering is only considered as a source of error in the determination of absorption.

The absorption coefficient can be calculated if the net vector irradiance and the scalar irradiance are known³. Højerslev⁴ built an *in situ* absorption meter based on Gershun's theory. Measurements based on Gershun's theory may not give accurate absorption estimates because the irradiance parameters are very sensitive to disturbance by surface waves and other experimental errors^{5,6}. These are mainly a consequence of the fact that the formula requires input measured across a small (in principle infinitesimal) distance and in a homogeneous water column.

Because of these difficulties inherent optical properties are usually measured in the laboratory. Different techniques were developed to do this. Absorption by clear samples is measured with low aperture optics; the beam attenuation coefficient is equal to the absorption coefficient because scattering is neglected, except in the blue. Absorption of turbid samples can be measured using high aperture optics to include as much scattered light as possible in the signal. Experimental difficulties of various nature beset the determination of the absorption coefficient of a suspension, mainly caused by light scattering and especially at low concentrations of particulate matter.

Haardt and Maske ⁷ described a method to collect all the scattered light using an integrating sphere and collimated incident light. In this method the actual distance covered by a photon travelling through the sample is longer than the geometrical distance because of multiple reflection inside the sphere. Elterman ⁸ and Fry and Kattawar ⁹ introduced an isotropically illuminated integrating cavity. Inside the instrument a homogeneous diffuse light field is assumed. The instrument needs to be calibrated because the actual length of the path traversed by a ray of light is unknown. Shibata *et al.* ¹⁰ invented the opal glass technique, similar to and simpler than the semi-integrating sphere technique. The technique aims to exclude photons passing the sample more than once, thus making calibration on the actual path length redundant. If single scattering is assumed, the measured absorption consists of inherent absorption a and part of the scattering coefficient. The scattering part is defined by the amount of scattered light not detected $(1-F(\theta_\alpha))b$ where $F(\theta)$ is the forward scattering probability and θ_α is the detection angle of the integrating sphere. For natural waters a major part of the scattering

coefficient is included because light is scattered mainly in forward directions ¹¹. Bannister ¹² used Monte Carlo calculations to assess errors in absorption coefficients induced by the type of cuvette used.

Because of its low concentrations particulate matter from surface water usually was concentrated before accurate absorption measurements could be made. Yentsch ¹³ filtered the samples and measured absorption of particulate matter present on the filter paper; this filter pad method is widely used. Multiple scattering is prominent and results in overestimation of absorption, this must be corrected for by determining an *ad hoc* calibration factor ¹⁴⁻¹⁶ known as the β -factor. Kirk ¹⁷ and Davies-Colley ¹⁸ resuspended the filtered material to avoid this. But systematic errors may result because of particle loss and formation and breaking up of flocs caused by the sample handling.

It may be better to measure the absorption on water samples using larger geometric path lengths than usual in a standard spectrophotometer. Zaneveld *et al.* ¹⁹ introduced a reflective tube absorption meter with collimated light, an internally reflecting cuvette and a high aperture radiance sensor. The measured spectra are corrected for scattering to obtain the absorption plus back scattering spectra comparable to those obtained by the opal glass method ¹⁰. The detector of the reflecting tube has 35° half angle field of view.

The absorption plus backscattering can also be measured with a technique that is the inversed method as done by Zaneveld *et al.* ¹⁹. With this technique the radiance attenuation is measured in an diffuse light field in such a way that all light forwardly scattered out of the normal direction is compensated by light scattered into this direction. This is true if the light in all directions has the same intensity. In our instrument such a light field is approximated by a Lambertian light source and radiance is measured at two distances from the light source. This way the detected fraction of forward scattered light is increased. A submersible absorption meter was designed to measure radiance attenuation *in situ* according to this reasoning. Working with this instrument sample handling on shipboard is avoided; it is an alternative way to determine absorption plus back scattering spectra in natural waters. Design, operation and calibration of this instrument and its performance in the field are described.

Table 1. Notations.

Symbol	Description
a	absorption coefficient, m^{-1}
a_h	absorption coefficient of aquatic humus, m^{-1}
a_w	absorption coefficient of pure water, m^{-1}
a_{chl}	absorption coefficient of chlorophyll containing particles, m^{-1}
b	scattering coefficient, m^{-1}
b_b	backscattering coefficient m^{-1}
b_f	forward scattering coefficient, m^{-1}
c	beam attenuation coefficient, m^{-1}
$F(\theta)$	forward scattering probability function, -
k	radiance attenuation coefficient, m^{-1}
k_{chl}	radiance attenuation coefficient of chlorophyll, m^{-1}
k_h	radiance attenuation coefficient of aquatic humus, m^{-1}
k_p	radiance attenuation coefficient of particulate matter, m^{-1}
k_w	radiance attenuation coefficient of water, m^{-1}
$L(z;\theta,\phi)$	radiance, $W m^{-2} sr^{-1}$
$L_*(z;\theta,\phi)$	path radiance, $W m^{-3} sr^{-1}$
Δl	path length, m
z	depth, m
α	apparent absorption coefficient, m^{-1}
α_p	apparent absorption coefficient of particulate matter, m^{-1}
$\beta(z;\theta,\phi)$	volume scattering function, $m^{-1} sr^{-1}$
θ	zenith angle, rad
θ_α	detection angle of the integrating sphere, rad
ϕ	azimuth angle, rad

2. THEORY

A list of the symbols used in the following equations is given in Table 1. The propagation of a beam of light in a plane parallel medium without internal light sources is

$$\frac{dL(z,\theta,\phi)}{dz} \mu = -cL(z,\theta,\phi) + L_+(z,\theta,\phi) \quad (1)$$

The first term on the right gives the radiance decrease per meter due to the beam attenuation c . The second term on the right is the path radiance L_+ . Path radiance is the increase in radiance per meter due to light scattered into a beam from all directions

$$L_+(z,\theta,\phi) = \int_{\phi'=0}^{2\pi} \int_{\theta'=0}^{\pi} \beta(z,\theta,\phi;\theta',\phi') L(z;\theta',\phi') \sin(\theta') d\theta' d\phi' \quad (2)$$

Using a lambertian light source the incident light has the direction $0 < \theta < \pi/2$. Light that applies $0 < \theta' < \pi/2$ is used to calculate path radiance. Light that has been scattered in the upward direction, $\pi/2 \leq \theta \leq \pi$, is considered lost.

Three cases are distinguished assuming single scattering, when the radiance attenuation is measured in such a light field:
Case 1. The sample volume only absorbs the light. This case is valid for measurements of radiance attenuation in clear samples. It is the most simple case. If radiance attenuation is measured perpendicular to a Lambertian light source and no scattering occurs than the radiance attenuation is

$$\frac{dL(z;0,0)}{dz} = -aL(z;0,0) \quad (3)$$

The path radiance in this case is zero. Dividing Equation 3 by $L(z;0,0)$ shows that radiance attenuation is equal to absorption.

$$k = a \quad (4)$$

Case 2. The sample volume only scatters the light. This case is a theoretical approach since measurements of radiance attenuation in surface water without absorption included do not exist. If measured in a scattering but no absorbing medium and assuming single scattering the radiance attenuation is

$$\frac{dL(z;0,0)}{dz} = -bL(z;0,0) + L(z;0,0) \int_{\phi'=0}^{2\pi} \int_{\theta'=0}^{\pi/2} \beta(z;0,0;\theta',\phi') \sin(\theta') d\theta' d\phi' \quad (5)$$

The second term on the right compensates for the light that was scattered forwardly out of the normal direction ($z;0,0$). Its integral is the forward scattering coefficient for a Lambertian light field.. So the measured radiance attenuation is the backscattering coefficient.

$$k = b - b_f = b_b \quad (6)$$

Case 3. The sample volume absorbs and scatters the light. This case is valid for natural waters. If measured in an absorbing and scattering medium the radiance attenuation is

$$\frac{dL(z;0,0)}{dz} = -cL(z;0,0) + \int_{\phi'=0}^{2\pi} \int_{\theta'=0}^{\pi/2} \beta(z;0,0;\theta',\phi') L(0;\theta',\phi') \exp\left(\frac{-az}{\cos(\theta')}\right) \sin(\theta') d\theta' d\phi' \quad (7)$$

It may be a good approximation to weight the contribution of radiance from all angles to the path radiance by the normalized volume scattering function. The volume scattering function of natural water samples is peaked forwardly. Radiance at high θ'

only has a small effect on the path radiance. It may be expected that the second term in Equation 7 is close to the forward scattering coefficient. So the measured radiance attenuation is

$$k \approx c - b_f \approx a + b_b \quad (8)$$

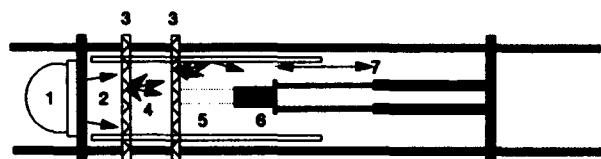


Figure 1. Schematic view of the submersible instrument built to measure *in situ* radiance attenuation. It consists of four units mounted in a frame. The first unit is constructed from: (1) a 220 V 800 W halogen lamp in a watertight housing. This projects light via (2) an internally white reflecting cylinder of 0.1 m length on a (3) 0.2 m diameter diffuser with diffusion factor 0.87. A homogeneous illuminated surface is obtained with a second diffuser (3). The intermediate cylinder (4) is filled with clear water. An infinite plane light source is approached with an internally mirroring cylinder (5) placed against the second diffuser. This cylinder is the sample compartment and contains ambient water; it is the second unit. The third unit is the radiance detector (6). It measures radiance at two preset distances in the diffuse light field. The fourth unit is a remote controlled pneumatic cylinder (7) which moves the radiance detector to the two positions necessary for a measurement.

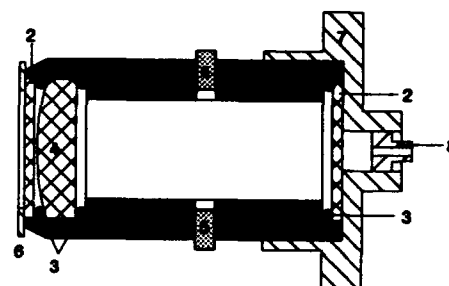


Figure 2. Radiance probe used in the submersible absorption meter. It has 1.7° half angle of view. The lens housing (1) has two glass windows (2) enclosed by O-rings (3) and mounting devices (6 and 7). An achromatic lens (4) is used to optimize projection of light spectral on the fibre entrance. Purging plugs (5) are attached to put dry air in the housing to prevent water vapour condensation. A glass fibre is attached at a connector (8) to transport the light to the spectrometer. The radiance probe is connected to a pneumatic cylinder with a mounting device (7).

3. DESIGN OF THE SUBMERSIBLE ABSORPTION METER

A submersible instrument (Figure 1) was built to measure radiance attenuation underwater in a diffuse light field. It consists of four units: a diffuse light source, a sample compartment, a radiance detector and a pneumatic cylinder to move the detector. Light is transported by a glass fibre to a diode array rapid scan spectrometer.

The diffuse light source consists of a halogen lamp in a watertight housing, a 0.2 m diameter white cylinder and two serially placed diffusers. The lamp is placed at the entry of the cylinder, one diffuser is inside the cylinder and the other at its end. Within 5 minutes no drift in light intensity and in its spectral distribution was found. The measurements are done within 15 seconds. The volume of water to be measured is contained in an internally mirroring cylinder of the same diameter as the one in the light source. The mirror was made of Scotchcal 5004 folio having 90-95 percent reflectivity. This way an infinite diffuse light field is approximated except for backscattering.

Radiance is detected in the direction of the irradiance vector at two distances from the light source by moving the detector with

a pneumatic cylinder with remote control. This distance can be adjusted to the optical depth of the water. Between measurements the water in the sample compartment is replaced by turbulence induced by repeated pneumatically moving the radiance detector. Tests in laboratory showed that the sample volume was refreshed within five repeated movements.

The radiance detector (Figure 2) consists of an achromatic doublet lens in a 25 mm diameter housing. The diameter of the radiance sensor must be large compared to size of suspended particles to avoid noise due to shading of the detector by particles close to it. Radiance is collected in a 1.7° half angle of view. A 40 m optical glass fibre transports the light to a Tracor Northern 6112 diode array rapid scan spectrometer. The fibres were mounted into a heavy duty reinforced PVC hose to prevent bending. An iron chain was mounted along the hose to prevent tensile forces breaking the fibers. Spectra were measured in the spectral range 400-800 nm with a 2 nm wavelength resolution.

Radiance attenuation k was calculated with the Lambert-Beer equation:

$$k = \frac{-1}{\Delta l} \ln \frac{L_2}{L_1} \quad (9)$$

where the path length Δl is the interval between the two sensor positions and L_1 and L_2 are radiances measured at both distances. L_1 was at 0.1 m and L_2 was at 0.22 m distance from the light source resulting in Δl is 0.12 m. Radiance attenuation of particulate matter k_p was calculated with

$$k_p = k - k_w - a_h \quad (10)$$

where k_w is the radiance attenuation of pure water and a_h is the absorption of aquatic humus.

Multiple scattering can become prominent in the recorded spectrum if the preset path length is too long. This is not desirable from the point of view of interpretation; it can be recognised (and avoided) by noting increased absorption by water in the 700-800 nm wavelength range. Measurements on turbid samples using path length of 0.12 m showed no increased absorption.

4. MATERIALS AND METHODS

4.1. Optical reference measurements

Optical measurements to compare with results from the submersible absorption meter were carried out with a Perkin Elmer $\lambda 16$ double-beam spectrophotometer. Spectra were measured in the 400-800 nm spectral range with 2 nm wavelength resolution with reversed osmosis water as a reference. The apparent absorption of particulate matter α_p was measured using 10 mm flow cuvettes and high aperture optics, consisting of a semi-integrating sphere with cuvettes placed at the entrance of the sphere. Radiance transmitted and scattered within 38° half angle of view was detected. Absorption of aquatic humus a_h was measured with low aperture optics using 100 mm cuvettes.

Aquatic humus was obtained by filtration of sub samples through a $0.2 \mu\text{m}$ Sartorius membrane filter. Particulate matter was concentrated from sub samples by centrifugation, the samples were decanted until a 10-times higher concentration resulted. The particulate matter was resuspended afterwards.

The total apparent absorption is the sum of the radiance attenuation of pure k_w , absorption of aquatic humus a_h and apparent absorption of particulate matter α_p :

$$\alpha = k_w + a_h + \alpha_p \quad (11)$$

The radiance attenuation spectrum of pure water is measured in reversed osmosis water. The absorption spectrum of aquatic humus is measured on filtered water against reversed osmosis water.

4.2. Algal suspension

Chlorella pyrenoidosa was grown in batch cultures on algal growth medium, chlorophyll *a* was at about 2 g m^{-3} at the time of the measurements. Experiments were done in a 0.2 m^3 tank, the algae were diluted in tap water filtered over a $0.2 \mu\text{m}$ Sartorius membrane filter. A concentration range of *C. pyrenoidosa* was prepared with chlorophyll *a* concentrations between 0 and 70 mg m^{-3} . The suspension was stirred to keep it homogeneous. Radiance attenuation spectra were measured in the concentration series. Apparent absorption spectra were measured as a reference in the *C. pyrenoidosa* at 2 g m^{-3} and 200 mg m^{-3} in the stock culture.

4.3. Field measurements

Triplicate measurements were carried out with the submersible absorption meter (see below) at 1 m depth in the Western Scheldt and quintuple measurements at 1 m and 5 m depth in the North Sea. From the extensive data set spectra were selected from stations where the results of multiple spectral scans were within 0.1 m^{-1} . Differences among scans occurred due to patchiness in the field (See 5.4). Water samples were taken for chemical and optical characterization in the laboratory.

4.4. Chemical measurements

Dry weight concentrations of particulate matter and inorganic fraction were determined according to Dutch norm NEN 6484²⁰. Chlorophyll *a* in algal cultures was determined after ethanol extraction according to Dutch norm NEN 6520²¹ and in field samples by high performance liquid chromatography²².

5. RESULTS

5.1. Laboratory test in clear water

The tank of 0.2 m^3 was filled with reversed osmosis water filtered over a $0.2 \mu\text{m}$ membrane filter. No efforts were made to remove all contaminants from the water. The water was deaerated by temporarily heating to avoid the formation of air bubbles during experiments. Radiance attenuation spectra were measured. Repeated measurements showed that radiance attenuation spectra are measured with 0.03 m^{-1} standard deviation.

The radiance attenuation spectrum of reversed osmosis water and absorption spectrum of pure water matched in the 500-700 nm wavelength range (Figure 3). The absorption spectrum of pure water is according to Smith and Baker²³. In the 700-800 nm wavelength range the radiance attenuation k_w was about 10 percent higher than the absorption of pure water, still being within the error margins of the pure water absorption spectrum. Pegau and Zaneveld²⁴ showed a temperature dependency of the water absorption spectrum. At 730 nm the water absorption changed 12 percent when comparing 5°C to 31°C water temperature. We used water at a temperature of 35°C . The radiance attenuation spectra of pure water as a function of temperature are in Buiteveld *et al.*²⁵. The radiance attenuation spectrum of reversed osmosis water differed from that of tap water, the spectral difference had the characteristic shape of aquatic humus absorption spectrum. The spectrum fits in first approximation an exponentially decreasing function with a slope of 0.013 nm^{-1} . We conclude that the absorption spectra and the radiance attenuation spectra using the instrument match when measured in clear solutions.

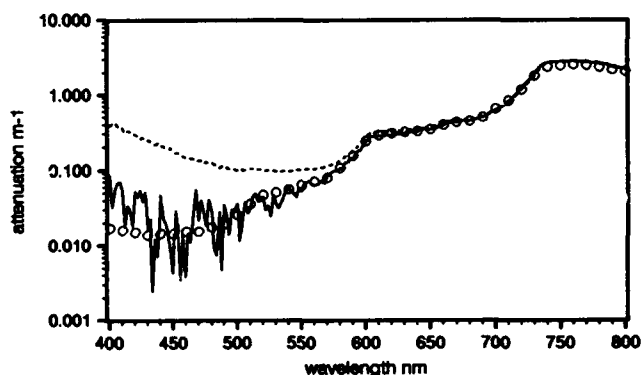


Figure 3. Absorption spectra of pure water and less pure water as used in experiments. ○: Absorption of pure water according to Smith and Baker (1981). Thin line: radiance attenuation of reversed osmosis water filtered over a $0.2 \mu\text{m}$ membrane filter. Dashed line: radiance attenuation of filtered tap water. The difference spectrum between the radiance attenuation spectra has the shape of the spectrum of aquatic humus.

5.2. Laboratory test in turbid water

Spectra measured with the submersible absorption meter in the concentration series of *C. pyrenoidosa* are shown in Figure 4. The lowest spectrum is from filtered tap water, including its humus. This radiance attenuation of tap water was subtracted from k . The radiance attenuation spectra of particulate matter k_p were calculated with Equation 10.

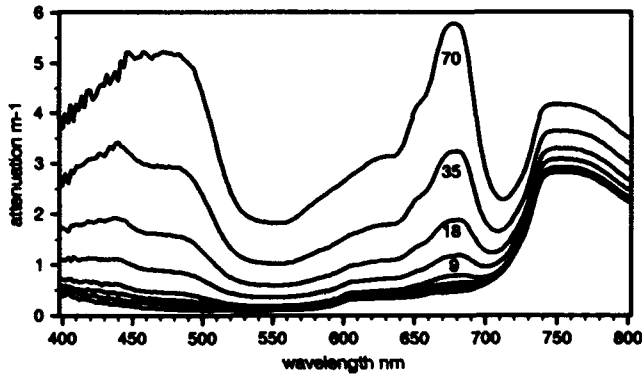


Figure 4. Radiance attenuation of a concentration series of *C. pyrenoidosa* measured with the submersible absorption meter. The lowest spectrum is from filtered tap water. Chlorophyll a range is 0-70 mg m⁻³. The upper spectrum (70 mg m⁻³) showed a decline in the 400-450 nm wavelength range. This decline is not explained yet.

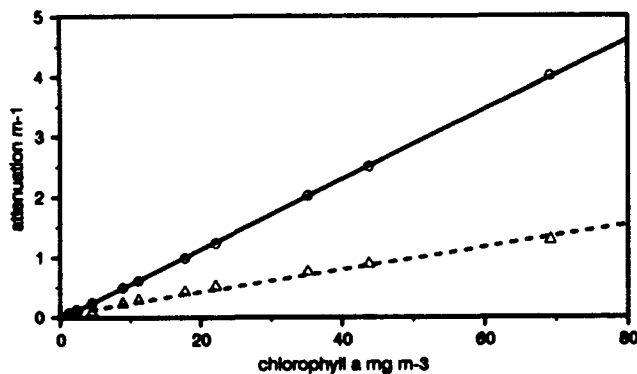


Figure 6. Linearity of radiance attenuation of *C. pyrenoidosa*, k_{chl} at 680 nm (○) and radiance attenuation of particulate matter k_p at 720 nm (△). Linear regression coefficient at 680 nm is $R^2=0.99958$ and at 720 nm $R^2=0.98803$.

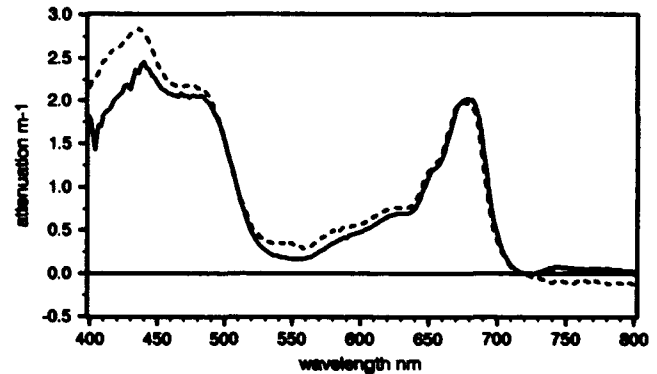


Figure 5. Inherent absorption of *C. pyrenoidosa* at 35 mg m⁻³ chlorophyll a calculated from radiance attenuation and apparent absorption measurements. The spectra were corrected according to Shibata *et al.*¹⁰ at 720 nm. The solid line k_{chl} was measured with the submersible absorption meter. It is representative for all other concentrations, noise level increased with decreasing concentration. The dashed line a_{chl} was measured with a semi-integrating sphere.

No real absorption by algae occurs in the 720-800 nm wavelength range. However the measured absorption spectra α_p and the radiance attenuation spectra k_p show significant attenuation in the 700-800 nm wavelength range (Table 2). This attenuation is attributed to light loss due to scattering and is usually corrected for according to the technique of Shibata *et al.*¹⁰. The inherent absorption spectra of algae can be calculated from the apparent-absorption spectra of particulate matter when assumptions according to Shibata *et al.* are made:

1. No real absorption by algae occurs in the 720-800 nm wavelength range.
2. The fraction of light scattered away from the aperture of the semi-integrating sphere is constant over the visible light range.

This effect of light loss cannot be corrected for when the particulate matter includes silt. The scattering and absorption characteristics of silt are largely unknown.

Under these assumptions a first order scattering correction was carried out; the value at $k_p(720)$ and $\alpha_p(720)$ were subtracted from the spectra k_p and α_p respectively. This way the inherent absorption spectrum a_{chl} and the radiance attenuation spectrum k_{chl} were

calculated (Figure 5), the spectra are closely matched. Absorption spectra measured with the submersible absorption meter a_{chl} in the range 400 nm to 500 nm were lower than those measured with the semi-integrating sphere. Cleveland *et al.*²⁶ found a similar result. Differences as high as 50 percent occurred between absorption spectra measured with their integrating cavity and absorption spectra measured according the technique of Mitchell and Kiefer¹⁶ in the blue light region. Calibration errors of the integrating cavity might have caused this, but Cleveland *et al.* also suggested a wavelength dependent scattering artifact as an explanation.

Zaneveld *et al.*¹⁹ used a correction factor for light scattered away from the detector as a percentage of the total scattering coefficient to compute the apparent absorption coefficient from measurements with the reflective tube absorption meter. This correction factor must be determined for different volume scattering functions. The results of this correction technique were comparable to the spectra measured directly with the submersible absorption meter.

The radiance attenuations $k_p(720)$ and $k_{chl}(680)$ ($= k_p(680) - k_p(720)$) increased linearly with the concentration of algae (Figure 6), showing that multiple scattering does not play a role in this concentration range. We conclude that radiance attenuation and absorption of turbid water match after the correcting method of Shibata *et al.*¹⁰ is applied.

5.3. Field tests

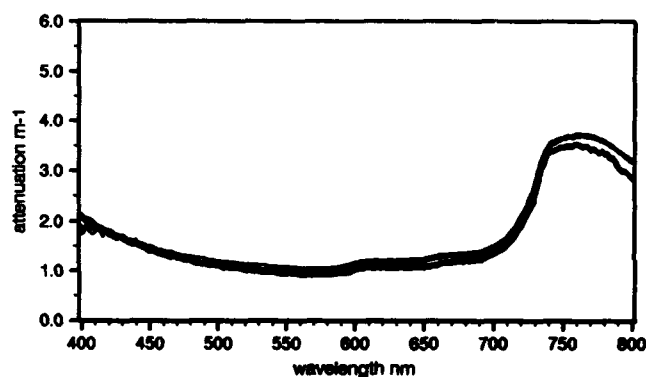


Figure 7a. Radiance attenuation k (thin lines) measured with the submersible absorption meter in the Western Scheldt estuary and total apparent absorption α (bold line) measured in the laboratory.

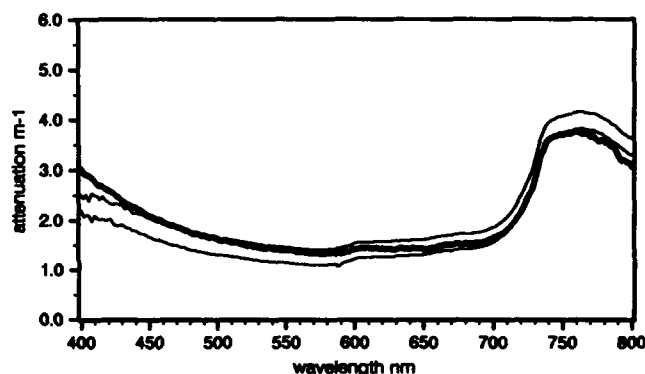


Figure 7b. Same notation as Figure 7a.

Table 2. The correction v to calculate inherent absorption spectra of algae from the absorption spectrum of particulate matter α_p or the radiance attenuation spectrum of particulate matter k_p were different. The calculation is a first order scattering correction¹⁰ at 720 nm wavelength. The $k_p(720)$ to $\alpha_p(720)$ ratio for *C. pyrenoidosa* was at about 15. The values were closer in the field measurements. Data presented must be regarded as illustrative for the situations studied. More research on this phenomenon is now in progress.

	Laboratory <i>C. pyrenoidosa</i>	Western Scheldt Silt	North Sea <i>P. mucus</i> + Silt
k_p	0.80	0.89	0.24
α_p	0.05	0.75	0.10

Field measurements were carried out at different stations in the Western Scheldt estuary in the southwest of the Netherlands and in the coastal area of the North Sea near the Netherlands. The concentration of aquatic humus in the Western Scheldt decreases

in the direction of the North Sea, but concentrations of suspended matter vary spatially and temporally in a more irregular way. Secchi Disk transparency ranged from 0.5 m to 1.5 m during measurements in the Western Scheldt. In the North Sea measurements were carried out near the Delta area by Walcheren, near Noordwijk and north of the island Texel. An algal bloom of *Phaeocystis mucus* occurred near Texel.

The radiance attenuation spectra measured in the Western Scheldt and the total apparent absorption spectra closely correspond (Figure 7). This does not agree with the results found for algal suspensions in the laboratory tank where the values of $k_p(720)$ and $\alpha_p(720)$ differed by a factor 15 (Table 2). This could be caused by the difference in scattering properties between algae and silt. The radiance attenuation of chlorophyll *a*, k_{chl} at 675 nm, and the radiance attenuation of silt k_p at 720 nm were calculated from the radiance attenuation measured in the field. Both were linearly correlated to concentrations of respectively chlorophyll *a* and total suspended matter (Figure 8a and 8b).

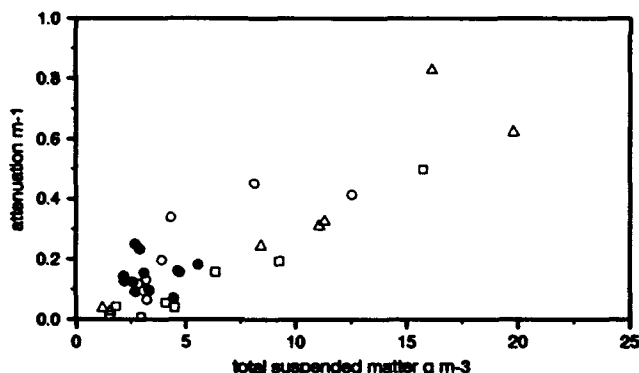


Figure 8a. Radiance attenuation of the particulate matter k_p at 720 nm from the North Sea measurements for 35 selected stations. Only stations were used where patchiness as seen by the submersible absorption meter was insignificant. The linear regression coefficient is $R^2=0.762$. The statistical error may be caused by variations in the volume scattering function of the suspended material. Also errors induced by the chemical analysis will have contributed. The symbols indicate the transects studied at Δ Walcheren ($R^2=0.838$), \square Noordwijk ($R^2=0.960$), \circ Texel in April ($R^2=0.671$) and \bullet Texel in June ($R^2=0.001$).

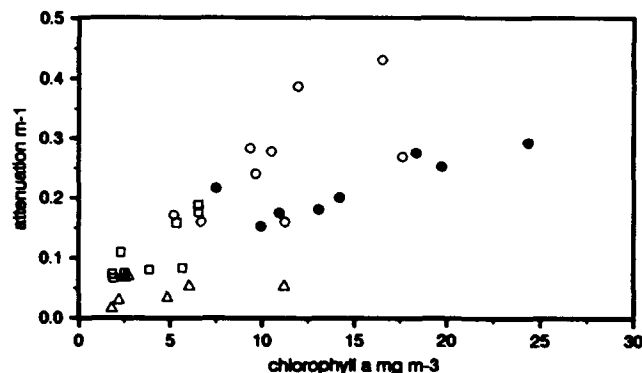


Figure 8b. Radiance attenuation k_{chl} of chlorophyll *a* at 675 nm for the same stations as used in Figure 8a. The linear regression coefficient was $R^2=0.557$. The statistical error may be caused by the chlorophyll *a* specific absorption differing between the transects. The Walcheren transect Δ mainly was dominated by *Rhizolenia delicatula* and a high silt load, ($R^2=0.045$). The Noordwijk transect \square showed *Cryptophytes spec.*, ($R^2=0.631$). The Texel transect in April \circ was dominated by *Phaeocystis mucus*, ($R^2=0.419$). The Texel transect in June \bullet mainly showed *Rhizolenia spec.*, ($R^2=0.686$).

5.4. High resolution temporal variation of optical water characteristics

An advantage of an *in situ* instrument as compared to laboratory measurements on field samples is the possibility to measure high resolution time series in the field. These can give insight to the occurrence of patchiness and allow the investigation of the processes associated with this phenomenon, as will be illustrated next. Six spectra were measured within five minutes in a bloom of *Phaeocystis mucus* near the island of Texel. The variation of these spectra around their mean is plotted in Figure 9, showing rapid variability of the concentration of algae: their patchiness on this time scale and on the spatial scale of the instrument. Also in one spectrum it appears that only the silt concentration varied.

Similar results were obtained in the Western Scheldt estuary, here the variation was dominated by rapid changes in silt concentration. Within three minutes radiance attenuation at one station changed by 2 m^{-1} , while Secchi disk transparency varied from 0.8 m to 0.5 m.

6. DISCUSSION

The design of this submersible absorption meter was based on close correspondence found between the path radiance gain coefficient under ambient light conditions and the fraction of scattering coefficient detected by the aperture of the integrating sphere²⁷. In other words the measured radiance attenuation is close to the measured absorption plus backscattering. The *in situ* application of this concept using artificial light leads to consistent results.

The adjustable path length, set by the two positions of the radiance sensor, makes the instrument scalable and suitable to measure a wide range of absorption coefficients. This kind of instrument allows absorbing plus backscattering characteristics to be measured under natural conditions. Sampling techniques may change the optical characteristics of the water constituents. The use of artificial light allows measurements of radiance attenuation at greater depth.

The submersible absorption meter measures radiance at two positions from the light source in a short time. The light source is required to be stable within this time interval but may drift in a larger time interval. If only one position is used then a high stability of the light source is required. The spectral signature of the light source can be improved using a Xenon lamp which has more light in the blue region.

The radiance attenuation spectra consist of several components. These can be determined with different techniques. Water absorption depends only on temperature²⁴. The known spectrum of water can be subtracted from the radiance attenuation spectrum. Eventual effects of multiple scattering can be recognized by a residual water absorption in the 700-800 nm wavelength range as multiple scattering increases path length and so absorption. In principle this can be corrected for. The absorption spectra of aquatic humus can be determined on shipboard and subtracted from the measured attenuation spectrum. However, this will be cumbersome if high time resolution is wanted. Default absorption spectra of aquatic humus can be used in this case²⁸. Target factor analysis can be a useful tool to decompose the spectral data.

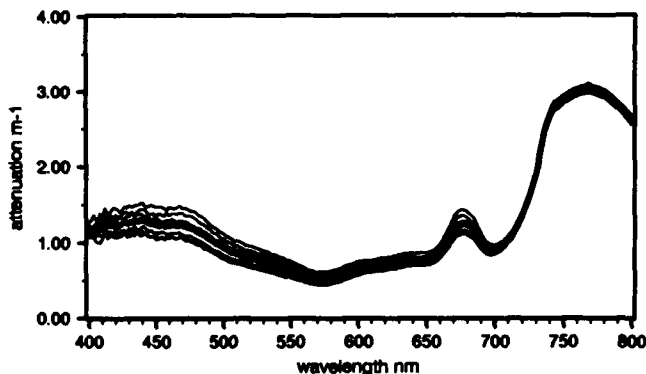


Figure 9a. Patchiness: rapid variability of the absorption of seawater *in situ* near the island of Texel in a bloom of *Phaeocystis mucus*. Six spectra of radiance attenuation were measured in a four minutes interval (thin lines), the bold line is the mean.

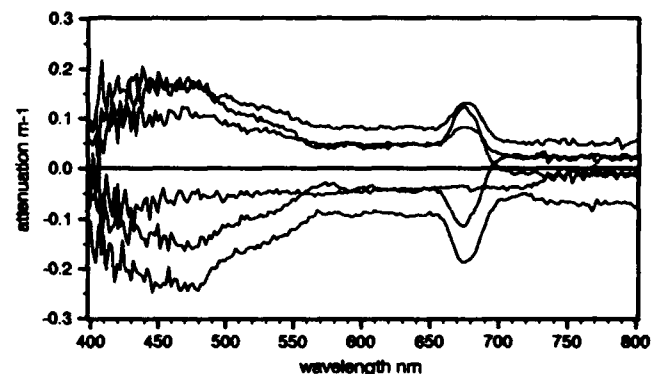


Figure 9b: The variation of the spectra in Figure 9a around their mean is plotted. These difference spectra demonstrate rapid changes in algal concentration on this time scale and on the spatial scale of the instrument. Changes in chlorophyll *a* had an amplitude of 70 percent. In one spectrum only the silt concentration varied.

7. ACKNOWLEDGEMENTS

We would like to express our thanks to J.C. Kromkamp of the Netherlands Institute of Ecological Research for use of the research vessel Luctor. We thank R. Wouts for his help during the North Sea cruises, this part of work was financed by the Dutch Remote Sensing Board (BCRS). We thank M. Donze for his critical comments on the manuscript.

8. REFERENCES

1. R.W. Preisendorfer, "*Hydrologic optics*", Vol. I: Introduction, U.S. Department of Commerce, 218 pp., 1976.
2. J.T.O. Kirk, "*Light and photosynthesis in aquatic ecosystems*", Cambridge university press, Cambridge. 401 pp., 1983.
3. A. Gershun, A., "The light field", J. Math. Phys. (Cambridge Mass.) 18: 51-151, 1939.
4. N.K. Højerslev, "A spectral light absorption meter for measurements in the sea", Limnol. Oceanogr. 20: 1024-1034, 1975.
5. J.E. Tyler, R.C. Smith & W.H. Wilson Jr., "Predicted optical properties for clear natural water", J. Opt. Soc. Am. 62: 83-91 1972.
6. J.R.V. Zaneveld, "An asymptotic closure theory for irradiance in the sea and its inversion to obtain the inherent optical properties", Limnol. Oceanogr. 34: 1442-1452, 1989.
7. H. Haardt & H. Maske, "Specific in vivo absorption coefficient of chlorophyll *a* at 675 nm", Limnol. Oceanogr. 32: 608-619. 1987.
8. P. Elterman, "Integrating cavity spectroscopy", Applied Optics, 9: 2140-2142, 1970.
9. E.S Fry & G.W Kattawar, "Measurement of the absorption coefficient of ocean water using isotropic illumination". Proc SPIE 925 (Ocean Optics IX), 142-148, 1988.
10. K.Shibata, A.A. Benson & M. Calvin, "The absorption spectra of suspensions of living micro-organisms", Biochimica et Biophysica Acta, 15: 461-470, 1954.
11. J.T. Petzold 1977. "Volume scattering functions for selected ocean waters." *Light in the sea*, J.E. Tyler, 152-174, (Benchmark papers in optics: V.3), Dowdon, Hutchinson and Ross, Stroudsburg, Pennsylvania: 1977.
12. T.T. Bannister, "Estimation of absorption coefficients of scattering suspensions using opal glass", Limnol. Oceanogr. 33: 607-615, 1988.
13. C.S. Yentch, "Measurement of visible light absorption by particulate matter in the ocean", Limnol. Oceanogr. 7: 207-217, 1962.
14. W.L. Butler, "Absorption of light by turbid materials, Journal of the Optical Society of America", 52: 292-299, 1962..
15. D.A.Kiefer & J.B. Soohoo, "Spectral absorption by marine particles of coastal waters of Baja California", Limnol. Oceanogr. 27: 492-499, 1982.
16. B.G. Mitchell & D.A. Kiefer, "Chlorophyll *a* specific absorption and fluorescence excitation spectra for light-limited phytoplankton", Deep-Sea Research, 35: 639-663, 1988.
17. J.T.O. Kirk, "Spectral absorption properties of natural waters: contribution of the soluble and particulate fractions to light absorption in some inland waters of south eastern Australia", Aust. J. Mar. Freshwater Res., 31: 287-297, 1980.
18. R.J. Davies-colley, "Optical properties and reflectance spectra of 3 shallow lakes obtained from a spectrophotometric study", New Zealand J. Marine Freshwater Res. 17: 445-459, 1983.
19. J.R.V. Zaneveld , R. Bartz & J.C. Kitchen, "A reflective-tube absorption meter", Proc. SPIE 1302 (Ocean Optics X), 124-136, 1990.

20. NEN 6484, "Water - Determination of the content of not dissolved material and its ignition residue", Nederlandse Norm Instituut, Delft, 4pp, 1982.
21. NEN 6520, "Water - Spectrophotometric determination of Chlorophyll *a* content", Nederlandse Norm Instituut, Delft, 6pp., 1981.
22. W.W.C. Gieskes, G.W. Kraay, A. Nontji, D. Setiapermana & Sutuno, "Monsoonal alteration of a mixed and layered structure in the phytoplankton of the euphotic zone of the Banda Sea (Indonesia), a mathematical analysis of algal pigment finger prints", *Neth. J. Sea Res.* 22: 123-137., 1988.
23. R.C. Smith & K.S. Baker, "Optical properties of the clearest natural waters (200-800 nm)", *Applied Optics* 20: 17-184, 1981.
24. W.S. Pegau & J.R.V. Zaneveld 1993. "Temperature-dependent absorption of water in the red and near-infrared portions of the spectrum". *Limnol. Oceanogr.* 38: 188-192, 1993.
25. H. Buiteveld, J.H.M. Hakvoort & M. Donze, "The optical properties of pure water" *Proc. SPIE 2258 (Ocean Optics XII)*, 1994.
26. J.S. Cleveland, R.M. Pope & E.S. Fry, "Spectral absorption coefficients measured with an integrating cavity absorption meter", *Proc. SPIE 1302 (Ocean Optics X)*, 176-186, 1990.
27. J.H.M. Hakvoort J. Krijgsman & M. Donze, "Upward radiance attenuation is an estimate of in-situ absorption: a comparison with laboratory measurements, In: J. Krijgsman, Thesis. *Optical remote sensing of water quality parameter. Interpretation of reflectance spectra*. Delft University Press: 173-188, 1994.
28. J. Krijgsman, Thesis. *Optical remote sensing of water quality parameter. Interpretation of reflectance spectra*. Delft University Press, 153-172, 1994.

SESSION 2

Bio-Optical Variability

Maintaining a phytoplankton bloom in low mixed layer illumination in the Bellinghausen Sea in the Austral Spring, 1992.

A.R. Weeks and I.S. Robinson

Department of Oceanography, The University, Southampton, SO9 5NH

J. Aiken and G. Moore

Plymouth Marine Laboratory, Prospect Place, Plymouth, PL1 3DH

ABSTRACT

A phytoplankton bloom was observed between 67.2°S and 68.5°S which extended over at least 4 degrees of longitude from 84° to 88°W in the Bellinghausen Sea. The northern boundary of the bloom was associated with a strong eastward flowing surface jet of low salinity water. The controlling factors for phytoplankton growth were explored by examining north to south transects of surface stability, inorganic nutrients, mean mixed layer irradiance and surface currents. The only parameter found to change along with the phytoplankton biomass was the mean mixed layer irradiance, which approached the light limitation thresholds for Antarctic phytoplankton. A hypothesis to explain the presence of the high concentrations of phytoplankton is a positive feedback mechanism in which the phytoplankton grow well in the low light conditions of the mixed layer. The high concentrations of biomass reduce the light sufficiently to allow low light-adapted phytoplankton to flourish, in contrast to the phytoplankton in the clearer waters north and south of the bloom.

1. INTRODUCTION

Southern Ocean waters are unusual for their oligotrophic characteristics even during the austral spring when the commencement of the solar heating season initiates ice melting and surface waters become stratified¹. The major inorganic nutrient levels stay relatively high throughout the austral summer² and therefore do not limit phytoplankton growth. Phytoplankton growth theory predicts an increase in phytoplankton biomass during spring due to the formation of stable lenses induced by ice-melting but these rapidly decay at the seaward edge by deep vertical mixing due to violent winds^{3,4,5}. High chlorophyll concentrations are typically only observed in isolated patches as the archive of chlorophyll measurements from the CZCS show⁶. By examining a spatially extensive bloom which lasted at least 6 weeks, this paper attempts to explain how a phytoplankton bloom is initiated and maintained in these waters, and discusses the limiting factors which may prevent widespread blooms in the Southern Ocean.

During winter the sea ice extends some 250km from the Antarctic coastline, and rapidly retreats at the start of the solar heating season. The classic model attributes the initiation of phytoplankton growth to the onset of stratification, provided surface nutrient levels are not bio-limiting⁷. However, this seems not to be applicable to Southern Ocean waters because recent studies in the marginal ice zone of the Weddell Sea report low phytoplankton concentrations in areas exhibiting near-surface stability, where the major inorganic nutrients are not limiting growth^{8,9}. Trace nutrient levels may limit the growth of phytoplankton. However Lancelot¹⁰ did not find any evidence of iron limitation in studies in the Weddell Sea.

The ice communities of phytoplankton are possible seed communities for those in open water. Lizotte¹¹ has shown that these ice communities are well adapted to low light conditions, typically photo-inhibition occur at 20Wm^{-2} . Any phytoplankton released into the water from melting ice would have these characteristics although in some species, such as the small pennates, photo-adaptation to higher light levels is extremely rapid. In contrast, larger diatoms are found to be extremely sensitive to and unable to survive a change from low to high light levels.

There is evidence that oceanic Antarctic phytoplankton only grow well between a small range of light levels. For example Lancelot¹² shows that ice cover greater than 40% prevents phytoplankton growth. In contrast, there is evidence of photo-inhibition when the underwater solar irradiance is greater than about 20Wm^{-2} ($100\ \mu\text{E m}^{-2}\text{s}^{-1}$)^{12,13,14}.

Lancelot¹² shows that during the period of ice retreat along the (0-20% ice cover) a significant phytoplankton biomass peak was observed even though the mixed layer depth was approximately constant during the transect along the 49°W meridian. Light levels are observed to vary inversely with chlorophyll concentrations. The results of her model show a shallowing of the mixed layer as the ice melted, and between 0-20% ice cover, a mixed layer depth of $\sim 60\text{m}$ and light winds an increase in the chlorophyll concentration due to growth. As the stable layer is maintained, and ice cover diminishes to zero the chlorophyll bloom is reduced.

Grazing pressure may be an important control for phytoplankton. In an area where there are large fluctuations in chlorophyll, one would expect similar fluctuations in phytoplankton groups, with those preferred by zooplankton populations to be in lower concentrations than those least preferred.

2. THE HIGH PHYTOPLANKTON BIOMASS REGION SAMPLED DURING DISCOVERY CRUISE 198.

The cruise took place from 11th November to 17th December 1992 and included an intensive grid survey in the Bellinghausen sea (Figure 1). A region of high chlorophyll was sampled between 67°S and 68°S which extended approximately from east to west (Figure 2). High phytoplankton values had been present in this area since before the first transect sampled by the James Clarke Ross on 12th November to after Discovery left the area on 10th December. Chlorophyll concentrations as high as 7.5 mg m⁻³ were measured. The northern boundary of the high phytoplankton patch coincided approximately with a density front¹⁵.

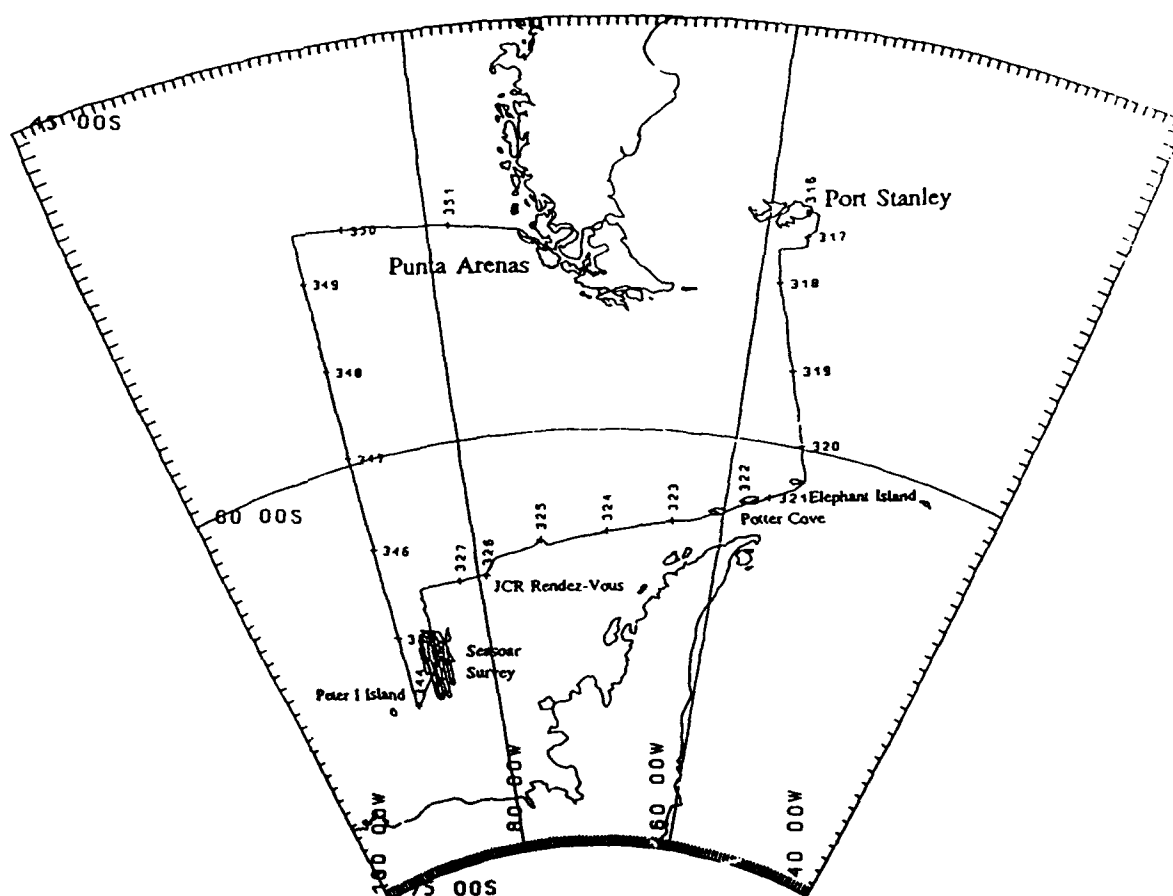


Figure 1. The cruise track for D198. The cruise commenced on 11th November 1992 from the Falkland Islands and terminated on 17th December 1992 in Punta Arenas, Chile.

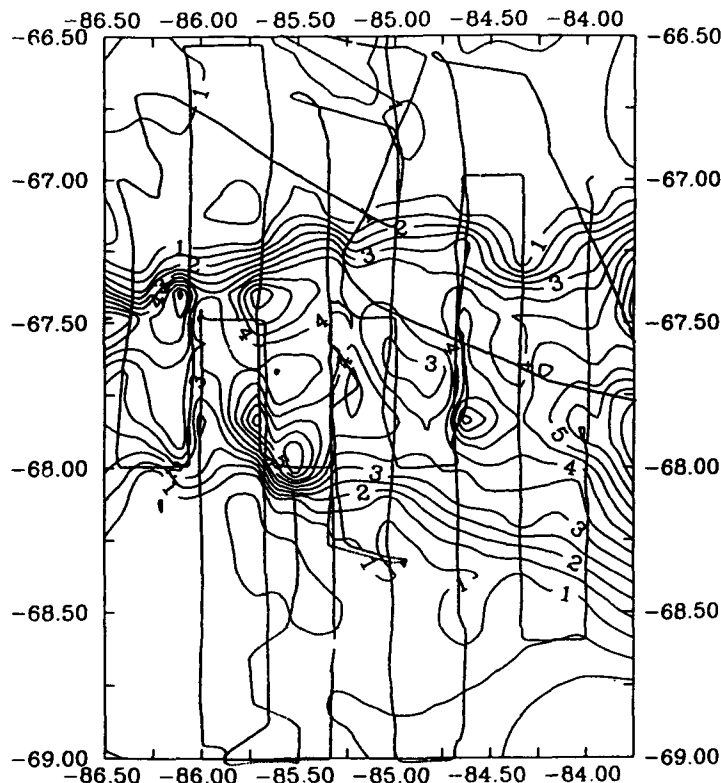


Figure 2. The region of the two surveys in the Bellinghausen Sea, an area centred on 85°W and between 65°S and 69°S. The surveys are merged in the diagram. Survey 1 was between 23-28/11/92 and Survey 2 was between 2-8/12/92. Underway chlorophyll values were sampled from water pumped from 3m below the surface through an Turner Designs fluorometer (Model 10-005); the *in vivo* fluorescence was calibrated using by comparing with chlorophyll values measured by a bench fluorometer (Turner Designs 10AU fluorometer).

To the north of the high chlorophyll region, between 65.0°S and 66.8°S, salinities were relatively high (>33.75) and chlorophyll values were in the order of 1 mg m^{-3} . Between 66.8°S and 67.2°S there was a low salinity band of water (<33.75) with high eastward velocities of $>10 \text{ cm s}^{-1}$ and up to 50 cm s^{-1} ¹⁶. The jet persisted between 67.2°S and 67.4°S and here chlorophyll values were high ($\sim 4 \text{ mg m}^{-3}$), as was salinity. Between 67.4°S and 68.2°S the velocities relaxed and chlorophyll remained high, but patchier than within the jet. Between 68.2°S and 70.0°S chlorophyll values were low. The boundary of the frontal jet appears to delineate a physical barrier to the northward extent of the high phytoplankton region. However it is less clear what the mechanism for the southern boundary was, and the transition to negligible chlorophyll values, between 68.0°S and 68.5°S, was much more diffuse than in the north.

The vertical structure of the upper part of the water column revealed two pycnoclines; the first was at a depth of 70m and the second between 150 and 200m. The deeper pycnocline, with both a temperature and salinity gradient across it, has been identified as the maximum depth of the winter mixed layer¹⁶. The shallower pycnocline was characterised by a halocline only and its origin may be due to summer ice melting, therefore having a shorter history than the deeper pycnocline. The mixed layer depth shallowed with distance to the south. During Survey 2 it was close to 100m at 67.0°S, whereas at 69.0°S it was only 58m. However most of the shallowing was between 67.0 and 67.6°. The high chlorophyll was restricted to the upper mixed layer, to 70m. This caused considerable shading to the waters below due to the enhanced attenuation of the solar radiance by the presence of the phytoplankton biomass.

The bloom was first discovered on 12th November by the James Clark Ross (JCR) while the area was still covered with ice, although the ice was broken enough to allow the ship to pass through it (Figure 3). During the first transect the ice reached as far north as 66.5°S. The bloom was sampled again on 19th November by the JCR, the ice extending to 67.3°N. RRS Discovery reached the area on 22nd November by which time the ice had retreated to ~69°S and then spent 15 days in the area repeatedly sampling the bloom. It was sampled again 4 days later along 88°W during the passage north. Overall the bloom was sampled over a period of 30 days, during which time chlorophyll levels remained high, typically greater than 4 mg m⁻³.

The aim of the work described in this paper was to examine the characteristics of the ocean that allowed such region of high phytoplankton biomass to develop and to be maintained, when all around it phytoplankton biomass concentrations were very low.

3. METHODS

Observations of water properties were made using a towed undulating system, the SeaSoar, and by sampling water from a pumped supply taken 3m below the surface when the ship was underway. The SeaSoar, developed from the Batfish¹⁷ has a depth range of 0-400m at a towing speed of 4 ms⁻¹ (8 knots) and uses a fully-faired conducting cable to communicate measurements in real-time from CTD sensors, a fluorometer and a PAR sensor. The

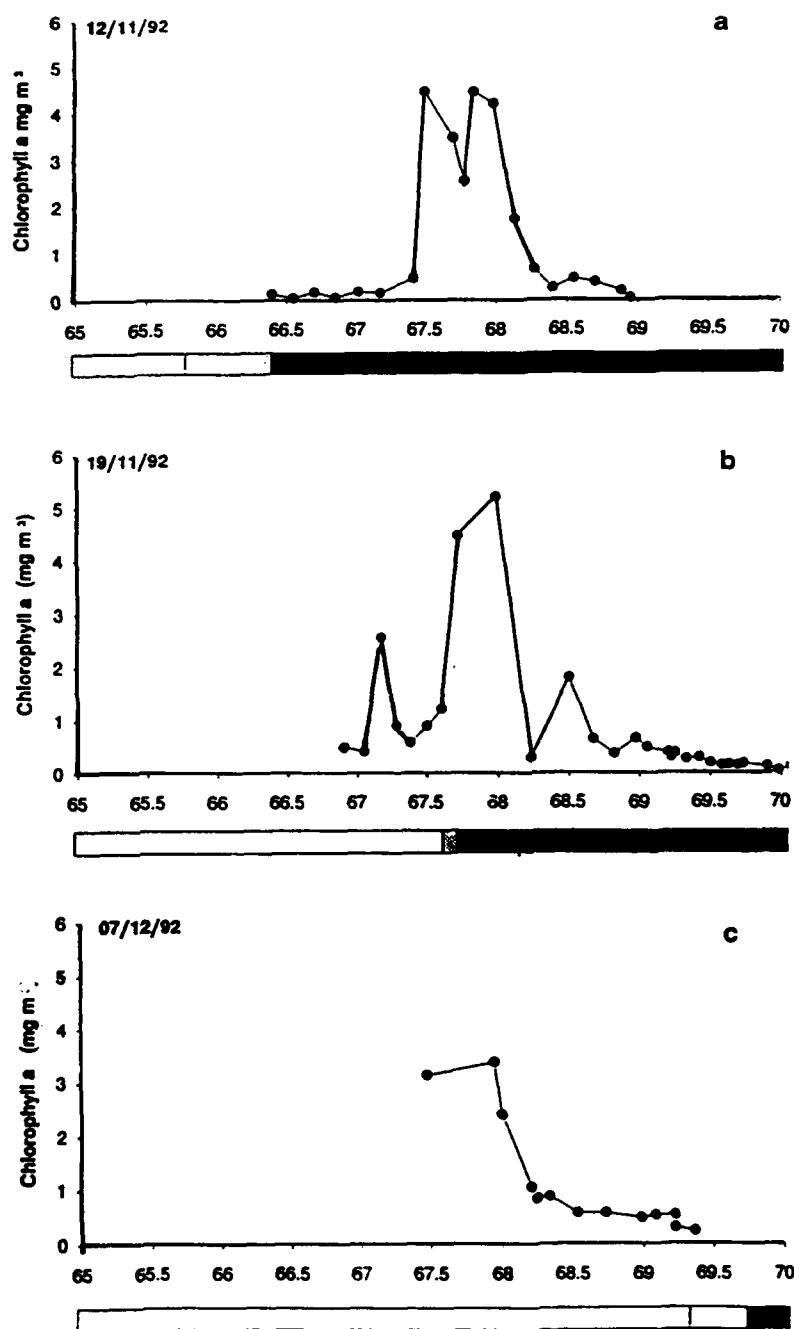


Figure 3. Transects along 85°W showing chlorophyll a (mg m⁻³), surface samples, and the retreat of the ice cover.

a) 12/11/92 b) 19/11/92 c) 7/11/92;

a) and b) from RRS James Clarke Ross, b) from RRS Discovery.

fluorometer (Chelsea Instruments SubAquatracker) is used to determine the phytoplankton chlorophyll concentration and the PAR sensor measures photosynthetically available radiation. SeaSoar operational methods follow those described in Fasham¹⁸. Data were averaged once per second giving a vertical resolution of 1m,. The undulation cycle length was 3km. Data were interpolated onto a two-dimensional grid, resolved to 8m in the vertical and horizontally to 0.04° latitude. Sigma-0 was calculated from measurements of conductivity, temperature and depth following the method described in Millero¹⁹.

Fluorescence measurements were calibrated and converted to chlorophyll concentrations by comparing fluorescence measurements with smaller data sets of extracted chlorophyll concentrations. These were obtained from the same body of water as the fluorometer, collected every hour from sub-surface water along the transects.

The downwelling irradiance PAR sensor and the other irradiance channels on the SeaSoar were calibrated before the cruise on an optical bench by comparing the sensor signal recorded with a standard detector (United Detector Technology (UDT) 81 radiometer) having NBS traceable calibration and giving measurements in $\mu\text{W cm}^{-2}$ ²⁰. Regression of the irradiance sensor signals and the light intensity measured by the UDT at a series of distances from a constant light source provide the calibration constants used to give measurements of relative intensity. The downwelling diffuse attenuation coefficient ($K_{d\text{PAR}}$) was calculated from the gradient of the downwelling PAR irradiance after resolution in 8m depth bins.

Downwelling above-surface PAR was measured using Didcot cosine collectors (spectral range: 400-700nm) located port and starboard on the forward mast. Calibration was carried out by the manufacturer prior to the cruise during installation of the sensors.

Surface currents were measured by means of a hull-mounted RD Instruments 150KHz an Acoustic Doppler Current Profiler (ADCP)²¹. The use of ADCPs for calculating current vectors are now routine²².

4. FACTORS CONTROLLING THE LOCATION OF THE PHYTOPLANKTON BLOOM

The northern and southern boundaries of the bloom may be influenced by a changing flow regime, by changing water masses which vary in terms of nutrients or mixed layer depths. The light available for growth may also be a limiting factor for phytoplankton growth. Grazing by zooplankton may rapidly reduce the phytoplankton biomass. The following section examines how these parameters changed with latitude from the region north of the front, to within the high chlorophyll region and to south of it. By identifying the parameters that varied significantly it should be possible to determine the likely cause of the persistence of the high phytoplankton values in the region.

The northern boundary of the bloom was associated with a density front (Figure 4), along which there was an eastward flowing jet. Between 67.4°S and 68.2°S there was a region of current flow with low velocities, which may be a possible accumulation zone for both phytoplankton and zooplankton. However north of this, between 67.2°S and 67.4°S the eastward flowing jet of water also had high phytoplankton. High biomass values may build up when currents slacken, allowing accumulation in the region, but the presence of the jet containing high biomass cannot be reconciled with this argument. In the south there was no real evidence of a frontal jet, which could provide a region for strong dispersal, but the velocities were higher here than within the phytoplankton maximum. However the surface current velocities (Figure 5) indicate the presence of an anticyclonic gyre. The central part of this would be expected to be a zone of accumulation, whereas the outer reaches a likely zone of dispersal.

The location of a phytoplankton bloom may be determined by the horizontal variation in the stability of the upper few hundred meters of the water column. The stability can be described by calculating the Brunt Vaisalla Frequency, defined as N where

$$N^2 = g \left[-\frac{1}{\rho} \frac{\delta \sigma_t}{\delta z} \right] \quad s^{-1}$$

However, when this was calculated from the 8m depth interval gridded data for section A in Survey 1, there was no apparent latitudinal variation in stability to account for the increased chlorophyll south of the surface front at 67°S. The values of σ_θ and N^2 are shown in Figure 6a and 6b.

It is possible that the major inorganic nutrients were biolimiting outside the region of high chlorophyll. However this was not found to be the case as values were generally high. For example inorganic nitrate values were 9-10 $\mu\text{mol l}^{-1}$ in the chlorophyll maximum, and 20 $\mu\text{mol l}^{-1}$ in the region to the north of the bloom where chlorophyll values were low. There is no evidence from our study that the bloom was limited by the major inorganic nutrients.

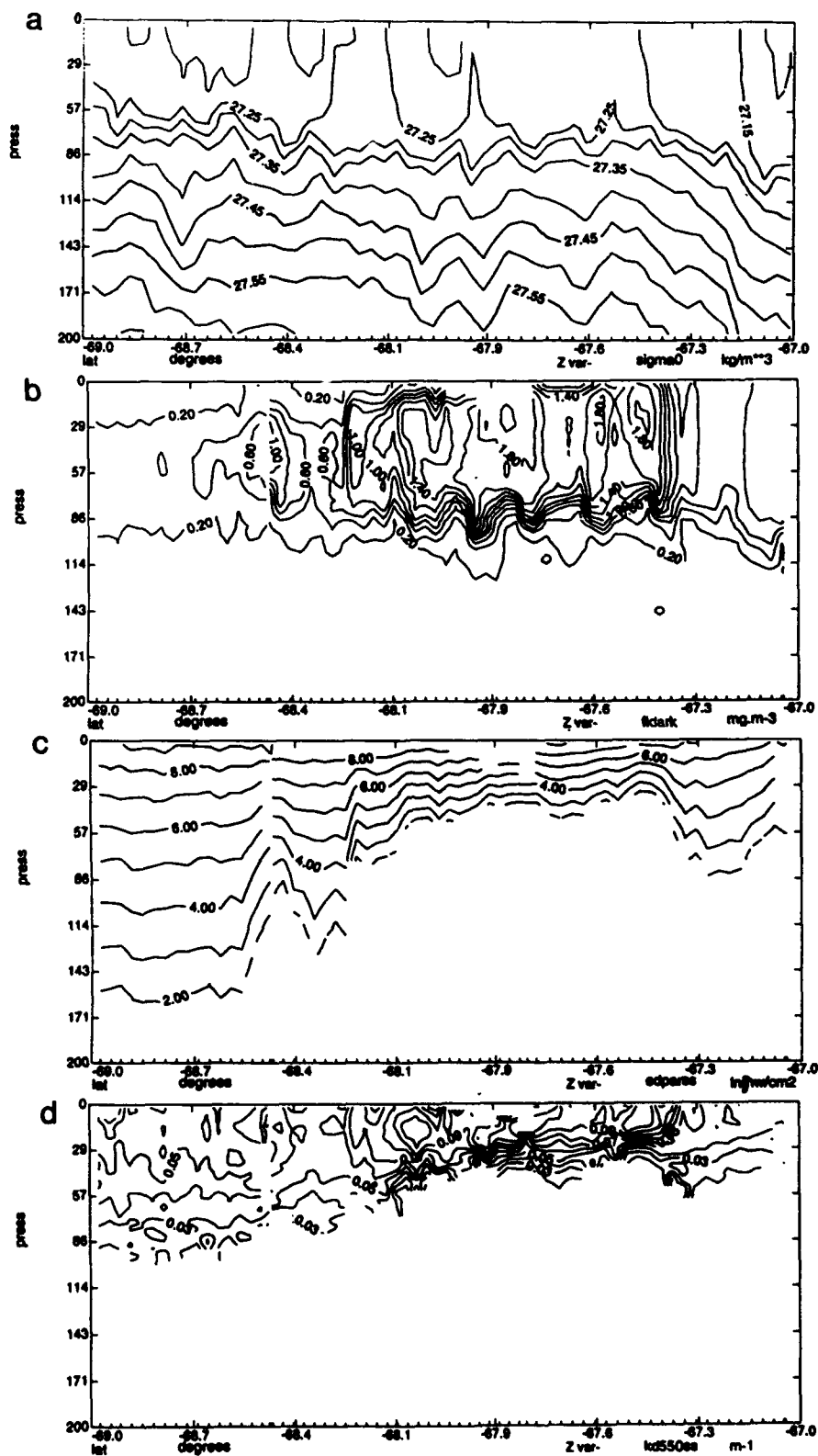


Figure 4. Section along transect B, survey 2 showing Seasoar data. a) Sigma-0. b) Chlorophyll from *in vivo* fluorescence (mg m^{-3}). c) Downwelling PAR ($\ln \mu\text{W cm}^{-2}$). d) Diffuse attenuation coefficient at 550nm (K_{4550}) (m^{-1}).

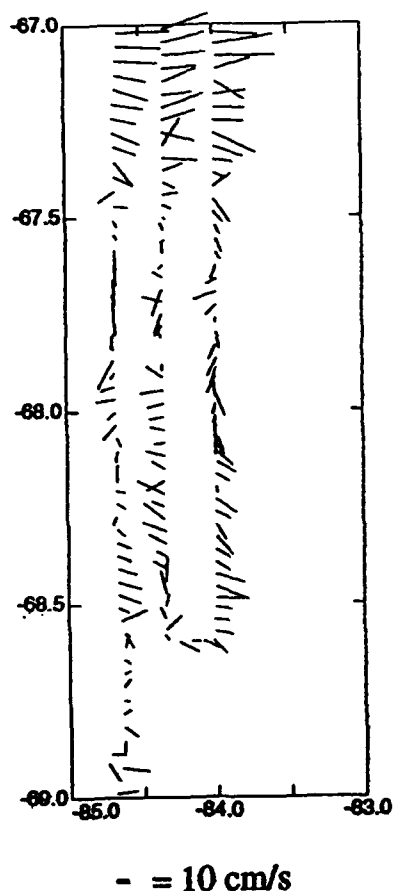


Figure 5. Surface currents, measured by ADCP (10 cm s^{-1}).

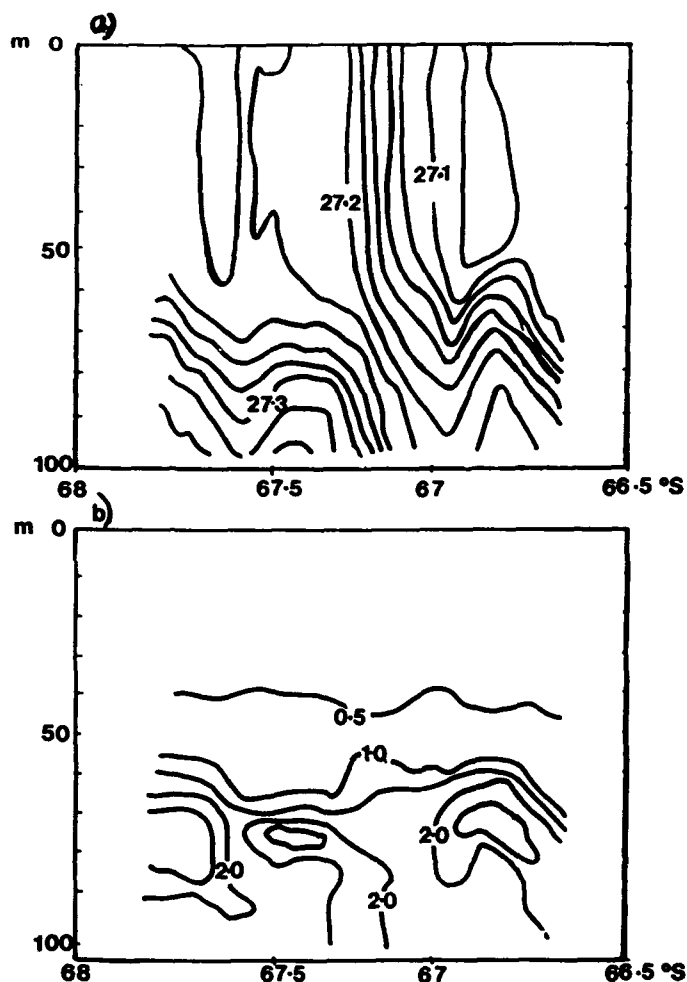


Figure 6. Diagram to show the well-mixed surface layer using Section A, from Survey 1 as an example. a) Sigma-0 (kg m^{-3}) and b) The Brunt Vaisala frequency (N^2) (cycles per hour).

The distribution of zooplankton in the surface mixed layer was closely associated with the phytoplankton biomass²³. There is no evidence that zooplankton grazing was great enough to significantly diminish the bloom in the surface mixed layer.

The effect of the phytoplankton bloom was to reduce significantly the amount of PAR penetrating into the upper ocean (Figure 4). The 1% light level was found in the region of the bloom at about 30m, whereas outside, it reached $> 80\text{m}$. The attenuation of the light can be attributed to the phytoplankton bloom as the diffuse attenuation coefficient for downwelling irradiance at 550 nm, the wavelength where absorption by chlorophyll and dissolved organic material is relatively small, shows a maximum at the same location as the bloom. When the mean values (for the top 50m) of K_{550} is compared with chlorophyll (Figure 7) there is a good relationship, implying that the attenuation is mostly attributable to the phytoplankton.

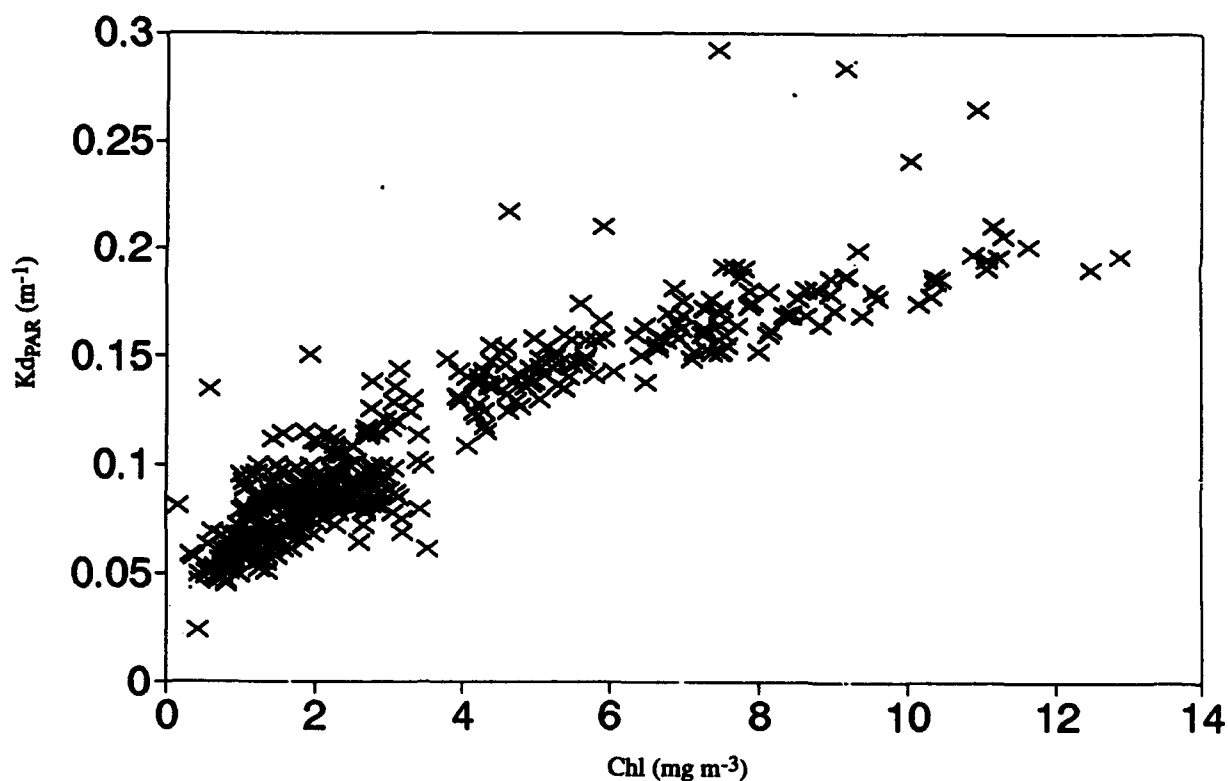


Figure 7. The relationship of K_{dPAR} (m^{-1}) and chlorophyll ($mg\ m^{-3}$) from SeaSoar; both are averaged over the top 50m.

These results show that there was no significant change in the depth of the mixed layer from 65°S to 69°S. Furthermore, although the inorganic nutrient levels were reduced in the high phytoplankton region, they were not biolimiting. However there is evidence of a change in current flow from north to south, with a central region of low currents associated with the high phytoplankton concentrations. However the fact that there were high chlorophyll values within the southern part of the jet suggests that current flow, and the forces of accumulation and dispersal were not the dominant factor in controlling growth. The zooplankton distributions in the surface mixed layer do not suggest high grazing pressure on the phytoplankton. The most significantly varying parameter is the light available in the mixed layer, due to the high attenuation by the phytoplankton biomass.

5. DISCUSSION

The penetration of PAR below the surface was strongly influenced by the phytoplankton biomass. In the bloom the mean illumination that the phytoplankton were exposed to as they circulated by turbulent mixing in the wind-mixed layer was considerably less than for those phytoplankton outside the bloom. A possible mechanism to sustain their growth within the bloom is that the high biomass restricts the mean mixed layer illumination. If they are low light-adapted phytoplankton having been seeded from ice communities, then those in the bloom would grow better than those outside it where the high light levels would inhibit growth. In other areas, the bloom, once established creates the shading necessary to nurture growth.

The transect along 85°W on 12/11/92 (Figure 3) shows that there was still ice cover as far north as 66.4°S and yet chlorophyll values up to 5 mg m⁻³ between 67.5 and 68.5°S. The phytoplankton biomass was high under the low light conditions under the ice. This suggests that the phytoplankton were adapted to low light conditions.

A hypothesis can be posed that phytoplankton of the low light-adapted species can only develop under the ice. Once established, however, as the ice thins and melts completely, the high biomass may continue to protect the phytoplankton from high illumination levels. Outside the bloom area, the phytoplankton in the mixed layer will be exposed to higher mean mixed layer illumination, and the low light-adapted phytoplankton will fare badly. This would imply that a critical parameter (shading/mixed layer depth) may have to be attained for optimal growth. There is evidence from the phytoplankton counts that the phytoplankton outside the bloom region were pale in colour and unhealthy, whereas those in the bloom were in good condition.

A comparison of mean light values and concentrations of chlorophyll, from in vivo fluorescence, in the mixed layer shows that in the region of the bloom the mean light levels were ~12 Wm⁻², whereas to the south of the bloom they increased to about 16 W m⁻² (Figure 8a). The mixed layer was determined as a difference in sigma-0 of less than 0.02. The mean mixed layer concentrations of chlorophyll and PAR_d were calculated simply by averaging the gridded data from the surface to the depth of the mixed layer. The values of PAR_d were close to the light saturation levels for Antarctic phytoplankton¹¹. So although PAR values above the surface values range from 0 - 300 W m⁻² over 24 hours, the phytoplankton circulating in the mixed layer received a much smaller amount of light due to their passage from dark to light waters as they circulated in the mixed layer.

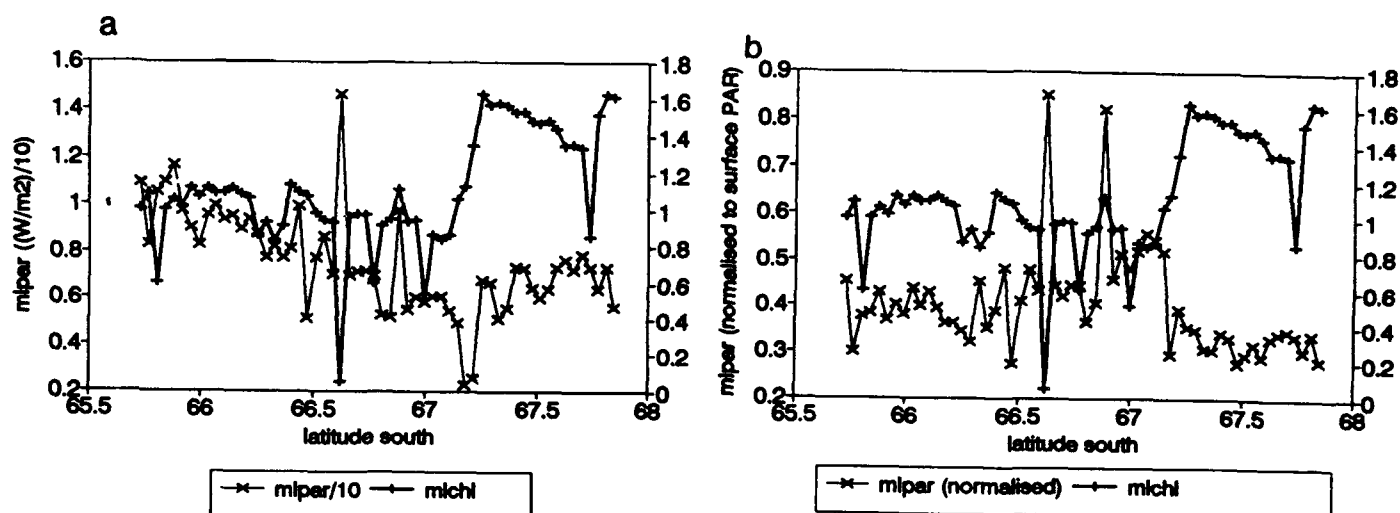


Figure 8. a) Mixed layer chlorophyll (mg m^{-3}) (from calibrated fluorescence) plotted versus mixed layer PAR_d from SeaSoar (24/11/92). This shows the inverse relationship between the parameters ($r=-0.62$). b) As a) but in this case PAR_d is normalised with surface PAR_d values.

When PAR_d is normalised to sub-surface light values an inverse relationship between mixed layer PAR_d and chlorophyll is observed (Figure 8b). The data is presented in a scatter plot (Figure 9) and the correlation is -0.616 , $N=59$. High mixed layer chlorophyll is correlated with low mixed layer light.

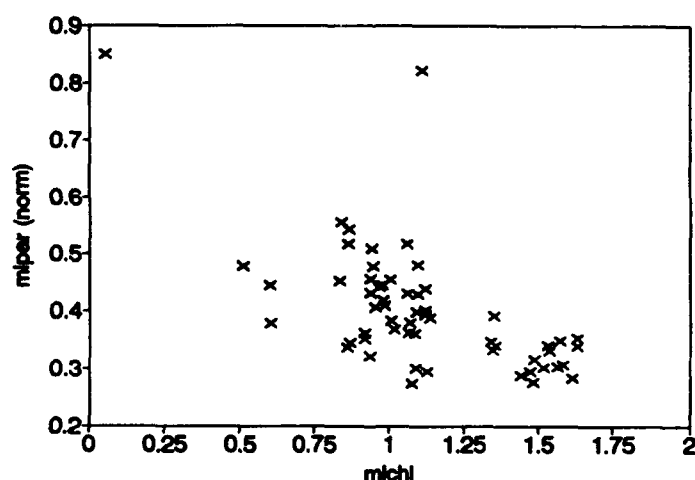


Figure 9. Mixed layer chlorophyll and PAR_d (normalised to surface PAR_d) between 65.5°S and 68.0°S , Survey 1, Section A.

6. CONCLUSIONS

The data presented suggests that the phytoplankton that circulated in the mixed layer were rather sensitive to a critical range of light levels. The growth of the low-light adapted phytoplankton may be controlled by a positive feedback mechanism. Our hypothesis is that blooms occurring under the ice must develop a critical biomass before the retreat of the ice so that they can be sustained by their own shade. This may be a delicate balance, depending on the rates of grazing by zooplankton. This mechanism may favour the larger diatoms like *Phaeocystis*, which are not the preferred food of zooplankton.

7. ACKNOWLEDGEMENTS

We would like to thank scientists from the James Clarke Ross for the chlorophyll a data presented in Figure 3; Derek Harbour, at Plymouth Marine Laboratory (PML) for the phytoplankton counts, and Bob Head (PML) for the inorganic nutrient data. The work was carried out by means of grants from the Natural Environment Research Council Special Topics for The World Ocean Circulation Experiment and for the British Antarctic Survey Southern Ocean Experiment. The authors gratefully acknowledge these grants.

8. REFERENCES

1. S.Z.El-Sayed. "Biological productivity of Antarctic waters; present paradoxes and emerging paradigms," Editors: S.Z.El-Sayed and A.P.Tomo, *Antarctic Aquatic Biology*, Vol. 7, pp. 1-23, Scott Polar Institute, Cambridge, U.K., 1983.
2. H.A.Sievers and W.D.Nowlin. "Upper ocean characteristics in Drake Passage and adjoining areas of the Southern Ocean, 39°W-95°W," *Antarctic Ocean and Resources Variability*, Editor: D.Sahrhage, pp.57-80, Springer-Verlag, Berlin, 1988.
3. O.Holm-Hansen, S.Z.El-Sayed, G.S.Francheschini and R.L.Cuhel. "Primary production and factors controlling growth in the Southern Ocean," In *Adaption within Antarctic ecosystems*, Editor: G.Llano, pp. 11-50, Gulf, 1977.
4. W.O.Smith and D.M.Nelson. "Phytoplankton bloom produced by a receding ice edge in the Ross Sea: spatial coherence within the density field," *Science*, Vol. 227, pp.163-166 1985
5. C.W.Sullivan, C.R.McClain. J.C.Cosimo and W.O.Smith. "Phytoplankton standing crops within an Antarctic ice edge assessed by satellite remote sensing," *Journal of geophysical research*, Vol. 93, pp. 12487-12498, 1988.
6. J.C.Cosimo, N.G.Maynard, W.O.Smith and C.W.Sullivan. "Satellite ocean colour studies of Antarctic ice edges in summer and autumn," *Journal of Geophysical research*, Vol. 95,6, pp.9481-9496, 1990.

7. H.U.Sverdrup. "On conditions for the vernal blooming of phytoplankton," *Journal du Conseil Permanent International pour L'Exploration de la Mer*, Vol. 18, pp.287-295,1953.
8. D.M.Nelson, W.O.Smith, L.I.Gordon and B.A.Huber. "Spring distributions of density, nutrients, and phytoplankton biomass in the ice edge zone of the Weddell-Scotia Sea," *Journal of Geophysical Research*, Vol.92, pp. 7181-7190, 1987.
9. C.Veth, C. Lancelot and S.Ober."On processes determining the vertical stability of surface waters in the marginal ice zone of the north-western Weddell Sea and their relationship with phytoplankton bloom development," *Polar Biology*, Vol.12, pp.237-243, 1992.
10. C.Lancelot, S.Mathot, C.Veth and H. de Baar. "Factors controlling phytoplankton ice-edge blooms in the marginal ice-zone of the northwestern Weddell Sea during sea ice retreat 1988:field observations and mathematical modelling," *Polar Biology*, Vol. 13, pp. 377-387, 1993.
11. M.P.Lizotte and C.W.Sullivan. "Photosynthetic capacity in microalgae associated with Antarctic pack ice," *Polar Biology*, Vol.12, pp. 497-502, 1992.
12. C.Lancelot, C.Veth and S.Mathot. "Modelling ice-edge phytoplankton bloom in the Scotia-Weddell sea sector of the Southern Ocean during spring 1988,". *Journal of Marine Systemes*, Vol. 2, pp.333-346, 1991.
13. R.I.Brightman and W.O.Smith. "Photosynthesis-irradiance relationships of antarctic phytoplankton during austral winter," *Marine Ecology Progress Series*, Vol.53, pp.143-151, 1989.
14. E.Saksung and O.Holm Hanson. "Photoadaptation in Antarctic phytoplankton:Variations in growth rate, chemical composition and *P* versus *I* curves," *Journal of Plankton Research*, Vol. 8, pp.459-473, 1986.
15. D.R.Turner. "Sterna 92 overview part 2: Spatial and temporal development of the 85°W bloom," *Deep Sea Research*, submitted.
16. R.T.Pollard, J.F.Read, J.T.Allen, G.Griffiths and A.I.Morrison. "On the physical structure of a front in the Bellinghausen sea," *Deep Sea Research*, submitted, 1994
17. J.G. Dessureault." "Batfish" A depth controllable towed body for collecting oceanographic data," *Ocean Engineering*,Vol.3, pp. 99-111,1976.
18. M.J.R.Fasham, P.M.Holligan and P.R.Pugh. "The spatial and temporal development of the spring phytoplankton bloom in the Celtic sea," *Progress in Oceanography*, Vol.12, pp.87-145, 1983.
19. F.J. Millero and A. Poisson. "International one-atmosphere equation of state of seawater," *Deep Sea Research*, Vol. 28A, pp. 625-629, 1981.
20. J. Aiken and I. Bellan. "A simple hemispherical, logarithmic light sensor," *SPIE, Ocean Optics VIII*, Vol. 637, pp.211-216.
21. G.Griffiths. "Using 3D GPS heading for improving underway Aacoustic Doppler Current Profiler data," *Journal of Atmospheroc and Oceanic technology*, submitted.
22. W.E.Woodward and G.F.Appell. Current velocity measurements using acoustic Doppler backscatter: a review," *IEEE Journal of Oceanographic Engineering* ,OE-11, pp.3-6, 1986
23. A.R.Weeks,G.Griffiths, H.Roe, I.S.Robinson, G.Moore, J.Aiken and A.Atkinson. "The distribution of backscatter from zooplankton during the spring bloom in the south east sector of the Pacific Ocean," *Deep Sea Research*, submitted.

Observing biologically induced optical variability in coastal waters

John J. Cullen*, Aurea M. Ciotti and Marlon R. Lewis

Dalhousie University, Department of Oceanography
Halifax, Nova Scotia, Canada B3H 4J1

* Also with: Bigelow Laboratory for Ocean Sciences
McKown Point, West Boothbay Harbor, Maine 04575

ABSTRACT

Biological and optical measurements were compared during studies in Bedford Basin, Nova Scotia. A principal objective was to evaluate a tethered spectral radiometer buoy, which measured downwelling irradiance at 490 nm and upwelling radiance in wavebands corresponding to the SeaWiFS satellite, along with the fluorescence of chlorophyll *a*. Movements of the buoy and changes in solar spectral irradiance influenced measurements. Nonetheless, records of upwelling radiance clearly described optical variability in the water. For example, blue:green radiance ratios were well correlated with water transparency, consistent with a published relationship, but for greener and more turbid waters than previously studied. Optical profiles, including diffuse attenuation at 3 wavelengths, detected a subsurface dinoflagellate bloom in August 1993. When the bloom was entrained into surface waters by afternoon winds, the radiometer buoy easily distinguished darker, red water from the background green water. During the study, a red:green radiance ratio and a measure of chlorophyll fluorescence (683 nm:670 nm radiance ratio) were well correlated with chlorophyll concentration near the surface, whereas green:blue ratios were not. Optical detection of a bloom during its development demonstrates that simple autonomous instruments might be used for detecting some phytoplankton blooms prior to significant environmental impact.

1. INTRODUCTION

Ocean color (water-leaving radiance) is an easily observed and immensely informative optical property. The magnitude and spectral distribution of water-leaving radiance depends on the characteristics of solar irradiance at the surface and the optical properties of the upper water column. These optical properties are strongly influenced by biogenic particles (phytoplankton¹, and to a lesser extent bacterioplankton and viruses²⁻⁴), which vary in concentration, size-distribution and cellular optical characteristics⁵. Thus, in the open ocean, local biological processes are largely responsible for the temporal and spatial variability in optical properties such as ocean color and water transparency. The situation is more complicated in coastal waters, because large and varying quantities of absorbing and scattering materials can be introduced to surface waters from sediments and terrestrial sources⁶. Nonetheless, phytoplankton are more abundant and variable near the coast^{7, 8}, and their optical properties are distinct from other absorbing and scattering materials⁹, so it is worthwhile to pursue optical methods for detecting biological variability in coastal waters.

Spatial and temporal variability in the concentrations and physiological properties of microscopic plankton has been studied for some time, but the optical manifestations of this variability are still being explored^{5, 10-13}. A central objective of our research program is to examine the links between optics and biology in the sea. One goal is to describe variability in phytoplankton biomass, community structure, and water transparency in terms of downwelling irradiance and upwelling radiance, measured at the surface in coastal waters with instruments that are appropriate for autonomous deployment on moorings or drifters. We describe here some preliminary observations and interpretations that may help with the analysis of data from optical buoys in coastal or open-ocean waters.

2. APPROACH

Biological and optical sampling was conducted from small (ca. 8 m) boats during 1992 and 1993 in Bedford Basin, near Halifax, Nova Scotia. Observations were made regularly during each spring, but ice and strong salinity gradients near the surface made it difficult to obtain reliable data on several of the sampling days. An intensive study was conducted from 17 to 20 August, 1993, during a predominantly subsurface bloom of the non-toxic dinoflagellate, *Gonyaulax digitale*¹⁴. Sets of observations were made each morning, near midday, and late afternoon. About one week subsequent to the study, anoxia

in the northern reaches of the Basin caused a fish kill that generated considerable public interest. Our optical observations from the week before made it easier to associate the anoxia with the decline of the dinoflagellate bloom.

2.1 Measurement of surface irradiance and near-surface upwelling radiance

A Tethered Spectral Radiometer Buoy (TSRB; Satlantic, Inc.) was deployed from the boat for about 1 h or less during each set of observations, drifting near the boat at the end of a 100 m conducting cable. It recorded downwelling solar irradiance at 490 nm (E_{d490} ; $\mu\text{W cm}^{-2} \text{ nm}^{-1}$) and upwelling radiance (L_u ; $\mu\text{W cm}^{-2} \text{ nm}^{-1} \text{ sr}^{-1}$) in seven wavebands corresponding to the six bands of the SeaWiFS ocean color satellite, and a channel for the fluorescence of chlorophyll *a* (Fig. 1). The TSRB is similar to the Expendable Spectral Radiometer¹⁵ (ESR) which is a drifter. The ESR transmits through the ARGOS satellite a statistical summary of measurements over the previous 1 h. With a sampling frequency of 1 s^{-1} , the TSRB is suited for examining the influence of short-term variability on those 1-h averages.

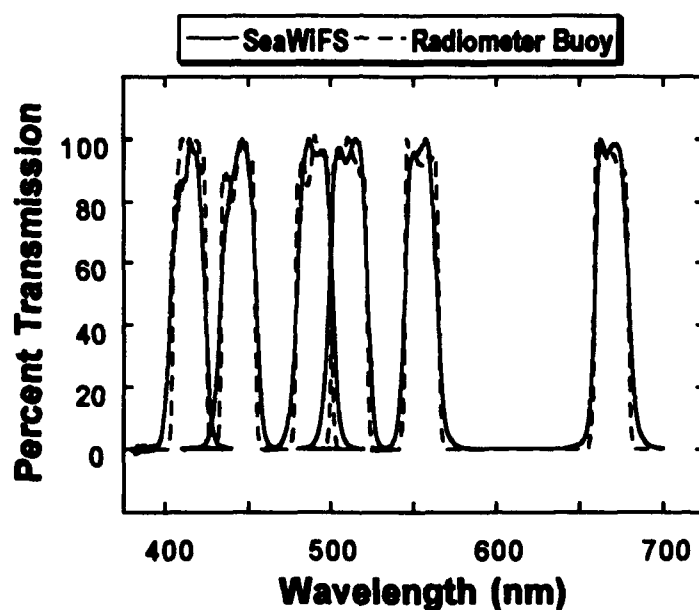


Fig. 1. Transmission characteristics of the filters on the TSRB (dashed line) compared to the SeaWiFS ocean color satellite (solid line). Nominal wavelengths are 412, 443, 490, 510, 555, and 670 nm. The TSRB has an additional band (10 nm half-band width) at 683 nm (not shown) for the estimation of fluorescence from chlorophyll 16, 17.

2.2 Vertical profiles of downwelling spectral irradiance

During 1992, an E_{d490} sensor was lowered and raised through the water column to estimate the attenuation of downwelling irradiance. Measurements were normalized relative to solar irradiance with reference to a Biospherical Instruments QSL-100 quantum scalar irradiance meter (400 - 700 nm) on deck, against a black background. Diffuse attenuation of downwelling spectral irradiance (K_{490} ; m^{-1}) was calculated for 0.5 m intervals, and averaged for up- and down-casts.

In August, 1993, a profiling K-meter was used to measure K at 3 wavelengths: 412, 510, and 555 nm (filters as in Fig. 1). Two sets of the three E_d sensors were attached to a frame, separated by 1.4 m. This distance is adjustable; for turbid coastal waters, a smaller separation would be better. The K-meter also measured pressure and temperature, and transmitted data to a logger on deck. Diffuse attenuation at each wavelength was calculated appropriately from the difference between the lower and upper sensors, and is reported for the mid-point depth.

2.3 Other measurements

A Sea-Bird Seacat 19 CTD was used for vertical profiles of temperature and salinity. It was equipped with a SeaTech transmissometer with a 25 cm pathlength and a SeaTech fluorometer. Beam attenuation (c ; m^{-1}) was corrected for the contribution from water by subtracting $0.364 m^{-1}$, as specified by the manufacturer. The fluorometer was saturated when it encountered the subsurface algal bloom.

Discrete samples for the measurement of chlorophyll *a* (Chl) and microscopic cell enumeration were taken from 0.5 cm I.D. Tygon hose, taped to exclude light. To achieve maximum vertical resolution and correspondence between profiles and discrete samples, the inlet was attached to the CTD very close to the fluorometer sensor. A small centrifugal pump (Little Giant, model 2E-N) provided propulsion. Samples for physiological measurements (not reported here) were taken from a Niskin bottle attached close to the CTD. The concentration of Chl was determined fluorometrically on triplicate samples, collected on Whatman GF/F filters, and extracted for at least 24 h at $-10^{\circ}C$ in the dark, using DMSO:90% acetone (1:3) as a solvent. The fluorometer (Turner Designs 10-005R with Corning filters and a blue lamp) was calibrated with Chl from Sigma.

3. EVALUATION OF THE RADIOMETER BUOY

Consistent with modern demands for radiometric accuracy, the TSRB is designed and calibrated to exacting specifications. Once the instrument is deployed, however, it encounters many insults that compromise accurate recording of Lu and Ed . Wave action is an obvious problem for a floating instrument, and all of our records show short-term variability associated with tilting and bobbing of the TSRB. Currents or wind can cause a tethered instrument to tilt in one direction; that problem will be discussed below. For long-term deployments, mechanical damage and fouling are concerns. One of our moorings was sheared by ice. An expendable drifter with inflatable flotation disappeared prematurely in the equatorial Pacific. Possibly, it attracted a shark. We address here the variability that was observed during relatively short deployments of the TSRB in a protected embayment.

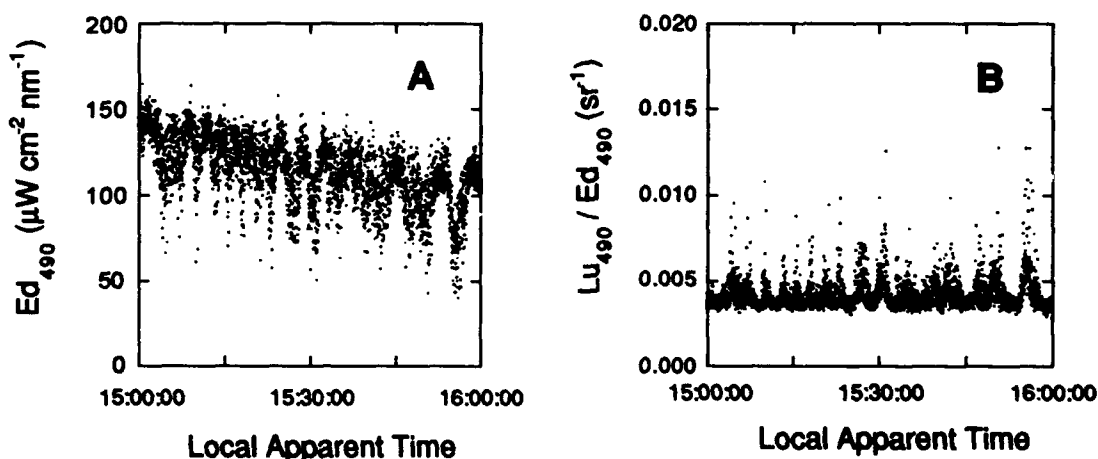


Fig. 2. Measurement from the TSRB on 9 August, 1992, in Bedford Basin, under clear skies and gentle winds, with little wave action. Atlantic Daylight time is 1 h 16 minutes later than local apparent time. A. Ed_{490} . B. TSRB reflectance at 490 nm [$R(490)_{TSRB}$, i.e., Lu_{490}/Ed_{490}].

3.1 Variability associated with orientation of the buoy

Data from a calm, clear afternoon illustrate the influence of orientation on measurements of Ed and Lu . During the deployment, the tilt of the tethered buoy, apparently caused by gentle currents and drifting of the boat, changed with a period of about 3 min, producing substantial artifactual variation in Ed_{490} (Fig 2A). A measure of reflectance (here referred to as $R(\lambda)_{TSRB} = Lu_{\lambda} / Ed_{490}$, units, sr^{-1}) was also affected severely (Fig. 2B). Longer-term changes (i.e., over 1 h), however, were

consistent with expectation. The relative decline of Ed_{490} , determined by linear regression, closely matched that predicted for clear skies at that time (Bird and Riordan model¹⁸, modified slightly). Changes in the upwelling radiance spectrum also matched model predictions: the ratio, $Lu_{412}:Lu_{670}$ declined 8% over the hour depicted in Fig. 2; similarly, the model, not completely tuned to local atmospheric conditions, predicted a decline of 6.4%. It seems that averaging data for 5-10 min would be adequate to obtain a good representation of Ed and Lu under these conditions.

Deviations associated with motion of the buoy can be described by subtracting the linear trend from the record of Ed_{490} . Comparison of $R(490)_{TSRB}$ with the Ed_{490} residual shows that estimated reflectance was strongly influenced by the orientation of the buoy. The nature of the relationship (Fig. 3A) is consistent with large changes of Ed as the sensor points toward and away from the sun, coupled with weak variation of Lu , as expected for a diffuse upwelling radiance field near the surface⁹. For less obvious reasons, the ratio, $Lu_{443}:Lu_{555}$ is also correlated with the Ed_{490} residual, indicating that tilting of the buoy caused about $\pm 15\%$ variation of that radiance ratio.

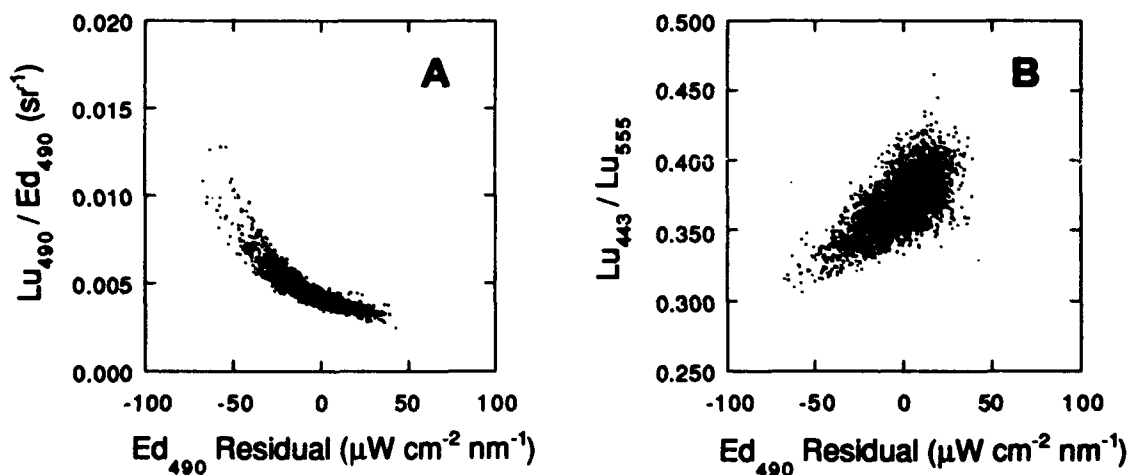


Fig. 3. Deviations of optical measurements as influenced by orientation of the buoy. Tilting of the buoy toward and away from the sun is represented by the residuals from a linear regression of Ed_{490} vs time. Same record as in Fig. 3. A. $R(490)_{TSRB}$ vs Ed_{490} residual. B. Lu_{443}/Lu_{555} vs Ed_{490} residual.

3.2 Variability from changes in solar spectral irradiance

Optical variability near the sea-surface is often described with upwelling radiance ratios¹⁹, and interpretation of these measures involves relating them to absorbing and scattering materials in the water^{20, 21}. It is thus desirable to account for any changes in upwelling radiance ratios that are due to variable spectral quality of solar irradiance. The direct solution is to measure Ed_{λ} at all wavelengths corresponding to Lu_{λ} , but that is not always practical or affordable. Instead, one could resort to solar radiation models of varying complexity to predict changes in clear-sky spectral irradiance during deployments. Compared to the variability in Lu ratios that we expect in coastal waters, predicted diel changes in ratios of solar spectral irradiance are fairly small (as shown in section 3.1) and well-behaved. Also, in the context of spectral variations discussed here, uniform cloud cover is close to spectrally neutral. Thus, if estimates of spectral reflectance were desired from TSRB data, it would seem reasonable to convert Ed_{490} measurements to Ed_{λ} using modeled solar spectra.

Partial clouds present a problem. When they don't block the sun, they can be good reflectors of sunlight, causing measurements of Ed exceeding clear-sky values (S. McLean, pers. comm.). When a cloud occludes the sun while much of the sky is clear, direct sunlight is attenuated to a greater extent than diffuse sunlight, which is relatively blue¹⁸. As a result, the longer visible wavelengths of solar spectral irradiance are differentially attenuated when patchy clouds block the sun, and upwelling radiance ratios shift toward the blue (Fig. 4). The effect is not overwhelming, but it is rapid, and could conceivably be misinterpreted if only Lu ratios were measured.

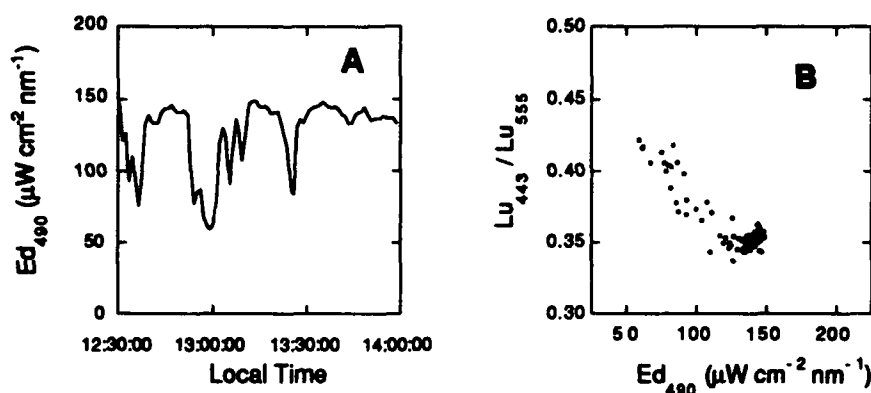


Fig. 4. The influence of patchy clouds on measurements from the TSRB. Observations from Redberry Lake, Saskatchewan, Canada, 9 June 1993. The water is green because light is absorbed principally by water and abundant dissolved organic matter. Chl was relatively low (ca. $1.5 mg m^{-3}$) and biologically-induced optical variability should have been slight²². A. Ed_{490} vs time during the passage of patchy clouds in front of the sun; 1-min averages. B. The ratio, $Lu_{443}:Lu_{555}$ vs Ed_{490} , showing that the blue:green ratio increased about 20% when a cloud blocked the sun.

3.3 Biologically-induced variability

Despite the potential for interference from extraneous factors, the TSRB has effectively detected biologically induced optical variability in coastal waters. For example, during a deployment in Bedford Basin, upwelling radiance ratios clearly showed the influence of a dinoflagellate bloom on near-surface optical properties (Fig. 5 and the following section). It is noteworthy that a rough measure of Chl fluorescence, the 683:670 upwelling radiance ratio, covaries strongly with the blue:green radiance ratio, a more conventional index of Chl which can be seriously compromised in coastal waters²³. When a measure of fluorescence covaries with a reflectance ratio determined by absorption and scatter, even during minor fluctuations, the patterns look more like biology and less like noise.

The importance of upwelled radiance in red wavelengths for the description of biological variability is illustrated by a comparison of radiance ratios with Chl (Fig. 6). Log-log plots can make relationships look better than they really are. Nonetheless, it is clear that both the $Lu_{683}:Lu_{670}$ and $Lu_{670}:Lu_{555}$ ratios were superior to green:blue (or blue:green) ratios for describing variability of Chl during this study. The result might not be surprising, considering that a red-tide event was observed. During the spring bloom of 1992, a different wavelength pair did a better job of predicting Chl ($Lu_{532}:Lu_{562}$ from an early filter set; data not shown, $R^2 = 0.9$, $n = 14$).

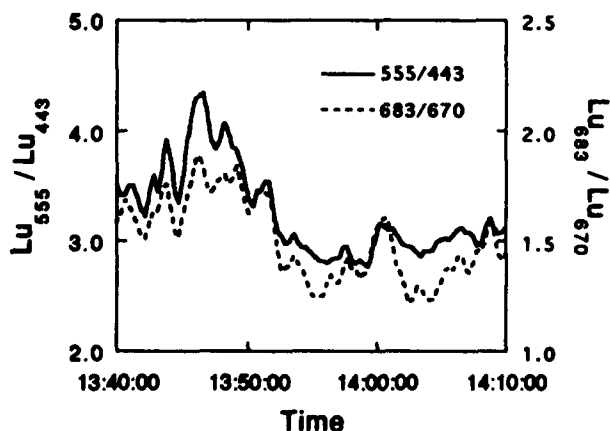


Fig. 5. Upwelling radiance ratios measured with the TSRB during a deployment on 18 August, 1993, between 13:40 and 14:10 local time. The buoy was drifting through patches of red water which appeared as a subsurface dinoflagellate bloom was entrained into the mixed layer. The ratio, $Lu_{555}:Lu_{443}$ is positively correlated with Chl in the open ocean. The ratio, $Lu_{683}:Lu_{670}$ is a crude measure of solar stimulated Chl fluorescence. For this plot, the two parameters have been scaled proportionally so that relative changes in each line are equivalent. Data were smoothed with a locally-weighted least squared error method with the closest 3% of the data considered (Kaleidagraph, Synergy Software).

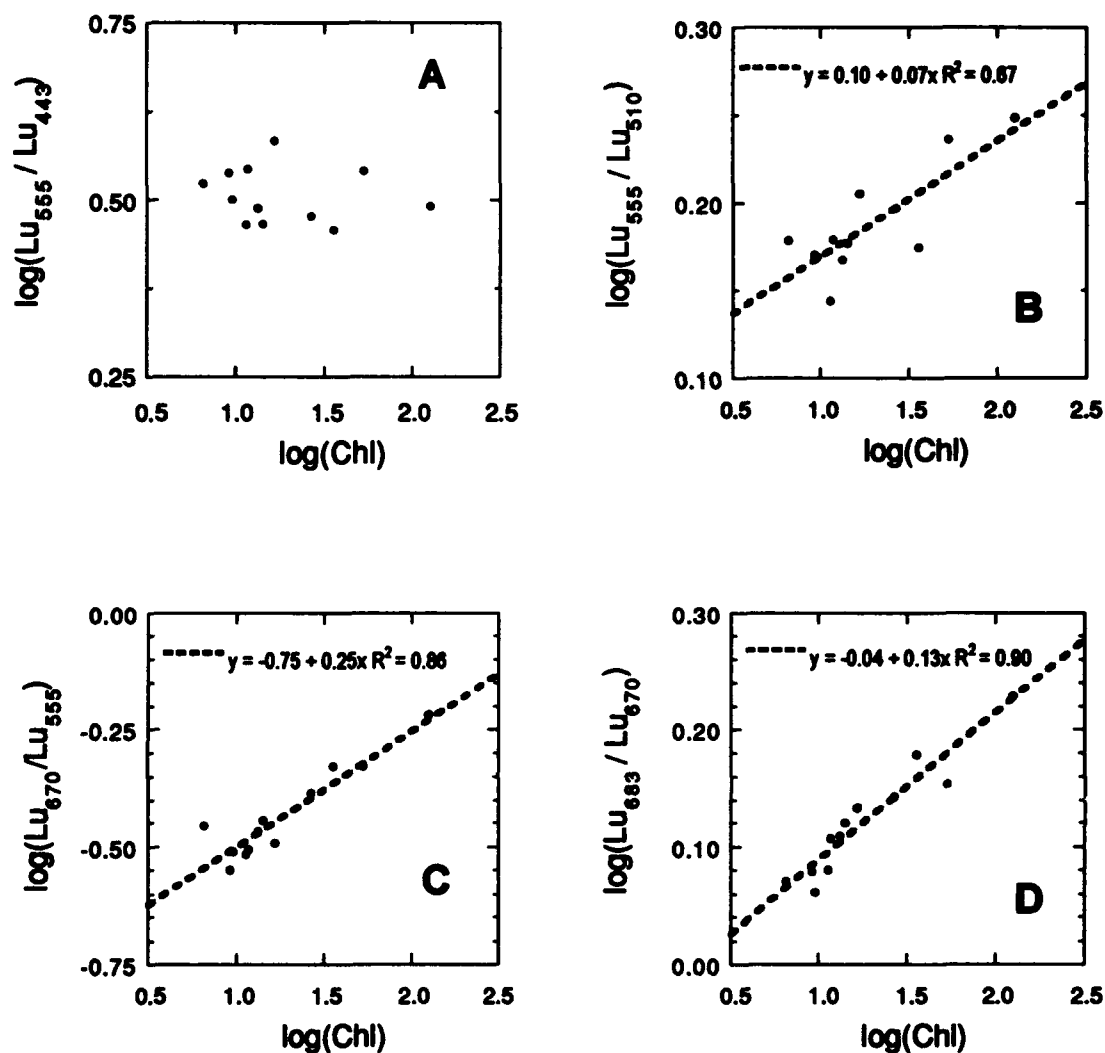


Fig. 6. Relationships between ratios of upwelling radiance and measurements of Chl (mg m^{-3}). Upwelling radiance from the TSRB was averaged for the 60 s closest to the time of sampling for Chl at 0.5 m. Regressions are for log-transformed data.

4. OPTICAL DETECTION OF A RED TIDE

The dinoflagellate bloom during August 1993 was detected in numerous ways. During equipment tests on the morning of August 6, an intense subsurface layer was observed in the thermocline at about 4 m. Beam attenuation exceeded 8 m^{-1} and the thickness of the subsurface peak was 1 m or less. Two weeks later, during the intensive study, a similar subsurface layer was observed each morning (Fig. 7A). The layer was composed of relatively large dinoflagellates, dominated by the non-toxic *Gonyaulax digitale* (30 - 45 μm). Small flagellated phytoplankton (3 - 5 μm) and other dinoflagellates (*Prorocentrum minimum*, 12 - 15 μm) populated the entire euphotic zone. Profiles of diffuse attenuation clearly distinguished the subsurface layer (Fig. 8A). During the afternoons, freshening winds eroded the thermocline, and the mixed layer intercepted the layer of dinoflagellates. When this happened, the water turned red as chlorophyll concentrations increased from roughly 10 - 30 mg m^{-3} to about 100 mg m^{-3} due to the entrained dinoflagellates. As wind-mixing continued to erode the thermocline, physical,

optical and biological properties became uniform in the surface layer (Fig. 7B), and volumetric concentrations of phytoplankton declined as deeper waters diluted the mixed layer population. Spectra of Lu_λ / Ed_{490} illustrate the strong differences between green and red water during initial entrainment (Fig. 8B). The red water was redder, of course, but it was also darker and had a much larger fluorescence signal at 683 nm. Similar spectral variations were reported by Carder and Steward⁹, but for their study area, brightness was greatly affected by variable detrital contributions.

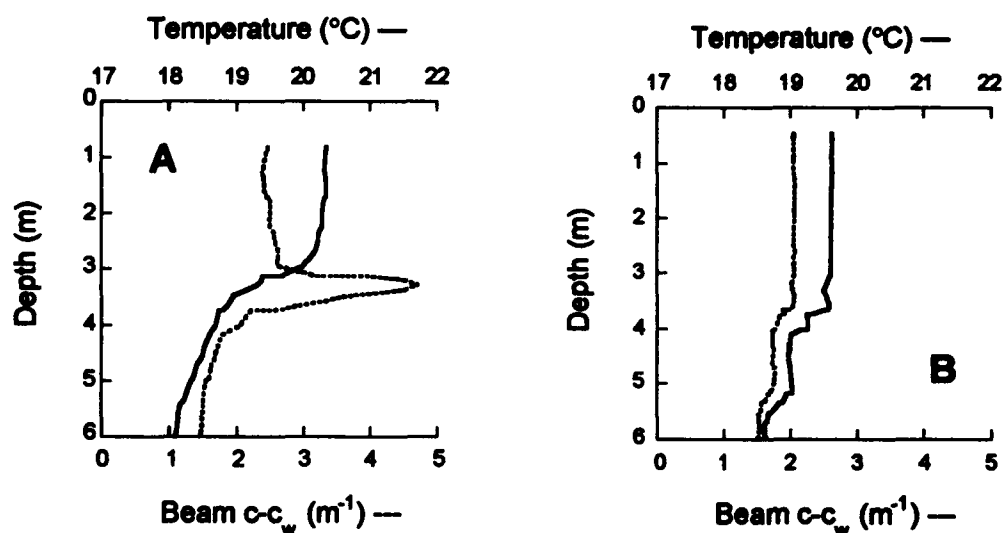


Fig. 7. Changes in the vertical distribution of the dinoflagellate bloom in Bedford Basin during August, 1993. Profiles of temperature (solid line) and beam attenuation, corrected for water ($c - c_w$, m^{-1} ; dashed line). A. Distribution typical of the morning and early afternoon, with the dinoflagellates predominantly confined to a subsurface layer: Aug. 18, 1350 h. B. Effects of wind-mixing: Aug. 18, 1720 h. The subsurface population and deeper water has been entrained into the mixed layer and the thermocline has been eroded.

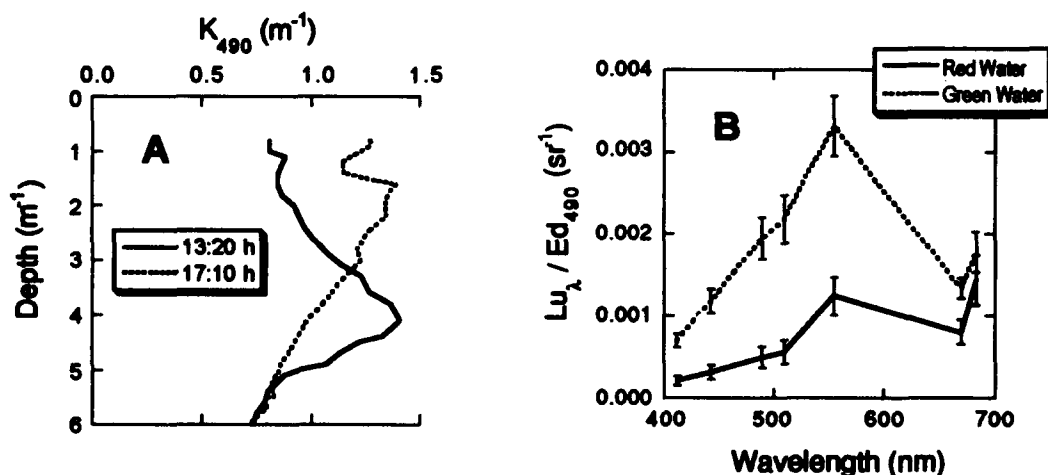


Fig. 8. Detection of the dinoflagellate bloom with passive optical measurements, Aug. 18, 1993. A. Diffuse attenuation of downwelling irradiance at 490 nm at 1320 h (subsurface peak) and 1710 h (after wind mixing). B. Spectra of $R(\lambda)_{TSRB}$ during a period of patchy entrainment of the dinoflagellates into the mixed layer (see Fig. 5): the red water spectrum is the average for 1345 - 1350 h, and the green water spectrum is for 1354 - 1359 h. Error bars are standard deviations.

5. DIEL OPTICAL VARIABILITY

Analysis of data from the open ocean demonstrate substantial diel variation in the optical properties of planktonic assemblages^{11, 24-26}, and recent laboratory studies have quantified changes in cellular scatter and absorption properties that contribute to these patterns^{12, 13}. Optical properties of the water are also influenced by the accumulation of growing cells during the day, and consumption by grazers at night¹¹. Because coastal waters are often rich in nutrients that can support rapid growth of phytoplankton, we expected to observe dynamic microbial populations with substantial diel changes in optical properties, detectable in reflectance, diffuse attenuation and beam attenuation. However, during our 1993 study, horizontal variability and vertical shifts of the dinoflagellate population strongly interfered with our quest, and diel patterns were difficult to discriminate.

Observations from other radiometer buoys reveal an interesting pattern that merits further examination. An expendable radiometer buoy moored in Monterey Bay, California showed a consistent and statistically significant diel pattern in radiance ratios, suggesting a 40% increase of Chl during the daytime (Fig. 9A). In contrast, records from the equatorial Pacific Ocean (Fig. 9B) show no significant difference between morning and evening radiance ratios. Such diel patterns (or lack thereof) should be studied further and considered in the design and analysis of remote-sensing studies.

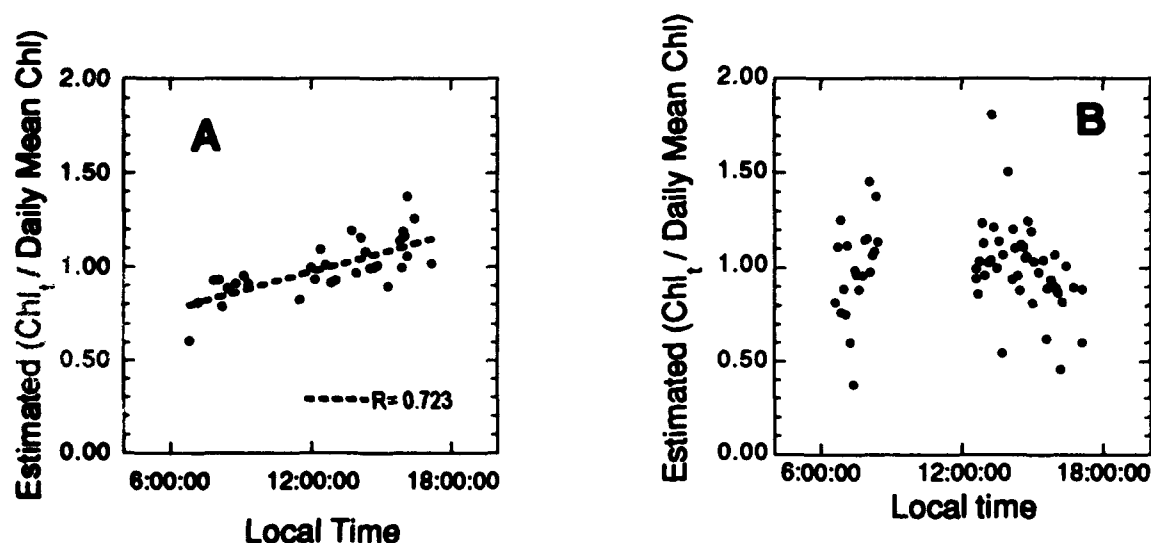


Fig. 9. Daily variation of Chl, as estimated from the ratio of $Lu_{443}:Lu_{555}$, measured by expendable spectral radiometers and transmitted as hourly averages. Chl algorithm according to Gordon²⁷. Data for each day were normalized to the average for the day. Data corresponding to low solar angles (criterion: $Ed_{490} < 20 \mu W cm^{-2} nm^{-1}$) were discarded. The gaps in data records correspond to periods when satellite communication was unavailable. A. Monterey Bay, California, September, 1992. B. Equatorial Pacific Ocean, between 1° and 5° S, September 1992.

6. RELATIONSHIPS BETWEEN OPTICAL PROPERTIES

It is hoped that measurements of upwelling radiance from the TSRB can be useful in extending the range of observations on which empirical and theoretical bio-optical models are based. Accordingly, one of our objectives was to relate measurements of upwelling radiance to profiles of diffuse attenuation. Results from August 1992 were very encouraging (Fig. 10A). Diffuse attenuation at 490 nm was strongly correlated with the ratio, $Lu_{443}:Lu_{555}$, and the relationship was almost exactly consistent with that presented by Austin and Petzold¹⁹, extending validation of the relationship to more turbid waters.

Some of the data from August 1993 were similar to the general relationship, but deviations can be seen, particularly in the two observations most representative of red tide at the surface. Since taxonomic groups of phytoplankton can differ substantially in size and pigmentation, hence in scattering and absorption properties, there is good reason to expect that pronounced changes in phytoplankton community structure would alter the type of relation presented in Fig. 10. Analysis of these deviations is underway.

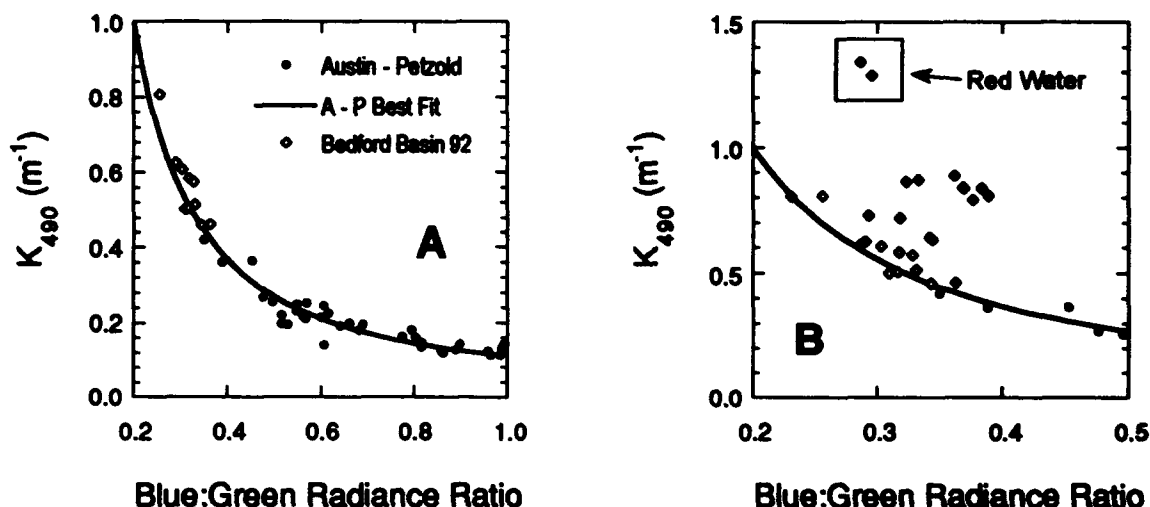


Fig. 10. Relationships between blue:green upwelling radiance ratios and diffuse attenuation at 490 nm: comparisons of data from Bedford Basin (Lu₄₄₃:Lu₅₅₅, collected with the TSRB, K_{490} estimated for the upper 2 m) and data presented by Austin and Petzold¹⁹ (filled circles, Lu₄₄₃:Lu₅₅₅ for radiance ratios ≤ 1.0), including the fit to their data, plotted on linear axes. A. Bedford Basin, August 1992 (open diamonds). B. An expanded view, with the same symbols as A, plus data from Bedford Basin, August 1993 (closed diamonds). The two points enclosed by a box represent red water at the surface.

7. DISCUSSION AND CONCLUSIONS

A principal objective of this research was to evaluate a radiometer buoy as a tool for observing biologically induced optical variability in surface waters. It was recognized that radiometric accuracy is not enough to ensure useful measurements; the instrument floats on the surface and records radiance and irradiance during chaotic movements in a highly variable photic environment. As expected, we found considerable "noise" associated with these movements, and as hoped, we found that suitable averaging yielded interpretable results. Further, the short-term deviations produced by movements of the buoy could be interpreted. The strong influence of tilting on estimated reflectance (inferred from Figs. 2B and 3A) indicates that any consistent effects on orientation (from tidal currents, for example) should be considered when designing long deployments and when interpreting records from those deployments. Expendable radiometers¹⁵, similar to the tethered version used here, must transmit averaged data. It appears that this is a fortunate constraint.

The determination of spectral radiance reflectance is important for describing optical variability in surface waters, and it is directly relevant to remote sensing. The TSRB measures E_d in only one narrow waveband, however, and upwelling radiance spectra will reflect (literally) variations in the spectral quality of solar irradiance as well as variability in the optical properties of the water. We suggest that models can be used to correct for predictable aspects of solar spectral variation, but under patchy clouds (Fig. 4), spectral shifts might cause problems.

Data from Bedford Basin demonstrated clearly that optical variability in the water could be observed despite interference from extraneous factors. The agreement of our measurements of radiance ratios and diffuse attenuation with the

compilation of Austin and Petzold¹⁹ is encouraging (Fig. 10A), as is the deviation associated with large dinoflagellates (Fig. 10B). It seems that the sensing systems used during this study provide data that are comparable to historical observations. The relationship between radiance ratios and Chl is unusual, though, with most of the useful information in the red wavebands (Fig. 6). This might be a special case, because red-water dinoflagellates caused much of the variability. It is nonetheless noteworthy that a signal from Chl fluorescence (Lu683/Lu670) was a good measure of pigment.

We have presented here some striking examples of biologically induced optical variability that would overwhelm subtler changes associated with particle dynamics in coastal waters that were unaffected by an algal bloom. Examples from expendable radiometer buoys (Fig. 9) indicate that other types of variation indeed exist. The presence of a strong diurnal increase in apparent pigment in coastal water, and no diurnal increase in the open ocean, is provocative and worthy of investigation.

Other instrument systems can observe biological dynamics more sensitively, or optical properties more accurately and thoroughly. We are interested in a radiometer buoy and a K-meter because they are suited for long-term deployments, either in moorings or as drifters (the K-meter would be replaced by a string of Ed sensors). As passive sensors measuring radiometric quantities, they are readily calibrated and are suitable for long-term studies of optical variability, and measurements in support of remote sensing. Similar sensor systems might be used for autonomous, long-term environmental monitoring and impact assessment. The detection of a red tide, both below the surface and in the mixed layer, demonstrates that radiometer/K-meter systems could be useful in early warning systems, for example at aquaculture sites. It seems clear that relatively simple optical instruments can be used to observe biologically induced optical variability in surface waters. However, it remains to be shown how sensitive and accurate the biological interpretations of optical variability can be.

8. ACKNOWLEDGMENTS

This work was supported by the U.S. Office of Naval Research, the U.S. Naval Research Laboratory, NASA, and NSERC Canada. The participation of AMC was supported by CNPQ, Brazil. We thank Carlos Freitas for help with sampling and data management, also Scott McLean and Norman Countway for technical support. We are grateful to Brian Schofield, boat captain and technical assistant in 1992, and to the Ships Division and small boat crews at the Bedford Institute of Oceanography for essential help.

9. REFERENCES

1. A. Morel, "Optical modelling of the upper ocean in relations to its biogenous matter content (Case I waters)," *J. Geophys. Res.*, Vol. 93, pp. 10749-10768, 1988.
2. A. Morel and Y.-H. Ahn, "Optical efficiency factors of free-living marine bacteria: Influence of bacterioplankton upon the optical properties and particulate organic carbon in oceanic waters," *J. Mar. Res.*, Vol. 48, pp. 145-175, 1990.
3. D. Stramski and D. A. Kiefer, "Light scattering by microorganisms in the open ocean," *Prog. Oceanogr.*, Vol. 28, pp. 343-383, 1991.
4. O. Ulloa, S. Sathyendranath, T. Platt and R. A. Quilones, "Light scattering by marine heterotrophic bacteria," *J. Geophys. Res.*, Vol. 97, pp. 9619-9629, 1992.
5. A. Morel, "Optics of marine particles and marine optics," *Particle analysis in oceanography*, S. Demers, (ed.), pp. 141-188, Springer-Verlag, Berlin, 1990.
6. K. L. Carder, R. G. Steward, G. R. Harvey and P. B. Ortner, "Marine humic and fulvic acids: Their effects on remote sensing of ocean chlorophyll," *Limnol. Oceanogr.*, Vol. 34, pp. 68-81, 1989.
7. R. W. Eppley, C. Sapienza and E. H. Renger, "Gradients in phytoplankton stocks and nutrients off southern California in 1974-76," *Est. Coastal Mar. Sci.*, Vol. 7, pp. 291-301, 1978.
8. J. J. Walsh, "Herbivory as a factor in patterns of nutrient utilization in the sea," *Limnol. Oceanogr.*, Vol. 21, pp. 1-13, 1976.
9. K. L. Carder and R. G. Steward, "A remote-sensing reflectance model of a red-tide dinoflagellate off west Florida," *Limnol. Oceanogr.*, Vol. 30, pp. 286-298, 1985.
10. T. D. Dickey, "The emergence of concurrent high resolution physical and bio-optical measurements in the upper ocean and their applications," *Rev. Geophys.*, Vol. 29 no. (3): pp. 383-413, 1991.
11. D. A. Siegel, T. D. Dickey, L. Washburn, M. K. Hamilton and B. G. Mitchell, "Optical determination of particulate abundance and production variations in the oligotrophic ocean," *Deep-Sea Res.*, Vol. 36, pp. 211-222, 1989.

12. S. G. Ackleson, J. J. Cullen, J. Brown and M. Lesser, "Irradiance-induced variability in light scatter from marine phytoplankton in culture," *J. Plankton Res.*, Vol. 15, pp. 737-759, 1993.
13. D. Stramski and R. A. Reynolds, "Diel variations on the optical properties of a marine diatom," *Limnol. Oceanogr.*, Vol. 38, pp. 1347-1364, 1993.
14. I. Amadi, D. V. Subba Rao and Y. Pan, "A *Gonyaulax digitale* red water bloom in the Bedford Basin, Nova Scotia, Canada," *Bot. Marina*, Vol. 35, pp. 451-455, 1992.
15. S. D. McLean and M. R. Lewis, "An expendable spectral radiometer drifter system (ESR)," *IEEE Proc. OCEANS '91*, Vol. 2, pp. 831-834, 1991.
16. R. A. Neville and J. F. R. Gower, "Passive remote sensing of phytoplankton via chlorophyll fluorescence," *J. Geophys. Res.*, Vol. 82, pp. 3487-3493, 1977.
17. H. Gordon, "Diffuse reflectance of the ocean: the theory of its augmentation by chlorophyll *a* fluorescence," *Appl. Optics*, Vol. 21, pp. 2489-2492, 1979.
18. R. E. Bird and C. Riordan, "Simple solar spectral model for direct and diffuse irradiance on horizontal and tilted planes at the Earth's surface for cloudless atmospheres," *J. Climate Appl. Meteor.*, Vol. 25, pp. 87-97, 1986.
19. R. W. Austin and T. J. Petzold, "Remote sensing of the diffuse attenuation coefficient of sea water using the Coastal Zone Color Scanner," *Oceanography from Space*, J.R.F. Gower, (ed.), pp. 239-256, Plenum Press, New York, 1981.
20. K. L. Carder, D. J. Collins, M. J. Perry, H. L. Clark, J. M. Mesias, J. S. Cleveland and J. Greenier, "The interaction of light with phytoplankton in the marine environment," *SPIE Ocean Optics*, Vol. VIII, pp. 42-55, 1986.
21. C. Roesler and M. J. Perry, "A robust model for determining *in situ* phytoplankton absorption and fluorescence emission spectra from reflectance," *J. Geophys. Res.*, submitted, 1994.
22. R. D. Roberts, M. S. Evans and M. T. Arts, "Light, nutrients, and water temperature as determinants of phytoplankton production in two saline, prairie lakes with high sulphate concentrations," *Can. J. Fish. Aquat. Sci.*, Vol. 49, pp. 2281-2290, 1992.
23. K. L. Carder, S. K. Hawes, K. A. Baker, R. C. Smith, R. G. Steward and B. G. Mitchell, "Reflectance model for quantifying chlorophyll *a* in the presence of productivity degradation products," *J. Geophys. Res.*, Vol. 96 no. (C11): pp. 20,599-20,611, 1991.
24. J. J. Cullen, M. R. Lewis, C. O. Davis and R. T. Barber, "Photosynthetic characteristics and estimated growth rates indicate grazing is the proximate control of primary production in the equatorial Pacific," *J. Geophys. Res.*, Vol. 97 no. (C1): pp. 639-654, 1992.
25. M. Stramska and T. D. Dickey, "Variability of bio-optical properties of the upper ocean associated with diel cycles in phytoplankton populations," *J. Geophys. Res.*, Vol. 97, pp. 17873-17887, 1992.
26. J. Marra, "Diurnal variability in chlorophyll fluorescence: observations and modelling," *SPIE Ocean Optics XI*, Vol. 1750, pp. 233-244, 1992.
27. H. R. Gordon, O. B. Brown, R. H. Evans, J. W. Brown, R. C. Smith, K. S. Baker and D. K. Clark, "A semianalytic radiance model of ocean color," *J. Geophys. Res.*, Vol. 93, pp. 10909-10924, 1988.

Optical backscattering measurements off the coast of Hawaii

Jeffrey M. Voss

SRI International
333 Ravenswood Avenue
Menlo Park, California 94025

Jeffrey H. Smart

Johns Hopkins University, Applied Physics Laboratory
Johns Hopkins Road, Laurel, Maryland 20723

ABSTRACT

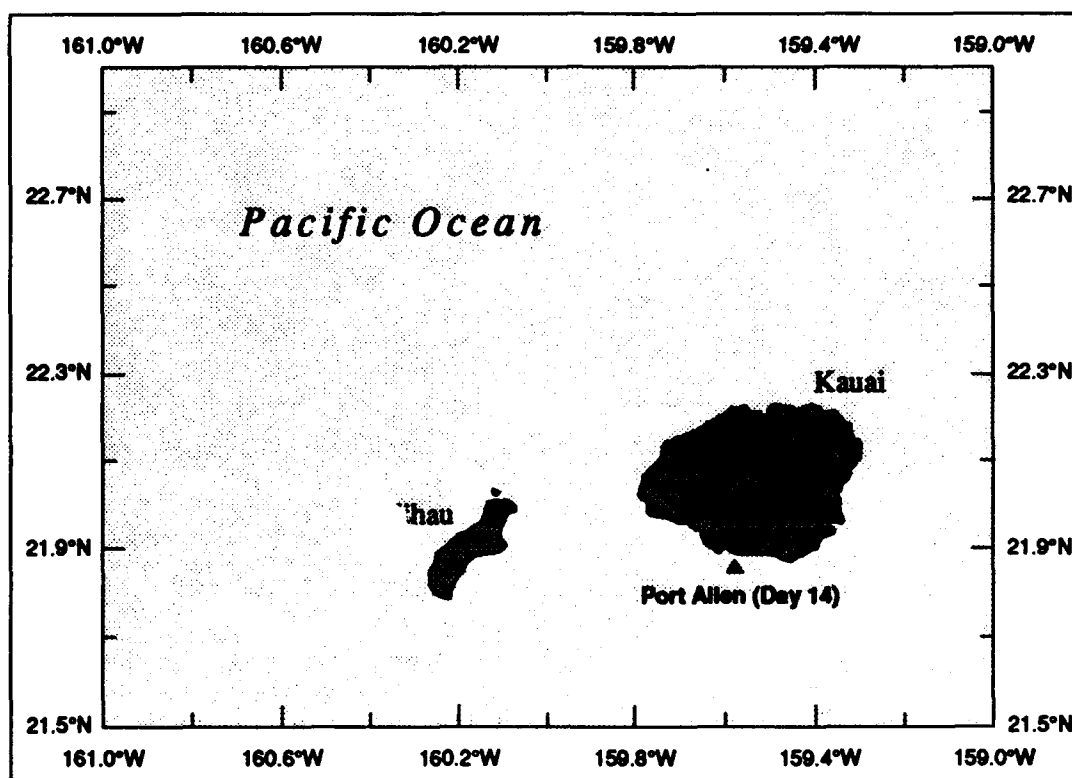
In a recent sea test, measurements of the volume scattering function (VSF) of clear sea water *in situ* at several angles were made. These measurements used the APL backscattering sensor, which measures the VSF at 170° ; the SRI Beta Pi sensor, which measures the VSF from 179° to 180° ; and the SRI backscattering sensor, which measures the VSF at a mean scattering angle of 150° . The intention of the testing was to quantify the enhanced backscattering feature at 180° relative to the scattering at more traditionally measured angles of the VSF. Measurements were made in both clear ocean water and Hawaiian coastal waters.

Analysis of the data has been combined with subsequent laboratory instrument intercomparisons to demonstrate that in clear ocean water there is relatively little enhanced backscattering, whereas in more turbid coastal water the feature is pronounced and is clearly higher than the VSF at 170° . Field data, including vertical profiles of optical backscatter in clear and coastal waters, are shown.

1. INTRODUCTION

During March 1993, a team of scientists from The Johns Hopkins University Applied Physics Laboratory (JHU/APL), SRI International, and the University of Miami conducted environmental measurements aboard the R/V Recovery I located in the open ocean northwest of Kauai and in an area close to Port Allen, Kauai (Figure 1). The ship measurement objective was to characterize the temporal and spatial variability of the optical conditions throughout the region. The measured optical properties included the volume scattering function (VSF) at 150° , 170° , and 180° , referred to hereafter as $B(150^\circ)$, $B(170^\circ)$, and $B(\pi)$, respectively. Other important measurements included the point spread function, the diffuse attenuation coefficient (K_d), and the beam attenuation coefficient (c). The Oceans XII paper entitled "Analysis of SeaTech Absorption Meter Characteristics and Comparisons to K_d Measurements," by J.H. Smart, discusses some of these measurements further.

The main objective of this paper is to examine the differences between the various backscattering sensors to determine whether or not there is an enhancement in the VSF at angles near π radians. Numerous investigators have reported enhancement of up to a factor of 2 in laboratory studies,¹ and previous at-sea experiments have suggested that remote sensing data could be reconciled with sea-truth profiles if an enhancement of about a factor of 2 existed between $B(170^\circ)$ and $B(\pi)$. Various investigators²⁻⁴ have shown that the VSF of sea water has a gradual increase from 120° to 170° , but Mie scattering computations⁴ and laboratory measurements¹ have predicted a narrow peak centered at 180° . With the exception of measurements by SRI's $B(\pi)$ system, all *in situ* measurements of $B(\pi)$ have actually been made at angles closer to 170° , and extrapolated to 180° . This experiment afforded the opportunity to determine whether this enhancement very close to 180° is significant in natural waters through *in situ*, nearly simultaneous measurements at 150° , 170° , and 180° (π).



p94-010/f1

Fig. 1. March 1993 general test location.

2. INSTRUMENT SUMMARY

The APL measurements included daily spatial transects of the area, made by using a towed paravane system housing a CTD, fluorometer, $B(170^\circ)$ sensor⁵, and beam transmissometer. APL measurements at fixed stations consisted of Optical Profiler System (OPS) casts. The OPS contains the same sensors as the paravane, together with irradiance sensors (Biospherical MER) and a 488 nm absorption meter (SeaTech).

SRI fielded several instruments from fixed stations, including the $B(\pi)$ sensor and $B(150^\circ)$ sensors at several wavelengths. The $B(\pi)$ sensor uses a collimated laser and CCD camera in a monostatic viewing geometry to measure and resolve the VSF at angles between 180° and 178° ⁶ at wavelengths between 456 and 532 nm. The $B(\pi)$ values shown in this paper are the average between 179° and 180° . Most of the testing was performed at 488 nm. The $B(150^\circ)$ sensors⁷ use either blue ($470 \text{ nm} \pm 35 \text{ nm}$) or green ($565 \text{ nm} \pm 15 \text{ nm}$) LEDs for illumination. SRI also deployed a spectral transmissometer and absorption meter operating at 456, 488, and 532 nm (WETLabs AC3).

The OPS, $B(\pi)$, and $B(150^\circ)$ sensors were deployed in casts while on station at positions marked on Figure 1. The OPS and $B(150^\circ)$ sensors provided continuous output profiles, whereas the $B(\pi)$ sensor provided output at discrete depths (usually spaced by 5 to 10 m).

3. "OPEN OCEAN" COMPARISON OF BACKSCATTER INSTRUMENTS

The best averaged 488 nm $B(170^\circ)$ and $B(\pi)$ profiles for clear ocean water are shown in Figures 2 and 3, respectively. The $B(\pi)$ values range from 5.7 to 6.6×10^{-4} /SR/m in the upper 65 m. The APL $B(170^\circ)$ values range from 6.3 to 6.9×10^{-4} /SR/m over the same depth interval. These values agree to within the 10% measurement accuracy of both instruments.

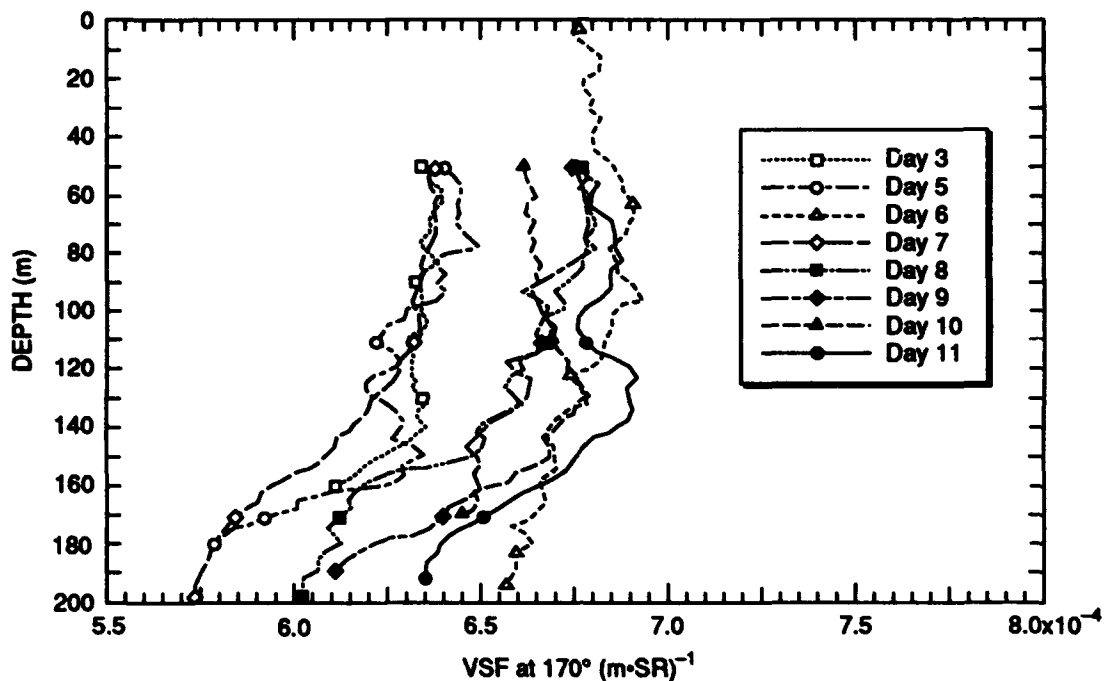
APL deployed two different $B(170^\circ)$ sensors, labeled as Unit 7 and Unit 9. Unit 9, which was used throughout most of the testing, was found to have a pressure hysteresis effect that affected data above 50 m, and the gain calibration was found to be 1.5 times too low in postcalibration. The data shown in Figure 2 have the corrected gain factor; these profiles exclude data above 50 m. Unit 7 and the corrected Unit 9 both agreed well with SRI $B(150^\circ)$ sensors during the postcalibration.

The main feature of both sets of backscattering data is that there are essentially no gradients in the upper 120 m. Below that depth, the data in Figure 2 show a significant decrease, consistent with the beam attenuation profiles in Figure 4 and the other optical and physical parameters measured throughout the experiment. During this experiment, the open ocean stratification was characterized by a well-mixed surface layer and a thermocline typically deeper than 100 m.

4. PORT ALLEN AREA MEASUREMENTS

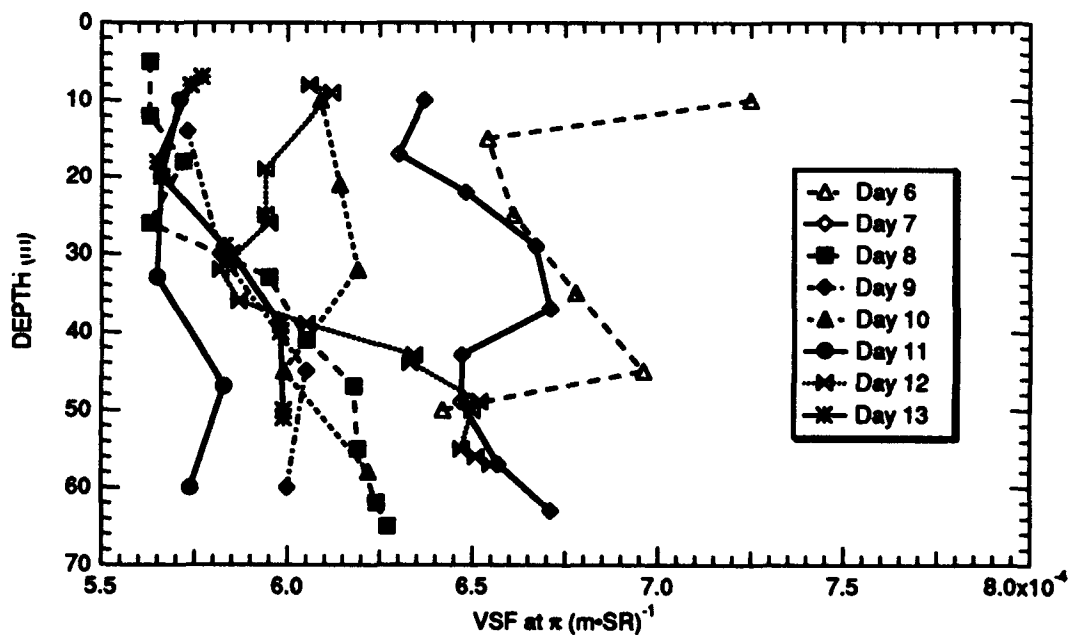
In addition to the data gathered in the very clear open ocean waters, we collected a limited data set close to the southwest shore of Kauai near Port Allen (shown on Figure 1). The objective was to determine whether enhanced backscattering occurs at 180° compared to that at angles $< 175^\circ$ in coastal waters. This objective was motivated by the facts presented in the Introduction. By making profiles of both devices through a sub-surface scattering layer, one should be able to detect the presence of any enhancement. In the open ocean waters, where there was no sub-surface scattering layer, no enhancement was measured.

To find a good candidate location for this experiment, the paravane (which contains a $B(170^\circ)$ sensor and a beam transmissometer) was tow-yo'ed near Kauai until a region was found having a sharp sub-surface maximum in the optical properties. The results of the subsequent profiles on day 14 with the various backscatter sensors are shown in Figure 5. The upper 50 meters of these profiles show a VSF of about 6.5×10^{-4} /SR/m⁻¹ with a sharply defined scattering layer peaking between 35 and 40 meters. The main result is that the additional scattering in the subsurface maximum appears to be nearly twice as high using the $B(\pi)$ sensor as it does using either the $B(170^\circ)$ or $B(150^\circ)$ sensor. The value outside of the scattering medium, however, does not exhibit any enhancement, suggesting that there is an intrinsic difference in the scatterers in the peak and those outside it. Similar results were found on the night of day 13 in a spot near Port Allen. Day 13 results were not as pronounced, because the sub-surface maximum was at the maximum depth that the $B\pi$ sensor could reach with the cable used.



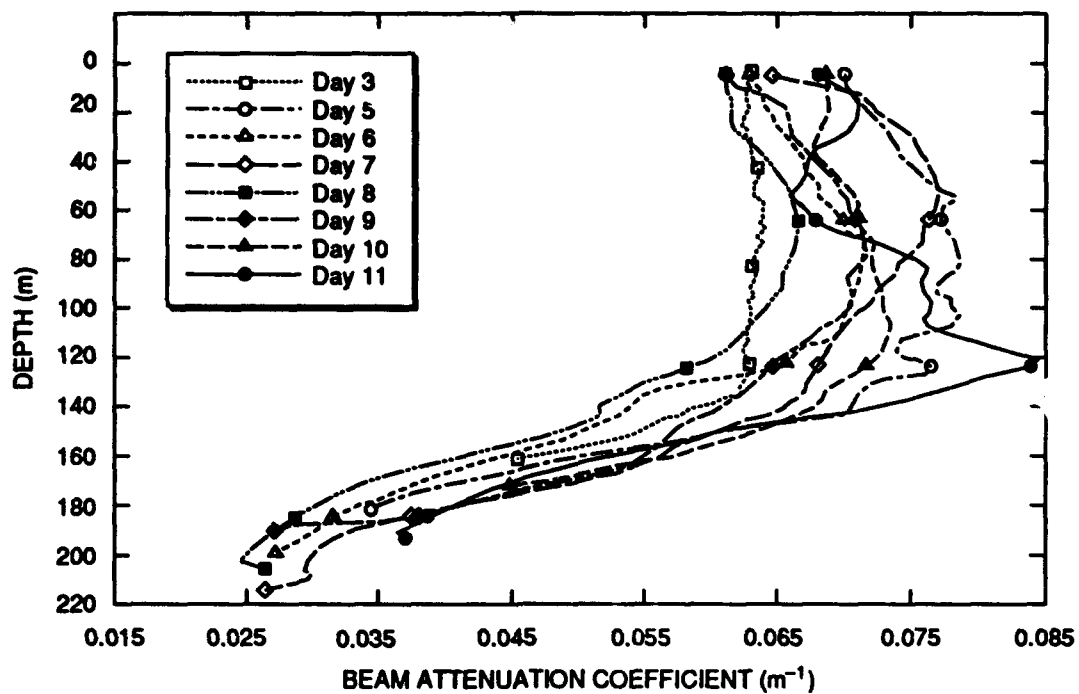
p94-010/12

Fig. 2. Best daily run APL $\beta(170^\circ)$ profiles. Unit 9 data clipped to avoid pressure-effect region and corrected based on post-test calibrations.



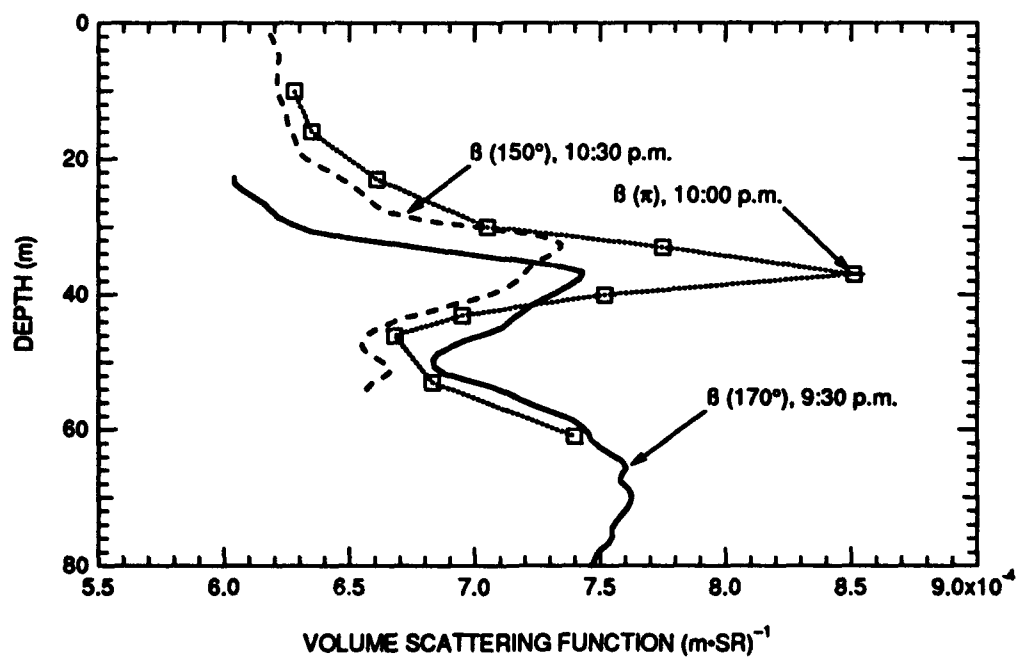
p94-010/13

Fig. 3. Open-ocean β_π measurements.



p94-010/14

Fig. 4. Summary of best estimates of daily c profiles in the open-ocean test area.



p94-010/15

Fig. 5. Enhanced $\beta\pi$ backscatter peak in coastal water.

5. DISCUSSION AND CONCLUSIONS

Figures 2 and 3, which show the clear water data for $B(170^\circ)$ and $B(\pi)$, respectively, indicate that there is no enhanced $B(\pi)$ feature in very clear water. This water showed very little scatterer concentration. Further tests in water with a scattering layer, shown in Figure 5, do support the possibility of enhancement within the scattering layer by as much as a factor of 2 between $B(170^\circ)$ and $B(\pi)$.

The data, while strongly suggesting the existence of an enhanced peak, are not entirely conclusive, primarily because the two profiles could not be measured simultaneously. (The sensors used the same cable, and therefore had to be operated sequentially.) Thus, it is possible (though unlikely) that the apparent enhancement arises from temporal variability, with the scattering properties actually increasing when the $B(\pi)$ sensor was lowered each night. The change in the depth of the sub-surface maximum from about 37 m in the 9:45 p.m. profile to about 30 m in the 10:30 p.m. profile shows that temporal variations, due to current, boat drift, or some other cause, occurred. To prove definitively that enhancement occurs, simultaneous profiles (or at least many contiguous profiles) would need to be collected.

The other requirement necessary to prove or disprove the existence of enhancement is the need for careful instrument intercalibration. APL and SRI conducted two days of intensive postcalibrations and cross comparisons using identical scattering targets and water conditions to produce the degree of agreement shown in Figure 5. For example, Figure 6 shows the results of one such comparison wherein increasing concentrations of scatterers were added to a tank of water to test the linearity and degree of agreement of the various sensors. APL's Unit 9 consistently measured a factor of 1.5 times too low in all tests, but when adjusted by this factor, produced values almost identical to those of the Unit 7 sensor. The solid line in Figure 6 indicates the APL values that would result in perfect agreement with the SRI values. The agreement is excellent for backscattering values $< 27 \times 10^{-4}/\text{SR/m}$, which is much higher than any seen during the course of the Kauai sea testing.

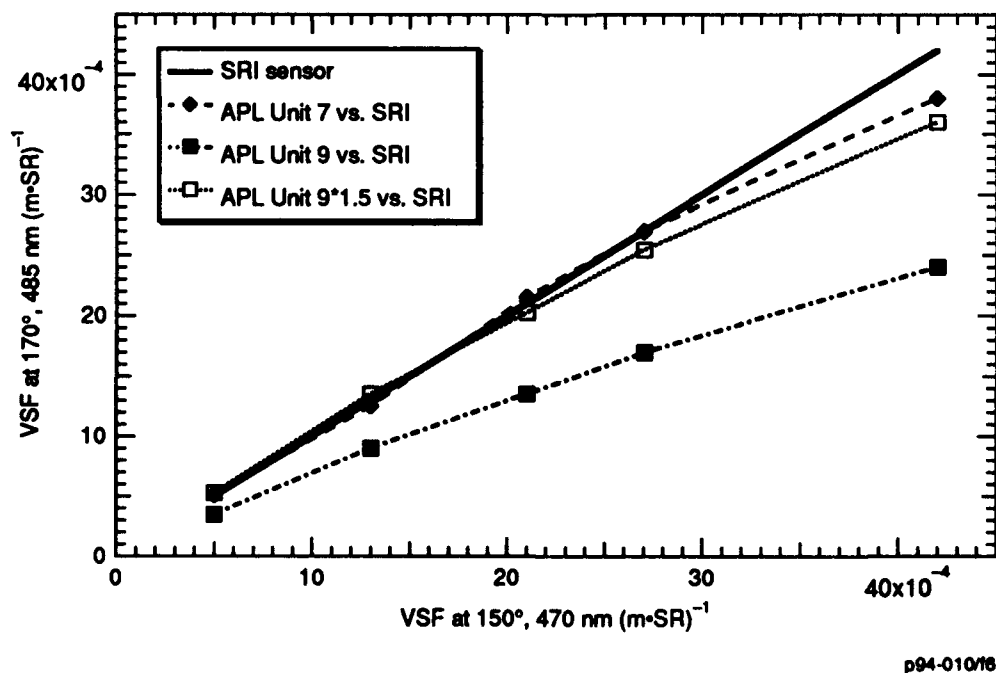


Fig. 6. Laboratory comparison between APL and SRI backscatter sensors.

6. ACKNOWLEDGMENTS

The authors wish to thank the many employees of APL and SRI who contributed to the development of these instruments and to the success of the experiment. We would additionally like to thank Dr. Gary Gilbert and the ONR Ocean Optics program for support in the development of the $\beta(\pi)$ sensor.

7. REFERENCES

1. Y. Kuga and A. Ishimaru, "Backscattering enhancement by randomly distributed very large particles," *Appl. Opt.* 28:2165-2169, June 1989.
2. T. J. Petzold, "Volume scattering functions for selected ocean waters," Visibility Laboratory, Scripps Institute of Oceanography, SIO Ref. 72-28, 1972, 79 pp.
3. N. G. Jerlov, "Scattering," Chapt. 2 in *Marine Optics*, Elsevier, New York, NY, 1976.
4. G. Kullenberg, "Observed and computed scattering functions," Chapt. 2 in *Optical Aspects of Oceanography*, N.G. Jerlov and E.S. Nielson, Eds., Academic Press, 1974.
5. J. H. Smart, "Variability in optical properties across the Gulf of Alaska," *Proc. of Oceans 91*, Honolulu, HI, October 1991.
6. R. A. Maffione and R. Honey, "Instrument for measuring the volume scattering function in the backward direction," SPIE Vol. 1750, *Ocean Optics XI*, pp 15-26, July 1992.
7. R. A. Maffione, D. Dana, and D. Honey, "Instrument for underwater measurement of optical backscatter," SPIE Vol 1537, *Underwater imaging, photography, and visibility*, pp 173-184, July 1991.

Instrumental considerations for deriving spectral photosynthetic absorption coefficients from total phytoplankton absorption

Mary E. Culver¹, Richard F. Davis² and Mary Jane Perry¹

¹School of Oceanography, WB-10, University of Washington, Seattle, WA 98195

²College of Oceanic and Atmospheric Sciences, Oregon State University, Corvallis, OR 97331

ABSTRACT

The phytoplankton absorption coefficient is primarily due to absorption by photosynthetic and photoprotective pigments. Absorption by photosynthetic pigments can be separated from that by other pigments by the former's ability to induce chlorophyll *a* (chl *a*) fluorescence. Chl *a* fluoresces at wavelengths between 660 and 760 nm with a distinct peak at 683 nm and a broad shoulder near 730 nm. The use of Basic Blue 3 as a quantum counter in spectrofluorimetry allows measurement of chl *a* fluorescence at 730 nm and hence, determination of phytoplankton fluorescence excitation spectra between 380 and 700 nm. Extension of measurements beyond 600 nm, the limit of the conventional quantum counter rhodamine B, allows direct comparison of the total absorption spectrum and the fluorescence excitation spectrum between 380 and 700 nm. Errors in the measurement of both types of spectra must be identified and minimized for reliable interpretation of either spectrum. Factors of primary importance include instrument-specific correction spectra for spectrofluorimeter configurations, accuracy in the absorption measurement, and sample handling. Accurate separation of spectral phytoplankton absorption coefficients into photoprotective and photosynthetic components will reduce the variability and errors in estimates of primary production based on optical models and will provide information on the photoadaptive state of the cells.

2. INTRODUCTION

The phytoplankton absorption coefficient is an inherent optical property, and its spectral shape and magnitude affects the diffuse attenuation coefficient, reflectance, and bio-optically modeled estimates of primary productivity. Particle-specific,¹ chemical,² and statistical^{3,4} methods that separate total phytoplankton absorption from particle absorption have been developed. Two classes of pigments are responsible for phytoplankton absorption: photosynthetic and photoprotective pigments. The phytoplankton absorption coefficient measured spectrophotometrically is suitable for models of light attenuation but overestimates absorption when used in productivity models, particularly in surface waters. The fluorescence excitation spectrum has been proposed as an alternative to improve estimates of photosynthetic phytoplankton absorption for modeling primary production.⁵

To generate a fluorescence excitation spectrum, a whole water sample is illuminated across the visible wavelengths while the emission of chlorophyll *a* (chl *a*) at 730 nm is monitored. This wavelength is a secondary emission peak for Photosystem II (PSII) chl *a*. The excitation spectrum represents the pigments involved in the transfer of energy from light-harvesting photosynthetic pigments to PSII chl *a* reaction centers.⁶ Absorption near 675 nm is dominated by chl *a* with minimal contributions by photoprotective or residual detritus pigments. The fluorescence excitation spectrum is normalized to the absorption at 675 nm allowing quantification of pigment absorption associated with PSII and, therefore, with photosynthesis.^{5, 7, 8}

Quantification of a fluorescence excitation spectrum depends on the use of a quantum counter to monitor variations in the intensity of the excitation irradiance during the course of a measurement. Previously, rhodamine B was used, and the excitation wavelengths were limited to those less than 600 nm because absorption by rhodamine B is minimal beyond this wavelength. The quantum counter 2,7-Bis(diethylamino)pheno-azoxonium chloride (Basic Blue 3) is effective for excitation wavelengths ranging

from the ultraviolet (240 nm) to 700 nm, thereby allowing both the blue and red peaks of chl *a* to be measured.⁹ Measurement of the red peak of chl *a* makes it possible to scale the fluorescence excitation spectrum to the absorption spectrum and to quantify fluorescence, typically reported in relative units, in units of the absorption coefficient [m^{-1}].

However, scaling the excitation spectrum to the absorption spectrum is not always successful. Often when phytoplankton cultures are adapted to low light, values for some regions of the excitation spectrum exceed those for absorption.^{7, 10, 11} To minimize this discrepancy, fluorescence excitation spectra must be properly corrected for variations in instrument optics, and the absorption measurement must be accurate. In each case, any short-term adaptation or physiological change in the state of the cells that may affect either fluorescence or absorption will affect the comparison and the quantification. The purpose of this paper is to analyze procedures for fluorescence excitation and absorption measurements. Fluorescence excitation correction procedures were modified for Basic Blue 3 to allow measurement throughout the visible spectrum, a requirement for quantification of fluorescence in phytoplankton. Absorption of phytoplankton cultures measured in suspension produce spectra which differ in shape and magnitude from those measured using the quantitative filter technique. The resulting fluorescence excitation and absorption spectra are compared for a phytoplankton culture grown at several light levels to separate photosynthetic from photoprotective pigments.

3. METHODS

3.1 Instrument optics

Correction procedures are necessary to minimize distortions in fluorescence spectra induced by instrument configuration. A significant amount of distortion can be removed from a spectrum by compensating for wavelength-specific variations in excitation irradiance.¹² The Spex Fluorolog 2 spectrofluorimeter monitors variations in the xenon lamp (450W) by using a beam splitter to focus a portion (Ω) of the excitation irradiance onto a quantum counter (QC) which has a photon yield and emission spectrum that is independent of excitation wavelength. The fluorescence of the quantum counter is measured by a reference photomultiplier tube (PMT) positioned behind the QC cuvette. Simultaneously, the sample is excited, and its fluorescence, collected at 90° from the excitation path and passed through two emission monochromators, is measured by a separate sample PMT. Fluorescence resulting from excitation at a wavelength (λ), measured by a PMT, is a function of the excitation irradiance (E), the absorption coefficient (a), the fluorescence efficiency (ϕ_f) and the effect of the PMT geometry (G) on detection. Fluctuations in lamp intensity are minimized by normalizing sample fluorescence to QC fluorescence. The fluorescence signal of a phytoplankton (phy) sample is recorded as the ratio (F_r) of the signal measured by the sample PMT, divided by that of the reference PMT:

$$F_r(\lambda) = \frac{F_{\text{phy}}(\lambda)}{F_{\text{ref}}(\lambda)} = \frac{[1 - \Omega(\lambda)] E(\lambda) a_{\text{phy}}(\lambda) \phi_{f-\text{phy}} G_{\text{sam-phy}}(\lambda)}{\Omega(\lambda) E(\lambda) a_{\text{QC}}(\lambda) \phi_{f-\text{QC}} G_{\text{ref-QC}}(\lambda)} \quad (1).$$

In addition to measurement in the ratio mode, an instrument-specific correction spectrum also is required to account for the differences in detection between the reference and sample PMT to completely remove the effects of instrument distortion from a spectrum. Primary factors include the wavelength-dependent efficiency of the beam splitter (Ω) and the viewing geometry of the reference and sample PMTs. Two methods, the quantum counter and the thermopile method, have been used to generate a correction spectrum.

The quantum counter method¹² entails placing the concentrated solution of QC, Basic Blue 3 (4.1 g l⁻¹ in ethylene glycol)⁹, in both the reference and sample positions and comparing the output of each PMT to generate a correction spectrum [$C_{\text{QC}}(\lambda)$]:

$$\begin{aligned}
C_{QC}(\lambda) &= \frac{F_{sam}(\lambda)}{F_{ref}(\lambda)} = \frac{[1 - \Omega(\lambda)] E(\lambda) a_{QC}(\lambda) \phi_{f-QC} G_{sam-QC}(\lambda)}{\Omega(\lambda) E(\lambda) a_{QC}(\lambda) \phi_{f-QC} G_{ref-QC}(\lambda)} \\
&= \frac{[1 - \Omega(\lambda)] G_{sam-QC}(\lambda)}{\Omega(\lambda) G_{ref-QC}(\lambda)}
\end{aligned} \tag{2}$$

The correction spectrum is applied by multiplying the fluorescence of a cell suspension measured in ratio mode $[F_r(\lambda); \text{eq. 1}]$ by the inverse of the correction spectrum $[C_{QC}(\lambda); \text{eq. 2}]$

$$\begin{aligned}
F_{corr}(\lambda) &= \frac{F_r(\lambda)}{C_{QC}(\lambda)} = \frac{F_{phy}(\lambda)}{F_{ref}(\lambda)} \frac{1}{C_{QC}(\lambda)} \\
&= \frac{[1 - \Omega(\lambda)] E(\lambda) a_{phy}(\lambda) \phi_{f-phy} G_{sam-phy}(\lambda)}{\Omega(\lambda) E(\lambda) a_{QC}(\lambda) \phi_{f-QC} G_{ref-QC}(\lambda)} \frac{\Omega(\lambda) G_{ref-QC}(\lambda)}{[1 - \Omega(\lambda)] G_{sam-QC}(\lambda)} \\
&= \frac{a_{phy}(\lambda) \phi_{f-phy} G_{sam-phy}(\lambda)}{a_{QC}(\lambda) \phi_{f-QC} G_{sam-QC}(\lambda)}
\end{aligned} \tag{3}$$

This method produces a corrected fluorescence spectrum for the phytoplankton sample $[F_{corr}(\lambda)]$, that is a function of the absorption and fluorescence efficiency of the QC and the viewing geometry. If the magnitude of the terms in the denominator of eq. 3 do not vary significantly with wavelength, this correction method is adequate.

The QC method for excitation correction has been used successfully with rhodamine B as the QC.^{6, 12, 13, 14, 15, 16} However, this method is not effective in this instrument configuration using Basic Blue 3 because the specific absorption coefficients of Basic Blue 3 vary across the visible spectrum more than those of rhodamine B. When Basic Blue 3 is used, the excitation irradiance penetrates to a variable extent within the cuvette as an inverse function of the spectral absorption coefficient (Fig. 1a,b). The absorption minima penetrate further into the cuvette; the fluorescence is emitted from the center of the cuvette and, in the sample position, passes at a right-angle through the center of the detection window. The result is high fluorescence at excitation wavelengths where absorption is minimal (Fig. 1b). At longer wavelengths (520 - 700 nm) the absorption coefficients are high, and excitation irradiance does not penetrate far into the cuvette. At these wavelengths maximal fluorescence is not aligned with the detection window, and the fluorescence measured is low but relatively constant (Fig. 1a). Reabsorption of photons emitted by the QC also may contribute to maintain a constant fluorescence output at longer wavelengths. The variation in the location of maximal emission intensity, and the resulting measurement of fluorescence intensity by the sample PMT, is expressed in the wavelength-dependent sample PMT geometry term $[G_{sam-QC}(\lambda)]$. When dilute samples are measured, the variation associated with right-angle geometry $[G_{sam-phy}(\lambda)]$ is small in contrast to the large variation associated with high concentrations of the QC Basic Blue 3.¹⁷ The QC method with Basic Blue 3 requires generation of an additional correction spectrum for $G_{sam-QC}(\lambda)$ to compensate for the low absorption by Basic Blue 3 in the blue region, which is a particular concern for phytoplankton measurements.

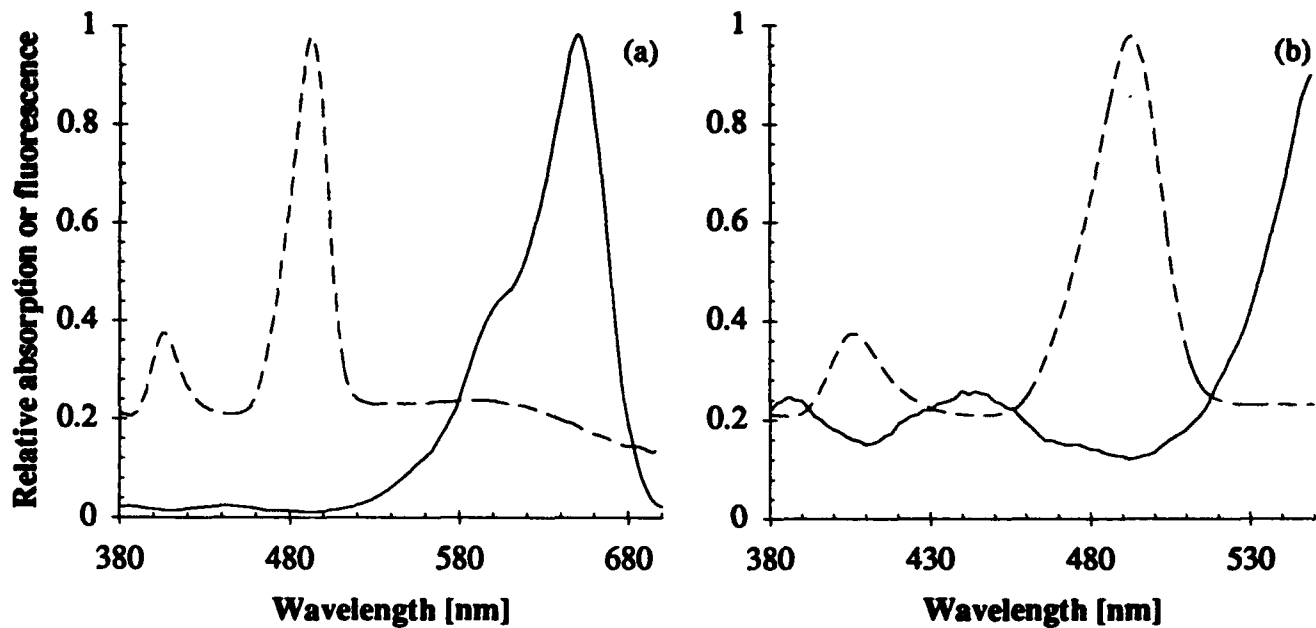


Fig. 1. Absorption of a dilute solution (solid) and fluorescence [CQC(λ); eq. 2; dashed] spectra for Basic Blue 3. The spectrum for 380 - 700 nm (a) shows constant fluorescence emission for longer wavelengths. Absorption minima in the blue wavelengths (b) correspond to increased fluorescence emission. Spectra are normalized to the maximum value for the specified wavelength range.

A variation of the thermopile method⁶ was used to generate a spectrum that adequately corrects for instrument optics using Basic Blue 3 with no additional correction procedures. A remote cosine detector for a LiCor scanning radiometer (1800-UW) was placed in the sample cuvette holder and incoming irradiance of several intensities was measured from 380 to 700 nm in 1-5 nm increments. Excitation irradiance intensity was varied by changing the size of the excitation monochromator slitwidth (1 to 15 nm). The radiometer half-maximum bandwidth is 8 nm; therefore, irradiance measured at any one wavelength/bandwidth combination was integrated to generate a single value $[(1-\Omega(\lambda)) E(\lambda)]$. Reference PMT voltages with the QC in the reference cell were monitored simultaneously with the radiometer measurements. A correction factor (C_T) was determined at each wavelength from a regression of reference PMT voltages $[F_{ref}(\lambda)]$ against the integrated irradiance measured at the sample cuvette holder $[(1-\Omega(\lambda)) E(\lambda)]$. The resulting slopes from the regression analysis were used to generate an excitation correction spectrum as a function of excitation wavelength $[C_T(\lambda)]$:

$$\begin{aligned}
 C_T(\lambda) &= \frac{F_{ref}(\lambda)}{[1 - \Omega(\lambda)] E(\lambda)} = \frac{\Omega(\lambda) E(\lambda) a_{QC}(\lambda) \phi_{f-QC} G_{ref-QC}(\lambda)}{[1 - \Omega(\lambda)] E(\lambda)} \\
 &= \frac{\Omega(\lambda) a_{QC}(\lambda) \phi_{f-QC} G_{ref-QC}(\lambda)}{[1 - \Omega(\lambda)]}
 \end{aligned}
 \tag{4}$$

When the thermopile correction spectrum ($C_T(\lambda)$; eq. 4) is applied to a phytoplankton fluorescence measurement in ratio mode ($F_r(\lambda)$; eq. 1),

$$\begin{aligned}
F_{\text{corr}}(\lambda) &= F_r(\lambda) C_T(\lambda) = \frac{F_{\text{phy}}(\lambda)}{F_{\text{ref}}(\lambda)} C_T(\lambda) \\
&= \frac{[1 - \Omega(\lambda)] a_{\text{phy}}(\lambda) \phi_{f-\text{phy}} G_{\text{sam-phy}}(\lambda)}{\Omega(\lambda) a_{\text{QC}}(\lambda) \phi_{f-\text{QC}} G_{\text{ref-QC}}(\lambda)} \frac{\Omega(\lambda) a_{\text{QC}}(\lambda) \phi_{f-\text{QC}} G_{\text{ref-QC}}(\lambda)}{[1 - \Omega(\lambda)]} \quad (5) \\
&= a_{\text{phy}}(\lambda) \phi_{f-\text{phy}} G_{\text{sam-phy}}(\lambda)
\end{aligned}$$

the resulting corrected spectrum is a function of the absorption coefficient and fluorescence efficiency of the phytoplankton sample and the viewing geometry of the sample PMT. If the absorption of the suspension is less than 2 m^{-1} , then the error due to viewing geometry [$G_{\text{sam-phy}}(\lambda)$] is less than 1% and additional correction is not necessary.¹⁷

The accuracy of the thermopile correction method [$C_T(\lambda)$] was verified by comparing the absorption and fluorescence excitation spectra for 90% acetone extracts of chl *a* and *b* (Sigma) and their acidified compounds. These standards have absorption spectra similar to whole phytoplankton cells yet lack the scattering properties and the complications of internal energy transfer encountered with whole cells; consequently, the absorption and fluorescence excitation spectra of the pure solutions should have identical shapes. Absorption was measured in a 1 cm cuvette using a SLM-Aminco dual beam spectrophotometer with 90% acetone as a reference. The fluorescence excitation spectra of optically dilute samples of extracted chl *a* and *b* were measured in ratio mode using emission at 730 and 710 nm, respectively. A blank spectrum of 90% acetone was subtracted from each excitation spectrum and the correction spectrum was applied to the output.

The double emission monochromators of the Spex Fluorolog 2 eliminate scattering errors from the fluorescence signal. To examine the effect of highly scattering particles on the optical pathlength of excitation irradiance, barium sulfate (BaSO_4) was added to the chl *a* and *b* acetone solutions. Concentrations of BaSO_4 ranged from 0.4 to 2 g l^{-1} . Absorption of these suspensions was measured in 10 cm cells.

3.2 Culture measurements

To compare the absorption and fluorescence excitation characteristics of whole cells, laboratory cultures of *Nitzschia closterium* (bacillariophyceae), *Isochrysis galbana* (chrysophyceae), and *Dunaliella tertiolecta* (chlorophyceae) were grown at several light intensities ranging from 5 to $700 \mu\text{moles quanta m}^{-2} \text{ s}^{-1}$ at 18°C . The cultures were maintained at the growth irradiance for a minimum of 10 generations before experimentation. Prior to measurement, the culture flask was placed in the dark for 30 min and then kept on ice in the dark until completion of all measurements to prevent cellular adaptation and growth.

Absorption was measured by concentrating the cells using centrifugation; then measuring the suspension in a 1 cm cuvette. To maximize the accuracy of the measurement and minimize the influence of scattering, the absorption of the sample was monitored repeatedly during the concentration procedure.¹⁸ Absorption also was measured by the quantitative filter technique using Whatman GF/F filters and correcting for pad absorption using two examples of β correction methods.^{16, 19}

Fluorescence excitation spectra were measured in ratio mode by exciting optically dilute cell suspensions in 1 cm non-fluorescent fused-quartz cuvettes from 380 - 700 nm (5 nm bandpass) and monitoring emission at 730 nm (10 nm bandpass). Each sample was warmed in a room temperature waterbath for 30-45 s before measurement. Three fluorescence replicates were measured both with and without 3-(3,4 dichlorophenyl)-1, 1-dimethylurea (DCMU). DCMU blocks electron transport from PSII to Photosystem I, thereby maximizing fluorescence from PSII.²⁰ A fresh aliquot was used for each

fluorescence excitation spectrum. The appropriate blank, either distilled water or distilled water with DCMU, was subtracted from the average of the three replicate samples. The spectra were corrected using the thermopile correction spectrum generated as described above (eq. 5). The excitation spectra of representative cultures preserved with ethanol and glutaraldehyde (final concentrations 5%) were also compared to spectra measured for fresh and DCMU-inhibited cultures.

4. RESULTS

4.1 Chlorophyll extracts

The corrected excitation spectra generated using the thermopile method [$C_T(\lambda)$] provided excellent agreement between the fluorescence excitation and absorption spectra for the 90% acetone extracts of chlorophyll standards (Fig. 2a,b); the QC method [$C_{QC}(\lambda)$] resulted in poor agreement in the blue region. The addition of white scattering, in the form of BaSO_4 particles, to the absorbing media did not affect the fluorescence spectrum of chl *a* (Fig. 3a). Scattering particles (Fig. 3b) did affect absorption by increasing the absorption coefficients and changing the spectral shape.

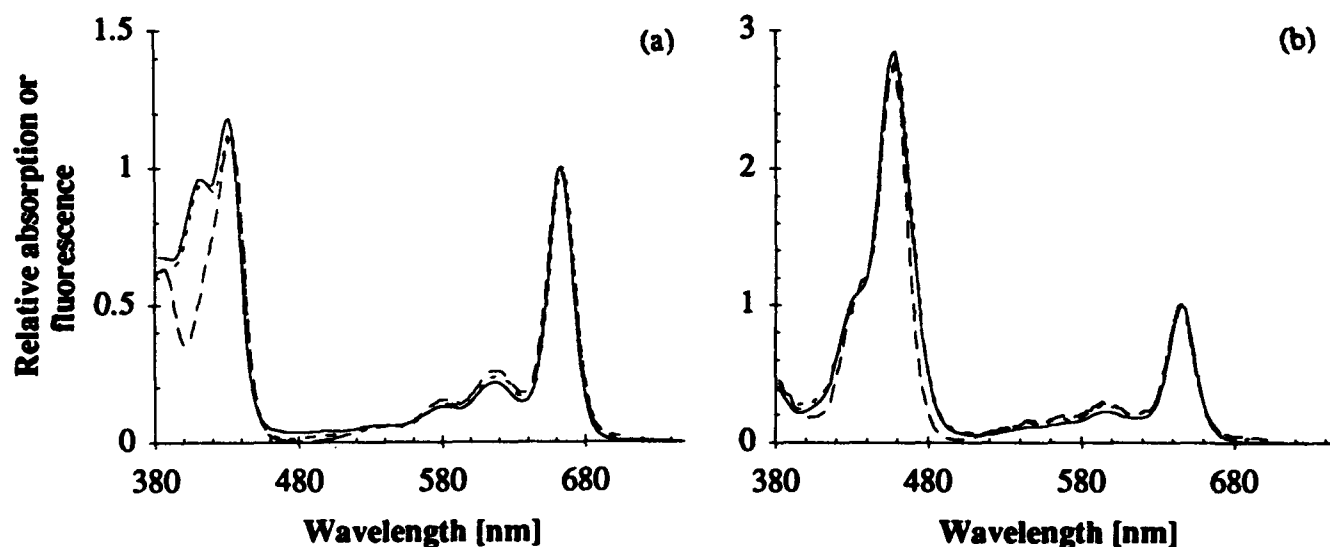


Fig. 2. Absorption (solid) and fluorescence spectra for acetone extracts of chl *a* (a) and chl *b* (b). The thermopile method of correction results in a fluorescence spectrum (dotted) that more closely represents absorption than the quantum counter method (dashed), particularly in the blue region of the spectrum.

4.2 Whole phytoplankton cells

The method for quantifying absorption of suspensions affects the comparison of absorption and fluorescence excitation spectra. Differences in the blue to red ratio for absorption spectra of phytoplankton cultures used in this paper varied by as much as 30% depending on the method used (Fig. 4a-c). For *Nitzschia closterium*, both the Mitchell and Kiefer¹⁶ and the Cleveland and Wiedemann¹⁹ model for filter pad absorption produced spectra with blue to red ratios slightly less than those of the 1 cm cuvette (Fig. 4a). Blue to red ratios for the other two species were overestimated using the filter pad method (Fig. 4b, c). To increase the accuracy of the absorption spectral shape and magnitude for cells in culture, a direct measurement of absorption using a suspension is preferable over using the filter technique. However, for field applications, suspension measurements rarely are possible.

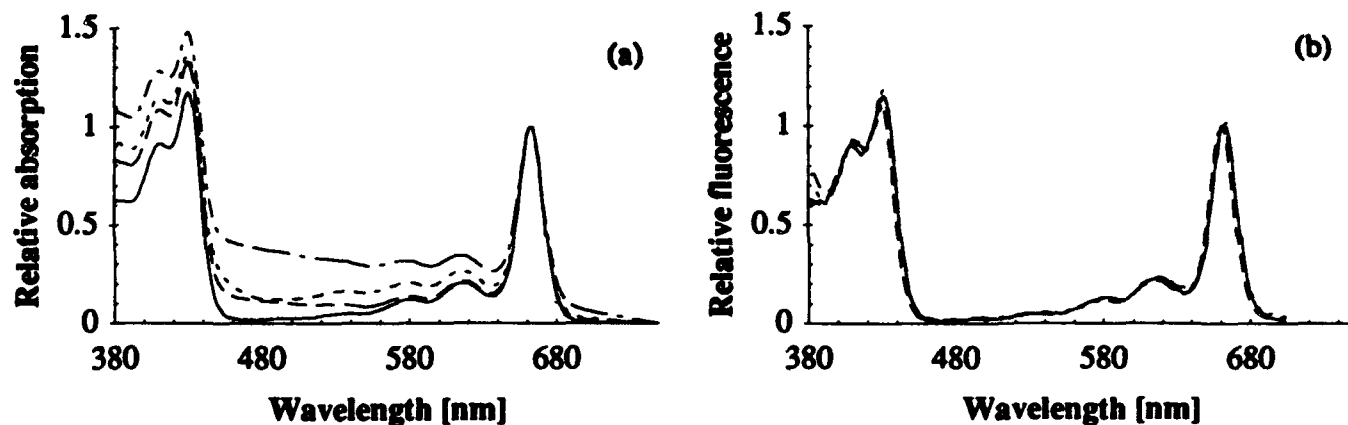


Fig. 3. Absorption (a) and fluorescence (b) spectra for acetone extracts of pure chl *a* (solid) normalized to the red peak. Increasing additions of BaSO₄ (0.4, 0.8, 2 g l⁻¹; dashed, dotted, and dot-dash lines, respectively) do not affect the shape of the fluorescence spectra yet significantly affect the spectral shape for absorption.

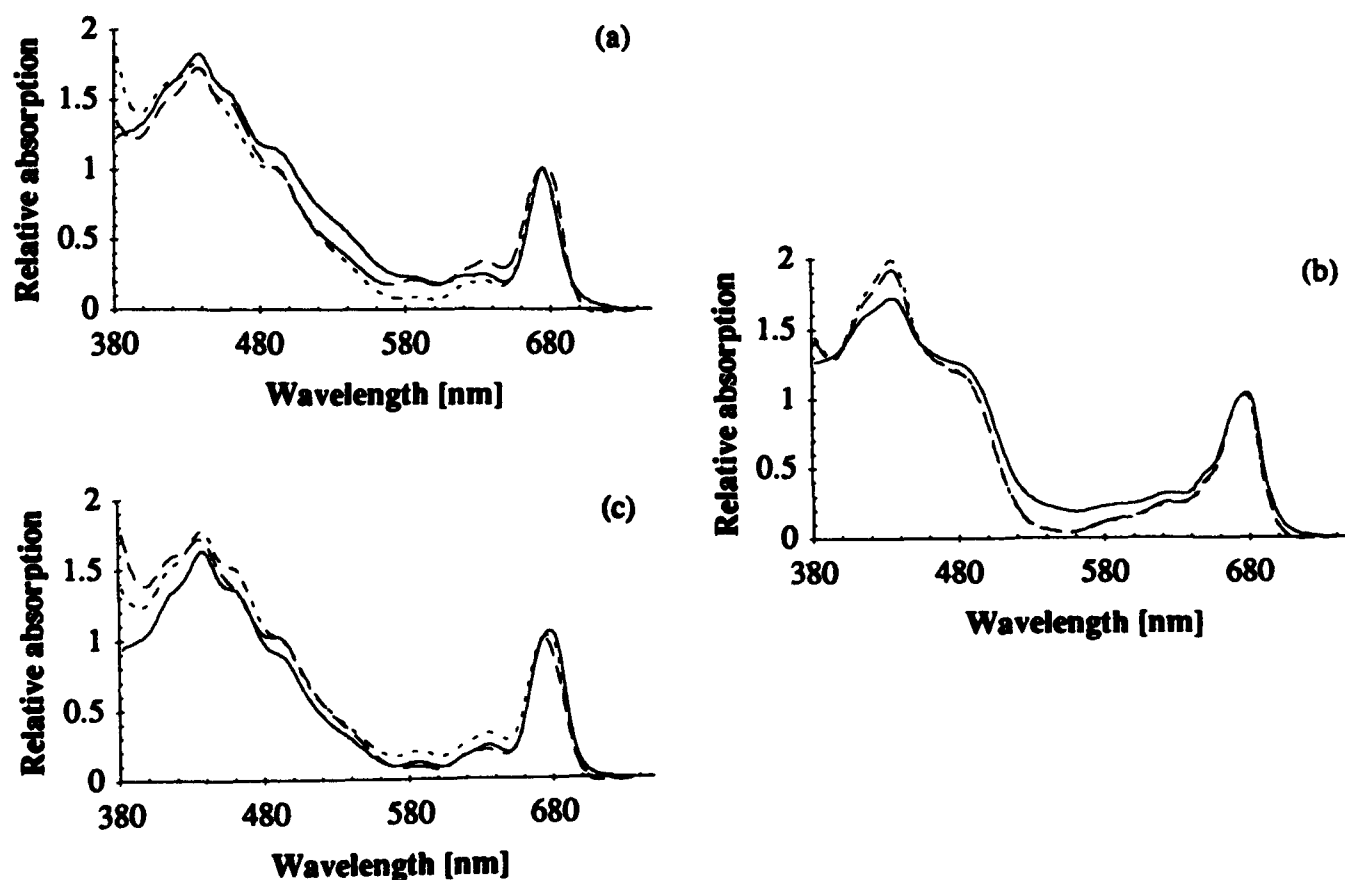


Fig. 4. Comparison of three methods of measuring absorption for *N. closterium* (a), *I. galbana* (b), and *D. tertiolecta* (c) normalized at the red peak. The quantitative filter technique adjusted for filter pad absorption and scattering using the method of Cleveland and Wiedemann (dotted) and Mitchell and Kiefer (dashed) result in a different spectral shape and magnitude than a suspension of concentrated cells in a 1 cm cuvette (solid).

The fluorescence excitation spectrum is similar in shape to the absorption spectrum due to the dominance of chl *a* absorption in the red region. For wavelengths influenced by accessory pigment absorption, there is a difference between absorption by photosynthetic pigments and total absorption (Fig. 5a-d), that is most obvious in the spectra of cells grown at high light intensity where photoprotective pigments are present. For *N. closterium*, the ratio of blue to red peaks for fluorescence is 1.4 compared to 2.0 for the total absorption of cells grown at the highest irradiance (Fig. 5a). These ratios for absorption decrease as growth irradiance decreases due to increasing packaging effects as cellular pigment concentration increases.^{21, 22, 23} The blue to red ratios for absorption and fluorescence become more similar at low growth irradiances as an increasing proportion of the absorption coefficient is due to photosynthetic pigments. The fluorescence and total absorption ratios are 1.3 and 1.4, respectively, for low-light-grown cells (Fig. 5d).

There is some discrepancy in the fluorescence and absorption spectra in the region from 550 to 650 nm if the spectrum is scaled to the red chl *a* peak. In this region, the fluorescence excitation spectrum may exceed total absorption, yielding a result with questionable interpretation. Because this is a region of minimum absorption for phytoplankton, the absorption measurement may be less accurate compared to other regions of the spectrum.¹⁶ The method of measuring absorption also will change the shape of the absorption spectrum, thereby affecting the degree to which fluorescence exceeds absorption (cf. Fig. 5).

During the course of the measurement (~45 s), the cells may undergo physiological changes that affect the fluorescence spectrum. Comparisons of fluorescence spectra between fresh and preserved samples showed some differences in shape and magnitude (Fig. 6a, b). DCMU additions to fresh cultures tends to produce a spectrum similar to that of the fresh cultures. The fluorescence spectra of cultures preserved with glutaraldehyde differed in spectral shape from fresh culture samples, as well as from cultures treated with ethanol and with DCMU. Glutaraldehyde cross-links proteins to preserve cell structure, yet may denature some proteins in the process of cross-linking. In Fig. 6, there appears to be a reaction between glutaraldehyde and the carotenoid pigments such that the contribution of carotenoid pigments (480 - 540 nm) to chl *a* fluorescence decreases. Cultures preserved with ethanol produced spectra with shapes similar to those of fresh cultures with a variable blue to red ratio and slightly lower fluorescence in the 550 to 650 nm region.

5. DISCUSSION

The use of rhodamine B as a quantum counter in spectrofluorimetric measurements allows spectrally-incomplete qualitative comparisons of absorption and fluorescence excitation between high and low-light adapted populations.^{13, 14} Comparisons between 400 and 550 nm showed a distinct difference in the spectral shapes of absorption and fluorescence, with the shape of the fluorescence spectrum changing to a larger degree in response to changes in irradiance. Quantification of the fluorescence measurement for use in bio-optical models of productivity requires using Basic Blue 3 as a quantum counter to provide measurement of both the blue and red chl *a* peaks.⁵

The excitation correction spectrum used to eliminate differences in optical paths between reference and sample cells depends on configuration and must be derived for each instrument. The use of a quantum counter (Basic Blue 3), which is different from that recommended by the manufacturer (rhodamine B), required an alternative method to generate the correction spectrum for the Spex Fluorolog 2. The accuracy of the correction spectrum, as well as a record of instrument performance, is easily checked by routine comparison of the absorption and excitation spectra of 90% acetone extracts of pure chl *a* or *b* or other commercially available standards.

Maintenance of the phytoplankton cultures on ice in the dark minimized changes in the cell physiology during the experiment. The variation in the absorption measurement was not large during the time required to concentrate the suspension. However, changes in the fluorescence excitation spectra were

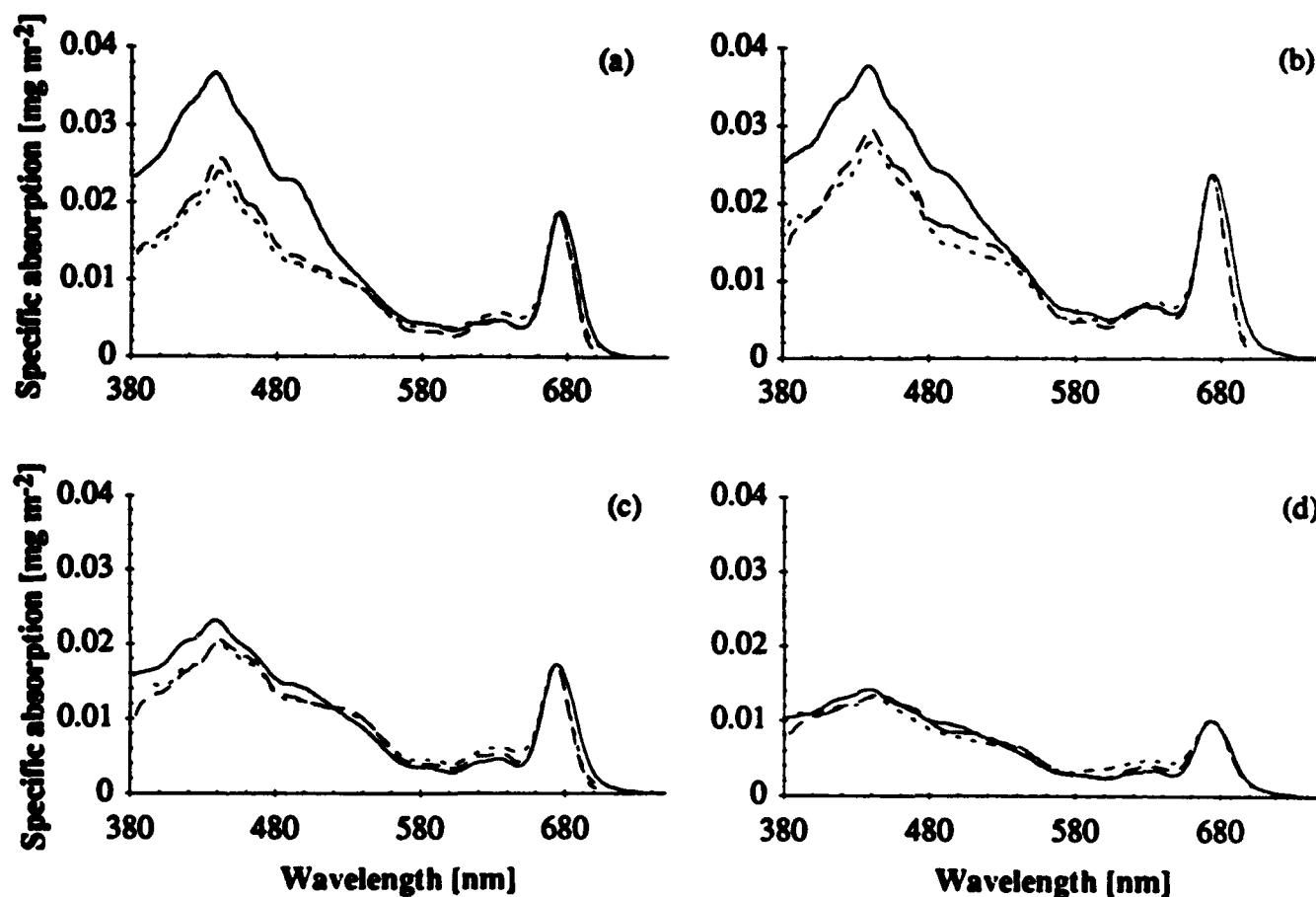


Fig. 5. Absorption (solid) and fluorescence spectra for fresh (dashed) and DCMU-treated (dotted) samples of *N. closterium* grown at light levels of 700 (a), 300 (b), 25 (c), and 5 (d) μmoles quanta m⁻² s⁻¹. The difference between total and photosynthetic absorption decreases as light level decreases and the proportion of pigments involved in photosynthetic, as opposed to photoprotective processes, increases.

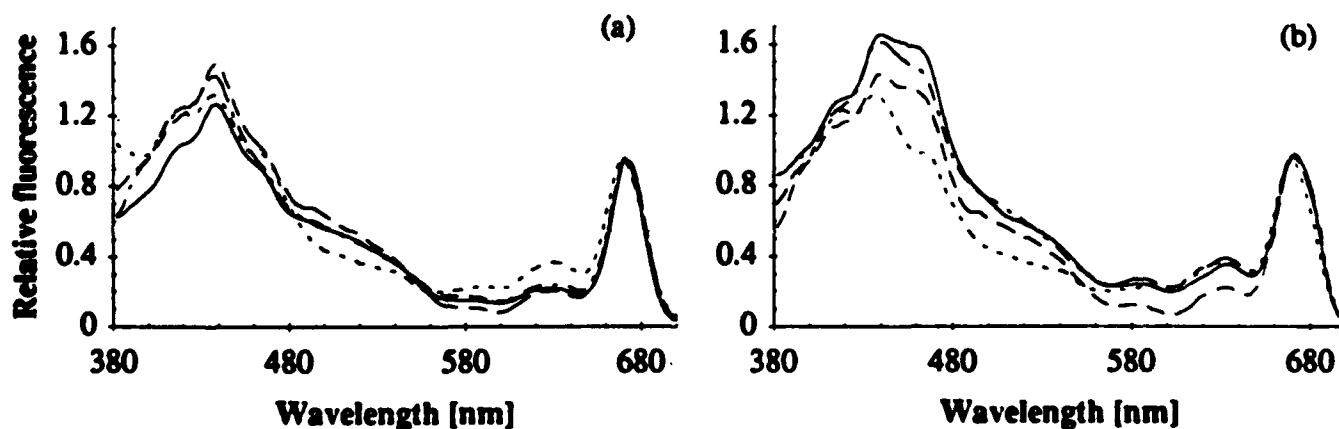


Fig. 6. Fluorescence spectra for fresh (solid), DCMU-treated (dot-dash), glutaraldehyde- (dotted), and ethanol-preserved (dashed) cultures of *N. closterium* (a) and *I. galbana* (b). Differences exist for each treatment throughout the spectrum.

noted within 10-15 min if cells were removed from the growth chamber and placed in the dark at room temperature. Placing the samples on ice after a pre-adaptation in the dark to maximize fluorescence provided the least variable excitation spectra over the 30-45 min period required to replicate measurements.

Suspension measurements of phytoplankton populations provide the most accurate values for absorption. Errors in the blue to red ratio of absorption, using the quantitative filter technique, range from 9 to 20% (Fig. 4). The quantitative filter technique relies on a correction factor generated using mixtures of species to correct for pad absorption.^{16, 19} This technique is the best available for measuring absorption by field populations; however, measurement of single species cultures requires generating a correction factor for each species to increase the accuracy of the measurement.²⁴

There remains, in some cases, the problem of excess photosynthetic over total absorption if the excitation spectrum is scaled to the absorption value at 675 nm. This method assumes that chl *a* present in Photosystem I contributes minimally to total absorption and that energy transfer to PSII chlorophyll *a* is completely efficient.⁷ Measurements of several species indicate that scaling the fluorescence value to 85% of the absorption will accommodate variations in energy and pigment distributions between photosystems; although the accurate scaling value will change with species and photoadaptation.⁷ Measurements made using *Nitzschia closterium* indicate some variation in the degree of discrepancy associated with photoadaptation.

Additional measurements of a range of species under differing environmental conditions will increase the accuracy in quantification of photosynthetic absorption and therefore the ability to interpret both laboratory and field results. Separating absorption by photosynthetic pigments from absorption by non-photosynthetic pigments and other particles, improves our understanding of the variability in the parameters used for bio-optical models of photosynthesis⁸ and also will prove useful in the interpretation of active and passive fluorescence emission signals in the field. Quantification of fluorescence may allow full development of the idea originally proposed by Yentsch and Yentsch²⁵ that fluorescence excitation spectra may be used to characterize phytoplankton populations by taxonomic groups.

6. ACKNOWLEDGMENTS

This work was supported by a National Defense Science and Engineering Graduate Fellowship and the Office of Naval Research (N00014-90-J-1091). We thank H. M. Sosik for discussion on the problems and merits associated with spectrofluorimetry.

7. LITERATURE CITED

1. R. Itturiaga and D. A. Siegel, "Discrimination of the absorption properties of marine particulates using a microphotometric technique," Ocean Optics IX, M. A. Blizard [ed.], Proc. SPIE 925, 277-287, 1988.
2. M. Kishino, M. Takahashi, N. Okami, and S. Ichimura, "Estimation of the spectral absorption coefficients of phytoplankton in the sea," Bull. Mar. Sci., 37, 634-642, 1985.
3. C. S. Roesler, M. J. Perry, and K. L. Carder, "Modeling *in situ* phytoplankton absorption from total absorption spectra in productive inland marine waters," Limnol. Oceanogr., 34, 1510-1523, 1989.
4. J. S. Cleveland and M. J. Perry, "A model for partitioning particulate absorption into phytoplanktonic and detrital components," Deep Sea Res., 41(1), 197-222, 1994.
5. E. Sakshaug, G. Johnsen, K. Andersen, and M. Vernet, "Modeling of light-dependent algal photosynthesis and growth: experiments with the Barents Sea diatoms *Thalassiosira nordenskioeldii* and *Chaetoceros furcellatus*," Deep Sea Res., 38(4), 415-430, 1991.
6. A. Neori, M. Vernet, O. Holm-Hansen, and F. T. Haxo, "Comparison of chlorophyll far-red and red fluorescence excitation spectra with photosynthetic oxygen action spectra for photosystem II in algae," Mar. Ecol. Prog. Ser., 44, 297-302, 1988.

7. G. Johnsen and E. Sakshaug, "Bio-optical characteristics and photoadaptive responses in the toxic and bloom-forming dinoflagellates *Gyrodinium aureolum*, *Gymnodinium galatheanum*, and two strains of *Prorocentrum minimum*," *J. Phycol.*, 29, 627-642, 1993.
8. H. M. Sosik and B. G. Mitchell, "Photosynthetically active absorption and quantum yield in the California Current," Abstract for The Oceanography Society, Third Scientific Meeting, Seattle, 1993.
9. U. Kopf and J. Heinze, "2,7-Bis(diethylamino)phenoazonium chloride as a quantum counter for emission measurements between 240 and 700 nm," *Anal. Chem.*, 56, 1931-1935, 1984.
10. H. Maske, and H. Haardt, "Quantitative *in vivo* absorption spectra of phytoplankton: detrital absorption and comparison with fluorescence excitation spectra," *Limnol. Oceanogr.*, 32(3), 620-633, 1987.
11. G. Johnsen, E. Sakshaug, and M. Vernet, "Pigment composition, spectral characterization and photosynthetic parameters in *Chrysochromulina polylepis*," *Mar. Ecol. Prog. Ser.*, 83, 241-249, 1992.
12. J. W. Hofstraat, K. Rubelowsky, and S. Slutter, "Corrected fluorescence excitation and emission spectra of phytoplankton: toward a more uniform approach to fluorescence measurements, *J. Plank. Res.*, 14(5), 625-636, 1992.
13. A. Neori, O. Holm-Hansen, B. G. Mitchell, and D. A. Kiefer, "Photoadaptation in marine phytoplankton: changes in spectral absorption and excitation of chlorophyll *a* fluorescence," *Plant Physiol.*, 76, 518-524, 1984.
14. J. B. Soohoo, D. A. Kiefer, D. J. Collins, and I. S. McDermid, "*In vivo* fluorescence excitation and absorption spectra of marine phytoplankton: I. taxonomic characteristics and responses to photoadaptation," *J. Plank. Res.*, 8(1), 197-214, 1986.
15. A. Neori, M. Vernet, O. Holm-Hansen, and F. T. Haxo, "Relationship between action spectra for chlorophyll *a* fluorescence and photosynthetic O₂ evolution in algae," *J. Plank. Res.*, 8, 537-548, 1986.
16. B. G. Mitchell and D. A. Kiefer, "Chlorophyll *a* specific absorption and fluorescence excitation spectra for light-limited phytoplankton," *Deep Sea Res.*, 35, 639-663, 1988.
17. K. D. Mielenz, "Photoluminescence spectrometry," Measurement of Photo-luminescence. Optical Radiation Measurements, K. D. Mielenz [ed.], vol. 3, pp. 2-88, Academic, New York, 1982.
18. A. Bricaud, A. Morel, and L. Prieur, "Optical efficiency factors of some phytoplankters," *Limnol. Oceanogr.*, 28(5), 816-832, 1983.
19. J. S. Cleveland and A. D. Weidemann, "Quantifying absorption by aquatic particles: a multiple scattering correction for glass-fiber filters, *Limnol. Oceanogr.*, 38(6), 1321-1327, 1993.
20. R. G. S. Bidwell, Plant Physiology, MacMillan, New York, 1974.
21. L. N. M. Duysens, "The flattening of the absorption spectrum of suspensions as compared to that of solutions," *Biochem. Biophys. Acta*, 19, 1-12, 1956.
22. J. T. O. Kirk, "A theoretical analysis of the contribution of algal cells to the attenuation of light within natural waters. I. general treatment of suspensions of pigmented cells," *New Phytol.*, 75, 11-20, 1975.
23. A. Morel and A. Bricaud, "Theoretical results concerning light absorption in a discrete medium, and application to specific absorption of phytoplankton," *Deep Sea Res.*, 28, 1375-1393, 1981.
24. A. Bricaud and D. Stramski, "Spectral absorption coefficients of living phytoplankton and nonalgal biogenous matter: a comparison between the Peru upwelling area and the Sargasso Sea," *Limnol. Oceanogr.*, 35(3), 562-582, 1990.
25. C. S. Yentsch and C. M. Yentsch, "Fluorescence spectral signatures: the characterization of phytoplankton populations by the use of excitation and emission spectra," *J. Mar. Res.*, 37, 471-483, 1979.

LIGHT ATTENUATION ON UNICELLULAR MARINE PHYTOPLANKTON.

Tadeusz Król, Maria Łotocka

Institute of Oceanology Polish Academy of Sciences
81-937 Sopot, ul. Powstańców Warszawy 55 POLAND

ABSTRACT

Sea phytoplankton plays a considerable role in the interactive processes between light and the sea. Its species composition and the physiological development phase influence the spectrum of the light attenuation coefficient in the sea. Laboratory measurements of light attenuation spectrum were carried out on three different phytoplankton monocultures of the unicellular green algae *Chlorella vulgaris* and the larger *Chlorella kesleri* and the blue-green alga *Chroococcus minor*. The cultures were subjected to chemical (NaOH and temperature) or physical (ultrasounds) factors which altered their internal cell structures. Distinct changes in the light attenuation spectrum were observed as a result of the modification of the internal cell structures. Light attenuation cross-sections of those phytoplankton cells were also determined.

1. INTRODUCTION

Phytoplankton is a part of the marine environment which has a significant influence on the light field in the sea and another light interaction process with the sea. However, the phytoplankton distribution in the sea is to a great extent dependent on the light field. This phenomenon leads to complex interactions between optical parameters of the sea water and the phytoplankton distribution in the near surface layer of the sea. The type of the phytoplankton as well as the phase of its physiological development influence the light attenuation coefficient and other optical parameters of natural sea waters. Satellite based estimations of the sea basins vitality are carried out using light emitted from the sea. This light is also a net product of the complex processes of light interactions with the marine environment, including phytoplankton.

A precise understanding of the mechanism of light interaction with phytoplankton cells can be helpful in creating accurate models which describe optical phenomena in the sea. Moreover it may lead to easier interpretation of information which is obtained via satellites as well as to understanding the influence of lighting on the primary production in the sea and ocean.

The process of light attenuation by phytoplankton is the net effect of light absorption and light scattering in its cells. Differences in the inner structures of the cells play a significant role in this phenomenon.³ Artificial changes of the inner structures of phytoplankton cells affect the phytoplankton's scattering properties and therefore influence light attenuation by its cells.

In order to verify this effect, laboratory investigations of light attenuation by three various phytoplankton suspensions were carried out. The suspensions were: a monoculture of spherical, unicellular *Chlorella vulgaris* and *Chlorella kesleri* and spherical *Chroococcus minor*. Tests were carried out on both live

cultures and cultures which were treated with chemical compounds or treated physically in order to change their internal structures.

This paper presents the results of these investigations

2. LIGHT ABSORPTION, SCATTERING AND ATTENUATION BY PHYTOPLANKTON

If a parallel beam of light of I_0 intensity illuminates a scattering medium of a thickness of d the intensity of the attenuated light I is described by the following formula:

$$I = I_0 \exp(-N C d), \quad (1)$$

where N is the concentration of scattering and absorbing particles and C is the mean attenuation cross-section of the particle. C is the sum of the scattering cross-section C_s and absorption cross-section C_a :

$$C = C_s + C_a \quad (2)$$

Both cross-sections C_s and C_a depend on optical parameters of the particles (complex light refraction coefficient) and their geometric parameters (size). Such a situation also occurs in the case of suspensions which are found in the marine environment including phytoplankton³ and microplankton.⁴ It was experimentally confirmed³ that in the process of light interaction with phytoplankton cells an important role is played by nonhomogeneities which occur in the inner structure of the cells (nucleus and the other parts). Interfering with the inner structures causes changes in the cells scattering properties including functions which create scattering matrix (Mueller matrix) i.e. intensity functions. Therefore, it must be assumed that the attenuation cross-sections of phytoplankton depend on the inner structure of the cells. The degree of the influence of the destruction of the inner structure on the scattering and attenuation cross-sections may vary for various wavelengths. This is due to the influence of the imaginary part of the refraction coefficient for all scattering structures including chlorophyll-protein centres. It is necessary to continue the investigations of the spectra of attenuation cross-sections.

The light scattering and therefore light attenuation by phytoplankton should be analysed at all levels of nonhomogeneities which occur in its cells⁵ as follows:

- at the level of the external size of the cells or organisms (C^e)
- at the level of the inner structures (C^i)
- at the level of macromolecular structures of protein molecules and chlorophyll-protein centres (C^m)

$$C = C^e + C^i + C^m \quad (3)$$

3. DESCRIPTION OF PHYTOPLANKTON CELLS

The following unicellular algae isolated from Baltic Sea phytoplankton were used in the tests.

a) *Chlorella vulgaris*.

Division: Chlorophyta

Class: Euchlorophyceae

Order: Chlorococcales

Family: Oocystaceae

Genera: *Chlorella* Beijernick 1890

Species : *Chlorella vulgaris* Beijernick

Chlorella vulgaris has spherical or ellipsoidal cells 3 to 10 μm in diameter, thin cellular wall and one chromatophore. This species is very common in fresh waters however it also occurs in the seas. For testing axenic culture of A176 *Chlorella vulgaris* was used which was extracted from the Baltic Sea phytoplankton at the Institute of Oceanology PAS in Sopot.²

b) *Chlorella kesleri*

Division: Chlorophyta

Class: Euchlorophyceae

Order: Chlorococcales

Family: Oocystaceae

Genera: *Chlorella* Beijernick

Species: *Chlorella kesleri* Fott and Nowakowa 1869

Chlorella kesleri has spherical always single cells up to 20 μm in diameter which are surrounded by a smooth cell membrane. It is very common in fresh waters and in waters with low saline concentrations.

c) *Chroococcus minor*

Division: Cyanophyta

Class: Cyanophyceae

Order: Chroococcales

Family: Gloeocapsaceae

Genera: *Gloeocapsa* (Kutzing) Holerbach emend 1983, Nageli, 1849 (*Chroococcus* Nageli 1849)

Species: *Gloeocapsa minor* (Kutzing) Holerbach

Chroococcus minor presents poorly defined spherical cells with diameter 3 - 8 μm . It creates oval or irregularly shaped colonies which are surrounded by a transparent jelly. It exist in inland waters e.g. Zalew Szczeciński (part of the Baltic Sea).

After the algae had been cultivated in a solid bactopectone medium for several days, the cells were washed with nutrients and then incubated for 7 days in order to adapt the organisms to a liquid medium.

The algae incubation was carried out in BBM (Bold Basal Medium),¹ with constant illumination of 150 $\text{mE m}^{-2} \text{s}^{-1}$ and at a temperature of $21^{\circ}\text{C} \pm 2^{\circ}\text{C}$.

Algae thus prepared were modified in order to obtain changes in the inner structure of the cells. Those modifications were carried out as follows:

- ultrasonic interaction with liquid culture *Chlorella vulgaris* using Ultrasonic Homogenizer 4710 Series (Cole Paxner) for a period of 10 minutes at a power of 30 W which caused disintegration of the cells inner structures but did not damage their walls,
- boiling algae for 10 minutes in 10% NaOH (sodium hydroxide) solution which caused the complete destruction of the interior of the cells.

Under microscopic investigations it was confirmed that only the walls of the empty cells remained. In addition to the above modified structures, the following cultures were used:

- live non modified cultures,
- acetone chlorophyll extracts of live cultures.

4. THE RESULTS OF LIGHT ATTENUATION MEASUREMENTS

The transparency of both live and modified cultures of phytoplankton cells were tested using a UV-VIS spectrophotometer (Zeiss). The measurements were carried out at the Institute of Experimental Physics at the University of Gdańsk. The cultures being tested were placed in flat cuvettes of 0.5 to 2 cm thickness. The cuvettes were illuminated with a beam of monochromatic light at various wavelengths about 1 cm in diameter.

At a distance of 0.4 m beyond the sample the light beam was registered by a photocell. Then it was compared with the same beam of light which went through the reference material i.e. pure nutrients (cultures) and acetone (extracts). Visible light wavelengths ranging from 0.36 μm to 0.78 μm were used.

Microscopic examinations were used to determine the actual concentrations of cells for tested samples and the concentrations of cells which relate to chlorophyll concentration in solution. Furthermore, the results obtained for the I/I_0 ratio were used to determine the spectra of the mean values of light attenuation cross-sections using the following formula:

$$C = \frac{-\ln\left(\frac{I}{I_0}\right)}{Nd} \quad (4)$$

The results of calculations aimed at determining the light attenuation of cross-sections of *Chlorella vulgaris*, *Chlorella kesleri* and *Chroococcus minor* are presented in Figures 1,2,3 for live cells (A), those treated with temperature (B) and those treated with ultrasounds (C). In addition, these figures show the spectra of the light absorption cross-section of the chlorophyll extract which has a concentration corresponding to the concentration in live cells (D). The modification of the inner structures of the phytoplankton's cells was changing optical properties of those cells.

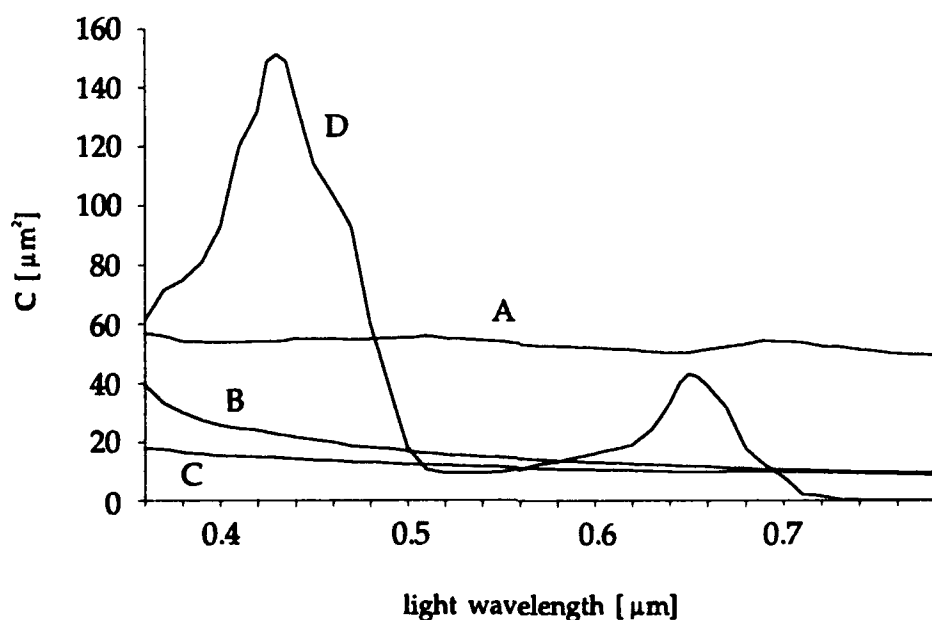


Fig. 1. Attenuation mean cross-sections spectra for *Chlorella vulgaris* cell. A - alive cell, B - thermally modified cell, C - ultrasonic modified cell, D - acetone extract of chlorophyll from one cell.

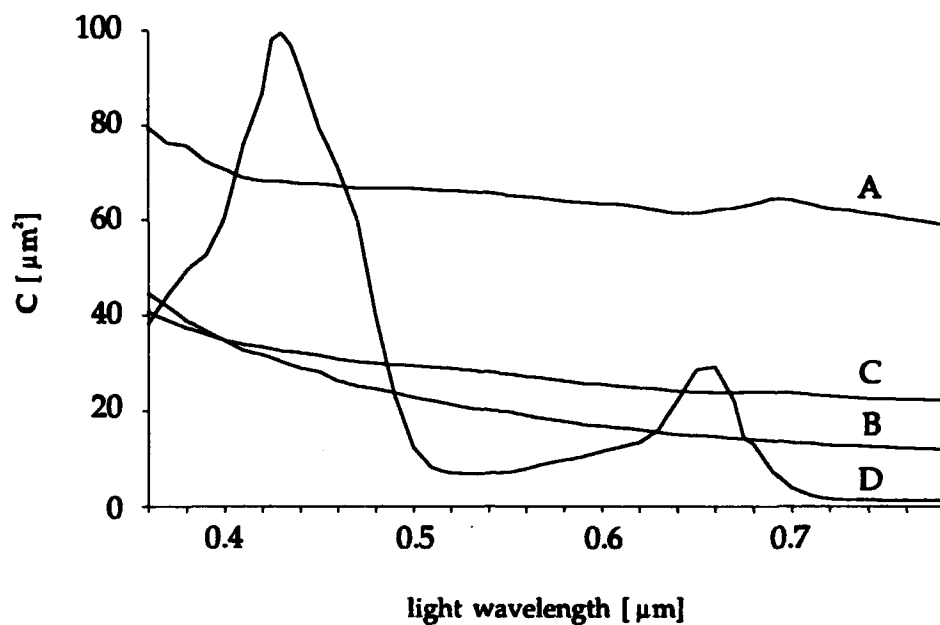


Fig. 2. Attenuation mean cross-sections spectra for *Chlorella kesleri* cell. A - alive cell, B - thermally modified cell, C - ultrasonic modified cell, D - acetone extract of chlorophyll from one cell.

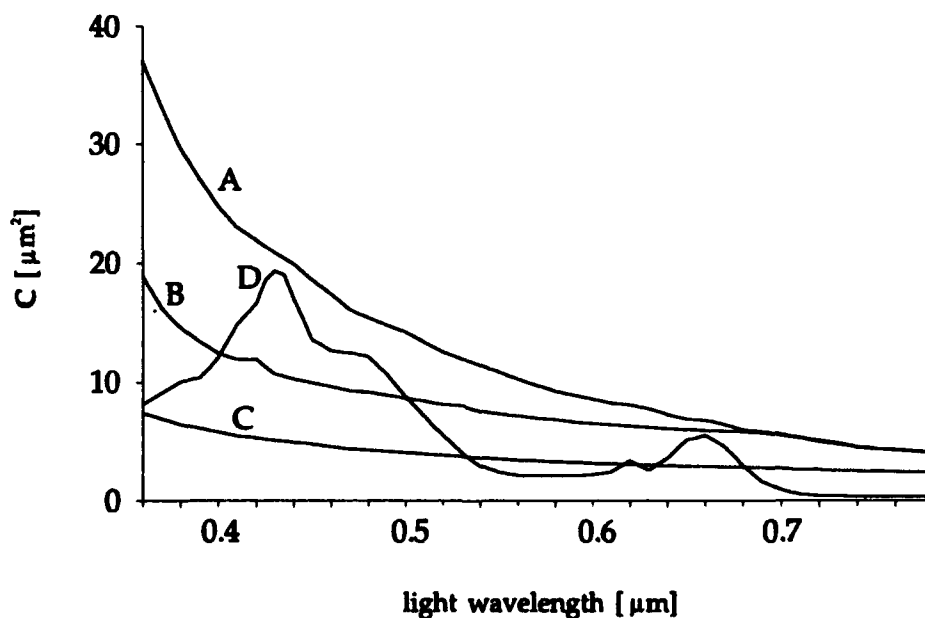


Fig. 3. Attenuation mean cross-sections spectra for *Chroococcus minor* cell. A - alive cell, B - thermally modified cell, C - ultrasonic modified cell, D - acetone extract of chlorophyll from one cell.

5. CONCLUSIONS

The dependence of light attenuation spectra by phytoplankton cells on the method and degree of inner structure destruction was confirmed

Significant changes of the spectrum of the light attenuation of tested phytoplankton cells as a result of inner structure modifications were confirmed.

In the process of light interaction with phytoplankton a decisive role is played by light scattering which is more significant than light absorption.

The influence of chlorophyll absorption on light attenuation cross-sections of the cells is insignificant.

In the process of light attenuation a significant role is played by the cells inner structures. For this process phytoplankton classification based on the organisation of inner structure is as important as the classification based on the size and shape of the cells.

In the case of *Chroococcus minor* the difference between the attenuation (absorption) of extracted chlorophyll in the maximum of absorption and attenuation of the whole cell is smaller than in the case of *Chlorella vulgaris* and *Chlorella kesleri* which were tested.

6. REFERENCES.

1. Bischoff H. W., Bold H. C., 1963, Phycol. Stud. 4, Univ Texas Public No 6318.
2. Gędziorowska D., 1983. Isolation of Baltic unicellular algae and obtaining axenic cultures for physiological and biochemical investigations. SiMO 41.
3. Król T., Zieliński A., Witkowski K., 1992, Light scattering on *Chlorella vulgaris* cell. SPIE Vol. 1750 Ocean Optics San Diego.
4. Morel A. Theoretical results concerning light absorption in a discrete medium and application to specific absorption by phytoplankton . Dep Sea Research. Vol 28A No 11.
5. Zieliński A., T. Król, D. Gędziorowska. 1987. The Influence of the Inner Structure of the *Chlorella vulgaris* Cell on the Light Scattering Properties. Bulletin of the Polish Academy of Sciences. Earth Sciences. Vol.35. No.2.

Diel variability of in vivo chlorophyll fluorescence in near-surface water layer

A.M. Chekalyuk and M.Yu. Gorbunov*

**Moscow State University, Dept. of Physics (*Dept. of Chemistry),
Moscow 119899, Russia**

ABSTRACT

The analysis of diel variations in fluorescence yield of chlorophyll-a (Chl-a) in vivo is presented in the paper, relying on recent field observations and laboratory studies, as well as on biophysical description of the relationship between photosynthesis and Chl-a fluorescence.

In general, the phenomenon is caused by the combined action of a number of environmental factors and physical processes in the near-surface water layer (changes in ambient irradiance, nutrient availability, vertical mixing, etc.). In particular, the variations in fluorescence yield due to "instant" changes and diurnal variations in ambient irradiance can be explained as the manifestations of "photochemical" and "non-photochemical" quenching of Chl-a fluorescence, respectively. The peculiarities of these regulations depends to a large extent on the nutrient supply of the cells.

Field studies of the diel variability in Chl-a fluorescence were carried out with a shipborne lidar system in the Baltic, Mediterranean, Black seas, and in the Atlantic ocean. As predicted by the model, we observed the maximal values of Chl-a fluorescence yield in the near-surface layer at night and its decrease in the noon. The max/min ratio varied from 3 to 1, depending on environmental conditions and, thus, on the functional state of photosynthetic apparatus. Non-photochemical mechanisms of "photoinhibitory" and energy-dependent quenching were found to be the major mechanisms of regulation of Chl-a fluorescence yield at a diurnal scale.

1. INTRODUCTION

The phenomenon of diel variability in algal chlorophyll-a (Chl-a) fluorescence is of particular significance when measuring in the nearsurface water column, where the ranges of variations in solar illumination and nutrient availability are maximum. Although changes in various parameters (cell concentration, Chl-a content per cell, etc.) can contribute to the overall variability of Chl-a fluorescence *in situ*, this effect is determined to a large extent by diurnal variations in Chl-a fluorescence quantum yield. In essence, the Chl-a fluorescence is a channel of energy dissipation accompanying photosynthetic conversion of absorbed light energy. The fluorescence yield is therefore subjected to regulation of an efficiency of primary stages of photosynthesis by environmental factors, such as ambient irradiance, nutrient availability, temperature.

The present paper is devoted to analysis of diel variability in Chl-a fluorescence, based on biophysical description, as well as on recent laboratory and field studies.

2. REGULATION OF PHOTOSYSTEM II PHOTOCHEMISTRY EFFICIENCY AND CHLOROPHYLL FLUORESCENCE BY AMBIENT IRRADIANCE

In vivo fluorescence of Chl-a accompanies the primary stages of photosynthesis (see as a review ¹). At a room temperature the major contribution to Chl-a fluorescence is emitted from photosystem II (PS2). Chl-a fluorescence yield depends to a large extent on a functional state of PS2 reaction centers (RCs). Due to unfavorable environmental conditions (e.g. nutrient limitation) some fraction of PS2 RCs can be photochemically inactive.²⁻⁴ If a potentially functional RC is open (i.e. the primary quinone acceptor Q_A is oxidized), a capture of excitation effectively drives non-cyclic electron transport. As in the dark all functional PS2 RCs are open, the quantum yield of fluorescence is minimal, and, to a first approximation, can be described as follows (similar to ⁴) :

$$\Phi_o = K_F / (K_F + K_D + f K_T). \quad (1)$$

Here K_F , K_D , and K_T denote the rate constants for three competitive ways of energy deactivation (fluorescence, non-radiative thermal dissipation, and trapping by RC, respectively); f is a fraction of potentially active RCs ($0 < f < 1$).

When functional PS2 RC is in the closed state with reduced Q_A (i.e. Q_A^-), the chain of electron transport is blocked and $K_T = 0$. This leads to corresponding increase in the probability of fluorescence emission. When all the PS2 RCs are closed (e.g. due to a saturating pump flash), the fluorescence yield reaches its maximum value

$$\Phi_m = K_F / (K_F + K_D). \quad (2)$$

As in the dark all functional RCs are open, the potential quantum yield of photochemistry in PS2 (Φ_p) is equal to the probability of exciton capture by functional RCs¹ :

$$\Phi_p = f K_T / (K_F + K_D + f K_T). \quad (3)$$

From (1) and (2) it follows, that

$$\Phi_p = (\Phi_m - \Phi_o) / \Phi_m, \quad (4)$$

and it can be easily estimated by measuring Φ_o and Φ_m magnitudes for dark-adapted algae. Note, that Φ_o is minimal when all RCs are potentially functional ($f = 1$), and tends to Φ_m with the increase in the fraction $(1-f)$ of inactive RCs under unfavorable changes in environment, resulting in corresponding decrease in Φ_p . According to laboratory measurements (² as well as our unpublished data) and field studies,^{5,6} the maximum potential efficiency of photochemistry in PS2 (when $f = 1$) for algae $\Phi_p = 0.65$ regardless of species examined and growth irradiance. In other terms, the maximum

$\Phi_{\text{m}}/\Phi_{\text{o}}$ ratio was found to be about 3 under nutrient-replete conditions. Based on this fact, $K_{\text{T}} = 2 (K_{\text{F}} + K_{\text{D}})$ in our model, and, to a first approximation, the fraction of functional PS2 RCs (f) can be estimated as $\{(\Phi_{\text{m}} - \Phi_{\text{o}})/\Phi_{\text{m}}\}/0.65$.⁷

In the presence of continuous light, photosynthetic reactions start their performance. In general, the actual efficiency of photochemistry in PS2 appears to be lowered in comparison with its potential value $\Phi_{\text{p}} = (\Phi_{\text{m}} - \Phi_{\text{o}})/\Phi_{\text{m}}$ measured in the dark (e.g. ^{1,7}). This results in corresponding changes in parameters of the Chl-a fluorescence. It is common practice to analyze the influence of ambient irradiance on *in vivo* Chl-a fluorescence in terms of 'photochemical' and 'non-photochemical' quenching (e.g. ^{1,7,8}).

In essence, various mechanisms of non-photochemical quenching play a protective role for photosynthetic apparatus under excessive levels of ambient irradiance.⁹ In spite of their different origin, these generally provide an increase in non-radiative thermal deactivation of excitation energy. Since the protective function of non-photochemical quenching is limited (both genetically and due to environmental regulation), at supraoptimal levels of irradiance the photo damage may occur in some of PS2 RCs, resulting in decrease in fraction of RCs, capable of photochemistry. In the context of our simplified model, these phenomena can be described by introducing a rate constant K'_{D} of thermal dissipation, and a fraction of functional PS2 RCs f' , both irradiance-dependent. In particular, the maximum (Φ'_{m}) and minimum (Φ'_{o}) fluorescence yields under ambient irradiance can be presented as follows:

$$\Phi'_{\text{o}} = K_{\text{F}} / (K_{\text{F}} + K'_{\text{D}} + f' K_{\text{T}}) , \quad \text{and} \quad (5)$$

$$\Phi'_{\text{m}} = K_{\text{F}} / (K_{\text{F}} + K'_{\text{D}}) . \quad (6)$$

Unlike the dark-adapted state, under ambient light the probability for exciton to be trapped by functional RCs

$$\Phi'_{\text{T}} = f' K_{\text{T}} / (K_{\text{F}} + K'_{\text{D}} + f' K_{\text{T}}) = (\Phi'_{\text{m}} - \Phi'_{\text{o}}) / \Phi'_{\text{m}} \quad (7)$$

does not describe the efficiency of photochemistry,¹⁰ as some fraction (1-A) of functional PS2 RCs appears in virtually closed state due to the relatively slow rate of Q_{A}^{-} reoxidation. This effect leads not only to decrease in the quantum yield of photochemistry Φ'_{p} , but also causes corresponding rise in actual yield of fluorescence Φ' as compared with its minimal for a given level of irradiance value Φ'_{o} . This effect is usually interpreted as a decrease in photochemical quenching.

To a first approximation, the resulting actual fluorescence yield Φ' can be determined as a sum of contributions from open and closed reaction centers.^{8,11} If we designate a fraction of the open functional PS2 RCs as A ($0 < A < 1$),

$$\Phi' = A \Phi'_{\text{o}} + (1-A) \Phi'_{\text{m}} \quad (8)$$

From (8) it follows that

$$A = (\Phi'_n - \Phi'_o) / (\Phi'_n - \Phi'_o) = Q_p, \quad (9)$$

where Q_p is a coefficient of photochemical quenching.¹²

Relying on the approach of Genty et al.¹⁰, the actual quantum efficiency of PS2 photochemistry under ambient irradiance (i.e. Φ'_p) can be estimated as

$$\Phi'_p = A \Phi'_n = A f' K_T / (K_T + K'_D + f' K_T) = (\Phi'_n - \Phi'_o) / \Phi'_n \quad (10)$$

Thus, Φ'_p can be obtained by measuring the actual (F') and maximum (F'_n) fluorescence levels, and calculating $(\Phi'_n - \Phi'_o) / \Phi'_n = (F'_n - F') / F'_n$.

Equations (5), (6), (8), and (10) provide a basis for analysis of the regulation of PS2 photochemistry efficiency and Chl-a fluorescence due to variations in ambient irradiance in different environmental conditions. In particular, the major peculiarities of diel variations in Chl-a fluorescence yield and Φ'_p in near-surface water layer can be explained relying on this approach.

Three major environmental factors control the observed diel variability in these parameters: nutrient availability, light history and current level of ambient irradiance. According to recent studies,^{2-4,13} the nitrogen and iron limitations can lead to significant changes in algal photosynthetic apparatus. In particular, these cause the reduction in the fraction (f) of functional PS2 RCs due to losses in the content of proteins, associated with PS2. Whereas the maximum fluorescence yield is independent upon functional state of PS2 RCs (see eq. (2), (6)), both the minimum "dark" fluorescence yield Φ'_o and the potential efficiency of PS2 photochemistry Φ'_p are subjected to changes under Fe or N limitation. From eq. (1) and (2) it follows, that Φ'_o will increase from its minimum value (about $1/3 \Phi'_n$), characteristic for nutrient-replete conditions, up to the level of maximum "dark" fluorescence yield Φ'_n (strong nutrient deficiency) with the reduction in f due to nutrient limitation. In contrary, the potential efficiency of photochemistry (see eq.(3)) will be lowered with decline of f in comparison with its maximum value 0.65. Under natural conditions, these "dark" magnitudes of Φ'_o and Φ'_p , determined by current situation with nutrient supply, define night values of the fluorescence yield and the potential efficiency of photochemistry in PS2.

After sunrise, when photosynthesis begins its performance, the increasing ambient irradiance leads to corresponding changes in the "starting" night values of fluorescence yields (both Φ'_o and Φ'_n) and PS2 photochemical efficiency. The non-photochemical quenching (Q_N) play an important role in this regulation. From the above model it is evident that the associated rise in non-radiative losses should affect the magnitudes of all related parameters (i.e. Φ'_o , Φ'_n , Φ'_T , and Φ'_p), but the

degree of its impact on each parameter is different.

The reduction in maximum fluorescence Φ'_m (see eq.6) must be more pronounced, regardless of PS2 RCs functional state. By contrast, a degree of decline in the minimum fluorescence yield Φ'_o will depend upon the fraction (f) of functional PS2 RCs. In nutrient-replete conditions under moderate ambient irradiance, when the major part of PS2 RCs are functional ($f \approx 1$), the manifestation of Q_N -induced decrease is minimal, as $K_T \approx 2(K_F + K_D)$, see eq.5. In contrary, under nutrient depletion (decrease in f) the minimum fluorescence yield must be not only higher as compared with replete conditions, but more sensitive to Q_N regulation. In a limiting case of full depletion ($f \approx 0$), the quantitative manifestation of Q_N should be similar to that one characteristic for Φ'_m (see eqs.5,6).

Under moderate irradiance levels, when Q_N is capable to protect PS2 RCs from photodestruction, the decrease in efficiency Φ'_T of exciton trapping by functional PS2 RCs is determined (eq.8) by the Q_N -related rise in K'_D , and in general its peculiarities with regard to nutrient supply are similar to those discussed above for Φ'_o (compare eq.5 and eq.7). Further increase of excessive irradiance can exhaust the protective potential of Q_N and cause inactivation of some PS2 RCs (Neale, 1987), i.e. the decrease in f' resulting in additional reduction in Φ'_T . The mechanism of Q_N -produced decrease in the actual efficiency of PS2 photochemistry Φ'_p can be described in that way (see eq.10).

Hand in hand with the non-photochemical quenching, the mechanism of virtual closure of a fraction ($1-A$) of functional PS2 RCs (i.e. light-induced decrease in photochemical quenching) is responsible for the light regulation of the actual fluorescence yield Φ' and the actual quantum efficiency of PS2 photochemistry Φ'_p (eq.8,10), leading to an increase in the former and a decrease in the later with a rise of ambient irradiance.^{1,7,8,10-12} From eq.8 it is evident that the greater is the difference between Φ'_o and Φ'_m , the more marked should be variations in Φ' due to the light-induced changes in A , a fraction of open PS2 RCs. Thus, the effect of changes in Q_p (e.g. due to fast changes in ambient irradiance) will be more pronounced in case of good functional state of photosynthetic apparatus (i.e. $f \approx 1$), e.g. under nutrient-replete conditions.

According to the laboratory and direct *in situ* measurements,^{8,15-17} this effect becomes noticeable even at a relatively low level of irradiance (e.g. $1-A \approx 0.2$ at the fluence rate of $15 \mu\text{mol quanta m}^{-2} \text{s}^{-1}$), and come into particular prominence at a moderate ones ($1-A \approx 0.80$ at $300 \mu\text{mol quanta m}^{-2} \text{s}^{-1}$). As a result, it plays a significant role in near-surface water layer in the sea.

One of the distinctions between photochemical and non-photochemical fluorescence quenching is the relaxation times for their response to changes in ambient irradiance. This time is several seconds for the photochemical quenching while it ranges from several to tens of minutes for the non-photochemical that (e.g. ^{1,9}). This distinction

is used for quantitative recording the contributions of these quenching mechanisms (see e.g. ¹⁸).

With regard to the non-photochemical quenching, there are several mechanisms potentially capable to contribute to this effect in natural conditions. These are a rise of light-induced pH gradient across thylakoid membrane (so-called " ΔpH -dependent" or "energy-dependent" quenching), alterations in xanthophyll cycle, photoinhibition of primary stages of photosynthesis resulting in inactivation of PS2 RCs and increase in the rate of non-radiative energy dissipation; photophosphorylation of polipeptides of the PS2 light-harvesting complex; spillover; and photodestruction of pigments and lipids of thylakoid membrane.^{1,9}

Under normal physiological conditions spillover and photophosphorylation are weakly displayed in intact cells.¹ The energy-dependent quenching decreases the variable fluorescence yield and is pronounced at irradiance levels of 30-300 $\mu\text{mol quanta m}^{-2} \text{s}^{-1}$ (^{9,19}). Excessive irradiance (over 1000 $\mu\text{mol quanta m}^{-2} \text{s}^{-1}$) may lead to photoinhibition^{1,20} of photosynthesis. Photodestruction, resulting in a marked decline of both Φ'_0 and Φ'_1 , may occur under prolonged (over 1 hour) action of strong ambient light (about 2000 $\mu\text{mol quanta m}^{-2} \text{s}^{-1}$ (²¹)).

3. METHOD AND INSTRUMENTATION

A lidar implementation⁶ of the pump-and-probe technique^{22,11,2} was applied in this study. As in case of conventional LIDAR systems, a *pump-and-probe* LIDAR provided remote measurements by using laser pulses for excitation of *Chl-a* fluorescence in sub-surface water layers. The distinction was that the fluorescence was alternately detected in response to the excitation by a single *probe* pulse and by the *probe* pulse following a *pump* pulse (see Fig.1). In the first case the actual (or minimal in night) *Chl-a* fluorescence intensity (Φ) was detected, in the second case - the maximum one (Φ_m). The function of the pumping laser pulse was to cause the transition of previously open RCs to the closed state at the moment of probe pulse action; the role of probe pulse - to induce *Chl-a* fluorescence to be detected.

Block diagram of a pump-and-probe lidar system is presented in Fig.2. It consists of two pulsed Nd:YAG-lasers, an optical system, including optical multichannel analyzer (OMA), and a computer for control over the system and data processing. All components of the lidar (excluding folding mirror) were mounted inside a ship laboratory. Pulses of the first laser (radiation wavelength - 532 nm; pulse duration - 10 ns; pulse power - 3.5 MW) were utilized as the pump ones to close initially open RCs PS II. The second laser generated the probe pulses (532 nm; 10 ns; 0.5 MW) to induce *Chl-a* fluorescence emission. A delay between the pump and the probe pulses in a double-pulse mode was about 30-50 μs . Gating the OMA system by 50 ns pulses synchronously with the probe laser pulses allow to avoid adverse contributions from ambient light and pump-induced fluorescence. Those parameters allowed pump-and-probe measurements of laser-induced *Chl-a* fluorescence in a sub-surface water layer (1-2 m depth) from a distance to water surface of 10-15 m, including prolonged day-and-night along-track monitoring at synoptic scale.⁶

An example of the pump-and-probe spectral-resolved measurement is presented in fig.1. All fluorescence data presented below are normalized to corresponding *Chl-a* concentrations at water surface, and to intensities of water Raman scattering I_R .

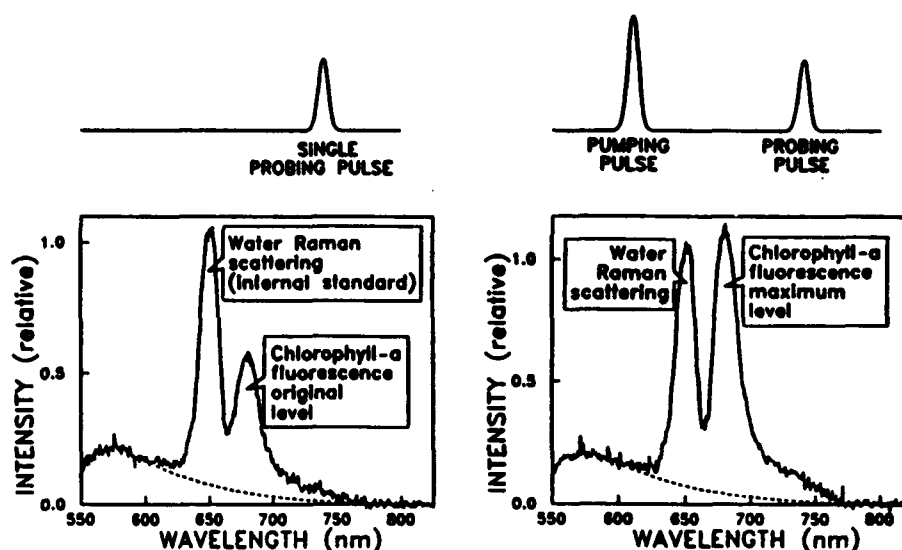


Fig.1. Typical spectra of return signal from sea water recorded in response to excitation by a single probe pulse (left) and by a probe pulse following a saturating pump one (right). The delay time between the pump and probe pulses is 40 μ s; the excitation wavelength 532 nm. The action of the pump pulse causes the closing of the initially open reaction centers of PS2, and, thus, an increase in the Chl-a fluorescence measured in response to the succeeding probe flash.

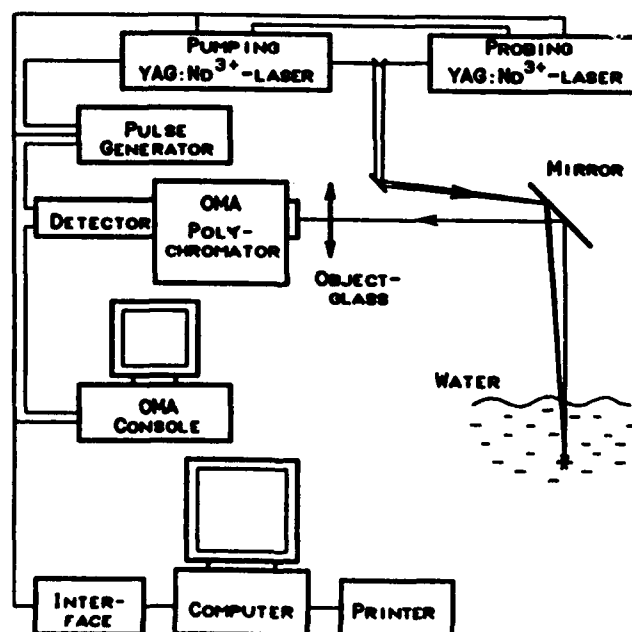


Fig.2. Block diagram of the pump-and-probe LIDAR system for measuring the pump-induced change in chlorophyll-a fluorescence of phytoplankton. The system consists of two frequency-doubled Nd:YAG-lasers for generating the pump and probe pulses, the detection system including an optical multichannel analyzer (OMA) to record the probe-induced fluorescent response, and a computer.

induced in the same water column by the laser excitation (for detail see ⁶). As detected I_R is linear-proportional to the energy of probe laser pulse, this approach provides a basis for remote estimates of relative variations in Chl-a fluorescence yield.

4. RESULTS AND DISCUSSION

A bright manifestation of environmental regulation of Chl-a fluorescence yield is the observed diurnal variations of Chl-a fluorescence in the near-surface water layer (e.g. ²³⁻²⁵). We studied this phenomenon with a shipborne lidar system in various environmental conditions during cruises in the Baltic, Mediterranean and Black seas, as well as in the Southern and North-Western Atlantic.

Diel variations of the actual Chl-a fluorescence F' , measured *in situ* with a single pulse excitation, and the maximum one F'_m , measured in pump-and-probe mode, are shown in Fig.3a,b. The data were obtained with a shipborne lidar during three days of measurements at the station in the Tyrrhenian Sea (the Mediterranean) in April of 1991. A diurnal rhythm of the actual efficiency of PS2 photochemistry $\eta = (\Phi' - \Phi'')/\Phi' = (F'_m - F')/F'_m$ is presented in Fig.3c. A dashed line presents diel variations in solar irradiance (E) measured at the sea surface. Due to sunny days, the maximum E magnitudes reached 1500 - 1800 $\mu\text{mol quanta m}^{-2} \text{s}^{-1}$.

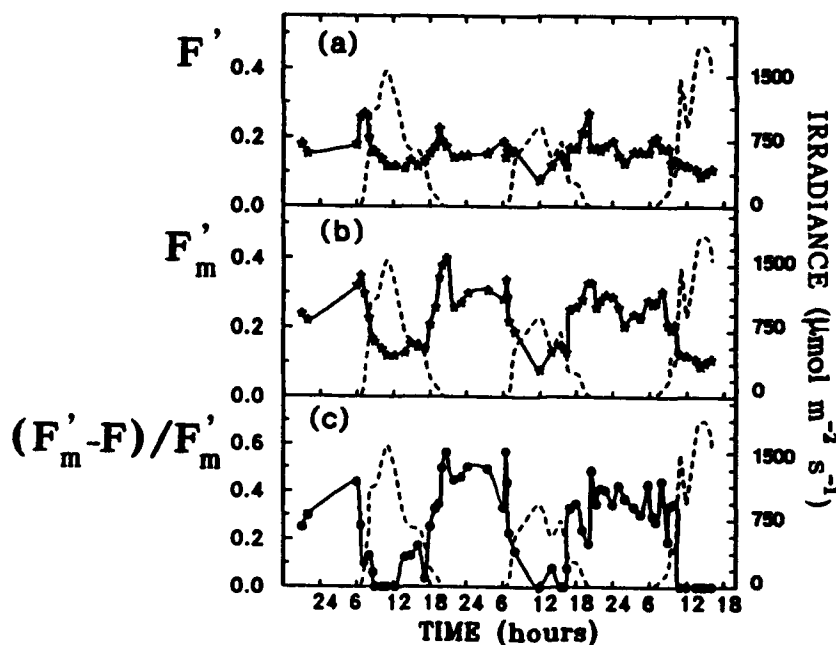


Fig.3. Diel variations of the actual Chl-a fluorescence F' (a), measured *in situ* with a single pulse excitation; the maximum one F'_m (b), measured in pump-and-probe mode; and the actual efficiency of photochemical reactions in PS2 $\eta = (\Phi' - \Phi'')/\Phi' = (F'_m - F')/F'_m$ (c).

The data were obtained with the shipborne pump-and-probe lidar during three days of measurements at the station in the Tyrrhenian Sea in April of 1991. A dashed line presents diel variations in solar irradiance at the sea surface.

At night, one could see weak variations in the actual fluorescence (Fig.3a) in the range from 0.15 to 0.17. During sunrise, F' increased by a factor of 1.5 as E weakly rose up to $20\text{--}30 \mu\text{mol quanta m}^{-2} \text{s}^{-1}$. Then, as the irradiation increased, F' showed a sharp decline, and under $E \geq 1000 \mu\text{mol quanta m}^{-2} \text{s}^{-1}$ it reached a steady state at the minimum level $F' = 0.1$. After noon, as long as the irradiation exceeded $300\text{--}500 \mu\text{mol quanta m}^{-2} \text{s}^{-1}$, F' remained at its noon level. The recovery in F' began only with a further decrease in irradiation in the evening. During the sunset, when E fell down to $20 \mu\text{mol quanta m}^{-2} \text{s}^{-1}$, a strong increase ($\approx 50\%$) in F' was observed. Then F' decreased down to its "dark" magnitude. The ratio of night maximum to noon minimum fluorescence (NT/NN ratio) was about 1.5. Note a marked decrease in the noon of the third day of measuring, when the irradiance reached its highest level of $1800 \mu\text{mol quanta m}^{-2} \text{s}^{-1}$. In general, the effect of diel modulation in F' was not too much pronounced, as it was predicted for the case of good functional state of PS2 RCs ($f \approx 0.6 - 0.7$, see below).

The diel variations in the maximum fluorescence F'_m were found to be much more pronounced (see Fig.3b). The value of NT/NN ratio was about 3 in that case, and while the night F'_m value were significantly higher than the corresponding F_o ones, there were observed no difference between F'_m and F' at noon: F'_m followed F' in detail. That indicated that variable fluorescence $F'_v = F'_m - F'_o$ (note, that $F'_m > F' > F'_o$) was fully inhibited under supraoptimal levels of ambient irradiance (more than $1000 \mu\text{mol quanta m}^{-2} \text{s}^{-1}$) in the subsurface water layer. A marked feature were also sharp increases in F'_m at the sunsets and sunrises.

Based on these data, diurnal variations in the quantum efficiency of PS2 photochemistry were calculated. The results presented in Fig.3c reveal that the potential capacity of PS2 for photochemistry was fairly high: $\Phi_p = (F'_m - F'_o)/F'_m = 0.4 + 0.5$, that corresponded to the fraction of functional PS2 RCs $f = \Phi_p/0.65 \approx 0.6 + 0.7$. The increases in Φ'_p were also observed at the sunrises and sunsets. Under moderate levels ($E < 1000 \mu\text{mol quanta m}^{-2} \text{s}^{-1}$) of ambient irradiance, Φ'_p inversely followed changes in E . In this irradiance range, these two curves look like the mirror images of each other. The major feature of Φ'_p curve is almost full inhibition of PS2 photochemical efficiency as the level of irradiance exceeded $1000 \mu\text{mol quanta m}^{-2} \text{s}^{-1}$. It is necessary to note, that in spite of apparent reduction caused by this effect, a rate of the gross photosynthesis (i.e. CO_2 assimilation or O_2 evolution) may be reasonably high due to high intensity of ambient irradiance (e.g. see Fig.5 in ⁷).

As predicted by the model presented in the previous chapter, the actual fluorescence yield Φ' should exhibit a similar behaviour under excessive light, as the the maximum one Φ' does. The experimental evidence of this phenomenon is presented in Fig.4. Three-days *in situ* measurements of the actual fluorescence F' (single-pulse excitation) were conducted with a shipborne lidar at a station in the Black Sea (April 1988). The overall situation was characterized by a decline of phytoplankton spring bloom, where the *Nitzschia sp.* was a dominant species. According to DCMU-based measurements in water samples taken from a surface, up to 90% of PS 2 RCs were inactive in that particular case (i.e. $f \approx 0.9$).

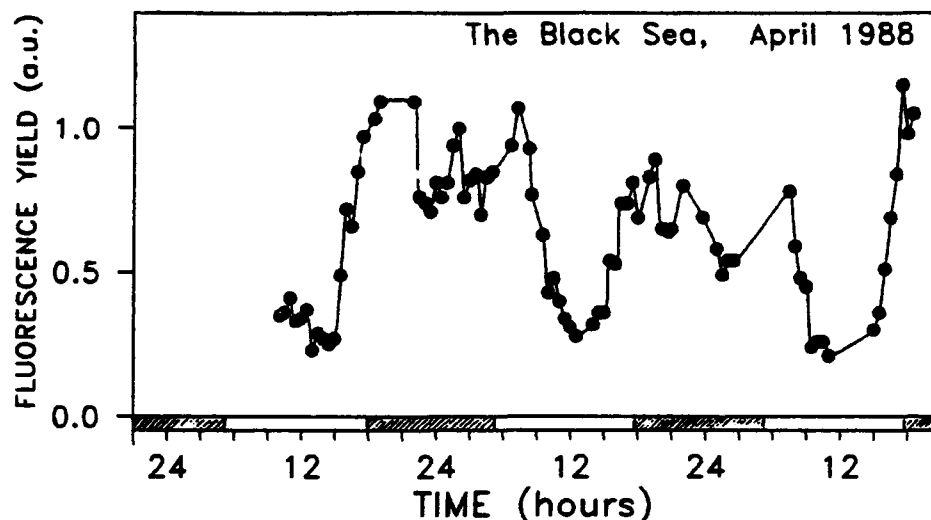


Fig.4. Diel variations in *in situ* Chl-a fluorescence yield measured with a shipborne lidar at a three-day station in the Black Sea (April 1988) at the stage of decline of phytoplankton spring bloom.

One can see a significant noon decrease in F' , the ratio of night maximum to noon minimum fluorescence $NT/NN \approx 3$, just like in the case of F' diel variations presented in Fig 3b. In general, all major peculiarities of the observed diel changes were similar in those two cases. It is remarkable, that in the later case there was completely different bio-optical situation in the area (the Tyrrhenian Sea, 1991), and the measurements were conducted with a different technique (pump-induced closure of PS2 RCs for F' measuring). Note, that the two F' curves presented in Fig.3a and Fig.4, measured with the same single-pulse technique, are much more distinct.

Similar data on the diel variations in F' were obtained with a shipborne lidar system in various environmental conditions in the Baltic Sea, and in the Southern Atlantic as well. These observations suggest that the peculiarities of the diel changes in Chl-a fluorescence F' in subsurface water layer are determined to a large extent by the regulation of the actual fluorescence yield Φ' caused by excessive levels of ambient irradiance. The degree of such regulation depends upon the functional state of PS2 reaction centers, i.e. is directly related to photosynthetic capacity of algae.

Mechanisms of diel variations in Chl-a fluorescence were studied under both laboratory and field conditions.²³ It has been found that for subsurface phytoplankton the main mechanisms of sunlight regulation of fluorescence yield were 'energy-dependent' fluorescence quenching, affecting at irradiances of $100 + 600 \mu\text{mol m}^{-2} \text{s}^{-1}$ and photoinhibition of primary photosynthesis processes by excessive light, that may dominate at irradiances more than $1000 \mu\text{mol m}^{-2} \text{s}^{-1}$.

5. CONCLUSION

The analysis of a regulation of Chl-a fluorescence yield and of the photochemical efficiency of photosystem 2 by ambient irradiance is presented in the paper. The model

is based on a simplified biophysical description and reveals that the manifestations of such regulation strongly depend upon the functional state of photosynthetic apparatus. Therefore, the nutrient availability should play an important role in related phenomena, determining to a large extent relative contributions of photochemical (Q_p) and non-photochemical (Q_N) quenching to the overall regulation. In particular, Q_N -produced diel variations in actual fluorescence yield Φ' should be more pronounced in case of nutrient deficiency, resulting in inactivation of PS 2 reaction centers. In contrary, Φ' is expected to be more sensitive to an "instant" variations in ambient irradiance (changes in Q_p) in nutrient replete conditions. The presented *in situ* field measurements with a shipborne lidar system provide evidence of the studied phenomena in various environmental conditions and generally support this approach.

Finally, we should stress that the presented model and the experimental results do not aspire to an accurate and comprehensive description of a fairly complicated phenomena related to the diurnal variability of Chl-a fluorescence *in situ*. Our goal was rather to emphasize a significant role of the diel changes in Chl-a fluorescence yield in the overall variations of Chl-a fluorescence in a subsurface water layer, and to show the relationship between manifestation of these changes and the functional state of photosynthetic apparatus of algae. Apparently, further, more detailed, laboratory and field studies of this phenomenon are required for its better understanding and for developing the more accurate theoretical description.

REFERENCES

1. G.H. Krause, and E. Weis, "Chlorophyll Fluorescence and Photosynthesis: the Basics," *Ann. Rev. Plant Physiol. Plant Mol. Biol.* vol.42, pp.313-349, 1991.
2. Z. Kolber, J. Zehr, and P.G. Falkowski, "Effects of Growth Irradiance and Nitrogen Limitation on Photosynthetic Energy Conversion in Photosystem II," *Plant Physiol.*, vol.88, pp.923-929, 1988.
3. M.Yu. Gorbunov, V.V. Fadeev, and A.M. Chekalyuk, "The use of laser saturation fluorometry for the study of mechanisms of chlorophyll-a fluorescence build-up in phytoplankton under conditions of mineral nutrition shortage," *Moscow Univ. Physics Bulletin*, vol. 47(4), pp.47-53, 1992.
4. R.M. Greene, R.J. Geider, Z. Kolber, and P.G. Falkowski, "Iron-induced changes in light harvesting and photochemical energy conversion processes in eukaryotic marine algae," *Plant Physiol.*, vol.100, pp.565-575, 1992.
5. Z. Kolber, K.D. Wyman, and P.G. Falkowski, "Natural Variability in Photosynthetic Energy Conversion Efficiency: a Field Study in the Gulf of Maine," *Limnol. Oceanogr.*, vol.35, pp.72-79, 1990.
6. A.M. Chekalyuk, and M.Yu. Gorbunov, "Laser Remote Sensing of Phytoplankton Photosynthetic Activity and Chlorophyll by Using a Shipboard Lidar System," In: *Laser Study of Macroscopic Biosystems*, Korppi-Tommola, J.E.I. (Ed.), *Proc. SPIE* 1922, pp.391-400, 1992.
7. Z. Kolber, and P.G. Falkowski, "Use of Active Fluorescence to Estimate Phytoplankton Photosynthesis *In Situ*," *Limnol. Oceanogr.*, vol.38, pp.1646-1665, 1993.
8. D.A. Kiefer, and R.A. Reynolds, "Advances in understanding phytoplankton fluorescence and photosynthesis, In: "Primary productivity and biogeochemical cycles in the sea", *Environ. Sci. Res.* 43. Plenum, p. 155-174. 1992.
9. B. Demmig-Adams, "Carotenoids and Photoprotection in Plants: a Role for the Xanthophyll Zeaxanthin," *Biochim. Biophys. Acta.*, vol.1020, pp.1-24, 1990.

10. B. Genty, J.-M. Briantais, and N.R. Baker, N.R., "The Relationship Between the Quantum Yield of Photosynthetic Electron Transport and Quenching of Chlorophyll Fluorescence," *Biochim. Biophys. Acta*, vol.990, pp.87-92, 1989.
11. P.G. Falkowski, and D.A. Kiefer, "Chlorophyll-a Fluorescence in Phytoplankton: Relationship to Photosynthesis and Biomass," *J. Plankt. Res.*, vol.7, pp.715-731, 1985.
12. O. van Kooten, and J.F.H. Snel, "The Use of Chlorophyll Fluorescence Nomenclature in Plant Stress Physiology," *Photosynth. Res.*, Vol.25, pp.147-150, 1990.
13. R.M. Greene, R.J. Geider, and P.G. Falkowski, "Effect of iron limitation on photosynthesis in a marine diatom", *Limnol. Oceanogr.*, vol.36, pp.1772-1782, 1991.
14. G.H. Krause, U. Behrend, "ΔpH-dependent chlorophyll fluorescence quenching indicating a mechanism of protection against photoinhibition of chloroplasts", *FEBS Lett.*, vol. 20(2), pp. 298-302.
15. P.G. Falkowski, and Z. Kolber, "Phytoplankton Photosynthesis in the Atlantic Ocean as Measured from a Submersible Pump and Probe Fluorometer in Situ," In: *Current Research in Photosynthesis IV*, Baltscheffsky, M. (Ed.), (London: Kluwer), pp. 923-926, 1990.
16. P.G. Falkowski, D. Ziemann, Z. Kolber, and P.K. Bienfang, "Role of Eddy Pumping in Enhancing Primary Production in the Ocean," *Nature*, vol.352, pp.55-58, 1991.
17. P.G. Falkowski, R.M. Greene, and R.J. Geider, "Physiological Limitations on Phytoplankton Productivity in the Ocean," *Oceanography*, vol.5, pp. 84-91, 1992.
18. U. Schreiber, W. Bilger, and U. Schliwa, "Continuous Recording of Photochemical and Non-Photochemical Quenching with a New Type of Modulation Fluorometer". *Photosynth. Res.*, vol.10, pp.51-62, 1986.
19. G.H. Krause, C. Vernotte, J.-M. Briantais, "Photoinduced quenching of chlorophyll fluorescence in intact chloroplasts and algae. Resolution of two components", *Biochim. Biophys. Acta.*, vol. 679(1), pp. 116-124, 1982.
20. S.B. Powles, "Photoinhibition of photosynthesis induced by visible light", *Annu. Rev. Plant. Physiol.*, vol. 35, pp. 15-44.
21. M.N. Merzlyak, S.I. Pogosyan, "Photodestruction of pigments and lipids in isolated chloroplasts", *Biol. Nauki (USSR)*, no.3, pp. 8-20, 1986.
22. D. Mauzerall, "Light-Induced Fluorescence Changes in *Chlorella*, and the Primary Photoreactions for the Production of Oxygen," *Proc. Natl. Acad. Sci. USA*, vol.69, pp.1358-1362, 1972.
23. D.A. Kiefer, "Fluorescent properties of natural phytoplankton populations", *Mar. Biol.*, no. 22, pp. 263-269, 1973.
24. A.M. Chekalyuk, A.A. Demidov, V.V. Fadeev, T.V. Lapshenkova, "Lidar mapping of phytoplankton and organic matter distributions in the Baltic Sea", In: *Laser Study of Macroscopic Biosystems*, Korppi-Tommola, J.E.I. (Ed.), *Proc. SPIE* 1922, 401-405.
25. M.Yu. Gorbunov, and A.M. Chekalyuk, "Lidar in Situ Study of Sunlight Regulation of Phytoplankton Photosynthetic Activity and Chlorophyll Fluorescence," In: *Laser Study of Macroscopic Biosystems*, Korppi-Tommola, J.E.I. (Ed.), *Proc. SPIE* 1922, 421-427, 1992.

The question of a nutrient effect on the bio-optical properties of phytoplankton

John Marra

Lamont-Doherty Earth Observatory of Columbia University,
Palisades, NY 10964

R.R. Bidigare

Dept. of Oceanography
University of Hawaii at Manoa, Honolulu, HI 96822

ABSTRACT

Although nutrient-limited growth of phytoplankton in the laboratory produces well-defined responses in the absorption coefficient, pigmentation, and quantum yield of photosynthesis, natural populations show only weak or inconclusive effects. Further analysis of the data from Biowatt-II, a seasonal study in the NW Atlantic in 1987, suggests two things. First, the phytoplankton absorption coefficient changes as a function of chlorophyll *a*, although photoprotectant accessory pigments are important in summer. Second, with the exception of one cruise, the data suggest that an estimated maximum quantum yield varies by less than 20%. Resolution of the issue of a nutrient effect may come with detailed measurements in a tropical region, in an ocean province without seasonally varying irradiance but having a strong seasonal signal in nutrient concentrations.

1. INTRODUCTION

We review here the available information and data pertaining to the subject of a nutrient effect on the bio-optical properties of phytoplankton. Such a review combines bio-optics with a central question in biological oceanography, namely, the nature and extent of nutrient limitation in the sea. It remains an open question whether nutrient supply limits physiological function, that is, rate processes, or whether nutrient supply standing crops. Falkowski et al.¹ have argued that nutrient limitation affects physiological rates in the ocean rather than standing crop, while the alternate view has been taken, for example, by Goldman.² In this sense, the bio-optical properties of phytoplankton may serve not only as a diagnostic for nutrient limitation, but contribute to the conceptual basis for how planktonic ecosystems function.

Cullen et al.³ compiled a review of several laboratory studies for this problem for the most recent Brookhaven symposium,⁴ the conclusion being that the evidence for nutrient effects on *P(I)* parameters is equivocal. Here we focus on at-sea investigations, however relying on laboratory research for initial guidance. While data collected at sea will be more difficult to interpret, that data will have the value of representing the conditions and activities of populations found in nature.

For the purposes here, the bio-optical properties we consider are absorption and quantum yield. These are important because they are directly linked to photosynthetic production, and are therefore critical to phytoplankton growth. For example, phenomenologically, photosynthesis can be expressed as the product of absorption and quantum yield, as in

$$P = \phi a_{ph} E, \quad (1)$$

where *P* is the rate of photosynthesis expressed either as carbon uptake or oxygen evolution per unit time, ϕ is the quantum yield (mols C or mols O₂ per mols photon), a_{ph} is the phytoplankton absorption coefficient (m⁻¹) and *E* is the irradiance (mols quanta m⁻² s⁻¹). Another, composite, parameter that has assumed importance is the changing rate of photosynthesis as a function of low values of irradiance, represented by α , that is, the slope of the photosynthesis-irradiance [*P(E)*] relationship where *E* is less than that which produces the maximum rate. The variable α is in units of [mg C m⁻³ h⁻¹ (μmols quanta m⁻² s⁻¹)⁻¹]. It can be shown that

$$\alpha = \phi_{max} a_{ph}, \quad (2)$$

where ϕ_{max} is the maximum photosynthetic quantum yield. Many of the studies considered below measure α by placing sub-sam-

ples of water in a specialized incubator and measuring the rate of photosynthesis at several irradiances. Usually, a_{ph} is normalized to chlorophyll, and designated a_{ph}^* , in which case α is expressed as α^B , also denoting a normalization to chlorophyll biomass. Most of the implied effect of nutrients is on the quantum yield of photosynthesis, and most of the studies involve variability in α .

2. A BRIEF LOOK AT LABORATORY INVESTIGATIONS

Although we focus on data from at-sea investigations, laboratory studies can identify important biochemical or physiological mechanisms. It is another question as to whether those mechanisms operate in the environment, or whether they occur to the exclusion of other, ecological, forces on natural populations. The assumption in applying laboratory results in the ocean is that the phytoplankton exhibit a community response to environmental change much like the physiological response by laboratory cultivated forms; an assumption, it can be argued, difficult to accept.

What these laboratory investigations have found is that nutrient limitation can affect both quantum yield and the absorption coefficient by pigments. The one effect of nutrients on quantum yield (where it has been calculated) is that maximum quantum yields decline with nutrient starvation.^{6,7} In contrast, nutrient-limited growth in the laboratory produces an increase in absorption.^{5,6} A mechanism for the increase in absorption was offered by Herzig and Falkowski⁸ whereby an increase in a_{ph}^* is associated with an increase in the quantity of accessory pigments, carotenoids, and chlorophyll *c*. Increases in absorption may be complicated, however, by the so-called 'package effect,' a phenomena representing a decrease in pigment-specific absorption resulting from self-shading by the chloroplasts.

In summary, we can identify two effects of nutrient limited growth on the bio-optical properties of phytoplankton, an increase in pigment-specific absorption, and a decline in the maximum quantum yield. In field investigations, these two parameters are not often measured. Instead, α has been used as the diagnostic for photosynthetic efficiencies. In their review, Cullen et al.³ found that in continuous culture, α was constant over a range of nutrient limited growth rates. (P_{max} stayed constant or increased in these same experiments.) α^B is a composite property, as equation (2) shows. Thus, while ϕ_{max} might decrease under nutrient limitation, it may be offset by increases in absorption. In the following, we review the major field studies which have estimated ϕ_{max} either through measurements of α^B and absorption (equation 2), or through measurements based on fluorescence.

3. THE EFFECT OF NUTRIENTS ON QUANTUM YIELD

3.1 The Springtime Sargasso Sea

One of the earliest studies to detect an effect of nutrient concentration on the quantum yield was by Cleveland et al.⁹ This was a study in the N. Sargasso Sea during and after the spring phytoplankton bloom. Cleveland et al. were able to compare conditions just as the water column was stratifying seasonally,^{10, 11} and again afterwards. They determined α^B , and measured phytoplankton absorption,¹² computing the maximum quantum yields. They concluded that there was no relationship between ϕ_{max} and concentrations of nitrate and ammonium. However, when plotted against "distance from the nitracline" (a representation for the nitrate flux into the surface zone) (Fig. 1), the data suggested a negative relationship: greater distance from the source of nutrients gave a lower value for ϕ_{max} .

The equation for the curve shown in Fig. 1 was given in the paper as

$$\phi_{max} = 0.0873 - 0.00050 \cdot e^{zn/10} \quad (3)$$

(where we have corrected an error in the published equation). Equation (3) and inspection of Fig. 1 shows the relationship to be not strong. For the equation, ϕ_{max} will decrease by a factor which is two orders of magnitude less than the maximum value, and by a depth (in the exponent) reduced to one tenth. That is, the distance from the nitracline has to increase to 50 m to see a decline in ϕ of the order of 50%. At 52 m, ϕ_{max} declines to zero. The equation was meant only to demonstrate the effect of nutrients on ϕ_{max} , and is not recommended in practice, for example, to possibly write a modification to equation (1) for the effect of nutrients on production. Another difficulty in using such parameterizations in modifications to equation (1) is that distance to the nitracline may be difficult to estimate.

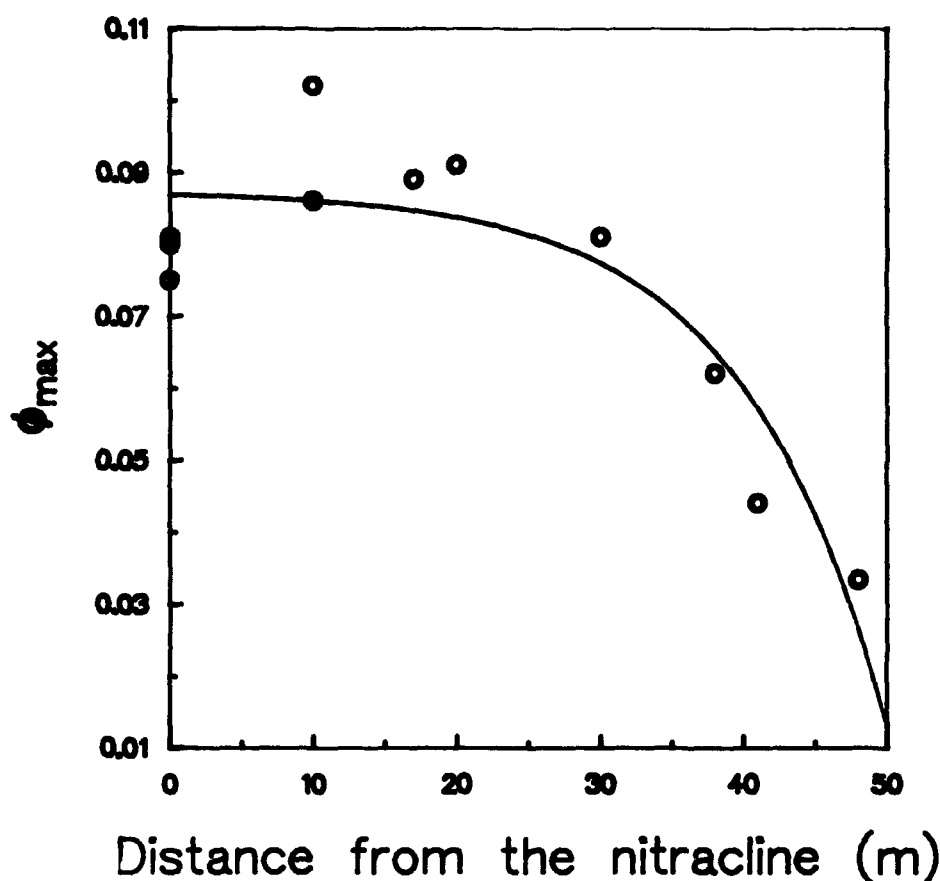


Fig. 1. Maximum quantum yield as a function of distance to the nitracline of the sample, adapted from ref. 9. The line is equation (3) in the text.

3.2. The Gulf of Maine, and an Eddy Near Hawaii

Soon after the Cleveland et al.⁹ work appeared, Kolber et al.¹³ examined fluorescent properties in phytoplankton along a nutrient gradient in the Gulf of Maine. The fluorescent properties are based on the fast-repetition-rate fluorescence technique pioneered in the ocean by these investigators. Two fluorescent properties are measured, one is the variable fluorescence and designated $\Delta\phi_{\text{sat}}$, and the other is a measure of the absorption coefficient. $\Delta\phi_{\text{sat}}$ is proportional to the quantum yield for photosynthesis. Thus, although they are proxy measures, they correspond to the needed quantities in equation (1). As in Cleveland et al.⁹ the distribution of variable fluorescence has a weak relationship to the depth of the nitricline. The correlation coefficient determined for the data, 0.63, suggests a significant relationship, but implies that 40% of the variation in the fluorescence parameter is caused by the supply of nutrients (again parameterized as the distance to the nitricline).

Stronger evidence for the fluorescence technique is presented in Falkowski et al.¹⁴ using the same parameter, $\Delta\phi_{\text{sat}}$. At one station in an oceanic eddy, chlorophyll-specific primary production and variable fluorescence are enhanced by 50%. Other data reported from this cruise, however, may not support the conclusion that nutrients (nitrate) strongly affect photosynthetic efficiency. Olaizola et al.¹⁵ use pigment data to show species changes between the inside and the outside of the eddy, an important factor in determining growth rates using variable fluorescence.¹⁶ The maximum in productivity and pigment biomass for the region of the eddy was not in the eddy itself, but outside, and estimated by the authors to be in the eddy's "wake."¹⁵ Unfortunately, no variable fluorescence data are reported for this station. One piece of evidence that helps the case is that the deep chlorophyll maximum in the tropical ocean almost certainly exists through photoadaptation to low irradiance, and not from an increase in biomass. Thus the pigment increase within the eddy means that a phytoplankton carbon increase would be greater than an increase in pigment alone, because

of the response to higher irradiances. It would also mean that the phytoplankton in the station in the wake of the eddy would have a higher carbon:chlorophyll ratio than is usual in the deep chlorophyll maximum of oligotrophic regions. Unfortunately, no particulate carbon analyses are reported for this interesting data set.

In summary, the two first studies discussed show only a weak dependence of nutrients on ϕ_{\max} . This might mean that there is no appreciable physiological effect, or that our means of gauging nutrient limitation in the marine environment is inadequate if not wrong. The studies of the eddy^{14,15} make a stronger case, yet here too there are uncertainties that result in less than compelling evidence.

3.3. The Spring Bloom in the Northwest Atlantic Ocean

Platt et al.¹⁷ determined α^B for phytoplankton populations during and after the spring bloom in the North Atlantic, and found that α^B increased by a factor of two (0.012 to 0.025) with nitrate concentration over the range of 0.2-2.0 μM . Because phytoplankton absorption is negatively correlated with biomass (chlorophyll), and because its relationship with α^B and ϕ_{\max} (equation (2)), they conclude that the increase in α^B with increase in nitrate must have been caused by a change in the maximum quantum yield rather than absorption.

A span of 0-2 μM is the entire seasonal range of nitrate in the western North Atlantic. It is not clear that we can extrapolate these results to other regions with higher nitrate values. For the equatorial Pacific,¹⁸ α^B 's are as low as that measured by Platt et al.,¹⁷ in the range of 0.02, but occur in water with much higher nitrate concentrations (4-8 $\mu\text{M NO}_3$). Studies in the Antarctic also show typical values of α^B but with an order of magnitude greater nitrate concentrations. In a warm-core ring, Dower and Lucas¹⁹ report α^B values ranging from 0.04-0.10 for nitrate concentrations of 1-2 μM (and with no discernible relationship). In the eastern North Atlantic, α^B 's are also high (0.02-0.06) for nitrate concentrations ranging from 3-6 μM .²⁰ [There is a question about these latter data since the P(E) parameters were determined from *in situ* ^{14}C -based production rather than in the usual manner; and it is possible that the statistical method used affected the outcome.] For the data in the equatorial Pacific and Antarctic, there is of course the possibility of limitation from other nutrients, such as iron.²¹ All in all, however, it is difficult to know what to conclude from these considerations of α^B . Platt et al.¹⁷ seem to have found a relationship that has statistical validity, however, it is not possible to extrapolate beyond the region in which they conducted their measurements. These data are further examined below.

4. THE BIOWATT-II DATA

A data set useful to this analysis is from the Biowatt-II experiment in 1987. Biowatt-II consisted of four cruises from early spring to late fall (March, May, August, and December), and encompassed a range of nutrient conditions, euphotic depths, etc. Absorption measurements are reported in Morrow et al.²² and Chamberlin,²³ pigment measurements using HPLC have been reported,²⁴ and well as measurements of carbon assimilation via the ^{14}C technique.²⁴ Mary Jane Perry conducted a program of P(E) measurements, and Ray Smith did BOPS profiles for spectral irradiance measurements. Thus, the data can be used to evaluate a variety of bio-optical properties, and their environmental determinants.

4.1. Photoprotectants and Absorption coefficient

We consider first the effects of nutrients on absorption coefficient, a_{ph} . Recall that an increase in absorption accompanied nitrate-limited growth in the laboratory, and that increased absorption could be related to the cellular production of accessory pigments.⁸ However, when phytoplankton experience more irradiance, one adaptive response is to produce photoprotective pigments to channel away excess irradiance.²⁴

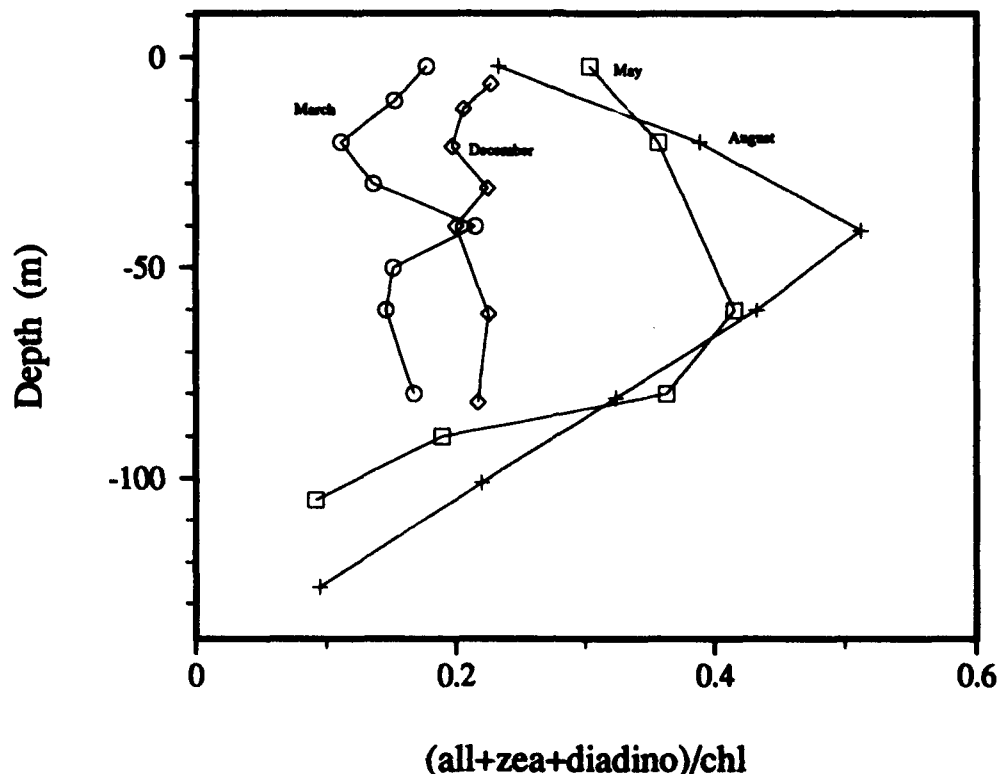


Fig. 2. Photoprotectant pigments (allo=alloxanthin, zea=zeaxanthin, diadino=diadinoxanthin) as a proportion of chlorophyll a (chl) for the four Biowatt-II cruises as a function of depth. (A plot as a function of irradiance looks the same.)

For the spring and summer cruises in Biowatt-II, the photoprotective pigments alloxanthin, zeaxanthin, and diadinoxanthin become a greater proportion of the chlorophyll pigment biomass than for the winter cruises and especially for August (Fig. 2). However, the primary agent of absorption remains chlorophyll *a*, being correlated with absorption coefficient (Fig 3a). Overall, 72% of the seasonal and depth variation in a_{ph} can be explained as a variation in chlorophyll *a*. The x-axis intercept can be interpreted as that absorption from accessory pigments. Thus they become important near the surface in the summer (with high light and low chlorophyll values), as indicated by the data points from May and August, and less important to absorption elsewhere. Deviations at higher values of chlorophyll also support the idea of other pigments participating in absorption in summer. the outliers below (greater absorption per nit chlorophyll) are from May and August, and those above are from March and December. During the summer, photoprotectants are responsible for about 40% of absorption.²⁴ Although we haven't spectrally-weighted the absorption coefficients, the data from May and August show higher values and with appreciable quantities of photoprotectants (Fig. 3b).

At least two conclusions can be drawn. First, whatever drives the change in chlorophyll *a* also, to some degree, drives the changes in the absorption coefficient. Conformity of the vertical distributions of a_{ph} and chlorophyll *a* for the Biowatt-II data has been previously noted.²² Second, photoprotectants do not strongly contribute to the variation in absorption during summer, although they are significant. While summer is a period of low nutrients, the change in pigment composition could be as easily ascribed to increases in irradiance. Similarly, the change in absorption may be from a reduced package effect in optically clear waters,²⁶ that is, a primary influence by irradiance.

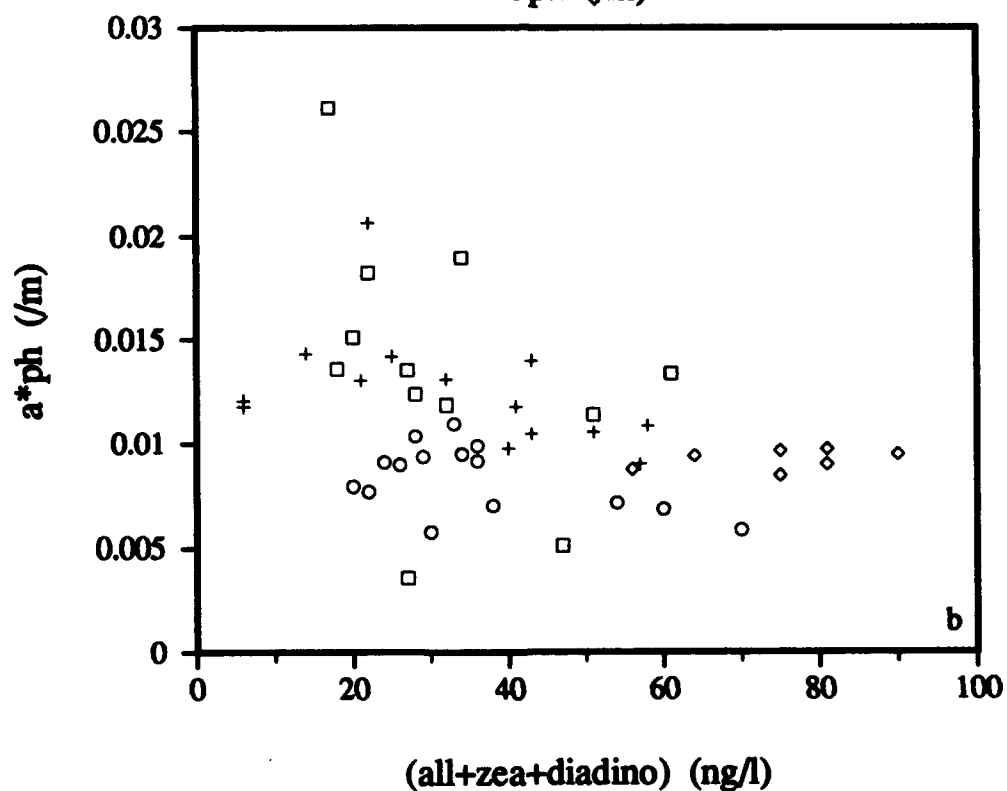
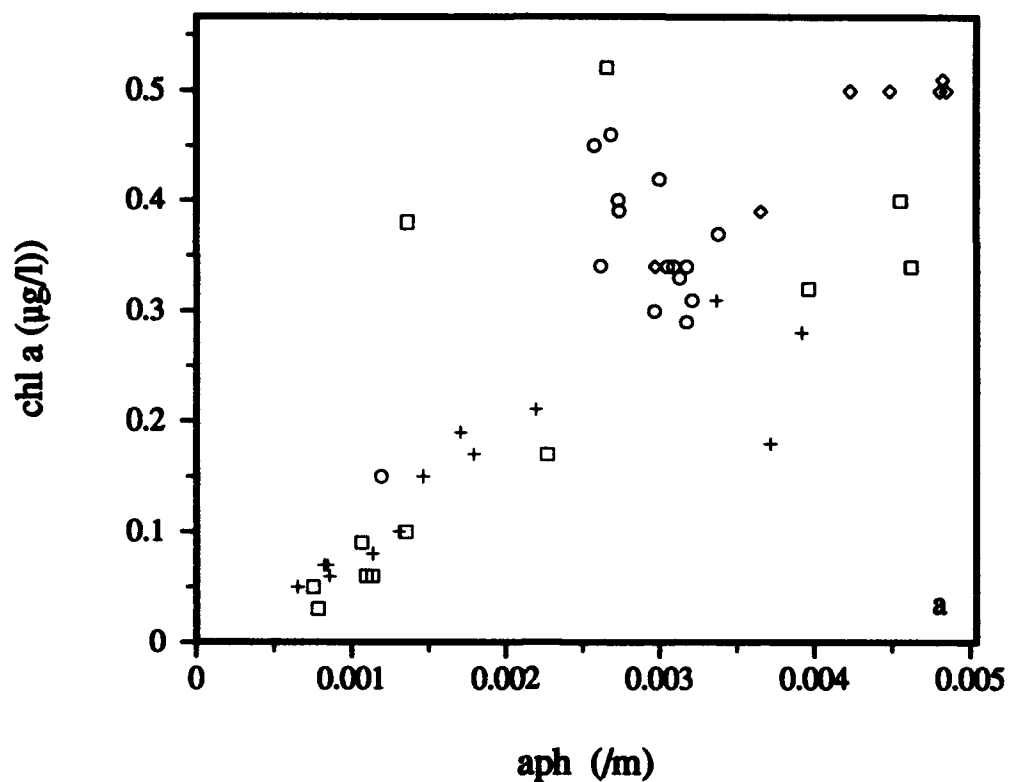


Fig. 3. Biowatt-II, 1987. (a) Chlorophyll a as a function of the absorption coefficient. (b) Chlorophyll-specific absorption [$\text{m}^2 (\text{mg chl a})^{-1}$] plotted against the quantity of photoprotectant pigments (see. Fig. 2). Circles=March cruise, squares=May, crosses=August, and diamonds=December.

4.2. Photosynthetic Efficiencies for Biowatt-II

The P(E) experiments in Biowatt-II used a broad-band blue filter. The data are from a variety of depths, although for the summer cruises, samples were more likely taken from deeper in the water column, in the vicinity of the chlorophyll maximum, or in the bottom half of the euphotic zone. The first thing to note about these estimates of α^B is their variability within cruises (Fig. 4). We have tried to analyze for the variability that can be measured, and conclude that it is probably caused in the method. For example, an ANOVA of these data shows that there is no clear variability in α^B with time of year, time of day, or depth in the water column. The variance instead must come from the procedure, such as between sample variability (because of the small sample size), the difficulty in measuring small signals (both in irradiance and uptake), and the possibility of a spectral dependence on the value determined.²³ The methods used in Biowatt-II are the same or similar to those used by other investigators, and to the extent that they can be intercompared, the high measurement variability noted on two of the Biowatt cruises, may mean that changes in quantum yield might possibly be incorrectly interpreted. Other studies^{27,28} failed to find an environmental factor, or suite of factors, to explain the variability seen in ϕ_{\max} .

For Biowatt-II, we had previously assumed a constant ϕ_{\max} [0.055 mols C (mols photons⁻¹)] in an analysis of the seasonal cycle of production obtained from the moored sensors.²⁵ We can also derive an independent estimate of ϕ_{\max} using the α^B determined from the P(E) data and the absorption data^{22,23} (using equation (2)), and therefore check for the internal consistency of the Biowatt-II data. The estimates of ϕ_{\max} from the P(I) measurements agree for the most part with the assumed value, with August being the exception. Nevertheless, the comparison gives some support to the use of a constant ϕ_{\max} .²⁵

Overall, for the Biowatt-II data, the clearest differences among the cruises can be explained through seasonal changes in irradiance. Nutrient supply may set the optical clarity of the water (a standing crop effect), and the phytoplankton community responds to this with differing populations, with different mixes of absorption, with photoprotective pigments, and (perhaps) changes in spectral efficiencies. There is no clear relationship among these with nutrients, although in August, the nitrate concentration was clearly at minimum, the nitracline at its deepest, and α^B at a seasonal minimum. To put the Biowatt-II data in a larger context, in Fig. 5 are plotted data from four investigations in the Northwest Atlantic, the before-mentioned works,^{9,17} data from Lewis et al.,²⁹ as well as the Biowatt-II data. Although by eye there appears to be a positive relationship, considering all the data, the correlation is not significant (t-test).

5. CONCLUSIONS

We believe that the data are as yet inconclusive in regard to an effect of nutrients on the bio-optical properties of phytoplankton. Published data show tantalizing trends, but with one exception,¹⁷ have little statistical validity. The Biowatt-II data do not bear out the findings of laboratory investigations, although on one cruise (August), a possible effect may have been indicated. The August exception warrants further measurements. Overall, the Biowatt-II data support the idea of only small changes in photosynthetic efficiency on the seasonal time scale, but how this is achieved remains unknown. The weight of evidence points to the importance of responses induced by irradiance. We may hypothesize, therefore that nutrient supply sets the biomass (and therefore the optical clarity), and irradiance governs the physiological rates.

Seasonally, nutrients and irradiance changes confound one another, or at least change in opposition, and the Northwest Atlantic is but one example of this. One region where the problem of a nutrient effect on bio-optical properties could be addressed is in an area such as the Arabian Sea. There, at a tropical latitude, solar irradiance changes only with cloud cover. Concentrations of nutrients in the surface layer change dramatically, mixed up or not with the twice-per-year monsoons.

7. ACKNOWLEDGMENTS

This research was supported by the Office of Naval Research. We thank all our colleagues in Biowatt for access to data from both Biowatt-I and Biowatt-II. Thanks also to M.J. Perry for comments on the manuscript, and to Joan Cleveland for assistance with data.

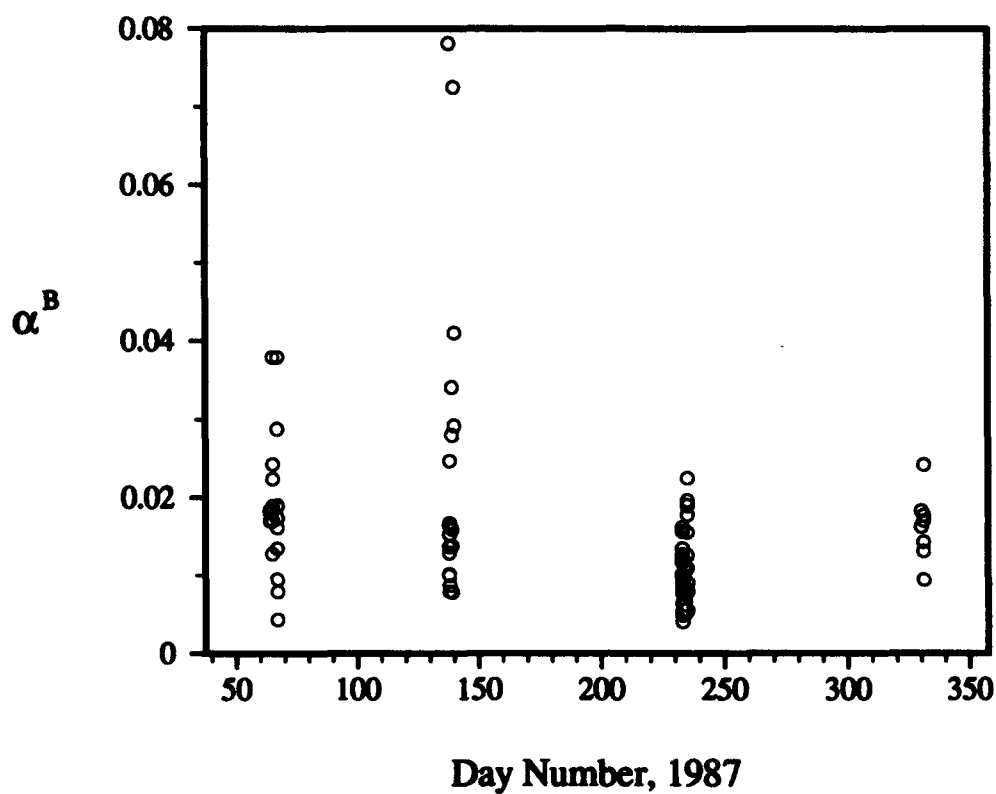


Fig. 4. Values of α^B measured on the four Biowatt-II cruises in March (Days 65,67), May (138,140), August (233,235) and December (321).

Table 1: Biowatt-II data (mean \pm stdev). Units are those given in Section 1.

Cruise	Date	α^B	a^*_{ph}	ϕ_{max}
1	6 March	0.018 ± 0.004	$0.007 \pm .001$	0.058
	8 March	0.024 ± 0.028	$0.009 \pm .001$	0.059
2	18 May	0.019 ± 0.020	$0.011 \pm .006$	0.040
	20 May	0.033 ± 0.021	$0.014 \pm .005$	0.054
3	21 August	0.009 ± 0.003	$0.013 \pm .004$	0.016
	23 August	0.013 ± 0.005	$0.012 \pm .002$	0.025
4	1 December	0.016 ± 0.004	$0.009 \pm .001$	0.041

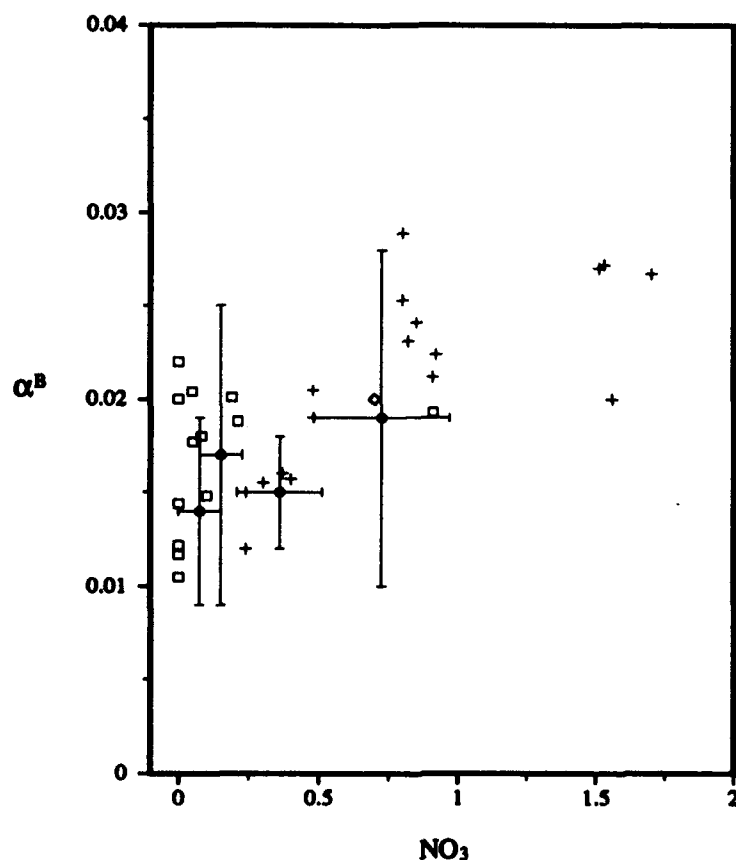


Fig. 5. Values from the NW Atl. Squares=Biowatt⁹ crosses=spring bloom¹⁷, circles=Biowatt-II, and diamonds=Sargasso Sea²⁹ Error bars are std. dev. Biowatt-II values differ from Table 1 in that there are not nutrient data for all α data.

8. REFERENCES

1. P.G. Falkowski, R.M. Greene, R.J. Geider, "Physiological limitations on phytoplankton productivity in the ocean," *Oceanography*, Vol. 30, pp. 311-321, 1992
2. J.C. Goldman, "Physiological processes, nutrient availability, and the concept of relative growth rate in marine phytoplankton ecology," *Primary productivity in the sea*, P.G. Falkowski (Ed.), pp. 179-194, Plenum Press, New York, 1980.
3. J.J. Cullen, X. Yang, H.L. MacIntyre, "Nutrient limitation of marine photosynthesis," *Primary production and biogeochemical cycling in the sea*, P.G. Falkowski, A.D. Woodhead (Eds.), Plenum Press, New York, 1992.
4. P.G. Falkowski, A.D. Woodhead (Eds.), *Primary production and biogeochemical cycling in the sea*, Plenum Press, New York, 1992.
5. M.S. Chalup, E.A. Laws, "A test of the assumptions and predictions of recent microalgal growth models with the marine phytoplankter *Pavlova lutheri*," *Limnol. Oceanogr.*, Vol. 35, pp. 583-596, 1990.
6. J.S. Cleveland, M.J. Perry, "Quantum yield, relative specific absorption and fluorescence in nitrogen-limited *Chaetoceros gracilis*

", *Mar. Biol.*, Vol. 94, pp. 489-497, 1987.

7. N.A. Welschmeyer, C.J. Lorenzen, "Chlorophyll-specific photosynthesis and quantum efficiency at subsaturating light intensities," *J. Phycol.* Vol. 17, pp. 283-293, 1981.

8. R.G. Herzig and Falkowski, P.G. "Nitrogen limitation in *Isochrysis galbana* (Haptophyceae), I. Photosynthetic energy conversion and growth efficiencies," *J. Phycol.* Vol. 25, pp. 462-471. 1989.

9. J.S. Cleveland, M.J. Perry, D.A. Kiefer, and M.C. Talbot, "Maximal quantum yield of photosynthesis in the northwestern Sargasso Sea," *J. Mar. Res.* Vol. 47, pp. 869-886. 1989.

10. J. Marra, R.R. Bidigare, T.D. Dickey, "Nutrients and mixing, chlorophyll and phytoplankton growth," *Deep-Sea Res.* Vol. 37, pp. 127-143, 1990.

11. R.R. Bidigare, R.C. Smith, K.S. Baker, "Oceanic primary production measurements of spectral irradiance and pigment concentrations. *Global Biogeochem. Cycles*, Vol. 1, pp. 171-186, 1987.

12. J.S. Cleveland, M.J. Perry, "A model for partitioning particulate absorption into phytoplankton and detrital components," *Deep-Sea Res.* Vol. 41, pp. 197-221, 1994.

13. Z. Kolber, K.D. Wyman, P.G. Falkowski, "Natural variability in photosynthetic energy conversion efficiency: a field study in the Gulf of Maine," *Limnol. Oceanogr.* Vol. 35, pp. 72-79, 1990.

14. P.G. Falkowski, D. Ziemann, Z. Kolber, P.K. Bienfang, "Role of eddy pumping in enhancing primary production in the ocean," *Nature*, Vol. 352, pp. 55-58, 1991.

15. M. Olaizola, D.A. Ziemann, P.K. Bienfang, W.A. Walsh, L.D. Conquest, "Eddy-induced oscillations of the pycnocline affect floristic composition and depth distribution of phytoplankton in the subtropical Pacific," *Mar. Biol.*, Vol. 116, pp. 533-542. 1993.

16. Z. Kolber, J. Zehr, P.G. Falkowski, "Effects of growth irradiance and nitrogen limitation on photosynthetic energy conversion in Photosystem II," *Plant. Physiol.* Vol. 88, pp. 923-929. 1988.

17. T. Platt, S. Sathyendranath, O. Ulloa, W.G. Harrison, N. Hoepffner and J. Goes, "Nutrient control of phytoplankton photosynthesis in the Western North Atlantic," *Nature* Vol. 356, pp. 229-231. 1992.

18. J.J. Cullen, M.R. Lewis, C.O. Davis, R.T. Barber, "Photosynthetic characteristics and estimated growth rates indicate grazing is the proximate control of primary production in the equatorial Pacific," *J. Geophys. Res.* Vol. 97, pp. 639-654, 1992.

19. K.M. Dower, M.I. Lucas, "Photosynthesis-irradiance relationships and production associated with a warm-core ring shed from the Agulhas Retroflection south of Africa," *Mar. Ecol. Progr. Ser.*, Vol. 95, pp. 141-154, 1993.

20. J. Kiddon, M. Bender, J. Marra, "Production and respiration in the 1989 North Atlantic spring bloom: an analysis of irradiance-dependent changes," *Deep-Sea Res.* (in press), 1994.

21. J.J. Cullen, "Hypotheses to explain high nutrient conditions in the open sea," *Limnol. Oceanogr.* Vol. 36, pp. 1578-1599, 1991.

22. Morrow, J.H., W.S. Chamberlin, D.A. Kiefer, "A two-component description of spectral absorption by marine particles," *Limnol. Oceanogr.* Vol. 34, pp. 1500-1509, 1989.

23. W.S. Chamberlin, "Light absorption, natural fluorescence, and photosynthesis in the open ocean," Ph.D. thesis, Univ. Southern Calif., 159 pp., 1989.

24. R.R. Bidigare, B.B. Prezelin, R.C. Smith, "Bio-optical models and the problems of scaling," Primary production and bio-

geochemical cycling in the sea, P.G. Falkowski and A.V. Woodhead (Eds.), pp. 175-212., Plenum Press, New York, 1992.

25. J. Marra, and others, "Estimation of seasonal primary production from moored optical sensors in the Sargasso Sea, *J. Geophys. Res.*, Vol. 97, pp. 7399-7412, 1992.

26. A. Bricaud, D. Stramski, "Spectral absorption coefficients of living phytoplankton and nonalgal biogenous matter: A comparison between the Peru upwelling and the Sargasso Sea," *Limnol. Oceanogr.* 35, pp. 562-582, 1990.

27. O. Schofield, B.B. Prezelin, R.C. Smith, P. M. Stegmann, N.B. Nelson, M.R. Lewis and K.S. Baker, "Variability in spectral and nonspectral measurements of photosynthetic light utilization efficiencies," *Mar. Ecol. Progr. Ser.*, Vol. 78, pp. 253-271. 1991.

28. O. Schofield, B.B. Prezelin, B.B. Bidigare, and R.C. Smith, "In situ photosynthetic quantum yield. Correspondence to hydrographic and optical variability within the Southern California Bight," *Mar. Ecol. Progr. Ser.*, Vol. 93, pp. 25-37, 1993.

29. M.R. Lewis, R.E. Warnock, T. Platt, "Measuring photosynthetic action spectra of natural phytoplankton populations. *J. Phycol.* Vol. 21, pp. 310-315, 1985

A Bio-optical Mapping Procedure for the North Atlantic Ocean

Dale A. Kiefer¹, Charles A. Atkinson², and Dan Ondercin³

¹Department of Biological Sciences
University of Southern California
Los Angeles, California 90089-0371

²Systems Science Applications
121 via Pasqual
Redondo Beach, California 90277

³Applied Physics Laboratory
Johns Hopkins Rd.
Laurel, Maryland 20707

ABSTRACT

We have developed a Bio-optical Profile Model which attempts to predict the vertical distribution of chlorophyll and the coefficients for diffuse downwelling irradiance attenuation and beam attenuation from measurements at the sea surface. In this paper we test the ability of this model to "fit" the vertical profiles measured at 117 stations in the North Atlantic. The stations range as far north as 60° N latitude and as far south as 26° N latitude. In general predicted values for the vertical distribution of chlorophyll and the beam attenuation coefficient fall within about 35% of measured values. In order to understand the pattern of distribution for the 7 tuning coefficients, we have calculated the principle components for the 7 X 117 matrix of "best-fit" values for the tuning coefficients. Such a calculation indicated that covariance among the 7 tuning coefficients was limited. It also indicated that variation in the scores for the dominant principle components were strongly dependent on the temperature at the sea surface and weakly dependent upon the concentration of chlorophyll at the sea surface. Finally, the relationship between the scores of principle components and the temperature-chlorophyll axes may provide a means of extrapolating the Bio-optical Profile Model in time and space.

1. INTRODUCTION

Satellite ocean color imagery provides detailed yet comprehensive information on spectral reflectance at the sea surface. In order to extract information about the bio-optical properties of the ocean from such imagery, we have developed a system of equations that predicts the vertical distribution of bio-optical properties from surface information. In particular our model is designed to predict the vertical distribution of chlorophyll *a*, the beam attenuation coefficient, and the diffuse attenuation coefficient. This Bio-optical Profile Model, which is a one dimensional description of the water column at a given location and time, has been recently described (Ondercin, Atkinson, and Kiefer, 1994), and it was tested during a single cruise in the northern waters of the North Atlantic. This test suggested to us that the coefficients found within the system of equations that form the model may vary with locale and that we needed to study the variability of these coefficients and then to develop a strategy to predict variability so that more accurate and realistic three dimensional maps can be produced from satellite imagery. This paper describes our initial study of the problem and our approach to predicting variability in the coefficients of equations that describe bio-optical relationships.

2. STRATEGY FOR PRODUCING 3 DIMENSIONAL BIO-OPTICAL MAPS FROM IMAGERY

Our strategy for producing 3 dimensional, bio-optical maps from satellite ocean color imagery is outlined in figure 1. As indicated, the production of such maps requires 4 types of information: (1.) remotely sensed information about the sea surface, surface chlorophyll (CZCS), surface temperature (AVHRR), and surface irradiance (GOES) (2.) databases on the depth of the surface mixed layer (Levitus, 1982). Other databases can also supply useful information such as the concentration of nitrate in upper waters (Glover and Brewer, 1988) and monthly averaged irradiance at the sea surface (Bunker Atlas) (3.) the Bio-optical Profile Model which predicts the vertical distribution of bio-optical properties at a given site (4.) a horizontal interpolation and extrapolation model which is used to predict variations in time and horizontal space of the value for the coefficients found in the Bio-optical Profile Model.

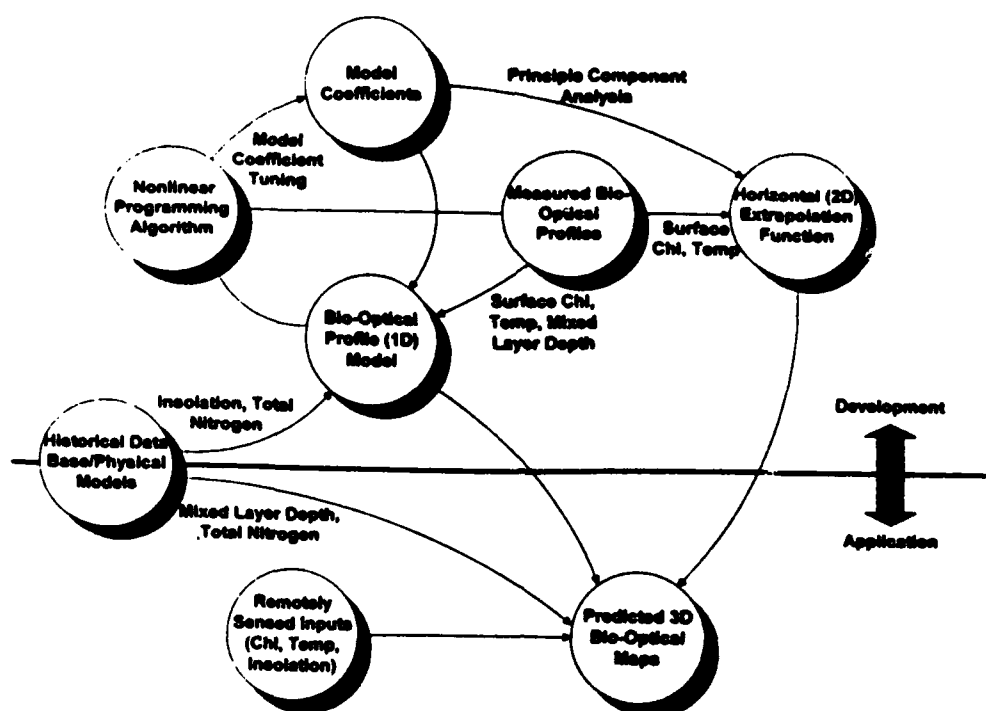


Figure 1. The components and flow of information that we propose to use in the mapping of bio-optical properties from satellite ocean color imagery.

In order to understand the magnitude and distribution of variability of the coefficients found in the equations of the Profile Model, the model must be tuned to measured profiles. Furthermore, to produce Basin scale and Global Maps the database used to tune the model must be large and diverse. The tuning process involves calculating the values of the variable coefficients (hereafter called tuning coefficients), such that the model calculation yields a χ^2 best fit of predicted values for chlorophyll and beam attenuation to the measured values at each station in the database. The 4 arrows linking "nonlinear programming algorithm", "model coefficients", "Bio-optical Profile Model", and "Measured Bio-optical Profiles" symbolizes the tuning process. Finally, the matrix of optimized values for the tuning coefficients at each station must be incorporated into a "horizontal (2 dimensional) extrapolation function" that will provide values for the tuning coefficients at locations and at times that differ from those of the database.

3. GENERAL DESCRIPTION OF THE BIO-OPTICAL PROFILE MODEL

The Bio-optical Profile Model is based upon three previous studies by Kiefer and Kremer (1981), Kiefer and Mitchell (1983), and Pak, Kiefer, and Kitchen (1988). The model is a description of the vertical distribution of the concentration, growth rate, and optical properties of phytoplankton and associated biogenous materials. The model is based upon a single element, that which is most limiting to the growth rate of the phytoplankton. In the north Atlantic this element is most likely nitrogen. The independent variables or inputs to the model are the sea surface values for scalar irradiance, the concentration of dissolved nitrogen (the sum of concentrations for ammonium, nitrate, and nitrite), the concentration of chlorophyll a at the sea surface, the temperature at the sea surface, and the depth of the surface mixed layer. This information provides a unique description of the vertical distributions for chlorophyll a, cellular nitrogen, the beam attenuation coefficient, and the scalar irradiance for photosynthetically active radiation.

The model consists of a system of equations that describe several types of relationships. One set of equations describes the relationship between the concentration of phytoplankton and detritus and the value of the diffuse and beam attenuation coefficients. Another set of equations describes the relationship between the ratio of phytoplanktonic cellular chlorophyll to cellular nitrogen and the conditions that determine the growth rate of the cells. The conditions that determine growth rate include temperature, light intensity, and nutrient concentration. The chlorophyll to nitrogen ratio of phytoplankton increases with decreases in light level and with increases in temperature and nutrient concentration. A third set of equations describes the relationships between the growth conditions of the phytoplankton, the vertical stability of the

water column, and the vertical distribution of light. The weakest assumption of the model is that within the euphotic zone the concentration of phytoplanktonic nitrogen is invariant with depth.

4. DESCRIPTION OF THE DATABASE

The 117 stations that form our database were sampled during 4 cruises conducted by the Applied Physics Laboratory, Johns Hopkins (Figure 2). In order to characterize the spatial structure of the upper ocean, APL designed and built a towed vessel, called the paravane, upon which were mounted a number of oceanographic sensors. The system profiles rapidly (1 m/s) to a depth of 140 m as the research vessel transits at speeds of between 2 to 5 m/s. The paravane acts much like an airplane in the water. The small vane on the underside of the vehicle moves back and forth, causing the vehicle to roll. With a fixed cable length, vehicle roll changes the direction of the wings' dynamic lift, causing the vehicle to rise as it moves perpendicular to the ship's course. The vane angle, and therefore the profiling characteristics of the vehicle, is controlled by a topside HP-9816 computer and a vehicle-mounted microprocessor. The instruments mounted on the paravane are Sea-Bird temperature and conductivity sensors, a Parascientific pressure transducer, a fluorometer, and a transmissometer (spectrally filtered at 490 nm, with a FWHM of 150 nm). Both the fluorometer and spectrophotometer were built by APL. In addition to the paravane, a rosette vertical profiler was built to provide high resolution vertical profile data and water and plankton samples. The vertical profiler not only measures the same parameters as the paravane, but also provides water samples from 5 liter Niskin bottles. These water samples were used to calibrate sensors.

All of the data from the two systems were collected at 12-Hz, calibration factors applied and the data averaged to 1-s intervals. The data from a paravane tow were divided into sections, with each section equal to one paravane undulation. Timers bins these sections were averaged into 1-m depth bins and stored in an array, with each row representing 1-m depth and each column representing one paravane undulation. In order to reduce the variance and the size of the data set without giving up too much vertical resolution, the paravane data was vertically averaged and binned over five meters and over five paravane oscillations (about 5 km) horizontally. To insure statistical independence between paravane oscillations, only oscillations that were nominally 50 km apart were used in the model development. A profile from a vertical profiler cast was obtained by averaging the data into 1-m depth bins. The vertical profiler data were also vertically averaged and subsampled over five

Datasets from four different cruises in the North Atlantic were combined into one to form the database used in the tuning of the model. The datasets included vertical profiler data obtained in August 1987 in the Sargasso Sea (within 100 km of 34°N 70°W) as part of the ONR special focus program BIOWATT; vertical profiler data obtained in March 1989 during a transect from the Canary Islands to Florida; paravane data obtained in August 1989 on a survey cruise between North Carolina and the Azores; and paravane data obtained in August 1991 during a transect from Ireland to 60°N 20°W and then to the Grand Banks as part of the ONR special focus program MLML. The fluorometer was calibrated by plotting measured voltages as a function of the concentration of chlorophyll a obtained from a water sample collected at the time of measurement. In turn the chlorophyll a in the water sample was measured by filtering the sample, extracting the pigments in acetone, and recording the fluorescence with a Turner 111 fluorometer (Parsons, Maita, and Lalli, 1984).

5. TUNING THE MODEL

The tuning process consisted of searching simultaneously for the values of the 7 tuning coefficients in the equations which would provide the best-fit between calculated profiles and measured profiles. Inputs to the Bio-optical Profile Model include the concentration of chlorophyll at the sea surface, which was measured directly, the irradiance, PAR, incident to the sea surface, which was obtained from the Bunker Atlas, and the depth of the surface mixed layer, which was determined from the measurements of temperature and salinity. The 4 of the 7 tuning coefficients of the model are found in the equations describing the relationship between the value of the beam attenuation coefficient at 499 nm and the diffuse attenuation coefficient of PAR and concentration of phytoplankton and detritus. The coefficients are the beam and absorption coefficient for detrital organic nitrogen and the nitrogen-specific, beam attenuation coefficient and the chlorophyll-specific absorption coefficient for phytoplankton. The remaining 3 tuning coefficients are the maximum photosynthetic quantum yield, the concentration of dissolved inorganic nitrogen in the surface mixed layer, and a factor that determines the rate of decrease in the concentration of biogenic nitrogen below the euphotic zone. The criterion of "best-fit" was the minimum of the χ^2 value for all measurements of chlorophyll and the beam attenuation coefficient collected at depth z within the upper 150 m. of the water column:

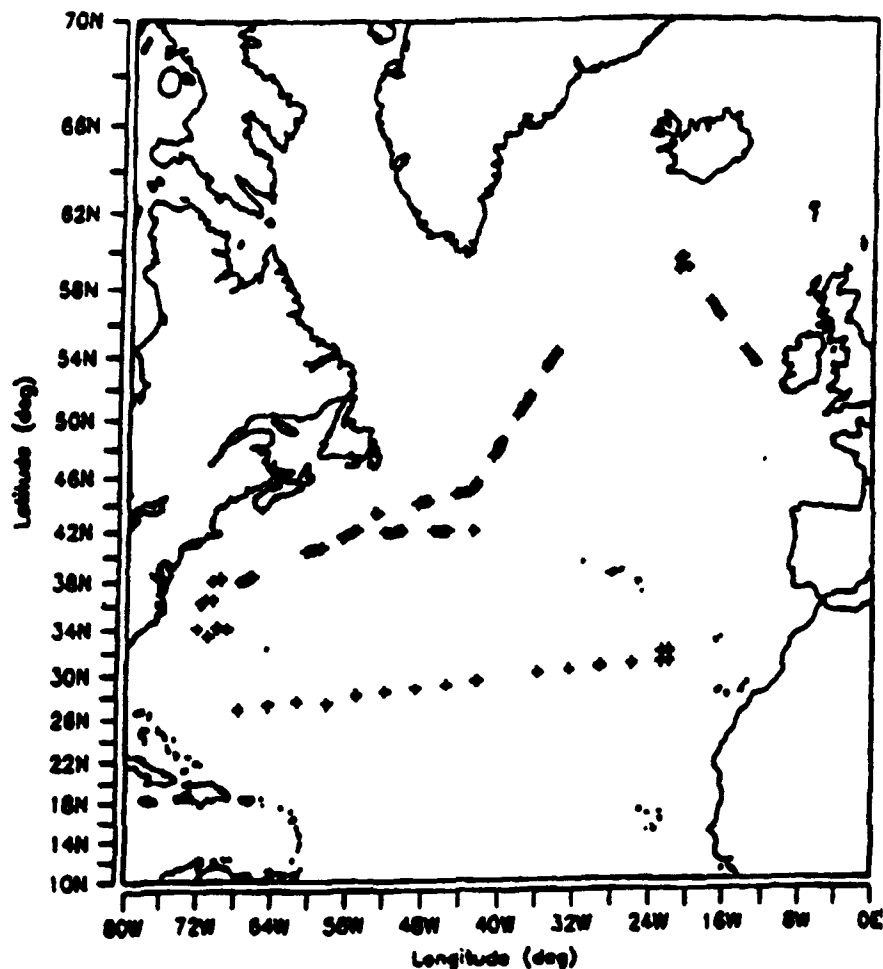


Figure 2. Map of the stations used to tune the Bio-optical Profile Model and thus used to calculate optimal values for the 7 tuning coefficients.

$$\chi^2 = \sum_{z=0}^{z=150} \frac{(pred.chl(z) - meas.chl(z))^2}{meas.chl(z)} + \frac{(pred.c(z) - meas.c(z))^2}{meas.c(z)}$$

We employed nonlinear programming software to make the search for the optimal values of the 7 coefficients. The search was constrained by restricting the value of each coefficient to fall within a specified and reasonable range.

Figures 3 and 4 are examples of fits that we obtained by tuning the model to individual stations. Figure 3 shows 3 pairs of predicted and measured profiles of chlorophyll and the beam attenuation coefficient obtained during August 1991 at the MLML mooring (60° N, 20° W). Figure 4 shows 3 pairs of predicted and measured profiles obtained during August 1989 in the western Sargasso Sea. We note in reference to the distribution of chlorophyll in the Sargasso Sea that the Bio-optical Profile Model provides a fairly good prediction of the depth and magnitude of the subsurface maximum in the concentration of chlorophyll a. In figure 5 we plot χ^2 values (percentage) as a function of the latitude and longitude for all 117 stations. We note from this figure that on the average predicted values within the water column of the beam attenuation coefficient and the concentration of chlorophyll are generally within 35% of the measured values.

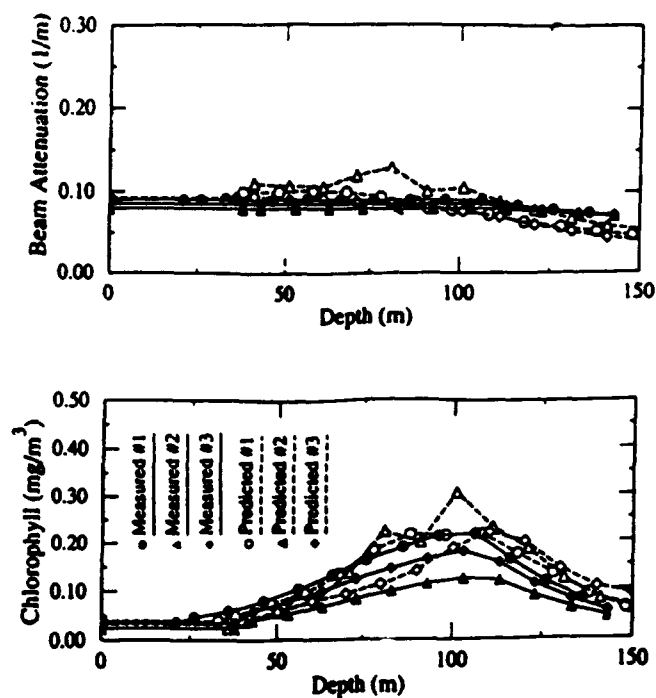


Figure 3. Predicted and measured profiles of the concentration of chlorophyll and the beam attenuation coefficient at three randomly selected stations sampled in August 1989 in the western Sargasso Sea. Open symbols are measured values and the corresponding filled symbols are predicted values.

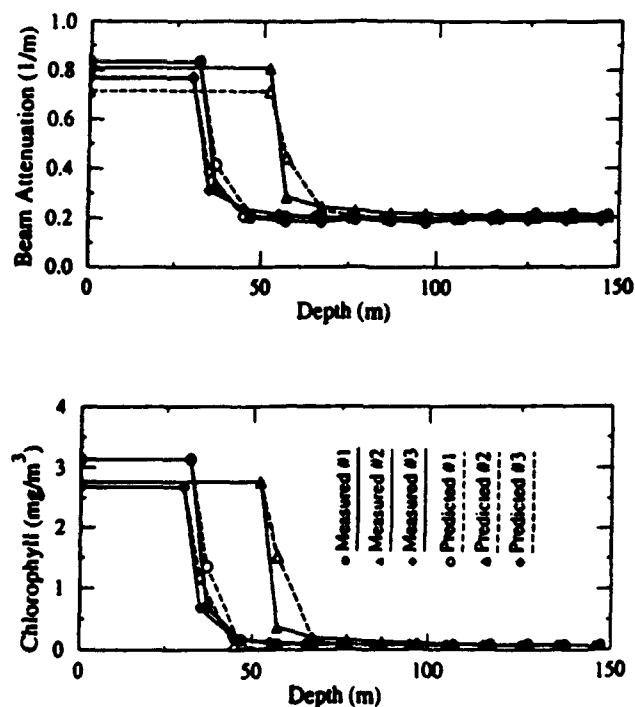


Figure 4. Predicted and measured profiles of the concentration of chlorophyll and the beam attenuation coefficient at three stations sampled in August 1991 in the northern North Atlantic. These stations were near the MLML mooring at 60° N, 20° W. Open symbols are measured values and the corresponding filled symbols are predicted values.

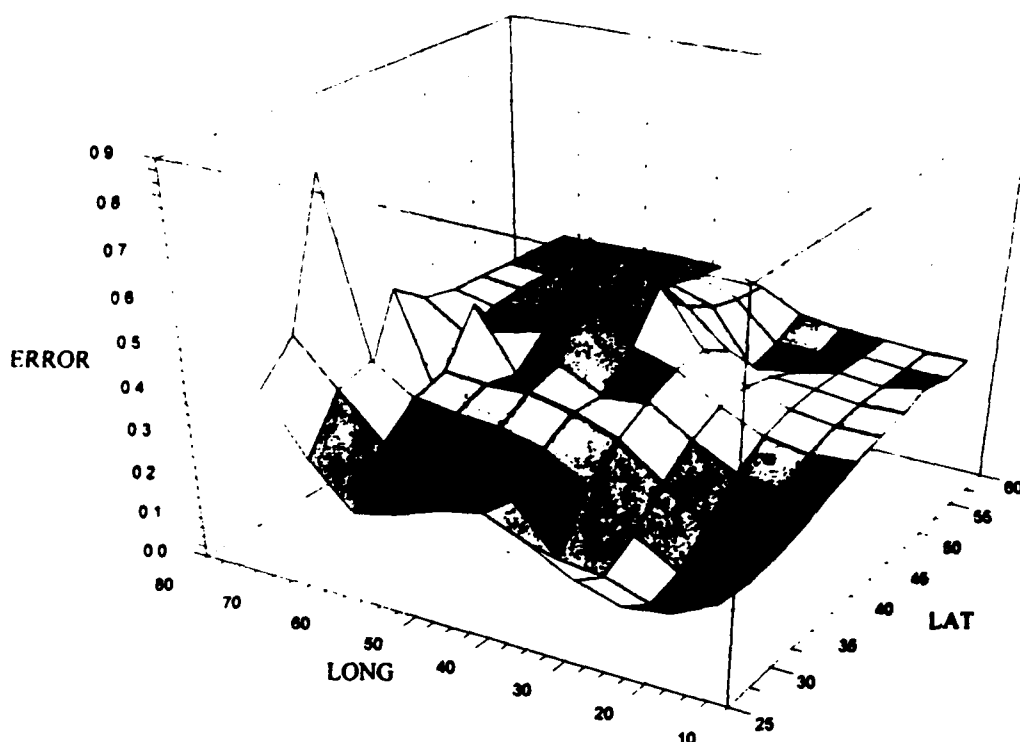


Figure 5. The spatial distribution of error in predicting the vertical distribution of chlorophyll and the beam attenuation coefficient for the 117 tuning stations.

6. PRINCIPLE COMPONENT ANALYSIS

The tuning process yielded a 7 X 117 matrix of values for the 7 tuning coefficients at the 117 stations. We then calculated the 7 principle components of this matrix following the procedures and definitions of Cooley and Lohnes (1971). (See also Estrada and Balasco, 1979.) Each principle component should be thought of as a vector determined by a set of 7 normalized values for each of the tuning coefficients. A linear combination of the mean values for the 7 tuning coefficients with the scores for each of the 7 principle components provides a complete description of the 7 X 117 matrix. The relationship between the principle components, the matrix of tuning coefficients, and scores can be summarized by an equation that describes the statistics for each of the 117 stations:

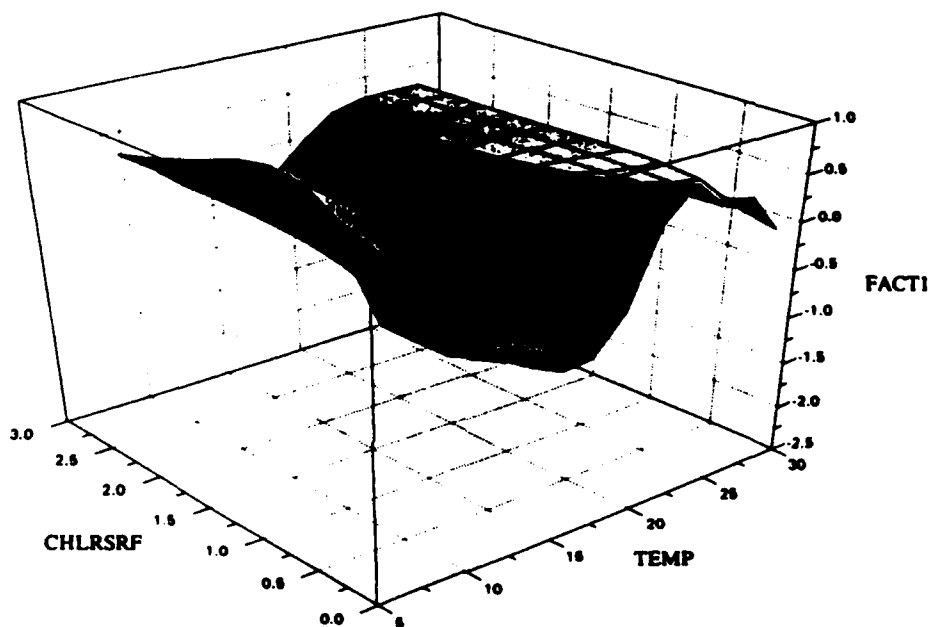
$$S(j) = \sum_{i=1}^7 \frac{F(i,j) * (x(i) - \bar{x}(i))}{s(i) * E(j)}$$

$S(j)$ is the score for principle component j . (j varies from 1 to 7.) In our case there are 117 values for $S(j)$, one for each station. $F(i,j)$ is the factor loading to parameter i on principle component j . $x(i)$ is the value of tuning coefficient i at given station, and $\bar{x}(i)$ is the mean value of tuning coefficient i for the 117 stations. $s(i)$ is the standard deviation of tuning coefficient i within the 117 stations. $E(j)$ is the eigenvalue of principle component j . The larger the eigenvalue of a given principle component the greater is the contribution of that component to variability in the tuning coefficients of the matrix.

The statistical analysis of the matrix of tuning coefficients indicated to us that the tuning coefficients did not strongly covary. This assertion is supported by the fact that the elements of the correlation matrix that we calculated for the tuning coefficients contained low values. Most elements contained values close to 0, and the highest value was about 0.49. In addition the lack of covariation among the tuning coefficients was also evident from the size of the eigenvalues for the 7

principle components. The first principle component accounted for 46% of the variability in the tuning coefficients, the second principle component accounted for 22% of the variability, the third principle component accounted for 8%, and the fourth component accounted for 7%. In our search for an interpolation/ extrapolation scheme for the mapping of the north Atlantic, we chose to examine the first 4 components.

In figure 6 we have plotted the scores for the first principle component for all stations as a function of the surface temperature and surface concentration of chlorophyll a at those stations. Before making such a plot, we attempted several other representation of the database, all of which were more complex. For example, plots in which we by-passed the calculation of principle components and simply plotted the value of the 7 tuning coefficients as a function of latitude and longitude were much more complex than those shown in figure 6. Likewise, plots of the scores of the first 4 principle components as a function of latitude and longitude were more complex than those shown here. In this figure we see that the surface describing the distribution of scores for the first and most important principle component is characterized by a strong, nonlinear dependence upon temperature and relatively weak dependence upon the concentration of chlorophyll a.



Figures 6. Plot of the scores for the first principle components of the matrix of values of the 7 tuning coefficients at all stations in the North Atlantic as a function of surface temperature and the surface concentration of chlorophyll a. When the scores for components are introduced into the equation above (along with mean values and standard deviations of tuning coefficients, and loading factors and eigenvalues for components values for the tuning coefficients can be predicted with defined accuracy.

Minimum values for scores are found at about 18°C and maximum values are found in the coldest waters sampled (about 8°C). High scores are also found in the warmest waters. In addition above 20°C scores for the first component vary little with increasing temperature. Three dimensional plots for the other 3 principle components were also relatively smooth and are generally less complicated than the surface of the first principle component. As is the case for the first component, variations in the temperature at the sea surface appeared to cause larger changes in the remaining three components than does changes in the concentration of chlorophyll at the sea surface. Because the plane defined by the temperature-chlorophyll axes in these plots is not completely filled with data, we are unsure of the complete shape of the surface that describes the relationship between the temperature-chlorophyll plane and the scores for the principle components. Despite this limitation in interpretation, we feel that this initial test is promising.

7. DISCUSSION AND CONCLUSION

The approach we present to interpolating and extrapolating in time and space one dimensional models in order to produce three dimensional maps is statistical. We tune the coefficients of our system of equations to the individual stations

of a database, we calculate the principle components of the matrix of values for these coefficients hoping to reduce the size of the matrix and to find significant relationships between the principle components and measurable coefficients such as temperature and chlorophyll concentration, and we then use these relationship to the predict the values for the coefficients in a four dimensions (x, y, z, t). An alternative approach has already been presented by Platt and Sathyendranath. (1988) and Mueller and Lange (1989). In this approach biogeographic regions are defined and located, and it is assumed that within these regions the values for coefficients remain constant. As an example, in Mueller and Lange's study of the vertical distribution of the diffuse attenuation coefficient, they defined 4 regions in the northeastern Pacific: the subarctic frontal regime, the California Current, the Alaskan gyre, and the central north Pacific. While these provinces are defined by patterns in large scale circulation and TS characteristics, Mueller and Lange found that the values for the coefficients found in the equations of their model were much less variable within the provinces than between provinces. Further research is required to determine whether the statistical approach which we present here or the more classical hydrographic approach is better.

In conclusion our study of the north Atlantic may be summarized by the following 4 points.

1. When tuned to individual stations in diverse waters of the north Atlantic, the Bio-optical Profile Model provides predictions of vertical distribution from surface properties that are generally within 35% of measured values.
2. The predictable relationship between scores and the plane of temperature-chlorophyll suggests that the principle components derived from our bio-optical model may provide a means of interpolating our 1 dimensional model both in time and horizontal space.
3. The scores for all 4 principle components all depended strongly on the surface temperature and less so on surface concentration of chlorophyll.
4. Since surface temperature and chlorophyll can be measured from satellite and vary with season and circulation, our interpolation scheme will be a dynamic feature in the creation of bio-optical maps. The bio-optical province imposes a more static description of the ocean.

5. ACKNOWLEDGEMENTS

This work was supported in part by the Oceanic Optics (grant N00014-93-1-0134) and the Biological Oceanography (grant N00014-93-1-0412) Programs of the U.S. Office of Naval Research, and NASA Ocean Biogeochemistry Program (grant NAGW-3574).

6. REFERENCES

1. W. W. Cooley and P.R. Lohnes, *Multivariate Data Analysis*, John Wiley & Sons, New York, 1971.
2. M. Estrada and D. Blasco, "Two phases of the phytoplankton community in the Baja California upwelling." *Limnol. Oceanogr.* 24, 1065-1080, 1979.
3. D.M. Glover and P. G. Brewer, "Estimates of winter time mixed layer nutrient concentrations in the North Atlantic", *Deep-Sea Res.*, 35(9), 1525-1546, 1988.
4. D.A. Kiefer and J.N. Kremer, "Origins of vertical patterns of phytoplankton and nutrients in the temperate, open ocean: a stratigraphic hypothesis", *Deep-Sea Res.*, 28(10), 1087-1105, 1981.
5. D.A. Kiefer and B.G. Mitchell, "A simple, steady state description of phytoplankton growth based on absorption cross section and quantum efficiency." *Limnol. Oceanogr.* 28, 770-776, 1983.
6. S. Levitus, "Climatological Atlas of the World's Oceans." NOAA Report, Geophysical Fluid Dynamics Laboratory, Princeton University 13, 173 pp., 1982.
7. J. Marra, T. Dickey, W.S. Chamberlin, C. Ho, T. Granata, D.A. Kiefer, C. Langdon, R. Smith, K. Baker, R. Bidigare, and M. Hamilton, "Estimation of Seasonal Primary Production from Moored Optical Sensors in the Sargasso Sea." *JGR.* 97, 7399-7412, 1992.

8. J. Marra, W.S. Chamberlin, and C. Knudson, "Proportionality between in situ carbon assimilation and bio-optical measures of primary production in the Gulf of Maine in Summer" *Limnol. Oceanogr.*, in press, 1992.
9. A. Morel, "Optical Modeling of the Upper Ocean in Relation to its Biogenous Matter Content (Case I Waters).", *J. of Geophysical Research*, 93 (C9 1988).
10. J.L. Mueller and R.E. Lange, "Bio-optical provinces of the Northeast Pacific Ocean: A provincial analysis." *Limnol. Oceanogr.*, 34(8), pp. 1572-1586, 1989.
11. D. Ondercin, C.A. Atkinson and D.A. Kiefer, "The Distribution of bioluminescence and chlorophyll during the late summer in the North Atlantic: maps and a predictive model.", *J. Geophys. Res.*, in press, 1994.
12. H. Pak, D. A. Kiefer, and J. C. Kitchen, "Meridional variations in the concentration of chlorophyll and microparticles in the North Pacific Ocean", *Deep-Sea Research*, 35 (7), pp. 1151-1171, 1988.
13. T.R. Parsons, Y. Maita and C. M. Lalli, *A Manual of Chemical and Biological Methods for Seawater Analysis.*, Pergamon Press, Inc., 1984.
14. T. Platt, "Primary production of the ocean water column as a function of surface light intensity: algorithms for remote sensing." *Deep-Sea Research*, Vol. 33(No. 2), 1986.
15. T. Platt and S. Sathyendranath, "Oceanic primary production: estimation by remote sensing at local and regional scales." *Science* 24(10), 1613-1620, 1988.
16. T. Platt, C. Caverhill and S. Sathyendranath, "Basin-Scale Estimates of oceanic primary production by remote sensing: the north Atlantic." *JGR*, Vol. 96(No. C8), 15147-15159, 1991.
17. E. Sakshaug, D.A. Kiefer and K. Andresen. "A steady-state description of growth and light absorption in the marine diatom *Skeletonema costatum*." *Limnol. and Oceanogr.* 43 (1), 198-205, 1988.
18. R.C. Smith, B.B. Prezelin, R.R. Bidigare and K.S. Baker. "Bio-optical modeling of photosynthetic production in coastal waters." *Limnol. Oceanogr.* 34 (8), 1524-1544, 1989.

SESSION 3

Closure

The optical properties of pure water

H. Buiteveld

Institute for Inland Water Management and Waste Water Treatment, Ministry of Transport and Public Works, P.O. Box 17,
8200 AA Lelystad, The Netherlands.

tel:+31-3200-70737 fax:+31-3200-49218

J.H.M. Hakvoort and M. Donze

Delft University of Technology, Faculty of Civil Engineering, P.O. Box 5048, 2600 GA Delft, The Netherlands

ABSTRACT

The optical properties of pure water are basic input data for many geophysical investigations such as remote sensing of surface water and underwater radiative transfer calculations. Knowledge of the spectral properties of components in surface water is required for accurate interpretation of measured reflection and attenuation spectra in terms of their concentrations. Also the sources and sizes of errors in the basic data must be known.

Absorption measurements were done with a submersible absorption meter in the temperature range 2.5 till 40.5 °C. The scattering of pure water is recalculated using the Einstein-Smoluchowski equation. The input for this equation is evaluated and the temperature dependency is included. New values for the absorption coefficient are given based on these results and analysis of data from the literature. Absorption in the wavelength range 300-550 nm is lower than presently used values. In the wavelength range above 700 nm the spectrum has a different shape. A formulation of the effect of temperature on the absorption spectrum is given.

1. INTRODUCTION

From reflectance spectra and attenuation spectra measured in the optical window concentrations of aquatic humus and suspended matter such as algae and silt in surface water are derived. Decomposition of measured spectra in terms of concentrations requires knowledge of the inherent optical properties of these components. Also the sources and sizes of errors in these basic data must be known. The inherent optical properties of pure water can be used to test and apply algorithms to decompose reflectance spectra and to calibrate instruments.

The inherent optical properties of surface water are the absorption coefficient a , the scattering coefficient b and the volume scattering function β . The beam attenuation c is the sum of the absorption and scattering coefficients. These properties depend only on dissolved and suspended matter in the water and water itself and not on the geometry of the light field. The coefficients are defined for an infinitesimally thin layer of medium, illuminated at right angles by a narrow parallel beam of monochromatic light. The fraction of the incident flux that is absorbed, divided by the thickness of the layer, is the absorption coefficient. The fraction of the incident flux that is scattered, divided by the thickness of the layer, is the scattering coefficient. The angular distribution of the scattered light is specified by the volume scattering function. The diffuse attenuation coefficient is an apparent optical property which depends on the geometry of the light field, it specifies the attenuation of solar irradiance in natural waters.

The optical properties of pure water were reviewed by Morel ¹, Smith and Tyler ² and Smith and Baker ³. Several methods were used to determine these properties. The beam attenuation coefficient of water can be measured by spectrophotometry and the absorption coefficient then is calculated by subtraction of the scattering coefficient from the beam attenuation coefficient. Optoacoustic measurements ⁴ yield absorption directly. Another way to derive the absorption coefficient of pure water is from measurements of the diffuse attenuation coefficient in very clear natural water ³. Smith and Baker ³ presented diffuse attenuation and absorption coefficients of water that are in common use now. These data were based on measurements from several sources and sound judgement as to what source to use. They arrived at the absorption spectrum in the following way:

1. At wavelengths smaller than 380 nm the spectrum was calculated from direct measurements of the diffuse attenuation coefficient.
2. At wavelength between 380 and 700 nm the spectrum was based on beam attenuation measurements of Morel and Prieur ⁵. In the wavelength range 600-700 nm these authors shifted their measured spectra in a vertical direction to obtain the same

- values as found by Sullivan⁶. So from 600 to 700 nm the results of Smith and Baker are based on Sullivan's work.
3. At wavelengths above 700 nm the average of beam attenuation data measured by Curcio and Petty⁷, James and Bridge⁸, Clark and James⁹ and Sullivan⁶ are used, as was done by Smith and Tyler².

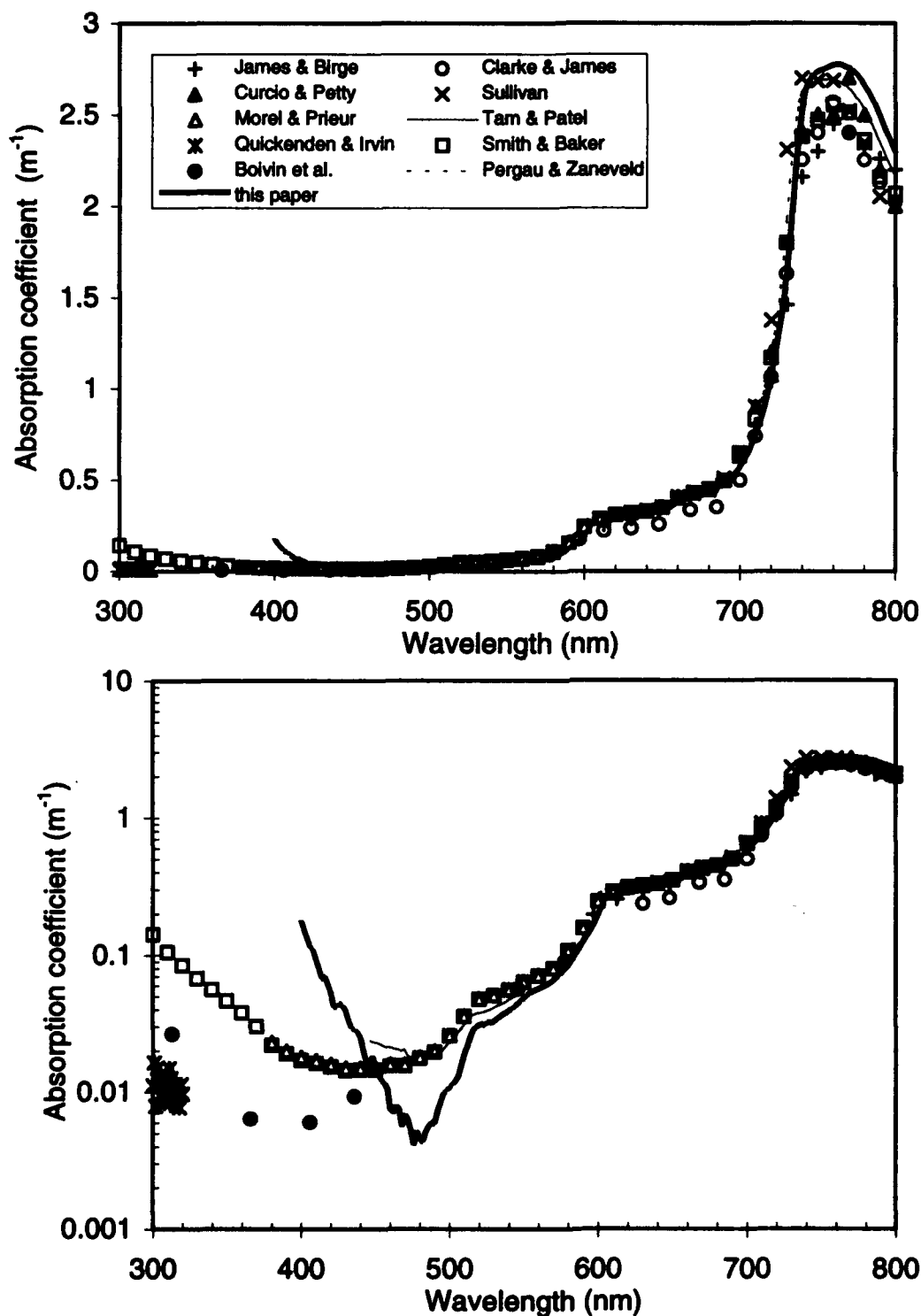


Figure 1 a and b. Absorption spectra (logarithmic and linear scale) used by Smith and Baker³ including our measurement and other recent measurements.

The shape of the water absorption spectrum in the visible wavelength range has the following characteristics. In the 300-700 nm wavelength range absorption is low. Published spectra show minima at 490 nm⁵, 480 nm⁴ or 380 nm¹⁰. This variation occurs due to impurities of the water as explained further on. The absorption increases with increasing wavelength and has shoulders at 510 nm, 600 nm and a small one at 660 nm. From 690 nm absorption increases rapidly until approximately 740 nm. At still higher wavelength the absorption decreases again. In Figure 1a and 1b the absorption spectra from Smith and Baker³ are shown together with our measurements and the values measured by Tam and Patel⁴, Boivin *et al.*¹⁰ Quickenden and Irvin¹¹ and at 21°C by Pegau and Zaneveld¹². Our values are the average of 16 absorption spectra between 10° and 40.5°C with a mean temperature of 20.1°C.

Among different authors differences between the absorption spectra are significant in the complete visible wavelength range. These must be explained by combinations of several possible errors:

1. False reflections of light in the optical equipment cause problems in the accurate determination of low attenuation coefficients. An extensive analysis of such errors is given by Quickenden and Irvin¹¹. Over a limited wavelength region this error results in a vertical shift of the spectrum, which may be positive or negative.
2. The values can be too high due to scattering by dust and micro air bubbles. Large particles lead to a vertical upward shift of the spectrum, small particles to an exponential increase with decreasing wavelength.
3. Absorption by other molecules than water also leads to overestimation of absorption. Large and complicated organic molecules, generally summarized as aquatic humus, begin to absorb significantly below 600 nm. This absorption increases in first approximation exponentially with lower wavelength, the exponent varies between 0.010 nm⁻¹ and 0.021 nm⁻¹¹³. Contamination of the water by significant concentrations of specific organic molecules and several ions leads to specific broad absorption bands in the ultra violet part of the spectrum.
4. Højerslev and Trabjerg¹⁴ observed that water absorption depends on temperature and Pegau and Zaneveld¹² found that this effect was especially large in the wavelength range 700-800 nm. This temperature effect was however until recently not identified as important. The spectral shape of this effect is one of the subjects of this paper.

In practice it is usually impossible to ascribe observed errors and differences among published spectra to these single causes. Boivin *et al.*¹⁰ and Quickenden and Irvin¹¹ measured attenuation coefficients in the 300-600 nm wavelength range which are significantly lower than the values reported before. This can probably be attributed to better purification of the water used¹¹. Højerslev and Trabjerg¹⁴ and Pegau and Zaneveld¹² measured the temperature dependence of the absorption coefficient. This effect increases with the absorption coefficient and it is strongest at the harmonics of the stretching of O-H bonds. In the range 400-600 nm Højerslev and Trabjerg¹⁴ found a temperature dependency of 0.0015 m⁻¹°C⁻¹. Pegau and Zaneveld¹² found a temperature dependency of 0.0071, 0.0092 and 0.0113 m⁻¹°C⁻¹ at respectively 755, 750 and 745 nm.

In this paper absorption measurements made with a submersible absorption meter¹⁵ in the temperature range 2.5 till 40.5 °C are given. The scattering of pure water is recalculated using the Einstein-Smoluchowski equation¹⁶. The input for this equation is evaluated and the temperature dependency is included. New values for the absorption coefficient are given based on these results and analysis of data from the literature.

2. ABSORPTION MEASUREMENTS

2.1 Materials and methods

Twenty five spectra of the sum of absorption and backscattering of pure water were measured with a submersible absorption meter¹⁵ in the temperature range from 2.5°C to 40.5°C. This submersible absorption meter measures radiance attenuation spectra in a Lambertian diffuse light field. If measured close to the light source the radiance forwardly scattered out of the normal direction is replaced by path radiance. The radiance attenuation approaches the sum of absorption and backscattering. In clear samples the radiance attenuation is equal to the absorption.

The sample compartment of the submersible absorption meter was filled with pure water. This was obtained by reversed osmosis followed by distillation. Conductivity of this water was 1.5 µS. A series of temperature was made from 2.5° to 40.5°C. Temperature was measured with an accuracy 0.05°C. Light reflection from the water surface into the sample compartment was prevented by a black absorption panel behind the radiance detector. Absorption spectra were measured over a path length of

0.120 m. At each temperature three spectra were averaged. Repeated measurements at a single temperature had a standard deviation of 0.03 m^{-1} .

2.2 Results

In Figure 1a and 1b the average of the spectra measured between 10 and 40.5 is shown. Averaging reduced noise; it is allowed since the dependence of absorption on temperature is linear (see below). This spectrum shows the general characteristics as described in the introduction. Most unsolved problems occur below 500 nm, considered in more detail in the discussion. In the 500-700 nm wavelength range good agreement occurs with the data of Tam and Patel. In the 700-800 nm wavelength range the measured spectra were up to 20 percent higher than the spectra of Smith and Baker³, here the temperature dependence is important.

The absorption spectrum of water as a function of temperature is shown in Figure 2. Absorption increases with temperature in the 400-780 nm wavelength range and decreases in the 780-800 nm range. The absorption maximum shifts towards a lower wavelength at increasing temperature. Absorption was linearly fitted to temperature at all wavelengths.

$$a(T) = a(20.1) + A(T - 20.1) \quad (1)$$

where $a(T)$ is the absorption at temperature T and A is the absorption increment due to temperature. The temperature dependency of absorption is plotted in Figure 3 along with the correlation between absorption and temperature.

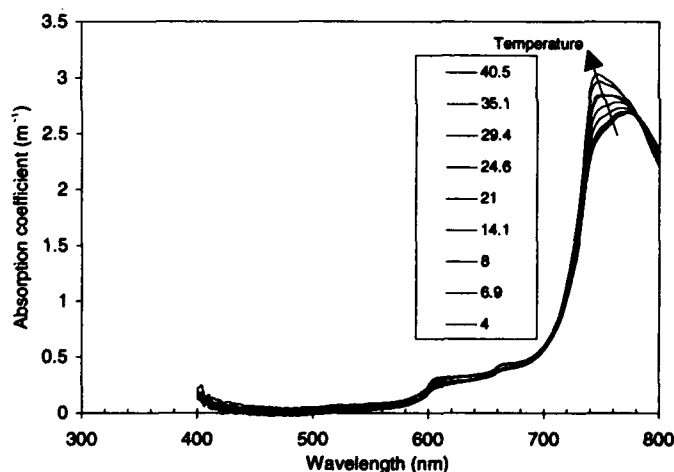


Figure 2. Absorption spectra of pure water measured with the submersible absorption meter for different temperatures.

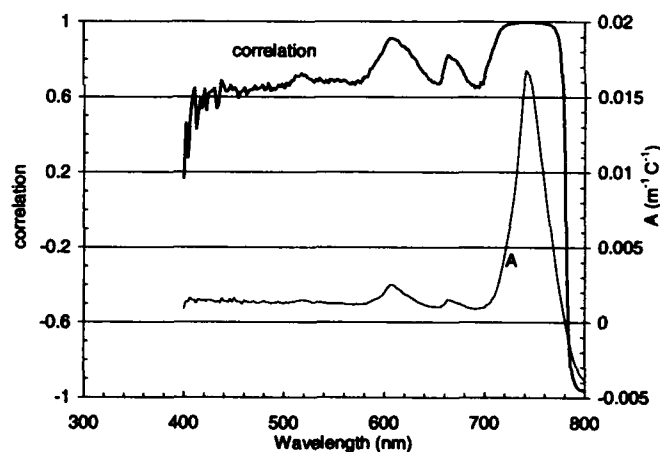


Figure 3. Spectrum of the temperature dependency (A) of the absorption coefficient of pure water and the correlation between the absorption coefficient and temperature

A has peaks in the same wavelength ranges where the shoulders and maximum absorption are found; 520, 606, 664 and 742 nm. At wavelengths below 580 nm the slope coefficient A is nearly constant at $0.0012 \text{ m}^{-1} \text{ } ^\circ\text{C}^{-1}$ and in agreement with Højerslev and Trabjerg¹⁴. A small peak around 520 nm can be seen, where A increases to $0.0015 \text{ m}^{-1} \text{ } ^\circ\text{C}^{-1}$. No peak was found at 550 nm as was predicted by Pergau and Zaneveld¹². Around the absorption maximum at 740 nm our measured absorption values are higher than those reported by Pergau and Zaneveld¹². Part of this difference may have been caused by their correction procedure; the spectra were adjusted in the vertical direction to the absorption at 685 nm as measured by Tam and Patel⁴. In doing so part of the temperature effect was discarded. However this does not completely explain the difference, because at 685 nm A is only $0.001 \text{ m}^{-1} \text{ } ^\circ\text{C}^{-1}$. Compared to Pergau and Zaneveld¹² our values for A are higher. Irvin and Pollard¹⁷ reported a value of A at 750 nm of $0.014 \text{ m}^{-1} \text{ } ^\circ\text{C}^{-1}$ which is in agreement with our results.

3. PROPOSED ABSORPTION SPECTRUM.

We arrived at an improved estimate for the absorption spectrum of pure water in the following way:

1. In the 300-394 nm wavelength range the spectrum according to Boivin *et al.*¹⁰ is used. Their measured data were interpolated to obtain absorption coefficients at fixed wavelength intervals.
2. In the 394-520 nm wavelength range the shape of the spectrum according to Smith and Baker³ is used, but the absolute values are changed by vertically shifting the spectrum such as to obtain a smooth fit at the lower wavelength with the data of Boivin *et al.*¹⁰ At the higher wavelength at 520 nm the constraint for a smooth fit is met by shifting the next section.
3. In the 520-604 nm wavelength range our measurements were used. The absorption coefficients were 0.01 m⁻¹ shifted to obtain a smooth fit with the data of Tam and Patel⁴.
4. In the 604-800 nm wavelength range the unmodified absorption spectrum as measured with the submersible absorption meter was used.

The results are given in Table 1 and in Figure 4. The measurements of Boivin *et al.*¹⁰ at 546 and 473 nm agree within a few percent. These values were not used in the numerical analysis. In the range below 400 nm we can choose between the values of Quickenden and Irvin¹¹ and Boivin *et al.*¹⁰ because both used highly purified water. Quickenden and Irvin¹¹ demonstrated the effect of subsequent purification steps on the water absorption spectrum. Probably a general feature visible in Figure 1 is that the absorption minimum in the spectrum shifts towards the ultra violet region with a higher degree of purification. Contamination causes exponentially increased attenuation coefficients towards the lower wavelengths. This criterium must be judged in combination with the value of the absorption. Absorption spectra with minima near 500 nm must be rejected for the low wavelength range. This also applies to our measurements in the 400-500 nm wavelength range.

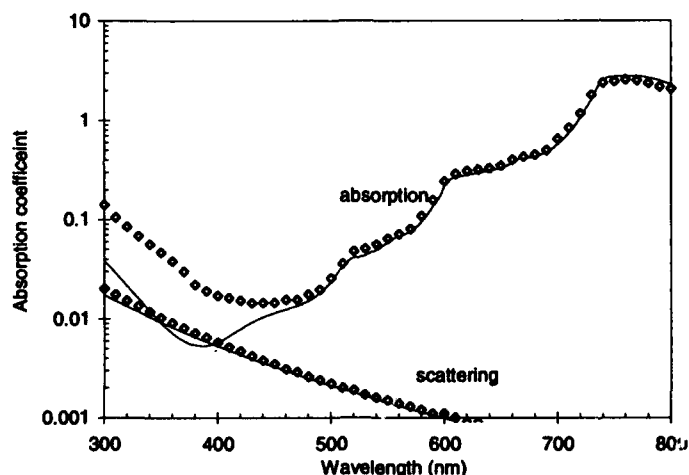


Figure 4. Spectra of absorption and scattering coefficient. The solid lines are the new values proposed and diamonds are the values given by Smith and Baker³

The data of Boivin *et al.*¹⁰ were selected because they used a longer cuvette than Quickenden and Irvin¹¹ and because they also made measurements in the visible part of the spectrum. Values for the attenuation coefficient were calculated for fixed wavelength intervals using fifth degree polynomial interpolation.

Our absorption measurements correspond well with the data of Tam and Patel⁴ between 600-700 nm. Therefore it is believed that these measurements are also accurate above 700 nm. Between 500 and 600 nm a small systematic difference remains.

Above 600 nm noise in a small wavelength region is generally much smaller than the systematic errors; the shape of water absorption spectra measured by different authors are very similar here. In contrast absolute values at single wavelength show larger differences. Boivin *et al.*¹⁰ arrived at an absolute error in their measurements of 0.007 m⁻¹ by direct experimental analysis of correction factors of their instrument. From our measurements we estimated the error in the absorption at 0.02 m⁻¹.

To align measurements from different sources it appears sometimes necessary to apply a vertical shift to the spectra, this may be

Table 1. Proposed values for absorption and scattering coefficients at 20 °C. The temperature dependence A derived from new measurements is included. Symbols: λ = wavelength (nm), a = absorption coefficient (m^{-1}), A = absorption increment due to temperature ($\text{m}^{-1}\text{°C}^{-1}$) and b = scattering coefficient (m^{-1}).

λ	a	A	b	λ	a	A	b	λ	a	A	b	λ	a	A	b
300	0.0382	-	0.0174	438	0.0102	0.0016	0.0036	576	0.0858	0.0012	0.0012	714	0.8445	0.0026	0.0005
302	0.0361	-	0.0169	440	0.0104	0.0014	0.0036	578	0.0896	0.0012	0.0012	716	0.9109	0.0032	0.0005
304	0.0341	-	0.0165	442	0.0106	0.0014	0.0035	580	0.0952	0.0012	0.0011	718	0.9871	0.0039	0.0005
306	0.0323	-	0.0160	444	0.0108	0.0013	0.0034	582	0.1008	0.0012	0.0011	720	1.0724	0.0046	0.0005
308	0.0305	-	0.0156	446	0.0110	0.0016	0.0034	584	0.1079	0.0013	0.0011	722	1.1679	0.0053	0.0005
310	0.0288	-	0.0152	448	0.0112	0.0013	0.0033	586	0.1159	0.0014	0.0011	724	1.2684	0.0061	0.0005
312	0.0272	-	0.0148	450	0.0114	0.0016	0.0033	588	0.1253	0.0014	0.0011	726	1.3719	0.0068	0.0004
314	0.0257	-	0.0144	452	0.0116	0.0014	0.0032	590	0.1356	0.0015	0.0011	728	1.4870	0.0077	0.0004
316	0.0242	-	0.0140	454	0.0118	0.0014	0.0031	592	0.1459	0.0016	0.0010	730	1.6211	0.008	0.0004
318	0.0228	-	0.0137	456	0.0120	0.0014	0.0031	594	0.1567	0.0016	0.0010	732	1.7872	0.0098	0.0004
320	0.0215	-	0.0133	458	0.0122	0.0012	0.0030	596	0.1700	0.0017	0.0010	734	1.9917	0.0114	0.0004
322	0.0203	-	0.0130	460	0.0124	0.0014	0.0030	598	0.1860	0.0018	0.0010	736	2.2074	0.0133	0.0004
324	0.0191	-	0.0126	462	0.0126	0.0014	0.0029	600	0.2224	0.0020	0.0010	738	2.3942	0.0152	0.0004
326	0.0180	-	0.0123	464	0.0128	0.0013	0.0029	602	0.2366	0.0022	0.0010	740	2.5319	0.0163	0.0004
328	0.0170	-	0.0120	466	0.0130	0.0013	0.0028	604	0.2448	0.0024	0.0010	742	2.6231	0.0168	0.0004
330	0.0160	-	0.0117	468	0.0133	0.0014	0.0028	606	0.2587	0.0025	0.0009	744	2.6723	0.0166	0.0004
332	0.0151	-	0.0114	470	0.0135	0.0014	0.0027	608	0.2653	0.0025	0.0009	746	2.7021	0.0161	0.0004
334	0.0142	-	0.0112	472	0.0138	0.0013	0.0027	610	0.2691	0.0024	0.0009	748	2.7216	0.0152	0.0004
336	0.0134	-	0.0109	474	0.0141	0.0013	0.0026	612	0.2715	0.0023	0.0009	750	2.7334	0.0143	0.0004
338	0.0127	-	0.0106	476	0.0144	0.0013	0.0026	614	0.2740	0.0022	0.0009	752	2.7413	0.0132	0.0004
340	0.0119	-	0.0104	478	0.0148	0.0014	0.0025	616	0.2764	0.0021	0.0009	754	2.7478	0.0122	0.0004
342	0.0113	-	0.0101	480	0.0152	0.0014	0.0025	618	0.2785	0.0020	0.0009	756	2.7542	0.0111	0.0004
344	0.0107	-	0.0099	482	0.0157	0.0013	0.0024	620	0.2810	0.0019	0.0009	758	2.7628	0.0102	0.0004
346	0.0101	-	0.0096	484	0.0162	0.0014	0.0024	622	0.2839	0.0018	0.0009	760	2.7710	0.0091	0.0004
348	0.0096	-	0.0094	486	0.0167	0.0013	0.0024	624	0.2868	0.0018	0.0008	762	2.7733	0.0081	0.0004
350	0.0091	-	0.0092	488	0.0174	0.0013	0.0023	626	0.2893	0.0017	0.0008	764	2.7742	0.0071	0.0004
352	0.0086	-	0.0090	490	0.0181	0.0013	0.0023	628	0.2922	0.0016	0.0008	766	2.7701	0.0061	0.0004
354	0.0082	-	0.0088	492	0.0189	0.0013	0.0022	630	0.2955	0.0015	0.0008	768	2.7610	0.0051	0.0004
356	0.0078	-	0.0086	494	0.0198	0.0014	0.0022	632	0.2988	0.0014	0.0008	770	2.7542	0.0042	0.0003
358	0.0075	-	0.0084	496	0.0209	0.0013	0.0022	634	0.3011	0.0013	0.0008	772	2.7482	0.0033	0.0003
360	0.0071	-	0.0082	498	0.0223	0.0013	0.0021	636	0.3038	0.0013	0.0008	774	2.7305	0.0025	0.0003
362	0.0069	-	0.0080	500	0.0238	0.0012	0.0021	638	0.3076	0.0012	0.0008	776	2.7097	0.0016	0.0003
364	0.0066	-	0.0078	502	0.0255	0.0014	0.0021	640	0.3111	0.0012	0.0008	778	2.6896	0.0009	0.0003
366	0.0064	-	0.0076	504	0.0273	0.0013	0.0020	642	0.3144	0.0011	0.0007	780	2.6590	0.0002	0.0003
368	0.0062	-	0.0075	506	0.0291	0.0014	0.0020	644	0.3181	0.0011	0.0007	782	2.6332	-0.0005	0.0003
370	0.0060	-	0.0073	508	0.0310	0.0014	0.0020	646	0.3223	0.0011	0.0007	784	2.6062	-0.0011	0.0003
372	0.0058	-	0.0071	510	0.0329	0.0013	0.0019	648	0.3263	0.0010	0.0007	786	2.5702	-0.0017	0.0003
374	0.0057	-	0.0070	512	0.0349	0.0014	0.0019	650	0.3315	0.0011	0.0007	788	2.5335	-0.0022	0.0003
376	0.0056	-	0.0068	514	0.0368	0.0014	0.0019	652	0.3362	0.0010	0.0007	790	2.4924	-0.0027	0.0003
378	0.0055	-	0.0067	516	0.0386	0.0015	0.0018	654	0.3423	0.0010	0.0007	792	2.4481	-0.0030	0.0003
380	0.0054	-	0.0065	518	0.0404	0.0015	0.0018	656	0.3508	0.0010	0.0007	794	2.4083	-0.0034	0.0003
382	0.0054	-	0.0064	520	0.0409	0.0014	0.0018	658	0.3636	0.0011	0.0007	796	2.3742	-0.0036	0.0003
384	0.0053	-	0.0063	522	0.0416	0.0015	0.0018	660	0.3791	0.0012	0.0007	798	2.3332	-0.0037	0.0003
386	0.0053	-	0.0061	524	0.0409	0.0014	0.0017	662	0.3931	0.0015	0.0007	800	2.2932	-0.0038	0.0003
388	0.0053	-	0.0060	526	0.0427	0.0014	0.0017	664	0.4019	0.0015	0.0006				
390	0.0054	-	0.0059	528	0.0423	0.0013	0.0017	666	0.4072	0.0015	0.0006				
392	0.0054	-	0.0058	530	0.0429	0.0013	0.0017	668	0.4098	0.0014	0.0006				
394	0.0054	-	0.0056	532	0.0445	0.0014	0.0016	670	0.4122	0.0014	0.0006				
396	0.0055	-	0.0055	534	0.0456	0.0013	0.0016	672	0.4150	0.0013	0.0006				
398	0.0056	-	0.0054	536	0.0470	0.0013	0.0016	674	0.4173	0.0013	0.0006				
400	0.0058	0.0009	0.0053	538	0.0480	0.0013	0.0016	676	0.4223	0.0012	0.0006				
402	0.0059	0.0014	0.0052	540	0.0495	0.0013	0.0015	678	0.4270	0.0011	0.0006				
404	0.0061	0.0014	0.0051	542	0.0503	0.0013	0.0015	680	0.4318	0.0011	0.0006				
406	0.0063	0.0016	0.0050	544	0.0527	0.0012	0.0015	682	0.4381	0.0010	0.0006				
408	0.0065	0.0015	0.0049	546	0.0544	0.0013	0.0015	684	0.4458	0.0010	0.0006				
410	0.0067	0.0015	0.0048	548	0.0564	0.0012	0.0014	686	0.4545	0.0009	0.0006				
412	0.0069	0.0013	0.0047	550	0.0588	0.0013	0.0014	688	0.4646	0.0010	0.0006				
414	0.0072	0.0015	0.0046	552	0.0611	0.0012	0.0014	690	0.4760	0.0009	0.0006				
416	0.0074	0.0015	0.0045	554	0.0631	0.0013	0.0014	692	0.4903	0.0009	0.0005				
418	0.0076	0.0014	0.0044	556	0.0646	0.0012	0.0014	694	0.5071	0.0009	0.0005				
420	0.0079	0.0015	0.0043	558	0.0658	0.0013	0.0013	696	0.5244	0.0010	0.0005				
422	0.0082	0.0014	0.0042	560	0.0672	0.0012	0.0013	698	0.5470	0.0009	0.0005				
424	0.0084	0.0015	0.0042	562	0.0686	0.0012	0.0013	700	0.5722	0.0010	0.0005				
426	0.0087	0.0015	0.0041	564	0.0699	0.0012	0.0013	702	0.5995	0.0012	0.0005				
428	0.0089	0.0015	0.0040	566	0.0718	0.0012	0.0013	704	0.6303	0.0012	0.0005				
430	0.0092	0.0014	0.0039	568	0.0734	0.0012	0.0012	706	0.6628	0.0013	0.0005				
432	0.0094	0.0013	0.0038	570	0.0759	0.0012	0.0012	708	0.6993	0.0016	0.0005				
434	0.0097	0.0014	0.0038	572	0.0787	0.0012	0.0012	710	0.7415	0.0018	0.0005				
436	0.0099	0.0013	0.0037	574	0.0819	0.0012	0.0012	712	0.7893	0.0021	0.0005				

due to differences in correction for specular reflection in the apparatus and to the presence of large particulate impurities. But also large differences occur in the shape of measured spectra. In practice it is usually impossible to ascribe observed errors and differences among published spectra to single causes.

4. THE SPECTRUM OF THE SCATTERING COEFFICIENT

The scattering of light by water is described by the Einstein - Smoluchowski equation¹¹. In this theory the scattering of light is attributed to fluctuations in the dielectric constant, caused by the random motion of molecules. It is therefore also known as the fluctuation theory. The spectra of the total scattering and the volume scattering are given by the following equations:

$$\beta(90) = \frac{2\pi^2 kT}{\lambda_m^4 \beta_T} n^2 \left(\frac{\delta n}{\delta p} \right)_T^2 \frac{6+6\rho}{6-7\rho} \quad (2)$$

$$\beta(\theta) = \beta(90) \frac{(1+\rho)+(1-\rho)\cos^2(\theta)}{1+\rho} \quad (3)$$

$$b = \frac{8\pi}{3} \beta(90) \frac{2+\rho}{1+\rho} \quad (4)$$

$$\frac{\delta n}{\delta p_T}(\lambda, T_c) = \frac{\frac{\delta n}{\delta p}(\lambda, 20) \cdot \frac{\delta n}{\delta p}(633, T_c)}{\frac{\delta n}{\delta p}(633, 20)} \quad (5)$$

Table 2 List of notations used in the Einstein-Smoluchowski equation.

b	total scattering coefficient, m^{-1}
k	Boltzmann constant; $1.38054 \cdot 10^{23} \text{ JK}^{-1}$
$n(\lambda, T_c, S)$	refractive index; $1.3247 + 3.3 \cdot 10^3 \cdot \lambda^{-2} - 3.2 \cdot 10^7 \cdot \lambda^{-4} - 2.5 \cdot 10^{-6} \cdot T_c^2 + (5.2 \cdot 10^{-2} \cdot T_c) \cdot 4 \cdot 10^{-5} \cdot S$
S	salinity 0/00
T	absolute temperature, K
T_c	temperature, °C
$\beta(90)$	volume scattering function at right angle Rayleigh ratio, $m^{-1} \text{ sr}^{-1}$
$\beta(\theta)$	volume scattering function, $m^{-1} \text{ sr}^{-1}$
β_T	isothermal compressibility, Pa^{-1} ; $(5.062271 - 0.03179 \cdot T_c + 0.000407 \cdot T_c^2) \cdot 10^{-11}$
θ	angle between the direction of the incident beam and the direction of observation, sr^{-1}
λ	wavelength, nm
λ_m	wavelength, m
ρ	depolarization ratio; 0.051
$\delta n / \delta p_T(\lambda, T_c)$	pressure derivative of n , Pa^{-1}
$\delta n / \delta p_T(\lambda, 20)$	pressure derivative of n at 20 °C as a function of wavelength, Pa^{-1} ; $(-0.000156 \cdot \lambda + 1.5989) \cdot 10^{-10}$
$\delta n / \delta p_T(\lambda, T_c)$	pressure derivative of n at 633 nm as a function of temperature, Pa^{-1} ; $(1.61857 - 0.005785 \cdot T_c) \cdot 10^{-10}$

The temperature dependence of the isothermal compressibility between 5°C and 35°C is given as a quadratic fit to the data of Lepple and Millero¹⁸. The refractive index of water is a function of wavelength, temperature, salinity and pressure. Empirical equations for this dependency are given by Mcneil¹⁸ and Matthäus²⁰. The formula given by Matthäus is reliable between 400 and 650 nm. We use the approximation given by Mcneil because it covers the greater wavelength range 350-800 nm. Values

calculated with this formula agreed within 0.01 percent with the values tabulated by Sager ²¹. For remote sensing applications only atmospheric pressure needs to be considered, and the equation reduces to the form given above.

The depolarization ratio is taken from Farinato and Roswell ²² who measured at 515 nm and 20°C. No discussion of the dependence of the polarization ratio on temperature and wavelength was found in the literature. The wavelength and temperature dependency of the pressure derivative of the refractive index are given by two independent linear approximations. The temperature influence was fitted to the data tabulated by O'Conner ²³ between 5°C and 35°C for 633 nm. The wavelength dependency is a linear approximation to the data of Evtushenkov and Kiyachenko ²⁴ measured at 20°C. The temperature and wavelength dependencies are combined to describe $\delta n/\delta p$ permitting a better representation.

Table 3. Rayleigh ratio calculated using Equation 2 for $T_c=20^\circ\text{C}$, measurement and calculation by Morel ¹ using a depolarization ratio of 0.09.

Wavelength (nm)	Rayleigh ratio ($\times 10^4 \text{ m}^{-1}$)		
	Equation 2	Morel	
		measured	calculated
			Pike <i>et al.</i>
366	4.67	4.53	5.32
405	3.07	2.90	3.42
436	2.26	2.12	2.49
546	0.89	0.83	0.94
578	0.71	0.66	0.73
633	0.48		0.49

Some spectral measurements of the Rayleigh ratio ($\beta(90)$) are given by Morel ¹ and shown in Table 2. The measured Rayleigh ratio is about 4 percent lower than described by Equation 2. Also the measurements of Pike *et al.* ²⁵ at 633 nm and at 22 °C agree well.

A consequence of this input into the Einstein-Smoluchowski equation is that in the temperature dependence of the total scattering a maximum at 15°C appears. From 15 till 30 °C the scattering coefficient decreases by 2.4 percent. The influence of salinity on the scattering is not studied here. According to Morel ¹ the scattering of sea water is 30 percent higher as compared with fresh water. Result of the calculations for fixed wavelength intervals are given in Table 2. The spectrum of the scattering coefficient is shown in Figure 4.

Relative errors in the input parameters of the scattering coefficient were estimated as follows:

1. 0.1 percent in the isothermal compressibility according to Lepple and Millero ¹⁸.
2. 2 percent in the pressure derivative of the refractive index.
3. less than 0.1 percent in the refractive index
4. 20 percent in the depolarization ratio.

This results in an relative error of about 6 percent in the total scattering coefficient and in the volume scattering function.

Morel ¹ used the Einstein-Smoluchowski equation with different input parameters, this result was adopted by Smith and Baker ³. Below 680 nm the numerical results of our interpretation are lower, above 680 nm they are higher. The difference is about 10 percent at 400 nm and 3 percent at 800 nm.

5. DISCUSSION

The inherent optical properties of pure water and the accuracy with which they are known have been reviewed here. Difficulties due to the recently discovered temperature dependence have been removed. It is seen that remaining systematic errors increase with decreasing wavelength. This leads to a problem in choosing the best values in practical applications, requiring a combination of measurements from several sources and sound judgement as to what source to use, a problem that becomes more difficult with decreasing wavelength.

It is arbitrary to choose a spectrum in the low wavelength range. Since impurity of the water sample is the largest source of error, it may be expected that the lowest spectrum measured is more or less automatically the best choice. Additionally the place of minimum absorption can be used to select. This minimum shifts toward lower wavelengths with less contaminations. The measurements of Boivin *et al* were adapted in this region because they found a minimum absorption at the lowest wavelength. However in the region between 300 nm and 500 nm these very low absorption may not be important in most practical problems because other components will be present even in clear ocean waters. The values given by Smith and Baker³ below 500 nm may therefore be the lowest which can be found in clear natural waters.

At wavelengths above 600 nm the absorption of water has a significant temperature dependency. Beyond 700 nm the differences between literature values increase up to 20 percent. The temperature effect on absorption is part of the explanation for these differences. But also other differences must be present since the difference spectra do not correspond accurately to the spectrum of the temperature effect.

The consequences of these proposed absorption coefficients must be evaluated in the various fields where the optical properties of water are used. Especially the temperature dependency of the absorption coefficient on the remote sensing signal in the red and near infra-red requires attention, such as procedures in remote sensing signal processing that may be sensitive to different water temperatures, atmospheric corrections using the darkest pixel method and chlorophyll determination from passive chlorophyll fluorescence.

In this study we used reversed osmosis water. There is however a general need for knowledge on absorption and scattering coefficients of sea water. The absorption coefficient and the temperature effect in sea water have to be studied.

6. ACKNOWLEDGEMENTS

The authors thank J. Krijgsman, G.B.J. Dubelaar and G.N.M Stokman for their comments and suggestions, Pegau and Zaneveld for supplying their original measurements and A.E.R. Beeker for assistance during the measurements.

7. REFERENCES

1. A. Morel, "Optical properties of pure water and pure sea water," in *Optical aspects of oceanography*, N.G. Jerlov and E. Steenman Nielsen, Eds, Acad. Press, London and New York, 1974.
2. R.C. Smith and J.E. Tyler, "Transmission of solar radiation into natural waters," in *Photochemical and photobiological reviews* Vol. 1. K.C. Smith Ed. Plenum Press, New York, 1976.
3. R.C. Smith and K. Baker, "Optical properties of the clearest natural water (200-800 nm)," *Applied Optics* 20, 177-184, 1981.
4. A.C. Tam and C.K.N. Patel, "Optical absorption of light and heavy water by laser optoacoustic spectroscopy," *Applied Optics* 18, 3348-3358, 1979.
5. A. Morel and L. Prieur, "Analysis of variation in ocean color," *Limnology and Oceanography* 22, 709-722, 1977.
6. S.A. Sullivan, "Experimental study of the absorption in distilled water, artificial sea water, and heavy water in the visible region of the spectrum," *J. Opt. Soc. Am.* 53, 962-968, 1963.
7. J.A. Curcio and C.C. Petty, "The near infrared absorption spectrum of liquid water," *J. Opt. Soc. Am.* 41, 302-304, 1951.
8. H.R. James and E.A. Bridge, "A laboratory study of the absorption of light by lake water," *Trans. Wisconsin Acad. Sci.* 31, 1-150, 1938.

9. G.L. Clark and H.R. James 1939, "Laboratory analysis of selective absorption of light by sea water," J. Opt. Soc. Am. 29, 43-55, 1939.
10. L.P. Boivin, W.F. Davidson, R.S. Storey, D. Sinclair and E.D. Earle, "Determination of the attenuation coefficient of visible and ultraviolet radiation in heavy water," Applied Optics 25, 877-882, 1986.
11. T.I. Quickenden and J.A. Irvin, "The ultraviolet absorption spectrum of liquid water," J. Chem. Phys. 72, 4416-4428, 1980.
12. W.S. Pergau and J.R.V. Zaneveld, "Temperature-dependent absorption of water in the red and near-infrared portion of the spectrum," Limnology and Oceanography 38, 188-192, 1993.
13. J. Krijgsman, "Optical remote sensing of water quality parameters," Thesis Delft University of Technology, Delft University Press, Delft, 1994.
14. N.K. Højerlev and I. Trabjerg, "A new perspective for remote sensing measurements of plankton pigments and water quality," Univ. Copenhagen Inst. Phys. Oceanogr. rep. 51. 1990.
15. J.M.H. Hakvoort, A.E.R. Beeker and J. Krijgsman, "An instrument to measure *in situ* visible light absorption in natural waters," in Ocean Optics XII, Proc SPIE 2258, 1994.
16. See, for example, M. Kerker, *The scattering of light and other electromagnetic radiation*. Acad. Press, New York and London, 1963.
17. W.M. Irvine and J.B. Pollack, "Infrared optical properties of water and ice spheres," Icarus 8, 324-360 (1968).
18. F.K. Lepple and F.J. Millero, "The isothermal compressibility of seawater near one atmosphere," Deep Sea Research 18, 1233-1254, 1971.
19. G.T. McNeil, "Metrical fundamentals of underwater lens systems," Optical Engineering 16, 128-139, 1977.
20. W. Matthäus, "Empirische Gleitungen für den Brechungsindex des Meerwassers," Beiträge zur Meereskunde 33, 73-78, 1974.
21. G. Sager, "Zur Refraction von Licht im Meerwasser," Beiträge zur Meereskunde 33, 63-72, 1974.
22. R.S. Farinato and R.L. Roswell, "New values of the light scattering depolarization and anisotropy of water," J. Chem. Phys. 65, 593-595, 1975.
23. C.L. O'Conner and J.P. Schlupf, "Brillouin scattering in water: The Landau-Paszek ratio," J. Chem. Phys. 47, 31-38, 1967.
24. A.M. Evtushenkov and Yu.F. Kiyachenko, "Determination of the dependence of liquid refractive index on pressure and temperature," Opt. Spectrosc. 52, 56-58, 1982.
25. E.R. Pike, W.R.M. Pomeroy and J.M. Vaughan, "Measurement of Rayleigh ratio for several pure liquids using a laser and monitored photon counting," J. Chem. Phys. 62, 3188-3192, 1975.

Influences of microbial particles on oceanic optics

Curtis D. Mobley

Applied Electromagnetics and Optics Laboratory
SRI International
333 Ravenswood Avenue
Menlo Park, CA 94025-3493

Dariusz Stramski

Department of Biological Sciences
University of Southern California
Los Angeles, CA 90089-0371

ABSTRACT

Inherent and apparent optical properties as measured in case 1 waters often deviate in seemingly random ways from values predicted by bio-optical models that parameterize the microbial composition of the water in terms of the chlorophyll concentration alone. We believe that this "random" variability in optical properties can be explained in terms of variability in the detailed microbial composition of the water, and we outline a research program for testing this hypothesis. Our approach combines laboratory experiments on monospecific microbial cultures, Mie scattering calculations, and radiative transfer numerical modeling. In addition to advancing our understanding of the marine optical environment (specifically the roles played by various microorganisms), this approach provides a unique means for improving bio-optical models and for developing new optical methods or algorithms for the study of biological processes in the upper ocean. We present here a few examples from preliminary results of this work. These examples show selected measures of the underwater light field for a hypothetical ocean that consists of pure water, viruses (typically 0.07 μm in size), heterotrophic bacteria ($\sim 0.5 \mu\text{m}$), cyanobacteria ($\sim 1 \mu\text{m}$), and small diatoms ($\sim 4 \mu\text{m}$) as optically significant components.

1. INTRODUCTION

There is great variability in the inherent optical properties (IOP's) of sea water. This variability in the IOP's induces a correspondingly large variability in oceanic apparent optical properties (AOP's), even after accounting for variability in the AOP's owing to variability in the incident lighting and sea state. Case 1 waters are those waters whose IOP's are determined primarily by the biological constituents of the water. Therefore, the variability in the IOP's of case 1 waters can be traced in large part to the variability in the microbial composition of such waters.

For our present discussion, we can qualitatively divide the natural variability of IOP's and AOP's into "systematic" and "random" parts. For example, it has long been recognized that variations in phytoplankton concentration, as expressed in terms of the chlorophyll *a* concentration *Chl* (in mg m^{-3}), cause systematic variations in the spectral absorption coefficient $a(\lambda)$ (in m^{-1} ; λ is the wavelength of light). The correlation between chlorophyll concentration and absorption is the basis for statistically derived bio-optical models that predict $a(\lambda)$ given *Chl* (e.g., Morel¹). Although such bio-optical models may satisfactorily predict *average* values of $a(\lambda)$ as obtained from water samples taken at many locations and times, such models say nothing about the *variability* of $a(\lambda)$ observed in different water samples, each of which has the *same* chlorophyll concentration *Chl*. This variability in measured $a(\lambda)$ values for a given *Chl* is "random" in the sense that measured $a(\lambda)$ values differ in a seemingly random manner from the

mean values predicted by bio-optical models. Any particular measured $a(\lambda)$ value can easily differ by a factor of two from the value predicted by a bio-optical model. Similar statements can be made for other IOP's, such as the spectral scattering coefficient $b(\lambda)$ (Gordon and Morel²), and for AOP's such as the diffuse attenuation coefficient for downwelling irradiance, $K_d(\lambda)$ (Morel³).

Our interest lies in understanding the "random" variability in IOP's and AOP's. *We believe that the "random" variability also can be explained in terms of the microbial composition of case 1 waters, if we progress beyond the overly simplified parameterization of microbial composition in terms of the chlorophyll concentration alone.* Consider, for example, one water body that has relatively many small cyanobacteria and relatively few large diatoms, which together give a total chlorophyll concentration of $Chl = 0.4 \text{ mg m}^{-3}$. Another water body with relatively many large diatoms and relatively few small cyanobacteria might also have $Chl = 0.4 \text{ mg m}^{-3}$. However, we expect that the optical properties of these two water bodies will differ noticeably. This is because bulk optical properties are determined by the optical properties of the individual particles, by the particle concentrations, and by particle size distributions, any of which may differ in the two water bodies just mentioned.

It is extremely difficult to separate unambiguously the optical effects of different classes of microbes in field experiments, because natural waters invariably contain many kinds of microbes. Our approach to understanding the optical roles of different microbes is therefore based on laboratory measurements made on monospecific cultures and on numerical modeling. Both the laboratory measurements and the numerical models give us a controlled environment in which we can vary input parameters (e.g., irradiance, particle types and concentrations) at will, and then observe the results.

Quantitative studies of how the microbial composition of a water body determines its IOP's requires first that we know the optical properties of individual microbes. These single-particle absorption and scattering properties depend not only on particle type, but also on the physiological state of the particular microbe (Stramski and Morel⁴) and on the time of observation over a day-night cycle (Stramski and Reynolds⁵). Once the single-particle optical properties are known (as functions of microbe type and physiological state), they can be convolved with measured or assumed concentrations to determine the bulk absorption and scattering properties of a given water body. The way in which we do this is outlined in Section 2.

In order to study how microbial composition affects the AOP's of a water body, we can insert the bulk IOP's into a radiative transfer model that connects the bulk IOP's with environmental conditions such as incident lighting, sea state, and bottom conditions and computes the radiance distribution throughout the water body. The radiance distribution immediately yields all quantities of interest to optical oceanographers: irradiances, K -functions, reflectances, and so on. Our radiative transfer model is described in Section 3.

In Section 4 we present some illustrative results of our approach to understanding how microbial composition leads to variability in the IOP's and AOP's of natural waters.

2. INHERENT OPTICAL PROPERTIES OF MICROBIAL PARTICLES

In our simulations, the needed IOP's are built up as sums of contributions from pure water and from the various microbial components of the water body. Thus the total absorption and scattering coefficients are given by

$$a(z, \lambda) = \sum_{i=1}^M a_i(z, \lambda) \quad \text{and} \quad b(z, \lambda) = \sum_{i=1}^M b_i(z, \lambda), \quad (1)$$

respectively, and the total scattering phase function is given by

$$\tilde{\beta}(\psi, z, \lambda) = \sum_{i=1}^M \frac{b_i(z, \lambda)}{b(z, \lambda)} \tilde{\beta}_i(\psi, \lambda). \quad (2)$$

Here, z is the depth and ψ is the scattering angle. The sums over i represent sums over the M components of the water body; we consider here $M = 5$ components. Accordingly, we let $i = 1$ label pure water and let $i = 2$ label viruses (typically $0.07 \mu\text{m}$ in size), $i = 3$ label heterotrophic bacteria ($\sim 0.5 \mu\text{m}$), $i = 4$ label cyanobacteria ($\sim 1 \mu\text{m}$), and $i = 5$ label small diatoms ($\sim 4 \mu\text{m}$). Note that the component absorption and scattering coefficients generally vary with both depth and wavelength (except for pure water, $i = 1$, for which a_1 and b_1 vary only with wavelength). For simplicity we assume that the component phase functions vary only with wavelength; this is reasonable because the phase function is determined by particle type. The component scattering coefficients b_i depend on particle concentrations, which generally vary with depth. Thus the total phase function does vary with depth, because of the b_i/b weighting factors on the component phase functions.

The component absorption and scattering coefficients are determined from basic relationships between the bulk optical coefficients and the single-particle properties (e.g., Morel and Bricaud⁶):

$$a_i(z, \lambda) = N_i(z) [\sigma_a(\lambda)]_i \quad (3)$$

$$b_i(z, \lambda) = N_i(z) [\sigma_b(\lambda)]_i \quad (4)$$

where $N_i(z)$ is the numerical concentration of particles (number of particles per m^3) representing the i^{th} component at a depth z , $[\sigma_a(\lambda)]_i$ is the absorption cross section (m^2 per particle) of a "mean" particle of the i^{th} component, and $[\sigma_b(\lambda)]_i$ is similarly the scattering cross section. Although the cross sections $[\sigma_a(\lambda)]_i$ and $[\sigma_b(\lambda)]_i$ do not describe any individual particle that actually exists, these quantities are single-particle properties in the sense that upon multiplication by the particle concentration, the bulk property of the particle suspension is obtained. In the present simulations we assume that the optical cross sections for a given microbial component do not vary with depth. In general, however, these cross sections may vary with the position of the microbial population within the water column, as a result of photoadaptive changes in cells or other physiological adjustments to varying growth conditions.

We here rely on an approach to determine $[\sigma_a(\lambda)]_i$, $[\sigma_b(\lambda)]_i$, and $\tilde{\beta}_i(\psi, \lambda)$ that is a combination of laboratory experiments with microbial cultures and theoretical modeling in the area of particle optics (e.g., Stramski and Kiefer⁷). This approach can be summarized as follows. First, the microorganisms of interest (say the i^{th} component in our equations above) are grown in laboratory culture under well defined conditions (e.g., irradiance, temperature, and nutrient supply). The spectral absorption and beam attenuation coefficients of these microbial suspensions are measured with a spectrophotometer using special geometrical configurations. These measurements are usually done in the spectral region from 350 to 750 nm with a 1 nm interval. The size distribution of microorganisms and their concentration are also determined with a microscope or electronic particle analyzer. From these data, the attenuation $[\sigma_c(\lambda)]_i$ and absorption $[\sigma_a(\lambda)]_i$ cross sections of the "mean" cell representing the examined population are calculated as the ratio of the bulk optical coefficients measured on the suspensions to the concentration of cells. The scattering cross section $[\sigma_b(\lambda)]_i$ is obtained as the difference $[\sigma_c(\lambda)]_i - [\sigma_a(\lambda)]_i$.

Next, the imaginary and real parts of the refractive index of microorganisms are derived from inverse calculations based on a theory of light absorption and scattering by a homogeneous spherical particle, which includes Mie scattering theory and some approximation for absorption efficiency (e.g., van de Hulst⁸, Bohren and Huffman⁹). The input to these inverse calculations is the measured size distribution as well as the absorption and attenuation efficiency factors as determined from the measurements. Finally, once the refractive index is determined, the Mie

scattering calculations are made in a direct way (again using the measured size distribution as input) to determine the phase function $\tilde{\beta}_i(\psi, \lambda)$ of the microorganisms.

The optical cross sections and phase functions for heterotrophic bacteria, cyanobacteria, and diatoms used in this study were obtained through the above described approach. Specifically, the data on unicellular cyanobacteria represent oceanic cells of the genus *Synechococcus* (strain WH8103) grown in a nutrient-replete culture under a day-night cycle in natural irradiance (Stramski *et al.*¹⁰). For the purpose of this study, we use the average values for the optical properties of these cells based on 15 measurements made during two days over a diel cycle. The data on small diatoms were similarly obtained from a diel experiment with the marine centric diatom *Thalassiosira pseudonana* (Stramski and Reynolds⁵). We here use the optical properties of these cells averaged from 25 measurements made over a day-night cycle during three days. The data on heterotrophic marine bacteria are averages of three experiments made with natural populations of such cells grown in unenriched seawater (Stramski and Kiefer⁷). No optical measurements of marine viruses are available, so we determined the optical properties of the particles from Mie theory, assuming a reasonable size distribution and refractive index with no absorption (Stramski and Kiefer¹¹).

For brevity, we present detailed results only at a wavelength of $\lambda = 443$ nm (which is the center of one of the CZCS and SeaWiFS ocean color satellite bands), although we are performing analogous calculations throughout the visible spectrum. Table 1 shows the single-particle absorption and scattering cross sections (m^2 per particle) and "typical" and "high" concentrations (particles per m^3) in case 1 waters for the four microbial types listed above. The "typical" concentrations shown in Table 1 are average values for case 1 waters. The "high" concentrations are representative of bloom conditions for cyanobacteria and for diatoms. These concentrations are based on Stramski and Kiefer¹¹. Figure 1 shows the scattering phase functions $\tilde{\beta}_i(\psi, \lambda = 443)$, as used in Eq. (2).

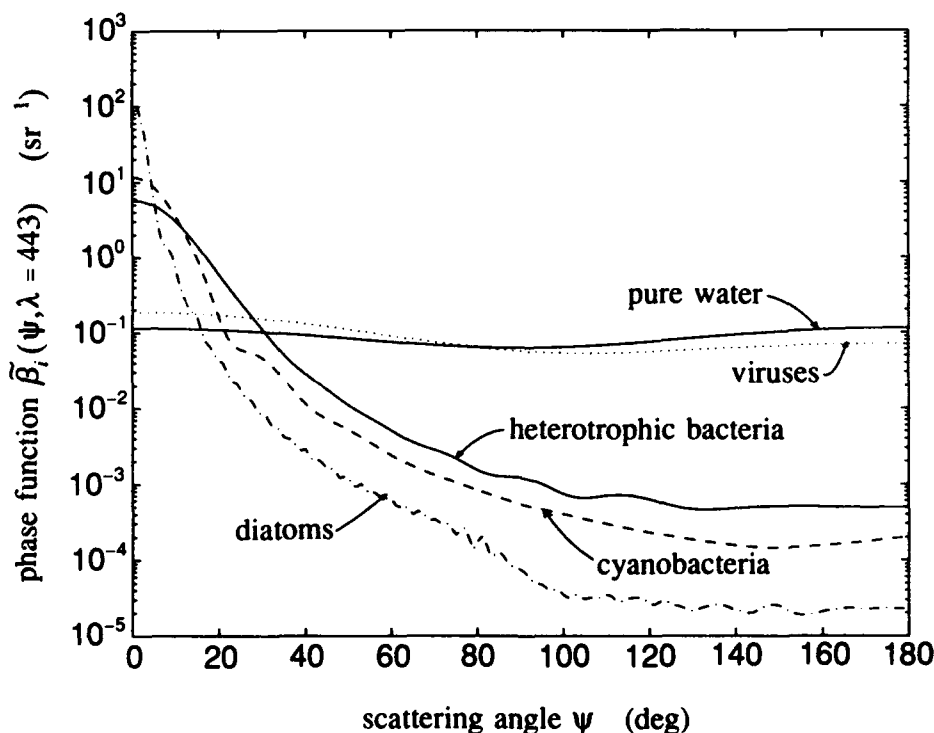


Fig. 1. Phase functions at $\lambda = 433$ nm for the five components as used in Eq. (2).

Table 1. Single-particle cross sections and albedos of single scattering at 443 nm, and concentrations, for microbial components.

component*	σ_a (m^2)	σ_b (m^2)	ω_o	typical concentration (m^{-3})	high concentration (m^{-3})
2	0.0	$4.406-18^\dagger$	1.00	$7.0+12$	$1.0+14$
3	$1.993-15$	$6.225-14$	0.97	$7.0+11$	$1.5+12$
4	$2.355-13$	$8.595-13$	0.78	$1.0+10$	$1.0+11$
5	$7.360-12$	$2.301-11$	0.76	$5.0+8$	$1.0+9$

* identified in the text

† $4.406-18$ means 4.406×10^{-18} , etc.

3. RADIATIVE TRANSFER NUMERICAL MODEL

The numerical model that we use to compute the radiance distribution is described in Mobley¹². The mathematical details of the model are given in great detail in Mobley^{13,14}. We therefore give only a qualitative description of the model here. It is compared with other numerical models in Mobley *et al.*¹⁵. The model as we use it in the present study is based on the following assumptions:

- The water body is horizontally homogeneous, but the IOP's can vary arbitrarily with depth. This reduces the problem to one spatial dimension: the depth.
- The air-water surface is represented by numerically determined radiance reflectance and transmittance functions that describe the time-averaged effects of a wind-blown sea surface that is covered by random capillary waves.
- The lower boundary of the water body can be either a Lambertian surface representing a sandy or muddy bottom at some finite depth, or an infinitely deep layer of water lying below the greatest depth of interest.
- The incident light falling onto the sea surface is specified by giving the radiance distribution of the sky, either from observed data or from analytic models of the sky radiance.
- The water does not contain any internal light sources such as bioluminescence, and inelastic processes such as fluorescence or Raman scattering are omitted.
- The radiance is monochromatic and unpolarized.

In order to solve for the radiance at a given wavelength, the model requires bulk IOP's as functions of depth, the sky radiance distribution, the wind speed (which determines the statistical nature of the random air-water surface), and the bottom type. Given this information, numerically efficient methods based on invariant imbedding theory are used to compute the full radiance distribution at prechosen depths within the water, as well as the radiance distribution leaving the water surface. Various irradiances and AOP's are obtained directly from the computed radiance distribution.

4. EXAMPLE SIMULATIONS

In order to illustrate our methods, we show results from simulations of water bodies composed of pure water plus one to four microbial components in typical or high concentrations. The five components as discussed in Section 2 and corresponding to the notation of Eqs. (1) and (2) are

- $i = 1$: pure water
- $i = 2$: marine viruses
- $i = 3$: heterotrophic marine bacteria
- $i = 4$: oceanic cyanobacteria (*Synechococcus*)
- $i = 5$: small diatoms (*Thalassiosira pseudonana*).

The data from Table 1 and Figure 1 of Section 2 provide the information necessary to construct the IOP's $a(443)$, $b(443)$ and $\beta_i(\psi, 443)$, which are needed as input to the radiative transfer model. For component 5 at a typical concentration, for example, we have

$$b_5(443) = (2.301 \times 10^{-11} \text{ m}^2) (5.0 \times 10^8 \text{ m}^{-3}) = 0.0115 \text{ m}^{-1},$$

which is about 2.4 times the corresponding scattering coefficient of pure water, $b_1(443)$. We place the sun at the zenith. The sun's direct beam contributes 70% of the total irradiance incident onto the sea surface, and a uniform sky radiance contributes the remaining 30%. The total irradiance incident onto the sea surface is set to $1 \text{ W m}^{-2} \text{ nm}^{-1}$; all radiometric quantities (such as L_u and E_o , discussed below) are scaled to this value. The wind speed is taken to be 5 m s^{-1} (although the sea state is of little importance for the sun at the zenith). We take the water to be homogeneous (IOP's independent of depth) and infinitely deep.

Figure 2 shows the effects of typical concentrations of the individual microbial components on the scalar irradiance $E_o(z, \lambda = 443 \text{ nm})$, as simulated by the radiative transfer model. The rightmost curve is that for pure water. The curve for pure water plus viruses at a typical concentration of $7.0 \times 10^{-12} \text{ m}^{-3}$ is indistinguishable from the curve for pure water only. The curve labeled "heterotrophic bacteria" is for pure water plus a typical concentration of heterotrophic bacteria, and so on. The curve labelled "all together" is pure water plus a typical concentration of each of the four microbial components. For pure water, a depth of $z = 100 \text{ m}$ corresponds to about 1.9 optical depths; for the case of all components together, 100 m is just over nine optical depths. Figure 2 is presented to illustrate the modeling process and the ease with which we can isolate the effects of individual microbial components on radiometric quantities. These simulations took only a few minutes on a Sun SPARCStation2 computer.

Table 2 shows near-surface values of three quantities frequently used in optical oceanography. L_u is the upwelling (zenith, or nadir-viewing) radiance, i.e., the radiance heading upward into a small solid angle centered on the zenith direction. K_d is the diffuse attenuation coefficient for downwelling irradiance E_d , and $R = E_u/E_d$ is the irradiance reflectance. Each of the values as seen in Table 2 is for $\lambda = 443 \text{ nm}$ and for $z \approx 0$, i.e., just below the sea surface. Because we have placed the sun at the zenith and taken the water to be homogeneous, there is not much variation of K_d and R with depth. The table includes values computed with both typical and high concentrations for the microbial components, in selected combinations.

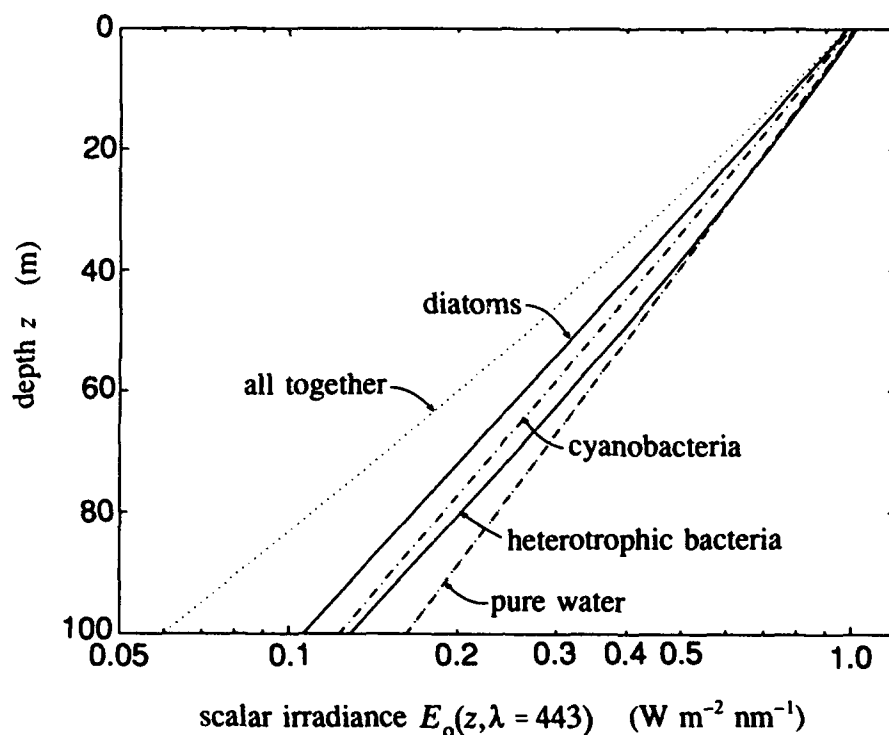


Fig. 2. Scalar irradiance for different combinations of pure water and microbial components.

Table 2. Upwelling radiance L_u , diffuse attenuation K_d , and irradiance reflectance R for various combinations of pure water and microbes. All quantities are at $\lambda = 443$ nm and at a depth just below the sea surface. The numbers in parentheses are the percentage change compared to the value for pure water seen in row 1.

simulation	L_u ($\text{W m}^{-2} \text{sr}^{-1} \text{nm}^{-1}$)	K_d (m^{-1})	R
1. pure water only	0.0136	0.0182	0.0496
2. typical viruses	0.0136 (0)	0.0182 (0)	0.0498 (0)
3. high viruses	0.0143 (+5)	0.0184 (+1)	0.0525 (+6)
4. typical heterotrophic bacteria	0.0130 (-4)	0.0201 (+10)	0.0507 (+2)
5. high heterotrophic bacteria	0.0129 (-5)	0.0222 (+22)	0.0532 (+7)
6. typical cyanobacteria	0.0119 (-13)	0.0207 (+14)	0.0437 (-12)
7. high cyanobacteria	0.0057 (-58)	0.0431 (+137)	0.0299 (-40)
8. typical diatoms	0.0111 (-18)	0.0221 (+21)	0.0405 (-18)
9. high diatoms	0.0094 (-31)	0.0260 (+43)	0.0343 (-31)
10. typical all together	0.0098 (-78)	0.0264 (+45)	0.0381 (-23)
11. cyanobacteria bloom	0.0053 (-61)	0.0488 (+168)	0.0212 (-57)
12. diatom bloom	0.0064 (-53)	0.0402 (+212)	0.0251 (-49)

A brief discussion of Table 2 is in order. The first row in the body of Table 2 gives values as computed for pure water only. The second row gives values for pure water plus a typical concentration of marine viruses; there is no significant change in L_u , K_d , or R compared to the pure-water case. At a high concentration, we see that viruses increase L_u by about five percent, K_d by one percent, and R by six percent, over the pure-water case. These increases are a consequence of the increase in scattering caused by the viruses: more light is now being backscattered from downward to upward directions, and so L_u and R increase. The loss of downwelling radiance to backscattering results in a slight increase in K_d . We note next (lines 4 and 5) that the addition of heterotrophic bacteria to pure water decreases L_u at 443 nm by a few percent. We are now seeing the combined effects of both absorption by the heterotrophic bacteria (recall that the viruses were assumed to be nonabsorbing) and of the dramatic change in the shape of the phase function of the heterotrophic bacteria compared to that of the viruses (which is very similar to that of pure water). The reflectance R increases with the addition of the heterotrophic bacteria. Pure water plus cyanobacteria (lines 6 and 7) leads to a decrease in both L_u and R . These qualitative differences in the behavior of R for heterotrophic and cyanobacteria are presumably a consequence of the fact that the cyanobacteria are relatively more efficient absorbers on a per-cell basis than are the heterotrophic bacteria. Recall from Table 1 that the single-scattering albedos are $\omega_0 = 0.97$ and $\omega_0 = 0.78$ for heterotrophic and cyanobacteria, respectively. Even trends such as the increase or decrease in R are difficult to predict *a priori*, and quantitative evaluations of such changes can be obtained only through numerical modeling.

The remaining lines of Table 2 show the results for pure water plus diatoms, for pure water plus all microbial components together at typical concentrations, and for two simulated phytoplankton blooms. To simulate the blooms, we simulated the water body as having all microbial components present at typical concentrations (as in line 10) except for the bloom component, which was set to the corresponding high concentration seen in Table 1.

We emphasize that even the qualitative behavior (e.g., increasing or decreasing L_u or R) seen in Table 2 holds only for these particular simulations at this wavelength. Even the trends can be opposite at other wavelengths. For example, simulations at $\lambda = 660$ nm using exactly the same microbial components and concentrations always show increases in L_u and R , compared to the pure-water values. This is presumably because the microbes remain highly scattering at 660 nm: the single-scattering albedos ω_0 are greater than 0.88 for all microbes.

We next consider simulations in which we hold the chlorophyll concentration Chl constant as we vary the concentrations of cyanobacteria and diatoms. In the first simulation, we take typical concentrations of all microbes except for the diatoms. For the diatoms, we use a concentration of $1.13 \times 10^9 \text{ m}^{-3}$, which is typical of bloom conditions. The average per-cell chlorophyll concentrations for cyanobacteria and diatoms as measured in the laboratory studies described in Section 2 are

$$Chl^*(\text{cyano}) = 5.235 \times 10^{-12} \text{ mg cell}^{-1}$$

and

$$Chl^*(\text{diatom}) = 3.091 \times 10^{-10} \text{ mg cell}^{-1}.$$

Thus the total chlorophyll concentration of the water is

$$\begin{aligned} Chl &= \left(5.235 \times 10^{-12} \frac{\text{mg}}{\text{cell}} \right) \left(1.00 \times 10^{10} \frac{\text{cells}}{\text{m}^3} \right) + (3.091 \times 10^{-10}) (1.13 \times 10^9) \\ &= 0.40 \text{ mg m}^{-3}. \end{aligned}$$

In the second simulation, we set the diatom concentration to its typical value and increased the cyanobacteria concentration to $4.7 \times 10^{10} \text{ m}^{-3}$, which is representative of a weak bloom. The chlorophyll concentration remains at

$$\text{Chl} = (5.235 \times 10^{-12}) (4.7 \times 10^{10}) + (3.091 \times 10^{-10}) (5.0 \times 10^8) = 0.40 \text{ mg m}^{-3}.$$

Table 3 shows the results at both $\lambda = 443$ and 660 nm for these two simulated blooms. There are several points to note in these results. First, at 443 nm both types of bloom significantly *decrease* L_u and R , from their pure-water values, whereas at 660 nm the blooms *increase* L_u and R . This is an example of the trends mentioned in the discussion of Table 2. But note also that when going from a diatom bloom to a cyanobacteria bloom, L_u and R *decrease* at 443 nm , whereas they *increase* at 660 nm .

Table 3. Results of simulations for which the chlorophyll concentration is held fixed at $C = 0.40 \text{ mg m}^{-3}$.

simulation	L_u ($\text{W m}^{-2} \text{ sr}^{-1} \text{ nm}^{-1}$)	K_d (m^{-1})	R
<u>$\lambda = 443 \text{ nm}$</u>			
pure water only, for reference	0.0136	0.0182	0.0496
typical cyanobacteria, high diatoms	0.00815	0.0313	0.0317
typical diatoms, high cyanobacteria	0.00721	0.0356	0.0285
<u>$\lambda = 660 \text{ nm}$</u>			
pure water only, for reference	9.300-5*	0.4164	3.365-4
typical cyanobacteria, high diatoms	1.191-4	0.4209	4.947-4
typical diatoms, high cyanobacteria	1.239-4	0.4207	5.315-4

* 9.300-5 means 9.300×10^{-5} , etc.

5. FUTURE WORK

The preceding discussion is intended only to illustrate our modeling process. This work is continuing at other wavelengths. We already have available the single-particle cross sections from 350 nm to 750 nm and the phase functions at ten selected wavelengths for the four microbial types discussed above. A proper simulation of case 1 waters must include additional microbial types, in particular the larger phytoplankton. Determination of the needed cross sections and phase functions is in progress.

Moreover, it is not sufficient to consider only average single-particle optical properties for a given microbial type or species, as we have done above. Stramski and Reynolds⁵ have shown, for example, that the single-particle absorption and scattering cross sections of *Thalassiosira pseudonana* can vary by 35 percent and 80 percent, respectively, between their minima near sunrise and their maxima near sunset. The coming availability of such data will allow us to study the optical consequences of intra-species variability, just as we have done above for inter-species variability in particle concentrations. More realistic simulations can also involve non-uniform vertical distributions of the concentrations of various microorganisms.

We note also that our methods are equally applicable to the analysis of case 2 waters, which may contain high concentrations of dissolved substances and mineral particles.

6. ACKNOWLEDGMENTS

This research was supported by the Oceanic Optics Program of the Office of Naval Research under contract number N00014-94-C-0114. Preparation of this paper was supported in part by Internal Research and Development funds from SRI International to author CDM. Michele Freed of SRI assisted greatly with the computations and figure preparation.

7. REFERENCES

1. A. Morel, "Light and marine photosynthesis: a spectral model with geochemical and climatological implications," *Prog. Oceanogr.*, **26**, 263-306, 1991.
2. H. R. Gordon and A. Morel, *Remote assessment of ocean color for interpretation of satellite visible imagery, A review*, in *Lecture notes on coastal and estuarine studies*, Springer Verlag, Berlin, 1983.
3. A. Morel, "Optical modelling of the upper ocean in relation to its biogeochemical matter content (Case 1 waters)," *J. Geophys. Res.* **93**(C9), 10749-10768, 1988.
4. D. Stramski and A. Morel, "Optical properties of photosynthetic picoplankton in different physiological states as affected by growth irradiance," *Deep-Sea Res.*, **37**, 245-266, 1990.
5. D. Stramski and R. A. Reynolds, "Diel variations in the optical properties of a marine diatom," *Limnol. Oceanogr.*, **38**(7), 1347-1364, 1993.
6. A. Morel and A. Bricaud, "Inherent optical properties of algal cells including picoplankton: Theoretical and experimental results," in *Photosynthetic picoplankton*, T. Platt and W.K.W. Li, editors, *Can. Bull. Fish. Aquat. Sci.*, **214**, 521-555, 1986.
7. D. Stramski and D. A. Kiefer, "Optical properties of marine bacteria," in *Ocean Optics X*, R.W. Spinrad, editor, *Proc. SPIE* **1302**, 250-268, 1990.
8. H. C. van de Hulst, *Light scattering by small particles*, John Wiley and Sons, New York, 1957.
9. C. F. Bohren and D. R. Huffman, *Absorption and scattering of light by small particles*, John Wiley and Sons, New York, 1983.
10. D. Stramski, A. Shalapyonok, and R. A. Reynolds, "Optical characterization of oceanic unicellular cyanobacteria grown under a day-night cycle in natural irradiance," *J. Geophys. Res.* (submitted), 1994.
11. D. Stramski and D. A. Kiefer, "Light scattering by microorganisms in the open ocean," *Prog. Oceanogr.*, **28**, 343-383, 1991.
12. C. D. Mobley, "A numerical model for the computation of radiance distributions in natural waters with wind-roughened surfaces," *Limnol. Oceanogr.*, **34**(8), 1473-1483, 1989.
13. C. D. Mobley, "A numerical model for the computation of radiance distributions in natural waters with wind-roughened surfaces," *NOAA Tech. Memo. ERL PMEL-75*, Pacific Mar. Env. Lab., Seattle, WA, 195 pp., Jan. 1988.
14. C. D. Mobley, *Light and Water: Radiative Transfer in Natural Waters*, Academic Press, San Diego, 592 pp, 1994.
15. C. D. Mobley, B. Gentili, H. R. Gordon, Z. Jin, G. W. Kattawar, A. Morel, P. Reinersman, K. Stamnes, and R. H. Stavn, "Comparison of numerical models for computing underwater light fields," *Appl. Optics*, **32**(36), 7484-7504, 1993.

Analytic phase function for ocean water

G.R. Fournier and J. L. Forand

Defence Research Establishment Valcartier
Courcellette, Quebec, G0A 1R0, Canada

1. ABSTRACT

Using a modified form of the anomalous diffraction approximation we have been able to derive in closed form an analytic expression for the phase function of Mie scatterers integrated over an inverse power law (Junge) size distribution. The analysis explains the apparent singularity seen experimentally at the forward scattering angle. Simple relationships are also derived that relate the inverse power law as a function of scattering angle in the near forward direction to the power law of the size distribution. The parameters of the formula are the relative index of refraction and the inverse power of the size distribution. A comparison is given between the analytic formula and exact integration of the Mie scattering for spheres. This new phase function is used in the analysis of forward angle transmissometer-nephelometer data collected by DREV in the Arctic, Atlantic and Pacific.

2. INTRODUCTION

Many empirical formulae have been suggested as empirical fits to the phase function of oceanic waters¹⁻⁷. They are often used in models of the light field and in analyses of optical system performance. Some work has also been carried out on fitting experimental phase functions to the exact Mie scattering solution numerically integrated over assumed or measured particle size distributions⁸⁻¹². The former solutions have the advantage of simplicity and analyticity. They allow some progress to be made in the treatment of difficult multiple scattering problems. However the parameters used and the forms chosen are not directly based on the physics of the problem. In general, no information about physical parameters such as the mean index of refraction or the particle size distribution can be extracted. The latter exact Mie solutions allow one to extract some information about the physical parameters from the phase functions. These solutions, being purely numerical, are extremely inconvenient to use when dealing with light propagation problems. The present work tries to address this dichotomy by using a simple set of approximations to derive from the basic physics an analytic phase function whose parameters can be related to a limited set of physically meaningful quantities.

3. DERIVATION OF THE PHASE FUNCTION

In order to obtain the phase function of an ensemble of spherical particles one must perform the following integral.

$$\beta(\theta) = \int_0^{\infty} \pi r^2 Q_s(x) P(\theta, x) F(r) dr \quad (1)$$

In equation 1, r is the particle radius and $x = 2\pi r/\lambda$, the particle size parameter. In this

case λ is the wavelength of the illuminating source. $Q_s(x)$ is the scattering efficiency which is defined as the ratio of the particle scattering cross-section to the geometric cross-section. $P(\theta, x)$ is the single particle scattering function normalized to unity when integrated over 4π steradians. $F(r)$ is the particle size distribution function.

It has been noted that to a first approximation the measured particle size distributions in the ocean follow an inverse power law (Junge distribution).

$$F(r) = \frac{C}{r^\mu}$$

Assuming a distribution of this type it is instructive to write equation 1 in terms of the particle size parameter x .

$$\beta(\theta) = C \left(\frac{2\pi}{\lambda} \right)^{\mu-3} \pi \int_0^\infty Q_s(x) P(\theta, x) x^{2-\mu} dx \quad (2)$$

It is interesting that, as was noted by Morel⁸, equation 2 predicts an inverse power relationship as a function of wavelength for the total scattering coefficient and that this is purely a property of the distribution function, independent of the particle shape. The only requirement is that the index also be independent of wavelength over the range of interest.

A second important conclusion can be drawn immediately from an analysis of equation 2: the phase function will be infinite in the forward direction ($\theta = 0$). This singularity occurs because in the large particle limit, $Q_s(x) = 2$ as required by Babinet's principle and $P(0, x) \propto x^2$. This last relationship is due to the fact that the width of the central forward diffraction peak of a finite object narrows inversely as the square of the size parameter and therefore the normalized amplitude of the scattering at $\theta = 0$ must increase as the square of x . It should be noted that this scaling is due to the wave nature of light and will apply even in the case of irregularly shaped finite particles with the proviso that the size parameter be replaced by some effective size parameter such as that of the volume equivalent sphere. Therefore, for any inverse power particle size distribution such that $3 \leq \mu \leq 5$, $\beta(0) \rightarrow \infty$.

From an analysis of equation 2 we can show that for small finite angles the scattering coefficient approaches infinity as an inverse power of θ . Chen¹³ has recently shown that for large particles with modest indices of refraction

$$P(\theta, x) = N(x)p(2x \sin(\theta/2)) \quad (3)$$

to a good approximation. $N(x)$ is the normalization factor obtained when one integrates the scattering function over the sphere and $p(z)$ is the unnormalized scattering function. If we now define two new variables $u = 2 \sin(\theta/2)$ and $z = xu$ and substitute them in equation 2, we obtain:

$$\beta(\theta) = C \left(\frac{2\pi}{\lambda} \right)^{\mu-3} \pi \frac{1}{u^{3-\mu}} \int_0^\infty Q_s(z/u) N(z/u) p(z) z^{2-\mu} dz. \quad (4)$$

The angular dependence in the kernel of equation 4 is now contained in the normalization factor $N(z/u)$ and in $Q_s(z/u)$. As mentioned previously for large particles which dominate

the scattering near the forward direction $Q_s = 2$ and $N(z/u) \propto z^2/u^2$. It therefore immediately follows by substitution of these expressions into equation 4 that in the near forward direction

$$\beta(\theta) \propto \frac{1}{u^{5-\mu}} \quad (5)$$

Since $u \rightarrow \theta$ for small values of θ the near forward scattering varies as an inverse power of θ . This corresponds to the small angle scattering behavior seen experimentally¹⁴. This behavior at and near $\theta = 0$ means that when a perfect nephelometer is operated very near the forward direction it will measure its own diffraction limit as the point where a roll over from the inverse power law occurs.

The conclusions we have reached are different from those of Morel⁸. The discrepancy arises because he has not taken into account the x^2 normalization factor in $P(0, x)$. For $\mu = 5$ the rate of divergence of $\beta(0)$ as a function of the upper limit of the integral in equation 2 is logarithmic. It is therefore extremely difficult to verify convergence numerically by integrating the phase function given by a Mie code over a particle distribution. Increasing the upper limit of integration by an order of magnitude only increases $\beta(0)$ by a small factor. Given the limited computer resources available at the time, the statements by Morel about the numerical convergence of $\beta(0)$ are perfectly understandable.

The relative index of oceanic particles is generally close to unity. This is precisely the regime where anomalous diffraction theory applies¹⁵. A simple expression for $Q_s(x)$ can be obtained in this regime. For real values of the relative index n ,

$$Q_s(x) = 2 - (4/\rho) \sin \rho + (4\rho^2)(1 - \cos \rho). \quad (6)$$

$\rho = 2(n - 1)x$ is the phase difference between an unscattered ray and the central ray through the particle. Equation 6 predicts a series of gentle oscillations that ultimately damp down to a constant value of 2 for large ρ . Although $Q_s(x)$ has a relatively simple expression, it does not lead to a simple expression when one tries to further integrate equation 2. We therefore replace it by the following approximate expression.

$$Q_s(x) = \frac{\rho^2/2}{(1 + \rho^2/4)} \quad (7)$$

This expression has the same asymptotes as equation 6 for both small and large particle sizes but does not model the oscillations. The hope is that since we will be performing an integral over a Junge distribution the contribution of the oscillations will be minimized. More accurate approximations could be used but at the cost of increased complexity in the final result.

The phase function is more difficult to model even in the anomalous diffraction approximation. For spheres it leads in general to expressions that cannot be reduced to simple functions¹⁵. However, Van de Hulst has shown that in the limiting case of small ρ the functional form of the anomalous diffraction phase function reduces to the same functional form as that given by Rayleigh-Gans theory. In the opposite limit of large ρ , the anomalous diffraction phase function converges for moderate angles to the standard diffraction theory result. These results have recently been confirmed by Klett¹⁶ and Chen¹³. Klett also shows

that polarization is maintained in the anomalous diffraction approximation. This means that all phase functions for unpolarized light will have the standard multiplication factor of $(1 + \cos^2 \theta)/2$. Note that this factor is independent of particle size and can therefore be immediately taken outside the integral for $\beta(\theta)$. Both the Rayleigh-Gans and the diffraction formulae involve Bessel functions. As in the case of the extinction efficiency these do not lead to simple results when the integral is carried out in equation 2. We have chosen to approximate the Rayleigh-Gans expression by a function which models the central peak. The resulting normalized phase function is given by

$$P(\theta, x) = \frac{1}{4\pi} \frac{(1 + 4x^2/3)}{(1 + u^2 x^2/3)}. \quad (8)$$

$$u = 2 \sin(\theta/2) \quad (9)$$

Substituting equations 7 to 9 into equation 2, performing a partial fraction decomposition of the kernel and integrating leads to the following result

$$\beta(\theta) = C\pi \left(\frac{2\pi(n-1)}{\lambda} \right)^{\mu-3} \frac{1 + \cos^2 \theta}{8 \sin(-\pi v)} \left[\frac{1}{(1 - \delta^2)\delta^v} \right] \\ \left([v(1 - \delta) - (1 - \delta^v)] + \frac{4}{u^2} [(1 - \delta^{v+1}) - (v+1)(1 - \delta)] \right). \quad (10)$$

Where

$$v = \frac{3 - \mu}{2} \quad (11)$$

and

$$\delta = \frac{u^2}{3(n-1)^2}. \quad (12)$$

4. DISCUSSION

From equations 10 to 12 it is easy to show that in the limit of small angles we obtain the same result as equation 5. We notice that the constant of proportionality depends on all the parameters but the inverse power ν of the phase function near $\theta = 0$ only depends on the inverse power μ of the particle size distribution function.

$$\nu = 5 - \mu \quad (13)$$

The slope of the phase function near $\theta = 0$ contains information only about the power law of the particle size distribution. As was mentioned previously the variation of the total scattering coefficient b will also be an inverse power γ of the wavelength.

$$\gamma = \mu - 3 \quad (14)$$

Equations 13 and 14 can be used to relate the wavelength dependence of the total scattering coefficient to the logarithm of the slope of the phase function as a function of angle in the near forward direction.

$$\gamma = 2 - \nu \quad (15)$$

We are currently attempting to verify this important relationship by using the experimental results of the NEARSCAT⁴ transmissometer-nephelometer. Figure 1 is a graph of γ against ν where the solid line is the theory and the squares are the data points from NEARSCAT. The dashed line is the least squares fit to the data. The slope for the two lines are the same but the intercept has a positive offset of .25 which we cannot explain at this time.

Figure 2 is a graph of the results of equation 10 plotted against numerical computations using both the full anomalous diffraction model and calculations from a Mie code. The index was 1.05 and the particle size power law had an exponent of 3.5. The expressions were integrated using an order 512 gaussian integration scheme from $x = .2$ to $x = 4000$. The results are not normalized. Both the Mie and the anomalous diffraction approximation were still not converged. In order to fully converge the computations special versions of the Mie code valid to $x = 100,000$ are required. We are currently working on improving the numerical algorithms in order to be able to compare our theory with properly converged Mie results. This illustrates the difficulty one can encounter when trying to estimate from theory the scattering behavior near $\theta = 0$.

Figure 3 is a graph of the experimental data of Petzold¹⁴ for San Diego harbor. The solid line is a fit to the data using equation 10. We chose this data because the scattering is almost exclusively due to particles. In this case the contribution of the water background scattering is negligible. The value of μ in equation 10 was chosen by using the measured slope as a function of θ ($\nu = 1.346$) in equation 13. The index was varied to obtain a best visual fit ($n = 1.12$). The absolute values were normalized at $\theta = .1^\circ$. The value of 1.12 for the mean index of refraction is compatible with the one given by Mie code integrations.

5. CONCLUSIONS

We have proven that for an inverse power particle size distribution there exists a singularity at $\theta = 0$ for all powers μ such that $3 \leq \mu \leq 5$. We have also shown that under mild restrictions, for small angles $\beta(\theta) \propto 1/\theta^{5-\mu}$. This leads to an interesting relationship between the inverse power of the small angle scattering and the inverse power of the total scattering coefficient as a function of wavelength. We have begun to verify this relationship using experimental data from our small angle nephelometer-transmissometer. We have derived a simple approximate parametric form for the oceanic phase function. We have attempted to compare this form with both Mie calculations and experimental data. Because of the difficult problems of numerical convergence our comparison with Mie results has met with limited success. We are currently trying to reformulate the numerical integration in a way that would allow direct comparisons to be made at more modest cost in computing time. The experimental fit gave encouraging results and equation 10 can be used for this purpose. The accuracy of the mean index values obtained is still up to debate at this time.

It should be noted in passing that the reality of the inverse power behaviour of scattering as a function of θ at small angles is a measure of the remarkable size extent of the Junge distribution. The reasons for the enormous apparent range of validity of this behavior are far from clear. Water turbulence, which would have an inverse power spectrum of $1/x^{11/3}$, could be involved. These effects need careful further study.

REFERENCES

1. L. Henyey and J. Greenstein, "Diffuse radiation in the galaxy", *Astrophys. J.*, Vol. 93, pp. 70-83, 1941.
2. D. Arnush, "Underwater light-beam propagation in the small-angle scattering approximation", *J.O.S.A.*, Vol. 62(9), pp. 1109-1111, 1972.
3. L.O. Reynolds and N.J. McCormik, "Approximate two-parameter phase function for light scattering", *J.O.S.A.*, Vol. 70(10), pp. 1206-1212, 1980.
4. G.R. Fournier, L. Forand, G. Pelletier and P. Pace, "NEARSCAT full spectrum narrow forward angle transmissometer-nephelometer", *Proceedings of SPIE*, Vol. 1750, San Diego, 20 July 1992.
5. W.H. Wells, "Theory of small angle scattering", in *Optics of the Sea*, AGARD Lect. Ser., No. 61, (NATO, 1973).
6. R.M. Lerner and J.D. Summers, "Monte Carlo description of time and space resolved multiple forward scatter in natural waters", *Applied Optics*, Vol. 21, pp. 861-869, 1982.
7. G.N. Plass, G.W. Kattawar and T.J. Humphreys, "Influence of the oceanic phase function on the radiance", *Journal of Geophysical Research*, Vol. 90C, pp. 3347-3351, 1985.
8. A. Morel, "Diffusion de la lumiere par les eaux de mer. Resultats experimentaux et approche theorique", in *Optics of the Sea*, AGARD Lect. Ser., No. 61, (NATO, 1973).
9. O.B. Brown and H.R. Gordon, "Two component Mie scattering models of Sargasso Sea particles", *Applied Optics*, Vol. 12, pp. 2461-2465, 1973.
10. M. Jonasz and H. Prandke, "Comparison of measured and computed light scattering in the Baltic", *Tellus*, Vol. 38B, pp. 144-157, 1986.
11. R. Reuter, "Characterization of marine particle suspensions by light scattering(I). Numerical predictions from Mie theory", *Oceanologica Acta*, Vol. 3, pp. 317-324, 1980.
12. J.R.V. Zaneveld, D.M. Roach and H. Pak, "The determination of the index of refraction distribution of oceanic particulates", *Journal of Geophysical Research*, Vol. 79, pp. 4091-4095, 1974.
13. T.W. Chen, "Simple formula for light scattering by a large spherical dielectric", *Applied Optics*, Vol. 32, pp. 7568-7571, 1993.

14. T.J. Petzold, "Volume Scattering Functions for Selected Ocean Waters," Scripps Institute of Oceanography, SIO Ref. 72-28, 1972.

15. H. van de Hulst, Light Scattering by Small Particles, Wiley, New York, 1957.

16. J.D. Klett and R.A. Sutherland, "Approximate methods for modeling the scattering properties of nonspherical particles: evaluation of the Wentzel-Kramers-Brillouin method", *Applied Optics*, Vol. 31, pp. 373-386, 1992.

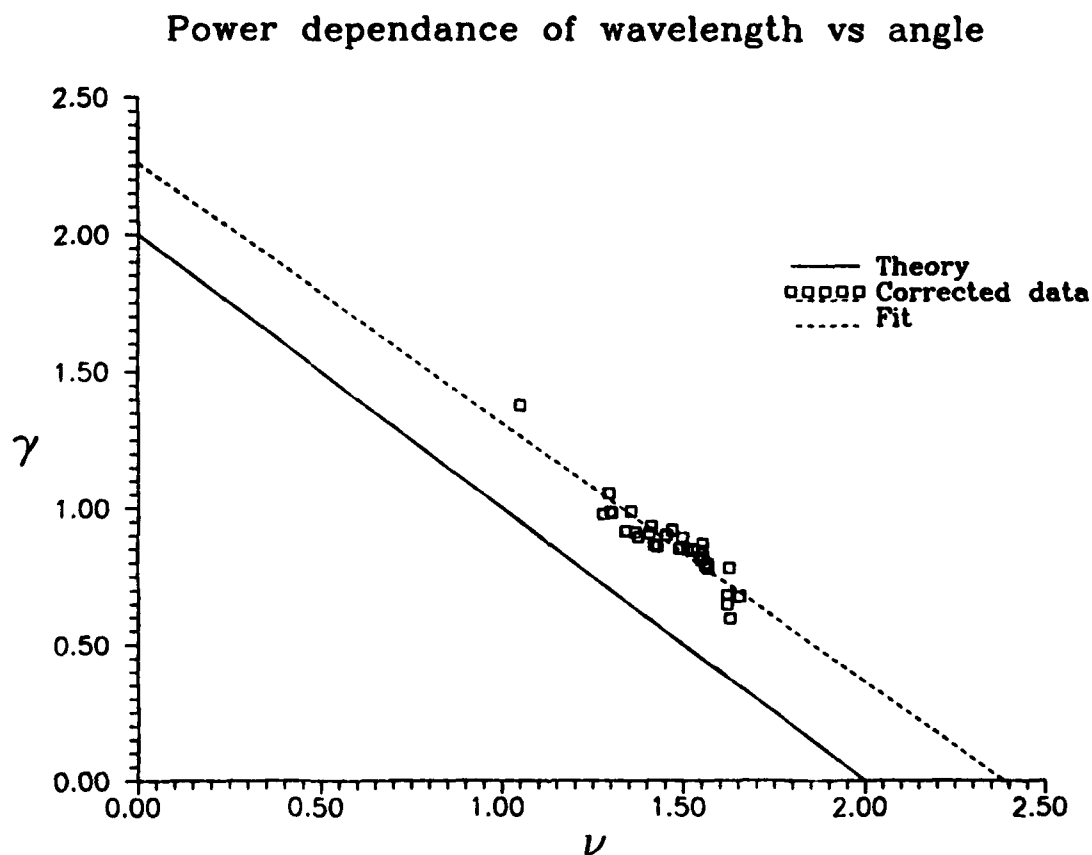


Figure 1. Plot of the inverse power γ of the total scattering coefficient as function of wavelength against the inverse power ν of small angle forward scatter.

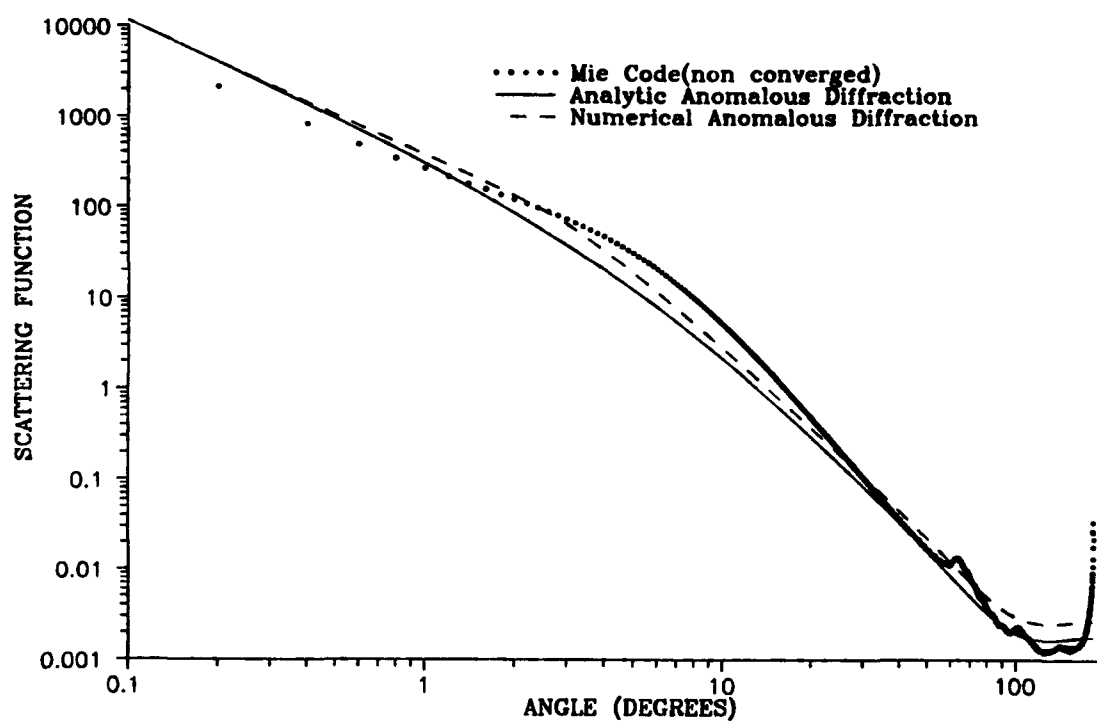


Figure 2. Comparison the analytic formula with the results of a numerically integrated Mie code and anomalous diffraction. ($\mu = 3.5, n = 1.05$)

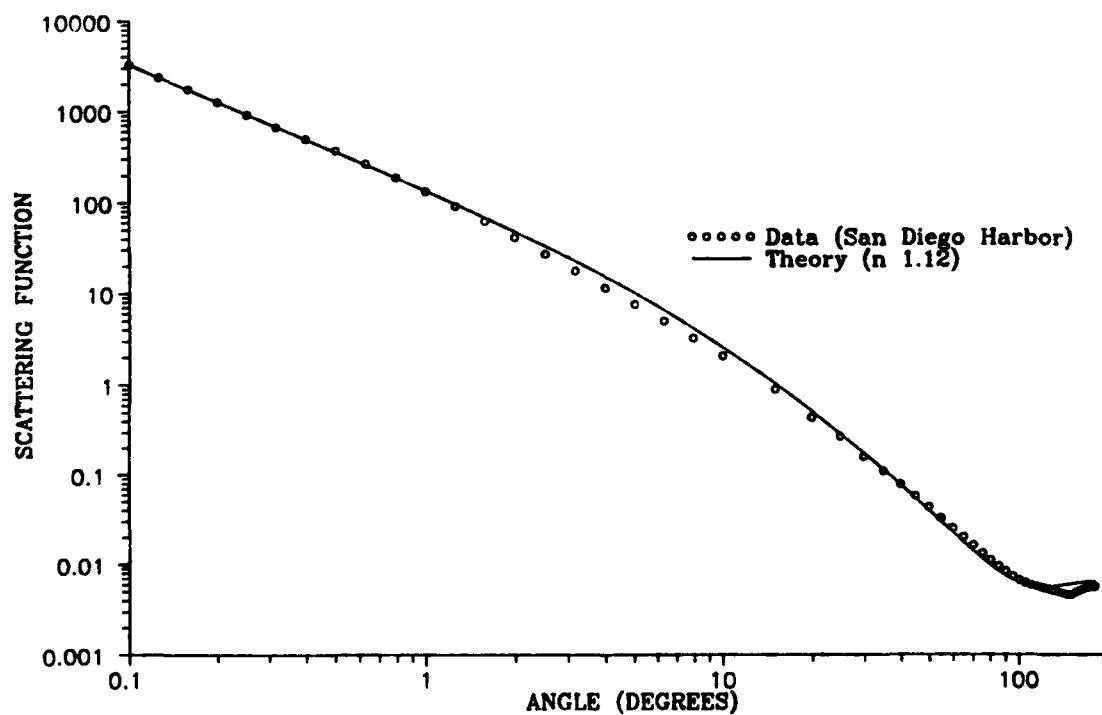


Figure 3. Comparison of the analytic formula with the Petzold data for San Diego harbor.

Geometrical light field parameters for improving remote sensing estimates of the backscattering coefficient for the marine hydrosol

Robert Hans Stavn

Department of Biology
University of North Carolina at Greensboro
Greensboro, NC 27412

Alan Dean Weidemann

Naval Research Laboratory
Code 7331
Coupled Dynamic Processes
Stennis Space Center, MS 39529

ABSTRACT

The backscattering coefficient of the marine hydrosol is recognized as an important optical parameter to extract from the radiance and irradiance data of the hydrosol. One of the more promising algorithms for extracting this parameter, utilizing remotely sensed reflectance, has been proposed by Zaneveld. He arrived at his algorithm by integrating the radiative transfer equation and simplifying the resultant geometrical shape factors of the light field in the algorithm. We have studied the implications of the simplified algorithm with the Naval Research Lab (NRL) optical model, a Monte Carlo simulation of the radiative transfer equation using standard absorption and elastic scattering coefficients for the water molecule, organic matter, and minerogenic matter. The known inputs of inherent optical properties can be used with the radiant flux outputs to check and verify algorithms that invert the measured irradiance streams for inherent optical properties. The results indicate that the inversion of the backscattering coefficient from remotely sensed reflectance is in error in the range of a 40% overestimate to a 10% underestimate of this parameter. The errors are dependent on both the solar angle and the constituents contributing to backscattering. Knowledge about the general shape of the backscattering function of a given hydrosol will be necessary for the most successful inversion algorithms.

2. INTRODUCTION

The propagation of light through the ocean, its diversion into biological and physical processes, and its reemittance into the atmosphere have been primary concerns of hydrologic optics. The algorithms related to ocean color and remote sensing are attempts to account for the various fates of light in the ocean based on the light that is sensed on a remote platform, either aircraft or satellites. A major goal is to invert the optical properties of the marine hydrosol from the properties of the remotely sensed light signal. From these data and relationships many processes can be studied, such as the primary production forced by the penetrating light field. One attempt to construct an algorithm for these purposes came from Zaneveld^{1,2}, based on radiative transfer theory. An important optical parameter to be inferred from this algorithm is the backscattering coefficient of the hydrosol, a significant factor in the generation of the nadir radiance, the major source of information for remote sensing.

The radiative transfer equation from radiative transfer theory relates the radiances and irradiances of the submarine light field to the inherent optical properties of the marine hydrosol. The inherent optical properties of the hydrosol, i.e. molecular properties, include total absorption $a_t(\lambda, z)$, total scattering $b_t(\lambda, z)$, and the volume scattering function $\beta(\gamma, \lambda, z)$. The wavelength dependence of the inherent optical properties and the light field itself will be implicit for the rest of this report. Zaneveld proposed an algorithm based on the remotely sensed reflectance, $RSR = L(\pi)/E_{\downarrow}$, the ratio of the nadir radiance to the downwelling scalar irradiance. He derived from the radiative transfer equation a functional relationship between the RSR, the total absorption coefficient, and the backscattering coefficient. The total scattering coefficient can be divided into forward scattering, b_f , and backward scattering, b_b , components. The total absorption and backscattering properties of the hydrosol are the most important in generating the remotely sensed signal. In this report we analyze Zaneveld's algorithm.

Monte Carlo methods provide the mode for analyzing the Zaneveld algorithm. We apply the NRL blue water model with appropriate extensions to account for biological components of open water and Case 1 type coastal waters of high phytoplankton and upwellings. The input parameters are the various inherent optical properties of the marine hydrosol and the output of the model is the irradiances generated by a particular hydrosol with two separate conditions of solar-skylight irradiation. Since we

know the backscattering coefficient a priori, it is possible to evaluate the Zaneveld algorithm's ability to determine the backscattering coefficient.

3. THEORY

Zaneveld formulated relationships to explain the propagation of the nadir radiance through the hydrosol derived from the radiative transfer equation. The propagation of any radiance through the hydrosol is given by:

$$\cos\theta \frac{dL(\theta, \phi, z)}{dz} = -cL(\theta, \phi, z) + L^*(\theta, \phi, z) \quad (1)$$

where

$$L^*(\theta, \phi, z) = \int_0^{2\pi} \int_0^\pi \beta(\gamma) L(\theta', \phi', z) \sin\theta' d\theta' d\phi', \quad (2)$$

and

$$\cos\gamma = \cos\theta \cos\theta' - \sin\theta \sin\theta' \cos(\phi - \phi'), \quad (3)$$

where $L^*(\theta, \phi, z)$ is the path function, $\beta(\gamma, z)$ is the volume scattering function for the angle between the θ, ϕ radiance trajectory and the θ', ϕ' trajectory of the radiance contributing a scattering component to the radiance, θ is the zenith angle, ϕ is the azimuth angle, z is the geometrical depth, and c is the beam attenuation coefficient which equals $(a_r + b_r)$, the absorption coefficient plus the total scattering coefficient. The path function represents the flux scattered into the radiance $L(\theta, \phi, z)$ from all other radiances $L(\theta', \phi', z)$ at depth z . Next restrict our consideration to the radiative transfer of the nadir radiance $L(\pi)$, no azimuth information needed

$$-\frac{dL(\pi, z)}{dz} = -cL(\pi, z) + L^*(\pi, z) \quad (4)$$

Assuming that the path function is continuous from 0 - π radians, we can divide Eq. (2) into a component integrated over the downwelling hemisphere and a component integrated over the upwelling hemisphere

$$L^*(\pi, z) = \int_0^{2\pi} \int_0^{\pi/2} \beta(\pi - \theta', z) L(\theta', \phi', z) \sin\theta' d\theta' d\phi' \quad (5)$$

$$+ \int_0^{2\pi} \int_{\pi/2}^\pi \beta(\pi - \theta', z) L(\theta', \phi', z) \sin\theta' d\theta' d\phi',$$

and

$$L^*(\pi, z) = f_b(z) \frac{b_b(z)}{2\pi} E_{\text{rad}}(z) + f_L(z) b_L L(\pi, z), \quad (6)$$

where $(\pi - \theta') = \gamma$, $f_b(z)$ is the backscattering shape factor at depth z , and f_L is the forward scattering shape factor. It is readily seen that backscattering contributes to the nadir radiance from the downwelling hemisphere and forward scattering contributes to the nadir radiance from the upwelling hemisphere. The mean value theorem of calculus allows us to define a function that replaces the volume scattering function under the first integral of Eq. (5) and remove the volume scattering function while the radiances of the downwelling hemisphere are integrated to give the downwelling scalar irradiance, E_{od} . The function that is equivalent to $\beta(\pi - \theta', z)$ is $f_b(z)b_b(z)/2\pi$ where the $f_b(z)$ backscattering shape factor accounts for the difference between the "mean backscattering function" and the volume scattering function in the backward scattering angles. The $f_b(z)$ function can be either greater than or less than one. Furthermore, the nadir radiance, $L(\pi, z)$, is removed from the second integral of Eq. (5) and the $\beta(\pi - \theta', z)$ function is integrated to give b_f . If the upwelling radiance distribution were perfectly uniform, then the nadir radiance multiplied by the forward scattering coefficient would give the forward scattered contribution to the nadir radiance. The forward scattering coefficient f_L accounts for any deviation of the above condition from the actual upwelling radiance distribution. Substituting Eq. (6) into Eq. (4)

$$-\frac{dL(\pi, z)}{dz} = -cL(\pi, z) + f_b(z)\frac{b_b(z)}{2\pi}E_{od}(z) + f_L(z)b_f(z)L(\pi, z) ,$$

recalling

$$\frac{dL(\pi, z)}{dz} = -k(\pi, z)L(\pi, z) ,$$

and substituting

$$RSR(z) = \frac{L(\pi, z)}{E_{od}(z)} = \frac{f_b(z)\frac{b_b(z)}{2\pi}}{k(\pi, z) + c(z) - f_L b_f(z)L(\pi, z)} . \quad (7)$$

In order to solve Eq. (7) we are required knowledge of the absorption coefficient and of the shape factors³. Zaneveld¹ estimated the range of the shape factors utilizing knowledge of sunny and overcast radiance distributions in the surface layers and Mie calculations estimating volume scattering functions for an assumed range of particle sizes and refractive indices. The reported range for f_b was 0.810 - 1.267 while that for f_L was 1.001 - 1.111. Zaneveld then concluded that, to within 30% error, the total backscattering coefficient could be determined if one assumed $f_b = f_L = 1.0$. The absorption coefficient would be determined by independent methods³.

Inversion attempts that ignore the geometry of the light field and the shape of the volume scattering function can be hazardous however^{4,5}. Thus, the approximation of unity for the two shape factors enumerated above is open to question, and Monte Carlo methods were employed to investigate the utility of these approximations. The NRL optical model, extended from blue water to coastal waters³, was used with known inputs for water, organic matter, and minerogenic matter. With the radiance output of this model and the known input of inherent optical properties, the f_b and f_L parameters can be calculated directly. The inversions made from Zaneveld's algorithm on the same data can be determined and compared with the known backscattering coefficient and the shape factors. The backscattering coefficient is determined by rearranging Eq. (7) after substituting $(a_T + b_T)$ for c

$$b_b(z) = \frac{L(\pi, z)}{E_{od}(z)} \cdot \frac{[k(\pi, z) + a(z) + b_T(1 - f_L)]}{[f_b/2\pi + L(\pi, z)/E_{od}(z)]} \quad (8)$$

This exact equation is then converted to the following when the shape factors have been assumed equal to unity

$$b_b(z) = \frac{L(\pi, z)}{E_{\text{sd}}(z)} \cdot \frac{[k(\pi, z) + a(z)]}{[1/2\pi + L(\pi, z)/E_{\text{sd}}(z)]} \quad (9)$$

4. METHODS

The NRL Blue Water model⁶ has been extended in this study to include events occurring from open ocean to coastal Case 1 waters. Scattering and absorption have been partitioned into the following components: algae, heterotrophic bacteria, detrital (organic), dissolved colored organic material (gelbstoff), quartz-like material, and molecular water. The model is parameterized to chlorophyll concentration and simulations were made in the range from 0.05 mg/m³ - 20.0 mg/m³. In keeping with an interest in such problems as utilizing remote sensing data to determine chlorophyll levels, the wavelength for all simulations was 440 nm. At this wavelength the effects of internal sources of radiation, water Raman scattering and organic fluorescence, were felt to be minimal so they were not included in the simulation. Internal sources can be included easily if necessary. The power of the Monte Carlo technique is the ability to study the individual effects of each and every component in the processes of absorption and scattering, then to extract which component appears to dominate. The algal component is further subdivided into two parts: a small cell component (Chlorophyll 1.0 mg/m³) and a large cell component (Chlorophyll > 1.0 mg/m³) which taken together are referred to as the "standard model." The two cell components were also used in the total chlorophyll range, however, to study the effects of the model assumptions. The criterion for division between "small" and "large" algal cells was a cellular diameter of 2µm. The small algal/cyanobacterial cell is felt to be typical of open ocean conditions and the larger cell model was felt to be typical of coastal-type conditions^{7,8}. The complete array of inherent optical properties and their sources are discussed in Weidemann and Stavn³.

The model simulations are carried out at solar zenith angles of 11° (air mass 1) and 60° (air mass 2) with 33.8% (air mass 1) and 52.4% of the global radiation due to skylight⁹. All simulations are for homogeneous conditions with a flat water/air interface.

The output of the Monte Carlo simulations, radiances and irradiances, is combined with the input of inherent optical properties to calculate values of f_u and f_L . Then the Zaneveld algorithm (Eq. 9) is used to estimate b_b for the marine hydrosol of a particular chlorophyll concentration and sky condition. The estimated b_b is then compared with the known b_b that was used in the Monte Carlo model to generate the radiance and irradiance output. The estimate of the error in b_b is made over one attenuation length ($1/K_d$) to conform with results of other studies indicating that 90% of the water-leaving radiance utilized in passive remote sensing studies is the result of interactions within the first attenuation length at the surface¹⁰. There were from 4 to 7 depth increments in each surface attenuation length in the model runs. At each depth increment b_b was estimated from Eq. (9) and the percent error was defined as

$$\bar{\epsilon} = \frac{b_b(\text{RSR}) - b_b(\text{actual})}{b_b(\text{actual})} \times 100 \quad (10)$$

The "mean percent error" was the average of calculations made from Eq. (10) over the depth increments that comprised one attenuation length.

5. RESULTS

Air mass 1 results for the mean percent error calculation and the backscattering shape factor are plotted in Fig. 1. We see that the mean percent error of the b_b estimate, for chlorophyll concentrations less than 1 mg/m³, are in the range of 35 - 48% with the values appearing to vary around the 38% level. The f_u values in the same chlorophyll range are about 1.34 - 1.41. Both the mean percent error and the f_u values drop precipitously as chlorophyll concentration increases beyond 1 mg/m³. At the maximum concentration of chlorophyll (20 mg/m³), the mean percent error drops to about 12% and the f_u value drops to about 1.02.

The air mass 2 results are plotted in Fig. 2. Here the mean percent error is about 10% at 0.05 mg/m³ chlorophyll concentration and it drops steadily to about 1% at 2 mg/m³. The f_u values in the same chlorophyll range are from about 1.04 to 0.98. The increase in chlorophyll concentration up to 20 mg/m³ results in a mean percent error of - 8% and an f_u value of about 0.85.

In Table 1. we have the results of f_u calculations partitioned among the components of the model and for air masses 1 and 2.

Each component makes a consistent contribution to the shape factor no matter what the chlorophyll concentration, so the results at 1 mg/m³ chlorophyll concentration were chosen as a "median" value of chlorophyll concentration with the individual component contributions essentially constant over the entire chlorophyll range.

Table 1. Shape Factors at 1 mg/m³ Chlorophyll, 0 m depth, 440 nm

	$f_{b \text{ total}}$	$f_{b \text{ water}}$	$f_{b \text{ quartz}}$	$f_{b \text{ bacteria}}$	$f_{b \text{ algae}}$
Air Mass 1	1.47	1.39	2.40	0.85	0.57
Air Mass 2	0.998	1.15	0.85	0.13	0.72

The f_b value for the total hydrosol changes, but the individual components do not -- the cause of the variation in the total f_b value is a weighted average of the component f_b values. The water component appears to have the strongest effect on the total f_b value while quartz-like material would be next in effect. This weighting changes with increase in chlorophyll and causes the total f_b to decrease with increase in chlorophyll as is seen in Figs. 1 and 2. The f_b values decrease from air mass 1 to air mass 2 with the exception of the algal component.

6. DISCUSSION AND CONCLUSIONS

The initial prediction of Zaneveld that the error in utilizing his algorithm would be approximately 30% is an adequate first order assertion. We see from the data in Fig. 1 and Fig. 2 however that this error range is not one of random error but rather of systematic error caused by at least two different factors: solar-sky radiance distributions and relative concentration of optically active components of the hydrosol. In open ocean water the error of estimate is consistently high (the backscattering coefficient is consistently overestimated) and greater than was predicted. As chlorophyll concentration increases and the Case 1 water becomes more coastal in quality the error of estimate for the backscattering coefficient decreases under air mass 1 conditions. The error of the backscattering estimate under air mass 2 conditions is lower in the open ocean and decreases with increase in chlorophyll; however the error becomes negative (the backscattering coefficient is underestimated). The variation in the error and the f_b coefficient is hyperbolic in the range 1 mg/m³ to 20 mg/m³ for both air mass conditions but the asymptotes differ. The algorithm based on Eq. (9) systematically overestimates the backscattering coefficient at low chlorophyll values under air mass 1 conditions and systematically underestimates the backscattering coefficient at high chlorophyll values under air mass 2 conditions.

The other pattern that appears in Figs. 1 and 2 is that the systematic error inherent in Eq. (9) can be explained in large part by the assumption that $f_b = 0$. The magnitude of the mean percent error is tracked well by the magnitude of f_b for all chlorophyll concentrations, and the f_b value will often serve to predict the error in the algorithm. At high chlorophyll concentrations the error is not predicted well by the f_b value so that the assumption about f_b is probably coming into play and making a contribution to the overall error of inverting the b_b value.

The changes in the patterns of the backscattering shape factor can be explained in part by the changes in the optically active components of the hydrosol. Quartz-like material especially has an extremely high f_b value under air mass 1 conditions and apparently is instrumental in stimulating high values of the total f_b in the open ocean, the increase in chlorophyll and thus of algae brings the f_b value down with increase of chlorophyll. Under air mass 1 conditions the components average out to an approximate value of 1.0 at 20 mg/m³ chlorophyll concentration. Under air mass 2 conditions the components of the hydrosol have a different backscattering shape factor because the radiance distribution is different and the volume scattering function is thus interacting in a new fashion with the radiance field. We must recall that the assumptions of Eq. (9) are essentially that the radiance distribution is uniform and that the backscattering lobe of all the hydrosol components is uniform. Thus we see the need for detailed examination of interactions of all possible hydrosol components in proposing remote sensing algorithms. The interactions of the hydrosol components with the radiance field are highly individual, and any increase in one component such as from an algal bloom or storm-derived delivery of excess minerogenic material into coastal waters has the potential of significantly altering the upwelling radiance signal in a complex fashion.

7. SUMMARY

1. Errors in estimating the backscattering coefficient occur systematically, not randomly.
2. Separate regimes can be identified: an open ocean high error system (Chlorophyll $< 1.5 \text{ mg/m}^3$), and a coastal/upwelling low error system (Chlorophyll $> 1.5 \text{ mg/m}^3$).
3. The geometrical shape factors associated with the submarine light field are strongly correlated with the errors of estimation of the backscattering coefficient.
4. Geometrical shape factors are a function of solar angle and particulate composition; they are required for the most accurate estimates from remote sensing.

8. ACKNOWLEDGEMENTS

We wish to acknowledge the continuing support of the Naval Research Laboratory through the Ocean Optics Characterization Program, and the Optics Program of the Office of Naval Research under grant # N00014-89-J-3137-P00005. Computer simulations are carried out in conjunction with the North Carolina Supercomputing Center, Research Triangle Park, NC, and the Primary Oceanographic Prediction System of the Naval Oceanographic Office, SSC, MS. This article represents NRL contribution # NRL/JA/7331-94-0037

REFERENCES

1. J.R.V. Zaneveld, "Remotely sensed reflectance and its dependence on vertical structure: a theoretical derivation," *Appl. Opt.*, 21, 4146-4150, 1982.
2. J.R.V. Zaneveld, "An asymptotic closure theory for irradiance in the sea and its inversion to obtain the inherent optical properties," *Limnol. Oceanogr.*, 34, 1441-1452, 1989.
3. A.D. Weidemann and R.H. Stavn, "Error in predicting hydrosol backscatter from remotely sensed reflectance," submitted to *J. Geophys. Res.*
4. R.H. Stavn and J.R.V. Zaneveld, "Geometrical shape factors in remote sensing algorithms for backscattering: partitioning and estimating," submitted to *J. Geophys. Res.*
5. R.H. Stavn and A.D. Weidemann, "Shape factors, two flow models, and the problem of irradiance inversion in estimating optical parameters," *Limnol. Oceanogr.*, 34, 1426-1441, 1989.
6. R.H. Stavn and A.D. Weidemann, "Optical modeling of ocean light fields: Raman scattering effects," *Appl. Opt.*, 27, 4002-4010, 1988.
7. A. Morel and A. Bricaud, "Inherent optical properties of algal cells including picoplankton: Theoretical and experimental results," *Can. Bull. Fish. Aquatic Sci.*, 214, 521-559, 1986.
8. A. Morel, Y.-H. Ahn, F. Partensky, D. Vaultot, and H. Claustre, "Prochlorococcus and Synechococcus: A comparative study of their optical properties in relation to their size and pigmentation," *J. Mar. Res.*, 51, 617-649, 1993.
9. D.T. Brine and M. Iqbal, "Diffuse and global solar spectral irradiance under cloudless skies," *Solar Energy*, 30, 447-453, 1983.
10. H.R. Gordon and A. Morel, "Remote assessment of ocean color for interpretation of satellite visible imagery," in *Lecture Notes on Coastal and Estuarine Studies*, R.T. Barber, C.K. Mooers, M.J. Bowman, and B. Zeitschel, eds., pp. 1-113, Springer Verlag, New York, 1983.

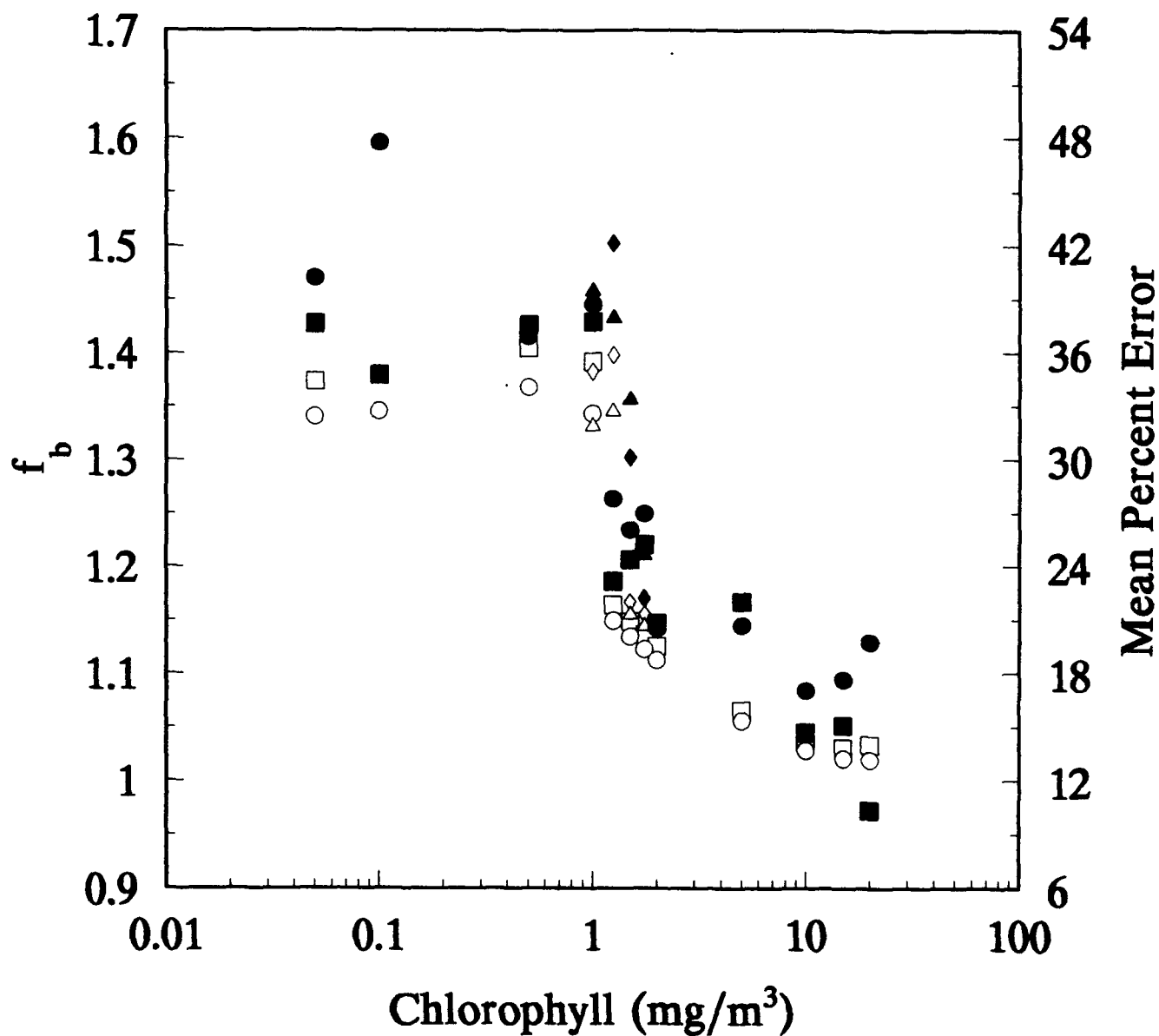


Figure 1. Backscattering shape factor f_b on left vertical axis and mean percent error of backscattering coefficient inversion on right vertical axis, air mass 1, 440 nm. For backscattering shape factor: \square = standard model with bacteria, \circ = standard model without bacteria, \diamond = small cell model with bacteria, \triangle = small cell model without bacteria. For mean percent error: \bullet = standard model with bacteria, \blacksquare = standard model without bacteria, \blacklozenge = small cell model with bacteria, \blacktriangle = small cell model without bacteria.

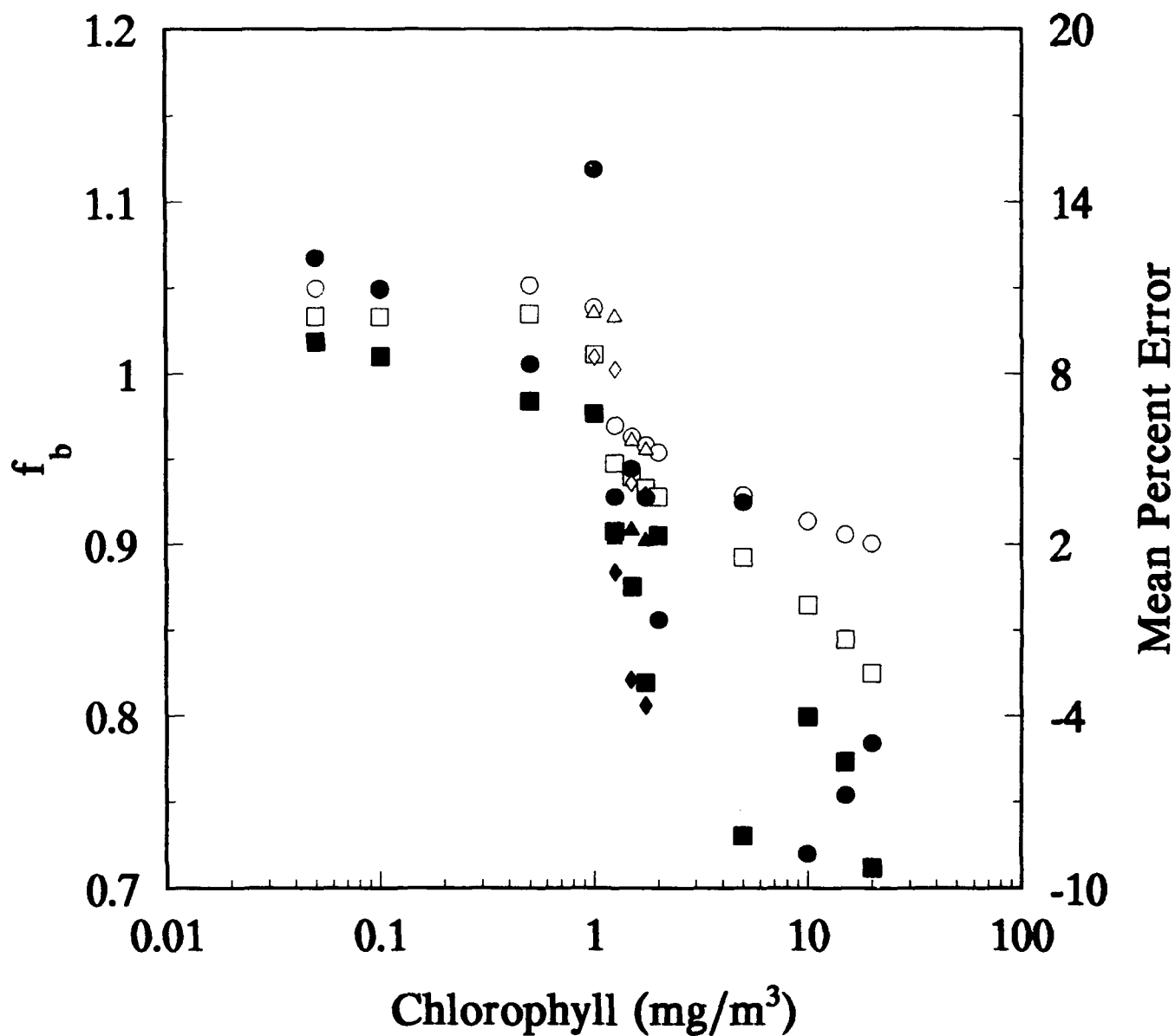


Figure 2. Backscattering shape factor f_b on left vertical axis and mean percent error of backscattering coefficient inversion on right vertical axis, air mass 2, 440 nm. For backscattering shape factor: \square = standard model with bacteria, \circ = standard model without bacteria, \diamond = small cell model with bacteria, \triangle = small cell model without bacteria. For mean percent error: \bullet = standard model with bacteria, \blacksquare = standard model without bacteria, \blacklozenge = small cell model with bacteria, \blacktriangle = small cell model without bacteria.

Comparison between different spectral models of the diffuse
attenuation and absorption coefficients of sea water.

Oleg V. Kopelevich

P.P.Shirshov Institute of Oceanology, Laboratory
of Ocean Optics, Moscow, Russia 117218

and

Yury V. Filippov

Student, Moscow Institute of Physics and Technology,
Dolgoprudny, Moscow Region, Russia 141700

ABSTRACT

The goal of this work is to verify of different spectral models of the diffuse attenuation and absorption coefficients of sea water and to work out recommendation of their using. It is shown the spectral models of the diffuse attenuation coefficient $K_d(\lambda)$ developed by Austin, Petzold, 1984 and by Volynsky, Sud'bin, 1992 correspond right each other, as well the models of Ivanov, Shemshura, 1973 and of Kopelevich, Shemshura, 1988 for calculation of the spectral absorption coefficient $a(\lambda)$ on the values of $K_d(\lambda)$. Theoretical foundation of the relation between $a(\lambda)$ and $K_d(\lambda)$ is given. The up-to-date physical model of the sea water light absorption is considered and checked by means of comparison with measured values of the attenuation coefficient at the ultraviolet and visible spectral ranges.

1. INTRODUCTION

The need for estimation of the spectral values of the sea water optical characteristic knowing only its value at a single wavelength is encountered often in practice. Especially in relation to the diffuse attenuation and absorption coefficients which spectral values determine the penetration and utilization of solar energy in upper ocean. In particular this problem arises concerning the remote sensing observations e.g. the CZCS or forthcoming SeaWiFS satellite ocean color sensors. The different spectral models of the diffuse attenuation and absorption coefficients have been developed up to date, and the comparison between them is important for their verification. For assessment of potential effects on marine phyto-plankton of increased UV radiation due to the stratospheric ozone depletion is necessary to know how the UV radiation penetrates into upper ocean, so a possibility of the extrapolation of the models to the UV region must be studied.

2. SPECTRAL MODELS OF THE DIFFUSE ATTENUATION COEFFICIENT

First spectral model of the diffuse attenuation coefficient K_d was developed by Jerlov^{1,2} in a state of the Jerlov water types. The problem was re-examined by Pelevin, Rutkovskaya³ in 1977-1979. They calculated the regression equations of the form

$$K_d(\lambda) = A(\lambda) + B(\lambda)K_d(\lambda^*), \quad (1)$$

where $\lambda^* = 500$ nm and λ ranged from 400 to 600 nm. The regression errors were less than 0.02 m^{-1} if $K_d(500) < 0.2 \text{ m}^{-1}$.

Similar approach was applied by Austin, Petzold in 1984⁴; the developed model was corroborated in 1990⁵ (the original model was based on data of 76 spectra of $K_d(\lambda)$ measured in tropical to mid-latitude waters; the

re-examination was on 83 spectra covering ocean latitudes from 24° to 77°). The regression equations were computed of the form (1); $K_d(490)$ was used as the input parameter. The spectral range was 350-700 nm with 5 nm step (values of the slope $B(\lambda)$ for 350, 355 and 360 nm were estimated by extrapolation); $K_d(490)$ values ranged from 0.025 to 0.245 m^{-1} ; standard deviations of the differences between the calculated and measured values of K_d were less than 0.03 m^{-1} for $\lambda < 650$ nm.

Volynsky, Sud'bin⁶ applied the expansion by the eigenvectors of the covariance matrix $M[K_d(\lambda_i), K_d(\lambda_j)]$ to approximate $K_d(\lambda)$ at the spectral range 410-590 nm

$$K_d(\lambda) = \overline{K_d(\lambda)} + \sum_{i=1}^n e_i \psi_i(\lambda), \quad (2)$$

where $\overline{K_d(\lambda)}$ are the mean values of $K_d(\lambda)$; $\psi_i(\lambda)$ are the eigenvectors of the covariance matrix M_{ij} ; e_i are the expansion coefficients. The total set of data included 333 spectra of $K_d(\lambda)$ and was subdivided into three subsets: 1. $K_d(500) < 0.11 m^{-1}$ ($N=177$); 2. $0.11 \leq K_d(500) < 0.6 m^{-1}$ ($N=84$); 3. Baltic Sea ($N=72$). For the joint set 1+2 the first term of the series (2) takes account 94.7% of the total dispersion, the two first terms 97.8%. It is of interest to compare the models^{4,6} with one input parameter within the range of $K_d(490)$ values comprised by the model⁴. Comparison was performed by calculating $K_d(\lambda)$ by means of the models AP⁴ and VS⁶ (the latter is Eq.(2) with $n=1$) for the selected values of $K_d(490)$ ⁴. Values of $K_d(\lambda)$ and $\psi_1(\lambda)$ were taken for the joint set 1+2⁶; the coefficient e_1 was found from (2) at the 490 nm: $e_1 = [K_d(490) - \overline{K_d(490)}] / \psi_1(490)$.

The differences $\Delta_i = K_d^{AP}(\lambda_i) - K_d^{VS}(\lambda_i)$ and ratios $\delta_i = \Delta_i / K_d^{VS}(\lambda_i)$ as well the standard deviation $s = \sqrt{1/m \sum_{i=1}^m \Delta_i^2}$ and the mean ratio $\delta = 1/m \sum_{i=1}^m \delta_i$ over the spectral range 410-590 nm were computed ($m=19$ with 10 nm step).

Table 1. The standard deviations and the mean ratios δ (comparison of the models AP and VS)

$K_d(490)$ $10^2, m^{-1}$	3	4	5	6	7	8	9	10	12	14	16	18
$s \cdot 10^2, m^{-1}$	0.5	0.5	0.4	0.4	0.3	0.3	0.3	0.3	0.4	0.5	0.6	0.7
$\delta, \%$	0.2	0.8	1.0	0.9	0.8	0.7	0.5	0.4	0.1	-0.1	-0.3	-0.5

Figure 1 shows examples of $K_d(\lambda)$ values calculated by models AP and VS for $K_d(490) = 0.03$ and 0.12 m^{-1} . As seen from Table 1 and Figure 1, the models AP and VS give results corresponding each other quite well. So we suppose both of the models are adequate for calculation of spectral values of $K_d(\lambda)$ from data at fixed wavelength. Advantage of the model AP is the more broad spectral range spread by that; of the model VS is a possibility of more accurate approximation with two or more eigenvectors in (2) if the values of K_d are known at two or more wavelengths.

3. RELATION BETWEEN $a(\lambda)$ AND $K_d(\lambda)$

Simple formula connecting a to K_d was given by Ivanov, Shemshura⁷

$$a = 0.81 K_d, \quad (3)$$

its accuracy is not worse than 20%. Kopelevich, Shemshura⁸ presented relation between a and K_d at the spectral range 410-590 nm in the form of linear regression

$$a(\lambda) = E(\lambda) + F(\lambda) K_d(500). \quad (4)$$

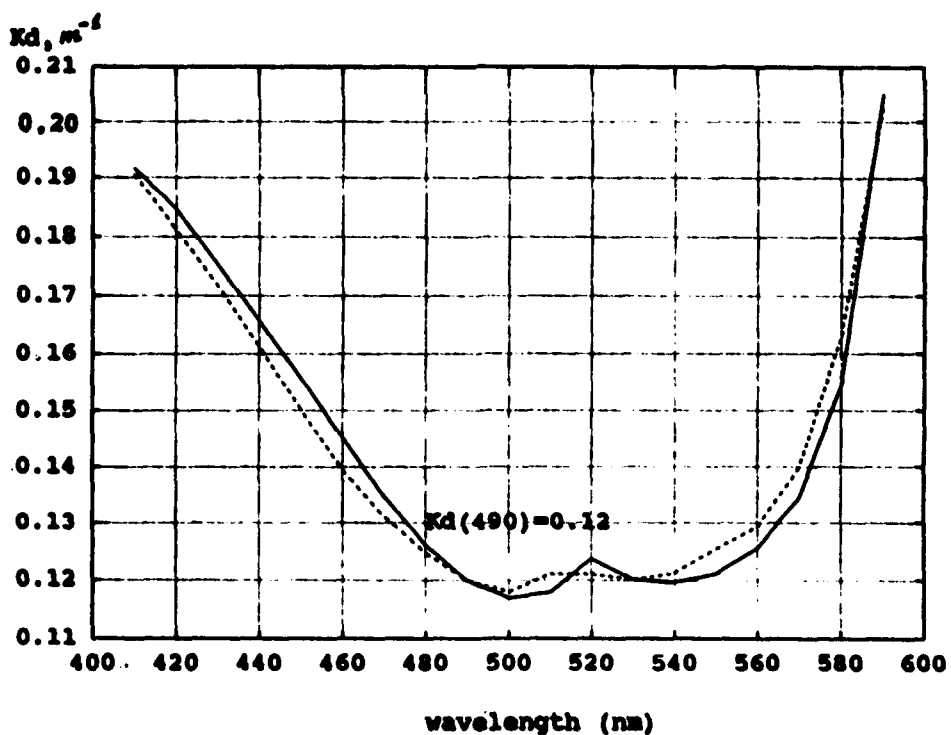
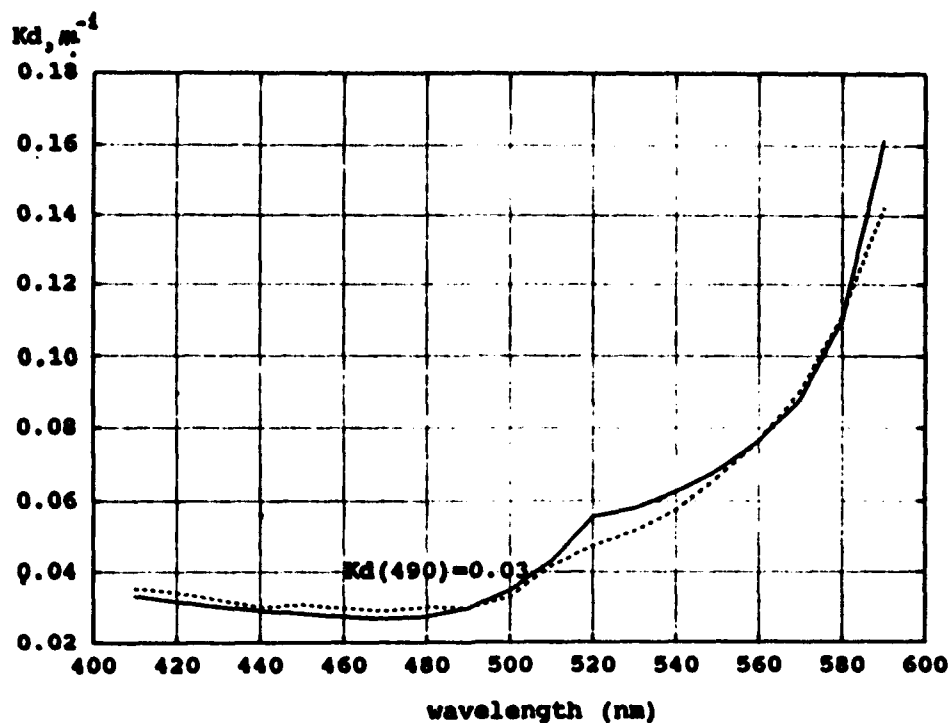


Fig.1. Comparison of values of $K_d(\lambda)$ as determined by means of the models of Austin, Petzold⁴ (solid line) and of Volynsky, Sud'bin⁶ (dashed); upper - $K_d(490) = 0.03 m^{-1}$, lower - $K_d(490) = 0.12 m^{-1}$.

49 spectra of $a(\lambda)$ and $K_d(\lambda)$ measured in Atlantic and Pacific were used; $K_d(500)$ values ranged from 0.027 to 0.49 m^{-1} ; the correlation coefficients were minimum at 590 nm (0.940) and maximum near 420-430 nm (0.993); the regression errors less than 0.02 m^{-1} . Table 2 and Figure 2 show the results of comparison between $a(\lambda)$ values computed by using (3) and (4) for the selected values of $K_d(490)^4$. The values of Δ_i , s_i , s and δ are calculated as above [$\Delta_i = a^{(3)}(\lambda_i) - a^{(4)}(\lambda_i)$].

Table 2. The standard deviations s and the mean ratios δ [comparison between (3) and (4)]

K (490) 10 ² , m	3	4	5	6	7	8	9	10	12	14	16	18
s 10 ² , m	0.5	0.4	0.4	0.4	0.4	0.4	0.4	0.4	0.5	0.6	0.8	0.9
δ , %	-11.3	-7.8	-5.8	-4.4	-3.4	-2.7	-2.1	-1.6	-0.9	-0.4	0.03	0.4

As seen in Table 2 and Figure 2, correspondence of the models (3) and (4) is quite satisfactory; it is a reason to believe the simple formula (3) can be applied for estimation $a(\lambda)$ on $K_d(\lambda)$ over the spectral range 410-590 nm.

Theoretical foundation of (3) can taken out from Gordon's work⁹. For the average diffuse attenuation coefficient $\langle K \rangle$ over the upper half of the euphotic zone can be led out the linear relation

$$\langle K \rangle / D_0 = 1.032 (a + b_b), \quad (5)$$

where a and b_b are the absorption and backscattering coefficients of sea water, D_0 is a parameter of the downwelling light field evaluated just beneath the surface; an average error of (5) is about 5%.

If a linear relation between b_b and a is assumed: $b_b = p a$, (5) can be rewritten

$$\langle K \rangle = 1.032 D_0 (1 + p) a = Q a, \quad (6)$$

We estimated $p(\lambda)$ by using available data of measurements of $a(\lambda)$ and $b_b(550)$ at the euphotic zone from 10 and 14 cruises of R/V «Dmitry Mendeleev» in Indian and Pacific oceans in 1973 and 1975. Spectral values of $b_b(\lambda)$ were calculated by using the model

$$b_b(\lambda) = (550/\lambda)^{1.7} [b_b(550) - b_b^{SW}(550)] + (550/\lambda)^{4.2} b_b^{SW}(550), \quad (7)$$

where $b_b^{SW}(550)$ is the backscattering coefficient of pure sea water (pure water + inorganic salts) at the 550 nm. The calculated values of p with their standard deviations and the Q^{-1} values at the 440, 480 and 550 nm are given at Table 3. The values of D_0 in (6) were taken from Gordon⁹; these values increase with the solar zenith angle (SZA) θ_0 so the ratio $Q^{-1} = a/\langle K \rangle$ decreases for the large SZA.

Table 3. The calculated values of p with their standard deviations s_p and $Q^{-1} = a/\langle K \rangle$

λ , nm	$p \pm s_p$	Q^{-1}			
		$\theta_0=0^\circ$	25°	40°	diffuse
440	0.25 +/- 0.13	0.75	0.71	0.67	0.73
480	0.27 +/- 0.12	0.74	0.71	0.66	0.64
550	0.11 +/- 0.05	0.86	0.82	0.76	0.73

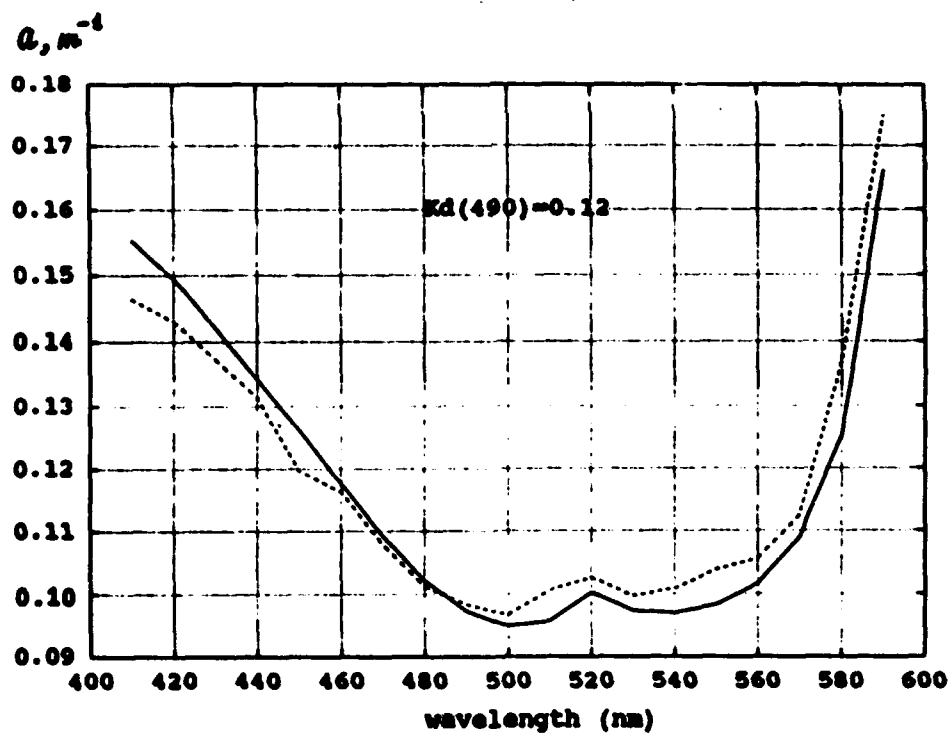
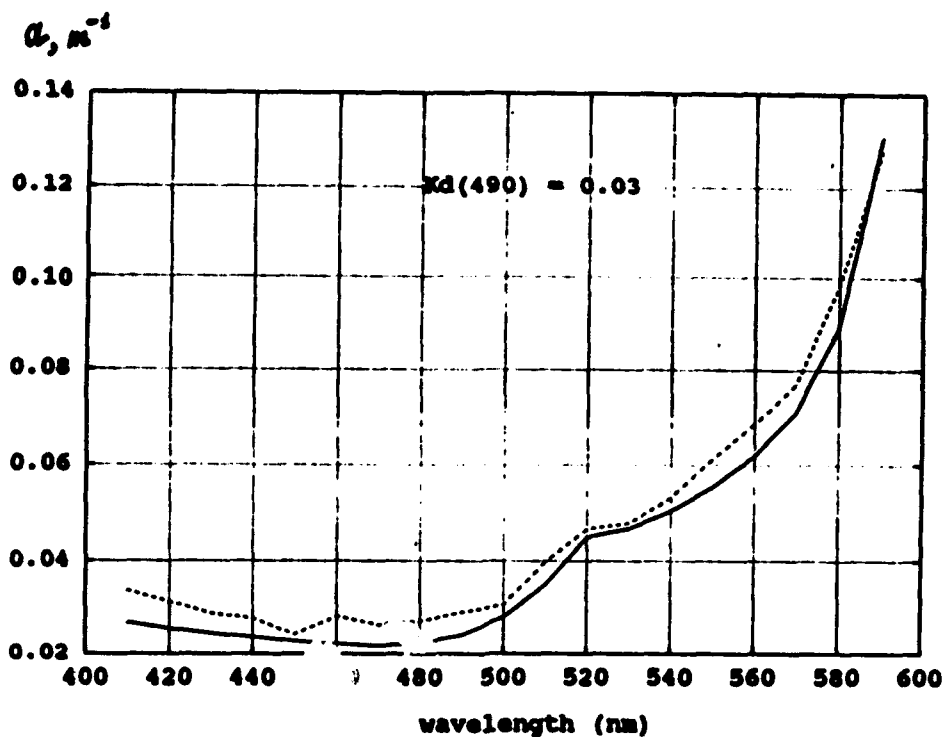


Fig.2. Comparison of values of $a(\lambda)$ as determined by means of Eq.(3) - solid line and (4) - dashed; upper - $K_d(490) = 0.03 m^{-1}$, lower - $K_d(490) = 0.12 m^{-1}$.

The ratios $Q^{-1} = a/\langle K \rangle$ at Table 3 differ from 0.81 within the limits of 20%, so the simple formula (3) proved to be correct theoretically for the small and medium SZA. As to the spectral dependency of the ratio $a/\langle K \rangle$, that has minimum corresponding to the maximum of sea water transmission (near 470--490 nm for oceanic water) where p is maximum. At the spectral range 440--550 nm D_0 depends weakly on the wavelength, but at the shorter wavelength range D_0 changes appreciably depending on the relation between direct and diffuse contributes of the incident solar flux.

4. PHYSICAL MODEL OF THE LIGHT ABSORPTION OF SEA WATER

Under «physical model» we understand a model showing a role of physical factors which cause the spectral absorption of light by sea water. Advantage of a physical model over a «statistical» which examples are given above, is that of giving general idea about physical structure of the phenomenon, and moreover allows to predict results out of range of existent measurement data; of course under condition of its adequacy to the phenomenon. Statistical model is valid only within a range of initial values of measured characteristics; for instance the models (1)–(4) are not valid at the ultraviolet spectral range, and a physical model only can be applied at the UV range at present for lack of statistical data of measurements there.

Of course physical models should be limited by the principal causing factors only. At the visible range these are the colored part of the dissolved organic matter («yellow substance»), phytoplankton pigments and pure water^{11,12}

$$a(\lambda) = a_y^{sp}(\lambda) c_y + a_{ph}^{sp}(\lambda) c_a + a_w(\lambda), \quad (8)$$

where $a_w(\lambda)$ is the spectral absorption coefficient of pure water; $a_y^{sp}(\lambda)$, $a_{ph}^{sp}(\lambda)$ are the corresponding specific absorption of yellow substance and phytoplankton pigments (the latter per unit Chl "a" concentration); c_y , c_a are the concentrations of yellow substance and Chl.

The more complex model including the absorption of nonchlorophyllous particles was suggested by Prieur, Sathyendranath¹³. In our opinion, there is no need to complicate a model if the more simple one gives good results^{11,12}.

The model^{11,12} is up-to-date in relation to new data for the pure water and yellow substance absorption^{10,14}.

Figure 3 shows the spectral values of the absorption coefficient of pure water according to the model^{11,12}, Morel, Prieur¹⁵ and Shifrin¹⁶. The first data are obviously understated; the second and third are in good correspondence except only two appreciable differences: near 440–460 nm and 520–560 nm. We analyzed these differences¹⁴ enlisting as control the measurement data of the diffuse attenuation coefficient in most clear ocean waters. As a result of the analysis the recommended value of $a_w(\lambda)$ are given by solid curve and Table in Figure 3.

As to the up-to-date values of the spectral absorption of yellow substance, the spectral curve is divided into two pieces: the 280--490 nm with $a_y^{sp}(\lambda)$ proportional $\exp(-0.017\lambda)$ and 500–680 nm with $a_y^{sp}(\lambda)$ proportional $\exp(-0.011\lambda)$ ¹⁴. Under this assumption $a_y^{sp}(\lambda) c_y$ in (8) is presented of the form

$$a_y^{sp}(\lambda) c_y = \begin{cases} a_y(390) \exp[-0.017(\lambda-390)], & \lambda \leq 490 \text{ nm}, \\ 0.154 a_y(390) \exp[-0.011(\lambda-500)], & \lambda \geq 500 \text{ nm} \end{cases} \quad (9)$$

The input parameter $a_y(390)$ is the constituent of the sea water absorption coefficient at 390 nm due to the yellow substance being presented; further we will denote that as a_y .

Note the model (8)–(9) has two input parameters: a_y and c_a , but it was shown above the spectral values $K_d(\lambda)$ and $a(\lambda)$ are possible to be approximated by using the models with one input parameter. The reasons of that were discussed^{11,12}: first the yellow substance is dominant factor of the sea water absorption causing

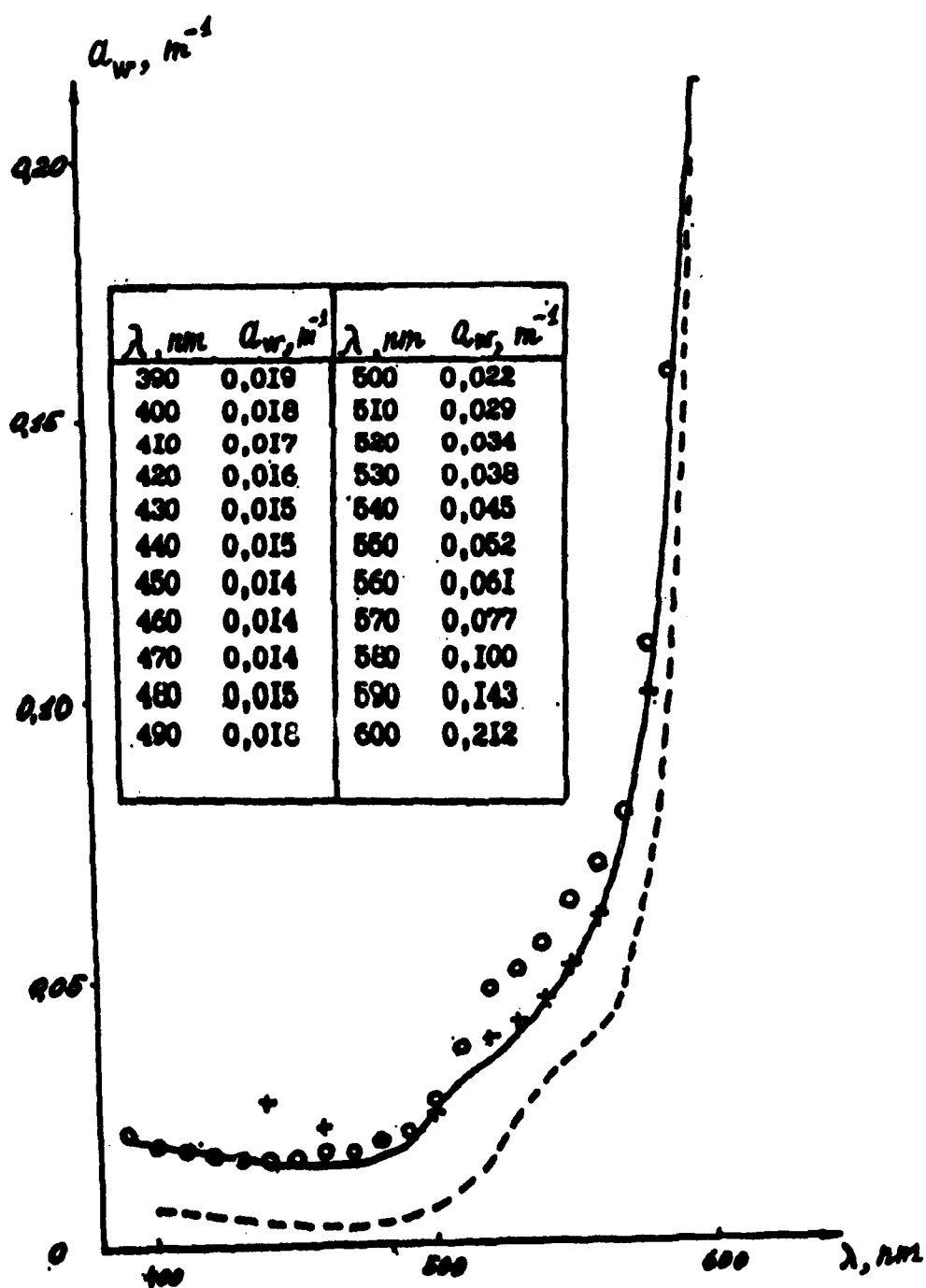


Fig.3. Spectral values of the absorption coefficient a_w, m^{-1} of pure water. o - Morel, Prieur¹⁵; +-Shifrin¹⁶; dashed curve - the values^{11,12}; solid curve and Table - recommended values.

its variability at $\lambda < 500$ nm; second there is a correlation between a_y and c_a in the waters of high bioproductivity.

For transformation the model (8)-(9) to the one-parametric a procedure as follows was used. The parameters a_y and c_a were computed by least squares technique for each of 12 spectra of $a(\lambda)$ at the spectral range 410-590 nm calculated from $K_d(\lambda)$ by means of (3) for 12 selected values⁴ of $K_d(490)$. The found parameters a_y and c_a allowed to approximate the starting spectra $a(\lambda)$ by means of the model (8)-(9) quite satisfactory: the standard error was 0.0053 m^{-1} if $K_d(490)=0.03 \text{ m}^{-1}$, and increased to 0.035 m^{-1} if $K_d(490)=0.18 \text{ m}^{-1}$. Then linear regressions of a_y on c_a and of c_a on a_y were computed by least squares technique

$$a_y = 0.261 c_a - 0.008, \quad (10)$$

$$c_a = 3.84 a_y + 0.03; \quad (11)$$

the standard errors of (10) and (11) are 0.002 m^{-1} and 0.007 mg m^{-3} .

We checked an applicability of the model (8)-(11) by using the spectra of the beam attenuation coefficient $c(\lambda)$ measured at the spectral range 270-590 nm in the Red Sea and Mediterranean during the 61 cruise of R/V «Dmitry Mendeleev»¹⁷. The model for calculation of spectra $c(\lambda)$ is

$$c(\lambda) = a(\lambda) + b_p(\lambda) + b_{sw}(\lambda), \quad (12)$$

where $a(\lambda)$ is according to (8)-(11), $b_p(\lambda)$ is the scattering coefficient of the suspended particles, $b_{sw}(\lambda)$ is the one of pure sea water. The spectral dependency of $b_p(\lambda)$ can be approximated by the hyperbolic law¹²

$$b_p(\lambda) = b_p(550) 550/\lambda, \quad (13)$$

where $b_p(550)$ is chosen as the input parameter; further that is denoted b_p .

The spectral values $b_{sw}(\lambda)$ are computed

$$b_{sw}(\lambda) = 2.07 \cdot 10^{-3} (550/\lambda)^{4.2}, \quad (14)$$

where $2.07 \cdot 10^{-3} \text{ m}^{-1}$ is the value of $b_{sw}(550)$ for $T=20^\circ \text{C}$ and $S=35\text{‰}$ ¹⁶.

Thus the model (12) has two input parameters: a_y and b_p . The ones were calculated by means of (12) from the measured values of $c(\lambda)$ at 410 and 590 nm. Then $c(\lambda)$ were calculated with the found values of the parameters a_y and b_p . At the range 400-590 nm the calculated values of $c(\lambda)$ coincided quite well with the measured ones: almost everywhere the differences were within 0.02 m^{-1} that corresponds to the error of the measurements.

It is of interest to check an applicability of the model (12) at the UV range 270-400 nm. For that it was necessary to prolong the specific absorption of the phytoplankton pigments $a_{ph}^{sp}(\lambda)$ to that spectral range because its values were limited by 400 nm. That was done by using the relative spectral curve of the chloroplast absorption published by Wolken, Strother¹⁸. The spectral values of $a_w(\lambda)$ were taken from Smith, Baker¹⁹.

We are interested in the waters of euphotic zone, so we chose 9 spectra of $c(\lambda)$ measured at the layer 0-25 m, calculated the input parameters a_y and b_p for each of them and computed $c(\lambda)$ according to the model (8)-(14). The calculated and measured values of $c(\lambda)$ happened to show systematic differences at the 270-400 nm which were maximum at 270 nm and decreased monotonously to the negligible ones at 400 nm. The only factor which influences at the UV region and is negligible at the visible is the inorganic salts. As a matter of fact Smith, Baker¹⁹ neglected of their absorption.

We computed the average differences $\bar{\Delta}(\lambda) = c_{\text{measured}}(\lambda) - c_{\text{calculated}}(\lambda)$ and attributed the ones to the absorption of inorganic salts $a_{is}(\lambda)$.

Table 4. The absorption coefficients of inorganic salts, m^{-1} .

λ	270	280	290	300	310	320	330	340	350	360	370	380	390
a_{is}	0.43	.32	.16	.11	.09	.08	.07	.06	.05	.04	.04	.03	.02

Note, these values correspond well to the measured ones by Copin-Montegut, Ivanoff, Saliot²⁰: $0.45 m^{-1}$ at 250 nm, $0.1 m^{-1}$ at 300 nm.

After such correction of the model (3)-(12) the calculated and measured values of $c(\lambda)$ coincide quite well: almost everywhere maximum differences are within 20%. Two examples of the comparison between the calculated and measured values of $c(\lambda)$ are shown by Figure 4.

5. ESTIMATION OF THE DIFFUSE ATTENUATION COEFFICIENT AT THE UV REGION ON THE ABSORPTION COEFFICIENT

Such possibility is given by (6) if the parameters p and D_0 are known. As before (see Section 3) we will investigate a change of the factor $Q = a/\langle K \rangle$. The parameter $p = b_0/a$ was calculated by means of (7)-(11) with addition of the absorption of inorganic salts $a_{is}(\lambda)$. The parameter a_y was found by using the measured values of $a(390)$ - see Section 3.

For the estimation of the parameter D_0 Gordon⁹ suggested the simplified equation under assumption of a cloud-free atmosphere and of a uniform radiance distribution of skylight

$$D_0 = f/\cos \vartheta_{ow} + 1,197 (1 - f), \quad (15)$$

where f is the fraction of direct sunlight in the downwelling irradiance and ϑ_{ow} is the solar zenith angle, both just beneath the surface (1,197 is the value of D_0 for the totally diffuse incident flux). The fraction f can be calculated

$$f = \frac{(1 - \rho_s)E_s}{(1 - \rho_s)E_s + (1 - \rho_d)E_d}, \quad (16)$$

where E_s , E_d are the direct solar and the sky irradiances above the surface; ρ_s , ρ_d are the surface reflectances for the direct and diffuse incident flux; for the flat surface ρ_s is the known function of the SZA, ρ_d is assumed as 0.066.

The values of E_s , E_d were computed by N.Krotkov, A.Vasilkov at our request by means of their model²¹; the ozone amount was 300 DU. Table 5 shows the average values of p and $a/\langle K \rangle$ for $\lambda = 290$, 320, 400 nm and the SZA 25, 30, 40, 60, 80° as well for the totally diffuse incident flux.

Table 5. The average values of p and $a/\langle K \rangle$ at the UV region

λ , nm	p	$a/\langle K \rangle$					
		$\vartheta=25^\circ$	30°	40°	60°	80°	diffuse
290	0.068	0.80	0.79	0.76	0.76	0.76	0.76
320	0.105	0.79	0.78	0.75	0.72	0.73	0.73
400	0.22	0.72	0.71	0.68	0.62	0.63	0.66

As seen the values of $a/\langle K \rangle$ increase appreciably at the UV region. The main reason of that is a decrease of $p(\lambda)$ caused by the sea water absorption increases at the UV more sharp than the backscattering. As concerns

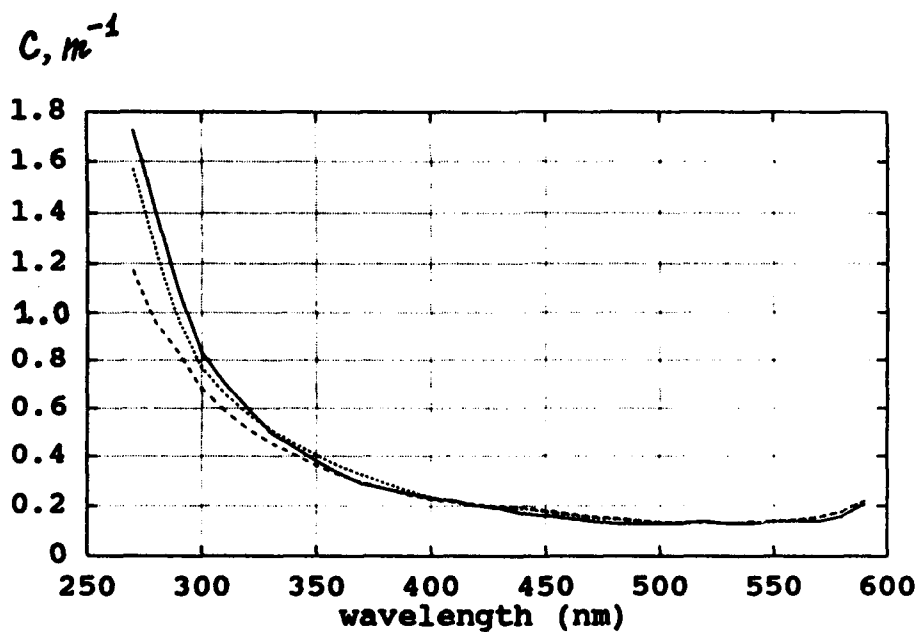
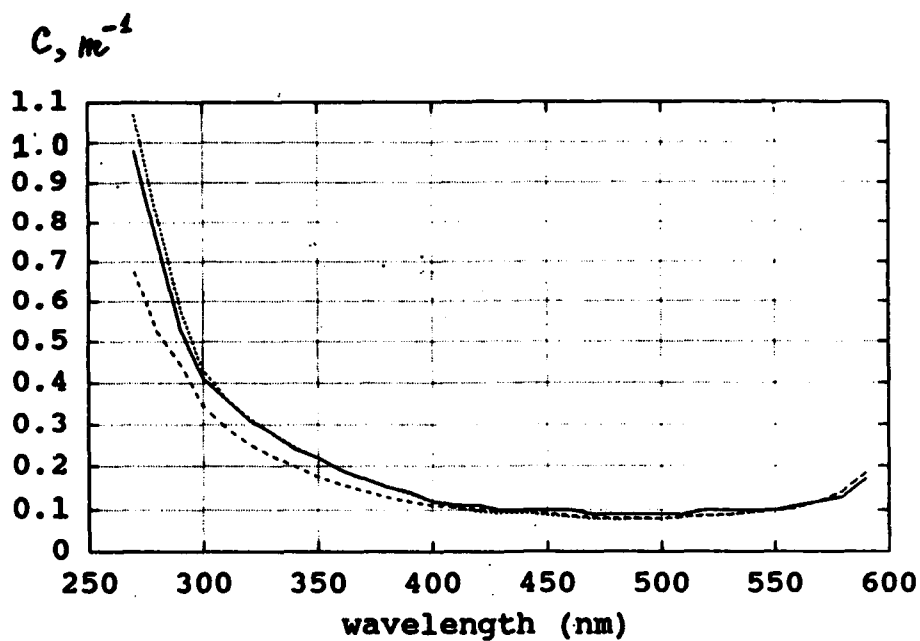


Fig.4. Validation of the model (8) - (12); solid curve - measured values of $c(\lambda)$, m^{-1} ; dashed curve - uncorrected calculated values; dotted curve - calculated values with correction; upper - South E. Mediterranean, depth 10m, lower - Central Red Sea, depth 25m.

the parameter D_0 , its values depend on f and the SZA. The larger SZA, the smaller f , and D_0 tends to its limit value 1,197. The shorter wavelength, the faster that goes. The ratio $a/\langle K \rangle$ is more stable in relation of the SZA for the shorter wavelength and closer to the value 0.81 in (3) even for the large SZA (see Table 5).

Summarizing the data of Tables 3, 5, we can conclude that the simple formula (3) appears to be applicable to the calculation of $K_d(\lambda)$ on $a(\lambda)$ and back at the UV and visible ranges for the small and medium SZA. The factor Q or Q^{-1} should be made more accurate for the future, but for rough estimates, Q^{-1} can be taken now as 0.8. In conjunction with the physical model of the spectral absorption that allows in principle to extrapolate the values of K_d obtained at the visible range to the UV. For the large SZA ($>40^\circ$) the parameter D_0 and the ratio $Q^{-1} = a/\langle K \rangle$ can be calculated by the method devised by Gordon⁹ for the field measurement or by means of proper model. Of course the model developed above needs to be validated by results of the field measurements.

6. ACKNOWLEDGMENTS

This work was supported by the USA State Department under Grant R 7 (Project «Triad» of the Program «Man and Biosphere»). We wish to express our gratitude to Drs. N.Krotkov and A.Vasilkov for giving us the results of calculation of the direct and diffuse components of the surface irradiance.

7. REFERENCES

1. N.G.Jerlov, *Optical Oceanography*, Elsevier Oceanography Series, Vol.5, Elsevier, Amsterdam, 1968.
2. N.G.Jerlov, *Marine Optics*, Elsevier Oceanography Series, Vol.14, Elsevier Scientific Publishing Co., Amsterdam, Oxford, New York, 1976.
3. V.N.Pelevin, «Solar radiation in ocean», *Optika okeana*, ed. A.S.Monin, Vol.1, pp.268-281, Nauka, Moscow, 1983.
4. R.W.Austin and T.J.Petzold, «Spectral dependence of the diffuse attenuation coefficient of light in ocean waters», *Ocean Optics VII*, Vol.489, pp.168-178, Monterey, 1984.
5. R.W.Austin and T.J.Petzold, «Spectral dependence of the diffuse attenuation coefficient of light in ocean waters: A re-examination using new data», *Ocean Optics X*, Vol.1302, pp.79-93, Orlando, 1990. ...
6. V.A.Volynsky and A.I.Sud'bin, «Statistical analysis of spectra of diffuse attenuation coefficient», *Okeanologia*, Vol.32, No.5, pp.821-829, 1992.
7. A.P.Ivanov, V.E.Shemshura, «Method of estimation of the light absorption coefficient in the sea», *Morskie Gydrofysicheskie Issledovania*, No.1(60), pp.110-118, 1973.
8. O.V.Kopelevich, V.E.Shemshura, «On possibility of estimation of the light scattering and absorption coefficients on the Secchi Depth», *Okeanologia*, Vol.28, No.5, pp.736-741, 1988.
9. H.R.Gordon, «Can the Lambert-Beer law be applied to the diffuse attenuation coefficient of ocean water?», *Limnol.and Oceanogr.*, Vol.34, No.8, pp.1389-1409, 1989.
10. O.V.Kopelevich, «Optical properties of ocean water», *Light scattering and absorption in natural and artificial dispersive media*, ed. A.P.Ivanov, pp.289-309, Inst.Phys. Belorussian Acad. Sci., Minsk, 1991.
11. O.V.Kopelevich, V.I.Burenkov, «On relation between the spectral values of the sea water light absorption coefficients, phytoplankton pigments, yellow substance», *Okeanologia*, Vol.17, No.3, pp.427-433, 1977.
12. O.V.Kopelevich, «Low-parametric model of sea water optical properties», *Optika okeana*, ed. A.S.Monin, Vol.1, pp.208-234, Nauka, Moscow, 1983.
13. L.Prieur and S.Sathyendranath, «An optical classification of coastal and oceanic waters based on the specific absorption curves of phytoplankton pigments, dissolved organic matter, and other particulate materials», *Limnol.and Oceanogr.*, Vol.26, No.4, pp. 671-689, 1981.
14. O.V.Kopelevich, S.V.Lutzarev, V.V.Rodionov, «The spectral light absorption by the «yellow substance» of the ocean water», *Okeanologia*, Vol.29, No.3, pp.409-414, 1989.
15. A.Morel and L.Prieur, «Analysis of variations in ocean color», *Limnol.and Oceanogr.*, Vol.22, No.4, pp.709-

722, 1977.

16. K.S.Shifrin, *Physical optics of oceanic water*, AIP, 1988.

17. O.V.Kopelevich, «Calculation of the spectral values of the sea water attenuation coefficient at the spectral range 270-590 nm from the measured values for two wavelengths», *Okeanologia*, Vol.22, No.3, pp.392-397, 1982.

18. J.J.Wolken and G.K.Strother, «Microspectrophotometry», *Appl. Opt.*, Vol.2, No.9, pp.899-907, 1963.

19. R.C.Smith and K.S.Baker, «Optical properties of the clearest natural water (200-800 nm)», *Appl. Opt.*, Vol.20, No.2, pp.177--184, 1981.

20. G.Copin-Montegut, A.Ivanoff, A.Saliot, «Coefficient d'attention des eaux de mer dans l'ultraviolet», *C. rend. Acad. Sci. Paris*, Vol.272, No.25, pp. B 1449- B 1456, 1971.

21. N.A.Krotkov, A.P.Vasilkov, «Ultraviolet radiation in the atmosphere-ocean system: a model study», SPIE Vol.2049 *Atmospheric Radiation*, ed. K.H.Stamnes, pp.244-255, 1993.

Detecting Raman scattering in the ocean by use of polarimetry

George W. Kattawar and Xin Xu

Center for Theoretical Physics, Dept. of Physics, Texas A&M University
College Station, Texas 77843-4242

ABSTRACT

We have developed a Monte Carlo program to calculate the complete four component Stokes vector for a coupled atmosphere-ocean system which also includes Raman scattering as well as a stochastic interface. Since the input to this program requires Mueller matrices for all scattering processes as well as the interface we had to derive the correct Mueller matrices for both Raman and elastic fluctuation scattering. We were then able to calculate the radiance, degree of polarization, orientation of the polarization ellipse, and the ellipticity of the radiation field at various levels within the ocean as well as just above the ocean surface. We found that the effect of Raman scattering on the polarization of the light field within the ocean is significant and can be detected by making polarimetric measurements within the ocean.

1. INTRODUCTION

The use of polarimetry in astronomy and atmospheric optics has provided additional information which has led to the characterization of the optical properties of scattering and absorbing media which was not possible with radiance data alone. An excellent review of the many ways polarimetry has been used successfully in these areas can be found in Gehrels¹. The use of polarimetry in ocean optics has been minuscule and a review of what has been done up to the middle seventies along with references can be found in Jerlov².

One of the first Monte Carlo programs written to compute the complete four component Stokes vector for a coupled atmosphere-ocean system was developed by Kattawar³, et. al., however, this study was only for elastic scattering. The inclusion of inelastic scattering has only been performed for scalar radiative transfer where all polarization effects have been neglected. It is the purpose of this paper to show how the inclusion of polarization into Raman scattering can provide us with another very good tool for detection of this very important process in ocean optics.

2. MONTE CARLO MODEL

For the calculations used in this study we have adopted the I, Q, U, V representation of the Stokes vector. For a complete definition of the Stokes vector and the corresponding 4x4 Mueller matrices relevant to ocean optics which transforms it the reader is referred to the paper by Kattawar and Adams⁴. Several quantities which are of particular importance are the degree of polarization, $P = (Q^2 + U^2 + V^2)^{1/2}/I$, the degree of linear polarization, $(Q^2 + U^2)^{1/2}/I$, the degree of circular polarization, V/I , the orientation of the polarization

ellipse, χ , where $\tan 2\chi = U/Q$ and the ellipticity $= \tan \beta$ where $\tan 2\beta = V/(Q^2 + U^2)^{1/2}$. Fig. 1 shows a geometric representation of some of these quantities.

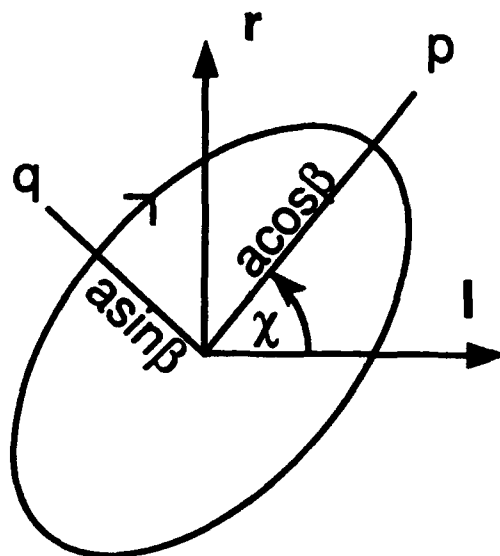


Fig. 1 Geometric description of the polarization ellipse where $a = I^{1/2}$ and the ellipticity, $\tan \beta$, is the ratio of the semiminor to the semimajor axis of the polarization ellipse. The angle χ gives the orientation of the polarization ellipse.

In order to include polarization dependent Raman scattering we had to derive the correct reduced Mueller matrix for this process. It is

$$m = \begin{pmatrix} 1 & \frac{(1-\rho)(c^2-1)}{(1+c^2)+(3-c^2)\rho} & 0 & 0 \\ \frac{(1-\rho)(c^2-1)}{(1+c^2)+(3-c^2)\rho} & \frac{(1-\rho)(c^2+1)}{(1+c^2)+(3-c^2)\rho} & 0 & 0 \\ 0 & 0 & \frac{(2-2\rho)c}{(1+c^2)+(3-c^2)\rho} & 0 \\ 0 & 0 & 0 & \frac{(2-6\rho)c}{(1+c^2)+(3-c^2)\rho} \end{pmatrix} \quad (1)$$

where $c = \cos \theta$, the cosine of the scattering angle and ρ is the depolarization ratio for incoming linearly polarized light which is polarized perpendicular to the scattering plane. In the ocean ρ is 0.17 for Raman scattering⁵ and 0.047 for elastic fluctuation scattering⁶. In Fig. 2 we show a plot of this matrix as a function of scattering angle for both Raman scattering and elastic fluctuation scattering. Raman scattering and elastic fluctuation scattering are in the same category; namely, one in which the medium contains the scattering units and their mirror units in equal number. The result here is consistent with the results in van de Hulst⁷. For forward scattering ($\theta = 0^\circ$), $m_{ij} \neq 0$ only when $i=j$ and $m_{22} = m_{33}$. For back scattering ($\theta = 180^\circ$), $m_{ij} \neq 0$ only when $i=j$ and $m_{22} = -m_{33}$. It should

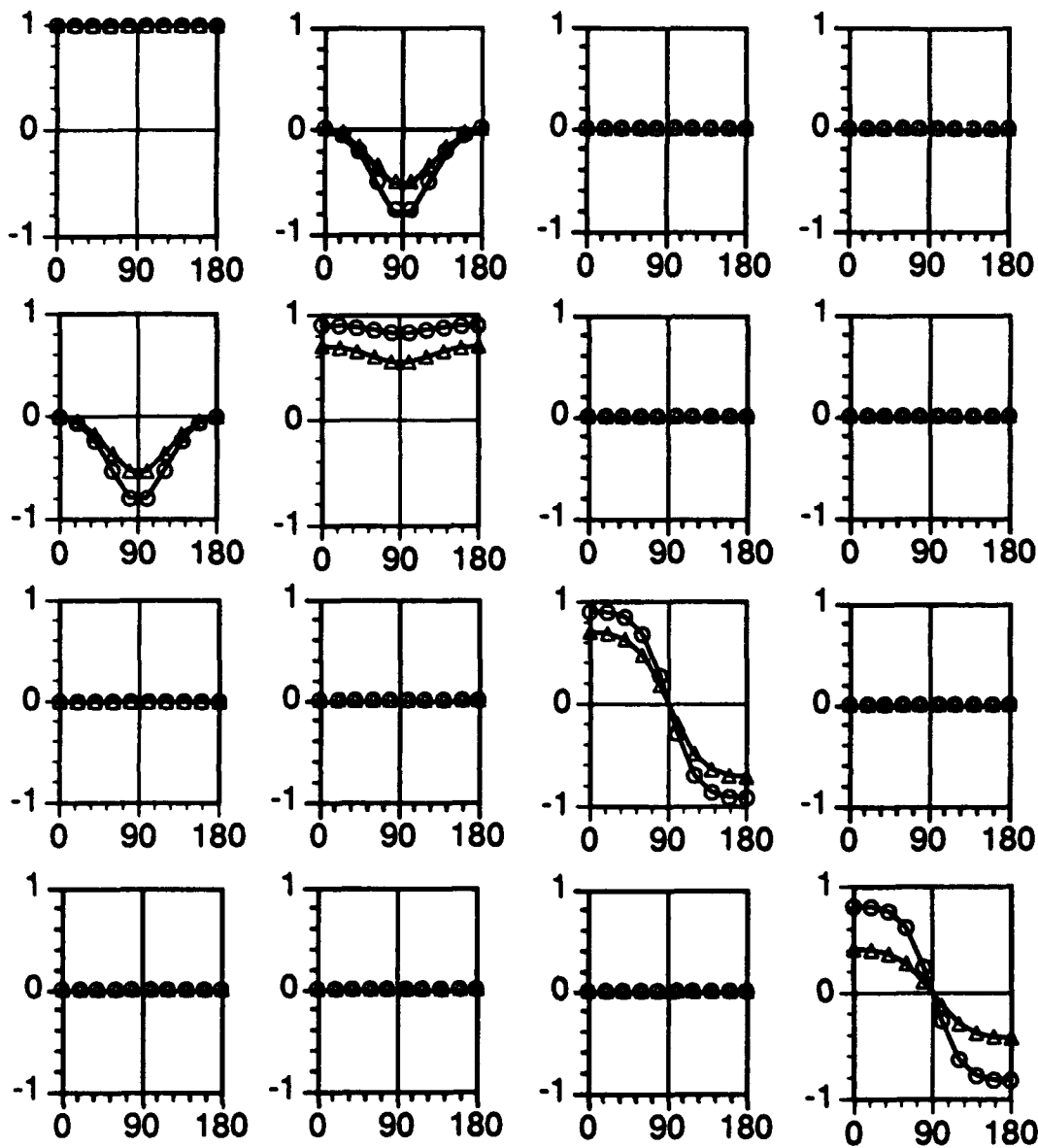


Fig. 2 Reduced Mueller matrix elements, m_{ij} , ($i=1, 2, 3, 4$ is the row index and $j=1, 2, 3, 4$ is the column index) for Raman scattering (open triangle) and fluctuation scattering (open circle). Each graph is a particular element (m_{ij}) of the Mueller matrix.

be noted that the m_{22} element is different from unity for both cases but for Raman scattering it is more pronounced. Another important point is that the m_{12} element, a measure of linear polarization, shows more complete polarization at 90° for elastic fluctuation scattering than for Raman scattering, which may cause significant differences in the degree of polarization for the two phenomena. Also for elastic fluctuation scattering $m_{44} \approx m_{33}$ while for the Raman scattering case these two elements have significant differences.

3. ATMOSPHERE-OCEAN MODEL

The Model we used for the atmosphere is the MAR-I model published by the International Association for Meteorology and Atmospheric Physics⁸. This model includes two layers and each layer has several types of aerosols whose size distribution can be represented by a log-normal distribution

$$\frac{dN_i(r)}{d(\log r)} = \frac{N_i}{\log \sigma_i^* \sqrt{2\pi}} \exp \left[-\frac{(\log r - \log r_i)^2}{2(\log \sigma_i^*)^2} \right] \quad (2)$$

where $N_i(r)$ is the number of particles of a certain type having radii smaller than r , and i represents different types of aerosols and $\log \sigma_i^*$, the standard deviation in $\log r_i$, is a parameter which has to be fitted empirically. The value of σ_i^* , r_i and N_i , as well as the optical refractive index and optical depth for the aerosols used in the model are given in Table 1. The total optical depth of the atmosphere is 0.22 and we assume the optical properties of the aerosols have no change in the spectral regions in our calculations.

The optical properties of the ocean for various spectral regions are listed in Table 2. The hydrosol size distribution used to calculate the reduced Mueller matrix was the same as that used by Takashima and Masuda⁹; namely,

$$\begin{aligned} \frac{dN(r)}{dr} &= k r^{-4} \quad , 0.1\mu\text{m} \leq r \leq 22\mu\text{m}, \\ \frac{dN(r)}{dr} &= 0 \quad , r > 22\mu\text{m} \text{ and } r < 0.1\mu\text{m} \end{aligned} \quad (3)$$

The complex refractive index for the hydrosols in their model was $n = 1.07 - 0.01i$. At the interface between the atmosphere and the ocean, both the reflected and refracted rays including the rays that undergo total internal reflection, were followed. We assumed the ocean interface to have a refractive index of 1.34 and surface wave effects were calculated using the Cox and Munk¹⁰ surface slope distribution.

To perform calculations for the radiation field at a certain wavelength (observation wavelength), the program must first be run at an excitation wavelength and when a Raman scattering event occurs, the photon is shifted to the observation wavelength, the optical properties of the ocean at this shifted wavelength are now used.

Table 1. Aerosol parameters used in calculations

r_i : mean radius
 τ_m : optical thickness of maritime haze model
 τ_c : optical thickness of continental haze model
 τ_r : optical thickness of Rayleigh scattering layer
 $\log \sigma_i^*$: the standard deviation in $\log r_i$
 N_i : the number of particles of type i
 n_i : the refractive index of particles of type i at 550 nm
 ω_0 : single scattering albedo

a) Continental Model (upper layer): $\tau_c = 0.025$, $\tau_r = 0.114$, averaged $\omega_0 = 0.891$

type	σ_i^*	r_i (μm)	N_i/N	n_i	ω_0
water-soluble	2.99	0.005	0.93876	$1.530 - 6.00 \times 10^{-3}i$	0.957
dust-like	2.99	0.50	2.27×10^{-6}	$1.530 - 8.00 \times 10^{-3}i$	0.653
soot	2.00	0.00118	0.06123	$1.750 - 0.440i$	0.209

b) Maritime Model (bottom layer): $\tau_m = 0.05$, $\tau_r = 0.031$, averaged $\omega_0 = 0.989$

type	σ_i^*	r_i (μm)	N_i/N	n_i	ω_0
oceanic	2.51	0.30	0.99958	$1.500 - 1.00 \times 10^{-8}i$	1.000
water-soluble	2.99	0.005	0.00042	$1.530 - 6.00 \times 10^{-3}i$	0.957

Table 2. Optical parameters (all in units of m^{-1}) of the ocean used in calculations

wavelength	a	b_{sw}	b_{hyd}	b_r	c	ω_0
417 nm	0.0156	0.0064	0.0443	0.00048	0.0663	0.7719
441 nm	0.0145	0.0049	0.0416	0.00038	0.0610	0.7685
486 nm	0.0188	0.0032	0.0373	0.00026	0.0593	0.6874
499 nm	0.0257	0.0029	0.0369	0.00023	0.0655	0.6076
518 nm	0.0470	0.0024	0.0354	0.00020	0.0848	0.4481
600 nm	0.2440	0.0014	0.0306	0.00011	0.2760	0.1163

a : absorption coefficient ¹³

b_{sw} : scattering coefficient for salt water ¹³

c : total extinction coefficient, $c = a + b_{sw} + b_{hyd}$

b_r : Raman scattering coefficient⁶

b_{hyd} : hydrosol scattering coefficient ¹⁴

$\omega_0 = (b_{sw} + b_{hyd}) / c$

This is the inelastic contribution to the total radiation field. The second phase consists of running the program for the observation wavelength to obtain the elastic component. The total radiation field will be the sum of the inelastic part and the elastic part with appropriate weighting to account for the difference in the solar flux at the excitation and observation wavelengths as well as the energy difference of the red shifted photons. It is important to note that to obtain absolute radiances one only has to multiply the results shown by the incoming solar flux at the *observation* wavelength. The four component Stokes vector (I, Q, U, V) is calculated for both parts and then transformed into radiance, degree and direction of polarization, as well as ellipticity.

4. RESULTS

4.1 Ocean without hydrosols

We chose 518 nm for the observation wavelength (corresponding to an excitation wavelength of 441 nm) for most of the calculations we will present because in our previous studies¹¹, we found that at this wavelength, Raman scattering is significant. The first set of results we will present hydrosol scattering is neglected in the ocean. In Figs.3(a)-3(d), we show the calculated radiance, degree of polarization, orientation of the polarization ellipse and ellipticity at various depths in the ocean (averaged over $0 < \phi < 30$) for an incident solar angle of 60° ($\mu_0 = -0.5$ and labeled by IB on the graphs). The calculated results without Raman scattering (labeled "elastic case") are also plotted on the same graph. The upward radiance is for the zenith angle range 0° - 90° and the downward radiance is for the range 90° - 180° . The critical angle for the refractive index chosen ($n=1.34$) is 132° and is labeled by CA on the graphs and the transmitted direct beam, labeled TB on the graphs enters the ocean at $\sim 140^\circ$. For the radiance, Fig. 3(a), we can see that at 80 m, for angles $\theta < 132^\circ$, the observed radiance without Raman scattering is much smaller than that with Raman scattering, especially for the upward directions. This is because the ocean is quite transparent at the excitation wavelength (441 nm) and the shifted part of the light, which is caused by Raman scattering at the excitation wavelength, is larger than the elastic part at the observation wavelength. Even at 10 m, the difference in radiance indicates that there is a significant amount of shifted light. Since the Mueller matrix elements for Raman scattering are different from those for elastic fluctuation scattering, the presence of a significant amount of Raman scattered light could cause a significant difference in polarization behavior. When we look at the degree of polarization, Fig. 3(b), we see that Raman scattering indeed causes some significant changes. First, Raman scattering decreases P_{\max} (the maximum degree of polarization as a function of zenith angle) relative to the elastic case. Secondly, P_{\max} decreases with depth when Raman scattering is introduced. This should be contrasted with the very small depth dependence for elastic scattering. This also implies that there is not a great deal of multiple scattering in the elastic case since multiple scattering in general tends to dilute the degree of polarization. Raman scattering doesn't, however, change the angle at which the maximum degree of polarization occurs (θ_{\max}). The larger degree of polarization for the detector at 10 m when the zenith angle is between 100° - 130° is caused purely by interface reflection. Raman scattering has no obvious effect on either the orientation of the polarization ellipse, Fig. 3(c), or the ellipticity, Fig. 3(d). This is to be expected since the reduced Mueller matrix elements $m_{34}=m_{43}=0$ for both Raman and elastic fluctuation scattering (see Fig. 2). There are two regions where elliptic polarization exists, one is within the critical angle ($\theta \sim 122^\circ$

which is caused by total internal reflection from the interface. Ivanoff and Waterman¹² explained this phenomena in their studies. It is due to the m_{34} element of the interface⁹. Another place is the peak outside the critical angle ($\theta=150^\circ$). This peak is caused by the aerosol in the lower layer of atmosphere; however, it is a *multiple* scattering effect and is not easy to quantify.

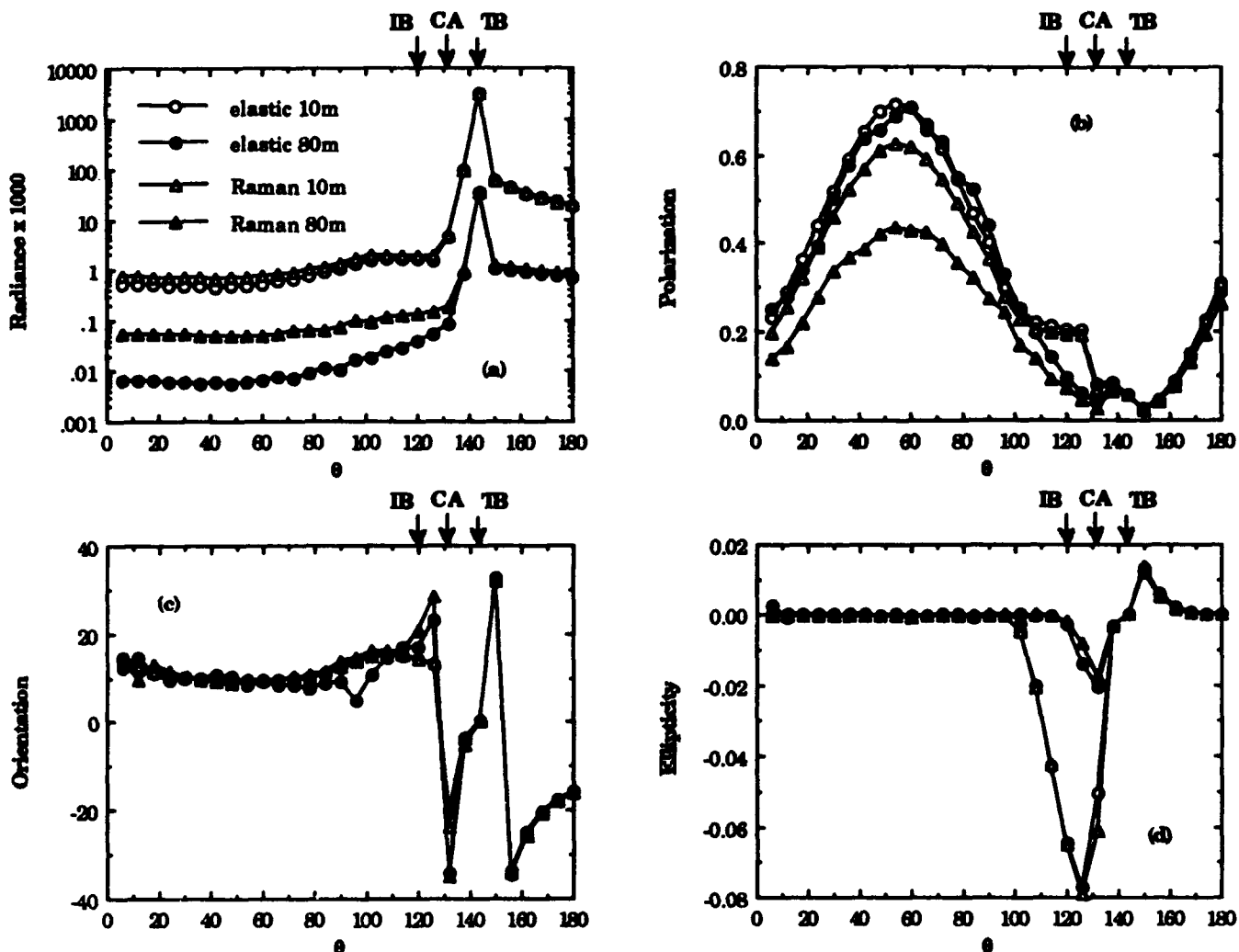


Fig. 3 (a) The radiance, (b) degree of polarization, (c) orientation, and (d) ellipticity as a function of zenith angle at various depths in the ocean for both elastic scattering (open symbols) and Raman scattering (filled symbols). The solar zenith angle is 60° , and the results are averaged over $0^\circ < \phi < 30^\circ$. IB denotes incident beam direction, TB denotes transmitted or refracted beam direction, and CA denotes the critical angle.

To see the origin of this peak we show in Fig. 4 the reduced Mueller matrix for the lower layer aerosol. What is noteworthy is the large m_{34} element. Without this element one cannot produce elliptic polarization from an unpolarized source. That is why there can be no ellipticity from a pure Rayleigh scattering atmosphere since $m_{34}=0$. In Fig. 5 we show the ellipticity for the detectors just above and just below the ocean surface.

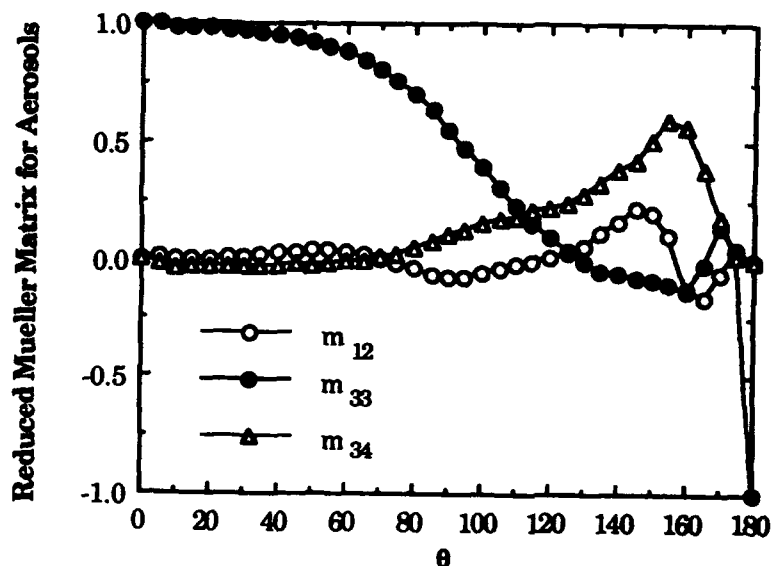


Fig. 4 Reduced Mueller matrix elements m_{12} , m_{33} , and m_{34} as a function of scattering angle for the lower layer aerosol.

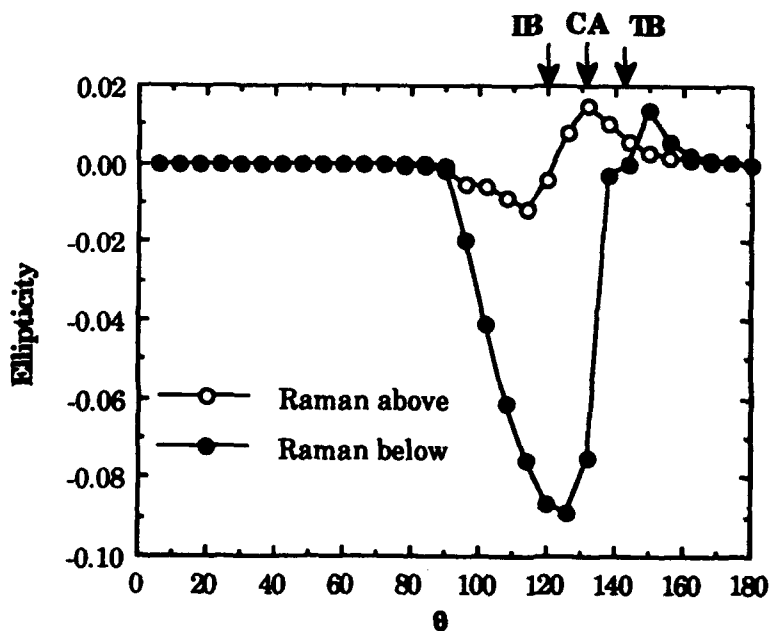


Fig. 5 The ellipticity as a function of zenith angle for detectors just above and just below the interface.

It can now be seen that the secondary peak appears first in the atmosphere and is then refracted into the ocean. To prove that it is indeed the m_{34} element of the lower layer aerosol which produces this secondary peak, we set the Mueller matrix element $m_{34}=0$ for the lower layer aerosol and the peak disappeared. We also found that this peak was not present when a pure Rayleigh scattering atmosphere was used. In Figs. 6(a)-6(d), the degree of polarization for different azimuth regions is plotted, the results were averaged over those regions indicated in the graph. We can see that θ_{\max} changes with different azimuth angles, and it is always close to the direction which is perpendicular to the direct beam. For upward directions, Raman scattering has a strong effect on the degree of polarization for regions with small ϕ , the degree of polarization also show strong depth dependence. When ϕ is close to 180° , there is almost no difference between the elastic and Raman scattering cases for the upward direction and also little depth variation. However, for the downward direction the Raman scattering case still shows strong depth dependence whereas the elastic case shows very little.

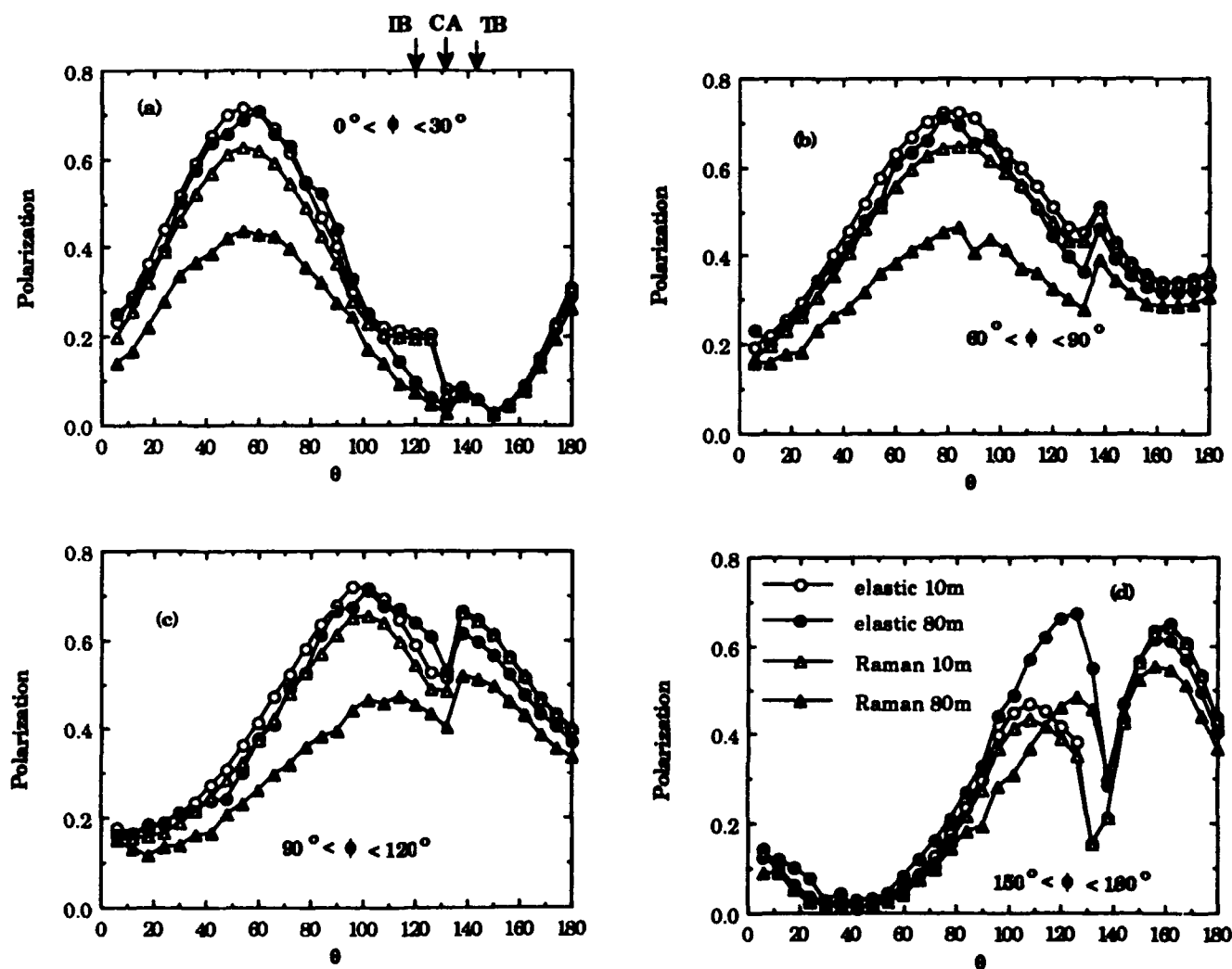


Fig. 6 The degree of polarization for four different azimuthal angle regions for the case considered in Fig. 3.

4.2 Ocean with hydrosols

We next considered the effect of hydrosols on the radiance and degree of polarization which is shown in Figs. 7(a)-(d). In general the addition of hydrosols doesn't change the behavior of the degree of polarization as a function of zenith angle in the upward direction; however, in the downward direction, the degree of polarization pattern has changed, for example, the small peak close to the direction of the direct beam broadens and becomes smaller. This broadening is due to a shift in the Babinet and Brewster neutral points which is extremely interesting and will be the subject for a future paper. Another noteworthy feature is in the ellipticity, Fig. 7(d). The small secondary peak which appeared in the hydrosol free case (see Fig. 3(d)) has now disappeared and a minimum has appeared. This is due to a small m_{34} element in the hydrosol Mueller matrix shown in Fig. 8. This demonstrates how sensitive the ellipticity is to subtle changes in the m_{34} elements of the Mueller matrices for both atmosphere and ocean

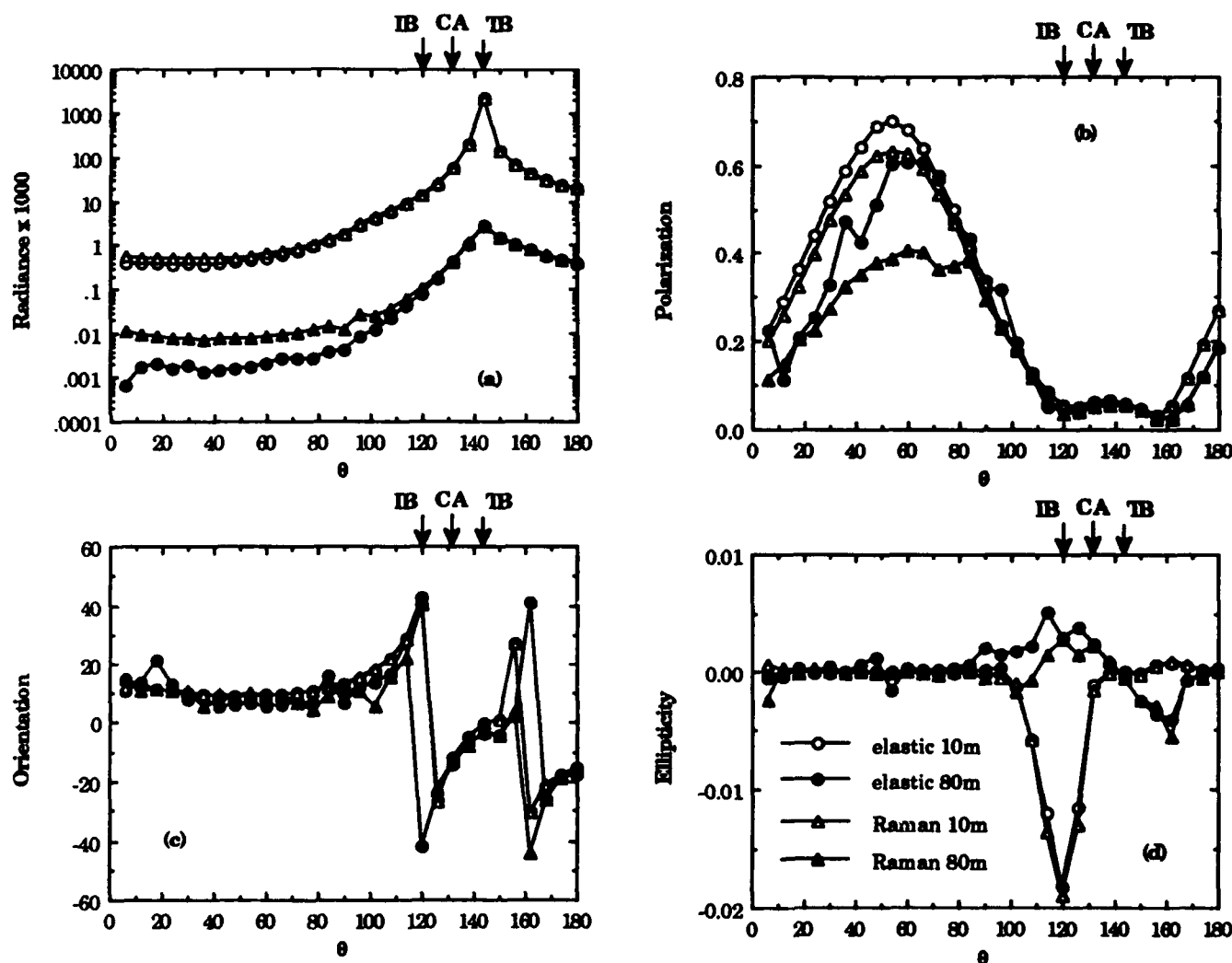


Fig. 7 Same as Fig. 3 but with the addition of hydrosols.

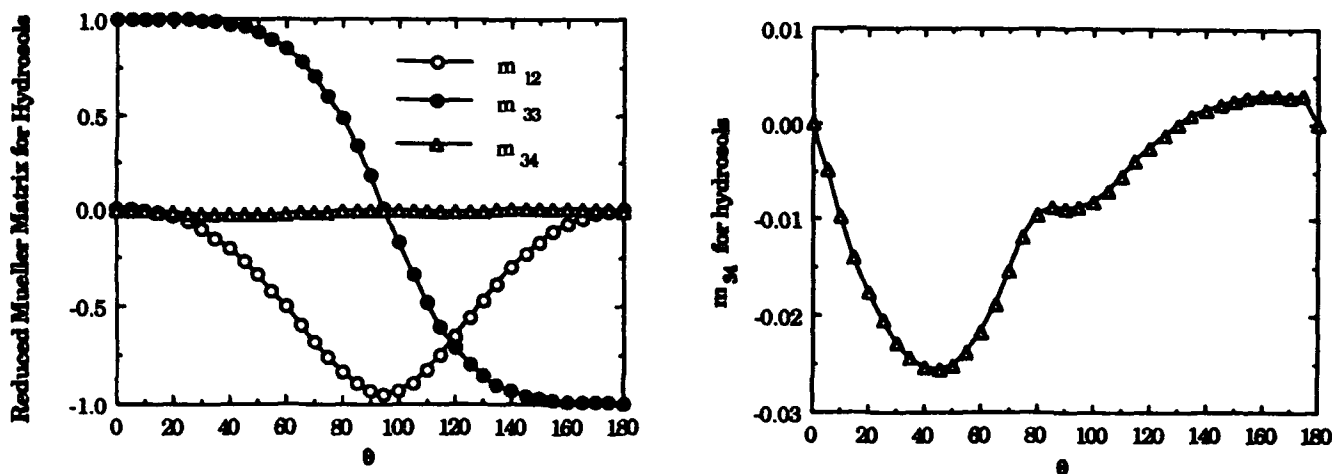


Fig. 8 Reduced Mueller matrix elements m_{12} , m_{33} , and m_{34} for hydrosols. The figure on the right is a magnified plot of the m_{34} element.

5. CONCLUSIONS

We have shown that Raman scattering can play an important role in determining the polarization of the underwater light field for certain spectral regions. The primary effect of Raman scattering is to decrease the degree of the polarization especially in the upward directions. The reason for this being that the Raman scattered signal, due to its high depolarization factor, produces less linear polarization than elastic fluctuation scattering (see Fig. 2). The beauty of using polarimetry is that since it uses *ratios* of Stokes vector components it isn't subject to absolute calibration. Hydrosol scattering produces little if any changes in the upward Stokes vector; however, it significantly affects the downward degree of polarization. One of the most interesting aspects of hydrosol scattering was the fact that it was able to shift the neutral points in the ocean. This opens a completely new way to monitor hydrosol scattering and will be the subject of a future paper. Another interesting effect we found was that the ellipticity was drastically affected by only small changes in the m_{34} element of the Mueller matrix. All of these facts taken together show the importance of using polarimetry to study the optical properties of the ocean.

6. ACKNOWLEDGMENTS

We would like to thank Charles N. Adams for providing some of the subroutines used in the Monte Carlo program. This work was partially supported by the Office of Naval Research under contract number N00014-89-J-1467.

7. REFERENCES

1. Planets, Stars and Nebulae, T. Gehrels, ed., The University of Arizona Press, Tucson, Arizona, 1974.
2. N. G. Jerlov, Marine Optics, Chap. 11, Elsevier Scientific Publishing Company, New York, 1976.
3. G. W. Kattawar, G. N. Plass, and J. A. Guinn, Jr., "Monte Carlo calculations of the polarization of radiation in the earth's atmosphere-ocean system," *J. Phys. Oceanogr.*, 3, 353-372, 1973.
4. G. W. Kattawar and C. N. Adams, "Stokes vector calculations of the submarine light field in an atmosphere-ocean with scattering according to a Rayleigh phase matrix: effect of interface refractive index on radiance and polarization," *Limnol. Oceanogr.*, 34, 1453-1472, 1989.
5. N. P. Romanov and V. S. Shulkin, "Raman scattering cross section of liquid water," *Opt. Spectrosc. (USSR)*, 38, 646-648, 1975.
6. B. R. Marshall, "Raman scattering in ocean water," Master's Thesis, Geography Dept. U. California at Santa Barbara, 1989.
7. H. C. van de Hulst, Light Scattering by Small Particles, Dover, New York, 46-57, 1981.
8. IAMAP, "A preliminary cloudless standard atmosphere for radiation computation," Section 2, 9-28, Boulder, CO., 1986.
9. T. Takashima and K. Masuda, "Degree of Radiance and polarization of the upwelling radiation from an atmosphere-ocean system," *Appl. Opt.* 24, 2423-2429, 1985.
10. C. Cox and W. Munk, "Statistics of the sea surface derived from sun glitter," *J. Mar. Res.* 13, 198-227, 1954.
11. G. W. Kattawar and X. Xu, "Filling in of Fraunhofer lines in the ocean by Raman scattering," *Appl. Opt.* 31, 6491-6500, 1992.
12. A. Ivanoff and T. H. Waterman, "Elliptical polarization of submarine illumination," *J. Mar. Res.* 16, 255-282, 1958.
13. R. C. Smith and K. S. Baker, "Optical properties of the clearest natural waters (200-800 nm)," *Appl. Opt.* 20, 177-184, 1981.
14. R. H. Stavn and A. D. Weidemann, "Optical modeling of clear ocean light fields: Raman scattering effects," *Appl. Opt.* 27, 4002-4010, 1988.

Multiple Scattering Metamorphosis of a Non-Gaussian Single-Scatter Phase Function

Brad D. Joelson and George W. Kattawar

**Center for Theoretical Physics, Dept. of Physics, Texas A&M University
College Station, Texas 77843-4242**

H. C. van de Hulst

**Sterrewacht Rijkuniversiteit Leiden
P.O. Box 5819, 2300 RA Leiden, the Netherlands**

ABSTRACT

Pulse broadening due to multiple scattering has long been of fundamental importance in the study of laser pulse transmission through the ocean as well as other diverse areas of science such as astrophysics, meteorology, and medical physics. The possibility of new imaging methods using multiple scattering techniques underscores the need to better understand this problem. We have used a Monte Carlo simulation to investigate the spatial and temporal spreading of a pulse ("Pulse Stretching") as it propagates through a medium due to small angle multiple scattering as described by van de Hulst and Kattawar¹. We will show the transformation of single scatter distributions into those predicted by the Central Limit theorem. We also derive the scattering property of the medium finding a simple relation between the phase function and the scattering parameter which connects the single scatter mean square scattering angle, $\langle \theta^2 \rangle$, and the multiple scatter expectation value, $\langle \theta^2 \rangle$, along with well defined limits of validity of the present theory in terms of the basic scattering parameters of the medium.

1. INTRODUCTION

The temporal and spatial spreading of a pulsed collimated beam due to small angle multiple scattering has been well studied. van de Hulst and Kattawar¹ presented a theory and gave a solution for the spread function of the beam. The introduction of a parameter inherently connected to the optical properties of the medium along with the region where this theory was applicable have yet to be studied in detail. This connection is of fundamental importance in many areas of imaging science which now includes tissue optics².

We have written a Monte Carlo program to emulate the entire scattering process of a semi-infinite medium of optical depth z and single scattering albedo ω_0 . Using the assumptions of van de Hulst and Kattawar¹ we studied cases where the phase function was truncated at a maximum scattering angle Θ_m . This allows us to study diverse forms of

single scattering while still maintaining the small angle scattering nature of the theory. In other words, with the use of a truncated phase function we can neglect moments higher than second order in the Legendre expansion of the product of the phase function and albedo. This is important since a diverging second moment leads to a different power law for the spread of the radiance with increasing optical depth³. We have chosen a Henyey-Greenstein phase function for almost all cases since we can produce isotropic to strongly peaked scattering by adjusting the asymmetry factor, g , with $g=0$ accounting for isotropic scattering and $g=1$ corresponding to a delta function. The one exception being that we also studied the case of pure Gaussian scattering. The Henyey-Greenstein was used to better understand multiple light scattering in turbid media such as human tissue as well as atmospheric and oceanic optics. The use of this phase function with various asymmetry values has been shown to properly describe photon dynamics *in vivo* of human and other mammalian tissue⁴.

The initial study done by van de Hulst and Kattawar¹ considered a collimated beam propagating in a homogeneous scattering medium. The beam spread was analyzed in the off-axis spatial coordinates (x_1, x_2) , the projected polar angles (θ_1, θ_2) , and the time-loss (path difference) t which is the difference between the actual and straight-through trajectories with the projected path differences satisfying the convolution $t=t_1+t_2$ (Figure 1). The latter result is a consequence of the small angle approximation of the problem. The joint distribution function was Laplace transformed in time-loss and Fourier transformed in spatial coordinates and projected angles. The complete solution to the temporal and spatial spread of the beam was obtained assuming the required inverse transformations could be performed and the scattering property of the medium was known. The radiance obtained could be used to calculate the energy fluence if dosimetry calculations were required.

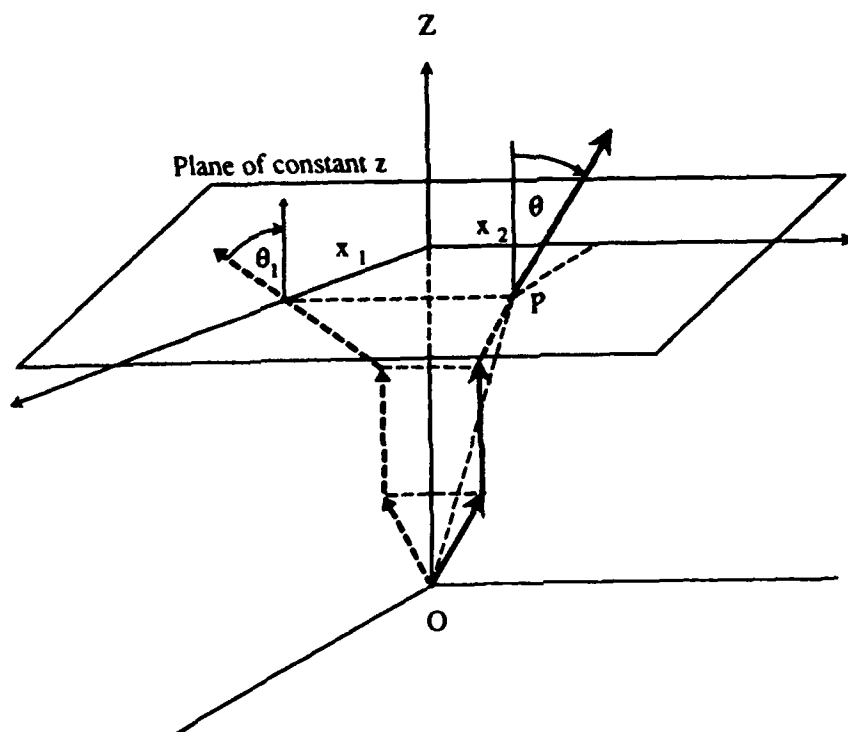


Fig. 1 Geometry used in describing the projected beam spread distribution function:
Solid line is three dimensional path and dashed line is its projection in the x_1 - Z plane.

2. THEORY

2.1) Radiances

The spatial and temporal spreading of a beam propagating radially in a homogeneous scattering medium is described by the equation of transfer⁵

$$\frac{df}{dr} = \sum_{i=1}^5 \frac{\partial q_i}{\partial r} \frac{\partial f}{\partial q_i} = -f + J \quad (1)$$

The radiance, $f(x_1, x_2, \theta_1, \theta_2, t; r)$, is a function of the five fundamental variables of the problem, x'_i , written in terms of their dimensionless optical depth quantities, $x_i = kx'_i$, shown here as $\{q_i\}$ with the speed of light set to unity. Throughout this manuscript primed quantities will refer to physical variables while the unprimed will be the corresponding dimensionless optical depth variables. All variables are implicitly dependent on the radial distance into the medium, r . The equation of transfer takes on the same form as van de Hulst and Kattawar derived but now the implicit dependence of the spread is in " r " not " z ". Thus, this equation will lead to the same distribution functions as derived by van de Hulst and Kattawar with slightly different parameters due to the new implicit dependence on " r ".

The contracted projected angular radiance in terms of θ_i , where a contraction is equivalent to an integration over the other independent variables is,

$$f(\theta_i) = \frac{1}{\sqrt{2\pi\sigma^2}} \exp\left(\frac{-\theta_i^2}{2\sigma^2}\right) \quad (2)$$

with a standard deviation given by

$$\sigma^2 = 2s_o r \approx 2s_o (1 + \theta_1^2) z \equiv 2s_\theta z \quad (3)$$

and

$$s_o = \frac{\omega_o}{4} \langle \Theta^2 \rangle \quad (4)$$

Thus, we have a new "corrected" scattering parameter based on the medium thickness due to the change in implicit variables.

The contracted projected time radiance cannot be readily solved. It involves an inverse Laplace transform which apparently needs to be done numerically. We can, however, solve for the contracted real space time-loss distribution which lends itself to a complete analytical solution since it is a convolution of the projected time-loss

distributions. This real space time-loss distribution readily follows when the inverse transform is analytically continued to the complex plane. It is

$$f(t) = \frac{\pi^2}{s_o r^2} \sum_{m=1}^{\infty} (-1)^{m+1} m^2 \exp\left(\frac{-m^2 \pi^2 t}{2s_o r^2}\right) \quad (5)$$

with

$$s_o r^2 \approx s_o (1 + 2\theta_i^2) z^2 \equiv s_i z^2 \quad (6)$$

This analytical form was also derived by Williamson⁶ and others. We again see a corrected form of the scattering parameter based on the thickness of the medium.

The differences in equations (3) and (6) will lead to an empirical definition of the region where the theory is valid. Note that the slightly different dependencies of s_θ and s_i are a result of the small angle approximation coupled with an implicit dependence of the beam spread in the radial direction, i.e., a plane of constant r instead of a spherical shell of radius r .

2.2) The Collimation Domain

We define the *Collimation Domain* as the region where the small-angle multiple scattering theory as described by van de Hulst and Kattawar is valid. Consider a general medium of radial depth r' with an extinction coefficient k . The optical depth of the medium is $r = kr'$. The extinction coefficient can be written as sum of scattering and absorption contributions, $k = k_{sca} + k_{abs}$. Focusing on small angle forward scattering we assume that we can separate the extinction coefficient's scattering contribution into a small angle (*sas*) and wide angle (*was*) component.

$$k = k_{sas} + k_{was} + k_{abs} = k_{sas} + \tilde{k}_{abs} \text{ with } k_{sas} = k_{sca} = \omega_o k$$

The diffuse radiation field set up in all directions by the "*was*" covers the forward direction and has a wide peak, but the radiance is much smaller than that set up by the beam in the *Collimation Domain*⁷. The competition of "*was*" with "*sas*" yields a rough estimate of the critical optical depth where the theory breaks down. This can be computed but appears to be too stringent. A better choice can be made empirically. This will be determined in the results. Calling this critical optical depth r_c , the bounds for the scattering contribution to the optical depth are

$$1 < r_{sca} << r_c$$

We also note that the beam cannot continue to spread indefinitely. This justifies an empirical definition. If we make a rough guess that θ_i will spread evenly between 0 and

$\pi/2$ this yields a width of $\langle \theta_i^2 \rangle = \frac{\pi^2}{12} = 0.82$. The real spread is due to small angle forward scattering, thus, an isotropic spread is an over estimate. The critical value $\langle \theta_i^2 \rangle$ reaches is 0.24 as the optical depth increases and we leave the *Collimation Domain*. Hence, the isotropic spread estimate is roughly 3 times too large in determining the endpoint of the domain for the steady state problem. The general problem which includes the temporal response of the beam is reached before this critical $\langle \theta_i^2 \rangle$ as s_θ and s_r physically represent the same quantity. Their required equivalence will decrease the estimate of r_c . This is expected in view of equations (3) and (6) which reflects the difference in depth dependence of these variables.

2.3) Truncated phase functions

The Monte Carlo process is a gradual spread in the radial direction. Hence, radiation traveling a distance r in a medium with a fundamental mean square angular deviation s_θ will arrive with an angular distribution in θ such that,

$$\langle \theta^2 \rangle \equiv 4s_\theta r \quad (7)$$

We examined the following phase functions:

Phase Function	Asymmetry (g)	Θ_m	s_θ
Isotropic*	$g=0$	5°	9.5173×10^{-4}
Isotropic	$g=0$	10°	3.8045×10^{-3}
Isotropic	$g=0$	20°	1.5179×10^{-2}
HG	$g=0.5$	5°	9.4813×10^{-4}
HG	$g=0.5$	10°	3.7484×10^{-3}
HG	$g=0.5$	20°	1.4357×10^{-2}
HG	$g=0.945$	5°	6.7075×10^{-4}
HG	$g=0.945$	10°	1.7941×10^{-3}
HG	$g=0.945$	20°	4.1950×10^{-3}
Gaussian	$\sigma^2 = 1.9046 \times 10^{-3}$	180°	9.5173×10^{-4}

* denotes distribution functions which are shown in the numerical results

2.4) Region of validity of the *Collimation Domain*

First we must consider the limits imposed on the *Collimation Domain*. The moments in θ scale as

$$\langle \theta_i^{2n} \rangle = \alpha (s_\theta z)^n, \quad n = 1, 2, \dots \quad (8)$$

while the temporal moments scale according to

$$\langle t_i^n \rangle = \beta (s_i z^2)^n, \quad n = 1, 2, \dots \quad (9)$$

with $n=1, \alpha=2$, and $\beta=1/6$ corresponding to the lowest non vanishing moments¹. Thus, the moments in projected angle all lead to the same scattering parameter, namely, s_θ as given by equation (3). Similarly, all the temporal moments lead to a scattering parameter, s_t , as determined by equation (6). Since the higher moments for each respective parameter has a higher power in the depth dependence they carry more error. Hence, the lowest non zero moments, $\{\langle \theta_i^2 \rangle, \langle t_i \rangle\}$, will be used throughout the calculations.

2.4.1) Lower limit of the *Collimation Domain*

We note that since the theory comes "on line" as a result of the Central Limit theorem the starting point for the region should only depend on the number of scatterings, or, in our homogeneous medium, the optical depth, r_{sca} .

2.4.2) Upper limit of the *Collimation Domain*

Equations (3) and (6) describe analytically the dependence of the scattering parameter on depth. These show that there is a strict region where the scattering parameter is uniquely determined by both these formulas. Since the scattering parameter is a measure of the optical properties of the medium we must have a consistent measure of it. This leads to an estimate of the endpoint based on the differing of the scattering parameter as determined by the spatial and temporal moments.

Considering a continuous beam where the temporal response has been integrated out, we arrive at a larger endpoint than that given by the full theory. This is simply a consequence of the lower depth dependence of the spatial as compared to the temporal moments. Making the aforementioned empirical estimate ($\langle \theta_i^2 \rangle \sim 1/4$) leads to

$$r_c < \frac{\omega_0}{8s_0} \quad (10)$$

for the spatially determined endpoint of the *Collimation Domain*. Of course, the actual endpoint is a matter of choice depending on the error the problem allows.

3. NUMERICAL RESULTS

3.1) Scattering parameter and the *Collimation Domain*

We show data for the 5°, 10°, and 20° truncation cases (figure 2). Beyond a 10° truncation the theory's ability to resolve the *Collimation Domain* realistically is limited since this leads to a large mean square single scattering angle. Fortunately, light scattering in turbid media such as the ocean and mammalian tissue is very forward⁸. This

lead us to focus on the smaller truncation angles (5°) when examining the contracted radiances of the Monte Carlo runs.

We fixed s_0 using the isotropic single-scatter at 5° and 10° cutoffs. The solid line plotted is the idealized theory, $s_0(1 + \langle \theta_1^2 \rangle)$, representing equation (3). The various other points are the Monte Carlo results of s_θ from equation (8) for all the phase functions considered. The agreement of the Gaussian with the Henyey-Greenstein phase functions of $g=0, 0.5$, and 0.945 obscures the multiple data points in figure 2A. In figure 2B we look at the overlap of s_θ and s_t of the isotropic phase function with $\Theta_m=5^\circ$. The analytic result for s_t and s_θ , (3) and (6), are again plotted as lines along with the Monte Carlo results generated from equations (8) and (9) which are represented as crosses. Figure 2C is a further demonstration of the fundamental scaling of the theory on $s_0 z$ along with a test of the "forwardness" of the phase function. It shows a Henyey-Greenstein phase function with $g=0.945$ for $\Theta_m=5^\circ, 10^\circ$, and 20° plotted similarly as (B) and (C).

3.1.1) Lower limit of the *Collimation Domain*

The beginning of the domain is purely a consequence of the Central Limit theorem. It depends only on the number of scatterings for which the scattering component of the optical depth, τ_{sca} , gives a statistical measure. The results are completely independent of the particular phase function. The same also holds for s_t as shown in figure 2B. Thus, the beginning depth of this region is a matter of choice which must be made depending on the allowed error. We think a reasonable choice is between two and three scatterings which was also arrived at empirically by Bucher⁹. At this point we have approximately 15% error between the theoretical and computational scattering parameter as determined analytically by equation (3) and numerically by equation (8). This optical depth also corresponds to the transition point during the metamorphoses of a non-Gaussian phase function's projected angle distribution. At this transition a Gaussian function of the same width as the distribution function will almost have an identical amplitude. We note that the lack of scattering initially translates into a scattering parameter which is too high according to theory (figures 2A and 2B).

The projected angle distribution functions shown in figure 3 are from optically thin runs which use an isotropic ($g=0$) of 5° truncation angle ($\Theta_m=5^\circ$). The solid lines in all the curves represent the analytical Gaussian function given by equation (2) with widths fixed using the Monte Carlo results in equation (8). The crosses represent the Monte Carlo calculation of these projected angle radiances. We see the persistence of the phase functions peak into the *Collimated Domain*. In the projected plane the isotropic distribution starts out circular with the radius of the truncation angle of 5° . This changes rather quickly into what appears to be a Gaussian form. Viewing this transformation we see that the single scattering distribution takes place tail first. The "kink" eventually works its way up the distribution giving the appearance that the metamorphoses takes place from the wings to the peak. This "kink" is a manifestation of the higher number of scatterings further off axis of the distribution function. This resolves itself by letting the peak retain its original single-scattering form longer than the wings. While in the *Collimation Domain* the contracted radiance never fully realizes a true Gaussian shape although the differences aren't appreciable except in the very forward direction at the

beginning of the domain. In fact, the validity of the Central Limit theorem implies that the peak region in the large optical depth cases is also a Gaussian but of a slightly different width. The deviations from the Gaussian nature in amplitude and width of the peak diminish with increasing optical depth, i.e., the "kink" works its way toward the peak. At a sufficient optical depth, depending on the mean square single-scatter, the peak zone has undergone a number of scatterings comparable to that in the wings which leads to a pure Gaussian form as predicted by the Central Limit theorem (see optically thick distribution functions in the next section). Before the critical optical depth, r_c , has been reached this is not fully realized. This is the reasoning behind the "pinched" appearance of the Monte Carlo radiances compared to their analytical counterparts.

3.1.2) Upper limit of the *Collimation Domain*

These results are based on the overlap of the values of the scattering parameters. We suggest $s_0 z = 0.1$ as the empirically estimated endpoint of the region. In figure 2B we have the scattering parameters given by equations (8) and (9) for $g=0$ and $\Theta_m=5^\circ$. The divergence of the analytical formulae, equations (3) and (6), occurs near an optical depth of $z=80$. Here the error between equations (3) and (6) is approximately equivalent to the error we chose as the starting point for the domain (15%). This endpoint must finally be determined by considering the allowed error of the problem.

If no temporal variables are required then we may work strictly with the scattering parameter s_0 . Here the empirically determined critical optical depth, r_c , given by equation (10) yields results with similar error as previously described (~20%). Again, the actual end point of the *Collimation Domain* is dependent on the error desired (figure 2). However, the empirical choice of the endpoint is a fairly accurate method since the beam cannot continue to spread forever. This resultant critical optical depth was obtained when the beam had spread to a width in the projected plane of 28° . This spread is about a factor of 3 lower than a uniform spreading from 0 to $\pi/2$. This resultant critical optical depth has a slightly larger error than that obtained for the full problem above, but its error bounds are near the same as we obtained in the beginning of the domain.

We varied s_0 considerably to check the limits of the "forwardness" of the scattering (figure 2C). This is really encompassed in the depth independent single-scattering parameter s_0 . Again we see the general agreement of various phase functions and the importance of the scattering parameter in the scaling of the medium. This scaling will be discussed more in later paper(s). A general region of validity with the above errors at the endpoints is obtained if we label the *Collimation Domain*

$$2 < r < r_c \quad (11)$$

with r_c empirically determined above both for the full and the steady state beam spread problem.

3.2) Contracted radiances

The distribution functions shown here are from runs which use an isotropic phase function ($g=0$) of 5° truncation angle ($\Theta_m=5^\circ$). The solid lines in all the curves represent the analytical formulae given by equations (2) and (5) respectively. These analytical functions were generated using equations (8) and (9) to fit the free parameter, i.e.,

$$s_\theta = \frac{\langle \theta_i^2 \rangle}{2z} \quad \text{and} \quad s_t = \frac{6\langle t_i \rangle}{z^2}$$

The crosses represent the Monte Carlo calculation of the contracted distribution function.

In the top of figure 4 we have the projected angle radiances at optical depths of 10 and 40 in a conservative medium. We see the same *quasi-Gaussian* nature as the optically thin cases within the *Collimation Domain*. At optical depths outside this domain the functions are Gaussian but the mean square scattering angle as predicted by theory does not hold (figure 2A). The Gaussian nature is a consequence of the Central Limit theorem, it is not necessary for the validity of the theory. Before this domain the shape of the single-scattering exists along with the Gaussian flavor of the wings as shown in figure 3.

The latter part of figure 4 represents the real space time loss (path difference) distribution for the same case as above. We have good agreement between the Monte Carlo and the analytical results given by equation (5) for cases within the *Collimation Domain*. The optically thin distributions, which are not shown, reveal no surprising results. They start from the Lambert-Beer law of pure exponential decay for the single scattering into the sharp rise followed by exponential descent for the optically thick cases relevant to the *Collimation Domain*. Outside the domain the theory fails to predict the fundamental form of the temporal radiance. This is the consequence of the planar approximation ($z = \text{constant}$) to the spherical shell ($r = \text{constant}$) which is the surface which actually describes the beam spread.

4. CONCLUSIONS

We have given a concise definition to the scattering parameter in terms of the phase function of the medium and angular spread of the beam. Our code built on the assumptions of van de Hulst and Kattawar allowed us to obtain the in-plane radiance and the real-space radiance as functions of the five fundamental variables of the problem. Thus, we have obtained the impulse solution temporally for the radiance. This allows us to compute the real temporal spread of an actual pulsed collimated laser simply by convolving the spread function of the laser with our temporal distributions. This should be of great use in studying such turbid media as mammalian tissue.

We have determined an empirical definition of the *Collimation Domain* ($2 < r < r_c$) where the small-angle forward scattering theory is valid. The wide variety of phase functions used shows the independence of this domain to the particular type of scattering excluding the demonstrated dependence on the mean square single scatter s_0 . The actual metamorphoses of the phase function into a multiple scattered radiance led to the

interesting *quasi-Gaussian* nature of the projected angle distribution while in the domain. These *quasi-Gaussians* were endemic to any phase function in the region of validity. Inside the domain a Gaussian profile for the projected angle distribution is of no importance to the theory. The distribution functions only become true Gaussians deep inside the domain leading to the conclusion that the single-scattering parameter, s_0 , and the optical depth are the variables of fundamental importance in determining the region of validity of the theory with the steady state problem exhibiting a deeper domain.

5. ACKNOWLEDGMENTS

This work was partially supported by the Office of Naval Research under contract number N00014-89-J-1467 .

6. REFERENCES

1. H. C. van de Hulst and G. W. Kattawar, "Exact spread function for a pulsed collimated beam in a medium with small-angle scattering", *Appl. Opt.*, to appear, 1994.
2. B. Chance, K. Kang and E. Sevick, "Photon Diffusion in Breast and Brain: Spectroscopy and Imaging", *Opt. and Photonics News*, 4, 9-13, 1993.
3. H. C. van de Hulst, "Scaling laws in multiple small-angle scattering with a non-Gaussian phase function", Unpublished, 1994.
4. S. L. Jacques, C. A. Alter and S. A. Prahl, "Angular Dependence of HeNe Laser Light Scattering by Human Dermis", *Lasers Life Sci.*, 1, 309-333, 1987.
5. V. V. Sobolev, A Treatise on Radiative Transfer, pp 240-244, D. Van Nostrand, Princeton, N.J., 1963
6. J. P. Williamson, "Pulse Broadening due to Multiple Scattering in the Interstellar Medium", *Mon.Not.R.astr.Soc.*, 157, 55-71, 1972.
7. A. Ishimaru, "Diffusion of light in turbid material", *Appl.Opt.*, 28, 2210-2215, 1989.
8. R. Marchesini, A. Bertoni, S. Andreola, E. Melloni and A. E. Sichirollo. "Extinction and absorption coefficients and scattering phase functions of human tissue *in vitro*", *Appl. Opt.*, 28, 2318-2324, 1989.
9. E. A. Bucher, "Computer simulation of light pulse propagation for communications through thick clouds", *Appl.Opt.*, 12, 2391-2400, 1973.

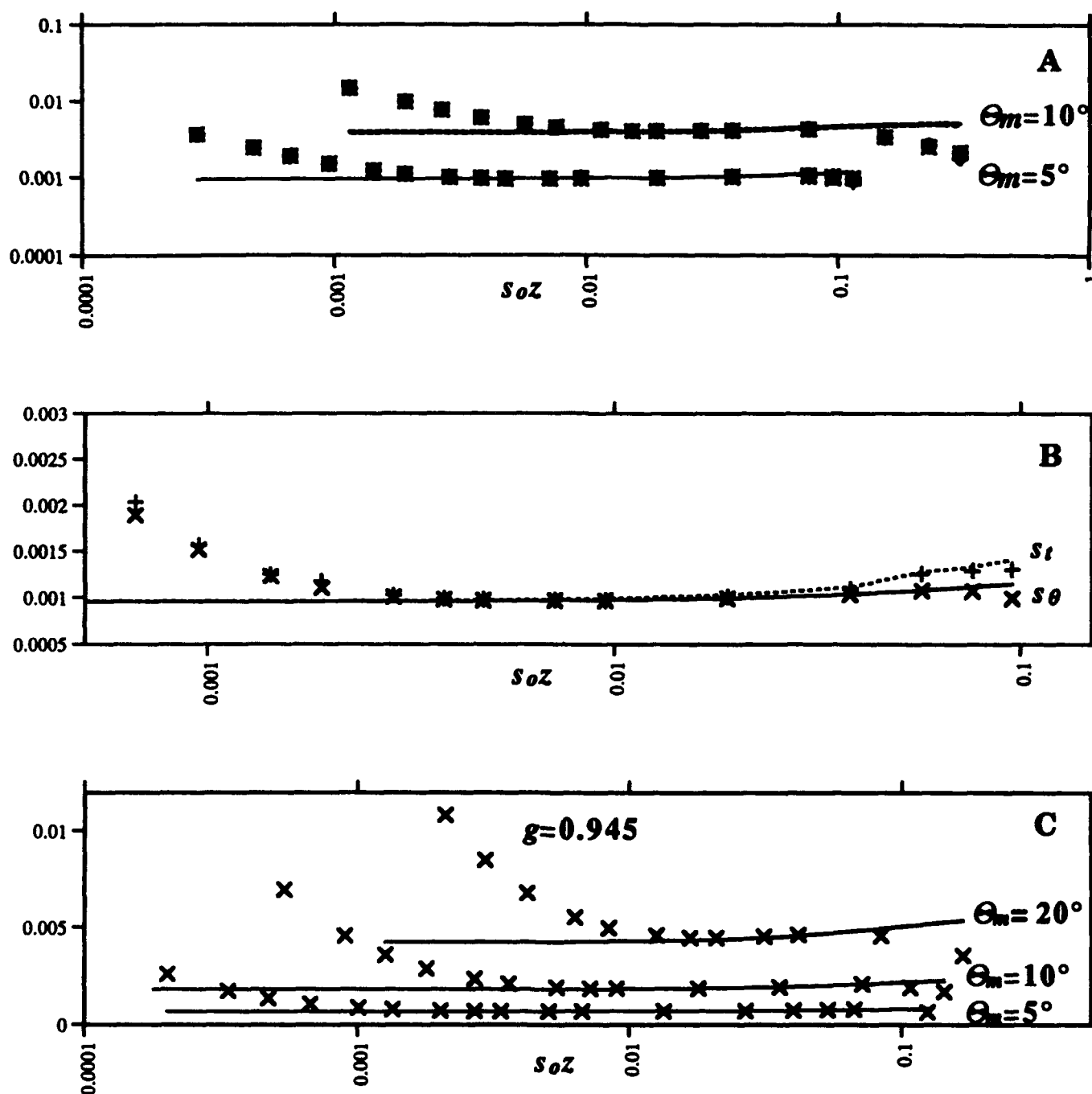


figure (2) In (A) the scattering parameter for the 5° and 10° phase functions in table 1 are plotted against the theoretical values as given by equation (3). (B) shows the scattering parameter of $g=0, \Theta_m=5^\circ$ as determined by equations (3) and (5). In (C) the scattering parameter for $g=0.945$ with $\Theta_m=5^\circ, 10^\circ$, and 20° is plotted against the theoretical values given by equation (3).

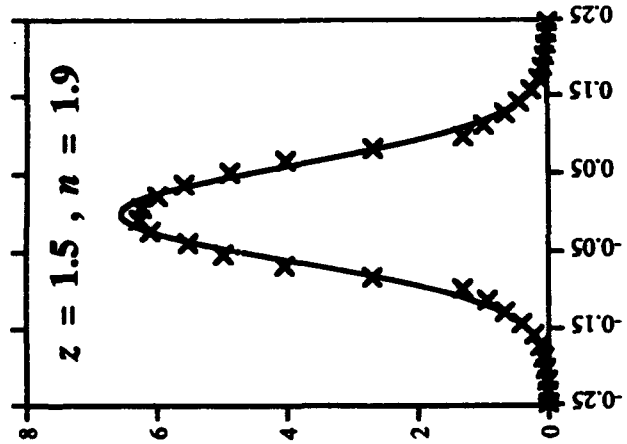
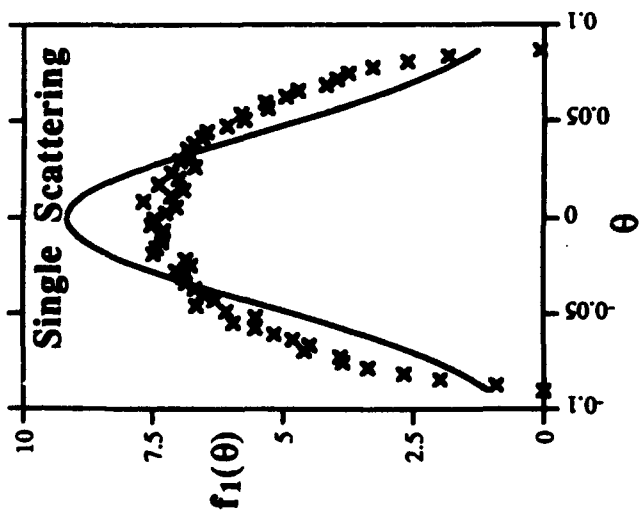
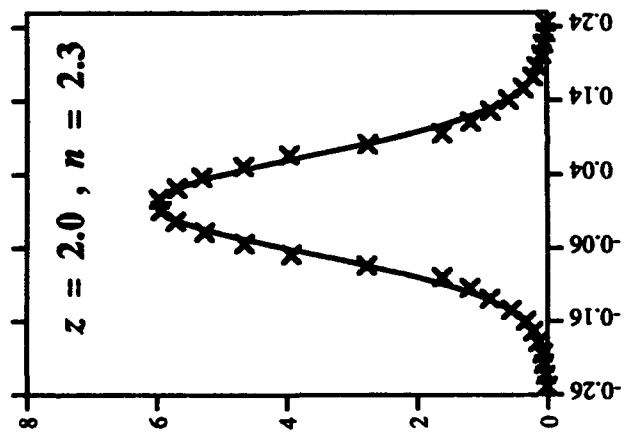
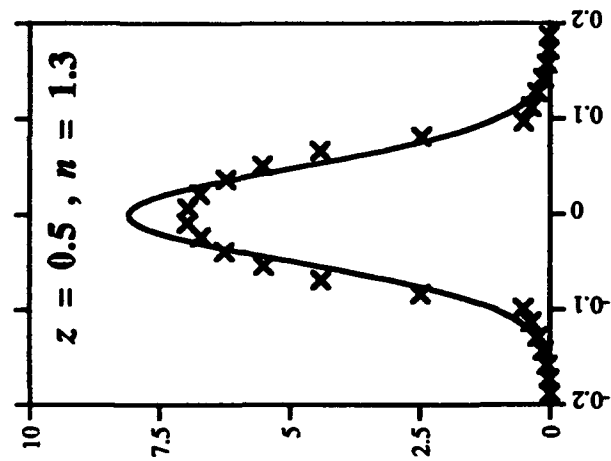
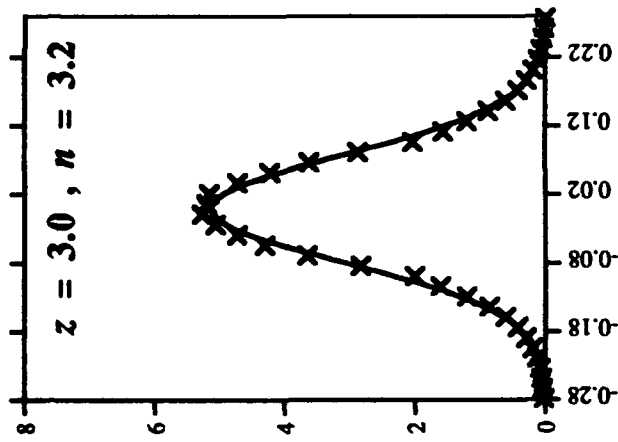
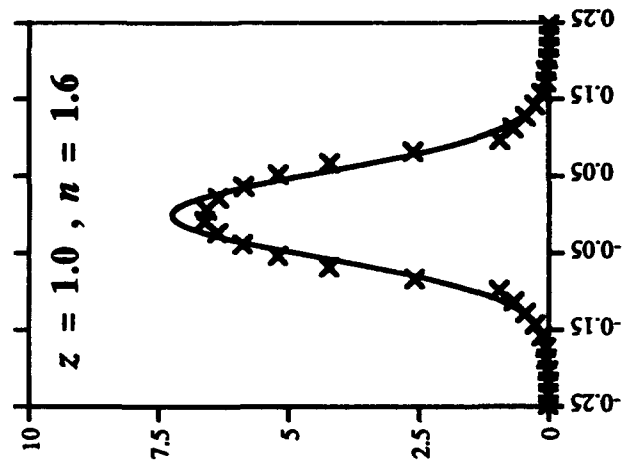


figure (3) $g=0, \theta_m=5^\circ$ projected angle radiance is shown for various small optical thicknesses.

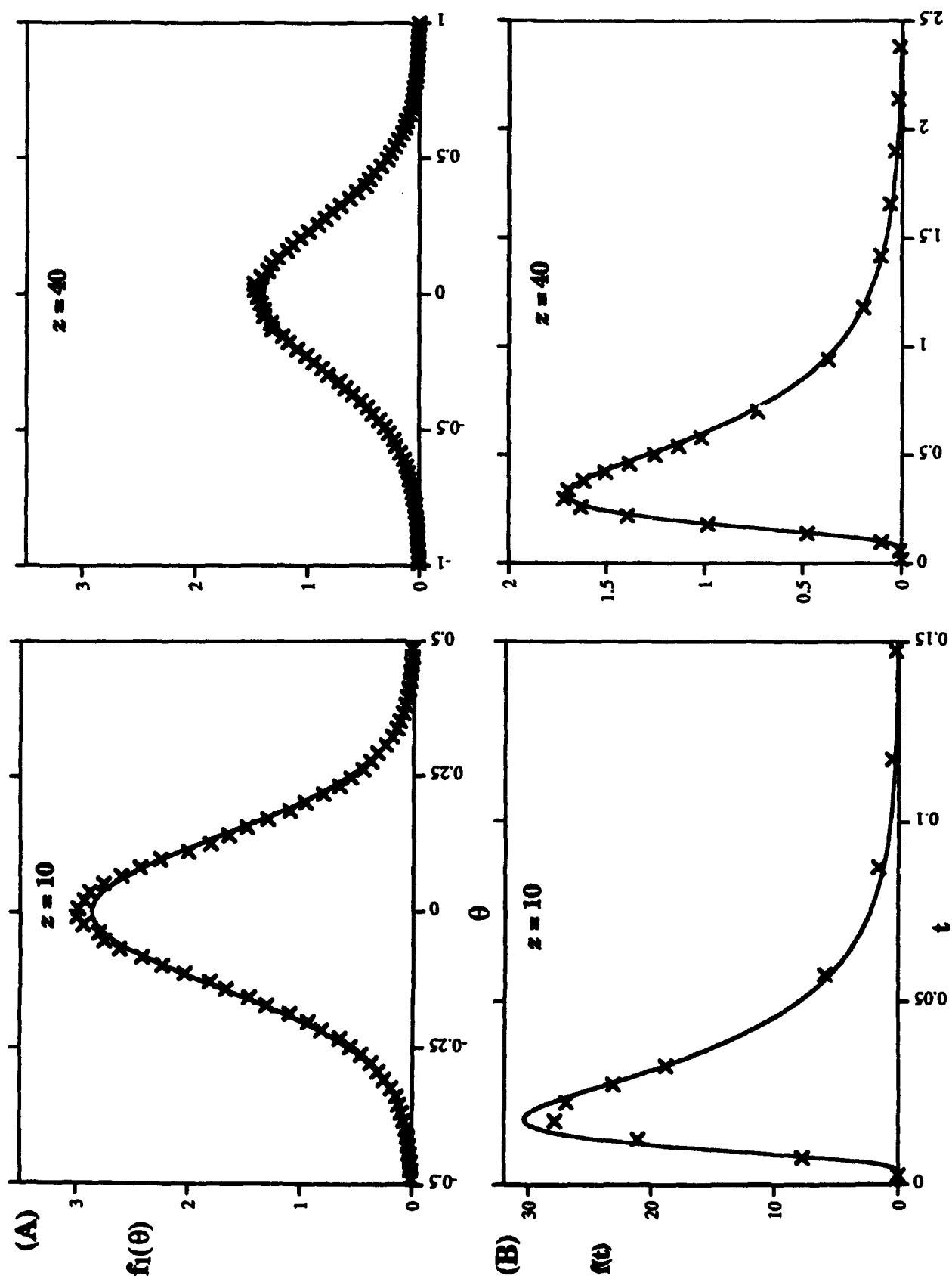


figure (4) In (A) $g=0$, $\theta_m=5^\circ$ projected angle radiances for optical depths of 10 and 40. In (B) $g=0$, $\theta_m=5^\circ$ temporal for optical depths of 10 and 40.

Light Scattering Induced by Turbulent Flow

D. BOGUCKI¹, A. DOMARADZKI², R. ZANEVELD³, T. DICKEY¹

¹ Ocean Physics Group, Department of Earth Sciences, University of Southern California, Los Angeles

² Department of Aerospace Engineering, University of Southern California, Los Angeles

³ College of Oceanic and Atmospheric Sciences, Oregon State University, Corvallis

ABSTRACT

Light scattering induced by turbulent flow in seawater has been studied and the effect of seawater turbulence on the propagation of a collimated light beam has been characterized. Inhomogeneities in the Refractive Index (IRI) of seawater are characteristic of turbulent flows. Our approach is to describe the interaction of light with IRI by solving Maxwell's equations. This set of equations is converted into the parabolized Helmholtz equation in the case of light propagating through water with IRI. We characterize the light scattering within a water parcel by the Volume Scattering Function (VSF). Field measurements of small-angle VSF exhibit a sharp peak which is orders of magnitude greater than that obtained from either laboratory measurements or Mie calculations for suspended particles. This has been postulated in the literature to be turbulence related. Our computer simulations show that the volume scattering function obtained is indeed characterized by an exponential decrease with scattering angle and is in quantitative agreement with *in situ* observations in the case of high temperature variance dissipation, χ . These results are in qualitative agreement with a previous study using the ray tracing technique. It appears that $O(1^\circ)$ is the upper limit of turbulent induced light scattering in the ocean.

1. INTRODUCTION

The passage of a coherent electromagnetic beam through a pure medium in turbulence results in a change of light velocity which in turn causes distortion in intensity and phase of the beam. Light propagation through the Earth's atmosphere has been studied extensively and many models have been developed to describe atmospheric turbulence (see for example the review by Strohbehn¹). Similar studies of the propagation of light in turbulent water are to date very sparse². The quantitative description of light scattering within a water parcel is given by the volume scattering function (VSF) (for example Spinrad³). Field measurements of small-angle scattering⁴ show that the VSF exhibits a sharp peak which is orders of magnitude greater than that obtained from either laboratory measurements of Spinrad³ or Mie type calculations for non-turbulent conditions⁵. This effect (*i.e.* peaking of volume scattering function at small angles) has been attributed to scattering by turbulence induced inhomogeneities in the refractive index of sea water (see Yura⁶). One of the main goals of this paper is to verify this conjecture.

Currently, increased use of optical detectors in the marine environment (for example biological oceanography and in underwater imaging and communications) makes quantifying the role of turbulence an important task. Fortunately, only small-scale fluctuations in the refractive index due to the flow field are relevant for light propagation. These small-scale features are only weakly dependent on the large-scale flow and thus are similar for different flow types⁷.

The interaction of light with fluid inhomogeneities associated with turbulence has long been utilized in laboratory observations of turbulence (*i.e.*, using the shadowgraph technique)⁸. This technique can also be used *in situ*, as was done to visualize a double-diffusive instability⁹.

It is extremely difficult to obtain optically clean water for laboratory experiments of light scatter due only to turbulence; thus we have chosen to do a numerical experiment. Any simplifying assumptions about the structure of turbulent flow fields can lead to unexpected errors¹⁰, and so we have chosen to use a direct numerical simulation. We propagate light through this modeled turbulent field to quantify the interaction of light scatter. Here we present the results of our numerical experiment.

2. THEORETICAL BACKGROUND

2.1. Inhomogeneities in the refractive index

Inhomogeneities in the refractive index (IRI) are characteristic of turbulent flows. Under typical oceanic conditions, these inhomogeneities appear to be temperature dominated. In general, however, the real part of the refractive index of seawater varies with changes of temperature, salinity, and pressure (changes in the imaginary part of the refractive index of water are negligibly small compared with the real part¹²). The effect of pressure can be neglected for spatial scales on the order of a meter or smaller. The variance of the IRI can be expressed as the sum of the variance associated with temperature and salinity: $\overline{(n^2)}^{1/2} = \overline{(n_T^2)}^{1/2} + \overline{(n_S^2)}^{1/2}$, where $\overline{(\)}$ denotes spatial averaging, n is the refractive index, and n_T and n_S are the contributions of temperature and salinity respectively.

In the ocean, background temperature and salinity induce quite different variance in the IRI. For example, data from the coastal region off Oregon (J. Moum, pers. comm.) show that variance of the refractive index due to temperature is much larger than that due to salinity. Thus, only temperature induced IRI will be considered in this study, so hereafter $n = n_T$.

The largest and smallest size of temperature inhomogeneities, and consequently of IRI, can be inferred from the observed oceanic rates of turbulent kinetic energy dissipation, ϵ . In the lowest limit, the spatial scale is approximately given by the Kolmogorov scale $2\pi(\nu^3/\epsilon)^{1/4}$, where ν is the molecular viscosity. Under typical oceanic conditions, dissipation is found to be between 10^{-9} and 10^{-6} W/kg¹³. Given this range of dissipation, the Kolmogorov length typically varies between 10^{-3} and 10^0 m. The contribution of the IRI on scattering is largest for the smallest IRI structures⁶. Therefore in this study we will concentrate on light scattering by IRI structures at the Kolmogorov scale.

2.2. Interaction of IRI with light

The interaction of light with IRI is described by Maxwell's equations. This set of equations, in the case of forward scattered light, can be converted into the parabolized scalar Helmholtz equation¹¹. In this equation, if light initially propagates along the z-axis, we have:

$$\left(\frac{\partial^2}{\partial x^2} + \frac{\partial^2}{\partial y^2}\right)\psi + 2ik\frac{\partial\psi}{\partial z} + k^2\left(\frac{n^2(r)}{n_0^2} - 1\right)\psi = 0 \quad (1)$$

where ψ represents the amplitude and the phase of the electric field, k is the light wavenumber, $n(r)$ is the spatially varying refractive index, and n_0 is the mean refractive index. We obtain the refractive index field from direct numerical simulation (DNS). This equation is derived from the full set of Maxwell's equations and is accurate as long as the propagating light creates small or moderate diffracting angles with respect to the propagation axis¹².

3. METHODS

To confirm the conjecture about importance of the light scattering by turbulence at small angles we have used data from Ruetsch and Maxey¹⁴. They simulated turbulent flow field data on a 96^3 grid point flow field with an embedded temperature field as a passive scalar. The Prandtl number used, $Pr = 0.5$, is not very realistic since Pr for water is 7. We use these data to model the temperature distribution. Thus here temperature spectra and velocity are similar.

The low Pr means that the smallest temperature structures will be somewhat larger than the structures in velocity. Therefore the presently used DNS data set does not reproduce representatively small temperature scales. This leads to an underestimate of the volume scattering function. For future work, we will use a simulation with $Pr = 7$.

The flow has a microscale Reynolds number of 60 (and 500 at the cube scale). This is small in comparison to typically observed geophysical flows where the Re is at least of order 10^6 in typical oceanographic applications and over scales of m. The disparity between the Re of realistic flows and that of the simulation is fortunately not an

important factor for the light scattering process. It can be shown that the largest contribution to light scattering comes from the smallest temperature scales which are locally isotropic⁷. Thus, in order to reproduce light scattering on the turbulent flow we only have to reproduce accurately small scale fluctuations of the scalar field. This can be achieved by scaling the simulated temperature distribution with field data.

Our observational dataset has been kindly provided by J. Moum from the TOGA-COARE experiment (Fig 1).

We use the spectral energy (E) and that of fluctuating temperature energy (E_T) to scale the simulated temperature field. The scaling was done in such a way that the ratio of E_T and E from the simulation is set equal to the ratio obtained from the *in situ* measurements for high wavenumbers. (assuming universal equilibrium range spectra). The scaling of the refractive index fluctuations reveals that they are strongly dependent on the observed ratio of ϵ to the rate of dissipation of temperature fluctuations χ . Thus in our simulations we keep ϵ constant (10^{-6} W/kg) which fixes the size of the smallest velocity scales. This is among the largest observed dissipation values, which ensures maximum IRI. We then chose two extreme cases of χ : weak ($10^{-11} \text{ K}^2/\text{s}$) and strong ($10^{-6} \text{ K}^2/\text{s}$). These cases are shown in the context of the observational data in Fig 2.

Both values were observed within the surface mixed layer (see Fig 1). The stronger one corresponds to mixing conditions like those at the base of the mixed layer (70 m) while the lower χ is similar to mixed layer values. We have chosen these extreme cases to examine the full range of variability for high ϵ . The high χ value is infrequent: it only made up 1% of the observational data set used here.

We solved equation (1) numerically using the pseudo-spectral second order method described in Strohbehn¹. The code was written in Fortran for the San Diego Cray C90. The result of simulating light propagation is that we obtain light intensity in W/m^2 and direction in *radians* at cross-sections of the sample cube perpendicular to light direction. Here we report the volume scattering function VSF at a given wavelength ($k = 10^7 \text{ m}^{-1}$) as the scattered radiant intensity I in a direction θ per unit scattering volume dV divided by the incident irradiance E

$$VSF(\theta) = \frac{dI(\theta)}{EdV}. \quad (2)$$

We also compare the results obtained by propagating light using the geometrical optics method (ray tracing).

4. RESULTS

We determined the spatial distribution of the complex $\psi(x, y)$ of the light after its passage through a simulated turbulent flow field using the parabolized Helmholtz equation. These data were converted into light distribution intensity and the VSF were estimated for each of the two cases of χ .

The emerging from the turbulent flow field irradiance distribution (Fig 3) has a banded structure reminiscent of shadowgraphs taken in laboratory experiments. It is also similar to the observed irradiance distribution obtained using the ray tracing technique¹⁵.

The relative variability of the irradiance $(E - E_0)/E_0$ is of order 10^{-7} in the case of weak χ and 10^{-4} in the case of strong χ . Despite this difference, the spatial distribution of the irradiance is the same. This may be because the Prandtl number is too small, that is the smallest temperature scales are not likely to be generated in the simulation. The smallest IRI are mostly associated with velocity structures; since both cases have the same ϵ , the light distribution would be the same. More importantly, the outgoing light is measured at 20 cm, which is within the pre-caustic (focusing) zone. The relative variability of the irradiance is thus not fully developed¹⁰, as the variability has not reached maximum value. Maximum variability is attained within distance of $O(m)$ from the turbulent volume given the parameters used. It may also be that the outgoing light pattern is independent of χ within a certain parameter range. This is a tantalizing result, but cannot be verified until higher Pr cases are examined beyond the pre-caustic zone, and for a range of ϵ values.

More quantitative results come from analyzing the VSF angle dependence (Fig 4).

Both cases show a similar functional form, which can be divided in three regions. For the smallest angles, the VSF changes very slowly, and there is a threshold beyond which no energy is propagated. From physical reasoning we expect a continuous function. The paucity of points is associated with numerical truncation used in light propagation

TOGA - COARE profile: asc124

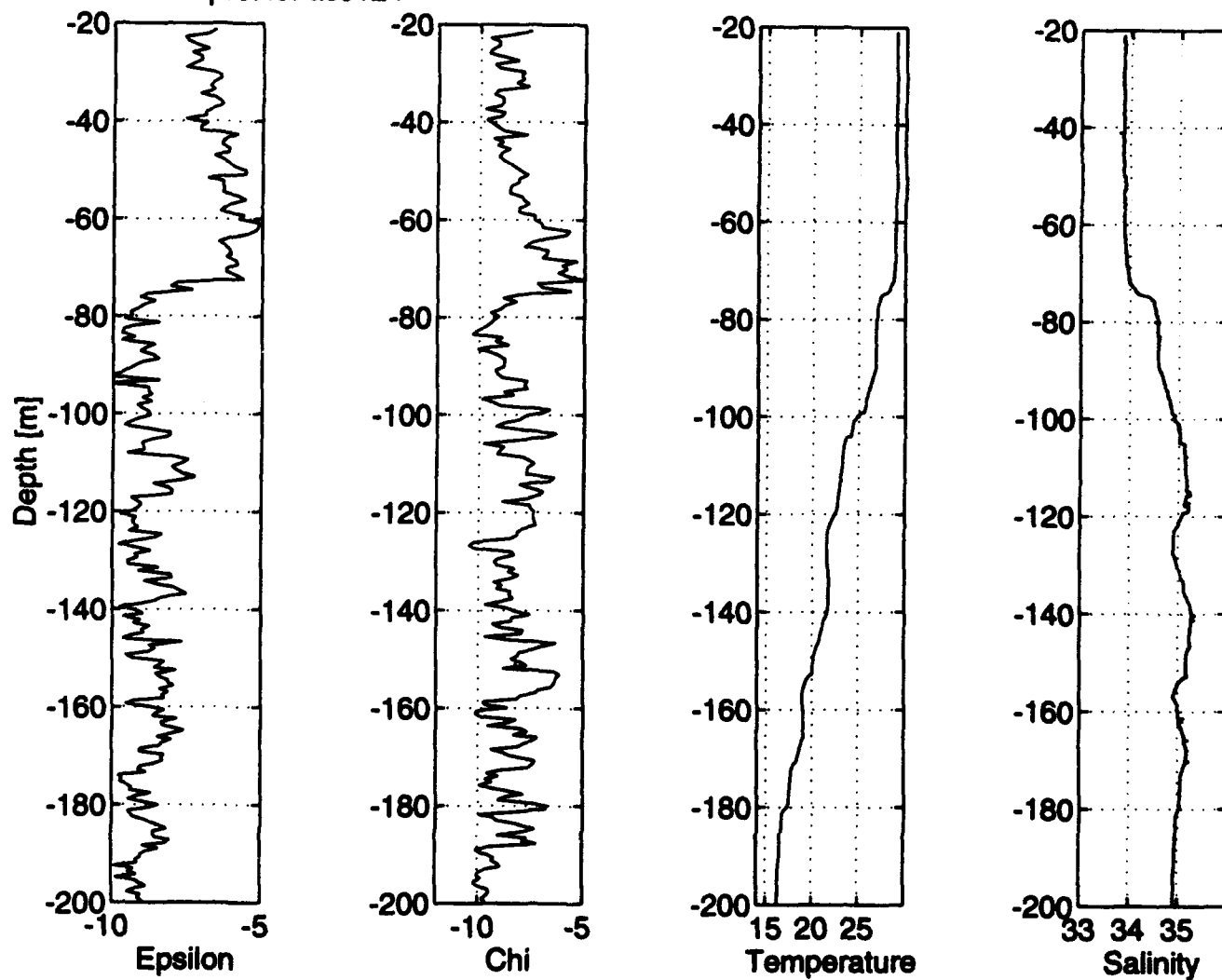


Figure 1:

Profile of ϵ , χ , temperature and salinity from TOGA-COARE experiment (courtesy J. Moum).
Our choice of ϵ and χ corresponds to the observed parameters between 60m and 80 m depth

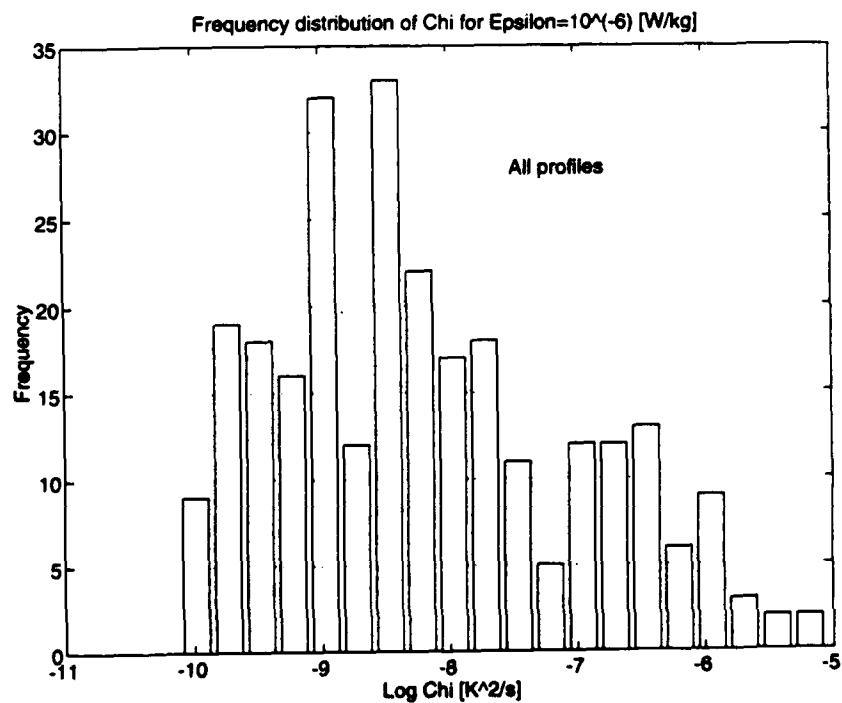
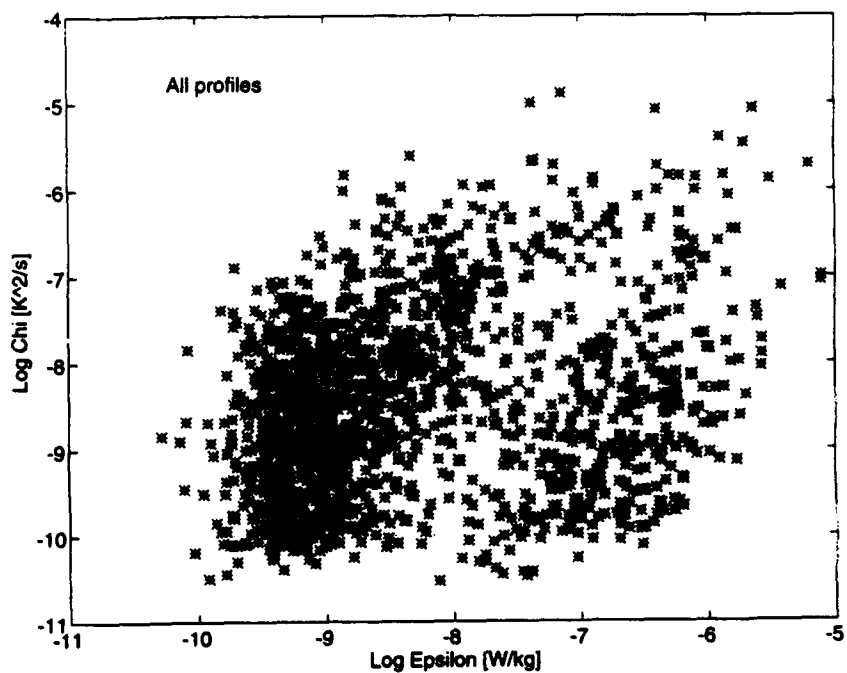


Figure 2:

A. Scatter-plot of the observed ϵ vs. χ in the observational data set. B. Frequency distribution of χ for the chosen $\epsilon = 10^{-6}$ W/kg.

$$0 < \text{Relative irradiance: } (E-E_0)/E_0 < 10^{-4}$$



Relative irradiance scale

Scattered light irradiance high Chi case

Side length: 20 cm



Side length: 20 cm

Figure 3:
Spatial distribution of the irradiance after its interaction with the turbulent flow.

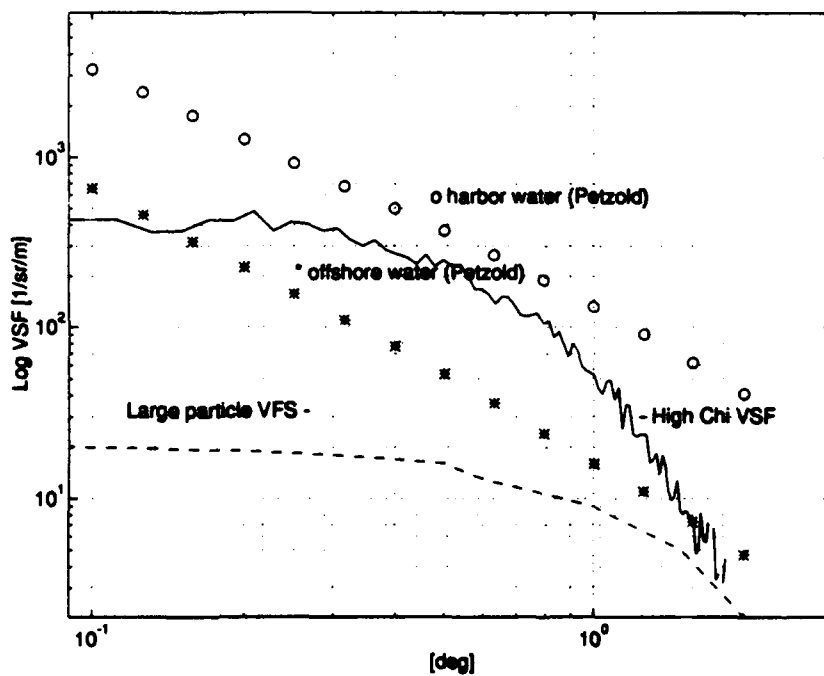
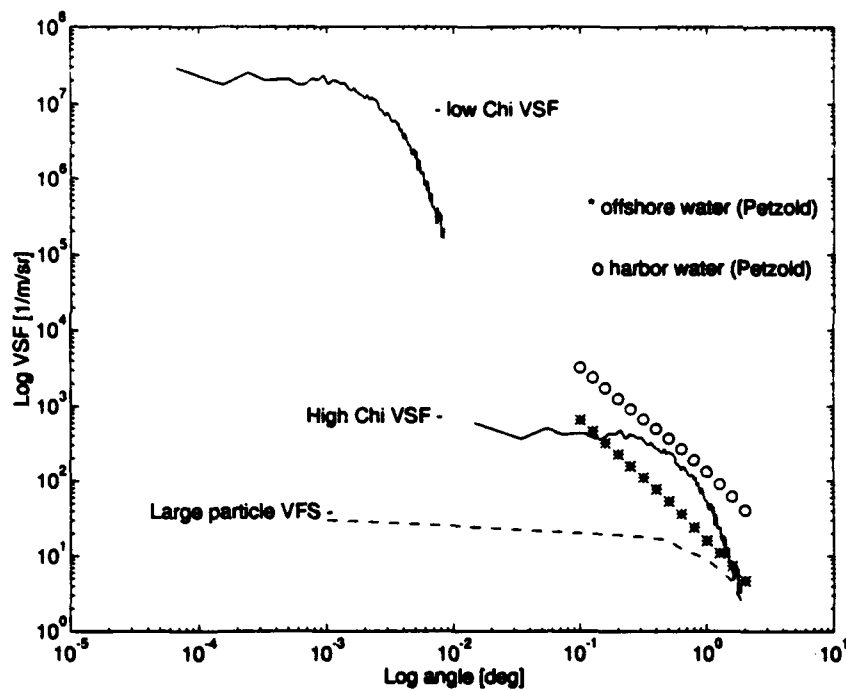


Figure 4:

A. Calculated VSF for two χ cases. VSF measured by Petzold⁴ and contribution to VSF from large particles⁵ is shown. B. High χ VSF case in log-normal representation with particles contribution to⁵ VSF and VSF observed by Petzold⁴

routine. For the largest angles, we observe random fluctuations around a constant VSF . This variability is again associated with numerical truncation error. The intermediate region is the main result. This region encompasses two orders of magnitude in scatter angle and three orders of magnitude in VSF . (This is consistent with tests carried out on the numerical solution of equation (1) for a known functions ψ and n , in which the dynamic range was at least three orders of magnitude.) In this region, the VSF decreases exponentially with the scatter angle. This behavior is consistent with the measurements of Petzold⁴ and the numerical simulation for Mie scattering on particles carried out by Shifrin⁵. We can observe this in Fig. 4. There we can see our results overlaid with the VSF observed by Petzold⁴ and compare the particle contribution to the VSF . As we see there the largest particle contribution is fairly constant between angle 0.1° and 1° and decreases rapidly for angles larger than 1° . At the same time for angles between 0.1° and 1° , the observed VSF (Petzold⁴) changes by 2 orders of magnitude similarly to our calculations. These observations were made in the fairly energetic offshore subsurface zone. Our modeled results for the case of high χ show agreement with his field measurements.

In the case of low χ , light is scattered between angles 10^{-4} of 10^{-2}° . For the case of high χ , light is scattered over a greater range to $O(1^\circ)$. Although the simulated high χ case gives scattered light at relatively large angles, this is an infrequent value for the oceanic environment. Nonetheless, uncertainties in optical measurements in seawater due to turbulence-induced scattering may reach up to 1° for high temperature variance situations.

The exponential decrease of the VSF with increasing angle was also independently observed in the simulations using the ray tracing technique¹⁵.

5. CONCLUSIONS

1. The light intensity distribution exiting the cube exhibits a banded pattern, similar to that observed in laboratory shadowgraphs.

The pattern obtained by solving the parabolized Helmholtz equation is similar to that obtained from the ray tracing technique.

2. The light intensity distribution for the two cases of χ values are identical. Thus the distribution is probably weakly dependent on the low Pr value and a consequence of sampling within the pre-caustic zone. It may also indicate that there is a parameter space for which light scatter intensity is driven by ϵ only.
3. The volume scattering function is characterized by an exponential decrease of VSF with scatter angle.
4. Our results suggest that turbulence may be responsible for the unexplained scatter at small angles observed in *in situ* experiments.
5. It appears that a scattering angle of 1° is the upper limit for turbulence-induced light scatter in the ocean. All measurements relying on light propagating in the ocean within this angle may be affected by turbulence.

6. ACKNOWLEDGMENTS

This work was funded by the Ocean Optics Program of the Office of Naval Research under contract number N 00014-94-1-0107. The simulations were carried out at the San Diego Super-computing Center. We thank the support staff for their assistance and efficiency. Dr. James Moum generously provided a very complete suite of oceanic turbulence measurements and Dr. Gregg Ruetsch made his DNS data available, as well as helpful discussion. We are also grateful to Drs. Dariusz Stramski and Mary-Elena Carr for many helpful comments and to Dr. Carr for assistance in manuscript preparation.

7. LITERATURE

1. J. W. Strohbehn, ed., *Laser beam propagation in the atmosphere*, Springer-Verlag, 1978.

2. C. R. Truman, "The influence of turbulent structure on optical phase distortion through turbulent shear flows", *AIAA Technology Conference*, 1992.
3. R. W. Spinrad, "Measurements of the volume scattering function at near forward angles for suspended oceanic particulates", *SPIE*, vol 160, pp. 18-22.
4. T. H. Petzold, "Volume scattering functions for selected ocean waters", *Technical Report U. of California San Diego*.
5. K. S. Shifrin, *Physical Optics of Ocean Water*, AIP Translation Series, 1988.
6. H. T. Yura, "Small-angle scattering of light by ocean water", *Applied Optics*, vol 10, No1, pp. 114-120.
7. G. K. Batchelor, "Small-scale variation of convected quantities like temperature in a turbulent fluid", *Journal of Fluid Mechanics*, vol. 5, pp. 113-133.
8. L. A. Vasilev, *Schlieren methods*, Israel program for scientific translations, 1971.
9. E. Kunze, A. J. Williams and R. W. Schmitt, "Optical microstructure in the thermohaline staircase east of Barbados", *Deep-sea Research*, Vol 34, No 19, pp. 1697-1704.
10. B. J. Uscinski, ed., *Wave propagation and scattering*, Clarendon Press, 1986.
11. A. S. Monin and A. M. Yaglom, *Statistical Fluid Mechanics*, MIT Press, 1981.
12. M. Born and E. Wolf, *Principles of Optics*, Pergamon Press, 1964
13. M. C. Gregg, "Diapycnal mixing in the thermocline", *Journal of Geophysical Research*, Vol 92, pp. 5249-5286.
14. G. R. Ruetsch and M. R. Maxey, "Small scale features of vorticity and passive scalar fields in homogeneous isotropic turbulence", *Physics of Fluids A*, Vol 6, pp. 1587-1597, 1991.
15. D. Bogucki, G. R. Ruetsch and T. D. Dickey, "A numerical study of the optical properties of a turbulent flow field with application for the marine environment", *Proceedings of the Third Oceanography Society Meeting*, Seattle, 1993.

An estimate of the average cosine for the radiance distribution resulting from a point source in the ocean.

Kenneth J. Voss
Physics Department, University of Miami,
Coral Gables, FL 33124

Robert A. Maffione
SRI International,
333 Ravenswood Ave., Menlo Park, Ca. 94025

ABSTRACT

We have shown in an earlier paper that by measuring the decay of the irradiance field due to a point source, the absorption coefficient of the medium can be determined. A central parameter in this method is the average cosine of the radiance distribution at each measurement point. From measurements of the Point Spread Function (PSF), an estimate of the average cosine can be determined. However, experimentally the PSF is routinely measured only to 12 degrees. We have also previously shown a method which relates the small angle PSF measurements to an empirically derived analytic formulation of the Beam Spread Function (BSF) which extends to 90 degrees. We will present an independent test of this method, and then use the BSF to determine the average cosine for varying ranges (from the point source) and water properties. In this way we can estimate how rapidly the average cosine varies, and its relative importance in the field measurements of the absorption coefficient with these techniques.

1. INTRODUCTION

One of the most important parameters in describing the propagation of light is the total absorption coefficient of the medium. This parameter is also one of the most difficult to properly measure. In almost every technique, light scattering can interfere with the measurement to some extent. Additionally there are unanswered questions about the variability of the absorption coefficient with changes in the measurement scale, the so-called "scales problem". Often the inherent optical properties of the medium, such as scattering and absorption, are required for prediction of the light field through radiative transfer modeling. In this case a large scale measurement technique is most appropriate. The most common method of measuring absorption on a large scale is through some variation of Gershun's Law.¹ This equation relates the average cosine of the light field and the falloff of scalar or vector irradiance with the absorption coefficient. Most commonly, the light source used, or proposed, is the natural solar illumination. In an earlier paper,² we discussed how a point source may be used as a light source and illustrated the differences in the resulting Gershun's Law when the light field exhibits spherical symmetry, rather than plane parallel symmetry as resulting from solar illumination. A key factor in this technique is the average cosine of the light field resulting from the point source. In this paper we will illustrate one method of estimating the average cosine, given small angle measurements of the PSF. With these results we will illustrate the predicted variation of the average cosine

2. BACKGROUND

In a previous paper, we showed that the absorption coefficient can be related to the irradiance attenuation from a point source using Gershun's Law in spherical coordinates. The equation relating these factors is:

$$a(z) = \bar{\mu}_r(z) \left[K_E(z) - \frac{2}{z} \right]$$

Where $a(z)$ is the absorption coefficient, $K_E(z)$ is the diffuse attenuation coefficient for vector irradiance from an isotropic source, z is the distance from the source, and $\bar{\mu}_r(z)$ is the radial average cosine:

$$\bar{\mu}_r(z) = \frac{E_r(z)}{E_o(z)}.$$

The $2/z$ factor is simply due to the inverse z^2 dependence of the spherically dependent light field. $K_E(z)$ is defined by:

$$K_E(z) = -\frac{1}{E_r(z)} \frac{dE_r(z)}{dz}.$$

So if $E_r(z)$ as a function of z is measured, and an estimate (or measurement) of $\bar{\mu}_r(z)$ is available, then $a(z)$ may be determined.

The PSF(θ, z), if known for all angles, can provide $\bar{\mu}_r(z)$:

$$\bar{\mu}_r(z) = \frac{\int PSF(\theta, z) \cos(\theta) d\Omega}{\int PSF(\theta, z) d\Omega}.$$

Where θ is the angle between the point source and incoming radiance (zero for radiance coming from the point source, π when going toward the point source). Unfortunately, because the PSF falls off very rapidly with angle, it is difficult to measure this function at large angles. The method we are currently using to measure the PSF was originally developed by Honey³ and involves a point source (a flashlamp) and a camera system. Descriptions of the instrument and calibration techniques have been discussed previously.⁴ However for this discussion it is relevant that this instrumentation only measures the PSF between 1-200 milliradians. Thus to obtain the PSF over a larger angular range, some numerical method must be used to extrapolate these data. We have described a method⁵ which uses an empirically derived equation for the Beam Spread Function (BSF) derived by Duntley and coworkers at the Visibility Lab, Scripps Institution of Oceanography.⁶ The empirical relationship of the beam spread vs. angle is given by the expression:

$$BSF(\theta) = \frac{E(\theta)}{P} = \frac{10 (A-C) \theta^B}{2 \pi z^2 \sin \theta} \quad (1)$$

where:

$$A = 1.260 - 0.375 (c z) [0.710 + 0.489(a/c)] - [1.378 + 0.053(c/a)] 10^{-cz} [0.268 + 0.083\{c/a\}]$$

$$B = 1 - 2(10^{-D})$$

$$C = \frac{1}{3} \{ [(\theta/F)^{3/2} + 1]^{2/3} - 1 \}$$

$$D = c z [0.018 + 0.011 (c/a) + 0.001725 c z]$$

$$F = [13.75 - 0.501 c/a] - [0.626 - 0.0357 c/a] c z + [0.01258 + 0.00354 c/a] (c z)^2$$

In these expressions $E(\theta)$ is the irradiance measured off-axis, P is the beam power, θ the angle (in degrees) with respect to the unscattered collimated light, c is the beam attenuation coefficient, z the range, and a the absorption coefficient. In the earlier paper we have shown a method to fit experimental ocean measurements with specific values of the a/c and cz parameters. To summarize this method:

1. Profiles of the beam attenuation with depth are used to determine the total optical pathlength, τ , for each PSF measurement.

2. From individual graphs of $\log(\text{PSF})$ vs. $\log(\text{angle}[\text{milliradian}])$ the slope, m , in the region between 4 and 100 milliradian is found. This step depends on the observation that the graph of the $\log(\text{PSF})$ vs. $\log(\text{angle})$ is almost linear in this region.

At this point one has a relationship for the PSF such that:

$$\text{PSF}(\theta) = B_1 \theta^{-m}.$$

where m is the slope of $\log(\text{PSF})$ vs. $\log(\text{angle})$. B_1 is related to the offset in this relationship.

3. Next one uses the observation that there is a regular relationship of m with τ . A relationship of the form $m = A * 10^{(-B\tau)}$ provided a good fit with the empirical equation for a given a/c . Figure 1 uses a new data set, obtained in clear water off of Hawaii, to illustrate the behavior of this function.

4. If one uses the fit from Fig. 1 and plots the resultant B on the curve in Fig. 2 a/c can be obtained. Note that this a/c may not be the real a/c in the water. It is the a/c which can be used to fit the experimental data to the empirical formula. In Fig 2 the values are shown for the calculations along with the value found previously for TOTO (Tongue of the Ocean, Bahamas), the coastal Pacific (PO), Sargasso Sea (SS) and Hawaii.

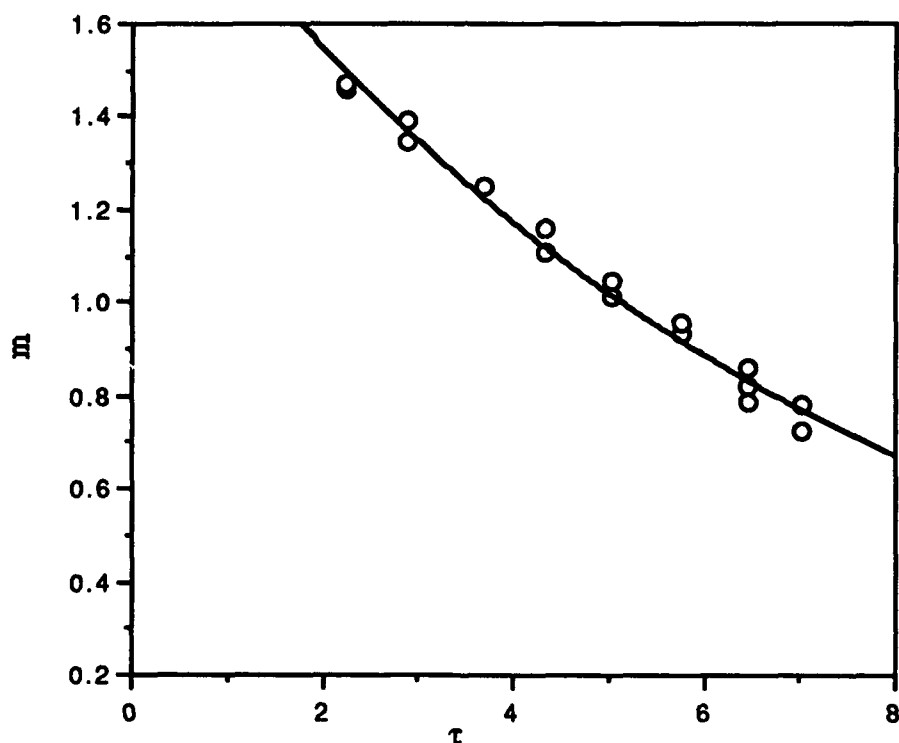


Fig 1) Illustration of functional fit of m vs τ for a data set taken off of Hawaii. This shows how a simple function will relate τ to m for a single data set. All data is from one cast with varying pathlengths in fairly homogenous water. This data was taken at 500 nm.

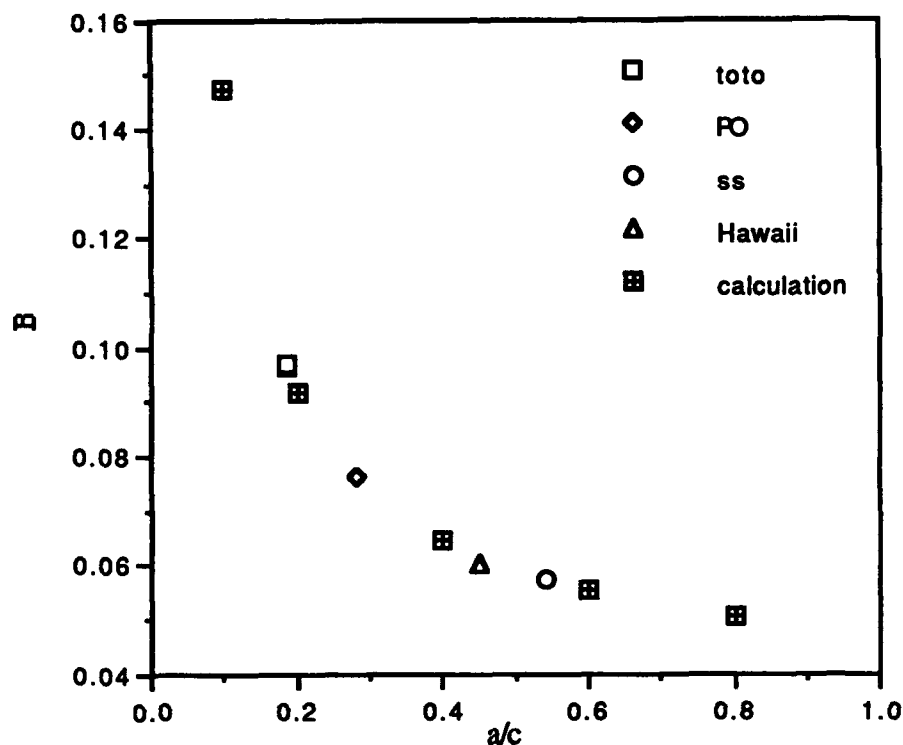


Fig. 2) Relation of a/c for empirical equation and the B coefficient found using m vs t . This graph shows both the results from the empirical equation (B found for each a/c value for the empirical equation) and the B resulting from the different cruise data. This graph enables one to find the correct a/c to use when extrapolating the PSF to larger angles.

5. It is also necessary to make correction to τ using the A derived in the above equation. The correction was empirically found to be:

$$cz = \tau - \log(A/2.158)/B$$

In the case of the Hawaii data this correction results in the addition of 0.41 to the optical pathlength found from the c profiles. This change is probably related to matching the physical size of the source in the oceanic measurements to that of the tank tests. It has a relatively small effect at large ranges, but increases the effective pathlength for short ranges.

After following the above steps, one can generate a PSF using the cz a/c and range (z) with which to compare to our experimental data. Two PSFs from the Hawaii data set, with extreme differences in optical pathlength, were chosen to illustrate the fit. In the short pathlength case τ was 2.23 (obtained from the beam attenuation profile) and the range was 32 m. The parameters needed for the empirical equation were $a/c = 0.45$ and $cz = \tau + 0.41$. The comparison of the experimental PSF and the calculated PSF are shown in Fig. 3. In the long pathlength case τ was 7.07, the range was 100m, and the other factors were constant. The comparison of the experimental data and the empirical equation for this case is shown in Fig 4. In both these cases the PSFs generated with the equation were normalized to the experimental data at 10 milliradians. As can be seen the fit is

very good over the range of the experimental data in both cases. The largest deviations appear at small angles in the shorter range data set and is undoubtedly caused by the finite size of the source appearing in our experimental data.

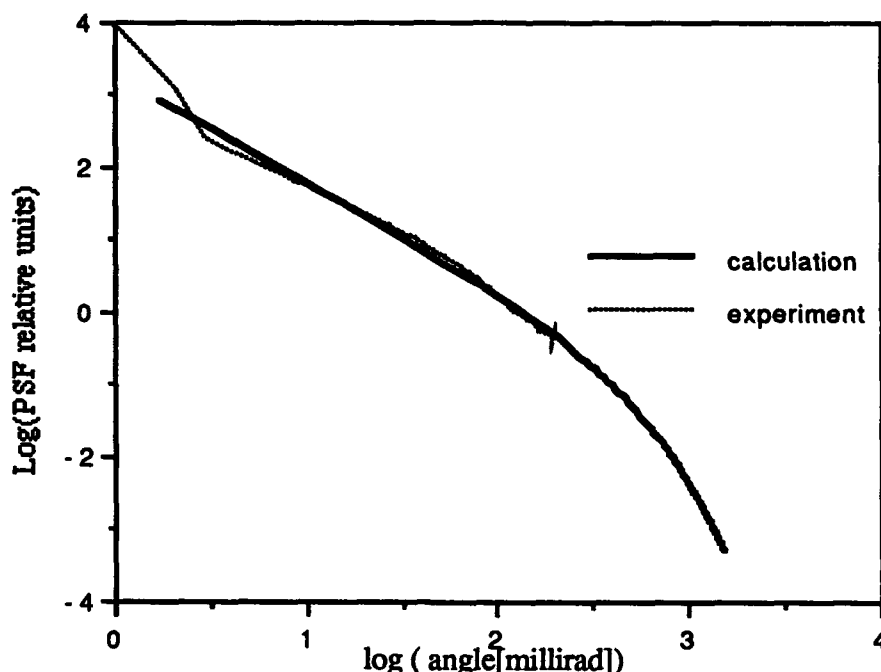


Fig. 3) Graph showing the extrapolated PSF and an experimentally measured PSF. Extrapolation using technique described in text. This data is for 2.23 optical depths, a range of 32 m. $a/c = 0.45$ and $cz = \tau + 0.41$. Data obtained at 500 nm.

3. AVERAGE COSINE

Our method for fitting the measured PSF to Duntley's equation allows us to estimate the average cosine. An important factor is that the extrapolation only extends to 90 degrees. The irradiance reflectance of the water can be used to estimate the error that neglecting the radiance from angles larger than 90 degrees might contribute. For solar illumination, the irradiance reflectance at 500 nm is approximately 5% (+/-5%) dependent on the constituents in the water column. Given a water reflectance of this magnitude, the average cosine for 0-90 degrees will overestimate the true average cosine by approximately 10%. This effect will be smallest when close to the source (very peaked radiance distribution) and largest when farther away from the source (more diffuse radiance distribution), and depend on the shape of the volume scattering function of the water.

In Figure 5 we show the variation of the average cosine, calculated with the empirical equation, for the 4 data sets. As can be seen, at short ranges (less than 3 attenuation lengths) the average cosine is larger than 0.9, thus has less of an affect on the absorption measurement. For larger distances however, the average cosine decreases substantially, thus must be taken into account when deriving the absorption coefficient from the irradiance decay. Some of the location dependent variation in the behavior of the average cosine can be removed if, instead of c attenuation lengths, the data is displayed versus b lengths. Since to first order, the width of the PSF (thus the slope, m) should be proportional to the number of scattering events, using b lengths instead of c lengths takes out the dependence on b/c (or a/c). This does remove some of the variations for short attenuation lengths (less than 3 b lengths) however for longer ranges the extra absorption involved in the large angles (longer pathlength) seems to remove the invariance on a . This is an area where we will be doing further work.

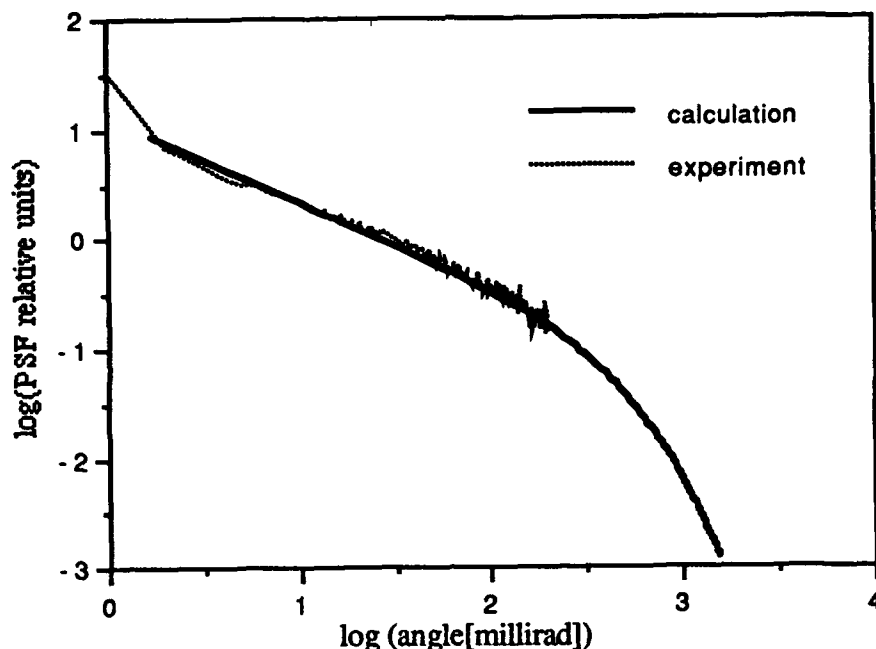


Fig. 4) Graph showing the extrapolated PSF and an experimentally measured PSF. Extrapolation using technique described in text. This data is for 7.07 optical depths, a range of 100 m. $a/c = 0.45$ and $cz = \tau + 0.41$. Data obtained at 500 nm.

The effects of the constituent measurements ($\bar{\mu}$, E , E' (the flashlamp irradiance output), and z on the absorption measurement can be found by a simple differentiation of the first equation. After taking the derivative and some substitutions the following equation can be found:

$$\left| \frac{da}{a} \right| = \left| \frac{d\bar{\mu}}{\bar{\mu}} \right| + \left| \frac{dz}{z} \right| + \frac{\bar{\mu}}{az} \left| \frac{dE}{E} \right| + \frac{\bar{\mu}}{az} \left| \frac{dE'}{E'} \right|.$$

Note that the first term on the right is the error in the determination in $\bar{\mu}$ and shows that the error in a is directly proportional to the error in the determination of $\bar{\mu}$ (or ignoring it completely). An error of 20% in $\bar{\mu}$, causes an error in a of 20%. The second error is due to measurement problems with separation of the source and collector. Neglecting problems with wire angle, most of these errors are on the order of 10 cm. At large distances this error term can go away, but it may be important at short distances. The third term is due to error in the measurement of the irradiance, and the fourth term is due to errors caused by the flashlamp variations. Both the third and fourth terms are most important at short distances, and can be minimized in homogenous waters by using least squares line fitting and other techniques which minimize the statistical deviations. Overall the average cosine term is the only term which enters the error budget directly. At short distances this term can be neglected, because the average cosine is very close to 1, however at longer distances, where the other terms are small this term must be taken into account.

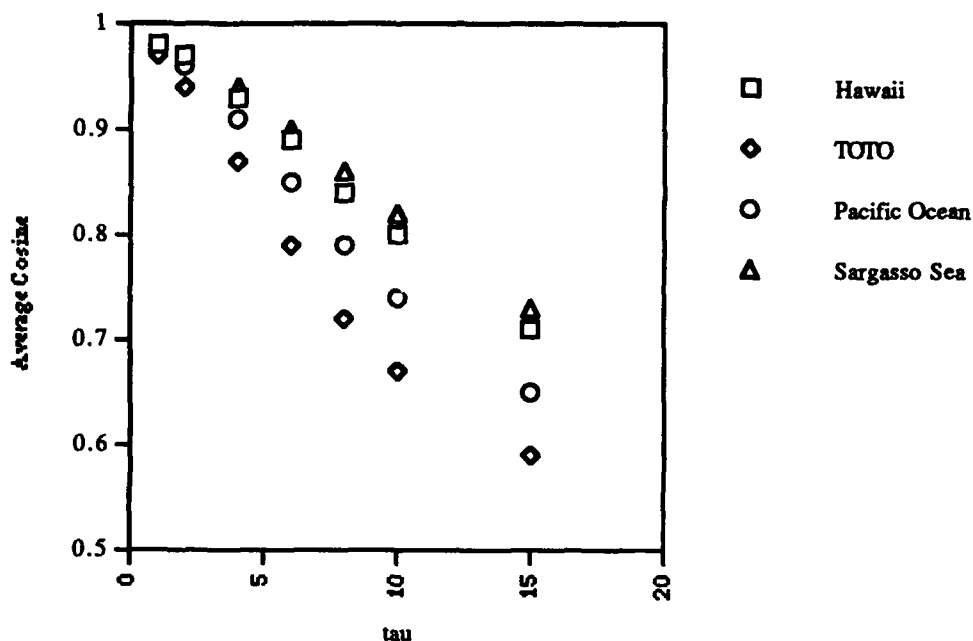


Fig. 5) Average cosine vs tau (τ). Average cosine derived from empirical extrapolation. Coefficients used in the extrapolation derived from the fitting procedure described in text. This method is based on measurements at for 500 nm. Illustrates that the average cosine can vary significantly in the first 15 attenuation lengths.

4. CONCLUSION

A method first presented in Voss for fitting the measured PSF to Duntley's empirically derived equation for the BSF, was used to extrapolate the measured PSF out to 90 degrees. The extrapolated PSF was then used to estimate the average cosine of the light field due to a cosine source embedded in the ocean. The method appears to work well and reveals a substantial change in the average cosine over a range of 15 optical lengths from the source. When simultaneous measurements of the PSF and the irradiance from an isotropic source are available, our average-cosine estimation technique can be used to improve the accuracy of estimating the absorption coefficient from the irradiance attenuation.

5. ACKNOWLEDGMENTS

This work has been supported by the ocean optics division of the Office of Naval Research. Additional support for field measurements was provided by the Applied Physics Laboratory, Johns Hopkins University. We also thank Albert Chapin for his help in the field measurements.

6. REFERENCES

- 1) Gershun, A. The light field, J. Math. Phys., Vol. 18, pp. 51-151, 1939.
- 2) R. A. Maffione, K. J. Voss, and R. C. Honey, Measurement of the spectral absorption coefficient in the ocean with an isotropic source. Appl. Optics, Vol. 32, pp. 3273-3279, 1993.

- 3) R. C. Honey, Beam spread and point spread functions and their measurement in the ocean, Ocean Optics VI, Vol. 208, pg. 242-248, 1979.
- 4) K. J. Voss and A. L. Chapin, Measurement of the point spread function in the ocean, Appl. Opt., Vol. 29, pp. 3638-3642, 1990.
- 5) K. J. Voss, Simple empirical model of the oceanic point spread function, Appl. Opt., Vol 30, pp. 2647-2651, 1991.
- 6) S. Q. Duntley, Underwater lighting by submerged lasers and incandescent sources, SIO Ref. 71-1, Scripps Institution of Oceanography, 1971.

SESSION 4

Coastal Waters I

Variations in bio-optical properties in the Greenland/Iceland/Norwegian-Seas

Runar Dalløkken, Roar Sandvik and Egil Sakshaug

Trondhjem Biological Station, The Museum, University of Trondheim
Bynesveien 46, N-7018 Trondheim, Norway

ABSTRACT

Diffuse attenuation coefficients for spectral irradiance $K_d(z, \lambda)$ and the total Chl *a* + Pheo *a* pigment-specific absorption of light by particles ($a_p^*(\lambda)$, algae + detritus), were determined during 2 cruises (Cardeep 2 and 3) in the Greenland/Iceland/Norwegian (GIN)-Seas.

The Cardeep 2 cruise (April - May 1993) represented a typical prebloom situation with deep mixing and low pigment concentrations. Particulate matter was dominated by phytoplankton. Cardeep 3 (July - August 1993) was characterised by large fluctuations in pigment concentrations and species composition.

The diffuse attenuation coefficient ranged from 0.064 to 0.130 m^{-1} (441 nm) for Cardeep 2 and 3, respectively. The pigment (Chl *a* + Pheo *a*) specific attenuation coefficient $K_d^*(\lambda)$ was compared with Morel's¹² non-linear model for light propagation of solar energy in the ocean and with the pigment specific absorption coefficient by particles, a_p^* . Our $K_d^*(\lambda)$ spectrum for the GIN-Seas was in good agreement (within 13 %) with values derived from Morel's¹² model for pigment specific light attenuation for 1 mg (Chl *a* + Pheo *a*) m^{-3} for wavelengths in the blue part of the spectrum. $K_d^*(\lambda)$ (apparent optical property) and $a_p^*(\lambda)$ (inherent optical property), were in good agreement except at wavelengths > 665 and < 441 nm. This was only true for the $a_p^*(\lambda)$ spectra for which the optical density from 750 - 800 nm was not subtracted^{7,8}. The higher values of $K_d^*(\lambda)$ relative to $a_p^*(\lambda)$ at 410 nm were probably due to small, but optically significant endogenous concentrations of yellow substances^{12,23} which enhance the blue part of the $K_d^*(\lambda)$ spectrum¹².

1. INTRODUCTION

The Greenland/Iceland/Norwegian (GIN)-Seas are sites of significant deep water formation in winter and play an important role in the export of carbon from the sea surface towards depth. Biological and physical processes therefore are of particular interest in this area. Models for the algal growth rate are crucial for quantifying primary productivity. Such models, in turn, require regional models of the pigment-specific light attenuation due to particles within the euphotic layer where photosynthesis occurs¹. Little *in situ* optical work has been done in the Greenland Sea area, however, bio-optical relationships for the region have been reported^{2,3,4}.

In such models the diffuse attenuation coefficient spectrum for downwelling irradiance $K_d(z, \lambda)$ is crucial because it describes quantitatively and directly the attenuation of downwelling solar radiation within the water column. $K_d(z, \lambda)$, is defined as the rate at which the natural logarithm of the downwelling irradiance $E_d(z, \lambda)$ is attenuated with depth z ⁵

$$K_d(z, \lambda) = - \frac{d(\ln(E_d(z, \lambda)))}{dz} \quad (1)$$

The main object of this work is to study the variation of the spectral properties of the underwater light field, and in particular the variation of $K_d(z, \lambda)$ and the pigment-specific attenuation coefficient spectrum for particulate matter $K_d^*(z, \lambda)$. We also look at the relative contributions of the attenuation of light by pure water, phytoplankton, and non-algal matter to the total $K_d(z, \lambda)$.

1.1. Abbreviations

λ Wavelength (nm)
 z Depth (m)
 $E_d(\lambda)$ Spectral downwelling irradiance [$\mu\text{W}(\text{cm}^2 \text{ nm})^{-1}$]

$K_d(\lambda)$	Attenuation coefficient spectrum for downwelling irradiance (m^{-1})
$K_w(\lambda)$	Attenuation coefficient spectrum due to pure water (m^{-1})
$K_s(\lambda)$	Attenuation coefficient spectrum for dissolved organic materials (m^{-1})
$K_d^*(\lambda)$	Pigment (Chl <i>a</i> + Pheo <i>a</i>) specific attenuation coefficient spectrum for downwelling irradiance ($\text{m}^2[\text{mg (Chl } a + \text{Pheo } a)]^{-1}$)
PAR	Photosynthetically available radiation ($\mu\text{mol quanta m}^{-2} \text{s}^{-1}$)
Z_{eu}	Depth of the euphotic zone, defined as the depth where PAR is reduced to 1% of its value at the surface (m)
C_{eu}	Mean pigment (Chl <i>a</i> + Pheo <i>a</i>) concentration within the euphotic zone (mg m^{-3})
OD_{susp}	Optical density of sample in suspension
OD_{fp}	Optical density of total particulate matter on filter
s	Clearance area of the filter (m^2)
V	Volume of filtered seawater (m^3)
a	Total absorption coefficient (m^{-1})
a_t	Absorption coefficient of total particulate matter (m^{-1})
a_p	Absorption coefficient of total particulate matter per unit of (Chl <i>a</i> + Pheo <i>a</i>) concentration ($\text{m}^2[\text{mg (Chl } a + \text{Pheo } a)]^{-1}$)
a_d	Absorption coefficient of particulate detrital matter (m^{-1})
a_{ph}	Absorption coefficient of living phytoplankton (m^{-1})
a_{na}	Absorption coefficient of non-algal materials (m^{-1})
a_s	Absorption coefficient of soluble materials (m^{-1})
S	Exponent in the spectral absorption law for detrital matter (nm^{-1})
$\bar{\mu}$	The mean cosine of the light field

2. MATERIAL AND METHODS

2.1. Cruises

Data for this study were collected at 38 stations during 2 cruises of the CARDEEP (Carbon Dioxide and Deep Water Formation)-program. The cruises were conducted during April/May (Cardeep 2) and July/August (Cardeep 3) 1993 in the Greenland/Iceland/Norwegian (GIN)-Seas. The stations covered a cruise track between $70^\circ - 76^\circ \text{N}$ and $15^\circ \text{W} - 25^\circ \text{E}$ and were in open water, except 4 stations on Cardeep 2 and 1 on Cardeep 3 which were in the marginal ice-zone.

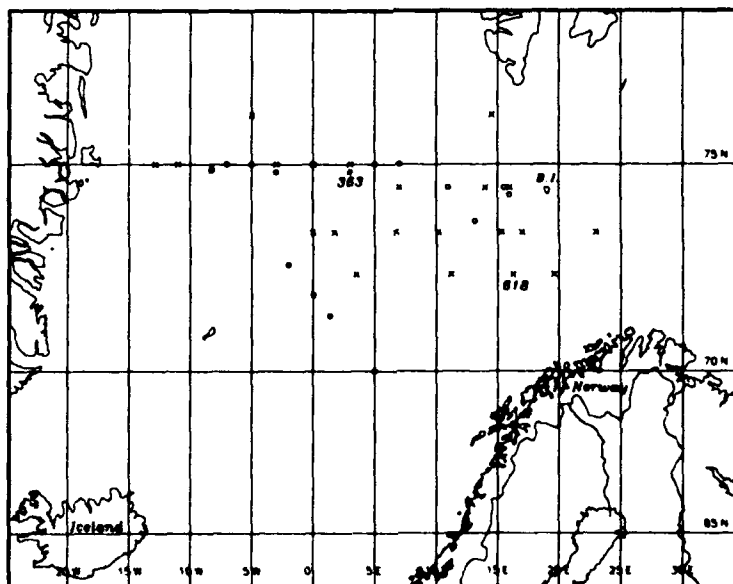


Figure 1 : Location map showing the 38 stations. Symbols (o) for Cardeep 2 stations and (x) for Cardeep 3 stations.

2.2. Continuous optical profiles

At each station measurements were made of spectral underwater downwelling irradiance (410, 441, 465, 488, 520, 550, 565, 589, 625, 656, 665, 683, 700 nm), upwelling irradiance (410, 441, 488, 520, 550, 565, 656, 683 nm), upwelling radiance (410, 441, 488, 520, 550, 565, natural fluorescence) and scalar irradiance (PAR) using a MER-1032 Reflectance spectroradiometer (Biospherical Instruments). A surface deck cell (2π PAR) was used simultaneously with the underwater MER during vertical profiling, making it possible to correct for surface light fluctuations during the measurements. The maximum working depth for the MER was 200 m.

The spectroradiometer package included sensors for conductivity and temperature (Sea Bird Electronics), and a stimulated Chl *a* fluorescence (excitation : 425 nm; emission 685 nm (Sea Tech)). These auxiliary instruments were interfaced with the MER. All data were multiplexed and transmitted on a multiconductor cable to a deck unit which transformed the signal to a digital format for storage on an IBM AT compatible computer. The combined cycle time (259 ms) and profile speed (0.3 m s^{-1}) resulted in a nominal sampling density of approximately 13 measurements of each variable per meter. All data were sorted by depth and averaged to 1m bins for further analyses.

2.3. Discrete water samples and particulate absorption spectra

Seawater was sampled using 30-l Niskin bottles, sample volumes were 0.5 - 4.0 l, filtered onto 25 mm glass-fibre filters (Whatman GF/F). All analyses, excluding phytoplankton enumeration and identification, were done aboard ship. Chlorophyll *a* (chl *a*) and pheopigment *a* (Pheo *a*) concentrations were determined by the method of Holm-Hansen *et al.*⁶ after extraction in 90 % acetone of samples which were filtered onto GF/F Whatman filters.

Optical densities of total particulate matter, ($OD_{fp}(\lambda)$), were measured directly on wet filters put onto a cover slip placed close to the photomultiplier of a Beckman DU60 (Cardeep 2) or a Hitachi 150-20 (Cardeep 3) spectrophotometer. An unused wetted filter was used as a blank. The optical density was measured at 1 nm intervals from 400 - 800 nm. During scans the wetness of the filters remained essentially unchanged.

2.4. Data preparation

From a total of 46 stations during 2 cruises, 38 stations were selected for further analyses. Criteria for inclusion of data included minimal ship-shadow effects on the submarine light field, constant irradiance at the surface during the cast and constant biological and physical properties within the mixed layer from which data were analysed.

Profiles of downwelling irradiance $E_d(z, \lambda)$ were used to calculate $K_d(z, \lambda)$, defined as the slope determined by linear regression of the natural log transformation of $E_d(z, \lambda)$ as a function of depth.

The mean optical density from 750 - 800 nm of $OD_{fp}(\lambda)$ was subtracted from all wavelengths as a scattering correction^{7,8}. $OD_{fp}(\lambda)$ values were converted to their respective optical density in solution $OD_{susp}(\lambda)$ by the method of Mitchell⁹. $a_p(\lambda)$ was estimated directly from $OD_{susp}(\lambda)$ by the relationship

$$a_p(\lambda) = \frac{2.3 OD_{susp}(\lambda)}{(V/s)} \quad (2)$$

We were not only interested in $a_p(\lambda)$, but also $a_d(\lambda)$ and $a_{ph}(\lambda)$. We have therefore used the decomposition method of Bricaud and Stramski¹⁰, as modified by Babin *et al.*¹¹. The method involves calculation of $a_{ph}(\lambda)$ as

$$a_{ph}(\lambda) = a_p(\lambda) - a_d(\lambda) \quad (3)$$

where $a_d(\lambda)$ can be expressed as

$$a_d(\lambda) = A \exp(-S\lambda) \quad (4)$$

A and S are constant for a given spectrum and variable among spectra. A and S were obtained numerically.

All the 38 stations were characterised by Case I waters as defined by Morel¹². This function describes the relationship between the depth of the euphotic zone (Z_{eu}) and the mean pigment concentration within the euphotic layer (C_{eu})

$$MC = 0.923 \log_{10} Z_{eu} + 0.385 \log_{10} C_{eu} - 1.308 \quad (5)$$

Positive values of MC (Morel's criterion) corresponds to case I waters.

3. RESULTS

Over the course of the study period we observed prebloom waters (Cardeep 2) with deep mixing (σ_t constant to at least ≥ 200 m depth except for ice edge stations with stratification) and postbloom (Cardeep 3) conditions with variable physical conditions. The depth of the euphotic zone (1 % light depth, PAR) during Cardeep 2 ranged from 40 - 66 m (mean Z_{eu} : 53 ± 5 m), and from 22 to 58 m on Cardeep 3 (mean Z_{eu} : 38 ± 8 m).

In the open water stations during Cardeep 2, pigment (Chl *a* + Pheo *a*) concentrations varied from 0.2 to 1.1 mg m⁻³ with a mean of 0.6 mg m⁻³. The pigment profiles were typically uniform over the measured depth range. The phytoplankton community was characterised almost entirely by *Phaeocystis* cf. *pouchetii* colonies in low concentrations. For Cardeep 3 we got a much more diverse phytoplankton assemblage. Pigment concentrations varied 20 - fold, from 0.2 - 4.0 mg m⁻³ with a mean value of 1.3 mg m⁻³. The phytoplankton community varied from almost pure *P. cf. pouchetii* to stations, which in addition to *P. cf. pouchetii*, had significant amounts of the diatoms : *Chaetoceros* spp., *Rhizosolenia* spp., *Pseudonitzschia* spp., *Corethron criophilum*, *Eucampia palustium*, *Leptocylindrus danicus*, and the coccolithophore *Emiliania huxleyi*. For pooled data (Cardeep 2 and 3; hereafter called GIN-93) the mean pigment concentration was 1.0 mg m⁻³.

Within the marginal ice zone the maximum pigment concentration in the euphotic zone reached 1.1 and 3.3 mg m⁻³ for Cardeep 2 and 3 respectively. The phytoplankton was typical for the sea-ice communities i. e. *Chaetoceros* spp., *Thalassiosira* spp., *Phaeocystis* cf. *pouchetii*, *Prorocentrum balticum* and *Eucampia palustium*.

3.1. Spectral distribution of downwelling irradiance

We here show two contrasting different situations with respect to attenuation of light (Fig. 2) : Station 363, a prebloom station with a mean (0 - 100 m) pigment concentration of 0.2 mg m⁻³, and a postbloom station with a mean pigment concentration of 4.0 mg m⁻³ within the upper mixed surface layer of 30 m.

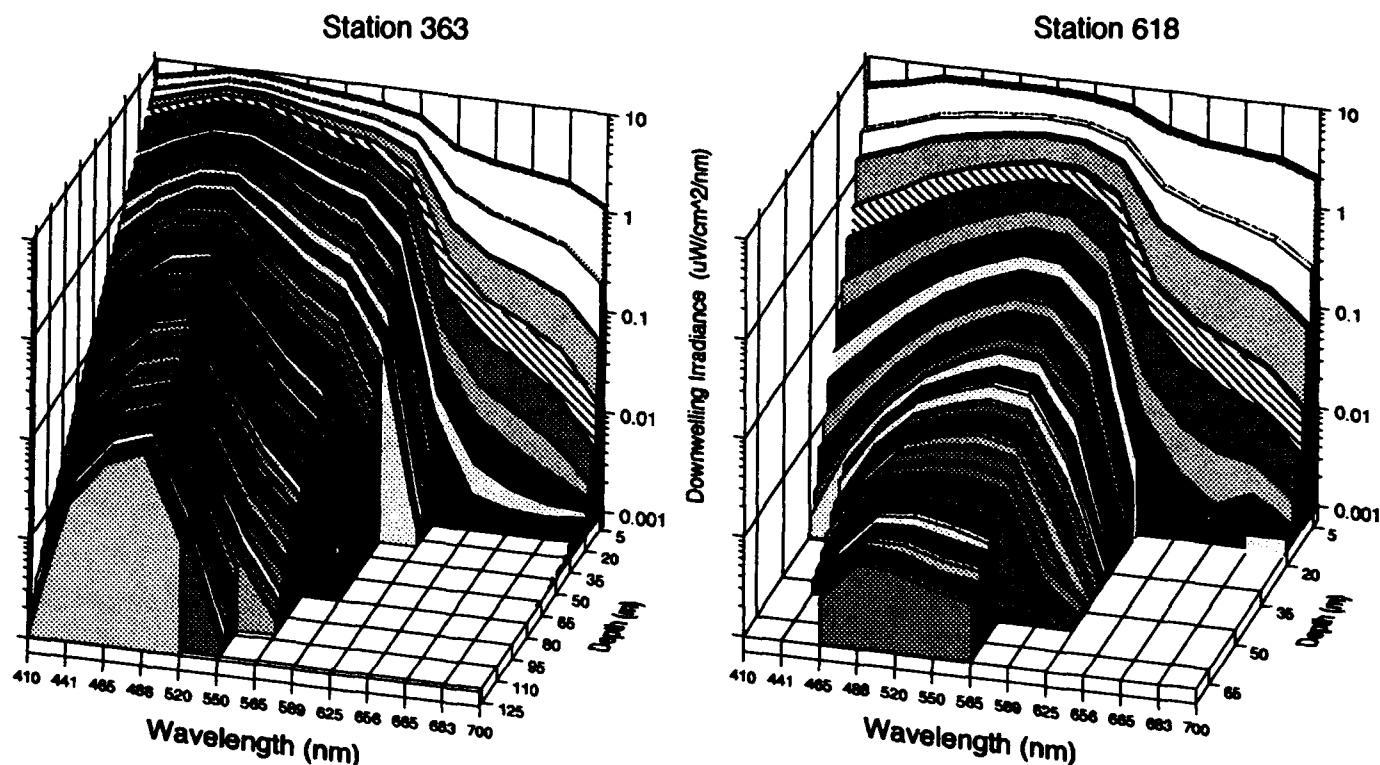


Figure 2 : Spectral distribution of downwelling irradiance $E_d(\lambda)$ for 12 discrete wavebands (410 - 700 nm) as a function of depth for two stations, plotted at 2.5 m depth intervals. Station 363 (prebloom) : pigment concentration 0.2 mg m^{-3} (0 - 100 m); station 618 (postbloom): mean pigment concentration 4.0 mg m^{-3} within the upper mixed (20 m) layer.

As a consequence of the different attenuation of the light within the photosynthetic waveband, the spectral composition of the downwelling flux changed progressively with increasing depth. The orange - red part of the spectrum (600 - 700 nm), was, however, attenuated within the upper 20 m due to the water itself which absorbs heavily in this region (Fig. 2).

For the low-pigment station, most of the light below 20 m was in the blue - green region (400 - 550 nm); i. e. the water itself absorbed poorly in this region^{12,13}. The waveband was narrowing with increasing depth. At 125 m depth, blue light (488 nm) was least attenuated (0.037 m^{-1}).

For the high-pigment station, the spectral distribution of $E_d(z, \lambda)$ in the red part of the spectrum was, as for the other station, due to the absorption of pure water in the upper 20 m. The blue region, however, was strongly attenuated due to pigmented particles. As for the pigment-poor station, the waveband was narrowing as depth increased, but in contrast, the peak was broader and shifted towards the green region.

3.2. The attenuation coefficient spectrum $K_d(\lambda)$ and its components

The diffuse attenuation coefficient for downwelling irradiance, $K_d(\lambda)$, was calculated for the upper mixed layers according to (1).

Mean values for $K_d(441)$ ranged from $0.064 (\pm 0.007)$ to $0.130 (\pm 0.045) \text{ m}^{-1}$ for Cardeep 2 and 3 respectively, and was $0.100 (\pm 0.042) \text{ m}^{-1}$ for all stations pooled together as an average. For Cardeep 2 stations, we observed only small changes in the $K_d(\lambda)$ because the pigment concentrations varied little during this cruise ($0.2 - 1.1 \text{ mg m}^{-3}$). The higher mean value of $K_d(\lambda)$ for the Cardeep 3 cruise, was consistent with higher mean pigment concentrations. At some stations (e.g. 618,

postbloom), we observed a higher detrital contribution than at any of the Cardeep 2 stations. The mean value of $K_d(550)$ was $0.095 (\pm 0.016) \text{ m}^{-1}$ during Cardeep 2 and 3, and was in good agreement with data reported by Trees³ (0.094 ± 0.009) m^{-1} for water masses between the Arctic Front and the East Greenland Polar Front.

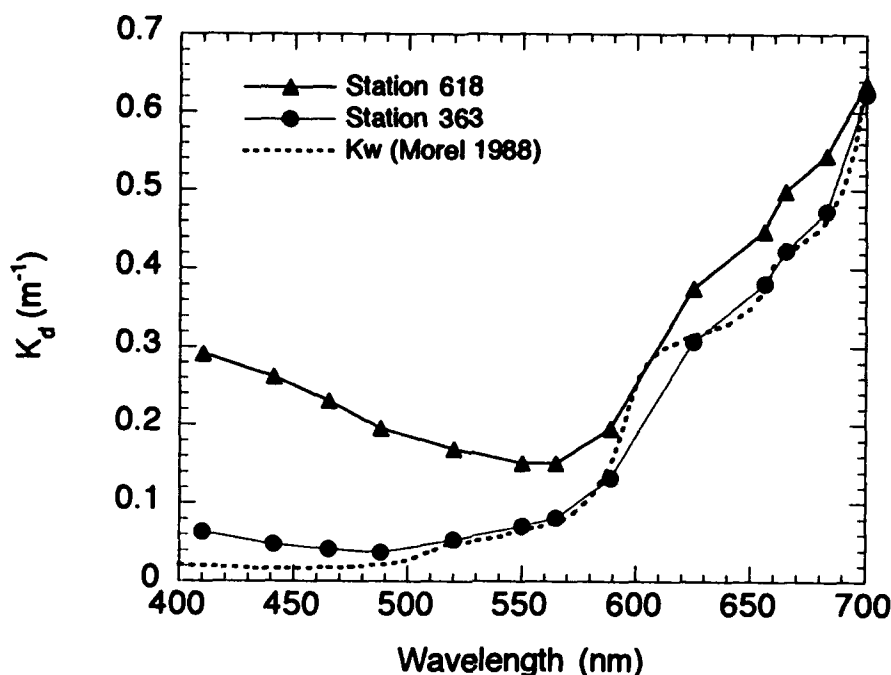


Figure 3 : Spectral variation in $K_d(\lambda)$ for stations 363 and 618, plotted together with the attenuation spectrum of pure water $K_w(\lambda)$. $K_w(\lambda)$ from Morel¹².

The $K_d(\lambda)$ spectrum for station 363 differed only slightly from the attenuation spectrum of pure water for wavelengths $> 520 \text{ nm}$ (Fig. 3). For wavelengths $< 520 \text{ nm}$, it was significantly higher. The $K_d(\lambda)$ spectrum for station 618 was significantly higher than that of station 363. This was caused by the higher pigment concentration within the layer for which $K_d(\lambda)$ was calculated, and a higher non-algal contribution (Fig. 5).

The nature of the underwater lightfield resulting from a given incident light field was determined by the inherent optical properties of the aquatic medium¹⁴. Assuming that $K_d(\lambda)$ is a "quasi-inherent" optical property¹⁵, we have used Beer's law to split the expression for $K_d(\lambda)$ as an inherent property into a sum of components

$$K_d(\lambda) = K_d^s(\lambda)[\text{Chl } a + \text{Pheo } a] + K_w(\lambda) + K_s(\lambda) \quad (6)$$

$K_d^s(z, \lambda)$ was determined as the slope of linear regression of $K_d(\lambda)$ on $(\text{Chl } a + \text{Pheo } a)$ (Table 1, Fig. 4). The intercept with the ordinate was the sum of attenuation due to water and soluble materials or particles which pass through the filter for pigment determination and therefor not directly attributable to the Chlorophyll-like pigments¹⁶.

Wavelength	$K_d^*(\lambda)$	$K_w + K_s$	r^2	Sign. level
410	0.069	0.049	0.814	<< 0.001
441	0.064	0.037	0.839	<< 0.001
465	0.055	0.033	0.823	<< 0.001
488	0.044	0.032	0.830	<< 0.001
520	0.032	0.053	0.799	<< 0.001
550	0.022	0.073	0.734	<< 0.001
565	0.019	0.085	0.684	<< 0.001
589	0.016	0.132	0.566	<< 0.001
625	0.018	0.304	0.276	< 0.001
656	0.017	0.387	0.278	< 0.001
665	0.020	0.433	0.354	< 0.001
683	0.021	0.478	0.321	< 0.001
700	n. s.	n. s.	n. s.	n. s.

Table 1 : Linear regressions for 38 case I stations. $K_d(\lambda)$ is the dependent variable and the mean (Chl *a* + Pheo *a*) for the respective depth interval is the independent variable. $K_d^*(\lambda)$ is the slope of this relationship and $(K_w + K_s)$ is the intercept with the ordinate. Coefficient of determination (r^2) and significance levels for the regressions are also presented.

From Table 1 it is obvious that there is a significant correlation between $K_d(\lambda)$ and the pigment concentration, but the significance level dropped for wavelengths > 589 nm.

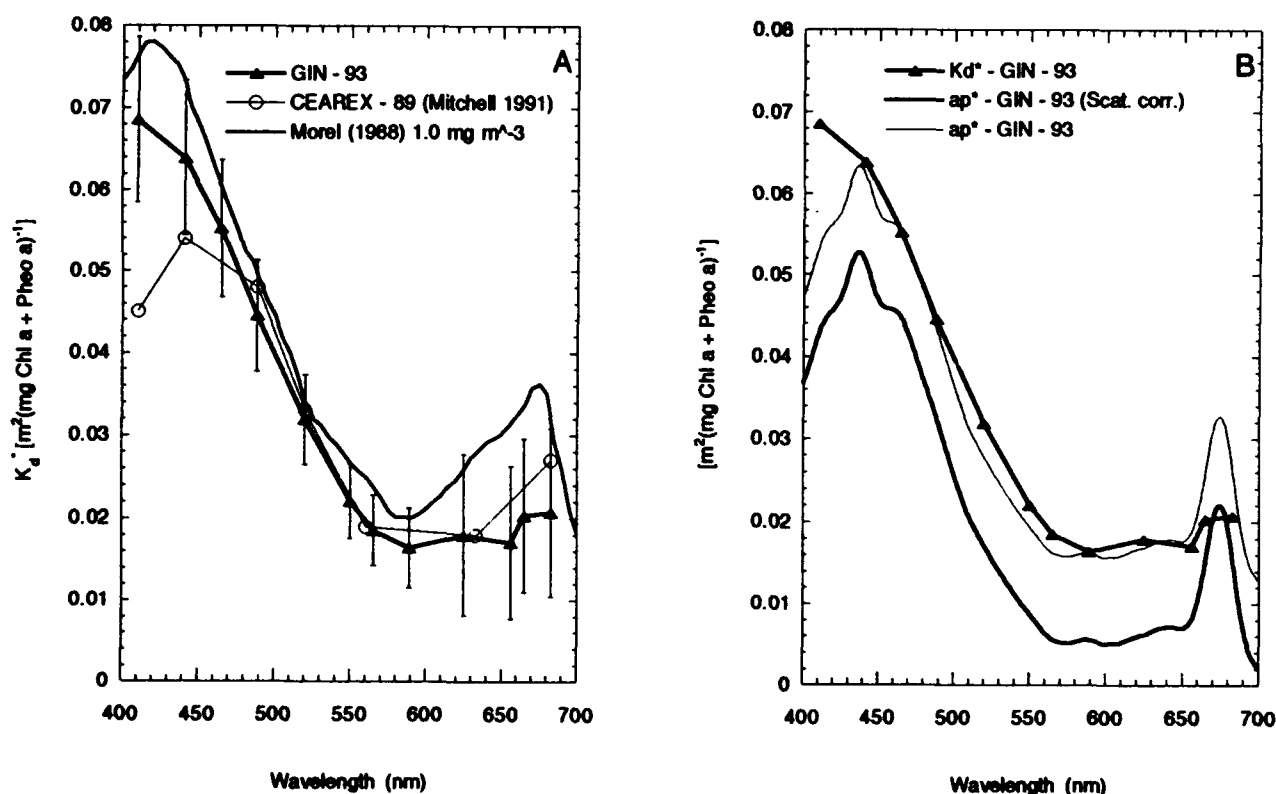


Figure 4 : Spectra of pigment specific attenuation coefficients $K_d^*(\lambda)$ for algal material (living and detrital), GIN-93 observations. The error bars represent 95 % confidence limits.

A : Our estimate for GIN-93 data (mean pigment concentration 1.0 mg m^{-3}) and data from Morel¹² for his non-linear model for 1.0 mg m^{-3} and CEAREX-89 data⁴ from the Fram Strait.

B : Our estimate of $K_d^*(\lambda)$ for GIN-93 together with mean values of $a_p^*(\lambda)$ for the same region. One of the $a_p^*(\lambda)$ spectra was corrected for scattering (mean value of the optical density between 750 - 800 nm subtracted) and the others not.

Our data are in good agreement with data from the non-linear model of Morel¹² in the blue - green waveband (within 13 % in the blue part). The CEAREX-89 (April, May) data from Mitchell⁴ were much lower in the blue end of the spectrum, but match our data well from 465 - 633 nm. Mitchell⁴ explained his low values at the blue end as a result of low light adaptation and the packaging effect⁴. Our data from Cardeep 2 (data not shown), show the same trend as the CEAREX-data with low values at the blue region. The Cardeep 2 data are much like the CEAREX-data (before onset of a spring bloom) where particles are dominated by phytoplankton.

When we compare $K_d^*(\lambda)$ (apparent optical property) and $a_p^*(\lambda)$ (inherent optical property) (Fig. 4 panel B), there is a good agreement except at wavelengths > 665 and < 441 nm. This was, however, true only for the $a_p^*(\lambda)$ spectrum for which the optical density from 750 - 800 nm was not subtracted before absorption coefficients were calculated^{7,8}.

3.3. Relative contributions of absorbing material to the total attenuation coefficient $K_d(\lambda)$

$K_d(\lambda)$ can be written as a function of inherent optical properties

$$K_d(\lambda) = \frac{a(\lambda) + b_b(\lambda)}{\bar{\mu}} \quad (7)$$

where $a(\lambda)$ and $b_b(\lambda)$ are the absorption and backscattering coefficients respectively, and $\bar{\mu}$ is the mean cosine of the light field. A good approximation of $K_d(\lambda)$ can be made by assuming $b_b \ll a$ for oceanic phytoplankton¹⁷. This leads (7) to

$$K_d(\lambda) = \frac{a(\lambda)}{\bar{\mu}} \quad (8)$$

The absorption coefficient $a(\lambda)$, which is an inherent optical property, can rigorously be written as

$$a(\lambda) = a_w(\lambda) + a_{ph}(\lambda) + a_{na}(\lambda) \quad (9)$$

where $a_{na}(\lambda)$ is defined as absorption by "non-algal" coloured matter (detritus, soluble materials, "gelbstoff").

The total pigment-specific particulate absorption $a_p^*(\lambda)$ varies depending on the relative fraction of detritus to phytoplankton. Partitioning the absorption coefficient to phytoplankton to non - phytoplankton is essential for modelling oceanic primary production¹⁸.

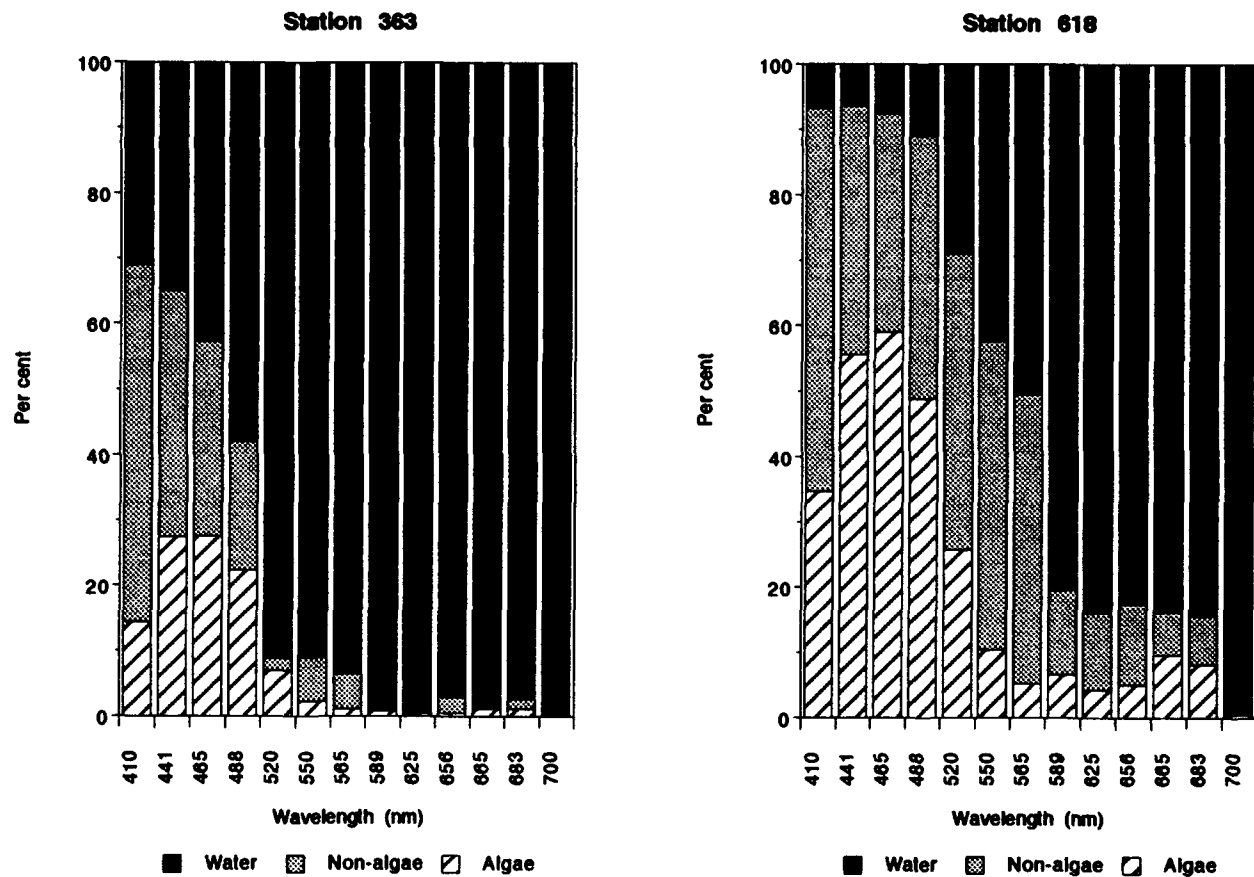


Figure 5 : Per cent contribution of absorbing material (water, algae and non-algal matter) to the total attenuation coefficient $K_d(\lambda)$ for downwelling irradiance

The relative contribution of algae (phytoplankton) absorption across the photosynthetic waveband (400 - 700 nm), was determined by (3). Non-algal absorption was estimated by subtracting values for pure water¹² and phytoplankton from the total attenuation coefficients $K_d(\lambda)$.

In the orange - red band, attenuation was dominated by the water itself regardless of the phytoplankton abundance. Light in the blue part of the spectrum was effectively attenuated by phytoplankton and to some extent non-algal matter specially at station 618. At station 363, 28% of the underwater light in the blue region (465 nm) was absorbed by phytoplankton. This is much lower than observed for the pigment-rich station (station 618) where 60% of the light attenuation was due to phytoplankton.

4. SUMMARY AND DISCUSSION

In our analyses, we observed changes in the blue part of the $K_d(\lambda)$ spectrum during GIN - 93 (Cardeep 2 and 3 cruises). This was mainly due to variations in pigment (Chl *a* + Pheo *a*) concentrations and phytoplankton assemblages during the two cruises. To some extent, contributions from non-algal materials played a role, particularly at some of the Cardeep 3 stations (postbloom stations) (Fig. 5).

Understanding the variability in $a(\lambda)$ is crucial for understanding variability in $K_d(\lambda)$, which is an apparent optical property of aquatic systems. Since $a_p(\lambda)$ dominates the variability in $a(\lambda)$ in oceanic waters with little terrestrial influence, it is among the most important parameters for a good description of the optical properties of aquatic systems⁹.

Particulate matter in the ocean consists of both phytoplankton and detrital particles. Detrital particles have high absorption in the blue part of the spectrum and therefore raising the $a_p(436):a_p(675)$ ratio. Samples from the GIN-93 cruises were characterised by blue-red absorption ratios close to blue-red ratios reported for phytoplankton culture spectra^{19,20,21}, and this is a strong indicator of low detrital influence. This was expected because most of the detrital material in the GIN-Seas presumably is derived from *in situ* biogenic processes. The deviation of field spectra from those reported from cultures must in large part be due to the previous history of biological dynamics within a particular water mass.

Spectral light attenuation models are important for the purpose of studying photobiological and physical phenomena related to absorption of solar energy¹. We have used Smith and Baker's²² linear model approach to obtain our $K_d^*(\lambda)$ for GIN-93. Our $K_d^*(\lambda)$ was 30 - 40 % higher than k_1 -values (pigment specific attenuation coefficient for pigment concentrations $< 1 \text{ mg m}^{-3}$) of Smith and Baker²² for wavelengths $< 600 \text{ nm}$.

Our results fit Morel's non-linear¹² model for pigment specific light attenuation (within 13 % in the blue part) (Fig. 4 panel A) better than Smith and Baker's²² discontinuous two-part linear model. The non-linear model of Morel¹² is also a two-component system: The water itself (constant) and the varying biogenic component. In the biogenic component, the phytoplanktonic cells and the other phytoplankton derivative materials are pooled together, and are variable¹². These features make this model more robust with respect to variation in the absorption coefficient due to differences in algal cell size and species composition. This is a valuable property when comparing prebloom and postbloom conditions.

Our data for the pigment specific attenuation coefficients $K_d^*(\lambda)$ for algal material (living and detrital) and the pigment specific absorption coefficient for total particulate matter $a_p^*(\lambda)$, were in good agreement except at wavelengths > 665 and $< 441 \text{ nm}$. Several investigators^{12,23} have shown that hardly measurable concentrations of yellow substances are not optically negligible and, thus, will enhance the pigment specific attenuation coefficient at the blue end of the spectrum¹².

The enhancement of $K_d^*(410)$, was probably due to endogenous yellow substances. Prieur and Sathyendranath²⁴ demonstrated that even in oceanic waters, the yellow substance concentration remained low and seemed to be related to the biological activity averaged over a long period rather than to the local and temporary phytoplankton content. This will have consequences for the regression analyses of $K_d(\lambda)$ versus pigment concentrations. Because the dissolved yellow substances pass through the filter for $a_p(\lambda)$ determination, they will not cause a rise in the $a_p^*(\lambda)$ spectrum corresponding to that of the $K_d^*(\lambda)$ spectrum.

5. ACKNOWLEDGEMENTS

This work has been supported by the Mare Nor program (The Research Council of Norway) (R. D.) and MAST/EN EE 104818 (European Subpolar Ocean Programme) (R. S.) both awarded to E. S. We wish to thank the Captain and the crew of R/V "Johan Hjort" for their professional support and patience during the Cardeep 2 and 3 cruises. We also wish to thank F. Rey (Institute of Marine Research, Bergen) for pigment data and S. O. Linde and K. Andresen (Trondhjem Biological Station) for carrying out the field work during the Cardeep 3 cruise.

6. REFERENCES

1. B. G. Mitchell and O. Holm-Hansen, "Bio-optical properties of Antarctic waters: Differentiation from temperate ocean models," *Deep-Sea Research*, Vol. 38, pp. 1009 - 1028, 1991.
2. E. Aas and G. Berge, "Irradiance observations in the Norwegian and the Barents Seas," *Institute Report Series*, Univ. of Oslo, Norway, No. 23, 42 pp., 1976.
3. C. C. Trees, J. Aiken, H-J. Hirche and S. B. Groom, "Bio-optical variability across the Arctic Front," *Polar Biology*, Vol. 12, pp. 455 - 461, 1992.
4. B. G. Mitchell, "Predictive Bio-optical Relationships for polar oceans and marginal ice zones," *Journal of Marine Systems*, Vol. 3, pp. 91 -105, 1991.

5. N. G. Jerlov, *Marine Optics*, Elsevier Oceanography Series, Vol. 14, Elsevier Scient. Publ. Comp., Amsterdam, 1976.
6. O. Holm-Hansen, C. J. Lorenzen, R. W. Holmes and J. D. H. Strickland, "Fluorometric determination of chlorophyll," *J. Cons. Perm. Int. Explor. Mer.*, Vol. 30, pp. 3-15, 1965.
7. D. A. Kiefer and J. B. Soohoo, "Spectral absorption by marine particles of coastal waters of Baja California," *Limnol. Oceanogr.*, Vol. 27, pp. 492 - 499, 1982.
8. B. G. Mitchell and D. A. Kiefer, "Determination of absorption and fluorescence excitation spectra for phytoplankton," *Marine Phytoplankton and Productivity*, O. Holm-Hansen, L. Bolis and R. Gilles editors, Springer-Verlag, Berlin, New York, pp. 157 - 169, 1984.
9. B. G. Mitchell, "Algorithms for determining the absorption coefficient for aquatic particulates using the quantitative filter technique," *Proceedings of the SPIE, Ocean Optics X*, Vol. 1302, pp. 137-148, 1990.
10. A. Bricaud and D. Stramski, "Spectral decomposition coefficients of living phytoplankton and nonalgal biogenous matter: A comparison between the Peru upwelling area and the Sargasso sea," *Limnol. Oceanogr.*, Vol. 35, pp. 562-582, 1990.
11. M. Babin, J. G. Theriault and L. Legendre, "Variations in the specific absorption coefficient for natural phytoplankton assemblages : Impact on estimates of primary production," *Limnol. Oceanogr.*, Vol. 38, pp. 154-177, 1993.
12. A. Morel, "Optical modeling of the upper ocean in relation to its biogenous matter content (Case 1 waters)," *J. of Geophys. Res.*, Vol. 93, pp. 10749-10768, 1988.
13. R. C. Smith and K. S. Baker, "Optical properties of the clearest natural waters (200 - 800 nm)," *Applied Optics*, Vol. 20, pp. 177 - 184, 1981.
14. J. T. O. Kirk, *Light and Photosynthesis in Aquatic Ecosystems*, Cambridge University Press, 1983.
15. K. S. Baker and R. C. Smith, "Quasi-inherent characteristics of the diffuse attenuation coefficient for irradiance," *Proceedings of the SPIE, Ocean Optics VI*, Vol. 208, pp. 60 - 63, 1979.
16. R. C. Smith and K. S. Baker, "The bio-optical state of ocean waters and remote sensing," *Limnol. Oceanogr.*, Vol. 23, pp. 247 - 259, 1978.
17. H. R. Gordon, "Can the Lambert-Beer law be applied to the diffuse attenuation coefficient of ocean water," *Limnol. Oceanogr.*, Vol. 34, pp. 1389 - 1409, 1989.
18. B. G. Mitchell, W. E. Esias, G. Feldman, R. G. Kirk, C. R. McClain, M. Lewis, "Satellite Ocean Color Data For Studying Oceanic Biogeochemical Cycles," *Proceedings IEEE*, pp. 280 - 287, 1991.
19. M. J. Perry and S. M. Porter, "Determination of the cross-section absorption coefficient of individual phytoplankton cells by analytical flow cytometry," *Limnol. Oceanogr.*, Vol. 34, pp. 1727-1738, 1989.
20. J. S. Cleveland and M. J. Perry, "A model for partitioning particulate absorption into phytoplanktonic and detrital components," *Deep-Sea Research*, Vol. 41, pp. 197-221, 1994.
21. H. Maske and H. Haardt, "Quantitative in vivo absorption spectra of phytoplankton: Detrital absorption and comparison with fluorescence excitation spectra," *Limnol. Oceanogr.*, Vol. 32, pp. 620-633, 1987.
22. R. C. Smith and K. S. Baker "Optical classification of natural waters," *Limnol. Oceanogr.*, Vol. 23, pp. 260 - 267, 1978.
23. A. Bricaud, A. Morel, L. Prieur, "Absorption by dissolved organic matter of the sea (yellow substance) in the UV and visible domains," *Limnol. Oceanogr.*, Vol. 26, pp. 43 - 53, 1981.
24. L. Prieur and S. Sathyendranath, "An optical classification of coastal and oceanic waters based on the spectral absorption curves of phytoplankton pigments, dissolved organic matter, and other particulate materials," *Limnol. Oceanogr.*, Vol. 26, pp. 671 - 689, 1981.

Chlorophyll sounding data in the bio-optical model of the Gulf of Gdansk spring bloom

Sergey V.Semovski,
Bogdan Woźniak,
Ryszard Hapter

Institute of Oceanology, Polish Academy of Science
P.O.Box 68, PL-81-712, Sopot, Poland,
Internet: siergej@ocean.iopan.gda.pl

ABSTRACT

In this study we propose a model of phytoplankton population dynamics in a marine ecosystem which include physical, biological and bio-optical parts. We discuss two different methods of contact chlorophyll observation assimilation to fit a model of 'in situ' data. As an example we simulate of the abnormal 1993 Gulf of Gdansk spring bloom during which extremely high chlorophyll concentration were observed. The data assimilation approach will serve as a base for more adequate underwater irradiance field simulations.

1. INTRODUCTION

In last decades it has been demonstrated^{1,2} that phytoplankton population models in marine ecosystem dynamics can prove the correct tool for describing spring blooms and annual cycles. Such models are usually based on the principles of hydrodynamics and population dynamics. The main parts of the model, however, are a bio-optical block for the underwater light field, and also the primary production simulation.

A problem of data assimilation in phytoplankton dynamics models can be solved by using the well-known data assimilation technique developed for hydrodynamic models^{3,4}. The problem of data assimilation from another sources in the dynamical models is also discussed. In some previous articles the problem of chlorophyll remote sensing data assimilation^{5,6} was state. Here we discuss the problem of chlorophyll sounding data assimilation in a model of phytoplankton spring bloom for a few points in the highly eutrophicated Baltic coastal zone. The model includes the vertical structure of the hydrooptical field simulation (underwater irradiance, spectral attenuation coefficient *etc.*).

During April-May 1993 there were a number of research cruises in the Gulf of Gdansk by Polish r/v 'Oceania'. Chlorophyll concentration, primary production and optical parameters were measured. The 1993 phytoplankton spring bloom was abnormal. Extremely high chlorophyll concentrations were observed determined in main part by nanoplankton *Cyclotella* diatoms species (about 2.5 mln cells on litre⁷). At some stations C_a (chlorophyll *a* + pheophytin *a*) concentrations of 100-200 mg/m³ were measured.

The problem of data assimilation is discussed in the model using a different numerical tools (optimal interpolation, parameters fitting). We discuss the possibility of various observed parameters being included in assimilation procedures (chlorophyll soundings, primary production *etc.*). The results of the data assimilation will serve as a tool for a more adequate underwater irradiance field description.

2. METHODS

The features of the Baltic phytoplankton field are described by a system of equations comprising mixing, sinking, growth as a function of light, temperature, nutrient availability as well as grazing and death by ingestion. Here we deal with a model without advection. The Baltic currents system impact and its changes with a wind direction will be a next step of the investigation. We use a set of coupled partial differential equations as a governing equations of the ecosystem simulation analysis².

$$\frac{\partial C_i}{\partial t} = K_z \frac{\partial^2 C_i}{\partial z^2} + w_s \frac{\partial C_i}{\partial z} + \mu_i(T, C_1, C_2, C_3) - \nu_i(T, C_1, C_2, C_3) - \gamma_i(C_i) + \xi, \quad (1)$$

where the subscripts denote the concentration at time t of the ecosystem components at depth z ; $C_1 \propto C_a$ — phytoplankton, C_2 — zooplankton, C_3 — nutrients (all in nitrogen units); K_z — kinematic eddy vertical diffusion coefficient, $[m^2 d^{-1}]$; w_s — vector sinking rate, $[m d^{-1}]$; μ_i — specific growth rate of system component concentration, $[d^{-1}]$; ν_i — specific ingestion rate of system component by 'herbivores', $[d^{-1}]$; γ_i — mortality rate, $[d^{-1}]$; T — temperature, $[^\circ C]$, ξ — δ -correlated random process with a σ^2 dispersion describing short-correlated fluctuations in mixing, depending on mixed-layer depth variability and random advection effects.

2.0 Physical model of mixing and sinking

The first term on the right-side of (1) is the diffusion term, which was assumed to be different for the upper and lower mixed layers, the second term accounts for vertical sinking (which does not apply to dissolved nutrients and zooplankton), and the remaining terms are the biological process terms. To solve this set of equations three separate numerical models are needed to obtain the values of the variables. These are: a physical 'mixing and sinking' model; a bio-optical model to obtain the available light irradiance at different depths; the phytoplankton primary production and a biological process model to describe the interactions between phytoplankton, zooplankton and nutrients as interaction between 'prey', 'predator' and 'substrate'.

Vertical diffusion coefficient K_z play a substantial role in every diffusion-advection model. It was computed⁸ that a vertical eddy coefficient for the plankton dynamic model was $1.88 m^2 s^{-1}$ for the wind-forced weak vertical stratification upper layer and $0.22 m^2 s^{-1}$ for the cessation of wind impulse. In the number of simulation studies there have been used values of K_z from a wide range^{9,12}.

Although laboratory sinking rates of diatoms¹⁰ range from only $1-10 m d^{-1}$, repeated daily field observation of the 1975 diatom spring bloom at 80-m depth in the Baltic Sea¹¹ indicated apparent sinking rates of $30-50 m d^{-1}$. Another field estimations² varies from $3-4 m d^{-1}$ to $90-100 m d^{-1}$. Values $w_s = 1-20 m d^{-1}$ were used for the plankton dynamics model^{2,9,12}.

We use for simulation values K_z , w_s in the ranges shown above. In Chapter 3.1 we will additionally state a problem of fitting these parameters by method of direct target function minimisation.

2.1 Biological model

Considering a population dynamics model of the 'phytoplankton – zooplankton – nutrients' system based on the general principles of population dynamics. For phytoplankton dynamics we have equation (1) in the form

$$\frac{\partial C_1}{\partial t} = K_z \frac{\partial^2 C_1}{\partial z^2} + w_s \frac{\partial C_1}{\partial z} + \omega(C_3)P(C_1) - \text{Cons}(C_1, C_2) - \gamma_1 C_1 + \xi, \quad (1.1)$$

where the primary production term $P(C_1)$ is defined in Table 1 (see Chapter 2.2), the nutrient limitation term and the consumption term are

$$\omega(C_3) = \frac{C_3}{k_s + C_3}, \quad \text{Cons}(C_1, C_2) = R_m \wedge C_1 C_2 [1 - \exp(-\wedge C_1)],$$

where k_s — the nutrient uptake half-saturation constant, $[mM/m^3]$ and we let $k_s = 0.2$ after¹. For zooplankton dynamics equation (1) has another form

$$\frac{\partial C_2}{\partial t} = K_z \frac{\partial^2 C_2}{\partial z^2} + (1 - \beta) \text{Cons}(C_1, C_2) - \gamma_2 C_2 + \xi, \quad (1.2)$$

and the corresponding nutrient dynamics equation is of the form

$$\frac{\partial C_3}{\partial t} = K_z \frac{\partial^2 C_3}{\partial z^2} + \beta \text{Cons}(C_1, C_2) + N_d(z) + \gamma_1 C_1 + \gamma_2 C_2 - P(C_1) + \xi, \quad (1.3)$$

Here the model parameters and variables are: γ_1, γ_2 — phytoplankton and zooplankton mortality rate, [d^{-1}]; R_m — max herbivore ingestion rate, [d^{-1}]; β — unassimilated fraction of herbivore grazing ration, dimensionless; A — Ivlev herbivore grazing constant, [m^3/mg], $N_d(z)$ — nutrient influx, [mM/m^3]. Typical values of the basic constants¹ are: $\beta = 0.3$, $A = 0.5$, $\gamma_1 = 0.1$, $\gamma_2 = 0.04$.

For the values of specific Baltic zooplankton-phytoplankton interaction parameters we used observed values¹³. It should be noted that zooplankton grazing is a complex process which depends on diurnal migrations of copepod grazers and of the variability of grazing stress during the year. In a previous models there have been used a different assumptions on grazing rates — from a constant¹ R_m to its variability during the spring bloom period² in the range 0.1–1. This range of variability agree with those for the Baltic¹³. We will use in this model values of R_m in the above stated range.

2.2 Bio-optical model and the primary production term

The primary production term $P(z)$ in equation (1.1) is responsible for the processes which define the carbon and energy cycles in the World Ocean. In a number of papers, different methods have been used to estimate primary production, like the simple one¹⁴, and more sophisticated methods^{15,16,17}.

However, most of these models were developed only for the Case 1 Waters (WC1) according to Morel terminology¹⁵. Another types of waters, so called Waters Case 2, which consist approximately 2% of the World Ocean, are the most productive ones. The eutrophicated Baltic waters can not be described by models suitable for WC1. In the Polish Institute of Oceanology there was developed the first authentic model of primary production for the Baltic waters¹⁸. This model are based on a data base of optical observations, C_a (chlorophyll a + pheophyn a) observations and quantum yield of primary production. The observations were made on a number of Polish and Russian research vessels cruises. We use this bio-optical model for the primary production term simulation (see Table 1).

3. CLIMATIC DATA, INITIAL CONDITIONS AND ASSIMILATION DATA

For the mixed layer depth computation and for the temperature data source for the primary production computation (see Table 1) we use a data base¹⁹. Mixed layer depth was computed from data¹⁹ using maximum gradient criteria. Initial nutrient data and nutrient inflow were taken from²⁰. We use a nutrient influx vertical structure as $N_d(z) = N_{d,0} \exp(-0.1z)$. Nutrient influx intensity $N_{d,0}$ was additionally used as a parameter in the assimilation procedure (see Chapter 4). In accordance to the ideas² we let grazing rate variable during the spring bloom period range from 0.1 to 0.9. We used climatic distribution of available daily natural irradiation on sea surface produced at the Hydrometeorological Centre of Russia in accordance with the algorithm in the paper²¹. As a observed C_a vertical profiles we use a fluorometric data produced by submersible fluorimeter 'Primprod' made by 'Ecomonitor' (Moscow). The chlorophyll- a pigment measurements on the base of simultaneous water samples was determined spectrophotometrically according to Strickland and Parsons procedure²².

Table 1. Model of the daily Baltic primary production¹⁸

Input parameters of the model are the chlorophyll *a* + pheophytin *a* concentration vertical profile $C_a(z)$ [mg·m⁻³], surface irradiance $E_d(\lambda, t, 0)$ [quanta·m⁻²·s⁻¹·nm⁻¹] and sea surface temperature T [°C].
Model formulas are:

1) Dependencies of total downward irradiance attenuation coefficients $K_d(\lambda)$ [m⁻¹], its phytoplankton component $K_{pl}(\lambda)$ [m⁻¹] and chlorophyll concentration C_a , are given:

$$\begin{aligned} K_d(\lambda) &= K_w(\lambda) + C_a \{ C_1(\lambda) \exp[-a_1(\lambda)C_a] + k_{d,i}(\lambda) \} + \Delta K(\lambda) \\ K_{pl}(\lambda) &= C_a \{ C_2(\lambda) \exp[-a_2(\lambda)C_a] + k_{c,i}(\lambda) \} \\ \Delta K(\lambda) &= 0.068 \exp[-0.014(\lambda - 550)] \end{aligned} \quad (T1)$$

The value constants $C_1(\lambda)$, $a_1(\lambda)$, $k_{d,i}(\lambda)$, $C_2(\lambda)$, $a_2(\lambda)$, $k_{c,i}(\lambda)$ and the attenuation of pure water $K_w(\lambda)$ see in¹⁷.

2) Dependencies of the photosynthesis quantum yield $\Phi(z)$ [atomC·quanta⁻¹] on underwater irradiance $EPAR(z)$ [quanta·m⁻²·s⁻¹] in PAR range (400-700 nm), sea surface chlorophyll concentration $C_a(0)$ and euphotic zone temperature T_e , are the next:

$$\begin{aligned} \Phi(z) &= \Phi_{\max} \frac{E_{PAR,1/2}}{E_{PAR,1/2} + E_{PAR}(z)}, \\ \Phi_{\max} &= \Phi_{MAX}(T_e) \frac{C_a(0)^{0.66}}{0.44 + C_a(0)^{0.66}}, \quad \Phi_{MAX}(T_e) = 0.0157(Q_{10})^{T_e/10}, \end{aligned} \quad (T2)$$

where the constants are: $E_{PAR,1/2} = 6.4 \cdot 10^{19}$ [quanta·m⁻²·s⁻¹] and $Q_{10} = 1.77$ (we let T_e approximately equal to sea surface temperature T)

Principles of computations of the some environmental characteristics of primary production in the sea:

1) Vertical profiles of spectral optical properties $K_d(\lambda, z)$ and $K_{pl}(\lambda, z)$ can be calculated on base of $C_a(z)$ using equations (T1);

2) Vertical profiles of the downward spectral irradiance $E_d(\lambda, t, z)$ [quanta·m⁻²·s⁻¹·nm⁻¹], the daily irradiance dose in the PAR spectral range $\eta_{PAR}(z)$ [quanta·m⁻²], the average downward irradiance in the PAR range $EPAR(z)$ [quanta·m⁻²·s⁻¹] and daily energy absorbed by phytoplankton $\eta_{PUR}(z)$ [quanta·m⁻³] can be calculated on base of $K_d(\lambda, z)$, $K_{pl}(\lambda, z)$ and input data of surface irradiance $E_d(\lambda, t, 0)$ by formulas:

$$\begin{aligned} E_d(\lambda, t, z) &= E_d(\lambda, t, 0) \left\{ \exp \left[- \int_0^z K_d(\lambda, z) dz \right] \right\} \\ \eta_{PAR}(z) &= \int_{t_r, 400nm}^{t_s, 700nm} \int E_d(\lambda, t, z) d\lambda dt \end{aligned}$$

where t_r and t_s are the sunrise and sunset times respectively;

$$EPAR(z) = \eta_{PAR}(z) / \Delta t$$

where $\Delta t = t_s - t_r$ is the period of daylight (from sunrise to sunset);

$$\eta_{PUR}(z) \approx 1.2 \int_{t_r, 400nm}^{t_s, 700nm} \int E_d(\lambda, t, z) K_{pl}(\lambda, z) d\lambda dt$$

3) Daily values of: vertical distributions of primary productions $P(z)$ [atomsC·m⁻³] and the total primary production in water column P_{tot} [atomsC·m⁻²] are calculated on base of known $\eta_{PUR}(z)$, $EPAR(z)$, $C_a(0)$, equations (T2), and by formulas:

$$P(z) = \Phi(z) \times \eta_{PUR}(z), \quad P_{tot} = \int_0^{z(P=0)} P(z) dz$$

where $z(P=0)$ is the depth at which primary production decrease to a level so small that it does not affect the overall production P_{tot} .

4 DATA ASSIMILATION IN A NUMERICAL PROCEDURE

Different methods of data assimilation in dynamical models can be proposed. In our previous paper⁶ for the remote sensing data assimilation there a simple method was used based on a optimal interpolation procedure with a time autocovariance function of chlorophyll field. A popular extended Kalman filter method³ usually will give better results but need a complicated numerical procedure. An ajoin-like method⁴ gives a possibility to study a model sensitivity to a parameters variability. There are a developments of ajoin procedures which can give an estimation of some model unknown parameters for the best fitting model to data⁴.

In our studies we use a simple procedure of data assimilation by means a exponential autocovariance function of chlorophyll field and modification of ajoin⁴ method for fitting the dynamics to data with a variation of some model parameters, which are: nutrient inflow, vertical sinking rate, vertical turbulent diffusion coefficients in upper layer and below.

The first assimilation procedure was proceeded by a simple method

$$C_1(t, z) = \alpha_0 C_1^{\text{model}}(t, z) + \sum_{i=1}^{N_{\text{obs}}} \alpha_i C_1^{\text{observed}}(t_i, z), \quad (2)$$

$$\alpha_0 + \sum_{i=1}^{N_{\text{obs}}} \alpha_i = 1, \quad \alpha_i = Q(t - t_i, z) / \sum_{j=1}^{N_{\text{obs}}} Q(t - t_j, z),$$

where $Q(t, z)$ — autocovariance function on a depth z , $t_i, i = 1, \dots, N_{\text{obs}}$ — moments of observations.

The second assimilation procedure can be described as a problem of determination of parameters values $\Theta = (\theta_1, \dots, \theta_N)$ which minimise the target function

$$J_0 = \sum_{i=1}^N \Gamma_i (\theta_i - \tilde{\theta}_i)^2 + \sum_{i=1}^M \sum_{t=1}^K \sum_{j=1}^L W_{ij} Q(t - t_j) [C_1^{\text{model}}(t, z_i) - C_1^{\text{observed}}(t_j, z_i)]^2 \quad (3)$$

with a dynamical conditions

$$\mathbf{P}^{t+1} - F(\mathbf{P}^t, \Theta) = 0, \quad t=1, \dots, K.$$

where matrix of model (1) variables $\mathbf{P}^t = (P_0^t, \dots, P_M^t)$, $P_i^t = P(z_i, t) = (C_1(z_i, t), C_2(z_i, t), C_3(z_i, t))$ in the regular time moments $\Omega: \{t = 1, \dots, K\}$, $F(\Theta)$ — dynamical operator of model (1). In equations (5) and (6) $\tilde{\Theta}$ is an aprioric estimation of parameter vector, $\Gamma_i \geq 0$ is an inversions of aprioric estimation error, $\mathbf{W} = (W_{ij})$ is a positive definite matrix which is an inversion of observation errors matrix, $Q_i(t)$ — covariance function of phytoplankton field on the depth z_i . For a detailed description of the ajoin technique see^{3,4}. We use a method of direct minimisation of target function (3) by the quasi-gradient procedure with a variation of a few of the model parameters (see below).

5. COMPUTATIONS RESULTS.

We produced the model computations for the three points in the Gulf of Gdansk (see Fig.1) for which we have a chlorophyll observations during the 1993 spring bloom (April 17, May 8, May 16) (see Fig.2). The distances between model points and Wistula mouth are different and ecosystem dynamic in the points differs in a nutrient influx and observed chlorophyll concentration C_a .

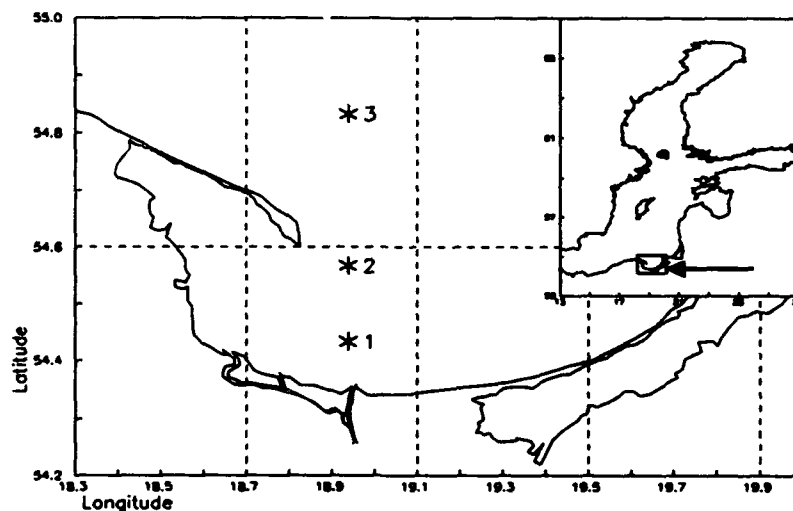


Fig.1. Positions of the simulation points.

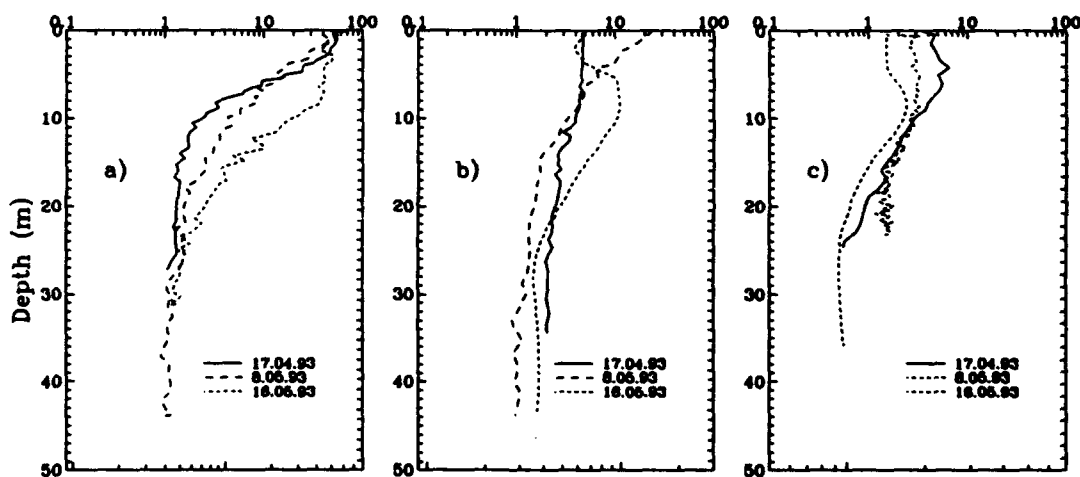


Fig.2. Chlorophyll observations ($\text{mg} \cdot \text{m}^{-3}$): (a) — point 1; (b) — point 2; (c) — point 3..

As a first step of simulation calculations were made of the model without data assimilation. Then data assimilation were produced in accordance with a method (2). It is assumed that chlorophyll observations were made without an errors. Then results of simulation on Fig.3 demonstrate 'dynamical interpolation' between observation points without any smoothing.

For the second step the method of direct target function minimisation (3) have been used. The variable parameters which are vertical sinking rate w_s , vertical diffusion coefficients $K_{z,1}$, $K_{z,2}$ for the upper and bottom layers and daily nutrient inflow intensity $N_{d,0}$. Fig.4 shows the chlorophyll time depth section of the initial state and phytoplankton time variability after data assimilation. The values of parameters before and after the assimilation procedure are presented in Table 2. Analysis of the final parameters values show that for the point 1 we have a very small final vertical sinking value. Such a value is necessary for the abnormal high chlorophyll concentration simulation. One of the possible explanation of this effect could be a lack of advection in model. For the point 1 situated near the Wistula mouth fresh water front the highest chlorophyll concentrations were observed. At this point, probably, it is not the vertical sinking but the advective transport of nutrients and phytoplankton determine the ecosystem dynamics. A complex model of ecosystem dynamics with a two or three-dimensional advection field will be a subject of our future studies.

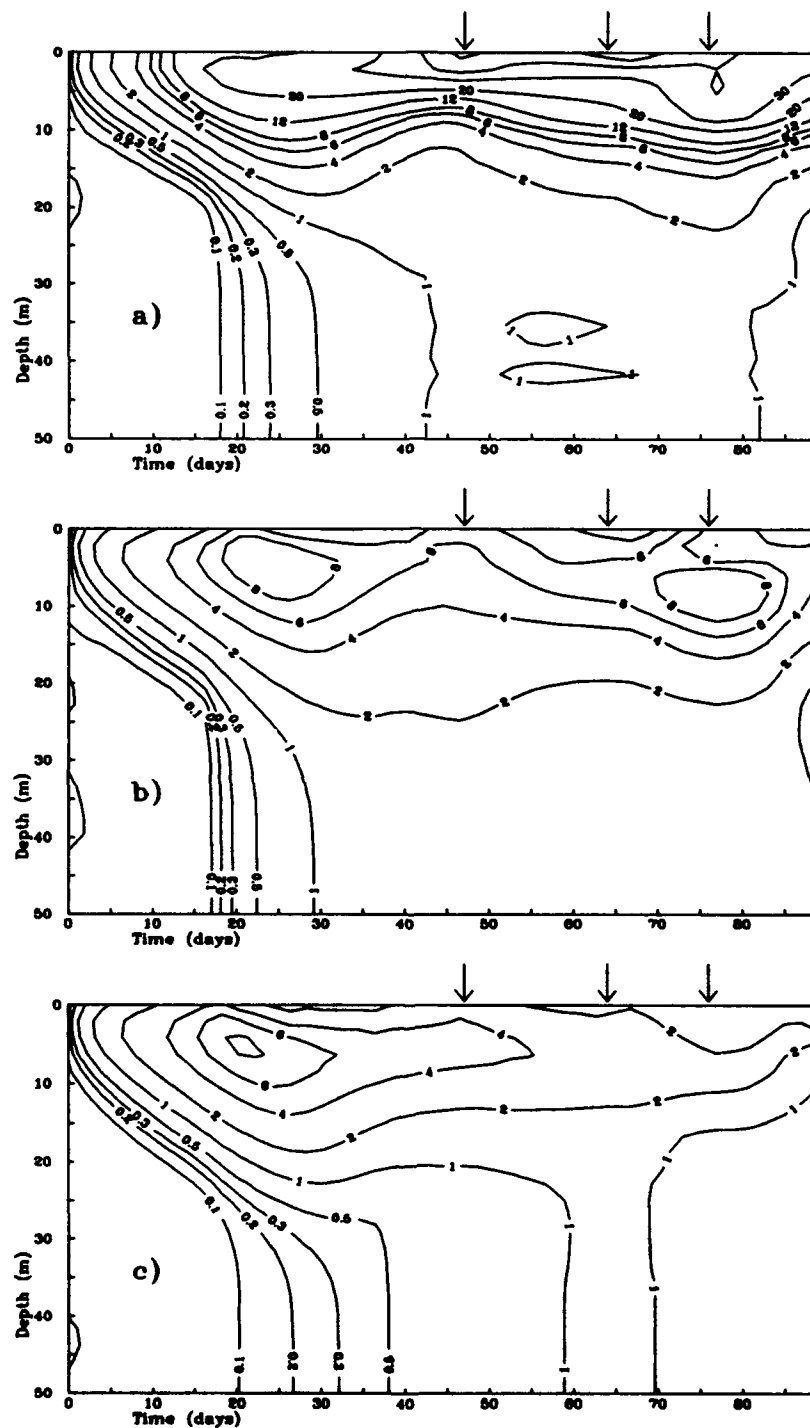


Fig.3. Model chlorophyll ($\text{mg}\cdot\text{m}^{-3}$) time-depth sections as a results of data assimilation procedure (2). (a) — point 1; (b) — point 2; (c) — point 3. Arrows on the top show the days of data assimilation.

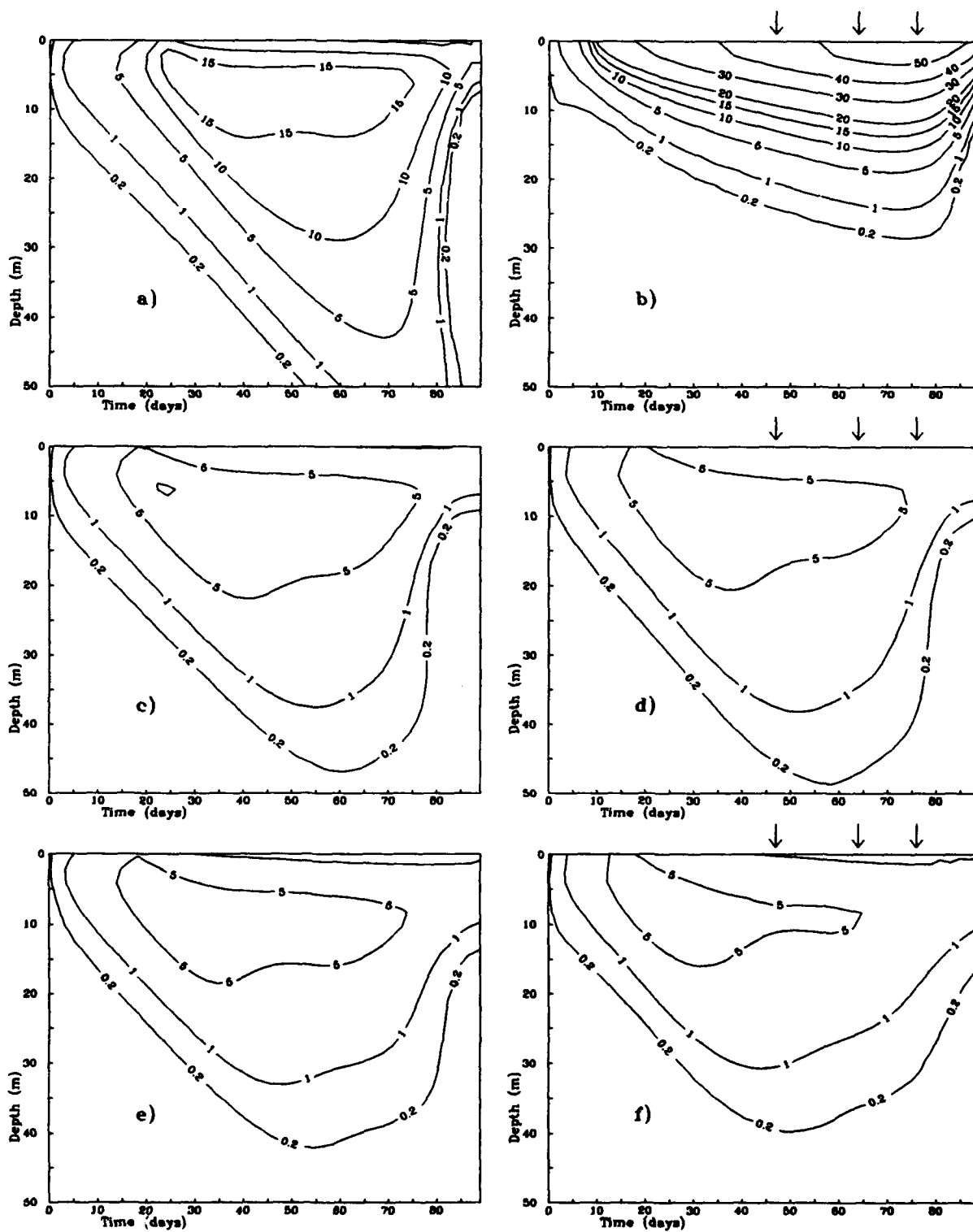


Fig.4. Initial model chlorophyll ($\text{mg}\cdot\text{m}^{-3}$) time-depth sections and a results of data assimilation procedure (3).
 point 1: (a) — initial, (b) — data assimilation; point 2: (c) — initial, (d) — data assimilation;
 point 3: (e) — initial, (f) — data assimilation; arrows show the days of data assimilation.

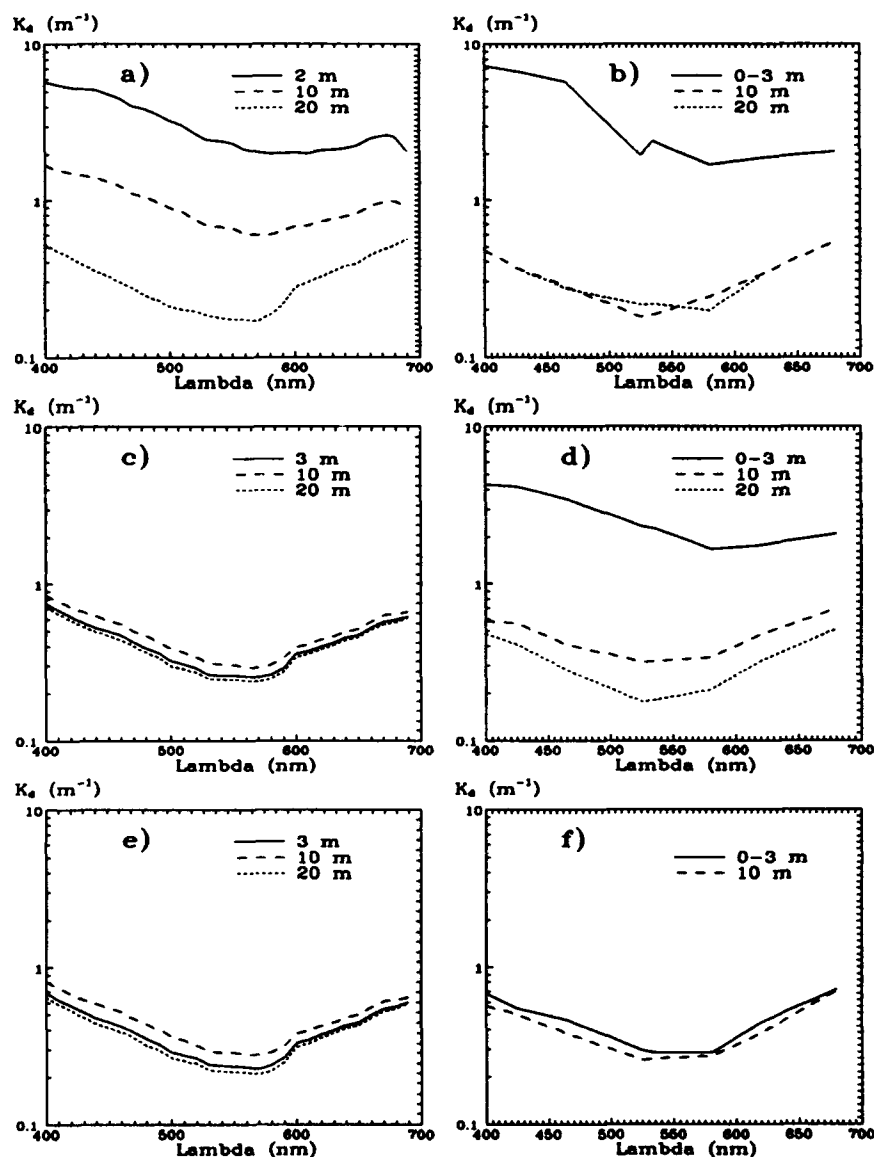


Fig.5. Observed and modelled spectral underwater light attenuation K_d (8.05.1993): point 1: (a) — model, (b) — observed; point 2: (c) — model, (d) — observed; point 3: (e) — model, (f) — observed;

Table 2. Initial and final values of parameters in data assimilation procedure (3).

	Point 1		Point 2		Point 3	
	Initial	Final	Initial	Final	Initial	Final
w_s [m·d ⁻¹]	1.0	0.04	1.0	1.08	1.0	0.88
$K_{z,1}$ [m·d ⁻¹]	0.8	0.94	0.8	1.34	0.8	1.3
$K_{z,2}$ [m·d ⁻¹]	0.4	0.4	0.4	0.4	0.4	0.34
$N_{d,0}$ [mM/m ³]	2.5	2.5	0.5	0.37	0.2	0.02

Not only chlorophyll data can be assimilate in bio-optical dynamical model. It's possible to state a problem of observed primary production, observed total downward irradiance attenuation coefficients $K_d(\lambda, z)$ or downward spectral irradiance $E_d(\lambda, z)$ assimilation in a model (1). The numerical procedure of data assimilation will be similar with a methods (2), (3).

In Fig.5 are presented the observed total downward irradiance attenuation coefficients K_d and equivalent modeled spectra of the K_d derived using a chlorophyll data assimilation by method (3). Spectral attenuation coefficient was calculated on the base of downwelled underwater vector light irradiance observations of 8 spectral bands by a profiler produced by IO PAS. We see that correlation of the observed underwater irradiance field with the modeled field is satisfactory for the highly eutrophicated zone (Point 1) and for open sea (Point 3), but is too smooth for the abnormal feature near Wistula river mouth. For the transition zone (Point 2) high surface K_d values can not be explained only by the chlorophyll and yellow substance model of Table 1. Probably, here we are observed with an effects of a other optical factors (dissolved organic and inorganic matter and other allochthonic admixtures).

6. CONCLUSIONS

Finally we can conclude that modern technique of marine bio-optical field and primary production simulation make it possible to describe marine ecosystems features typical situations. For an abnormal chlorophyll concentrations on a high eutrophicated regions accuracy of model is temperate. Data assimilation methods can produce an estimation of unknown model parameters or can be a sort of 'dynamical interpolation and smoothing'. Future research will give us a new tools for remote sensing data assimilation. We need methods which include in this assimilation procedure other data sources such as primary production estimated by a 'pump and probe' fluorimeter²³.

7. ACKNOWLEDGEMENTS

The authors express their gratitude to Dr. Anton Staśkiewicz (IO PAS) who have put their calculated data at our disposal, M. Ostrowska (IO PAS) and Yuri Konev (Moscow State University) who took part in experimental observations as well as Mark Dowell (IRSA, JRC, Ispra) for the help in manuscript preparation.

8. REFERENCES

1. J.S. Wroblewski, "A model of the spring bloom in the North Atlantic and its impact on ocean optics," *Limnol. Oceanogr.*, Vol.34, No. 8, pp.1563-1571, 1989.
2. W.W. Gregg and J.J. Walsh, "Simulation of the 1979 spring bloom in the mid-Atlantic bight: a coupled physical/biological/ optical model," *J. Geophys. Res.*, Vol.97, No.C4, pp.5723-5743, 1992.
3. M. Ghil and P. Malanotte-Rizzoli, "Data assimilation in meteorology and oceanography," *Adv. Geophys.*, Vol.33, pp.141-265, 1991.
4. W.C. Thacker and R.B. Long, "Fitting dynamics to data," *J. Geophys. Res.*, Vol.93(C2), pp.1227-1240, 1988.
5. J. Ishizaka, "Coupling of Coastal Zone Color Scanner data to a physical-biological model of the southeast U.S. continental shelf ecosystem, 2, An Eulerian model," *J. Geophys. Res.*, Vol.95, No.C20, pp.183-200, 1990.
6. S.V. Semovski and B. Woźniak, "Assimilation of monthly CZCS data in the bio-optical model of the North Atlantic annual phytoplankton cycle," *Proceedings of the Second Thematic Conference "Remote Sensing for Marine and Coastal Environments"*, 31.01-2.02.1994, New Orleans, USA, Vol.1, pp.281-292, 1994.
7. M. Plinski, *Private communications*.
8. J.S. Wroblewski and J.G. Richman, "The nonlinear response of plankton to wind mixing events — implication for larval fish survival," *Journ. of Plankton Res.*, Vol.9, pp.103-123, 1987.
9. H.G. Fransz, J.P. Mommaerts and G. Radach, "Ecological modelling of the North Sea," *Netherl. Journ. of Sea Res.*, Vol.28(1/2), pp.67-140, 1991.
10. T.J. Smayda, "The suspension and sinking of phytoplankton in the sea," *Oceanography and Marine Biology Annual Review*, Vol.8, pp.353-414, 1970.
11. B. Boungen, K. Brockel, V. Smetacek and B. Zeitzscel, "Growth and sedimentation of the phytoplankton spring bloom in the Bornholm Sea (Baltic Sea)," *Kieler Meeresforschung Sonderheft*, Vol.5, pp.49-60, 1981.

12. O.P. Savchuk, A.A. Kolodocha and E.Sh. Gutsabbath, "Simulation of the matter cycle in the Baltic ecosystem," *16 Conference of the Baltic Oceanographers*, Kiel, Vol.2, pp.921-931, 1988.
13. E. Styczyńska-Jurewicz and M. Łotocka, "Zooplankton-phytoplankton interaction evaluated by pigment analysis," *Proceedings of the 21th European Marine Biology Symposium*, Gdansk, pp.471-483, 1989.
14. W.M. Balch, R. Evans, L. Brown, G. Feldman, C. McClain and W. Esaias, "The remote sensing of ocean primary productivity: use of a new data compilation to test satellite algorithms," *J. Geophys. Res.*, Vol.97(C2), pp.2279-2293, 1992.
15. A. Morel, "Light and marine photosynthesis: a spectral model with geochemical and climatological implications," *Progr. Oceanog.*, Vol.26, pp.263-306, 1991.
16. T. Platt, C. Caverhill and S. Sathyendranath, "Basin-scale estimates of ocean primary production by remote sensing: the North Atlantic," *Journ. of Geophys. Res.*, Vol.96(C8), pp.15.147-15.159, 1991.
17. B. Woźniak, J. Dera and O.J. Koblenz-Mishke, "Modelling the relationship between primary production, optical properties, and nutrients in the sea," *Ocean Optics XI, Proceedings SPIE*, Vol.1750, pp.246-275, 1992.
18. B. Woźniak, S.V. Semovski, R. Hapter, M. Ostrowska and S. Kaczmarek, "Algorithm for estimating primary production in the Baltic from remotely sensing," *Studia i Materialy Oceanolog., Marine Physics*, in press, 1994.
19. W. Lenz, "Monatskarten der Temperatur der Ostsee, dargestellt für verschiedene Tiefenhorizonte," *Dt. Hydrogr. Z., Egr.-H. R.B.*, No.11, Hamburg, 1971.
20. J. Jędrasik and M. Kowalewski, "Transport model of pollutants in the Gulf of Gdansk," *Studia i Materialy Oceanolog., Marine Chemistry*, No.64, pp.61-75, 1993.
21. G.G. Girdiuk, B.N. Egorov, and S.P. Molevskii-Molevich, *Definition of the radiance balance of the ocean surface*, Gidrometeoizdat, Sankt-Petersburg, 135 p., (in Russian), 1992.
22. L.D.H. Strickland and T.R. Parsons, "A practical hand-book of sea water analysis," *Canada Bulletin of Fisheries Research*, 1968.
23. Z. Kolber and P.G. Falkowski, "Use of active fluorescence to estimate phytoplankton photosynthesis in situ," *Limnol. Oceanogr.*, Vol.38(8), pp.1646-1665, 1993.

Solar ultraviolet radiation penetration and photochemical effect on colored dissolved organic matter in coastal waters

Alexander P. Vasilkov

P.P. Shirshov Institute of Oceanology
Moscow, 117218 Russia

ABSTRACT

The photochemical effect of solar ultraviolet radiation on colored dissolved organic matter has been recently revealed. This effect consist in change of spectral absorption of sea water in the UV band. In present paper the experimental data are parameterized to include this effect into radiative transfer theory. Radiative transfer model is developed for calculation the spectral UV flux at different depths in the sea. Resulting nonlinear radiative transfer equation is solved by the consequent iteration method with using quasi-single scattering approximation. Calculations of the spectral irradiance within 290-400 nm band were carried out for different solar zenith angles and for different total amount of ozone. Model of spectral optical properties of sea water inherent to coastal zone was used. By convolution of irradiance spectra with the DNA action spectrum the biologically effective UV dose rates were calculated. It is shown that solar UV-light effect on the colored dissolved organic matter absorption leads to about of 40% increase of the DNA dose rates at depth 4 m.

1. INTRODUCTION

Depletion of Earth's ozone layer resulting from the growing industrial emissions to the atmosphere is now in great interest of research scientists. Increased levels of biologically harmful UV-B radiation (280-320nm), resulted from ozone layer depletion, could affect the aquatic ecosystems. One of the important effects of enhanced levels of UV-B radiation is the reduction in the productivity of phytoplankton. This effect is conclusively confirmed by laboratory findings^{1,2} and field observations in the Bellinghausen Sea (Antarctic), showing a reduced water column productivity of Antarctic phytoplankton under conditions of ozone hole (total ozone less than 200 Dobson Units, DU) in comparison with productivity outside the hole.³ Enhanced UV-B radiation could also decrease the global sink of carbon dioxide into the oceans, thereby augmenting greenhouse effect and affecting other long-term global biogeochemical cycles.⁴ The effect of increased UV radiation on phytoplankton is particularly important for coastal regions where great part of World Ocean primary production is produced.

The quantitative assessment of UV effects on aquatic organisms requires an accurate knowledge the in-water radiation

field. For predictive capability it is necessary to model levels of spectral irradiance existing within natural waters as a function of total ozone amount, solar zenith angle, depth and values of optical properties of the sea water. For these purposes a radiative transfer model for propagation UV radiation in the atmosphere-ocean system has been developed in papers^{5,6}. In this paper spectral irradiance is calculated at different depths for different solar zenith angles and total ozone amounts. Depth dependence of biologically effective UV dose rates for marine phytoplankton are also given.

Recently the effect of the solar UV radiation on water absorption has been reported⁷. Change of water absorption due to this effect is about of 20÷40% at wavelength 290 nm. For accurate calculation of UV irradiance this effect would be included into radiative transfer model.

In present paper the parameterization of the effect of solar UV radiation on water absorption is fulfilled. Change of water absorption is considered as change of the dissolved organic matter (DOM) absorption in dependence on ratio of UV-B flux to UV-A flux. Resulting nonlinear radiation transfer equation is solved by consequent iteration method with using quasi-single scattering approximation. The paper gives some calculated examples of spectral irradiance under action of considered effect. Depth dependence of biologically effective UV dose rates for unshielded DNA is calculated at considered effect in action. Maximum enhancement of DNA dose rates resulting from considered effect attains about of 40% at depth 4 m.

2. UV RADIATION EFFECT ON THE DOM ABSORPTION AND ITS PARAMETERIZATION

It is well known that sufficiently rigid UV radiation destroys the DOM and consequently decreases the water absorption. Recently evidence of solar UV radiation effect on the DOM absorption has appeared^{7,8}. In paper⁸ the in situ photodegradation of aquatic humic substances by underwater UV radiation was studied. Decrease of water absorption at wavelengths 250 nm and 365 nm has been established. This decrease was long-term and appeared to be proportional to total time of exposure (over 5 days). Another, short-term effect of the solar UV radiation on water absorption has been reported in paper⁷. Most remarkable feature of revealed effect is its convertible nature. During first part of light time of a day the decrease of water absorption in the UV-B spectral band was revealed and later water absorption increased up to the former values. Reverse change of water absorption was revealed in the UV-A spectral band: at first the water absorption increase was observed and later the restoration of the former values of absorption was observed. The exposure of water samples in quartz ampoules on ship board showed change of water absorption identical to change of the in situ samples. Water "clearance" in the UV-B spectral band and water "darkness" in the

UV-A spectral band are explained by the photochromatic transformation of some component of the DOM under action of the solar UV radiation.

To include these changes of the DOM absorption into radiative transfer model one needs the parameterization the UV radiation effect on the DOM absorption. We shall consider only short-term, convertible effect of UV radiation on the DOM absorption because these changes of absorption during a day attain considerable values 20-40% (at wavelength 290 nm)⁷. Changes of absorption due to long-term effect of UV radiation on water absorption are significantly less (decrease of absorption at wavelength 250 nm is about of 20% during over 5 days)⁸.

Comparison of daily changes of the DOM absorption and the time dependence of ratio of UV-B irradiance to UV-A irradiance shows their close correlation. Therefore we can assume that relative change of the DOM absorption at fixed wavelength 290 nm is determined by the instant values of solar irradiance:

$$(\Delta a / a)_{\lambda=290} = F(E_B / E_A) \quad (1)$$

Here E_B and E_A are UV-B and UV-A irradiances:

$$R \equiv E_B / E_A = \int_{290}^{320} E_{\lambda} d\lambda / \int_{320}^{400} E_{\lambda} d\lambda \quad (2)$$

In first approximation the function $F(R)$ is taken to be linear: $F(R) = k_1 R + k_2$, where k_1 and k_2 are the regression coefficients. Spectral dependence of change of the DOM absorption is described by the function $f(\lambda)$ which approximates the experimental data:

$$\Delta a(\lambda) / \Delta a(290) = f(\lambda) \quad (3)$$

Note that $f(\lambda) < 0$ in the UV-B spectral band, $f(290) = -1$ and $f(\lambda) = 0$ at wavelength approximately equal to 340 nm.

Then we can write the radiative transfer equation for water medium in following form:

$$\mu \frac{\partial L_{\lambda}}{\partial z} + [b_{\lambda} + a_{\lambda} + a(290)F(E_B/E_A)f(\lambda)] L_{\lambda} = \frac{b_{\lambda}}{4\pi} \int_{4\pi} L_{\lambda} x(\gamma) d\Omega \quad (4)$$

Here $\mu = \cos \theta$ is cosine of zenith angle, L_{λ} is spectral radiance, z is depth, b_{λ} is spectral scattering coefficient, a_{λ} is absorption coefficient of sea water in absence of effect of UV radiation on water absorption, $\Delta a = a(290)F(E_B/E_A)f(\lambda)$ is change

of DOM absorption due to effect of UV radiation on water absorption, $x(\gamma)$ is the normalized volume scattering function in dependence on scattering angle γ . Boundary condition takes place just below the ocean surface:

$$z = 0 \quad L_\lambda = E_\lambda^S / \mu_0 \delta(\mu - \mu_0) \delta(\phi - \phi_0) + L_\lambda^d(\mu, \phi) \quad (5)$$

where E_λ^S is the direct solar irradiance, μ_0 is cosine of the solar zenith angle in water, ϕ_0 is the solar azimuth angle, L_λ^d is diffuse radiance in dependence on zenith angle μ and azimuth angle ϕ .

3. APPROXIMATE SOLUTION OF THE RADIATIVE TRANSFER EQUATION

It can be easily seen that the radiative transfer equation (5) becomes nonlinear under photochromatic transformation of the DOM. A possible approach to solve this equation is the consequent iteration method. We are restricted the first approximation, resulted in taking the ratio $R = E_B / E_A$ as one at absence of effect of solar UV radiation on the DOM absorption. Resulting equations are solved in quasi-single scattering approximation⁹.

Ocean water is the strong absorption medium with highly anisotropic scattering. Therefore the quasi-single scattering approximation of radiative transfer equation⁹ can be used for calculation of spectral irradiance. This approximation is based on following assumptions: (a) single scattering in upward direction; (b) multiple scattering in downward direction in accordance with delta-function.

Quasi-single scattering approximation gives the simple expression for beam transmittance: $T_\lambda^b = \exp(-K_\lambda z / \mu)$, where K_λ is the diffuse attenuation coefficient, $K_\lambda = a + b_b$, b_b is the backscattering coefficient. Here the water column is supposed to be homogeneous. In the zero approximation, that is in absence of the photochromatic effect, spectral irradiance at depth z can be written as

$$E_\lambda(z) = E_\lambda^S T_\lambda^b(\mu_0) + \int_0^{2\pi} d\phi \int_0^{\mu_1} L_\lambda^d(\mu, \phi) T_\lambda^b(\mu) \mu d\mu \quad (6)$$

There E_λ^S is the spectral irradiance for direct solar radiation just beneath the ocean surface, μ_1 is the cosine of the total internal reflection angle $\theta_1 \approx 49^\circ$, $L_\lambda^d(\mu, \phi)$ is the angle distribution of sky radiance after surface refraction.

If the photochromatic effect is taken into account the beam transmittance in the first approximation becomes as following:

$$T_{\lambda}^b = \exp(-K_{\lambda}^0 z/\mu) \exp\left[a^0(290) f(\lambda) \int_0^z F(R^0) dz / \mu\right] \quad (7)$$

There superscript zero denotes parameters taken in the zero approximation, that is in absence the photochromatic effect. Parameter R^0 depending on depth is calculated on base of (2) and (6). Putting expression (7) into formula (6) one obtains solution of the nonlinear radiative transfer equation (4) in the first approximation.

For calculations of UV irradiance the boundary conditions at sea surface and the model of spectral optical properties of sea water are required. The water surface is supposed to be flat. Refraction of radiance on the surface takes place in accordance with the Fresnel law. Angular distribution of radiance incident on sea surface was calculated by numerical method which is a modification of the discrete ordinate method^{5,6}. It simulates the effects of multiple scattering for inhomogeneous plane-parallel cloudless atmosphere. It takes into account absorption by ozone, molecular and aerosol scattering. The calculations of UV spectral radiance were carried out with a wavelength resolution of 2 nm in UV-B region (290-320 nm) and 5 nm in UV-A region (320-400 nm).

Model of the optical properties¹⁰ includes the spectral dependencies of absorption coefficients for pure sea water and dissolved organic matter (DOM), backscattering coefficients for pure water and particulate matter (PM) :

$$a(\lambda) = a_w(\lambda) + a_0 \exp[-k(\lambda - \lambda_0)]; \quad b_b(\lambda) = b_b^w(\lambda) + b_0(\lambda/\lambda_0)^{-m} \quad (8)$$

There a_0 is the DOM absorption at wavelength λ_0 , $k=0.015\text{nm}^{-1}$ is coefficient, b_0 is the PM backscattering coefficient at wavelength λ_0 , m is parameter. Values of absorption coefficient for pure sea water $a_w(\lambda)$ were taken from paper¹¹.

4. RESULTS

The developed model has been used to investigate influence of the photochromatic effect on a set of optical and biological characteristics: (a) spectral absorption of sea water; (b) spectral distribution of UV flux at different depths; (c) depth dependence of biologically effective UV dose rates for unshielded DNA. Input parameters of the model are following: (a) total amount of ozone Ω ; (b) solar zenith angle θ_0 ; (c) aerosol optical thickness τ at wavelength λ_0 ; (d) DOM absorption coefficient at wavelength λ_0 ; (e) ratio of PM backscattering coefficient to DOM absorption coefficient at wavelength λ_0 ; (f) power in spectral

dependence of backscattering coefficient m . Preliminary calculations have shown that most important input parameters were total amount of ozone, solar zenith angle and DOM absorption coefficient. Other input parameters play less significant role in propagation UV radiation in sea water⁶. Optical properties of sea water were chosen as typical for coastal waters.

Influence of solar UV radiation on the sea water absorption expressed as ratio of absorption coefficient at effect in use to one without it $a(\lambda)/a^0(\lambda)$ is shown in Fig.1. Input parameters are following: solar zenith angle $\theta_0=30^\circ$, total amount of ozone 300 DU, DOM absorption coefficient $a_0(290)=1\text{m}^{-1}$, ratio $b_0/a_0=0.05$, parameter $m=1$, aerosol optical thickness $\tau=0.1$ at wavelength 400 nm. Value of DOM absorption coefficient corresponds to coastal sea waters. All these input parameters are used invariable in following calculations. The data on Fig.1 demonstrate the rapid reduction of effect of UV radiation on water absorption with depth increasing. Maximum change of water absorption (about of 30%) takes place just beneath sea surface and change of water absorption becomes less 10% at depth equal approximately to 3 m. Rapid reduction of considered effect with depth is explained by strong attenuation of UV-B radiation in coastal waters.

Effect of solar UV radiation on water absorption causes change in spectral irradiance. Ratio of irradiance at effect in use to one without it E_λ/E_λ^0 is shown in Fig.2. The photochromatic effect is pronounced in the UV-B spectral band where increase of irradiance attains about of two times at depth 1 m. Change of spectral irradiance in the UV-A spectral band is insignificant. Emphasis of effect in the UV-B spectral band is especially important for biological community because just UV-B radiation is biologically harmful.

The biological effect of UV radiation is ordinary described by action spectrum. Biological dose rate of UV radiation is expressed as weighted integral:

$$D(z) = \int_{290}^{400} E_\lambda(z) A(\lambda) d\lambda \quad (9)$$

where $A(\lambda)$ is an action spectrum. UV dose rates were calculated using the action spectrum for unshielded DNA (Setlow's spectrum). This spectrum was taken from paper¹² where its absolute values were given. DNA dose rates were calculated for two cases: at the photochromatic effect in use and in its absence. Ratio of these dose rates $D(z)/D^0(z)$ is shown in Fig.3 for different solar zenith angles and total amounts of ozone. The photochromatic effect on DNA dose rates increases with the solar zenith angle diminishing and the total ozone amount reducing. Maximum effect reveals at

depth about of 4 m where increase of dose rate at effect in use attains approximately 40%.

Biologically effective UV enhancement ratio resulting from reduction of the total ozone column can be determined as ratio of dose rate at less amount of ozone to dose rate at greater amount of ozone¹²: $r=D(250)/D(400)$. This ratio can be named as the radiation amplifier factor analogous to routine determination of this factor at one percent decrease of ozone amount. The depth dependence of ratio r at the photochromatic effect in use is shown in Fig.4a for different solar zenith angles. This ratio decreases rapidly with depth increasing due to rapid attenuation of UV-B radiation. The photochromatic effect leads to increase of influence of ozone depletion on DNA dose rate. In Fig.4b the ratio of radiation amplifier factor at effect in use to one without effect is shown. The photochromatic effect is pronounced for small solar zenith angles. Increase in the radiation amplifier factor at the photochromatic effect in use attains 6+10% in 30+70° region of solar zenith angles.

5. CONCLUSION

The radiative transfer model has been developed which includes recently revealed effect of the solar UV radiation on water absorption. To include this effect into radiative transfer model the parameterization of the effect is fulfilled. Change of water absorption due to this effect is considered as change of the DOM absorption in dependence on ratio of UV-B flux to UV-A flux. Resulting nonlinear radiative transfer equation has been solved by consequent iterations method with using the quasi-single scattering approximation. Calculations show that spectral irradiance near wavelength 290 nm increases approximately in two times at depth 1 m when the effect of UV radiation on water absorption is included into calculations.

By convolution of calculated spectral irradiance with Setlow's action spectrum for unshielded DNA the depth dependence of biologically effective UV dose rates are calculated for different solar zenith angles and total ozone amounts. Effect of solar UV radiation on water absorption is pronounced at lower ozone amounts and higher solar elevations. Maximum enhancement of DNA dose rates resulting from considered effect attains about of 40% at depth 4 m. Effect of UV radiation on water absorption leads to 10% increase of radiation amplifier factor determined as ratio of DNA dose rates at reduction of total ozone amount from 400 DU to 250 DU.

The effect of solar UV radiation on water absorption is especially important for coastal waters with great content of the DOM.

6. ACKNOWLEDGMENT

The research reported in this paper was supported by the USA State Department under grant R7 (project "Triad" of the program "Man and Biosphere"). Author expresses his gratitude to Dr.

N.Krotkov who provided the data of atmospheric calculations.

7. REFERENCES

1. R. Worrest and D.P.Hader, "Effect of stratospheric ozone depletion on marine organisms," *Environmental Conservations*, Vol.16, 261-263, 1989.
2. S.Z.El-Sayed, F.C.Stephens, R.R.Bidigare and M.Ondrusek, "Effect of ultraviolet on antarctic marine phytoplankton," *Antarctic Ecosystems, Ecological Change and Conservation*, ed by K.R.Kerry and G.Hempel, pp.379-385, Springer-Verlag, Berlin, 1990.
3. R.C.Smith, B.B.Prezelin, K.S.Baker, R.R.Bidigare, N.P.Boucher, T.Coley, D.Karentz, S.MacIntyre, H.A.Matlic, D.Menzies, M.Ondrusek, Z.Wan, K.J.Waters, "Ozone depletion: ultraviolet radiation and phytoplankton biology in Antarctic waters," *Science*, Vol.255, 952-959, 1992.
4. SCOPE, Effects of Increased Ultraviolet Radiation on Global Ecosystems, 1992.
5. N.A.Krotkov and A.P.Vasilkov, "Theoretical model for prediction of ultraviolet radiation in the atmosphere-ocean system," *IRS'92: Current Problems in Atmospheric Radiation*, Proc. Intern. Radiation Symp., ed. S.Keevallic and O.Karner, 555-558, A.DEEPAAK publishing, Hampton, 1993.
6. N.A.Krotkov and A.P.Vasilkov, "Ultraviolet radiation in the atmosphere-ocean system: a model study," *Atmospheric Radiation, Proc. EUROPE series*, ed. K.H.Stamnes, SPIE Vol.2049, 244-255, 1993.
7. I.A.Samokhina and A.S.Tibilov, "Variation of the sea water attenuation coefficient in UV spectral band due to the solar radiation action," *Izvestiya USSR Academy of Sciences, Atmosph. Oceanic Phys.*, Vol.25, 98-102, 1989.
8. H.De Haan, "Solar UV-light penetration and photodegradation of humic substances in peaty lake water," *Limnol. Oceanogr.*, Vol.38, 1072-1076, 1993.
9. H.R.Gordon, "Simple calculation of the diffusive reflectance of the ocean," *Appl. Opt.*, Vol.12, 2803-2804, 1973.
10. O.V.Kopelevich, "Optical properties of the sea water," *Ocean Optics, Physical Optics of the Ocean*, Vol.1, (in Russian), pp.150-235, Nauka, Moscow, 1983.
11. R.C.Smith and K.C.Baker, "Optical properties of the clearest natural waters," *Appl. Opt.*, Vol.20, 177-186, 1981.
12. F.E. Quate, B.M.Sutherland and J.C.Sutherland, "Action spectrum for DNA damage in alfalfa lowers predicted impact of ozone depletion," *Nature*, Vol.358, 576-578, 1992.

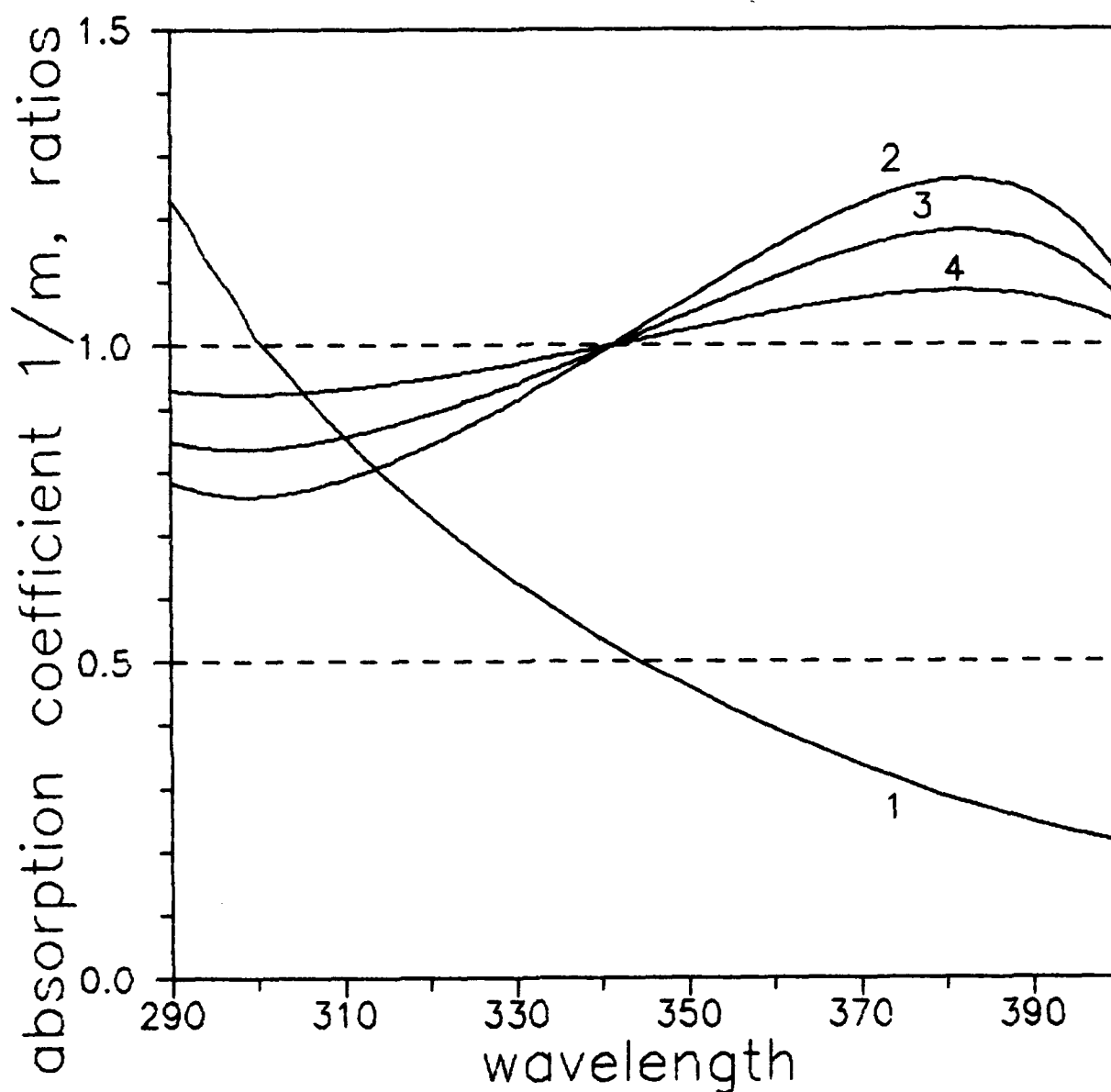


Fig.1. Absorption coefficient of sea water $a^0(\lambda)$ in absence of the photochromatic effect (curve 1) and ratio of absorption coefficient at effect in use to one without effect $a(\lambda)/a^0(\lambda)$. Curve 2 corresponds to depth $z = 0$ m, curve 3 corresponds to $z = 1$ m and curve 4 corresponds to $z = 3$ m. Solar zenith angle is equal to 30° , total ozone amount is equal to 300 DU.

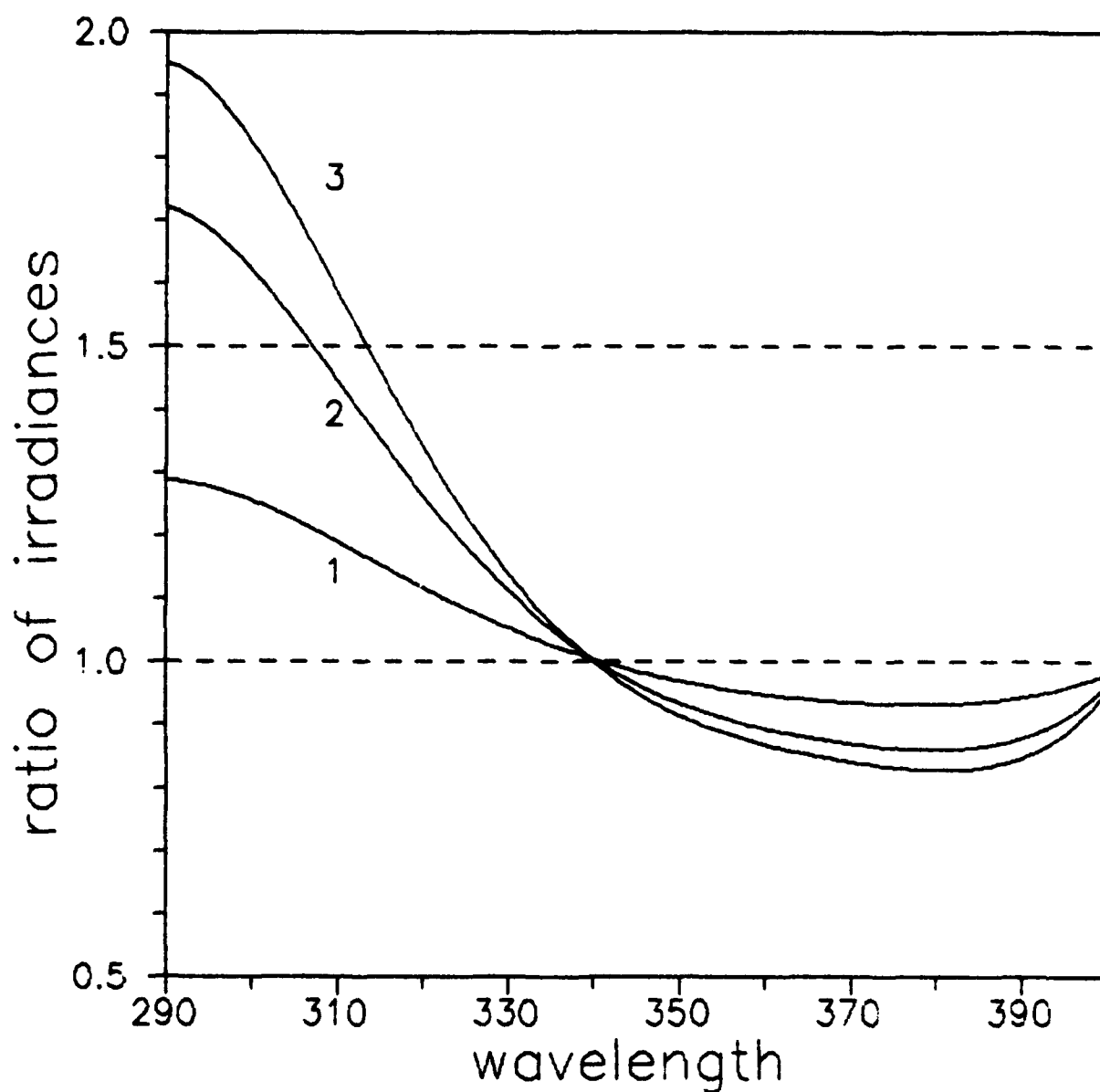


Fig.2. Ratio of spectral irradiance at the photochromatic effect in use to one without effect for different depths. Curve 1 corresponds to depth $z = 1$ m, curve 2 corresponds to $z = 3$ m and curve 3 corresponds to $z = 5$ m. Solar zenith angle is equal to 30° and total ozone amount is equal to 300 DU.

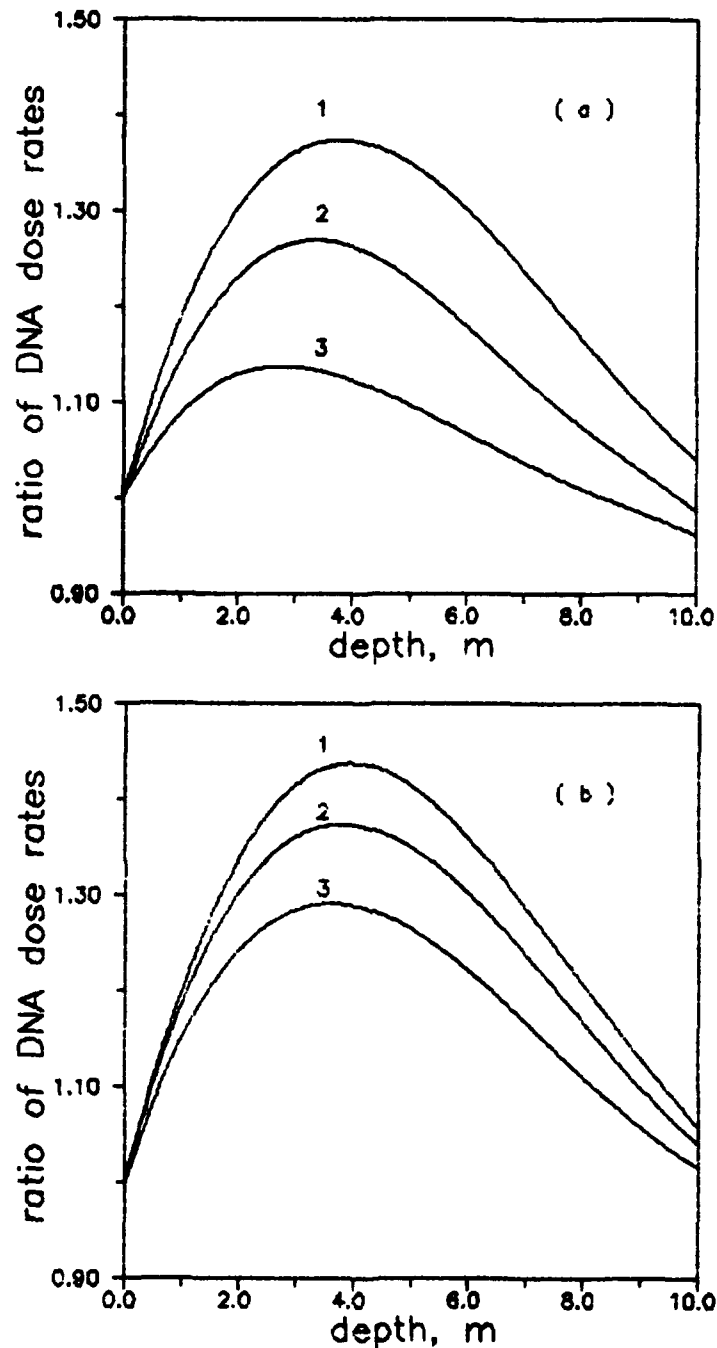


Fig.3. (a) Ratio of DNA dose rate at the photochromatic effect in use to one without effect $D(z)/D^0(z)$ for different solar zenith angles θ_0 . Curve 1 corresponds to $\theta_0 = 30^\circ$, curve 2 corresponds to $\theta_0 = 50^\circ$ and curve 3 corresponds to $\theta_0 = 70^\circ$. Total ozone amount is equal to 300 DU. (b) Analogous ratio of DNA dose rates for different total ozone amounts Ω . Curve 1 corresponds to $\Omega = 250$ DU, curve 2 corresponds to $\Omega = 300$ DU and curve 3 corresponds to $\Omega = 400$ DU. Solar zenith angle is equal to 30° .

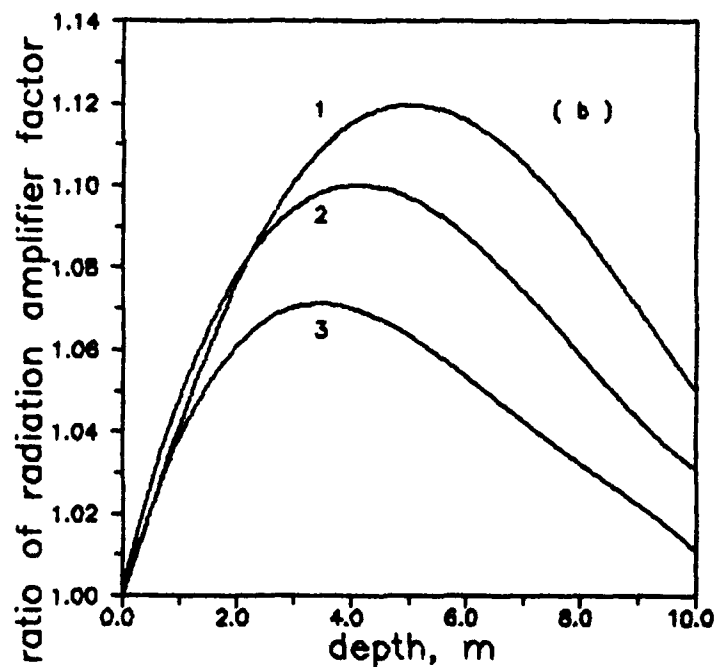
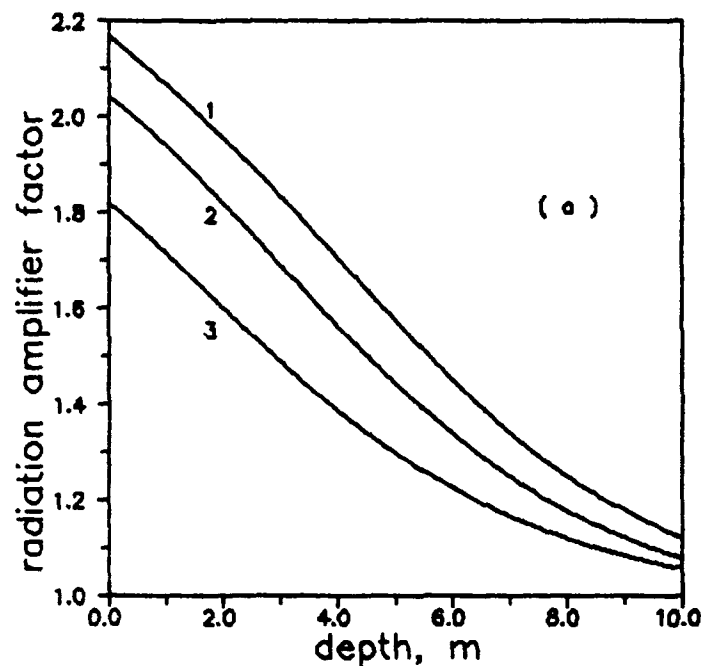


Fig.4. (a) Radiation amplifier factor $r = D(250)/D(400)$ for DNA dose rate showed at the photochromatic effect in use for different solar zenith angles θ_0 . Curve 1 corresponds to $\theta_0 = 30^\circ$, curve 2 corresponds to $\theta_0 = 50^\circ$ and curve 3 corresponds to $\theta_0 = 70^\circ$. (b) Ratio of radiation amplifier factor at the photochromatic effect in use to one without effect r/r^0 for different solar zenith angles. Numbers at curves are the same.

Effects of surface waves and sea-bottom
on self-shading of in-water optical instruments.

Jacek Piskozub

Institute of Oceanology, Polish Academy of Sciences
ul. Powstańców Warszawy 55
81-712 Sopot, Poland

ABSTRACT

Calculations of self-shading for an instrument measuring upward irradiance were conducted with a Monte-Carlo radiance transfer algorithm. The algorithm included Cox-Munk wave-slope probability function and simulation of diffusion on sea-bottom allowing incorporation of rough and/or shallow sea in the simulations. The effect of the self-shading phenomenon was calculated in function of instrument radius, sea-water absorption, surface roughness (depending on assumed wind velocity up to 15 m/s) depth of the instrument, its height over bottom and bottom albedo (both diffusive and reflective one).

1. INTRODUCTION

The problem of self-shading by in-water optical instruments has been discussed during last few years. It is an inherent problem of upwelling radiance and irradiance measurements in sea. Since every photon of upwelling radiance (assuming no light sources) must have passed the instrument depth on the way down to come back from beneath, it is obvious that some of them are blocked by the instrument housing. The effect of self-shading was first calculated Gordon and Ding² in 1991. However in their paper they did not consider sea-surface roughness and influence of sea-bottom in shallow basins. This author used his own Monte-Carlo algorithm for solving the radiance transfer equation in the sea. It included a numerical representation of rough sea surface as well as light diffusion on simulated bottom. The object of the calculations was to determine how much the two additional phenomena affect the self-shading of in-water instruments.

2. MATERIALS AND METHODS

The instrument measuring upwelling irradiance was imagined as a circular disk of radius R floating at a depth d under the sea surface. The sensor itself is treated as a *point* at the center of the disk. No attempt was made to make calculations for a sensor of non-zero diameter as the effect of making the sensor *finite* was already extensively discussed in

aforementioned paper by Gordon and Ding. Of course the assumed shape of the instrument (being in reality rather cylinder or a cone) makes the calculated values of self-shading an understatement.

Photons in the Monte-Carlo algorithm, used in the calculations, were traced in the natural forward direction. Absorption ended a photon's history, i.e. no partial photons were traced to make the physical meaning of the algorithm easier to analyze^{3,4}. The price for that was paid in time-efficiency of the program. The history of every photon that reached the assumed instrument's depth on its return way upwards was then traced back to see if it passed through the instrument on its way down. Each of multiple downward passes for a given photon were counted as each adds to unperturbed downward irradiance on the level of the instrument. The ratio of such photons to all photons upwelling through the instrument depth (again including multiple passes) is the sought ratio of self-shading (i.e. relative error of upwelling irradiance measurement). Similarly, by counting not photons but their cosines, the effect of self shading on vector upwelling irradiance can be calculated. If the photons are included only if they come to the instrument from a narrow solid angle, analogous ratio represents relative error of upwelling radiance coming from the center of that angle. All three possibilities are incorporated in the computer program. However, results shown below are mostly irradiation ones as this is the most frequently measured parameter of upwelling light in the sea.

The algorithm allowed introducing of a layered sea with different absorption α and total backscattering b coefficients. This was however not used in present calculations; water column is homogeneous to make the simulations simpler to analyze. Similarly only a point source of photons simulating the sun was used; light scattered in the atmosphere (skylight) was left out in most calculations to study dependence of self-shading on sun zenith angle. A standard scattering phase function for open ocean sea-water was used.

The roughness of sea surface was introduced by using Cox-Munk¹ probability distribution of wave slopes. The parameters defining the distribution are azimuth and velocity of wind producing the sea-surface waves. Each time a photon reached zero depth, including the moment it leaves atmosphere, an inclination of the element of wave surface is randomly chosen. Reflection or refraction is chosen according to Fresnel law in the co-ordinates of the surface element. The effect of visibility of the element by the incident photon is taken into account by accepting only slopes for which a $[0,1)$ range random number is smaller than cosine of the surface element's normal to the photon direction. There are some limitations to the method. Photons reflected or refracted into the wrong hemisphere (e.g. upwelling photon reflected *upwards* on an extremely sloped surface element) must be rejected. All surface events are assumed to happen at zero depth as Cox-Munk distribution gives no information on actual height of a surface element. No shading of the surface element by neighboring waves can be taken into account, distorting calculations especially for low sun angles. The Cox-Munk distribution is defined only for wind velocities up to 15 m/s.

Sea-bottom reflectance was assumed to be a uniform diffusion with some reflection added to simulate a forward tilted reflectance phase function. Both diffusive and reflective albedo

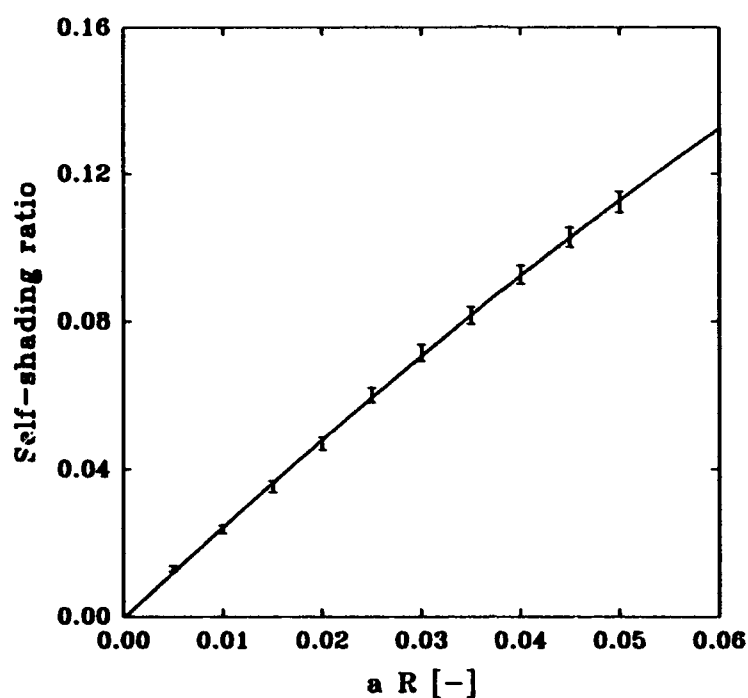


Fig 1. Dependence of upwelling irradiance relative error on aR product.
 ($d = 0$ m, $D = \infty$, $\omega = 0.8$, $\theta = 40^\circ$, $v = 0$ m/s)

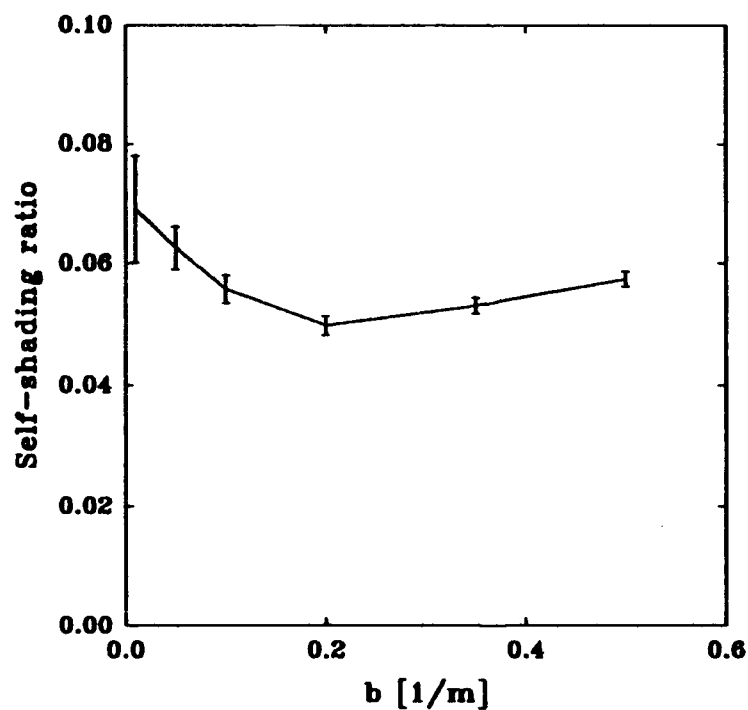


Fig 2. Dependence of upwelling irradiance relative error on absorption a
 ($d = 0$ m, $D = \infty$, $b = 0.1$ m⁻¹, $\theta = 40^\circ$, $v = 0$ m/s)

could be changed separately. Only level (horizontal) bottom was considered in the calculations.

The calculations presented were carried out partly on PC 486 50 MHz in Institute of Oceanology, Sopot and partly on a Sun Sparc Sever 630 MP in Remote Sensing Laboratory of GKSS Forschungszentrum Geesthacht, Germany. All results for rough sea-surface model presented here were calculated using 4 million photons. Calculations for each million photons took 45-100 minutes for the PC used and 20-45 minutes for the Sun Workstation depending on solar zenith angle and degree of sea roughness..

3. RESULTS AND DISCUSSION

It is obvious from dimensional analysis that changing of absorption a (with proportional change of total scattering b to keep photon survival probability $\omega = b/(a+b)$ constant) is equivalent to changing all sizes l so that product al remains unchanged. Therefore relative error in measurement of upwelling irradiation due to self-shading must be a function of aR , where R is the radius of instrument shading. This relative error will be called further self-shading ratio as it represents the ratio of upwelling photons blocked by instrument shading to the number of upwelling irradiance photons in the absence of the instrument. Figure 1 shows dependence of self-shading ratio on product aR for photon survival probability $\omega=0.8$. For reasonable values of aR the relationship is almost linear. Moreover, as Figure 2 shows self-shading has almost no dependence on scattering for constant a . This result, consistent with Gordon and Ding², means that self-shading ratio practically does not depend on ω .

The results presented so far have been calculated for a flat-surfaced sea. One of aims of this paper was to investigate how the effect of self-shading changes in presence of waves on the surface. Fig. 4 shows its dependence on the degree of surface roughness (defined in used Cox-Munk model of sea-surface by wind velocity v) for various solar zenith angles. The angle of simulated wind direction to solar azimuth was $\vartheta=45^\circ$. Because, as mentioned above, Cox-Munk distribution gives no information on actual height of surface elements, instrument depth was chosen at $d=2\text{m}$, just under the zone of actual waves. Calculated self-shading decreased for greater solar zenith angles θ (sun closer to horizon). This is caused by better direct illumination of volume just under the instrument when sunlight is more slanted. However, the effect of surface waves turned out to be rather subtle. Self-shading error in upwelling irradiance decreases a little with growing sea-surface roughness for greater solar zenith angles. For low zenith angles there is almost no dependence on wind speed.

The effect of different directions of wind generating ocean waves on self-shading was also studied. Fig. 5 shows results for several wind directions relative to solar azimuth ϑ and two values of aR product. There is a noticeable dependence of self-shading on the wind azimuth. However the values for different azimuths do not differ more than one standard deviation for 4 million photons used. The linear regression line for the calculated values is

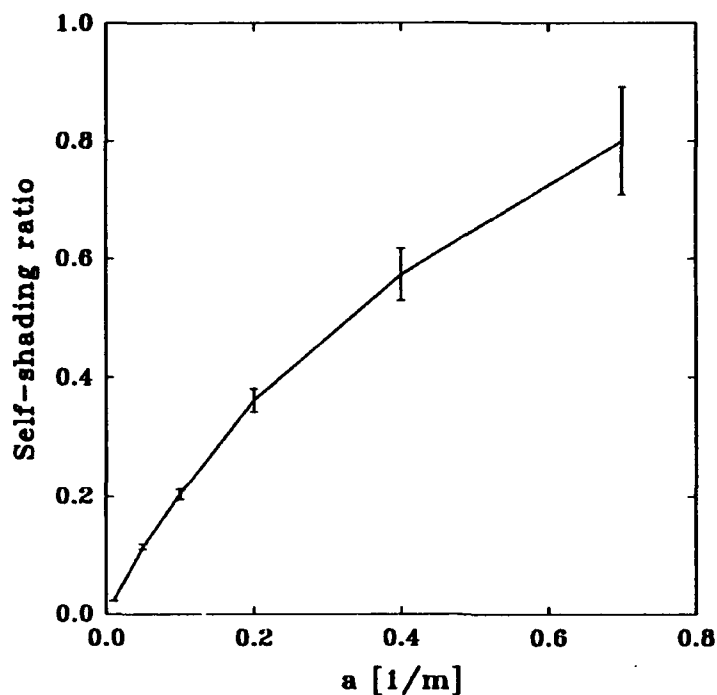


Fig 3. Dependence of upwelling irradiance relative error on total scattering b ($d = 0$ m, $D = \infty$, $a = 0.025$ m⁻¹, $\theta = 40^\circ$, $v = 0$ m/s)

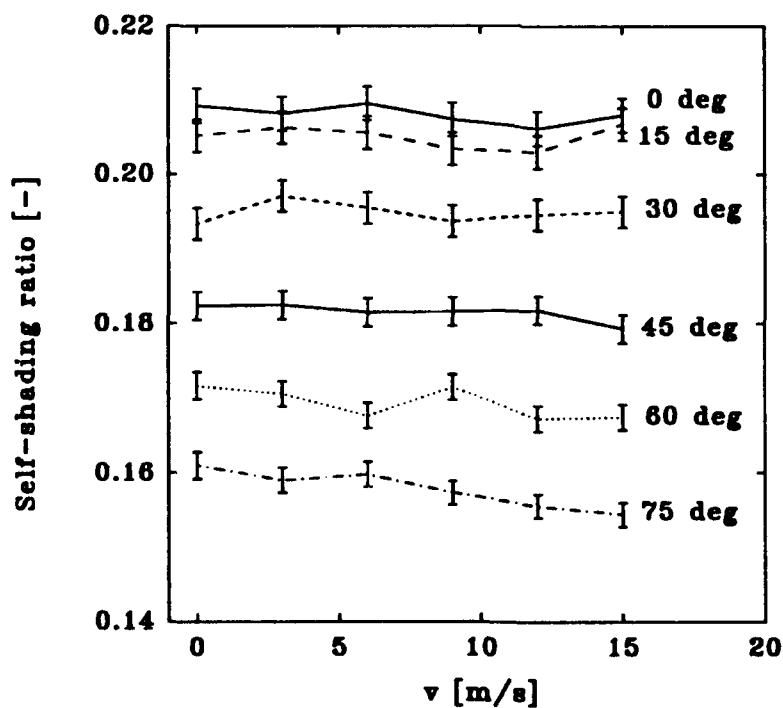


Fig 4. Dependence of upwelling irradiance relative error on solar zenith angle θ and wind velocity v ($d=2$ m, $D = \infty$, $aR=0.1$, $\omega=0.8$, $\vartheta=45^\circ$)

shown for comparison. Especially for $aR=0.1$ the values lie very close to the regression line.

Figure 6 shows the effect of bottom on self-shading ratio. The calculations were done for the instrument hanged $d=20$ m under sea surface; distance to bottom was varied by changing bottom depth (D - depth of the bottom). As expected, close to the bottom almost all upwelling photons must have passed through the instrument on their way down. This leads to very high values of upwelling irradiance error close to the bottom. However a few meters above bottom this ratio decreases even under its value for bottomless sea. This could be caused by greater fraction of highly slanted photon paths for photons diffused on bottom than in unperturbed light field in water.

The effect of bottom albedo A_b on self-shading for an instrument close to the bottom was studied. Calculations were done for an instrument floating 1 m over the bottom. Light returning from the bottom was 80% homogeneous diffusion, 20% geometric reflection ($\eta=0.2$) to simulate a forward-elongated angular reflection function. Figure 7 shows that the darker the bottom the bigger is the upwelling irradiance error. Surprisingly for albedos greater than 0.2 the bottom effect practically saturates. There is almost no further decrease in self-shading ratio for highly reflective bottoms. Influence of angular bottom reflection function on self-shading for upwelling irradiance was studied by varying the reflective fraction of albedo η . Figure 8 presents the results. The self-shading error depends linearly on this parameter. It means the less elongated is the angular reflection function (the more diffusive the bottom) the smaller becomes error introduced by self-shading.

4. CONCLUSIONS

The results of numerical Monte-Carlo simulations of the self-shading of in-water instruments measuring upwelling irradiance show that introducing rough sea-surface does not lead to changing the maximum instrument sizes estimated by Gordon and Ding². Surface roughness does lead to a small decrease in self-shading error but only for high solar zenith angles. Influence of direction of wave-inducing wind may be neglected.

Calculations show that at small height over sea bottom (comparable to instrument diameter) there is a significant increase in self-shading error for upwelling irradiance. However, instrument floating higher but still in the zone of bottom visibility experiences smaller values of self-shading error due to the change in light field that diffusive bottom introduces. This effect is particularly strong for ideally diffusive and whitish bottoms.

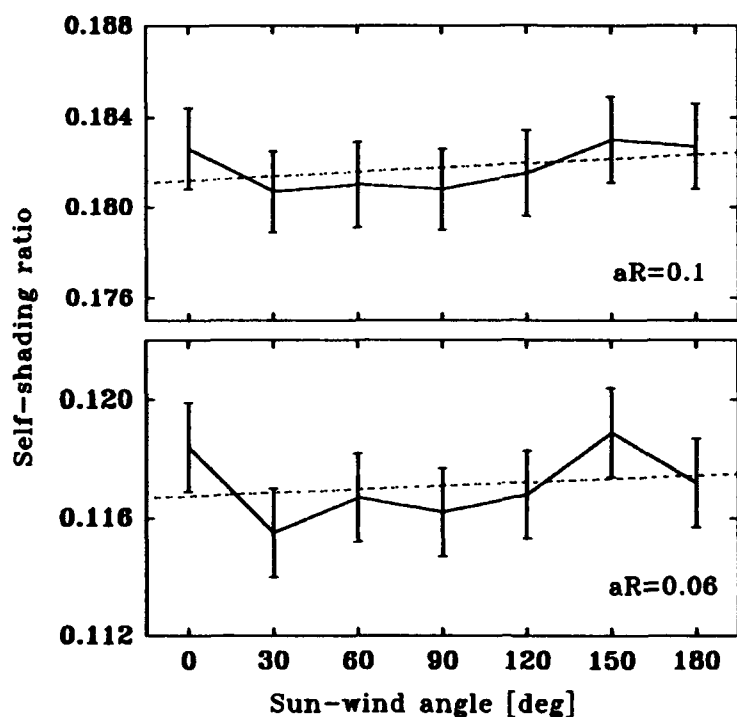


Fig 5. Dependence of upwelling irradiance relative error on sun-to-wind azimuth angle ϑ ($d = 2$ m, $D = \infty$, $aR = 0.1$, $\omega = 0.8$, $\theta = 45^\circ$, $v = 15$ m/s)

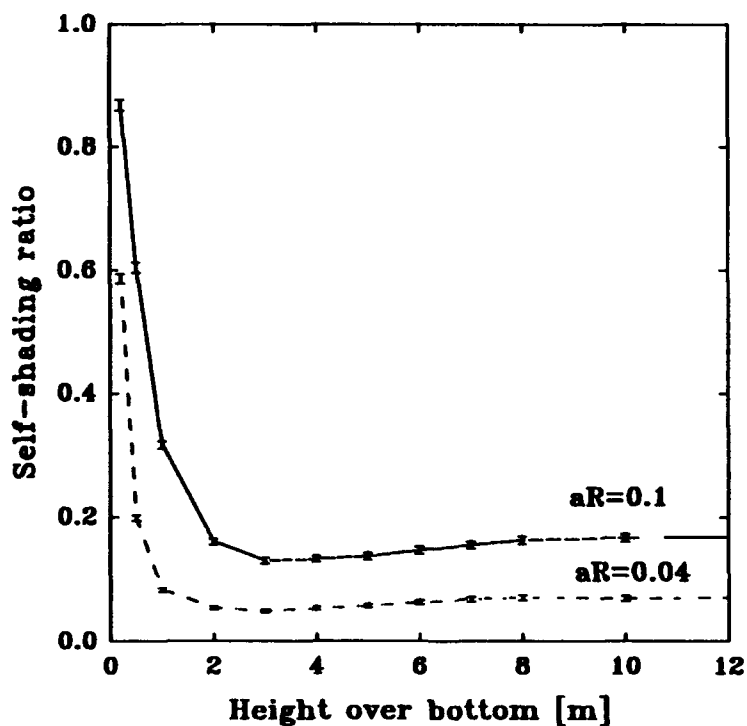


Fig 6. Dependence of upwelling irradiance relative error on height of instrument over bottom $D-d$ ($d = 20$ m, $A_b = 0.1$, $\eta = 0.2$, $a = 0.1$ m $^{-1}$, $\omega = 0.8$, $\theta = 45^\circ$, $v = 15$ m/s)

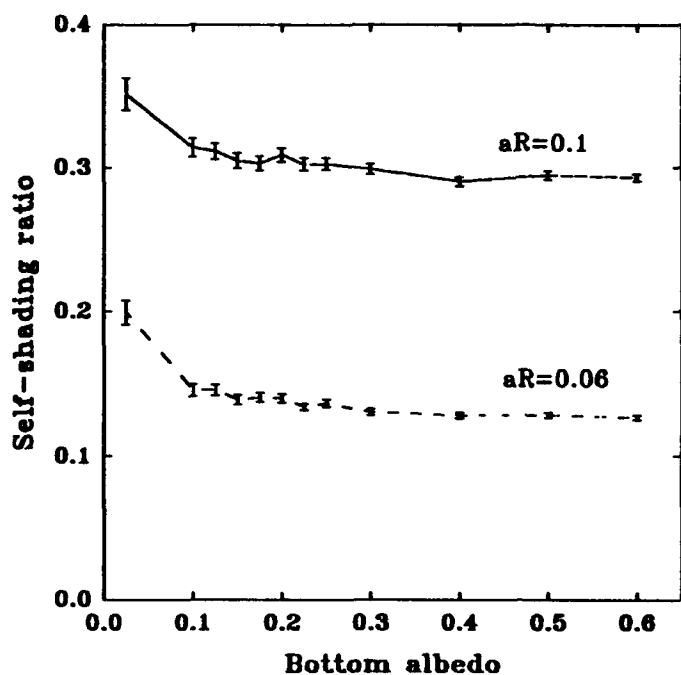


Fig 7. Dependence of upwelling irradiance relative error on bottom albedo A_b
 ($d=20\text{m}$, $D=21\text{m}$, $\eta=0.2$, $a=0.1\text{ m}^{-1}$, $\omega=0.8$, $\theta=45^\circ$, $v=15\text{ m/s}$)

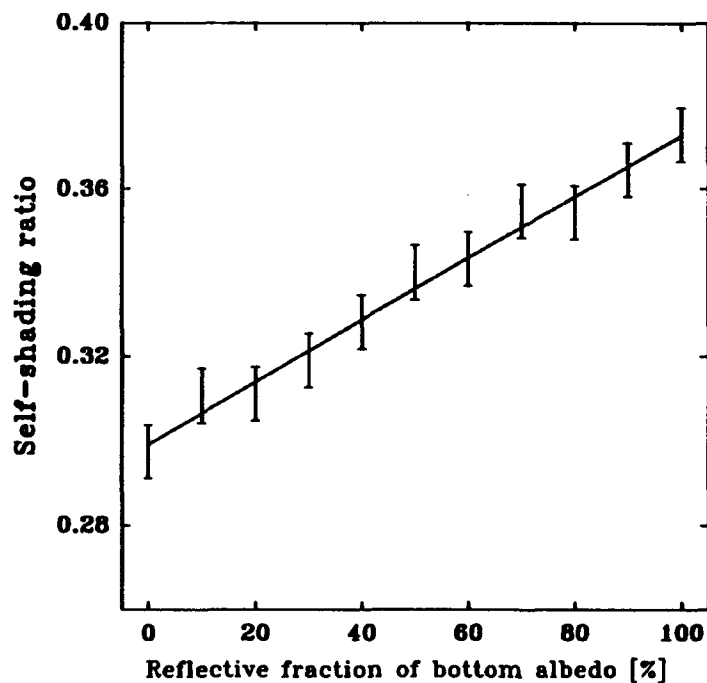


Fig 8. Dependence of upwelling irradiance relative error on reflective fraction of albedo η
 ($d=20\text{m}$, $D=21\text{m}$, $A_b=0.1$, $a=0.1\text{ m}^{-1}$, $\omega=0.8$, $\theta=45^\circ$, $v=15\text{ m/s}$)

5. ACKNOWLEDGMENTS

Author would like to express his appreciation to Dr. Roland Doerrfer of GKSS Forschungszentrum Geesthacht for some helpful suggestions during my DAAD stipendium in Germany that were genesis of this paper and consent for remotely using computing time on a Sun Sparc Server in his laboratory

6. REFERENCES

1. Cox C., Munk W.H., 1956: Slopes of the sea surface deduced from photographs of sun glitter, Scripps. Inst. Oceanogr. Bul. 6, 9.
2. Gordon H.R., Ding K., 1992: Self-shading of in-water optical instruments, Limnol. Oceanogr., 37, 3, p. 491.
3. Kattawar G.W., Plass G.N., 1972, "Radiative transfer in the Earth's atmosphere-ocean system: II. Radiance in atmosphere and ocean", J. Phys. Ocean, 2, 146-156.
4. Lenoble L. (ed.), 1985, "Radiative transfer in scattering and absorbing atmospheres: standard computational procedures", A. Deepak Publishing, Hampton, VA, USA

High resolution vertical profiles of spectral absorption, attenuation, and scattering coefficients in highly stratified waters

Collin S. Roesler and J. Ronald V. Zaneveld

College of Oceanic and Atmospheric Sciences, Oregon State University, Corvallis, Oregon 97331

ABSTRACT

Profiles of spectral attenuation and absorption were measured *in situ* with a WET Labs AC-9; scattering coefficients were calculated by difference. Closure of the absorption and scattering coefficients was obtained on this limited data set for *in situ* and discrete sample measurements. Centimeter-scale fine structures were observed in the vertical profiles. Total absorption coefficients were dominated by the phytoplankton component. Total attenuation coefficients were dominated by scattering although the effects of strong absorption were apparent in both the attenuation and scattering spectra. The vertical structure of absorption and scattering were not spatially coherent, nor were the vertical structures of phytoplankton and non-phytoplankton absorption. The strongest spatial coherence was observed between the non-phytoplanktonic component absorption and particle scattering coefficients. The spectral absorption coefficients of the *in situ* phytoplankton component exhibited decreasing blue to red absorption ratios as a function of depth and spectral flattening of the blue absorption peak indicative of photoadaptation. The results of this study indicate that centimeter-scale analyses of component inherent optical properties are possible with *in situ* optical instrumentation.

1. INTRODUCTION

The inherent optical properties (IOPs; absorption, scattering, and their sum, attenuation) determine the magnitude and spectral quality of light transmission through the water column and light emission from the ocean surface. Absorption of visible and infrared energy determines the transfer of heat in the upper ocean. Absorption of solar energy by phytoplankton drives photosynthesis and results in production of stored chemical energy. For these varied reasons, determination of the IOPs of components in natural waters is a primary goal for oceanographers of all disciplines.

Historically, absorption coefficients were determined spectrophotometrically on water samples collected at discrete depths. Attenuation coefficients were determined with single wavelength *in situ* transmissometers. Recent advances in optical technology have resulted in new *in situ* instrumentation to measure absorption and attenuation at discrete wavelengths^{1, 2, 3, 4}. The first order of investigation is to determine if instrument closure can be obtained by quantitatively comparing the IOPs measured *in situ* to those measured on discrete water samples. The second order of investigation is to determine if the IOPs can be separated into contributions by the various components in natural waters^{5, 6}. The purpose of this study was to verify closure of the IOPs and application of a component model in natural waters.

2. METHODS

Water samples and optical measurements were collected in East Sound, Orcas Island, Washington in May 1993. The euphotic zone was determined to be less than 12 m (S. McClain, pers. comm.). The water column was dominated by a large bloom of chain-forming diatoms (*Chaetoceros* spp.) with a range in chlorophyll a concentrations of 5 to 20 $\mu\text{g l}^{-1}$.

Profiles of absorption, a , and attenuation, C , coefficients were measured with a WET Labs AC-9² at wavelengths, $\lambda = 412, 456, 488, 532, 560, 650, 660, 676$, and 712 nm. Data were collected at 6 Hz and

bin averaged to account for flushing rate of the sample cells to arrive at independent sample measurements. Absorption and attenuation values were calibrated relative to pure water⁷. The *in situ* spectral absorption coefficients were partitioned into contributions by the phytoplankton and non-phytoplankton components, $a_p(\lambda)$ and $a_{np}(\lambda)$, respectively, using the model and coefficients of Roesler et al.⁶. The model was modified for the wavelength 456 nm instead of 436 nm by setting the maximal blue to red absorption peak ratio to 1.5 and scaling it to the pheopigment to chlorophyll ratio.

Water samples were collected at seven depths in the upper 12 m of the water column from a siphon system with intake immediately adjacent to the intake for the AC-9. a and c were monitored during water collection at each depth to determine the natural variations in optical properties. Samples were filtered on combusted glass fiber filters (Whatman GF/F) and then either extracted in 90% acetone for 48 hours in a freezer, and analyzed fluorometrically for chlorophyll and pheopigment concentrations or scanned spectrophotometrically for particulate absorption spectra⁸. Absorption spectra for gelbstoff were determined spectrophotometrically in 10 cm quartz cuvettes from the filtrate. Particle size distributions were measured over the diameter range 0.5 to 150 μm with a Galai CIS100 Particle Analyzer. This instrument determines particle diameters from the time of transit of a laser beam as it intersects the midsection of a particle (C. S. Roesler and M. E. Culver, unpub. data). The shape of the voltage trace during the interaction is used to reject off-center interactions.

3. RESULTS

3.1 Correction of the reflecting tube absorption meter

The absorption by particulate and dissolved material in the ocean is minimal in the red region of the spectrum. The absorption signal measured at 712 nm is therefore assumed to be due primarily to scattering and can be used to correct the entire spectrum for scattering⁹. Scattering errors in the reflecting tube absorption meter, $\epsilon_b(\lambda)$, were determined from the measured absorption signal at 712 nm scaled spectrally to the attenuation spectrum:

$$\epsilon_b(\lambda) = \epsilon_b(712) * \frac{b(\lambda)}{b(712)} \quad (1a)$$

where

$$b(\lambda) = c(\lambda) - a'(\lambda) \quad (1b)$$

$a'(\lambda)$ is the uncorrected absorption coefficient and

$$\epsilon_b(712) = a'(712) \quad (1c)$$

Corrected absorption coefficients were then determined by:

$$a(\lambda) = a'(\lambda) - \epsilon_b(\lambda) \quad (2)$$

The scattering error was of the same order as the absorption coefficient at 456 nm in these waters, and approximately 30% of the scattering coefficient.

3.2 Closure between *in situ* and discrete determinations of the inherent optical properties

Corrected absorption coefficients were calculated from static measurements made with the AC-9 during water collection. These coefficients exhibited a range in absorption of 0.05 to 0.4 [m^{-1}] over the approximately two minute time period of water collection at each depth (Fig. 1a). Total absorption

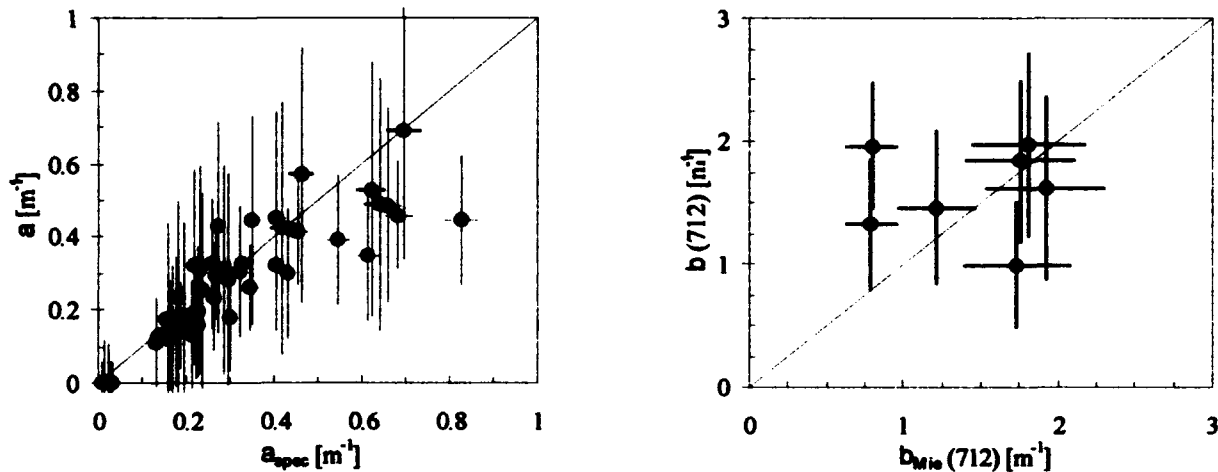


Fig. 1. (a) Absorption coefficients for all wavelength determined with the AC-9 at discrete depths, a , and determined spectrophotometrically, a_{spec} . a_{spec} is the sum of spectrophotometrically-determined absorption coefficients for the particulate and dissolved fractions of the water sample. The error bars associated with a indicate the ± 1 standard deviation of the natural variability in a observed at the depth of water collection during the time of collection. The error bars associated with a_{spec} are attributed to errors in the beta correction for particulate absorption spectra determined on a filter pad⁸. The line is the 1:1 although the regression fit slope and intercept are not significantly different from one and zero, respectively ($p < 0.001$).

(b) Scattering coefficients at 712 nm as determined by the AC-9, $b(712)$, and as estimated from Mie theory using measured particle size distributions, $b_{\text{Mie}}(712)$. $b(712) = \alpha(712)$ since $a(712)$ was set equal to zero. Error bars associated with b indicate the ± 1 standard deviation of the natural variability in b observed at the depth of water collection during the time of collection. The error bars associated with $b_{\text{Mie}}(712)$ are attributed to variability in the measurement of the particle size distribution function. The line is the 1:1. Regression analysis was not statistically significant.

coefficients (minus the water contribution) were calculated from the spectrophotometric measurements:

$$a_{\text{spec}}(\lambda) = a_p(\lambda) + a_g(\lambda) \quad (2)$$

where the subscript spec indicates a spectrophotometrically determined absorption coefficient, the subscripts p and g indicate measurements made on the particulate and gelbstoff fractions of discrete samples. Within this natural variation, the absorption coefficients determined from the AC-9 and spectrophotometer compared favorably (Fig. 1a). While there is the suggestion of a non-linear trend in the data, the slope obtained from linear regression is not significantly different from 1 ($p < 0.001$).

Scattering coefficients were determined from the AC-9 measurement of attenuation at 712 nm. These coefficients exhibited a range of 0.5 to 0.75 [m^{-1}] in natural variability. Scattering coefficients were calculated from Mie theory for homogeneous particles and measured particle size distributions in the absence of absorption at 712 nm^{10,11}.

$$b_{\text{Mie}}(712) = \sum_{i=1}^n N_i Q_{bi} \pi \frac{d_i^2}{4} \quad (3a)$$

The subscript Mie indicates the calculated scattering coefficient, N_i is the concentration of particles with diameter d_i and Q_{bi} is the scattering efficiency for individual particles given by:

$$Q_{bi} = 2 - \frac{4}{\rho} \sin \rho + \frac{4}{\rho^2} (1 - \cos \rho) \quad (3b)$$

where ρ is the size parameter of the particle relative to the wavelength of light ($\lambda = 712 \text{ nm}$),

$$\rho = \frac{4 \pi d_i}{\lambda} (n - 1) \quad (3c)$$

and n is the refractive index of the particles relative to water. Particle size distributions, measured from 0.5 to 150 μm were extrapolated to 0.01 μm using the \log_{10} slope calculated over the range 1 to 4 μm to better predict the population of scattering particles (Fig. 2). Values of n were scaled from 1.15 for small refractive particles of 0.01 μm diameter to 1.05 for larger less refractive particles of diameters $\geq 4 \mu\text{m}$ (Fig. 2).

Scattering coefficients determined from *in situ* measurements and calculated from Mie theory were found to covary within the range of natural variability observed in b and within the error of the b_{Mie} calculation (as determined by the standard deviation in N_i values) (Fig. 1b).

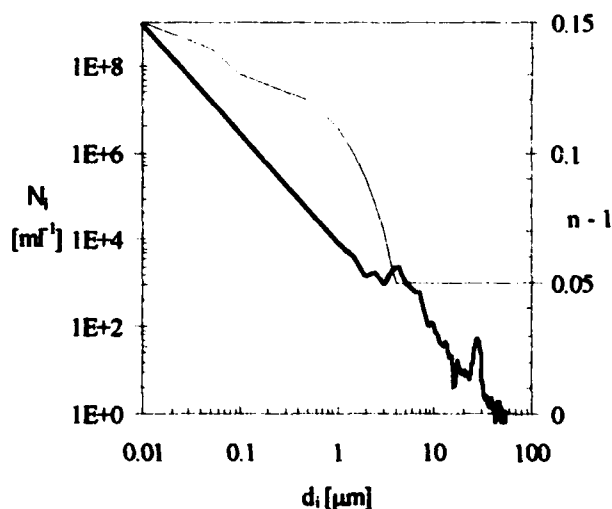


Fig. 2. Example of the measured particle size distribution function (bold solid line) and the relative index of refraction (light solid line) used in the Mie scattering model. The size distribution from 0.01 to 0.5 μm was extrapolated from the \log_{10} slope calculated from 0.5 to 4.0 μm .

3.3 Vertical distribution of the spectral inherent optical properties

Profiles of corrected absorption and scattering coefficients illustrate the large variability in the distribution of absorbing and scattering material in these waters. Autocorrelation of unsmoothed a profiles indicate the presence of features 2 to 5 centimeters thick with a range in absorption coefficient of 0.25 m^{-1} (Fig. 3). A 10-cm boxcar smoothing window was used for subsequent analysis.

The overall trend in a was different than that for b (Fig. 4a). a was maximal at approximately 5m while b was maximal at the surface. The subsurface maximum in a at 4.8 m was due almost exclusively to

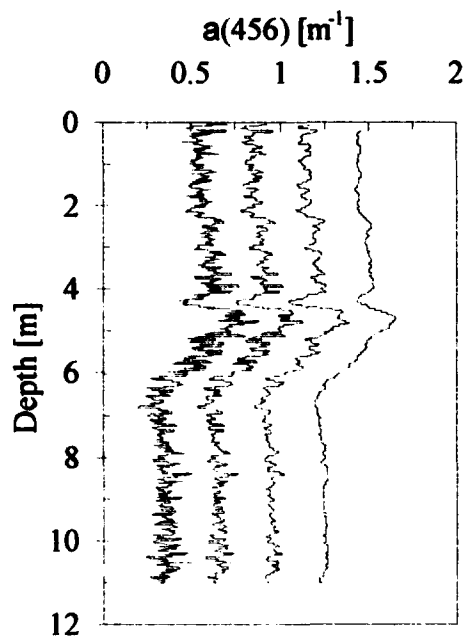


Fig. 3. Examples of the vertical profile of absorption measured with the AC-9 at 456 nm. The profile on the far left is the unsmoothed data corrected for scattering and for the residence time of fluid in the sample tube. The three offset profiles on the right are the same data smoothed with moving boxcar windows of 4 cm, 10 cm, and 40 cm, respectively.

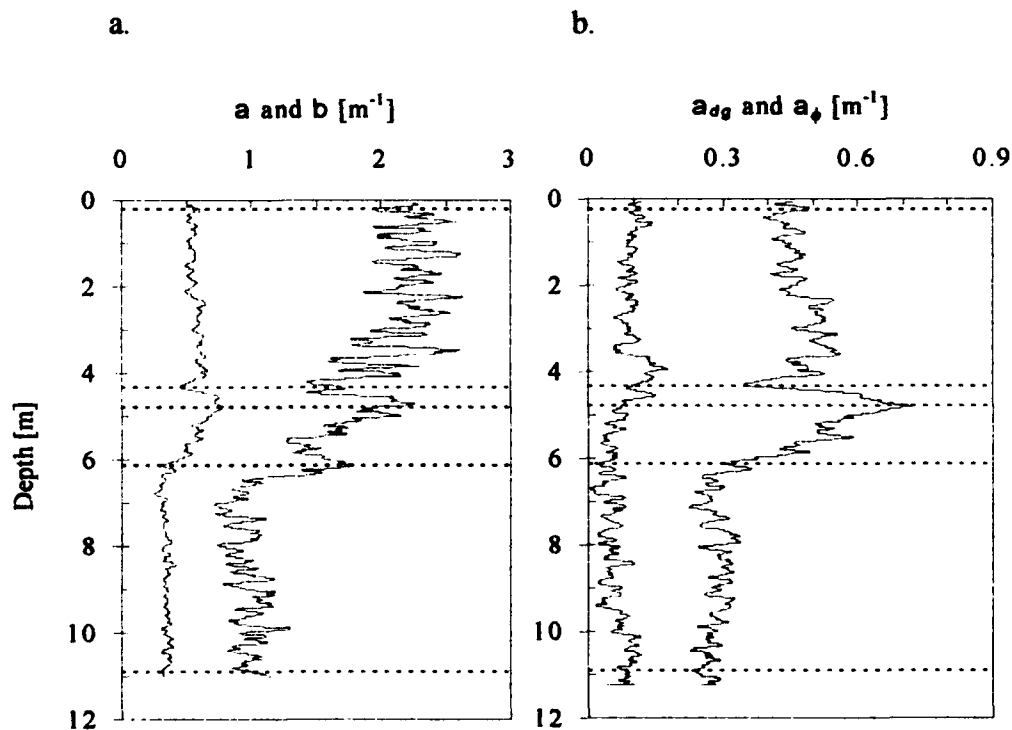


Fig. 4. (a) Absorption, a (left), and scattering, b (right), profiles measured with the AC-9 at 456 nm. Data are smoothed with a 10 cm moving boxcar window. Depths for absorption and scattering spectra are indicated by dashed lines. (b) Vertical profiles of absorption by the phytoplanktonic, a_p (right) and non-phytoplanktonic, a_{np} (left), particulate components as determined from the measured total absorption coefficient and the model of Roesler et al.⁶

the phytoplankton component (Fig. 4b). A slight enhancement of the non-phytoplankton absorbing component was observed just above the phytoplankton maximum at 4 m.

Five depths were selected in the profile to examine the differences in the spectral distribution of the IOPs. The selection criteria were used to highlight regions of spatial coherence and incoherence between a and b and also to examine the depth dependent changes in the absorption coefficient associated with phytoplankton. As expected from Fig. 4b, the *in situ* spectral absorption coefficients strongly resembled phytoplankton absorption coefficients (Fig. 5a). This is not surprising given the large concentrations of

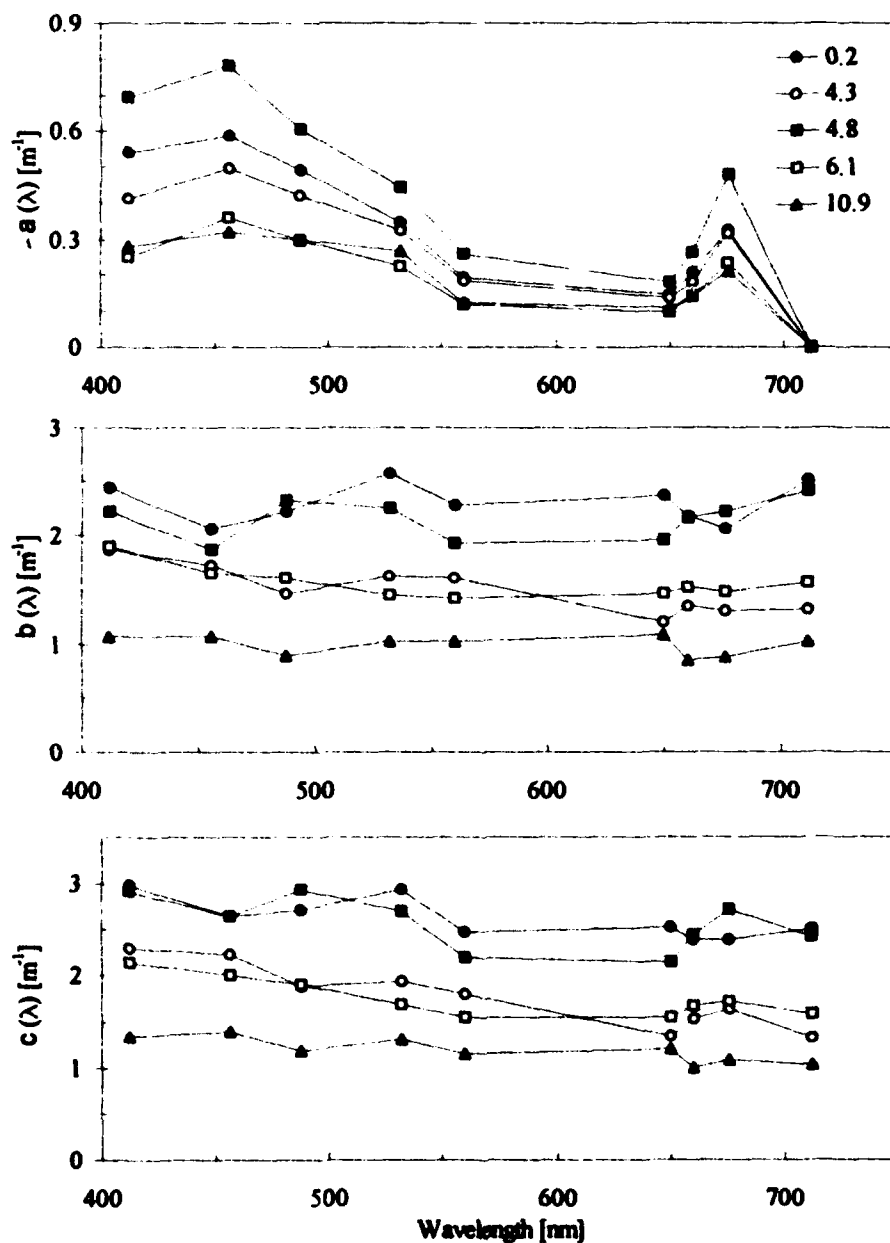


Fig. 5. Spectral (a) absorption, (b) scattering, and (c) attenuation coefficients measured with the AC-9 at the depths shown in Fig. 4.

phytoplankton in these waters. The spectral trend in c and b were approximately flat although there were features associated with the strong absorption coefficients (Fig. 4 b and c).

The large scale vertical distribution of a_p and a_{dg} were not visually coherent (Fig. 6a). Both components exhibited subsurface maxima but that of a_p was more than a meter deeper than the maxima in a_{dg} . On the scale of tens of cm the two components also appeared to be incoherent. The non-phytoplankton component is comprised of the non-planktonic particles and dissolved material. Since particles will contribute significantly to the scattering coefficients, it is expected that a_{dg} will be spatially coherent with b if a_{dg} is dominated by particle absorption. While the spatial coherence between a_{dg} and b is similar in the large scale, there are features in a_{dg} that are not observed in b, suggesting that there is significant structure in gelbstoff absorption or in the ratio of particle absorption to scattering (Fig. 6b).

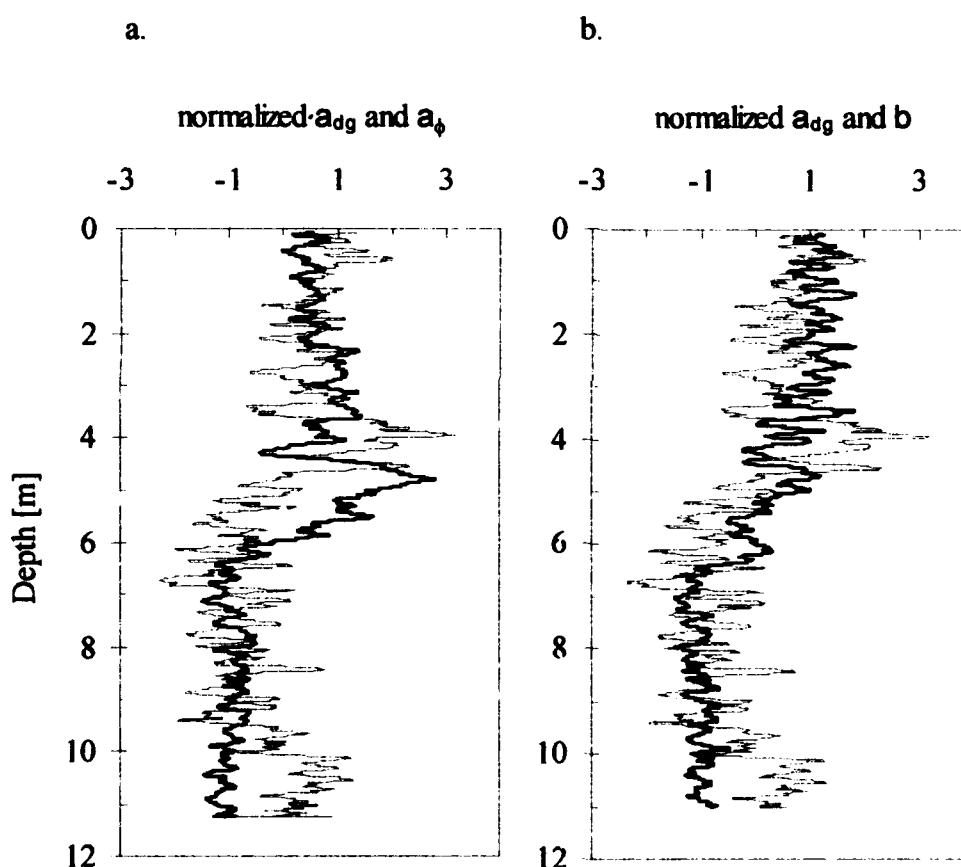


Fig. 6. (a) Normalized (differenced from mean and scaled to standard deviation) absorption coefficients at 456 nm for the phytoplanktonic (bold solid) and the non-phytoplanktonic (light solid) absorbing components. (b) As in part a for the non-phytoplanktonic absorbing component (light solid) and the scattering coefficient (bold solid).

The absorption spectra for the phytoplankton and non-phytoplankton components are shown in Fig. 7. The magnitude of the $a_{dg}(\lambda)$ coefficients are variable and estimated by the model while the spectral composition is a constant defined by the input parameter for spectral slope of the exponential (Fig. 7a). The shape of the estimated $a_p(\lambda)$ is variable throughout the water column (Fig. 7b). In particular, the ratio of

$a_p(456):a_p(532)$, indicative of the relative concentrations of chlorophyll *a* to accessory carotenoid pigments, varies with depth. Normalizing the spectra to the red chlorophyll *a* peak (676 nm) allows the effects of pigment composition and pigment packaging to be qualitatively assessed (Fig. 7c). There is a decrease in the blue to red absorption peak ratio of $a_p(\lambda)$ as well as the suggestion of flattening of the blue absorption peak that increases from the surface relative to 12 m.

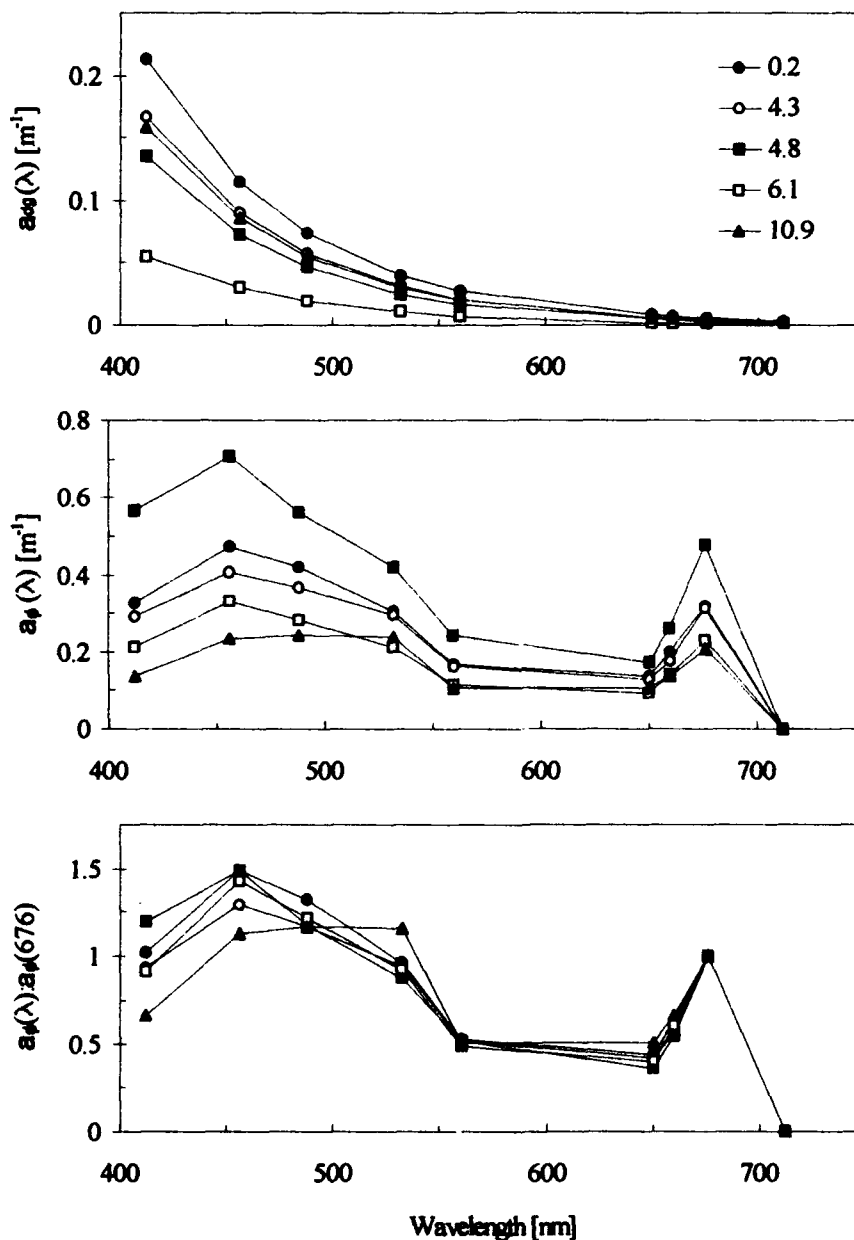


Fig. 7. Spectral absorption coefficients for the non-phytoplanktonic (a), and phytoplanktonic (b), components at the depths shown in Fig. 4. (c) Phytoplankton absorption spectra normalized to the chlorophyll *a* peak at 676 nm.

The single scattering albedo, ω_o , was calculated from the ratio of scattering to attenuation coefficients (Fig. 8a). The value of ω_o ranged from 0.7 to 0.8 with the largest variations occurring beneath the subsurface phytoplankton maximum. The smallest variability was observed in the upper 4 m, coincident with the mixed layer (P. Donaghay, pers. comm.). The mixed layer was also characterized by generally larger ω_o values of 0.8.

The ratio of a_{dg} to a_p also exhibited the largest variability below the mixed layer and below the subsurface phytoplankton maximum (Fig. 8b). Within the mixed layer the non-phytoplanktonic component of absorption decreased from the surface to the depth of the subsurface a_{dg} maximum at 4 m.

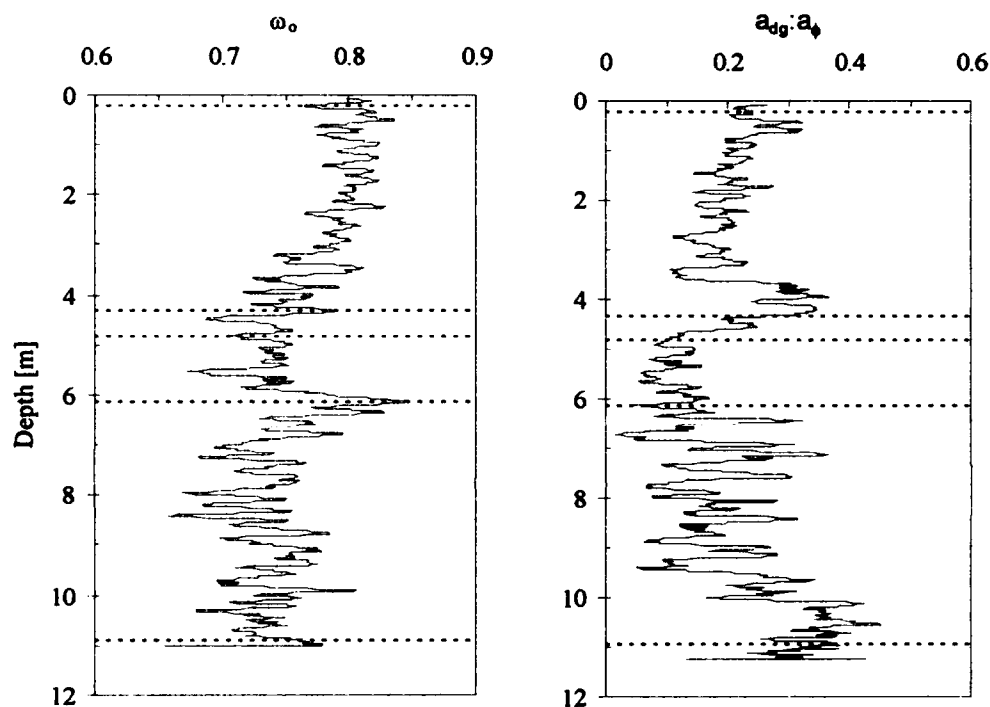


Fig. 8. Vertical distribution of (a) $\omega_o = b(456):c(456)$ and (b) $a_{dg}:a_p$ at 456 nm. Horizontal dashed lines as in Fig. 4.

4. CONCLUSIONS

The absorption coefficients determined *in situ* and in the spectrophotometer were in good agreement within the observed range of natural variability. The dominant absorbers were phytoplankton which appear to be very patchy in their horizontal distribution and lead to the factor of 4 variation in a . However, the relationship between a_{spec} and a suggests that there is closure between the two methodologies. This phenomenon is not always observed¹². Perhaps the difference can be accounted for by the improved design of the *in situ* instrument and in the improved spectrophotometric methodology⁸.

The absolute range in scattering coefficients was found to be only a factor of two throughout the water column and thus the relationship between measured and modeled scattering coefficients should not be considered proof of closure. However, that the two estimates of scattering are generally within the observed natural variability and the methodological error is very encouraging for future closure approaches. An

obvious next step in this analysis would be to determine to what degree changes in the scattering coefficient can be attributed to changes in the concentration of particulate material or to changes in the size distribution of particulate material¹³.

The scattering and attenuation coefficients were observed to be approximately flat across the spectrum as would be expected for the polydisperse particle population observed in these waters¹¹. However, at depths characterized by the largest absorption coefficients, features were observed in the b and c spectra. These were most likely due to anomalous dispersion and diffraction, a phenomenon which has been recently modeled for phytoplankton-dominated particle populations as was observed in this study¹⁴. These results indicate that the effects of strong absorption coefficients cannot be ignored in the modeling of spectral attenuation and scattering coefficients.

Bio-optical models very often assume that phytoplankton covary with other pigmented or suspended materials in order to estimate chlorophyll concentrations¹⁵ or IOPs¹⁶. While this covariance may be true to a first approximation, it has been shown that indicators of phytoplankton biomass such as absorption coefficients or chlorophyll concentration are not good predictors of IOPs in vertical profiles¹³ or over large geographic regions¹⁷. Results from this study indicate the lack of coherence between phytoplankton absorption and other absorbing components or between non-phytoplanktonic absorption and scattering occurs even over centimeter scales as a function of depth. This non-covariance may be reflecting variations in the concentrations of the components with depth or variations in the absorption and scattering efficiencies of the components with depth. Because the direct measurement of IOPs is now possible *in situ*, in particular spectral scattering coefficients, better models can be developed that do not assume covariance between the components.

The ability to separate the IOPs into contributions by functional groups increases the utility of the *in situ* instrumentation. Small scale features in the vertical profiles of the IOPs can be attributed to specific functional groups such as phytoplankton, non-phytoplanktonic particles, and dissolved material. Further, the spectral resolution of the *in situ* instruments is sufficient to observe changes in phytoplankton absorption spectra over very small spatial scales. Changes in pigment composition and pigment packaging, associated with photoadaptation, were observed over the euphotic zone in this study. In combination with high resolution fluorometric instrumentation¹⁸, these changes could be used in the future to investigate small-scale variations in the physiological status of phytoplankton populations in the ocean.

The values of ω_0 were consistent with those measured by Petzold¹⁹ for San Diego Harbor water, although the values of a and b observed in East Sound were a factor of two larger. Within the vertical profile of ω_0 is the suggestion of structure related to photoadaptation in the phytoplankton absorption coefficient. The general decrease in ω_0 with depth in the mixed layer in the presence of relatively invariant absorption coefficients demonstrates that the absorption efficiency per scatterer, in this case phytoplankton, increases with depth. This observation is consistent with the phytoplanktonic photoadaptive response of increased pigment absorption with depth.

The spatial scales of the small scale structures and the magnitude of the variability in the IOPs were found to be relatively constant throughout the water column, with the exception of the large subsurface maxima in a_p at 5 m and in a_{dg} at 4 m. This indicates that the fine structure in IOPs is independent of concentration of the components, and further that physical processes, as opposed to biological processes, are the likely sources of the observed variability. In the case of biological processes, such as local growth, the variability would be expected to scale as a function of the concentrations of the biological components. In order to improve the understanding of the biological and physical forces that lead to the development and maintenance of fine scale structures in the ocean, simultaneous measurements of physical, optical and biological parameters on highly resolved spatial scales is required²⁰.

5. ACKNOWLEDGMENTS

This research was supported by the Office of Naval Research Ocean Optics Program Grant No. N0014-93-10150. The authors wish to thank Casey Moore for use of the AC-9, Percy Donaghay for the water sampling siphon, Scott Pegau for field assistance and calibration of the AC-9, and Richard Davis for comments on the manuscript.

6. REFERENCES

1. J. R. V. Zaneveld, R. Bartz, and J. C. Kitchen, "A reflecting tube absorption meter," *SPIE Ocean Optics X*, 1302, 124-136, 1990.
2. C. C. Moore, J. R. V. Zaneveld, and J. C. Kitchen, "Preliminary results from and in-situ spectral absorption meter," *SPIE Ocean Optics XI*, 1750, 330-318, 1992.
3. J. R. V. Zaneveld, J. C. Kitchen, A. Bricaud, and C. C. Moore, "Analysis of in-situ spectral absorption meter data," *SPIE Ocean Optics XI*, 1750, 187-200, 1992.
4. A. Bricaud, C. S. Roesler, and J. R. V. Zaneveld, "In situ methods for measuring the inherent optical properties of ocean waters," in review *Limnol. Oceanogr.*, 1994.
5. L. Prieur and S. Sathyendranath, "An optical classification of coastal and oceanic waters based on the specific spectral absorption curves of phytoplankton pigments, dissolved organic matter, and other particulate materials," *Limnol. Oceanogr.* 26, 671-689, 1981.
6. C. S. Roesler, M. J. Perry, and K. L. Carder, "Modeling in situ phytoplankton absorption from total absorption spectra in productive inland waters," *Limnol. Oceanogr.* 34, 1510-1523, 1989.
7. C. C. Moore, J. R. V. Zaneveld, and J. C. Kitchen, "Characterization and calibration of a nine wavelength attenuation and absorption meter (ac-9)," *SPIE Ocean Optics XII*, this issue, 1994.
8. C. S. Roesler and M. J. Perry, "Minimizing errors in the determination of particulate absorption spectra, beta revisited," submitted to *Limnol. Oceanogr.*, 1994.
9. J. R. V. Zaneveld, J. C. Kitchen and C. C. Moore, "Correction of a reflecting tube absorption meter", *SPIE Ocean Optics XII*, this issue, 1994.
10. H. C. van de Hulst, Light scattering by small particles, Dover, New York, 1981.
11. A. Bricaud and A. Morel, "Light attenuation and scattering by phytoplanktonic cells: a theoretical modeling," *Appl. Opt.* 25, 571-580, 1986.
12. W. S. Pegau, J. S. Cleveland, W. Doss, C. D. Kennedy, R. A. Maffione, J. L. Mueller, R. Stone, C. C. Trees, A. D. Weidemann, W. H. Wells, J. R. V. Zaneveld, "A comparison of methods for the measurement of the absorption coefficient in natural waters, submitted to *J. Geophys. Res.*, 1994.
13. J. C. Kitchen and J. R. V. Zaneveld, "On the noncorrelation of the vertical structure of light scattering and chlorophyll a in case I waters," *J. Geophys. Res.* 94C, 20,236-20,245, 1990.
14. J. R. V. Zaneveld and J. C. Kitchen, "The effects of anomalous dispersion and diffraction on the inherent optical properties near an absorption peak as determined by various models of phytoplankton structure," submitted to *J. Geophys. Res.*, 1994.
15. H. R. Gordon and A. Morel, Remote assessment of ocean color for interpretation of satellite visible imagery. A review, Lecture Notes on Coastal and Estuarine Studies, Springer-Verlag, New York, 1983.
16. A. Morel, "Chlorophyll-specific scattering coefficient of phytoplankton. A simplified theoretical approach," *Deep-Sea Res.*, 34, 1093-1105, 1987.
17. C. S. Roesler and M. J. Perry, "A robust model for determining in situ phytoplankton absorption and fluorescence emission spectra from reflectance," submitted to *J. Geophys. Res.*, 1994.
18. T. J. Cowles, R. A. Desiderio, N. Potter, and C. C. Moore, "Steep gradients in phytoplankton biomass in Eastern Boundary Currents," *EOS*, 75, 141, 1994.
19. T. J. Petzold, "Volume scattering functions for selected ocean waters," SIO Ref. 72-78, 1972.
20. T. J. Cowles and R. A. Desiderio, "Resolution of biological microstructure through in situ fluorescence emission spectra," *Oceanography*, 6, 105-111, 1993.

SESSION 5

Coastal Waters II

Effects of Vertical Chlorophyll Structure and Solar Irradiance on Remote Sensing Ocean Color Spectrum

Robert A. Arnone

Naval Research Laboratory, Stennis Space Center, MS 39529
Telephone: 601 688-5268 Fax: 601 688-4149 e-mail: arnone@nrlssc.navy.mil

Richard W. Gould

Sverdrup Technology, Stennis Space Center, MS 39529

Ramon A. Oriol

Planning Systems Incorporated, Slidell, LA

Gregory Terrie

Naval Research Laboratory, Stennis Space Center, MS 39529

ABSTRACT

A model has been developed to investigate the influence of the subsurface chlorophyll profile on the complete spectral water-leaving radiance (ocean color) from 400 - 700 nm. The spectral reflectivity of vertical chlorophyll layers is modeled and coupled with the spectral incident irradiance at the sea surface. Model results indicate similar water-leaving radiance signatures can be obtained from different subsurface chlorophyll profiles. This model provides an interpretation of remote sensing ocean color signatures and possible subsurface structure.

The inherent optical properties of the backscatter and absorption coefficient which are determined from the vertical chlorophyll profile for Case I waters¹ are used to calculate the subsurface spectral reflectivity at layer depths. Subsurface reflectivity models are coupled with an atmospheric model² of the incident solar irradiance spectrum. The atmospheric irradiance model was run for different cloud cover and different optical depths (ozone, aerosol). The coupled model results compute the remote sensing color spectrum (upwelling radiance) at the sea surface. The study shows the effect of a varying chlorophyll maximum depth and intensity on the upwelling radiance distribution and the ocean color signatures.

1. INTRODUCTION

In the open ocean, where the optical properties are driven largely by absorption from chlorophyll concentration, the resulting ocean color spectrum at the sea surface is affected by the vertical profile of the chlorophyll structure. Previous investigations have shown that non-uniform profiles influence the blue - green upwelled radiance ratio at the sea surface^{3,4,5}. The blue - green ratio is used in remote sensing algorithms to estimate chlorophyll concentration. Ocean color imagery from the Coastal Zone Color Scanner for example has been used to determine the chlorophyll pigment concentration^{6,7}; results are based on the integrated chlorophyll concentration in the first attenuation depth⁸. The vertical chlorophyll profile can change significantly in the first attenuation length⁹. The chlorophyll maximum acts as a strong absorbing layer that occurs at different depths⁵ and significantly influences the ocean color spectrum especially when it is located within the first attenuation length^{9,10}. Gordon³ examined the effect of non-uniform chlorophyll profiles on the reflectivity at 440 and 550 nm. Gordon's improved bio-optical algorithms were modeled using Monte Carlo simulations in which he observed differences in surface reflectivity between the non-uniform chlorophyll and the depth averaged chlorophyll to be of the order of 20-25%.

Both the proximity of the layer to the surface and the intensity of the chlorophyll maximum layer affect the color spectrum sensed at the surface. Gordon and Clark⁸ speculated that an intense chlorophyll concentration occurring just under the surface can be estimated to have a similar blue green radiance response as a uniform chlorophyll profile of lower concentration such that the integrated chlorophyll is the same. However, we are not certain how the complete visible spectrum responds to the non-uniform chlorophyll profile.

Besides the spectral reflectivity within the water, the ocean color is influenced by the incident intensity and spectrum of the solar irradiance. This incident solar spectrum is reflected at different layers as it penetrates the water column and is scattered to the surface. The visible solar irradiance intensity and spectrum are influenced by the aerosol and ozone optical depths and the percentage of cloud cover ^{2,12}.

The objective of this paper is to determine the effect of the chlorophyll profile on the color spectrum. A two flow layer reflectance model based on non-uniform chlorophyll profile and varying solar irradiance will be used to show the resulting remote sensing reflectance and upwelling radiance from 400 - 700 nanometers at 5 nm intervals. The effort is aimed at determining whether unique solutions to the non-uniform chlorophyll structure and solar irradiance can be extracted from the ocean color spectrum. The results are intended to locate additional visible regions that can be used to define the vertical chlorophyll structure. These results will provide improved interpretation of ocean color spectra that can originate from subsurface structure and will enhance our understanding of satellite ocean color imagery.

2. MODELS

The formulation of the vertical chlorophyll model is based on discrete chlorophyll concentrations within distinct layers. For each layer the spectral irradiance reflectance R_λ , defined as the ratio of upwelling to downwelling irradiance, is computed. We have taken the reflectance relationship:

$$R_\lambda = 0.33 b_\lambda / a_\lambda \quad 1$$

for Case I waters with small absorption, a_λ , compared to the backscattering, b_λ , ¹³. Following the work of Morel ¹, where $a = \mu K_d$, the layer reflectance can be computed as:

$$R_\lambda = (0.33 / \mu) (b_\lambda / K_d) \quad 2$$

where the mean cosine, μ is computed by iteration ¹. Using this relationship, Morel, showed that b_λ and K_d can be empirically related to the chlorophyll concentration, Chl, by:

$$b_\lambda = 0.5 bw_\lambda + 0.3 * [Chl^{0.62} [0.002 + 0.021 (5 - .25 \log Chl) * (550/\lambda)]] \quad 3$$

and

$$K_d = Kw_\lambda + X_{c\lambda} Chl^{\epsilon_\lambda} \quad 4$$

(see Morel¹ for symbols)

From these equations the R_λ can be computed for each layer in a chlorophyll profile in addition to the inherent and apparent optical properties.

To model the upwelling radiance (ocean color, Lu_λ), the R_λ is coupled to the solar irradiance at the sea surface, $Ed_{\lambda 0}$ and penetrated to depth, z by:

$$Lu_{\lambda z} = \{R_{\lambda z} * Ed_{\lambda z} / Q\} + \{Lu_{\lambda(z-1)} \exp^{-K_d z}\} \quad 5$$

In this study Q ¹², which is the ratio of the downwelling radiance to upwelling radiance, is assumed to be π , although it is recognized that this parameter changes with both wavelength and depth. Further investigations are required to improve this estimate.

The remote sensing reflectance, $R_{rs\lambda}$ is computed as the summed upwelling radiance reaching the surface (eq. 5) divided by the downwelling irradiance:

$$R_{rs\lambda} = Lu_{\lambda 0} / Ed_{\lambda 0} \quad 6$$

The total $R_{rs\lambda}$ computed in this way is very much dependent on the vertical resolution of the chlorophyll profile increments. We use a layer increment of 5 m in this model to approximate *in situ* measurements.

The solar spectral irradiance at the sea surface, $Ed_{\lambda 0}$, is approximated using a modified model originally developed by Bird^{2,12}. Bird's model has been modified to include cloud cover estimates and aerosol optical thickness

from CZCS La_{870} data. The model utilizes coincident monthly climatological databases as inputs for percent cloud cover, aerosol concentration and ozone concentration to compute the solar spectrum. For a specific time, latitude and longitude, the direct clear sky irradiance (i.e. the solar contribution) as given by Bird²:

$$Ed_{\lambda 0} = \cos(Z) H_{0\lambda} T_{r\lambda} T_{a\lambda} T_{o\lambda} T_{w\lambda} T_{u\lambda},$$

7

where H_0 is the extraterrestrial spectral irradiance, T_r , T_a , T_o , T_w , and T_u , are the transmittance functions for Rayleigh scattering, aerosol extinction, ozone absorption, water vapor absorption, and uniformly mixed gas absorption, respectively. Next, the diffuse irradiance term is computed as a function of the percent cloud cover. The total irradiance at the sea surface is the sum of the direct and the diffuse components.

A schematic of the model showing the interaction of the chlorophyll profile, layer reflectance, solar irradiance and the upwelling radiance is presented in figure 1.

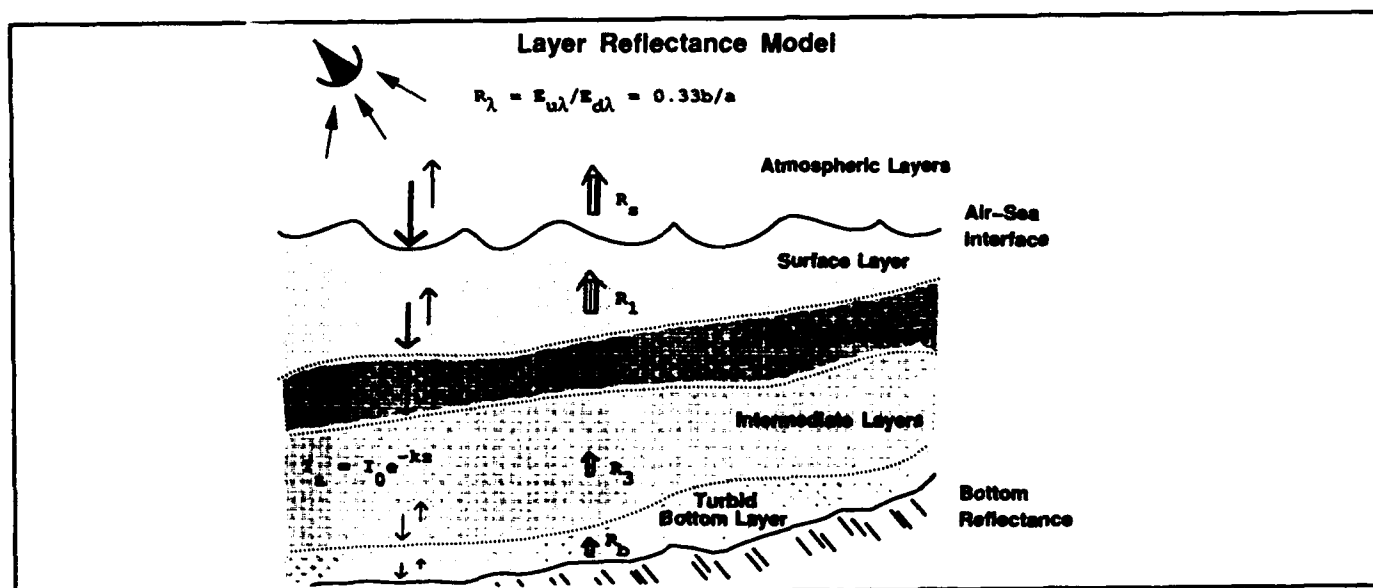


Figure 1 - Model interaction of non-uniform layer reflectance with solar irradiance and upwelling radiance.

The depth-weighted chlorophyll concentration $\{Chl\}$ to a depth of one attenuation length (z_{90} , penetration depth), for a non-uniform profile as computed by Gordon and Clark³:

$$\{Chl\} = \frac{\int_0^{z_{90}} C_z f_z dz}{\int_0^{z_{90}} f_z dz}$$

8

where:

$$f_z = \exp \left[- \int_0^z 2K_{(\lambda, z')} dz' \right]$$

9

Here the depth integrated chlorophyll of the non-uniform profile is assumed equal to the depth integrated chlorophyll of a uniform profile. The upwelling radiance, Lu_1 at the surface has been used to estimate the satellite weighted chlorophyll concentration $[Chl]$ using ratios of 3 blue green channels⁴:

$$[Chl] = 1.12979 * \{Lu443/Lu550\}^{-1.71} \quad \text{for } chl < 1.5 \text{ mg/m}^3$$

10

and

$$[Chl] = 3.32659 * \{Lu520/Lu550\}^{-2.44} \quad \text{for } chl > 1.5 \text{ mg/m}^3$$

11

The [Chl] computed from the model's upwelling radiance (eq. 5) is compared with the depth-integrated [Chl] to compute the error. This error can be attributed to inaccuracies in the coefficients of equation 10 and 11 and inconsistencies of these coefficients with Morel's equation 4 since these relationships were empirically determined from different data sets.

3. RESULTS

The following results used the solar irradiance spectra shown in figure 2¹². The parameters used to compute the 3 atmospheric types are shown in the table below. The three atmospheric types used represent average conditions in the Western Mediterranean (I), cloud dominated in the North Atlantic (II) and elevated aerosols off the African (III). All solar irradiance spectra were generated at 1300 hours for mid January 1979. The differences in intensity and spectral response are assumed to be largely the response of the clouds cover and the aerosol concentration. Note the irradiance spectrum corresponding to high cloud coverage, is lower and has a more diffuse spectral response than the other two spectra. As has been shown¹², the aerosol concentration has a stronger influence in the shorter than in the longer wavelengths.

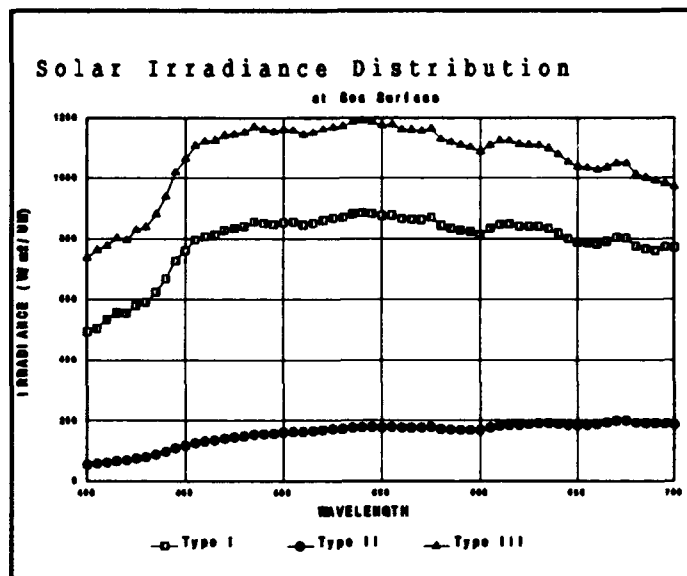


Figure 2- Solar irradiance at the sea surface for different atmospheres.

Table 1. - Parameters Used for Solar Irradiance Atmospheres

Atmosphere Type	Hour	Angstrom Coefficient	Aerosol - La670 ($\mu\text{W}/\text{cm}^2/\text{nm}$)	Ozone Dobsons	Cloud %
I - W. Med.	1300	0.0	0.61	304	41
II - N. Atlantic	1300	0.0	0.19	341	76
III - African Coast	1300	0.0	1.26	316	36

First using atmosphere type I, we examined the spectral R_{up} and upwelling radiance for *uniform* chlorophyll profiles (5 m layers) ranging from 0.03 to 5 mg/m^3 (figure 3 and 4). The hinge point at $\sim 520\text{nm}$ is clearly shown at low concentrations ($< 1 \text{ mg}/\text{m}^3$) with a spectral shift to $\sim 560\text{nm}$ at higher concentrations (5 mg/m^3). The shape of the upwelling radiance (figure 4) at the sea surface is similar to the reflectance spectra (figure 3) above 460 nm, but is different in the blue spectrum. The peak of the upwelling radiance (figure 4) shifts from 450 nm to 490 nm with increasing chlorophyll concentrations ($< 1 \text{ mg}/\text{m}^3$). The noticeable decrease from the peak to the shorter wavelengths (450 to 400 nm) is attributed to the rapid decline in solar irradiance intensity.

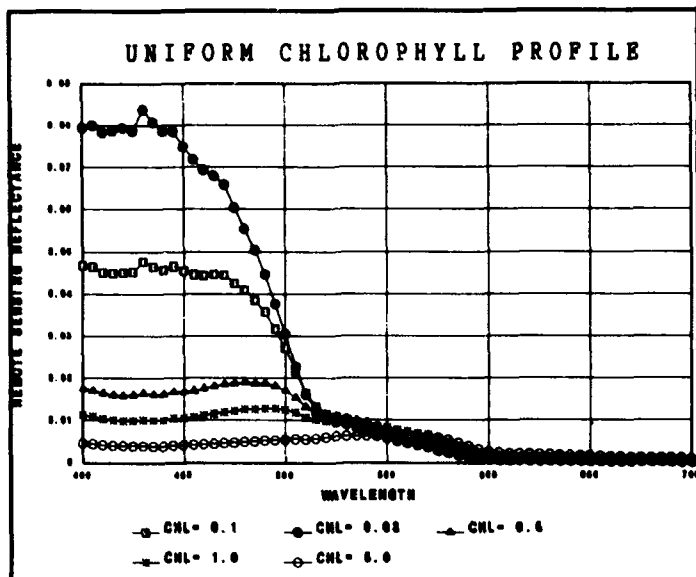


Figure 3 - Remote sensing reflectance, R_{rs} for uniform chlorophyll profiles of varying concentration.

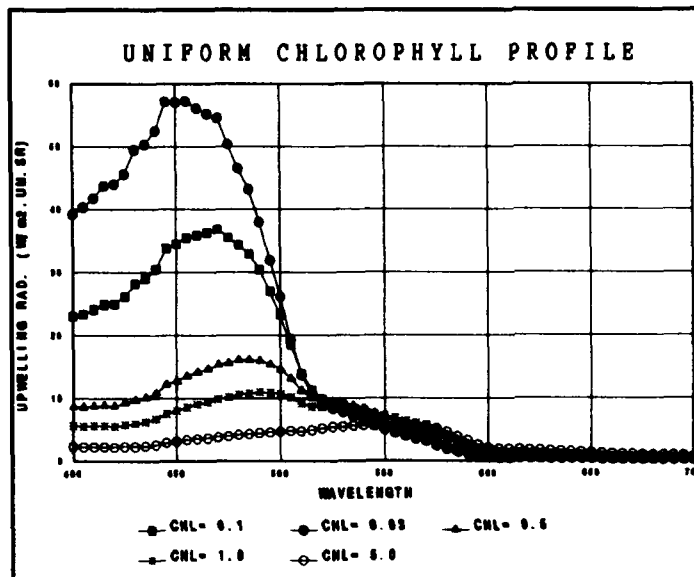


Figure 4 - Upwelling radiance for uniform chlorophyll profiles of varying concentration.

A non-uniform chlorophyll profile was selected from a data set in the Oran/Almeria front in the Western Mediterranean in Oct, 1986 having a maximum concentration (chl_{max}) of 1.3 mg/m^3 at 25 m (figure 5). The layer reflectance (figure 6) shows the hinge point at 520 nm. The chl_{max} at 25 meters has the "darkest" reflectance of all the layers at wavelengths less than 520 nm and the brightest reflectance at wavelengths greater than 520 nm. The downwelling and upwelling radiance at each depth layer are shown in figures 7 and 8. Comparison of the depth-weighted chlorophyll concentration of 0.361 mg/m^3 from the profile to the chlorophyll concentration computed from the blue green ratio (0.275) indicates an error of 23.9 %.

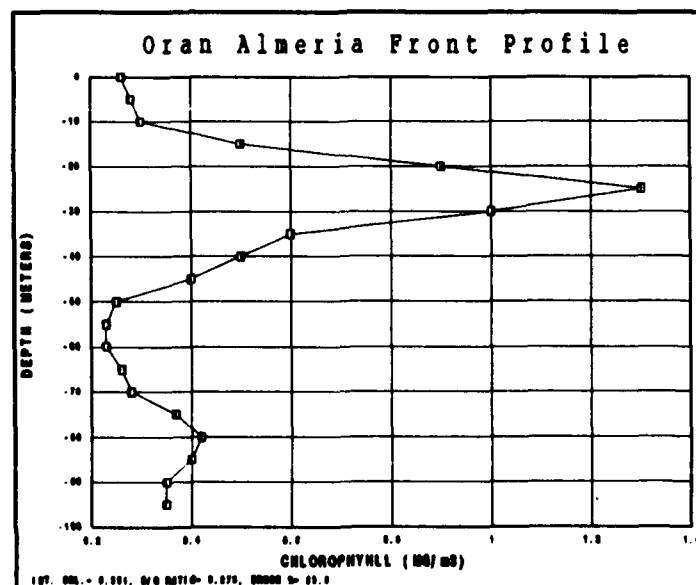


Figure 5 - Chlorophyll profile at the Oran/Almeria Front, Western Mediterranean. Penetration depth at 490 nm is 17 m.

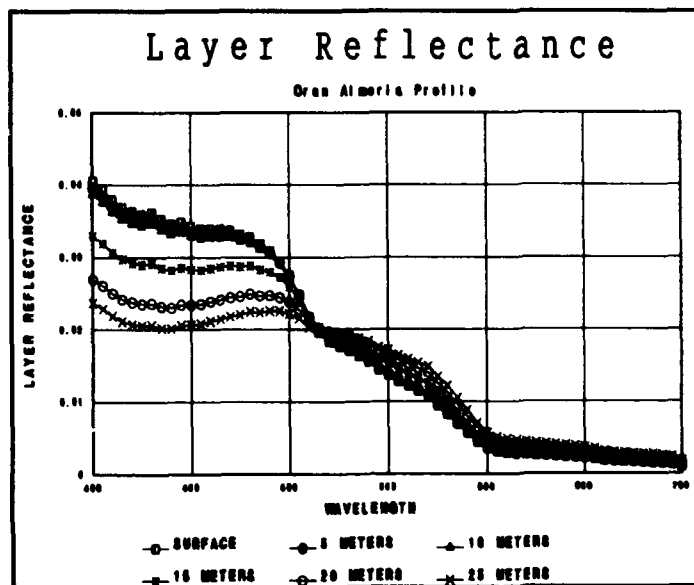


Figure 6 - Layer reflectance for O/A profile.

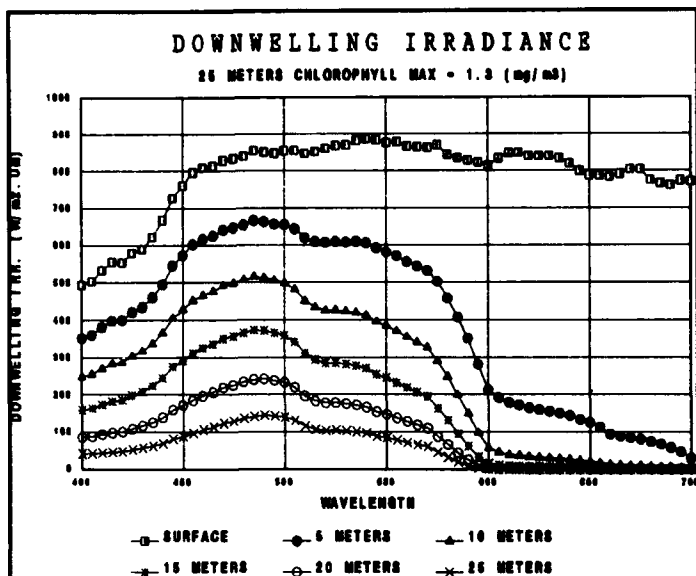


Figure 7 - Downwelling irradiance for O/A profile.

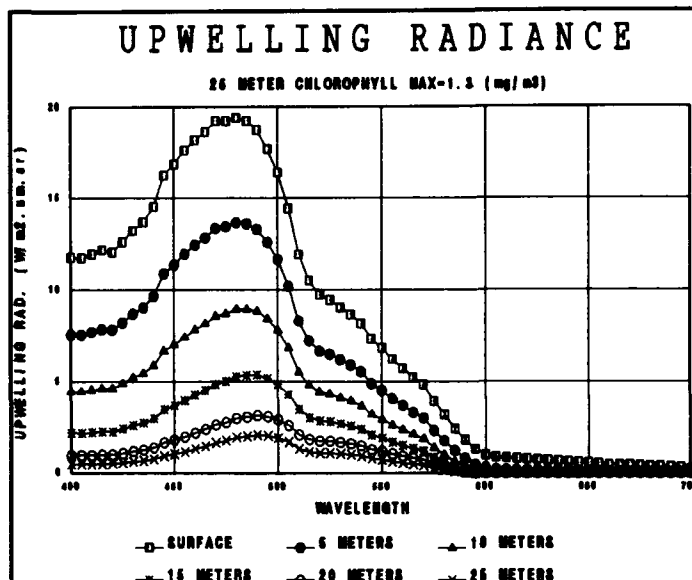


Figure 8 - Upwelling radiance for O/A profile.

The influence that the depth of the chl_{max} has on the color spectrum is shown through a sequence of model runs where this layer is migrated from 20 m to the surface at 5 meter increments (figure 9). Note that the intensity of the chl_{max} is fixed at 1.3 mg/m^3 and that the depth-weighted chlorophyll, {CHL} changes for each profile from 0.452 mg/m^3 @ 20 m to 0.677, 0.965, 1.092 to 0.782 at the surface. The resulting surface upwelling radiances (figure 10) shows that at 15 m, the "dark" chlorophyll layer is not strongly affecting the surface ocean color and highest upwelling radiances are observed. As the chl_{max} is shifted up to 15 and 10 meters, a corresponding decrease in the upwelling radiance is observed. (Note also the spectral peak of the radiance increases to longer wavelengths and a hinge point occurs at 540 nm.) This decrease in upwelling radiance is proportional to the increase in depth-weighted chlorophyll. As the chl_{max} reaches the surface, an increase in the radiance occurs. Here, the surface radiance intensities at 490 nm (the crest of the spectra) are equal to the radiance intensities when the chl_{max} is at 10. However, differences do occur in the spectrum both in the blue and red. Note that the radiance increase is directly proportional to the decrease in {CHL} (0.782) observed when the chl_{max} reaches the surface.

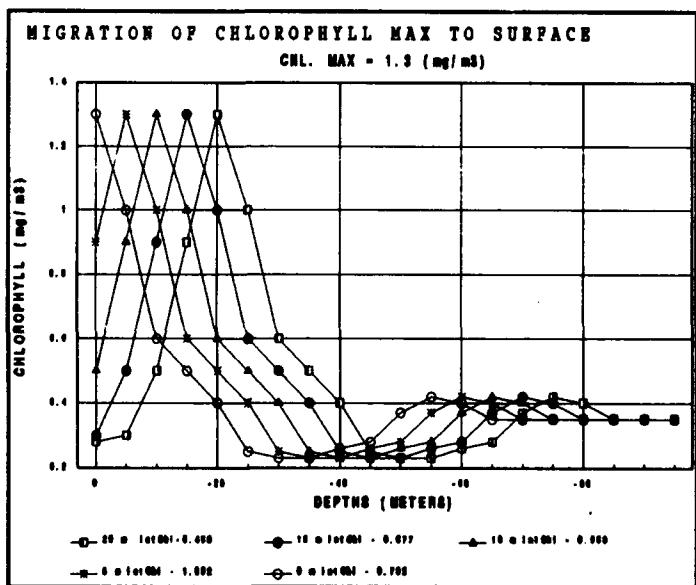


Figure 9 - Sequential vertical chlorophyll profiles, migrating the Chl_{max} to surface.

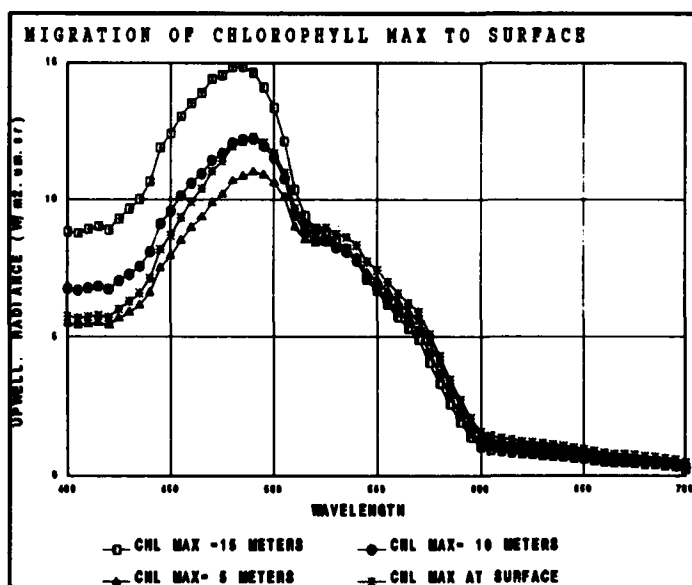


Figure 10 - Surface upwelling radiance for sequential Chl_{max} depths.

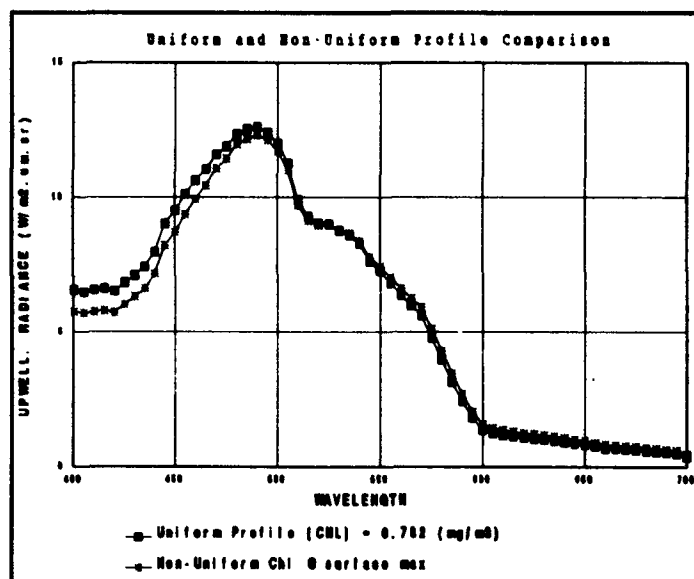


Figure 11 - Uniform and non-uniform profile for surface chlorophyll maximum.

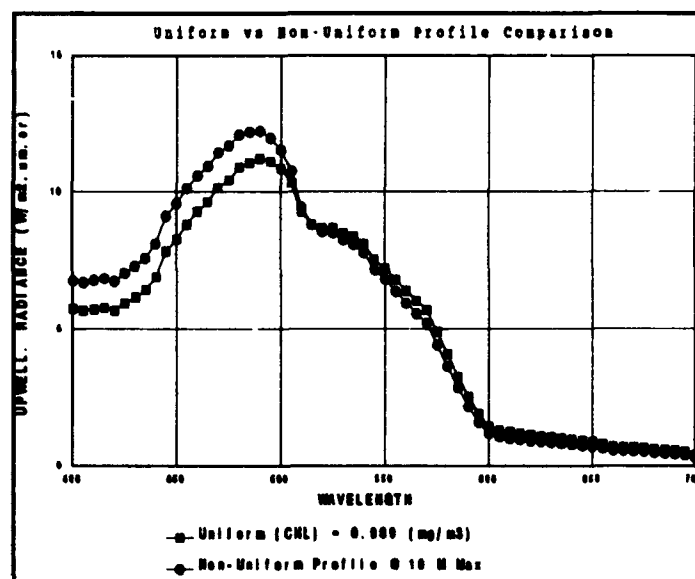


Figure 12 - Uniform and non-uniform chlorophyll profiles (Chl_{max} at 10 m).

The shape of the upwelling radiance was compared between the non-uniform profile and a uniform profile. According to equation 8^a, a uniform profile with a depth-weighted chlorophyll concentration {CHL} equal to a depth-weighted chlorophyll concentration from a non-uniform profile should have a similar water-leaving radiance spectrum. The profile with a surface chlorophyll maximum of 1.3 mg/m³ and decreasing with depth was used in determining the surface upwelling radiance in figure 11. The depth-weighted chlorophyll concentration of 0.783 mg/m³ from this profile was used to derive the upwelling radiance spectrum for a uniform profile with the same chlorophyll concentration. Figure 11 shows differences in the two spectra, with the upwelling radiance from the uniform profile being generally greater for wavelengths shorter than 520 nm. Notice that at 550 and 443 nm the radiance values are similar and form the basis for using the blue green ratio to estimate [CHL]. In this profile the uniform spectrum exceeded the non-uniform spectrum in the shorter wavelengths.

Additional profiles for a chl_{max} of 1.3 mg/m³ at 10 m were used to determine the depth weighted chlorophyll {CHL} of 0.969. The upwelling radiance from a uniform chlorophyll at this concentration are shown in figure 12. Here the uniform profile underestimates the radiance spectrum in the shorter wavelengths (<520 nm). The peak of the two spectra, at ~490nm shows a 20% difference. The spectra are linked at the hinge point at 520, but clearly differences in the spectra will always occur. These spectral differences are associated with the differences between the uniform and non-uniform structure. Ratios of the spectra will reduce the error especially if they bracket the hinge point of 520 nm. Thus the 443 to 550 nm ratio is a reasonable choice for estimating the approximate chlorophyll spectrum.

The effect of the intensity of the chl_{max} on the upwelling radiance spectrum is shown by varying the concentration of a fixed profile (figure 13). Concentrations from a profile with a 10 m chl_{max} (figure 9) were multiplied by 1, 0.75, 0.5 and 0.25 corresponding to chl_{max} concentration to 1.3, 0.98, 0.65 and 0.33 mg/m³. The strong decrease in the upwelling radiance corresponds to an increase in chl_{max} intensity (figure 13). For these spectra, the peak radiance shifts slightly from 470 to 485 nm; however, note that the spectra remain constant at wavelengths greater than 530 nm.

The influence of the atmospheric type, I, II, and III on the upwelling radiance is shown for a non-uniform profile with a chlorophyll layer of 1.3 mg/m³ at 10 m (figure 14). The solar irradiance intensity is clearly observed in the upwelling radiance. Notice that more diffuse solar irradiance (atm. type II) has a comparable diffuse upwelling radiance response. The changes in the spectral response between 440 to 480 in type I and II are observed in the shape of the upwelling radiance.

The results of the model runs used in this paper are presented in Table 2.

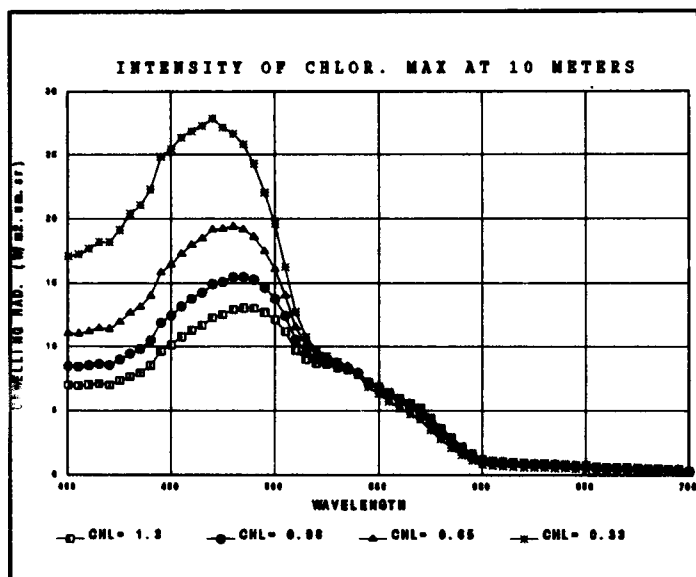


Figure 13 - Upwelling radiance from changing intensity of the Chl_{max} .

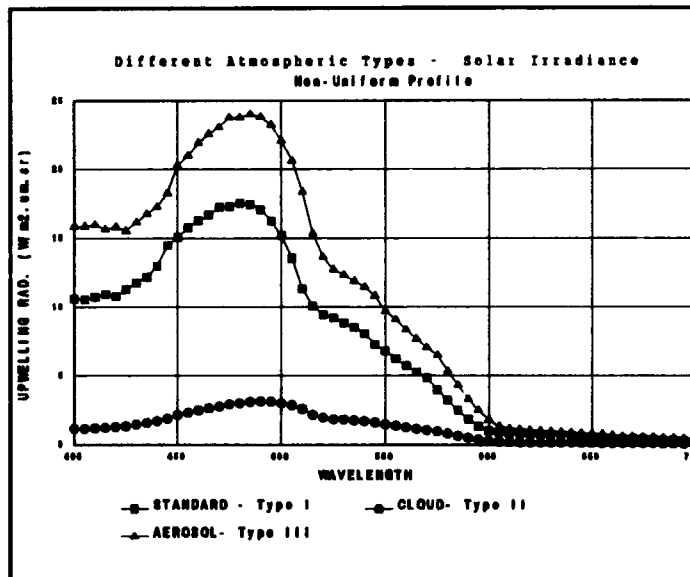


Figure 14 - Upwelling radiance from changing atmospheric solar irradiance type.

4. CONCLUSIONS

A model has been developed to characterize the vertical layer reflectance for chlorophyll profiles. Layer reflectance are used with different solar irradiance spectra to determine the spectral upwelling radiance. The model assumes the chlorophyll profile can be partitioned into reflectance layers based on the relationship with absorption and scattering. The depth resolution of the chlorophyll layers affects the upwelling radiance distribution. The spectral shape of the upwelling radiance were modeled for different vertical structures and were compared with modeled spectra for uniform chlorophyll profiles.

For low chlorophyll concentration ($< 1 \text{ mg/m}^3$), the hinge point occurs at 520 nm, whereas at higher concentrations, $> 5 \text{ mg/m}^3$, the hinge point extends to 560 nm. The intensity of upwelling radiance at the surface (ocean color) is shown to decrease as the "dark" subsurface chlorophyll layers migrate toward the surface. The radiance intensity is closely coupled to the depth-weighted chlorophyll concentration in the first attenuation length⁸. However, the shape of the upwelling radiance spectra is different for uniform and non-uniform vertical structure. Model runs for a uniform profile and a non-uniform chlorophyll show that similar radiances at 520 nm occur, if the depth weighted chlorophyll $\{Chl\}$ is used for the uniform profile. However, differences appear to occur at other wavelengths. This suggests the depth-weighted $\{Chl\}$ is not adequate for reproducing the complete upwelling radiance distribution. This also suggests that using the complete upwelling radiance spectrum can provide improved estimates of the vertical structure.

The difference between the actual depth-weighted chlorophyll concentration $\{Chl\}_d$ of a non-uniform profile and that computed based on the $Lu_{443,520,660}$ ratios $\{Chl\}^8$ is approximately 20-30% for different vertical structures. These appear related to some inconsistencies in data sets used in the empirical relationships. Ratios of upwelling radiance, especially bracketing the hinge point of 520 nm will tend to minimize the differences previously discussed in the uniform and non-uniform structure.

As the chlorophyll layer is closer to the surface and within the penetration depth, the model showed better agreement between the depth-weighted $\{Chl\}$ calculated from the profile and the chlorophyll estimated using the blue green ratio $[Chl]$. However, if the chlorophyll layer is at the surface the model shows a negative error ($\{Chl\} < [Chl]$).

In addition to the locations of the chlorophyll maximum layer, the intensity of the chlorophyll layer at depth influences the upwelling radiance at the surface. By changing the layer intensity from 1.3 to 0.33 mg/m^3 at 10 m, the modeled upwelling radiance was shown to change in intensity and wavelength.

This represents a preliminary investigation of the spectral response of the upwelling radiance (ocean color) arising from the vertical chlorophyll structure. Methods of understanding the complete spectral response are required to define the uniqueness of the upwelling radiance spectrum from different vertical profiles. Understanding the upwelling radiance spectrum will help interpretation of the remote sensing ocean color spectrum.

5. ACKNOWLEDGEMENTS

The authors express their appreciation to A. Weideman and L. Estep for helpful discussions. This research was support by the Naval Research Laboratory, "Littoral Remote Sensing Simulation Program" PE 0601153N and the Naval Research Laboratory, Advanced Research Initiative " Upper Ocean Forced Dynamics - Arabian Sea" Program Element 0601153N.

6. REFERENCES

1. Morel, A., Optical modeling of the upper ocean in relation to its biogenous matter content (case 1 waters). J. of Geophys. Res. Vol. 93, No C9 p10749-10768, 1988.
2. Bird, R. E., A simple solar spectral model for direct-normal and diffuse horizontal irradiance. Solar Energy 32:461-471, 1984.
3. Gordon, H.R., Diffuse reflectance of the ocean: Influence of nonuniform phytoplankton pigment profile. App Optic Vol 31 no 12 p2116-2129, 1992.
4. Sathyendranath, S and T. Platt, Remote sensing of Chlorophyll: Consequence of nonuniform pigment profile, Applied Optics Vol 28, No 3 p 490-495, 1989.
5. Lewis, M.R., J. J. Cullen, and T. Platt, Phytoplankton and Thermal Structure in the Upper Ocean: Consequences of Non uniformity in Chlorophyll Profile, J.of Geophy. Res, Vol 88, No c4 p2565-2570, 1983.
6. Gordon, H. R., D. K. Clark, J. W. Brown, O. B. Brown, R. H. Evans and W. W. Broenkow, Phytoplankton pigment concentration in the middle Atlantic bight; comparison of ship determination and CZCS estimates. Applied Optics, Vol. 22, N20, 1983
7. Arnone, R.A. D. A. Wiesenburg and K. D. Saunders. The origin and characteristics of the Algerian Current. J. of Geophy. Res. Vol 95 C2 p1587-1598, 1990.
8. Gordon, H. R. and D. K. Clark, Atmospheric effects in remote sensing of phytoplankton pigments. Boundary Layer Meteorology, Vol. 18, p299-313, 1980.
9. Platt, T. C., S. Caverhill and S. Sathyendranath, Basin-scale estimates of ocean primary production by remote sensing: The North Atlantic. J. Geophys. Res. Vol 96 C8 p15147-15159, 1991.
10. Gordon, H. R. and W. R. Mc Cluney, Estimation of the depth of sunlight penetration in the sea in remote sensing. Applied Optics, Vol. 14, N2, p. 413-416, 1975.
11. Arnone, R.A., G. Terrie and R.A. Oriol, Coupling surface chlorophyll and solar irradiance in the North Atlantic. Marine Technology Society Journal Nov. Vol 27, No.1 Spring, 1993.
12. Austin, R., The remote sensing of spectral radiance from below the ocean surface, in *Optical Aspects of Oceanography*, edited by N.G. Jerlov and E.S. Niesen, pp 317-344, Academic, San Diego, Calif, 1974.
13. Gordon, H.R., O. B. Brown, and M. M. Jacobs, Computed relationships between the inherent and apparent optical properties of a flat homogeneous ocean. Appl. Opt. Vol 14 p 417-427, 1975.

Table 2 - MODEL RUN RESULTS
All with Type I atmosphere

Chl_{max} Depth m (layer thickness)	$\text{Chl}_{\text{intensity}}$ mg/m ₃	Z_{90} @ 490 nm Penetration Depth	$\{\text{Chl}\}_{\text{pro}}$ mg/m ₃	$[\text{Chl}]_{\text{b/g}}$ mg/m ₃	% Error
35 (5)	1.3	19	0.304	0.252	17.01
30 (5)	1.3	18.7	0.308	0.261	15.35
25 (5)	1.3	17.5	0.361	0.275	23.90
20 (5)	1.3	15.85	0.458	0.33	27.29
15 (5)	1.3	13.39	0.677	0.452	33.21
10 (5)	1.3	11.39	0.969	0.740	23.63
5 (5)	1.3	10.84	1.092	1.098	-0.60
0 (5)	1.3	13.05	0.782	1.047	-33.85
15 (1)	1.3	14.622	0.554	0.455	17.94
10 (1)	1.3	12.67	0.784	0.776	1.07
10 (1)	0.97	14.76	0.584	0.541	7.30
10 (1)	0.65	17.81	0.393	0.334	15.04
10 (1)	0.33	23.66	0.196	0.148	24.49
Uniform (1)	0.03	36.25	0.03	0.28	5.41
Uniform (1)	0.10	28.25	0.10	0.075	24.65
Uniform (1)	0.50	15.60	0.50	0.483	3.37
Uniform (1)	1.0	11.02	1.0	1.174	-17.4
Uniform (1)	5.0	4.25	5.0	4.38	12.41
Uniform (5)	0.03	36.25	0.03	0.19	37.05
Uniform (5)	0.1	28.25	0.1	0.064	36.01
Uniform (5)	0.5	15.60	0.50	0.496	0.77
Uniform (5)	1.0	11.02	1.0	1.116	-11.56
Uniform (5)	5.0	4.25	5.0	39.46	21.08

Remote sensing of coastal water quality

Kai Sørensen

Norwegian Institute for Water Research, Norway

Eyvind Aas

University of Oslo, Department of Geophysics, Norway

ABSTRACT

In the turbid and yellow substance rich waters of the outer Oslofjord the turbidity and the Secchi disk depth have been successfully determined by remote sensing, with the TM channels of Landsat 5. Similar attempts to determine the total suspended matter and the beam attenuation coefficient at 520 nm have been less successful, and the content of chlorophyll-*a* is the most difficult to estimate, if at all possible with this sensor.

Observations in the green and red parts of the spectrum give the best correlation. The method requires that a few field measurements and samples are taken, and the constants of the algorithms will vary from case to case. These results and the possible causes of the variation are discussed.

Established optical theory for the backscattering of light from the sea to the atmosphere is tested by optical measurements. The results indicate that so far we are not able to predict the ratio between the radiance from nadir in the sea and the downward irradiance from given absorption and scattering coefficients.

1. INTRODUCTION

The use of satellite remote sensing data for monitoring coastal water quality has until a few years ago been of limited extent in Norway. With new satellites and airborne sensors an increasing interest for using such technology has been established. The State Pollution Control Authority of Norway have applied this type of data in a few monitoring projects. The present investigation is part of an on-going project between the Norwegian Institute for Water Research and the Department of Geophysics for the optimal use of satellite data in monitoring water quality. The work is based on several monitoring and remote sensing projects executed in the area. An important point has been to test the established optical theory concerning the backscattering of light from the sea to the atmosphere.

The success of estimating a water quality parameter from a passive satellite remote sensing signal depends on the relation between the water-leaving radiance and the water parameter, and on how precisely one can correct for the atmospheric contribution to the signal. A lot of work has been done to solve this last problem, but very little validation of the different "atmospheric corrections" seems to have been made. And still much work remains to be done before the satellite radiance can be transferred directly into information that can be used in long term monitoring, without the use of ground truth data. In coastal waters and fjords optical remote sensing data can relatively easily be used to monitor water quality when combined with field data¹. The use of field observations reduces several problems (e.g. the atmospheric contribution) and simplifies the interpretation of the satellite data. Also the combined approach of different high (e.g. Landsat and Spot) and low resolution (NOAA) satellite sensors will improve the monitoring in near coastal waters². Due to the frequent cloud cover in the area the combination of several satellite sensors will increase the number of available satellite data.

The main area of investigation has been the outer Oslofjord, including the Hvaler archipelago and the north-eastern part of the Skagerrak in the south of Norway (Figure 1). Some fresh water localities (lakes and rivers) near the coastline which drains into the fjords and coastal waters are also included in the investigation. The coastal waters (case 2) have high and variable concentrations of inorganic suspended sediments, phytoplankton and yellow substance, which make the interpretation of the remote sensing signals into useful water quality parameters more difficult than in offshore (case 1) waters. This coastal area and especially the Hvaler archipelago is influenced by fresh water from the river Glomma. During the last decade several toxic algal

blooms have occurred in the Skagerrak, e.g. the *Chrysocromulina polylepis* bloom in 1988³, and this has focused on improvement of the methods for monitoring the area, with the use of oceanic buoys and remote sensing technology.

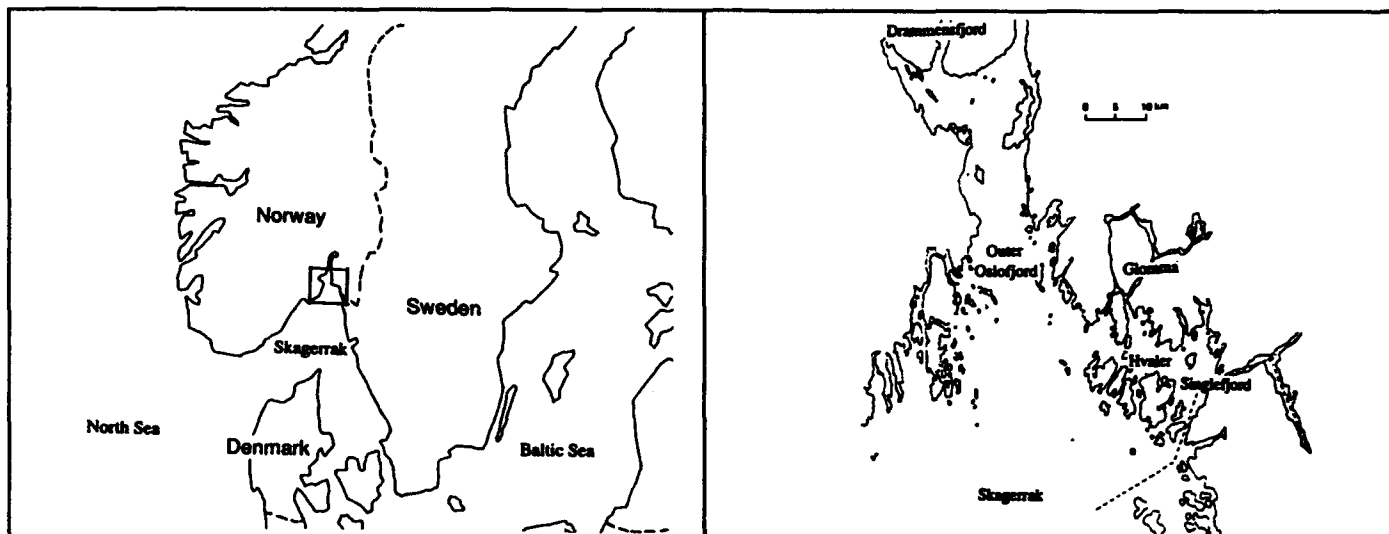


Figure 1. The main area of investigation in the south of Norway and the north-eastern part of the Skagerrak.

2. OBSERVATIONS AND METHODS

2.1 Satellite observations

The satellite data used in the investigation are from the Thematic Mapper (TM) sensor onboard the Earth Observation Satellite Landsat-5, which consist of the channels TM1-4 within the visible and near infrared part of the spectrum. The satellite recordings are geometrically and radiometrically corrected at Esrange in Kiruna. The calibration constants of the TM channels for transferring the digital numbers from the CCT to satellite radiance [$W m^{-2} \mu m^{-1} sr^{-1}$] are those applied by Markham and Barker⁴ and Epema⁵.

The number of pixels used for extracting the digital values at the stations was about 5×5 pixels. With a pixel resolution of 30×30 m the mean digital value will represent an area of about 150×150 m. Comparison of satellite data with field data have been performed for 6 situations in the period 1986 to 1988, and covers the seasonal period May to September.

2.2. Field observations

The field data are collected from different projects in the area in the period 1986-1991. The observations include the Secchi disk depth S , [m], and the beam attenuation coefficient at 520 nm, c , [m^{-1}], measured with a Martec transmissometer. The vertical attenuation coefficient of quanta irradiance, k [m^{-1}], between the surface and the Secchi disk depth, was obtained with a LI-COR meter. The salinity was determined with different salinity sensors. Water samples were collected at the surface (0.5 m) and analysed for total suspended matter, TSM [mg/l], turbidity, Turb [FTU], chlorophyll- a , Chl- a [$\mu g/l$], and dissolved coloured material or yellow substance, $a_y(380)$ [m^{-1}]. TSM was measured by filtration onto a preweighted Nucleopore filter ($0.4 \mu m$). Turbidity was measured with a Hach Turbidimeter and chlorophyll- a with a spectrophotometric method. Dissolved organic material (yellow substance) was measured with a Perkin Elmer Lambda-5 spectrophotometer on water samples filtered through glassfiber filters (GFF). The yellow substance content was expressed as $a_y(380)$, and was calculated from $a_y(390)$, $a_y(400)$, $a_y(430)$, and $a_y(450)$ by means of the average relation given by Højerslev⁶:

$$a_y(\lambda) = a_y(\lambda_0) e^{-0.014(\lambda - \lambda_0)}$$

where λ is the wavelength in nm.

3. RESULTS

3.1. Secchi disk depth, turbidity and absorption.

Secchi disk depth is used for both sea and fresh water monitoring. It is a simple method and can easily be used by local personnel and fish farmers to collect important ground truth data for calibration of satellite data. It is probably one of the few optical parameters used in routine monitoring programs, and in many projects it is the only parameter that gives any optical information about the water masses. The Secchi disk depth is influenced by both particles and dissolved material, and is related to the water-leaving radiance, and thus to the remote sensing signal.

The test area was divided into 6 subareas where the water was expected to have different contents of particles and yellow substance. Large differences in the optical behaviour of the water masses will result in errors if we want to transfer or extrapolate an algorithm from one area to another. It was therefore of interest to test the optical characteristics of the different water types. The areas involved are:

1. North-eastern Skagerrak
2. Outer Oslofjord
3. Inner Oslofjord
4. Singlefjord
5. Fresh water
6. The Hvaler archipelago

The Hvaler archipelago and the outer Oslo fjord are influenced by high concentrations of particles from the river runoff, especially during spring from April to June. The annual mean water transport in the Glomma River is approximately $700 \text{ m}^3/\text{s}$, but can reach $2500 \text{ m}^3/\text{s}$. Smaller amounts of fresh water enter the area from the Drammens River, and low saline water is coming up from the Baltic Sea along the Swedish west coast. The particle concentration in the area varies from less than 1 to 20-25 mg/l during spring, and the corresponding Secchi disk depth from 8-10 meters to less than 0.5 meter.

The Secchi disk depth is well correlated with the vertical attenuation coefficient of the quanta irradiance, k (Figure 2). Since k as a first approximation will be a function only of the absorption coefficient, and not of the scattering coefficient, the Secchi disk depth will thus give us an estimate of the absorption of the water mass.

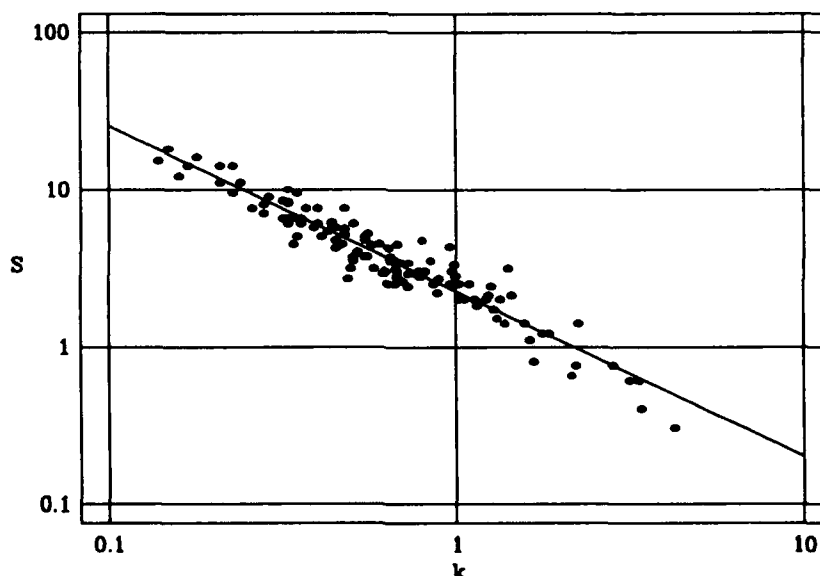


Figure 2. The relationship between Secchi disk depth (S) and the vertical attenuation coefficient of quanta irradiance (k).

The relationship between the Secchi disk depth and the amount of suspended material expressed as turbidity is presented in Figure 3 in a log-log diagram. The mean values for the inverse Secchi disk depth are plotted against turbidity for the different water types in Figure 4.

The turbidity is a measure of the scattering properties of the water mass, and thus of the particle content, while the Secchi disk depth represents the absorption. The relationship between S and $Turb$, demonstrated by Figure 3 and 4, indicates that although the concentrations of the optical components may vary from one area to another, the overall specific optical properties remain the same.

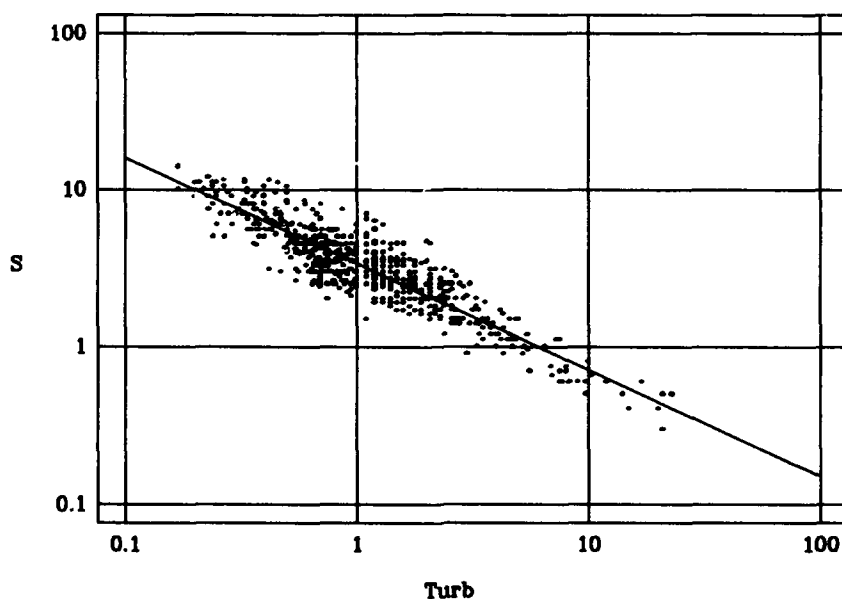


Figure 3. The relationship between the Secchi disk depth (S) and turbidity ($Turb$).

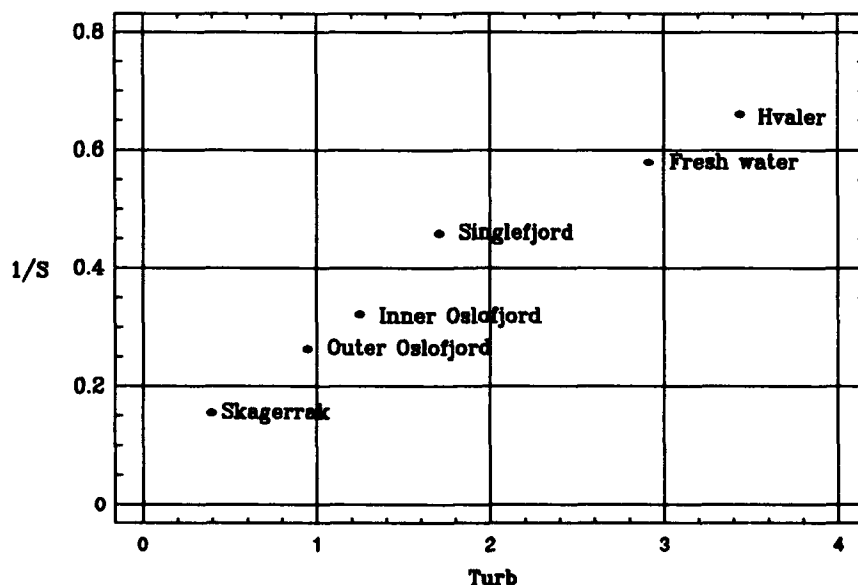


Figure 4. The relationship between the mean inverse Secchi disk depth ($1/S$) and the mean turbidity ($Turb$) for different areas.

3.2. Yellow substance content

The variation of the yellow substance concentration in the coastal area is shown as a function of the salinity in Figure 5. In the figure and Table 1 are shown some typical values from other neighbouring water masses given by Højerslev⁷. There seems to be a crude linear relation between the salinity and the amount of yellow substance in the present data. The typical values from the Hvaler archipelago and the Oslofjord are exceeding the typical values from both the German Bight and the Baltic Sea (Table 1).

Practically no correlation was found between the dissolved substances, given as $a_y(380)$, and the phytoplankton (Chl-*a*) or the amount of particles (Turb), but there was a weak correlation between the Secchi disk depth and $a_y(380)$. High values of $a_y(380)$ in the area will reduce the upward radiance, especially in the TM1 channel and to a smaller extent in the channels TM2 and TM3, and the TM1 should be avoided in the algorithms for the water quality parameters S and Turb.

Table 1. Typical values of yellow substance, $a_y(380)$, and salinity from the investigated area, compared with data from the surrounding seas.

Location	$a_y(380)$, m ⁻¹	Salinity, PSU
Hvaler archipelago	3.60	11
Oslo fjord	1.60	21
German Bight ¹	1.50	31
Baltic Sea ¹	0.96	8
North Eastern Skagerrak	0.57	27
North Sea/Atlantic ¹	0.07	35

1) values from Højerslev⁷.

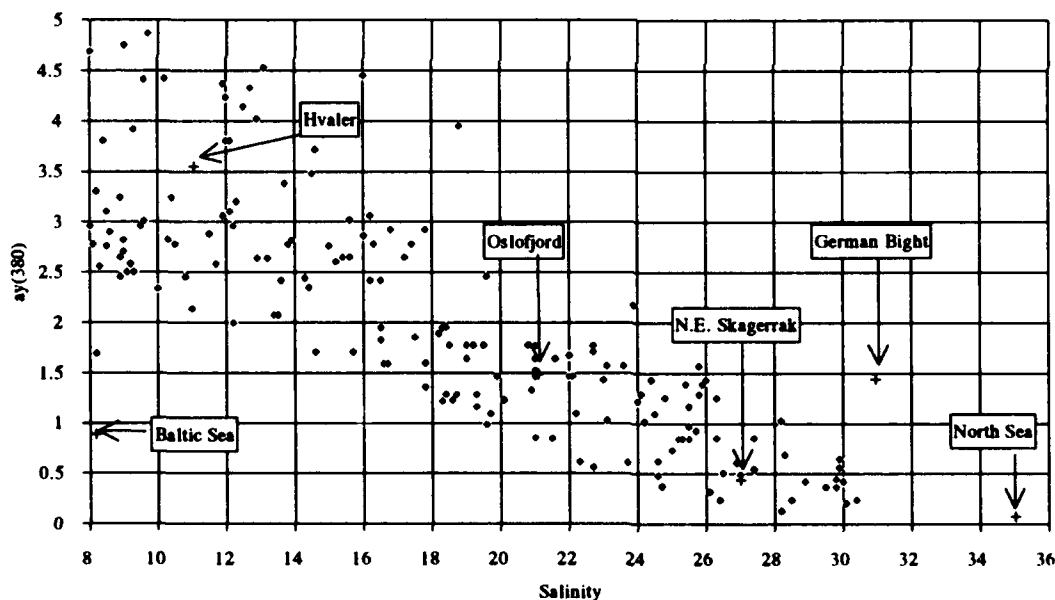


Figure 5. The relationship between yellow substance, $a_y(380)$, and salinity in the surface water of the coastal area in the north-eastern Skagerrak. Typical values from the area and the surrounding seas are indicated.

3.3. Satellite radiance and water quality parameters

The inverse value of the Secchi disk depth was tested against the marine radiance, L_{sea} , for the four TM channels after a first order correction for the atmospheric radiance by using the minimum radiance in clear water (dark object subtraction technique). The radiance was normalized for sun elevation and the sun-earth distance. The correlation is strong in the green (TM2) and red (TM3) parts of the spectrum, but weakens towards the blue and infrared parts as seen by

$$\frac{1}{S} = 0.137 + 0.097 L_{sea_{TM1}} \quad r^2 = 47 \% \quad N = 88$$

$$\frac{1}{S} = 0.126 + 0.074 L_{sea_{TM2}} \quad r^2 = 76 \% \quad N = 88$$

$$\frac{1}{S} = 0.203 + 0.072 L_{sea_{TM3}} \quad r^2 = 85 \% \quad N = 88$$

$$\frac{1}{S} = 0.254 + 0.181 L_{sea_{TM4}} \quad r^2 = 42 \% \quad N = 88$$

The upward radiance from the sea will depend on both the absorption and the scattering coefficients (see chap. 4), while the Secchi disk depth in these waters seems to be primarily a function of the absorption. The absorption in the blue part of the spectrum due to chlorophyll-*a* and yellow substance will then influence the Secchi disk depth more than the satellite signal, and this could explain some of the weaker correlation for the TM1 channel. The radiance signal for the near infrared channel TM4 will come from only a thin layer in the surface (high water absorption), which can explain some of the weaker correlation. Water absorption in the atmosphere will also be more dominant in this channel.

Experiences from measurements of the spectral distribution of the upward radiance in this area have shown that the radiance obtains its maximum values in a broad spectral band between approximately 550 and 650 nm⁸. The satellite signal from TM2 and TM3 will approximately cover the spectral range from 520 to 690 nm. In view of this and the strong correlations for these channels given above, we have chosen to use the mean radiance $L_{sea_{TM23}}$ of the two channels. Within the the range of measurements the inverse Secchi disk depth, $1/S$, fits a linear function of the mean satellite radiance:

$$\frac{1}{S} = 0.153 + 0.074 L_{sea_{TM23}} \quad r^2 = 83 \% \quad N = 88$$

Figure 6 shows the observed values of S from the six cruises as a function of $L_{sea_{TM23}}$, after a first order correction, together with the average relation given above.

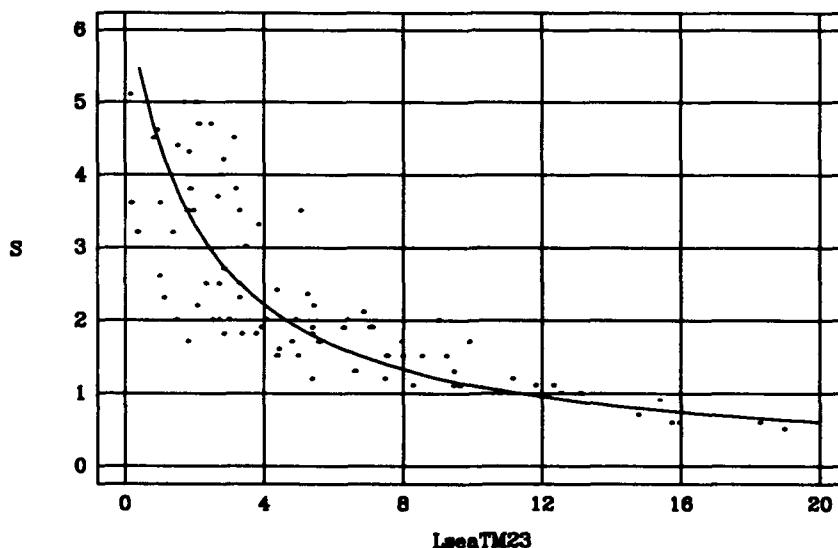
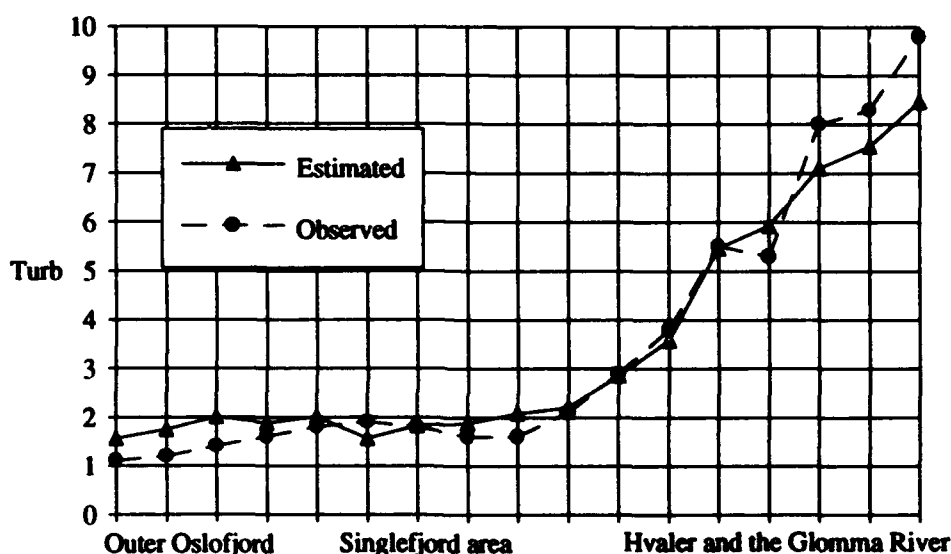


Figure 6. Observations of the Secchi disk depth S and the mean normalized radiance $L_{sea_{TM23}}$, and the average relation between the quantities. $L_{sea_{TM23}}$ is here only corrected for the clear water radiance.

This relation, together with at least two good recordings of the Secchi disk depth from the area at the actual date, covering as large a part of the gradient as possible, can be used to estimate the Secchi disk depth with a satisfactory resolution and accuracy.

$$Turb = 0.521 + 0.397 Lsea_{T_{M3}} \quad r^2 = 84 \% \quad N = 88$$



The correlation between the total suspended matter, TSM, and the radiance from TM3 was found to be much weaker than for the turbidity. One explanation may be that the TSM also includes the organic material (e.g. phytoplankton) which has a lower reflectance than the inorganic material. The Secchi disk depth was also better correlated with the turbidity than with the TSM. Tests for the attenuation coefficient c at 520 nm show even weaker correlation with the satellite radiance.

4. THEORETICAL RELATIONSHIPS

By expressing the irradiance ratio R as

$$R = \frac{E_u}{E_d} = f \frac{b_b}{a} \quad (1)$$

where E_u is upward irradiance, E_d downward irradiance, b_b the backward scattering coefficient, a the absorption coefficient and f a dimensionless quantity⁹, and introducing

$$Q = \frac{E_u}{L_u} \quad (2)$$

where L_u is the radiance from nadir in the sea, it becomes possible to write

$$\frac{L_u}{E_d} = \frac{L_u}{E_u} \frac{E_u}{E_d} = \frac{R}{Q} = \frac{f b_b}{Q a} \quad (3)$$

It has often been assumed that L_u should be proportional to the ratio $\frac{b_b}{a}$, which requires that E_d and the ratio $\frac{f}{Q}$ are constant.

We have no direct observations of b_b and a , but as substitutions we have applied the turbidity and the Secchi disk depth.

One of the many obtained results during the project is that

$$S = -0.043 + \frac{2.43}{k} \quad r^2 = 90 \% \quad N = 126 \quad (4)$$

where k is the vertical attenuation coefficient of the quanta irradiance between the surface and the Secchi disk depth. By assuming that $\frac{1}{a}$ is proportional with $\frac{1}{k}$ it may be expressed as

$$\frac{1}{a} = A_0 + A_1 S \quad (5)$$

where A_0 and A_1 are constants. Another assumed proportionality could be

$$b_b = B_0 + B_1 \text{Turb} \quad (6)$$

where B_0 and B_1 are constants. (3) can then be written

$$\begin{aligned} \frac{L_u}{E_d} &= \frac{f b_b}{Q a} = \frac{f}{Q} [A_0 B_0 + A_1 B_0 S + A_0 B_1 \text{Turb} + A_1 B_1 S \text{Turb}] \\ &= C_0 + C_1 S + C_2 \text{Turb} + C_3 S \text{Turb} \end{aligned} \quad (7)$$

In this expression the C 's are constants, provided $\frac{f}{Q}$ is constant.

For the six cruises the results were

$$L_{sea_{TM23}} = 3.82 - 0.39S + 1.98Turb - 0.55STurb \quad r^2 = 86 \% \quad N = 88 \quad (8)$$

$$L_{sea_{TM23}} = 0.54 + 1.96Turb \quad r^2 = 81 \% \quad N = 88 \quad (9)$$

It is seen that the equation (8), based on physical reasoning, does not improve significantly the correlation with the satellite radiance, as compared with the single-component relation (9).

By introducing

$$\gamma = \frac{b_b}{b} \quad (10)$$

and

$$c = a + b \quad (11)$$

where b is the scattering coefficient, (3) becomes

$$\frac{L_u}{E_d} = \frac{f\gamma}{Q} \frac{b}{a} = \frac{f\gamma}{Q} \left(\frac{c}{a} - 1 \right) \quad (12)$$

Substitution of $\frac{1}{a}$ from (5) gives the relation

$$\frac{L_u}{E_d} = D_0 + D_1c + D_2cS \quad (13)$$

However, it was found that (13) gave no better correlation than relations with only one independent variable. We think that the lack of success for (8) and (13) may be due to significant variations in the ratio $\frac{f}{Q}$.

5. CONCLUSIONS

We have shown that the combined use of TM data from the green and red parts of the spectrum and a few field measurements of Secchi disk depth or turbidity can produce reasonably good water quality information. The radiometric sensitivity and the broad spectral band width of the TM channels will limit the number of parameters that can be determined, but in coastal waters with high amounts of suspended material such satellite data will be useful.

The State Pollution Control Authority has developed a classification system where the Secchi disk depth is one of many parameters used to classify water quality. It is our opinion that both Secchi disk depth and turbidity determined from remote sensing can be used in this context, and that it will improve the monitoring in coastal waters.

Our attempts to estimate total suspended material from the satellite signals were somewhat less successful, probably because the TSM is not an optical quantity. For the chlorophyll content it was not possible to obtain any general relationship at all. We think that with the present satellite sensors chlorophyll in coastal waters can only be estimated in very special cases.

The tests of relations between the satellite radiance and different optical quantities based on optical theory did not give any significant better correlation than the more simple statistical relationships. The most plausible explanation may be that the ratio f/Q is not as constant as assumed, but varies considerably in these waters.

6. ACKNOWLEDGMENTS

The field work was part of projects supported by the State Pollution Control Authority and the Norwegian Institute for Water Research. The work is based on data from earlier investigations in collaboration with Tommy Lindell at the Centre of Image Analysis, Uppsala.

7. REFERENCES

1. K. Sørensen, E. Aas, B. Faafeng and T. Lindell. "Remote sensing of water quality - Further development of optical satellite remote sensing as a method for monitoring of water quality." *Norwegian Institute for Water Research. Report no 2860* (In Norwegian), March 1993, Oslo.
2. K. Sørensen, T. Lindell, and J. Nisell. "The information content of AVHRR, MSS, TM and SPOT in the Skagerrak Sea". *Proceedings from the 12th Canadian Symp. on Rem. Sensing*. Vancouver 1989.
3. T. Lindell, K. Sørensen, G. Larsen and J. Nisell. "Remote sensing and the vertical distribution of the *Chrysochromulina polylepis* bloom in the Skagerrak in 1988." *Norwegian Institute for Water Research. Report no 2666*, Des. 1991, Oslo.
4. B. L. Markham and J. L. Barker. "Thematic Mapper bandpass solar exoatmospheric irradiances". *Int. J. Remote Sensing*, Vol 8, No 3, 517-523, 1987.
5. G. F. Epema. Determination of planetary reflectance for Landsat-5 Thematic Mapper tapes processed by Earthnet (Italy). *ESA Journal*, Vol 14, 1990.
6. N. K. Højerslev. "Natural occurrences and optical effects of Gelbstoff." *Univ. Copenhagen, Dep. Geophys., Rep. 50*, 1988.
7. N. K. Højerslev. Pers. comm. (rep. in prep.).
8. L. H. Petterson, Ø. Frette, O.M. Johannessen, K. Sørensen, E. Svendsen, G. Borstad, R. Kerr, and J. F. R. Gower, J.F.R., 1990. Norwegian remote sensing spectroscopy for mapping and monitoring of algal blooms and pollution - NORSMAP'89. *NRSC Technical Report 28*. 90102/05, Bergen.
9. A. Morel and B. Gentili. "Diffuse reflectance of oceanic waters. II. Bidirectional aspects", *Appl. Opt.*, 32, 6864-6879, 1993.

Extending Coastal Zone Color Scanner estimates of the diffuse attenuation coefficient into Case II waters

Richard W. Gould

Sverdrup Technology, Building 2105
Stennis Space Center, MS, 39529

Robert A. Arnone

Naval Research Laboratory
Remote Sensing Branch, Code 7240
Stennis Space Center, MS, 39529

ABSTRACT

An iterative technique has been developed to improve Coastal Zone Color Scanner (CZCS) estimates of upwelled subsurface water radiances (L_w) in Case II waters. Regional relationships between the diffuse attenuation coefficient measured at 490 nm (K490) and L_w measured at 443, 520, and 550 nm were developed using data collected in the northern Gulf of Mexico in April 1993. These relationships are used to iteratively adjust the aerosol contribution to the total radiance measured at the sensor.

The open-ocean assumption that there is no water-leaving radiance at 670 nm (the CZCS channel used to estimate aerosol radiance) is not valid in coastal areas with a high sediment load; reflectance from suspended sediment can result in a significant signal at 670 nm. If the sediment signal is not considered the aerosol contribution is overestimated during the atmospheric correction of the CZCS data. Subsequently, the calculations of L_w are underestimated, even to the point of negative radiances calculated in extremely turbid areas. Because the L_w are used in the geophysical algorithms to estimate K490 and pigment concentration, these derived products are overestimated in Case II waters if the 670 nm radiance is not partitioned into aerosol and sediment components.

1. INTRODUCTION

Estimates of upwelled subsurface water radiances at 443, 520, 550, 670, and 750 nm were provided by the CZCS during its operational lifetime from 1978 to 1986. These radiance measurements have been used to calculate oceanic bio-optical parameters such as the diffuse attenuation coefficient and phytoplankton pigment concentration, generally to within an accuracy of approximately 30-40%^{1,2}. Similar relationships are anticipated in algorithms utilizing data from the next generation of ocean color sensors, such as the Sea-Viewing Wide Field Sensor (SeaWiFS) currently scheduled for launch in late 1994 or early 1995, the Japanese Advanced Earth Observing Satellite (ADEOS) scheduled for launch in 1996, and the Moderate Resolution Imaging Spectroradiometer (MODIS), scheduled for launch in 1999.

Most of the research to date has focused on open-ocean, Case I waters, where optical properties are dominated by phytoplankton absorption and their correlated particulate and dissolved degradation products. Many current research programs, however, are shifting attention to coastal, Case II waters, where optical properties are strongly influenced by scattering from suspended sediments and absorption by colored dissolved organic matter (CDOM). Current algorithms must be reviewed to assess their validity in Case II waters, and if necessary adjustments must be made.

The current atmospheric correction routine for CZCS data, described in Gordon et al.², assumes that the total radiance recorded by the sensor in each of the five wavelength channels is the sum of three components: the water-leaving radiance (L_w , which is the upwelled subsurface radiance, L_u , pushed through the air/sea interface), the aerosol path radiance, and the Rayleigh path radiance (which results from Rayleigh scattering). To estimate aerosol radiance, however, an assumption is made that the radiance in the 670 nm channel is due entirely to path radiance by atmospheric aerosols and Rayleigh scattering. Open-ocean, clear-water regions are essentially "black" at this wavelength, or totally absorbing, so the water-leaving radiance should be zero in this channel. The Rayleigh scattering component can be calculated from the

satellite viewing geometry, so the aerosol radiance at 670 nm can be calculated by subtraction.

Aerosol radiances in the remaining channels are calculated from the 670 nm aerosol radiance using the angstrom exponent formulation for the wavelength dependence, with ozone transmittance and incident solar irradiance considered. Once the aerosol and Rayleigh components have been determined for each channel, the water-leaving radiances are calculated as the total, sensor-measured radiances minus the aerosol and Rayleigh radiances. Equations describing these relationships are presented in the Algorithm section.

While the aerosol assumption is valid for most of the world ocean, in coastal regions where there is a high suspended sediment load, water-leaving radiance at 670 nm (L_w670) may be significantly greater than zero due to reflectance from sediment in the red portion of the spectrum^{4,10,11}. This error results in an overestimate of the aerosol radiance component, which propagates through the atmospheric correction algorithm and causes the radiances in the remaining channels to be underestimated. In extreme cases of aerosol overestimation in turbid regions, water-leaving radiance calculations even result in negative values. The 443 nm channel is the first to go negative, but negative values in the 520 and 550 channels have been observed as well. These radiances are subsequently used in geophysical algorithms to derive estimates of the diffuse attenuation coefficient and pigment concentration, which are therefore also in error (overestimated), if they can be calculated at all.

Previous relationships between the diffuse attenuation coefficient measured at 490 nm ($K490$) and ratios of upwelled subsurface radiances at CZCS wavelengths, such as those described by Austin and Petzold¹ (referred to as A/P), were developed for Case I waters with a maximum $K490$ value of approximately 0.4 m^{-1} . In order to improve estimates of $K490$ in certain areas or in extremely turbid regions, regional K relationships or additional Case II relationships may be required. In this paper, we evaluate these hypotheses by developing new regional relationships based on data collected during an April 1993 cruise in Case I and Case II waters in the northern Gulf of Mexico (GOMEX-1 cruise). These new relationships are compared to previously described relationships.

In addition, a coastal iterative algorithm is presented that partitions the total 670 nm radiance measured at the sensor into aerosol and water-leaving radiance components. The iterative algorithm utilizes two separate equations to estimate $K490$, based on either the L_{443}/L_{550} radiance ratio or the L_{520}/L_{550} radiance ratio, and adjusts the radiances by successively reducing the aerosol radiance until the radiance ratios yield similar estimates of $K490$. The iterative radiance algorithm is based on earlier work by Smith and Wilson¹⁰ and Mueller¹¹ (hereafter referred to as the S/W and M iterative algorithms). The new algorithm is compared to the previously described S/W and M iterative algorithms and the benefits and disadvantages are discussed.

The iterative radiance algorithm has been implemented in an automated processing system developed by the Naval Research Laboratory (NRL). The automated system, described by Oriol et al.³, can process a full-resolution, two minute CZCS scene from Level-1 raw data to Level-3 geographically registered products in less than 10 minutes (on a Silicon Graphics Crimson computer), with very little operator intervention. A complete data base of CZCS imagery in the Gulf of Mexico collected over the lifespan of the sensor has been created using the automated processing system (approximately 850 scenes). Similar data bases are under development for the Sea of Japan and the Arabian Sea.

2. METHODS

During a cruise in the northern Gulf of Mexico in April, 1993, a suite of bio-optical measurements were made at 28 stations along transects extending from extremely turbid coastal Case II waters into clear, offshore Case I waters. Station locations are shown in Figure 1 of Gould et al.⁴ Measurements included spectral upwelling counts, collected with a Research Support Instruments (RSI) scanning radiometer, as well as calibrated upwelling and downwelling radiance and irradiance, collected with a multi-channel environmental radiometer (MER). Although the RSI provides only photon counts, the data are collected spectrally at 2 nm intervals from 400-700 nm. The MER provides calibrated radiance values but only at 7-12 preset wavelengths. RSI and MER data processing is described in Gould et al.⁴ and Mueller and Trees⁵. The calibrated subsurface upwelling radiances were ratioed and used to model the measured $K490$ values.

During the GOMEX-1 cruise, downwelling irradiance was measured at 486 nm, so the diffuse attenuation coefficient for downwelling irradiance was calculated at 486 nm, not 490 nm. The K value at 490 nm used to formulate the regression relationships was derived from K at 486 nm using the K spectral relationship described by Austin and Petzold⁶. The coefficients required for the conversion from K at 486 nm were linearly interpolated from the values at 485 and 490 nm provided in that paper.

In addition, upwelling radiance at 520 nm, a wavelength required in the CZCS algorithms, was not measured by the MER during the GOMEX-1 cruise (the closest wavelengths were 489 and 531 nm), so a three-step wavelength conversion routine was developed. The conversion routine uses spectral upwelling count data from the RSI scanning radiometer as well as calibrated upwelling radiance data from the MER. Correlations and linear regression relationships were formed in an effort to estimate upwelling radiance at unmeasured wavelengths.

The first step in the three step conversion requires converting from radiance values at MER wavelengths to RSI upwelling counts at the same wavelengths. The MER radiances vs. the RSI upwelling counts are plotted in Figure 1A, with the polynomial regression line overlaid (data from the coastal stations did not fall along the regression line, possibly due to problems with the RSI instrument in turbid waters, so they were excluded from the analysis). The MER to RSI relationship appeared to be wavelength independent over the wavelength range used (400 - 590 nm). In addition to the model error, however, another source of error enters into the application of the MER to RSI conversion routine; the equation is subsequently applied to data at the coastal stations, even though no coastal data were used to derive the relationship.

For the second step, the RSI counts at MER wavelengths were converted to RSI counts at CZCS wavelengths. If the two wavelengths are not separated by more than 4-30 nm (depending on the wavelengths), simple linear regression equations relating the MER wavelengths (independent variable) to the CZCS wavelengths (dependent variable) can be used, with R^2 values ranging from 0.76 to 0.99 (determined from a correlation analysis of the GOMEX-1 RSI data over all wavelengths).

K490 data from the GOMEX-1 cruise were separated into three categories: Stations with $K < 0.13$, stations with $0.13 < K < 0.4$, and stations with $K > 0.4 \text{ m}^{-1}$ (see Figure 2 in Gould et al.⁷). These station groupings were formulated based on visual similarities in the spectral curves, correlation analyses using both RSI and MER data, and principal component analysis using the MER data.

Regressions of MER wavelengths to CZCS wavelengths were derived for each of the three groups of stations. These station groupings, which are based on the K values, correspond to offshore, mid-regions, and coastal locations. Of the 14 RSI stations from the GOMEX cruise, 6 were from low-K offshore areas, 2 were from mid-K areas, and 3 were from high-K coastal areas (three coastal stations were not used due to possibly erroneous data). Additional data from a cruise to Tampa Bay in June 1993 were combined with the corresponding GOMEX stations and all were used to derive the regression equations. These included 3 Tampa Bay stations from mid-K areas and 9 that were from high-K regions. RSI counts at 531 nm vs RSI counts at 520 nm for the coastal, high-K stations are plotted in Figure 1B, with the regression line overlaid.

The third step of the wavelength conversion process requires inverting from RSI counts at 520 nm to radiance at 520 nm. Rather than formulating a new model which would add another source of error, the "inverse" of the second order polynomial equation from step one was used. In this manner, errors introduced during the modeling of step one tend to cancel in step three. Note that this equation was formulated with data at MER wavelengths but is being applied in this step to data at CZCS wavelengths (specifically 520 nm) because we are assuming the relationship is independent of wavelength.

To summarize, a the three-step wavelength conversion routine was developed to obtain estimates of subsurface upwelled radiance at 520 nm from measurements of upwelled radiance at 531 nm. MER-measured radiance values at 531 nm are first converted to RSI count values at the same wavelength using a second order polynomial regression equation. The RSI counts at 531 nm are then converted to RSI counts at 520 nm using simple linear regression equations (separate equations are used for each of the three station groupings). Finally, RSI counts at 520 nm are converted back to radiance values at the same wavelength using the inverse of the quadratic equation from step one. This wavelength conversion routine has also been employed to estimate radiances at SeaWiFs wavelengths to aid in the development of algorithms for that sensor.

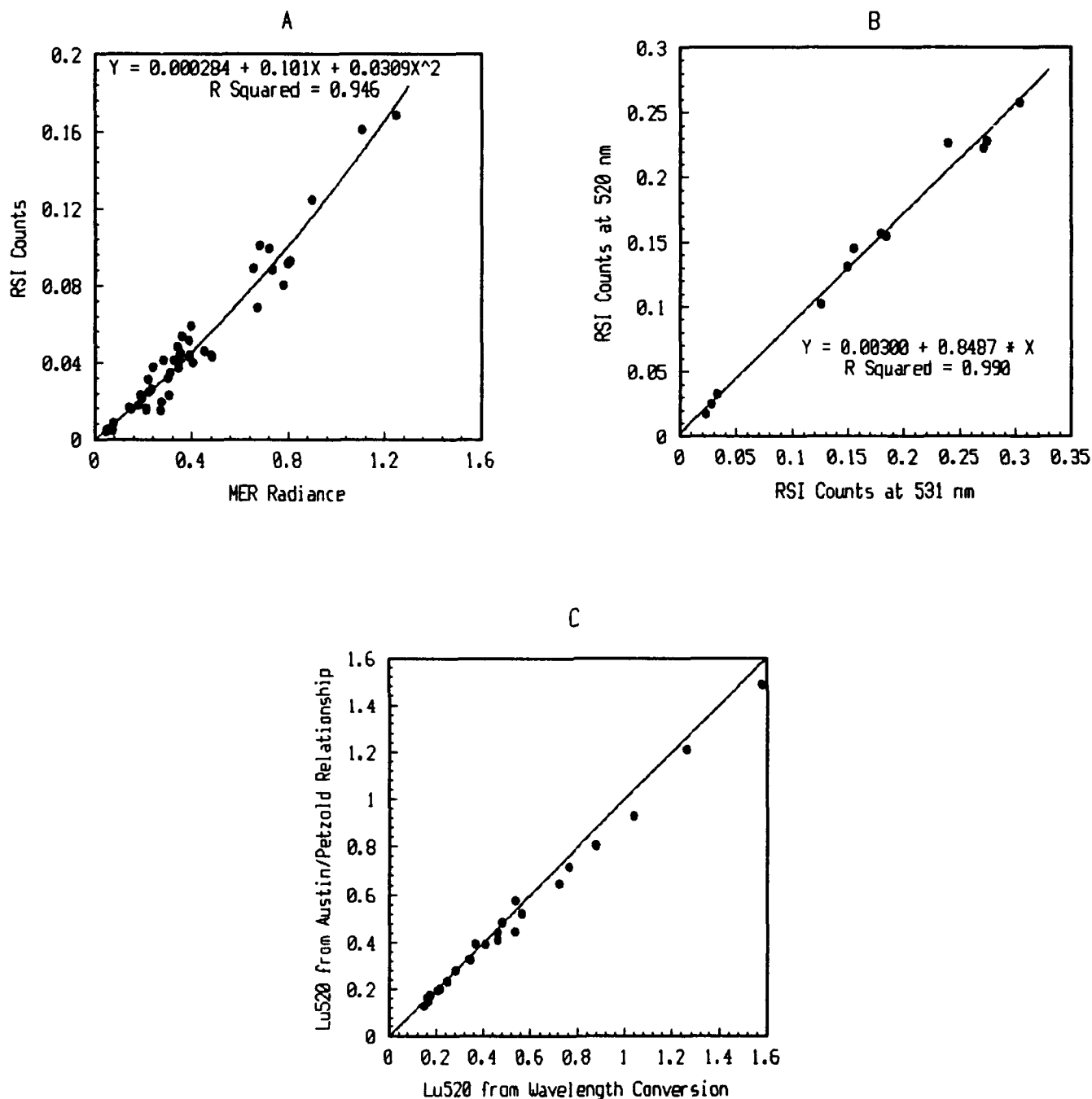


Figure 1. Conversion from radiance at 531 nm to radiance at 520 nm. A. Conversion from upwelling radiance at MER wavelengths to RSI upwelling photon counts at the same wavelengths. B. Conversion from RSI upwelling counts at 531 nm to RSI upwelling counts at 520 nm, for coastal stations where $K > 0.4 \text{ m}^{-1}$. C. Comparison between L_{w520} estimated from wavelength conversion routine to L_{w520} estimated using Austin/Petzold relationship between L_{w443} , L_{w520} , and L_{w550} (Equation 1).

Because measurements of upwelled radiance were made at 443 and 550 nm, $L_u(520)$ was also calculated by solving equation 12 in A/P¹ for $L_u(520)$:

$$L_u(520) = 1.111 [L_u(443)]^{(0.258)} [L_u(550)]^{(0.742)} \quad (1)$$

In Figure 1C, calculations of $L_u(520)$ using equation 1 are plotted against $L_u(520)$ estimates calculated using the three-step wavelength conversion routine. Points falling on the solid line indicate a one-to-one correspondence between the two estimates. The results compare very favorably, except at high radiance values, where the wavelength conversion estimate exceeds the A/P estimate. Assuming that the wavelength conversion estimates are more correct than the A/P estimates, this indicates that, for certain stations where high values of $L_u(520)$ were calculated, the relationship between the 443, 520, and 550 radiances does not follow the A/P relationship. The stations where this discrepancy was the greatest were located in shallow water (less than 30 meters) off the coast of Florida, suggesting that the data there might have a component of bottom reflectance in the measurements.

3. ALGORITHM DEVELOPMENT

The relationship between the 443/550 upwelled radiance ratio and K490 that was described by Austin and Petzold¹ was developed using mainly Case I data with a maximum K value of approximately 0.4 m⁻¹. Data collected during the GOMEX-1 cruise in the northern Gulf of Mexico extended into extremely turbid Case II waters with a maximum K490 value of 1.3 m⁻¹ recorded. The relationship between the $L_u(520)/L_u(550)$ ratio and K490 that was described by Mueller et al.⁷ was based on data collected in Case II waters from various locations, including San Francisco Bay. We believe a re-evaluation of these equations is warranted to ascertain whether new algorithms are required for Case II waters or whether there are regional dependencies that require further analysis. For simplicity, relationships between K490 and the $L_u(443)/L_u(550)$ radiance ratio will be referred to as K1 relationships and those between K490 and the $L_u(520)/L_u(550)$ ratio as K2 relationships.

In many coastal areas, very low water-leaving radiances in the 443 nm channel may result from strong absorption by chlorophyll. Sensor limitations and errors in the atmospheric correction routine may make it impossible to accurately retrieve an estimate of $L_u(443)$ in those regions, thereby inducing errors in the estimation of K490 if algorithms containing the $L_u(443)/L_u(550)$ ratio are used. To alleviate this problem, Mueller et al.⁷ recommended branching to a K490 algorithm based on the 520/550 ratio in locations where K exceeds 0.16 m⁻¹, and we have adopted this procedure.

Relationships similar to those originally presented by Austin and Petzold between the $L_u(443)/L_u(550)$ upwelled radiance ratio and K490 were prepared using data from the GOMEX-1 cruise (see text and Figure 3 in Gould et al.⁴). At K values greater than about 0.2 m⁻¹, discrepancies were detected between the historical relationship and a new regression equation fit to the GOMEX-1 data. However, the data collected during the GOMEX-1 cruise were acquired under widely varying conditions of cloud cover, ranging from clear skies to complete overcast, and widely varying solar zenith angles, whereas the data used by Austin and Petzold were restricted to more cloud-free conditions.

In order to correct for these differences, the GOMEX-1 data have been normalized for downwelling irradiance using the relationship suggested by Mueller⁸:

$$\frac{L_{wn}(\lambda_1)}{L_{wn}(\lambda_2)} = \frac{L_u(\lambda_1) F(\lambda_1) E_d(\lambda_2)}{L_u(\lambda_2) F(\lambda_2) E_d(\lambda_1)} \quad (2)$$

where $L_u(\lambda_i)$ and $E_d(\lambda_i)$ are the measured upwelled radiance and downwelled irradiance and $F(\lambda_i)$ is incident solar flux at the top of the atmosphere (Neckel and Labs⁹) at wavelengths λ_i ($i = 1, 2$). We neglect the slight wavelength dependence of the Fresnel transmittance of the sea surface so that this term cancels out in the ratios when converting from upwelled subsurface radiance to water-leaving radiance, i.e., $L_{wn}(\lambda_1)/L_{wn}(\lambda_2) \approx L_u(\lambda_1)/L_u(\lambda_2)$ for wavelengths between 400-700 nm.

The effect of normalization is illustrated in Figure 2. The lines in Figures 2A and B represent a one-to-one correspondence between the normalized and non-normalized data. The normalization procedure has no effect on the ratio if the data points fall along the $y = x$ line. Whereas the normalized 443/550 ratio exceeds the non-normalized ratio for nearly all data points, the 620/550 data points cluster along the line indicating that the normalization procedure had little effect on that ratio.

K1 and K2 relationships derived using normalized GOMEX-1 radiance ratios are plotted in Figures 3A and B, with the Austin/Petzold (A/P) K1 and Mueller et al. (MTA) K2 equations overlaid as dotted lines. Notice that the normalized GOMEX-1 data now fall very close to the A/P K1 line, but the GOMEX K2 relationship still varies significantly from the MTA K2 equation.

To calculate estimates of water-leaving radiance in each channel, the equation for the atmospheric correction of CZCS data as defined by Gordon et al.³ can be rearranged and expressed as follows:

$$L_w(\lambda) = t_d(\lambda)^{-1} [L_t(\lambda) - L_r(\lambda) - L_a(\lambda)] \quad (3)$$

where $L_t(\lambda)$ represents the total radiance recorded at the sensor, $L_r(\lambda)$ represents the Rayleigh scattering contribution, $L_a(\lambda)$ represents the aerosol scattering contribution and $t_d(\lambda)$ is the diffuse transmittance of the atmosphere, for wavelengths $\lambda = 443, 520, \text{ and } 550 \text{ nm}$. The aerosol radiance at each wavelength can be estimated from the aerosol radiance at 670 nm:

$$L_a(\lambda) = \left(\frac{\lambda}{670} \right)^n S(\lambda, 670) L_a(670) \quad (4)$$

where n is the Angstrom coefficient to account for the wavelength dependence of aerosol radiance and $S(\lambda, 670)$ represents the product of the ratios of ozone transmittances and incident solar irradiances at wavelengths λ and 670 nm. Aerosol radiance at 670 nm is calculated from:

$$L_a(670) = L_t(670) - L_r(670) - t_d(670) L_w(670) \quad (5)$$

The initial assumption (which is modified during the iterative process) that $L_w(670) = 0$ reduces Equation 5 to:

$$L_a(670) = L_t(670) - L_r(670) \quad (6)$$

Thus, the initial estimate of $L_a(670)$ is taken as the total radiance measured by the sensor at 670 nm minus the Rayleigh radiance (which is calculated for each wavelength from the known sun/satellite viewing geometry). If $L_w(670)$ is greater than zero, $L_a(670)$ will be overestimated, and this error will propagate through the atmospheric correction routine resulting in underestimates of the $L_w(\lambda)$ s.

The standard processing routine stops at this point, and the iterative algorithm begins, in order to estimate a non-zero value for $L_w(670)$ in turbid areas. After initial estimates of $L_w(\lambda)$ are obtained for the 443, 520, and 550 nm channels, K490 is calculated using both the K1 and K2 equations if all three of the initial $L_w(\lambda)$ estimates are positive:

$$K1 = 0.0883 \left[\frac{L_w(443)}{L_w(550)} \right]^{(-1.491)} + 0.022 \quad (7)$$

$$K2 = 0.1650 \left[\frac{L_w(520)}{L_w(550)} \right]^{(-4.576)} + 0.022 \quad (8)$$

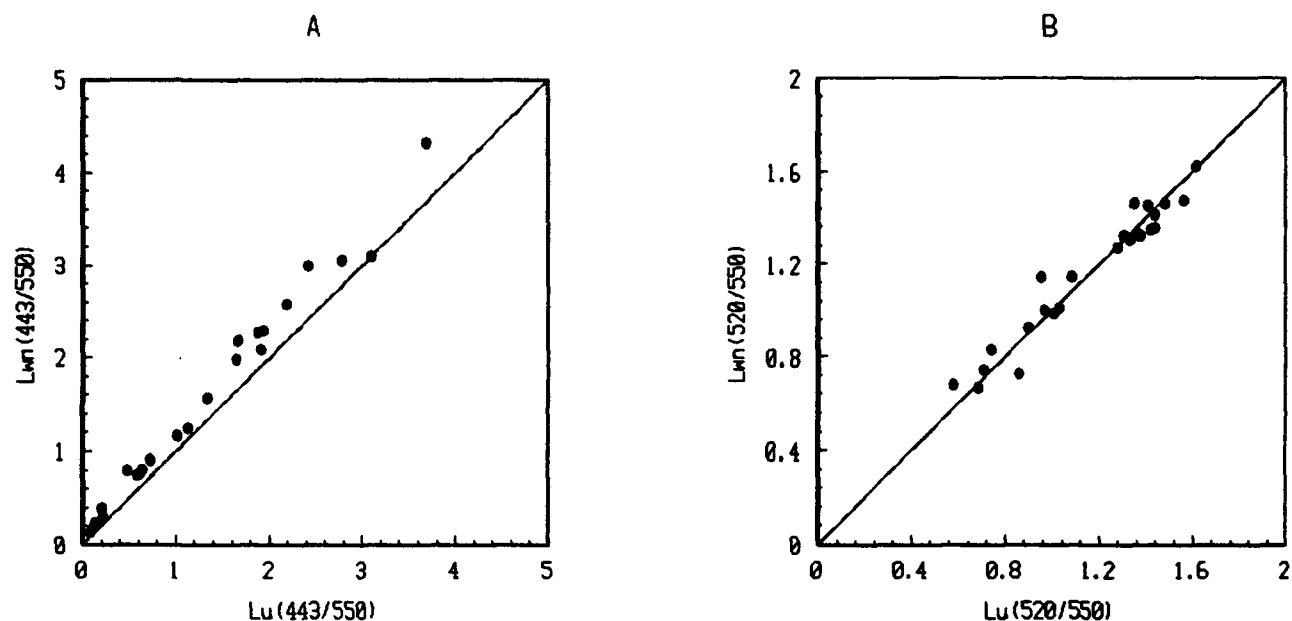


Figure 2. Normalized water-leaving radiance ratios (L_{wn}) vs. non-normalized subsurface upwelling radiance ratios (L_u). A. 443/550 ratio. B. 520/550 ratio.

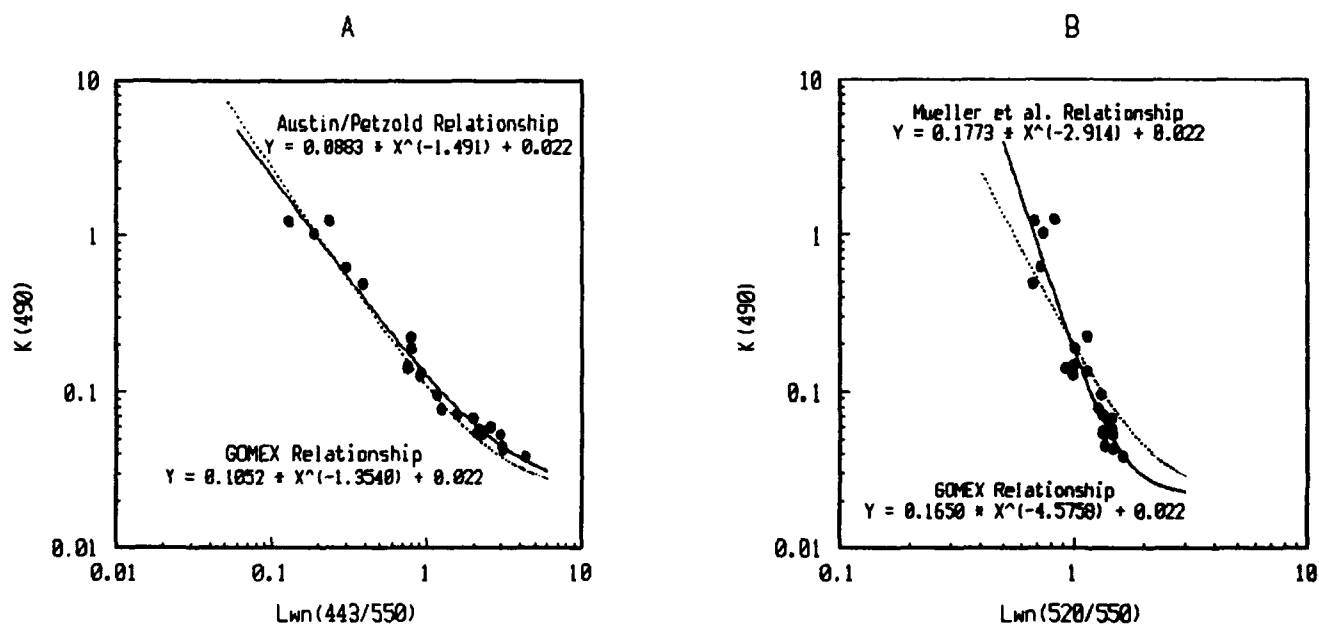


Figure 3. Normalized water-leaving radiance ratios vs. $K490$. The data plotted are from the April, 1993, GOMEX-1 cruise in the northern Gulf of Mexico. A. $L_{wn}(443/550)$ ratio. The least-squares regression fit to the data is represented by the solid line (GOMEX relationship); the Austin/Petzold relationship is overlaid as the dotted line. B. $L_{wn}(520/550)$ ratio. The least-squares regression fit to the data is represented by the solid line (GOMEX relationship); the Mueller et al. relationship is overlaid as the dotted line.

The K1 equation is the original A/P relationship and the K2 equation was derived using normalized GOMEX-1 data (see Figures 3A and B). The $L_u(\lambda)$ s are subsurface values calculated by pushing the $L_w(\lambda)$ s down through the air/sea interface.

At this point, the iterative algorithm operates if either of two conditions is met: 1) the initial K1 estimate exceeds 0.16 m^{-1} (indicating the possibility of turbid water and a non-zero value for $L_w(670)$), or 2) any of the initial $L_u(\lambda)$ estimates are negative (indicating an obvious overestimation of the aerosol radiance). Generally, in turbid areas the $L_u(443)$ radiance is the first radiance to go negative, followed by the $L_u(520)$ and finally the $L_u(550)$ as suspended sediment concentration increases and the aerosol radiance is increasingly overestimated. Thus, if $L_u(520)$ or $L_u(550)$ are negative $L_u(443)$ is likely to be negative as well.

If condition 1 is satisfied, a new estimate of $L_u(443)$ is calculated by setting the K1 and K2 equations equal and solving for $L_u(443)$:

$$L_u(443) = \left(\frac{K2 - 0.022}{0.0883} \right)^{(-0.6707)} L_u(550) \quad (9)$$

The assumption here is that the K2 estimate of K490 is more correct than the K1 estimate because it is based on the 520/550 ratio rather than the 443/550 ratio. There are problems related to measuring $L_u(443)$ in coastal areas (low values due to strong absorption of this wavelength by chlorophyll) and the Angstrom formulation for the wavelength dependence of the aerosol radiance magnifies aerosol errors as wavelength distance from 670 nm increases.

If condition 2 is satisfied, $L_u(443)$ is set to a low, positive value (0.01 radiance units). As stated in Mueller¹¹, the magnitude of the radiance adjustment required to restore $L_u(443)$ to a positive value can be interpreted as the minimum overestimate of aerosol path radiance at 443 nm.

Using the new estimate of $L_u(443)$ from condition 1 or 2, an estimate of $L_u(670)$ is then calculated:

$${}^m L_u(670) = {}^{m-1} L_u(670) + \frac{t_d(443) [{}^m L_u(443) - {}^{m-1} L_u(443)]}{t_d(670) S(443, 670) \left(\frac{443}{670} \right)^n} \quad (10)$$

following Mueller¹¹, where the leading superscript m denotes the iteration number ($m = 0$ for initial estimates, 1 for first iteration values, and so on). $L_u(670)$ is then calculated from $L_u(670)$ and substituted into Equation 5, and Equations 3 and 4 are used to calculate new estimates of water-leaving radiances at the other wavelengths. With the new radiance estimates, new estimates of K1 and K2 are calculated using Equations 7 and 8, and the iteration process repeats until the K values agree to within 0.1 units.

At pixels where iteration occurs, the K1 estimate will be greater than the K2 estimate, so the K1 estimate will be lowered by setting it equal to K2 and calculating a new (higher) $L_u(443)$. The algorithm constrains iteration to only those pixels that satisfy condition 1 or 2 above and whose K1 estimate exceeds the K2 estimate. Iteration will not occur if K2 exceeds K1 because we cannot increase the aerosol radiance term (which would be required to increase the K1 estimate up to the K2 estimate) because the $L_u(670)$ term cannot be reduced further; it is already set to an initial value of zero.

The rationale behind the algorithm is to start iterating at some value of K490 where suspended sediment may begin to play a role in the attenuation of light. At that point there will be a significant $L_w(670)$ signal due to reflectance by sediments at this wavelength and we can no longer attribute all of the radiance in the 670 nm channel to aerosols. Based on previously reported results and GOMEX-1 cruise data which indicates a change in the spectral shape of upwelling light near a K value of 0.16 m^{-1} , so we have chosen this value as the minimum K value at which to begin iterating. In addition, iteration will also occur at pixels where the initial $L_u(443)$ estimate is negative, because the estimate of aerosol radiance at that pixel is obviously too high.

In coastal areas, where the 443 nm radiance is too low to measure accurately by the sensor, we assume that the 520 radiance is more correct and branch from a K1 algorithm to a K2 algorithm to estimate K490. However, if the K1 and K2 values are forced to agree closely in the iteration scheme, branching would not be necessary. There are cases where the iteration cannot remove enough aerosol to force the K estimates to agree, so the branching is still required. The west Florida shelf in Figure 4 is one such example; the initial K1 estimate is much larger than the initial K2 estimate and the radiance ratios do not conform to the relationships specified in the K1 and K2 equations (Equations 7 and 8), possibly due to contamination from bottom reflectance in the signal.

In this way, the aerosol radiance estimate at each pixel (where condition 1 or 2 is satisfied) is successively decreased by partitioning some of the total 670 nm radiance into an $L_w(670)$ term. If convergence is not achieved within 10 iterations, processing ceases, the pixel is flagged, and a message is written to a log file. A check to prevent negative aerosol calculations is also implemented in the algorithm, and another check prevents any iteration if the initial aerosol concentration is less than 0.10 radiance units (unless the initial $L_w(443)$ was negative, in which case it is set to 0.01, new $L_w(\lambda)$ s are calculated for 520, 550, and 670 nm, and control returns from the iterative subroutine to the main processing program).

4. RESULTS

Statistical results of the various K models evaluated are presented in Table 1. Normalized and measured (non-normalized) GOMEX-1 radiance data were fit to the A/P and MTA models, as well as the new regression models developed in this study (Equations 7 and 8), and the mean bias and standard error of prediction were calculated. The mean K from the GOMEX-1 data was calculated at 486 and 490 nm; the value of 0.2727 listed under the "Mean K from Data" column in Table 1 corresponds to the mean of the attenuation coefficient measured at 486 nm and the value of 0.2650 corresponds to the mean of the coefficient converted to 490 nm. The L_w520 estimates used in the K2 equations were derived using the three-step wavelength conversion routine described in Section 2.

Except for the A/P model, a better fit to the GOMEX-1 data is obtained if measured rather than normalized radiance data are used in the models. However, the samples span a wide range of cloud cover conditions and solar zenith angles, so we believe that the data should be normalized using Equation 2 before analysis. The standard error of prediction is a measure of the dispersion of the data points about the regression curve. The standard errors of the normalized MTA and GOMEX-K2 models are very similar, but the mean bias of the GOMEX-K2 model is smaller and the data fit the curve in Figure 3b with an R^2 value of 0.88. The rather high standard errors associated with all the models indicate a large degree of scatter in the data.

The iterative algorithm has been applied to approximately 850 CZCS scenes of the Gulf of Mexico. Figure 4 shows the results for the October 8, 1979 image. In the top panel (Figure 4a), K490 estimates derived using Gordon's standard atmospheric correction routine ($L_w670 = 0$ for all pixels) are shown. Land is black and cloud pixels are flagged grey. Increasing K values are depicted by increasingly warmer colors (i.e., blue pixels represent low K values and red pixels represent high K values). White areas along much of the Gulf coast indicate where unrealistically high K values were calculated or where K values could not be calculated at all, due to negative radiance estimates (resulting from overestimates of aerosol radiance).

In Figure 4B, K490 results for the same image processed using the iterative algorithm are shown. Notice that the coastal pixels that were previously flagged white now have reasonable K values assigned. Notice also that the iteration algorithm has reduced the K estimates for many of the coastal pixels by increasing the radiance estimates. The black line on the image, extending to the southwest from Mobile Bay, marks the location of a transect where pixel values were dumped for a quantitative comparison of processing results (see Figure 5).

Figure 4C shows the distribution of L_w670 calculated using the iterative processing. Although ground truth verification of the results is not available, the higher radiance values closest to shore and in bays, presumably indicating higher suspended sediment concentrations there, are reasonable and realistic.

Table 1. Statistical comparison of K490 models.

	Model	Mean K from Data (m ⁻¹)	Mean K Estimated from Model	Mean Bias	Standard Error S_K	$\frac{S_K}{\text{Mean K}} \times 100$
K from 433 550 ratio	Austin/Petzold, Measured	0.2727	0.4804	0.2077	0.6046	221.7%
	* Austin/Petzold, Normalized	0.2650	0.2611	-0.0039*	0.1753	66.2%
	GOMEX-K1, Measured	0.2727	0.2718	-0.0009	0.1215	44.6%
	GOMEX-K1, Normalized	0.2650	0.2607	-0.0043	0.1460	55.1%
K from 520 550 ratio	Mueller et al., Measured	0.2727	0.2359	-0.0368	0.1981	72.6%
	Mueller et al., Normalized	0.2650	0.2211	-0.0439	0.2469	93.2%
	GOMEX-K2, Measured	0.2727	0.2577	-0.0150	0.2137	78.4%
	* GOMEX-K2, Normalized	0.2650	0.2361	-0.0289	0.2462	90.6%

* Recommended Models

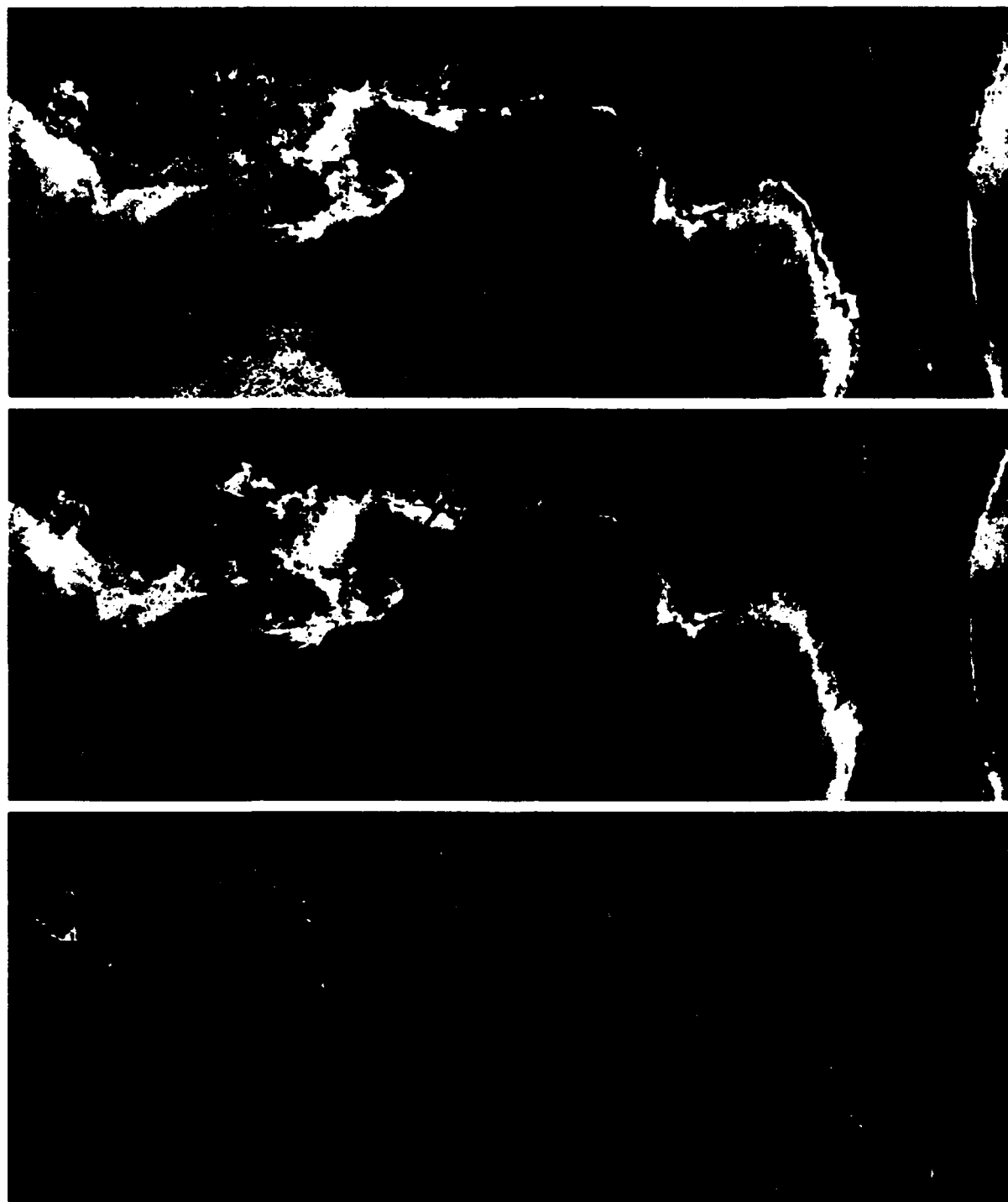


Figure 4. October 8, 1979 CZCS image of the northern Gulf of Mexico. A. K490 image processed with the standard Gordon algorithm. The white pixels along the coast represent unrealistically high K estimates ($> 4.8 \text{ m}^{-1}$) or negative radiances where K could not be estimated. B. K490 image processed with the iterative algorithm. C. Water-leaving radiance at 670 nm from the iterative algorithm.

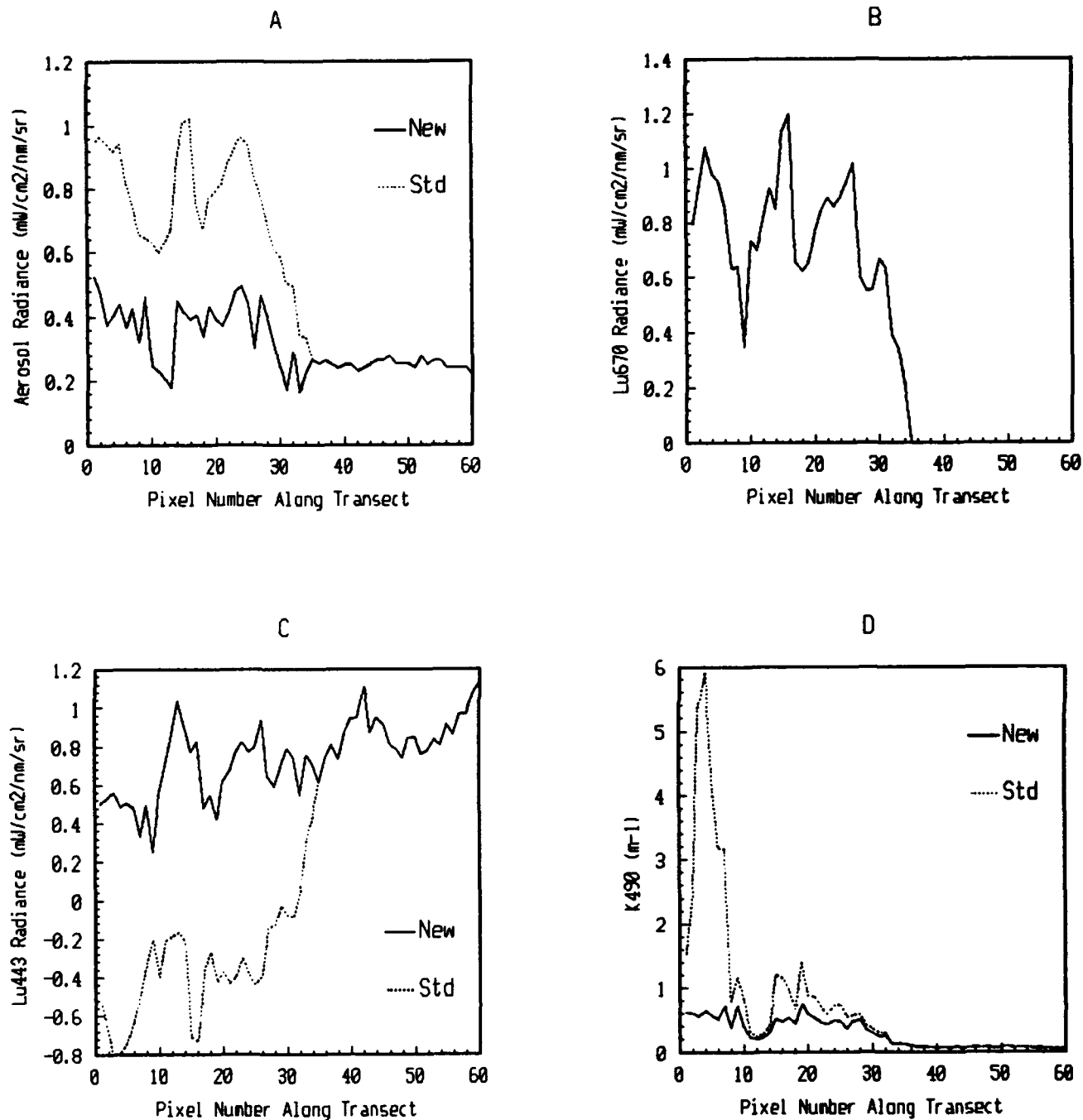


Figure 5. Comparison between standard (Gordon) processing and new iterative processing on CZCS image from October 8, 1979, for pixel values along a transect extending southwestward from Mobile Bay (see Figure 4B). Pixel #1 corresponds to the northern end of the transect. A. Aerosol radiance. B. L_{670} radiance (the solid line represents L_{670} from the iterative processing; there is no L_{670} estimated from the standard algorithm). C. L_{443} radiance. D. K_{490} estimate.

Plots of aerosol radiance, L_{670} , L_{443} , and K490 vs. distance along the transect out of Mobile Bay are presented in Figure 5 (the north end of the transect corresponds to pixel number 1 in the figures). ASCII data values along the transect were dumped from each of these four output image files to allow comparisons between the standard processing algorithm (Figure 4a) and the new iterative algorithm (Figure 4b). The dashed lines in each figure indicate results from the standard algorithm and the solid lines indicate the new results using the iterative approach. There are no differences in the results from approximately pixel number 35 to the end of the transect because iteration did not occur there (neither condition 1 nor condition 2 described in Section 4 was met).

In Figure 5a, notice that the iterative algorithm has successfully reduced the aerosol radiance in Mobile Bay at the northern end of the transect while maintaining the general shape of the curve. The partitioning of the 670 nm channel into aerosol and water-leaving radiance terms is shown in Figure 5b, where it is apparent that the reduction in aerosol radiation in Figure 5a corresponds to an increase in the L_{670} term.

The reduction in the aerosol radiance also translates into an increase in the 443 nm radiance (Figure 5c) and a decrease in the K490 estimates (Figure 5d). With the standard processing algorithm, unrealistically high K values over 5. m^{-1} were calculated. Also, negative 443 radiance values were calculated for the first 32 pixels along the transect (K values could still be calculated with the standard processing because a K1/K2 branching routine was employed so that the K490 value was derived from the 520/550 ratio); the iterative routine has increased these to positive values.

5. DISCUSSION

A statistical analysis of the various K models has been completed and the results are presented in Table 1. Although the recommended K1 and K2 models do not yield the lowest standard errors, we believe that the objective is not necessarily to achieve the "best fit" based on an error analysis, but to employ the models that have been tested most thoroughly in a variety of locations and were cast from the strongest physical foundation.

We suggest the continuing use of the Austin/Petzold K1 equation for consistency with past analyses. After normalization, the GOMEX-1 data fell very close to the Austin/Petzold line. We do not believe that the slight error reduction gained by utilizing the normalized GOMEX K1 equation justifies its use, as the Austin/Petzold relationship has proven robust in a variety of locations representing both Case I and Case II waters. The Mueller et al. K2 equation, however, was originally developed from a limited data set, does not fit the GOMEX data, and has not been adequately evaluated in other regions, so we recommend the normalized GOMEX K2 relationship (presented here as equation 8), with the caveat that additional validation is required in other areas. Although the non-normalized GOMEX K1 and K2 equations provide better fits to the GOMEX data (lower standard errors), it makes more physical sense to normalize the data to approximate the clear sky conditions required for satellite estimates even though we are introducing additional sources of error into the K calculation (errors in measuring E_d and in the estimation of F in Equation 2, Gordon¹²).

By implementing an iterative radiance algorithm in coastal areas and branching from the K1 equation to the K2 equation at K490 values greater than 0.16 m^{-1} , improved estimates of derived geophysical parameters have been obtained. The iterative algorithm is similar to ones developed by Mueller¹¹ and Smith and Wilson¹⁰, but with several differences. The M algorithm adjusts radiance estimates by iterating on chlorophyll relationships and the S/W algorithm iterates based on a relationship between the 443, 550, and 670 nm radiances. The algorithm presented here iterates on K490 relationships that have been specifically tested and tuned for the region where they are employed (the northern Gulf of Mexico). Also, the S/W algorithm does not handle negative initial radiance estimates in any channel and the M algorithm handles negative estimates in only the 443 channel; the algorithm presented here will iterate if any or all of the channels are negative. As with the M iterative algorithm, this algorithm tends to overestimate L_{670} in some cases, as evidenced by dark areas in several of the aerosol scenes.

Additional effects of the iterative procedure on radiance relationships are under further investigation and deserve mention. By iterating until the K1 and K2 estimates of K490 agree, we are forcing the radiance estimates into a pre-defined relationship (that was determined using *in situ* measurements collected under specific environmental conditions) and we are effectively removing the source of any deviation from this relationship. Our assumption is that the source of the deviation is an error in the aerosol radiance, but the deviations could be due to a variety of factors, including a spectral

component of bottom reflectance, absorption by CDOM, or scattering by coccoliths, if those factors differentially affect measured radiances in the 443, 520, 550, or 670 nm CZCS channels. Whatever the source, it is removed by adjusting the aerosol radiance and placing the "excess" radiance into the L_{w670} term.

Sources of error in the iterative algorithm include model error in the K1 and K2 relationships and errors associated with the conversion from K486 to K490 and the conversion from L_{w531} to L_{w520} . Future efforts to extend coastal CZCS estimates of K490 further inshore involve the development of a high-resolution land mask to apply over the data after processing all pixels as water. The current methodology is based on a threshold technique using the 750 nm channel as a land/water discriminator and frequently causes very turbid water pixels to be flagged as land pixels and excluded from processing.

6. SUMMARY

Regional algorithms relating subsurface upwelling radiances to K490 were developed using data from Case I and Case II waters in the northern Gulf of Mexico. The K1 relationship based on the 443/550 ratio was very similar to the historical relationship described by Austin and Petzold¹ if normalized radiances were used in the calculations. The K2 relationship based on the 520/550 ratio deviated significantly from the equation formulated by Mueller et al.⁷ (the comparison suffers somewhat, however, because the L_{w520} values used in the derivations presented here were not actually measured, but calculated from the L_{w531} measurements).

An iterative radiance algorithm that incorporates the Austin/Petzold K1 equation and the new K2 equation was developed in conjunction with a K-branching algorithm to improve CZCS estimates of water-leaving radiances in turbid coastal areas. The algorithm partitions the total radiance measured by the sensor at 670 nm into components related to aerosol path radiance and sediment reflectance (in addition to the Rayleigh scattering component), rather than neglecting the sediment contribution by assuming that L_{w670} is zero. The radiance estimates in the remaining CZCS channels are therefore increased (because less aerosol radiance is subtracted during the atmospheric correction of the data) and the derived geophysical parameters are reduced to realistic levels. In addition, satellite-derived K490 and pigment concentrations can now be calculated in areas where they were previously unretrievable (due to negative radiance estimate calculated with the standard processing routine).

7. ACKNOWLEDGEMENTS

The authors wish to acknowledge P. Martinolich and S. Oriol for helpful discussions and for their assistance with software development and image processing. J. Mueller graciously provided the MER radiance data collected during the GOMEX-1 cruise. This research was supported by the 6.2 MCM Coastal Optics Program, P.E. 0602435N, and the NRL 6.1 Upper Ocean Forced Dynamics Program, P.E. 0601153N.

8. REFERENCES

1. Austin, R.W. and T.J. Petzold, "The determination of the diffuse attenuation coefficient of sea water using the Coastal Zone Color Scanner," In *Oceanography from Space*, J.F.R. Gower, Ed., pp. 239-256, Plenum Press, New York, 1981.
2. Gordon, H.R., D.K. Clark, J.W. Brown, O.B. Brown, R.H. Evans, and W.W. Broenkow, "Phytoplankton pigment concentrations in the Middle Atlantic Bight: comparison of ship determinations and CZCS estimates," *Applied Optics*, Vol. 22, pp. 20-36, 1983.
3. Oriol, R.A., P.M. Martinolich and R.A. Arnone, "Development of an 800 meter bio-optical database from satellite ocean color for applications in coastal processes," In *Proceedings of the Second Thematic Conference on Remote Sensing for Marine and Coastal Environments*, Vol. 2, pp. 271-282, ERIM, Ann Arbor, MI, 1994.

4. Gould, R.W., R.A. Arnone and J.L. Mueller, "Optical relationships in Case II waters and their application to coastal processes and remote sensing algorithms," In *Proceedings of the Second Thematic Conference on Remote Sensing for Marine and Coastal Environments*, Vol. 2, pp. 283-294, ERIM, Ann Arbor, MI, 1994.
5. Mueller, J.L. and C.C. Trees, "Ocean optical properties measured during Naval Oceanographic Office cruise 330789," *CHORS Technical Memorandum No. 005-91*, 1991.
6. Austin, R.W. and T.J. Petzold, "Spectral dependence of the diffuse attenuation coefficient of light in ocean waters", In *Ocean Optics VII*, Proc. of SPIE, Vol. 489, pp. 168-178, Bellingham, WA, 1984.
7. Mueller, J.L., C.C. Trees and R.A. Arnone, "Evaluation of Coastal Zone Color Scanner diffuse attenuation coefficient algorithms for application to coastal waters," In *Ocean Optics X*, Proc. of SPIE, Vol. 1302, pp. 72-80, Bellingham, WA, 1990.
8. Mueller, J.L., "Coastal Ocean Optics Planning Applications of Ocean Color Remote Sensing: Atmospheric Corrections Error Estimates," *CHORS Technical Memorandum No. 006-93*, June 1993.
9. Neckel, H. and D. Labs, "Improved data of solar spectral irradiance from 0.33 to 1.25 μ ," *Solar Physics*, Vol. 74, pp. 231-249, 1981.
10. Smith, R.C. and W.H. Wilson, "Ship and satellite bio-optical research in the California Bight," In *Oceanography from Space*, J.F.R. Gower, Ed., pp. 281-294, Plenum Press, New York, 1981.
11. Mueller, J.L., "Effects of water reflectance at 670 nm on Coastal Zone Color Scanner (CZCS) aerosol radiance estimates off the coast of central California," In *Ocean Optics VII*, Proc. of SPIE, Vol. 489, pp. 179-186, Bellingham, WA, 1984.
12. Gordon, H.R., "Reduction of error introduced in the processing of coastal zone color scanner-type imagery resulting from sensor calibration and solar irradiance uncertainty," *Applied Optics*, Vol. 20, pp. 207-210, 1981.

Origin of the Kattegat waters

Niels Kristian Højerslev

The Niels Bohr Institute, Geophysical Department,
Haraldsgade 6, DK-2200 N, Copenhagen, Denmark

ABSTRACT

The Kattegat region forms a transition zone between the Baltic Sea and the North Sea. Baltic Sea water being brackish and high in yellow substance mixes with saline and dense North Sea water which are either low or high in yellow substance.

Yellow substance combined with salinity are most suitable for water mass classification in the region since the Baltic water is characterized by a low salinity in combination with a high yellow substance content, whereas the North sea waters originates either from the Atlantic having extremely high salinities and low yellow substance content or from the German Bight which has an intermediate to high salinity and a very high yellow substance content exceeding the one in the Baltic proper. Measurements of salinity and yellow substance in the Kattegat allow the construction of yellow substance/salinity diagram which serve the same purposes as the classical temperature/salinity diagram where the latter is not applicable in coastal areas. The yellow substance/salinity diagrams also permit discolouration studies resulting from mixing of Case 1 waters and Case 2 waters rich in yellow substance.

1. INTRODUCTION

Classical water mass classification is based on the following 3 concepts:

Water types,
Water masses, and
Conservative parameters.

Here, 3 different water types are defined based on 25 years of measurements done mainly by the author in the Baltic proper, the Belt Sea, the Sound, the Kattegat, the Skagerrak, off the Danish west coast, the Danish Wadden Sea, the German Bight, the Central North Sea, the Norwegian Sea and the North Atlantic.

A water mass is simply defined as a mixture being completely mixed with 2 or more water types. For the Kattegat it is assumed that all the water masses encountered here are resulting from mixing of at most the 3 water types listed in the above table. This assumption is justified to a high degree.

Conservative parameters are those describing a quantity which are neither produced or removed/consumed locally. One such example is salinity. In the classical salinity/temperature analysis temperature is also considered to be a conservative property but this is not so in say the upper 100 meters. Daylight penetration in the upper ocean produces sensible heat locally due to light absorption leading to increase in temperature. In other words: Classical T-S analysis is inappropriate in shelf mixing studies.

Yellow substance can however be considered to behave like a conservative property in shelf waters (*e.g.* Højerslev, 1988) because it is a very stable chemical mixture of humic and fulvic acids. In the Kattegat region mixing time scales are of the order of days - weeks so the assumption that yellow substance is conservative is absolutely justified. The small mixing time scales in the Kattegat imply moreover that yellow substance measured either in terms of light absorption or fluorescence become the same. This is contrasting in the Baltic where mixing time scales can be of the order of decades. Here, the fluorescence might even double with depth for constant light absorption (Højerslev, 1971, 1981, 1982 and 1988 for some details).

2. THEORY

Yellow substance is measured in terms of light absorbance in a spectrophotometer in a 10 cm cuvette *i.e.* A_{10} at 380 nm (actually from 280 nm to 900 nm). The unit for yellow substance is the light absorption coefficient, a_y (380 nm) m^{-1} or briefly, a_y . The following relation is valid:

$$a_y (380 \text{ nm}) = 23.3 \cdot A_{10} \text{ m}^{-1} \quad (1)$$

Selection of 380 nm allows full use of the of measured yellow substance encompassing the last 25 years. Assume now that a water mass has been sampled at a specific position and depth in the Kattegat region having the salinity/yellow substance characteristics (S , a_y). The following 3 equations can then be stated by combinations of the assumptions given in the Introduction as well as the water mass characteristics (S , a_y):

$$q_B + q_N + q_G = 1 \quad (2)$$

$$8 \cdot q_B + 35 \cdot q_N + 31 \cdot q_G = S \quad (3)$$

$$0.96 \cdot q_B + 0.07 \cdot q_N + 1.50 \cdot q_G = a_y \quad (4)$$

From measured i.e. known (S , a_y) it is possible to calculate the mixing fractions q_B , q_N and q_G in the Kattegat water mass and thereby the mixing of two Case 2 waters (Baltic and German, B + G) and a mixture of two Case 1 waters (Central North Sea and North Atlantic, N). The q -parameters represent a fraction per sample volume say, per litre. If, say the percentage of all German Bight water in the whole Kattegat region is asked for the bathymetry has to be known beforehand. The calculation is rather straight-forward and will not be dealt with here. It was only brought forward to stress the difference between the German Bight water fraction in a sample and in the region.

3. RESULTS

Salinity/yellow substance data pairs, (S , a_y) for October and March 1992 are depicted in Figs. 2 and 3. Small fluxes of German Bight water into the Kattegat are expected to be small during fall and high during spring. This is reflected in the 2 salinity/yellow substance diagrams.

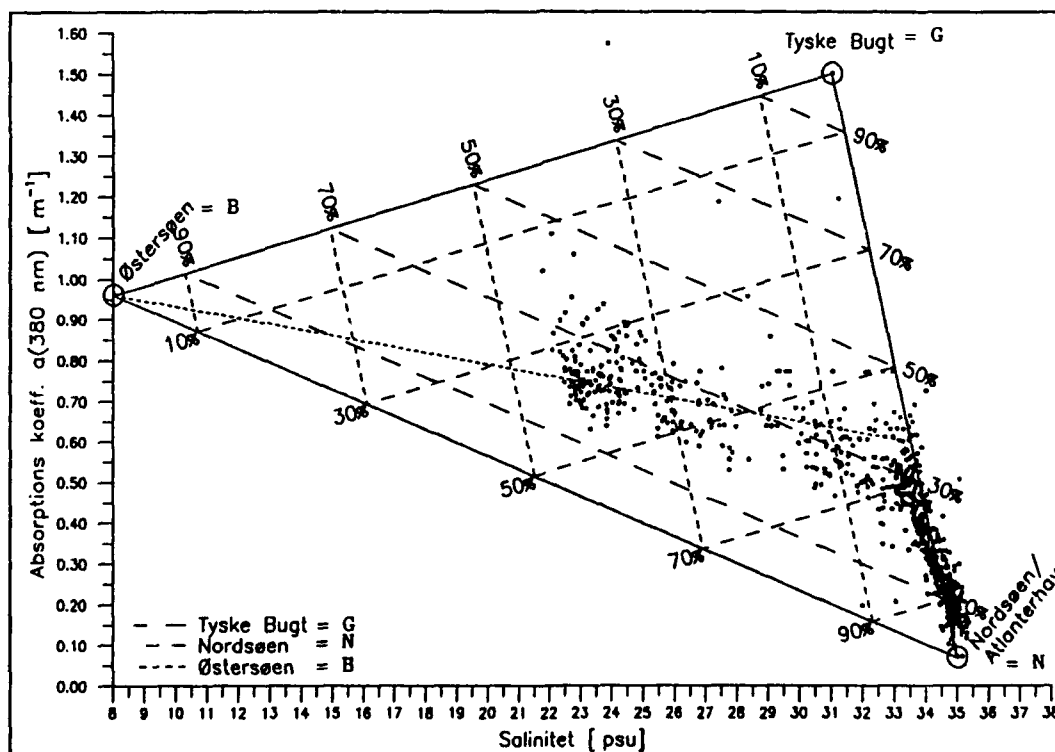


Fig. 2. Salinity/yellow substance diagram for October, 1992.

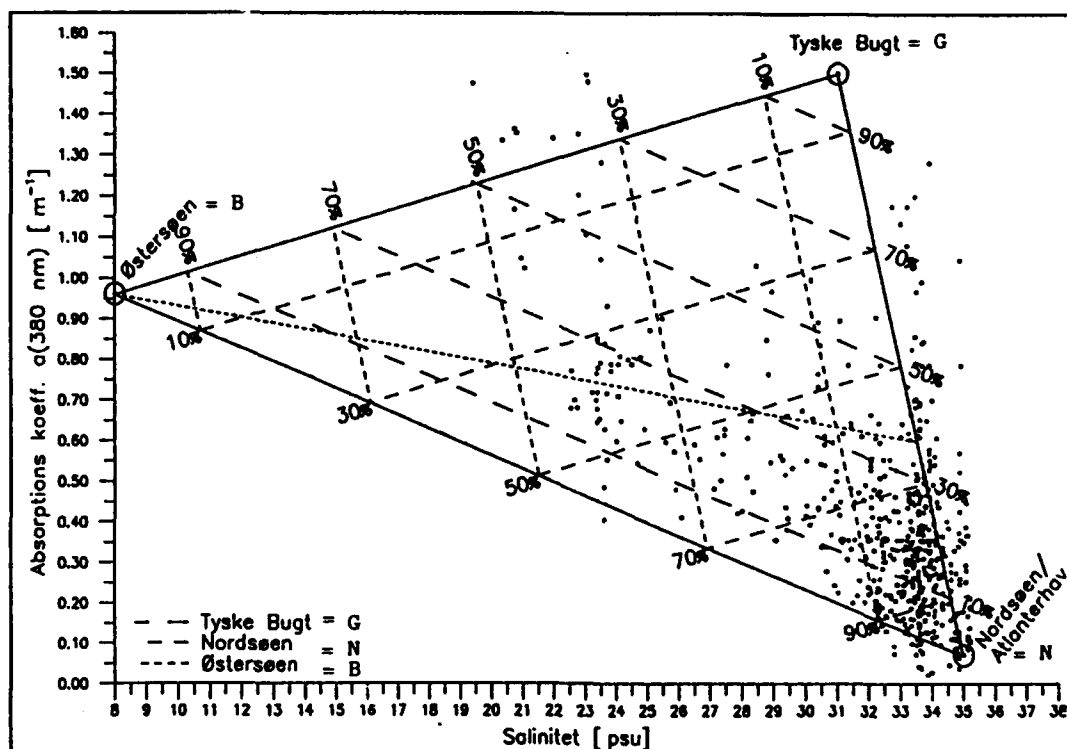


Fig. 3. Salinity/ yellow substance diagram for March, 1992

(S , a_y) has been sampled in one case along the section presented in Fig. 4 and q_B , q_N and q_G have been calculated by use of Eqs. (2), (3) and (4) as functions of depths.

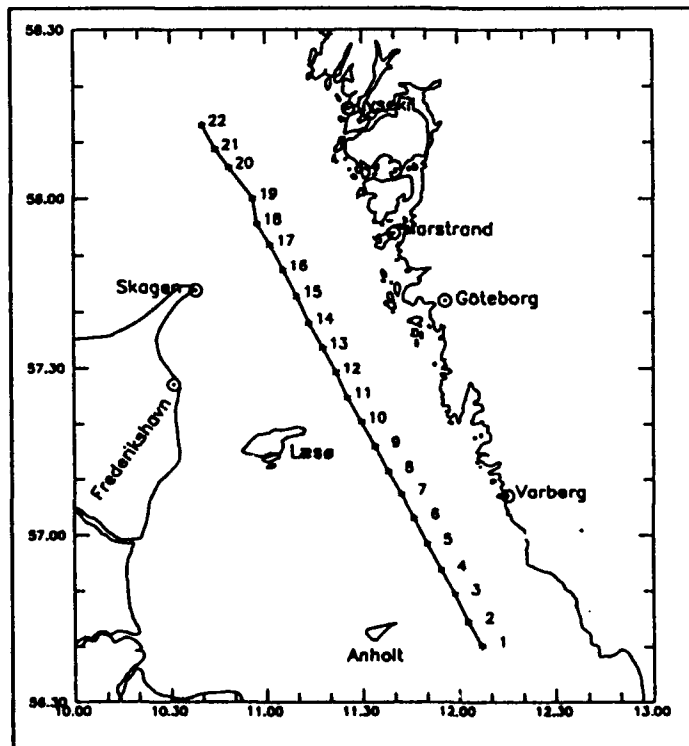
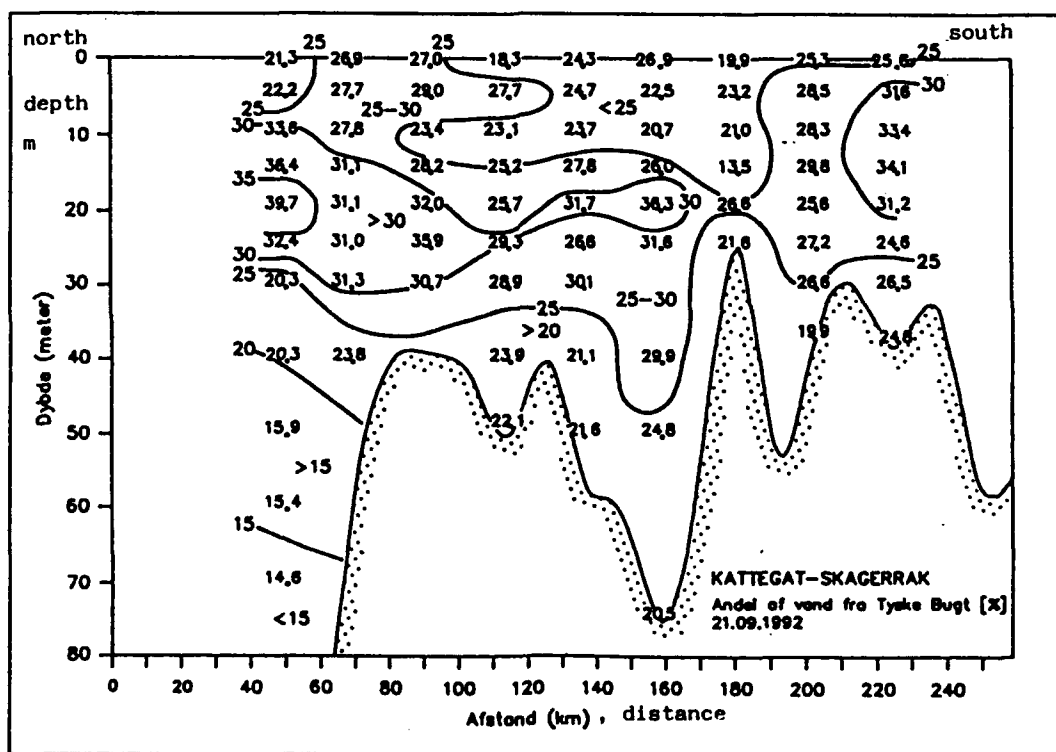


Fig. 4. Sampling section of salinity and yellow substance in the Kattegatt. Sampling depths: 0, 5, 10, 15, 20, 25, 30, 40, 50, 60 and 70 metres.

The results of these calculations are presented in Figs. 5, 6 and 7. As to be expected a large fraction ~ 80% of Central North Sea - North Atlantic water is intruding the deeper part of the Norwegian Trench to the northern part of the Kattegat. It was also expected to find a high fraction of brackish, light Baltic water in the Kattegat surface waters ~ 40%. What is unexpected however, is the fact that the fluxes of German Bight water into the region is not only rather small but also having maximum fractions q_G in the intermediate layers. This implies that the colour of the surface waters in the Kattegat is dominated by mixing of Baltic Case 2 water and Central North Sea - North Atlantic Case 1 water. This is of crucial importance for making interpretations of remote colour measurements over the Kattegat region.



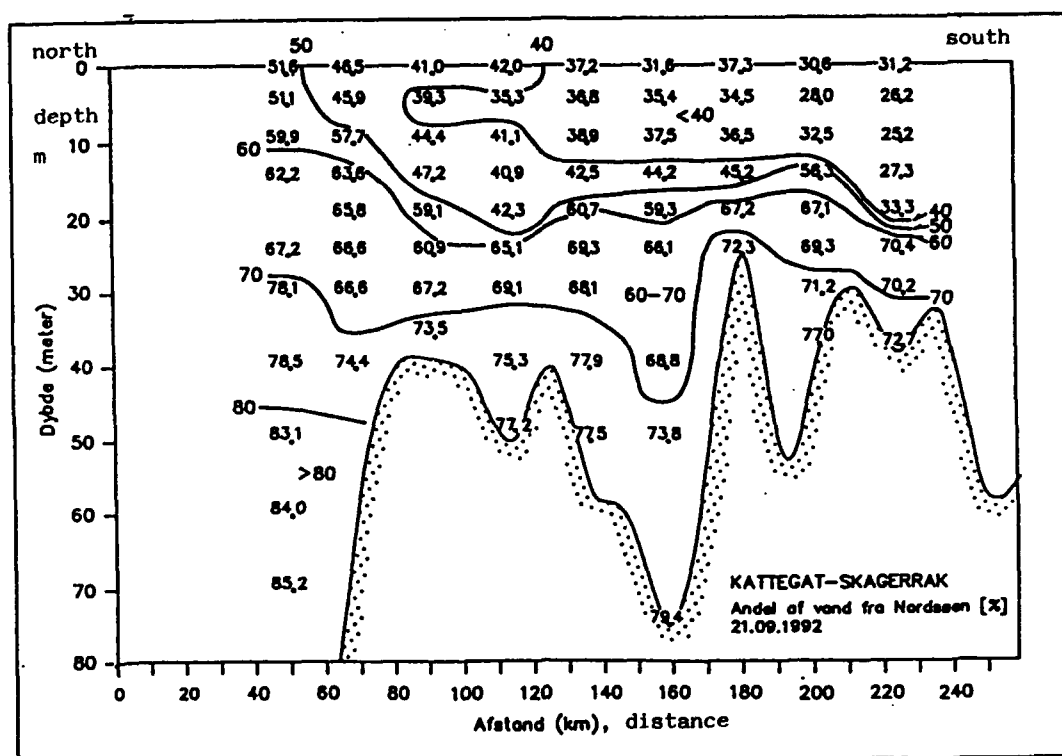


Fig. 6. $q_N \times 100\%$ versus depth for the section depicted in Fig. 4.

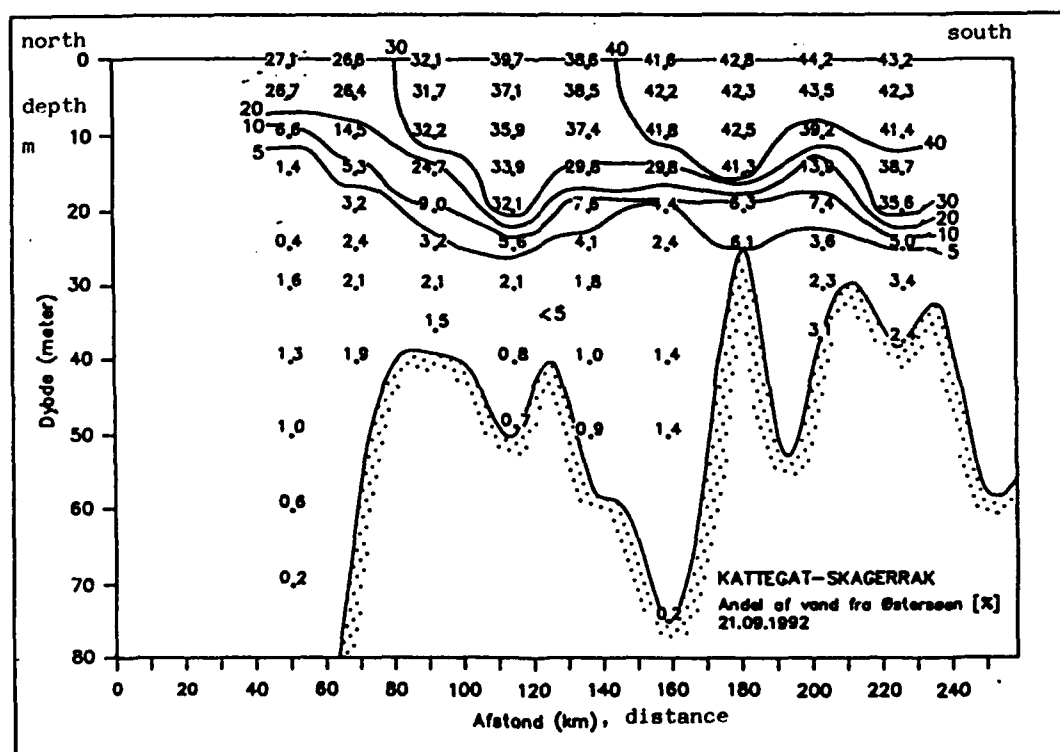


Fig. 7. $q_E \times 100\%$ versus depth for the section depicted in Fig. 4.

4. DISCUSSIONS

The water types from the Baltic Sea, Central North Sea - North Atlantic and the German Bight are represented by the 3 (S, a_y) - values $(8, 0.96)$, $(35, 0.07)$ and $(31, 1.50)$, respectively. If the assumption, that any kattegat water mass is formed by mixing of the above mentioned water types all (S, a_y) data pairs should stay within the two triangles in figs. 2 and 3. This condition is essentially fulfilled for the fall situation, Fig. 2 but not quite so for the spring situation, Fig. 3. It can thus be argued that the German Bight water type maybe should be defined as $(S, a_y) = (34.5, 1.80)$ instead of $(31, 1.50)$. Now, this would not be in accordance with common hydrographic practice. Here, it suffices to state that picking the $(34.5, 1.80)$ value leads only to minor changes in the statements concerning the Kattegat region and that the region then will be slightly less influenced by the "German Bight" water.

5. CONCLUSIONS

Yellow substance is a most suitable tracer in shelf waters combined with salinity. Both quantities in combination allow calculations of mixing ratios among other things which can be of real importance for making full use of passive remote sensing of sea surface colours.

Yellow substance is in addition a crucial quantity for inverting the spectral water leaving radiances into phytoplankton pigments like chlorophyll. Accordingly, yellow substance is one of the key parameters in colour studies of surface shelf waters.

6. ACKNOWLEDGEMENTS

This work is based on much efforts from crews and colleagues who all contributed both professionally and personally. My list is long but a few have been selected. Due thanks are given to Bo Lundgren and Henning Hundahl for many good years and cruises, to Thorkild Aarup, Niels Holt and not to forget, Nils Jerlov. Among the many fine research vessels, I have selected r/v Helland-Hansen, its crew and Captain Magnus Hauge for their outstanding guidance and assistance during the early years.

7. REFERENCES

1. N.K. Højerslev. "Tyndall and fluorescence measurements in Danish and Norwegian waters related to dynamical features", Rep. Inst. Phys. Oceanogr., Univ. Copenhagen, 16: 12 pp, 1971.
2. N.K. Højerslev. "Optical water mass classification in the Skagerrak and the Eastern North Sea", Proc.: The Norwegian Coastal Current Symp., Voss 1980, pp. 331-339, 1981.
3. N.K. Højerslev. "Yellow substance in the sea. The role of solar ultraviolet radiation in marine ecosystems. Ed.: J. Calkins. Plenum Press, New York and London, pp. 263-281, 1982.
4. N.K. Højerslev. "Natural occurrences and optical effects of Gelbstoff. Rep. Inst. Phys. Oceanogr., Univ. Copenhagen, 50. 30 pp., 1988.

Use of ERS-1 and Landsat imagery for monitoring coastal water properties and current circulation

Marius Necsoiu¹, Cora Braescu¹, Nicolaie Oprescu², Vasile Diaconu³, Mihai Burca⁴

¹Institute of Optoelectronics, Remote Sensing Department, Bucharest, Romania

²Technical University of Civil Engineering Bucharest, Romania

³Institute of Marine Research, Constanta, Romania

⁴Maritime Hydrographic Directorate of the Navy, Constanta, Romania

ABSTRACT

Imagery and digital tapes (CCT) from ERS-1 and Landsat, regarding the Black Sea coastal zone of Romania have been analysed with special emphasis on turbidity, current circulation, waste disposal plumes and convergent boundaries between different water masses. Landsat image radiances, were correlated with "in-situ" measurements of suspended sediment concentration.

Colour density slicing helped delineate the suspended sediment patterns more clearly and differentiate turbidity levels. A good correlation was found, sediment concentrations as function of depth, since the bands penetrate different depths, ranging from several meters to several centimetres, respectively.

The wind speed dependence of the microwave brightness temperature of the sea is interpreted primarily for small scale wave structure at wind speeds below 10m/s and from increasing coverage of sea foam at higher wind speeds.

1. INTRODUCTION

The advantages of remote sensing have been recognised, as being the only method that gives a good description over large areas. The aim of this study is to present preliminary results about correlation of information, prevailed from optical satellite data, with "in-situ" measurements, for monitoring of suspended sediment and of chlorophyll, using complementary multitemporal data (i.e. radar) to determine the range of hydro-meteo conditions under which dynamic features and current circulation can be observed.

Monitoring of suspended sediment has always been of great interest for the coastal geomorphologists, since it is fundamental for obtaining the solution of various problems, such as the sediment balance of enclosed bays, or simply the use of suspended sediment as a tracer for studying the circulation in the coastal and near-shore environments, that can be subsequently used for planning of waste disposal and for pollution monitoring.

From an ecological point of view, suspended matter and pigment concentration are

very important parameters. Both of these parameters play an important role in the process of primary production, whereas suspended matter is also a transportation medium for micropollutants.

The Landsat data, used for monitoring suspended matter and chlorophyll, was acquired on the 24 July 1975, in a period of heavy floods of the Danube river (fig.1).

For analysing the Landsat MSS data we used an automatic segmentation process that examines simultaneously taken images, coming from different spectral channels, performing a low-level data fusion.

Referring to the radar data, 3 ERS-1 C-band images, 2 at the ascendant and one at the descendant node, were collected. ERS-1 SAR has the potential for detection and monitoring of coastal processes, as demonstrated by studies acquired by Seasat SAR. Vesecky and Stewart (1982) report that SAR has the capability to detect features such as fronts, eddies, current shear and bathymetry, over a range of scales. The high resolution capabilities, combined with the available synoptic view, will improve our understanding of fine scale coastal processes, providing a method for monitoring meteorological effects.

The test area selected was at env. 80 km North of Constanta, which is partially included in the Danube Delta region (fig.2). The chosen area, with its specific ecosystem, inland lakes (Razelm, Sinoe), land and sea, was selected because of the available "in-situ" measurements.

2. DATA ANALYSIS

2.1. Landsat data

The segmentation step consists in dividing a sea area into regions that differ in terms of suspended matter. No a-priori knowledge is required about the sea conditions. The segmentation operator is based on a low-level data fusion.

The procedure consists of the following steps: first, a noise reduction is carried out (for each image) by applying a modal filter, which replaces the grey level of the current pixel with the most probable one in a mask of 7*7 pixels. Then, each image was locally analysed on square windows of predefined size (64*64 pixels). The grey level histogram was used to evaluate the local situation, without appreciable distortion caused by noise. The threshold technique applied for each image will separate regions, with different water masses.

After merging this set of small regions, the next step consists in creation of individual graphic planes, each plane (bitmap) covering a different type region (which was then assigned an only grey-value - fig.3). The contour of these zones was then drawn (using an edge detection filter), and superimposed on the original image.

To compare the results with the original data, channels 4 and 5 are displayed (fig.4,5), together with the contours of the homogeneous regions, detected by the segmentation process. For a correct visualisation, the grey levels have been distributed (stretched) in order to facilitate the interpretation by the human user.

2.1. ERS-1 SAR PRI data

As reference for ERS-1 image registration, the first data acquired at (27.04.1993) was

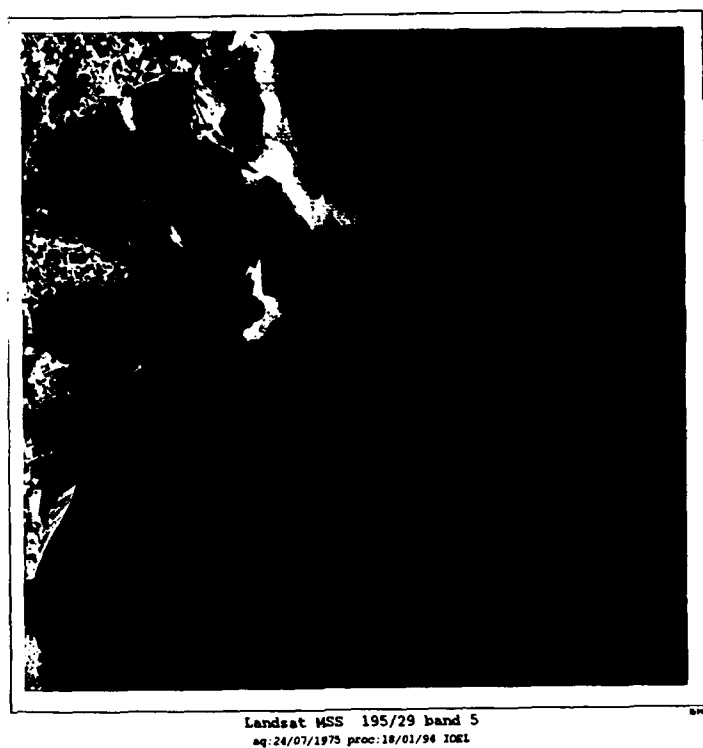


Fig.1. An overview of the Danube Delta and the coastal zone of the Black Sea.

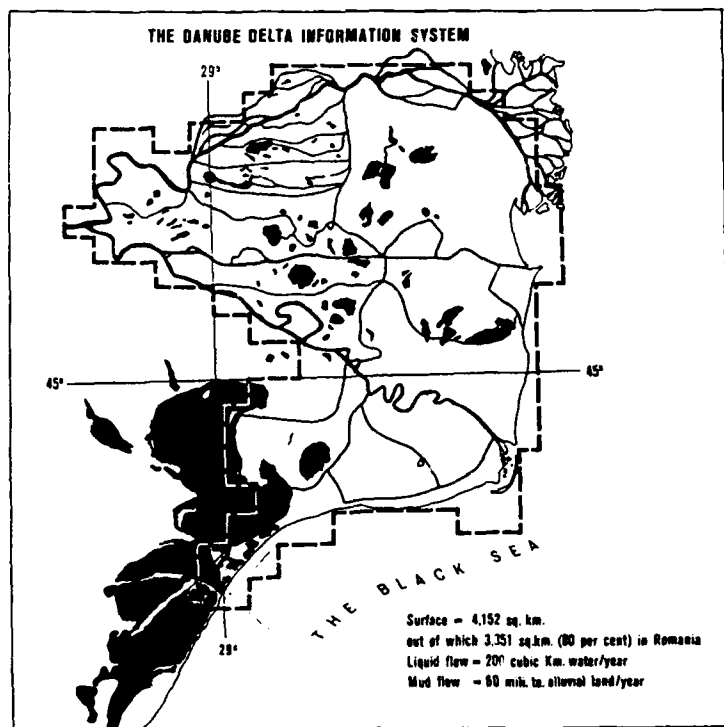


Fig.2. The test area, partially included in the Danube Delta region.

chosen (table 1). Since ERS-1 keeps a very stable orbit, with often less than 1000 meters latitudinal difference, images from repetitive orbit 891 were registered with few match points, by a relative shift of images.

A major problem is that the backscatter from the ocean surface is plagued with speckle. The multiplicative noise of SAR images causes difficulties to visual perception. Generally, the image variation is proportional to the backscatter coefficient. This implies that a proper filtering process is needed in a way that underlying geophysical signal, boundaries, linear features are preserved while removing the non-geophysical variance. The related to radar interference pattern test area is heterogeneous, due to presence of a complex ecosystem: land, coastal lakes, sea. Conventional filters such as Mean, Median Edge Enhancement do not account for the scene heterogeneity while adaptive filters, like Frost, do. Table 2 lists all the filters applied at the image acquired on 27.04.1993, with the corresponding overall results in statistics.

Table 1. Satellite data used

Sensor	Date of acquisition	Frame	Orbit
ERS-1 SAR	27.04.1993,2015	891	9320 ascendant
ERS-1 SAR	06.07.1993,2015	891	10322 ascendant
ERS-1 SAR	11.09.1993,0830	2709	11274 descendant

Table 2. Statistical parameters of original and filtered ERS-1 SAR PRI image
Dim 960 x 960 pixels area.

	Min.	Max.	Mean	o	Skewness*	Kurtosis*
Original data	0	1650	111	131	2.38	6.38
Mean filter 3 x 3	0	1243	110	123	2.06	4.04
Mean filter 5 x 5	0	1027	110	119	1.84	3
Mean filter 7 x 7	0	962	109	116	1.81	2.53
Median filter 3 x 3	0	1312	109	122	2.12	4.42
Median filter 5 x 5	0	1078	107	116	1.96	3.32
Median filter 7 x 7	0	963	106	113	1.88	2.83
Frost Adaptive 3 x 3	0	1530	111	123		

*) These 2 values are derived from comparing the distribution of the value to an ideal Gaussian "standard" distribution.

Skewness - when positive, the right side of the distribution curve is "steeper" than the left. When negative, the left side is "steeper".

Kurtosis - when positive, the data is more "spiky" than a standard distribution. When negative, the data is more broadly-distributed than a standard distribution.

As it is shown in table 2, the information on ocean backscatter appears to be contained in 11-bit range data. Hence compression of the data to 8-bit to assist data handling in terms of computer space and screen display need not involve a loss of dynamic range.

A more efficient computing method than the usual bit shift the data, losing some least and most significant bits is presented below. The input data (16 bit) was applied first a threshold technique, with the range:

$$(Z_{ij} - 2\sigma Z_{ij}, Z_{ij} + 2\sigma Z_{ij})$$

where Z_{ij} is the grey level of the observed SAR pixel. Then the data is furtherly shrinked to fit in 8-bit range.

The 8-bit images are studied either as full resolution scenes (960 x 960 pixels) or averaged over blocks of 3 x 3 pixels to provide synoptic view of an area. This improves the quality of data, reducing the speckle by averaging effectively multiplying the number of looks by 3.

Fig.6 shows 4 registered subsections (3 ERS-1 and 1 Landsat images) for 5 x 5 km (960 x 960 pixels) of land-sea zone near Portita and fig.7 histograms for ERS-1 27.04 and 06.07 scenes; the histogram of the ERS-1 11.09 is approximately in the same range and profile like the ERS-1 06.07 scene. Most relevant for detecting sea surfactants is the image acquired at 11.09.1993 in light winds (4 m/s), with wind direction from SW and the maximum deviation between wind and current direction about 20.

Table 3. In situ measurements for test area on ERS-1 SAR PRI images

Image	Orbit 9320	Frame 891	Orbit 10322	Frame 891	Orbit 11274	Frame 2709
Date	27.04.1993		06.07.1993		11.09.1993	
Wind direction	S		S		SW	
Wind speed	2		7		4	
Sea state	2		3		2	
Sea visibility	5		5		1	
Land visibility	15		15		0,5	
Air temperature	11,7		20,6		15,3	
Sea temperature	9,2		16,3		18,1	

This images prove the ability of SAR to detect fronts over a range of wind conditions. Close inspection of tones in vegetated area shows differences in coastal vegetation patterns. Lakes reflectivity is clearly different than the sea reflectivity in some portions.

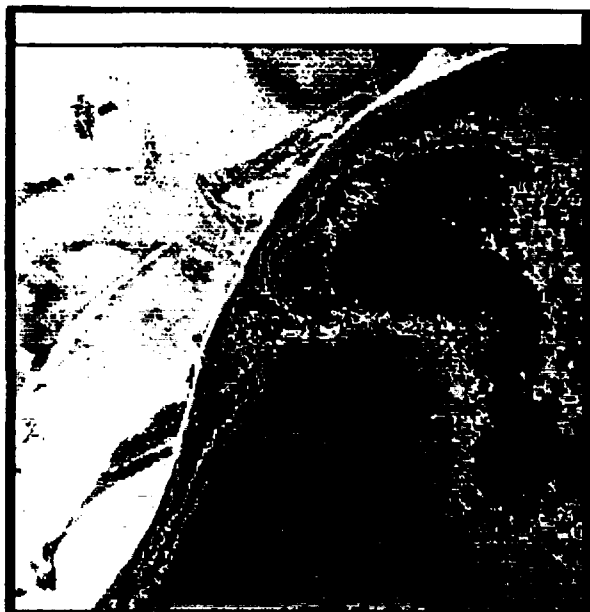


Fig.3.

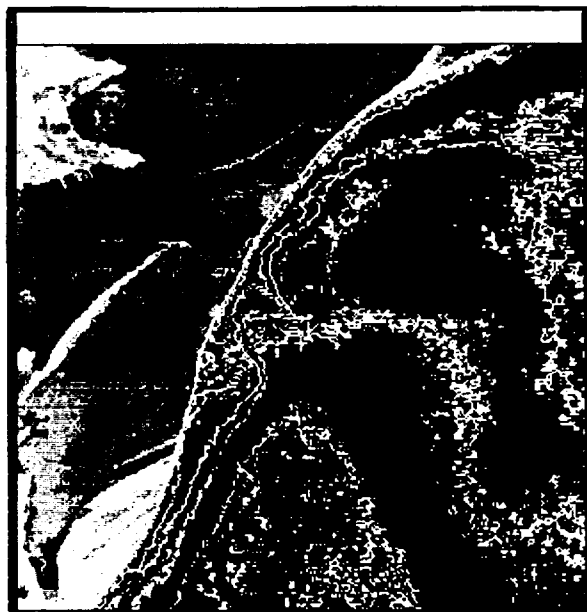


Fig.4.



Fig.5.

Fig.3. Bitmaps covering different water type regions.

Figs.4-5. Region contours superimposed on original images (MSS 4,5).

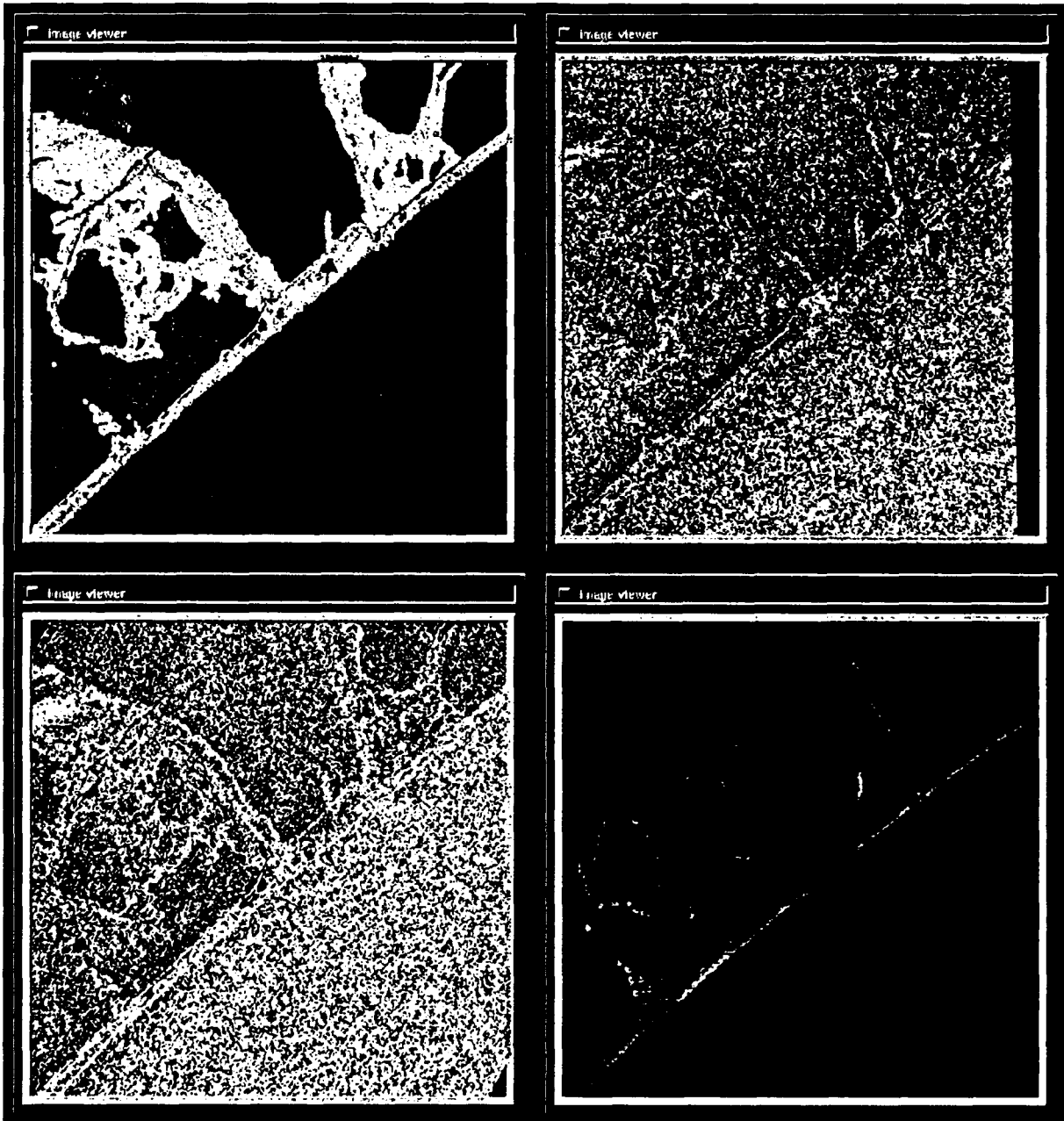


Fig. 6. 4 registered subsections (3 ERS-1 and 1 Landsat) of a land-sea zone, included in the test area.

3. DISCUSSIONS

3.1. Landsat data

In the processed Landsat images, two sources of continental contributions of sediments are clearly visible: one (centre left of the image) includes the gateway between the inland lake Sinoe and the Black Sea and the other one (top right) corresponds to the sediment discharges and dispersion regime, in the sea region of the Danube Mouths.

The processed image reveals a good consistency with the "in-situ" measurements (table 4). The measurements were taken on 3 profiles, env. parallel to the shore line, using 2 fixed reference points; the coordinates (X,Y) are relative to one of these points. In consequence, the analysis of the obtained results, corroborated with the terrain measurements, led us to the following conclusions:

Table 4: Data obtained by "in-situ" measurements, on the test area
(TSM = Total Suspended Matter; ISM = Inorganic Suspended Matter; OSM = Organic Suspended Matter)

X	Y	T.S.M. g/m ³	I.S.M. g/m ³	O.S.M. g/m ³
205.0	417.2	15.6	5.0	10.6
227.0	249.7	22.0	9.4	12.6
240.6	122.1	11.2	3.8	7.4
243.6	22.1	17.4	7.4	10.0
244.0	-94.7	12.4	4.4	8.0
298.1	-129.6	13.6	5.8	7.8
286.7	-23.7	12.2	3.6	8.6
267.2	123.1	13.2	4.6	8.6
246.9	233.3	15.4	6.2	9.2
280.4	362.0	20.6	8.6	12.0
460.8	440.9	15.0	6.2	8.8
436.3	269.0	11.8	2.6	9.2
427.2	109.3	17.8	9.0	8.8
409.2	-16.0	8.8	1.4	7.4
388.2	-156.5	14.0	3.6	10.4

- in the merging region, the suspended matter concentration, which varied from a few mg/l to tenths of mg/l, in the 4 and 5 spectral bands have reflectances (seen as different grey level values) between 28-17 and respective between 24-13 (grey level values are comprised between 0-255).

- in the 6 spectral band, the merging zone is not as evident as in the 5 and 4 bands; along the shore line, till the end of the image, there are relative high reflectance values areas (10-16) on the background of the sea water (6-7), indicating the presence of high quantities of chlorophyll.

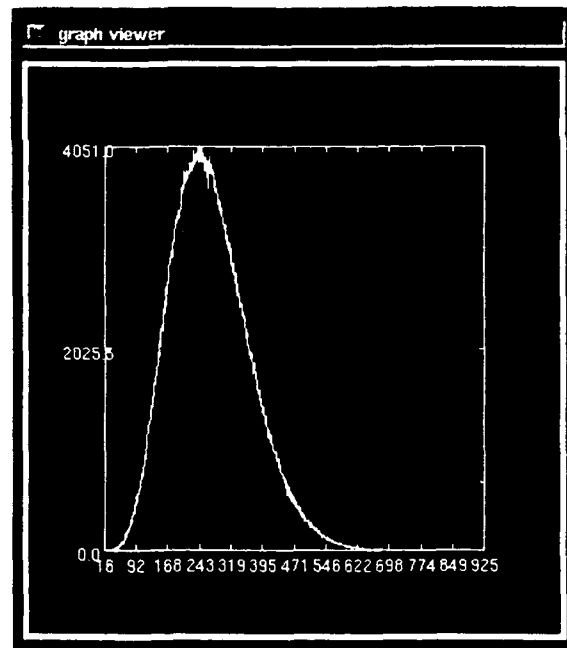
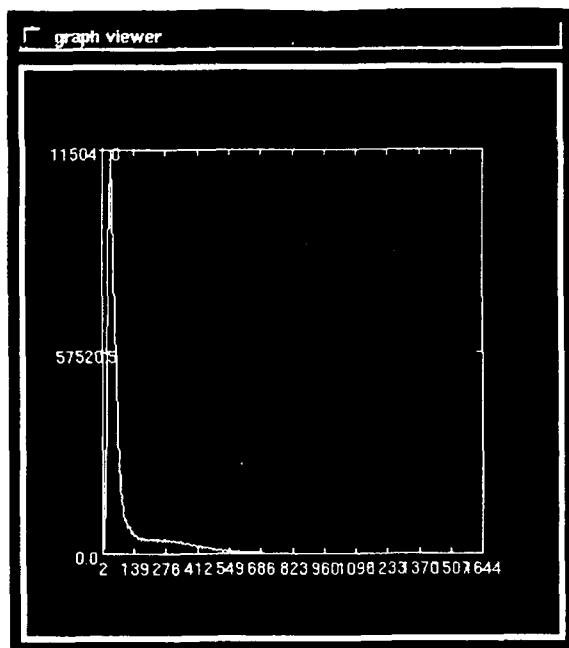


Fig.7. Histograms for the ERS-1 SAR.PRI images, acquired on 27.04.1993 and 06.07.1993.



Fig.8. Small scale turbulence, near Portita.

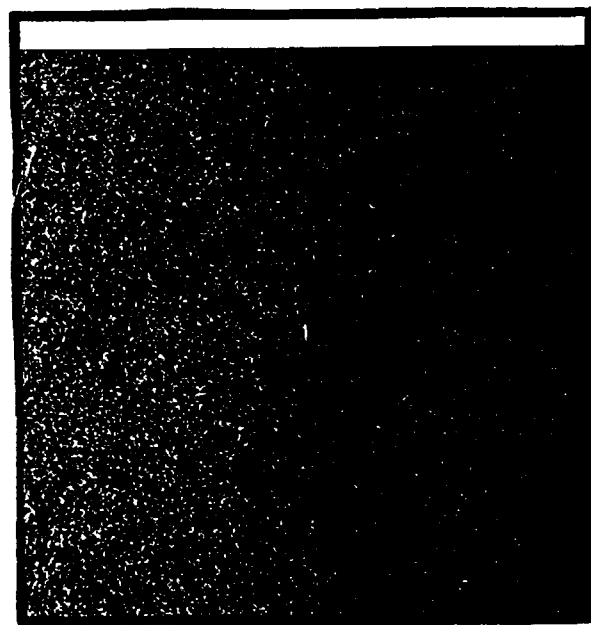


Fig.9. Surface slicks, observed on the 11.09.1993 SAR.PRI image.

3.2 ERS-1 SAR PRI data

Typical expressions of mesoscale upper ocean current features in radar images can be characterised by two types, eddies (including jets and vortex pairs) and ocean current fronts. These expressions are caused by the surfactants, short wave-current interaction along shear and convergence dominated frontal boundaries, and rapid shifts in the surface wind stress connected with strong ocean thermal fronts.^{5,6} Eddies are usually manifested in SAR images through wave-current interaction outlining the curved shape of the eddy or indirectly through the presence of surfactants.

In fig.8 the SAR image obtained near Portita shows a small scale turbulence aligned in the direction of the larger scale eddy orbital motion. The spiralling lines suggest convergence towards the eddy centre. Indications of convergence suggest that this cyclonic eddy may be important for the distribution and concentration of chlorophyll a, algae. The turbulence, in turn, leads to convective motion in the water that can bring organic material present in the upper layer of natural surface film.⁴ In addition, the film edge may reflect the short waves that propagate oblique angles to the edge, thus limiting the advance of short wave roughness through the slick covered region.

The image acquired on 11.09.93 gives us also the possibility to visualise sand waves dominated by slicks on the slightly roughened sea surface (fig.9). The observations of bottom topography with imaging radar is widely known after the SEASAT mission in 1978. Since 1984, Alpers and Henning have noted that this surprising imaging mechanism consists of three steps:

- interaction between flow and bottom topography which causes variations in the surface current velocity;
- variations in the surface current velocity give rise to modulations in the water wave spectrum;
- modulation in the wave spectrum show up as spatial variation in radar backscatter. Now this theory is generally accepted.

The decrease in velocity and therefore convergence of some small surface waves produces the bright return and viceversa. With the exception of high wind conditions the main bathymetric features in the region are regularly detected as a bright/dark signature.

However, in the case of SAR imaging, in addition to the above mentioned amplitude or cross-section modulation, phase modulation may also contribute to the imaging. The surfactants are presumably related to biological productivity in the sea. For them, to concentrate at the surface and to make visible slicks, there is both an upper and lower wind speed limit. At a too low wind speed, the surface will be too smooth for the SAR to measure a return signal whether surfactants are present or not. At a too high wind speed, roughness due to dominances over that due to the surfactant, and patterns due to wave-induced circulation replace those due to the large scale patterns.

4. CONCLUSIONS

The intention of this study is to find the best methods for investigating the specific

features of the coastal zones of the Black Sea. Unfortunately the quantity of "in-situ" data correlated with the optical satellites Landsat MSS and TM was poor. However, the image acquired on the 24 July 1975 shows a good correlation between the "in-situ" measurements and the reflectivity. In future, to obtain quantitative maps, a large quantity of "in-situ" measurements are required in order to correlate the data on the composition and size of suspended sediment with the spectral response of the MSS (4,5) and TM (1,2) channels.

About the ERS-1 SAR images, they were acquired in 1993, at the ascendant and descendant nodes, and demonstrate the ability of the SAR to repeatedly detect both small and large (kilometres) scale features, under variable wind condition. In addition, observation of swell and coastal refraction patterns may provide useful input for modelling the beach processes.

Images acquired at 27.04.93 and 11.09.93 (wind speed less than 4 m/s) shows excellent perturbation on the slightly roughened sea surface.

There is no doubt that ERS-1 SAR data will open up interesting new opportunities for the scientific study of complex coastal sea dynamical processes and lead the way for operational monitoring by satellite SAR for coastal management purposes.

5. ACKNOWLEDGEMENTS

We would like to acknowledge the contributions made by the team from Remote Sensing Department, IOEL about possibilities and limitations of the technique available.

We are very grateful to dr. Vincenzo Beruti, from ESA-ESRIN for providing the ERS-1 SAR images.

6. REFERENCES

1. V.DaMolo, et.al, "Monitoring of coastal water quality through integration between "in situ" measurements and remote sensing data", *Proceedings of the 9-th Earsel Symposium*, Espoo - Finland, 1989.
2. J.F.Vesecky, R.M.Stewart, "The observation of ocean surface phenomena using imagery from Seasat synthetic aperture radar", *Journal of Geophysical Research*, 87,1982.
3. W.Alpers, I.Hennings, "A theory of the imaging mechanism of underwater bottom topography by real and synthetic aperture radar", *Journal of Geophysical Research* 89,1984.
4. J.F.Vesecky, E.S.Kasischke and R.A.Shchuman, "Marine microlayer effects in the observations of internal waves by SAR", *ERIM research report to DARPA*, 65,1988.
5. J.A. Johannessen et al. "Detection of surface current features with ERS-1 SAR", *Proceedings of the Second ERS-1 Symposium*, ESA Publishing Division, ESA SP-361, October, 1994.
6. J.A. Johannesen et al. "Coastal ocean studies with ERS-1 SAR during NORCSEX'91", *Proceedings of the Second ERS-1 Symposium*, ESA Publishing Division, ESA SP-359, February, 1993.

Investigation of the geochemistry of dissolved organic matter in coastal waters using optical properties

Paula G. Coble and M. Michele Brophy

University of South Florida, Department of Marine Science
140 Seventh Avenue South, St. Petersburg, FL 33701-5016

ABSTRACT

Naturally-occurring dissolved organic matter (DOM) is a major component of ocean color signatures, especially in coastal transition zones. Accurate characterization of DOM optical properties is crucial for accurate measurement of chlorophyll from remotely-sensed color data and for modelling spectral light penetration in the ocean. Correlation between optical properties and concentration of DOM could potentially be exploited to evaluate dissolved versus particulate carbon fluxes on a global scale.

Determination of DOM optical properties is made difficult by low absorption coefficients and by generally featureless absorption spectra. In coastal areas, changes in the humic acid: fulvic acid ratio of gelbstoff from riverine to marine environments cause significant changes in the spectral slope parameter but are difficult to predict a priori and impossible to measure without extracting gelbstoff from seawater. Fluorescence is orders of magnitude more sensitive than absorption and can be used to distinguish between gelbstoff from terrestrial and marine sources without preconcentration of water samples.

Our recent results from a wide variety of natural waters show that DOM optical properties are a function of physical, chemical, and biological processes. Detailed fluorescence spectroscopy shows changes in the optical properties of gelbstoff related to the onset of marine productivity in coastal transition zones which are indicative of changes in chemical composition of DOM. The magnitude of observed changes in optical properties caused by production of new marine gelbstoff and its subsequent transformation not only effects spectral absorption and reflectance in seawater but also can provide important geochemical information on carbon cycling in the ocean. In this paper, we will discuss our efforts to use fluorescence to aid interpretation of variability in gelbstoff spectral slopes for development of next generation chlorophyll algorithms and for development of an optical tracer of geochemical processes involving dissolved organic carbon (DOC).

2. INTRODUCTION

Colored DOM (CDOM) in natural waters is responsible for the blue fluorescence of seawater,¹ and has been called fulvic acid,² gelbstoff or yellow stuff,³ and aquatic humus.⁴ Many articles have been written on the chemical properties and structure,^{2,5-12} optical properties,¹³⁻¹⁷ distribution in natural waters,^{13,18-19} and problems in the measurement of gelbstoff and humic substance,²⁰⁻²⁴ including numerous review volumes.²⁵⁻²⁶ In the last ten years, satellites and LIDAR have also been used to detect gelbstoff.²⁷⁻³¹

Gelbstoff is thought to comprise 25% of the total dissolved organic carbon (DOC) pool in the ocean,³²⁻³³ although the amount of DOC that is fluorescent has been estimated at 20-70%.³⁴⁻³⁵ The major source of gelbstoff in coastal regions of the ocean is from river runoff of terrestrially-derived humic and fulvic acids. Marine humic substances away from continental margins have a distinctly different chemical structure and origin as determined by ¹³C-NMR,¹ H-NMR and other spectroscopic methods,^{6,36} elemental analysis, stable isotope analysis, radiocarbon content, and biomarker content.^{8,37} Terrestrial humic substances are more aromatic and have higher C:N and H:C ratios than do marine humic substances, and many possible structures have been proposed.^{5,10,38-42} Marine humic material is thought to be derived from decomposition products of marine organisms, either directly as unutilized macromolecules,⁴³ or indirectly by condensation of smaller, non-fluorescent compounds.¹³ Although humic substances in freshwater and seawater have dissimilar sources and differ chemically, previous reports of similarities and differences in optical properties have been

contradictory in many cases. Discrepancies in measurements may be due to comparison of measurements from different regions of the spectrum, failure to correct for differences in instrumental configuration, interdependence of excitation and emission spectra, or inherent differences in the fluorescence properties of DOM from different sources.

Interest in gelbstoff measurements is driven by two major goals. The first is to understand and correct for gelbstoff interference in estimates of chlorophyll concentrations derived from ocean color measurements. In areas where gelbstoff concentrations are high, as in coastal regions, much of the absorbance in the blue region is due to DOM and not chlorophyll,^{28,44-48} and gelbstoff fluorescence can be a significant component of the upwelled radiance in waters containing low amounts of chlorophyll.⁴⁹⁻⁵⁰

The second major goal is to use gelbstoff concentrations to estimate the role of DOC in the global carbon budget. Fluorescence of CDOM is a useful indicator of DOC transport from rivers to oceans,⁵¹⁻⁵⁴ from sediment porewaters to overlying bottom waters,⁵⁵ and possibly of new DOC from the euphotic zone to deepwater. It is also an indicator of potential photochemical reaction rate for some compounds.⁵⁶ The effects of these processes on gelbstoff concentrations and optical properties have not been investigated.

Since fluorescence of gelbstoff in natural waters is more easily and conveniently measured than absorbance, fluorescence has been extensively used in regions where gelbstoff concentrations are very low. Moreover, a very high degree of correlation between gelbstoff fluorescence and absorbance have been shown.^{31,57} Recent improvements in fluorescence spectroscopy, including laser excitation sources, highly sensitive multichannel detectors, and rapid-scan monochromators, make collection of high resolution natural fluorescence data possible within a few minutes.⁵⁸⁻⁵⁹ Application of these techniques to the study of seawater DOM has demonstrated that optical properties can be used to distinguish between water masses from various sources.⁶⁰⁻⁶¹

This paper is intended partially as a review of the optical properties of gelbstoff and partially as an illustration of new insights gained when one uses a broader window for observation of those optical properties. Specific examples obtained by extending absorbance and fluorescence measurements into the UV range and by using multiple excitation wavelengths to observe fluorescence spectra will be presented. The focus will be on how the optical properties of CDOM vary spatially in coastal regions, what they reveal about the chemical composition of gelbstoff, and which are most useful for discerning the geochemistry of DOM in the oceans.

3. METHODS

Water samples were collected at 28 stations in the northwestern Gulf of Mexico between the Mississippi River outflow and the mouth of Tampa Bay. Samples from all locations were filtered through GF/F (Whatman) filters and stored frozen for up to four months prior to analysis. Excitation-emission matrix spectroscopy was performed using a SPEX Fluorolog II using a previously described method.⁶² Absorbance was measured versus MilliQ (Millipore) water in 10 cm quartz cuvettes on a Hitachi UV3300. All absorbance spectra were corrected for scattering by subtracting the absorbance value at 700nm.

4. OPTICAL PROPERTIES

The general optical properties of gelbstoff have been known for many years. It is yellow in color and emits a blue fluorescence when excited by near UV light. Absorption coefficients increase exponentially from visible to UV wavelengths. Measurement of absorption coefficients in seawater are difficult without a long path spectrophotometer, and corrections must be made for errors due to scatter.¹⁵ Measurement of fluorescence has suffered from difficulties in correcting for errors due to absorption by optical components of different instruments. Measurements of both types have rarely been made at wavelengths shorter than 350 nm, where much of the CDOM optical signal is located, and even more rare are studies in which all the relevant optical parameters have been measured on the same samples. The parameters of interest include: absorption coefficient from 250 nm to 700 nm, fluorescence intensity, excitation maximum ($E_{x_{max}}$), emission maximum ($E_{m_{max}}$), and fluorescence efficiency, which is the ratio of fluorescence to absorption (F/a).

4.1 Gelbstoff absorption coefficients and spectral slope.

Typical absorption spectra for gelbstoff from a coastal region are shown in Figure 1 for samples collected in the Gulf of Mexico. Stations 1 and 2 were in the plume from the Mississippi River and the other stations were farther offshore in the clear, oligotrophic waters of the Gulf Loop Current. As expected, absorption coefficients decrease in the offshore direction. Values for the coefficients are within the range of published values for other areas.^{15,17} The natural logarithm transformation is more effective at linearization of data from highly absorbing samples than from "bluewater" samples.

Least squares regression fits of the log transformed absorption data versus wavelength generate a slope parameter, S , which has been used to extrapolate gelbstoff absorption measurements from the UV to the visible range,¹⁵ and to compare optical properties of aquatic humic substances from different natural waters.¹⁴ The spectral slope factor of gelbstoff absorbance was initially shown to be independent of water mass type between 375-500 nm.¹⁵ However, it has recently been shown that S is both wavelength dependent and water mass type dependent when calculated over two shorter intervals, 370-440 and 440-565 nm. Spectral slope increases with decreasing wavelength of measurement and with increasing fulvic acid to humic acid ratio.¹⁷

Results from the Gulf of Mexico support both sets of previous results. Values of S were calculated over four wavelength intervals (Table 1). Spectral slopes in two of these ranges, 280-312 nm and 365-435 nm, are plotted as a function of CDOM fluorescence in Figure 2. Slopes for the UV range are much higher than for the blue range, and both sets of data show strong dependence of S on fluorescence intensity. Since fluorescence correlates highly with gelbstoff absorption coefficient, this result indicates a change in spectral slope with gelbstoff concentration. Wavelength dependence is minor for samples with high gelbstoff content, but changes exponentially as gelbstoff content decreases. What is surprising is the reversal in the sign of the concentration dependence. Spectral slopes calculated over intermediate wavelength ranges fall between these two extremes, with downward curvature between 365-404 nm and insignificant to slight upward curvature between 312-365 nm (Table 1).

Table 1. Spectral slopes of absorption coefficient calculated between different wavelength intervals using the equation: $a(\lambda) = a(\lambda_0) \exp [-S(\lambda - \lambda_0)]$, λ in nm.¹⁵ Data are from surface waters of the Gulf of Mexico. Number of observations equals 26 for each calculation, s.d. is standard deviation.

λ_0	λ	S	s.d.
280	312	0.0257	± 0.0056
312	365	0.0175	± 0.0018
365	404	0.0157	± 0.0025
404	436	0.0146	± 0.0031
365	436	0.0151	± 0.0027

The changes in S with gelbstoff concentration reflect the greater degree of curvature in the log-linear absorption data of "bluewater" samples shown in Figure 1. This feature has previously been attributed to UV oxidation of organic matter at the short visible wavelengths and to an increase in absorption due to inorganic constituents in open ocean waters.¹⁵ It has been shown recently that the photobleaching rate and the rate of production of low molecular weight organic compounds are proportional to the absorption coefficient for gelbstoff.⁵⁶ The effects of radiation below 312 nm are mitigated by strong absorbance of these wavelengths by water molecules. Selective photodegradation of gelbstoff components which absorb in the blue range of the visible spectrum and concomitant production of new, lower molecular weight compounds which absorb most strongly in the UV may explain the observed curvature of the open ocean samples.

The observed changes in S could also be caused by the production of new organic material by biological activity. Compounds such as proteins, amino acids, and carbohydrates all absorb more strongly in the UV than in the visible

range. Evidence for a diurnal cycle in UV-absorbing compounds from the equatorial Pacific Ocean supports this possibility (Coble, unpublished). For the Gulf of Mexico data discussed in this paper, chlorophyll values were very low in the offshore, low gelbstoff samples, so photodegradation is a more likely explanation. However, these data indicate that the spectral slope of gelbstoff absorption in the UV range may provide a useful indicator of extent of photodegradation versus other geochemical processes. Such processes include dilution between freshwater and seawater which would be expected to decrease gelbstoff absorption without changing S, and biological activity which would change both S and gelbstoff concentration.

4.2 Fluorescence properties

Gelbstoff is also fluorescent, with emission peaks at 420–450 nm from excitation at 220–250 and 320–350 nm.^{61,63,64} The detailed spectral excitation and emission information obtained using high resolution fluorescence spectroscopy,^{61,62} provides a more complete view of optical properties and chemical composition of aquatic humic substances than measurements of a single excitation and emission spectrum. In this technique, emission spectra are measured between 270 and 710 nm at forty separate excitation wavelengths between 260 and 455 nm, generating an excitation-emission matrix (EEM). Excitation and emission maxima can be independently determined from these EEMs. Furthermore, absorption coefficients at each excitation wavelength can be used to generate relative fluorescence efficiencies over the entire matrix. The biggest advantage to the technique, however, is that it is sensitive enough so that no preconcentration or extraction of CDOM from seawater is necessary, thus eliminating the potential for chemical alteration or selective retention of certain components which hamper other techniques used for CDOM measurement and characterization.

Figure 3 shows EEMs from a pure solution of quinine bisulfate and from a typical coastal water sample. Both topographic and three-dimensional views are shown to better illustrate both relative intensities and location of maxima. The excitation spectrum of a pure compound, when properly corrected,^{63,65} should be the same as the absorption spectrum.⁶⁶ The shape and position of the emission maximum is usually independent of excitation wavelength, with only its intensity variable. Likewise, the position and shape of excitation maximum is independent of the wavelength at which emission is monitored. This results in round contours in a topographic view of an EEM for a simple, single fluorophore such as quinine bisulfate (Fig. 3, left). Notice that quinine sulfate has a second fluorescence maximum from UV excitation at 260 nm. The actual maximum is beyond the lower excitation limit for this EEM, however the fact that emission maximum occurs at the same wavelength, 450 nm, for both excitation maxima indicates that both peaks are due to the same fluorophore.

The EEM for the naturally-occurring aquatic humic material, taken from the Columbia River Estuary, differs from the quinine bisulfate EEM in several respects. The fluorescence maximum in the region of 340/430 nm, which has been used for most previous measurements of gelbstoff fluorescence, shows an elongated fluorescence maximum in topographic view (peak C in Fig. 3). The position of the emission maximum shifted towards the red as light of successively longer wavelength is used for excitation. This is indicative of a mixture of fluorescent compounds, or the presence of a complex fluorophore in which energy can be transferred internally, and is consistent with conclusions from chemical analyses that aquatic humic substances are chemically complex and difficult to characterize. The peak at 260/450 (peak A) probably represents humic substances fluorescence at a second excitation wavelength, although the emission maximum for this peak is not always at the same wavelength as that at $Ex=340$ nm, and the relative intensity of the two peaks is also somewhat variable. Both of these observations suggest some variability in the composition and relative concentrations of the fluorophores responsible for these peaks in natural waters. The fact that gelbstoff excitation spectra have two maxima has largely been overlooked by previous studies, possibly because spectra have not been corrected.⁶⁵ An additional peak at $Ex/Em = 275/310$ (peak B) indicates that components other than aquatic humic substances are present in natural waters. The peak B maximum is located in the region where proteins and the amino acid tyrosine have fluorescence maxima,⁶⁶ although the chemical identity of this peak in natural waters has not yet been verified.

The positions of Ex_{max} and Em_{max} of gelbstoff fluorescence are other optical parameters of interest. Fluorescence and excitation maxima have been found to vary with observation wavelength not only within the EEM of a given sample, but also between samples of different origin, with Em_{max} for samples from offshore shifted towards the blue relative to Em_{max} for coastal samples.⁶⁷ Excitation maxima of marine samples are also blue-shifted relative to Ex_{max} for riverine

samples.⁶⁸ Variations in spectral shape could present problems when algorithms are dependent upon such factors as F_{\max} , peak width at half height,⁵⁰ and normalization to Raman peaks.²⁹ Variation in spectral shape is also indicative of a difference in chemical composition of the sample, with blue-shifted excitation and emission generally indicative of a higher relative proportion of lower molecular weight compounds.

An example of variability in Em_{\max} and spectral shape is shown in Figure 4 for samples from Rio Madeira (a tributary of the Amazon River) and from the coastal waters of the Gulf of Maine. At $Ex = 310$ nm, the variation in Em_{\max} is largest, with fluorescence maxima offset by as much as 40 nm. Spectral shapes are also different at $Ex = 310$ nm (Fig. 4A), with marine samples showing a greater amount of blue fluorescence and terrestrial samples showing more green fluorescence. At $Ex = 350$ nm (Fig. 4B), the Em_{\max} appear to be only slightly offset, but the freshwater Rio Madeira sample still has more long wavelength fluorescence. At $Ex = 430$ nm (Fig. 4C), spectral shape and position of Em_{\max} are the same for both samples. These results may explain the apparent discrepancy in previous studies as to whether or not there was a difference in Em_{\max} for different natural waters. The position of the Em_{\max} is dependent on choice of excitation wavelength, and measurements at a single excitation cannot be extrapolated to other wavelengths. Excitation maxima also occur at slightly shorter wavelengths for marine samples than for riverine samples, making it impossible to quantify either of these parameters without using some type of multispectral fluorescence technique.

The differences in Ex_{\max} and Em_{\max} also clearly demonstrate compositional changes in gelbstoff between nearshore and offshore regions. Although the cause of these differences is still poorly understood, measurement of optical parameters can be used to characterize the relative contribution of each type to CDOM of a given sample.

4.3 Fluorescence efficiency and estimation of absorption coefficient from fluorescence.

A high degree of correlation has been found between fluorescence and absorption coefficient in the regions studied thus far, but errors in retrieval of gelbstoff absorption coefficients can be as high as a factor of 2.^{31,48} Since estimates of fluorescence efficiencies of gelbstoff vary up to 2.5-fold for a wide range of water types,^{14,67,69} part of the error in estimation of absorption from fluorescence is due to variability in chemical composition rather than to measurement errors.

The data from the Gulf of Mexico (Fig. 5) are in agreement with these previous findings. The correlation coefficient for the relationship between absorption coefficient and fluorescence for the entire data set is $r=0.97$. Estimates of errors in absorption coefficient range from 10% at high values to 60% at low values of absorption ($0.09 - 1.88 \text{ m}^{-1}$). Fluorescence to absorption ratios vary by a factor of 2.5 over the entire data set, with highest values in river plume samples.

Regression equations for total integrated fluorescence versus absorption coefficient also show some variation with wavelength at which fluorescence is excited (Table 2). The slope of the regression line increases between 300 and 350 nm, indicating more fluorescence per light absorbed at the longer wavelengths. The magnitude of the effect is somewhat exaggerated by inclusion of the river plume data, however variability in F/a is another indicator of variability in chemical composition of the CDOM in seawater.

The more detailed variability in F/a for individual samples from the Gulf of Mexico can readily be seen in absorption-normalized EEMs (Fig. 6). The top panel shows a surface water sample from within the Mississippi River plume. The F/a maximum at $Ex/Em = 400/480$ nm occurs at longer wavelengths than the maximum in fluorescence intensity ($Ex/Em = 320/420$ nm). The middle panel shows a surface sample from Station 10, which is farther offshore. The normalized EEM has a shape similar to that at Station 1, but the overall F/a values are lower by a factor of 2-2.5. The bottom panel shows a normalized EEM for a subsurface sample also taken at Station 10 at the depth of the chlorophyll maximum. This EEM clearly shows a second peak located at $Ex/Em = 310/405$ nm. These spectra are indicative of the different nature and composition of gelbstoff which cannot be observed with single point determinations of optical properties.

Table 2. Least squares regression data for total integrated fluorescence intensity (ppb QS) as a function of absorption coefficient (m^{-1}) for surface data from the Gulf of Mexico. Fluorescence data from excitation at each wavelength, λ_i listed in table were integrated between $(\lambda_i + 10)$ and $(\lambda_i + 250)$ nm and regressed versus absorption coefficient measured at the appropriate excitation wavelength. S = slope \pm standard error; I = intercept \pm standard error; r = correlation coefficient; n = number of observations.

Wavelength (a; Ex(λ)nm)	S	I	n	r ²
300	511 \pm 25	-106 \pm 199	28	0.94
320	634 \pm 28	-97 \pm 163	28	0.95
350	819 \pm 41	-98 \pm 141	28	0.94

Since the parameter of interest in remote sensing of chlorophyll is the absorbance due to gelbstoff at 436 nm, the absorbance maximum of chlorophyll, several optical parameters of gelbstoff were investigated to see which was the best predictor of $a_g(436)$. Absorption coefficients at 280, 312, 365, and 404 nm are all highly correlated with absorbance at 436 nm, as is fluorescence at 455 nm excited at 350 nm. None of these parameters, however, is as good a predictor of $a_g(436)$ as is the spectral slope calculated between 365-436 nm.

5. GEOCHEMICAL APPLICATIONS

Dissolved fluorescence due to gelbstoff has previously been shown to vary with salinity⁵¹⁻⁵⁴ and DOC^{34,70-72} in coastal regions, and to increase with depth in open ocean areas.^{51,54,61,73,75} In oligotrophic areas, however, gelbstoff fluorescence and DOC concentration are inversely related due to photodegradation in surface waters.⁶² A positive correlation has been found between DOC and gelbstoff fluorescence in sediment porewaters and in the water column directly above organic-rich sediments, although this appears to be a minor source of gelbstoff in the ocean.⁵⁵

These observations provide the basis for optical measurement of geochemical properties of seawater which could be exploited on remote sensing or *in situ* platforms. Despite potential problems with regional dependence of correlations and non-linearities due to biological or photochemical processes, preliminary results indicate that optical measurements of gelbstoff may prove very useful over limited temporal and spatial scales.^{12,16,23,29} Addition of measurements at multiple wavelengths to maximize the compositional information retrieved could extend the applicability of this approach by increasing the number of measurable parameters.

The protein-like fluorescence (peak B in Fig. 3, right) is of special interest in the study of geochemistry of seawater for several reasons. Its protein-like nature, as evidenced both by its spectral properties and by its distribution patterns,^{62,64,65,76} suggests that it is associated with biologically-produced DOC that is younger and more labile than humic material. Its distribution is uncoupled from that of gelbstoff fluorescence and it behaves non-conservatively in estuaries, thereby providing an independent tracer of processes other than mixing. Its fluorescence at 300-340 nm can be more intense than gelbstoff fluorescence, especially in productive regions, and it may therefore be important in radiance budgets of UV light in the ocean.

6. CONCLUSIONS

The ability to rapidly measure DOM fluorescence with high resolution at multiple wavelengths has led to a revised and expanded view of the natural fluorescence of seawater. Such parameters as spectral shape of absorption and fluorescence curves, position of excitation maximum, position of emission maximum, and relative fluorescence efficiency provide

information pertaining to the chemical composition of CDOM in natural waters, but are dependent upon the wavelengths at which measurements are made as well as on the source of the sample. Accurate measurement of DOM fluorescence parameters requires multichannel excitation and collection of emission spectra rather than single point determinations. Two channels at $\lambda_{\text{ex}} = 310$ and 350 nm could be used for differentiation of marine vs. terrestrial DOM. Excitation at 270 nm would permit measurement of protein-like fluorescence. Direct measurement of the contribution of gelbstoff fluorescence to chlorophyll fluorescence could be obtained by collecting an emission spectrum at excitation 435 nm, the same wavelength used for excitation of chlorophyll *a*.

Two distinct pools of CDOM can be identified in coastal regions based on optical properties. Transition between the two types is due to some combination of physical mixing, biological activity, and geochemical transformation, but what actually happens is poorly understood. Additional studies focused in the coastal transition zone will lead to an improved understanding of DOM geochemistry as well as to improved algorithms for conversion of ocean color to dissolved and particulate carbon concentrations.

7. ACKNOWLEDGEMENTS

The following people provided samples or assistance in this research: F. Prahl, J. Hedges, C. Roessler, M.J. Perry, A. Nowell, T. Peacock, R. Steward, R. Arnone and J. Hesler. Financial support from Office of Naval Research (#N00014-92-J-1210, #N00014-93-1-0167) and the National Science Foundation (#OCE-9116497).

8. REFERENCES

1. K. Kalle. "Fluoreszenz und Gelbstoff im Bottnischen und Finnischen Meerbusen," *Dt. hydrogr. Z.* 2:117-124. 1949.
2. S. Oden. "The humic acids, studies in their chemistry, physics and soil science," *Kolloidchemische Beihefte* 11:75-260. 1919.
3. K. Kalle. "Zum Problem der Merreswasserfarbe." *Ann. Hydrog.* 66:1-13. 1938.
4. E. T. Gjessing. "Physical and chemical characteristics of aquatic humus," *Ann Arbor Science*, Ann Arbor. 1976.
5. D. H. Stuermer and G.R. Harvey. "Humic substances from seawater," *Nature (London)* 250:480-481. 1974.
6. P. G. Hatcher, R. Rowan, and M.A. Mattingly. " ^1H and ^{13}C NMR of marine humic acids," *Org. Geochem.* 2:77-85. 1980.
7. M. A. Wilson, P.F. Barron, and A.H. Gillam. "The structure of humic substances as revealed by ^{13}C -NMR spectroscopy," *Geochim. Cosmochim. Acta* 45:1743-1750. 1981.
8. J. R. Ertel and J.I. Hedges. "Bulk chemical and spectroscopic properties of marine and terrestrial humic acids, melanoidins and catechol-based synthetic polymers," In: *Aquatic and Terrestrial Humic Materials*, R.F. Christman and E.T. Gjessing, eds. Ann Arbor Science, Ann Arbor, Michigan. pp. 143-163, 1983.
9. P. G. Hatcher. "Symposium on early diagenesis and formation of humic substances," Amer. Chem. Soc., Seattle, Washington. March 20-25. 1983.
10. G. R. Harvey, D. A. Boran, L. A. Chesal, and J. M. Tokar. "The structure of marine fulvic and humic acids," *Mar. Chem.* 12:119-132. 1983.
11. A. Spitzzy and V. Ittekkot. "Gelbstoff: An uncharacterized fraction of dissolved organic carbon," Appendix 1, In: "The influence of yellow substances on remote sensing of sea-water constituents from space," Vol. II. H. Grassl, R. Doerffer, and W. Jager, eds. ESA Contract No. RFQ3-5060/84/NL, GKSS Research Centre Geesthacht, D-2054 Geesthacht, FRG, December 1986.
12. D. Diebel-Langohr, R. Doerffer, R. Reuter, F. Dorre, and T. Hengstermann. "Long term stability of gelbstoff concerning its optical properties," Appendix 6, In: "The influence of yellow substances on remote sensing of sea-water constituents from space," Vol. II. H. Grassl, R. Doerffer, and W. Jager, eds. ESA Contract No. RFQ3-5060/84/NL, GKSS Research Centre Geesthacht, D-2054 Geesthacht, FRG, December 1986.
13. K. Kalle. "The problem of the gelbstoff in the sea," *Oceanogr. Mar. Biol. Ann. Rev.* 4:91-104. 1966.
14. R. G. Zepp and P.F. Schlotzhauer. "Comparison of photochemical behavior of various humic substances in water: III. Spectroscopic properties of humic substances," *Chemosphere* 10:479-486. 1981.
15. A. Bricaud, A. Morel, and L. Prieur. "Absorption by dissolved organic matter of the sea (yellow substance) in the

UV and visible domains," *Limnol. Oceanogr.* 26:43-53. 1981.

16. R. Reuter, D. Diebel-Langohr, R. Doerffer, F. Dorre, H. Haardt, and T. Hengstermann. "The influence of gelbstoff on remote sensing of seawater constituents from space," Appendix 3, In: *"The influence of yellow substances on remote sensing of sea-water constituents from space," Vol. II.* H. Grassl, R. Doerffer, and W. Jager, eds. ESA Contract No. RFQ3-5060/84/NL, GKSS Research Centre Geesthacht, D-2054 Geesthacht, FRG, December 1986.

17. K. L. Carder, R.G. Steward, G.R. Harvey, and P.B. Ortner. "Marine humic and fulvic acids: Their effects on remote sensing of ocean chlorophyll," *Limnol. Oceanogr.* 34:68-81. 1989.

18. L. M. Mayer. "Geochemistry of humic substances in estuarine environments," pp. 211-232, In: *"Humic Substances in Soil, Sediment, and Water: Geochemistry, Isolation, and Characterization,"* G.R. Aiken, D.M. McKnight, R.L. Wershaw, and P. MacCarthy, eds. John Wiley & Sons. New York. 692 p. 1985.

19. G. R. Harvey and D.A. Boran. "Geochemistry of humic substances in seawater," pp. 233-247, In: *"Humic Substances in Soil, Sediment, and Water: Geochemistry, Isolation, and Characterization,"* G.R. Aiken, D.M. McKnight, R.L. Wershaw, and P. MacCarthy, eds. John Wiley & Sons. New York. 692 p. 1985.

20. G. R. Aiken. "Isolation and concentration techniques for aquatic humic substances," pp. 363-386, In: *"Humic Substances in Soil, Sediment, and Water: Geochemistry, Isolation, and Characterization,"* G.R. Aiken, D.M. McKnight, R.L. Wershaw, and P. MacCarthy, eds. John Wiley & Sons. New York. 692p. 1985.

21. J. A. Leenheer. "Fractionation techniques for aquatic humic substances," pp. 409-432, In: *"Humic Substances in Soil, Sediment, and Water: Geochemistry, Isolation, and Characterization,"* G.R. Aiken, D.M. McKnight, R.L. Wershaw, and P. MacCarthy, eds. John Wiley & Sons. New York. 692 p. 1985.

22. J. Fischer and H. Grassl. "On the selection of an optimized channel for measuring yellow substance from space within the 380 to 475 nm domain," Appendix 7, In: *"The influence of yellow substances on remote sensing of sea-water constituents from space," Vol. II.* H. Grassl, R. Doerffer, and W. Jager, eds. ESA Contract No. RFQ3-5060/84/NL, GKSS Research Centre Geesthacht, D-2054 Geesthacht, FRG, December 1986.

23. R. Reuter, W. Albers, K. Brandt, D. Diebel-Langohr, R. Doerffer, F. Dorre, and T. Hengstermann. "Ground truth techniques and procedures for gelbstoff measurements," Appendix 8, In: *"The influence of yellow substances on remote sensing of sea-water constituents from space," Vol. II.* H. Grassl, R. Doerffer, and W. Jager, eds. ESA Contract No. RFQ3-5060/84/NL, GKSS Research Centre Geesthacht, D-2054 Geesthacht, FRG, December 1986.

24. G. R. Aiken. "A critical evaluation of the use of macroporous resins for the isolation of aquatic humic substances," pp. 15-28, In: *"Humic Substances and Their Role in the Environment,"* F.H. Frimmel and R.F. Christman, eds. John Wiley & Sons Ltd. @ S. Bernhard, Dahlem Konferenzen. 1988.

25. F. H. Frimmel and R.F. Christman, eds. *"Humic Substances and Their Role in the Environment,"* John Wiley & Sons Ltd. @ S. Bernhard, Dahlem Konferenzen. 1988.

26. E. M. Perdue and E.T. Gjessing, eds. *"Organic Acids in Aquatic Ecosystems,"* John Wiley & Sons Ltd. @ S. Bernhard, Dahlem Konferenzen. 1990.

27. M. P. F. Bristow, D.H. Bundy, C.M. Edmonds, and P.E. Ponto. "Airborne laser fluorosensor survey of the Columbia and Snake rivers: simultaneous measurements of chlorophyll, dissolved organics and optical attenuation," *Int. J. Remote Sensing* 6:707-1734. 1985.

28. J. R. Fischer, Doerffer, H. Grassl, I. Hennings, and M. Tormahlen. "An inverse technique for remote detection of suspended matter, phytoplankton and yellow substance from CZCS measurements," Appendix 5, In: *"The influence of yellow substances on remote sensing of sea-water constituents from space," Vol. II.* H. Grassl, R. Doerffer, and W. Jager, eds. ESA Contract No. RFQ3-5060/84/NL, GKSS Research Centre Geesthacht, D-2054 Geesthacht, FRG, December 1986.

29. D. Diebel-Langohr, T. Hengstermann, and R. Reuter. "Identification of hydrographic fronts by airborne lidar measurements of gelbstoff distributions," In: *Marine Interfaces Ecohydrodynamics.* J.C.J. Nihoul, ed. Elsevier. Amsterdam, pp. 569-590, 1986.

30. K. Gruner, R. Reuter, and H. Smid. "A new sensor system for airborne measurements of maritime pollution and of hydrographic parameters," *GeoJournal* 24:103-117. 1991.

31. F.E. Hoge, A. Vodacek and N.V. Blough. "Inherent optical properties of the ocean: Retrieval of the absorption coefficient of chromophoric dissolved organic matter from fluorescence measurements." *Limnol. Oceanogr.* 38:1394-1402. 1993.

32. Thurman, E.M. *"Organic Geochemistry of Natural Waters,"* Nichoff & Junk Publ. 1985.

33. P. M. Williams and E.M. Druffel. "Dissolved organic matter in the ocean: Comments on a controversy," *Oceanogr.*

1:14-17. 1988.

34. R. W. P. M. Laane and L. Koole. "The relation between fluorescence and dissolved organic carbon in the Ems-Dollart Estuary and the western Wadden Sea," *Neth. J. Sea Res.* 15:217-227. 1982.
35. R. W. P. M. Laane and K.J.M. Kramer. "Natural fluorescence in the North Sea and its major estuaries," *Neth. J. Sea Res.* 26:1-9. 1991.
36. J. I. Hedges, P.G. Hatcher, J.R. Ertel, and K.J. Meyers-Schulte. "A comparison of dissolved humic substances from seawater with Amazon River counterparts by ^{13}C -NMR spectrometry," *Geochim. Cosmochim. Acta* 56:1753-1757. 1992.
37. J. I. Hedges. "Compositional indicators of organic acid sources and reactions in natural environments," In: *"Organic Acids in Aquatic Ecosystems,"* E.M. Perdue and E.T. Gjessing, eds. John Wiley & Sons Ltd. @ S. Bernhard, Dahlem Konferenzen. pp. 43-63, 1990.
38. M. M. Kononova. *"Soil Organic Matter,"* Pergamon, Elmsford, N.Y. 544p. 1966.
39. R. W. P. M. Laane. "Comment on the structure of marine fulvic and humic acids," *Mar. Chem.* 15:85-87. 1984.
40. W. Ziehm. "Evolution of structural model from consideration of physical and chemical properties," In: *"Humic Substances and Their Role in the Environment,"* F.H. Frimmel and R.F. Christman, eds. John Wiley & Sons Ltd. @ S. Bernhard, Dahlem Konferenzen. pp. 113-132, 1988.
41. D. L. Norwood. "Critical comparison of structural implications from degradative and nondegradative approaches," In: *"Humic Substances and Their Role in the Environment,"* F.H. Frimmel and R.F. Christman, eds. John Wiley & Sons Ltd. @ S. Bernhard, Dahlem Konferenzen. pp. 133-148, 1988.
42. H.-R. Schulten and M. Schnitzer. Corrected fluorescence excitation spectra of fulvic acids. Comparison with the UV/visible absorption spectra. *Sci. Tot. Environ.* 62:157-161. 1993.
43. C. S. Yentsch, and C.A. Reichert. "The interrelationship between water-soluble yellow substances and chloroplastic pigments in the marine algae," *Bot. Marina* 3:65-74. 1961.
44. N. K. Hojerslev. "Assessment of some suggested algorithms on sea colour and surface chlorophyll," In: *Oceanography from Space*, J.F.R. Gower, ed. Plenum. New York. pp. 347-353, 1981.
45. J. Fischer, R. Doerffer, and M. Russo. "The influence of yellow substance on remote monitoring of water substances in coastal waters," Appendix 2, In: *"The influence of yellow substances on remote sensing of sea-water constituents from space,"* Vol. II. H. Grassl, R. Doerffer, and W. Jager, eds. ESA Contract No. RFQ3-5060/84/NL, GKSS Research Centre Geesthacht, D-2054 Geesthacht, FRG, December 1986.
46. A. Schmitz-Peiffer and H. Grassl. "Remote sensing of coastal waters by airborne lidar and satellite radiometer," Part. 1: A model study. *Int. J. Remote Sensing* 11:2163-2184. 1990.
47. A. Schmitz-Peiffer, T. Viehoff, and H. Grassl. "Remote sensing of coastal waters by airborne lidar and satellite radiometer," Part. 2: Measurements. *Int. J. Remote Sensing* 11:2185-2204. 1990.
48. G. M. Ferrari and S. Tassan. "On the accuracy of determining light absorption by "yellow substance" through measurements of induced fluorescence," *Limnol. Oceanogr.* 36:777-786. 1991.
49. W. G. Witte, C. Whitlock, R. Harriss, J. Usry, L. Poole, W. Houghton, W. Morris, and E. Gurganus. "Influence of dissolved organic materials on turbid water optical properties and remote-sensing reflectance," *J. Geophys. Res.* 87:441-446. 1982.
50. D. Spitzer and R.W.J. Dirks. "Contamination of the reflectance of natural waters by solar-induced fluorescence of dissolved organic matter," *Appl. Opt.* 24:444-445. 1985.
51. E. K. Duursma. "The fluorescence of dissolved organic matter in the sea," In: *Optical Aspects of Oceanography*. N. G. Jerlov and E. Steemann Nielsen, eds. Academic Press, N. Y. pp. 237-256, 1974.
52. R.W.P.M. Laane. "Composition and distribution of dissolved fluorescent substances in the Ems-Dollart Estuary," *Neth. J. Sea Res.* 15:88-89. 1981.
53. P. Berger, R.W.P.M. Laane, A.G. Ilahude, M. Ewald, and P. Courtot. "Comparative study of dissolved fluorescent matter in four West-European estuaries," *Oceanologica Acta* 7:309-314. 1984.
54. K. Hayase, M. Yamamoto and H. Tsubota. "Behavior of natural fluorescence in Sagami Bay and Tokyo Bay, Japan - Vertical and lateral distributions," *Mar. Chem.* 20:265-276. 1987.
55. R.F. Chen, J.L. Bada and Y. Suzuki. "The relationship between dissolved organic carbon (DOC) and fluorescence in anoxic marine porewaters: Implications for estimating DOC fluxes," *Geochim. Cosmochim. Acta* 57:2149-2153. 1993.
56. R. J. Kieber, X. Zhou, and K. Mopper. "Formation of carbonyl compounds from UV-induced photodegradation of humic substances in natural waters: Fate of riverine carbon in the sea," *Limnol. Oceanogr.* 35:1503-1515. 1990.
57. G.M. Ferrari and S. Tassan. "Evaluation of the influence of yellow substance absorption on the remote sensing

of water quality in the Gulf of Naples: A Case Study," *Int. J. Remote Sensing* 13:2177-2189. 1992.

58. G. D. Christian, J.B. Callis, and E.R. Davidson. "Array detectors and excitation-emission matrices in multicomponent analysis," In: E.L. Wehry, ed. *Modern Fluorescence Spectroscopy*, v. 4. Plenum Press, New York. pp. 111-165, 1981.

59. C. H. Lochmuller and S.S. Saavedra. "Conformational changes in a soil fulvic acid measured by time-dependent fluorescence depolarization," *Anal. Chem.* 58:1978-1981. 1986.

60. S. E. Cabaniss and M.S. Shuman. "Synchronous fluorescence spectra of natural waters: tracing sources of dissolved organic matter," *Mar. Chem.* 21:37-50. 1987.

61. P. G. Coble, S. Green, N.V. Blough, and R.B. Gagosian. "Characterization of dissolved organic matter in the Black Sea by fluorescence spectroscopy," *Nature* 348:432-435. 1990.

62. P. G. Coble, K. Mopper, and C.S. Schultz. "Fluorescence contouring analysis of DOC Intercalibration Experiment samples: A comparison of techniques," *Mar. Chem.* 41:173-178. 1993.

63. O.F. Donard, C. Belin and M. Ewald. "Corrected fluorescence excitation spectra of fulvic acids. Comparison with the UV/visible absorption spectra," *Sci. Tot. Environ.* 62:157-161. 1987.

64. K. Mopper and C.A. Schultz. "Fluorescence as a possible tool for studying the nature and water column distribution of DOC components," *Mar. Chem.* 41:229-238. 1993.

65. M. C. Ewald, C. Belin, P. Berger, and J.H. Weber. "Corrected fluorescence spectra of fulvic acids isolated from soil and water," *Environ. Sci. Technol.* 17:501-504. 1983.

66. J. R. Lakowicz. "*Principles of Fluorescence Spectroscopy*," Plenum Press. New York. 496 p. 1983.

67. O. F. X. Donard, M. Lamotte, C. Belin, and M. Ewald. "High sensitivity fluorescence spectroscopy of Mediterranean waters using a conventional or a pulsed laser excitation source," *Mar. Chem.* 27:117-136. 1989.

68. P.G. Coble. "Excitation-emission matrix characterization of marine and terrestrial DOM in seawater," (submitted). 1994.

69. S.A. Green. "*Applications of fluorescence spectroscopy to environmental chemistry*," Ph.D. Thesis. WHOI-92-24. 1992.

70. P. L. Smart, B.L. Finlayson, W.D. Rylands, and C.M. Ball. "The relation of fluorescence to dissolved organic carbon in surface waters," *Water Res.* 10:805-811. 1976.

71. G. S. Karabashev and A.I. Agatova. "Relationship of fluorescence intensity to concentration of dissolved organic substances in ocean water," *Oceanol.* 24:680-682. 1984.

72. F.G. Prahl and P.G. Coble. "Input and behavior of dissolved organic carbon in the Columbia River Estuary," In: *Change in fluxes in estuaries: Implications from Science to Management*, Joint ECSA/ERF Conference 13-18 Sept. 1992. Polytechnic SW, Plymouth, UK (in press). 1994.

73. M. A. Ivanoff. "Au sujet de la fluorescence des eaux de mer," *Comp. Rend. Acad. Sci. (Paris)* 254:4190-4192. 1962.

74. K. Hayase, J. Tsubota, and I. Sunada. "Vertical distribution of fluorescent organic matter in the North Pacific," *Mar. Chem.* 25:373-381. 1988.

75. R. F. Chen and J.L. Bada. "Seawater and porewater fluorescence in the Santa Barbara Basin," *Geophys. Res. Lett.* 16:687-690. 1989.

76. E. D. Traganza. "Fluorescence excitation and emission spectra of dissolved organic matter in sea water," *Bull. Mar. Sci.* 19:897-904. 1969.

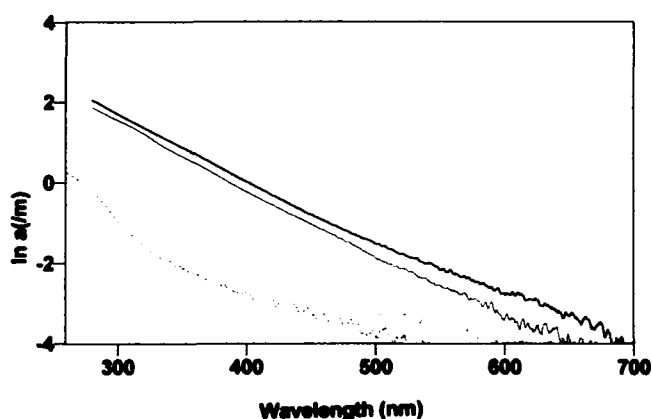


Figure 1. Natural logarithm of absorption coefficient (m^{-1}) versus wavelength for four representative samples from Gulf of Mexico surface water. Curves are from (top to bottom) Sta. 2 and 1, (Mississippi River plume) and 10 and 3 (Loop Current).

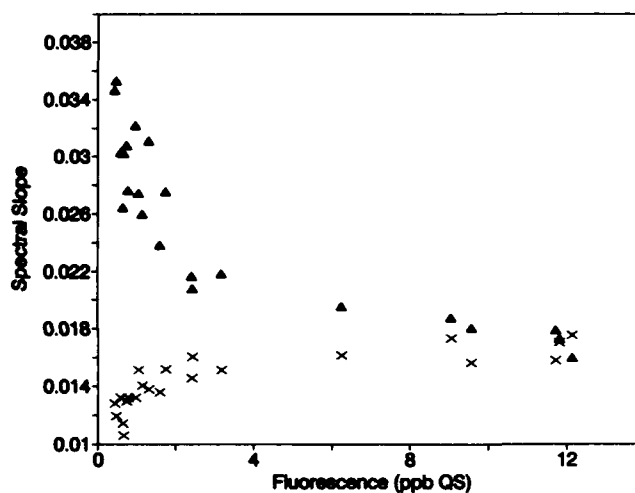


Figure 2. Absorption spectral slope versus fluorescence intensity (parts per billion quinine bisulfate equivalents)⁶². Filled triangles represent spectral slopes calculated between 280 and 312 nm, and Xs represent calculations over the interval from 365 to 436 nm. See Table 1 caption for equation used in calculations.

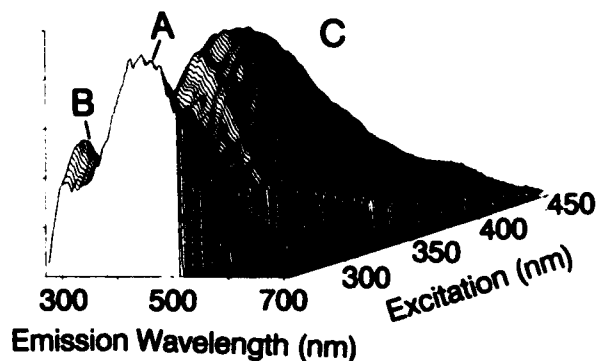
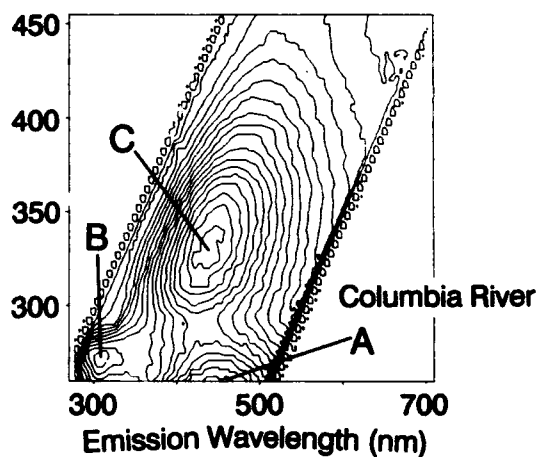
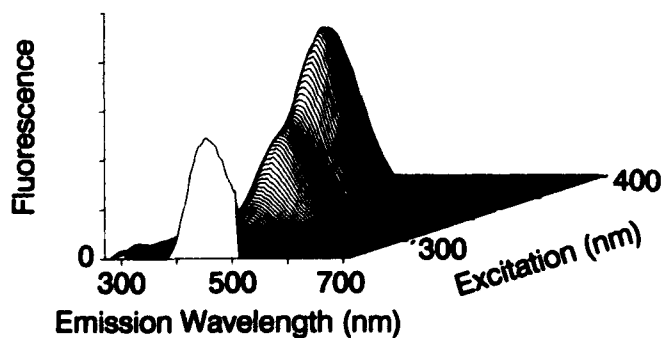
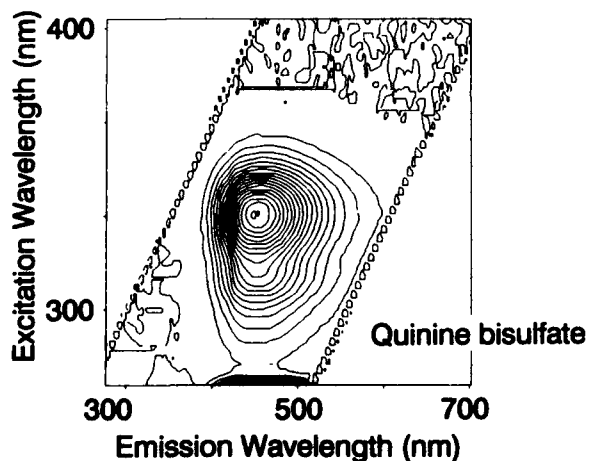


Figure 3. EEMS for quinine bisulfate (left) and Columbia River Estuary water (right). See text for explanation of peak labels.

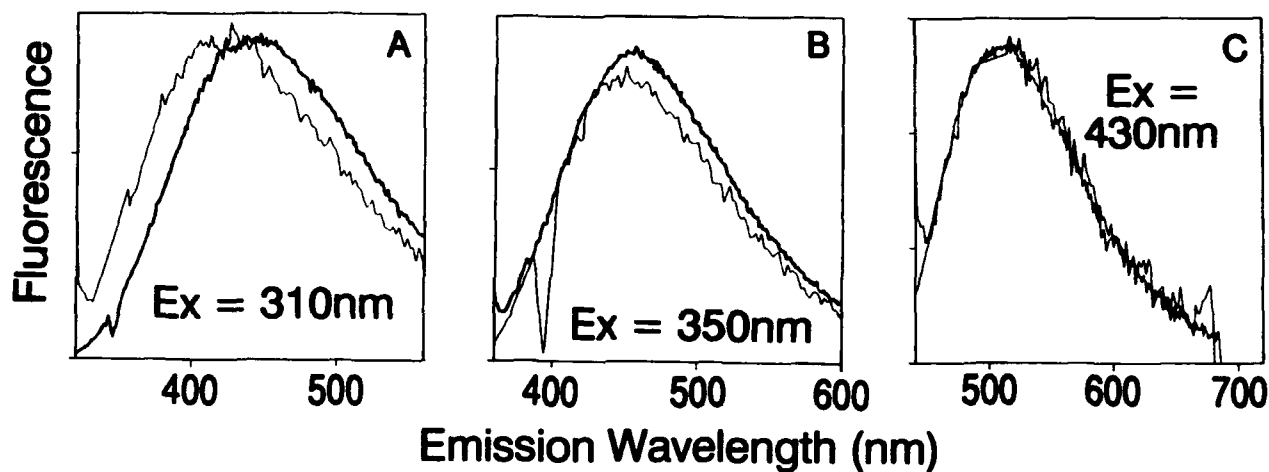


Figure 4. Fluorescence emission spectra as a function of excitation wavelength for a freshwater sample from Rio Madeiro, a tributary in the Amazon River System (heavy line), and from a seawater sample from the Gulf of Maine (light line). Fluorescence intensities are relative and have been set to full scale for each panel.

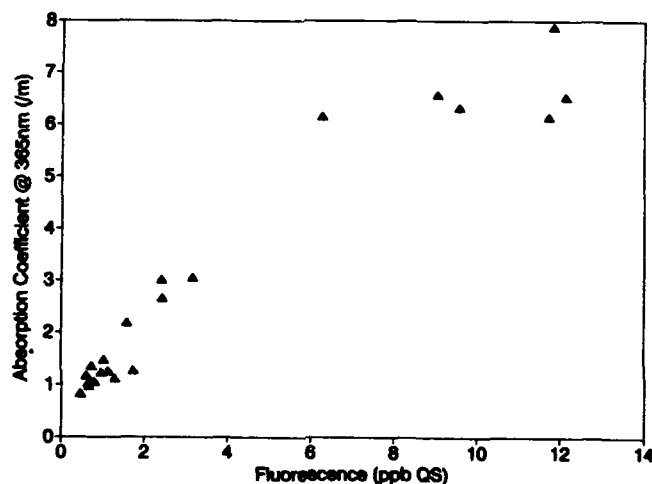


Figure 5. Absorption coefficient at 365 nm (m^{-1}) versus fluorescence intensity (parts per billion quinine bisulfate equivalents)⁶² for surface waters of the Gulf of Mexico.

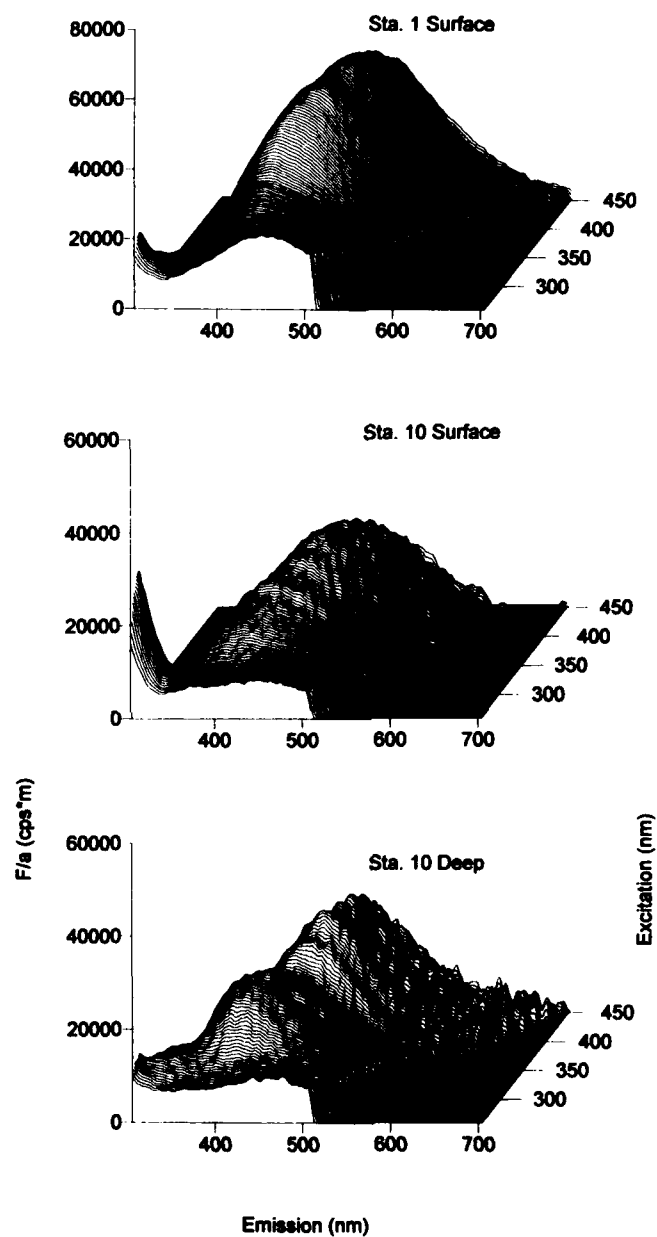


Figure 6. Absorption normalized EEMS for three types of water sample collected in the Gulf of Mexico. Station numbers as in Fig. 1. F/a units of counts per second * m can be converted to ppb QS * m by multiplying by 1.52×10^{-4} .

SESSION 6

Lidar

Airborne laser depth sounding. System aspects and performance.

Ove Steinvall, Kurt Koppari, Ulf Karlsson

Swedish Defence Research Establishment (FOA), Dept.3
P.O. Box 1165, Linköping, SWEDEN.
FAX: +46 13 13 16 65

ABSTRACT

In Sweden work on airborne depth sounding lidar has taken place during more than ten years. Activities include the development of a helicopter borne lidar called FLASH¹⁻³ as well as instrumentation (HOSS) for in situ measurement of the optical water parameters⁴. These instruments have been used in rather extensive field trials some of which will be discussed in more detail.

Recently we have been engaged in analysis of lidar data to determine system performance and possible ways to optimise that in relation to lidar parameters and anticipated bottom depth and topography. Examples from that analysis will be presented. Comparisons between laser and acoustic soundings will be presented.

The FLASH system has been further developed into two operational systems called Hawk Eye with Saab Instruments as the main contractor and Optech Inc. as the main subcontractor. The first of these two systems has now been delivered for helicopter installation and acceptance flights. Data from Hawk Eye will hopefully be available at the time of the meeting and will be discussed. FOA are members of the Hawk Eye project team together with the Swedish Hydrographic Service, the Swedish Navy and the Swedish Material Administration (FMV).

1. INTRODUCTION.

Airborne laser depth sounding (lidar bathymetry) is one of the most promising techniques for rapid and high density sounding of shallow waters. This promise also includes high mobility, cost effectiveness and easy administration due to a low need of manpower. The oceanographic lidar can be extended to include remote sensing of the water optical parameters, chlorophyll monitoring, oil slick detection and classification, fish detection and more. Although the great majority of remote sensing results of oceans, lakes and rivers come from passive sensors (visible, IR and microwave) the lidar adds another dimension in the form of depth resolution and at least some degree of absolute measurement capability which is hard to obtain by passive sensors. Data fusion between passive and active optical sensors for remote sensing seem to be a promising method to further increase the data quality and area coverage. However little data fusion work has so far been presented in hydrographic remote sensing.

Oceanographic lidars have lately been developed and used in Sweden (FLASH^{1,2}, Hawk Eye^{3,5}), USA (AOL^{6,7}, ABS NORDA⁸, OWL⁹, SHOALS¹⁰), Australia (LADS^{11,12}, WRELADS¹³), Canada (LARSEN-500¹⁴), Russia (Chaika¹⁵, Makrel-II¹⁶, GOI¹⁷) and China (BL0L¹⁸).

Due to the development in short pulse high prf green laser technology and the rapid development in data handling, storage and processing, scanning lidars are now in operational use. So far however the number of publications on performance compared with experimental data are very few especially in situations with irregular bottoms. This paper will try to address some of these issues.

2. HOW, WHEN AND WHY TO USE LIDAR BATHYMETRY ?

Lidar bathymetry has some more or less obvious advantages as mentioned above. The airborne operation and the minimum depth achievable (≈ 1 m) allow operation in areas difficult for ships such as archipelagos with numerous small islands, reefs and narrow ship routes. The rapidness enables resurvey in areas where the depths are often changing such as sand bottoms. The minimum depth of about 1 m is of importance in waters with frequent yachting. The high area coverage rate (today typically 20 km² per hour at 5 m spot distance or 80 km² at 10 m distance) is especially valuable with regard to the vast areas classified as inadequately or not surveyed. In a recent IHO study¹⁹ it was concluded that these areas are 71 % of the almost 97 207 900 km² under consideration for nautical purposes.

The purpose of lidar bathymetry can range from accurate and spatially dense depth sounding to a more rapid but less dense and accurate sounding for locating areas of interest for more detailed surveys or for different military purposes. In general lidar bathymetry is always a complementary technique and should therefore often be combined with acoustic or mechanical methods. The optimum and most economic way of combination these different techniques will gradually develop from experimental experience.

lidar bathymetry is always a complementary technique and should therefore often be combined with acoustic or mechanical methods. The optimum and most economic way of combination these different techniques will gradually develop from experimental experience.

One must however remind of the operational limitations of lidar bathymetry and how these limitations affects the planning and use of the sensor. From our experimental experience the most important limitations are given below:

Table 1. Limitations of lidar bathymetry.

Depth penetration	≤ 4 KD (day) and ≤ 5 KD during night
Cloud, fog, sea smoke	Esp. low clouds and fog can affect the operation
Strong winds	Affects the ability to accurate follow flight lines at low helicopter speeds
Sea state	High sea state esp. white and broken water affects accuracy and maximum penetration.
Scattering layers and other inhomogenities in the water column	May limit penetration and have to be sorted out in the post processing as false bottoms.
Bottom roughness vegetation	Rises the question of the smallest feature that can be measured within the beam footprint. Dense vegetation may result in underestimating the depth.
Hardware limitations	If every wave form is to be stored with high amplitude and time resolution, and real time imaging capability is needed this puts a high load on computer power and signal handling. Today this limit is about 200 Hz. The use of future high prf laser will stress this even more.

2.1 Depth penetration

The strongest limitation is the depth penetration. This is related to the system attenuation G (m^{-1}) which determines the maximum depth penetration D_{max} which is given by

$$D_{max} = \ln(P^* / P_{min}) / 2G \quad (1)$$

where $P^* \approx S \cdot \rho / H^2$, H being altitude, ρ the bottom reflectivity and S the system parameter defined as a product of laser peak power, receiver aperture, and loss factors due to surface reflection, limited field of view and optical system efficiency. P_{min} is the minimum power for bottom detection which during daytime usually is limited by solar background radiation and during night time by detector and other electronic noise. Putting typical system parameters for a lidar bathymeter into the above formula one arrives at values for $G \cdot D_{max} \approx 3-6$ depending on daylight level and parameter choice. Due to the exponential attenuation a large increase in the system parameter S (e.g. by a factor of 10) gives only a marginal increase in D_{max} ($\Delta D_{max} \approx \ln(10)/2G \approx 4$ m for $G = 0,3 m^{-1}$). For large FOV-diameters on the surface ($>$ bottom depth) the system attenuation G is approximated by the diffuse attenuation K .

The diffuse attenuation K can be measured by special instrumentation like the HOSS (see below) or by relating K to the Secchi disc depth (D_{secchi}). The Secchi disc depth is obtained as the maximum depth at which a submerged white disc can be observed. The relation between the inherent contrast C_0 of the disc and the apparent contrast C_D as seen by the observer is given by Duntley²⁰ for vertical observation:

$$C_D = C_0 e^{-(c+K)D} \quad (2)$$

We have observed the following empirical relation between K and the collimated beam attenuation coefficient c (observations made in the Baltic Sea):

$$K \approx 0.136 + 0.092 \cdot c \quad (3)$$

If we assume an inherent contrast $C_0 = 40$ (this is for a disc reflectivity of 82 %²¹) and a threshold value of $C_{Dsecchi} = 0.0066$ ²¹ formula (2) gives $c+K = 8.70/D_{secchi}$. If we combine this with (3) we find the following relation between the daylight penetration depth D_{max} ($\approx 4/K$) and the Secchi disc depth as:

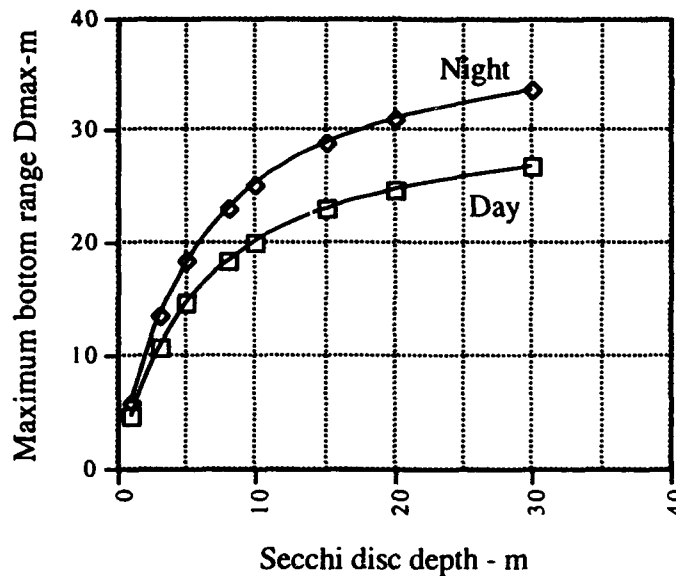


Figure 1. Maximum bottom range (against a flat bottom with about 10 % reflectivity) for a state of the art lidar bathymeter.

$$D_{max} = 4.368 * D_{Secchi} / (0.136 * D_{Secchi} + 0.8) \quad (4)$$

The formula (4) is illustrated in figure 1 together with the 25 % increase in depth obtained during night time.

The turbidity as measured by K-meter or by Secchi disc depth differs in that K-meters can be made true profiling instruments and thus reveal scattering layers close to the bottom for example, which a Secchi measurement may miss totally or at least not resolve in depth. Turbidity is often a strong function of season and geographic location. River outlets for example will often have a much more turbid water than the surrounding sea. Recent weather especially storms heavily affect the turbidity.

One way of monitoring the turbidity for bathymetric planning is to have Secchi disc or K-meters and different locations of interest. If the areas are large a combination of such measurements and the use of satellite or airborne multispectral cameras is motivated. In doing so a rapid and efficient way of monitoring seasonal and geographical changes of water quality is possible. This was done for LANDSAT data and correlated to Secchi disc data²².

2.2 Atmospheric limitations

The prime limitation of the atmosphere is to reduce the amount of signal reaching the receiver. If we for simplicity assume a homogeneous atmosphere between platform and the sea surface the reduction of depth penetration ΔD_{atm} due to atmospheric transmission loss can simply be written:

$$\Delta D_{atm} = \ln(T_{atm}^2) / 2G = \ln(e^{-2\sigma H}) / 2G = H\sigma / G \approx 3.9H / V * 1/G \quad (5)$$

where σ is the atmospheric extinction coefficient at the laser wavelength which generally is close enough to the 550 nm wavelength used in defining visibility to justify the relation $\sigma \approx 3.9/V$ where V is the meteorological visibility range V (looking downwards). For a system with FOV diameter at the surface larger than the depth we can assume $G \approx K$ and formula (5) can be used to estimate the depth loss. In general $V \gg H$ and this loss is negligible but if for example the visibility is so low that the water surface hardly is seen ($V \approx H$) from the operating altitude the loss can be substantial ($\approx 3.9/K$). Figure 2 shows the loss vs. visibility V and for different K -values.

We have observed another problem arising during winter time when "sea smoke", a haze layer just above the water surface, can interfere and trigger the surface measuring / slant range IR-channel which results in a shift of the signal so that the bottom echo may fall out of the measurement range usually set to 50 meters or so. An example of this can be seen in figure 3. One way to avoid this problem is to have more criteria on the surface return for example using the raman signal which would be a more stringent time marker for the water surface.

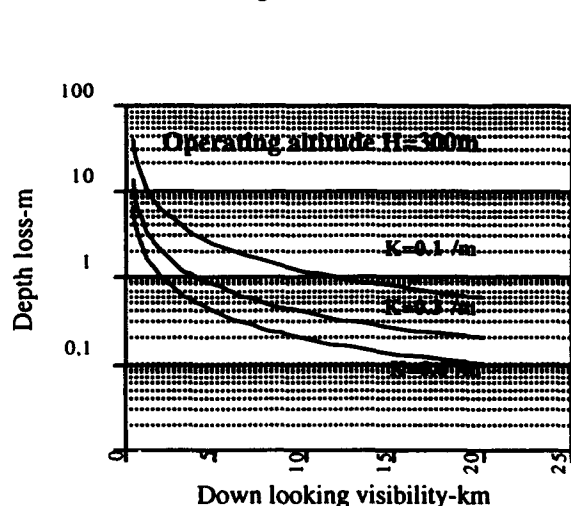


Figure 2 Depth loss due to atmospheric transmission at 300 m operating altitude for different K-values.

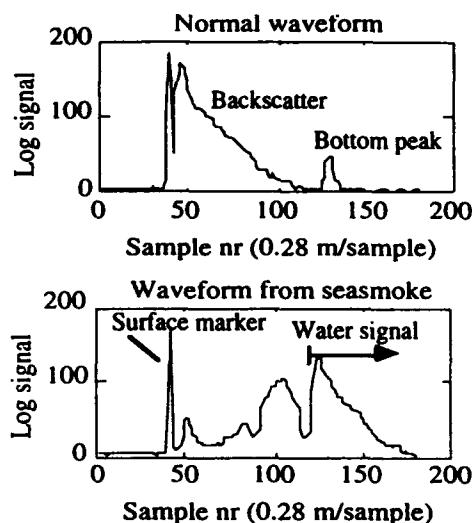


Figure 3. Example of wave forms with and without sea smoke (haze) close to the water surface.

Feigils²³ has recently pointed out a potential problem with a scattering component from the atmosphere reaching the receiver at the same time as the bottom signal. This signal is thought to come from the laser radiation hitting the water surface reflected upwards to the atmosphere and down to the water surface again and then reflected up to the receiver. To estimate the importance of this component we note that the energy of the bottom signal from depth D can be written:

$$E_b = \rho_b E_0 T_{opt} [T_{atm}^2(H)] (1 - \rho_0)^2 F_2 \frac{\cos^2 \theta}{(n_w H + D)^2} \frac{A_R}{\pi} \exp(-2GD) \quad (6)$$

with E_0 as the outgoing laser pulse energy, T_{opt} the optical loss in the receiver, A_R the receiver aperture, T_{atm}^2 the two-way atmospheric transmission, F_2 a loss factor due to small receiver field of view ($F_2 \leq 1$), A_R the receiver area, H the platform altitude, θ the angle of incidence on the water surface and n_w the water index of refraction. The bottom reflectivity is ρ_b and ρ_0 is the Fresnel reflectance (≈ 0.02 at 532 nm wavelength). G is the system attenuation coefficient. Feigils²³ gives the following estimate of the energy E_{ba} of the atmospheric scattering contribution at the time of the bottom pulse ($\theta = 90$ degr. assumed):

$$E_{ba} = E_0 T_{opt} A_R \rho_0^2 [T_{atm}^2(n_w D + H)] \beta_{atm} \frac{c\tau}{2} \frac{1}{(n_w D + H)^2} \quad (7)$$

where β_{atm} is the atmospheric back scatter coefficient, c the velocity of light in the air and τ the laser pulse length. By taking the ratio between (7) and (6) and noting that $H \gg D$ and $\rho_0 \ll 1$ we get

$$2GD \approx \ln \left[\frac{E_{ba}}{E_b} \frac{2F_2 \rho_b}{\pi \beta_{atm} c \tau n_w^2 \rho_0} \right] \quad (8)$$

It is of interest to estimate the depth at which $E_b = E_{ba}$ for different visibility's V . Assuming a laser pulse length $\tau = 5$ ns and $F_2 = 0.5$ (reasonable for a 50 mrad receiver FOV at 200-300 m altitude and looking at 20 m returns) we arrive at the following approximate relation for $2GD$:

$$2GD \approx \ln[6826 * V^{0.69}] \quad (9)$$

where we used the relation $\beta_{\text{atm}} = 0,0263(3,91/V)^{0.69}$ cited in Feigils²³ article. For visibility's as low as $V=0,3$ km the expression (9) estimates $GD \approx 4$ i.e. the atmospheric scattering contribution might become comparable with the bottom peak energy at the approximate range limit during day time ($GD \approx KD \approx 4$). For higher visibility's ($V > 1$ km is probably a lower practical limit for good and safe operation) the atmospheric contribution $E_{ba} \ll E_b$ during the assumption of small receiver field of view (FOV) loss (F_2). For much smaller FOV there might be some effects by the atmospheric scattering in that it may hide the bottom peak. Note however that the atmospheric scattering contribution to the wave form is a slowly decaying function vs time compared with the bottom echo.

2.3 Wind influence and sea state.

The wind influences the system operation in several ways. First through the ability to fly along the straight flight lines and secondly through the waves generated by the wind.

The relation between flying speed V , swath width S , laser prf f and spot density a is $V*S = f*a^2$. For spot densities $a = 5$ m and $S = 200$ m for example a 200 Hz laser gives $V = 25$ m/s which is rather low for a helicopter making its flight wind sensitive. Therefore the planning of a mission must include the wind in setting up the flight lines. It is best to fly against the wind to make it easy to hold steady course. The wind can cause the helicopter to turn more towards the wind which makes the scanner to sweep a narrower swath a bit to the side of that planned. There may be a trade off between swath width S , spot density a and the helicopter velocity V . If the speed is low relative to wind this may result in "gaps" in the coverage. The cloud base may also affect the swath width. Lower altitude means that a narrower swath can be used and this enables higher flight speed for constant spot density.

The waves influences the system operation and accuracy in several ways. In summary the waves will break up the beam, refract the beam, influence depth measured as the difference between surface signal and bottom signal, distort the surface signal leading to saturation or loss for the green signal in both directions. We will comment these effects.

The wavy surface breaks the beam in a complicated manner which is superimposed on the beam pattern falling into the water. This beam break up is not very well modelled and may influence the depth accuracy in the first few optical depths. After many optical depths multiple scattering in the water tend to smear out this effect.

The wave refraction which is most important for large swells where the whole beam may refract on the same wave slope. This results both a in a position error on the bottom and a depth error. The wave slope is coupled to the wind velocity by the Cox-Munk relations²⁴. In this way maximum errors can be estimated as a function of wind velocity assuming that the whole beam falls on the same wave slope. Figure 4 shows the maximum errors on the beam position and depth error introduced by the refraction²⁵. Assuming wind velocities of 10-12 m/s as practical upper limits for operation we can estimate the maximum position error on the bottom as 5-10 % of the depth. This error is hard to compensate for as the wave slope is difficult to measure for every laser shot. The maximum refraction depth error is according to figure 3 between 1-2% of the depth. This error is again difficult to compensate for due to the above reasons. One way to reduce the influence of refraction is to widen the beam to cover at least two wave crests. The waves affect the interface return. In many systems the IR return is used to measure the time position for the water surface. The angle of incidence will also affect the magnitude of the IR-return. The IR return may be lost when the water surface is calm and in such a case the green signal must be used to establish the surface reference. This can be specular or a volume return from the water just below the surface. This "flip-flop" effect²⁶ can theoretically be about 0,5 meter for K-values between 0,1-0,3 m^{-1} . The magnitude of the specular return depends heavily on wind and off nadir beam angle. Guenther²⁷ has shown results from calculations of these effects. For low wind speed and nadir angles both the magnitude and the standard deviation of the surface return is large. For larger winds and nadir angles the signals are weaker but also less variable which is important from an operational point of view. From the diagram in ref. 27 it can be seen that a nadir angle of 20° results in a fairly constant loss factor relative to a perfect lambertian surface of about 0,01. For small nadir angles a small change in wind speed will have a dramatic effect on the surface return. There might also be as much as an order of magnitude difference between up/down and crosswind directions. In summary there is a strong effect on the interface return by the wind but that should be possible to minimise by proper system design and choice of nadir angle.

For strong winds the influence of white caps must be taken into account. Koepke²⁷ has measured the reflectance and surface coverage of whitecaps. The reflectance of fresh foam is about 55 % in the visible but the aging and spread leads to

an effective reflectance of ρ_e about 22 %. How the foam actually affects the beam penetration and is unclear but the effect is probably "worse" than just reducing the bottom signal by $(1-\rho_e)^2$. The surface fraction covered with foam is given by Koepke according to figure 5. For a wind speed of 10 m/s about 1 % of the area will be foam covered. This probably means that less than 1 % of the laser shots are "lost".

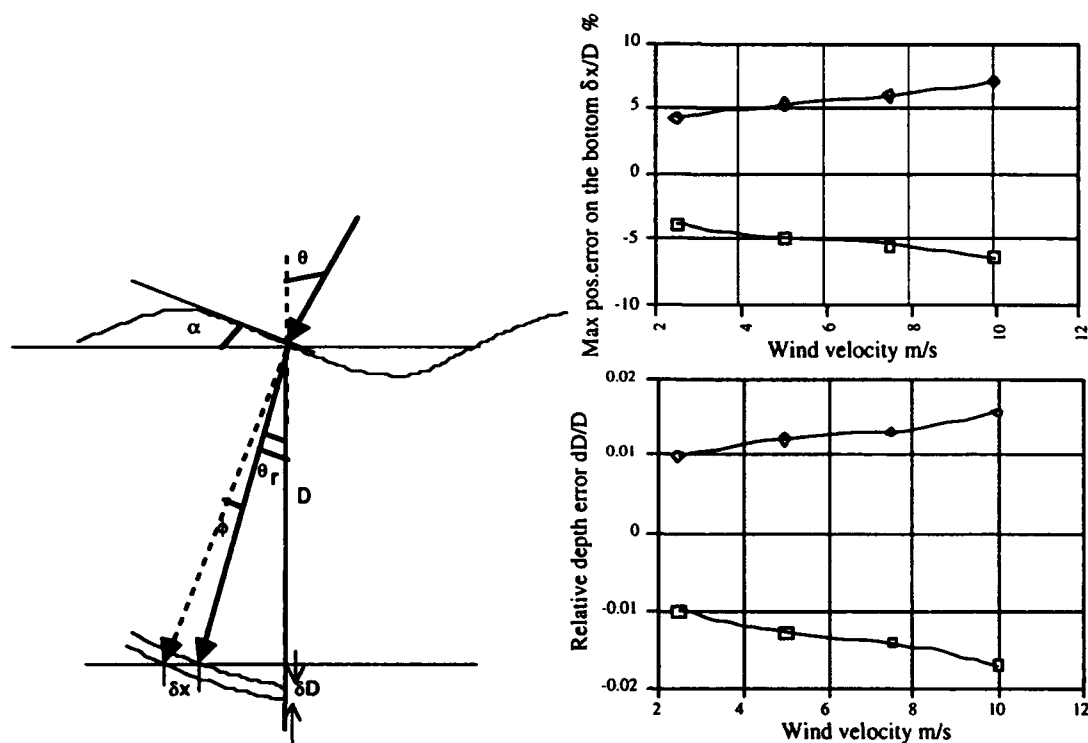


Figure 4. Estimate of maximum error due to wave refraction. Upper right shows the bottom position error and right below the relative depth error which may exceed 1 % of depth. These type of errors are hard to correct for.

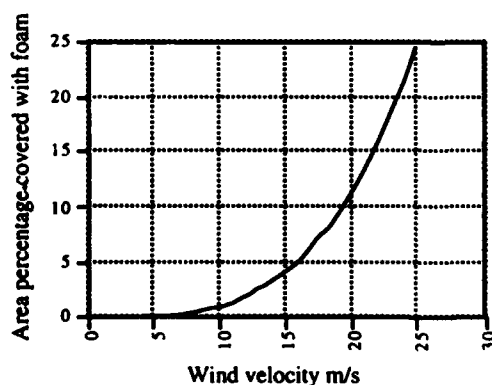


Figure 5. Percentage of surface covered with foam as a function of wind speed. Data from Koepke²⁷.

Since the depth is calculated by the difference in arrival times of the surface and bottom returns the depth includes wave height information. The wanted depth is that referred to the mean surface level and thus wave height correction is necessary. The problem is analysed by Thomas and Guenther²⁹. The wave heights are derived from the slant path measurements using collinear IR and green beams and vertical accelerometer data for taking out the aircraft motion from swell. It is shown that no slant range available (IR-dropout) will lead to a short term error (< 6 seconds for the accelerometer sampling time of $1/64$ sec. and standard deviation of the acceleration = 0.1 ms^{-2}) of $1/4$ of the wave height h . With the data acc. to table 2 we see how the depth error due to wave correction depends on system parameters (figure 6). The random variation of slant range (σ_r) was assumed to be 0.1 m. However there are reasons to believe that this random error is larger due to geometric pulse stretching at the surface and to the fact that different parts of the beam footprint may

contribute differently to the surface return (due to facets giving glint returns). For σ_r ranging from 0,1-0,5-1 m (other par. to table 2) the depth error increases from 0,03-0,11-0,21 m for the case of no IR dropout.

2.4 Scattering layers and other inhomogenities in the water column.

The scattering in the water broadens the beam which gives a depth bias which can be both positive and negative (positive for "deep" biases, negative for shallow). The bias depends on the scattering length $s \cdot D$ and the nadir angle θ . Guenther³⁰ has studied this bias in great detail by Monte Carlo simulation. In general this bias is rather small as can be seen in figure 7. In order to use this bias correction the scattering coefficient has to be known or estimated (for example from the wave form decay which for large FOV gives K and for small FOV $c = a + s \approx K + s$). We conclude from figure 7 that a smaller uncertainty in the s -value has a small impact on the bias. This also include the case where the water column is inhomogenous. For many cases an estimate of the average scattering should be enough. On the other hand the scattering layers may, if they are strong, be interpreted as bottoms. One example is shown in figure 8 from our experimental data. More examples are discussed under experimental results.

Table 2. Parameters for estimating error in wave height correction of the depth.

Flight altitude H	300 (m)	Wave height stand. dev.	0,3 (m)
Beam aiming error	1 (mrad)	Half filter length	5 (sec.)
Nadir angle	20 (°)	Sample time acc. data	1/64 (sec.)
Slant range error	0,1 (m)	Acc. error in altitude	0,1 (ms ⁻²)

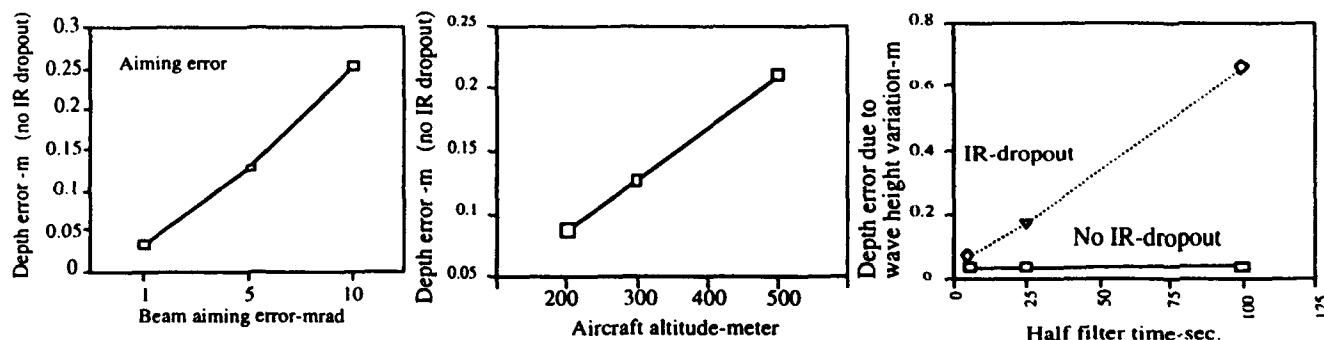


Figure 6. Depth error in wave height correction due to beam stabilisation, altitude and integration time. Data according to table 1. Diagrams are based upon formulas in ref. 29.

2.5 Bottom roughness and vegetation.

The depth accuracy analysis for lidar bathymetry presented in the literature has almost exclusively dealt with horizontal flat bottoms. However real bottom are seldom that ideal. Therefore we have investigated the influence of bottom topography by wave form simulations. The theoretical simulations are based on the analytical formulas for beam propagation by Lutomirski³². We have looked at 3 topography situations (figure 9). We have investigated the wave forms for different bottom slopes and for three different water types (clear, "mean", turbid cf table 2). Figure 10 shows example of wave forms for the slopes 0°, 10° and 20°. We can also see the influence on the bottom pulse shape depth using the 50 % threshold with the pulse echo in linear scale. For the echo extraction we find that the contrast C defined as the ratio A/B where A is the bottom peak amplitude above the extrapolated back scatter level B according to figure 11. The signal to noise ratio for the bottom echoes defined as $SNR = A^2/\text{var}(N(t))$ where N is the noise signal well out of the depth range for bottom and water back scatter.

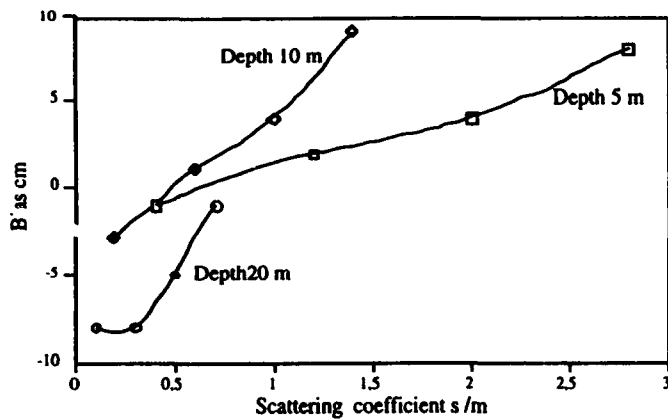


Figure 7. Depth biases vs. scattering coefficient and for different depth. Nadir angle 20° and FOV diam. = depth As can be seen from the figure this correction is rather small.

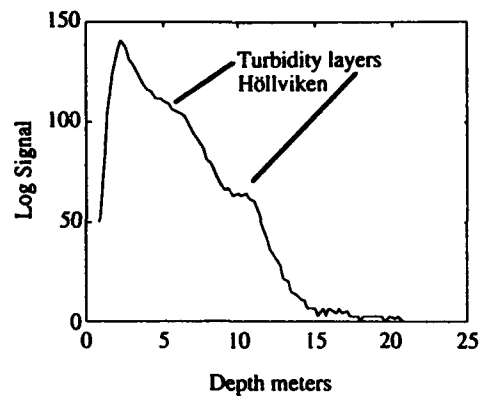


Figure 8. Turbidity layers measured with FLASH.

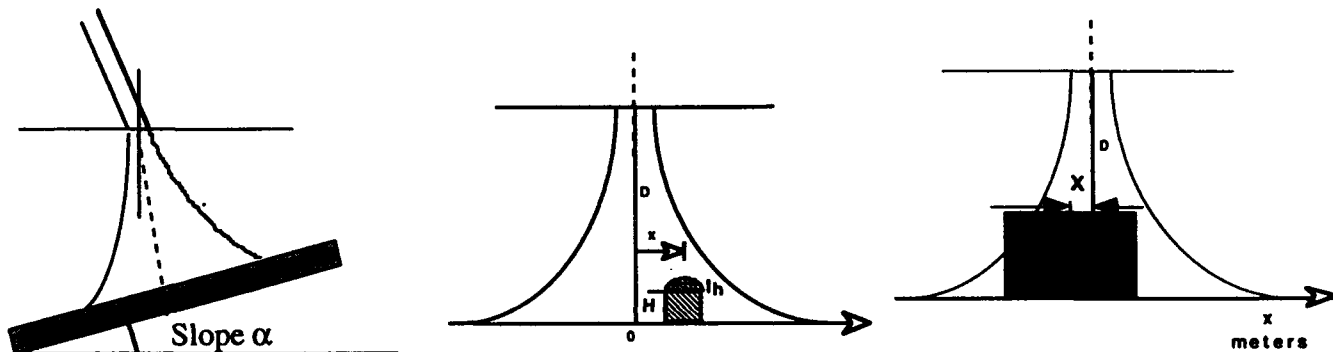


Figure 9. Bottom models used in the simulations. Left sloping bottom, middle stone ($1 \times 1 \times 1 \text{ m}^3$) and right step like bottom. Variables: slope angle, position relative to the beam (x) and depth. Besides that the water quality and system parameters were varied.

Table 3. Water parameters used in simulation.

WATER PARAMETER	"Clear" water	"average"	"turbid"
Diffuse att. K	0,17 /m	0,25 /m	0,35 /m
Sc. coeff. s	0,35 /m	0,8 /m	1,3 /m
Beam att. c	0,5 /m	1 /m	1,6 /m
Albedo w_0	0,7	0,8	0,9
Backsc. coeff. β	0,0014 /msr	0,0025 /msr	0,0032 /msr
Rms sc. angle	0,39 /rad	0,40 /rad	0,41 /rad

Figure 11 b shows the contrast C as a function of bottom slope angles. These curves are also fairly symmetrical around the zero slope angle. Note the very steep bottoms (slopes above 25°) will "smear out" the pulse within the footprint giving a very low contrast and difficulty for detection even if the SNR is high. A possibility of confusing the bottom echo with that of a turbidity layer which also can give a broad echo is obvious. Also note that the contrast is much higher for the clear water model than for the models of average and turbid water. This is what to be expected. A strange fact that can be noted is that the contrast for the turbid and average waters are so similar. This might be partly explained by the smaller differences if the scattering parameters between these two waters in relation to the difference against clear water.

For 5 m depth the offset tolerance for detection of the stone is $\pm 2 \text{ m}$ which correspond to a 4 m shot distance for certain detection. If we increase the depth the sensitivity for an offset is smaller. At 10 meters depth (figure 12) the offset tolerance for resolved wave forms with two peaks is $\pm 4 \text{ m}$ while the corresponding figure at 5 m depth is $\pm 2 \text{ m}$. If the peaks are not

fully resolved, detection with a 50 % threshold will miss stone detection because the wave form amplitude originating from the stone will in general be much smaller than that from the surrounding bottom at least for the assumed receiver field of view (FOV) and flight altitude (50 mrad and 300 m altitude).

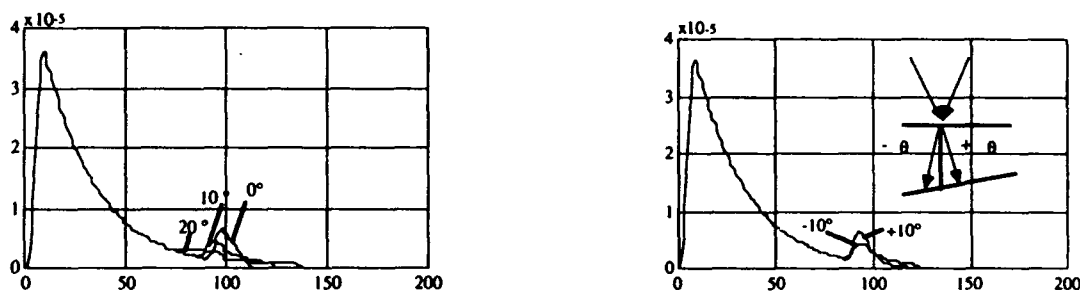


Figure 10. Left: Examples of wave forms (linear scale) from different bottom slopes. We can see how the slope is affecting the pulse shape so that more shallow depths are detected as they will be within the broadened beam. Right: Different bottom pulse shapes for the slopes indicated in the figure. Horizontal scale 1 ns/div. (=11,12 cm).

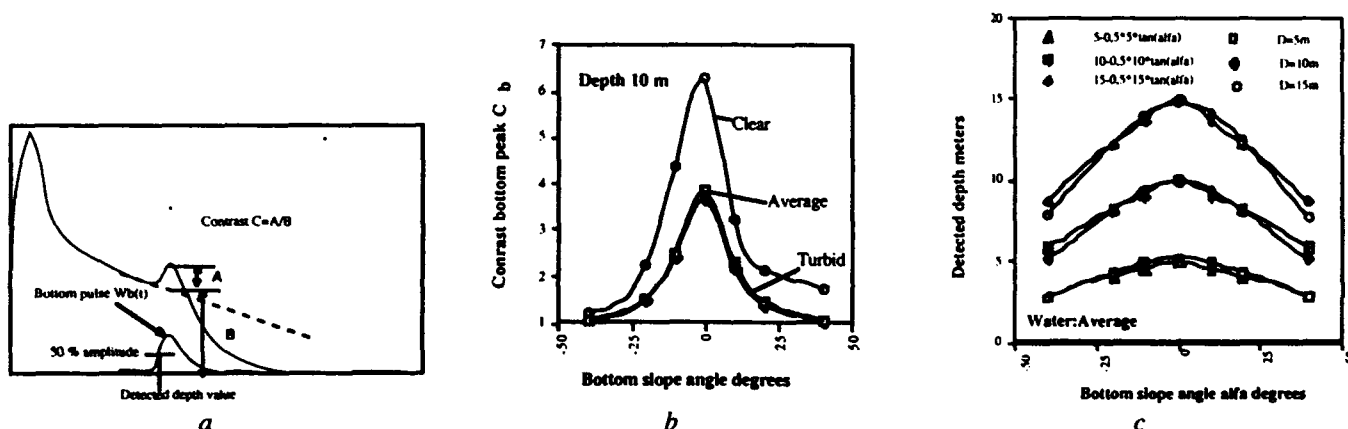


Figure 11a. Definition of contrast and definition of the depth detection procedure. 11 b. Bottom contrast vs. slope angle 11 c.: Comparison between depths using a simple geometric model where we assume a beam footprint as half the depth and calculates the smallest depth within that footprint and the depths detected by simulation.

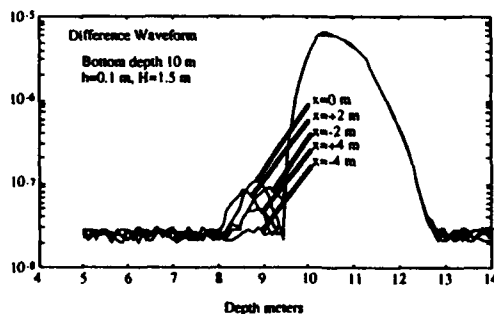


Figure 12. Wave forms from a $1 \times 1 \times 1 \text{ m}^3$ stone. straight below the beam centre at the surface respectively with a 2 m offset. Linear scale. Bottom depth 10 meters. Simulation of difference wave forms (water back scatter removed). Stone with $h = 0.1 \text{ m}$ and $H = 1.5 \text{ m}$ (cf. figure 9). Bottom depth 10 meters. Water: clear.

If the receiver field of view is reduced we can increase the stone peak relative to the surrounding bottom peak and a 50 % threshold will give the correct (shallowest) depth. Figure 13 gives an example of this. For a large FOV it seems reasonable to detect at two positions in the rising edge not to miss any shallow feature. Figure 14 shows the detected depth from the stone and from bottom at 5 and 10 m. Note the large variation due to position of the stone relative to the beam position at the surface. This depth bias can, as in the case of a sloping bottom, be explained by the geometric path difference. This is

seen in figure 14 a where the "geometric" depth according to Pythagoras ($D(x) = D*[1+(x_0/D)^2]^{0.5}$) is plotted together with that obtained from simulation. In figure 14 b the receiver field of view is varied. Note the sharp increase of the detectability for smaller FOV:s (contrast and SNR for the stone increases). For smaller FOV:s the detected depth for the stone is closer to the true depth. In figure 14 c the depth and contrast for a $1*1*1\text{ m}^3$ stone at 10 meters are shown vs. FOV. The bottom contrast increases for larger FOV:s. The depth of the stone is slightly increased for larger FOV. The conclusion from the above is that reducing the receiver field of view is motivated to ensure capture of smaller features in shallow waters. The reduced FOV results however in a smaller maximum depth. We have done similar simulations as for small stones for a "step like" bottom. The main difference to that case is that the depth variations due to position of the "step" are much smaller. Figure 15 shows detected depths vs. step position for a large surface of 4 m^2 at 5 meters and 3 meters above bottom. The depth variation for $|x_0| \leq 2.5\text{ m}$ (5 m spot distance) is smaller than 0,1 m. The contrast for the detection at 5 meters is of course higher and maximises for $x_0 = 0$ meters as expected.

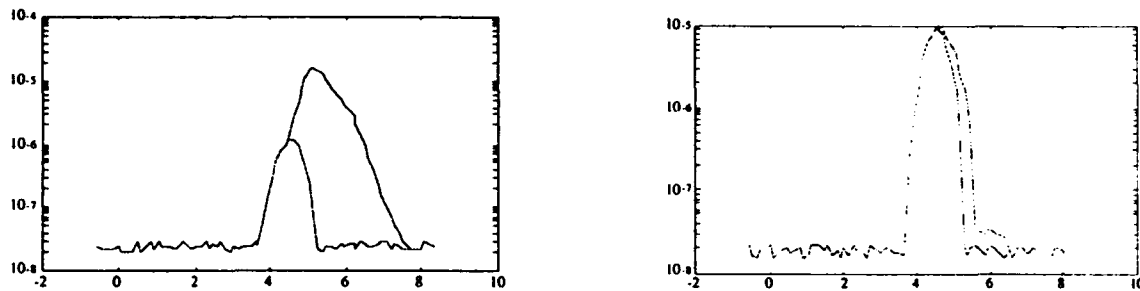


Figure 13. Difference wave forms from a $1*1*1\text{ m}^3$ stone at 5 meters bottom depth. Left shows the wave form with full field of view (50 mrad corresponding to 15 m at the surface) and right shows the result for 10 mrad FOV. In both cases the stone offset from the beam centre at surface is 1 m ($x = 1\text{ m}$). Water: clear.

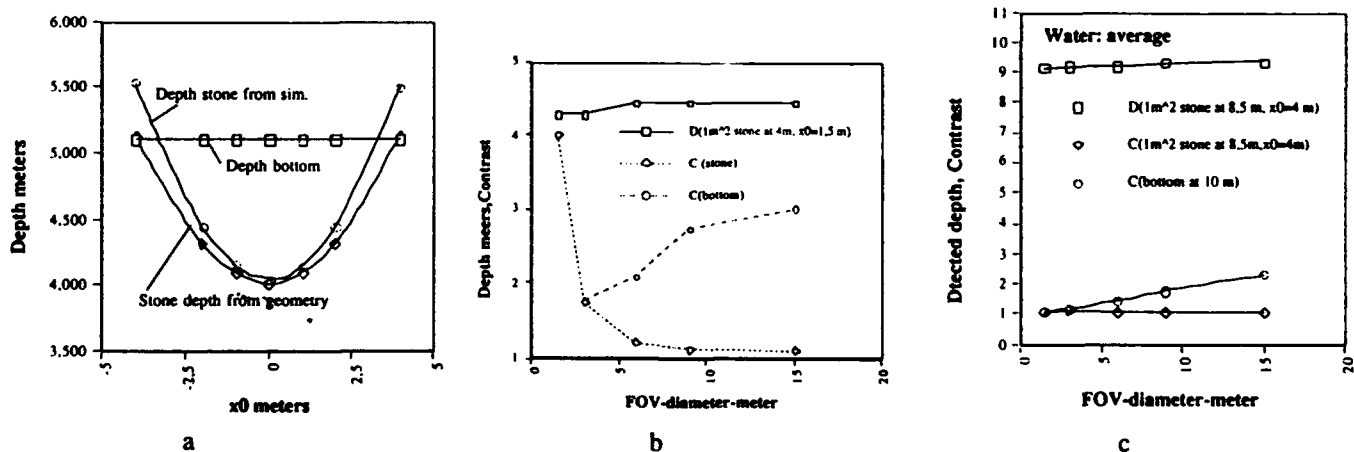


Figure 14a. Detected depth from 1 m^3 stone at 5 m depth. Note the large variation of depth depending on the stone position x_0 relative to the beam centre at the water surface. Water: clear. 14b. Variation of depth and contrast vs. receiver field of view diameter (FOV-diameter). $1*1*1\text{ m}^3$ stone on a 5 m bottom and displaced $x_0 = 1.5\text{ m}$ from beam centre. at the water surface. Note the sharp increase of detectability (contrast) for small FOV-diameters. 14c. Depth and contrast for a 1 m^3 stone at 10 meters.

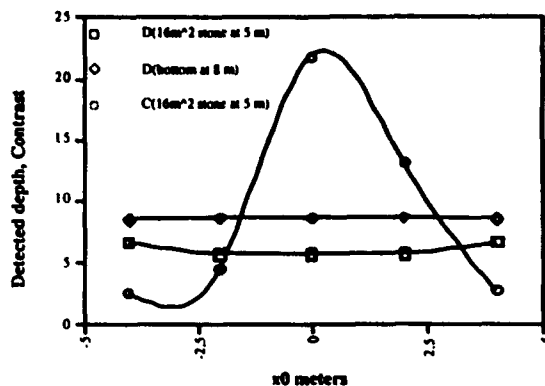


Figure 15. Detected depth and contrast for a steplike bottom.

2.6. Hardware limitations.

Today state of the art lidar bathymeters have about 10-200 Hz pulse repetition frequency. The swath width is limited by the maximum angle of incidence relative to the water surface of about 30° . This translates to a swath width slightly larger than the altitude. Assuming dense coverage ($a = 5$ m) the reasonable helicopter speed of 50 knots (25 m/s) leads to a swath width of about 200 m. Future diode pumped laser technology will be about 10 times as efficient as today's flash lamp pumped systems. Assuming the same electrical power this efficiency can be used to increase from today's 5 mJ, 200 Hz to 5 mJ, 2 kHz or more using an all solid state and reliable laser. This 10 fold prf increase can be used in many ways, one is denser sounding another is high flight speed and higher surface coverage rate etc. One can also think of using larger pulse energies 100 mJ-1 J and use diffractive elements to split up the beam to fit the avalanche detector arrays now under development. This puts less demand on the scanner frequency but higher demand on the signal processing system in handling parallel channels.

The storage of every wave form together with real time depth imagery drive the signal processing electronics to the commercial limits. Future higher prf systems may benefit from partially relying on real time depth algorithms with part of the storage wave forms as controls points. Finally lidar bathymetry is coming into full operational use right now. The system reliability can fully be evaluated first after some years of use in various climate situations.

3. EXPERIMENTAL EFFORTS

In Sweden work on airborne depth sounding lidar has taken place during more than ten years. Activities include the development of a helicopter borne lidar called FLASH¹⁻³ as well as instrumentation (HOSS)⁴ for in situ measurement of the optical water parameters. The FLASH system has been further developed into two operational systems called Hawk Eye with Saab Instruments as the main contractor and Optech Inc. as the main subcontractor.

3.1 The Flash system

For detailed description of the system we refer to ref. 2-3. In short the FLASH system is a helicopter borne lidar bathymeter with key functions in real time depth imaging and programmable scanning³². Figure 16 shows a real time display in the normal flying mode and the hovering mode of operation.

Table 4. FLASH system parameters

"Green" receiver:	Scanner:
PMT, 20 cm telescope, filter 1,2 nm	Programmable, semicircular scan pattern at 20° angle of inc. in normal mode.
FOV outer 5-50 mrad, inn. bl. 0-10 mrad	Hovering mode: $\pm 20^\circ$ in y (^ nose dir.)
"IR" receiver:	+35° / -5° in x (in nose dir.)
Coax. with green, av. photo diode,	Storage:
Land/water discriminator.	Data: Sensor parameters, navigational data.
Rec. Electronics:	Full wave forms every 6th wave form at 200 Hz, all wave forms at 62 Hz.
Log. amplifier: 80 dB.	Video recorder.
Le Croy digitizer: 2,5 ns sampling at 8 bits.	Navigation:
Constant fraction discr. for slant range.	Motorola mini ranger later replaced by GPS.
Slant range resolution 8 cm.	Presentation:
Real time echo extraction.	Wave form, depth coded colour display



Figure 16. Real time depth colour display from the FLASH system. Left shows the normal mode when flying. Swath width 200 m, altitude 300 m, spot distance 5 m, semicircular scan with 20° nadir angle. Right shows the hovering mode with a = 2 m shot distance. In both modes the operator can choose the shot distance and in the hovering the subarea to be searched. Colour code can be adopted to the range interval of interest. In this example deep blue (black here) is about 20 m and light blue (white) is 1.5 m.

3.2 The Hawk Eye system.

The FLASH system has been further developed into two operational systems called Hawk Eye (figure 17) As mentioned before these systems are intended to be more suitable for accurate depth sounding. Main differences include:

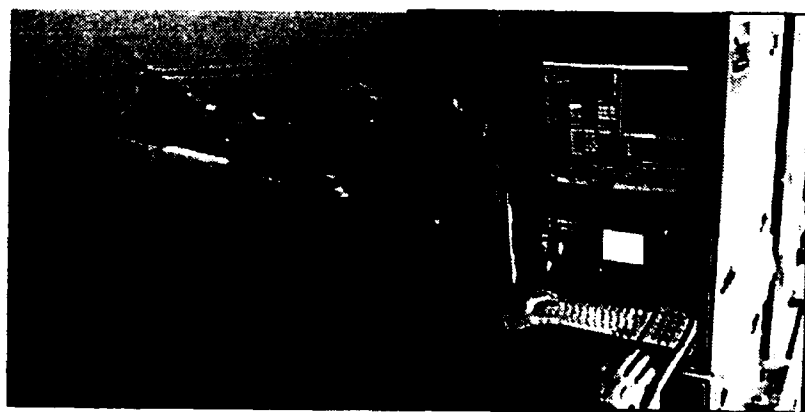


Figure 17. The HAWK EYE system at present under testing (June 1994).

- Pod mounted transceiver system.
- Better wave form sampling (10 bits, 1ns).
- Storage of every wave form.
- Better signal handling especially for echo extraction.
- Better scanner accuracy.
- Inertial reference system plus GPS.
- More compact and easy installation.
- Built in planning and mission software.
- PMT replaced by APD for the green channel.

3.3 The HOSS system.

The in situ profiling instrument called HOSS (Hydro Optical Sensor System)⁴ is designed to operate from a helicopter or from a ship. HOSS collects data during its up and down movement at a vertical speed of 0,5 m/s. The optical sensors measures daylight attenuation (K), beam attenuation (c), single scatter (s) and back scatter (β). The absorption (a) and the albedo (w_0) are derived.

3.4. Water parameters.

The main part of the HOSS measurements were made in the Baltic. Below (figure 18) we show some examples of correlation between different water parameters measured by HOSS. Such relations are of large operational value as they correlate those parameters which are difficult to estimate from lidar directly (e.g. the scattering coefficient s) to those which are easier to estimate from the wave form such as the diffuse attenuation K. Typical correlation coefficients in the Baltic were found to be between 0,5 and 0,7 for K vs. s and c and for β vs. s. Measurements were taken both during winter and summer. Typically the summer values for K, s and c are 50-100 % higher than those obtained during winter time.

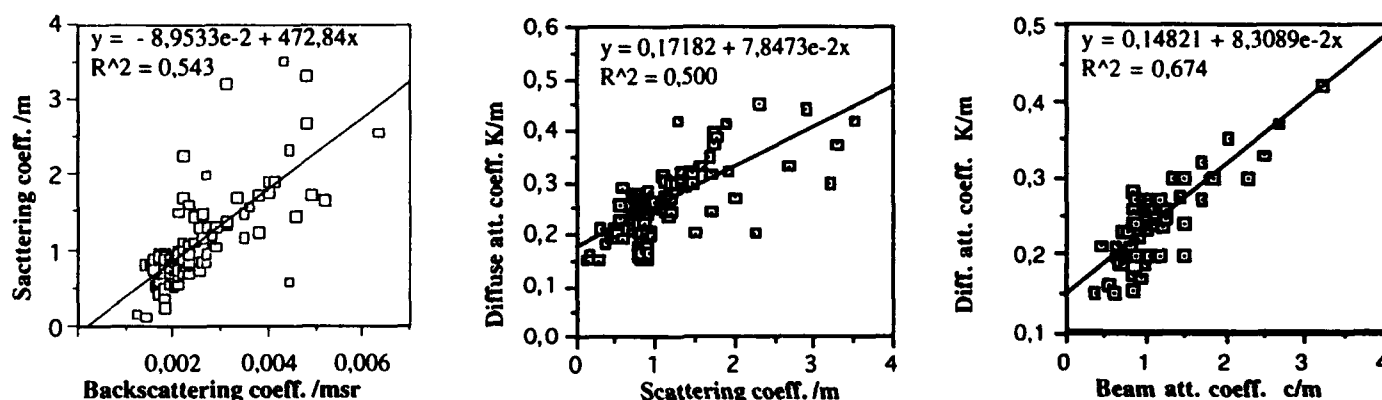


Figure 18. Correlation between various optical water parameters as measured by HOSS in the Baltic during 1989-92.

The maximum depth penetration correlates for a large receiver field of view (FOV) diameter (about the depth) well with $1/K$ as shown in fig. 19. For a known bottom reflectivity this can be used to estimate K. The value of G depends on the receiver field of view (FOV) or more directly to the receiver spot size on the water surface. This relation has been studied by the multiple scattering results obtained by Gordon³³. We have investigated G using the back scatter decay and the bottom peak decay both of which are expected to follow the relation $\exp(-2GD)$ with depth D. The underlying assumptions are a homogenous water body and bottom. Figure 20 and 21 show G from back scatter and bottom echo respectively obtaining $G \approx K$ (FOV diameter 15 m). Table 5 show the comparison between different ways of estimating G given two types of water. The back scatter decay method fails as soon as the water column is inhomogeneous. This is shown by table 5 and by figure 22. The system attenuation G is depending on the FOV as pointed out by Gordon³³ and in our earlier paper². Figure 23 a shows G for various FOV combinations. As expected the attenuation increases with smaller FOV or larger blocking. In this water the decrease of FOV from 48 to 8 mrad (corresponding to a surface diameter of 14,4 to 2,4 m) and no inner blocking according to Gordons article should result in a system attenuation

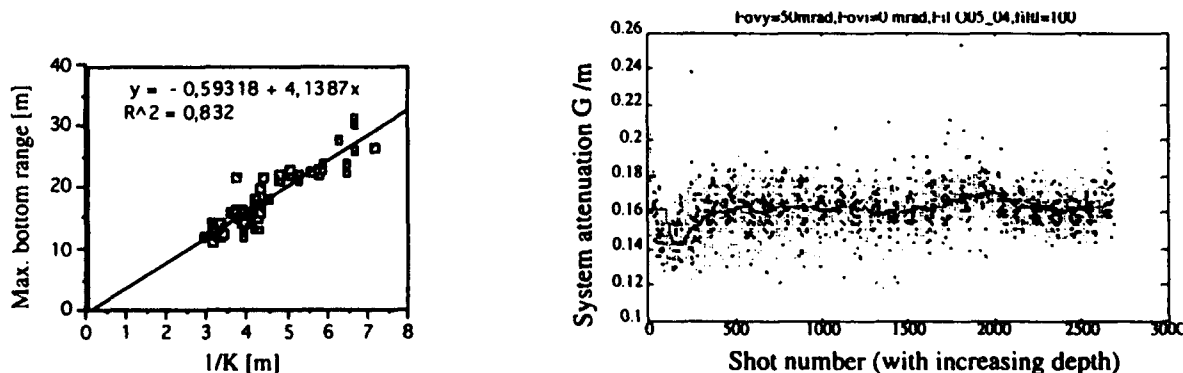


Figure 19. Maximum bottom range (Rb) scales

Figure 20. Measured system attenuation coefficient G

approximately as $R_b \approx 4,14/K$.

from the back scatter slope. 3000 wave forms were used.

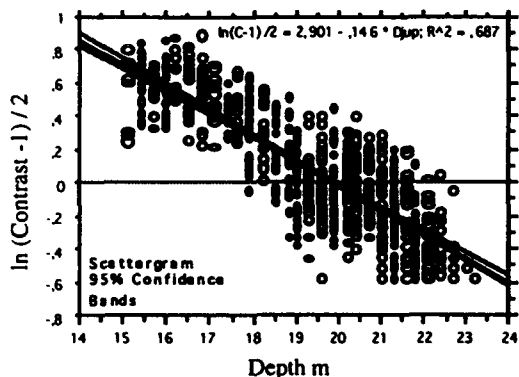
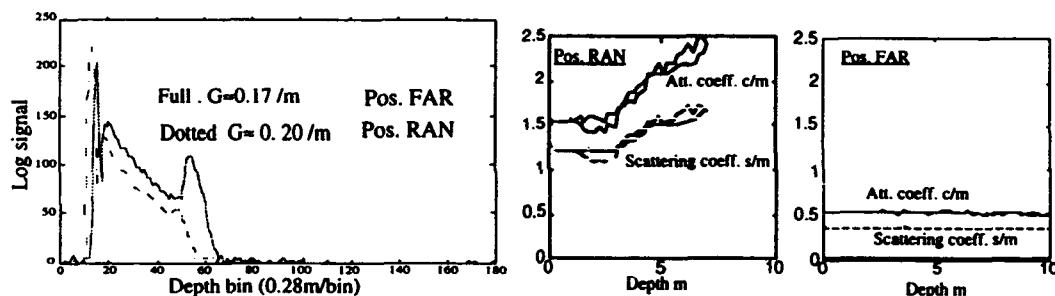


Table 5. Estimate of system att. G

Method	Position FAR	Position RON
HOSS	0.160-0.165/m	$\approx 0.30/m$
Bottom range	0.16-0.20	0.28-0.33
Backsc. decay	0.162 ± 0.014	0.17 ± 0.014
Bottom decay	0.146 ± 0.05	No echo in noise

Figure 21. Measured bottom peak decay (as contrast C relative to noise) for estimating system att. coeff. $G \approx 0,146/m$. About 800 wave forms were used.

between (0,15-0,17) to (0,23-0,27) depending on the choice of scattering phase function. We measured $0,162 \pm 0,010$ to $0,228 \pm 0,007$ which compares rather well with the theoretical results. Figure 23 b shows comparisons between G -measurements and those inferred from Gordon results. Also indicated in figure 23 c is the range loss obtained by reducing the filed of view in that type of water ($c \approx 1/m$). As pointed out earlier in the paper reducing the FOV of the receiver has the potential advantage of improving the horizontal resolution but at the cost of some range loss.



Water parameters: (average values):

FAR: $K = 0,17/m$, $s = 0,32/m$, $c = 0,45/m$, $b = 0,0017/msr$

RON: $K = 0,30/m$, $s = 1,38/m$, $c = 1,70/m$, $b = 0,0031/msr$

Figure 22 Wave forms from two water types. Measurement of G from back scatter gives a value of $G \approx 0,17/m$ for the clear water (FAR) in acc. with depth range. In the other example (RAN) the back scatter decay heavily underestimates G (0,20/m instead of 0,30/m because the turbidity is not homogenous with depth as indicated by the profiles obtained by HOSS.

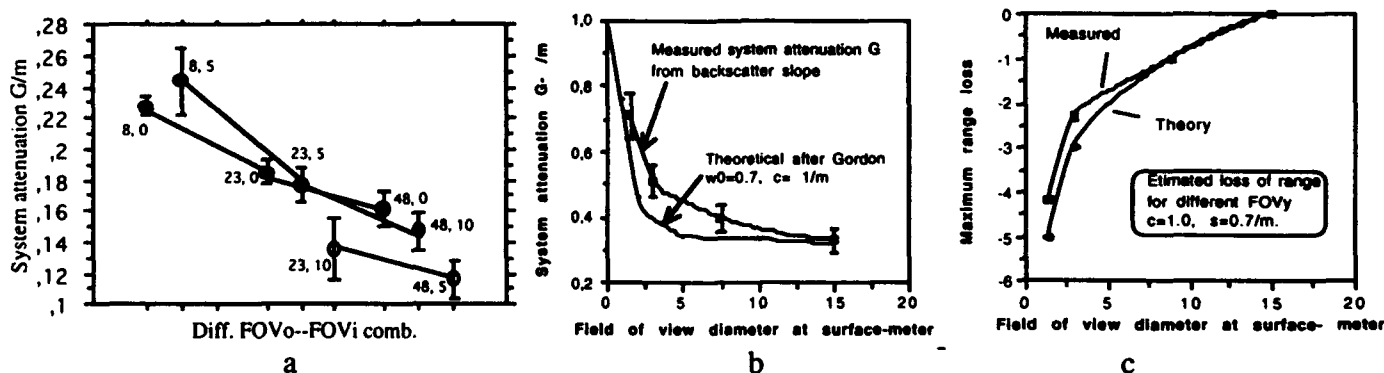


Figure 23a: System attenuation (obtained from back scatter slope) for various combinations of outer field of view and inner blockings. 23 b: The measured value of the system attenuation as a function of the field of view diameter compared with theoretical simulations by Gordon³³ 23 c: Measured and estimated (by analytical modelling) maximum range loss based on the results bottom peak decrease.

3.5 Resolution, small feature detection.

Due to beam broadening, system time resolution and propagation induced time response the lidar system has lower limits on both shallowest depths, depth resolution and horizontal resolution. At present systematic trials are under way to investigate these limits. We will here give some examples from the FLASH system that indicate what one can expect from the technology in well designed operational systems.

The shallowest depth that the FLASH real time echo extractor (simple peak finder) could handle was about 1.4 m. Some times even 1.1 m depth could be resolved (fig.24). With the new Hawk Eye, which uses a separate shallow detector, channel and post processing shallow depths down to 1 m seems feasible. Next question is the depth resolution between features on the bottom. To study this problem we used a reference target made as an "Olympic rostrum" with 3 flat nets 2*2 m² each and placed next to each other (figure 25). By altering the distance between the nets (reflectivity about 20 %) we could measure depth resolution, pulse amplitudes and horizontal resolution. Figure 26 show an example of a real time image of the reference target indicating that in part of the target the system could resolve two peaks coming from the nets separated by 1.5 m. The shot distance a was 1 m and the apparent horizontal size of the target was estimated to 4*7 m² to be compared with the true projected area of 2*6 m². The depth to the deepest part of the target was 16.7 meters. Bottom range was about 21 meters. "The blurring" may be attributed to the long scanning time (160 Hz, $a = 1$ m and 50*50 m² scanned gives 16 sec.) and the lack of compensation for the helicopter drift. Figure 27 gives examples of pulses from the reference target.

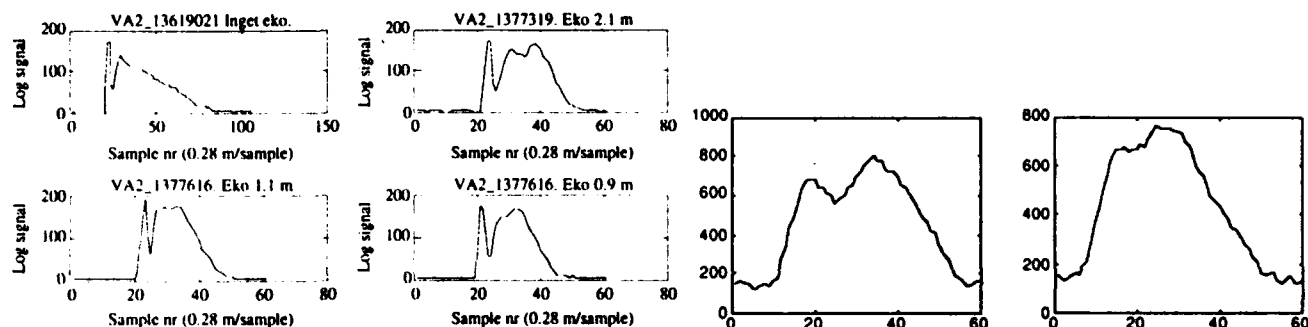


Figure 24. Example of the shallow depth wave forms from FLASH (left) and Hawk Eye (right). In the FLASH system the real time extractor generally could measure depth down to 1.4-1.5 m. In Hawk Eye each sample corresponds to 0.11 m.

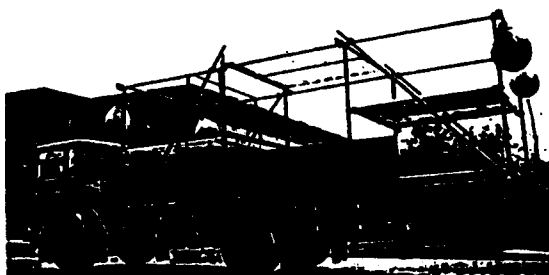


Figure 25. The reference target.

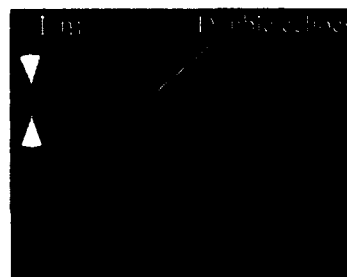


Figure 26. Real time image of the reference target at 15-17 m depth.

Tests were made with boxes on the bottom to investigate the possibility to see smaller features on the bottom. To a first approximation the small target detection is a contrast problem. If we adopt the designations from figure 11 a the contrast for a feature well above the bottom to be depth resolved can be approximated with the expression:

$$C = A/B = [\rho_f A_f + (A_b - A_f) \rho_w] / [A_b \rho_w] \quad (10)$$

where A_f is the top cross sectional area of the feature, A_b the beam area at the depth of A_f and ρ_f the diffuse reflectivity of the feature. The equivalent water reflectivity ρ_w can (for not too turbid waters) be approximated by $\rho_w = \pi \beta c_w \tau / 2$ where β is the water back scatter coefficient, c_w the velocity of light in the water and τ the laser pulse length. Using the above formulas together with beam broadening calculations based on Lutomirski³¹ and $\rho_f = 5\%$ we can estimate the

minimum cross section of the feature to be observed against the water back scatter curve (figure 28 a,b). As a contrast threshold for detection we set $C = 1,2$. As can be seen from figure 28 b the minimum feature size is about 1 m at 10 m depth and 2 m at 20 m. Water model according to table 3. We found by experiments that these theoretical calculations were in accordance with observations.

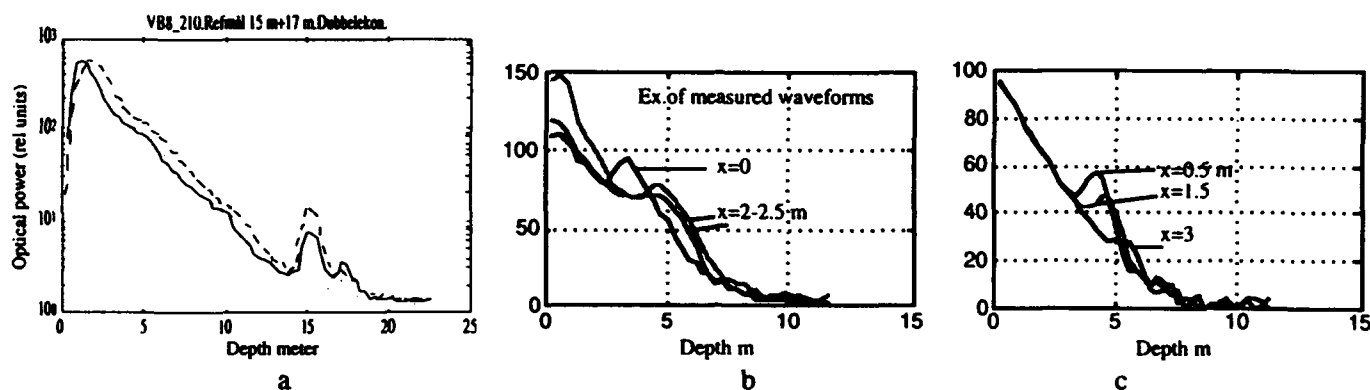


Figure 27 a: Pulses from the reference target. Double echoes are resolved when the separation is larger than about 1.4 m. 27b: Pulses from a bottom feature at about 4 meters depth. When hovering above this feature the pulses at different depths are explained by the fact that the laser beam hits beside the target and not right above. This can thus introduce depth errors. 27c: The same results as in 27 b obtained by wave form simulations.

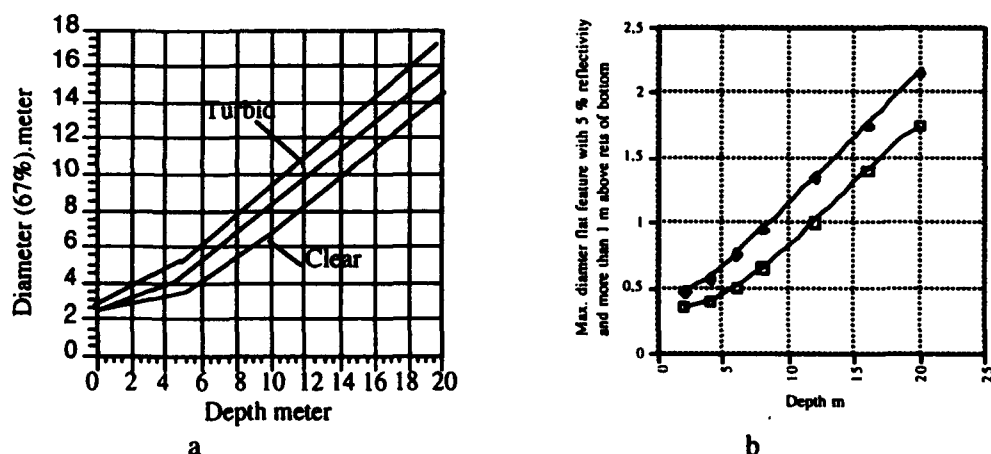


Figure 28 a: Beam broadening (67 % of energy diam.) as a function of depth. Water model according to table 3. Beam size at surface 2 m. 28b: minimum cross section size of smallest depth resolved feature that can be seen against the water background.

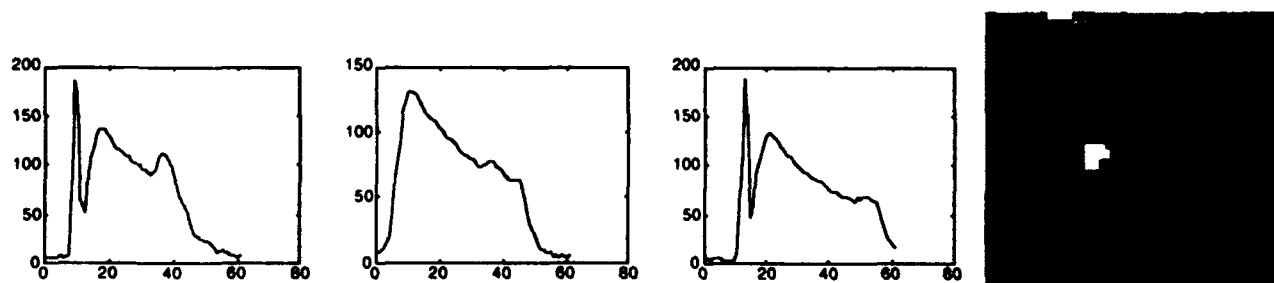


Figure 28c: Example of target signal from a target box with height 1,15 m and cross area of 0,4 m². The white pixel corresponds to the left wave form, where only the target are resolved. The black pixel corresponds to the middle wave form, where both the target and the bottom are resolved. The wave form to the right corresponds to a gray pixel, where only the bottom are detected.

3.6 Depth accuracy.

Wave heights

The FLASH system did not have an INS-system why full wave height compensation could not be done. We did compensate for the short fluctuation (small waves) taking the relatively large scanner induced slant path variation into account (figure 29, 30).

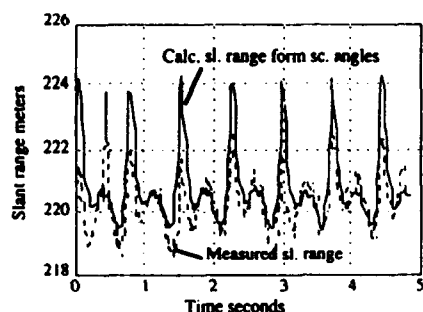


Figure 29. Scanner induced slant range variations.

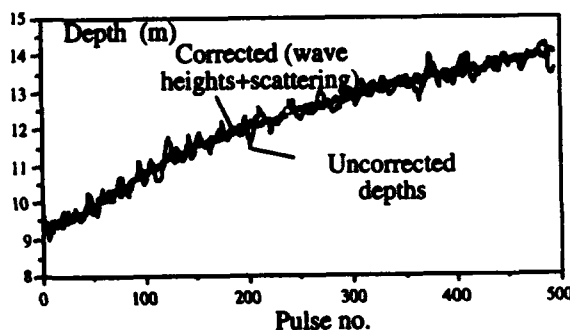


Figure 30. Corrected depths due to wave heights and scanner effects.

Turbidity layers

Turbidity layers may limit depth penetration and introduce false bottoms if not postprocessing is done with enough care. Figure 31 shows examples of a thin and thick scattering layer respectively. As can be seen from these examples the discrimination of scattering layers based upon pulse shape only may not be sufficient.

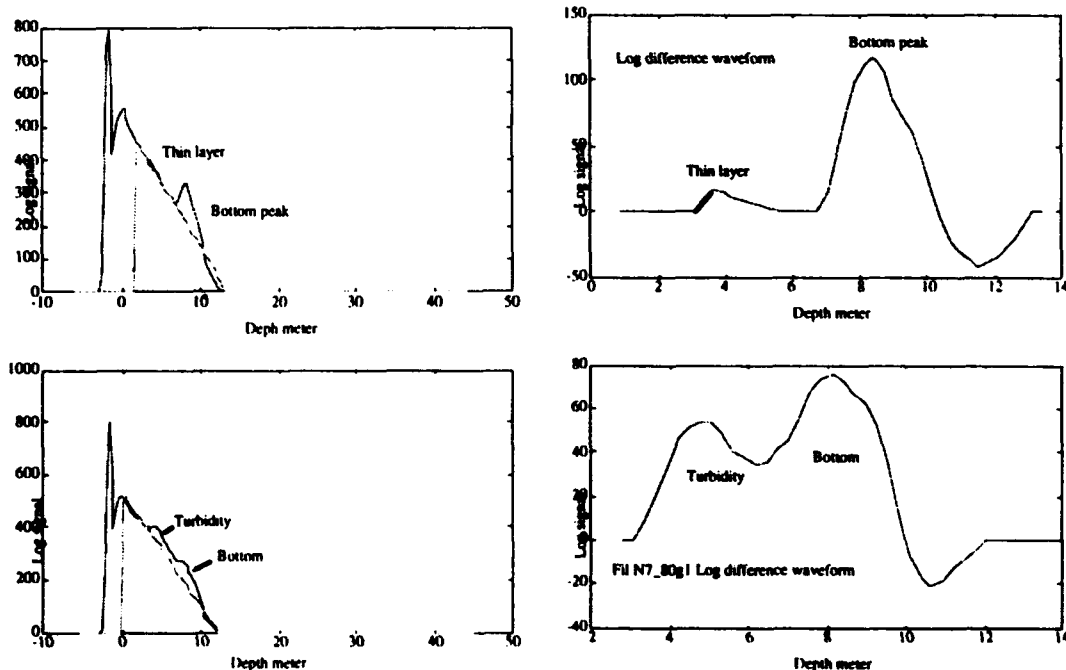


Figure 31. Examples of thin and thick layer signal in relation to the bottom signal. Log difference waveform refer to a log signal with the homogenous backscatter subtracted.

Scan angles

We made statistical tests (using ANOVA) about the hypothesis that the detected depths did not depend on the scanner angles being either in X (in helicopter nose direction), Y or nadir. Figure 32 shows detected depths and bottom echo contrast (echo amplitude divided by back scatter / noise level if no echo should be present) for different angles. For the total angle of incidence relative to nadir we find that there are small differences in both depth and contrast, although the depth variation in this case could probably be attributed to a weak bottom slope. There are not any significant angle of incidence effects after correction of the refraction. The example investigated corresponded to scattering length $s \cdot D = 4$. For larger $s \cdot D$ values propagation biases may be so large that they show significance.

If we compare the results with theoretical simulations we find that we should expect very small depth differences as a function of scanner angle (about 10 cm) but we find that the contrast should change. To the first approximation there is a difference for the shortest water paths of 3 % at an angle of incidence of 20 degrees, which means less than 0,4 m for this data set. However this is compensated for when calculating the depth. The contrast difference is however larger than what should be expected from this small depth difference. The effect of slant angle of incidence is here to "stretch" the echo.

The angle of incidence will affect the detected depth and the bottom echo amplitude. During some of the swaths we noticed that there was a depth bias between the left and right parts of the swaths. Figure 33 shows examples of wave forms from different parts of the swath. The wave form consists of an artificial surface marker that is positioned in time about 1 meter (depending on PMT voltage) above the true surface which is controlled by the slant range measurement made by the 1,06 μm channel. As our real time echo extractor picked the "true surface" from the position of the surface peak, the variation between that peak and the position of the beginning of the green wave form will result in depth variations. As we have not seen this phenomena more than a few times we conclude that one possible explanation might be due to surface waves that affected the IR- or green return differently depending on angle of incidence and flight direction relative to the wave propagation. The angle of incidence will also affect the magnitude of the IR-return. During calm conditions IR-dropout may occur which also affects the depth accuracy as the surface form of the green return might be either specular or coming from a volume return just below the surface. This "flip-flop" effect can theoretically be about 0,5 meter for K-values between 0,1-0,3 m^{-1} .

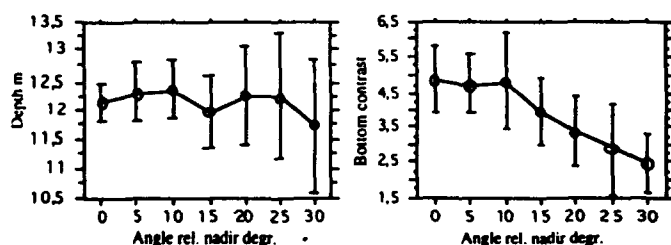


Figure 32. Detected depths and bottom echo contrast for different scanner angles for a rectangular scan during hovering. Av. water parameters: $K = 0,17 / \text{m}$, $s = 0,32 / \text{m}$, $c = 0,45 / \text{m}$, $\beta = 0,0017 / \text{msr}$.

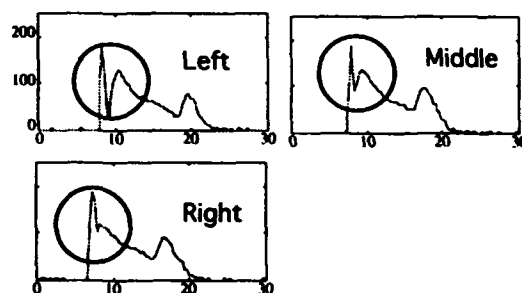


Figure 33. Waveforms from different parts of the swath. Note the time difference between the surface marker and the start of the green return.

Receiver FOV effects.

A smaller FOV may improve the horizontal resolution and thus improving detectability and depth accuracy for small depth resolved bottom features. The interesting question then arises whether FOV has any significant impact on depth accuracy for plane bottoms. Normally the FLASH system operates at 300 m altitude and with 50 mrad outer FOV (15 m FOV diam. at surface) and no inner blocking. The inner blocking is useful to suppress the strong returns from the surface and the layer just below. We thus found it motivated to investigate the FOV effects on the bottom contrast, detected depth for a plane bottom. The typical number of pulses within each FOV set is about 100.

Figure 34 shows the results for detected depth and bottom contrast as a function of FOV. We have chosen data from hovering above a $50 \times 50 \text{ m}^2$ area at 12.5 m depth and believed to be flat and horizontal. The water parameters were: $K = 0,17 / \text{m}$, $s = 0,32 / \text{m}$, $c = 0,45 / \text{m}$, $B = 0,0017 / \text{msr}$. The ANOVA tests does not support any significant effects on bottom depths and contrast versus the used field of views. Error sources are scan angle effects and bottom variations.

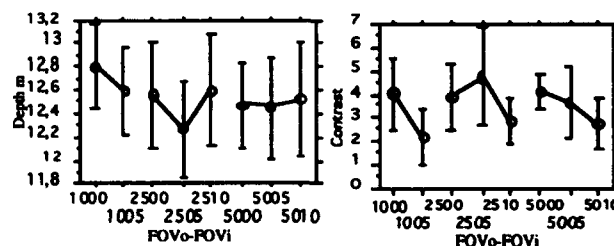


Figure 34. Detected depth and bottom contrast for combinations of outer field of view and inner blockings. Key: 2510 = 25 mrad FOVo and 10 mrad inner blocking.

Topography, vegetation.

As said in the beginning of the paper that for irregular bottoms the dominating depth error is the uncertainty of the beam position relative to the shallowest bottom feature. In figure 35 we give an experimental verification of this by showing detected depth vs. beam position (obtained from scanner angles) for a 1 m wide flat target well above bottom.

Vegetation, if dense, may underestimate the depth. One way of compensating for this effect may be to fit a pulse from the "hard bottom" at the same depth to the deepest tail of the return and calculate two depths based on first leading edge and that of the fitted hard return.

Position errors, repeatability

The perhaps easiest way to isolate positioning errors from other errors is to fly the same flight line in opposite direction. This will reveal systematic positioning errors of the platform. An example is illustrated in figure 36 where a severe positioning offset was revealed. For a displacement of 250 m the profiles fitted very well to each other. Smaller error that could be attributed to error in positioning the beam relative to the scanner can be detected by positioning land marks.

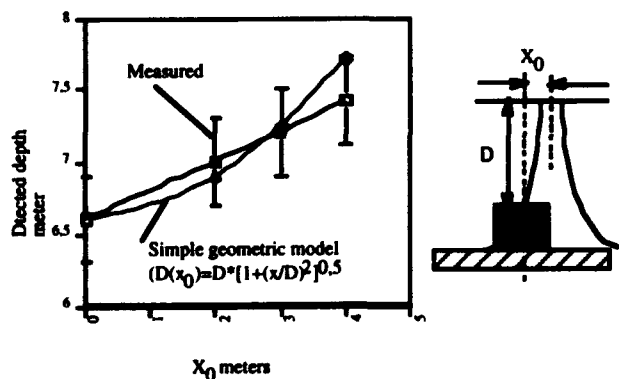


Figure 35. Measured and calculated depth for various position of the feature relative to the beam.

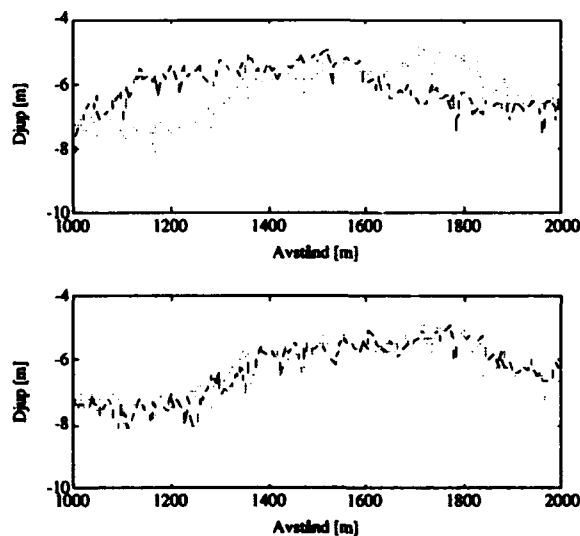


Figure 36. Example of detected positioning offset (by time error between GPS and sored time) when flying the same line in opposite directions. A displacement of 250 m gave a severe error.

Comparison laser-acoustic data

Before comparing the laser and acoustic data it should be noted that the FLASH system was not a full worthy bathymeter in many aspects. For example, FLASH did not save all wave forms and the real time echo extractor was not intended for accurate depth measurements. Further there was no inertial reference system which makes wave height compensation very difficult and reduces the positioning accuracy of the helicopter. All these drawbacks have been taken into account in the Hawk Eye system. Figure 37 shows a pair wise comparison between laser and acoustic depth data. The agreement is good with a small offset of 17,8 cm. The deviation is larger at large depths where the laser approaches the max. range level.

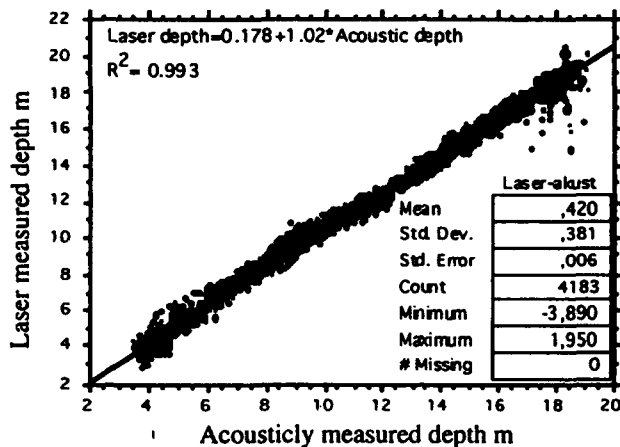


Figure 37. Comparison between acoustic and laser generated depths.

4. CONCLUSIONS.

We have tried to summarise the system and operational aspects of lidar bathymetry based on our experience from the FLASH system. The results obtained support the assumptions that the lidar is a very valuable tool for rapid and accurate depth sounding. We have also pointed out the limitations due to the environment and the system capability. At the time of writing analysis of the Hawk Eye data is under way. The results presented here are mostly taken from FLASH campaigns.

5. ACKNOWLEDGEMENTS.

The FLASH system was developed under contract from the Swedish Material Administration (FMV) and the interaction with FMV Radar, Optronics Section in Stockholm and FMV Testing Directorate in Linköping is greatly acknowledged. The never ending support from the Swedish Navy Staff and the 11. Helicopter Division has been of great value. The collaboration with the Swedish Hydrographic Department has been very inspiring. Finally we want to thank our subcontractors Optech Inc., Saab Instruments and AWA as well as other colleagues at FOA.

6. REFERENCES.

1. O.Steinvall et.al. " Laser depth sounding in the Baltic Sea", *Appl.Optics*, vol.20, no.19, pp. 3284-86, October 1981.
2. O. Steinvall, K. Koppari and U. Karlsson," Experimental evaluation of an airborne depth sounding lidar ",*Optical Engineering*, vol.32, no.6, pp 1307-21, June 1993.
3. K. Koppari, U. Karlsson and O. Steinvall, Airborne Laser Depth Sounding in Sweden, *Proceedings U.S. Hydrographic Conference '94*, pp. 124-133, April 18-23, 1994 Norfolk USA.
- 4.S.Svensson, C.Ekström, B.Ericsson and J.Lexander," Attenuation and scattering meters designed for estimating laser system performance", *SPIE proceedings Ocean Optics IX* vol.925, pp.203-212, 1988.
5. P.Thureson, "SHOALS-Hawk Eye", *International Laser Bathymetry Seminar* 3-4 May, Ronneby, Sweden, 1994.
6. Hoge F.E., Swift R.N., Frederick E.B. "Water depth measurement using an airborne pulsed neon laser system", *Applied Optics*, vol. 19.,no. 6,pp 871-883, 1980.
7. Hoge F.E.,Wright C.W., Krabill W.B., Buntzen R.R., Gilbert G.D.,Swift R.N.,Yungel J.K.,BerryR.E. " Airborne Lidar detection of subsurface oceanic scattering layers", *Applied Optics*, vol. 27, no. 19, 3969-3977,1988.

8. Curran T., Keck T., Contarino V.M., Harris M.M., Haimbach S.P., "Digital ABC Laser Sounder Bathymetry", *Proc. SPIE Ocean Optics IX*, vol. 925, pp 242-249, 1988.
9. Lutomirski R., Haimbach S., Curran T. and Gibbons J., " Performance modelling and analysis of the Ocean Water Lidar (OWL) Hydrographic System, *Proceedings U.S. Hydrographic Conference '94*, pp. 200-205, April 18-23, 1994 Norfolk USA.
10. W.J.Lillycrop, L.E. Parson, L.L. Estep, P.E. Larocque, G.C. Guenther, M.D. Reed and C.L. Truitt, " Field testing of the U.S. Army Corps of engineers airborne lidar hydrographic survey system", *Proceedings U.S. Hydrographic Conference '94*, pp. 144-151, April 18-23, 1994 Norfolk USA.
11. Penny M.F., Billard B., Abbot R.H. " LADS-the Australian Laser airborne Depth Sounder", *Int. J. Remote Sensing*, Vol. 10, no. 9, pp 1463-1497, 1989.
12. C. Setter and R.J. Willis, " LADS-from development to hydrographic operations", *Proceedings U.S. Hydrographic Conference '94*, pp. 134-143, April 18-23, 1994 Norfolk USA.
13. M.F. Penny et.al. " Airborne laser hydrography in Australia", *Appl. Optics* vol.25, no.13, pp. 2046-58, July 1986.
14. Banic J., Sizgoric S., O'Neill R. "Scanning lidar bathymeter for water depth measurement", *Proc. SPIE*, vol. 663, 187-195, 1986.
15. Abroskin A.G., Bunkin A.F., Vlasov D.V., Gorbunov A.L., Mirkamilov D.M. " Natural experiments on laser sounding with the "Chaika" system", *Remote Sising of the Ocean*, Moscow: Nauka, 23-38, 1986 (in russian).
16. Abramochkin A.I., Zanin, V.V., Penner I.E., Tikhomirov A.A. Shamanov V.S. " Airborne polarization lidar for atmospheric and hydrospheric studies", *Optika Atmosfery*, vol.1, no.2, 92-96, 1988 (in Russian).
17. Tsetkov E.A. " Lidar related shipboard and aircraft measurements," Report at the *Technical Seminar on Issues in Lidar and Ocean*. Naval Ocean Systems Center San Diego, CA, Oct.1-21991.
18. Liu Shi-Shen, " Estimate of maximum penetration depth of lidar in coastal water of the China Sea" *Proc. SPIE Ocean Optics X*, vol. 1302, 655-661, 1990.
19. Kerr, A.J., "IHO laser bathymetry recommendations", *International Laser Bathymetry Seminar*, 3-4 May, Ronneby, Sweden, 1994.
20. Duntley S.Q., "The visibility of submerged objects" Final report, Visibility Lab. Mass. Inst. Tech., 72 p, 1952.
21. Tyler J.E., "The Secchi disc" *Limnology and Oceanography*, vol. XIII, no1, pp.1-6, 1968.
22. L.T. Lindell, O.Steinvall, M.Jonsson and T.Claesson, " Mapping of coastal -water turbidity using LANDSAT imagery, *Int.J. Remote Sensing*, vol.6, no.5, pp.629-642, 1985.
23. V.J. Feigels, "Lidars of Oceanographical Research: Crioteria for Comparison, Main Limitations, Perspectives", *SPIE vol. 1750 Ocean Optics XI*, 1992.
24. Cox, G and Munk, W., "Measurement of the surface roughness of the sea from photographs of the sun's glitter", *J. of Opt. Soc. Am.*, vol. 44, no.11, pp 838-850, 1954.
25. O. Steinvall, K.Koppari and U.Karlsson, " Corrections for postprocessing of laser bathymetry data", FOA report A 300 79-3.1, May 1993 (in Swedish).
26. Guenther G.C., Mesick H.C., "Automated Lidar Waveform Processing" *Proc. US Hydro Conf.* April 12-15, 1988, Baltimore.
27. Guenther, G.C., "Wind and nadir angle effects on airborne lidar water "surface" returns", *Proc. SPIE Ocean Optics VIII*, pp. 277-286, 1986.
28. Koepke P., "Effective reflectance of oceanic white caps", *Appl. Optics* vol. 23, no.11, pp 1816-1824, 1984.
29. R.W.L. Thomas and G.C. Guenther, " Water surface detection strategy for airborne laser bathymter", *Proc. U.S. Hydro Conf.*, 1991.
30. G.C. Guenther, "Airborne Laser Hydrography, System Design and Performance Factors", *NOAA Professional Paper Series*, National Ocean Service, Rockville, 1985. Library of Congress nr.: 65-600602.
31. R.F. Lutomirski, "An analytical model for optical beam propagation through the maritime boundary layer", pp.110-122, *SPIE Ocean Optics V*, vol.160, 1978.
32. R. Axelsson, O. Steinvall and P. Sundberg, "Programmable scanner for laser bathymetry", *International Hydrographic Rev.* vol.67, no.1, pp.161-170, January 1990.
33. H.R. Gordon, "Interpretation of airborne oceanic lidar effects of multiple scattering", *Applied Optics*, vol.21, no.16, pp 2996-3001, August 1982.

Underwater laser imaging system with large field-of-view

G.R. Fournier, D. Bonnier and J. L. Forand

Defence Research Establishment Valcartier
Courcelette, Quebec, G0A 1R0, Canada

1. ABSTRACT

Two years ago we designed built and tested a ROV mounted range-gated imaging system. This narrow field of view system (60 mr) had a range of from 4 to 6 times that of a conventional camera with floodlights in the strongly scattering waters typical of harbor approaches. During the sea trials a scanning transmissometer-nephelometer system (NEARSCAT) was operated simultaneously with the imaging system. This has allowed us to validate a simple model that evaluates the performance of the imaging system. Given that the target covers at least one pixel at the maximum range of interest the model predicts that for the same laser power and under the condition where the field of illumination is matched to the field of view there is no performance penalty in increasing the field of view. In order to test this result we have built and deployed a second generation underwater imaging system whose field of view and field of illumination are matched and continuously variable from 60 mr to 600 mr in water. The laser source was also upgraded in power by a factor of 10 to a water cooled, 2-kHz, 400 mw doubled Nd:YLF laser. The light is collected by a 7-cm diameter zoom lens. The detector is a gated image intensifier with a 7-ns gate and a gain which is continuously variable from 500 to 1,000,000. An on-board image processor has been added to the system. It allows us to frame integrate in real-time and thus further improve system performance. This processing and the high repetition rate of the laser, which ensures a lack of speckle, both contribute significantly to the clarity of the images.

2. INTRODUCTION

LUCIE is but one of several different types of active imaging devices that have been proposed and built¹. Several constraints fixed the specific design we used for the LUCIE underwater imaging system. The first goal was to produce a system whose total power could be furnished by a remotely operated vehicle (ROV). This dictated the use of an efficient and compact laser source. The second goal was to produce images that would ease the work of the operator of the vehicle when searching for objects lying on or near the sea bottom. Since the vehicle is often in motion, the images must be generated and displayed either at full television frame rates or, at a minimum, several frames per second. Given the above conditions, range-gated imaging becomes the preferred solution.

During trials at sea, an in-situ tunable transmissometer-nephelometer² is operated simultaneously with the LUCIE system. This allows us to have the spectral curves of absorption and scattering coefficients at the same time, depth and location. These fundamental parameters are necessary for evaluating the performance of the imaging system and validating transmission, scattering and imaging models. This data has allowed us to test

a simple model of range gated imaging³⁻⁵

3. SYSTEM DESCRIPTION

The LUCIE system has been previously described in detail³⁻⁵ and is shown in outline in figure 1. The system is housed in three cylinders 30 cm in diameter by 60 cm in length. These cylinders are interconnected and bolted to a frame which is attached to the ROV through pneumatic linkages. This allows the camera to be tilted and panned with respect to the vehicle. The entire assembly is neutrally buoyant in order to reduce the load on the ROV. One cylinder contains the laser system. The camera is housed in the adjoining cylinder and the computer and control electronics in the third cylinder. The cylinders are filled with nitrogen to avoid condensation on the optical surfaces. The system is designed to dive up to 200 m. It should be emphasized that no particular care was taken to package tightly the present experimental device and that its size could be considerably reduced in an operational system.

Figure 2. is a block diagram of the LUCIE imaging system. The laser source is a 2-kHz diode-pumped Nd:YLF, model TFR from Spectra Physics. It has a pulse length of 7 ns with an average power of 1 W at 2 KHz. This model is equipped with a temperature stabilized frequency doubler which gives an average power at 527 nm of 500 mW. The 527 nm laser beam passes through a zoom system consisting of two consecutive diverging lenses and goes out into the water through a laser quality quartz window which is anti-reflection coated on the inside surface. The beam divergence in water can be varied from 60 mr to 600 mr by simply changing the lens spacing. The beam intensity profile is roughly circular and gaussian in the radial direction.

The light is collected by a 7-cm diameter zoom lens with a continuously variable focal length from 11 mm to 110mm. The lens system has a motorized iris, focus, and zoom. The camera is a double stage micro channel plate intensified gated CCD with full frame transfer. The CCD is kept at -20 C by a double stage Peltier cooler. The luminous gain can be continuously varied from 500 to 1×10^6 by applying a control voltage with a 12 bit D/A converter. The gain settings were calibrated using a tungsten-halogen standard reference source. The threshold sensitivity is 5×10^{-7} lux. The number of active pixels is 488 in the horizontal(H) direction and 380 in the vertical(V) direction. The pixel size is $12\mu\text{m}$ (H) by $18\mu\text{m}$ (V). The image dimensions at the cathode of the intensifier are 11.4 mm (H) and 8.8 mm (V). The camera can be switched from an ungated mode to a range gated mode by applying a TTL pulse to an electronic high voltage relay. In the pulse mode of operation the gate width is 7 ns, a good match to the laser pulse length. The total illuminated length in water is 2 meters. With a target centered in the gate the scattered light comes from a volume of water extending 1 meter. The delay between the gate pulse and the laser pulse can be varied in 1 ns increments by applying a voltage with a D/A converter. This delay was calibrated in the water tank facility. The gate delay can be tied to the focus setting of the lens system. This considerably simplifies the operation of the device and ensures that only the scattering occurring near the target is seen by the camera system. It should also be noted that in one mode of operation the laser beam zoom can be tied to the camera zoom, again simplifying the operation of the system. In that case the fields of view and the field of illumination are matched.

The analog video link from the ROV to the ship was designed to maintain a bandwidth of 7 MHz with some noise immunity. The camera and the frame grabber produce a standard NTSC television signal. The receiver aboard the ship is designed to compensate for the high frequency losses in the cable. With the compensating circuit the 3 db point occurs at 8MHz. The signal is flat within 1 db limits up to 5 Mhz. This exceeds the specification of the super VHS VCR system and ensures the recording and display of high quality images.

All functions aboard LUCIE are monitored and controlled by a single board IBM compatible computer. The on board frame grabber can operate in pass-through mode and in slow-scan mode. In slow scan the camera CCD clock can be slowed down and image frames taken at any desired rate. This is equivalent to averaging a number of frames before display.

4. SEA TRIALS

In 1992, our original tests of the first version of LUCIE were carried out in Patricia Bay at a mean depth of 35 m. This inlet is on the east side of Vancouver island. Another more extensive set of trials was recently carried out both in Patricia Bay and in Esquimalt harbour at a mean depth of 45 m. In both cases a frame supporting several targets was first lowered to the bottom. The targets were white on a black background. One target is a standard television resolution pattern framed by an hexagonal border. The other target is a set of vertical bars of various widths. It can be used to measure the square wave modulation transfer function.

During each dive a narrow forward angle transmissometer-nephelometer² was lowered to within 2 meters of the bottom. Absorption and scattering spectra were taken and analyzed. This allows us to characterize the performance of LUCIE in terms of extinction, absorption and scattering lengths.

Figure 3 is a graph of the absorption and scattering spectra on a low turbidity day in 1992. The scattering length is 3.0 meters and the absorption length is 6.25 meters at 532 nm. From the width of the forward scattering peaks, we estimated the scatterers to be of relatively small size. The daily variations which we monitored closely are strongly correlated with the tidal flow. Figure 4 shows the absorption and scattering spectra on a corresponding low turbidity day in 1993. The scattering length is 1.8 meters and the absorption length is 7.5 meters at 527 nm. The daily variations were again shown to be related to the tidal flow.

Detailed images have been shown previously³⁻⁵. The maximum useful imaging distance was established by using the bar target. The widest bar is 2.5 cm in width and the smallest is 0.8 cm wide. At maximum range the 0.8 cm bars are still resolvable but the noise is considerable. In these conditions LUCIE can resolve objects which subtend 0.5 mr. At that limiting resolution the range was 12 m in 1992. A range of 11 meters was obtained in 1993. In the 1992 trial we estimate that the performance of LUCIE was limited by the loss of signal due to absorption and scattering. The gate width and laser pulse length of 7 ns were sufficiently short to ensure that the backscatter from the illuminated volume resulted in a negligible loss of contrast. In the 1993 trial, at the longest ranges, we obtained images with signals considerably above noise and with the scattered photon component dominating the image. This is due to the fact that in this latter case, scattering was much

larger than absorption. These images are suitable candidates for image enhancement and we are currently proceeding with their analysis.

5. PERFORMANCE ESTIMATE

In principle the range limit of range gated imaging systems can be estimated given the absorption and scattering data. Our results for both versions of LUCIE can be explained to first order by a very simple theory⁴⁻⁵. In the narrow angle forward direction the scattering phase function follows an inverse power law⁶ as a function of θ . Arnush⁷ has solved beam propagation problem in the small angle scattering approximation using the following representation for the phase function.

$$P(\theta) = \frac{e^{-\frac{t}{t_s}}}{(2\pi\theta_s\theta)} \quad (1)$$

We have found that a value of $\theta_s = .04$ gives an order of magnitude fit to both of our scattering functions. The laser beam half width is then given by

$$w = z\sqrt{\theta_0^2 + \frac{2sz\theta_s^2}{3}} \quad (2)$$

where z is the target distance from the laser, s is the scattering coefficient and θ_0 is the initial beam divergence half angle. In our case θ_0 is 30 mr in water. When the phase function is assumed to follow a gaussian form¹⁰ the factor of 2/3 in equation 3 is merely replaced by 1/3. That such different forms give rise to such similar results shows the insensitivity of laser beam broadening to the exact form of the phase function in the case where small angle scattering dominates.

Given the beam broadening of a radially symmetric laser beam of either gaussian or "flat top" radial intensity profile, the performance of an imaging system can be evaluated⁴. For an N frame average the range is thus obtained by solving the following non-linear equation.

$$\left(\frac{I_t}{\sqrt{N}P_0}\right) = \frac{R_t D^2 e^{-(2a+s)z}}{8\pi z^2 [\theta_0^2 + 2sz\theta_s^2/3]} \left(\frac{4\theta_0^2}{h^2}\right) \quad (3)$$

In the above equation, I_t is the threshold sensitivity of the camera in watts per meter squared. P_0 is the laser power in watts. θ_0 is the beam divergence angle in radians which, for optimum performance, is set equal to the field of view. a and s are the absorption and scattering coefficients in units of inverse meters. D is the diameter of the camera lens. h is the vertical dimension of the image on the intensifier front surface. R_t is the target reflectivity and z the distance of the target from the imaging system.

As was shown in a previous work⁵ it is instructive to rearrange equation 3 in terms of the following parameters.

$$G = \frac{\sqrt{N}}{2\pi} \left(\frac{P_0 R_t}{I_t}\right) \left(\frac{D}{h}\right)^2 \quad (4)$$

$$V = (2a + s)z \quad (5)$$

$$F = \frac{2}{3} \left(\frac{\theta_s}{\theta_0} \right)^2 \left[1 + 2 \frac{a}{s} \right]^{-1} \quad (6)$$

Equation 3 can therefore be rewritten as:

$$G(2a + s)^2 = e^V V^2 (1 + FV) \quad (7)$$

G groups together the intrinsic system parameters. V contains the direct dependence on the type of water in which the system operates. F is a measure of the effect of the laser beam broadening on the system. Figure 5 is a plot of V as a function of $G(2a + s)^2$ for different values of F . It is at first glance somewhat surprising that the range performance of the system improves with a larger field-of-view for the same laser power. This is a consequence of the fact that the FOI and FOV are matched. For a sufficiently small FOV a significant fraction of the illuminating photons are diffused out of the image and lost to the system. However, when the FOV is sufficiently large, most of the scattered laser photons fall on the image and the range performance therefore improves.

Bounds can easily be established for the various components of equation 7. G can range from .1 to 10^6 . F goes from $2/3$ to $2 \times 10^{-3}/3$. As we move from harbour waters to the deep open ocean, $(2a + s)^2$ goes from 10 to 4×10^{-3} . The points show the measured performance of LUCIE. From the NEARSCAT data, on day 1 the scattering coefficient at 532 nm was 0.33 m^{-1} and the absorption coefficient 0.16 m^{-1} . On day 2 the scattering coefficient was 0.53 m^{-1} and the absorption coefficient 0.12 m^{-1} . If we substitute these numbers into equation 7 and assume a target reflectivity of 1 we obtain as a maximum range 14 m for the conditions prevailing on day 1 and a maximum range of 11.5 m for day 2. This result is conservative since the bar target was detected at 15 m on day 1.

As is shown the simple theory predicts reasonably the performance of two different systems under very different operating conditions. Considering the simple assumptions made in deriving the received intensity, the accuracy is at first glance surprising. Upon closer analysis the dominant factor in determining the range is the $(2a + s)z$ exponential dependence. The error of the estimate is therefore most likely due to the inherent error in the measurement of the absorption and scattering coefficients. This situation is the opposite of that found in the atmosphere where the denominator in equation 3 dominates over the exponential dependence.

6. CONCLUSIONS

We have developed a simple theory which predicts to first order the performance of range gated imaging systems. The results of tests carried out with both a low power narrow field-of-view system and a high power variable field-of-view version under substantially different water clarity conditions are in close agreement with this theory. We now have a substantial data base of range gated underwater images and corresponding scattering and absorption spectra which we are analyzing in order to evaluate the effectiveness of various image processing techniques. LUCIE at present has shown a range increase of 3 to 5 times that of a conventional imaging system in waters which are typical of harbours and their approaches.

7. REFERENCES

1. D.J. Holloway, "Underwater imaging", Proceedings of SPIE, Vol. 980, San Diego, 18 August 1988.
2. G.R. Fournier, L. Forand, G. Pelletier and P. Pace, "NEARSCAT full spectrum narrow forward angle transmissometer-nephelometer", Proceedings of SPIE, Vol. 1750, San Diego, 20 July 1992.
3. G.R. Fournier, D. Bonnier, L. Forand and P. Pace, "LUCIE ROV mounted laser imaging system", Proceedings of SPIE, Vol. 1750, San Diego, 20 July 1992.
4. G.R. Fournier, D. Bonnier, L. Forand and P. Pace, "Range Gated underwater laser imaging system", *Optical Engineering*, September 1993.
5. J.L. Forand, G.R. Fournier, D. Bonnier and P. Pace, "LUCIE: A Laser Underwater Camera Image Enhancer", Proceedings of IEEE Oceans'93, Vol. III, pp 187-190, Victoria, November 1993.
6. T.J. Petzold, "Volume Scattering Functions for Selected Ocean Waters," Scripps Institute of Oceanography, SIO Ref. 72-28, 1972.
7. D. Arnush, "Underwater light-beam propagation in the small-angle scattering approximation", *J.O.S.A.*, **62**(9), 1109-1111 (1972)
8. W.G. Tam and A. Zardecki, "Multiple scattering of a laser beam by radiational and advective Fogs", *Optica Acta*, **26**(5), 659-670 (1979)

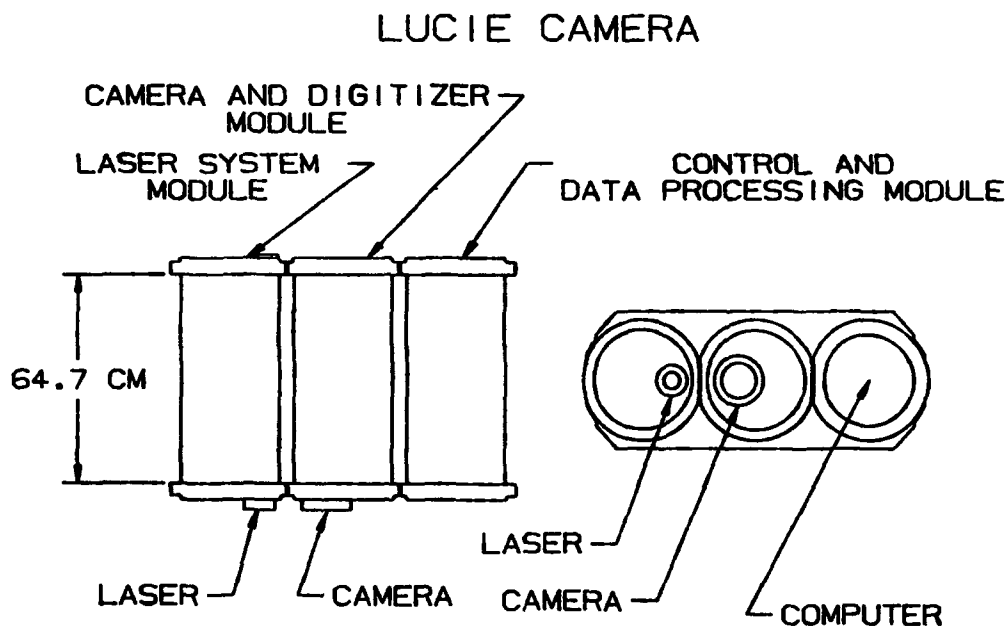


Figure 1. Outline of the LUCIE system.

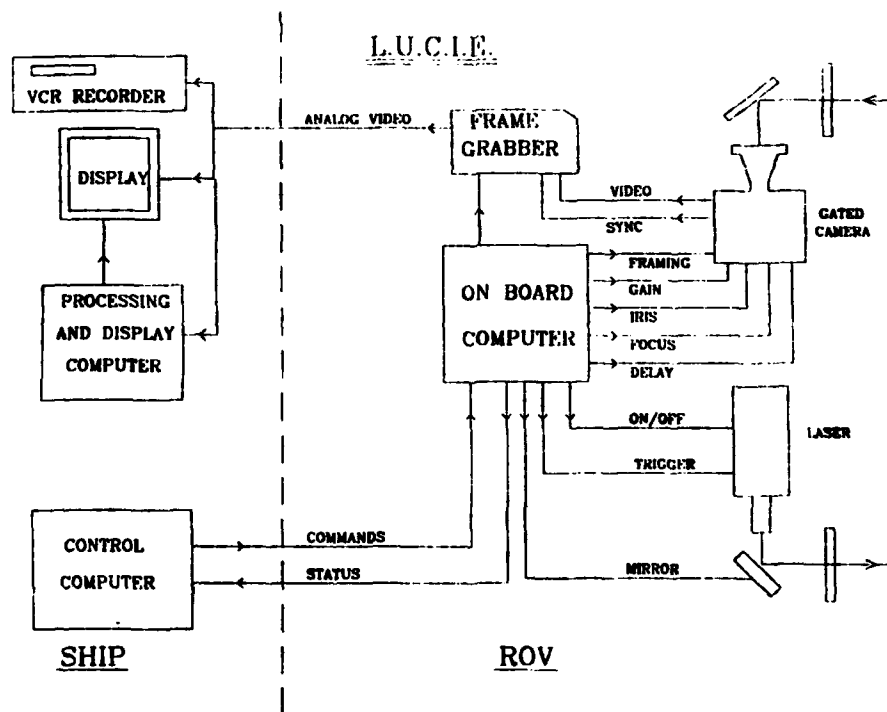


Figure 2. Schematic of the optics and electronics.

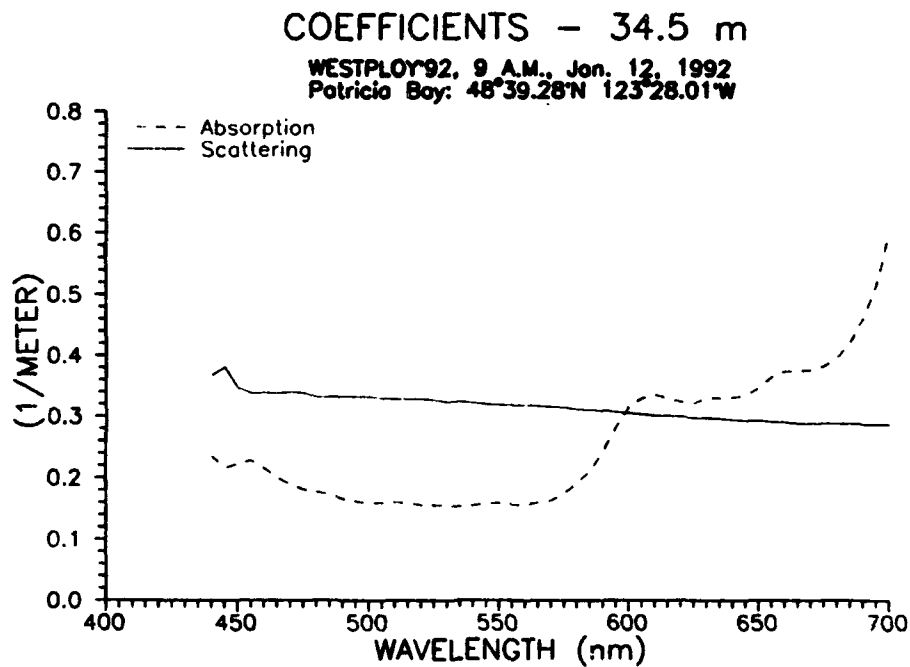


Figure 3. Scattering and absorption spectra for the 1992 trial.

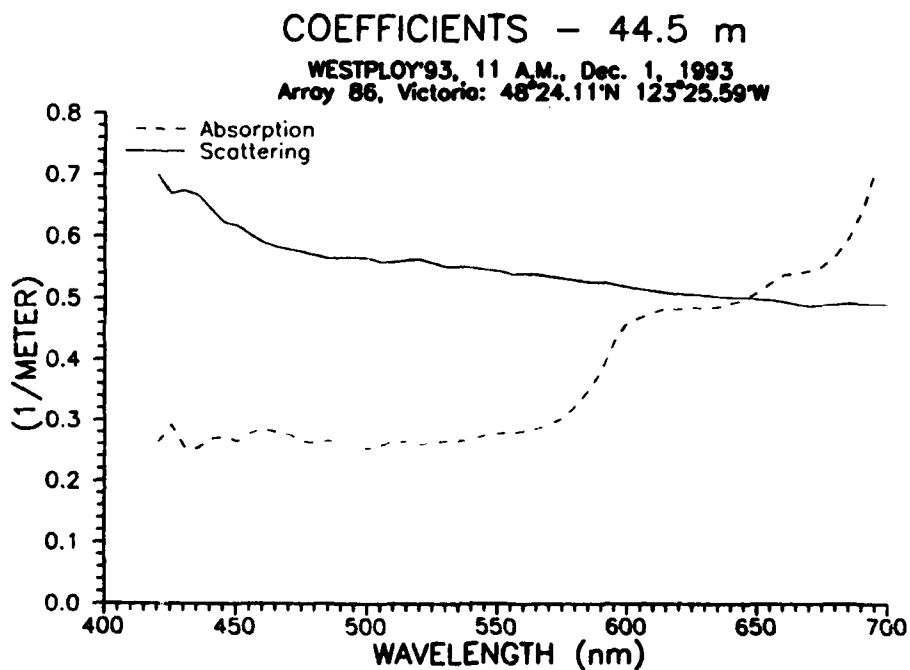


Figure 4. Scattering and absorption spectra for the 1993 trial.

Normalized Performance

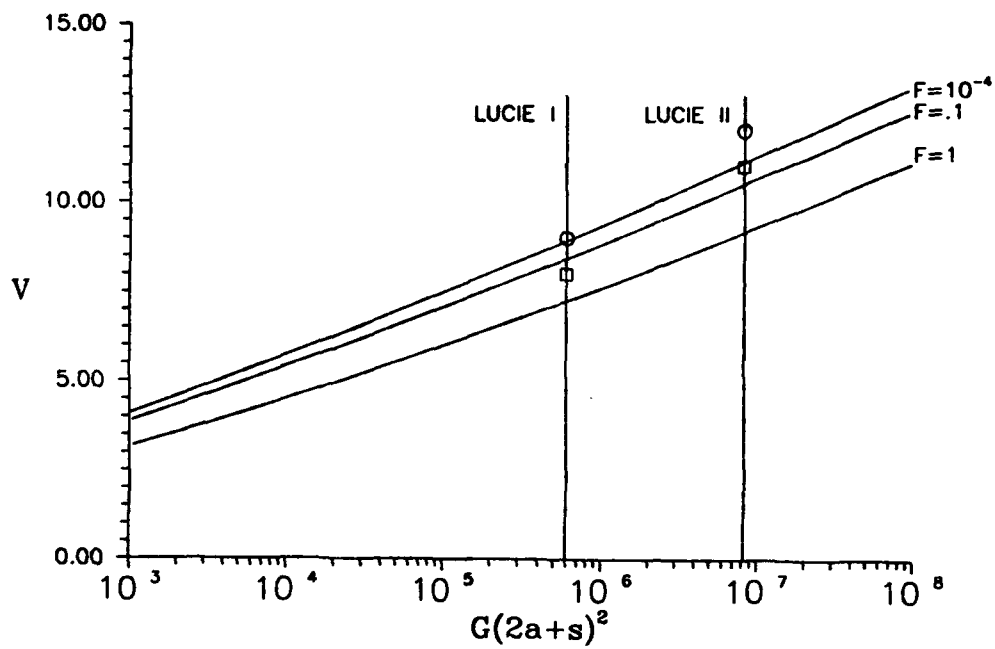


Figure 5. Non-dimensional plot of the range performance of gated systems. The circles are the measured system performance and the squares the predicted system performance.

Multiple surface channels in SHOALS airborne lidar

Gary C. Guenther

National Ocean Service, NOAA
1315 East-West Highway
Silver Spring, Maryland 20910

Paul E. LaRocque

Optech, Inc.
100 Wildcat Road
North York, Ontario, Canada M3J 2Z9

W. Jeff Lillycrop

U.S. Army Corps of Engineers
3909 Halls Ferry Road
Vicksburg, Mississippi 39180

ABSTRACT

Airborne laser hydrography is the process of measuring the depth of coastal waters, for the purpose of nautical charting, by firing a pulsed laser beam into the water from an airborne platform. In this application of LIDAR (Light Detection and Ranging), the times of flight for signals detected from the reflection of the light pulse off the air/water "surface" interface and off the sea bottom are converted into slant range distances from which the water depth can be determined. The interaction of a light pulse with the surface and near-surface region of the water column involves a number of complex phenomena which depend on environmental conditions and system parameters, and great care must be taken in system design and data processing to obtain an accurate, reliable, and unambiguous result. The SHOALS system records data for three independent channels which contain surface information. Two of these, the infrared, which is effectively an interface return, and Raman, which is strictly a volume return, are used singly or in concert to ensure that these goals are met. Results from the green channel are ambiguous due to the uncertain nature of the origin of that energy (between interface reflection and volume backscatter), and are not used. Field test results indicate that easily detectable returns were received in both infrared and Raman channels under virtually all test conditions. The use of independent surface channels also permits operation at extremely shallow depths. Excellent delineation of tidal erosion "cuts" through nearly exposed "mud banks" was obtained in Florida Bay for use in flow modeling programs.

1. INTRODUCTION

The Scanning Hydrographic Operational Airborne Lidar Survey (SHOALS) is a hydrographic survey system recently developed for the U.S. Army Corps of Engineers and the Canadian Department of Science, Industry, and Technology by Optech, Incorporated.¹ SHOALS consists of a computer-controlled airborne laser transceiver capable of measuring 200 soundings per second using a pulsed, frequency-doubled Nd:YAG laser. Both green and collinear infrared pulses are utilized. The pod-mounted system operates from a Bell 212 helicopter,

flying at from 200 to 1000 meters altitude, with a speed of from 0 to 100 knots. With the standard 20-degree off-nadir scanning angle, the swath width surveyed is half the aircraft altitude. The helicopter is being provided by the National Oceanic and Atmospheric Administration (NOAA) Aircraft Operations Center, and the system will be operated by John E. Chance & Associates.

The most important requirements of an airborne laser hydrography system are vertical and horizontal accuracy and depth penetration; we will deal here with the aspects of vertical accuracy. The depth which must be determined is the vertical distance between some reference height and the sea bottom. Different references are used for different purposes by different agencies. For nautical charting, NOAA's Coast and Geodetic Survey typically uses "mean lower low water" (MLLW) as a reference. Depths are first measured with respect to the mean water surface and then corrected to MLLW through the use of a tide corrector which references the mean water level at a given location to MLLW. This approach requires that tides be measured constantly during the hydrographic survey (as well as before and/or after, in order to establish an accurate datum).

In this approach, which is currently used by all operational airborne laser hydrography systems,¹⁻⁴ the depth is determined by differencing the measured distances from the airborne platform to the water surface and to the bottom. The distance to the surface must thus be determined with an accuracy better than that required of the overall depth measurement. Although different measurement techniques and procedures are used in the different systems, it is generally true that the measurements are affected by the presence of waves on the water surface, and that in order to achieve the best possible vertical accuracy, the mean water level at the locations of the sounding pulses must be obtained as a spatial average of local water surface heights.

An alternate approach, which should become practical in the near future, involves the use of the satellite-based Global Positioning System (GPS) with kinematic differential carrier-phase tracking⁵ and "on-the-fly" (OTF) ambiguity resolution⁶ to provide a highly accurate (several centimeter) measure of the vertical height of the surveying platform with respect to the ellipsoid while the vertical distance from the platform to the sea bottom is being simultaneously measured. The "ellipsoid" refers to a standard mathematical ellipsoid of revolution which has been chosen as a best fit to the surface of the earth -- as a whole or at some specified location. Examples which are in current use are termed "WGS84" and "NAD83". If the tidal datum at a given location is also measured with respect to the ellipsoid using GPS, the water depth with respect to that tidal datum can be determined without the need of measuring the tidal heights at the time of the hydrographic survey.

It is important to note that even if GPS techniques are adopted for obtaining depths by measuring the distance to the bottom relative to the ellipsoid, the distance to the water surface must still be accurately measured, because the light pulse travels a fraction of the distance to the bottom in air and the remainder in water, for which the speed of light is significantly slower. For either method, given a detectable surface return, the resulting depth error is roughly one-quarter of the error in the surface height measurement plus three-quarters of the error in the altitude estimate.^{7,8} The benefit for using the GPS approach is that a wave correction procedure to convert local surface heights to the mean water level, a complex and computationally intensive process in software, would not be necessary. The former approach, however, with its calculation of a mean water level, does have an advantage in that it permits depth estimation even for (a limited number of) pulses whose surface returns are missing, with a depth error related to one-quarter of the physical wave height.

It is clear that accurate measurement of the transit time of the green sounding pulse, or a collinear equivalent, to the surface of the water is imperative for every airborne lidar hydrography system. SHOALS has three potential surface channels. Waveforms are digitized from detectors at wavelengths of 1064 nm (infrared), 647 nm (red), and 532 nm (green). The measurement of the time to the surface is determined by the detection of any of these singly or with "priority logic" which defaults to a lower priority channel should the signal in a higher priority channel be missing.

2. THE GREEN SURFACE RETURN

The sounding beam which must penetrate the water to the bottom is green in all airborne laser hydrography systems because that is the wavelength for which attenuation in typical coastal waters is minimized⁹ so that depth penetration is maximized. The use of the green beam for surface detection, however, is a problem. In order to cover a swath under the aircraft, the laser pulses are scanned across the flight path at or up to off-nadir angles as large as 20 degrees. For laser light to be reflected back into a co-located (monostatic) receiver from the air/water interface, water waves must present facets perpendicular to the incoming pulses. Since the presence of gravity waves with such large slopes would likely resuspend bottom sediments and make the water too turbid for satisfactory penetration to the bottom, one must depend on wind-generated capillary waves with centimeter-order wavelengths. If sufficient wind is not blowing, the average facet angle may be too small,^{10,11} and the interface reflections in the direction of the receiver may not be sufficient for detection.

The green pulses, however, having passed through the interface, are partially backscattered off particulate material entrained in the water column. The peak of this volume backscatter signal, being much stronger than a typical bottom return, is relatively strong and easily detected in the absence of an interface return. Since it arises from the water column, this return arrives later than the interface return by a time differential which depends primarily on the temporal pulse width and pulse location algorithm but also on water clarity. For the 5 to 7 nanosecond pulse widths typical of lasers in current use for this application, this would lead to unacceptably large depth errors in the 20-70 cm range¹² (30-40 cm for a leading-edge 50% linear fractional threshold pulse location algorithm)¹³ if the volume return were mistaken for an interface return, which could easily happen.

If the origin of each pulse were known and unique, those perceived to be volume returns could be corrected to the interface by the application of predicted biases based on models and/or field measurements. Neither case, however, is true. For most wind conditions and moderate off-nadir angles, the surface return origin can "flip-flop" unpredictably back and forth from pulse to pulse¹⁴ according to the sea surface statistics. One pulse might, for example, strike a mass of capillaries piled up near a gravity wave crest and give a big interface return, while the next might hit a flat trough area and yield nothing but volume. The observed behavior will be a strong function of wind and off-nadir angle with much stronger and more numerous interface-dominated returns arising at off-nadir angles under, say, ten degrees and mostly volume-dominated returns at larger angles.

In general, pattern recognition to determine the origin of an individual return is not practical, as the lidar "surface" return is a linear combination of interface and volume backscatter energy whose character can be very "mixed". A green surface return waveform can have a leading edge with some fraction dominated by interface energy while the peak location is dominated by the volume return.¹⁵ The arrival time of green surface returns is thus an inaccurate measure of surface location. Unless interface returns can be guaranteed, which is a rare occurrence at the larger off-nadir angles preferred for a cost-

effective swath width and for minimizing the uncertainty in the propagation-induced bias corrector,¹⁶ the use of green surface returns is likely to lead to unacceptably large depth measurement errors.

Laser designers take note: if an otherwise satisfactory laser (in terms of pulse energy and repetition rate) are developed with a pulse width (FWHM) of two nanoseconds or less, this error would shrink to within the vertical accuracy error budget and make irrelevant much of the remainder of this paper.

3. THE INFRARED SURFACE RETURN

The natural wavelength of a Nd:YAG laser is at 1064 nm in the infrared (IR). Frequency doubling these pulses to 532 nm is an inefficient process, and a great deal of IR energy is left over. This energy can be put to good use by sending it to the water surface either as a narrow, collinear beam as in SHOALS or as a broad, vertical beam as in the Australian LADS system.

The Fresnel reflection characteristics of infrared energy from the air/water interface are basically the same as in the green. Because the diffuse attenuation coefficient of water is much greater at this IR wavelength (by a factor of 50-100x over the green¹⁷), the physical origin of any detectable IR volume backscatter is limited to a region much closer to the interface. Thus the IR surface return resulting from a 5-7 ns pulse width can provide accurate surface timing regardless of its interface or volume character.

There are several problems, however, with this signal. By far the biggest is that, in the absence of an interface return, the volume return may be too weak to detect due to the greater attenuation. If so, operation of a collinear IR beam at larger off-nadir angles would be constrained to more windy conditions which are not necessarily desirable. Evidence is growing from SHOALS field data, however, that for most if not all cases of interest, the IR volume return may be strong enough for typical coastal waters to be detected by a sensitive receiver. The SHOALS IR channel is approximately 50 times more sensitive than the green surface (and shallow bottom) channel, and additionally, the laser output in the IR is three times greater than in the green. A minor problem which can affect the performance of an IR surface channel is early returns from above the surface caused by puffs of condensed water vapor (sea smoke) or bird strikes.

Another use of IR in SHOALS is the discrimination of returns from land. Land returns must be recognized and excluded from the wave correction process, because otherwise they would affect the calculation of the mean water level. The technique utilized is a comparison of signal levels from two cross-polarized IR channels. This application, too, could be compromised by excessively low signal strength. It is also possible for the land/water discrimination to be confused by interface reflections from extremely thin layers of water on land areas.

4. THE RAMAN SURFACE RETURN

The dominant, elastic (on-frequency) scattering processes for light in natural waters are either molecular (Rayleigh) or particulate (Mie, Tyndall) in origin. Raman backscatter, named after its discoverer, Sir Chandrasekhara Raman (1888-1970), is, in general, an inelastic process in which the energy of an incident photon is either increased (anti-Stokes) or decreased (Stokes), and the wavelength of the exiting photon is correspondingly shorter or longer. The vibrational modes of the O-H stretch in liquid water yield a set of broad Stokes lines representing the different structural species (monomer, polymer, etc.); together these compose a band with a wavenumber (frequency reduction) centered at

roughly 3350 cm^{-1} and a width of about 700 cm^{-1} .¹⁸ The resulting scattering process converts a small portion of the incident green lidar pulses at 532 nm into weak pulses of red light centered at about 647 nm.

It was felt that SHOALS would benefit from the time and amplitude information of the Raman backscatter signature returning from the water in the form of these pulses of red light. SHOALS is the first system to use Raman returns for hydrographic purposes. Prior applications of the use of an airborne, water Raman lidar include the estimation of oil film thickness,¹⁹ the normalization of laser-induced fluorescence returns for the estimation of the concentration of chlorophyll and phycoerythrin,²⁰ and a proposal for sub-surface temperature estimation.²¹ Raman backscatter also plays an important role in the spectral redistribution of energy, such as the production of red light in deep ocean waters, which can seriously confuse irradiance and attenuation measurements.²²

The Raman scattering cross section is a very strong function of the wavelength, varying as the inverse fourth power of the emission wavelength,²³ which yields stronger returns with ultraviolet excitation than with green. It would be nearly seven times stronger, for example, at tripled Nd:YAG (355 nm) than for doubled Nd:YAG. The cross section at 90 degrees has been measured at $8.2\text{E-}34\text{ m}^2/\text{molecule-sr}$ at 488 nm;²⁴ this is equivalent to $5.4\text{E-}34\text{ m}^2/\text{molecule-sr}$ at 532 nm. The depolarization ratio (the ratio of the perpendicularly polarized intensity of Raman scattered energy to the parallel polarized component) for water is about 0.16,²⁵ which means the parallel component is roughly six times stronger. For this depolarization ratio, the intensity of the parallel component is three times greater in the forward and backward directions than at 90 degrees.²⁶ (The perpendicular component is isotropic.) Multiplying the above cross section by three for the backscatter direction and by $3.3\text{E}28\text{ molecules/m}^3$ (the number density of water) yields a Raman backscattering coefficient of $5.4\text{E-}5\text{ m}^{-1}\text{ sr}^{-1}$. This is roughly one-third the on-frequency backscattering coefficient for distilled water,²⁷ ten times less than deep ocean water, and 30 to 100 times less than typical coastal waters.²⁸

This cross section is, however, large enough to provide a lidar return signal of sufficient strength to be easily detected and used for surface identification, particularly at lower flight altitudes. Indeed, during the initial SHOALS field tests (January 1994), the amplifier gain in this channel had to be reduced to preclude unexpected saturation of the digitized signal. This return can be inadvertently augmented slightly by laser-induced fluorescence. The long wavelength tail of the phycoerythrin peak, the broad spectrum of dissolved organic materials, and the short wavelength tail of the chlorophyll peak can all contribute energy to the 17-nm optical bandpass of the red (Raman) channel.²⁹ Although these signal sources would beneficially increase the received signal-to-noise ratio, they cannot be depended upon, and the effects are relatively minor. The Raman signal can be reduced or suppressed by the existence of an oil film.¹⁹ For this reason, it is beneficial to have the IR channel as a backup.

The Raman return is desirable because its origin is unambiguous, being strictly from the volume and having no interface component, and because it has comparatively little dependence on wind speed or nadir angle. Since it is a volume return, a bias corrector must be applied to move the time measurement back to the interface. This bias corrector, which has the same characteristics as that for elastic scattering, is slightly smaller than for the green return since the diffuse attenuation coefficient is a bit greater for the returning red pulses, and depends on the pulse location algorithm and water clarity. The Raman bias corrector can be predicted from an analytic model,¹² and this model can be validated in field data by comparison with IR returns when both are present. Another beneficial characteristic of Raman returns is that they will not be generated by sea smoke, because the number density of water molecules in fog is much less than in a mass

of liquid water. It remains to be seen from field data if bird feathers are fluorescent enough to produce a false return.

In very shallow waters, only a few meters deep, weak Raman bottom returns can be detected from the reflection of forward scattered red light and Raman conversion of the green bottom reflection. A leading-edge pulse location algorithm is thus required rather than a pulse-shape sensitive detector such as a constant-fraction discriminator (CFD) or an energy detector such as a matched filter.

The Raman return can also be useful in the land/water logic. The presence of a return in the Raman channel indicates either a significant thickness (magnitude yet to be determined) of water or fluorescence from items on land such as vegetation. The latter can be rejected by application of an adaptive amplitude threshold.

5. SHOALS SIGNAL PROCESSING

Because of the uncertainty of the depth of the origin of the green return, that channel will never be used for depth determination in either hardware or software, although the information may be used for diagnostic purposes. The availability of both IR and Raman information lends great redundancy and virtually ensures the detection of surface returns under all expected conditions. It also provides the ability to detect in software, by intercomparison on a pulse-to-pulse basis, anomalous situations which might compromise accuracy. Timing differences greater than a set threshold, for example, can be used as a pulse rejection criterion.

In addition to providing real-time hardware surface detection, SHOALS also records digitized waveforms for each of the above three channels which contain surface information so that these can also be processed later in software if desired. Depths may be calculated using surface timing from either hardware or software detection. The former runs faster, but the latter, in some cases, may be more accurate. Timing differences between hardware and software surface detection can be constantly monitored during post-flight data processing. The probability of successful surface returns in each surface channel, for both hardware and software detection, is also available. Depths which may have been missed or mistaken by the hardware, due perhaps to incorrect threshold settings, can be resurrected in processing by using software surface detection.

The use of independent channels for surface detection also permits the measurement of extremely shallow depths for which the surface and bottom returns in the green channel are merged, as long as the bottom returns are significantly stronger, which they typically are at a 20-degree off-nadir angle. Software processing is preferred here for greatest accuracy. From preliminary field data recently acquired in a SHOALS survey in the Florida Bay region of Everglades National Park sponsored by NOAA's National Ocean Service, it seems that SHOALS will be useful in depths as shallow as one meter. This provides the added benefit of being able to use the system in such environmentally sensitive wetland areas. The Florida Bay data, for example, dramatically delineates the network of very shallow tidal "cuts" (Figure 1.) eroded through the large mud banks which restrict the flow of water in the region. This data is expected to be useful in modeling the transport phenomena in this endangered region.

6. CONCLUSIONS

The utilization of independent infrared and Raman surface channels in the SHOALS airborne lidar hydrography system provides reliable, unambiguous, and accurate surface location, for depth determination, at a 20-degree off-nadir angle. This permits a usable sounding

swath width under the aircraft equal to half of the flight altitude, independent of wind conditions. It also permits the scanner pattern to avoid near-nadir incidence where the receiver is subjected to a very difficult amplitude dynamic range and where the variation in propagation-induced depth bias with unknown water clarity parameters is quite large.¹⁶ There appears to be no inherent reason why this angle could not be increased even further if that were desirable. Post-flight processing software can be used to provide the highest possible accuracy and rejection of anomalous data.

7. ACKNOWLEDGMENTS

Conception, funding, design, construction, testing, and operation of the SHOALS hardware and software have involved over one hundred people, all of whom deserve high praise for jobs well done. The SHOALS system was jointly funded by Headquarters, U.S. Army Corps of Engineers, Operations, Construction, and Readiness Division, and the Department of Industry, Science, and Technology, Canada.

8. REFERENCES

1. W.J. Lillycrop, L.E. Parson, L.L. Estep, P.E. LaRocque, G.C. Guenther, M.D. Reed, and C.L. Truitt, "Field testing of the U.S. Army Corps of Engineers airborne lidar hydrographic survey system," Proc. U.S. Hydro. Conf. 1994, The Hydrographic Society Spec. Pub. No. 32, 144-151, April 1994.
2. C. Setter and R.J. Willis, "LADS -- From development to hydrographic operations," Proc. U.S. Hydro. Conf. 1994, The Hydrographic Society Spec. Pub. No. 32, 134-139, April 1994.
3. K. Koppari, U. Karlsson, and O. Steinvall, "Airborne laser depth sounding in Sweden," Proc. U.S. Hydro. Conf. 1994, The Hydro. Society Spec. Pub. No. 32, 124-133, April 1994.
4. J. Vosburgh, "Larsen lidar -- past experience, present system, continuing refinements -- from a hydrographic perspective," Proc. U.S. Hydro. Conf. 1994, The Hydrographic Society Spec. Pub. No. 32, p.206, April 1994.
5. B.W. Remondi, "Kinematic GPS results without static initialization," NOAA Technical Memorandum, NOS NGS-55, National Geodetic Information Center, Maryland, USA, 1991.
6. S.L. Frodge, R.A. Barker, D. Lapucha, B.W. Remondi, and B. Shannon, "Results of real-time testing of GPS carrier phase ambiguity resolution on-the-fly," Inst. of Navigation, ION GPS93, Salt Lake City, Nevada, USA, 1993
7. R.W.L. Thomas and G.C. Guenther, "Water surface detection strategy for an airborne laser bathymeter," Proc. SPIE Ocean Optics X, 1302, 597-6911, April 1990.
8. G.C. Guenther and R.W.L. Thomas, "Determine mean water depth and data quality factors: SHOALS laser waveform post-flight data processing module," version 1.51, 1993 -- company proprietary.
9. N.G. Jerlov, Marine Optics, Elsevier Scientific Pub., Amsterdam, 1976.
10. G. Cox and W. Munk, "Measurement of the roughness of the sea surface from photographs of the sun's glitter," J. Opt. Soc. Am., 44, 11, 838-850, 1954.
11. K.J. Petri, "Laser radar reflectance of Chesapeake Bay waters as a function of wind speed," IEEE Trans. Geoscience Electronics, GE-15, 2, 87-96, 1977.

12. G.C. Guenther, "Airborne laser hydrography: system design and performance factors," NOAA Professional Paper Series, National Ocean Service 1, National Oceanic and Atmospheric Administration, U.S. Department of Commerce, Washington, D.C., 385 pp., 1985.
13. G.C. Guenther and R.W.L. Thomas, "Error analysis of pulse location estimations for simulated bathymetric lidar returns," NOAA Technical Report, OTES 1, 51pp, July 1981.
14. G.C. Guenther, "Wind and Nadir Angle Effects on Airborne Lidar Water 'Surface' Returns," Proceedings SPIE Ocean Optics VIII, 637, 277-286, 1986.
15. G.C. Guenther and H.C. Mesick, "Analysis of airborne laser hydrography waveforms," Proc. SPIE Ocean Optics IX, 925, 232-241, 1988.
16. G.C. Guenther and R.W.L. Thomas, "Effects of Propagation-Induced Pulse Stretching in Airborne Laser Hydrography," Proceedings SPIE Ocean Optics VII, 489, 287-296, 1984.
17. J.E. Tyler and R.W. Preisendorfer, The Sea, M.N. Hill, Ed., Wiley-Intersci.(NY), 1962.
18. G.E. Walrafen, "Raman spectral studies of the effects of temperature on water structure," J. Chem. Phys., 47, 1, 114-126, July 1967.
19. F.E. Hoge and R.N. Swift, "Oil film thickness measurement using airborne laser-induced water Raman backscatter," Appl. Opt., 19, 19, 3269-3281, Oct 1980.
20. F.E. Hoge and R.N. Swift, "Airborne mapping of laser-induced fluorescence of chlorophyll-a and phycoerythrin in a Gulf Stream warm core ring," Advances in Chemistry Series 209, Mapping Strategies in Chemical Oceanography, A. Zirino, Ed., 353-372, 1985.
21. D.A. Leonard, B. Caputo, and F.E. Hoge, "Remote sensing of subsurface water temperature by Raman scattering," Appl. Opt., 18, 11, 1732-1745, June 1979.
22. R.H. Stavn and A.D. Weidemann, "Optical modeling of clear ocean light fields: Raman scattering effects," Appl. Opt., 27, 19, 4002-4011, Oct. 1988.
23. R.M. Measures, "Analytical use of lasers in remote sensing," p.323 in Analytical Laser Spectroscopy, N. Omenetto, Ed., Wiley-Interscience (NY), p.295-410.
24. B.R. Marshall and R.C. Smith, "Raman scattering and in-water ocean optical properties," Appl. Opt., 29, 1, 71-84, Jan 1990.
25. C.H. Chang and L.A. Young, "Seawater Temperature Measurement from Raman Spectra", Research Note 920, N62269-72-C-0204, ARPA Order No. 1911, July 1972.
26. S.P.S. Porto, "Angular dependence and depolarization ratio of the Raman effect," J. Opt. Soc. Am., 56, 11, 1585-1589, Nov 1966.
27. J.E. Tyler, Limnol. Oceanog., 6, 451, 1961.
28. T.J. Petzold, "Volume scattering functions for selected ocean waters," SIO Ref. 72-78, Scripps Inst. of Oceanography, Visibility Laboratory, San Diego, Calif., 79pp., 1972.
29. W.M. Houghton, R.J. Exton, and R.W. Gregory, "Field investigation of techniques for remote laser sensing of oceanographic parameters," Rem. Sens. Env., 13, 17-32, 1983.



Figure 1. The Rabbit Key channels in Florida Bay as delineated by the SHOALS airborne lidar hydrography system.

The surrounding black areas are unsurveyed. The irregular, vertical black area is a short section of a very shallow (less than one meter depth) mud bank running north and south. It is black because the depths are too shallow to be detected with the given software parameterization. The horizontal features are the "cuts" of interest to modelers which range in depth from one to three meters. The lidar swath width evident at the survey line ends (along the sides of the figure) is 100 meters. There are roughly one million color-coded soundings in the area.

Optical properties of the sea water for a short pulse

Kusiel S. Shifrin and Ilja G. Zolotov

Oregon State University, College of Oceanic and Atmospheric Sciences
Corvallis, Oregon 97331-5503

ABSTRACT

The present work consists of two parts. In the first part, the principal results of the scattering theory of ultra short light pulses (USLP) by a small spherical particle, are briefly outlined. In the second part, the peculiarities of the USLP scattering by marine suspension are examined.

1. INTRODUCTION. PECULIARITIES OF THE USLP SCATTERING BY A SMALL PARTICLE.

General calculational formulae for optical characteristics of a small particle in light pulse field are given in^{1,2}. In these works, a case is considered of irradiation of a sphere with a radius a by a pulse of an arbitrary shape, with a duration T . It is supposed that a particle is irradiated by electromagnetic field by the following expression:

$$\vec{E}_i = \vec{E}_0 g(\tau) e^{i\omega_0 \tau} \quad (1)$$

It is a modulated plane wave propagating along the OZ axis with the carrier frequency ω_0 , phase $\tau = t - z/c + \psi$ and envelope $g(\tau)$. The values $\vec{E}_i, \vec{E}_0, t, z, c$ are commonly used symbols in optics. The initial phase ψ determines the pulse position on the time axis relative to the time origin t . The origin of coordinate is situated at the particle centre. Using the Fourier theorem, we can represent a pulse as an infinite set of plane waves. The scattering of an every plane wave is calculated with the Mie formulae. The total field scattered in the given direction is calculated as a sum of individual fields originated by individual plane waves. Such is a general interpretation of the pulse scattering in¹. It provides a complete solution to the problem.

When using the Fourier theorem, negative frequencies appear in the calculations. They can be eliminated in the following manner. Let $G(\omega)$ is the Fourier image of the pulse envelope $g(\tau)$. By the shift theorem³ (p. 14), the Fourier image $g(\tau) e^{i\omega_0 \tau}$ is equal to $G(\omega - \omega_0)$. It follows that the incident field

$$E_i(\omega_0, t) = \vec{E}_0 \int_{-\infty}^{\infty} G(\omega - \omega_0) e^{i\omega \tau} d\omega. \quad (2)$$

The function $G(\omega)$ as a Fourier image of the real function $g(\tau)$ satisfies the condition $G(-\Omega) = G^*(\Omega)$. This allows us to write the formula (2) in the following form:

$$\vec{E}_i = \vec{E}_0 \left\{ \int_0^{\infty} G(\omega - \omega_0) e^{i\omega \tau} d\omega + \int_0^{\infty} G^*(\omega + \omega_0) e^{-i\omega \tau} d\omega \right\} \quad (3)$$

There is no negative frequency in the formula (3). It represents the pulse field as an infinite set of two types of plane waves: $\exp[i\omega(t - z/c)]$ and $\exp[-i\omega(t - z/c)]$ correspondingly, with the amplitudes $E_0 G(\omega - \omega_0) \exp[\pm i\omega \psi] d\omega$. The field scattering for both wave types are related by a simple expression. This relationship is examined in⁴. We are not going to use in the calculations the second term in (3); we will consider only such pulses which have the filling coefficient $\ell_0 = \omega_0 / \tilde{\omega} > 1.5$ ($\tilde{\omega} = 2\pi/T$ is the frequency corresponding to the pulse duration T). For these pulses, the function $G(\omega)$ peaks sharply at $\omega = \omega_0$; it is practically equal to zero at $|\omega - \omega_0| \geq \tilde{\omega}$. However, the second term in (3) should be considered for pulses with wider spectra (that is, for shorter pulses).

The response of a receiver to a signal is proportional to the total incoming energy for the period of reception, namely,

$$W_s = \frac{c}{8\pi} \int_{-\infty}^{\infty} \text{Re} [\vec{E}_s \times \vec{H}_s^*] dt$$

By the Rayleigh-Parceval theorem⁵ (p. 112), the integral of the square of a function with respect to t from $-\infty$ to $+\infty$ is equal to the integral of the square of its Fourier spectrum modulus with respect to ω from $-\infty$ to $+\infty$. This enables all optical characteristics of a particle to be represented as single integrals with respect to ω . The condition $\ell_0 \geq 1.5$ and the Rayleigh-Parceval theorem considerably simplify the calculations.

The intensity of linearly polarized light $I^0(\vartheta, \phi)$ scattered in the direction (ϑ, ϕ) is determined by the formula

$$I^0(\vartheta, \phi) = \frac{cE_0^2}{8\pi} \left(\frac{1}{k_0 r} \right)^2 \int_{-\ell_0}^{\infty} V_0(s) \left[|S_1(\vartheta, s)|^2 \sin^2 \phi + |S_2(\vartheta, s)|^2 \cos^2 \phi \right] ds \quad (4)$$

Here S_1 and S_2 are the Mie amplitudes⁶; $s = (\omega - \omega_0) / \tilde{\omega}$ is the dimensionless frequency;

$V_0(s) = \left[w(s) \ell_0 / (s + \ell_0) \right]^2$; $k_0 = 2\pi / \lambda_0$; $w(s)$ is the Fourier image of the envelope $g(\tau)$. For the Gaussian pulse, at $g(\tau) = \exp(-\pi \tau^2 / T^2)$, $w(s) = \exp(-\pi s^2)$. It is easy to show that at $T \rightarrow \infty$, the formula (4) transforms into the Mie formula for the monochromatic wave scattering with the frequency $\omega = \omega_0$.

In¹, the effect of the pulse duration T on scattering characteristics is considered. The calculations show that pulses begin affect the scattering pattern at $T \leq 50T_0$ (T_0 is the period of a carrier wave). For the visible range ($\lambda_0 = 0.5 \mu\text{m}$), this means that $T \leq 0.1 \text{ ps}$, for the IR range ($\lambda_0 = 10 \mu\text{m}$) $-T \leq 2 \text{ ps}$, for the microwave range ($\lambda_0 = 1 \text{ cm}$) $-T \leq 2 \text{ ns}$. The pulse influence amounts to the smoothing of interfering effects. Qualitatively, it is similar to changes arising under the transfer from the monodisperse to polydisperse scattering.

2. PECULIARITIES OF SCATTERING BY MARINE SUSPENSION PARTICLES.

The calculations in¹ were performed in the approximation of single scattering by atmospheric aerosol. For hydrooptics, the pattern obtained in^{1,2} should be amplified. It is necessary to make clear:

- How do optical characteristics of typical marine suspension particles change under pulse irradiation?
- How does the pulse scattering pattern in sea water change in conditions of spectral extinction?
- How does a pulse affect the phase function shape (or, more exactly, mean cosine of the scattering angle) which determines light field in sea water?

a) The first question was studied in⁷. In this work, efficient scattering and backscattering cross-sections Q_{sca} and Q_{back} are calculated for terrigenous and biogenic suspension components. Radiation with $\lambda_0 = 0.532 \mu\text{m}$ is considered (the range of sea water maximum transmittance) for pulses of the duration $T = 0.27 \cdot 10^{-14} \text{ sec}$; $0.33 \cdot 10^{-14} \text{ sec}$ and 10^{-14} sec . Terrigenous particles are supposed to have radii up to $2 \mu\text{m}$, biogenic ones- up to $10 \mu\text{m}$. For Q_{sca} of terrigenous particles, the maximum difference with monochromatic values takes place at the radius interval $0.8-1.5 \mu\text{m}$; for biogenic particles it is at $4-7.5 \mu\text{m}$ and $9-10 \mu\text{m}$. These differences are not big; they reach 10-15%. The situation is different for Q_{back} . In this case, polychromatic (pulse) coefficients Q_{back} significantly differ from monochromatic ones. The latter undergo strong interference oscillations. For pulse Q_{back} , these are smoothed. For terrigenous particles, the coefficient Q_{back} increases monotonously with the radius; for biogenic ones it is practically constant.

b) The extinction index $c(\omega)$ and phase function of sea water depend on the frequency. Because of that, when a pulse propagates in sea water, the pulse signal shape changes all the time (as opposed to the atmosphere). As a result, integral (with respect to spectrum) characteristics of the medium depend on the path of radiation. In order to describe this phenomenon, one should introduce a transmittance function depending on the pulse path. Strictly speaking, it is impermissible to introduce characteristics of an elementary volume for the given pulse duration, because they would be different for beams with different pre-existing conditions. It is necessary first to

determine the photon path distribution. This distribution can be found from the solution of the nonstationary transfer equation. Usually, it is given as a function $p(h)$. It is the probability function for a photon to have a path h in a turbid medium. At that, the factor $p(h) \exp[-c(\omega)h]$ appears in the expression under integral of the formula (4) and of other similar formula in¹ for other optical characteristics. In order to conceive what kind of changes takes place, let us consider the structure of a straight beam which travelled the path h . For this beam, $p(h)=1$.

Let a pulse emitting from a source has the Gaussian shape, its frequency characteristic with respect to the intensity is $w^2(s) = \exp(-2\pi s^2)$, where $s = (\omega - \omega_0) / \tilde{\omega}$ is the dimensionless frequency. The energy density within the frequency range $d\omega$ is

$$\frac{dW_i}{d\omega} = \frac{cE_0^2}{8\pi\tilde{\omega}} w^2(s).$$

The density is symmetric about frequency, with the centre at $\omega = \omega_0$. Practically all the pulse energy is concentrated within the frequency range $0.3 \omega_0 - 1.7 \omega_0$. Let the carrier wavelength (in vacuum) is $\lambda_0 = 0.532 \mu\text{m}$ and the pulse duration $T=0.27 \cdot 10^{-14}$ sec. In this case, the spectral range occupied by a pulse is equal to $0.32 - 1.55 \mu\text{m}$. This interval corresponds to $-1 \leq s \leq 1$. It is determined by the level 0.002 of the maximum pulse amplitude. A pulse keeps these characteristics until it enters sea water.

It is possible to account for the change of the pulse frequency characteristic using the additional multiplier $\exp(-c(\omega)h)$, where h is the path of a pulse in sea water. In order to estimate the extinction effect of an incident pulse in sea water, it is necessary to set the extinction index as a function of frequency (or of wavelength). Data on $c(\omega)$ of sea water were taken from^{8,9}. The distribution of energy density in frequency is calculated for different path h , depending on the wavelength with the formula: $\exp[-2\pi s^2 - c(\omega)h]$.

Let us consider the behaviour of the energy density of an incident pulse when it passes across a sea water layer of different thickness. The calculational results for sea water layers of the thickness h from 5 to 50 m, depending on the wavelength λ , are shown in Fig. 1. On the same figure, the energy characteristic of the initial Gaussian pulse at $h=0$ is shown (the solid line).

It is seen from Fig. 1 that as a pulse passes through sea water, its energy distribution in wavelength changes substantially. In parallel with the evident decrease of maximum, the carrier wavelength shifts in the direction of shorter waves. However, most significant changes concern the spectral range length occupied by the pulse. As h increases, it decreases abruptly (several times), especially from the side of longer waves. In other words, the known pulse "widening" takes place. It is possible to conclude that pulse effects under its propagation in sea water manifests themselves for much shorter pulses in comparison with air.

c) The mean cosine of the scattering angle $\langle \cos \theta \rangle$ is determined by the integral of the product of the phase function and the cosine of the scattering angle θ with respect to this angle. For monochromatic scattering, the explicit expression for this value as a series in Mie coefficients is presented in^{6,10}. By analogy with the formula for the efficiency for pulse scattering Q_{sca} in¹, it is possible to obtain $\langle \cos \theta \rangle$ for pulse scattering:

$$\langle \cos \theta \rangle = \frac{\sqrt{2}}{\pi^2 Q_{\text{sca}}} \left(\frac{\lambda_0}{a} \right)^2 \sum_{n=1}^{\infty} \int_{-\infty}^{\infty} V_0(s) \left[\frac{n(n+2)}{(n+1)} \text{Re} \{ a_n(s) a_{n+1}^*(s) + b_n(s) b_{n+1}^*(s) \} + \frac{2n+1}{n(n+1)} \text{Re} \{ a_n(s) b_n^*(s) \} \right] ds \quad (5)$$

We calculated $\langle \cos \theta \rangle$ for terrigenous ($m=1.15$) and biogeneous ($m=1.03$) marine suspension particles from this formula. The results are shown in Figs. 2 and 3. Both for $m=1.15$ and $m=1.03$, the curves $\langle \cos \theta \rangle$ for pulse scattering practically coincide with those for monochromatic scattering. In other words, they are independent of T . For small particles, all phase function component are of the Rayleigh type, and $\langle \cos \theta \rangle = 0$. As particle enlarge, $\langle \cos \theta \rangle$ increases abruptly. At $a=0.5 \mu\text{m}$, the curves become asymptotic. For $m=1.15$, $\langle \cos \theta \rangle = 0.9$; for

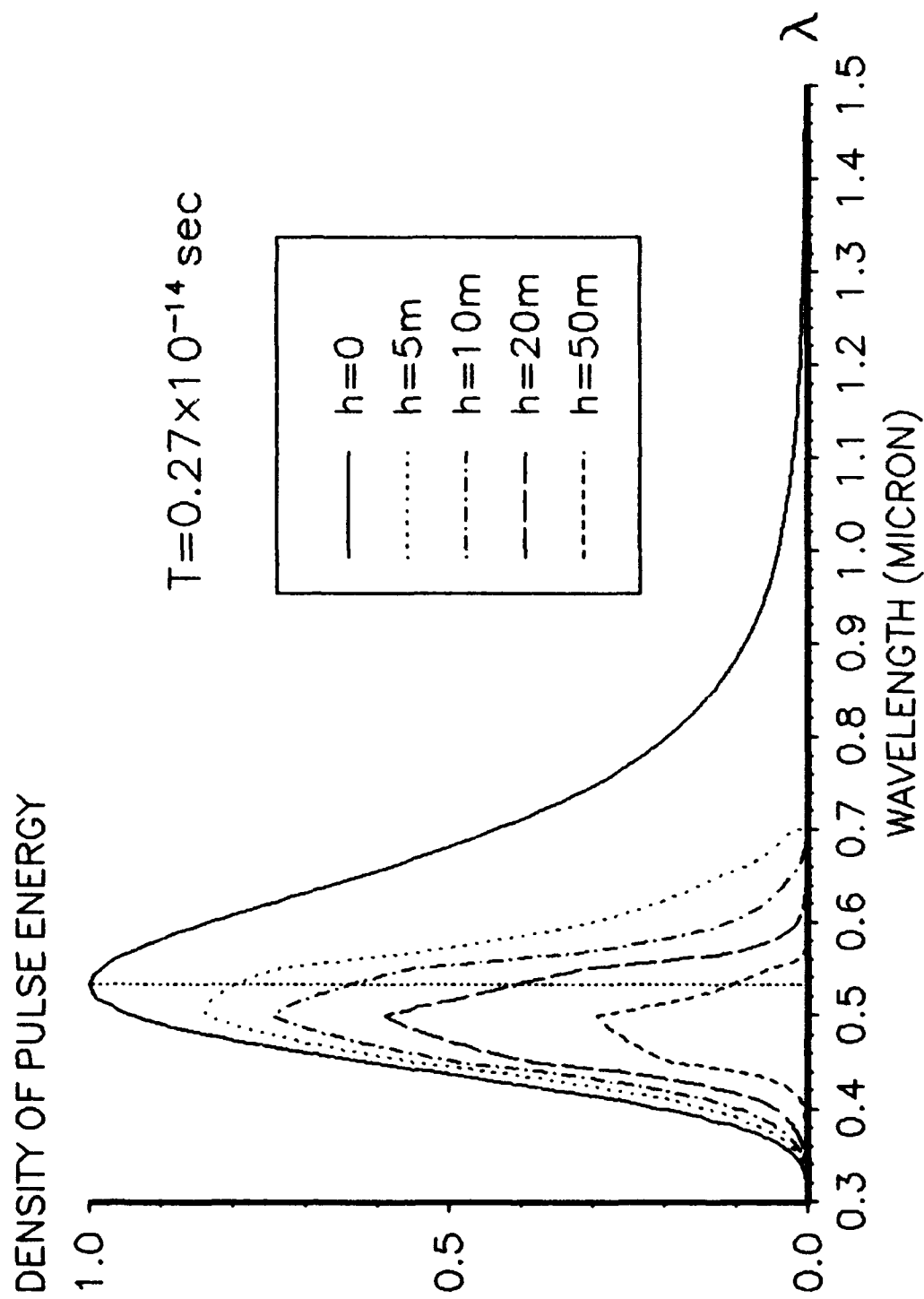


Fig.1 . The relative distribution of the pulse energy density at different pulse paths in sea water.

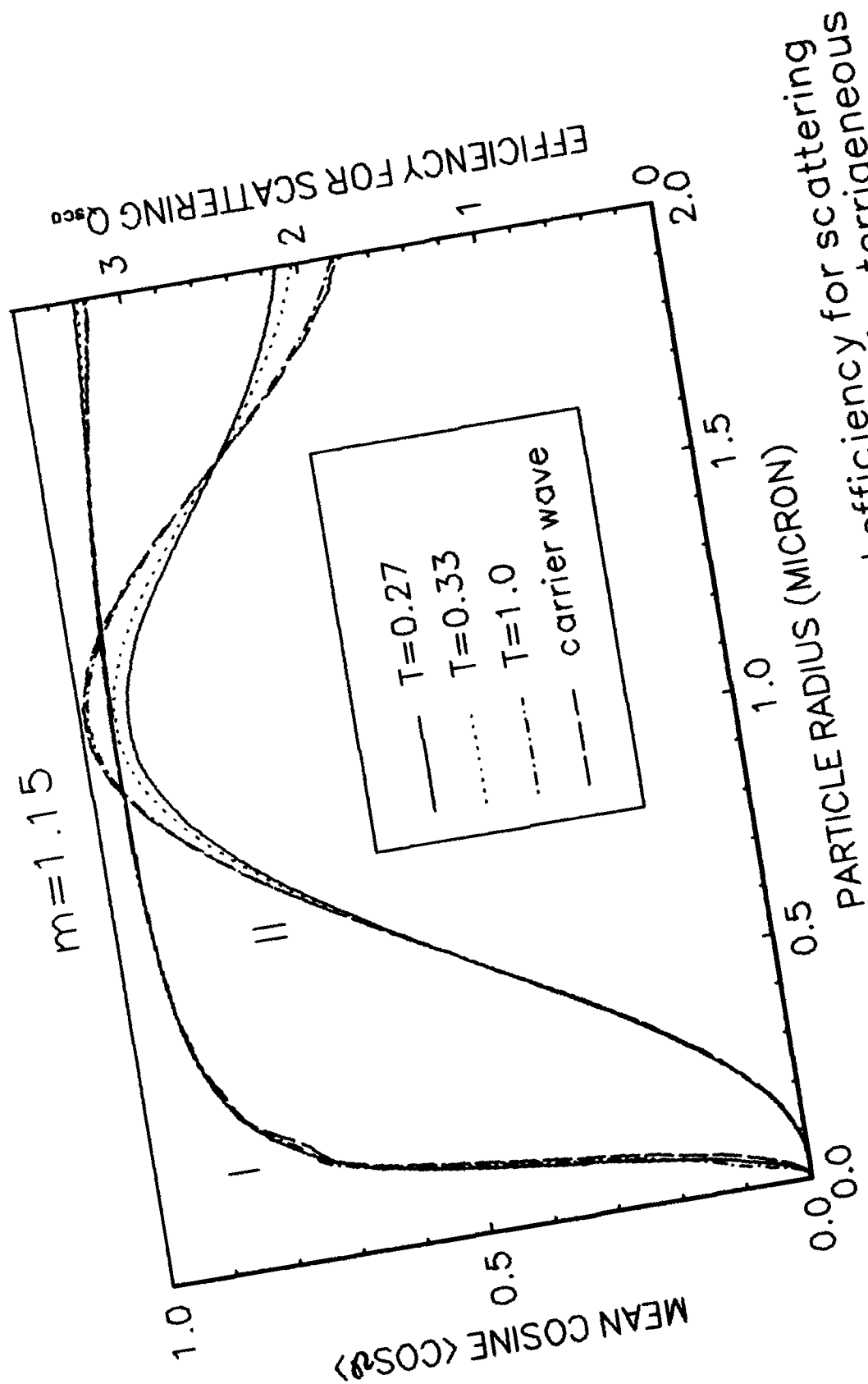


Fig.2. The mean cosine $\langle \cos \vartheta \rangle$ (I) and efficiency for scattering Q_{sca} (II) for pulses of different durations T for terrigenous component of sea suspension

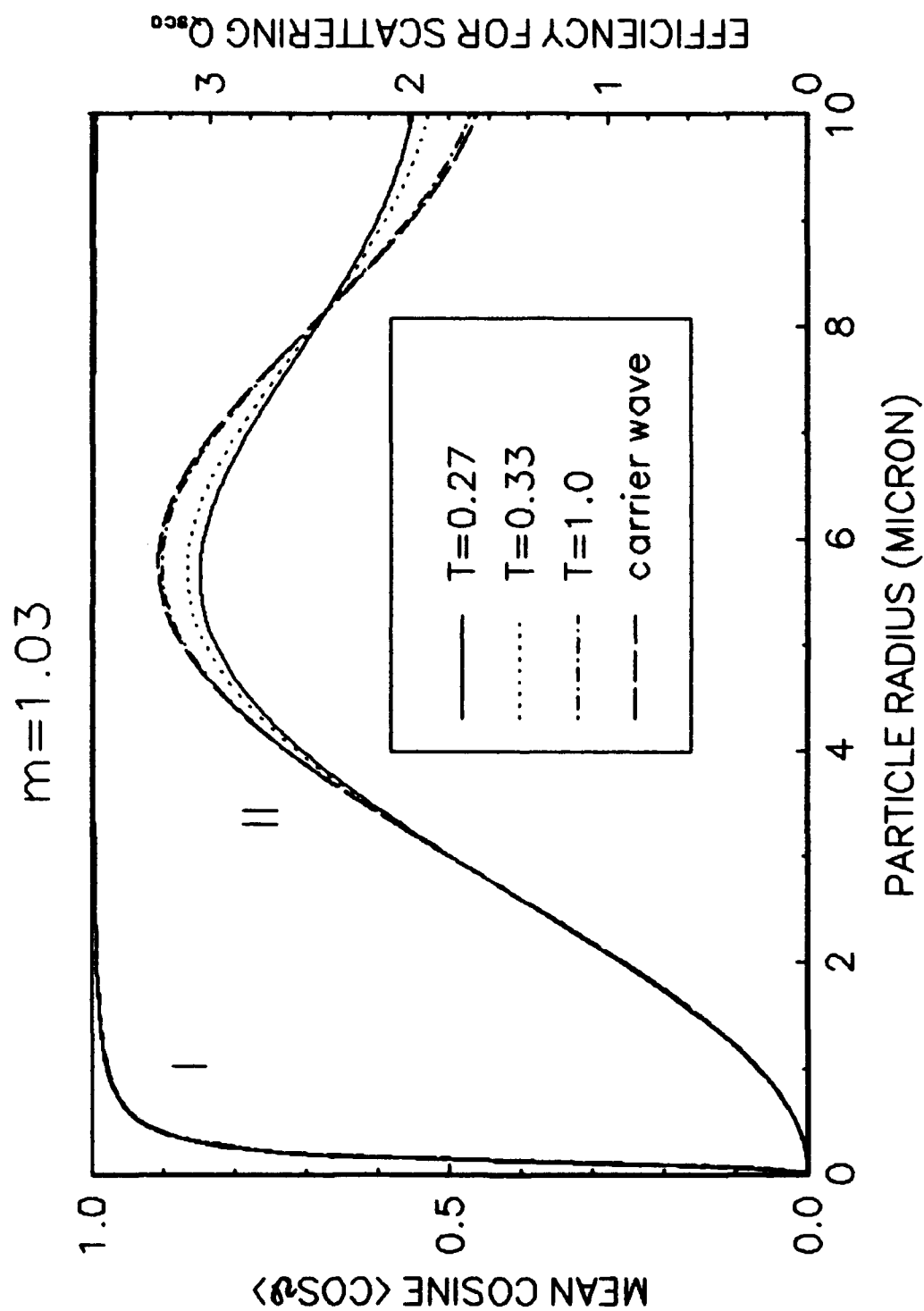


Fig.3. The mean cosine $\langle \cos \vartheta \rangle$ (I) and efficiency for scattering Q_{sca} (II) for pulses of different durations T for biogeneous component of sea suspension.

$m=1.03$, $\langle \cos \theta \rangle = 0.99$. It is possible to explain these values. For large particles, light consists of the diffracted beam and the beam described by geometrical optics. For $m=1.03$, practically the entire geometrical beam passes in the forward direction. Because of that, a portion of $\langle \cos \theta \rangle$ associated with it is high. For $m=1.15$, a portion of light scattered sidewise and back are much more than for 1.03. As a result, the magnitude of $\langle \cos \theta \rangle$ at $a \rightarrow \infty$ for $m=1.15$ is much less than for 1.03. This is seen also from data in⁸. In this work, the calculated dependence of $\langle \cos \theta \rangle$ at $a \rightarrow \infty$ on m is presented in Table 4.7. It is seen that $\langle \cos \theta \rangle$ at $a \rightarrow \infty$ decreases as m increases.

In Figs. 2-3, alongside with curves $\langle \cos \theta \rangle$, curves $Q_{sca}(a)$ are presented for the same cases. We see that the pulse duration differently affects the amount of scattered light and the scattered angle mean cosine. The reason is just that the formula $\langle \cos \theta \rangle$ has the additional scattering angle cosine under the integral. This averaging turns out to be very significant. As its result, all peculiarities of pulse scattering vanish. This effect is similar to what is going on in light field when we pass from the brightness distribution to the illumination distribution (see⁸ p. 11). At that, all details of the spatial distribution vanish.

3. CONCLUSION.

Let us list the principal results.

1) Optical characteristics of marine suspension particles depend not only on the pulse duration, but also on the carrier frequency. The light extinction in sea water causes an additional monochromatization of radiation and brings particle optical characteristics closer to their values at water transparency bands.

2) Although phase functions for pulses and monochromatic radiation are noticeably different (as it was demonstrated with Q_{back}), these differences practically vanish for mean cosine.

4. ACKNOWLEDGMENTS.

This work was supported by the Office of Naval Research (ONR) under Grant N0001490J1132. We thank ONR for this support. We also thank Professor J. Ronald V. Zaneveld for his personal support and for discussions on individual questions.

5. REFERENCES.

1. K. S. Shifrin and I. G. Zolotov, "Quasi-stationary scattering of an electromagnetic pulse by a spherical particle". *Appl. Opt.*, (submitted).
2. K. S. Shifrin and I. G. Zolotov, "Non-stationary scattering of electromagnetic pulses by spherical particles". *Appl. Opt.*, (submitted).
3. A. Papoulis, *The Fourier integral and its applications*. McGraw-Hill Book Company, Inc., 1962.
4. K. S. Shifrin and I. G. Zolotov, "Remark about the notation used for calculating the electromagnetic field scattered by a spherical particle". *Appl. Opt.*, 32, 5397-5398, 1993.
5. R. N. Bracewell, *The Fourier transform and its applications*. McGraw-Hill Book Company, 1978.
6. H. C. Van de Hulst, *Light scattering by small particles*. New York, John Wiley & Sons, Inc., London, Chapman & Hall, Ltd., 1957.
7. K. S. Shifrin and I. G. Zolotov, "Optical characteristics of suspended marine particles for short light pulses". *Journ. Geoph. Res.*, (submitted).
8. K. S. Shifrin, *Physical Optics of Ocean Water*. AIT, 1988.
9. A. Ivanoff, *Introduction a L'Océanographie*. Tome II, Paris, Librairie Vuibert, 1975.
10. C. F. Borhen and D. R. Huffman, *Absorption and scattering of light by small particles*. Wiley, New York, 1983.

Interferometric analysis of the spatial coherence of a laser beam propagating in sea-water
and through the wavy air-water interface

A. Perennou, J. Cariou, J. Lotrian

Laboratoire de Spectrométrie et d'Optique Laser
Université de Bretagne Occidentale
Faculté des Sciences et Techniques
6, Avenue Le Gorgeu
29285 BREST Cédex

ABSTRACT

To study the influence of sea-perturbations on an optical wavefront in coherent detection through the air-sea interface, we have used two experimental methods based on interferometric techniques. We use Michelson Interferometry and Fourier transform to determine wavefronts deformations after double passage through a wavy air-water interface. We consider the statistical aspect by using the averaged Fourier spectra over many independent realisations. Then, a spatial coherence analysis of light scattering in turbid water is presented: the module of the degree of spatial coherence across the beam section is measured by a Mach-Zehnder interferometer.

I - INTRODUCTION

Optical heterodyne detection used in air-borne hydrographic systems will be severely perturbed by the refraction effects caused by the rough surface of sea-water and by the scattering effects of the sea medium on spatial coherence. Misalignment of the reference beam with the signal wavefront will reduce the heterodyne efficiency ρ given by ^{1,2}:

$$\rho = \frac{\left| \int_A U_S(x,y) \cdot U_L^*(x,y) dx dy \right|^2}{\int_A U_S(x,y) \cdot U_S^*(x,y) dx dy \int_A U_L(x,y) \cdot U_L^*(x,y) dx dy} \quad (1)$$

where U_S and U_L are the normal distributions of the signal field and the local field, respectively, A is the area of the detector and the asterisk represents the complex conjugate.

In this paper we report an experimental study using interferometric imaging technique, to evaluate the distortion effects of the optical wave front in laboratory configuration.

We first study the wave front distortion through a wavy air-water interface with a Michelson interferometer: a linear fringe pattern is obtained, for a non-perturbed medium, which gives a reference "spatial carrier" frequency. Then, the wave front distortion is analysed with the spatial Fourier spectrum of the fringe pattern. We describe some statistical aspects of the wave front deformation in relation with the number of the averaged patterns: a statistical treatment can give useful information from the spreading of Fourier spatial spectra of interferometric images.

In section 3, a spatial coherence analysis of light scattering in turbid water, illuminated by a laser source is presented. We use a Mach-Zehnder interferometer to measure the module of the degree of spatial coherence across the beam section in relation with the scattering properties of the medium disturbing the fringes visibility.

II- PERTURBATION ON AN OPTICAL WAVEFRONT PROPAGATING THROUGH THE WAVY AIR-WATER INTERFACE.

2.1- EXPERIMENTAL SET UP :

The aim of this experimental study is to determine the wave front deformations after double passage through a wavy air-water interface³⁻⁶. The experimental arrangement is shown in figure 1. An optical wave front Σ_s of the signal, after its double passage through a perturbed air-water interface is coherently added to a reference plane wave front Σ_r into a Michelson interferometer. The intensity of the fringes pattern, in the observation plane is given by:

$$i(x,y) = a(x,y) + b(x,y) \cdot \cos(2\pi u_0 x + \Phi(x,y)) \quad (2)$$

Where $a(x,y)$ describes the background variations and $b(x,y)$ is related to the local contrast of the interference fringes; $\Phi(x,y)$ describes the local phase relation between Σ_r and Σ_s ; u_0 is the "spatial carrier" frequency in the x direction: it is created by tilting the reference wave Σ_r of an angle θ_0 with the plane wave-front Σ_s coming from a plane interface; in this case

$$u_0 = \frac{\sin \theta_0}{\lambda} \quad (3)$$

The laser is a frequency-doubled Nd:YAG laser which generates 10 nS pulses of green light at 532 nm. Each interference pattern is recorded on a CCD camera (512 X 512 pixels). A laboratory tank was used to obtain a wavy air-water interface. A variable air-speed system was mounted at the top of the tank on one side to produce wavelets.

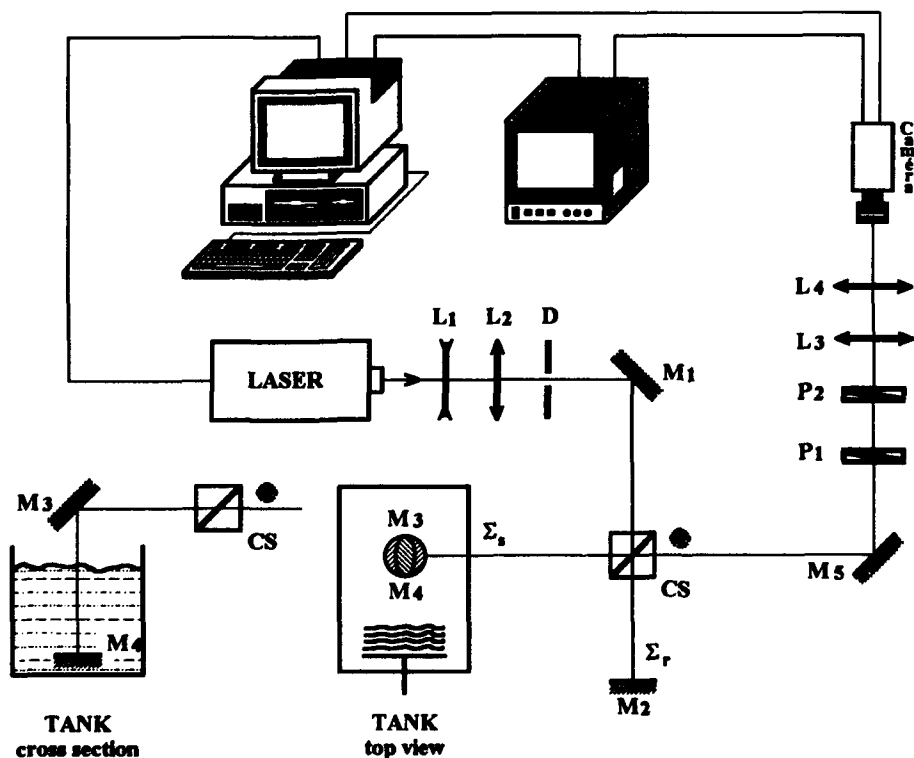


Figure 1 :

Details of experimental set-up

C.S : Beam splitter cube

D : Diaphragm

L1,L2,L3,L4 : Lenses

M1,M2,M3,M4 : Mirrors

P1,P2 : Polarizers

2.2- PHASE DISTRIBUTION :

Using the random aspect of the perturbed water surface needs an interferometric investigation using only one interferogram pattern a time because the sea surface is in constant evolution. We use the Fourier transform to analyse interference fringes to get the wave front topography following Gorecki ⁷, Kreis ⁸ and Takeda ⁹.

In order to show the variety of different patterns after passage through the air water interface, we have presented two examples of instantaneous interferograms in figure 2. We observe phase variation of several time π and we can see the effect of perturbations on fringes orientations and densities.

These examples show the necessity of a statistical treatment.

2.3- STATISTICAL ASPECT OF INTERFEROGRAM ANALYSIS :

The heterodyne detection efficiency is a function of the angle θ between the signal and the reference wavefronts. θ depends of the slopes variations of the air-water interface.

We use the same experimental arrangement as previously (figure 1), and we make a summation of different instantaneous Fourier spectra ⁹ to obtain the spectral intensity:

$$I_T(u, v) = \sum_{i=1}^N I_i(u, v) = \sum_{i=1}^N (A_i(u, v) + C_i(u - u_0, v) + C_i^*(u + u_0, v)) \quad (4)$$

where $I_i(u, v)$ is the instantaneous Fourier spectrum of $i(x, y)$ obtained over a laser pulse. By using u_0 it is possible to separate the non-perturbed part of the signal from the background $A(u, v)$ of the spectrum. The wave front shape is determined by the spatial frequencies u and v .

The spectra have been calculated by a fast Fourier transform based on a Danielson-Lanczos algorithm¹⁰. The Fourier transform will consist of three peaks, one located at the origin of the spectral plane ($u=128, v=128$), which correspond to the background of the interferogram pattern. The two other are located symmetrically at the frequencies $(u_0, 0)$ and $(-u_0, 0)$. The frequencies around u_0 are the interesting part of the Fourier spectra because they are generated by a nearly plane wave corresponding to a uniform phase.

Figures 3 show the stability of the Fourier spectrum for a same wind ruffled water surface in the case of averaged Fourier Spectra over 50, 100 and 800 independent realisations. The spectra is here composed on 256×256 pixels. On the two first spectra (fig. 3a, 3b) the part of the non-perturbed interface does not appear.

We can see in figure 3c the presence of the two peaks. This result is important because it shows that the interesting signal is much more important than the noise. $|I(u, v)|$ converge toward a statistical law : it shows that the signal to noise ratio will have a limited value. With this type of averaged Fourier spectrum, we can apply coherent detection with a relatively good heterodyne efficiency; We can choice the number of acquisitions in relation with the perturbed air-sea interface.

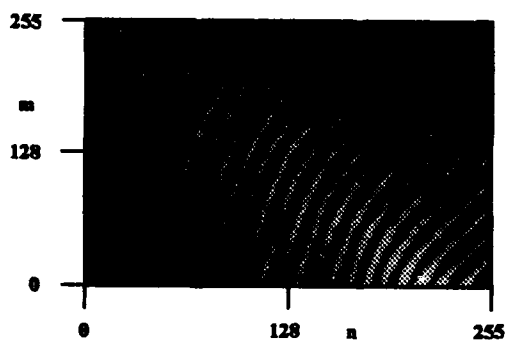
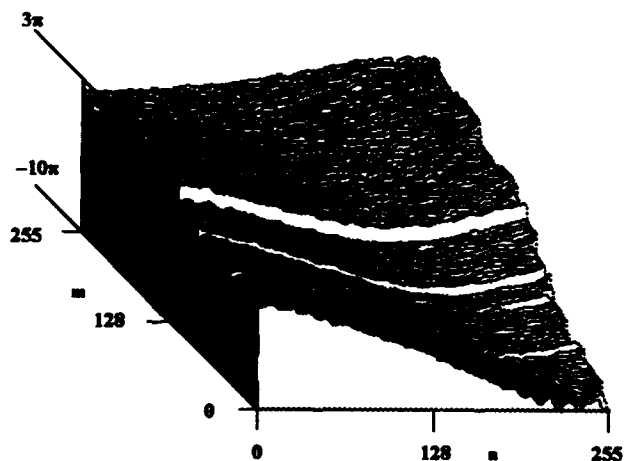


FIGURE 2-a :

Interferogram pattern : $i(n,m)$
The air-water surface is
perturbed by ruffled wind.

Image size on detector :
6mm x 4mm



Phase distribution : $\Phi(n,m)$

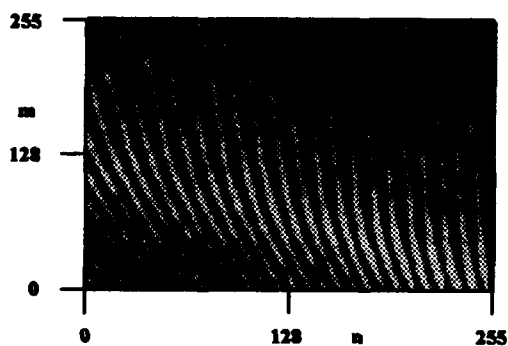
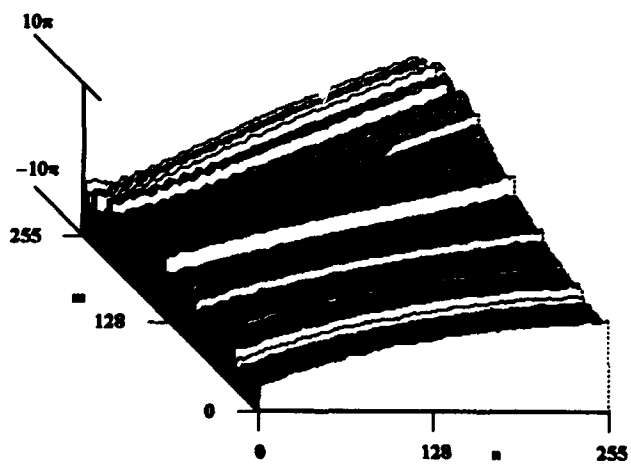


FIGURE 2-b :

Interferogram pattern : $i(n,m)$
The air-water interface is
perturbed by ruffled wind.

Image size on detector :
6mm x 4mm



Phase distribution : $\Phi(n,m)$

FIGURES 3

Averaged Fourier spectra over many independent realisations.

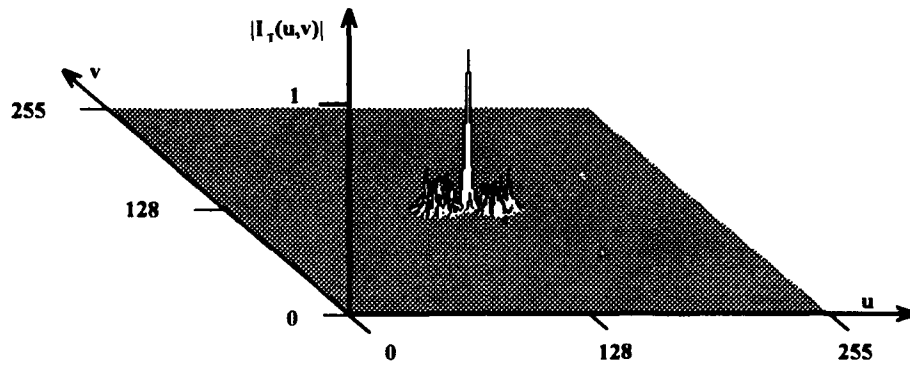


Figure 3.a : Fourier spectrum over 50 realisations.

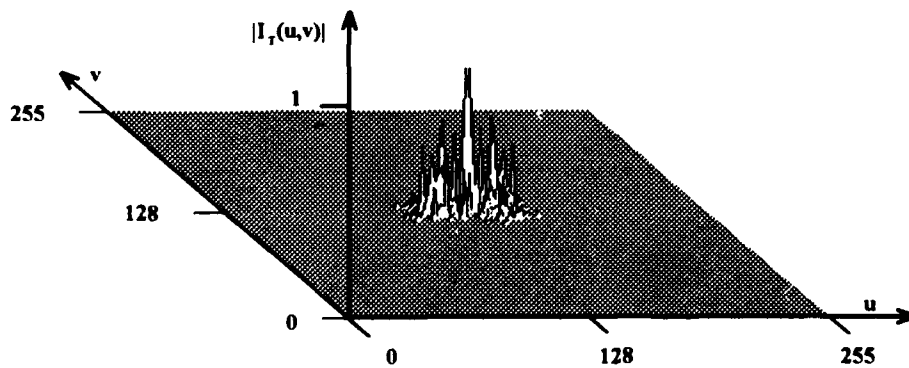


Figure 3.b : Fourier spectrum over 100 realisations.

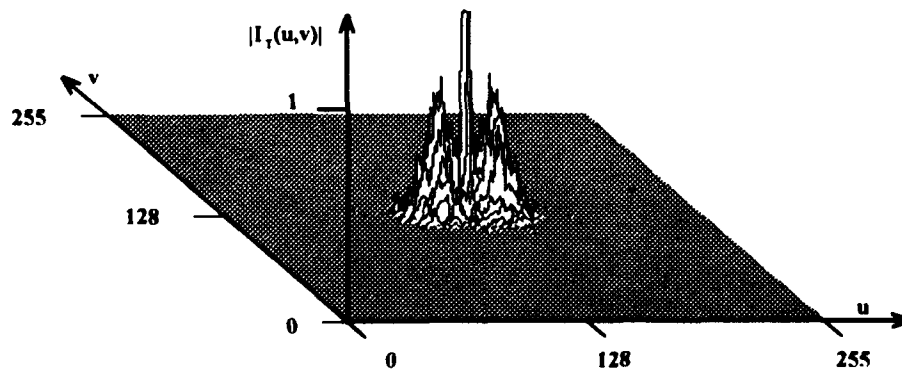


Figure 3.c : Fourier spectrum over 800 realisations.

III- EVALUATION OF THE SPATIAL COHERENCE OF A LASER BEAM PROPAGATING IN SEA WATER.

3.1- EXPERIMENTAL SET UP :

In this section we only report an experimental study concerning the scattering effect on the spatial coherence of the laser beam. We have used the well know theory of partial coherence developed by Wolf^{11,12} and based on the mutual coherence function $\Gamma_{12}(\tau)$. If $U_1(x,y,t)$ and $U_2(x,y,t)$ are the electromagnetic fields produced by a coherent source the mutual coherence function in a observation plane (x,y) is :

$$\Gamma_{12}(\tau) = \Gamma_{12}(x,y,\tau) = \langle U_1(x,y,t+\tau)U_2^*(x,y,t) \rangle \quad (5)$$

where the brackets denote a time average and τ is a time delay.

By normalising the mutual coherence, we obtain the complex degree of coherence :

$$\gamma_{12}(\tau) = \frac{\Gamma_{12}(\tau)}{\sqrt{\Gamma_{11}(0)}\sqrt{\Gamma_{22}(0)}} \quad (6)$$

In practice the delay time τ introduced between the interfering beams is very small and it is then possible to simplify the formula. When τ is very much smaller than the coherence time, we can define the degree of mutual intensity $\gamma_{12}(0)$:

$$\gamma_{12}(0) \approx \gamma_{12}(\tau) \quad (7)$$

$\gamma_{12}(0)$ describes the spatial coherence of the light. For heterodyne applications, we shall restrict ourselves to the important case of quasi-monochromatic light ($\Delta\nu \ll \bar{\nu}$). The theoretical expressions take a simpler form in this case : the degree of mutual coherence can be determinate by the measurement of the visibility $V(x,y)$ of fringes :

$$|\gamma_{12}(0)| = V(x,y) \cdot \frac{I^{(1)}(x,y) + I^{(2)}(x,y)}{2\sqrt{I^{(1)}(x,y) \cdot I^{(2)}(x,y)}} \quad (8)$$

Where the visibility is given by

$$V(x,y) = \frac{I_{\max} - I_{\min}}{I_{\max} + I_{\min}} \quad (9)$$

Different techniques for measuring the degree of coherence over all the beam section have been developed¹³⁻¹⁴ Here, we use a Mach-Zehnder interferometer to obtain the spatial correlation function after propagation through scattering water: this technique allows measurements of $|\gamma_{12}(0)|$ for every points of the wave front.

Fringe patterns are initially created by tilting the reference wave of a small angle θ with the plane wave front. If we make equal the path lengths for the reference and the signal beam and if θ is small, then the time difference τ between the two paths will be small compared to the coherence time. When these conditions are satisfied, $|\gamma_{12}(\tau)|$ is not very different from $|\gamma_{12}(0)|$ for quasi-monochromatic light.

We use the experimental arrangement of figure 4. The laser is the same than for the precedent experiment. The detection is made on a CCD array (512 x 512 pixels). The diffuse beam propagates through a cylindrical tank of 5,4 m length. Scattering in the medium is produced by kaolinite particles ($\phi_{\text{mean}} = 3,5 \mu\text{m}$; relative index $n=1,15$) suspended in the water and characterized by an absorption coefficient c .

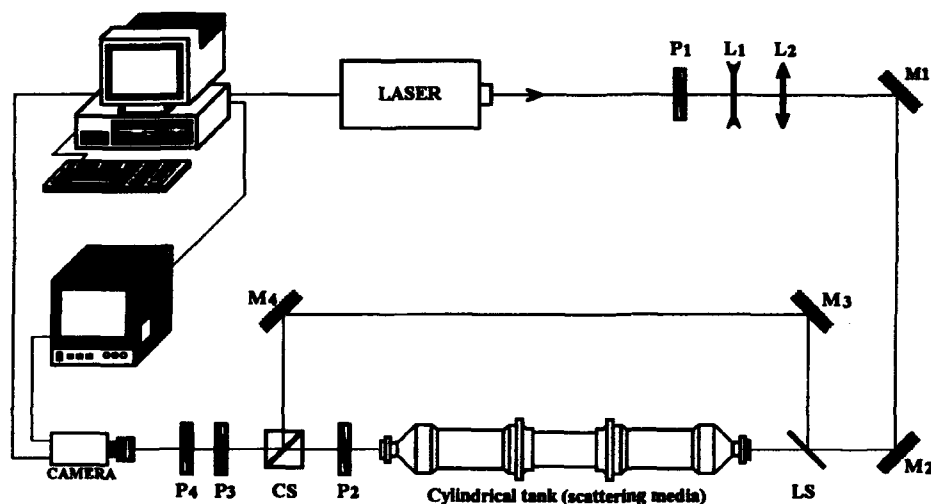


Figure 4 :

Details of experimental set-up

C.S ,L.S : Beam splitter cube

L1,L2: Lenses

M1,M2,M3,M4 : Mirrors

P1,P2 ,P3,P4 : Polarizers

3.2- RESULT :

Transverse analysis of the beam was made for three positions of the camera to cover all the wave front (Total size of matrix array : 6 mm X 4,5 mm). The effect of scattering on spatial coherence is shown in figure 5 for two absorption coefficients c ($c=0,69 \text{ m}^{-1}$, $c=1,47 \text{ m}^{-1}$). Each part of the fringe patterns is recorded during a laser pulse (10 ns) and is digitalized over 512 X 512 pixels. Local deformations of fringes result from aberrations of optical elements and from instabilities of reference beam propagating in air (optical path length > 7m).

In the case of equal intensities illumination of the two beams ,the visibility $V(x,y)$ was calculated for each interferogram and the value of $|\gamma_{12}(x)|$ was then determined. We have presented the averaged transverse evolution of $|\gamma_{12}(x)|$ on figures 5 under each interference pattern. Each plot is the mean of $|\gamma_{12}(x)|$ calculated over the width of the interferogram and results from 12 recorded patterns. The module of spatial coherence shows a constant high level for $c < 1,20 \text{ m}^{-1}$ ($|\gamma_{12}(x)| \approx 0,8$). The degree of spatial coherence decreases in the periphery of the beam section as the absorption coefficient increases, but remains constant in the center of the beam.

In figures 6, the histograms give a global description of the spatial coherence evolution for different values of c . Each histograms results from coherence coded images calculated from 12 recorded interference patterns. By this method, we can access directly important parameters:

- the mean value of $|\gamma_{12}(x)|$ which is approximately given by the maximum value on the graph.
- the variations of the spatial coherence which is represented by the spreading of the histogram.

In this analysis, we give the mean histogram for three positions of the camera, so, for each absorption coefficient and for a tank length of 5,4 m we have three histograms: the effect of scattering on the laser beam is immediately observable.

For $c < 1 \text{ m}^{-1}$, we have narrow peaks with high means values for the right, the left and the center of the beam (figure 7-a). We have a high level of spatial coherence with low variations over the beam. This configuration is favourable to coherent detection.

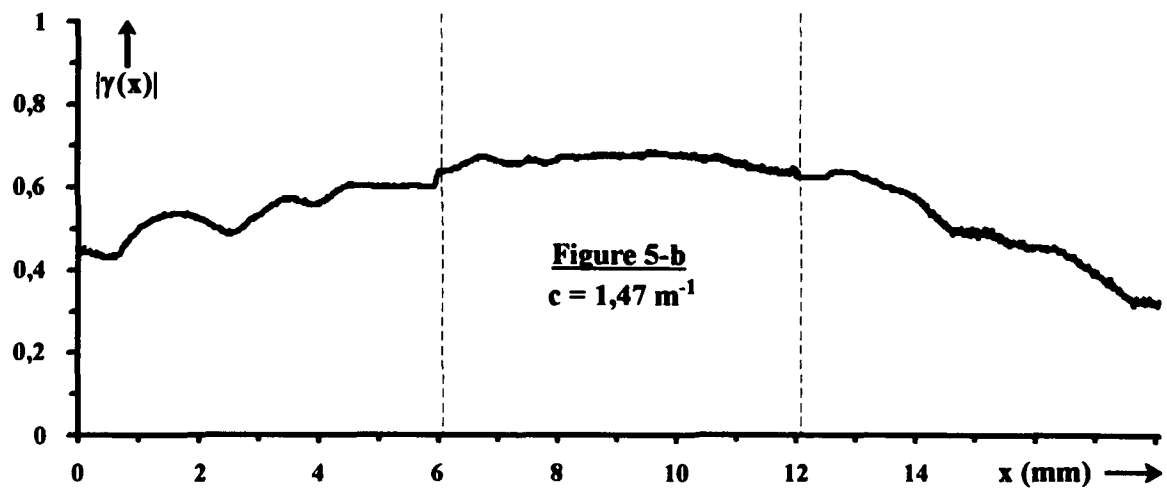
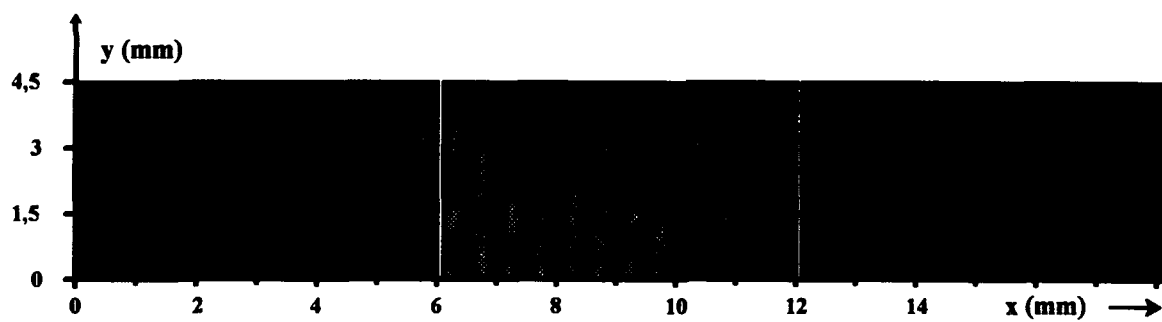
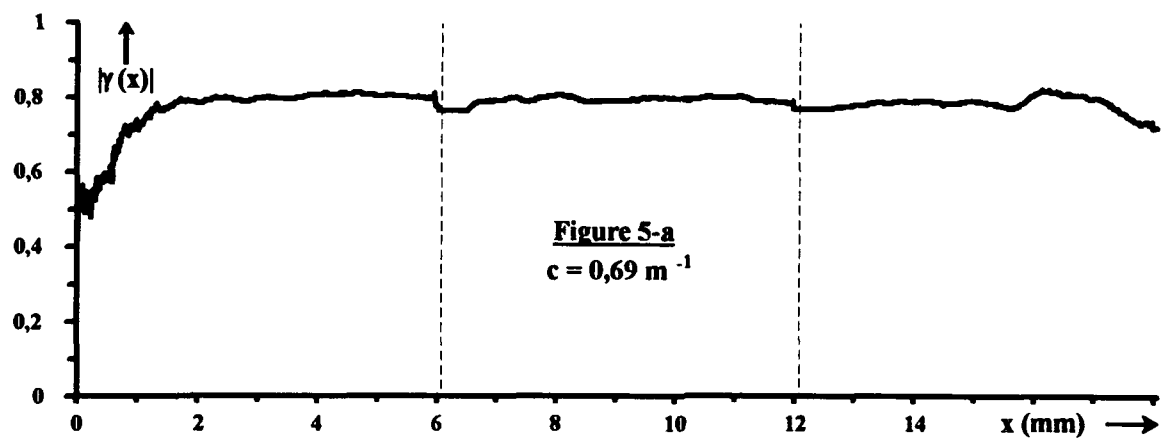
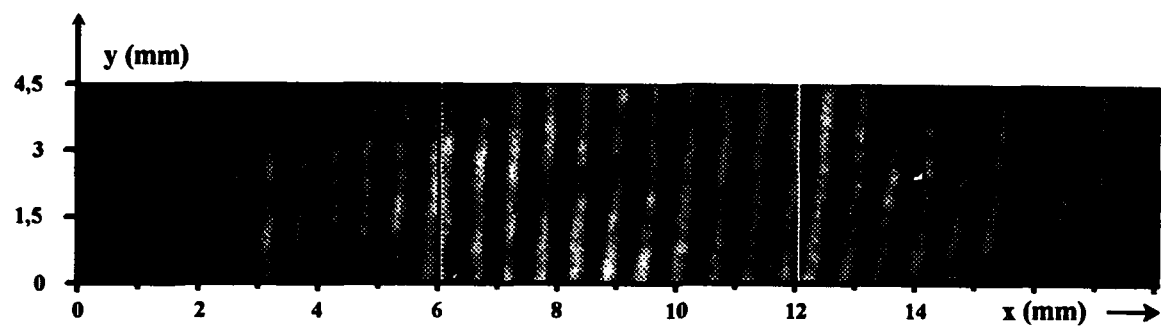


FIGURE 5: fringe patterns and evolution of spatial coherence for different absorption coefficients.

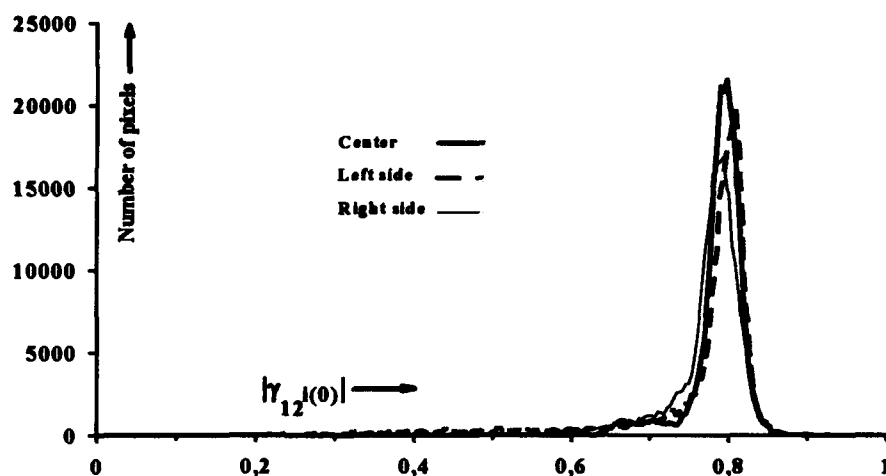


Figure 6-a

$c = 0,34 \text{ m}^{-1}$

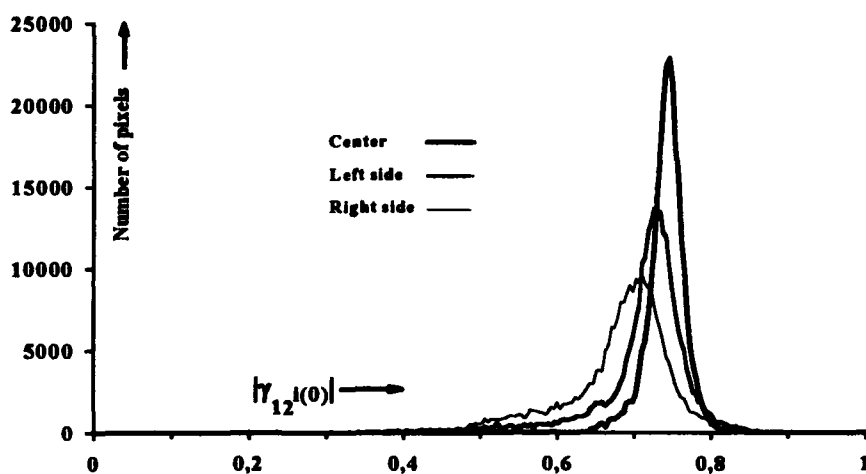


Figure 6-b

$c = 1,26 \text{ m}^{-1}$

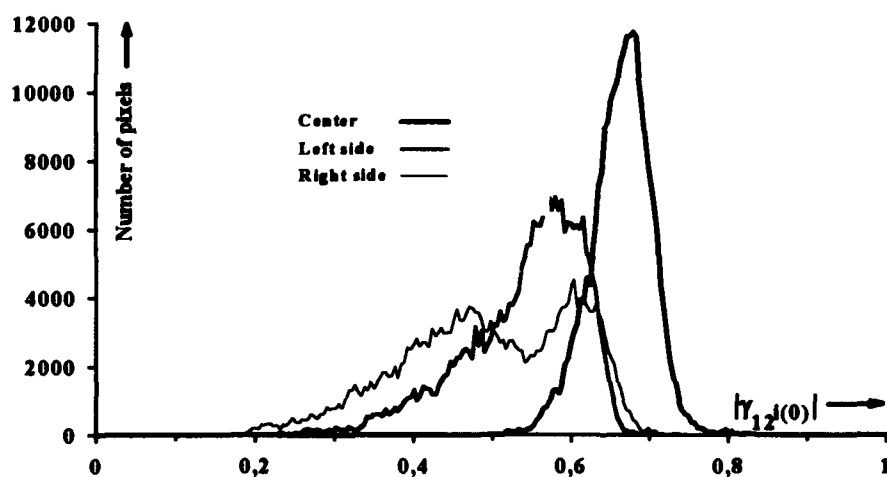


Figure 6-c

$c = 1,47 \text{ m}^{-1}$

FIGURE 6 : Histograms of the averaged $|\gamma_{12}(0)|$ for the right, the left and the center of the light beam for different absorption coefficients.

For $c = 1,26 \text{ m}^{-1}$ and $c = 1,47 \text{ m}^{-1}$, the histograms of $|\gamma_{12}(0)|$ is represented on figures 6-b and 6-c. Here we can easily observe the evolution of spatial coherence over two regions. First, at the center of the beam, we have sensibly the same evolution as in the previous case. We still have a narrow peak, so we have small variations of $|\gamma_{12}(0)|$ and we can see a small decrease of the mean value of $|\gamma_{12}(0)|$. The second region represents the two sides of the laser beam : the loss of spatial coherence is here given by a smaller mean value and by a stronger spreading of the histogram of $|\gamma_{12}(0)|$. If we assume that the spreading of the histogram increases in the two sides and at the center of the beam with the scattering effect, then the possibility to use the coherence of the laser light appears to be difficult only for very turbid waters ($c > 1,5 \text{ m}^{-1}$).

IV- CONCLUSION

Two experimental methods using interferometric images and Fourier transform has been developed to analyse beam transformations in sea medium.

First, we have analyse air water interface roughness. The results can be use to analyse the heterodyne efficiency in air-borne hydrographic systems using optical coherent detection. We have seen that a statistical treatment of the problem can give useful informations given by the spreading of Fourier spatial spectra. The choice of the number of realisations is important and depends of the air-sea perturbations.

Then we have evaluated the spatial coherence, in relation with the scattering effect of sea-water; we have observed that for most of the sea-waters ($c < 0,5 \text{ m}^{-1}$ for 5,4 m length) the central part of the laser beam will conserve a good spatial coherence and so permit coherent detection. The kaolinite particles used in our experiments can be present in sea-water and simulate the absorption effect of usual sea-water¹⁵. Our result can then be applied in ocean detection, but they don't take into account the random variations in salinity and temperature which will also distort the wave fronts by turbulence effects.

V - REFERENCES

- 1- Veldkamp W.B., "Holographic local-oscillator beam multiplexing for array heterodyne detection", Appl. Opt. V 22 N°6, pp 891-900, 1983
- 2- Tanaka T., Taguchi M. and Tanaka K., "Heterodyne efficiency for a partially coherent optical signal", Appl. Opt. V 31 N°25, pp 5391-5394, 1992
- 3- Kravtsov Yu A. and Saichev A.I., "Effect of double passage of waves in randomly inhomogeneous media", Sov.Phys.Usp. V 25 pp. 494-508, 1983
- 4- Tapster P.R., Weeks A.R. and Jakeman E., "Observation of backscattering enhancement through atmospheric phase screens", J. Opt. Soc. Am. A 6, pp. 517-22, 1989
- 5- Welch G. and Phillips R., "Simulation of enhanced backscatter by a phase screen", J. Opt. Soc. Am. A 7, pp. 578-84, 1990
- 6- Mavroidis T., Salomon C.J. and Dainty J.C., "Imaging a coherently illuminated object after double passage through a random screen", J. Opt. Soc. Am. A 8, pp. 1003-1013, 1991
- 7- Gorecki C., "Interferogram analysis using a Fourier transform method for automatic 3D surface measurement", Pure Appl. Opt., V.1, N°2, pp.103-110, 1992
- 8- Kreis T., "Digital holographic interference phase measurement using the Fourier-transform method", J. Opt. Soc. Am. 8, pp. 47-55, 1986

- 9- **Takeda M., Ina H. and Kobayashi S.**, "Fourier-transform method of fringe-pattern analysis for computer-based topography and interferometry", *J. Opt. Soc. Am.* 72, pp. 156-60, 1982
- 10- **Press W.H., Brian P.F., Teukolsky S.A. and Vetterling W.T.**, *Numerical Recipes "Fourier transform Spectral methods"*, chap 12, pp. 381- 453, Cambridge University Press, 1987
- 11 - **M. Born and E. Wolf**, *Principles of optics* 6th edition, Pergamon, New York, 1983
- 12 - **M.J. Beran and G.B. Parrent**, *Theory of partial coherence*, Prentice-Hall, Englewood cliffs N.J. 1964
A.S. Marathay, *Element of optical coherence theory*, John Wiley and Sons, 1982
- 13 - **H.W. Wessely and J.O. Bolstad** "Interferometric technique for measuring the spatial correlation function of optical radiation fields" *J.O.S.A.* V.60 p.678-682, 1970
- 14 - **C. Joenathan** "Vibration fringes by phase stepping on an electronic speckle pattern interferometer : an analysis" *A.O.* V.30 p.4658-4665, 1988
- 15 - **J Lotrian, J.Cariou, Y. Guern and A.Bideau- Mehu** "Etude temporelle de la retrodiffusion d'un faisceau laser dans les eaux de mers" *Contrat DRET-UBO N° 84-155*, 1986

Applicability of Lidar Remote Sensing Methods for Vertical Structure Investigation of Ocean Optical Properties Distribution

V.I. Feigels

St. Petersburg Institute of Fine Mechanics & Optics
14 Sablinskaya st., St. Petersburg, 197101 Russia
e-mail: vfeigels@ipmo.spb.su

and Yu.I. Kopilevich

S.I. Vavilov State Optical Institute
3 Pochtamtskaya st., St. Petersburg, 190000 Russia
e-mail: hydroopt@soi.spb.su

ABSTRACT

The results of theoretical study of the problem of detectability of vertical profiles of hydrooptical characteristics in sea water column with the help of airborne lidars are presented. The used approach is based on the developed theory of retroreflected light pulse formation in scattering medium with angular anisotropy of volume scattering function and Sakett's discriminability criterion; the effects of solar illumination, sea surface waves, and atmospheric backscattering are taken into account, as well as the internal noise factors of lidar transmitter and receiver.

The recommendations are formulated for system parameters optimization for separate subsurface water layers detecting in various hydrooptical situations and different environmental conditions.

1. INTRODUCTION

Practically all of the actually functioning modern lidar systems¹⁻¹¹ are specially designed for bottom depth measurement in continental shelf areas. Nevertheless it is evident that on a level with depth data, the shape of registered lidar signal contains an information on hydrooptical characteristics of the sea water layers from the surface to the bottom. Some attempts to solve the inverse problem, that is to obtain the hydrooptical characteristics of the sounding water column by the shape of registered lidar signals, are reported in¹²⁻¹⁶.

One of the difficulties in the problem of lidar sounding data inversion is related to the situations when anomalously high levels of backscattered light intensity from within distinct layers of sea water are registered^{12,13}. The physical nature of the phenomenon is of special interest, first of all, for bathymetry, because the sharp peaks at the slope of a lidar signal cause additional problems in the bottom reflected pulse recognition¹⁴. At the same time the fine structure of scattering characteristics of sea water is an important part of the whole picture of the optical properties of the world's oceans.

The problem of "enhanced backscattering" from separate horizons was discussed in¹⁷⁻²⁰. The analysis presented there was based on the developed theory of backscattered light pulse formation within the sea water column¹⁷ with the account for anisotropy of the volume scattering function (VSF) in the backward direction. The supposition on a sharp peak existence in the angular dependence of VSF around 180° confirmed by the recent field measurement²¹, allows to give a satisfactory explanation for the above mentioned and some other anomalous results of lidar sounding experiments. The proposed interpretation connects the enhanced signal values with the presence of distinct, rather thin layers of sea water characterized by contrast high values of the volume backscatter coefficient, $\beta(\pi)$, practically independent of the value of total backward scattering coefficient b_b .

In this paper the described theory of lidar echo-signal kinetics is applied to the problem of recognition of the fine structure of vertical distribution of sea-water optical parameters with the help of remote sounding lidar systems. For the task, the optimal parameters of the optical receiving system are found to differ generally from the optimal values of the same parameters for bathymetric applications (cf. ^{8,18,22}). The established dependencies of lidar effectiveness on the sounding pulse power, receiver lens diameter and field of view (FOV), as well as on the width of optical filter band pass, demonstrate some unexpected features for different external conditions.

2. THE THEORETICAL MODEL FOR LIDAR BACKSCATTER SIGNAL

It is clear that generally the shape of a lidar signal from sea water column depends of the full set of the medium light scattering characteristics, integral ones as well as differential. For the following analysis the closer definition of some of the parameters is essential.

The volume scattering function (VSF), $\beta(\theta)$, is the scattered radiant intensity in a direction θ relative to the direction of incidence per unit scattering volume divided by the incident irradiance. The value of $\beta(\theta)$ for the angle $\theta = 180^\circ$ is the volume backscatter coefficient, $\beta(\pi)$.

In practice all the known in situ measurements of VSF, prior to the paper ²¹, were restricted to the scattering angles not greater than $170^\circ - 175^\circ$, the maximal angle being limited by the used instrument construction. Interpretation of collected data to obtain an estimate for the volume backscatter coefficient was based on the assumption of smooth VSF variation around 180° . So the result of an extrapolation of measured points to 180° was taken for the desired estimate; we denote the value by $\tilde{\beta}(\pi)$, to distinguish it from the true magnitude of $\beta(\pi)$.

The backward scattering coefficient, b_b , is defined as

$$b_b = 2\pi \int_{\pi_1}^{\pi} \beta(\theta) \sin\theta \, d\theta.$$

A significant correlation is found in ²³ (see also review in ²⁴) for the parameters b_b and $\tilde{\beta}(\pi)$, as well as for b_b and $\beta(170^\circ)$. It worth mentioning the extraordinary high values of the correlation coefficient for the established relations. A very important regression statistic for correlation between $\beta(170^\circ)$ and attenuation coefficient, c , was obtained in ²⁴ for different regions.

Let us introduce a one more parameter, the small-angle scattering coefficient, b_α , which is equal to the integral of VSF over the solid angle around 0° in which the essential part (80 - 90%) of scattered light radiance is concentrated:

$$b_\alpha = 2\pi \int_0^\alpha \beta(\theta) \sin\theta \, d\theta.$$

The new quantity may be applied to obtain the two-side estimate for the effective attenuation coefficient (cf. ^{14,15,16,19}):

$$(c - b_\alpha) < k < c$$

Now everything is ready to formulate the model for lidar signal used in the following analysis.

In the light field of the sounding laser beam propagating through the water in forward direction, two radiation components may be distinguished ²⁵ -

- 1) weakening radiance of the incident beam (coherent component), and
- 2) diffuse scattered radiance constituent (incoherent component), formed by the small-angle scattering of the incident beam.

According to this, the power, $P_{bw}(h)$, of the signal at the input of lidar receiver caused by backscattered radiation from within the water layer at the depth h , may be expressed^{17,18} by the sum,

$$P_{bw}(h) = P_{bw}^c(h) + P_{bw}^i(h) \quad (1)$$

where the first term ($P_{bw}^c(h)$) is related to the coherent component, and the second ($P_{bw}^i(h)$) - to the incoherent component of the sounding light beam. As it is shown in¹⁷, $P_{bw}^c(h)$ is proportional to $\beta(\pi)$:

$$P_{bw}^c(h) = C \beta(\pi) e^{-2ch}, \quad (2)$$

while $P_{bw}^i(h)$ is proportional to a certain mean value of VSF in the back hemisphere, that is, in view of slight variations of VSF outside of a small vicinity of 180° , to $\bar{\beta}(\pi)$:

$$P_{bw}^i(h) = C \bar{\beta}(\pi) e^{-2ch} [e^{2b_w h} - 1], \quad (3)$$

To explain an unexpectedly high level of lidar return signal from a separate sea-water layer, it is sufficient to assume a considerable anisotropy of the VSF in backward direction, i.e. the difference between $\bar{\beta}(\pi)$ and $\beta(\pi)$, at the locations corresponding to the "anomalous" experimental points. Indeed, the increase of $\beta(\pi)$ in the upper layer of the water column, where the first term in (1) determines the essential part of the signal, may be the cause for the observed backscattering enhancement. The variations of $\beta(\pi)$ do not contradict the above mentioned correlation of optical parameters, if only the value of $\beta(\pi)$ is relatively invariable.

The two-component model (1) for the lidar signal allows to explain also another phenomenon well known to the authors: in lidar bathymetric survey in shallow waters, the contrasts of the bottom are usually found to be several times smaller compared with theoretical predictions. Really, according to²⁶, the relation, M , of the light pulse power reflected from the bottom (P_{bot}) to power backscattered by the water-body (P_{bw}) is given by the formula

$$M = P_{bot} / P_{bw} = (\rho_{bot} / \pi) / \rho_w, \quad (4)$$

where ρ_{bot} is the bottom reflectivity coefficient, and parameter ρ_w is usually identified with $\bar{\beta}(\pi)$

$$\rho_w = 0.5 \bar{\beta}(\pi) \tau c / n,$$

where c - the velocity of light in the air,

τ - the laser pulse duration,

n - the refraction index of the water.

However, when the model (1) is used for the case of rather small depth, ρ_w in (4) must be substituted with $\beta(\pi)$, and if a prominent peak in VSF around 180° ²¹ is assumed to exist, (4) gives a quit realistic estimate for bottom contrast.

3. THE ESTIMATION OF LIDAR SYSTEM EFFECTIVENESS FOR TURBID LAYERS DETECTION

The basis for the following analysis is a test for comparison of different lidars. In the applied criterion Sakitt's D -index of discriminability²⁷ is used, which was found to be extremely effective for the purpose^{8, 28}.

The magnitude of D -index is defined as the measure of distinguishability between two probability distributions, (A) and (B), for the random quantities at the detector input. For the case in question the distribution (B) corresponds to the signal registered in the presence of a layer of turbid water at a given depth, while (A) describes the background situation of homogeneous profile of optical characteristics in the water column.

D -index is determined by the chosen detection criteria, and its value depends on the two first moments of signal distribution. It makes it possible, for the analysis of various factors affecting the detection ability, to use D -index directly, omitting the calculation of acquisition probability. It is the way to compare the effectiveness of various lidar system and to optimize a given system parameters for a concrete task.

The parameter D for a subsurface layer detection is determined by the expression (cf. ⁸)

$$D = \frac{\Delta P_{bw}}{[(c_1 P + B^2) \cdot (c_1(P - \Delta P_{bw}) + B^2 - \epsilon_{bw}^2 \cdot \Delta P_{bw}^2)]^{1/4}} \quad (5)$$

where ΔP_{bw} is the increase in backscattered signal from within the layer; it may be calculated with the use of formulae (1) - (3). P is the sum,

$$P = P_{bw} + P_s + P_{ba}.$$

of the light pulse power backscattered by the water-body (P_{bw}), the power of the sun light exposure (P_s), and the signal (P_{ba}) caused by the backscattering in the atmosphere

$$c_1 = e(1 + b_d)/(\Delta t S_{ph}),$$

e is the electron charge;

$(1 + b_d)$ - parameter, accounting for additional contribution of PMT dynodes to the shot noise;

Δt - discretization time interval;

S_{ph} - PMT photocathode spectral sensitivity;

$$B^2 = \epsilon_{bw}^2 P_{bw}^2 + \epsilon_s^2 P_s^2 + \epsilon_{ba}^2 P_{ba}^2 + \epsilon_{sys}^2 (P - P_s)^2,$$

where ϵ_{bw}^2 , ϵ_s^2 and ϵ_{ba}^2 are the normalized variances of the signals P_{bw} , P_s , and P_{ba} correspondingly, caused by the sea surface roughness; the variances are rather complicated functions of surface waves characteristics, platform altitude, receiver FOV and so on ²⁹⁻³¹. ϵ_{sys}^2 is the normalized variance of the total signal due to laser light returned to the receiver, caused by the system instability (the laser pulse power fluctuations, the random variations in the PMT amplification and so on).

4. THE OPTIMIZATION OF RECEIVER FIELD OF VIEW

To illustrate the approach to the problem of lidar system development on the basis of D -index we consider the evaluation of one of the most important parameters, the receiver FOV. Let the layer be characterized by 20%-increase in parameter $\beta(\pi)$ and 4-times increase in $\beta(\pi)$. The calculations are presented for two cases - (I) the layer depth is 20 m, $c = 0.5 \text{ m}^{-1}$; (II) the layer depth is 10 m, $c = 0.2 \text{ m}^{-1}$. The other sounding conditions are as follows (cf. ⁸):

wind velocity above the sea surface	- 5 m/s;
meteorological visibility	- 5 km;
system instability, ϵ_{sys}	- 5 %
zenith sun angle	- 45°.
laser source divergence	- 5 mr.

The results obtained for the cases (I) and (II) are shown in Figures 1 and 2, correspondingly, for the three values of the lidar platform altitude, $H = 100$ m; 300 m and 500 m. All the calculations of D -index are carried out with the help of PC program program "OCEAN - SCIENTIFIC" (OS) for Windows 3.1 (created with the author's participation for EG&G Washington Analytical Services Center, Inc.^{32,33}), modified with the account for two-component model (1). The program uses the few-parametric model for sea-water optical characteristics^{34,35}. One of the purpose of the OS program is to compare the effectiveness of different lidar systems for the given task and specific conditions, including water quality and meteorological situation;

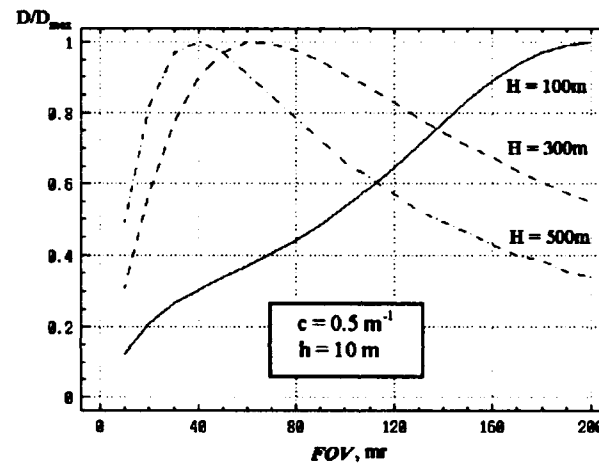


Figure 1. Normalized D -index versus FOV-angle for case (I)

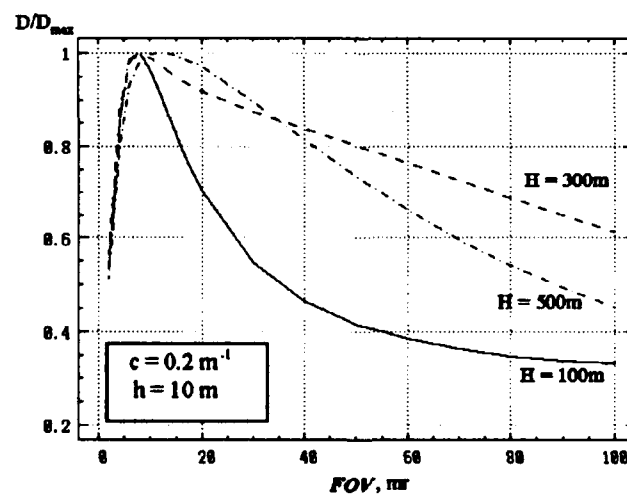


Figure 2. Normalized D -index versus FOV-angle for case (II).

It is seen that the optimal values of FOV for the given external conditions, are:

case (I):

FOV > 200 mr for $H = 100$ m;
FOV = 60 mr for $H = 300$ m;
FOV = 45 mr for $H = 500$ m.

case (II):

FOV = 8 mr for $H = 100$ m;
FOV = 8 mr for $H = 300$ m;
FOV = 12 mr for $H = 500$ m.

The obtained results may be easily explained with the help of two-component model of lidar signal described in Section 2. In the case (I) the optical thickness of the water column above the layer to be detected is rather big, and the incoherent component, $P_{bw}^i(h)$, is the main constituent of the $P_{bw}(h)$ from (1) [see (2) and (3)]. So the signal from the layer, and therefore D -index, are determined by the increase in $\beta(\pi)$ only. The extremum in D dependence of FOV is the result of the increase in P_s (proportional to FOV) and the simultaneous grows (as FOV^2) of the noise caused by the sun light exposure, which diminishes the magnitude of D -index. The results for the case (I) are practically identical to those for bathymetric application^{8,36}.

Case (II) is quite another thing. The optical thickness of the water above the layer is rather small, so, in view of (2) and (3), the coherent component, $P_{bw}^c(h)$, is the principal term in (1). The main contribution into P_{bw} , and hence into D , is related to $\beta(\pi)$. It is evident that the growth of FOV when it is much greater than the incident light beam divergence, involve the increase in $P_{bw}^i(h)$, which cause a negligible effect, and the diminution D due to the noise. The optimal value of FOV, as it must be expected, is close to the value of incident laser beam divergence and does not depend practically on the platform altitude.

5. THE EFFECT OF LASER POWER, RECEIVER APERTURE AREA, AND FILTER BANDPASS

Let us consider formula (5) when geometrical parameters (platform altitude, bottom depth, receiver FOV) and water quality are fixed. Then the two limiting cases may be distinguished:

A. "night" conditions ($P_s = 0$), unperturbed sea surface ($\epsilon_{bw} = \epsilon_s = \epsilon_{ba} = 0$), and negligible system instability ($\epsilon_{sys} = 0$);

B. "bright-day" conditions, rough sea, and considerable system instability, when

$$c_1 P \ll B^2; \quad P \approx P_s.$$

For the case A one has

$$D = \frac{\Delta P_{bw}}{\sqrt{c_1} P_{bw}} - \sqrt{P_T A_R} \quad (6)$$

while in the case B

$$D = \frac{\Delta P_{bw}}{\epsilon_s P_s} - \frac{P_T}{\Delta \lambda} \quad (7)$$

where A_R is the effective aperture area of receiver

P_T - the laser transmitter power

$\Delta\lambda$ - the receiver spectral selector bandpass

The Eq.(7) leads to an unexpected conclusion: the effectiveness of lidar system does not depends on receiver aperture area, when background light power exceeds significantly the echo-signal from the layer to be detected. It is obvious that the effect of the width of spectral selector bandpass is especially strong in the case "B", in contrast to the night conditions (case "A").

Note that according to (6) and (7) the lidar effectiveness is proportional to a power of the laser pulse power, P_T :

$$D \sim P_T^\alpha; \quad \frac{1}{2} \leq \alpha \leq 1$$

where the limiting values of the exponent, α , correspond to the cases "A" ($\alpha = 1/2$) and "B" ($\alpha = 1$).

6. CONCLUSIONS

The two-component model of laser pulsed echo-signals from the water column with the account for the volume scattering function anisotropy in the backward direction is applied to the problem of recognition of the fine structure of vertical profiles of sea-water optical parameters with the help of remote sounding lidar systems.

The ability of a lidar system to register an optically contrast layer of the sea water is considered on the basis of D -index of discriminability analysis.

Some recommendations are formulated for system parameters optimization for separate subsurface water layers detecting in various hydrooptical situations and different environmental conditions; the effects of solar illumination, sea surface waves, and atmospheric backscattering are taken into account, as well as the internal noise factors of lidar transmitter and receiver.

The optimal value of receiver field of view for detection of near-surface turbid water layers is found to differ abruptly from the optimal value of the parameter for lidar bathymetry.

The established dependencies of lidar effectiveness on the sounding pulse power, receiver lens diameter, and the width of optical filter band pass, demonstrate some unexpected features for different external conditions.

7. ACKNOWLEDGMENTS

The authors would like to thank Gary C. Guenther (NOAA), and Dr. R. W. L. Thomas (EG&G) for their attention to the work and helpful discussions.

8. REFERENCES

1. Lillycrop W.J., Banic J.R., "Advancements in the U.S. Army Corps of Engineers Hydrographic Survey Capabilities: The SHOALS System", *Marine Geodesy*, v.15, 177-183, 1992.
2. Lillycrop W.J. et. al. "Field Testing of the U.S. Army Corps of Engineers Airborne Lidar Hydrographic Survey System", *Proc. U.S. Hydrographic Conference '94*, SP 32, 200-205, 1994.
3. Sizgoric S., Banic J., Guenther G., "1970-1990: Airborne Lidar Hydrography Status", *EARSEL Advances in Remote Sensing*, v.1, No 2, 95-100, 1992.
4. Lutomirski R., Halmbach S., Curran T., and Gibbons J. "Performance Modelling and Analysis of the Ocean Water Lidar (OWL) Hydrographic System". *Proc. U.S. Hydrographic Conference '94*, SP 32, 200-205, 1994.

5. Penny M.F., Billard B., Abbot R.H. "LADS - the Australian Laser Airborne Depth Sounder," *Int.J.Remote Sensing*, v.10, No.9, 1463-1479, 1989.
6. Setter C., Willis R.J., "LADS - from Development to Hydrographic Operation", *Proc. U.S. Hydrographic Conference '94*, SP 32, 134-143, 1994.
7. Kervern G., Le Gall A., Toullec B., "Airborne Laser Bathymetry: a Novel Technique for Shallow Water Monitoring", *Proc. SPIE*, v. 1714, 74-80, 1992.
8. Feigels V.J. "Lidars for Oceanological Research : Criteria for Comparison, Main Limitations, Perspectives", *Proc. SPIE Ocean Optics XI*, v.1750, 473-484, 1992.
9. Feigels V.J. and Kopilevich Yu.I., "Russian Airborne LIDARs for Oceanography", *Proceedings from Geophysical Technology Transfer Initiative Symposium & Workshop, "Russian Airborne Geophysics & Remote Sensing", September 13 -17, Golden, Colorado, 1992*, *Proc. SPIE*, v.2111, 127-141, 1993.
10. Steinvall O., Koppari K., Karlsson U. "Experimental Evaluation of an Airborne Depth Sounding Lidar", *Proc. SPIE*, v. 1714, 108-126, 1992.
11. Koppari K., Karlsson U., Steinvall O., "Airborne Laser Depth Sounding in Sweden", *Proc. U.S. Hydrographic Conference '94*, SP 32, 124-133, 1994.
12. Billard B., Abbot R.H. and Penny M.F., "Airborne Estimation of Sea Turbidity Parameters from the WRELADS Laser Airborne Depth Sounder", *Appl. Opt.*, v.25, No.13, 2080-2088, 1986.
13. Hoge F.E., Wright C.W., Krabill W.B., Buntzen R.R., Gilbert G.D., Swift R.N., Yungel J.K., Berry R.E. "Airborne Lidar Detection of Subsurface oceanic scattering layers," *Appl. Opt.*, v.27, No. 19, 3969-3977, 1988.
14. Billard B., Wilsen P.J., "Sea Surface and Depth Detection in the WRELADS Airborne Depth Sounder. *Appl. Opt.*, v.25, No. 13, 2059-20667, 1986.
15. Phillips D.M., Abbot R.H., Penny M.F. "Remote Sensing of Sea Water Turbidity with an Airborne Laser System," *J.Phys.D: Appl.Phys.* v.17, 1749-1758, 1984. Printed in Great Britain.
16. Phillips D.M. and Koerber B.W., "A Theoretical Study of an Airborne Laser Technique for Determining Sea Water Turbidity," *Aust. J. Phys.*, v.37, No 1, 75-90, 1984.
17. Kopilevich Yu.I. and Feigels V.J. "Characteristics of Light Backscattering by Sea Water and Lidar Sounding of Water Column", *Proc. SPIE*, v.2048, 212-228, 1993.
18. Feigels V.I. and Kopilevich Yu.I., "Remote Sensing of Subsurface Layers of Turbid Sea Water with the Help of Optical Lidar System", *Proc. SPIE*, v.2048, 342-353, 1993.
19. Kopilevich Yu.I, Svetlykh A.A., and Feigels V.I., "On Interpretation of Some Anomalies in the Shape of Lidar Signal from Upper Sea-Water Layers", *Proc. SPIE*, v.2112, 1993.
20. Kopilevich Yu.I. and Feigels V.J., "Theoretical Model for Backscattered Pulse Kinetics and Interpretation of Some Anomalies in Lidar Remote Sensing Data" (in this issue).
21. Maffione R.A. and Honey R.C., "Instrument for Measuring the Volume Scattering Function in the Backward Direction", *Proc. SPIE* v.1750, 15-26, 1992.

22. Svetlykh A.A. and Feigels V.I., "A Gain in LIDAR Performance Provided by Increase of Pulse Repetition Rate and Narrowing Optical Filter Band", *Proceedings from Geophysical Technology Transfer Initiative Symposium & Workshop, "Russian Airborne Geophysics & Remote Sensing", September 13 -17, Golden, Colorado, 1992, Proc.SPIE, v.2111, 75-94, 1993.*
23. Petzold T.J., Volume Scattering Functions for Selected Ocean Waters. S10 Ref. 72-28, *Scripps Institution of Oceanography, Visibility Laboratory, San Diego, Calif., 79pp, 1972.*
24. Smart J.H., "Empirical Relationship between Optical Properties in the Ocean", in *Ocean Optics XI*, Gary D. Gilbert, Editor, Proc. SPIE 1750, 276-298 (1992).
25. Ishimaru A., *Wave Propagation and Scattering in Random Media*, Vol.1, Academic Press, New York - San Francisco - London, 1978.
26. Steinvall O., Klevebrant H., Lexander J , Widen A. "Laser Depth Sounding in the Baltic Sea," *Appl. Opt.*, v. 20, No.19, 3284-3286, 1981.
27. Sakitt B. "Indices of Discriminability," *Nature*, v.241, 133-134, 1973.
28. Egan J.P. *Signal Detection Theory and ROC Analysis*, Academic Press, NY, 1975.
29. Dolin L.S., Levin I.M. *Theory of Underwater Vision (Reference book)*, Leningrad, Gidrometeoizdat, 1991, (in Russian).
30. Veber V.L. "Backscattering Signal in Pulsed Optical Sounding of the Upper Ocean Layer through a Rough Surface," *Izv. AN SSSR. Fizika atmosfery i okeana (Izvestiya, Atmospheric and Oceanic Physics)*, v.24, No.6, 647-656, 1988.
31. Luchinin A.G. "On Some Features of a Backscattered Signal at Laser Probing of Sea Upper Layer trough a Rough Surface," *Izv. AN SSSR. Fizika atmosfery i okeana (Izvestiya, Atmospheric and Oceanic Physics)*, v.23, No.9, 976-982, 1987.
32. Feigels V.I., Kopilevich Y.I. *Ocean-Scientific for Windows. Basic Concepts, Description of the Theory*, EG&G Washington Analytical Services Center, Inc., 1993.
33. Feigels V.I., Kopilevich Y.I. *Ocean-Scientific for Windows. User's Guide*, EG&G Washington Analytical Services Center, Inc., 1993.
34. Feigels V.I. "LIDAR Modeling", Report at the Technical Seminar on Issues in LIDAR and Ocean. Naval Ocean Systems Center. San Diego, CA. October 1-2, 1991.
35. Dolin L.S., Levin I.M., Kopelevich O.V., Feigels V.I. " Few-Parameter Models of Light Field at the Sea and Integral Parameters of Phase Functions of Water." *Izv. AN SSSR. Fizika atmosfery i okeana (Izvestiya, Atmospheric and Oceanic Physics)*, v.24, No 11, 17-22, 1988.
36. Feigels V.I. "Optimization of LIDAR field of view for airborne bathymetric measurements" // *Laser'90: IV national conference and technical exhibition with international participation "Laser and Their applications". Abstracts.* October 23-26, 1990, Plovdiv, Bulgaria,- p.110-111.

Theoretical Model for Backscattered Pulse Kinetics and Interpretation of Some Anomalies in Lidar Remote Sensing Data

Yurij I. Kopilevich

S.I. Vavilov State Optical Institute
3 Pochtamtskaya st., St. Petersburg, 190000 Russia fax: (812) 312-9383
e-mail: hydroopt@soi.spb.su

and Victor I. Feigels

St. Petersburg Institute of Fine Mechanics & Optics
14 Sablinskaya st., St. Petersburg, 197101 Russia fax: (812) 232-0574
e-mail: vfeigels@ipmo.spb.su

ABSTRACT

A new theoretical approach is suggested for the problem of backscattered light signal kinetics under the pulsed illumination of sea water column. The developed model uses the small-angle-scattering approximation for the sounding and backscattered light beams and takes into account the angular anisotropy of volume scattering function (VSF) in the back hemisphere. The predictions of the theory are supported by the results of laboratory experiments with model scattering media.

On the base of the model, an interpretation is proposed for some anomalies in the shape of lidar signals registered in airborne sounding experiments. The interpretation of the effect of "enhanced backscattering" from separate sea water layers is shown to be consistent with the recent unique measurements of VSF in the vicinity of 180° and revealed fine structure of vertical profiles of the backscattering coefficient.

The physical nature of the effect is discussed. The recently obtained theoretical results allows to suppose that, along with high concentration of large biological particles, coherent light backscattering by refractive turbulence in the corresponding water layers may be the cause of enhanced echo-signals from isolated depth levels.

1. INTRODUCTION

The basic application of airborne lidar systems is bottom depth measurements in continental shelf areas¹⁻¹¹. However some progress was achieved in the problem of estimation of hydrooptical characteristics of the sea water layers by the shape of registered lidar signals¹²⁻¹⁶. To obtain the values of the effective attenuation coefficient (K) and a backscatter parameter (B) from the signals of a laser-based airborne hydrographic system the lidar equation for the power, $P(h)$, returned to the airborne receiver from the depth h , is applied in the form^{12,13}

$$P(h) = B e^{-2Kh}. \quad (1)$$

The "backscatter parameter", B , is supposed to be proportional to the volume backscattering coefficient, $\beta(\pi)$ ¹²,

$$B = C \beta(\pi); \quad (2)$$

with the quantity, C , depending only on lidar transmitter and receiver parameters. For near-coastal shoal regions with strongly forward-stretched volume scattering function (VSF), absorption gives the main contribution to the effective attenuation coefficient, K , in (1), so that

$$K \approx a \quad (3)$$

(a is the light absorption coefficient) with the accuracy of 5% - 20% depending on single-scattering albedo, $\omega = \frac{(c-a)}{c}$ (c is the attenuation coefficient).

In several lidar sounding experiments performed in turbid near-shore waters anomalously high levels of backscattered light intensity from within distinct layers of sea water were registered. The signals in question were obtained near Carnac Island in Western Australia¹² and southeast of Wallops Island in Atlantic Ocean (VA, USA)¹⁷; analogous waveforms were observed with the GOI lidar system^{18,19} in a series of experiments carried out in 1988 at the Black Sea (coastal zone near the peninsula of Petzunda)¹⁹. The observed high backscatter was often associated with the shallower inshore regions; the corresponding layer depth did not exceed 10 m.

The attempts to use the Eq.(1) for water optical parameters estimation in the situations in question leads to a confusion. The point may be explained with the example shown in Figure 1, where the results of some lidar signals processing are given in the form of "K - B diagram".

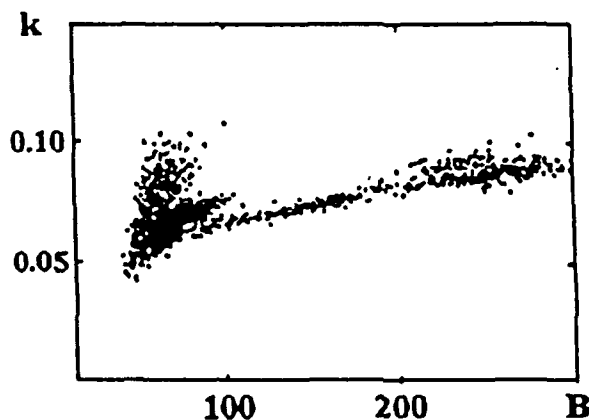


Figure 1. (reproduced from¹²). Scatter diagram of attenuation against backscatter for data collected in a pass over the Gulf of St. Vincente.

It is seen that the points on "K-B diagram" corresponding to high B values, displace a relation between the two parameters, which seems to be remarkably different from the well known data of optical oceanology. It is significant that the registered backscatter enhancement (variations in magnitude of B for 5 - 6 times) are not followed by noticeable attenuation growing (K values remain in the limits of 0.06 - 0.08 m^{-1}); according to Eq.(3) it implies the approximate constancy of the absorption coefficient, a . The available data of independent contact measurements of the attenuation coefficient carried out at the same locations²⁰ do not demonstrate any significant variations of c with depth at the corresponding horizons. So the value of the scattering coefficient, b ,

$$b = c - a,$$

has to remain nearly constant (with possible variations for no more than 10 - 20%), when B [and hence $\beta(\pi)$, by virtue of (2)] suddenly becomes 5 - 6 times greater. This contradicts to the well known results²¹ concerning the strong connection between $\beta(\pi)$ and b .

An attempt to clarify the situation described above was first made in²². The presented analysis is based on the developed theory of backscattered light pulse formation within the sea water column²³ with the account for anisotropy of the volume scattering function (VSF) in the backward direction.

It is evident that the anisotropy do affect abruptly the level of lidar signal from water body and the registered pulse shape in the case of stratified sea water. The point is that in typical airborne lidar experiment geometry the angle under which the receiver aperture is seen from a point in the scattering volume is of the order of 1 mr, so a lidar system with spatially coherent sounding laser beam registers directly backscattered light from upper layers of water column. In the same time the angular broadening of light beam due to scattering by sea water and finite field-of-view (FOV) of receiver results in the fact that for lidar echo-signal from water layers at considerable depth the determining parameter is a certain mean value of VSF in the back hemisphere. The supposition on a sharp peak existence in the angular dependence of VSF around 180° seems to be consistent with the known unique measurements of volume scattering phase function in the vicinity of backward direction.

The physical nature of the "enhanced backscattering" from separate sea-water layers is of special interest. In this paper two possible mechanisms for the effect are discussed; the first of them (see ²²) is connected with the assumption of high concentration of large biological particles at corresponding horizons. We propose here an alternative explanation: according to presented theoretical results, coherent light backscattering by refractive turbulence in separate water layers may be the cause of enhanced echo-signals.

2. THEORY OF LIDAR ECHO-SIGNAL

The known physical models of lidar signal formation (see, e.g., ^{14, 16, 24}) are based on radiation transfer theory; they usually characterize backscatter by a single parameter and presuppose, more or less obviously, the VSF to be constant through the whole back hemisphere. Thus, for a quantitative account of light backscattering anisotropy, that is angular dependence of VSF around 180° , it is necessary to develop an adequate theory of backscattered light pulse kinetics in discreet random medium.

We first consider the field of the sounding laser beam in sea water. Let $L = L(\mathbf{r}, \mathbf{k}, t)$ be the radiance of the beam propagating in the forward direction along Oz -axis of cartesian co-ordinates where $\mathbf{r} = \{\mathbf{r}_1, z\}$, $\mathbf{r}_1 = \{x, y\}$; \mathbf{k} is the unit vector, $\mathbf{k} = \{k_1, k_2\}$, $k_z > 0$; t is the time.

It is convenient to distinguish two radiation components of the field L ²⁵ -

- 1) weakening radiance of the incident beam (coherent component), L_c , and
- 2) diffuse scattered radiance constituent (incoherent component), L_i , so that $L = L_i + L_c$.

In terms of the small-scattering-angle approximation ²⁶, L_i and L_c are the solutions for the following problems:

$$\begin{cases} \hat{A}L_c(\mathbf{r}, \mathbf{k}, t) = 0, & z > z_0 \\ L_0(\mathbf{r}, \mathbf{k}, t)|_{z=z_0}, & k_z \approx 1 \end{cases} \quad (4)$$

$$\begin{cases} \hat{A}L_i(\mathbf{r}, \mathbf{k}, t) = (1 - \alpha) \int \beta_+(\mathbf{k}, \mathbf{k}') L_i(\mathbf{r}, \mathbf{k}', t) d^2\mathbf{k}'_1 + (1 - \alpha) \int \beta_+(\mathbf{k}, \mathbf{k}') L_c(\mathbf{r}, \mathbf{k}', t) d^2\mathbf{k}'_1, & z > z_0 \\ L_i(\mathbf{r}, \mathbf{k}, t)|_{z=z_0} = 0 \end{cases} \quad (5)$$

where

$$\hat{A} \equiv \frac{1}{nv} \frac{\partial}{\partial t} + \frac{\partial}{\partial z} + \mathbf{k}_1 \nabla_1 + c, \quad \nabla_1 \equiv \left\{ \frac{\partial}{\partial x}, \frac{\partial}{\partial y} \right\}$$

is the differential operator for the radiation transfer equation in the small-angle approximation, v is the speed of light in air, n is the refractive index of the water. $L_0(\mathbf{r}, \mathbf{k}, t)$ is the initial radiance distribution in $z = z_0$ plane, caused by the laser source. The VSF is assumed to be given by the sum,

$$\beta(\theta) = (1 - \alpha), \quad \beta_+(\theta) + \alpha\beta_-(\theta) \quad (6)$$

where β_+

$$\beta_+(\theta) = 0, \quad \theta > \theta_+,$$

describes the sharp peak of forward scattering by the water, and

$$\beta_-(\theta) = 0, \quad \theta \leq \theta_-;$$

α is a small parameter of the problem. Note that β_{\pm} , and therefore β , are normalized according to the equality,

$$2\pi \int_0^{\pi} \beta_{\pm} \sin\theta \, d\theta = b$$

The distribution of backscattered light radiance, $\beta^-(r, k, t)$, $k_z < 0$, in the first order of perturbation theory in small parameter α from (6), is the solution for the radiation transfer equation with spatially distributed source, Q^- ,

$$Q^-(r, k, t) = \alpha \int \beta_+(k' k) L_c(r, k', t) d^2 k'_1 \quad (7)$$

caused by single large-angle scattering of the forward-going radiance $L = L_i + L_c$. The quantity, $P(t)$, of the signal, registered by a lidar receiver at the moment t , is expressed via L by formula (we consider monostatic scheme)

$$P(t) = \int d^2 r_1 \int d^2 k_1 \int dt' \tilde{L}_0(r_1, k, t - t') L^-(r, k, t')|_{z=z_0} \quad (8)$$

where $\tilde{L}_0(r_1, k, t)$ is the receiver instrument function,

$$\int d^2 r_1 \int d^2 k_1 \int dt \tilde{L}_0(r_1, k, t) = \Sigma \Omega,$$

Σ is the effective area and Ω is the angular aperture of the receiver (FOV).

With the help of the optical reciprocity theorem^{27,28} formula (8) may be rewritten in the form²⁴

$$\begin{aligned} P(t) &= \int d^3 r \int d^2 k_1 \int dt' Q^-(r, -k, t') \tilde{L}(r, k, t - t') = \\ &= \alpha \int d^3 r \int d^2 k_1 \int d^2 k'_1 \int dt' \tilde{L}(r, k, t - t') L(r, k, t') \beta_-(k' k) \end{aligned} \quad (9)$$

with Q^- from (7) and forward-propagating radiance field \tilde{L} , caused by "fictitious" radiation source with the spatial, angular and temporal characteristics just equal to those of lidar receiver. Assuming the receiver FOV to be sufficiently narrow to ensure the applicability of the small-angle approximation for radiance \tilde{L} , the latter may be divided into the two components, \tilde{L}_c and \tilde{L}_i , analogous to $L_{c,i}$. Then \tilde{L}_c is the solution for problem (4) with the boundary condition

$$\tilde{L}(r_1, k, t')|_{z=z_0} = \tilde{L}_0(r_1, k, t')|_{z=z_0}, \quad k_z \approx 1,$$

and \tilde{L}_i satisfies equation (5) with \tilde{L}_c instead of L_c . So, finally, we derive

$$\begin{aligned} P(t) &= \alpha \int d^3 r \int d^2 k_1 \int d^2 k'_1 \int dt' \beta_-(k' k) [\tilde{L}_c(r, k, t - t') L_c(r, k', t') + \\ &\quad \tilde{L}_i(r, k, t - t') L_c(r, k', t') + \tilde{L}_c(r, k, t - t') L_i(r, k', t') + \tilde{L}_i(r, k, t - t') L_i(r, k', t')] \end{aligned} \quad (10)$$

Let us take the following assumption on characteristic angular scale, θ_* , of the variation of $\beta(\pi)$ in the vicinity of $\theta = \pi$. The angular width of the L_c -component of the radiance L , as well as the corresponding quantity for \tilde{L}_c , are supposed to be small compared with θ_* . Conversely, the divergencies of the incoherent components L_i and \tilde{L}_i , in the depth range of interest are much greater than θ_* . According to that, the integration over k_1 and k'_1 in (10) may be carried out:

$$P(t) = \int dt' \int d^3r \left\{ \beta(\pi) \tilde{E}_c(r, t-t') E_c(r, t') + \tilde{\beta}(\pi) [\tilde{E}_c(r, t-t') E_i(r, t') + \tilde{E}_i(r, t-t') E_c(r, t') + \tilde{E}_i(r, t-t') E_i(r, t')] \right\} \quad (11)$$

where $\beta(\pi) = \alpha \beta_-(\pi)$ [see (6)], $\tilde{\beta}(\pi)$ is a certain mean value of VSF $\beta(\theta)$ in the back hemisphere, and $E_{c,i}$ and $\tilde{E}_{c,i}$ are the irradiance distributions corresponding to the radiances $L_{c,i}$ and $\tilde{L}_{c,i}$.

Note that in the case of isotropic backscattering, that is for $\beta(\pi) = \tilde{\beta}(\pi)$, expression (11) is converted to the well known formula used in ²⁴. When the values $\beta(\pi)$ and $\tilde{\beta}(\pi)$ differ significantly, our Eq. (11), with regard for different spatial localization of irradiances caused by coherent and incoherent components, predicts certain peculiarities in signal form, $P(t)$.

Let excitation pulse be δ -shaped, and the receiver have infinite time-resolution. For further simplification we restrict the range of considered depth values by the inequalities,

$$\frac{z^2}{H^2} \ll n^2; \quad \frac{z^2}{H^2} \left[1 + z \frac{b(1-\alpha)}{3} \right] < \frac{U_0^2}{\gamma^2}, \quad \frac{\tilde{U}_0^2}{\gamma^2},$$

where U_0 and \tilde{U}_0 are the initial angular divergences for source beam and receiver, correspondingly; H is the lidar altitude above the sea surface; γ is the mean square value of the scattering angle, $\gamma \ll \pi/2$. With the assumptions Eq. (11) gives

$$P(t) = \frac{W T^2 \Sigma \Omega v}{2\pi n H^2 (U_0^2 + \tilde{U}_0^2)} \left[\beta(\pi) e^{-2cz} + \tilde{\beta}(\pi) e^{-2cz} (e^{-2b_1 z} - 1) \right] \quad (12)$$

Here W is the incident light pulse energy, coefficient $T < 1$ is introduced to account for the light energy losses due to surface reflection; the depth value, z , is related to moment t ,

$$t = \frac{H + z n}{v},$$

and $b_1 = b(1-\alpha)$ is the effective coefficient of volume small-angle scattering (see (6)).

The latter formula allows one to suggest an explanation for the anomalous shape of lidar signals described in Section 1, and the form of "K - B diagram" in Figure 1. Really, if at the given horizon, z , the inequality holds:

$$\beta(\pi) > \tilde{\beta}(\pi),$$

while for the upper layer of sea water $\beta(\pi) \approx \tilde{\beta}(\pi)$, then the received signal $P(t)$ at the corresponding moment increases in comparison with preceding values, and the "enhancement coefficient" is

$$\frac{\beta(\pi) - \tilde{\beta}(\pi)}{\beta(\pi)} e^{-2b_1 z}.$$

So the effect of signal enhancement may be essential when the depth of the layer is not too big, and the first ("coherent") term in (12) [cf. (11)] determines the essential part of the signal.

Note that due to the approximation used to come to expression (12), the dependence of an optically contrast layer detectability on lidar system FOV is neglected. The important dependence is considered in details in ²⁹.

According to the interpretation suggested here, the anomalously high levels of lidar signals from separate horizons are connected with an abrupt variation of relation of $\beta(\pi)$ to $\beta(\pi)$. It is obvious that big value of $\beta(\pi)/\beta(\pi)$ indicates special optical properties of the sea water in the corresponding layer. Unfortunately, the available data of contact measurements of hydrooptical characteristics seems not to confirmed the presence of such layers. The problem is discussed in the following Section.

3. THE PROBLEM OF MEASUREMENT OF VOLUME BACKSCATTER CHARACTERISTICS

In practice all the known *in situ* measurements of VSF, prior to the paper ³⁰, were restricted to the scattering angles not greater then $170^\circ - 175^\circ$, the maximal angle being limited by the used instrument construction. Interpretation of collected data to obtain an estimate for the volume backscatter coefficient was based on the assumption of smooth VSF variation around 180° . The result of an extrapolation of measured points to 180° was taken for the desired estimate; it seems reasonable to associate it with the mean value of VSF in the back hemisphere introduced in Eqs. (11), (12); so we denote the value by $\beta(\pi)$.

The backward scattering coefficient, b_b , is defined as

$$b_b = 2\pi \int_{\pi/2}^{\pi} \beta(\theta) \sin\theta d\theta.$$

A significant correlation is found in ²¹ (see also review in ³¹) for the parameters b_b and $\tilde{\beta}(\pi)$, as well as for b_b and $\beta(170^\circ)$. It worth mentioning the extraordinary high values of the correlation coefficient, r^2 , for the established relations:

$$b_b = 5.92 \tilde{\beta}(\pi) - 0.00185 \quad (r^2 = 0.98);$$

$$b_b = 6.18 \beta(170^\circ) - 0.00176 \quad (r^2 = 0.97).$$

Perfectly analogous results, confirming the connection between the parameters, are obtained by the authors ²⁹:

$$b_b = 5.21 \beta(170^\circ) - 5.216 \cdot 10^{-5} \quad (r^2 = 0.96)$$

What for the "true" backscatter coefficient of sea water, R.A.Maffione and R.C.Honey ³⁰ in Monterey Bay were the first to measure direct scattering in the vicinity of 180° . Their results show the significant anisotropy of VSF.

The analysis ²³ of the method used in ³⁰ allows to expect the real VSF distribution to have a more prominent spike peak in backward direction then the registered one. The difference between measured angular distribution and "true" VSF is easily explained on the base of the theory described in Sec.2. The point is that when a cw laser is used, the registered signal is the result of integration over all distances, $0 < z < \infty$, and in view of comparatively slow descent of incoherent irradiances, E_i and \tilde{E}_{ij} , $P(r)$ contains a significant "isotropic" part produced by the terms in (11), proportional to $\beta(\pi)$.

Fig. 2 shows the results of numerical modeling of angular distribution of registered backscattered signal from medium with VSF of the form

$$\beta(\pi - \theta) = \beta(\pi) \exp\left(-\frac{\theta^2}{\Delta^2}\right) + \tilde{\beta}, \quad \Delta < \pi/2. \quad (13)$$

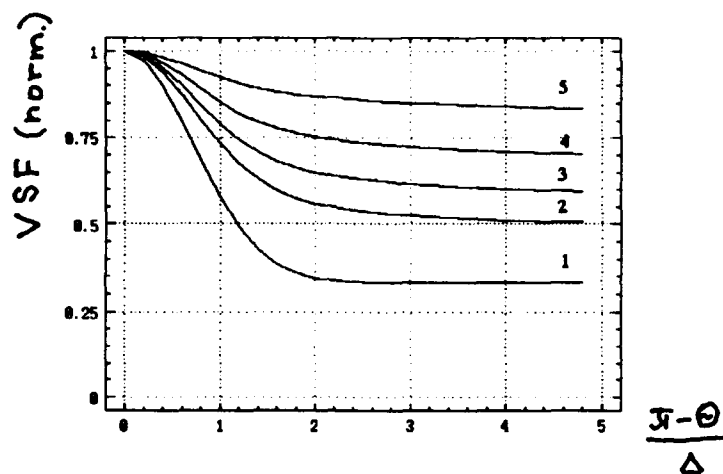


Figure 2. Model VSF from (13) with $\beta(\pi)/\beta_0 = 2$ (curve 1) and numerically calculated angular distribution of backscattered intensity (curves 2 - 5) for $\frac{\gamma^2}{\Delta^2} = 2$ and different values of $b(1 - \alpha)/c$: (2) - 0.6; (3) - 0.7; (4) - 0.8; (5) - 0.9.

Note that the size of receiver entrance pupil was supposed here to be "infinite"; for finite values of the parameter some additional signal descent with θ is observed.

There are some experimental evidence³² for the fact of strong stratification of the volume backscatter coefficient: extremely high values of $\beta(\pi)$ are found to be concentrated in a rather thin layer (several meters thick), and it's depth varies diurnally.

The theory of lidar signal formation described in sec.2 uses the supposition of a sharp peak existence in the angular distribution of VSF around 180° . The proposed interpretation connects the enhanced signal values with the presence of distinct thin layers of sea water characterized by contrast high values of the volume backscatter coefficient, $\beta(\pi)$, practically independent of the value of total backscatter coefficient b_0 . Several possible mechanisms to be responsible for the effect of "enhanced backscattering" are discussed in the following Sections.

4. ENHANCED BACKSCATTERING: HYDROSOLE PARTICLES

We now consider the two backward scattering characteristics, $\beta(\pi)$ and $\tilde{\beta}(\pi)$, for monodispersive hydrosol ensembles.

Two parameters may be considered for separate particle - the backscatter efficiency, e_π ,

$$e_\pi = 4\pi \frac{\sigma_\pi(\pi)}{\sigma_g}$$

($\sigma_\pi(\theta)$ is the differential scattering cross-section and $\sigma_g = \pi a^2$ is the geometrical cross-section of the particle with radius a), and the mean efficiency of scattering into back hemisphere, \tilde{e} ,

$$\tilde{e} = \frac{2}{\sigma_g} \int_0^\pi \sigma_\pi \sin\theta d\theta.$$

It is clear that for a given concentration of suspended particles in water, the following proportionalities hold:

$$\beta(\pi) = e_{\pi}; \quad \tilde{\beta}(\pi) = \bar{e}.$$

Figure 3, *a* and *b*, show the numerically calculated particle size effect on the parameters e_{π} and \bar{e} for optically soft spherical particles (relative refractive index 1.05).

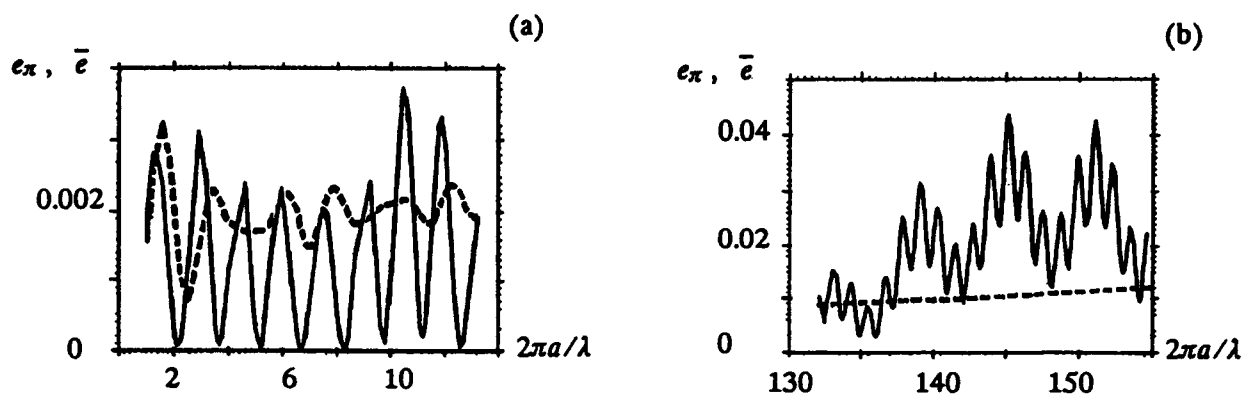


Figure 3. Backscatter efficiencies e_{π} (solid curves) and \bar{e} (dashed curves) against the diffraction parameter $2\pi a/\lambda$ of spherical particle with radius a .

It is seen that for small particles with radii close to the wavelength of light, λ , the inequality $e_{\pi} < \bar{e}$ is typical, while for large particles (tens of λ and more) the most probable is the inverse inequality, $e_{\pi} > \bar{e}$.

Even more prominent examples of angular anisotropy of backscattering ($e_{\pi} \gg \bar{e}$) are demonstrated by two-layered particles. Figure 4 shows the form of scattering phase function in the vicinity of angle $\theta = \pi$ for spherical particle with optically soft core ($n_{core} = 1$) of radius equal to $24 \mu\text{m}$ and coat thickness of $1 \mu\text{m}$ ($n_{coat} = 1.52$); the computations³³ were performed with the help of modified algorithm BHCOAT³⁴ for $\lambda = 514 \text{ nm}$.

One more possible mechanism that explains the narrow peak formation in the angular intensity distribution around 180° of light scattered by sparse hydrosol, relates to the well known effect of coherent enhanced backscattering³⁵⁻³⁷. While it is not probable to observe the classic variant of the effect due to multiple scattering by ensemble of suspended particles in sea water, the backscatter enhancement may be caused by coherent multiple scattering of light inside separate sufficiently large particles with strong enough irregular optical inhomogeneities of internal structure. It is just typical for some biological objects in sea water, like alga cells (coccolithophorids, diatoms, etc.)^{38,39}. It must be noted that the biological particles usually concentrates at distinct horizons⁴⁰, in conformity with the considered lidar data.

5. ENHANCED BACKSCATTERING: REFRACTIVE TURBULENCE

The problem of light scattering by a volume of random medium with weak refractive index inhomogeneities was discussed in well-known monographs and manuals (see, e.g.⁴¹⁻⁴³). According to the classical formula given in the papers, the scattered intensity is proportional to the effective scattering volume, V , and is caused by incoherent summation of contributions from separate elements of the medium. For radiation wavelength λ the "incoherent scattering" cross-section for a given scattering angle, τ , is determined by singled out harmonic component of spatial spectrum $\Phi_{\epsilon}(\mathbf{x})$ of dielectric permittivity fluctuations with the period

$$k(\theta) = \frac{2\pi}{\mathbf{x}(\theta)} = \frac{\lambda}{2 \sin^2 \theta/2} = \frac{\pi}{k \sin^2 \theta/2} \quad (14)$$

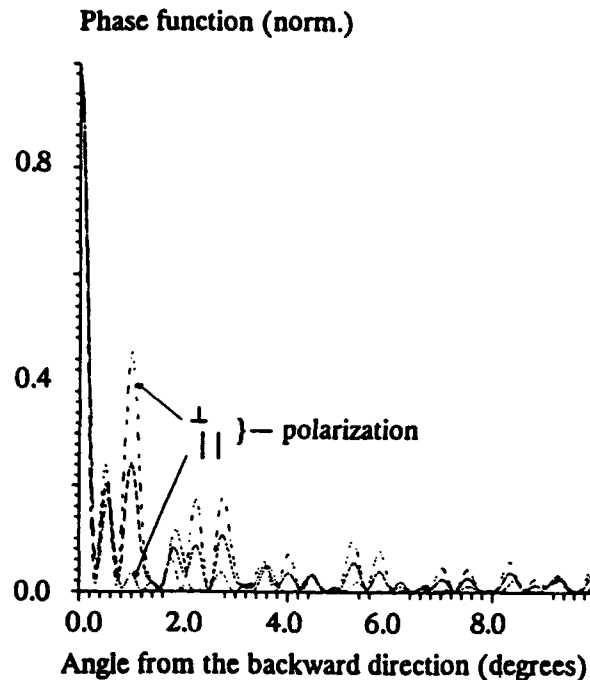


Figure 4. Numerically calculated scattering phase function for two-layered spherical particle.

where $k = 2\pi/\lambda$ is the incident radiation wave number. The result corresponds to the Bragg condition for diffraction of waves on spatial structures.

The spectrum $\Phi_s(\kappa)$ decreases rapidly in the dissipation interval, where l_0 is the internal scale of turbulent fluctuations⁴⁴. So for backward direction, that is for $\theta \approx \pi$, the spectral density at the spatial frequency $\kappa(\theta) = 2\pi/\lambda(\theta)$ becomes negligibly small for wavelength $\lambda < 2l_0$. Since the internal scale for sea-water turbulence is measured by millimeters⁴⁴, the incoherent backscattering of visible light is practically absent.

Theoretical analysis carried out by one of the authors⁴⁵, reveals an additional component of light scattering cross-section by a layer of random medium. The corresponding angular distribution of scattered radiation is concentrated in a narrow solid angle around backward direction. The effect is shown to be caused by coherent summation of light fields scattered by elementary layers, and may be regarded as an analogy to the phenomenon of weak photon localization in 1-D structures⁴⁶.

Let h be the thickness of the turbulent medium layer, and S be the effective area of illuminated plane boundary of the layer. We consider the case when incident light beam direction is perpendicular to its boundary, and scattering angles, θ , are in the vicinity of backward direction, that is

$$|\pi - \theta| < 1. \quad (15)$$

According to⁴⁵, the total differential cross-section, $\sigma(\theta)$, may be written as the sum,

$$\sigma(\theta) = \sigma_c(\theta) + \sigma_i(\theta). \quad (16)$$

The first term in (16) corresponds to the "coherent backscattering":

$$\sigma_c(\theta) = \frac{S k^2}{8} \int_{-\infty}^{\infty} \Phi_\varepsilon(\sqrt{\xi^2 + k^2(\pi - \theta)^2}) d\xi, \quad (17)$$

and does not depend on h (it is assumed that $h \gg l_0$). The second term in (16) is given by the formula

$$\sigma_i(\theta) = \frac{\pi h S k^4}{2} \Phi_\varepsilon(x(\theta)) \quad (18)$$

where

$$x(\theta) = 2 k \sin \theta / 2 \quad (19)$$

Eq.(17) coincides with the expression for "incoherent" scattering cross-section from ⁴¹⁻⁴³. Really, $V = S h$ is the effective scattering volume of turbulent medium, and the argument, $x(\theta)$, of Φ_ε in (18) [see Eq.(19)] corresponds to the harmonic component of the spectrum with period given by Eq. (14).

It is evident that for visible light scattering in backward direction "incoherent" component σ_i is the negligible addition to σ_c .

To obtain a quantitative estimate for the effect of backscattering by refractive turbulence in the sea water on lidar signal we use the gaussian model of the spectrum

$$\Phi_\varepsilon(x) = \frac{\langle \varepsilon^2 \rangle l_0^3}{(2\pi)^{3/2}} \exp\left(-\frac{x^2 l_0^2}{2}\right),$$

where $\langle \varepsilon^2 \rangle$ is the variance of dielectric permittivity fluctuations. Let $l_0 \approx 1$ cm, and $h \approx 10$ cm (the value corresponds to the sounding pulse duration of 1 ns). Then according to (17) the equivalent value of effective volume backscattering coefficient for refractive turbulence, $\beta_r(\pi)$ is

$$\beta_r(\pi) = \frac{\sigma_i(\pi)}{S h} \approx 4 \cdot 10^9 \langle \varepsilon^2 \rangle$$

The values of $\langle \varepsilon^2 \rangle$ for refractive turbulence in the ocean are known to lie in the range from 10^{-14} to 10^{-10} ⁴⁷, and thus for $\beta_r(\pi)$ we have

$$\beta_r(\pi) \approx 4 \cdot 10^{-5} - 4 \cdot 10^{-1} \text{ (m SR)}^{-1}.$$

The maximal values of $\beta(\pi)$ registered in optical back-scatter measurements ³² [$10^{-3} \text{ (m SR)}^{-1}$] get into the middle of the range. So the quantitative estimates show the backscattering by turbulent layers in water column produce noticeable contributions to signal registered in lidar experiments, and thus the effect under consideration has to be taken into account when interpretation of laser remote sounding data is carried out. It seems that the coherent backscattering by intensive refractive turbulence may cause the anomalously high lidar signals from separate horizons near the jump in temperature and/or salinity profiles.

6. CONCLUSIONS

The developed theory of backscattered light signal kinetics under the pulsed illumination of sea water column takes into account the angular anisotropy of volume scattering function in the back hemisphere. On the base of the theory, an interpretation is proposed for anomalously high levels of lidar signals from separate sea water layers registered in airborne sounding experiments. The explanation connects the enhanced echo-signals with the presence of distinct thin layers of sea water characterized by contrast high values of the volume backscatter coefficient. The interpretation is shown to be consistent with the measurements of VSF in the vicinity of 180° and revealed fine structure of vertical profiles of the backscattering coefficient.

Two possible mechanisms to be responsible for the effect of "enhanced backscattering" are discussed; first of them presuppose the presence of high concentration of large biological particles at corresponding horizons. An alternative explanation is based on presented theoretical results concerning backscattering of light by refractive turbulence.

The quantitative estimate shows that the coherent backscattering by intensive turbulence in separate layers near the jump in temperature and/or salinity profiles may be the cause for anomalously high lidar signals from corresponding horizons.

7. ACKNOWLEDGEMENTS

The authors would like to thank Dr. Alexander S. Tibilov and Dr. George B. Sochilin of State Optical Institute for useful discussions and encouragement. We are grateful to the London Office of Naval Research and SPIE for financial assistance to support our travel to "Ocean Optics XII" Conference.

8. REFERENCES

1. Haimbach S.P., Mesick H.C., Byrnes H.J., and Hickman G.D., "Optical Bathymetry for the U.S. NAVY: a Field Measurement Program," *Proc. SPIE Ocean Optics IX*, v. 925, 214-221, 1988.
2. Abroskin A.G., Bunkin A.F., Vlasov D.V., Gorbunov A.L., and Mirkamilov D.M., "Natural experiments on laser sounding with "Chaika" system". In: *Remote Sensing of the Ocean*, Nauka, Moscow, 23-38, 1986 (in Russian).
3. Banic J., Sizgoric S., and O'Neill R., "Scanning Lidar Bathymeter for Water Depth Measurement," *Proc. SPIE*, v. 663, 187-195, 1986.
4. Lillycrop J. and Banic J.R., "Advancements in the U.S. Army Corps of Engineers Hydrographic Survey Capabilities: The SHOALS System", *Marine Geodesy*, v.15, 177-183, 1992.
5. Penny M.F., Abbot R.H., Phillips D.M., et al., "Airborne Laser Hydrography in Australia," *Appl. Opt.*, v. 25, No.13, 2046-2058, 1986.
6. Penny M.F., Billard B., and Abbot R.H., "LADS - the Australian Laser Airborne Depth Sounder," *Int.J.Remote Sensing*, v.10, No.9, 1463-1479, 1989.
7. Steinvall O., Klevebrant H., Lexander J., and Widen A., "Laser Depth Sounding in the Baltic Sea," *Appl. Opt.*, v. 20, No.19, 3284-3286, 1981.
8. Liu Zhi-Shen, "Estimate of Maximum Penetration Depth of Lidar In Coastal Water of the China Sea," *Proc. SPIE Ocean Optics X*, v.1302, 655-661, 1990.
9. Feigels V.J., "Lidars for Oceanological Research : Criteria for Comparison, Main Limitations, Perspectives", *Proc. SPIE Ocean Optics XI*, v.1750, 473-484, 1992.
10. Feigels V.J. and Kopilevich Yu.I., "Russian Airborne LIDARs for Oceanography", Proceedings from Geophysical Technology Transfer Initiative Symposium & Workshop, "Russian Airborne Geophysics & Remote Sensing", September 13 -17, Golden, Colorado, 1992, *Proc. SPIE*, v.2111, 127-141, 1993.

11. Svetlykh A.A. and Feigels V.I., "A Gain in LIDAR Performance Provided by Increase of Pulse Repetition Rate and Narrowing Optical Filter Band", Proceedings from Geophysical Technology Transfer Initiative Symposium & Workshop, "Russian Airborne Geophysics & Remote Sensing", September 13 -17, Golden, Colorado, 1992, *Proc.SPIE*, v.2111, 75-94, 1993.
12. Billard B., Abbot R.H., and Penny M.F., "Airborne Estimation of Sea Turbidity Parameters from the WRELADS Laser Airborne Depth Sounder", *Appl. Opt.*, v.25, No.13, 2080-2088, 1986.
13. Phillips D.M., Abbot R.H., and Penny M.F., "Remote Sensing of Sea Water Turbidity with an Airborne Laser System," J.Phys.D: *Appl.Phys.* v.17, 1749-1758, 1984. Printed in Great Britain.
14. Phillips D.M. and Koerber B.W., "A Theoretical Study of an Airborne Laser Technique for Determining Sea Water Turbidity," *Aust. J. Phys.*, v.37, No 1, 75-90, 1984.
15. Billard B., "Remote Sensing of Scattering Coefficient for Airborne Laser Hydrography," *Appl. Opt.*, v.25, No. 13, 2099-2108, 1986.
16. Gordon H.R., "Interpretation of Airborne Oceanic Lidar: Effects of Multiple Scattering," *Appl. Opt.*, v.21, No. 16, 2996-3001, 1982.
17. Hoge F.E., Wright C.W., Krabill W.B., Buntzen R.R., Gilbert G.D., Swift R.N., Yungel J.K., and Berry R.E., "Airborne Lidar Detection of Subsurface oceanic scattering layers", *Appl. Opt.*, v.27, No. 19, 3969-3977, 1988.
18. Bystrov V.V., Svetlykh A.A., and Sochilin G.B., "Helicopter-mounted Laser Bathymeter", In: Proceedings of Workshop "Ecological Problems of European North", September 3-8, 1990, Arkhangelsk, 239-240, 1991 (in Russian).
19. Zenchenko S.A., Malevich I.A., Pranovich V.I., Svetlykh A.A., Svintilov M.V., Sochilin G.B., and Utenkov B.I., "Amplitude- time Structure of the Full Shape of Backscattered Signal from Combined Trace "Atmosphere - Hydrosphere" for Laser Excitation", *Kvantovaya Elektronika*, v.14, No.11, 2381-2384, 1987.
20. Phillips D.M. and Scholz M.L., "Measured Distribution of Water Turbidity in Gulf St. Vincent", *Aust. J. Mar. Freshw. Res.*, v.33, No. 5, 723-737, 1982.
21. Petzold T.J., *Volume Scattering Functions for Selected Ocean Waters*. S10 Ref. 72-28, Scripps Institution of Oceanography, Visibility Laboratory, San Diego, Calif., 1972.
22. Kopilevich Yu.I, Svetlykh A.A., and Feigels V.I., "On Interpretation of Some Anomalies in the Shape of Lidar Signal from Upper Sea-Water Layers", *Proc. SPIE*, v.2112, 112-123, 1993.
23. Kopilevich Yu.I. and Feigels V.J. "Characteristics of Light Backscattering by Sea Water and Lidar Sounding of Water Column", *Proc. SPIE*, v.2048, 212-228, 1993.
24. L.S.Dolin and V.A.Savel'ev, "Characteristics of Back Scattering Signal at Pulse Radiation of Turbid Medium by a Narrow Directional Light Beam," *Izv. AN SSSR. Fizika atmosfery i okeana (Izvestiya, Atmospheric and Oceanic Physics)*, v.7, No.5, 505-510, 1971.
25. Ishimaru A., *Wave Propagation and Scattering in Random Media*, Vol.1, Academic Press, New York - San Francisco - London, 1978.
26. Bravo-Zhivotovsky D.M., Dolin L.S., Louchinin A.G., and Savel'ev V.A., "On the Structure of a Narrow Light Beam in the Sea Water," *Izv. AN SSSR. Fizika atmosfery i okeana (Izvestiya, Atmospheric and Oceanic Physics)*, v.5, No.2, 160-167, 1969.

27. Case K.M. and Zweifel P.F., *Linear Transport Theory*, Addison-Wesley Publ. Co., Reading, Ms - Palo Alto - London - Don Mills, Ont., 1967.
28. Dolin L.S. and Levin I.M., *Theory of Underwater Vision (Reference book)*, Gidrometeoizdat, Leningrad, 1991 (in Russian).
29. Feigels V.I. and Kopilevich Yu.I., "Remote Sensing of Subsurface Layers of Turbid Sea Water with the Help of Optical Lidar System", *Proc. SPIE*, v.2048, 342-353, 1993.
30. Maffione R.A. and Honey R.C., "Instrument for Measuring the Volume Scattering Function in the Backward Direction", *Proc. SPIE Ocean Optics XI*, v.1750, 15-26, 1992.
31. Smart J.H., "Empirical Relationship between Optical Properties in the Ocean", *Proc. SPIE Ocean Optics XI*, v.1750, 276-298, 1992.
32. Maffione R.A. (private communication).
33. Bogdanov V.L., Kopilevich Yu.I., Lukomskij G.V., and Sochilin G.B., "Backscatter Anisotropy and the Shape of Retroreflected Lidar Pulse from Sea Water", Proceedings from Geophysical Technology Transfer Initiative Symposium & Workshop, "Russian Airborne Geophysics & Remote Sensing", September 13 -17, Golden, Colorado, 1992, *Proc. SPIE*, v.2111, 95-126, 1993.
34. Bohren C.F. and Huftman D.R., *Absorption and Scattering of Light by Small Particles*, Wiley, New York, 1983.
35. Van Albada M.P. and Lagendijk A., " Observation of Weak Localization of Light in a Random Media", *Phys. Rev. Lett.* v.55, No 24, 2692-2695, 1985.
36. Wolf P.E. and Maret G., "Weak Localization and Coherent Backscattering of Photons in Disordered Media", *Phys. Rev. Lett.*, v.55, No 24, 2696-2699, 1985.
37. Kuga Y. and Ishimaru A., "Retroreflectance from a Dense Distribution of Spherical Particles", *J. Opt. Soc. Am. A1*, 2100-2105, 1984.
38. Meyer R.A., "Light Scattering from Biological Cells: Dependence of Backscatter Radiation on Membrane Thickness and Refractive Index", *Appl. Opt.*, v.18, 585-588, 1979.
39. Aas E., "Influence of Shape and Structure on Light Scattering by Marine Particles", *Univ. Oslo, Inst. Rep. Series*, 53, 112 pp., 1984.
40. Kopelevich O.V. and Sergeeva O.M., "Studies of the Vertical Stratification of Phytoplankton in the Ocean with the Aid of the Small-Angle Light Scattering Meter", *Oceanology*, v. 18, No. 6, 1070 -1076, 1978.
41. Tatarski V.I., *Wave Propagation in a Turbulent Atmosphere*, Dover, New-York, 1961.
42. Rytov S.M., Kravtsov Yu.A., and Tatarski V.I., *Introduction to Statistical Radiophysics. Part II. Random Fields*, Nauka, Moscow, 1967.
43. Ishimaru A., *Wave Propagation and Scattering in Random Media*, Vol.2, Academic Press, New York - San Francisco - London, 1978.
44. Monin A.S. and Yaglom A.M., *Statistical Hydrodynamics. Part I, Part II*, Nauka, Moscow, 1965, 1967 (in Russian).
45. Kopilevich Yu.I. "Coherent Backscattering of Light by Turbulent Atmosphere", *Opt. Spectrosc.*, 1994 (in publ.)

46. Yoo K.M. and Alfano R.R. "Photon Localization in a Disordered Multilayered System", *Phys. Rev. B*, v.39, No.9, 5806-5809, 1989.

47. K.N.Fedorov, *Fine Thermohalin Structure of the Ocean*, Nauka, Moscow, 1978 (in Russian).

Studies of optical ringing in sea water

Gary D. Gilbert and Mark H. North

Code 754

Naval Research and Development Division
San Diego, California 92107

ABSTRACT

A Monte Carlo model is used to examine the effect of water turbidity on the temporal storage of photons. Multiple scattering can store light in increasing scattering orders. It is hypothesized that this light will be present in a LIDAR gate when signal photons return from a distant target and will generally exceed the backscatter predicted by single scatter models. A photon's mean survival time in a turbid medium is the product of the medium's absorption coefficient at the photon's wavelength times the speed of light in the medium. For very clear ocean water ($a=0.023 \text{ m}^{-1}$ @ 480 nm) this is about 190 nanoseconds, the time that it would take a laser pulse to travel to and return from a target 20 meters distant. The model considers an unbounded body of water illuminated by light from a pulsed laser beam. An irradiance receiver collocated with the laser transmitter is the detector. Future studies will use radiance detectors of varying field subtenses. Storage is studied as the absorption and scattering constituents of the water are incrementally varied in multiples of those found in clearest sea water. Single scatter albedos ranged from about 0.2 to 0.85 to span naturally occurring conditions. Results for this geometry show multiply scattered light surpassing singly scattered light returns for paths of the order of a volume attenuation length or less.

1. INTRODUCTION AND BACKGROUND

Laser and LIDAR (Light Detection And Ranging) system technology has advanced such that a number of systems are being used in the underwater environment. For the first time large data bases of LIDAR performance are available. When this data is compared to modeling predictions of performance it is often the case that modeled Signal to Noise Ratios (SNR) in the LIDAR receiver's range bin (or gate for imaging systems) are greater than the actual measured SNRs. This study investigates the hypothesis that a possible cause of this measured versus modeled SNR excess is the relatively long time that it takes scattered light in water to be absorbed. This phenomenon is called Optical Ringing. It is analogous to echoing sound reverberation in SONAR. It is not the same phenomenon as the "laser pulse tail" which is often cited as a possible cause for modeling versus measured differences.

1.1 Optical ringing

Optical ringing in a scattering/absorbing medium is quite simply related to the mean time that it takes a photon to be absorbed. Preisendorfer¹ discussed the temporal behavior of light fields. He made an analogy between the transient photon storage in a turbid medium and the transient response of electronic charge, q , in a simple series circuit of a battery of voltage, V , a capacitor of capacitance, C , and a resistor of resistance, R . The series circuit has a time constant given by RC for the capacitor charge or discharge. If the battery is switched into the circuit for an instant of time, the voltage appearing across the resistor will be spread in time and be proportional to $\exp(-t/RC)$.

A turbid medium "stores" light in the scattered light field analogous to the capacitor storing charge. The "stored" light bounces around until dissipated by absorption in the medium. Absorption is thus analogous to the circuit's resistance. The greater the ratio of scattering to absorption the greater the fraction of light stored in increasingly higher scattering orders at each successive scattering event. A convenient measure of the ratio of scattering to absorption is given by the single scattering albedo of a medium, $\omega_0 = b/(a + b)$ where a is the already mentioned volume absorption coefficient and b is the volume scattering coefficient both in units of m^{-1} . Preisendorfer showed that for a pulse of finite duration the ratio of energy in the n th scattering order to the original pulse energy varied as the n th power of the single scatter albedo, ω_0^n . A large single scatter albedo means a larger stored light field.

A photon's mean survival time in a turbid medium, T , analogous to the circuit's RC time constant is given by the quotient of the medium's absorption coefficient, a , at the photon's wavelength, λ , times the speed of light, c (m/sec), in the medium. Hence $T = (ac)^{-1}$ with units of seconds. For very clear ocean water ($a=0.023 \text{ m}^{-1}$ @ 480 nm) T is about 190 nanoseconds.

The implication is that a photon scattered near the LIDAR as a pulse transmits outward has some probability of surviving and reaching the receiver at the same time that it would take an unattenuated photon to travel to and return from a 20 meter distant target. An important question is ... what is this probability? But first, what relevance is it to LIDAR modeling?

1.2 Optical ringing's relevance to LIDAR SNR

The SNR for a LIDAR range (or alternatively, time) bin or gate may be defined as the ratio of the energy (or photon number) in the bin returned from the target to the shot noise of the energy from the water backscatter and ambient background appearing in the bin. The SNR for a range bin in terms of number of photons is given as $SNR = (n_s)^2 / \sigma_b^2$. Here n_s is the number of signal photons and σ_b^2 is the noise variance due to non-signal background light often dominated by water backscatter. (Noise-in-signal, dark current noise, and other noise sources are neglected for discussion purposes.) For range gates far from the sea surface, Poisson statistics apply to the background term. Thus the noise variance of the background equals the background mean, i.e. $\sigma_b^2 = n_b$ where n_b is the mean number of photons due to background returned in the bin. The SNR becomes $SNR = (n_s)^2 / n_b$. The importance of background photons is evident in this representation. For every 10 fold increase in mean background photons SNR decreases by 10 dB. This is roughly equal to a decrease in LIDAR performance of one attenuation length in range. Thus uncertainty in the knowledge of background photon quantities translates directly into uncertainty in LIDAR performance predictions.

In most analytic models of the LIDAR system the number of photons n_b from water backscatter is proportional to $\beta(\pi) c \delta t / 2n$ where $\beta(\pi)$ is the scattering phase function at π radians, c is the speed of light, δt is the width of the time bin in seconds, and n is the refractive index of seawater. These analytic models assume that the only light returned to this bin from the initial laser pulse has been singly scattered from the water at the bin's range. No account is taken of the possibility that multiple scattered light might survive with possible consequences to SNR.

2. APPROACH

Our first thought in designing a program to investigate Optical Ringing was to use a combination of modeling calculations and laboratory measurements in a one meter square wide by 8 meter long tank. This idea was soon discarded. A photon would require about 70 nanoseconds to make a round trip traverse of the 8 meter long tank. In the radially unbounded sea scattered photons returning in 70 nanoseconds would necessarily come from a hemispherical volume of 8 meters radius centered on the LIDAR source/receiver aperture. This required geometry could not be obtained in our narrow laboratory tank and our budget was not sufficient to mount an at-sea experiment. A modeling approach was dictated. A favorable feature of the modeling approach was that the scattering order of a photon reaching the receiver could be determined. Real photodetectors can't discriminate scattering order and thus an experimentalist would be forced to interpret measurements with reference to some type of modeling predictions anyway.

2.1 The Model

The modeling approach is a weighted return ² Monte Carlo method. Figure 1 is a sketch of the geometry. A perfectly collimated (zero divergence) pulsed source and an irradiance collector are located at the x,y,z origin. The source pulses are photon packages (temporal δ -functions) directed along the z axis. (The number of photons in a package corresponds to the a user input laser pulse energy given in joules.) For this initial study an irradiance collector collocated with the source accounted for the returned photon weights. (In future studies this collector will be replaced with a radiance collector with a finite field of view like a LIDAR receiver.)

With reference to the figure, a photon package with a weight equal to 1 is transmitted into the water. The water has an absorption coefficient of a , a scattering coefficient of b , and a scattering phase function $\beta(\theta)$ obtained from McLean³ as an analytical fit to Petzold's measurement⁴ of $\beta(\theta)$. a and b establish an attenuation length for the water of $(a + b)^{-1}$ meters. A random number generator selects a number from 0 to 1. If the number is less than the fraction $a/(a+b)$, the photon weight is tallied as absorbed and leaves the calculation. A new photon package is started. If the random number is greater than $a/(a+b)$ then a weighted scatter return is sent back to the receiver.

Weights are calculated as follows. From the point in space where the scattering event occurs the angle from the photon package's direction before scattering back to the irradiance receiver, θ_B , is computed from geometry. (For the on-axis first order scattering this angle is always the 180 degrees found in the analytic LIDAR models. For all higher orders the angle

ranges anywhere from 0 to 180 degrees.) The angular subtense in steradians of the irradiance collector aperture as seen from this scattering location is computed. Knowing the angle θ_B from the photon package's pre-scatter direction back to the collector and its angular subtense from the scattering point, a weighted return W_{ti} to the collector is computed as the product of the value of the scattering phase function $\beta(\theta_B)$ times the solid angle subtended by the collector. The subscript 'i' represents the i-th scattering order. This weight represents the probability that photons scattered at that point in space would have returned to the collector. Forced return means that every scattering event contributes to the calculation. No scattering events are lost.

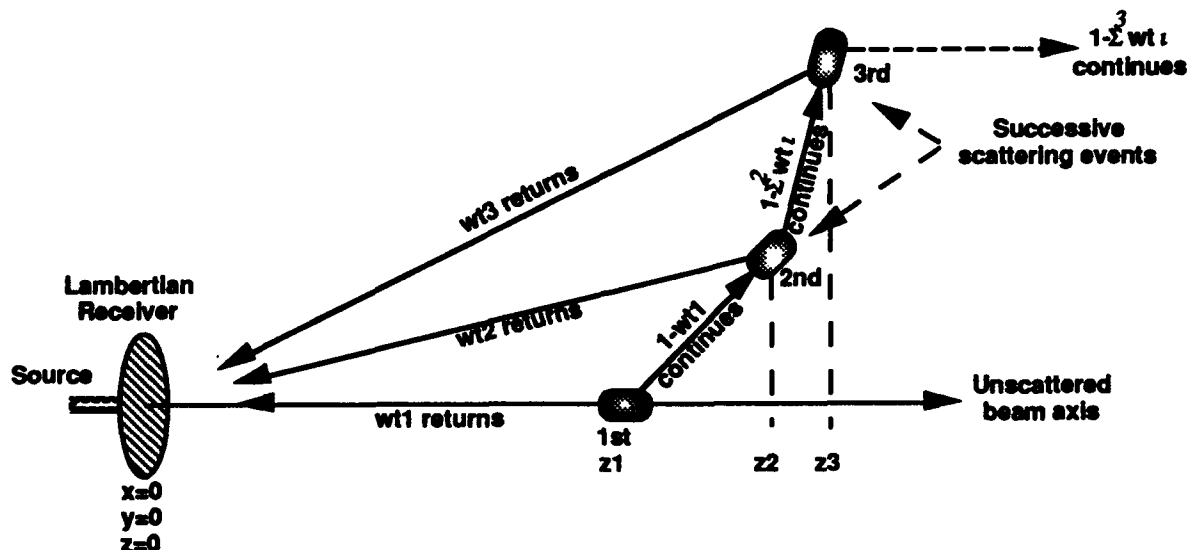


figure 1 Model geometry for weighted Monte Carlo scattering

Each scatter event weight returned to the receiver is multiplied by a factor, $\exp[-(a+b)D]$. This accounts for the attenuation of the weight when returned from the scattering event position at a distance D from the collector. A slight error of underestimation is introduced as photons scattered on the way back to the collector are assumed to be absorbed and thus leave the calculation.

The total distance traveled by the scattered photon weight is computed i.e. the travel path distance from the source to the scattering location plus the distance from the scattering location back to the detector. This travel distance is divided by the speed of light in water to obtain the time that the weight returns to the detector. The returned weight is then stored in a time bin corresponding to the return time and scattering order by adding it to the sum of previous weighted scattering events. Three storage registers are available for the first three scattering orders. A fourth register records the sum of fourth and greater order scattering events. Each register has 1001 bins of 1 nanosecond resolution to record photon arrivals from 0 to 1000 nsecs.

The continuing scattering photon package's weight is then reduced by the weight returned to the collector and sent in a new direction. The new scattering direction is obtained using the random number generator and the $\beta(\theta)$ function to select a new polar scattering angle and a uniform 2π distribution to choose a new azimuthal angle. The new direction is checked to ensure that it is not toward the detector. If it is, the random number generator selects a direction away from the detector. The reduced photon package moves in the new direction and the process is repeated. After N scatters the photon package weight is given as

$$W_{t\text{photon}} = 1 - W_{t1} - W_{t2} - \dots - W_{tN}.$$

If not absorbed during this process, the photon package continues until its weight falls below a predetermined value. A new photon package is then started from the source.

At the end of a typical run of 10 million photon packages the recorded data included the total number of absorbed photons, the total number of scattered photons, their scattering order, and their arrival times at the detector. The relative importance of higher order scattering contributions to the returned light was thus quantified.

2.2 Range of single scatter albedos

Table 1 gives the values of absorption and scattering coefficients pertaining to the results shown in this paper. The table is ordered in terms of increasing single scatter albedo, $\omega_0 = (b/(a+b))$. The absorption and scattering coefficients used for the first run, mc1, were taken from measurements made in the North Central Pacific Ocean off the Hawaiian Island of Kauai. The absorption and scattering coefficients for the other three cases were made up by taking multiples of either the mc1 absorption and/or scattering values to obtain a range of albedos. This allowed the study of light storage as media changed over a range of albedos representative of predominantly absorbing to predominantly scattering water.

TABLE 1
Range of optical properties studied

Case #	Absorption a (m^{-1})	Scattering b (m^{-1})	Albedo ω_0
mca3	0.138	0.042	0.23
mc4	0.023	0.023	0.50
mc1	0.023	0.046	0.65
mc2	0.023	0.126	0.85

3. RESULTS AND DISCUSSION

3.1 Successive temporal peaking of scattering orders

The first case, mc1, modeled the waters off Kauai, Hawaii. Figure 2 displays the results for this run as a composite plot of each scattering order. The purpose of showing this graph is to note the different time slopes for the scattering orders and to observe how each successively higher scattering order dominates the total return for a time. (Displays are not shown for the other runs but are similar.) The total return is the sum of all orders and is what would be seen by a real detector. A real detector could not discriminate the scattering order associated with each received photon.

The data has been smoothed with a ten point Hamming window lowpass filter implemented on an Excel spreadsheet. Data has not been decimated. Note that the y-axis has units of photoelectrons. This is a display option of the Monte Carlo program which scaled photons to photoelectrons received for a specific LIDAR laser and receiver characteristic.

Note the succession of scattering order contributions to the total return. Early in the record (0 to 40 nanosecs) total return is dominated by first order scatter. However as time increases the first order return decreases at a greater rate than the second order return. A time is reached where the second order return is greater than the first and second order becomes the dominant return in the total. This sequence is repeated with each successive order as time increases. Finally after about 200 nanoseconds, total scatter return is comprised almost exclusively of fourth order and greater scatter. Table 2 lists the times in nanoseconds at which each order exceeded the previous order in magnitude.

TABLE 2
Times in nanoseconds when N+1 st scattering order exceeds Nth scattering

N+1 >	N @	nanoseconds
2	1	41
3	2	106
4 and greater	3	197

The apparent upturn of first order scattering for times near 800 nanoseconds is simply an artifact of the Excel plotting routine and the filtering process which puts energy from first order scatter into late bins which in fact received no first order scatter contributions. This compresses the apparent time axis and causes the upturn. Data shown in the next section has been truncated in time such that this artifact would not be present.

Figure 3 is another representation of the mc1 data in figure 2. This figure plots first order scatter together with the sum of all greater orders as a function of incidence time on the receiver in nanoseconds. This display emphasizes the relatively early time (40 nanoseconds) at which the higher order scattering surpasses first order scatter back to the detector.

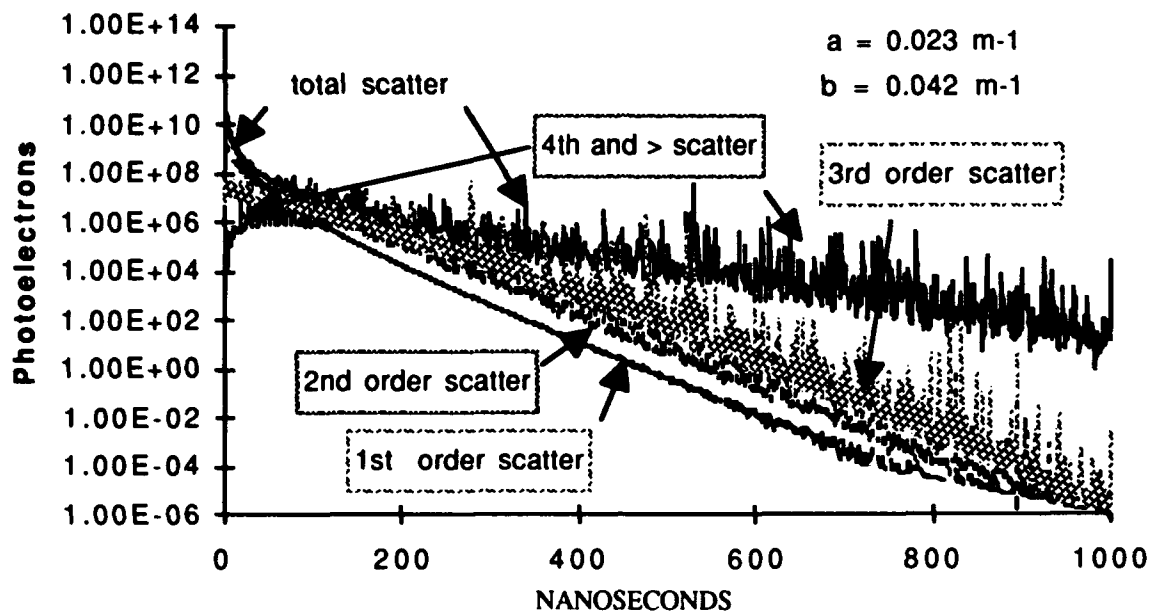


figure 2 Example of time return of all scattering orders for albedo $\omega_0 = 0.65$ (case mc1)

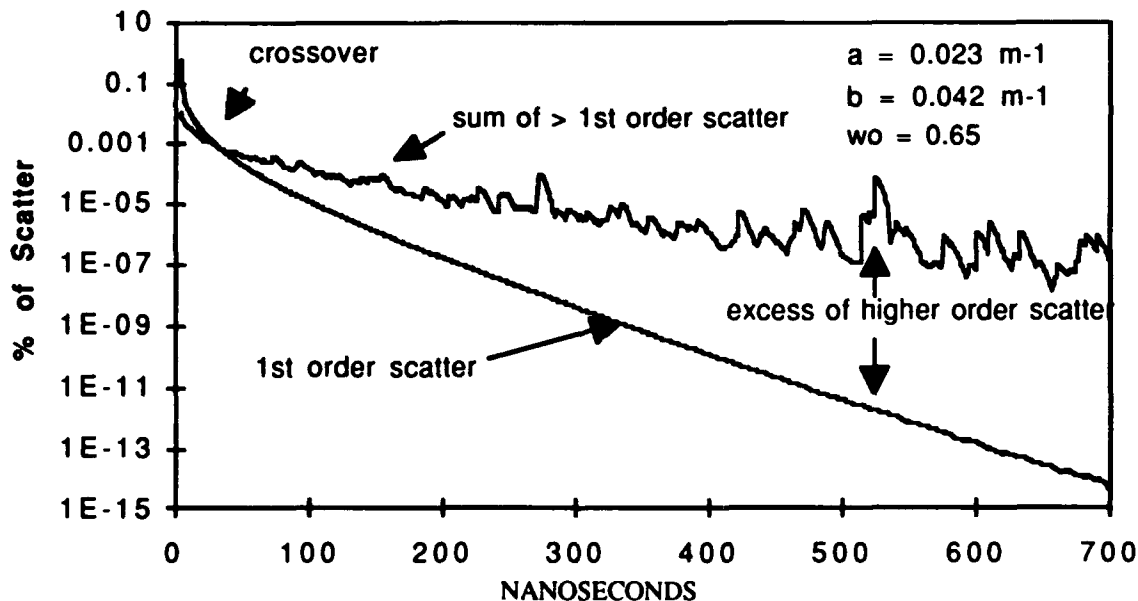


figure 3 1st order scattering versus sum of all higher scattering orders for albedo $\omega_0 = 0.65$ (case mc1)
note crossover point at 40 nanoseconds

3.2 Higher order scattering optical ringing with varying albedo

Figures 4 to 7 are the total return and the first order scattering return for all of the cases covering the range of increasing albedos shown in Table 1. The total return is the sum of all scattering orders. Note that the units of the x-axis for each figure has been transformed from nanoseconds of survival time into range to a target given in terms of volume attenuation lengths defined as $(a+b)^{-1}$. The logic for this conversion is that if a scattered photon survived and returned to the receiver in a time, t , then the distance that an on axis unscattered photon would travel to and be reflected from an on axis target in the same

time t would be ct/n . The one way range in meters would thus be $ct/2n$. This one way range divided by the attenuation length $(a+b)^{-1}$ thus represents the range in units of attenuation lengths which is a preferred form for quantifying optical system performance. Normalization to attenuation lengths allows the comparison of performance for the range of albedos studied. Table 3 will show for the four cases how this normalized measure is related to time.

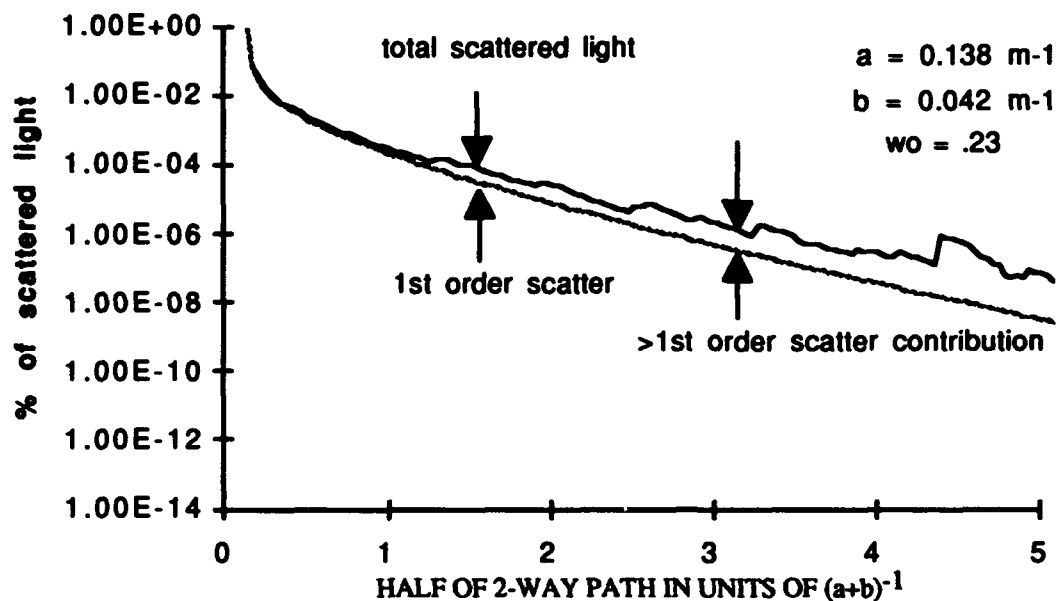


figure 4 Total and 1st order temporal scatter return for low albedo $\omega_0 = 0.23$ (case mc3a)

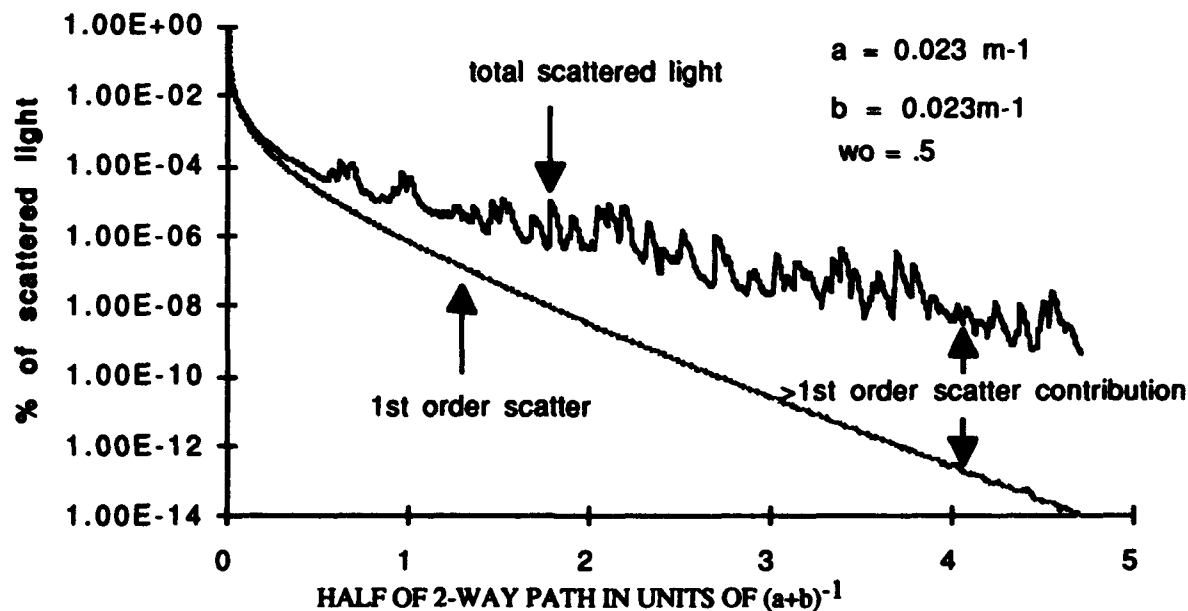


figure 5 Total and 1st order temporal scatter return for medium albedo $\omega_0 = 0.50$ (case mc4)

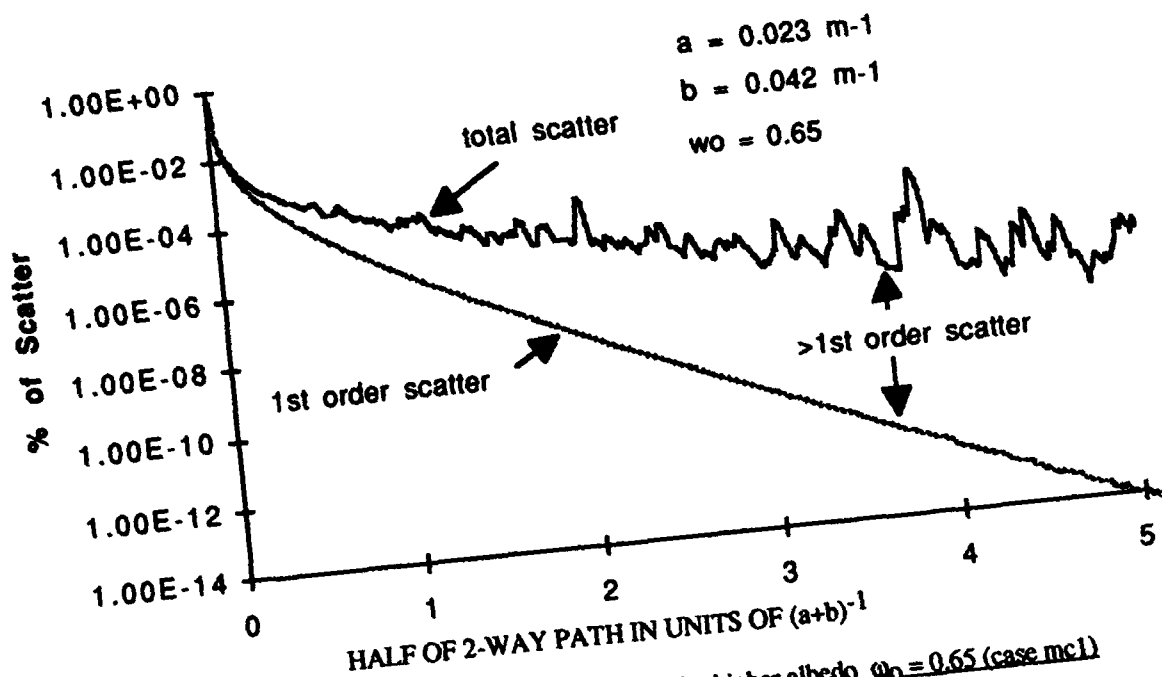


figure 6 Total and 1st order temporal scatter return for higher albedo $w_0 = 0.65$ (case mc1)

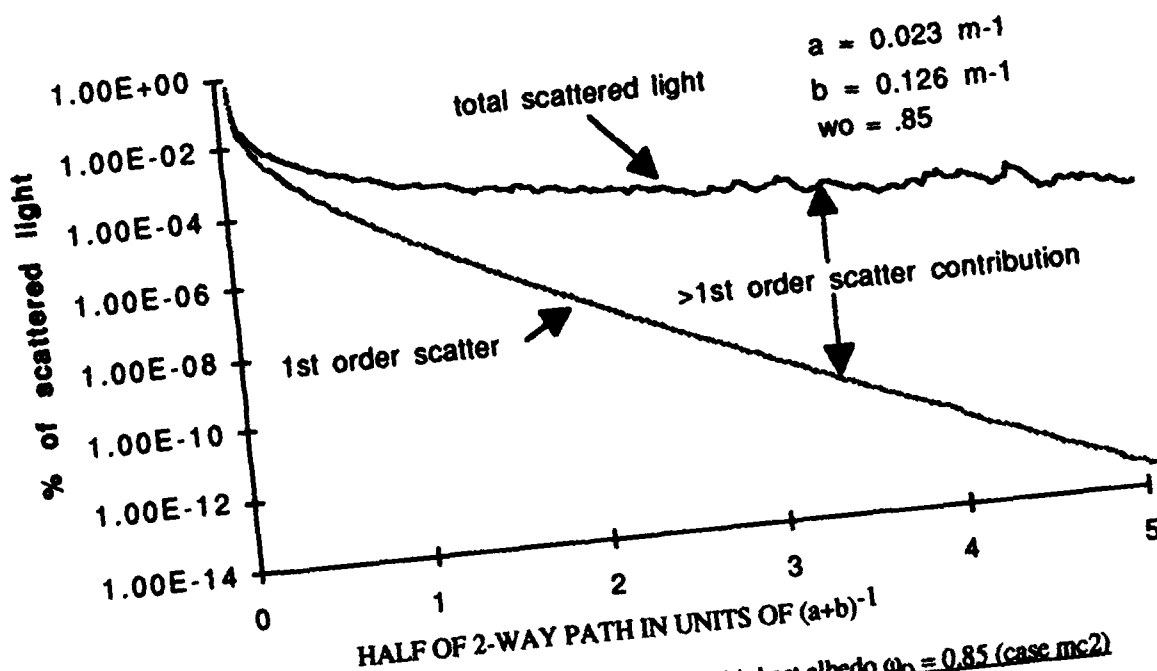


figure 7 Total and 1st order temporal scatter return for highest albedo $w_0 = 0.85$ (case mc2)

Two general trends can be seen with increasing albedo in the figures. The first is that in water of increasing albedo the range to a target in units of attenuation length at which higher order scatter exceeds first order scatter decreases. This is shown in Table 3 both in range units of $(a+b)^{-1}$ which would be relevant for system performance consideration measured in terms of $(a+b)^{-1}$ and in terms of absolute return time. Note that the return time does not vary inversely as the albedo. What

is surprising in the Table are the very short ranges (ca. 0.2 to 1.3 attenuation lengths) at which multiple scatter becomes important.

TABLE 3
Range and times as a function of albedo where scatter from 2nd and higher orders exceed 1st order scatter

Case #	figure	albedo ω_0	range multiple scatter > 1st order scatter in $(a+b)^{-1}$	time multiple scatter > 1st order scatter in nanosecs
mc3a	4	0.23	1.332	37
mc4	5	0.50	0.331	64
mc1	6	0.65	0.256	35
mc2	7	0.85	0.201	12

The second trend is shown in Table 4. It concerns the absolute value of the ratio of first order to total scatter at return times corresponding to a target range of 4 attenuation lengths. (This range was chosen arbitrarily to represent a typical LIDAR performance range.) The ratio decreases with increasing albedo in an extreme way. It may be seen that for the cases presented first order scatter contributions are several orders of magnitude less than total scatter at this 4 attenuation length range.

TABLE 4
Ratio of single scatter to total scatter for times corresponding to returns from 4 attenuation lengths

Case #	figure	albedo ω_0	ratio of 1st order to total scatter at $4(a+b)^{-1}$
mc3a	4	0.23	0.16
mc4	5	0.50	5.9×10^{-5}
mc1	6	0.65	1.0×10^{-6}
mc2	7	0.85	1.6×10^{-7}

4. SUMMARY AND FUTURE WORK

A Monte Carlo model has been used to examine the effect of Optical Ringing in water on the time dependent behavior of multiply scattered light returned to an irradiance collector collocated with a pulsed collimated light source. The results indicate that the multiple scattered component which is generally neglected in analytic LIDAR modeling may be of more importance than previously thought.

The next step in this study will be the replacement of the irradiance collector with a radiance detector in the Monte Carlo code. The behavior of the multiple scattered component will then be studied as the radiance detector's field of view is varied over solid angles of typical gated imaging systems and LIDARs.

5. ACKNOWLEDGMENTS

We thank Dr. Allan Gordon of NRaD for support of this work through the NRaD IR&D program for FY 1994, Mr. Jon Schoonmaker for help in figure preparation and computation, Dr. Stephen Stewart for computer facility advice, and Dr. John McLean for use of his scattering phase function representation.

6. REFERENCES

- 1 Preisendorfer, R.W., Hydrologic Optics, v. III, pp. 49-133, NOAA, Honolulu HI, 1976.
- 2 Cashwell, E.D. and C.J. Everett, The Monte Carlo Method for Random Walks, p.14, Pergamon Press, NY, 1959.
- 3 McLean, J., Personal communication, Arete, Tucson, AZ, 1994.
4. Petzold, T. J., Volume Scattering Functions for Selected Ocean Waters, SIO Ref. 72-78, Scripps Institution of Oceanography, U. California, San Diego, 1972.

Some aspects of wide beam imaging lidar performance

R. N. Keeler

Kaman Aerospace Corporation
1111 Jefferson Davis Highway, Suite 700
Arlington, Virginia 22202

and B. L. Ulich

Electro-Optics Development Center, Kaman Aerospace Corporation
3460 East Britannia Drive
Tucson, Arizona 85706

ABSTRACT

In recent years, broad area imaging lidar systems have been applied to ocean applications. These lidars have now been operated in the field since 1988. These systems possess certain intrinsic advantages over narrow angle systems, and can measure, while deployed, the very oceanographic properties on which their performance depends.

BACKGROUND

Imaging lidar systems have a number of special features not previously used in airborne ocean lidar systems. The concept itself, developed in the summer of 1987 and subsequently reduced to practice in the field^{1,2} is based on mature technology; the solid state diode pumped Nd:YAG laser³, which had been in production and in the field since 1989 and was successfully tested in October, 1993 (with a design frozen in 1991). The lidar receiver, an ICCD camera has been in the field since 1988^{4,5,6}. The scanner provides a greater area coverage and has also been tested⁷. With the scanner, a beam homogenizer⁸ was used. The use of such a configuration in this basic concept is based on the superiority of broad area lidar imaging systems over narrow area or "spot" systems using a photodetector.

BROAD AREA-NARROW AREA LIDAR COMPARISON

For a number of years, lidar research was carried out using narrow beam or "spot" systems. This was because for a given energy per pulse and for a single pulse greater depths could be attained using a narrow, collimated beam. These types of lidars were used in bathymetric application, where only intermittent soundings needed to be taken. However, when the broad area systems were first deployed, and area coverage became an issue, it soon became obvious that the performance of these systems far exceeded that of the previous narrow beam systems. This improved performance was explained^{9,10} as the result of previous workers not fully having understood the role of optical scattering in the ocean

combined with the requirement for complete area coverage. Briefly, this can be illustrated in terms of illumination of underwater targets in the ocean. Recalling the following definitions of oceanographic optical quantities, c is the extinction coefficient in units of meter^{-1} , in a formalism used among physical oceanographers¹¹. The extinction coefficient, c is equal to the sum of the total scattering coefficient, b , and the absorption coefficient, a . This is nothing more than the statement that a given photon with a given direction of motion can be either scattered or absorbed (or continue on its path); or that a narrow beam of light can be attenuated by either absorption or scattering. Thus, one can write

$$c = a + b \quad (1)$$

or as used in the physics community,

$$K_{\text{total}} = K_a + K_s \quad (2)$$

As a historical note, Equation (1) was often stated as defining the extinction coefficient, a quantity which could be apportioned into two quantities a and b ; a was defined as an absorption component, and b a scattering component. These are rather inexact definitions, as compared to the later, more exact Equation (2). The reason for the previous inexact definitions reflected problems in measuring c , and a caused by the inability to deal with small angle forward scattered light. Earlier researchers used the absorption coefficient interchangeably with the irradiance attenuation coefficient. Problems with this procedure will be discussed later in this paper. Also, the measurement of c was not well developed at this time; hence, the earlier inexactitude in defining these terms. Although measurements of a were first made in some 20 years ago, only recently has reliable hardware appeared which can measure both c and a . Because of the early interpretations of Equation (1) the physics notation of Equation (2) will be used in most of this paper.

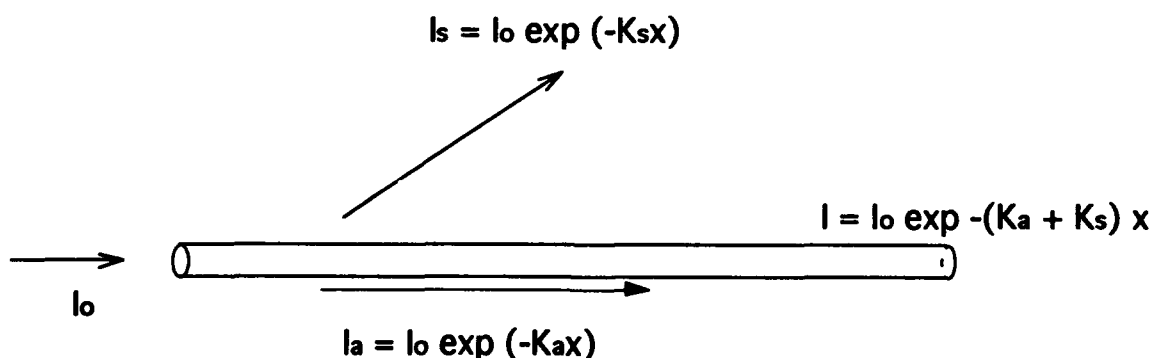


Figure 1

The coefficients K_a and K_s appear in the equations governing the propagation of light in a turbid medium. For a very narrow beam, this is shown in Fig. 1, using the physics notation:

Here, a beam with initial intensity I_0 is attenuated by both absorption and scattering. Figure 1 represents, of course, the narrow angle or spot system. The extinction coefficient is frequently measured during sea trials, and it is the quantity which appears in the equation for Secchi depth as a function of sea turbidity. In Fig. 1, The initial light intensity, I_0 , is then attenuated according to the relationship

$$I = I_0 e^{-(K_a + K_s)d} \quad (3)$$

where d is the depth below the surface of the ocean, for example. If an object is at the depth d , it will be illuminated by a light intensity I , given by (3). At the observing lidar camera, the reflective return from the object is the "signal", and so (3) can be written

$$S_n \sim e^{-2(K_a + K_s)d} \quad (4)$$

for the narrow angle or spot system.

Consider now the performance of a system using broad area illumination. In this configuration, a cylindrical element within the wide area illuminated light field is shown in Figure 2.

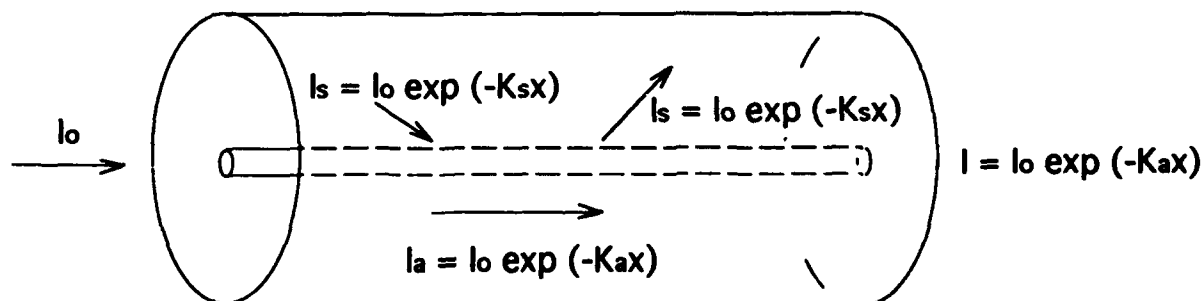


Figure 2

That part of the beam within the cylinder is attenuated as before, and a certain amount of light is scattered out of the cylindrical element. Because this cylindrical element is immersed in the interior of the broad area illuminated element, it is surrounded by elements identical to itself. Therefore, the amount of light scattered out of the element is replenished by light scattering back into the initial element from all the surrounding elements. In this case, the attenuation of light in the cylindrical element under consideration is given by $\exp(-K_a d)$, not by

the term $\exp -(K_a + K_s)d$ as in the narrow angle case. Here, the attenuation is given by $e^{-K_a d}$ on the path down to the target and by the relationship $e^{-(K_a + K_s)d}$ on the path back to the camera. Thus

$$S \sim e^{-(2K_a + K_s)d} \quad (5)$$

The terms in Equation (4) and (5), ($a = K_a$ and $b = K_s$) bear a rough relationship to each other. This situation is best summarized in Fig. 3¹², and will be used in comparing the two methods of illumination.

Returning to Equation (4) and (5) and comparing the signal return from a narrow angle system with that returning from an equivalent cylinder in a broad area illuminated light field, we obtain:

$$\frac{S_a}{S_b} = e^{-K_s d} \quad (6)$$

It should be noted that the expression irradiance attenuation coefficient of Figure 3 is often used synonymously with the term diffuse attenuation coefficient.. Fig. 3 is a plot of the irradiance attenuation coefficient, K_d vs. the total scattering coefficient, K_s . The irradiance attenuation coefficient is a measure of the attenuation of sunlight with depth, usually measured with narrow band filters. It should be noted that the irradiance attenuation coefficient, K_d of Figure 3 is more commonly referred to as the diffuse attenuation coefficient. It has been argued by Ivanov¹³ that there is a close correspondence between K_a and K_d so the two quantities will be used interchangeably. It can be seen that if a typical value from Figure 3. is used assuming

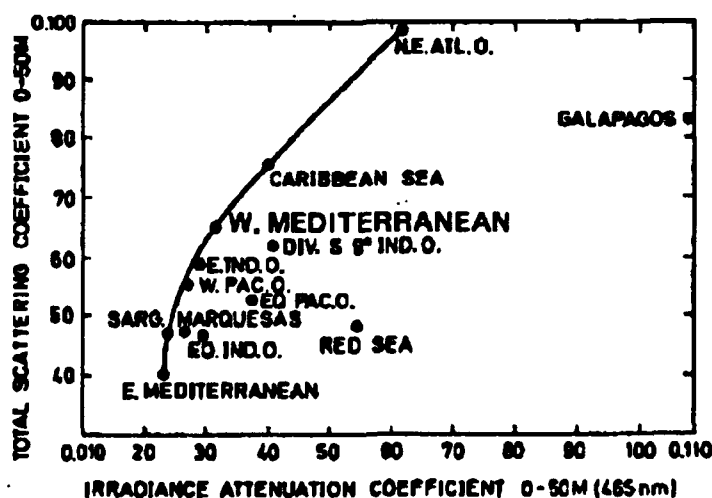


Figure 3: Total Scattering Coefficient vs. Irradiance Attenuation Coefficient, m^{-1}

that $K_a = 0.05 \text{ m}^{-1}$ (referred to by oceanographers as 20 meter water with 20 meters the e-folding length for the given K_a), K_s will be ~ 0.085 . Then, the performance of the narrow angle system will be degraded by a factor of $\exp(K_s d)$. At 20 meters depth, this represents a loss of a factor of ~ 5.5 in signal, and the loss in signal strength is exponential in depth.

Another consideration is that Figure 3 represents data for a wavelength of 465 nm, at depths from the surface down to 50 meters. These data are more relevant to littoral waters than might appear at first glance, because as will be shown later on in this paper, littoral waters can be quite clear.

This analysis is simplistic. We have ignored the effects of multiple scattering, finite receiver FOV, return signals from illuminated regions beyond the FOV, finite beam divergence, and non conservative scattering effects. And, the presence of a signal only is not sufficient for a measurement or detection to be made. In fact, noise must be taken into account. Sunlight is one source of noise. It can be minimized by use of narrow bandpass optical filters. This source of noise will be the same for both cases. The case of backscattering "noise" is a little more complicated, since it is a consequence of the downward transmitted light field. It varies by a factor of \sqrt{E} , (with E the energy per pulse) rather than E , so the exponential effects of depth on signal still dominate. Of course, when an object is observed in obscurity, this particular "noise" becomes the signal, and its presence is necessary for the observation to be made.

Other assumptions have been made, for example, the spreading of the broad area beam will be more pronounced than that of the narrow angle beam since the beam must be expanded to cover a larger area. In this example, the illuminating beams are both assumed to be originating at an infinite distance in a non-scattering, non- attenuating medium; the atmosphere.

Finally, it must be assumed that even if light scattering out of the cylindrical volume element shown in Figures 1 and 2 at angles between 90° and 180° does reenter the small cylindrical, element as in Figure 3, it will be back scattered and will never reach the underwater target. This effect is small, as this part of K_s is only about 1/20 of the total. This and many of the others effects ignored in this simple analysis mentioned previously will be accounted for in the monte-carlo calculations to be described shortly. In any case, the attenuation of light in the ocean is exponential, and dominates Equation (2). The other effects cited are second order and far less significant.

Consider a lidar system with pulse repetition rate prf , and beam area A . The geometric sweep rate (area covered per unit time), R , is given by

$$R = \text{prf} \cdot A, \quad (7)$$

where it is assumed that each pulse covers new water and does not overlap with water previously covered.

If E is the energy per pulse, then the output power (Pwr) of the laser is given by

$$Pwr = ppr \cdot E \quad (8)$$

Dividing (8) by (7) gives

$$\frac{Pwr}{R} = \frac{E}{A} \quad (9)$$

where E/A is the energy fluence per unit area.

Now consider two systems (e. g., a broad beam system and a narrow beam system) that have the same power output and the same geometric sweep rate. The equation above shows that in this case, they must also have the same energy fluence, E/A at the surface.

This means that if broad and narrow angle systems operate with the same average power and are required to map or place under total area surveillance a given area, the fluence per unit area delivered by the laser transmitter for both systems is identical.

The next part of this paper is intended to achieve a more precise estimate of the differences between the performance of the two systems. In practice, analysis of spot or narrow beam systems has shown that while their attenuation characteristics are much stronger than those predicted by $\exp(-2K_d)$, they are not well approximated by $\exp(-K_t)$. This is because the "real" system geometry falls between the idealized narrow beam, which is chosen to be an unrealistically narrow beam and the infinitely broad wide area system. Therefore, use of monte carlo techniques is called for. It will now be shown below that the fluence per unit area measured at the center of the beam below the surface will be larger for the wide beam system than for the narrow beam system regardless of depth. This should be true across the entire beam area, although these calculations have not yet been made.

Consider a point on the transmitter beam axis at some depth d. Assume that the energy fluence per unit area is uniform over the transmitter beam and that the circular cross section of the beam has radius R. Also, assume that the beam is collimated, i. e. that all photons are originally directed parallel to the beam axis. We are interested in studying the behavior of this maximum fluence as a function of beam radius and depth d.

It can be shown mathematically that the ratio of the energy fluence per unit area at depth d to the energy fluence per unit area in the beam at the surface is equal to the probability that any given transmitted photon will fall within a circle of radius R at depth d. Note that photons may fail to reach depth d by being absorbed or being permanently back scattered. The mathematical equivalence of the calculation of fluence at the origin to the problem of computing a "capture"

probability makes it a simple matter to compute the solution by monte-carlo simulation for any volume scattering function.

The volume scattering phase function used in the monte-carlo calculations is

$$\phi(\theta) = \frac{\kappa_{\pi} \theta_0}{2\pi(\theta_0^2 + \theta^2)^{3/2}}, \quad (10)$$

where $\kappa_{\pi} = 1.175$. This value is chosen so that the phase function will integrate to unity with respect to solid angle, for $0 \leq \theta \leq \pi$. The value of $\theta_0 = .06$ radians (3.4 degrees) is used in the calculations below as described by McLean and Voss¹⁵.

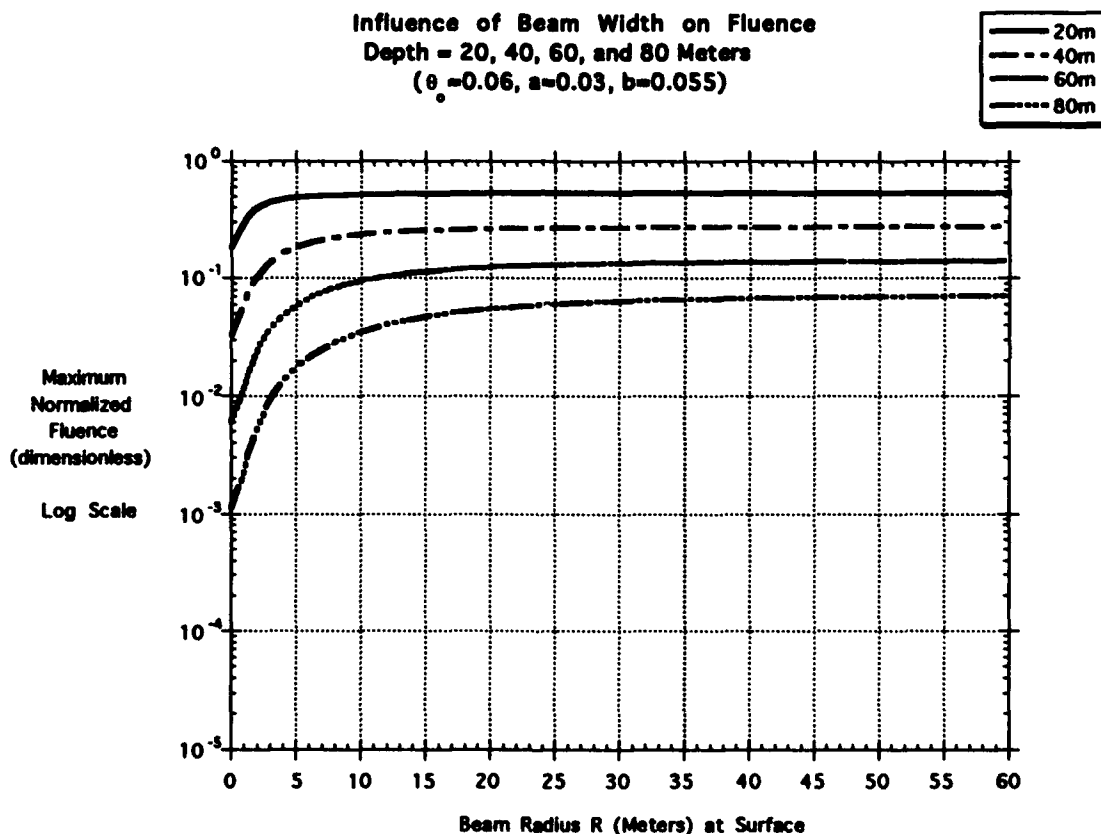


Figure 4a

Figures 4a and 4b show the effect of varying the beam radius at the surface on the irradiance at a given depth. Parameters for coastal water are chosen, with the diffuse attenuation coefficient of 0.03 m^{-1} , and the scattering coefficient 0.055 m^{-1} . This water is "33 meter water" For this water type, the extinction coefficient is equal to $0.03 + 0.055 = 0.085 \text{ m}^{-1}$. Note that the values plotted give the ratio of the energy fluence per unit area on the beam axis to the energy fluence per unit area

of the beam on the surface. Recall that surface fluence must be the same for both wide and narrow beam systems

Figure 4a shows the results. In this class of water, the effects of varying beam width are shown. At 20 meters depth, increasing beam width to values in excess of 5 meters has little further effect on the irradiance. At 80 meters, however, the beam radius at the surface must be increased to 20-25 meters before the maximum normalized irradiance levels off. There is an increase of nearly a full order of magnitude in irradiance at 80 meters when the beam radius is increased from 5-25 meters.

In Figure 4b, the irradiance is plotted on a linear scale, and the effect of varying beam angle is shown in more detail.

Lidar systems generally can function up to four or five e-folding lengths at a maximum (although the Russians claim better performance), so a 33 meter depth is the relevant curve. If a narrow angle system is searching for detail the size of one meter, then the beam diameter on entry into the ocean should be no more than three

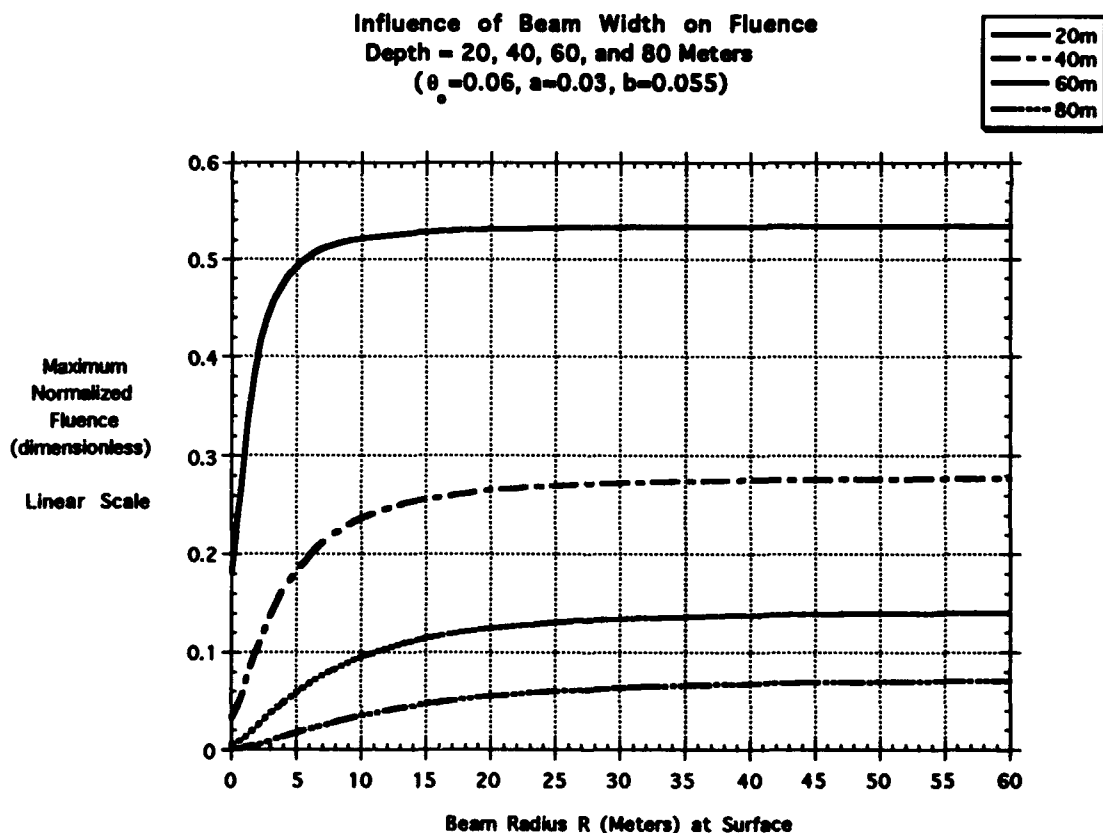


Figure 4b

meters to retain the signal from one part of the area irradiated without it being swamped by noise and other signals. (If the signal return occupies a square meter, then it is reduced by a factor of ten with respect to noise if the area illuminated is ~ 10 square meters in a system using a time resolved photo detector) Then an increase in beam diameter from 3 to 15 meters increases the irradiance by a factor of ~ 1.5 ; the effect is even more striking when 1 and 2 meter diameter beam diameters are used; factors of two to four are then involved.

There is a natural compatibility of wide area illuminating systems and imaging cameras, and small area with the time resolved photo detector approach. In the latter approach, however, the electrical signal must be picked off at the desired depth, then assembled real time into a mosaic. Gating is not necessary, since the signal is time resolved. With a imaging camera, gating is necessary, but the mosaic of pixels is already present in each frame.

There is another problem associated with platform stability and error tolerance. In the narrow beam system, illumination and imaging errors of only one or two feet could be very significant. For broad area systems, a foot or two at the edge of the area viewed is trivial and taken account of in the natural frame overlap. The overlap is easy to accommodate in the large area system; for the narrow beam system, this type of overlap is significant, and accommodating it could lead to a degradation in sweep rate. It makes little sense to speak about homogenizing the beam of a spot system; on the other hand, a wide area beam can be very effectively homogenized, and spread into a square or rectangular shape, leading to very efficient area coverage.

In conclusion, a wide area system will always outperform a narrow area system, given the requirement of total area coverage and a given average power allotment for both systems.

IMAGING LIDARS FOR OCEAN OPTICAL MEASUREMENTS

One unanticipated advantage of imaging lidar systems is their ability to make real time oceanographic measurements in operational environment. To evaluate the significance of this capability, it is necessary to understand some of the basic physics and optics of the ocean environment.

The geometry and mathematical formalism for light propagation into a flat calm ocean are well understood^{16, 17, 18, 19}. Some investigators have also pursued the effects of wave action on light propagation and image formation^{20,21,22}. But the two quantities upon which a lidar performance depends, are the absorption coefficient, K_a , and the backscattering coefficient β_r . Both these ocean optical properties appear in the basic equations governing radiation transport in the ocean. The absorption coefficient K_a , closely related to the diffuse attenuation coefficient as outlined previously, is the property which determines how deep the

light from a lidar can penetrate the ocean, and to what extent the light returning from a target is attenuated.

A plot of the variation of K_d with wavelength is shown in Figure 5. Ocean and littoral water is divided into five classes¹² with the more turbid riverine waters represented by Roman numerals. It can be seen that for the clear deep ocean waters (Class I), the optimum wavelength of ~ 470 nm, in the blue portion of the spectrum. This "Jerlov Peak" (for transmission) shifts slightly to longer wavelengths until the spectrum for Class III water is virtually flat. The transparency of the ocean at various locations is beyond the scope of this paper, but is discussed in References 4 and 11.

K_a appears in the general equation which results from the ideal geometry and can be written in terms of the photons arriving at a given pixel from a target:

$$S = \frac{\eta \lambda \Psi T_{out} T_{in} T^2 \Gamma E_o A_{pixel} e^{-2K_a d}}{hc(2n f)^2 A_{beam}(h, d)} \quad (11)$$

and from the ocean

$$N = \frac{\eta \lambda \beta_{\pi} \Psi \pi T_{out} T_{in} T^2 E_o A_{pixel}}{(2n f)^2} \int_{d_1}^{d_2} \frac{e^{-2K_a d}}{A_{beam}(hd)} dd \quad (12)$$

(11) and (12) are written as being expressions of signal and noise, since it is customary to think of ocean backscattering as noise when trying to image a reflective target within a given camera gate. In the obscuration mode, however, this "noise" becomes the signal, as the target signature is an absence of photons arriving from the area subtended by the target. Thus β_{π} remains important, as it is now the source of the signal.

Equations (11) and (12) are basic, and variations and improvements have been introduced to radiation transport codes which take into account the effects of solar noise (which has proven to be less of a problem than anticipated), wave action, and other effects. The point to be made here is that to the first order, hardware performance depends on two intrinsic properties of the ocean; K_a , the absorption coefficient, and β_{π} , the backscattering coefficient at 180° . At relatively shallow depths (ignoring multiple scattering) the majority of light originating at the transmitter and returning from the ocean can be assumed to be backscattered at an angle of 180° . As seen in Figure 5, K_a is a strong function of wavelength for almost all open waters.

Figure 5 also makes clear the desirability of operating at "blue" wavelengths in deep ocean and most littoral waters. This led earlier to a search for a blue laser for strategic submarine communications, and an excimer laser

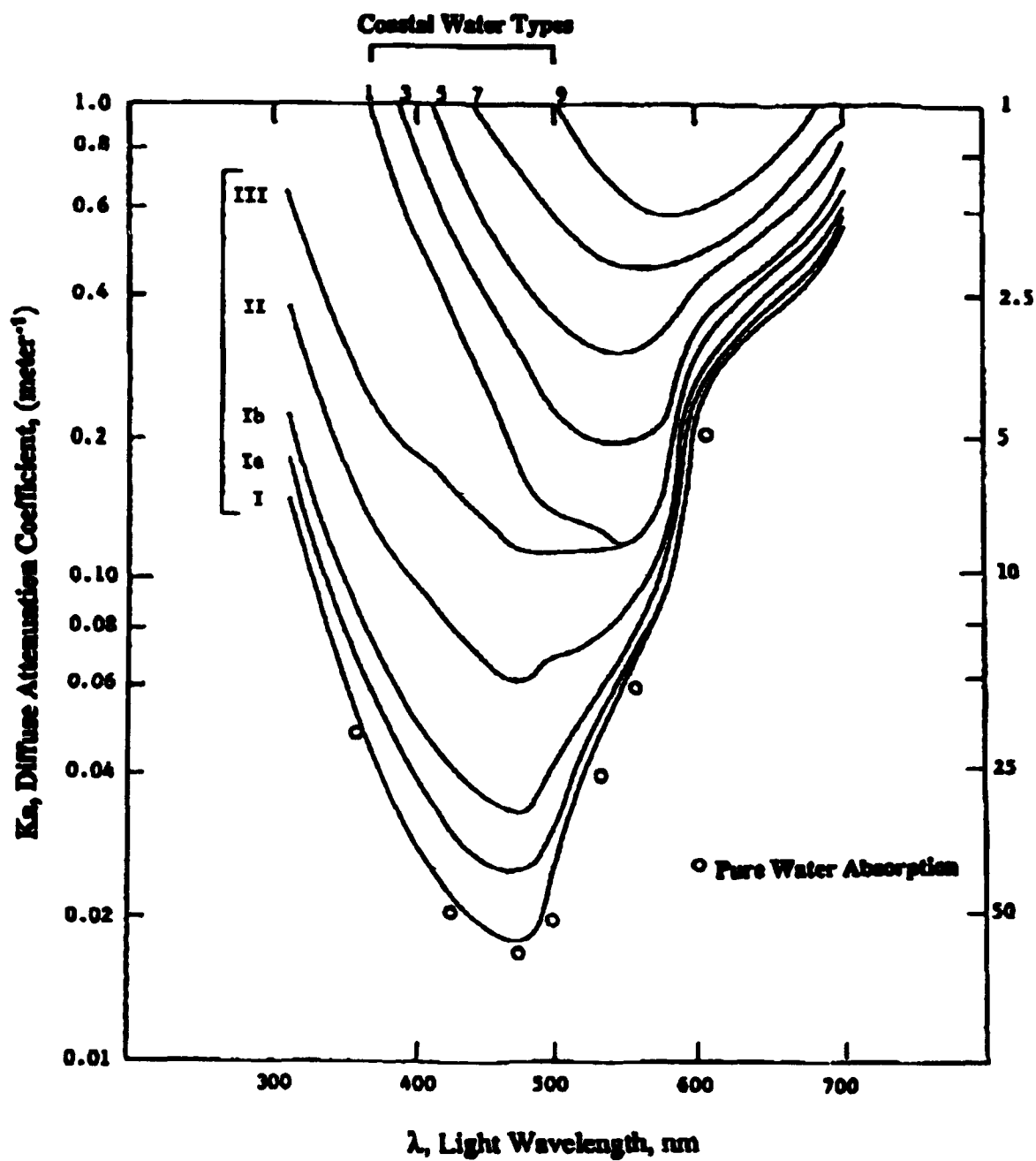


Figure 5

concept proposed by Dr. Ralph L. Burnham of the Naval Research Laboratory was actually used successfully in the "Yankee Blue" SLC (Submarine Laser Communications) experiment, although a later program "TALC" used an all solid state laser downlink transmitter (NdYAG) successfully, and a flashlamp pumped alexandrite laser uplink. The program then was held in abeyance, awaiting the appearance of a more reliable all solid state laser for operation in the blue wavelengths. Again, it should be noted that the mature portion of the system, the diode pumped NdYAG laser was the most successful of the transmitters used.

As stated previously, it has been difficult to obtain a reliable laser transmitter operating in the blue region of the optical spectrum (440-480 nm). In fact, no such transmitter has yet been fielded. The diode pumped all solid state NdYAG laser has been deployed extensively for various applications including ocean lidar use. As for a blue laser, such a device has recently been patented for lidar applications⁷. This laser transmitter represents the merger of two mature technologies; diode pumping of TiSAF laser rods, and laser pumping of TiSAF.

The claim has been made that in much area of the world's oceans, the water is Jerlov Class II. A look at various mosaics constructed from Nimbus satellite data²³ and Secchi Disc Atlas²⁴ support this claim. The theory behind these predictions has been given previously²⁵. Typical data are shown in Fig. 6 and Fig. 7 for the Persian Gulf.



Figure 6

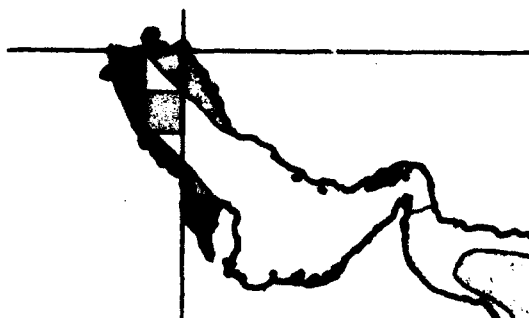
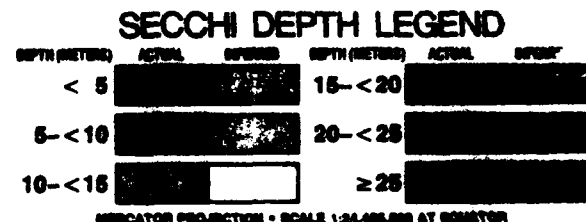


Figure 7



It could be inferred that this water is of the worst quality-Class II-III. Therefore, it could be argued from Figure 5 that it would not make a great deal of difference what wavelength is used in a lidar system. Any transmitter wavelength operating in the range of ~450 nm to 550 nm should be appropriate. This conclusion is subject to question, however. Recent K_a measurements made in the Persian Gulf by an imaging lidar system during its successful deployment there indicate that the water is far clearer than these surface measurements would indicate. These results are shown in Table I, and compared with the Nimbus, CZCS and Secchi results.

The K_a measurements were taken by the lidar system in the following way. The camera images two adjacent gated regions underwater. The camera gain setting is recorded and compared with the gain setting at an adjacent. As shown before^{3,10}, K_a is given by:

$$K_a = \frac{\ln(G_j / G_i)}{2(d_j - d_i)} \quad (13)$$

with G the gain settings, and d the gate depth. The Nimbus, CZCS and Secchi measurements are obtained in the usual way.

The possibilities are threefold for this disagreement; first, that only the most shallow depths are emphasized in the previous measurements; or second, these comments really pertain to a narrow angle system, and that the relationships between K_d , K_a and K_s are not well understood for these cases. It now appears that the performance of ocean lidars may not be reliably predicted without direct measurements by the Lidar system itself, which directly measures the absorption coefficient K_a or by in situ measurements of the extinction coefficient, downwelling irradiance attenuation coefficient or absorption coefficient. Finally, the case of the Persian Gulf may be anomalous, because the completion of a dam system on the Tigris and Euphrates Rivers after these data were taken may have led to a significant decrease in the amount of silt carried into the Persian Gulf. Perhaps the other types measurements will be useful some time in the future, but at present, they must be deemed unreliable. In this case of the Persian Gulf the lidar deployed performed far better than expected because of greater water clarity than previous data suggested.

Table 1

	CZCS/Nimbus	Secchi	Imaging Lidar
K_a , m ⁻¹	Class III or worse	Class III or II	~0.05 to 0.2 (class I _a to III)

THE BACKSCATTER COEFFICIENT

In Eq. (2) of the previous section, an expression is given for the photons on a pixel due to light reflected from the ocean. Part of this expression is the light "reflected" from the water;

$$N = \frac{\eta \lambda \beta_{\pi} \Psi \pi T_{out} T_{in} T^2 E_o A_{pixel}}{(2nf)^2} \int_{d_1}^{d_2} \frac{e^{-2Kd}}{A_{beam}(hd)} dd \quad (14)$$

This represents the light backscattered into the ICCD camera originating within a given gate, or spatial "slab". The constant β_{π} is the scattering function $\beta(\theta)$ at $\theta = 180^\circ$. In this analysis sunlight and multiple scattered light from the target is ignored. Recalling that to the first order the light received at the camera of a monostatic imaging lidar system is reflected at 180° , it can be seen that knowledge of the magnitude of β_{π} is very important for making accurate predictions of ocean Lidar performance. β_{π} is related to the scattering coefficient by:

$$b = K_s = \int_{4\pi} \beta(\vartheta) d\omega = 2\pi \int_0^{\pi} \beta(\vartheta) \cos \theta d\vartheta \quad (15)$$

The scattering coefficient is the sum of Rayleigh Scattering, Raman Scattering, Tyndall Scattering, Brillouin Scattering and Mie Scattering²⁶. For the purest water, Mie Scattering is negligible, as it is the result of scattering from dispersed particulates.

To the first approximation (single scattering), the backscatter from (or reflectivity per unit observed area of) a slab of ocean water is given by the relationship:

$$\rho_s = \frac{\pi \beta_{\pi}}{2} \int_{d_1}^{d_2} e^{-K_s z} dz = \frac{\pi \beta_{\pi}}{2K_s} [e^{-K_s d_1} - e^{-K_s d_2}] \quad (16)$$

In the case where it is desired to image in obscuration, and to optimize the signal (which in this case is the backscatter from the water) the upper (shallower) gate is taken as the target depth and the lower gate is taken as infinity. That is in order to collect all the ocean backscatter possible for better contrast with the shadow, or obscuration portion of the image, thus maximizing signal to noise ratio for this way of observing the target.

Then, equation (16) becomes

$$\rho_s = \frac{\pi\beta_\pi}{2K_a} e^{-K_a d} \quad (17)$$

It should be noted, however, that for deeper, larger targets the β_π of Equations (15) (16) and (17) becomes an effective β_π at greater depths ($\sim 3-4 K_a d$). Since $\beta(\theta)$ is maximum (in the backscattering direction) at $\theta = 180^\circ$ the diffuse nature of the field at depth tends to produce an "effective" $\beta_{\pi e}$ since the camera now receives a significant amount of doubly scattered light returning from scattering angles slightly less than 180° (the Mie back scattering peak), and with an intensity less than β_π . In general, therefore, one would expect a wide angle system to observe a larger β_π than a small angle system, and a experimental measurement with ocean optics equipment specifically designed to measure β_π observing an even larger β_π .

In general, oceanographers are not particularly interested in β_π . The light in this narrow backscattering cone of $1/2^\circ$ to 1° represents less than one part in 10^6 of the total incident light²⁷. Data on $\beta(\theta)$ are scarce. The first published work was by Kullenberg²⁸. This investigator used a Mie model to correlate his results. Based on other considerations, he concluded that the majority of scattering was due to particles larger than $1-2 \mu$ thus justifying the Mie model. The correlation led to a very sharp 180° peak and β_π more than an order of magnitude higher than his nearest measured $\beta(\theta)$ for $\theta = 130^\circ$. This result was subsequently ignored, perhaps because of the inadequacy of the Mie model, particularly at 180° , since ocean particulate matter is known not to be spherical. Estimates, for the most part, came from Petzold²⁹, and Oishi³⁰, and were simple extrapolations from data at smaller angles. There were no data available at 180° and the beam patterns of the various small spot systems were not homogeneous enough to permit any inference of β_π .

In the summer of 1990, extensive tests were carried out at CSS, Panama City, to calibrate the codes. Two weeks were spent overflying and imaging various underwater targets. As the analysis by Metron of these results began to unfold, a major discrepancy became evident. It was now possible to infer values of β_π 2-4 times greater than the previous extrapolations. As a result of the 1990 Magic Lantern results, a meeting was held at NOSC, San Diego on February 21, 1991 to discuss the problem. No conclusions were reached, but as a result, Stanford Research Institute was funded specifically to make measurements of β_π , a difficult and challenging experimental task. That work proceeds, and has now been published in the open literature³¹; but a number of questions still remain³². Most recently, an experiment carried out off Port Allen, Hawaii indicated that the enhanced β_π arises from Mie-like scattering from particulates in the water³³.

During imaging lidar tests in October, 1992, a calibrated underwater target was imaged by the ICCD camera lidar receiver; and these results were consistent with ocean backscatter images interpreted on the basis of previous radiometric calibrations. The use of calibrated underwater targets to obtain β_π has been proposed previously³⁴. The preliminary results are shown in Table 2. Note that

using three different techniques, results were obtained indicating values of β_π significantly greater than those predicted by the Petzold extrapolation.

Table 2

β_π	Predicted (Petzold)	Integrated	Radiometric	Target Comparison
	$\beta_{\pi 0}$	$\sim 2.3 \beta_{\pi 0}$	$\sim 3\beta_{\pi 0}$	$\sim 4\beta_{\pi 0}$

The designation $\beta_{\pi 0}$ refers to the value extrapolated from Petzold²⁹. The integrated column refers to an assembly of data fitted to the most probable β_π , and the last two columns refer to a statically calibrated camera, and imaging against a calibrated target in the ocean. These data require further analysis recalling that the β_π measured by the lidar system is an effective β_π whose value will decrease with increasing depth as the ambient light field becomes more diffuse. Obviously, more data on $\beta(165^\circ-180^\circ)$ are needed, as well as β_π measurements taken in the same water and at the same time.

SEA STATE AND IMAGING LIDAR PERFORMANCE

It is obvious that sea state can have a profound effect on signal to noise ratio. For illumination at nadir, the main problem is false alarms caused by focusing and defocusing taking place within the first 15 or 20 feet. There are ways of minimizing this noise, which fall beyond the scope of this paper³⁵. A more serious problem is the attempt to increase sweep rate by broadening the swath area and increasing the maximum viewing angle to 45° . This results in serious degradation of the signal due to shadowing, reflection, total internal reflection, defocusing and absorption.

Table 3 is based on a smooth ocean nadir signal normalized to 1.0; the modified Pierson-Moskowitz wave spectrum³⁶ was used, and sea states 1 and 3 were used for comparison.

It can be seen that any attempt to use such a sharp incidence angle would lead to a serious loss of depth, probability of detection, and sweep rate. In the case of the sweep rate, if the probability of detection was at its minimum permissible level in a flat sea at 45° inclination, the minimum permissible angle in a state one sea would be $\sim 35^\circ$. Thus, in a State 1 sea, the sweep rate would be halved. In a State 3 sea, the minimum permissible angle would be $\sim 25^\circ$. The sweep rate would be decreased by a factor of between three and four. The computer codes used to calculate the numbers quoted in Table 3 were normalized to data obtained in previous at sea tests, using various off nadir angles of incidence in various sea states.

In the calculations made for Table 3, the signal return at nadir is arbitrarily set at 1.0 for both sea states, showing the strong effect of sea state on off nadir

operation of all types of lidars. The effect at nadir at the various sea states will be less for the wide area than the spot systems because of a filling effect from adjacent regions analogous to the situation described in the first part of this paper.

Table 3

Angle from vertical; Lidar Transmitter and Receiver, deg.	Normalized Signal	
	Sea State 1	Sea State 3
0	1.0	1.0
20	0.74	0.62
40	0.33	0.26
60	0.16	0.07

In conclusion, the use of imaging lidar for making oceanographic measurements has led to two new discoveries, both important for the operation of ocean Lidar systems; anomalously high β_{π} , and ocean turbidity less than anticipated in certain coastal waters.

IMAGING LIDAR RECEIVERS

Gated intensified CCD cameras serve as receivers in the imaging lidar systems developed at Kaman. These receivers share a common basic configuration, although certain component variables are selected to optimize for the specifics of particular applications. An image intensifier tube, fiber optically coupled to a solid state sensor forms the heart of the unit with sensor support electronics, and a front end, imaging optic system completing the assembly.

The image sensor is a high-speed frame-transfer CCD of 256 x 256 format with 16 μ m square pixels in a contiguous (100% fill factor) array. On-chip pixel binning (2x2 or 4x4) can be easily implemented when a reduced format of larger effective pixels is sought. The sensor support electronics includes readout / timing control, analog signal amplification, 8 bit digitization and finally, fiber optic transmission of the outgoing video signal.

The intensifier tubes used in these Receivers are all 18 mm format, MCP wafer tubes (Gen2 or Gen3) with specific configuration tailored for the application. Conventional S20 (multialkali) photo cathodes (Gen2) having quantum efficiencies at the system wavelength of 12% to 15% have generally been used

although recent units have been built using the relatively new GaAsP cathode (Gen3) material yielding quantum efficiencies of 40% to 50%. When required, conductive underlays have been added to achieve sufficient gating speed; generally 5 to 10 nsec turn-on (rise-time) is sought.

Where the application dictates higher net gain than offered by the single stage MCP tube, a second stage (Gen1) tube has been cascaded. This device has the added benefit of providing magnification to match the CCD's format to that of the intensifier tube. For the single stage configurations, the coupling fiber optic is tapered to achieve that desired format matching. The optimum resolution is achieved with the single stage Gen3 configuration, where a tube point spread function (PSF) of 50 to 60 μ m (FWHM) can be achieved in gated operation, yielding a good match for the effective (magnified) sensor array.

The entire intensifier support electronics have been packaged in a single module providing the interface between externally supplied logic and/or low-level analog control commands, and the operating voltage applied at the intensifier tube to achieve desired gate and gain operation.

Lens systems designed to maximize F/# (i. e., collecting aperture given the needed focal length) are used to form the object scene image on the intensifier photo cathode. A 172 mm F/1.9 lens is being used for the narrow field configuration (nominal 2.72°) where multiple Receiver fields-of-view are mosaicked to achieve a large, high resolution instantaneous FOV for the system. A 90 mm F1 lens has been selected for the comparatively wide FOV (nominal 6.85°) used when multiple Receiver FOVs are stacked to achieve system depth coverage. For all cases a narrow bandpass filter is integrated onto the front of the lens assembly to provide sunlight background rejection. The bandpass is located coincident with the system wavelength with width minimized subject to FOV constraints (3nm to 6 nm).

These and similar types of camera systems have been deployed in numerous lidar field tests as well as in the Persian Gulf during Desert Storm.

SUMMARY

The introduction of wide area imaging lidar systems has revolutionized the field of ocean lidar surveillance. The concepts described herein have been reduced to practice in the field, including a successful wartime deployment. In addition, a number of phenomena not fully understood have been observed. Eventual understanding of these effects can significantly influence the performance of future imaging ocean lidar systems.

ACKNOWLEDGEMENTS

The authors would like to express their personal gratitude to the following personnel from Metron, Inc.; Dr. Henry R. "Tony" Richardson for providing numerous significant physical insights to us while assisting us in preparing this

manuscript; to Ms. Maria K. Hopgood of Metron for carrying out the monte-carlo calculations, and to Ms. Maribeth Dwyer for assistance with the graphics. We would also like to acknowledge the significant assistance of Dr. Jack Lloyd of the Coastal Systems Station, Panama City, Florida for providing us with a detailed and critical review of our manuscript and providing us with numerous comments reflecting his many years of experience in working with various types of ocean lidar systems.

REFERENCES

1. Ulich, B. L., "Imaging Lidar System", U. S. Patent 4,862,257, August 29, 1989
2. Ulich, B. L., et al., "Imaging Lidar System" U. S. Patent 4,964,721, Oct. 23, 1990
3. Keeler, R. N., "Imaging Lidar Systems and K-Meters Employing Tunable Fixed Frequency Laser Transmitters", U. S. Patent 5,091,778, Feb. 25, 1992
4. Ulich, B. L. et al., "Lidar System Incorporating Multiple Cameras for Obtaining a Plurality of Subimages", U. S. Patent 4,967, 270, Oct. 30, 1990
5. Ulich, B. L. and Kent Pflibsen, "Method and Apparatus for Three Dimensional Range Resolving Imaging", U. S. Patent 5,249,046, Sept 24, 1993
6. Ulich, B. L., "Imaging Lidar System for Shallow and Coastal Water" U. S. Patent 5,243,541, Sept. 7, 1993
7. Kaman, C. H. et al. "Imaging Lidar System" U. S. Patent 5,231,401, July 27, 1993
8. Pflibsen, Kent and A. Stuppie, "Laser Beam Homogenizer" U. S. Patent 5,303,084, April 12, 1994
9. Keeler, R. N., H. R. Richardson and M. Hopgood, "The Relative Efficiency of Wide Area and Narrow Area Illumination in Airborne Ocean Lidar Systems", Proceedings of the Second Annual ITEMS Conference, June 8- Washington, DC, J. Powell, ed., Armed Forces Communications and Electronics Association, Vienna, Virginia, 1993
10. Ulich, B. L., Method and Apparatus for Determining K Factor, U. S. Patent 4,936,024, July 7, 1988
11. Jerlov, N. G., Marine Optics, Elsevier, New York, N. Y., p 4, 1976
12. Jerlov, N. G. Medd. Oceanogr. Inst. Göteborg Ser. B 8, 40 pp, 1961

31. Maffione, R. A. and R. C. Honey, Ocean Optics XII, SPIE Vol. 1750, p 15, SPIE, Bellingham Washington, 1992
32. Feigels, V. St. Petersburg Institute of Fine Mechanics and Optics, private communication, February 17, 1994
33. Maffione, R. and J. Smart, paper, this conference.
34. Daniels, K., R. N. Keeler and M. Cantor, "Optical Buoys and Towed Bodies for Oceanographic Measurements by Imaging Lidar" U. S. Patent 5,311,272, May 10, 1994
35. Zege, Eleonora P., I. L. Katsev and A. S. Prikhach, "Visibility Range of the Underwater Objects" Izv. Akad Nauk SSSR, Fiz. Atm. Okean 29, 337 (1993)
36. Cox, C. S. and W. H. Munk, Bull. Scripps Inst. Oceanogr. Univ. Calif. 6, 401 (1956)

13. Ivanov, A. P., Ye. I. Afonin, I. M. Gurskiy, M. N. Kaigorodov, V. D. Koslov and B. Ye. Shemshura, *Izv. Akad. Nauk SSSR, Fizika Atmosferiy i Okeana*, v. IX, no. 10, 1101(1973) The relationship cited by these workers was $K_i \sim 0.86 K_a$ so the assumption made in this paper that $K_i \sim K_a$ tends to mitigate the poor performance of spot systems indicated by Eq. (6). The situation is somewhat worse than indicated herein.
14. Mobley, C. D., et al., *Appl. Opt.* **32**, 7484 (1993)
15. McLean, J. W. and K. Voss, *Appl. Opt.* **30**, 2027 (1991)
16. Luchinin, A. G. et al., *Izv. Akad. Nauk SSSR, Fiz. Atmos. Okeana* **18**, 850 (1982)
17. Preisendorfer, R. W., *J. Quant Spectrosc. Radiat. Transfer* **8**, 325 (1968)
18. Jerlov, N. G., "Optical Oceanography", Elsevier, New York, N. Y. 1968
19. Bravo-Zhivotovsky, D. M., *Izv. Atmosph. Ocean Physics* **5**, 83(1969)
20. Lutomirsky, R. F. et al, Pac. Sierra Res. Corp., Report 1898A, Nov., 1989
21. McLean, J. W. *Appl. Opt.* **30**, 7484 (1991)
22. Bravo-Zhivotovsky, D. M. et al. "Theory of Optical Image Transfer in Water" *Optika Okean I, Fizicheskaya Optika Okeanov*, Nauka, Moscow (1983)
23. "Oceanography from Space-Global Ocean Color", U. S. Global Ocean Flux Study Planning Office, Woods Hole Oceanographic Inst, Woods Hole, MA, July 1987
24. Arnone, R. A. Coastal Secchi Depth Atlas, NORDA Report 83, July, 1985
25. Estep, Lee and R. A. Arnone, *Photographic Engineering and Remote Sensing* **59**, 345 (1993)
26. Jerlov, N. G., *Marine Optics*, Elsevier Press, New York, N. Y., 1976
27. Honey, R. C., NOSC Rpt. "Optical Backscattering Mtg.", February 21, 1991, G. D. Gilbert, ed. Naval Ocean Systems Center
28. Kullenberg, G., et al. *Univ. Copenhagen Inst. Phys. Ocean. Rep.* **19** (1972)
29. Petzold, T. J., SIO Report 72-78 dtd Oct., 1972, NADC, Warminster, Pa.
30. Oishi, T., *Appl. Opt.* **29**, 4658(1990)

SESSION 7

Instrumentation II

ANALYSIS OF SEA TECH ABSORPTION METER CHARACTERISTICS AND COMPARISONS TO K_d MEASUREMENTS

Jeffrey H. Smart

Johns Hopkins University/Applied Physics Laboratory
Johns Hopkins Rd, Laurel, Md 20723

ABSTRACT

A Sea Tech single wavelength (488 nm) absorption meter (known as the "a-meter") has been deployed in the Florida Straits and in the open ocean near Kauai. The instrument has been evaluated to assess its performance in measuring the diffuse attenuation coefficient (K_d) so that the numerous problems associated with traditional K_d measurements can be avoided. (Traditionally, one measures downwelling irradiance, which requires daylight and suffers from the effects of clouds, ship shadowing, instrument tilting, surface wave focussing, and Raman transpectral scattering.) **The main result of this evaluation is that the a-meter generally provided profiles that agreed with traditional K_d profiles to within about 0.003/m, and the instrument did not suffer from any of the problems of irradiance measurements.** It did, however, require the use of knowledgeable deployment, maintenance, and calibration techniques and the use of essential supporting measurements in order to obtain this degree of accuracy. This paper describes these aspects of how to effectively use the a-meter and provides representative examples of simultaneous traditional K_d profiles.

1. INTRODUCTION

In studies of ocean optics we frequently need to measure the diffuse attenuation coefficient, defined as

$$K_d(\lambda, z) = -(1/E_d)(dE_d/dz) \quad (1),$$

where $E_d(\lambda, z)$ is the depth profile at a given wavelength of downwelling solar irradiance. Therefore, this parameter can only be measured during daylight, and it suffers from fluctuations in the light caused by the effects of clouds, ship shadowing, instrument tilting, surface wave focussing, and Raman transpectral scattering (Reference 1). Various investigators have sought to make equivalent measurements using artificial light sources in order to avoid the problems associated with ambient light, and in order to measure K_d at night. For example, Honey (Reference 2) estimated K_d by using an E_d sensor that was successively raised and lowered in depth relative to an underwater strobe light. That method requires good alignment between source and receiver, as well as highly accurate measurements of relative separation distances (R) to account for the $1/R^2$ light loss. A more robust approach was developed by Zaneveld (Reference 3), who used a modified beam transmissometer. In his device a collimated light beam is surrounded by a reflecting tube so that most of the light scattered out of the beam is reflected back into the detector at the end of the tube. Therefore, to a good approximation, the only loss in light is due to absorption and to backscattered light. Thus this "absorption meter" (referred to hereafter as the a-meter) is really designed to measure $a + b_b$ (References 3 and 4), where a is absorption and b_b is that portion of scattering that occurs in the backward hemisphere, defined as

$$b_b = 2\pi \int_{\pi/2}^{\pi} \beta(\theta) \sin\theta \, d\theta \quad (2).$$

The instrument has also been referred to as a K-meter because

$$K_d \approx a + b_b \quad (3),$$

(References 4 and 5). This device has been improved and sold commercially by Sea Tech, Inc.

The Applied Physics Laboratory (APL) purchased a Sea Tech single wavelength (488 nm) absorption meter, and we have deployed it in two field tests to date: in the Florida Straits (January 1993) and in the open ocean near Kauai (March 1993). The instrument

has been evaluated to assess its performance in measuring the diffuse attenuation coefficient (K_d) so that the numerous problems associated with traditional K_d measurements can be avoided. **The main result of this evaluation is that in the March test the a-meter generally provided profiles that agreed with traditional K_d profiles to within about 0.003/m, and the instrument did not suffer from any of the problems of irradiance measurements.** It did, however, require the use of knowledgeable deployment, maintenance, and calibration techniques and the use of essential supporting measurements in order to obtain this degree of accuracy. (Reference 4 describes maintenance and deployment techniques.) With regard to the supporting measurements, one must obtain a concurrent profile of the total beam attenuation coefficient (c), and c should be accurate to $\approx 0.01/\text{m}$ because the raw a-meter output has a component that depends on c and therefore must be removed. Second, an at-sea calibration technique is needed, such as the distilled water reservoir/pumping system used in our field tests.¹ This calibration is needed because the instrument's calibration can change with time, especially if it has to be opened for repairs. Finally, to obtain high quality profiles, one needs to carefully screen the raw data for measurement artifacts. The presence of bubbles in the sensing volume will greatly distort the measurements, and this condition is frequently encountered within the first five minutes after the instrument has been lowered into the water. (An experienced user will monitor the sensor's output before lowering the instrument beyond a few meters depth.) Furthermore, as shown in Figure 1, sporadic large noise spikes also occur during a profile, and these need to be removed in post-cast processing. (These spikes may be caused by the passage of bubbles or relatively large particles, fish larvae, etc. through the sensor.) One should also carefully examine the unedited c -meter and $\beta(170^\circ)$ profile to verify that there are no corresponding spikes in those sensors because the presence of such spikes in the c -meter and $\beta(170^\circ)$ profiles would imply that the spikes are real features, not noise.

2. OBJECTIVES

The main objective of this paper is to show that the Sea Tech a-meter is generally capable of providing highly accurate profiles (good to $\pm 0.003/\text{m}$) of K_d both at night and during the day. A second objective is to describe what a user needs to do to achieve this degree of accuracy. The Appendix provides additional information on how to perform at-sea calibrations without having a pure water pumping system, and it describes the sensitivity of a-meter data to the accuracy of the calibrations.

3. INSTRUMENTATION

The data described in this paper come from the Optical Profiler System (OPS). The OPS consists of a suite of instruments: a Biospherical Instruments MER1048, a Sea-Bird conductivity/temperature/depth (CTD), a Sea Tech absorption meter, a beam transmissometer, a 170° backscatter sensor (hereafter referred to as the $\beta(170^\circ)$ sensor), and a fluorometer. (The last three instruments were designed and built at APL.) The MER1048 contains sensors that measure downwelling and upwelling irradiance (E_d and E_u , respectively) at the following wavelengths: 410, 441, 475, 488, 507, 540, 570, and 589 nm. It also contains sensors that measure upwelling radiance (L_u) at the same wavelengths. The E_d and E_u sensors have a cosine corrected acrylic plastic diffuser/collector, and the L_u sensors have a field of view defined by 8 Gershun Tube elements having anti-reflection baffles and a 10.2° half angle field of view. The half power bandwidth is 10 nm over a temperature range of 0 to 30°C . The spectral stability over this same temperature range is 2 nm. The response to light more than 100 nm outside a sensor's passband is one part per million relative to the peak response. All sensors are calibrated using a spectral irradiance standard that is traceable to the National Bureau of Standards. Dynamic range is 12 bits and sensor time constants are 0.1 s.

The MER1048 also includes a built-in depth sensor which is operational to a depth of 200 m and which has a total error less than 0.25% of full scale. The typical resolution is 0.1 m. A built-in 2-axis tilt sensor suite provides data on instrument orientation. The

¹ As briefly described in Reference 4, the water calibration involves a distilled (or preferably reverse osmosis filtered) water reservoir, that is continuously filtered through a coarse filter followed by a $0.2\ \mu$ filter. The pump must have a magnetic clutch to avoid oils getting into the water. As described in Appendix 1, the APL system was able to provide water that was measurably cleaner than the deepest, clearest water off Kauai, which had $K_d \approx 0.028/\text{m}$ and $c \approx 0.035/\text{m}$. For pure sea water, $K_d = 0.0217/\text{m}$ and $c = 0.023/\text{m}$.

OPS has ports for connection of external sensors, which include the beam transmissometer, the $\beta(170^\circ)$ sensor, and the fluorometer. Two FSK ports receive frequency-encoded data from the Sea-Bird temperature and conductivity sensors.

Another external port is used to power the absorption meter data, and the data from the absorption meter is sent directly to the MER's deck box (via RS485) where it is appended to the MER's serial data stream before it is sent into the topside computer. The a-meter uses its own internal light source and therefore is useful either at night or during the day. The daytime K_d profiles, computed directly from the OPS 488 nm downwelling irradiance sensor, were used to ground truth the a-meter profiles.

Two different fluorometers were used with the OPS, but only one gave sufficiently stable profiles to use as an independent comparison with the a-meter. A limited number of these stable sensor profiles are available to provide an independent comparison with the a-meter profiles.

4. DESCRIPTION OF DATA

As discussed in the previous section, in order to ensure the accurate measurement of K_d , more than one instrument was used when possible. This section describes representative comparisons between these instruments. (Another paper in these proceedings describes the comparison between the APL $\beta(170^\circ)$ backscatter device and the SRI $\beta(\pi)$ backscatter instrument.) K_d was determined by several independent means, including K_d computed from downwelling irradiance (sunlight) profiles, from K_d estimated using the Sea Tech a-meter, and from K_d computed from the fluorometer.

A detailed analysis of the a-meter data is provided in Reference 6. The results were that the a-meter generally provided profiles that agreed with traditional irradiance K_d profiles to within about 0.003/m, and the instrument did not suffer from any of the problems of irradiance measurements. Typical comparisons between average² profiles obtained from K_d derived from irradiance and the a-meter are shown by the solid lines in Figure 2. In some cases (as in Figure 2b), the two methods gave essentially identical results, and in other cases (as in Figure 2a), there was an offset between the two methods of ≤ 0.003 /m. In the latter case, the a-meter profile also had a smaller sub-surface maximum than the K_d profile, but the accuracy of the latter is suspect because the peak occurs at a depth of 150 m where light levels are approaching the system noise level for the irradiance detectors. (The Figure 2b data also show a consistent offset below about 130 m.)

The dashed lines in Figure 2 show the degree of agreement that can be achieved between the K_d and a-meter profiles if the latter are "empirically corrected." The first correction method is to compute a linear least squares fit between the two mean profiles and then to apply that mean fit to the a-meter profile. For example, the Figure 2a fit indicates that the original a-meter data be multiplied by 1.42 (essentially this is the same as applying a gain factor correction to the data) and then to subtract 0.0085/m (an offset correction). The linear least squares fit computed for the Figure 2b data, which agree very well without a correction, gives a gain factor of 0.85 and an offset of +0.0041/m. Fits to six other sets of average profiles show a range of gains from 0.85 to 1.42, with offsets ranging from -0.0085 to +0.0085/m. In each case, gains less than 1.0 have positive offsets, and vice versa. The wide variability in these coefficients is an indication of the lack of statistical reliability in the fits. It turns out that the a-meter data can generally be corrected just as well (and in a less complicated way) using a simple DC offset ($K_d - a$) that ranges from -0.0035 to +0.0055 /m. In Figure 2, the result of applying this mean offset to the a-meter profile is shown by the profiles with the short, thin lines, and the result of applying the linear least squares fit is shown by the thicker dashed lines. In general, these two correction schemes gave almost identical results, as shown here.

It is tempting to attribute the DC offset between the a-meter and the K_d profile to the sun angle effects predicted by Kirk (Reference 7). That is, when the sun is not at zenith, the effective pathlength of sunlight is increased by a small amount, thereby increasing K_d from its zenith value. The data shown in Figure 2a come from early to mid-morning, whereas those in Figure 2b data come from nearer to midday. Therefore Kirk's analysis would predict that K_d will be biased slightly high in 2a compared to 2b, and that is exactly what we observe. Although this argument seems plausible, it can not account for the negative biases (up

² The data in each figure were all gathered at one location, and there was generally little temporal variability during this test. The purpose for using *average* profiles, instead of individual ones, is to increase the statistical accuracy in the K_d profiles, which tend to be noisy due to the effects of instrument tilt, sunlight fluctuations, etc.

to $-0.0035 / \text{m}$) that were also observed when the sun was not at zenith. As discussed further below, the biases seem more related to the a-meter output than to sun angle effects, and there is even some evidence that drifts in the c-meter may affect the values of K_d computed from the a-meter.

As mentioned above, special care was taken with the a-meter in the areas of maintenance and calibration. Nevertheless, the unit we were using still occasionally exhibited unexplained drifts, as illustrated in Figure 3. Here the irradiance-derived K_d profiles exhibit no temporal variability, but the a-meter data seem to wander around by as much as $0.01/\text{m}$ over a five hour period. (The K_d data are only shown for a portion of this period because the later profiles were acquired after sunset. Although some of the variability in the a-meter data after 16:34 could be real, the suspicious drift between 16:09 and 16:34 casts doubt on the absolute accuracy of the subsequent profiles.) This problem was eventually traced to a broken wire, but it serves to illustrate the value in making independent measurements of key parameters.

During this field test the a-meter was found to consistently measure the *structure* of the K_d profile, although as discussed above DC offsets of up to about $\pm 0.005/\text{m}$ were needed to obtain agreement in absolute values. Some of these offsets could have been the fault of DC drifts in the c-meter profiles, because the "corrected" a-meter profiles are obtained via the following equation provided in Reference 3:

$$a_c = \frac{(a_r - F)}{(1-F)} \quad (4),$$

where F is an empirical correction factor, nominally 0.14, and a_r is the raw (but temperature compensated) absorption value computed from the a-meter data. This equation indicates that if c increases by $\sim 0.01/\text{m}$, then a_c decreases by $\sim 0.0015/\text{m}$. As illustrated in Figure 4, occasions did occur where the raw a-meter profiles were essentially identical, but the corrected ones had a DC offset, due entirely to the change in the c meter profiles. If the increase in c were real in these profiles, it would be reasonable to expect a to increase also, whereas the opposite appears to be true here. These results suggest that the c meter data may also be subject to DC changes of up to $\sim 0.01/\text{m}$.

Another standard way to obtain K_d is to use a fluorometer (which contains a light source designed to induce florescence in ambient pigments) and to calibrate it in terms of total chlorophyll pigment content.³ One then typically uses either the Gordon-Morel empirical regression (Reference 8), or the Smith-Baker empirical fit (Reference 9), to convert the chlorophyll concentration profile to a K_d 490 nm profile. (In practice, if one has sufficient simultaneous measurements of K_d and of chlorophyll concentration, then a regression can be computed that best fits the data at hand, thus removing some of the uncertainty of using the published fits from other ocean data sets.) The main advantage of fluorometer profiles is that they can be used at night as well as during the day. The disadvantages are 1) the need for obtaining bottle samples, 2) the labor involved in processing them, and 3) the need for two sets of regressions (converting from florescence to chlorophyll, then to K_d .) If we do not care about chlorophyll concentrations, these disadvantages can be avoided by directly regressing the raw fluorometer voltages against the corresponding irradiance-derived K_d . We can then apply this regression to subsequent fluorometer profiles, and we can use these profiles as another validity check on the a-meter profiles.⁴

This approach was applied to data obtained on Test Day 12, and the results for two typical sets of simultaneous K_d profiles are shown in Figure 5. All three methods of measuring K_d give essentially the same profile. The main difference is that the

³ Bottle samples are obtained at various depths and chlorophyll extraction and measurement techniques are then applied to these samples. One obtains a measure of the concentrations of chlorophyll a and of phaeophytin, and their sum is what is used to infer K_d .

⁴ With this methodology, the fluorometer data become linked to the irradiance-derived K_d data, and they do not provide a completely independent comparison to the a-meter data. However, the fluorometer has the advantage that it does not suffer from cloud contamination, surface wave focussing, ship's shadow, etc., so by calibrating it with a "good" K_d profile, we have a more reliable sensor for use on subsequent casts, including those performed at night.

fluorometer-derived K_d profile has a narrower sub-surface maximum than the sunlight-derived K_d profile, so that between 120 and 170 m depth the latter is consistently higher. A careful examination of the fluorometer data shows that the narrower peak is caused by a change in the relationship between fluorometer voltage and K_d that occurs below 120 m. As shown in Figure 6, a single linear least squares fit (indicated here by the dashed line) is not really appropriate over the full depth range of our profiles. The most reasonable explanation is that as depth increases, the contribution of phaeophytin relative to chlorophyll is increasing, and it is well known that the florescence of phaeophytin is much lower than it is for chlorophyll.

5. CONCLUSIONS

Despite our careful attention to sensor calibrations and cleaning, we still have several unresolved questions relating the performance of the a -meter. During the March test, absolute zero changes occurred ($\sim 0.005/m$) on at least two different occasions. Also, even when we used a constant set of calibration constants, it was possible to obtain an average a profile greater than the average K_d profile in the morning, and then to have the reverse happen in the afternoon. (The differences were $\sim \pm 0.003/m$). During the January test, in order to obtain good agreement between the a -meter and K_d profiles, we had to use either an abnormally high c -meter correction factor, or else we had to use a pure water calibration factor *below* the measured value. Further study of these anomalies is needed to more fully characterize the capabilities and limitations of this instrument.

6. ACKNOWLEDGEMENTS

The author would like to thank Drs. Michael DeWeert and Dan Ondercin for their advice and suggestions. Drs. DeWeert and Ondercin also participated in the Hawaii cruise to acquire the data analyzed in this paper. The work of our electrical engineer, Kirk Decker, was essential to accomplishing the interface from the a -meter to the OPS, and to maintaining and calibrating the device.

7. REFERENCES

1. Smart, J.H., "Seasonal and Spatial Variations in the Attenuation of Light in the North Atlantic Ocean," Johns Hopkins APL Tech. Dig., Vol 14, 1993
2. Honey, R. C. and C. A. Priore, "In Situ Characterization of Seawater Using a Computerized Suite of Optical Instruments," AGARD Symposium on Propagation Factors Affecting Remote Sensing, Oberammergau, Germany, May 1983
3. Zaneveld, R., et al, "A Reflective-Tube Absorption Meter," SPIE Vol 1302, Proc. of Ocean Optics X," (1990) pp 124-134
4. Sea Tech, Inc, "Selectable Wavelength Absorption Meter User's Manual," Corvallis, OR 97339, March 27, 1992
5. Kitchen, J. C. and J. Ronald V. Zaneveld, "On the noncorrelation of the vertical structure of light scattering and chlorophyll a in Case I Waters, (Journal of Geophysical Research, Vol. 95 No. C11 pp 20,237-20,246) Nov 1990
6. Smart, J.H., "Analysis of Sea Tech Absorption Meter Characteristics and Comparisons to K_d Measurements," JHU/APL Internal Memorandum STE-93-091, July 1993
7. Kirk, J. T. O., "Dependence of relationship between inherent and apparent optical properties of water on solar altitude," (Limnol Oceanogr., 29(2), 350-356) 1984
8. Gordon and Morel, Remote Assessment of Ocean Color for Interpretation of Satellite Visible Imagery- A Review, Springer-Verlag, NY, 1983.
9. Baker, K.S. and R.C. Smith, "Bio-optical Classification and Model of Natural Waters. 2," Limnol. Oceanogr. 27:500-509, 1982.

APPENDIX

WATER CALIBRATION RATIO (WCR) RELATIONSHIPS

1. How to Correct In-situ Water Calibration Ratios to Pure Water Values

This appendix describes how a WCR value measured in ocean water can be corrected to reflect the value associated with pure sea water, and it describes the sensitivity of the a-meter measurements to small changes (or errors) in the WCR. Ideally, one wants to use pure water to obtain the Water Calibration Ratio (WCR). For *impure* water, one can apply the following correction.

$$V_{sig} = V_w e^{-(K_d - K_{dw}) L}, \text{ where}$$

V_{sig} is the measured voltage at the signal output, V_w is the voltage that would be measured in pure water, K_{dw} is the attenuation coefficient for pure water, and L is the pathlength (in meters) of the a-meter. The WCR, which is V_{sig}/V_{ref} , will also be decreased by $e^{-(K_d - K_{dw}) L}$. For $K_d = 0.03/\text{m}$ and $L = 25 \text{ cm}$, and using the pure water value of $K_{dw} = 0.0217$, then V_{sig} is attenuated by:

$$\begin{aligned} V_{sig} &= V_w e^{-(0.03 - 0.0217) 0.25\text{m}} \\ V_{sig} &= 0.998 V_w \end{aligned}$$

This result also means that the WCR is 0.998 times the true value, so if the measured WCR value at $K_d = 0.03/\text{m}$ is 0.7623, then the corrected WCR @ $K_d = 0.0217/\text{m}$ is 0.7638. As shown in the following derivation, this correction leads to an increase in the corrected a-meter reading of 0.009/m, which is a 30% correction when $K_d = 0.03/\text{m}$.

2. Effect on Absorption Meter Measurements of Changing Water Calibration Ratios

Let CR = corrected signal ratio = $\frac{V_{sig}}{V_{ref} + V_{ref}(KR(20 - T_{ref}))}$, where KR is the temperature

coefficient of the a-meter, which was measured at Sea Tech to be $0.00035/^\circ\text{C}$. Also, let CF = calibration factor = T_{theo} / WCR , where T_{theo} is the transmissivity of pure water ($T_{theo} = 0.9950$).

$$\begin{aligned} \text{Then } a_t &= -4 \ln(\text{CR} \cdot \text{CF}) \\ &= -4[\ln(\text{CR}) + \ln(\text{CF})] \\ &= -4[\ln(\text{CR}) + \ln(\text{Theo}) - \ln(\text{WCR})] \\ a_t &= -4\{\ln(\text{CR} \times \text{Theo}) - \ln(\text{WCR})\}. \end{aligned}$$

Now if we change to a new WCR (call it WCR') then

$$a_t^1 = a_t - 4 \ln(\text{WCR}) + 4 \ln(\text{WCR}'), \text{ or } a_t^1 - a_t = 4 \ln\left(\frac{\text{WCR}'}{\text{WCR}}\right), \text{ and}$$

$$a_t^1 = a_t + 4 \ln\left(\frac{\text{WCR}'}{\text{WCR}}\right)$$

For example, if $\text{WCR}' = 0.7619$ and $\text{WCR} = 0.7591$, then $a_t^1 - a_t = 0.015/\text{m}$.

To determine a similar relationship for the "corrected" a value, denoted a_c , recall

$$a_c = \frac{(a_t - Fc)}{(1-F)}. \text{ Therefore,}$$

$$a_t = (a_c)(1-F) + Fc$$

(1)

Now one can use the relationship derived above for a_c^1 to obtain a_c^1 :

$$a_c^1 = a_c + 4 \ln \left(\frac{WCR'}{WCR} \right)$$

$$a_c^1 = \frac{[a_c + 4 \ln \left(\frac{WCR'}{WCR} \right)] - Fc}{(1-F)}$$

$$a_c = (a_c^1)(1-F) + Fc - 4 \ln \left(\frac{WCR'}{WCR} \right) \quad (2)$$

Subtracting (2) from (1) yields

$$0 = (a_c - a_c^1)(1-F) + 4 \ln \left(\frac{WCR'}{WCR} \right), \text{ or}$$

$$a_c^1 = a_c + \frac{4 \ln \left(\frac{WCR'}{WCR} \right)}{(1-F)}$$

Note: $\left(\frac{WCR'}{WCR} \right)$ is generally ≈ 1 , and $\ln(1+x) \approx x$ for $|x| \ll 1$. Therefore

$$a_c^1 \approx a_c + 4 \left[\left(\frac{WCR'}{WCR} \right) - 1 \right] / (1-F).$$

3. Temporal Stability of the Water Calibration Ratio

Sea Tech has said that it is normal for the efficiency of the reflecting tube in the a-meter to decrease with time such that the WCR decreases by ~ 0.01 over 6 months. We performed a crude check on this degradation by measuring the change in the ratio V_{sig}/V_{ref} over the 12 days of the March 1993 sea test. The results suggest that this ratio decreased from ~ 0.761 to ~ 0.755 over this period of intense usage, and this rate implies a change much greater than 0.01 over a 6 month period. On the other hand, between August 1992 and June 1993 the WCR changed by about 0.01. More data are needed to determine how the combination of time and usage affect the rate of decay of the WCR.

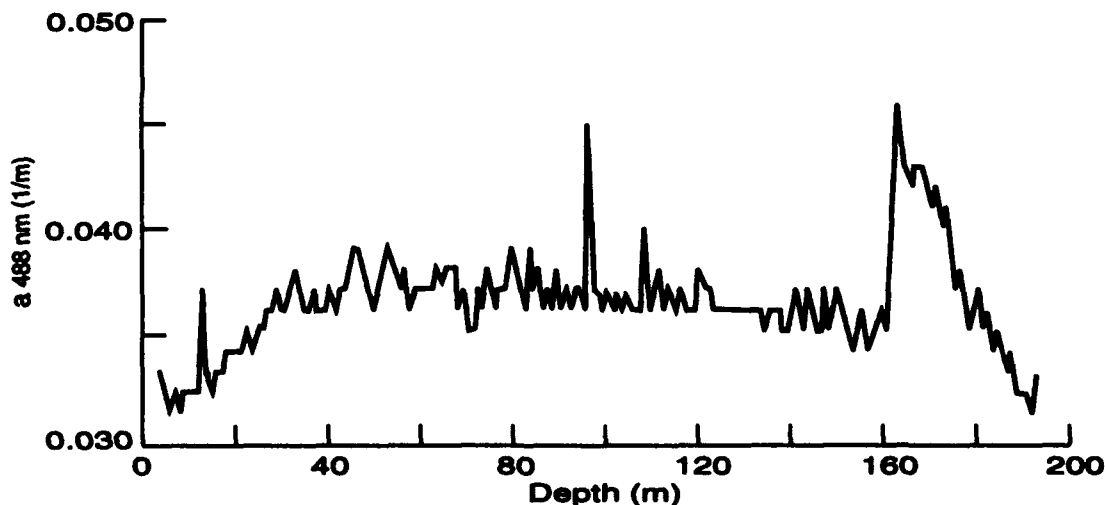


Figure 1. Example of Unedited a Meter Profile. The spikes at 15, 95, and 110 m appear to be instrument noise and such features are routinely cut out of the profiles before applying a 10 m vertical low pass filter.

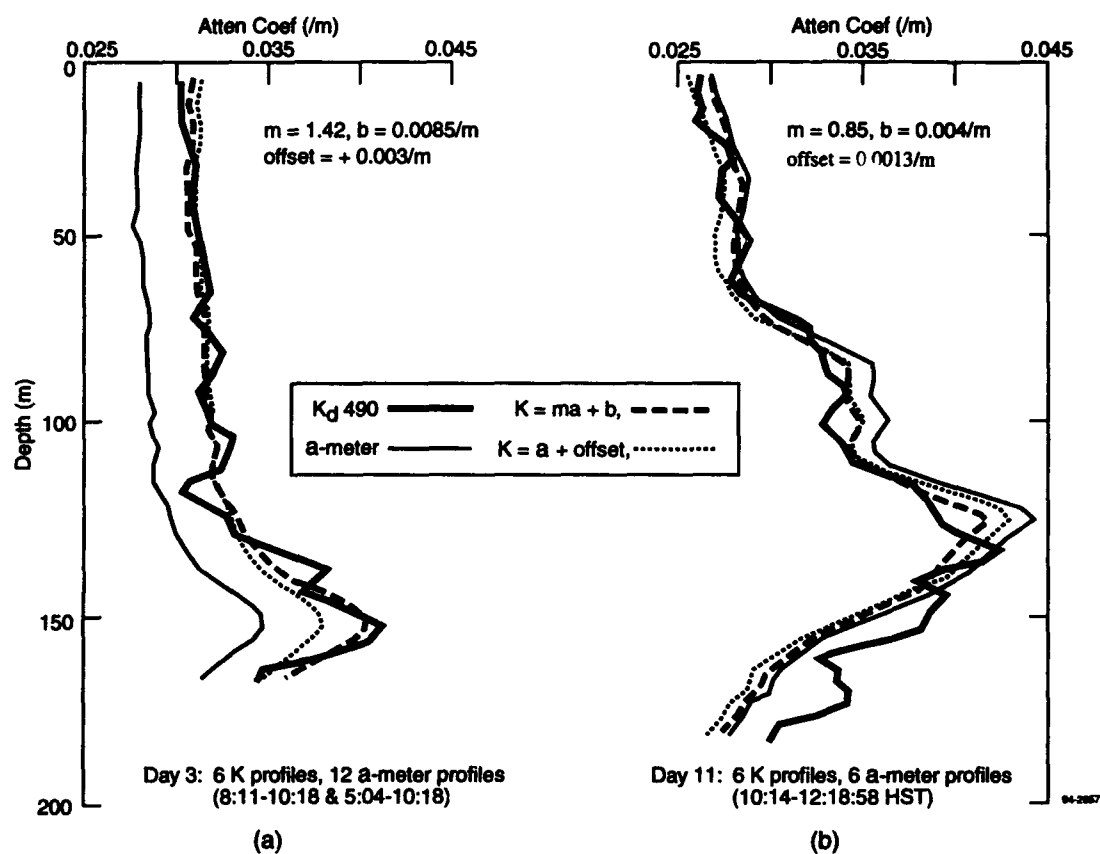


Figure 2. Mean a -meter Profiles having (a) Lower and (b) Same Mean Values Compared to K_d Profiles. Data from Mid-March 1993. Dashed lines are fits to K_d data using a -meter data.

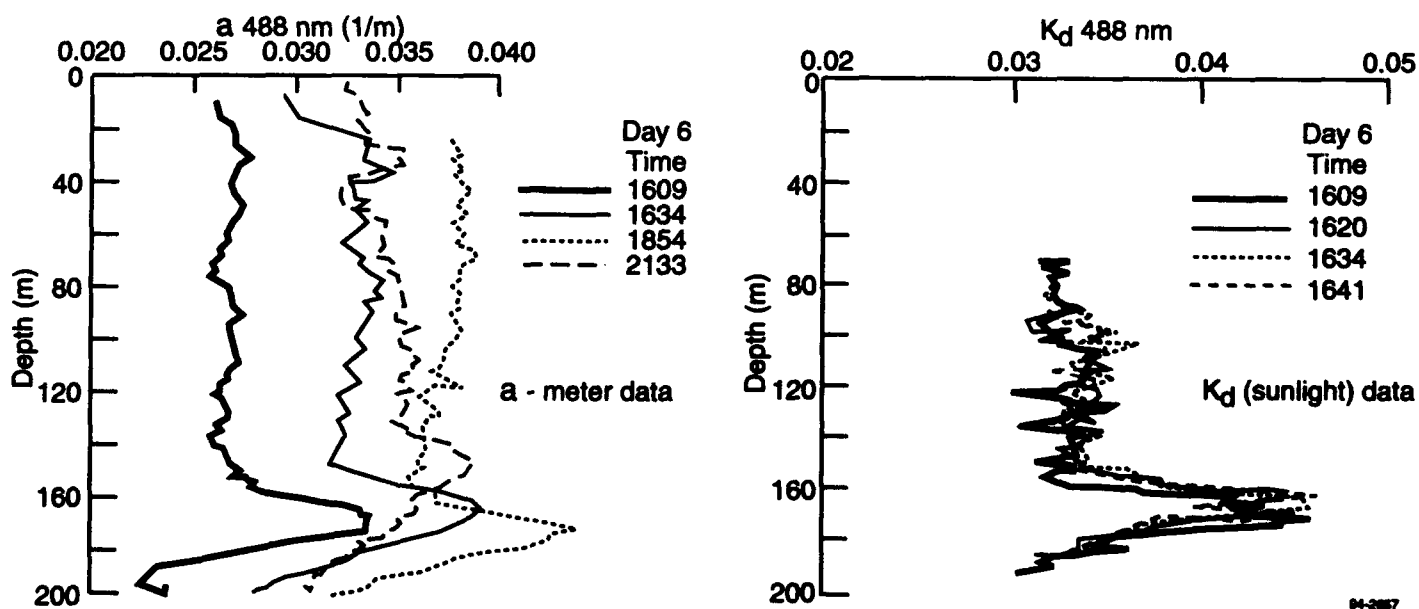


Figure 3. Profiles Exhibiting Unexplained DC Shifts in the a -meter Data. Note that the K_d Profiles do not show the DC shifts exhibited by the a -meter between the casts at 16:09 and 16:34.

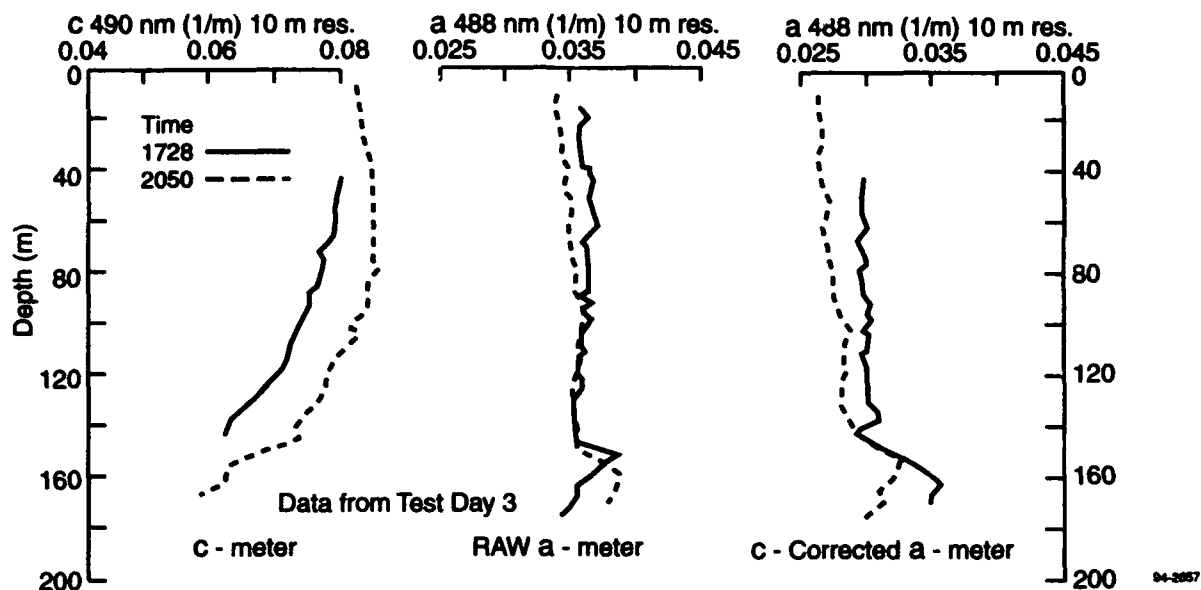


Figure 4. Profiles Showing How the c-Correction (Eqn. 4) Can Introduce Biases Between a-meter Profiles that Otherwise Had Similar Readings. (See data between 80 and 120 m depth.)

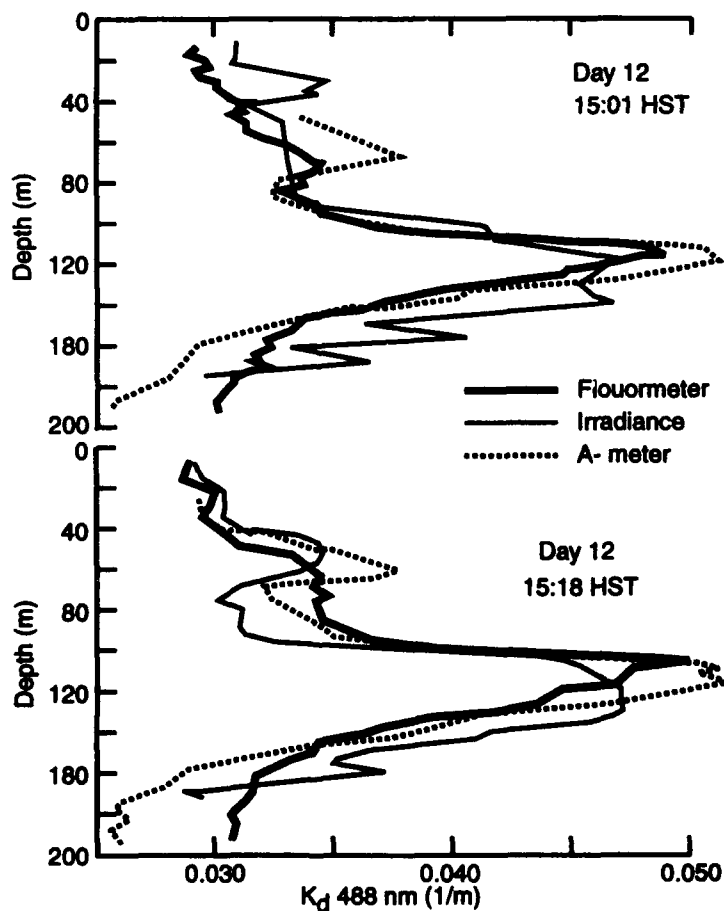


Figure 5. Comparisons Among a-meter Profiles, K_d Profiles Inferred from Fluorometer Data, and K_d Computed from Sunlight.

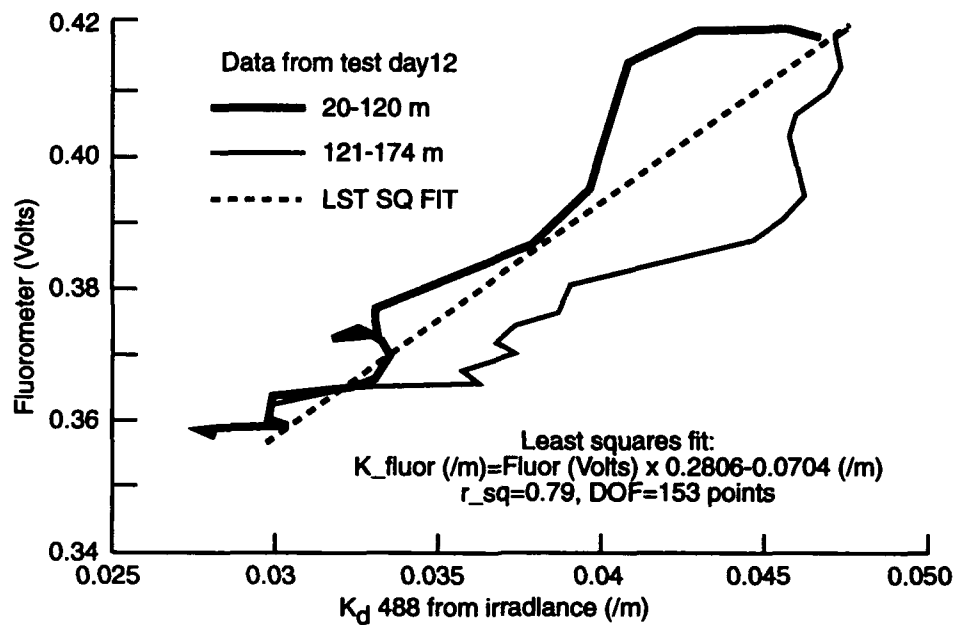


Figure 6. Plot of Raw Fluorometer Voltage Versus Sunlight-Derived K_d . Note the change in slope below 120 m depth.

A photometer for the continuous measurement of Calcite-dependent light scatter in seawater

Katherine A. Kilpatrick, William M. Balch
University of Miami, Rosenstiel School for Marine and Atmospheric Science,
Miami, Florida 33149

Yuntao Ge, Kenneth J. Voss
University of Miami, Physics Department,
Coral Gables Florida 33124

ABSTRACT

Biogenically-produced calcite represents a significant source of light scatter in the ocean, poorly defined in space and time. One reason for this lack of observations is that standard shipboard techniques for measuring light scatter are slow and labor intensive. We describe an automated photometer for measuring 90° light scatter due to calcite on time scales as short as a minute. Raw seawater continuously flows through a 1 mL glass cuvette illuminated by a helium-neon laser. A photodiode is used to measure the 90° light scatter of particles in the incident beam. During each sampling interval, a calibrated addition of weak acid lowers the seawater pH to dissolve the calcite and another 90° light scatter measurement is made. Standard curves are prepared using calcium carbonate coccoliths from the coccolithophore *Emiliania huxleyi*. The relationships between acid-labile light scatter and coccolith abundance give an r^2 of 0.96-0.99. The light scatter photometer is coupled to a fluorometer, temperature and salinity probe to relate the suspended calcite concentration to algal distributions and hydrography. We show some examples of its performance at sea.

1. INTRODUCTION

In recent years, there has been much interest in the phenomenon of mesoscale coccolithophore blooms. These blooms increase the visible reflectance of seawater from 2-5% to values as high as 25%. The spectral effect of these blooms results in a color change of the water from blue to a turquoise. Sightings of this condition have been noted as "whitings" in ship's logs from around the world¹. Many of these white water blooms have been reported to be predominantly composed of the coccolithophorid *Emiliania huxleyi*² but can also be caused by other coccolithophore species³. The coccolithophoridae order of phytoplankton are covered with calcium carbonate scales (coccoliths) which can dramatically affect the shape and magnitude of the volume scattering function. In blooms of coccolithophores, as much as 75% of the total backscatter is due to calcite coccoliths⁴. Our estimates suggest that even in non-bloom conditions calcite may represent 10-20% of the total backscatter. Backscatter due to these calcite particles dramatically changes ocean reflectance as seen by remote sensing ocean color satellites.

The impact of calcite on the backscattering coefficient has been assessed by measurement of the volume scattering function before and after dissolution of the calcite particles⁴. This measurement is extremely tedious to perform, which limits sample frequency. We report here the development of an automated flow thru 90° light scatter instrument which can be calibrated to the coccolith concentration.

2. OPTICAL INSTRUMENT DESIGN

The scattering meter uses a 5mW CW He-Ne laser at 632.8nm as the light source (Fig. 1). Light from the laser passes through a glass beam splitter which sends a portion of the light (4%) to a 10

mm² silicon photodiode(Melles Griot 13DSI007) which is used to monitor the laser power. The remaining light travels thru a lens which focuses the beam on a 1 cm glass cuvette. The light scattered to 90° is collected by a plano-convex 25.4 mm focal length lens which focuses the light onto another photodiode detector (Melles Griot 13DSI007). This geometry gives a full acceptance angle of 22 degrees. Each of these detectors have independent gain adjustments. Voltage from each diode is passed to a pre-amp and amplifier and the analog signal from each is converted to digital form by a 16 bit A/D board in the computer controller (286 PC). The signal detector voltage is divided by the laser monitor voltage to compensate for any changes in laser power during sampling.

3. DATA ACQUISITION

The instrument was fitted with a microvolume 0.5 ml rectangular flow thru cuvette. A small glass mixing coil was placed on the bottom entry port of the cuvette. Seawater was continuously pulled thru the system by a peristaltic pump at 11.6 ml per minute resulting in a 10 second turnover time of water in the cuvette. It is important that the sample be pulled rather than pushed thru the system because the delicate cells and particles can be damaged as they pass over the pump head, dramatically changing the shape and hence the optical characteristics. Every minute for a 30 second duration a second peristaltic pump was activated injecting 0.3 % glacial acetic acid at a rate of 0.23 mL per minute upstream of the mixing coil, into the stream line, dropping the pH to 5.8. As the acidified sample passed around the mixing coil, calcite in the sample dissolved. Previous lab results have demonstrated that a pH of 5.8 was not low enough to damage the cultured phytoplankton cells on this time scale (unpublished data.). The amount of light scatter before and after the addition of the acid was recorded. If calcite was present in the sample then the 90° light scatter was greater in the non-acidified (calcite present) than the acidified (calcite dissolved). The difference in scatter was proportional to the amount of calcite in the sample, henceforth this will be referred to as acid-labile light scatter. In the absence of calcite, no change in light scatter was detected.

A Turner 1-11 fluorometer configured for in- vivo chlorophyll fluorescence and an Inter-Oceans temperature and salinity probe were also in the flow stream. All data were collected on an IDS Turbo 286 computer with a National Instruments 16 channel A/D board and Labtech Notebook software. During along-track measurements seawater came from the ship's seawater chest (2m depth), then through stainless steel pipe to the ship's lab. Data was collected at 3 minute intervals. Hourly discrete samples were analyzed for extracted chlorophyll and particulate calcite.

Vertical profiles were obtained with a pumping system, the hose of which was attached to a CTD rosette. The hose was raised at 2 meters per minute with a maximum possible depth of 120 meters. The seawater was brought into a large tub on deck for debubbling, where a Little Giant pump in the bottom of the tub moved the water into the main lab.

4. ANALYTICAL METHODS

Particulate calcite was determined by flame photometric atomic absorption spectroscopy (Perkin Elmer model 2380). One liter of seawater was filtered onto a pre-combusted Whatman GFF 25mm filter. The filter was rinsed with 20mM borate buffer, pH 8.0 to remove interstitial seawater. Filters were then frozen for later analysis. Samples were processed by digesting filters in 2 mL of 50% trace-metal clean hydrochloric acid and maintained in a water bath at 40°C overnight. Eight mL of 1% lanthanum chloride were added to the sample, then centrifuged to remove the filter. Dissolved calcium in solution was analyzed by absorption at 422.7nm. using a 10cm flame. The instrument was calibrated using a commercial calcium standard from Fisher Scientific. The *in vivo* chlorophyll fluorescence was calibrated by linear regression with discrete

samples. The extracted chlorophyll and phaeopigment concentrations were determined by the method of Yentsch and Menzel⁵ as modified by Holm-Hansen⁶. Particles and cells were enumerated in a Palmer Maloney counting chamber using an epi-fluorescence microscope with a polarization attachment.

5. CALIBRATION OF THE GE-METER

The linearity of the detector was checked using a series of neutral density filters. A culture of the coccolithophore *Emiliana huxleyi* at a concentration of 9.62×10^2 cells ml^{-1} and 8.75×10^3 coccoliths ml^{-1} was pumped thru the cuvette at 3.5 ml per minute. Combinations of neutral density filters were placed in front of the signal detector to attenuate the 90° light scatter of the sample and the voltage of each detector was recorded. The ratio of the signal to laser monitor was found to have a linear response over 3 orders of magnitude (Fig.2). The detector was able to discriminate between 0.2 μm filtered distilled water (Milli-Q) and filtered seawater with a signals of 0.639 and 0.785, respectively. These values are within the mid-range of the dynamic response of the detectors set at the lowest gain. A dilution series was measured of seawater containing only free coccoliths from *E. huxleyi* (Fig. 3). The data in this figure represents the total 90° light scatter for the sample which includes both seawater and coccoliths. The curvilinear response is due to the fact that below 10,000 coccoliths ml^{-1} most of the total 90° light scatter is due to water. The instrument was found to be sensitive to 1,000 coccolith ml^{-1} and remained linear past 90,000 coccoliths ml^{-1} which represents bloom conditions (Fig. 4). This range of concentrations of coccoliths represents 0.2-20 μg of inorganic Carbon per liter as calcite, assuming 0.2pg of carbon per coccolith⁷.

6. DATA ANALYSIS

The data from the scattering meter was continually acquired at a rate of one sample every 0.2 seconds. As the acid pump was triggered on and off, the resulting data stream over a 1 minute period had a square wave appearance when calcite was present. The minimum duration of the plateaus in the wave form was about 20 seconds with a 10 second transition interval between the peak and trough as the calcite dissolved. A 40 point average was applied to the data during the 10 second interval before the acid pump was triggered on or off. The non-acidified and acidified data were independently smoothed using a 4 point running average. Since determination of the acidified and non-acidified value were not synchronous, rapidly changing light scatter caused an artifactual value for the acid labile light scatter. To correct for this, data from the non-acidified samples were interpolated to the time of the acidified sample. The acidified value subtracted from the interpolated, non-acidified data point represented the acid labile light scatter.

7. FIELD DATA

Surface data collected from 2°N-1°N latitude along 140°W longitude during the JGOFS equatorial pacific cruise in August-September 1992 are shown in figure 5. A hydrographic front and an increase in chlorophyll fluorescence occurred between 1.6°-1.5°N. This front was associated with a decrease in temperature (Fig.5A). The total 90° light scatter (non-acidified) began increasing at 1.6°N but remained high until 1.3°N even though chlorophyll had begun to decrease (Fig.5B). The non-acidified and acidified 90° light scatter were the same from 1.9°N to 1.65°N and again between 1.34°N to 1°N. The acid labile 90° light scatter had a small peak at 1.65°N with three major peaks between 1.44° to 1.32°N.(Fig. 5C). These acid labile peaks were not located in the region of highest chlorophyll concentrations. Calcite as carbon ranged from 2.2-5.0 μg per liter along the transect. Differences in sample size and frequency between the light

scatter and calcite measurements precluded a direct comparison, however the two values generally co-varied over the transect.

A depth profile from the vertical pumping system at 12°N 140°W in the equatorial Pacific is shown in Figure 6. Values for acid labile 90° light scatter were close to zero for most of the profile with a well defined peak at about 50m (Fig.6A). Broad peaks in both chlorophyll and total 90° light scatter occurred at 75m (Fig.6B), 25 meters below the peak in acid labile 90° light scatter, suggesting that coccolithophores were living above the chlorophyll maximum. Samples of particulate calcite taken from a rosette cast 12 hours prior to the pump profile showed a peak in calcite carbon at 45m.

8. CONCLUSIONS

Acid labile light scatter calibrated well to coccolith concentration in the lab cultures ($r^2=0.99$) and varied rapidly over short spatial scales both in the vertical and horizontal. Future work will involve absolute calibration of the detector at various gains and improved sampling design such that a direct comparison between acid labile light scatter and particulate calcite can be made at sea. This instrument will be a useful shipboard tool for high resolution mapping of calcite particles in the sea.

9. ACKNOWLEDGEMENTS

W.M.B. and K.A.K. were supported by the Ocean Optics program of the Office of Naval Research (N0014-91-J-1048), National Science Foundation (OCE-9022227), and NASA(NAGW2426). K.J.V. and Y.G. were supported by ONR (N0014-90-J-1505).

10. REFERENCES

1. Brongersma-Sanders, M. (1957) "Mass mortality in the sea". Mem. Geol. Soc. Am., 67, 941-1010.
2. Holligan, P.M., Viollier, M., Harbour, D.S., Camus, P. and Champagne-Phillipe, M. (1983) "Satellite and ship studies of coccolithophore production along a continental shelf edge". Nature, 304, 339-342.
3. Balch, W.M., Eppley, R.W., Abbott, M.R., Reid, F.M. (1989) "Bias in satellite-derived pigment measurements due to coccolithophores and dinoflagellates". J. Plank. Res., 11, 575-581.
4. Balch, W.M., Holligan, P.M., Ackelson, S.G., Voss, K.J. (1991) "Biological and optical properties of mesoscale coccolithophore blooms in the Gulf of Maine". Limnol. Oceanogr., 36, 629-643.
5. Yentsch, C.S. and Menzies, D.W. (1963) "A method for the determination of phytoplankton chlorophyll and phaeophytin by fluorescence". Deep-Sea Res., 10, 221-231.
6. Holm-Hansen, O., Lorenzen, C.J., Holmes, R.W., Strickland, J.D.H. (1965) "Fluorometric determination of chlorophyll". J. Cons. perm. int. Explor. Mer., 30, 3-15.
7. Balch, W.M., Holligan, P.M., Kilpatrick, K.A., (1992) "Calcification, photosynthesis and growth of the bloom-forming coccolithophore, *Emiliania huxleyi*". Cont. Shelf Res., 12, 1353-1372.

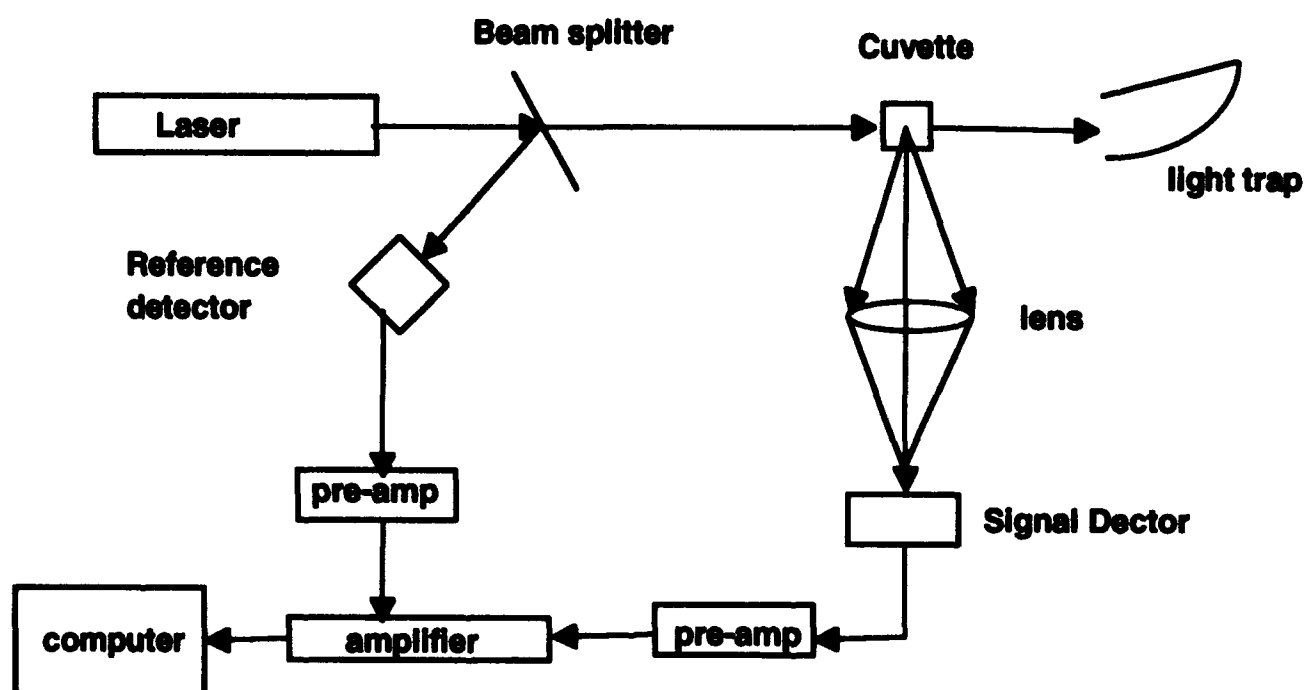


Figure 1 Scattering meter optical layout

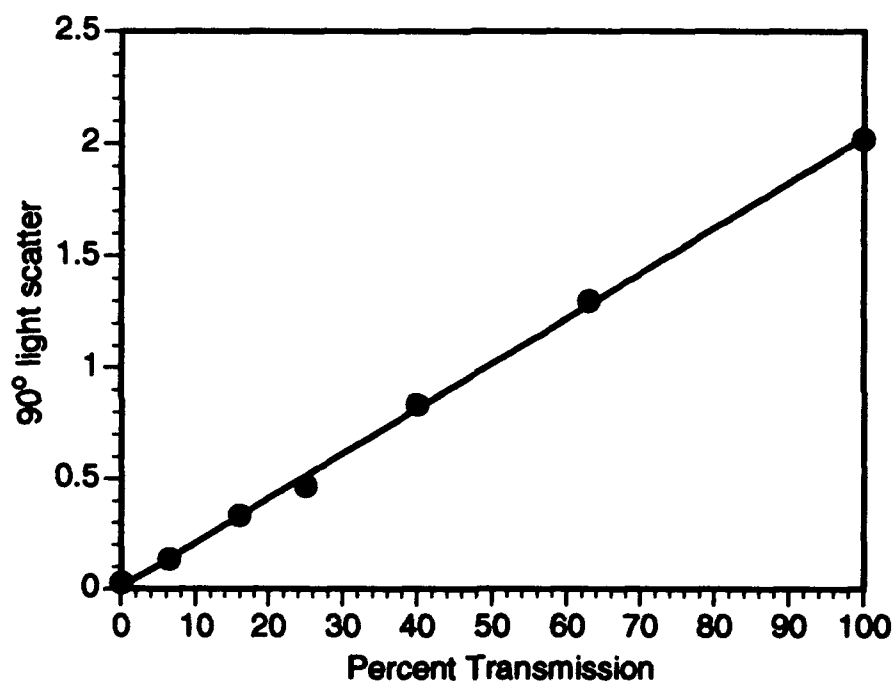


Figure 2 Linearity response of the Signal detector: The scattered light was attenuated with neutral density filters.

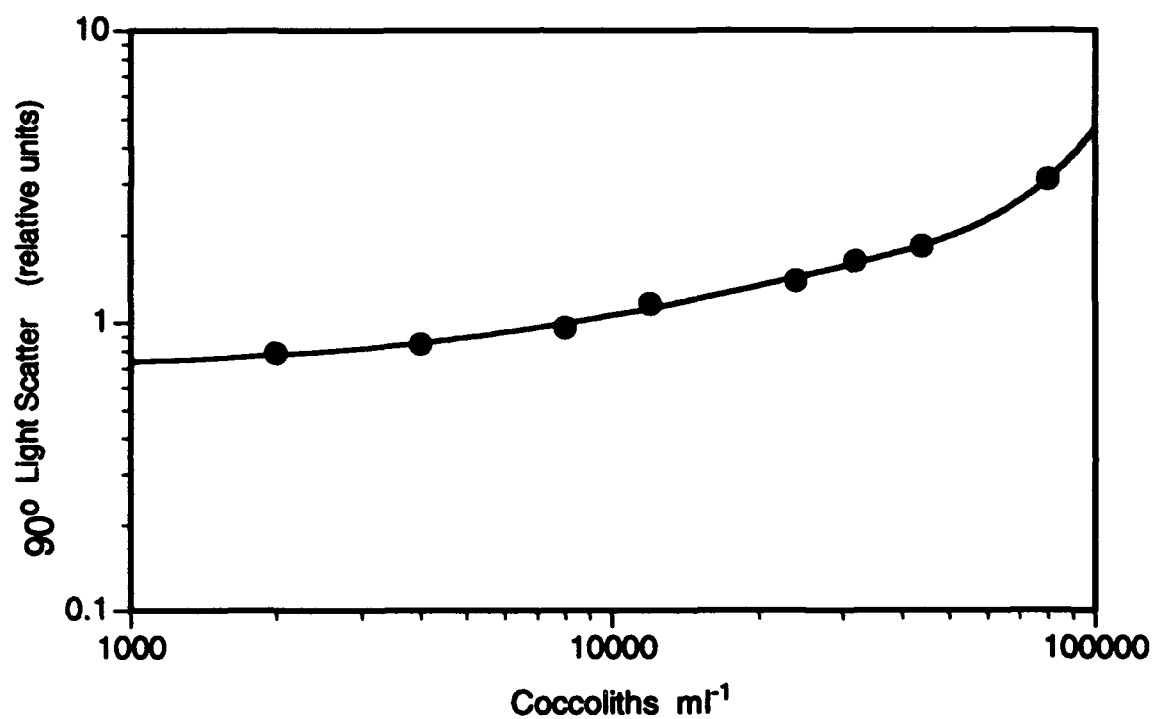


Figure 3 Dector response to increasing coccolith concentration: The data represent the contribution of both seawater and coccoliths to the total 90° light scatter signal.

$$f(x) = 2.875192E-5 * x + 7.279035E-1 \quad R^2 = 9.912294E-1$$

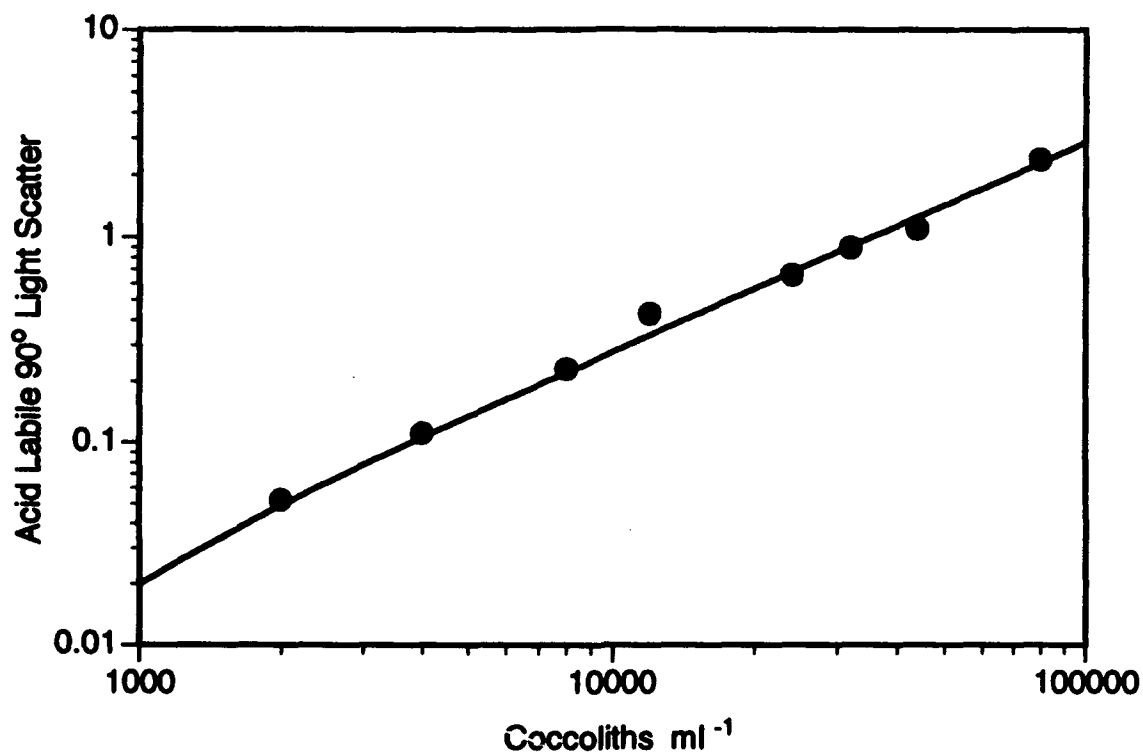


Figure 4 Acid-labile 90° light scatter versus coccolith concentration.
The acid-labile value is calculated as the difference between the total and acidified light scatter.

$$f(x) = 2.878954E-5 \cdot x + -8.955551E-3 \quad R^2 = 9.902170E-1$$

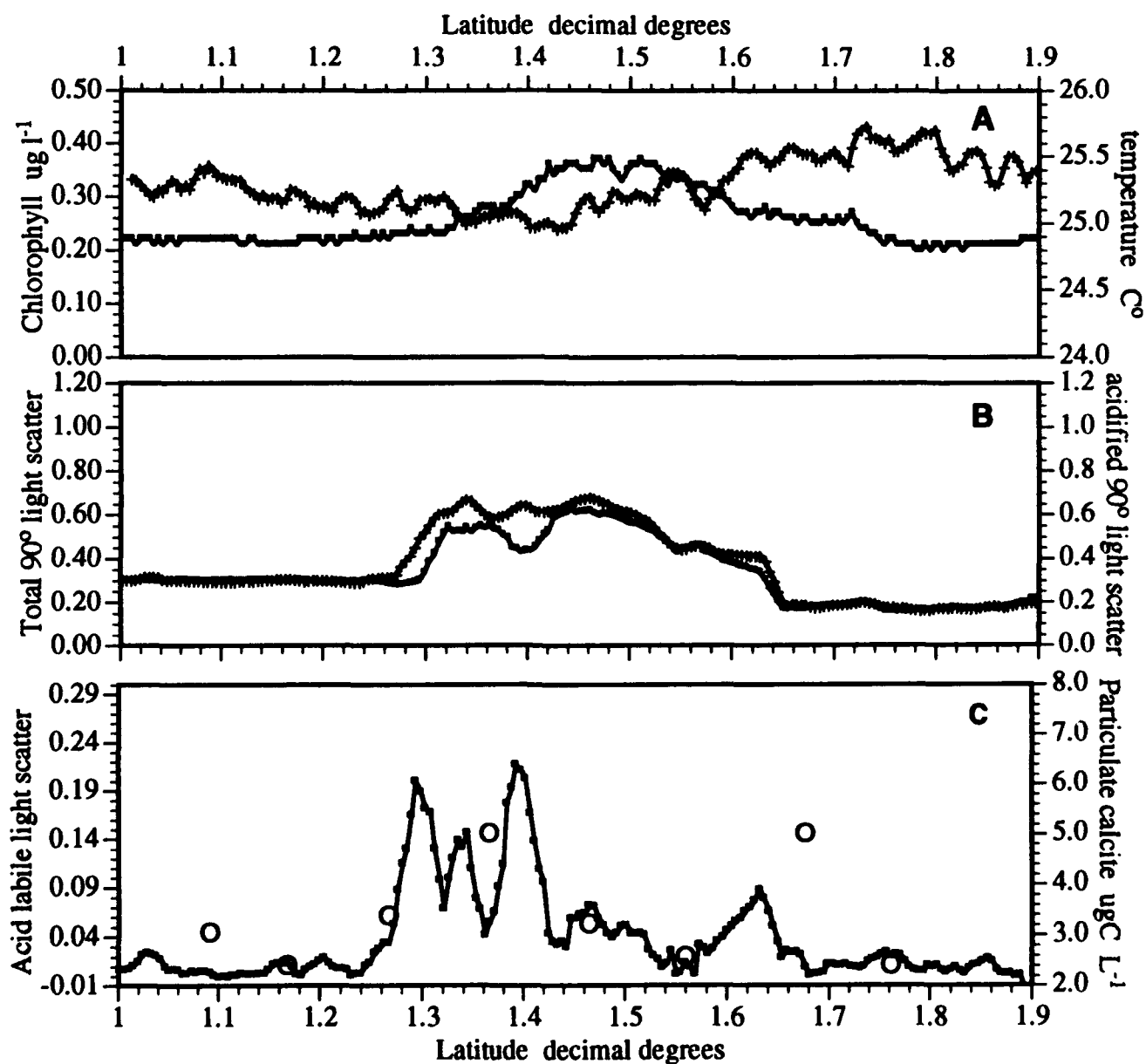


Figure 5 Portion of Transect from Equatorial Pacific along 140W Longitude.

A. + Temperature, • Salinity; B. + Total 90 $^{\circ}$ light scatter, • acidified light scatter;
C. • Acid labile light scatter, o Particulate Calcite.

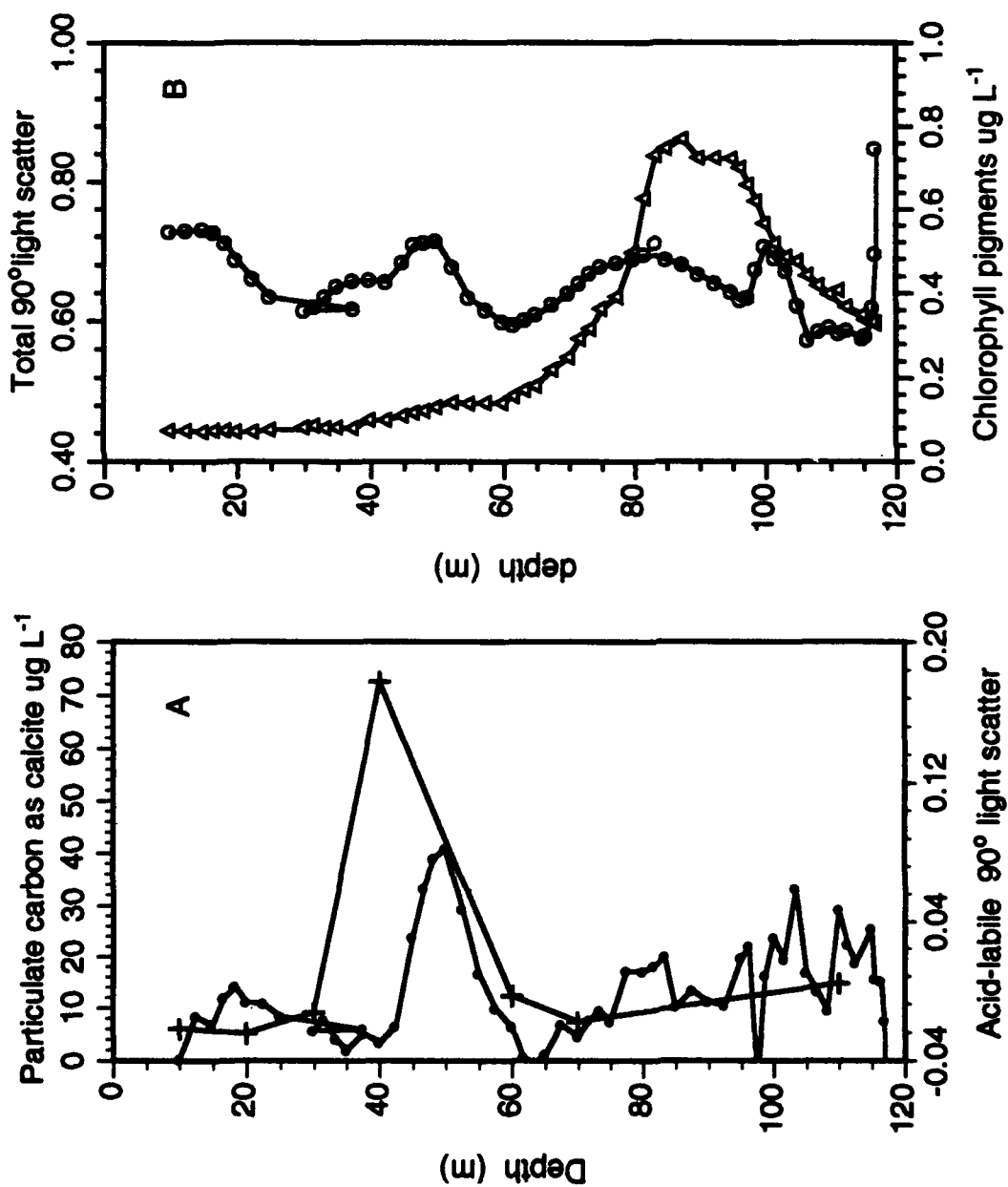


Figure 6, Vertical profile 12N 140W in the Equatorial Pacific

A; + Particulate inorganic Carbon as calcite, \bullet acid-labile 90° light scatter; B: Δ chlorophyll ug L^{-1} ,
 O Total 90° light scatter

New instrument for measuring the scattering
coefficient and the concentration
of suspended particles in turbid water

L. S. Dolin

Institute of Applied Physics, Russian Academy of
Sciences, 46, Uljanov Ul., Nizhny Novgorod, 603600

I. M. Levin and T. M. Radomysl'skaya

P.P.Shirshov Institute of Oceanology, St. Petersburg Branch,
Russian Academy of Sciences, 11, Tavricheskaja Ul.
St. Petersburg, 193015

ABSTRACT

A new method of measuring the total scattering coefficient b of turbid water is described. The method is based on measuring the irradiance and radiance from a point isotropic source. It is shown that the method accuracy can be improved by using the empirical relations between b and some integral parameters of the scattering phase function. A simple scattering meter "Turbido" based on this method has been designed, patented, calibrated, and tested. The instrument is intended for in situ measurements of b and concentration of suspended particles C in tap and natural waters. In the red spectral region the measurement range of b is $0.18-18 \text{ m}^{-1}$, C ranges from 0.3 to 30 mg/l. The advantage of the instrument compared with nephelometers is its simplicity and weaker dependence of its readings on sizes of suspended particles.

1. INTRODUCTION

At present, the hydroopticians have no instruments for measuring the scattering coefficient b , which would be as simple and reliable as instruments for measuring the attenuation coefficient c . The scattering coefficient is usually determined by measuring either the volume scattering function $\beta(\theta)$ or its value at a given scattering angle θ_0 . In the first case, b is calculated by integration of $\beta(\theta)$ over entire solid angle, in the second case, it is expressed through $\beta(\theta)$ by empirical equations, e.g.¹

$$\log b = 0.86 \log \beta(6^\circ) - 0.56. \quad (1)$$

The shortcoming of these methods results from the necessity of using rather high-powered light sources and high-sensitive receivers for measuring weak light signals, as well as arrangements for angle selection and second processing. The accuracy of determining b from Eq.(1) may be too low.

Here we describe a new method of measuring b ². The advantages of this method lie in its simplicity and high enough accuracy. The method is based on measuring radiance and irradiance from a point isotropic source placed in the water.

2. ALGORITHM OF DETERMINING THE SCATTERING COEFFICIENT

The apparent radiance of point isotropic source in turbid medium is attenuated with distance r according to the Bouguer law

$$L = L_0 \exp(-cr), \quad (2)$$

where L_0 is the inherent source radiance, $c = a + b$, a is the absorption coefficient. This law holds within the limits $br \leq \tau_0$, provided the source size (d) is small enough.

Attenuation of irradiance from such a source with high accuracy is computed from³

$$E = 0.25 \pi d^2 r^{-2} L_0 \exp[-(a + b \varphi_{45}) r], \quad (3)$$

where φ_{45} is the scattering probability for the scattering angle range $\theta \geq 45^\circ$. It is related to average cosine of the scattering phase function by the regression⁴

$$\varphi = 0.880 - 0.885 \langle \cos \theta \rangle. \quad (4)$$

If the irradiance meter and the radiance meter (receivers 1 and 2 in Fig.1) are placed at a distance $r < \tau_0/b$ from the source, the aperture angle of radiance meter being d/r , then the ratio of radiant powers at the detectors of both receivers ($P_1 = \Sigma_1 E_1$ and $P_2 = 0.25 \Sigma_2 L \pi d^2 r^{-2}$) is given by

$$P_1/P_2 = (\Sigma_1/\Sigma_2) \exp[(1-\varphi_{45})br], \quad (5)$$

where Σ_1 and Σ_2 are the areas of entrance pupils of the receivers.

Provided that the receivers form signals u_1 and u_2 which are proportional to P_1 and P_2 , the scattering coefficient can be expressed through the ratio of these signals:

$$b = A \ln(u_1/u_2)/r + b_0, \quad (6)$$

$$A = (1 - \varphi_{45})^{-1} = (0.12 + 0.885 \langle \cos \theta \rangle)^{-1}. \quad (7)$$

The value of b_0 in Eq.(6) depends on receiver parameters (Σ_1 and Σ_2 , amplification of the electronic section, etc.). It turns out to be zero when the receivers are balanced to suit the condition $u_1 = u_2$ for $b = 0$.

3. SOURCES OF MEASUREMENT ERRORS

The unknown factor A in Eq.(6) does not prevent measuring b with a rather high accuracy. Long-standing investigations of the inherent optical properties in various regions of the World Ocean have shown that $\langle \cos \theta \rangle$ ranges from 0.75 to 0.98. According to Eq.(7), the corresponding values of A lie in a range between 1.013 and 1.276. Therefore, without a priori information about the value of $\langle \cos \theta \rangle$, the error of determining b by Eq.(6) will not exceed 11.5%, if the real value of A in this equation is replaced by the

average value $\langle A \rangle = 1.145$.

The accuracy of measurement of b can be increased through using correlative relations between b and scattering phase function asymmetry coefficient K ^{3,5}, and between K and $\langle \cos \theta \rangle$.⁶ Data on the ranges of K , $\langle \cos \theta \rangle$, and A in waters with $b > 0.05 \text{ m}^{-1}$ and in very pure waters ($b < 0.05 \text{ m}^{-1}$) are presented in Table 1. Besides, Table 1 contains average values of A and maximal relative errors (δb) of determining b by Eq.(6), provided that A in this equations takes the value of $\langle A \rangle$, depending on the measurement range of b .

Table 1

b	$b > 0.05 \text{ m}^{-1}$	$b < 0.05 \text{ m}^{-1}$
K	22-170	12-22
$\langle \cos \theta \rangle$	0.87-0.98	0.75-0.87
A	1.013-1.12	1.12-1.28
$\langle A \rangle$	1.07	1.20
$\delta b (\%)$	5.0	6.5

In accordance with data in Table 1 the following algorithm may be used for determining b . Let the factor A in Eq.(6) be equal to 1.07. If the result of measurement is $b' > 0.045 \text{ m}^{-1}$, we take that $b = b'$. If $b' < 0.045 \text{ m}^{-1}$, we take $b = 1.12 b'$. As a result, the error of determining b caused by variations of A will decrease to 5% for $b > 0.05 \text{ m}^{-1}$ and to 6.5% for $b < 0.05 \text{ m}^{-1}$.

The "base" of the instrument (r) and size of the light source (d) should be chosen with account of the condition that in a given range of b the exponential law for radiance (Eq.(2)) is valid. It means that radiance of scattered light (L_s) in r - direction must be much smaller than that of direct (unscattered) light (L_d).

As a result of scattered light entering the receiver 2 the instrument will read an underestimated value of b :

$$b' = b (1 - \delta b), \quad (8)$$

the relative systematic measurement error being dependent on the L_s/L_d ratio as

$$\delta b = A \ln (1 + L_s/L_d) / br. \quad (9)$$

From results of small-angle diffusion approximation of the radiation transfer theory³ the following formula can be written

$$\delta b = \frac{1}{B} \ln \frac{2 \exp B + \exp(-B) - 3 + NB}{1 - \exp(-B) + NB}, \quad (10)$$

where $B = br/A \approx 0.9 br$, $N = 8\langle\theta_{45}^2\rangle/(3\psi^2)$, $\langle\theta_{45}^2\rangle$ is the variance of the scattering phase function, calculated within the angle range $0 < \theta < 45^\circ$, $\psi = d/r$ is the aperture angle of the receiver 2. Note, that both φ_{45} and $\langle\theta_{45}^2\rangle$ are related to $\langle\cos\theta\rangle$ through linear regressions⁴.

The curves of constant values of δb and the area of the values $\delta b < 0.01$ on the coordinate plane N, B , shown in Fig.2, demonstrate that the systematic measurement error caused by violation of the Bouguer law will be excluded if $N > 300$ and $B < 5$ ($br < 5.5$). The value of $\langle\theta_{45}^2\rangle$ ranges from 0.026 to 0.087⁴. Accordingly, the condition $N > 300$ will be fulfilled in any water if $\psi < 1.5 \cdot 10^{-2}$ rad.

4. ARRANGEMENT AND PARAMETERS OF THE INSTRUMENT

The measurement method was realized in the instrument "Turbido" which has been designed, manufactured, calibrated, and tested. This instrument is intended for rapid in situ measurements of the scattering coefficient and concentration of suspended particles in the tap water and sewage, in natural waters (rivers, lakes, coastal waters), and in cooling reservoirs of the thermoelectric power stations and nuclear power stations. Its measurement range is $b = 0.18-18 \text{ m}^{-1}$ in the red spectral region (600-700 nm). It makes possible measurements of water turbidity in a range of 0.5-50 FTU (Formazine Turbidity Units) and concentration of suspended particles in a range of 0.3-30 mg/liter. The instrument consists of two cable-connected parts: submersible data unit and portable measuring unit.

The data unit is designed in the form of two hermetic boxes connected by a rigid framework (Fig.1), which does not prevent water flowing in the space between the boxes, but protects the receivers from outer lighting. The distance between the box illuminators ("base") is $r = 25 \text{ cm}$. The magnitude of r was computed with the requirement that the designed measurement accuracy be provided in a given range of b . In one of the boxes a light source (light-diode) is placed just ahead of the illuminator. The radiant power of the source is about 20 mW, the radiant intensity being constant in a range of angles within 90° , which enables one to consider the source as isotropic. Two coaxial receivers are situated in the other box. The photo-diode placed directly behind the illuminator measures the irradiance. The radiance meter consists of a lens with a focal length $f = 50 \text{ mm}$, a screen with a hole, 0.5 mm in diameter, and a photo-diode situated behind the screen. The screen is placed in the plane of the source image formed by the lens. The size of the hole is equal to the source image size, therefore the entire unscattered light passing through the lens, falls on the photo-diode. The signals from the photo-diodes after amplification and processing enter the measuring unit in the form of currents i_1 and i_2 . In the measuring unit the currents are converted to the voltages $u_1 = i_1 R_1$ and $u_2 = i_2 R_2$. The calculator forms the signal

$$S = M \ln (u_1/u_2). \quad (11)$$

Setting instrument readings to zero is performed by changing the resistance R_2 . In doing so the condition $S = 0$ ($u_1 = u_2$) is fulfilled for $b = 0$. Controlling the scale factor M enables one to fit the instrument scale to a given value of A/r in Eq.(6) or to graduate the instrument by turbidity samples. The instrument has a two-bit digital indicator, graduated in FTU, and current output of 0-5 mA. Electrical power supply is

autonomous (from a 9V-battery) and from the mains 220 V, 50 Hz . Power consumption is not greater than 2 W. The overall dimensions of the instrument are 0.5 x 0.25 m.

The digital indicator shows the values of turbidity with an accuracy of about 10% in the range 1-50 FTU ($b = 0.36-18 \text{ m}^{-1}$) and about 20% for 0.5 FTU. The current output provides a measurement accuracy not worse than 10% in the entire measurement range.

The dependence of readings of "Turbido" and nephelometer on suspended particle size computed according to the Mie theory shows that readings of "Turbido" depend on particle size more weakly than that of nephelometer (provided that particle concentration is constant). Besides, the radiant power measured in "Turbido" is 4-5 orders of magnitude larger than in nephelometer. This provides simplicity of the instrument.

5. ACKNOWLEDGEMENTS

The authors wish to thank Dr. Victor I. Feigels and Igor V. Bronshtein from St.Petersburg Institute of Fine Mechanics and Optics (St.Petersburg), and Dr. Peter A. Kapustin, Vladislav J. Kallistratov, and Lev B. Gordeev from the Institute of Applied Physics, Russian Academy of Sciences (N.Novgorod), who took part in designing and testing of the first and second versions of the "Turbido". Thanks are also due to Dr. Eduard B. Achnazarov, President of Scientific and Industrial Corporation "Ecology" (St.Petersburg), who supported development and designing of the instrument.

6. REFERENCES

1. V. I. Burenkov, B. F. Kel'balichanov, and O. V. Kopelevich, "Methods of measuring sea water optical properties", *Ocean Optics*, Vol. 1, Nauka Publ., Moscow, pp. 114-139, 1983 (in Russian).
2. I. G. Bronshtein, L. S. Dolin, I. M. Levin, T. M. Radomysl'skaya, and V. I. Feigels, "Method of determination of scattering coefficient and the arrangement for its realization" (patent of Russian Federation No 1784092), *Bull. of Inventions*, No 47, 1992 (in Russian).
3. L. S. Dolin and I. M. Levin, *Theory of underwater imaging (handbook)*, Gidrometeoizdat Publ., Leningrad, 1991 (in Russian).
4. L. S. Dolin, O. V. Kopelevich, I. M. Levin, and V. I. Feigels, "Few-parameter models of light fields in the sea and integral characteristics of the scattering phase function of water", *Izv. Atmos. Ocean. Phys.*, Vol. 24, No 11, pp. 893-896, 1988.
5. V. I. Man'kovsky, "Spectral changeableness of the asymmetry coefficient of sea water scattering phase function ", *Okeanologia*, Vol. 24, No 1, pp. 63-69, 1984 (in Russian).
6. V. I. Man'kovsky, V. A. Timofeeva, V. E. Shemshura, "Relations between the integral characteristics of the scattering phase function in the sea and oceanic waters ", *Optics of sea*, Nauka Publ., Moscow, pp. 38-44 , 1983 (in Russian).

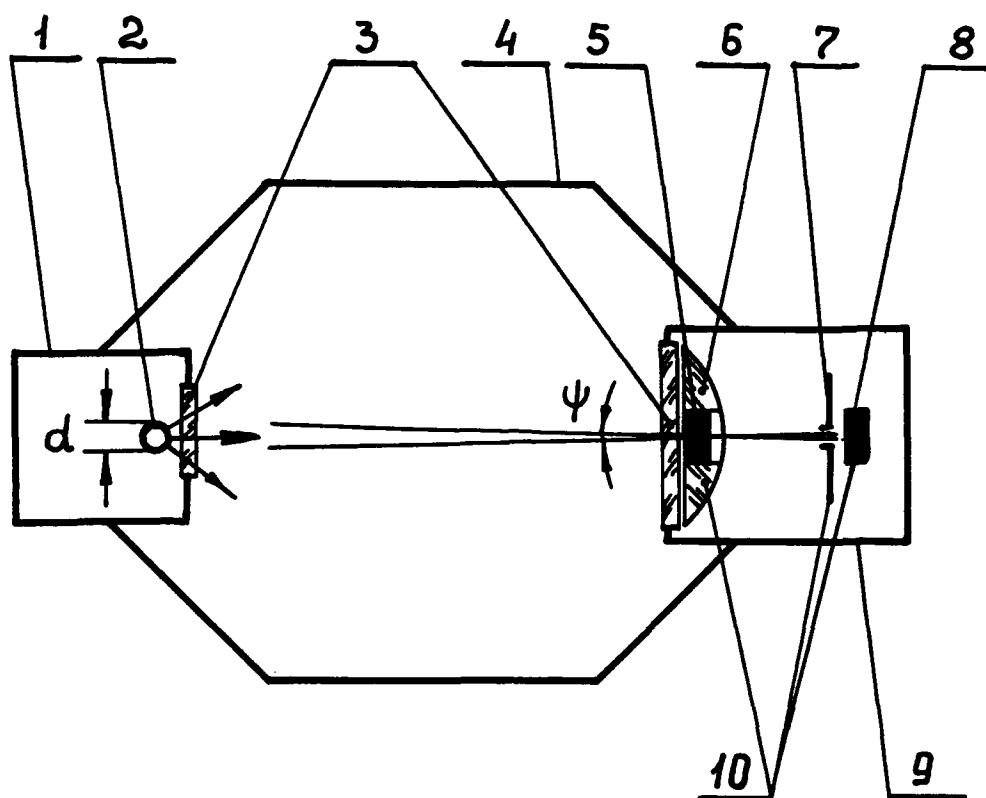


Figure 1. Schematic diagram of the submergible data unit of "Turbido"

- | | |
|-----------------------------------|----------------------------------|
| 1. Transmitter box. | 2. Light source (light-diode). |
| 3. Illuminators. | 4. Rigid framework |
| 5. Receiver 1 (irradiance meter). | 6. Lens. |
| 7. Screen with a hole | 8. Photo-diode |
| 9. Receiver box. | 10. Receiver 2 (radiance meter). |

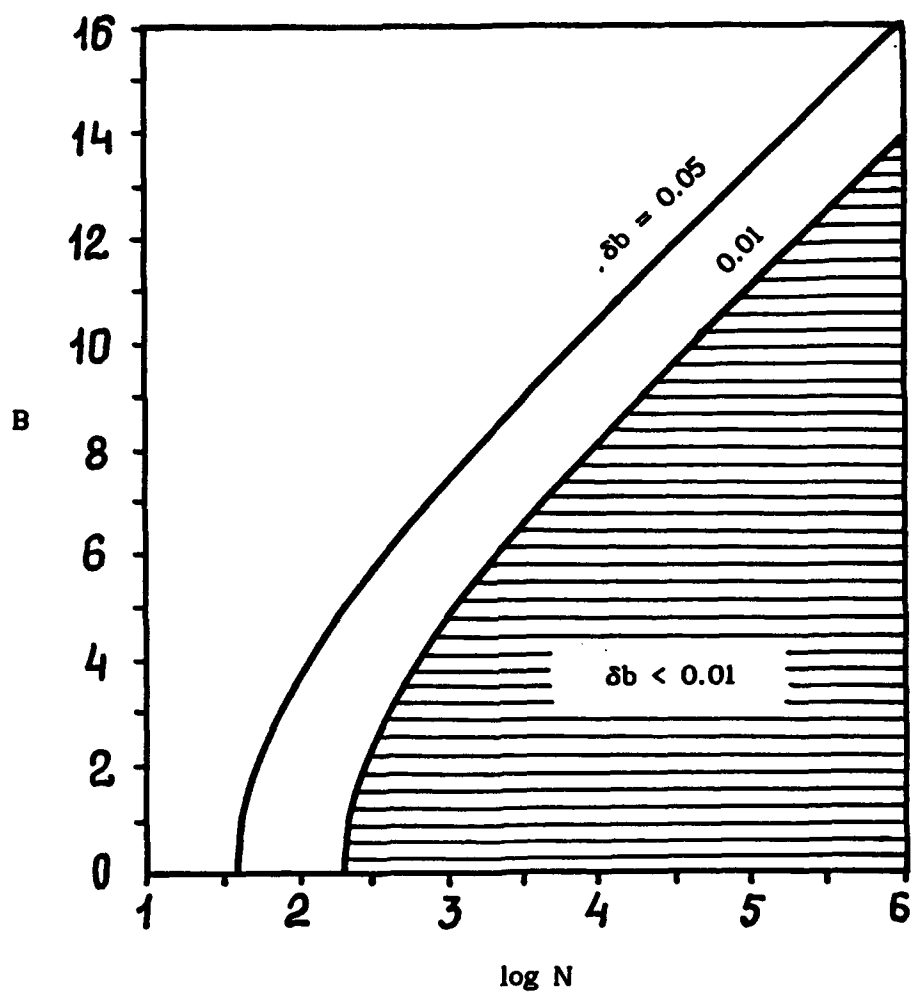


Figure 2. Curves of the constant values of the measurement error δb and the area of the values $\delta b < 0.01$ in the coordinate plane $\log N, B$.

Monte Carlo modelling of the light field in reflective tube type absorption meters

J.H.M. Hakvoort

Faculty of Civil Engineering, Delft University of Technology
PO Box 5048, 2600 GA Delft, The Netherlands

R. Wouts

(Author for communication)

Netherlands Institute of Ecological Research, Centre for Estuarine and Coastal Ecology
Vierstraat 28, 4401 EA Yerseke, The Netherlands

ABSTRACT

The light field in reflective tube type absorption meters was modelled with Monte Carlo methods. The entrance light field was varied and the systems geometry was varied together with the inherent properties of a test medium. This enabled us to calculate the radiance attenuation as a function of the field of view for several variants of a reflective tube absorption meter. It was found that an instrument with a Lambertian entrance light field and a small field of view measures the sum of absorption and backscattering with an error less than 2-5%. This result is independent of the shape of volume scatter functions for surface water. For small fields of view the reflectivity of the cylinder was found not to be critical.

1 INTRODUCTION

The propagation of light through a suspension of particles can be described with two parameters only: the absorption coefficient and the volume scattering function of the medium. These so-called inherent optical properties depend on the physical properties of the constituents of the medium. The inherent optical properties of a sample of water contain all information about its constituents that is obtainable by optical bulk measurements. As a second step in analysis it can be attempted to translate these properties into chemical and physical characteristics, aquatic humus, silt and concentrations of algal pigments. With this approach these water quality parameters can be monitored by monitoring the changes in the inherent optical properties.

Measuring the absorption coefficient of turbid water samples is not trivial. Suspended matter causes light loss by scattering, which leads to an over-estimation of the absorption coefficient. This error is minimised with an optical configuration that ensures that most of the scattered light is intercepted by the detector. Examples are the Ulbricht sphere¹⁶, the semi-integrating sphere and the opal glass method^{14, 13}. The disadvantage of the Ulbricht sphere is that although it measures absorption only, the path length does not necessarily equal the geometrical path length. A disadvantage of the opal glass method is that only light scattered into the forward direction can be measured. Total reflection, caused by the refractive index difference between glass and air, restricts the angle of intercepted light further when measurements are done on a sample contained in a glass cuvet. This leads to an effective field of view of approximately 38 – 41°. A variation of the opal glass method is the filter pad method¹⁷ which uses particle-laden filters as diffusor. These methods are generally used in laboratory work but sample treatment introduces further errors. Automated monitoring of inherent properties is not possible this way and *in situ* measurements are therefore preferable. Several instruments have been built to do this.

Zaneveld *et al.*¹⁸ built a reflective tube absorption meter. In this design a silver coated (second surface) glass tube reflects the forward scattered light of a collimated beam towards a detector with a large field of view. The path length travelled by scattered photons is not equal to the geometrical path length of the tube. Further errors are introduced by the backscattered light and by reflection at the tube boundary. Therefore field data must be corrected with laboratory measurements on suspensions with similar scattering properties. If both beam attenuation and absorption measurements are used for this correction the error in the absorption coefficient will be $\pm 3\%$ of the total scattering. Radiative transfer in the reflective tube absorption meter was modelled with Monte Carlo techniques by Kirk⁷.

Table 1: Characteristics of the submersible absorption meter.

tube	Diameter 25 cm	Length 50 cm	Reflectivity 93%		
detector	Diameter 2.5 cm	Fov 1.5°	Wavelength 400-800 nm	Resolution 1.2 nm	Remark path length adjustable over 5-20 cm

Other instruments make use of the integrated equation of radiative transfer^{3, 9}. The resolution of this method is set by the limiting distance over which irradiance changes may be measured. In photo-acoustic spectroscopy, another method, the sound pulses generated by changes in volume after absorption of light by a sample are measured; sound intensity is proportional to absorbed energy^{15, 1}. Fry and Kattawar² proposed to apply the integrating cavity to measure absorption *in situ*².

The submersible absorption meter developed by Hakvoort *et al.*⁶ is based on the fact that in a diffuse (Lambertian) light field, light scattered out the beam is always compensated for. A detector looking in one direction towards a Lambertian light field should therefore measure absorption plus backscattering, as long as the light field remains diffuse over the whole path length. A Lambertian light field is made from a flat diffuse light source contained in a reflecting cylinder. Physical dimensions and characteristics of the instrument are given in Table 1. In this paper the equation of radiative transfer is solved numerically with Monte Carlo techniques for this instrument and for similar designs. The influence of several design parameters on the performance of such an absorption meter is studied and their optimum choice determined.

2 THEORY

The propagation of light through a medium can be described by the equation of radiative transfer. In a plane parallel medium without internal sources this can be written as

$$\cos(\theta) \frac{dL(z; \theta, \phi)}{dz} = -c(z)L(z; \theta, \phi) + L_{\star}(z; \theta, \phi). \quad (1)$$

Here $L(z; \theta, \phi)$ is the radiance at depth z , normal to the plane of stratification, in a solid angle $d\omega$ centred around direction (θ, ϕ) . θ is the angle with respect to the zenith and ϕ is the azimuth angle. The first term on the right gives the radiance decrease per meter due to the beam attenuation c . The beam attenuation is the sum of absorption a and scattering b . The second term on the right gives the path radiance: ie. the gain in radiance due to light scattered into a beam from all directions,

$$L_{\star}(z; \theta, \phi) = \int_0^{2\pi} \int_0^{\pi} \beta(z; \theta, \phi; \theta', \phi') L(z; \theta', \phi') \sin(\theta') d\theta' d\phi'. \quad (2)$$

Here β is the volume scattering function. It is customary to substitute μ for the cosine of the zenith angle. If there is rotational symmetry around the optical axis of the system and the z -dependence of the beam attenuation and scattering is negligible, the equation of radiative transfer can be rewritten as

$$\mu \frac{dL(z; \mu)}{dz} = -cL(z; \mu) + \frac{1}{2} \int_{-1}^1 p(\mu, \mu') L(z; \mu') d\mu', \quad (3)$$

with

$$p(\mu, \mu') = \frac{1}{2\pi} \int_0^{2\pi} \beta(\mu, \phi; \mu', \phi') d\phi'. \quad (4)$$

Integro-differential equations are difficult to solve, also by numerical means, but with the quasi-single scattering approximation⁴ this equation can be rewritten in a simple form for zenith radiance. The quasi-single scattering approximation is based on the fact that the volume scattering function is strongly peaked in the forward direction. The approximation consists of forcing photons that are not backscattered to scatter forward perfectly and hence to remain in the beam. Backscatter can be treated in two ways, the backscattering part of the original volume scattering function can be used or backscattering can be replaced by isotropic backscattering. Mathematically this can be

Table 2: Notations.

Symbol	Description	unit
$L(\vec{r}, \vec{s})$	radiance at position \vec{r} , direction \vec{s}	$\text{J/s sr}^{-1} \text{m}^{-2}$
$L_*(\vec{r}, \vec{s})$	path radiance at position \vec{r} , direction \vec{s}	$\text{J/s sr}^{-1} \text{m}^{-2}$
E_{0d}	downward scalar irradiance	$\text{J/s sr}^{-1} \text{m}^{-2}$
a	absorption coefficient	m^{-1}
b	scattering coefficient	m^{-1}
b_f	forward scattering coefficient	m^{-1}
b_b	backward scattering coefficient	m^{-1}
c	beam attenuation	m^{-1}
$\beta(\theta)$	volume scatter function	$\text{m}^{-1} \text{sr}^{-1}$
mfp	mean free path	m
$P(s)$	probability distribution function	
$F(t < s)$	probability mass distribution	
θ	zenith angle	rad
ϕ	azimuth angle	rad
μ	$\cos(\theta)$	
$\text{rand}(a, b)$	random deviate uniformly distributed between a and b	
$\delta(x)$	Dirac-delta function	

described with a delta function for forward scattering and an isotropic distribution for backscattering. The volume scatter function then becomes

$$\beta(\theta) = \begin{cases} b_b/2\pi & \text{if } -1 \leq \cos(\theta) < 0 \\ b_f\delta(\theta)/2\pi & \text{if } 0 \leq \cos(\theta) < 1. \end{cases} \quad (5)$$

Substituting this in the radiative transfer equation we get for zenith radiance

$$\frac{dL(z)}{dz} = -(a + b_b)L(z) - \frac{b_b}{2\pi}E_{0u}(z). \quad (6)$$

With $E_{0u}(z)$ the upward scalar irradiation. From the definition for beam attenuation we find

$$\frac{-1}{L(z)} \frac{dL(z)}{dz} = a + b_b + \frac{b_b}{2\pi}E_{0u}(z)/L(z). \quad (7)$$

As long as the last term on the right side is small this expression will be $\approx a + b_b$. This analytical solution of the equation of radiative transfer suggests that the submersible absorption meter as built by Hakvoort *et al.* should work in situations where the quasi-single scattering approximation is valid. If multiple scatter can be ignored the absorption meter should work for any phase function. In the real instrument the light field will not be completely diffuse due to absorption; only the entrance light field can be made diffuse. Volume scattering functions as found for surface water are strongly peaked in the forward direction but are not perfect delta functions. Therefore Monte Carlo modelling will be used to solve the equation of radiative transfer for several different geometries. In reality a detector always has a finite field of view therefore the angular distribution of the light field was studied.

3 MATERIAL AND METHODS

In a Monte Carlo model normalised radiance is interpreted as the probability of finding a photon in a particular direction. The beam attenuation coefficient is interpreted as describing the probability for a photon to travel a certain distance before any interaction with the medium takes place, i.e. before absorption or scattering. If scattering by water is ignored then the absorption by water can be subtracted from the total beam attenuation to give the beam attenuation by the particles in suspension. Then we can interpret the absorption as absorption by particles only. The ratio a/c gives the probability that the outcome of an interaction with the medium will be absorption of a photon. The normalised volume scattering function is interpreted as to give the probability that a photon trajectory will deviate from its current trajectory by a certain scattering angle. Volume scattering function as measured by Petzold¹⁰ were used. Reflectivity is interpreted as the probability that a photon hitting a wall will be reflected.

In our coordinate system the light source is placed at z -position 0, centred around the origin and emitting light upwards. The detectors are placed on the z -axis facing the light source. Direction cosines depend on the zenith angle, θ , ie. the angle with respect to the z -axis and the azimuth angle, ϕ , ie. the angle in the xy -plane with respect to the x -axis.

All random deviates, except for the uniform probability distribution, were calculated with the transformation method¹¹. That is generate a random number and interpret this as the area under the graph of the desired probability distribution. Then find the value for which this area is reached, this is the random deviate we need. This involves solving the inverse of the mass distribution of the probability distribution. If for a given mass distribution function the inverse of its probability distribution function could be found analytically the transformation method was used directly. If not, the inverse probability function was calculated with the Newton-Raphson method. If the probability mass function was available in tabular form its distribution function was calculated with the trapezium rule. Hunt search¹¹ in combination with the transformation method results in the interval that contains the random deviate. A random value uniformly distributed in this interval was chosen.

To avoid statistical correlation between the random deviates selected the number of times a random number is generated should not exceed 5% of the period of the random number generator. In our simulations not more than 10^7 photons employing approximately 10 random numbers each were generated. The period of the generator is approximately $16 * (2^{31} - 1)$, much larger than the number of times a random number was generated.

The model follows generated photons one at a time. The length of each step made by the photon is determined by the position closest to the current position, the position of reflection, the position of interaction with the medium or the position of detection. Photons moving past the boundary of the tube are no longer followed. Backscattering can be quite large, so the position of the last detector was chosen before the end of the tube. If the photon is reflected its direction cosines are recalculated when the photon survives the reflection. If interaction with the medium takes place it is decided whether the photon is scattered or absorbed. When scattering takes place the new direction cosines are calculated. If the photon is detected, its current angle with respect to the z -axis is logged.

The light field as calculated by the model is analysed by adding all photons that arrived at a given position while travelling in a direction with a zenith angle smaller than or equal to the field of view of a detector. A straight line is fitted through the (natural) logarithm of these cumulative distributions and the direction coefficient is taken as the measured radiance attenuation. For each geometry of an absorption meter the ratio of this number with the true absorption is calculated. This procedure is only valid when the light field changes exponentially, ie. when Lambert-Beers law is valid. If the light field does not decrease exponentially the radiance attenuation is calculated from $-1/z \ln(I_0/I(z))$, with z the position of the last detector.

4 RESULTS

4.1 Collimated beam

A reflective tube with the same diameter and length as the reflective tube absorption meter developed by Zaneveld *et al.*, illuminated by a collimated beam, was modelled. Table 3 gives the parameters that were used with the model. The results should be directly comparable with the Monte Carlo modelling of a reflective tube as done by Kirk⁷. The model developed there was slightly more refined since the motion of a photon in the cylinder wall was taken into account, as appropriate for a second surface reflector. Our model assumes a first surface reflector. Also the method of analysing the data differs slightly. Only the number of photons at position $z = 0$ and at the position of the last detector are taken into account by Kirk. In our model the calculation of the radiance attenuation coefficient is influenced by light intensities at intermediate positions as well. So statistical fluctuations are less important. This is only valid if the light field decreases exponentially. Figure 1a shows the result of varying the ratio b/a , agreement between our model and the calculations done by Kirk is better than 5%. Figure 1b shows the result of varying the reflectivity of the cylinder wall. The figures also show the ratio of the measured radiance attenuation to $a + b_r$. As can be seen the measured radiance attenuation is better correlated with $a + b_r$ than with a .

Table 3: Parameters used in the model. Each simulation consists of following 10^6 photons.

light source	collimated	lambertian
tube length [m]	0.25	1
tube diameter [m]	0.01	0.25
tube reflectivity	0...100%	0...100%
field of view	0...90°	0...90°
c [m^{-1}]	0...2.2	2 & 10
a [m^{-1}]	0.1 & 0.2	0.18...9.1
b [m^{-1}]	San Diego Harbor	San Diego Harbor, Tongue of the Ocean, Southern California

4.2 Lambertian light source

A configuration similar to the submersible absorption meter as built by Hakvoort *et al.* illuminated with a Lambertian light source was modelled. Table 3 gives the parameters that were used with the model. Figure 2a compares the measured radiance attenuation with the true absorption and Figure 2b compares the measured radiance attenuation with the the sum of true absorption and backscattering. The true beam attenuation is kept constant at 2 while the true absorption and scattering were varied. The reflectivity of the tube was set to 100%. Petzold's San Diego Harbor volume scattering function was used. It can be seen that the calculations for the smallest field of view still suffer from statistical noise. The trend of the curves is that measured radiance attenuation goes to $a + b_s + \epsilon$, with ϵ a few percent of the true absorption. It can be seen in the figures that measured radiance attenuation with a field of view of 8.5° is almost indistinguishable from true absorption, the difference is approximately 10%. This is supported by the measurements of Hakvoort *et al.*⁵. They describe measurements of upwelling radiance attenuation with a field of view of approximately 8.5° . Upward radiance attenuation was found to be strongly dependent on the absorption. No theoretical reasons were given to explain this.

Figures 3a and b compare the measured radiance attenuation with true absorption and backscattering when the reflectivity of the tube is varied. The true absorption was set to 0.4 m^{-1} and the scattering was set to 1.6 m^{-1} . The smallest fields of view are not much affected by the reflectivity of the tube, the larger fields of view are.

Figures 4a and b compare the measured radiance attenuation with true absorption and backscattering when the field of view is varied and the volume scattering function is varied. From Figure 4b it can be seen that the difference between the volume scattering functions can be completely attributed to difference in backscattering. This indicates that the absorption meter is quite insensitive for the shape of the volume scattering function.

5 CONCLUSION AND DISCUSSION

We found that for a reflective tube type absorption meter with an Lambertian entrance light field the radiance attenuation as measured with a detector with a small field of view almost equals the true absorption plus backscattering. The model developed can be a useful tool to investigate the influence of design parameters as size and reflectivity of the cylinder wall.

With some modifications the model can be used to calculate the reflection in a reflective tube. This makes it possible to model reflection as measured in large scale enclosures as developed by Rijkeboer *et al.*¹². The model could also be used to estimate the effect of shadowing by the finite size of a detector.

6 ACKNOWLEDGEMENTS

This is publication no. 722 of the NIOO-CEMO. The authors like to thank prof. M. Donze for his critical comments. This work was supported by grants from the National Remote Sensing Board (BCRS) and the National Institute for Coastal and Marine Management (RIKZ).

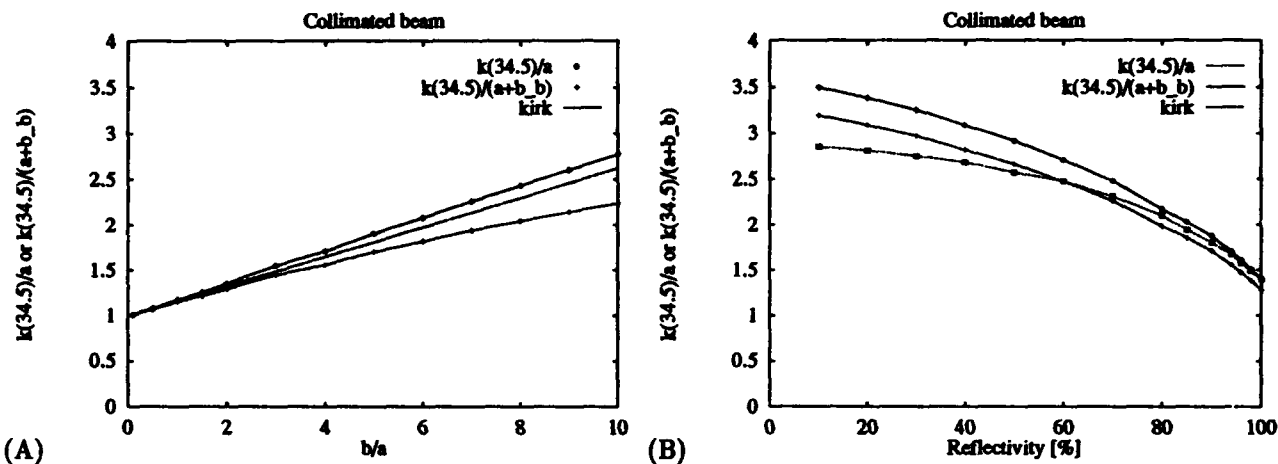


Figure 1: (A) Radiance attenuation of the light field in a reflective tube illuminated with a collimated beam. The absorption is kept constant at 0.2 m^{-1} , the ratio b/a is varied and the reflectivity is set to 94%. Petzold's San Diego Harbor volume scattering function is used. The ratio of measured attenuation to true absorption and absorption plus backscattering for a field of view of 34.5° is shown. Also shown is the ratio of attenuation to absorption as calculated by Kirk. (B) Similar to (A) but the reflectivity is varied, $b = 0.4$ and $a = 0.1$.

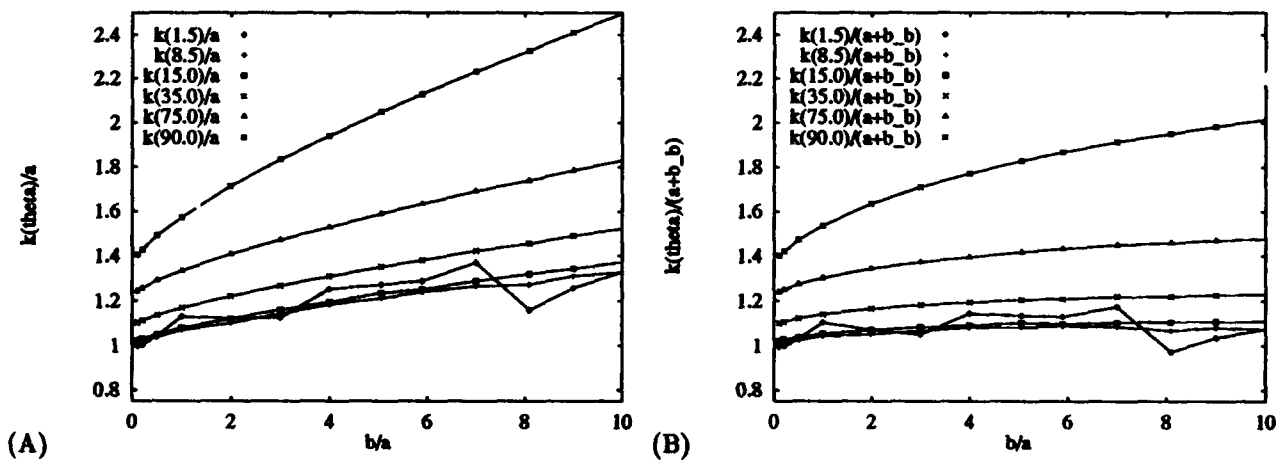


Figure 2: Radiance attenuation of the light field in a reflective tube with a Lambertian initial light field. The beam attenuation is kept constant at 2 m^{-1} and the reflectivity is set to 100%. Shown are the ratios of measured radiance attenuation to true absorption (A) and to the sum of true absorption and backscattering (B) as measured with different fields of view when the ratio b/a is varied. Path length amplification becomes important for large fields of view. The radiance attenuation for a field of view of 1.5° is influenced by statistical noise.

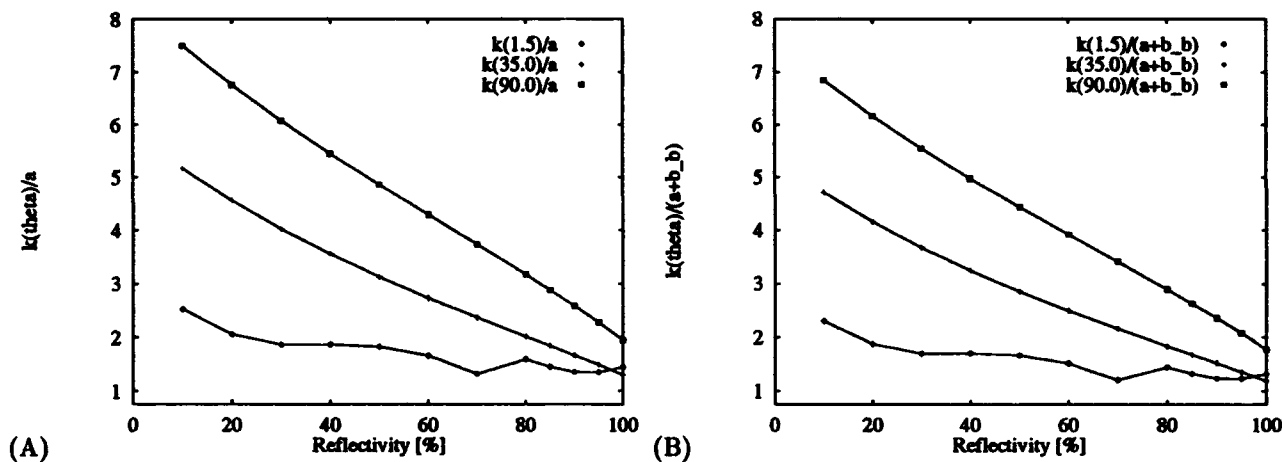


Figure 3: Radiance attenuation of the light field in a reflective tube with a Lambertian initial light field. The beam attenuation is kept constant at 2 m^{-1} , the absorption is set to 0.4 m^{-1} and the scattering is set to 1.6 m^{-1} . Shown are the ratios of measured radiance attenuation to true absorption (A) and to the sum of true absorption and backscattering (B) as measured with different fields of view when the reflectivity of the tube is varied. The radiance attenuation for a field of view of 1.5° is influenced by statistical noise.

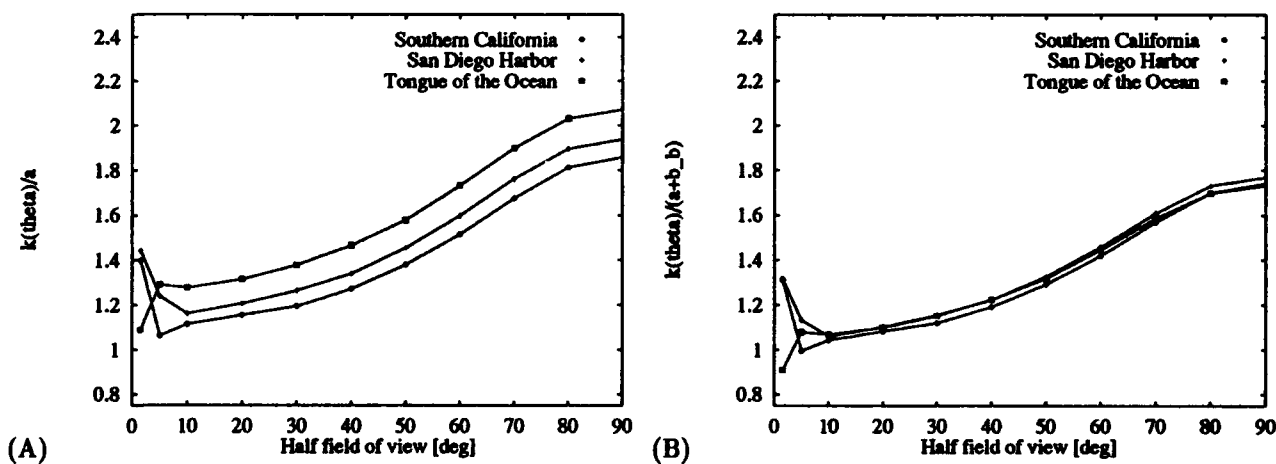


Figure 4: Attenuation of the light field in a reflective tube with a Lambertian initial light field. The beam attenuation is kept constant at 2 m^{-1} , the absorption is set to 0.4 m^{-1} and the scattering is set to 1.6 m^{-1} . Shown are the ratios of measured radiance attenuation to true absorption (A) and to true absorption plus backscattering (B) as measured with different volume scattering functions when the field of view is varied. The values for small fields of view are influenced by noise in the simulation.

A.1 Light Sources

The simulations were done with a Lambertian light source and a collimated beam. For each light source a uniform distribution of photons over the source area is assumed. For a Lambertian light source the flux seen from any direction has to be equal therefore the probability for a photon to have a zenith angle, θ , is $\cos(\theta) \sin(\theta)$. The direction cosines can then be calculated from zenith and azimuth angles generated according to

$$\theta = \arcsin \sqrt{\text{rand}(0, 1)} \quad \phi = \text{rand}(0, 2\pi). \quad (8)$$

A collimated beam is generated by setting the zenith angle to 0.

A.2 Beam attenuation

The medium is characterised by a beam attenuation c . For a beam with N_0 photons travelling in a certain direction this means that $N_0(1 - \exp(-cs))$ are left after a distance s . This allows us to set a mean free path length for a photon during which no interaction with the medium takes place. The probability mass function and the probability distribution function are given by

$$P(s) = c \exp(-cs) \quad (9)$$

$$F(t < s) = \int_0^s P(t) dt = 1 - \exp(-cs). \quad (10)$$

After inversion a mean free path is calculated by:

$$\text{mfp} = -\ln(1 - \text{rand}(0, 1)) / c. \quad (11)$$

A.3 Scattering

The angular deviation of the new trajectory with respect to the old trajectory is governed by the volume scattering function $\beta(\theta)$. The probability mass and distribution function are

$$P(\theta) = \int_0^{2\pi} \beta(\theta) d\psi = 2\pi\beta(\theta) \quad (12)$$

$$F(\theta' < \theta) = 2\pi \int_0^\theta \beta(\theta') \sin(\theta') d\theta'. \quad (13)$$

The volume scatter functions used are the ones measured by Petzold.

The direction cosines of the new trajectory of the particle can be calculated from the current direction cosines and from a generated deviation, θ , and a generated azimuth angle, ϕ , around the current trajectory.

A.3.1 Direction cosines after scattering

A trajectory of a particle can be described by the following direction vector

$$\vec{s} = (dx, dy, dz) = (\cos \varphi \sin \vartheta, \sin \varphi \sin \vartheta, \cos \vartheta), \quad (14)$$

with zenith angle, ϑ , and azimuth angle, φ . We want to find a new direction vector,

$$\vec{s}' = (dx', dy', dz') = (\cos \varphi' \sin \vartheta', \sin \varphi' \sin \vartheta', \cos \vartheta'), \quad (15)$$

which makes a angle θ with the old vector but whose direction is further arbitrary. See Figure 5 for the angles involved. From the following results of spherical trigonometry,

$$\frac{\sin A}{\sin a} = \frac{\sin B}{\sin b} = \frac{\sin C}{\sin c}, \quad (16)$$

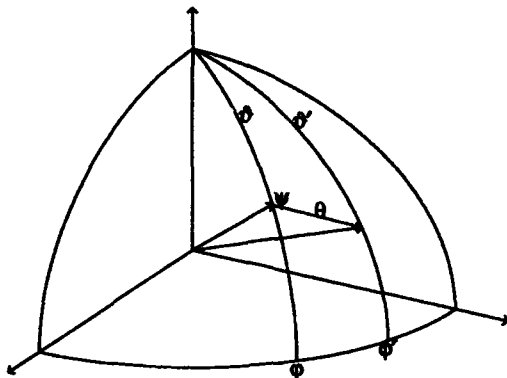


Figure 5: Direction cosines after scattering. This figure shows the angles involved when calculating the direction cosines after scattering over θ of a beam having direction ϑ, φ initially.

$$\sin b \cos C = \cos c \sin a - \sin c \cos a \cos B, \quad (17)$$

$$\cos b = \cos c \cos a + \sin c \sin a \cos B. \quad (18)$$

we can derive the new direction vector. From equation 16 it is found that

$$\begin{aligned} \frac{\sin \vartheta'}{\sin \phi} &= \frac{\sin \theta}{\sin(\varphi' - \varphi)} \\ dy' \cos \varphi - dx' \sin \varphi &= \sin \theta \sin \varphi. \end{aligned} \quad (19)$$

With equation 17 we get

$$\begin{aligned} \sin \vartheta' \cos(\varphi' - \varphi) &= \cos \theta \sin \vartheta - \sin \theta \cos \vartheta \cos \phi \\ dx' \cos \varphi + dy' \sin \varphi &= \cos \theta \sin \vartheta - \sin \theta \cos \vartheta \cos \phi. \end{aligned} \quad (20)$$

Multiply 19 with $\sin \varphi$ and 20 with $\cos \varphi$ and subtracting gives

$$dx' = \cos \theta dx - \sin \theta [\sin \phi dy + \cos \phi dz] / \sqrt{1 - dz^2}. \quad (21)$$

Multiply 19 with $\cos \varphi$ and 20 with $\sin \varphi$ and subtracting gives

$$dy' = \cos \theta dy + \sin \theta [\sin \phi dx - \cos \phi dz] / \sqrt{1 - dz^2}. \quad (22)$$

With equation 18 we get

$$\begin{aligned} \cos \vartheta' &= \cos \vartheta \cos \theta + \sin \vartheta \sin \theta \cos \phi \\ dz' &= dz \cos \theta + \sqrt{1 - dz^2} \sin \theta \cos \phi. \end{aligned} \quad (23)$$

REFERENCES

- 1 G. Bennet, E. Fry, and F. Sogandares. "Photothermal Measurement of the Absorption Coefficient of Water at 590 nm." In Ocean Optics VIII, number 637 in Proc. Soc. Photo-Opt. Instrum. Eng., pages 172-180, 1988.
- 2 E. Fry and G. Kattawar. "Measurement of the absorption coefficient of ocean water using isotropic illumination." In Ocean Optics IX, number 925 in Proc. Soc. Photo-Opt. Instrum. Eng., pages 142-148, 1988.

- 4 H. R. Gordon. "Simple Calculation of the Diffuse Reflectance of the Ocean." *Appl. Opt.*, 12(12):2803-2804, 1973.
- 5 J. Hakvoort, J. Krijgsman, and M. Donze. "Upward Radiance Attenuation is an *in situ* Estimate of Absorption; a Comparison with Laboratory Measurements." In J. Krijgsman, PhD Thesis, Dept. of Civil Engineering, Delft University of Technology, januari 1994.
- 6 J. H. M. Hakvoort, A. E. R. Beeker, and J. Krijgsman. "An instrument to measure *in situ* visible light absorption in natural waters." submitted to SPIE Ocean Optics XII, 1994.
- 7 J. T. O. Kirk. "Monte Carlo modeling of the performance of a reflective tube absorption meter." *Appl. Opt.*, 31(4):6463-6468, 1992.
- 8 J. Krijgsman. Optical Remote Sensing of Water Quality Parameters: Interpretation of Reflectance Spectra. Thesis Delft, Delft University of Technology, Dept. of Civil Engineering, januari 1994.
- 9 E. O'Mongain, K. Moore, S. Plunkett, O. Zalloum, R. Doerffer, J. Fischer, T. Oishi, M. McGarrigle, and J. Kennedy. "MARAS: An instrument for the characterisation of the light field in the ocean."
- 10 T. J. Petzold. "Volume Scattering Functions for selected Waters." SIO Ref. 72-87, 1972. Scripps Institution for Oceanography, Calif.
- 11 W. H. Press, S. A. Teukolsky, W. T. Vetterling, and F. B. P. Numerical Recipes in C. The art of Scientific Computing. Cambridge University Press, Cambridge, second edition, 1988c1992.
- 12 M. Rijkeboer, F. d. Bles, and H. J. Gons. "Laboratory scale enclosure: concept, construction and operation." *J. Plankton Res.*, 12(1):231-244, 1990.
- 13 K. Shibata. "Spectrophotometry of intact biological materials, absolute and relative measurements of their transmission, reflection and absorption spectra." *J. Biochem.*, 45(8):599-623, 1958.
- 14 K. Shibata, A. A. Benson, and M. Calvin. "The absorption spectra of suspensions of living micro-organisms." *Biochimica et Biophysica Acta*, 15:461-470, 1954.
- 15 A. Tam and C. Patel. "Optical absorptions of light and heavy water by laser optoacoustic spectroscopy." *Appl. Opt.*, 18:3348-3358, 1979.
- 16 R. Ulbricht. "Die bestimmung der mittleren räumlichen Lichtintensität durch nur eine Messung." *Elektrotechnische Zeitschrift*, 29:595-597, 1900.
- 17 C. S. Yentsch. "Measurement of visible light absorption by particulate matter in the ocean." *Limnol. Oceanogr.*, pages 207-217, 1962.
- 18 J. R. V. Zaneveld, R. Bartz, and J. C. Kitchen. "A reflective tube absorption meter." In Ocean Optics X, number 1302 in Proc. Soc. Photo-Opt. Instrum. Eng., pages 124-136, 1990.

The BBOP Data Processing System

Jens C. Sorensen, M.C. O'Brien, Daniel Konnoff and D.A. Siegel

Center for Remote Sensing and Environmental Optics
and
Department of Geography
University of California, Santa Barbara
Santa Barbara, CA 93106, USA

ABSTRACT

The sheer volume of profiling spectroradiometer data is increasing dramatically as global change research programs are placing more emphasis on the evaluation of spatial and temporal structure of ocean biogeochemical cycles. For example, the Bermuda BioOptics Project (BBOP) collects over 1000 profiles each year in order to link time-series observations of primary production rates to bio-optical parameters. It is likely that these trends will continue as there are several satellite ocean color sensors that are planned to be deployed between now and the end of the century. However, these vast amounts of data must be calibrated, processed, reduced, analyzed, and interpreted in a timely manner. Here, we present a computer data processing for efficiently achieving this goal, in terms of both computational and human resources. The processing system is comprised of a suite of ANSI C++ programs that read and operate on a specified file format, the lowest common denominator (LCD) data file. The LCD file contains all relevant data and metadata (which include calibration information and at-sea comments) in a single ASCII file. UNIX shell scripts are used in the control of data flow as well as error and log handling. The final product is a binned spectroradiometer data set with relevant derived parameters included ($K_d(z, \lambda)$, $R_{rs}(z, \lambda)$, $E_d(0^-, \lambda)$, etc.) that may be disseminated to other groups or data bases. At UCSB, we have been using the BBOP system for the past two years and the system is available for use by other research groups.

1. INTRODUCTION

It is well recognized that ocean optics data sets have huge potential for addressing many aspects of ocean biogeochemical cycles (cf., Dickey and Siegel, 1993). To be effectively used in interdisciplinary studies, such as the Joint Global Ocean Flux Study (JGOFS), optical data sets must be made available in a timely manner. For example, in order to effectively collaborate with other investigators in the JGOFS Bermuda Atlantic Time-series Study (BATS), we (the Bermuda Bio-Optics Project, BBOP) must provide and interpret ocean optical data sets on the same time scale as our BATS collaborators are able to work up pigment, primary production and water chemistry data. In addition, the calibration and validation needs of the upcoming Sea Viewing Wide Field-of-view Sensor (SeaWiFS) satellite ocean color mission requires processed ocean optics data in near real-time (e.g., McClain et al., 1993).

In our opinion, a major stumbling block in the dissemination and utilization of bio-optical data sets has been the lack of efficient and straight-forward data processing schema. Bio-optical data sets have several characteristics which make their "final" products difficult to produce quickly. First, they tend to be large (several Mb each) due to high data sampling rates and a diverse parameter range. Second, many profiles (10's to 1000's) are often made during a single cruise due to experimental design and the at-sea ease of making these profiles. Recalculation of measured parameters is another characteristic of profiling spectroradiometer data sets that is often necessary, as radiometric calibrations are at times uncertain (Mueller and Austin, 1992). Each year, the BBOP sampling collects over 1000 spectroradiometer profiles and the instrument is re-calibrated at UCSB four times each year. In order to effectively meet our scientific and collaboration goals, we must efficiently process and analyze these data.

In anticipation of this large volume of data as well as the rapid turn-around requirements imposed by the calibration and validation of satellite data sets, we developed a new data processing system for large volumes of multispectral profile data. In what follows, we will introduce the structure and data flow of the BBOP data processing system. This manuscript is intended as a simplified overview, and not as a detailed users guide (see Siegel et al. 1994 for a users guide).

2. PHILOSOPHY

As with any data processing system, there are several conceptual and philosophical positions that need to be taken based on the scientific goals of the project and the available resources. In no specific order, the goals of the BBOP data processing system are to:

- utilize existing spectroradiometer analysis methods,
- rapidly produce final archival data sets,
- minimize human intervention steps,
- maximize the number of data quality assessment/assurance checks,
- generate fully self-describing data sets
- provide data files in ASCII which is easily read and edited,
- make quick looks easy to obtain at several stages of processing,
- include processing documentation in the data files at each step,
- work on many present and future computer platforms,
- allow much of the data reduction to be accomplished by an experienced undergraduate student.

As a limitation imposed by the number of casts generated and the imposed rapid turn-around requirements, we are unable to manipulate each profile individually. Therefore, in order to assure data quality, many efficient quality assessment and control steps must be implemented. Known sensor problems must be corrected or "flagged". Examples of known sensor problems include low signal to noise ratios in irradiance and radiance channels near the dark current values and obvious spiking in data fields due to acquisition errors. These problems require that the affected data values be replaced with trap flags ($-9.9e+35$) so that no processing is performed on these spurious fields. In addition, the quality of the data for some applications is affected by events occurring during collection, including excessive package tilts and variations in incident illumination during a cast due to changes in cloud cover. These events require that entire data records be qualified. In these cases, a new field is created containing a flag which defines the quality of the data based on data values in one or two fields. Data records containing either of these flags (trap or quality) can be later deleted or accepted by making simple threshold comparisons.

Provisions also must be made for unknown and unexplained sources of error. These may be simple, the complete failure of a channel, or insidious, the slow change in a calibration constant. To catch these errors, plots must be made of several important quantities on a regular basis. These may be spectra of calculated diffuse attenuation coefficients, reflection ratios or simply profiles of processed CTD variables. The BBOP data processing system streamlines the plotting of important parameters by allowing quick output of selected variables as simple ASCII files which are easily read and manipulated by plotting programs.

The documentation of data processing procedures is often neglected in many data processing schemes. For example, it is essential to trace changes in calibration constants. Things as simple as the digital filtering method used are also important characteristics imposed upon a data set. As part of the BBOP data processing system, processing documentation is added automatically to the data file so that every data user knows explicitly what was done to the data file.

3. LCD FILE FORMAT

At the heart of the BBOP processing system is the LCD file (least common denominator data set) and its structure. The LCD file is self-contained, with all pertinent header, calibration and processing history included. This system is somewhat redundant since much of the header and calibration data will be identical for all casts in a cruise; however, the benefits of easy access to calibration constants and processing history far outweigh the cost of slightly larger data files. During the first 18 months of the BBOP project, we have required 20 different calibration files due to changes in spectroradiometer calibration, ancillary instruments and collection software. Record keeping has been simplified by recording all calibration information within each data file. The LCD file can be stored in a compressed format to save disk space.

The LCD file is organized into five major sections separated by keywords in brackets (< >). The header portion, <cruise_info>, consists of general information about the cast gleaned from several sources. The <sampld_parameters> and <derived_parameters> sections contain a list of the contents of the data fields found in the <data> section. The <sampld_parameters> section also contains the calibration constants. At the end of the LCD

file is the <filters_used> section which contains a record of all BBOP programs applied to the file as well as any statistical output generated by the programs. Excerpts of a LCD file are shown below after some processing.

Example of a LCD file:

```
<cruise_info>
filename a111292f
date 11-12-1992
position 31 17.96 64 18.81
cruise b50
...
castid      index      lmer_time      ldepth
a111292f.dt1 2.5000000e+01 1.8150000e+01 1.3406400e+00
a111292f.db1 4.9100000e+02 1.3502500e+02 1.2275800e+02
a111292f.ubl 5.2000000e+02 1.4727500e+02 1.2317100e+02
a111292f.ut1 9.2000000e+02 2.4760000e+02 1.1174000e+00
<sampled_parameters>
led410 0. 4.547500e-02 1.603000e-03
...
<derived_parameters>
kc-led410
...
<data>
-9.900000e+35 3.457528e+01 3.790249e+01 4.242258e+01 ...
...
<filters_used>
...
bscalc -fr led410 1 20 hmdqa111292f.lcd.1 bhmdqa111292f.lcd.1
#stats ---> samples = 19 abdev = 1.663616e-01 int = 3.457528e+01 slope = 9.904044e-01 min
= 9.872207e+00 max = 3.772964e+01 mean = 2.863836e+01 stdDev = 1.364106e+00 var =
1.101210e+00 confidence(95) = 1.381770e+00
bbopkc -fs led410 10 bhmdqa111292f.lcd.1 kbhmdqa111292f.lcd.1
...
```

3.1. Building the LCD file

The LCD file structure is required by all BBOP filters and scripts. The choice of a conversion program depends on the software used to collect the data. If the data have been collected with Biospherical Instrument's M24-PROF software, the LCD file can be created with the BBOP program, mer2lcd. The LCD file is created from the card, binary and calibration files. The output is an LCD file containing all the necessary features with an abbreviated header which can be augmented later or concurrently by using the BBOP shell script smklcd (see section 4.1). Once the LCD file is completed, it is ready for processing using the BBOP filters.

4. BBOP FILTERS

The BBOP filters are a suite of UNIX programs designed to perform a variety of functions in the processing of LCD data files (Table 1). The filters are designed as stand alone programs that can be applied to LCD files directly or embedded in shell scripts. The BBOP Filters are built using g++ (gcc) version 2.4.0 and are stable on Sun Sparc, DEC Ultrix, and Silicon Graphics platforms. The BBOP filters will either replace data values within the <data> section of the LCD file and/or add new data fields. New data field names are placed in the <derived_parameters> section and can be operated on by most of the filters in the same way as those in the <sampled_parameters> section.

All filters share certain fundamental features:

- Filters read and operate on an external ASCII file and create an output file with a name specified by the user (with the exception of bbopbin, which creates the outfile name using the infile name).
- Filters require that LCD files contain all the keywords described above.
- Filters append their command lines to the <filters_used> section of the output file.
- Filters will not operate on a field if the same filter and arguments have been used before or if the new field name already exists.

FILTER	DESCRIPTION
mer2lcd	creates the LCD file from the card, binary and calibration files
bboprecal	recalibrates sampled parameters based on new scales and offsets
bbopradq	compares data to thresholds and replaces them with trapflags if below
bbopangq	compares package angle data to a constant and writes a quality flag
bbopkq	calculates incident irradiance changes over a depth interval and writes a quality flag
bbopdespike	flags spikes based on thresholds and forward first difference and/or slope difference, replacing data with a mean of windowed points
bbopmovavg	smooths data using a moving arithmetic mean window (boxcar)
bboph2o	calculates water properties using UNESCO FORTRAN routines
bbopbin	breaks the cast into profiles, sorts the profiles on depth and averages data over depth intervals creating new LCD files for each profile.
bscalc	extrapolates data to a NULL depth over a specified depth window
bbopkc	calculates attenuation coefficients
bboptrans	performs transformation operations (log, sqrt, sin, etc.) on data
bbopmath	performs simple math operations with data by columns, or by one operand and a scalar
bbopfutil	extracts or removes fields from a LCD file and writes the result as a new LCD file
bbopdeflag	removes or keeps lines of data based on flag values and thresholds
bbopstrip	extracts LCD data columns and writes them to a simple ascii file

Table 1. Filters used in the BBOP data processing system.

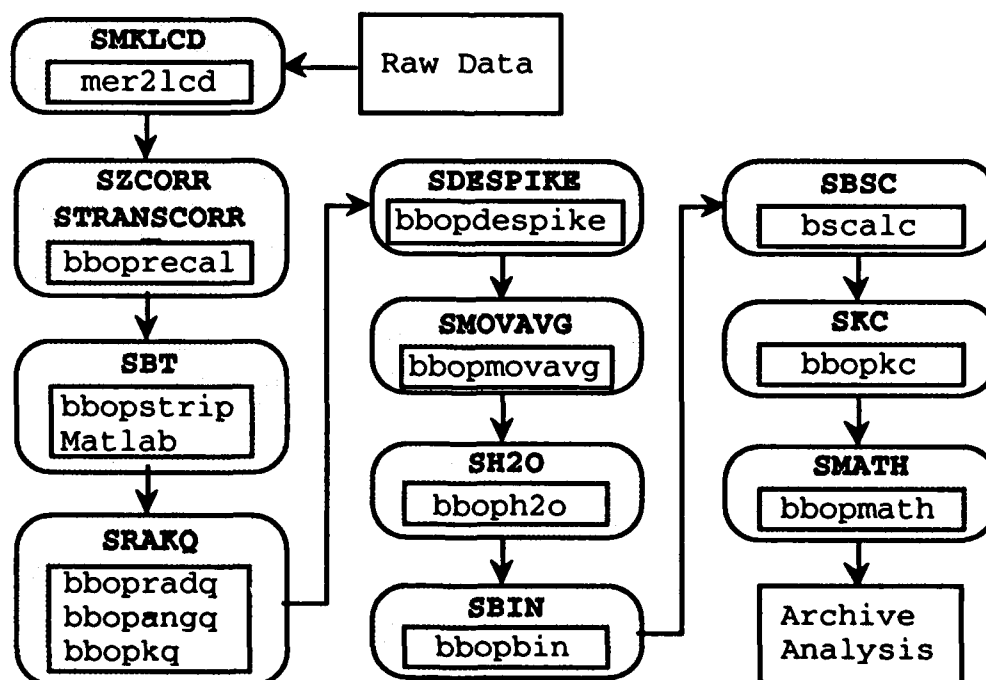


Figure 1: Schematic cartoon tracing some of the processing steps used in BBOP. The outer shell holds the shell script(s) which intern call the BBOP filter(s) within the box. The resulting files are binned, qualified LCD files for archiving.

4.1. Linking BBOP filters with scripts

The flow of data processing is controlled using UNIX shell scripts written in the bourne and bash shells. These scripts can create and extract header information, build LCD files and call graphics packages and/or BBOP filters. The scripts are used to point to the appropriate directories, automate processing, check for errors in execution and update log files. Figure 1 illustrates the overall structure of the BBOP processing system. The scripts currently used are summarized in Table 2. The scripts calling individual BBOP filters can be run singly, or more commonly, are combined in a global script (scmds). By combining the scripts and utilizing the UNIX environment we are able to automate the entire data processing system. The following is an example of the global script scmds, processing a recalibrated LCD file through completion:

```
#!/local/gnu/bin/bash
lcd_file=`basename $1`
logfile=$PWD/log/${lcd_file}.log
{
    echo -n "$lcd_file : "; date
    srakq $1&&\
    sdespike q${lcd_file}&&rm q${lcd_file}&&\
    smovavg dq${lcd_file}&&rm dq${lcd_file}&&\
    sh2o mdq${lcd_file}&&rm mdq${lcd_file}&&\
    sbin hmdq${lcd_file}&&\
    { for filename in `ls hmdq${lcd_file}.*`
    do
        sbsc $filename&&\
        skc b${filename}&&rm bhmdq${lcd_file}.*&&\
        smath kb${filename}
    done }
    date
} 2>&1 | tee -a $logfile
```

The "&&" construct allows the following command to be executed only if the command preceding it is successful (returns a zero exit value). This insures that if one step fails, the running of the script on a particular file will stop. The standard output of each script is sent to a log file for each LCD. Each script called in scmds, prefixes a unique letter to the input file name. For example, hmdqa010193.lcd indicates that the scripts srakq, sdespike, smovavg and sh2o have been run on the LCD file a010193.lcd. In scmds, most intermediate LCD files are removed, with the exception of the files that precede and follow bbopbin, which are later archived. Files are available for quick looks at any step within the processing sequence.

SCRIPT	DESCRIPTION
smklcd	creates the LCD file from the card, binary and calibration files and cruise notes
szcorr	recalculates the pressure channel using a new cruise offset
stranscorr	recalculates the transmissometer channel using the new cruise air calibration and dark offset.
sbt	determines tops and bottoms of profiles using an interactive Matlab [®] script and inserts the castid table into the LCD header section.
srakq	qualifies data based on dark value thresholds, instrument tilt, and constant surface illumination intensity.
sdespike	despikes conductivity, temperature, fluorometer and transmissometer channels twice (two passes)
smovavg	smoothes despiked conductivity, temperature, fluorometer and transmissometer channels.
sh2o	calculates salinity, sigma, sigma-t, potential temp and sigma-theta
sbins	breaks cast into profiles, sorts and averages data into 1m bins

sbsc	extrapolates below surface irradiance and radiance to a NULL depth over a predefined window using the robust algorithm
skc	calculates attenuation coefficients over a 10m moving window
smath	calculates irradiance and radiance products and ratios
sdeflag	removes data lines containing trapflags
sloop	a simple looping program for passing file names to other scripts
scmds	automates the entire BBOP processing system (see example script above)

Table 2. UNIX shell scripts used in the BBOP data processing system.

5. DATA PROCESSING STEPS

5.1. Bottom-top indexing (*sbt*)

Because the LCD file must eventually be split into individual profiles, each cast is examined to determine the tops and bottoms of down- and up-casts. Initially, we pursued an automated method of marking these points, but found that the great variety in the shape of the time vs. depth curve made this determination prohibitively complicated. We decided that the time vs. depth curve must be evaluated *manually* for each cast. There are any number of ways this could be done, we have chosen to use Matlab[®] as a graphical user interface to allow a trained user to interactively select these points. A table comprised of a header line and corresponding indices and depths is inserted into the <cruise_info> section of the LCD file (see the example LCD file above). These indices and depths are points marking the tops and bottoms of the profiles within the cast. Once these data are inserted, the first line of the table, beginning "castid" functions as a list of keywords. The data within this table are used by *bbopkq* in anticipation of the binning process and then by *bbopbln*.

5.2. Recalibration:

Recalibration may be necessary due to changing instrument calibration constants, at sea atmospheric pressure offsets and/or changing transmissometer offsets. The BBOP filter *bboprecal* converts data from engineering units to voltages using the scale and offset values from the <scaled_parameters> section and converts back to engineering units using the scale and offset values from the command line. The new scale and offset constants are inserted following the variable name in the <scaled_parameters> section maintaining a calibration history within the LCD file. Recalibration is not implemented for Seabird (CTD) sampled parameters or derived fields.

5.3. Data qualification

Because our approach minimizes human intervention, we have attempted to maximize the number of data quality assessment/assurance checks that are made as part of our BBOP data processing. The first data qualification uses *bbopradq* to assess the ambient light levels for each channel. When ambient light levels fall below some predefined level, the individual data fields are replaced by a trap flag ($=-9.9e+35$). At all later stages of BBOP processing, flagged fields are not operated upon. Lines containing these flags can be later deleted using *bbopdeflag* or in an application program.

The *bbopangq* filter qualifies lines of data based on the orientation of the radiometer in the water, since spectral data may be compromised by excessive tilting of the instrument. This filter creates a new field containing a quality flag rather than replacing data in a field.

Accuracy of the diffuse attenuation coefficient calculation is strongly dependent on a constant intensity of incident radiation during the calculation time interval. *bbopkq* is used to identify the segments of the cast over which surface illumination is steady enough for the diffuse attenuation coefficient to be accurately determined. *bbopkq* uses the castid table information to perform its qualification in anticipation of binning and calculation of attenuation coefficients (*bbopkc*; section 5.8). *bbopkq* calculates the standard deviation and the mean of the first difference for the group of points centered at each data line within the user-selected depth interval (in meters) over which the attenuation coefficients will be calculated. The user also specifies a threshold values for the standard deviation and maximum first difference with which *bbopkq* compares its calculated values and writes a quality flag into a new field dependent upon the results of the comparison. Later, these flag values can be used to assess the quality of the calculated diffuse attenuation coefficients (see figure 2).

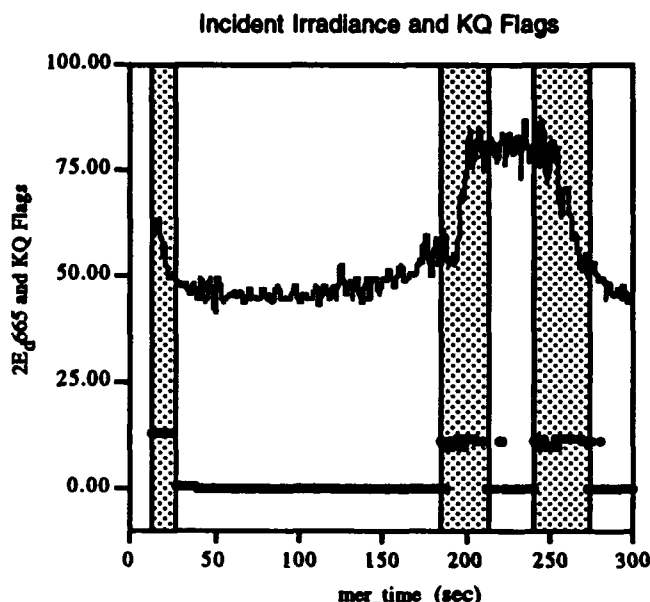


Figure 2. Incident downwelling irradiance (solid) and KQ flags produced by *bbopkq*. Regions of non-zero KQ flags (shaded) indicate periods where the calculation of $K_d(z, \lambda)$ may be uncertain due to variable incident irradiance. Lines of data can be later deleted or accepted using *bbopdeflag* and user specified flag thresholds.

are accounted for using a single-pole digital filter. The following parameters are calculated: salinity, *in situ* density, σ_t , potential temperature, σ_θ , and coefficients of thermal and saline expansion.

5.6. Binning

A cast may contain from one to several up or down profiles (yo-yo's) and hence, may not be monotone in depth. The binning filter, *bbopbln*, uses the information from the castid table to break up the LCD file into individual daughter profiles that are sorted based on pressure and compacted using arithmetic averages over a pressure interval ($\text{bin} \pm \delta p$). The resulting pressure field for each binned profile is also binned to evaluate the "true" depth of each binned data record. Each daughter LCD file retains the complete header and processing history of the original LCD file and contains 2 new <derived_parameters> fields named *bin_m*, where "m" is the interval chosen by the user, and *bin_pts*, containing the number of raw bandwidth data records that have been averaged into that bin. If the file is missing pressure interval data near the surface, *bbopbln* fills in the lines for the missing bins with trap flags such that the binned LCD file begins at its lowest bin interval (i.e., 1.0) and increases monotonically.

5.7. Null depth extrapolations

The determination of optical fluxes just beneath the sea surface, or at NULL depth, are of obvious relevance for ocean color remote sensing (e.g., Dickey and Siegel, 1993; McClain et al., 1993). The direct determination of NULL depth optical signals is particularly difficult due to high levels of surface wave glint noise and uncertain water depth determinations. In order to provide accurate data at a NULL depth ($z = 0$) for the irradiance and radiance channels, profiling data sets must extrapolate their signals to the sea surface. The BBOP filter *bscal* employs an algorithm which statistically extrapolates a depth profile to the surface over a user-specified depth interval. *bscal* allows the user to specify both the upper and lower bounds in the extrapolation interval and the log-transformed fields are extrapolated to the sea surface using the Beer-Lambert relation (Smith and Baker, 1986; Siegel and Dickey, 1987). Two extrapolation algorithms are currently available, the standard chi-square (χ^2) algorithm and a robust algorithm which eliminates points greater than 2 standard deviations from the mean (Press et al., 1990). *bscal* does not make any derived fields, but rather

5.4. Despiking and smoothing

Two types of digital low-pass filters are used to reduce spurious data values (spikes) within the BBOP data processing system. The first filter (*bbopdespike*) uses two criterion (either together or individually) to flag potential data spikes. Flagged values are either replaced with arithmetic means over a user defined window or trap flags if no valid (nonflagged) data exists within that window. The criteria are based upon either a forward first difference and/or a forward slope difference compared to specified threshold values. The second filter, *bbopmovavg*, uses a moving arithmetic mean (boxcar) with the window size defined by the user. Despiking and smoothing are carried out on temperature, conductivity, transmissometer and fluorometer fields only. Both the despiking and moving average filters create new fields, leaving the input field untouched.

5.5. CTD calculations

bboph2o calculates water characteristics using the standard UNESCO FORTRAN routines and writes the calculated parameter as a new field in the LCD file. *bboph2o* must have despiked temperature and conductivity data to produce a smooth salinity profile. Time constant differences between the conductivity and temperature sensors

creates a new line of data at the top of the <data> section with "0" in the bin_m field and trap flags in any field for which the extrapolation was not calculated. Statistics for the extrapolation fits are included following the command line in the <filters_used> section (see the example LCD file above).

5.8. Attenuation coefficient (K) calculations

The BBOP filter *bbopkc* calculates the attenuation coefficient ($K_d(z, \lambda)$) at each binned depth interval using the Beer-Lambert relation by employing a sliding regression window. This procedure is similar to that employed by Smith and Baker (1984) and Siegel and Dickey (1987). The user specifies the channel, algorithm and depth window over which to perform the regressions using either standard chi-square or robust algorithms (Press et al., 1990). We decided not to normalize the underwater irradiance fields to simultaneous above water irradiance data for the $K_d(z, \lambda)$ calculations. Our approach is to select profiles that are free from perturbations, and to create composites of profiles based on *bbopkq* KQ flags. This choice was done as it is unclear whether the normalization would be relevant in a quickly changing irradiance field due to passing of small convective cloud elements. Further, we are uncertain whether a surface irradiance normalization routine will mask any variations associated with the incident radiance distribution. The depth window used with *bbopkc* should be the same as was used for *bbopkq*.

5.9. Simple math and transformation calculations

A variety of "utility" BBOP filters are also available. For example, *bbopmath* performs simple math operations on LCD data fields (add, subtract, multiply, ratio), and adds a new field to the data section. *bboptrans* performs simple math transformations (log, exp, sin, asin, sqrt, etc...) on the data and adds a new field to the data section. Both these tools are used in the final stages of processing to produce spectral ratios and reflectance ratios as well as calculate the beam attenuation coefficients for the transmissometry field.

6. CONCLUSIONS AND AVAILABILITY

The BBOP data processing system has allowed us to meet our data processing goals. By making this system available to the community we hope that other investigators will benefit from the investments made at UCSB and to make incremental improvements to the existing system. It is intended that investigators will customize and/or rewrite the filters and scripts to suit their own needs and systems as well as contribute suggestions for improvement. This processing system and source code are available to anyone via anonymous ftp from [eos.ucsb.edu \(/pub/BBOP/soft\)](ftp://eos.ucsb.edu/pub/BBOP/soft). However, the BBOP data processing system is not intended as a software product. The usual free software licensing caveats apply.

7. ACKNOWLEDGMENTS

The development of the BBOP data processing system was supported by NSF (OCE 90-16372) and by NASA (NAGW-3145). Support from Digital Equipment Corporation's flagship research project, Sequoia 2000, is also gratefully acknowledged.

8. REFERENCES

- Dickey, T.D., and D.A. Siegel, (eds.), 1993: *Bio-Optics in U.S. JGOFS*. Report of the Bio-Optics Workshop, U. S. JGOFS Planning and Coordination Office, Woods Hole, MA, p 180.
- McClain, C.R., W.E. Esaias and others, 1992: *SeaWiFS Calibration and Validation Plan*. NASA Tech Memo. 104566, Vol 3, S.B. Hooker and E.R. Firestone, Eds. 41 pp.
- Mueller, J.L. and R.W. Austin, 1992: *Ocean Optics Protocols*. NASA Tech Memo. 104566, Vol 5, S.B. Hooker and E.R. Firestone, Eds. 45 pp.
- Press W.H., S.A. Teukolsky, W.T. Vetterling and B.P. Flannery, 1990: *Numerical Recipes in C: The Art of Scientific Computing*, Cambridge Univ. Press, 994 pp.
- Siegel, D.A., D. Konnoff, M.C. O'Brien, J. C. Sorensen, and E. Fields, 1994 (to appear): *BBOP Sampling and Data Processing Protocols*. U.S. JGOFS Planning and Coordination Office, Woods Hole, MA.
- Siegel, D.A., and T.D. Dickey, 1987: Observations of the vertical structure of the diffuse attenuation coefficient spectrum. *Deep-Sea Res.*, 34, 547-563.
- Smith, R.C. and K.S. Baker. 1984: The analysis of ocean optical data. *Ocean Optics VII*, SPIE Vol. 489. pp. 95-126.
- Smith, R.C. and K.S. Baker. 1986: Analysis of ocean optical data. *Ocean Optics VIII*, SPIE Vol. 637. pp. 95-107.

The use of a laser stripe illuminator for enhanced underwater viewing

S Tetlow & R L Allwood

**Marine Technology Centre, Cranfield University,
Cranfield, Bedfordshire, MK43 0AL, UK**

ABSTRACT

A laser-based illumination system that can be incorporated into the existing underwater viewing system of current remotely operated vehicles (ROVs) has been investigated. A stripe of projected laser light is scanned over the target and resultant image frames are processed and combined to produce a computer generated composite image.

Initially, the system was characterised through trials in the underwater optical test facility at Cranfield where water conditions are easily controlled. Subsequently, further work was carried out on a self-contained underwater unit at a flooded quarry in Leicestershire.

Several advantages of this technique have been identified from the laboratory and field trials. Scanning the laser source allows greater control of the lighting envelope resulting in more optically uniform images. Contrast improvements of 300% and range improvements of 50% over orthodox systems have been measured. The use of image processing allows a greater degree of flexibility in image presentation and because this methodology is based on a standard underwater camera, it is complementary and can be fitted retrospectively at relatively low cost.

Applications are seen to exist in ROV navigation and structural inspection.

1. INTRODUCTION

Separating the lighting from the camera, reducing the beam spread and the use of multiple spotlights to replace a single floodlight are all measures that can be employed to improve underwater images when using conventional illumination^{1 & 2}. The basis for all these improvements is the reduction of the so called common backscatter volume. By simple geometrical considerations, this can be further reduced by the use of a stripe of light projected perpendicular to the camera to light source axis. Since the use of a stripe of light only illuminates a part of the intended target, the stripe has to be scanned to cover the whole target or the forward motion of the vehicle can be used in the case of an ocean bottom survey type application. The result in each case is a sequence of images and the illuminated part of the target can be extracted from each individual image by a number of image processing techniques. In this way the backscatter caused by the outgoing laser stripe is effectively removed. The extracted stripes are then added together to produce a composite image. Depending on the stripe separation algorithm employed, this process may be carried out in real time by hardware implemented image processing.

This technique was first proposed by Jaffe^{3,4 & 5} using an incoherent lighting source. Such a source could be produced simply and cost-effectively. The major problem with such a source is in producing a stripe with clean edges, and even illumination along its whole length. With a laser source the optical properties of the stripe were likely to be far superior. Until recently, lasers operating at suitable wavelengths have been costly and too fragile for such applications. However, the availability of high power, rugged, solid-state green light emitting lasers, has stimulated further investigation of this technique.

2. LABORATORY LASER STRIPE MEASUREMENTS

Measurements on the formation and characteristics of laser stripes were carried out in a small (4 x 4 x 3 metres deep) research tank. The sides were painted black to minimise reflections and all external light could be excluded by the use of a floating cover. To avoid power limitation constraints in these experiments, a 5 W Argon ion laser was used. Since it was impractical to house this laser underwater, its beam was delivered into the water through a window at one end of the tank. This also allowed the scanning system to be placed in an easily accessible location. A standard underwater SIT camera and a 1 kW, 80° beam divergence, incandescent underwater lamp were mounted on a wet frame such that the laser scanner and lamp were separated from the camera by 0.5 m. This arrangement allowed an effective viewing range of 3.5 m to the opposite wall and is shown in Figure 1.

Particulate matter in the form of a Bentonite slurry was added to the water to increase the turbidity. The absorption function of the water was not altered. With the water circulation system used, it was found that a homogeneous turbidity could be maintained throughout the field of view. Bentonite could be removed by allowing it to settle or by filtering through sand for rapid water cleaning.

2.1 Image and target plane measurements

In order to investigate the effect of the scattering medium on the projected stripe and compare the stripe at the target to the stripe perceived by the camera, simultaneous measurements were taken in the target and image planes. These were undertaken by projecting a 3 cm wide laser stripe onto the black surface of the tank wall which was considered as the target plane. The target plane profile was measured by scanning a submersible photocell vertically through the horizontal stripe. This was carried out for a range of turbidities having attenuation coefficients between 0.25 m^{-1} and 1.4 m^{-1} . Simultaneously, images obtained with the SIT camera were displayed and vertical cross sections through the image of the stripe were measured. These results, presented side by side for a range of turbidities, are shown in Figure 2.

From Figure 2, it can be seen immediately that the stripe is always present in the target plane even though it is not always present in the image plane. This is to be expected, since as the number of scattering events increases, backscattered light from the outgoing sheet of light is of greater intensity than the light from the relatively weak stripe. This effect is clearly seen in pseudocoloured images of the outgoing laser sheet. Bright near field backscatter events also cause the automatic camera iris to shut down which increases the depth of field of the camera, thus exacerbating the problem further. Hence in turbid conditions, the stripe methodology is limited in exactly the same way as a conventional lighting system and this is demonstrated by the similarity of the images produced by the two systems.

The target plane measurements reveal that the laser methodology of producing a stripe is successful even in turbid water. For the technique to be successful, a good stripe boundary is necessary to allow easy extraction of the stripe area by image processing techniques. As scattering increases, the stripe is seen to spread as expected but a clear stripe is still present when the camera is conventionally backscatter limited. Thus it is the SIT camera that is the limiting component of the system and future work will address the use of alternative cameras.

2.2 Stripe formation

Forming the beam into a stripe was obviously fundamental to this technique and various methods were investigated. The initial criterion was for the stripe length to be able to match the field of view of the camera used. For this reason, acousto-optical deflectors were not considered due to the limited deflection angles attainable. The three techniques investigated were the use of passive optical components such as cylindrical lenses, polygon scanners and galvanometer scanners. The passive optical component approach was attractive because of its simplicity and low cost. However, if this approach was taken to stripe formation, an active scanner would still be necessary to scan the stripe over the target.

In order to carry out a comparison of each scanner against conventional lighting, a black and white bar target was used. The target was illuminated at 3.5 m range in various turbidities and horizontal cross sections were taken from images obtained as shown in Figure 3.

The characteristics of images obtained with the conventional illuminator are as expected. In clear water a good image is obtained which is shown by good contrast in the cross section. As the turbidity increases, the contrast decreases and a difference in overall light intensity across the image is seen as light at the edges is attenuated more because it has travelled slightly further. This is the familiar "tunnelling" effect common to underwater images.

Contrast in all three scanner methods is seen to be better than the conventional lamp. However, in the passive and polygon scanner, the longer pathlength for the illuminating beam at the edge of the image results in an intensity fall off at increased turbidity. This is not seen with the galvanometer scanner. In this case, the amount of light delivered to any particular point will depend on the function used to drive the scanner, which in these experiments was a sine function. This results in the concave shape to the cross section seen for the galvanometer scanner in clear water as more light is delivered to the edges as the mirror slows and reverses direction. This effect is advantageous however in more turbid water as more light is delivered where most attenuation occurs. The result is the flatly illuminated cross section shown for the image of the target taken when the attenuation coefficient = 0.68 m^{-1} . This technique can be extended such that if a galvanometer scanner is used to form the stripe, a driving function can be selected to provide even illumination for a particular turbidity. This would result in evenly illuminated images without recourse to computer compensation.

2.3 Stripe contrast measurements

With no recognised standard to assess underwater viewing systems known to the authors, the black and white bar target provided a good method to compare the performance of various stripes against the conventional light source. In an attempt to measure a continuum of results from a conventional beam shape to a narrow stripe, various stripe thicknesses were projected by diverging the beam prior to the scanner. By the use of a diverging lens it was also possible to produce an illuminator in which the beam spread was matched to the field of view of the camera at the required distance. Contrast measurements from the target images were similar to those taken when illuminating with the conventional lamp which indicated that the lamp was well matched geometrically for the system at a range of 3.5 metres.

Contrast values from the target images were measured and are plotted as a function of turbidity in Figure 4. It can be seen that target contrast is improved over the conventional illuminator in all cases and as the stripe thickness is reduced, reducing the backscatter volume results in increased contrast. It is interesting to note that the laser stripe system does not provide significantly better results at high turbidities ($<1 \text{ m}^{-1}$) in this configuration.

3. BUILDING STRIPES INTO 2-DIMENSIONAL IMAGES

For the stripes to be used in an imaging system, they have to be isolated from the rest of the image and several stripes "sewn" together to form a complete composite image. Modified thresholding, temporal differencing and edge finding algorithms were developed to isolate the stripes from the individual images. Both water turbidity and the processing speed dictate which particular algorithm is most suitable. In selecting an algorithm, consideration also has to be given to the way in which the image processor is triggered as the stripe is scanned over the target. For instance temporal differencing can easily accommodate overlapping stripes whereas a simple thresholding algorithm would result in areas of image saturation when overlapping stripes were added together.

There is considerable advantage in having an image processing system producing the final image as the user can decide in what format the final images are presented. For example, as well as conventional images composed of a series of adjacent stripes, the use of narrow stripes and appropriate spacing results in structured type imaging which might be more appropriate for tasks such as navigation in a steel jacket structure. A hybrid image has been developed that uses narrow, closely spaced stripes. In this way, spatial information is represented and reflective information at the edges of the stripes gives conventional

imaging information. The close proximity of the stripes allows the eye to use this information as for a normal image. In this way, normal imaging information is provided with the advantages of structural imaging. Finally, because the final images are computer based, they can easily be incorporated into other computer based systems such as an inspection data base or stored on optical disks.

4. OPEN WATER TRIALS

Although the closed environment of the tank allowed careful control of the scattering properties of the water, it did not allow viewing over longer distances to be carried out. For this purpose, an underwater laser scanning unit was built to allow stripe illumination to be produced at open water test sites. The electrical power requirements for the Argon ion laser used in the laboratory work precluded its use and so a diode-pumped, frequency-doubled Nd:YAG laser capable of delivering 10 mW cw radiation of 532 nm wavelength was used. The laser scanning unit and conventional illuminator were mounted at a fixed separation from the camera.

In order to avoid the effects of surface reflections, the viewing system was suspended pointing downwards under a boat and the target beneath lowered to progressively greater distances. All work was carried out at night to minimise the effects of stray ambient light. Contrast measurements were taken from target images using the conventional light and the laser stripe. Although the principle of the technique was demonstrated with this arrangement, the 10 mW output of the laser proved to be power limited at extended ranges. Figure 5 shows an image of the target illuminated with the conventional source, a single frame from the stripe illuminated target and a synthesized composite image of the whole target. Despite power limitations, images were obtained at ranges 50% greater than those with the conventional system in water with an attenuation coefficient of 0.8 m^{-1} .

5. CONCLUSIONS

Based on the laboratory and open water trials, the following possible advantages of using a laser stripe for underwater viewing have been identified:

1. The technique provides enhanced contrast of images (or greater viewing range) as a result of reducing the backscatter volume in classical considerations.
2. Optically flat images are obtainable (no image drop off at edges) if an appropriate scanner driving function is used to deliver light appropriate to the optical path.
3. There are no depth of field limitations since the image processing system automatically locates the stripe in the camera image plane.
4. An image processing based system allows flexibility in the type of images produced, eg. structured images for navigation, hybrid user defined image or high contrast flat image for inspection.
5. A laser scanner may be added as an illuminator to existing imaging systems.
6. Solid state green light emitting lasers can be used which require modest power and are suitably reliable for the given environment.
7. The system can be used from a stationary platform.
8. Images are readily incorporated into computer based inspection systems.
9. The technique can be incorporated into photogrammetry systems for enhanced accuracy.

ACKNOWLEDGMENTS

The authors would like to thank Elf Aquitaine UK (holdings) plc for funding the research.

REFERENCES

1. Lawrence E Mertens, "In-Water Photography. Theory and Practice", John Wiley & Sons, 1976 SBN 471 59630 2
2. S Q Duntley, "Underwater Lighting by Submerged Lasers and Incandescent Sources", University of California, Scripps Inst of Oceanography, Visibility Laboratory, San Diego SIO Ref 71-1 June 1971. US Naval Contract N00014-69-A-0200-6013
3. Jules S Jaffe and Chris Dunn, "A Model-Based Comparison of underwater Viewing Systems", SPIE Vol 925 Ocean Optics IX (1988)
4. Jules S Jaffe, "Computer Modelling and the Design of Optimal Underwater Imaging Systems", IEEE J. Ocean Engineering Vol. 15 No 2 April 1990
5. Jules S Jaffe, "Sensors for Underwater Robotic Vision : Status and Prospects", Proc 1991 IEEE Int. Conf. on Robotics and Automation. 9-11 April 1991 Sacramento, California.

4 Metres

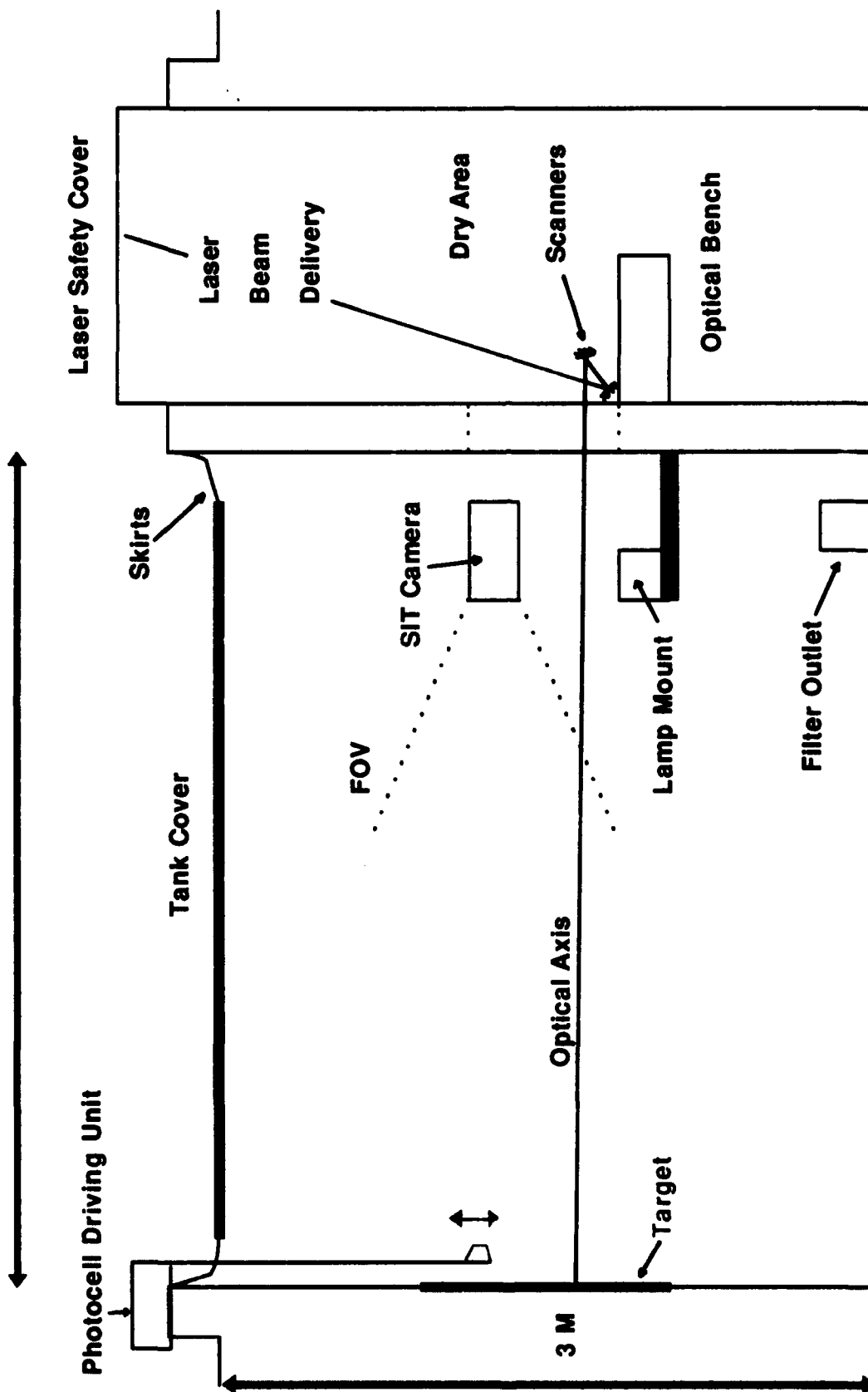


FIGURE 1 - Underwater optical laboratory

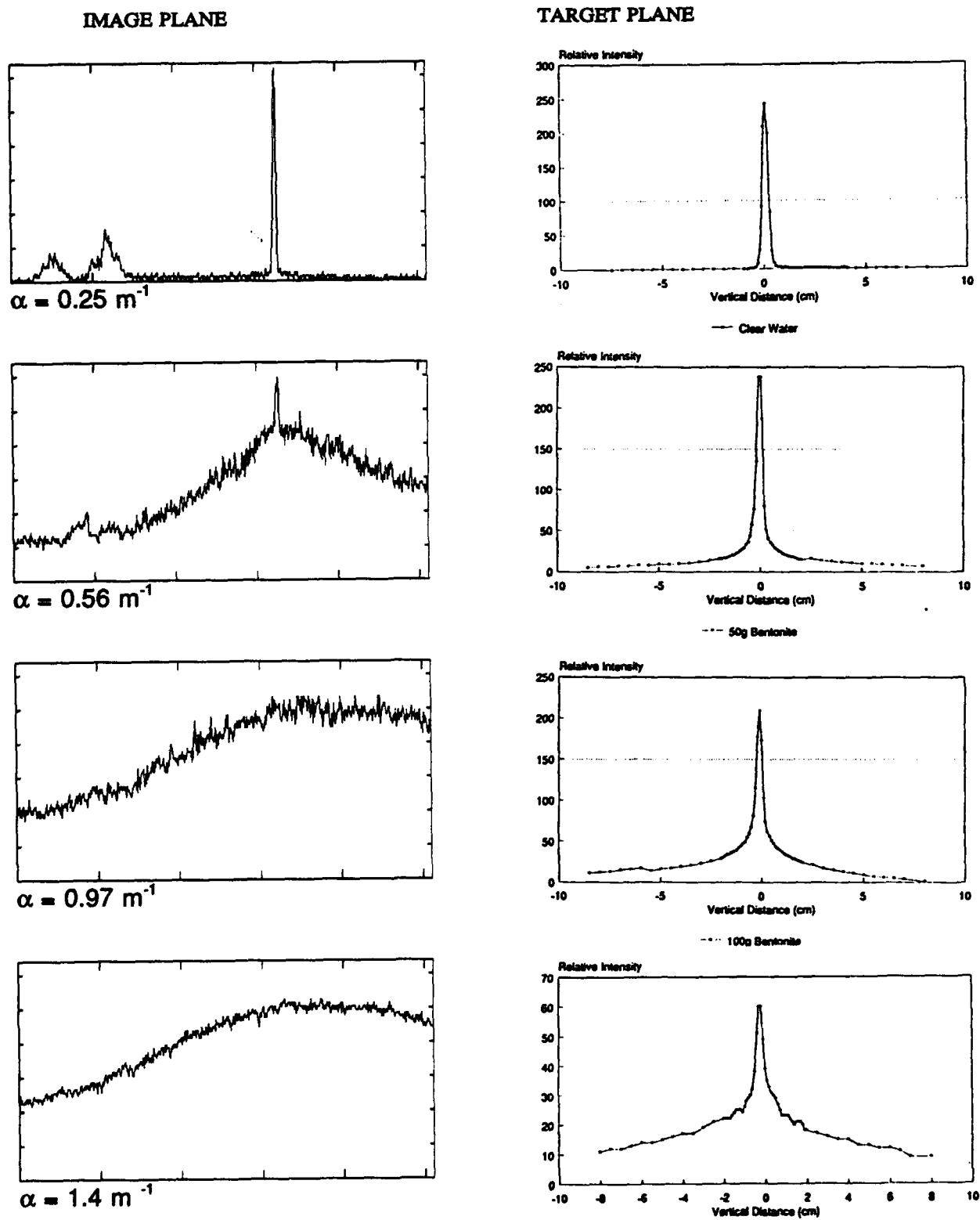


FIGURE 2 - Comparison of vertical cross sections taken through a horizontal laser stripe in the image and target plane

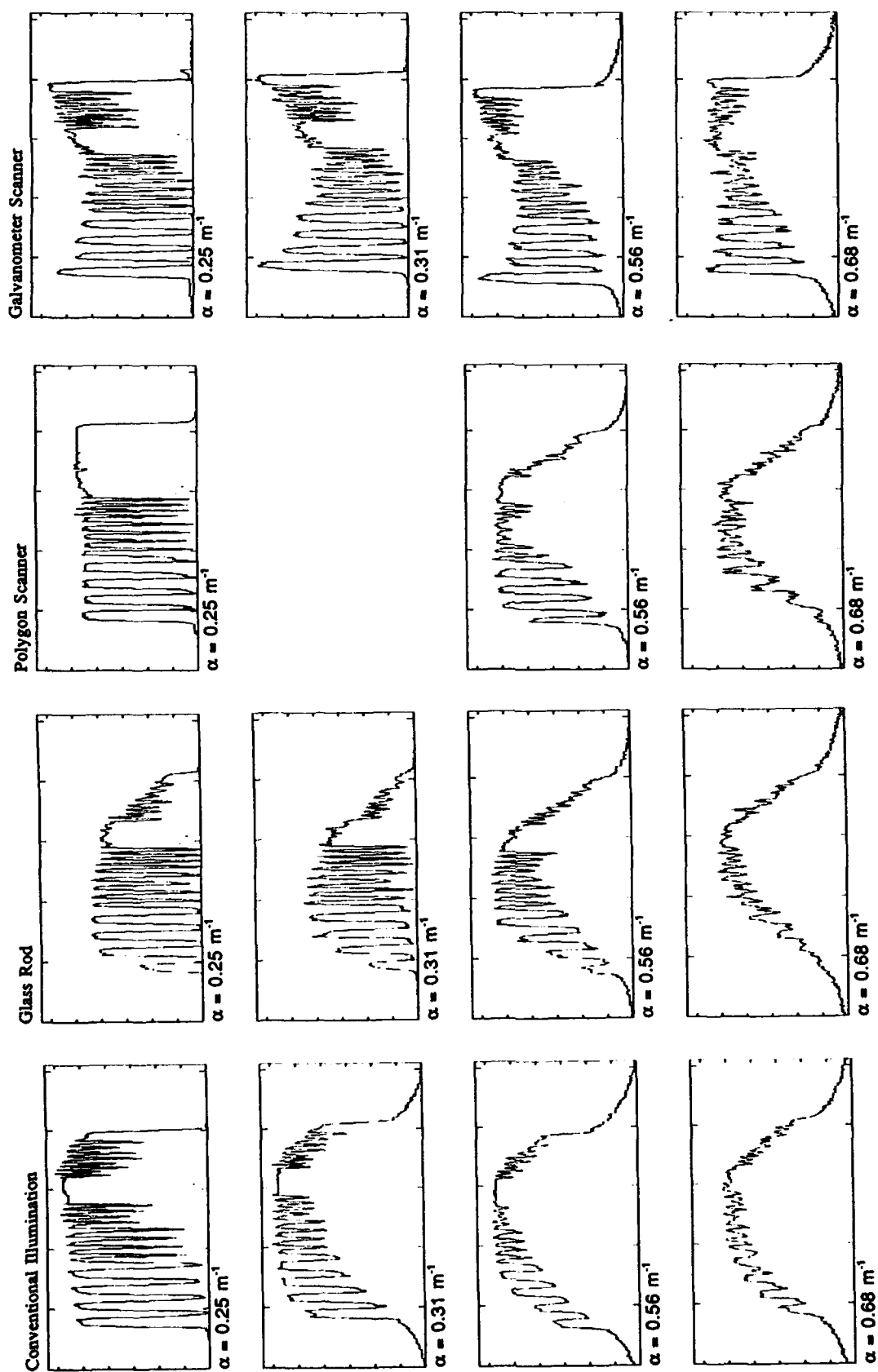


FIGURE 3 - Horizontal cross section of a black and white bar target illuminated with the three stripe forming techniques

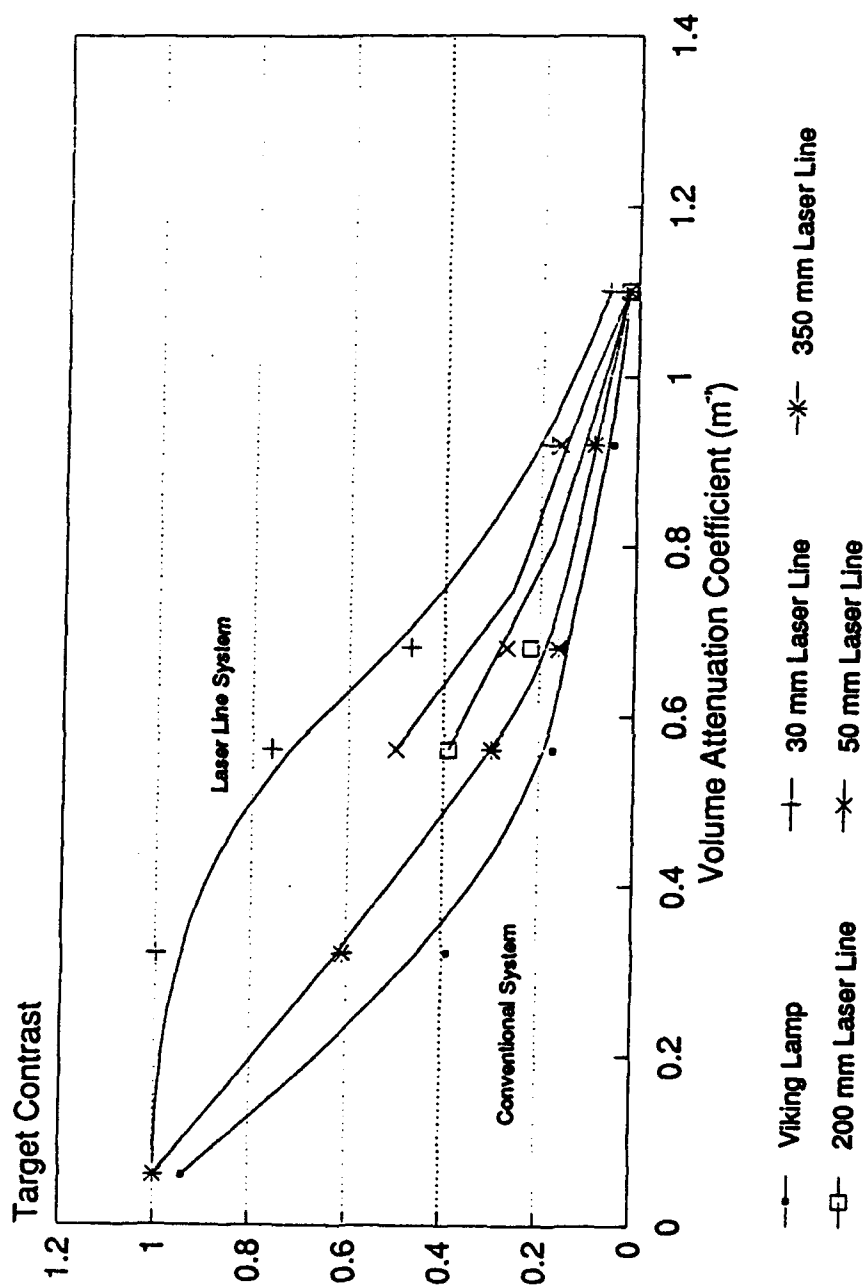


FIGURE 4 - Image contrast vs turbidity for laser stripes

A New Type of Scatterometer for Measuring the Small Angle Volume Scattering Function of Seawater and the Experiments in the East China Sea

Huang Xiao-sheng, Zhang Jin-long, Chen Wei-biao, ZHANG Ting-lu
He Ming-xia and Liu Zhi-shen

Ocean Opt-Electronic Institute
Ocean University of Qingdao
Qingdao 266003, China

ABSTRACT

The small angle volume scattering function (SAVSF) of the seawater is one of the most important ocean optical parameters, which influences the laser beam propagation and the underwater image properties, so the in situ data of SAVSF have a great importance in ocean optics and in many applications. We have built a new type of scatterometer for measuring the SAVSF of the seawater. The instrument uses a underwater imaging system to measure the optical transfer function (OTF) of the seawater body, then the SAVSF can be calculated. The configuration of the scatterometer is presented and the main performance is analyzed. The results of in situ experiments in the East China Sea are also presented.

1.INTRODUCTION

There are large amount of opaque organic particles in the natural seawater, whose size is larger than light wavelengths and whose index of refraction is near that of water. According to the Mie scattering theory, we know that there are strong forward scattering in the natural seawater. In the coastal zone water there are a large amount of mineral particles which increase the forward scattering according to the diffraction theory. So, forward scattering is dominant, the most of scattered light energy is distributed about the light propagation direction, the small angle scattering ($<5^\circ$ or $<10^\circ$) is more strong and the large angle scattering may be neglected in many important applications. So SAVSF is one of the key parameters which influence underwater laser beam propagation and underwater image properties, because scattering decides the broadening of laser beam and the blurring of the images. SAVSF is a important inherent optical parameter in underwater laser communication, ocean lidar sounding, lidar bathymetry, underwater vision systems etc.. But scattering in the natural water is a complicated physical process, it is difficult to be calculated directly, because the particles have various shapes and optical properties. So in situ measurement is the most important method to get available SAVSF data.

The convenient methods of measuring SAVSF usually use collimate laser beam which passes a water body and measure the light energy angular distribution", we have measured the SAVSF up to 0.01° successfully, using collimate laser beam and zero block filter in the laboratory". But it is very difficult to keep high alignment accuracy in situ measurements, so the in situ instruments for measuring SAVSF are usually complex and expensive.

The water body is a liner spacial invariant system according to the information optics theory, the optical properties of seawater can be described by OTF which is depended on the attenuation coefficient c and the volume scattering function $\beta(\theta)$, the relationship between them is":

$$\beta(\theta) = B^{-1}(c + \ln(OTF)/r)$$

B^{-1} : inverse Fourier-Bessel transform

c : attenuation coefficient of seawater
 β : volume scattering function of seawater
 r : the optical path in the water body

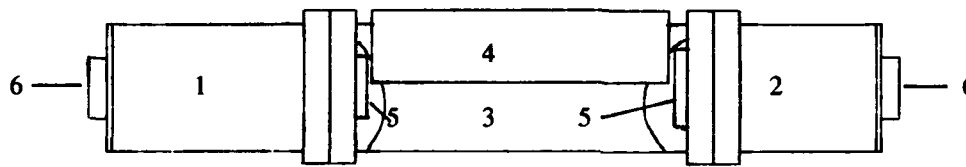
We measure the OTF of water body with defined length r , if the attenuation coefficient c is known, then β can be calculated. The details of the principle is given by another paper presented in this proceeding".

Our new type of the small angle scatterometer is based on this principle. An underwater imaging system is used to measure a image passed through water body, OTF can be get from the original and blurred image. The main advantages of the method are that there are no necessary of high alignment accuracy, so the system is stable and available for severe in situ conditions, and that the configuration is simple and stable, the coast is lower. Since white light source is used, there are no speckle effect and spectral SAVSF data should be obtained if a spectral filter is used.

2. THE INSTRUMENT

2.1 The configuration of the instrument

Fig.1 shows the diagram of our new scatterometer.



- 1: light source box
- 2: camera box
- 3: connector
- 4: shade
- 5: glass window
- 6: window for operation

Fig.1 diagram of the small angle scatterometer

Our scatterometer is composed of 3 parts mainly, the light source box, the camera box and the connector.

A fluorescent lamp tube is used as a light source, and a battery is used as a power supply. A Lamber's body is illuminated, a slip is located in front of the Lamber's body, and the direction of the slip is parallel to the lamp tube, so we have a spread line light source with 1-mm wide and 80-mm long, which is used as a original 1 dimension image. Such light source has high efficiency and good stability. All of the elements are mounted in the light source box, which is water tight and has a aperture with 80-mm diameter protected by a water tight glass window.

A video camera records the blurred image passing through the water body contained in the connector. The lens has 90-mm focal length. The detector is a 512×512 CCD array and the scan line is perpendicular to the line source. A press sensor is used to detect the depth. The images are tape recorded, and also the information of time and depths. All of that are set in the water tight camera box. The aperture with 70-mm diameter is protected by a glass window too.

The two boxes have 180-mm diameter and 350-mm length. There are operation windows at the trails of the two boxes for necessary operations.

The connector is made of steel cylinder as the same diameter as the boxes. The inside diameter is 164-mm and the length is 720-mm. The effective length of the contained water body is 680-mm and the effective view field is from 100-mm to 160-mm. Many 20-mm holes are arranged on the cylinder's wall permitting the exchange of the inside water when the scatterometer is sinking. A shade is mounted over the cylinder to obstruct the downward irradiance, which is strong in the sea. Some upward irradiance, which is weak in the sea, goes into the cylinder through the holes at the cylinder bottom, but only the light scattered near the 90° direction could be received by the detector and it is the weakest scattering in such direction. In addition to, there are two apertures inside the cylinder to repress the background.

2.2 Analysis of the performance of the instrument

The effective view field 100-mm is used and the work distance is about 720-mm, so the upper limit of the angular range is about 4.0° . Because of the symmetry of the image, the line light source is off-axis, and the upper limit of the angular range can be extended to 5° or larger.

The angular resolution is determined by the line number of the CCD array. For 512 line of the CCD array, the angle resolution is about 0.015° . The 0.01° angular resolution can be obtained by interpolation and the 0.01° lower limit of the angular range can be get by extrapolation according to monotonicity of the SAVSF. The angular range and the angular resolution can be changed by changing the effective view field from 100-mm to 160-mm.

Because of the 1 dimension image and the CCD scan line is perpendicular to the line light source, so we average the central 100 rows data to calculate the OTF, and SNR is increased ten times.

The main performances index of our new scatterometer are:

- the length of water body: 680-mm
- the measuring range: $0.01^\circ \sim 5^\circ$
- the angular resolution: 0.01°
- the maximum working depth: -100-m
- the full length: 1500-mm
- the full weight: 60-kg

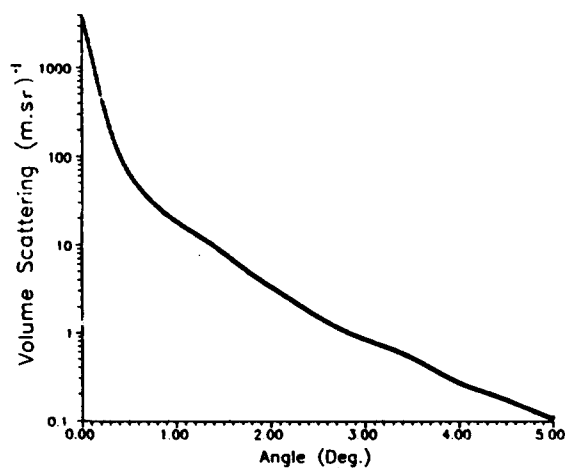
3. THE IN SITU EXPERIMENTS

In October, 1993, we get 5 sets of SAVSF data from the East China Sea using our new scatterometer. At every points, we collected original data at different depths, the maximum depth was - 60-m. The data processing was outline using the method presented in ours another paper¹. The typical results are listed in Fig.2.

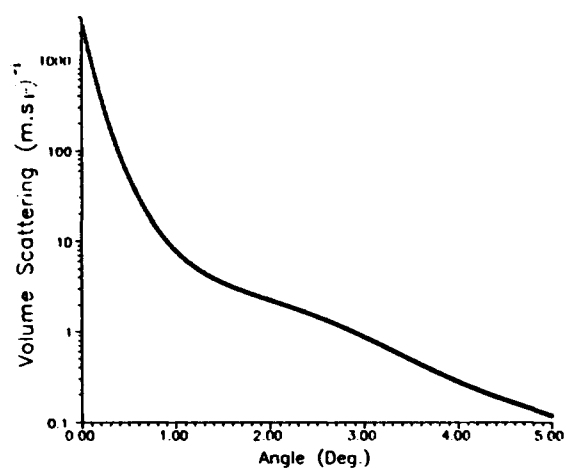
This research work was supported by a grant from the National Science Foundation of China.

REFERENCES

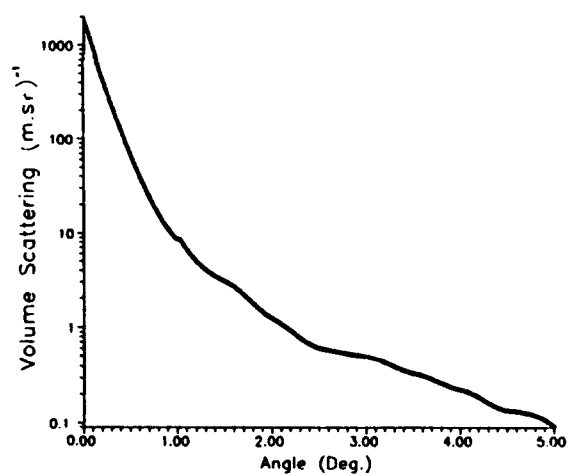
- [1] S.Q.Duntley, "Light in the Sea," J. Opt. Soc. Amer., Vol. 53 pp.214-233, 1963.
- [2] T.J.Petzold, "Volume Scattering Function for Selected Ocean Waters," in *Light in the Sea*. Edited by J.E.Tyler pp.152-174, 1977.
- [3] Liu Zhi-Shen & He Ming-Xia, "Fourier Optics Method of Radiative Transfer in the Ocean," Scientia Sinica (Series A) Vol.29, No.4, 1986.
- [4] Zhang Ting-Lu et al, "An Image Transmission Method of Measuring Small Angle Scattering Function Of Seawater," in procceding *SPIE OCEAN OPTICS XII*, 1994.



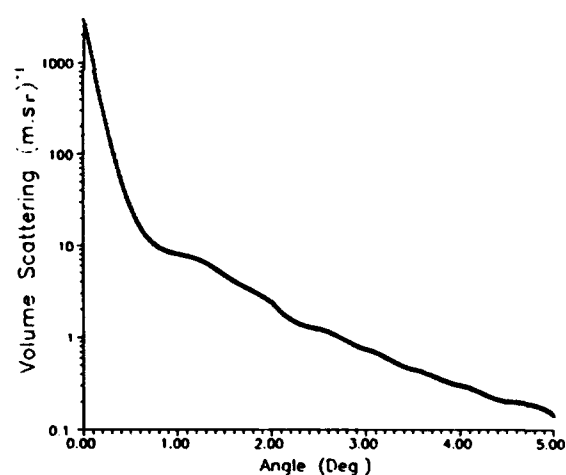
Station 1: Water Depth 25 m



Station 10: Water Depth 5 m



Station 9: Water Depth 25



Station 9: Water Depth 55 m

Fig.2 The measured SAVSF curves from different locations and different depths

An Image Transmission Method for Measuring Small Angle Scattering Function of Seawater

Zhang Ting-lu, Huang Xiao-sheng, Liu Zhi-shen

Ocean Opt-electronic Institute
Ocean University of Qingdao
Qingdao 266003, CHINA

ABSTRACT

The small angle scattering function of seawater(SASF) is a significant parameter of ocean optics, and has an important role on the underwater transmission of image and narrow beam. In this paper, we have described the image transmission method of measuring SASF and the system which we have set up for measuring SASF by the method. We have get much data using the experiment system with different water path range. The measurement results agree with the theory.

1. INTRODUCTION

Modern Ocean Optics is very concerned with the small angle scattering function of seawater(SASF). Since 1980s, with the rapid development of the underwater laser communication, Lidar and underwater laser image system, the characteristics of under laser transmission need to be studied in detail. Laser is a narrow beam light, and has strong directivity. The theory of transmission shows that the SASF is an important parameter. Since 1960s, some methods of measuring SASF have been developed^{1,2}, but there are some shortcomings. At present, there is no universally accepted method for measuring SASF in ocean survey, and the data of SASF are very limited. So, a new method is needed in ocean optics measurement.

In Optics, there are some well-considered methods for measuring the optical transfer function, for example the method of optical Fourier analysis and optical-electrical Fourier analysis. These methods can be used to measure the space angular frequency attenuation characteristics of the optical transparent medium. The space angular frequency attenuation reflects the spreading of the collimation light beam and point light source through the transparent medium. That is called beam spread function (BSF) and point spread function (PSF) of the transparent medium. This paper is based on the idea. By measuring the PSF of seawater, we can obtain the SASF according to the Fourier Optics method of radiative transfer in the ocean.

2. PRINCIPLE

An image $f(x,y)$ being transmitted through the water path distance R , it will become the blurred image $g(x,y)$. If the point spread function is $psf(x,y)$, they satisfy the relation

$$g(x,y) = f(x,y) \otimes psf(x,y) \quad (1)$$

Where: \otimes is the convolution operation.

Therefor, if the standard image $f(x,y)$ is known, we can obtain the PSF of the water path from measuring the deterioration image $g(x,y)$ by the certain data processing methods. The simple images are usually selected as the standard images, for example point or line. The line is more available for the practical system. At first, we obtain the line spread function by measuring the edge blurring of line image, and then get the two-dimension PSF according to the rotational symmetry of the seawater PSF.

By the Fourier Optics method of radiative transfer in the ocean, OTF is the Fourier-Bessel transform of the PSF:

$$\text{OTF}(\phi, R) = 2\pi \int_0^{\theta_0} R^2 \text{psf}(\theta, R) J_0(2\pi\phi\theta) \theta d\theta \quad (2)$$

Where: ϕ is the angular frequency, R is the water path distance, θ_0 is the maximum integral angle.
Another, OTF can be expressed as:

$$\text{OTF}(\phi, R) = \exp[-(c - \Xi)R] \quad (3)$$

Where: c is the beam attenuation coefficient.

Ξ is the Fourier-Bessel transform of the scattering phase function.

The angle of the scattering phase function is limited by the view field of measurement, so the scattering phase function obtained by the above method is called small angle scattering function.

3. EXPERIMENT

In order to verify the feasibility of measuring SASF by the image transmission method, and to get the various parameter which is needed in the design of in-situ small angle scatterometer, we have set up a system in lab.

The system (As showed in Fig.1) consists of a white light source, a standard object, a water tank, a video camera, an image sampling board and a pc-computer. The volume of the water tank is 30X30X40cm, the uniformity and transparency of its bottom glass are good. The standard object is the narrow split (its width is 1 mm), and placed on the tank bottom. The white light source under the water tank is the uniform diffused light, and illuminates the standard object. The standard image is transmitted in the water, and captured by the camera on the top of the tank. The signal of the camera is sent to the computer by the image sampling board, and then processed by the computer. The process of experiment is as follows:

- (a). No water in the tank, captured the image of standard object by camera
- (b). Add 10cm height water in the tank, captured the image of standard object by camera.
- (c). add 10cm height water in the tank again, captured the image of standard object by camera.
- (d). Repeat (c).

So, we can obtain three blurred images and one standard image. These are all our raw data.

4. DATA PROCESSING

The data captured by camera is two-dimension data, we need one-dimension data. In order to eliminate the edge effect, we select the average of 200 rows on the centre of image as one-dimension data. Another, in order to get higher angle resolution and wide view field, the image of standard object is not on the centre of view field, but on the right side or left side. By the symmetry of scattering, we can get the right (or left) side data using left (or right) side data.

In solving the equation (1) for PSF, it is an ill-conditioned problem, if linear method is used. To avoid the ill-conditioned problem, we use the Monte Carlo method to solve the equation.

At the end, the SASF can be solved by the formulas (2), (3) and (4).

5. RESULTS AND ANALYSIS

$\text{Psf}(r)$, $\text{psf}(r)$ and $\text{psf}(r)$ are the point spread functions with the three different water path distance r (10cm),

$r_1(20\text{cm})$ and $r_1(30\text{cm})$. By the transmission theory, they satisfy the equations:

$$\begin{aligned} \text{psf}(r_2) &= \text{psf}(r_1) \otimes \text{psf}(r_1) \\ \text{psf}(r_3) &= \text{psf}(r_1) \otimes \text{psf}(r_2) \end{aligned} \quad (4)$$

From Fig.2, the measured PSFs agree well with the calculated PSFs. So, the measurement results of PSF agree with the theory. This confirms the correctness of PSF measured by the method based on this paper.

From the data of $\text{psf}(r_1)$, $\text{psf}(r_2)$ and $\text{psf}(r_3)$, we have obtained the corresponding SASFs β_1 , β_2 and β_3 . (As showed in Fig. 3). In principle, the three SASFs should be same for the same water. Fig.3 shows that the three SASFs are same within the error. But there is more error in the larger angle. In the larger angle, β_3 is bigger than β_2 , and β_2 is smaller than β_1 .

The scatterance of the short water path distance is less than that of long water path distance. Some of the Scatterance of short water path distance is too small to detect for the camera in the larger angle because of the limitation of the camera sensitivity. If the high sensitivity camera are used, the error may become less.

The angle resolution of the system based on the method of this paper can reach 0.01° , its measurement angle range is $0.01^\circ \sim 5^\circ$. The system has the advantages as following: simple structure, convenient operation and high angle resolution.

This research work was supported by a grant from the National Science Foundation of China.

6. REFERENCE

1. Duntley, S.Q., "Light in the sea", J. Opt. Soc. Am., 53: 214-233, 1963.
2. Petzold, T.J., "Volume Scattering Function for selected ocean waters", SIO Ref., 72-78: 79pp, 1972.
3. McCluney, W.R., "Multichannel forward scattering meter for oceanography", Appl. Opt., 13: 548-555, 1974.
4. Kneneth, J. Voss, et al., "Measurement of the point spread function in the ocean", Appl. Opt., Vol. 29, No.25, 3638-3642, 1990.
5. Liu Zhi-shen, He Ming-xia, "Fourier Optics Method of Radiative Transfer in the ocean", Scientica Sinica (Series A) Vol. 29, No.4, 1986.
6. Zhang Ting-lu, Liu Hai, "De-bluring the underwater image using the method of Monte Carlo", SPIE Vol.2258 Ocean Optics XII, 1994.

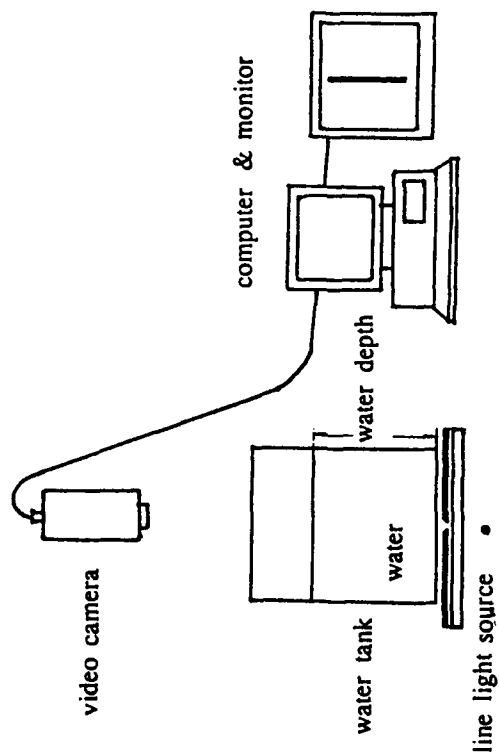


Fig.1 Diagram of the laboratory experiment

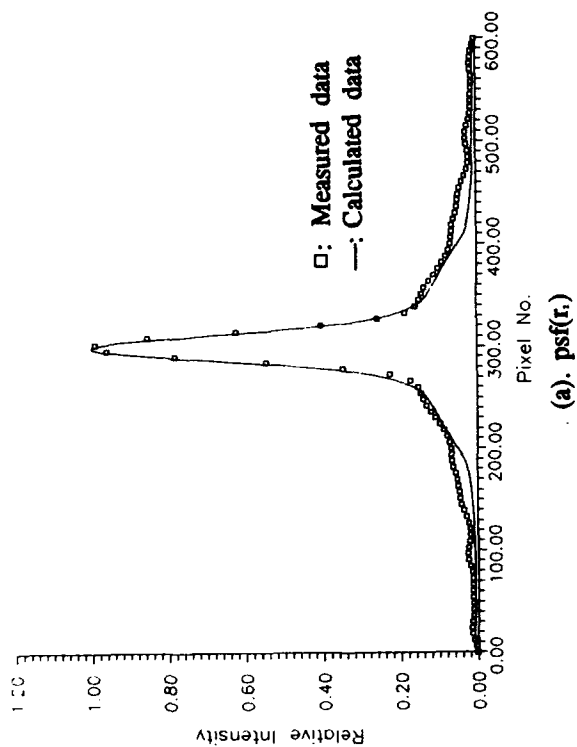


Fig.2 The comparison between the measured and the calculated PSF

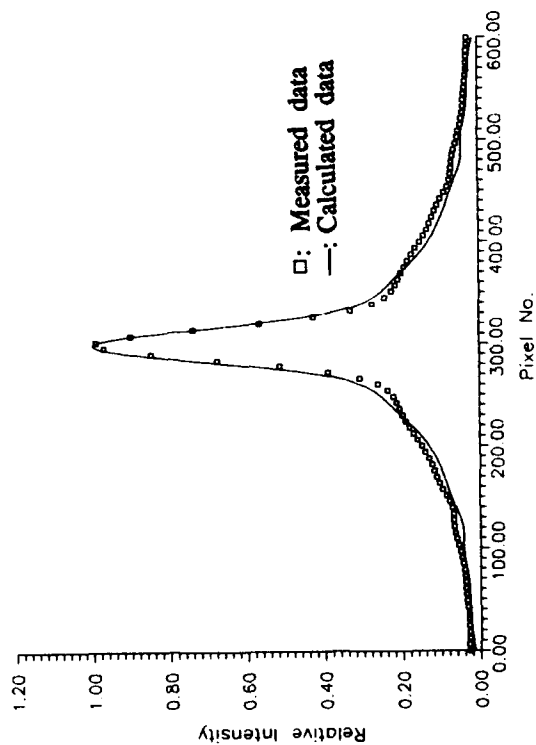


Fig.2 (b). psf(r.)

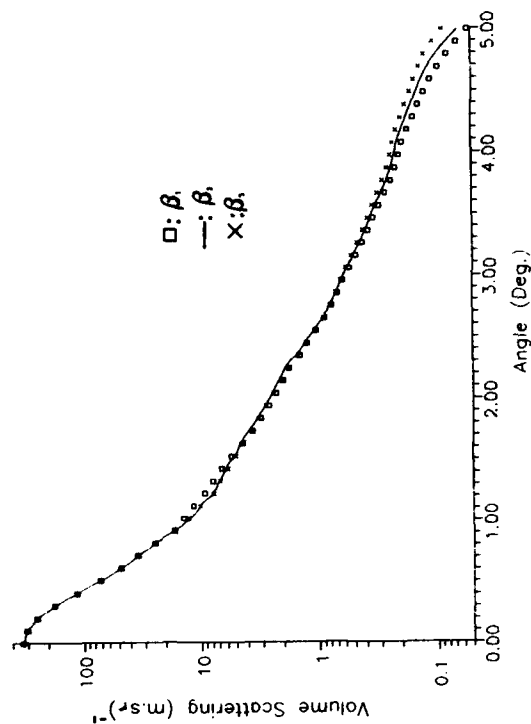


Fig.3 The comparison of β , β , β .

De-blurring the Underwater Image Using the Method of Monte Carlo

Zhang Ting-lu, Liu Hai

Ocean Opt-electronic Institute
Ocean University of Qingdao
Qingdao 266003, CHINA

ABSTRACT

Because of the scatterance of water, underwater image will be deteriorated. It is necessary to restore the image for the underwater photography and underwater robot vision. In this paper, we have simulated the process of the image blurred under the water, described the steps of de-blurring the underwater image using Monte Carlo method, and restored the blurred image in the different random noise by this method. The results of restoration are satisfactory.

1. INTRODUCTION

An image being transmitted in the water will be blurred unavoidably. That is harmful for the underwater photography and underwater robot vision. Since 1960s, the mechanism which the image is blurred had been studied from the theory and experiment^[1,2]. The point source will be blurred, when it is transmitted through the water. It is caused by the scatterance of water. One image is regard as the space distribution of many point sources. All point sources of the image are scattered simultaneously through water path, and spread identically. It is called the space invariance for the image transmission. Mathematically the image transmission is a process of convolution. It is showed as:

$$g(x,y)=f(x,y)\otimes \text{PSF}(x,y)$$

Where: $g(x,y)$ is the blurred image received

$f(x,y)$ is the original image to be retrieved

$\text{PSF}(x,y)$ is the point spread function of water

\otimes is the convolution operation

Solving the above equation is a problem of image restoration in the image processing. Although the method of solving the equation by linear restoration is simple, it has an insolvable problem -- ill-conditioned problem. We use the method of non-linear image restoration -- Monte Carlo method to process the simulation image blurred in the different noise, and get good results.

2. THE METHOD OF THE DE-BLURRING IMAGE BY MONTE CARLO

The main idea of the method is as follows: One image is divided into many pixels, and the pixels value of the image is composed of particles, every particle has certain energy. The total number of particles is known, so the total energy of the image is definite. One particle is located on a pixel randomly, only it satisfies the criterion. After all particles are distributed, the object image will be restored. We will show the process of image restoration by one-dimension image in the following.

The process of image transmission in water satisfies the following equation:

$$g(y_m)=f(x_n)\otimes \text{psf}(y_m-x_n)+n_0$$

Where: $f(x)$ is the object image, $x=(x_1, x_2, \dots, x_n)$
 $g(y)$ is the blurred image, $y=(y_1, y_2, \dots, y_m)$
 n is the random noise
 \otimes is the convolution operation

At the beginning, we suppose that the object space is empty. While a particle (its energy is d) is distributed at the location x , its energy will be added on the image plane at the form of continuous distribution of the point spread function.

The first particle being distributed on the location x , the accumulated image is:

$$g^{(1)}(y_m) = d_0 \cdot \text{psf}(y_m - x_n)$$

The second particle being distributed on the location x , the accumulated image is:

$$g^{(2)}(y_m) = g^{(1)}(y_m) + d_0 \cdot \text{psf}(y_m - x_n)$$

For the same reason, the k th particle being distributed on the location x , the accumulated image is:

$$g^{(k)}(y_m) = g^{(k-1)}(y_m) + d_0 \cdot \text{psf}(y_m - x_n)$$

And the next particle being distributed on the location x , the new accumulated image is:

$$g^{(k+1)}(y_m) = g^{(k)}(y_m) + d_0 \cdot \text{psf}(y_m - x_n)$$

$g^{(k+1)}(y_m)$ divides the known image data $g(y_m)$:

$$r_m = g^{(k+1)}(y_m) / g(y_m) \quad (m=1, 2, \dots, M)$$

We suppose that R is the maximum value of r . At the same time, there is a adjustable minimum R . Only $R \leq R$, this distributing is reasonable. The meaning of Minimum R is: when R becomes less, any location x distributing is not reasonable. Repeat above procedure, while all particles are distributed completely, the object image will be restored.

3. SIMULATION EXPERIMENT

For the convenience, we use one-dimension image instead of two-dimension image in the simulation experiment. Of course, the method is also available for two-dimension image.

At first, we do the convolution of the original image and the point spread function, add the random noise to get a blurred image. Then we consider the point spread function and the blurred image as the known factor, and use the Monte Carlo method mentioned to restore the image.

In the experiment, the point spread function used is a typical function measured on the sea (Fig.1), and the original image is also a representative. The maximum of random noise is 5% and 10%.

4. RESULTS AND ANALYSIS

From the simulation experiment, we draw the following conclusions:

(1). After the image have been blurred, it is distorted beyond recognition, and its contrast is very small. But through the restoration processing using the Monte Carlo method, the clear images are restored.

(2). The relative mean square error of restored image is 2% with no noise, 7.8% with 5% random noise, and 12.8% with 10% random noise. From the shows of Fig.2 (a),(b) and (c), the quality of restored images is high with noise or less noise, and the bigger the noise is, the more the error of restored image is. Another, the bigger the pixel value changes in a location, the more the restoration error in the location.

(3). This method is an effective method for de-blurring the underwater image. Its advantages are: high ability against the noise, less retraining conditions, no ill-conditioned problem and fast computing.

This research work was supported by a grant from the National Science Foundation of China.

5. REFERENCE

1. Romanova, L.M., "Non-stationary light field deep in a turbid medium illuminated by a narrow beam". *Izv. Atmos. Oceanic Phys.*, 5:354-363, 1969.
2. Wells, W.H. and Todd, N.N., "Loss of resolution in water as a result of multiple small-angle scattering", *J. Opt. Soc. Am.* 59:686-691, 1969.
3. Hodara, H., "experimental results of small angle scattering", In: *Optics of the sea. AGARD Lect. Ser.*, No. 61: 3.4-1-3.4-17, 1973.
4. Andrews, H.C., and Hunt, B.R., Digital Image Restoration, Prentice Hall, INC., 1977.

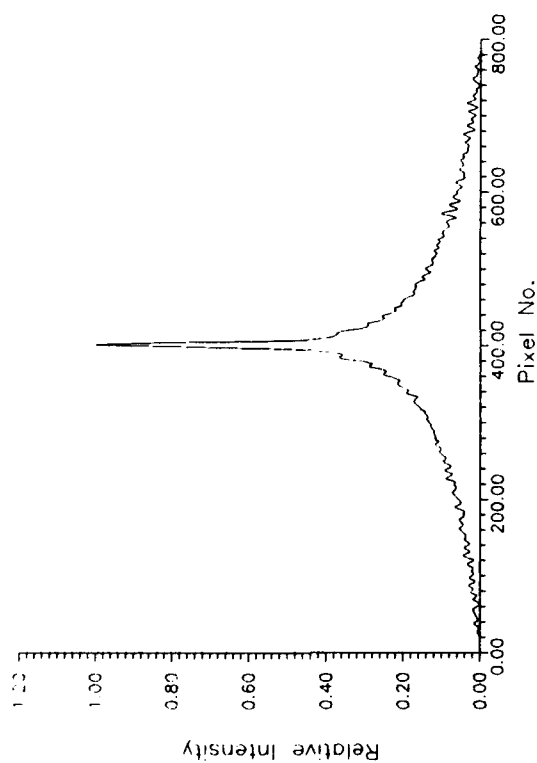


Fig. 1 The typical point spread function of seawater

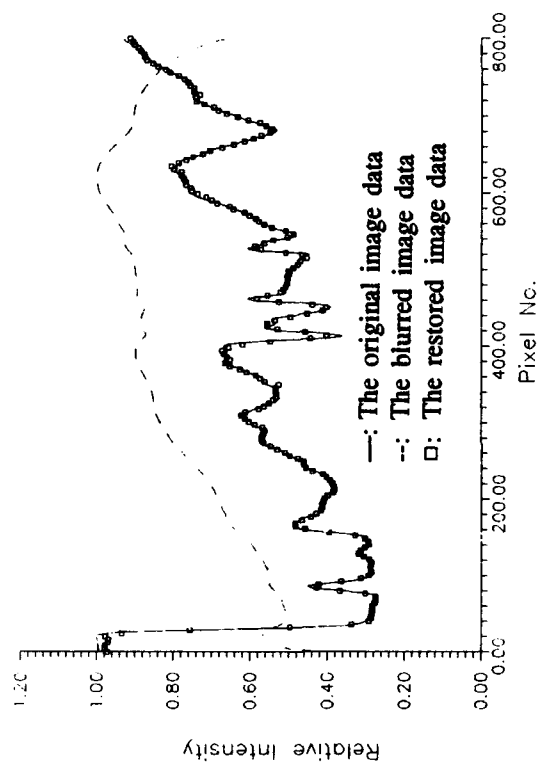
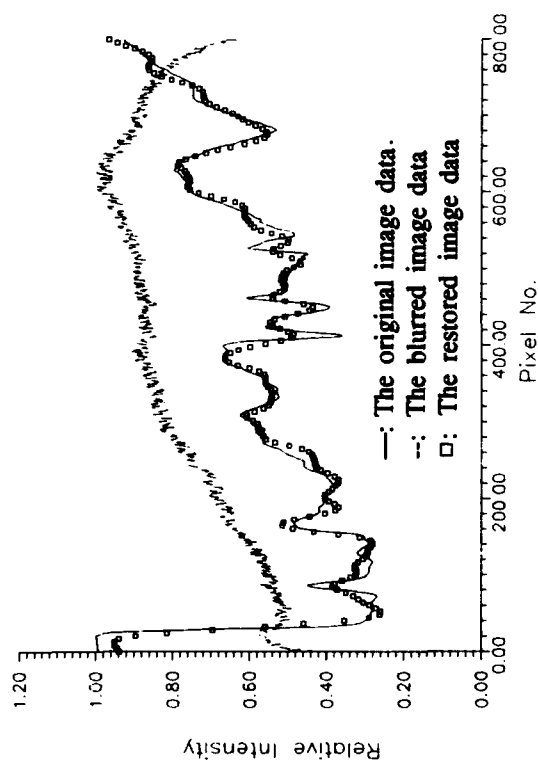
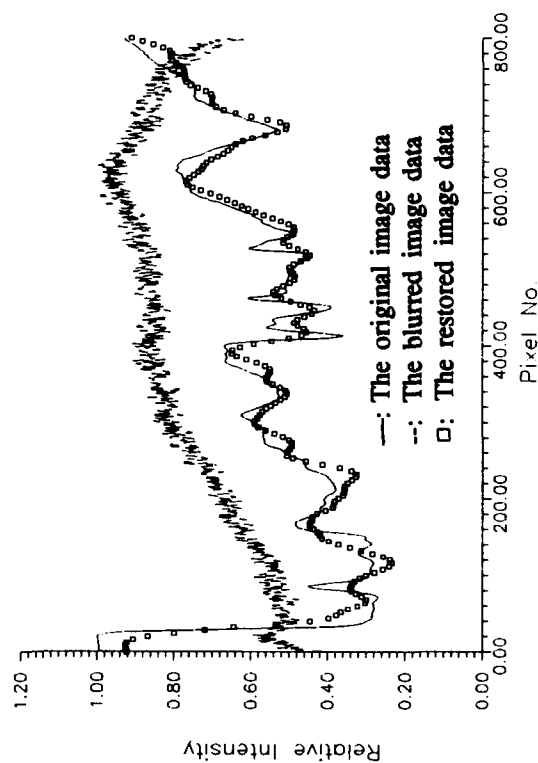


Fig. 2(a). With no noise



(b). With 5% random noise



(c). With 10% random noise

Fig. 2 The comparison of the original image, blurred image and restored image

SPECTRAL FLUORESCENCE AND SCATTERING OF CYANOBACTERIA AND DIATOMS HELD BY OPTICAL TWEEZERS

G.J. Sonek and Y. Liu

Department of Electrical and Computer Engineering, and Beckman Laser Institute
University of California, Irvine CA 92717

R.H. Iturriaga

Department of Biological Sciences
University of Southern California, Los Angeles, CA 90089

ABSTRACT

Optical tweezers is a term used to describe the optical force generation and confinement process by a highly focused laser beam. The forces exerted by the tweezer are sufficient to confine and move cells and particles without physical contact. When integrated with fluorescence or scattering detection, the laser tweezer can become a powerful instrument for the rapid characterization of the optical properties of isolated organic marine particulates and phytoplanktonic cells, from which bulk properties may be inferred. This technique offers the advantage of studying planktonic cells and organisms in their natural environment by confinement without immobilization, thereby preserving the spectral absorption and fluorescence properties of the samples under study. Herein, we report, for the first time, on the measurement of the spectral fluorescence and scattering of cyanobacteria and diatoms which have been confined by an optical tweezer. Cell culture samples of *Nanochloris* and *Skeletonema* ranging in size from ~ 2 to 4 μm were confined using ~ 30 mW from a focused Nd:YAG laser ($\lambda = 1060 \text{ nm}$). Fluorescence was simultaneously excited in the 350 - 400 nm wavelength range and detected using a diffraction grating and CCD array, while scattering was detected in a backscatter geometry. Fluorescence emission of picoplanktonic cyanobacteria (*Synechococcus*) type DC-2 showed a characteristic peak centered at 565 nm, when excitation was set within 520 - 540 nm. Preliminary data shows the characteristic emission peak from the *chlorophyll a* pigment (685 nm) for both samples, as well as spectral features that may be related to other photosynthetic pigments.

1. INTRODUCTION

The ability to systematically measure the optical properties of single marine particles, and their perturbations, is important to the understanding of how individual microscopic particles, specific types of particles, and collections of different particles, govern the bulk or macroscopic ocean optical parameters. The study of marine particle fluorescence¹⁻³ and scattering^{4,5} is well known. Optical tweezers⁶, with the ability to confine and manipulate single cells and organisms, offer several unique advantages over the conventional techniques of flow cytometry and microphotometry in marine particle optical measurements. These include: (1) confinement in the sample's natural environment without destructive immobilization, (2) preservation of spectral scattering, absorption, and fluorescence, due to the *in-situ* nature of the measurement, and (3) the ability, over time, to examine individual particles, or classes of

particles, with respect to size, shape, orientation, interaction with multiple particles, and absorption and fluorescence efficiencies. Described herein are preliminary experimental results which show that fluorescence spectra and scattering signatures can be acquired from single phytoplankton cells and cyanobacteria suspended in their natural medium using the optical tweezer technique. Furthermore, the sampling of particle populations facilitates the microscopic study of intrasample and intersample variability. Hence, optical confinement may provide yet another means to study in the field the inherent optical properties (IOPs) of marine particulates, their parametric dependences, and how single particle properties relate to the bulk optical properties for optical closure.

2. METHODS

Fluorescence and scattering measurements were performed on a microscope system that combines laser trapping and fluorescence, as shown in Fig. 1. The system consists of a primary infrared laser beam ($\lambda = 1060$ nm), emitting up to 200 mW, that is interfaced to an inverted optical microscope. The basic optical tweezer is formed by focusing the circularly polarized laser beam onto the sample from below the sample chamber via a high magnification, oil immersion microscope objective (e.g. 100X, 1.3 N.A.). A special chamber, consisting of thin parafilm sheets sandwiched between microscope coverslips, is used to confine the cells in suspension. The tweezer is converted into a high resolution fluorescence - scattering microscope by collinearly coupling a secondary optical beam through the same objective lens. Using the same focusing optics, light from a UV source (200 W Hg arclamp) is used to excite fluorescence, while general illumination is provided by an optical condenser system that resides above the sample chamber. Single particle fluorescence is collected by the same objective used to form the laser trap, and passed through a pinhole. The light is then collimated, dispersed by a diffraction grating, and ultimately focused onto a cooled CCD detector array. A personal computer acquires the spectral data over a 400 nm bandwidth in ~ 100 ms. S/N ratios in excess of $10^3:1$ are achieved with high spatial resolution (> 1 μm). For light scattering studies, a third beam is brought into the system (HeNe laser, $\lambda = 632.8$ nm), and the scattered light collected along the same optical path. To measure "bulk" properties, the focusing objective was reduced in magnification to 10X or 20X, thereby enabling hundreds of particles to be studied at once in the same field of view.

Three cell types were used in laboratory experiments, including nanochloris and skeletonema phytoplankton cells ($\sim 2 - 4$ μm diameter), and synechococcus cyanobacteria (~ 0.5 μm diameter). Cells were cultured in F2 medium, and left under daylight illumination, at $\sim 23^\circ\text{C}$, until experiments were performed. The cultures were then transferred into sample chambers and placed within the trapping - fluorescence microscope. Using the minimum amount of laser power required for trapping cells of a given size (~ 30 mW for 3 μm cells, < 10 mW for 0.5 μm cells), individual cells were confined, and exposed to UV light for 0.1 sec. Experiments performed included a comparison of bulk and single cell fluorescence spectra for excitation at 350 nm, a study of fluorescence as functions of UV exposure time and confinement time within the tweezer, and measure of backscattering from single cells, over an angular range of $\pm 20^\circ$ at the scattering wavelength of 632.8 nm.

3. RESULTS AND DISCUSSION

In our first set of experiments, samples of nanochloris phytoplankton were studied. The results of comparing fluorescence spectra from an individual cell and that of the bulk are shown in Fig. 2. When the data is normalized, both spectra display the characteristic peak of *chlorophyll a* emission at 685 nm. The bulk spectrum is nearly identical, with the exception of a long-wavelength shoulder centered at ~730 nm, indicating that there is some batch variation. For five different single cells identically exposed to UV light, and measured within a time period of ~ 3 min., individual spectra differed only in their intensity of fluorescence, as shown in Fig. 3. These differences may arise from changes in the chlorophyll content per cell, photoadaptation, or biomass variations⁸. However, changes in fluorescence emission can also be induced via extended UV exposure, as shown in Fig. 4 for the skeletonema cell. While a 0.1 sec. exposure time results in strong emission at 685 nm and 730 nm, respectively, the intensity of fluorescence clearly decreases, almost by a factor of 2, with increasing exposure time, indicating that some photobleaching has occurred. Variations in fluorescence intensity from cell to cell may, therefore, have more than one origin.

A second series of experiments focused on measuring the fluorescence emission from the cyanobacteria, *synechococcus*. Here, given the small size of the samples (~0.5 μm), the optical trapping process is close to its practical limit for single cell confinement. For cells or particulates much smaller in size, it is nearly impossible to confine just a single sample at a given time. A bulk measurement, made with a low magnification microscope objective by collecting light from several hundreds of cells, is shown in Fig. 5. A bulk nanochloris spectrum is included for comparison. The significant features here include an intense fluorescence peak at 565 nm, and a less intense peak at 650 nm. Surprisingly, the emission spectra taken from four different *synechococcus* samples, as shown in Fig. 6, exhibit very large variations in emission intensity at designated wavelengths. At the single cell level, spectral features now appear not only at 565 nm and 650 nm, as in the bulk, but also at 600 nm and ~675 nm. The long wavelength peaks are attributed to *chlorophyll a*, while the shorter wavelength features (565, 600 nm) are likely to be derived from the *phycoerythrin* photosynthetic pigments. The variations in spectral features from sample to sample can be better understood when the fluorescence from an individual *synechococcus* sample is monitored for an extended period of time. While confining the same sample within an optical trap for a period of five hours, and measuring the fluorescence emission every hour, it is found that the intensities of the 565 nm and 676 nm peaks decay and grow in a complementary fashion, as shown in Fig. 7. When Figs. 6 and 7 are interpreted together, the results suggest that the observed intrasample variability is related to the measurement of fluorescence at different stages in the cell's natural growth or death cycle. Hence, the optical tweezer, as a non-invasive immobilization tool, has facilitated the temporal study of a single cyanobacteria species in its natural environment.

Lastly, to demonstrate that light scattering can also be accomplished within the tweezer system, backscattering signals from individually trapped nanochloris cells were measured. These results are shown in Fig. 8. At four scans per sample, and four different samples measured, the signatures display variations that may be shape or orientation related. The scans cover an angular range of $\sim \pm 20^\circ$ ($x = 0.09^\circ$), centered around 180° . The backscatter signals appear to be consistent from sample-to-sample and run-to-run, respectively. This data is more difficult to

interpret with respect to particle size, refractive index, or absorption than standard Mie theory results, given the fact that, in this case, Lorenz-Mie scattering results from the use of a highly focused Gaussian beam geometry. However, this geometry may offer the potential advantage of enhanced scattering sensitivity to the particle's index, absorption coefficient, non-sphericity, or stratified layer structure, based upon the coherent nature of the scattering process.

4. CONCLUSION

Optical tweezers have been used for the first time to confine phytoplankton and cyanobacteria, so that in-situ fluorescence and scattering measurements could be made on individual cell samples. Both fluorescence and scattering reveal intrasample and intersample variability in terms of spectral shape, and the magnitude and angular distribution of scattering. While nanorchloris and skeletonema samples show strong *chlorophyll a* fluorescence at 685 nm, the much smaller synechococcus samples exhibit their strongest emissions at 565 nm and 650 nm, with much greater intrasample variability. The methods presented herein should provide marine biologists and oceanographers a new means to study, in detail, the physiology of individual cells and marine particulates, and their contributions to the bulk oceanic optical properties under a variety of environmental conditions.

5. ACKNOWLEDGMENTS

This work was supported by the National Science Foundation, under grant BIR-9121325. The work of R. Iturriaga was supported the Office of Naval Research Ocean Optics Program, Contract N00014-89-J-1047.

6. REFERENCES

1. D.A. Kiefer, "Chlorophyll a fluorescence in marine centric diatoms: responses of chloroplasts to light and nutrient stress," *Mar. Bio.* vol. 23, 39-46 (1973).
2. C.S. Yentsch and D.A. Phinney, "Fluorescence spectral signatures for studies of marine phytoplankton," in *Mapping Strategies in Chemical Oceanography*, A. Zirino ed. (Am. Chem. Soc., Washington, DC 1985).
3. R. Iturriaga and S.L. Bower, "Microphotometric analysis of the spectral absorption and fluorescence of individual phytoplankton cells and detrital matter," in *Current Methods in Aquatic Microbial Ecology*, P. Kemp, J. Cole, B. Sheer, and E. Sheer, eds. (Lewis Publishers, Miami FL 1992).
4. T.J. Petzold, "Volume Scattering Functions for Selected Ocean Waters," Scripps Institute of Oceanography, SIO Ref. 72-28 (1972).
5. D. Stramski and D.A. Kiefer, "Light scattering by microorganisms in the open ocean," *Prog. Oceanog.* vol. 28, 343-383 (1991).
6. A. Ashkin, J.M. Dziedzic, J.E. Bjorkholm, and S. Chu, "Observation of a single-beam gradient force optical trap for dielectric particles," *Opt. Lett.* vol. 11, pp. 288-290 (1986).
7. S.L. Bower and R. Iturriaga, "Preparation of natural phytoplankton communities to preserve spectral fluorescence properties," SPIE Vol. 1750 *Ocean Optics XI*, 224 -232 (1992).
8. J. Marra, "Diurnal variability in chlorophyll fluorescence: Observations and Modeling," SPIE Vol. 1750 *Ocean Optics XI*, 233-244 (1992).

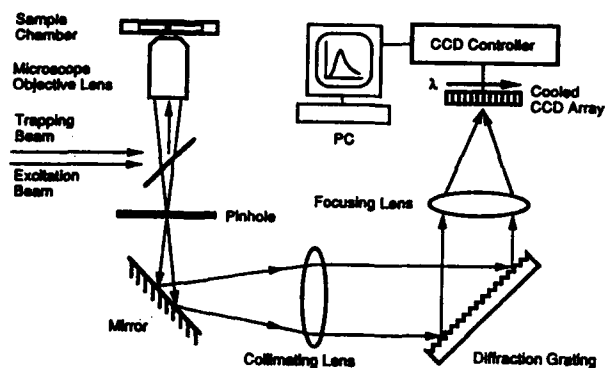


Fig. 1. Optical system for *in-situ* particle confinement and the measurement of fluorescence and scattering.

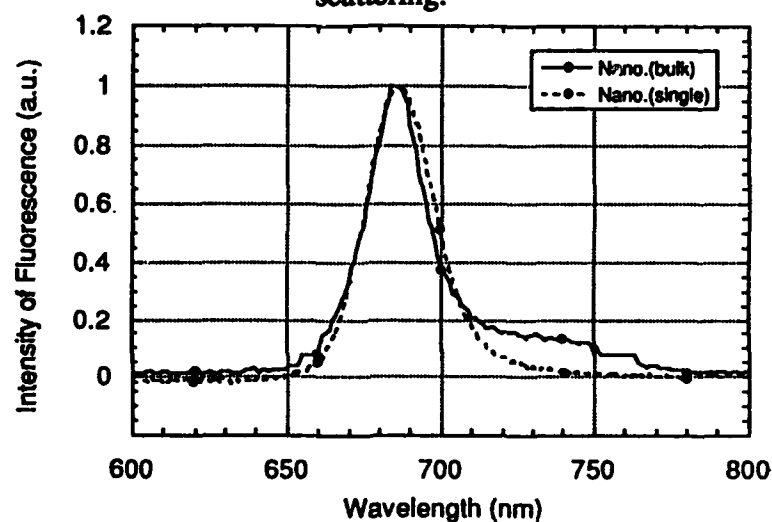


Fig. 2. Comparison of bulk and single cell fluorescence signals from a 2 μm nanochloris cell.

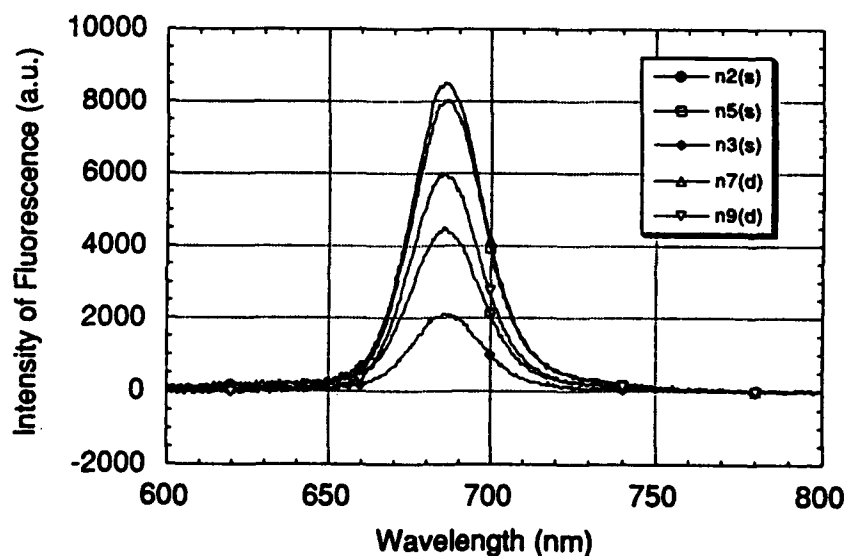


Fig. 3. Fluorescence signals from five different nanochloris samples.

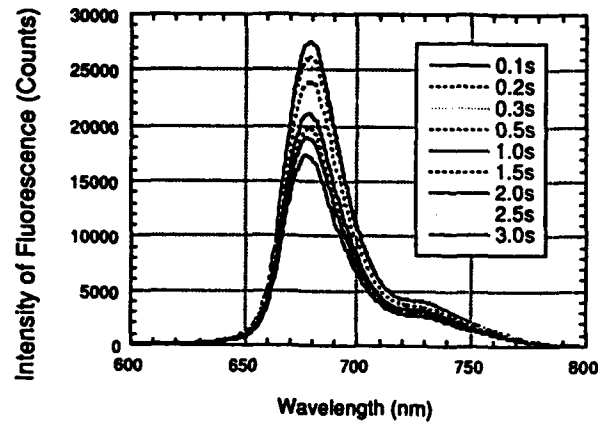


Fig. 4. Example of UV photobleaching in an optically trapped skeletonema cell.

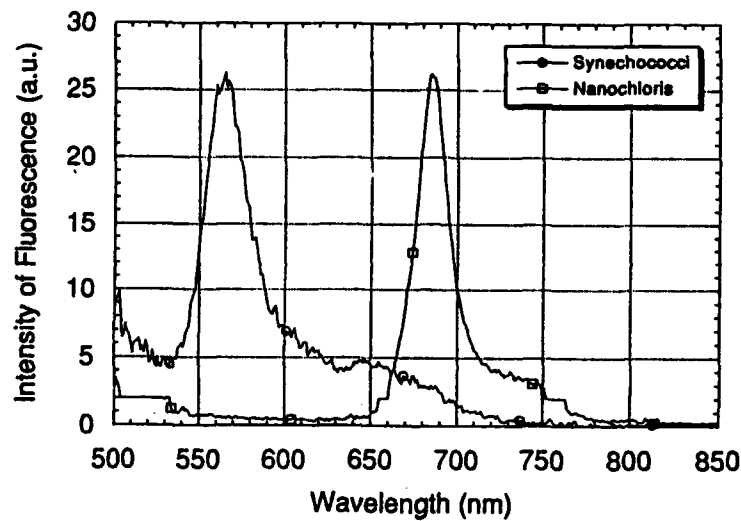


Fig. 5. Bulk fluorescence signals from the phytoplanktonic and cyanobacteria cells nanochloris and synechococcus.

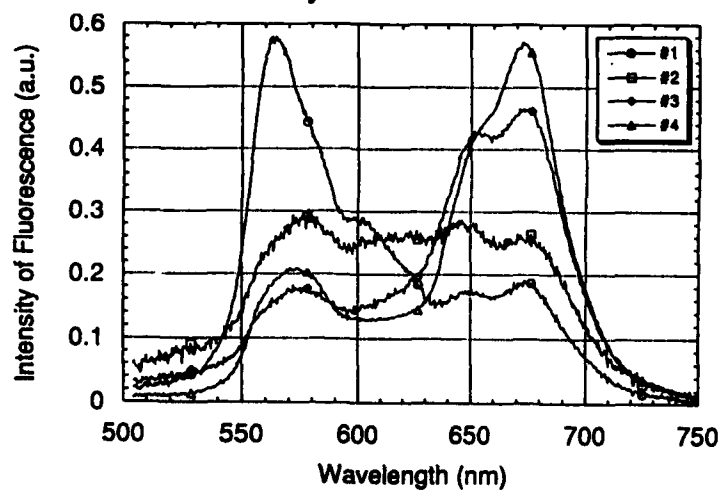


Fig. 6. Intensity of fluorescence for four different synechococcus cells, each confined by the optical tweezer at a slightly different time.

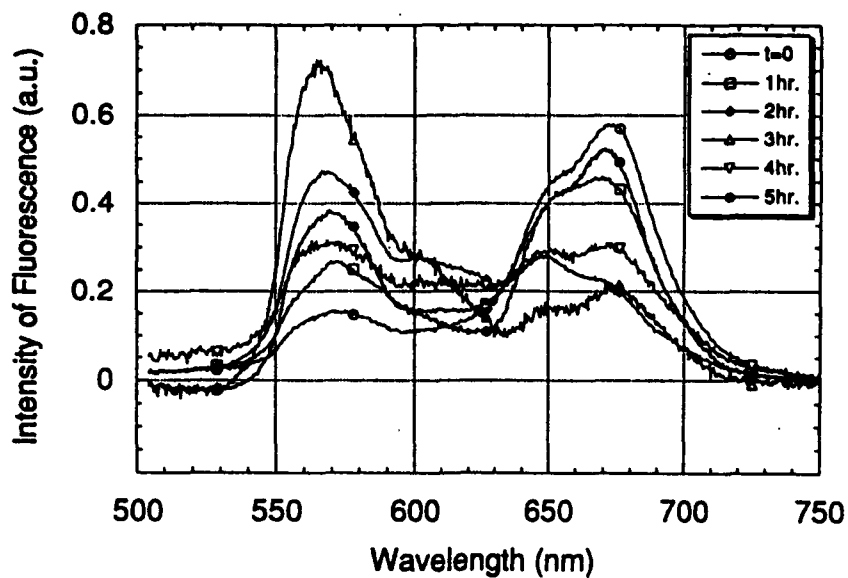


Fig. 7. Time-dependent fluorescence from a single cyanobacteria sample, confined by an optical tweezer for more than five hours, with fluorescence sampled every hour.

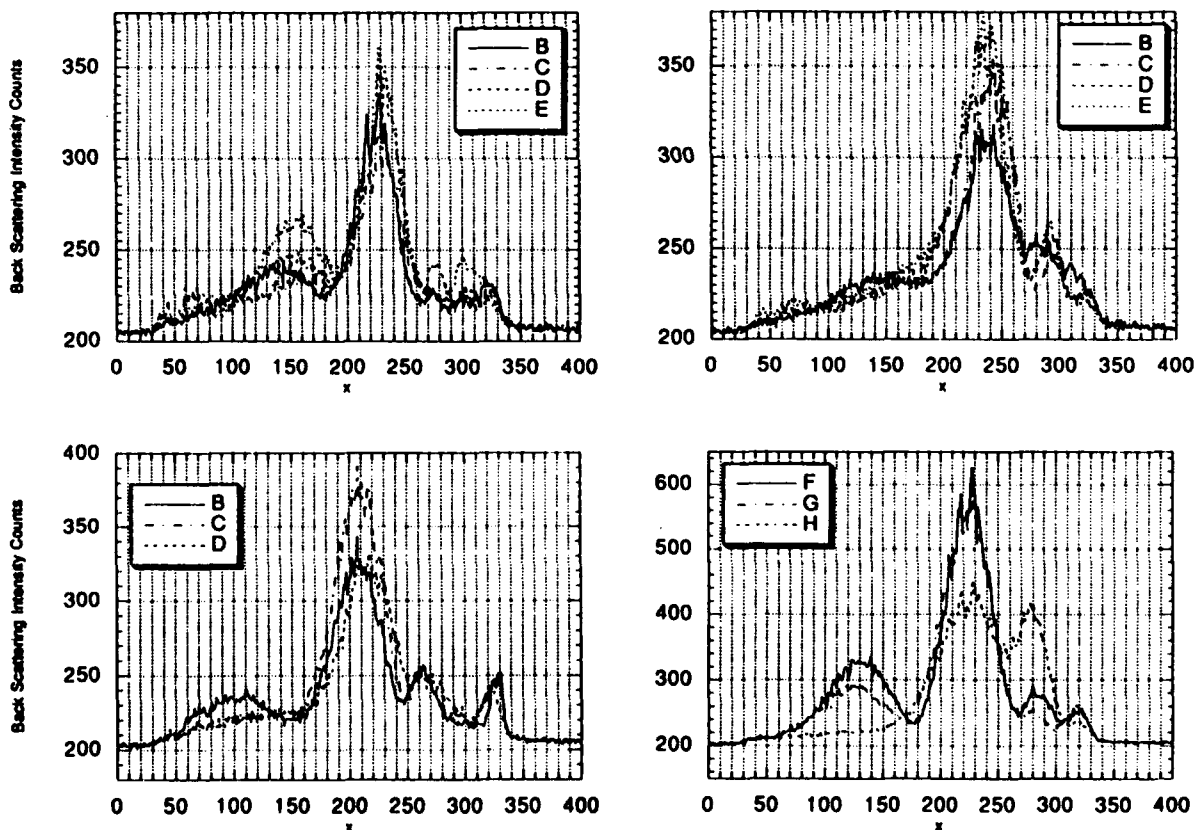


Fig. 8. Backscattering signals from individually trapped nanochloris cells.

SESSION 8

Environmental

Data base of oceanic optical properties

G.R. Fournier

Defence Research Establishment Valcartier
Courcellette, Quebec, G0A 1R0, Canada

M. Jonasz

M. Jonasz Consultants, 217 Cadillac Street
Beaconsfield, Quebec, H9W 2W7, Canada

1. ABSTRACT

An extensive data base of the optical properties of the ocean has been established. The phase function data has been analyzed using a modified form of the anomalous diffraction approximation. Results are presented for the fitted values of the index of refraction, inverse power of the size distribution, total scattering, forward to backward scattering ratio, backscatter, mean cosine and second moment of the scattering distribution. The size distribution data base has been analyzed using a new algorithm which allows the size distribution to be decomposed in a set of zero order log-normal distributions. We have found that this approach allows us to model measured distributions more accurately than by using inverse power laws of varying powers over sub-ranges of the data. The data is presented both in terms of the standard parameters of the log-normal and in terms of total integrated component amplitude, mode location and half width. This latter form is relatively independent of the model distribution used. Statistical correlations between the various parameters are given. We have found that the data base defines a working envelope of optical parameters that should be useful to the designer of underwater optics.

2. INTRODUCTION

We have gathered in computer readable form an extensive data base of the optical properties of the ocean which contains over 200 phase functions, 500 particle size distributions and an extensive reference on the refractive index of particles in suspension in seawater¹. The data was obtained from our own files and by an extensive literature search. The data base contains phase functions and particle size distributions measured in the Atlantic, Pacific, Baltic and Antarctic.

The analysis of such an extensive data base presents some serious problems. We have decided to model both the phase function and the particle size distributions and to extract from the models as many optically relevant parameters as possible. This effort should be considered only as a first attempt to systematically present the data.

3. PHASE FUNCTIONS

Assuming that the particle size distributions follow an inverse power law, we have recently derived from the anomalous diffraction approximation a simple approximate an-

alytic formula for oceanic phase functions².

$$\beta(\theta) = C\pi \left(\frac{2\pi(n-1)}{\lambda} \right)^{\mu-3} \frac{1 + \cos^2 \theta}{8 \sin(-\pi v)} \left[\frac{1}{(1 - \delta^2)\delta^v} \right] \\ \left([v(1 - \delta) - (1 - \delta^v)] + \frac{4}{u^2} [(1 - \delta^{v+1}) - (v+1)(1 - \delta)] \right). \quad (1)$$

Where

$$u = 2 \sin(\theta/2) \quad (2)$$

and

$$v = \frac{3 - \mu}{2} \quad (3)$$

and

$$\delta = \frac{u^2}{3(n-1)^2}. \quad (4)$$

In the above equations, $\beta(\theta)$ is the phase function. C is the front constant of the particle size distribution and μ is the inverse power of the same distribution. n is the index of refraction of the particles relative to that of water and λ is the wavelength of the light source used by the nephelometer.

Equation 1 models well the overall shape of the phase function. However it is not by itself a good enough to fit the data over the entire angular range to a relative accuracy of a few percent. In order to obtain this accuracy we must model the phase function more precisely in the back hemisphere. After some study we added an empirical term to equation 1. The resulting form is as follows.

$$\beta(\theta) = A \left(\frac{1 + \cos^2 \theta}{2} \right) \left[\frac{1}{(1 - \delta^2)\delta^v} \right] ([v(1 - \delta) - (1 - \delta^v)] \\ + \frac{4}{u^2} [(1 - \delta^{v+1}) - (v+1)(1 - \delta)]) + De^{-\alpha w}. \quad (5)$$

$$w = 2 \cos(\theta/2) \quad (6)$$

Equation 5 was used to fit the data base of scattering functions. A nonlinear simplex type fitting algorithm was used. The relative least squares error was minimized. All the data points had a relative error less than 10%. It should be noted that when the equipment measured only one polarization state of the scattered light the $(1 + \cos^2 \theta)/2$ term was modified accordingly.

Figure 1 is a graph of $(n-1)^2$ against μ , the inverse power of the particle distribution function. No apparent correlation can be seen. The mean value of the index is $n = 1.17$. This is within the range computed by other workers³. Figure 2 is a graph of the amplitude A against μ . A definite trend can be seen where the amplitude tends to sharply decrease as μ increases. Figure 3 is a graph of D against μ . Except for a tendency of the values to bunch between 10^{-4} and 10^{-3} , no significant trend can be seen. Finally, figure 4 is a plot α against μ . Once again, no correlations are apparent. Note that the line seen at

a value of $\alpha = 6$ is merely due to the upper bound that was set in the fitting program. Given the large range of water types which the data base covers this lack of clear trends is not surprising. We are now analyzing more closely the cases where data is available at both the very small angles and the larger angles simultaneously. Being pegged at both ends of the angular spectrum, these phase functions narrow down considerably the range of suitable parameters in the fit. At this point, equation 5 should only be considered as a compact way of expressing the phase function data.

Several parameters which are useful in the computation of the underwater light propagation can be derived from the phase function information. The total scattering coefficient is given by:

$$s = 2\pi \int_0^\pi \beta(\theta) \sin(\theta) d\theta. \quad (7)$$

The ratio of the radiation scattered in the forward hemisphere to that scattered in the back hemisphere is given by:

$$R = \frac{\int_0^{\pi/2} \beta(\theta) \sin(\theta) d\theta}{\int_{\pi/2}^\pi \beta(\theta) \sin(\theta) d\theta}. \quad (8)$$

The mean cosine, which is extensively used in the two stream model, is defined as:

$$\overline{\cos \theta} = \frac{\int_0^\pi \beta(\theta) \cos(\theta) \sin(\theta) d\theta}{\int_0^\pi \beta(\theta) \sin(\theta) d\theta}. \quad (9)$$

The normalized second moment, which is used to compute beam spreading, is given by:

$$\overline{(2 \sin(\theta/2))^2} = \frac{\int_0^\pi \beta(\theta) (2 \sin(\theta/2))^2 \sin(\theta) d\theta}{\int_0^\pi \beta(\theta) \sin(\theta) d\theta}. \quad (10)$$

Figure 5 is a graph of the total scattering coefficient s against μ . The range of values illustrates the variety of water types contained in the data base. No significant correlation is apparent. Figure 6 is a plot of the forward to backward scattering ratio. Figure 7 is a graph of the backscatter coefficient $\beta(\pi)$. The results cover once again a large dynamic range. Figure 8 is a graph of the mean cosine. The values are generally greater than .95. This is an indication of the dominance of the forward scatter in water due to the large size of the scattering particles. As seen in figure 9, the second moment is very often less than 10^{-1} . This small value is again an indication of the dominance of the forward scatter due to the large particle sizes.

In order to improve on the present results, an improved fitting formula with fewer arbitrary parameters is required. As shown by Klett⁴, the backscatter coefficient in the limit of small relative index is given by a simple formula. We are attempting to use this result to relate the D parameter to n and μ . A more in depth study is also required to see if μ can be related to n in the cases for which a full set of angular values of scattering are available⁵⁻⁶. Pending this work, the results we have shown at present indicate only that

the experimental phase functions can be modelled to a reasonable accuracy by a simple 5 parameter function.

4. SIZE DISTRIBUTION DECOMPOSITION

The present database of particle size distributions contains 433 distributions measured by 12 researchers in various regions of the Atlantic, Pacific, Indian Ocean and the Baltic Sea. Most of these distributions (412) were obtained using a Coulter counter. For the sake of consistency we have chosen to only analyze these latter distributions.

As was mentioned in the first part of this paper one can represent in an average way the particle size distribution by a power law. This approach, while modelling well the overall behavior of real oceanic distribution functions, does not allow a more detailed analysis of the substructure often seen in such data. We have developed an algorithm that decomposes particle size distributions into a sum of log-normal distributions⁷. These sub-components are automatically sorted in order of statistical significance by applying the Fischer test.

The log-normal distribution is given in standard notation by the following formula:

$$p_m(d) = C_m d^m \exp[-(\log(d/d_m))^2 / (2\sigma_m^2)], \quad (11)$$

where m is the order of the log-normal and d is the diameter of the particles. We will use the 0th order log-normal in our analysis. By taking the log of both sides of equation 11 and performing some simple algebraic transformations we have:

$$\log p_0(d) = [\log C_0 - \log^2 d_0 / (2\sigma^2)] + [\log d_0 \ln 10 / \sigma^2] \log d - [\ln 10 / (2\sigma^2)] \log^2 d. \quad (12)$$

Equation 12 is a second order polynomial in $\log d$. Standard least squares fitting algorithms can therefore be used to obtain the coefficients for a given data set of $p_0(d)$. Simple algebra can then be performed to extract the estimated values of d_0 , σ and C_0 .

The curve fitting is based on the assumption that the size distribution is composed of a cascade of log-normal components each of which dominates in a particular size interval. In principle, if one can identify the size range over which a component dominates, one can determine the parameters of the corresponding log-normal by applying the least squares algorithm to the log-log transformed original data. In order to perform this identification, the algorithm repeatedly scans the data set using a window whose width is systematically increased. Given the moderate number of data points representing typical size distributions of marine particles, we can evaluate the quality of fit to the data for all possible window positions and widths. The best component found during this systematic search is then subtracted from the data set. This difference set becomes the new data set. In the new data set only the differences which are greater than a fixed fraction of the previous version of the data set are retained for analysis. The procedure terminates when either there are not enough data points left, no log-normal component can be found or the number of components exceeds a preset maximum. Only the most statistically significant components are kept. Further details of the procedure can be found in our previous work⁷.

Figure 10 shows a typical distribution with a data set extending over a substantial size range. The four log-normal sub components are shown for reference along with their sum.

The fit to the data is excellent. For the 412 data sets in the data base we have identified 912 log-normal components. Some distributions taken over relatively narrow size ranges can be completely modelled by a single component. This feature seems to be due to the small size range of the data as we have noticed that the distributions taken in similar waters but over larger size ranges are generally decomposed into several components.

Significant correlation between the diameter at which the peak of the distribution D_{peak} occurs and the maximum value of the distribution function itself FD_{max} can be seen in figure 11. The equation of the straight line fit is given by:

$$FD_{max} = 3.645D_{peak}^{-2.2}. \quad (13)$$

A similar correlation between the width of the log-normal component and D_{peak} can be seen in figure 12.

$$width = 1.368D_{peak}^{-.9} \quad (14)$$

The significant correlation between $width$ and D_{peak} ($r^2 = .991$) is a consequence of the constraint that the envelope of the sum of all components of the particle size distribution is approximately described by an power law. Thus the smaller the D_{peak} , the narrower must the component be.

We have recently attempted to see if correlations could be found between the for the total surface area and the total volume of the sub components. This work is so far inconclusive and we believe that the problem is due to the extremely long tail of the 0th order log-normal distributions. When one tries to evaluate the moments of such a distribution one finds that the most significant contributions come from a size range that is many widths removed from the peak or even centroid of the distribution. This requires an extreme extrapolation away from the size range over which the parameters of the distribution itself were determined. Other distributions such as higher order log-normal functions would alleviate the problem. Such distributions would require a full nonlinear least squares fitting algorithm. These algorithms require a good set of initial guesses to converge. The estimate of the width, peak location and peak height given by the present algorithm could be used to provide this input. The present method can be therefore considered as a required first step in the analysis of particle size distributions into more physically based probability distributions.

5. CONCLUSIONS

We have analyzed an extensive data base of oceanic phase functions by a new approximate formula based on the anomalous diffraction approximation and assuming a power law distribution for the particle size distribution. Even though the fit to the phase functions themselves is excellent, no significant correlations could be found at this time. A more rigorous derivation of the approximating expression is required. In particular, the backscatter correction must be directly related to the relative index of refraction and the inverse power of the distribution function.

We have decomposed a data base of experimental data sets of particle size distributions into 0th order log-normal components. Significant correlations were seen between the location and value of the peak of the distribution functions as well as between the width

and peak location of the same functions. Analysis of the higher moments of the distribution function, such as total area and total volume, indicate that, because of its long tail, the 0th order log-normal distribution is not an appropriate form for the evaluation of such quantities. The present method must be considered as a necessary step to obtain the initial estimates of the parameters of more realistic distributions. These estimates could then be used in a full nonlinear fitting algorithm.

6. REFERENCES

1. M. Jonasz, "Scattering functions of sea water, and size distributions, refractive indices, shapes, and compositions of marine particles", DREV contract report 4528/01-XSK
2. G.R. Fournier and J.L. Forand, "Analytic phase function for ocean water", Proceedings of SPIE, Vol. 2258, Bergen, Norway, 13 June 1994.
3. J.R.V. Zaneveld, D.M. Roach and H. Pak, "The determination of the index of refraction distribution of oceanic particulates", Journal of Geophysical Research, Vol. 79, pp. 4091-4095, 1974.
4. J.D. Klett and R.A. Sutherland, "Approximate methods for modeling the scattering properties of nonspherical particles: evaluation of the Wentzel-Kramers-Brillouin method", Applied Optics, Vol. 31, pp. 373-386, 1992.
5. T.J. Petzold, "Volume Scattering Functions for Selected Ocean Waters," Scripps Institute of Oceanography, SIO Ref. 72-28, 1972.
6. C.H. Whitlock, L.R. Poole, J.W. Usry, W.M. Houghton, W.G. Witte, W.D. Morris and E.A. Gurganus, "Comparison of reflectance with backscatter and absorption parameters for turbid waters", Applied Optics, Vol. 20, pp. 517-522, 1981.
7. M. Jonasz and G.R. Fournier, "Approximation of the size distribution of marine particles by a sum of log-normal functions", Submitted to Deep Sea Research, 1994

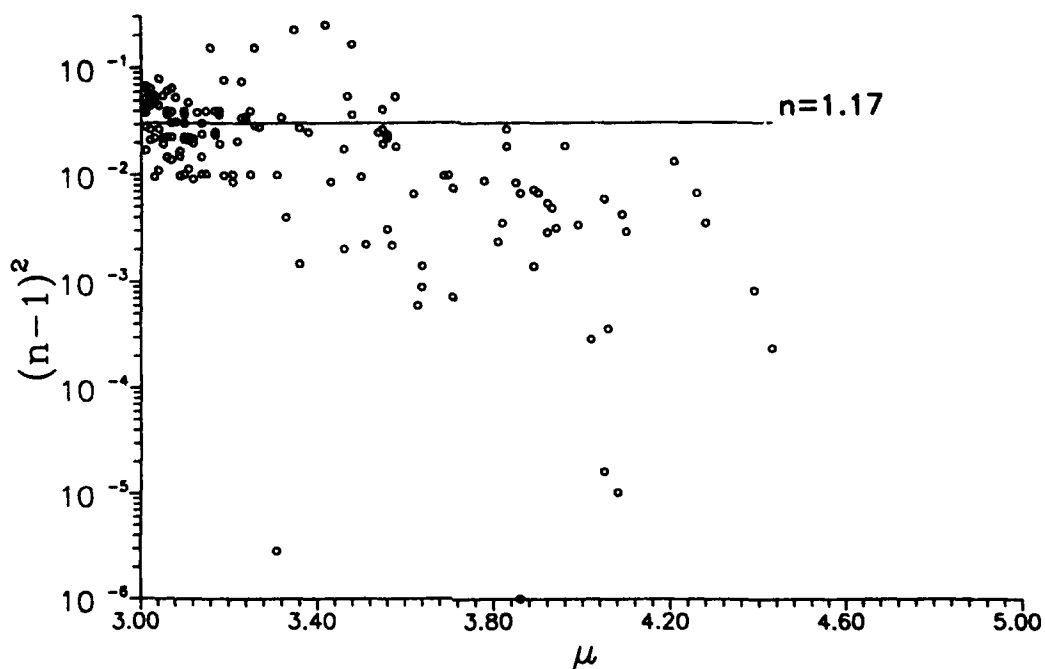


Figure 1. Plot of the index of refraction factor against the power of the particle size distribution function μ . The average index is 1.17.

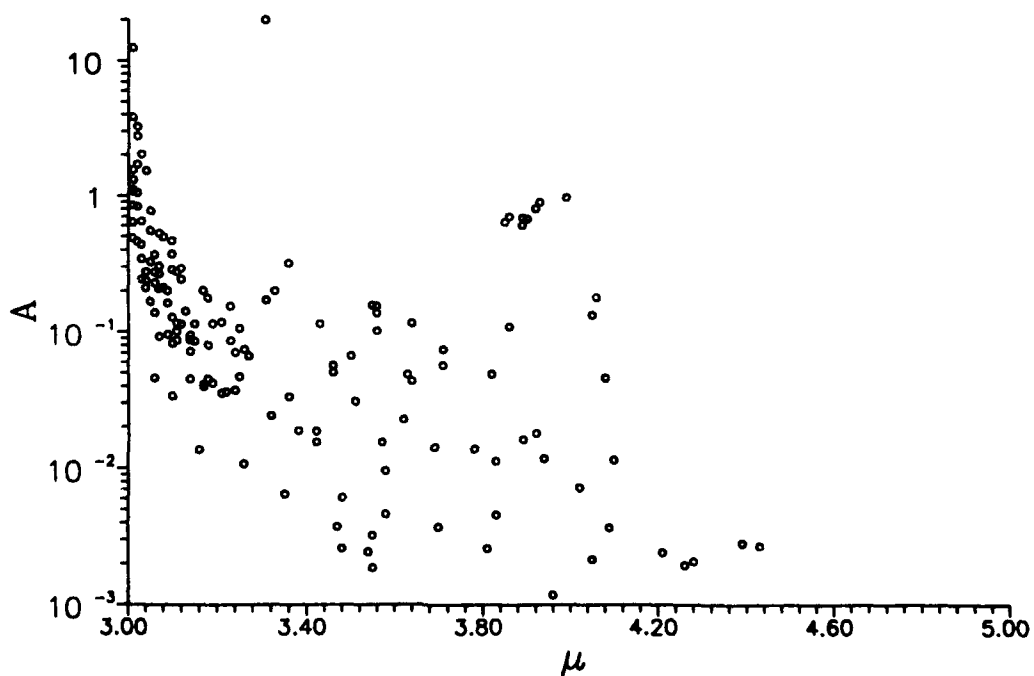


Figure 2. Plot of the amplitude parameter against the power of the particle size distribution function μ .

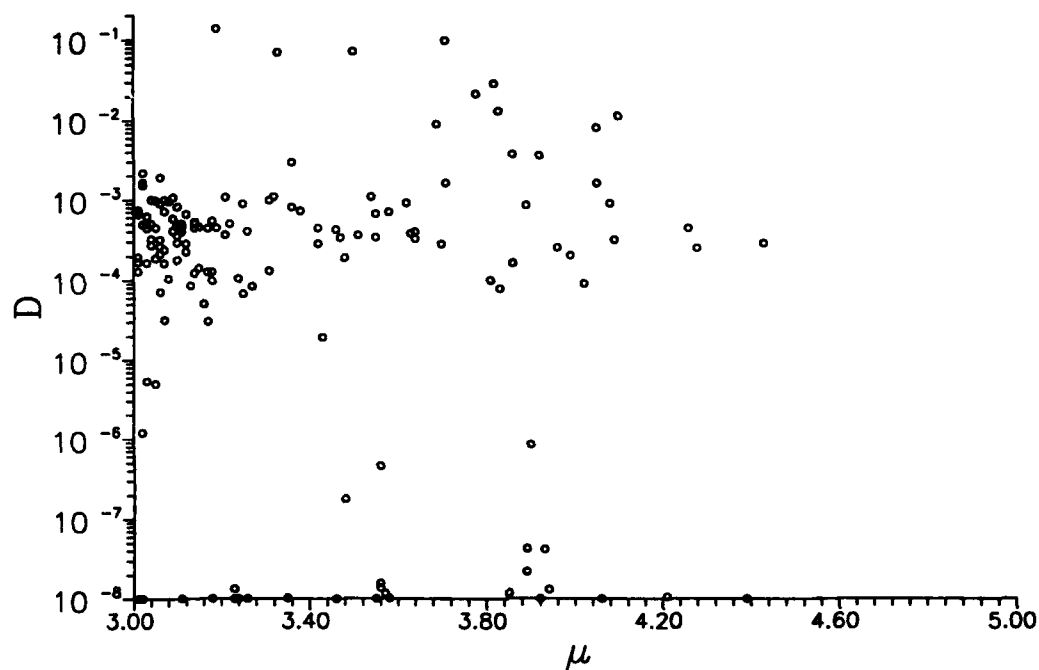


Figure 3. Plot backscatter amplitude parameter against the power of the particle size distribution function μ .

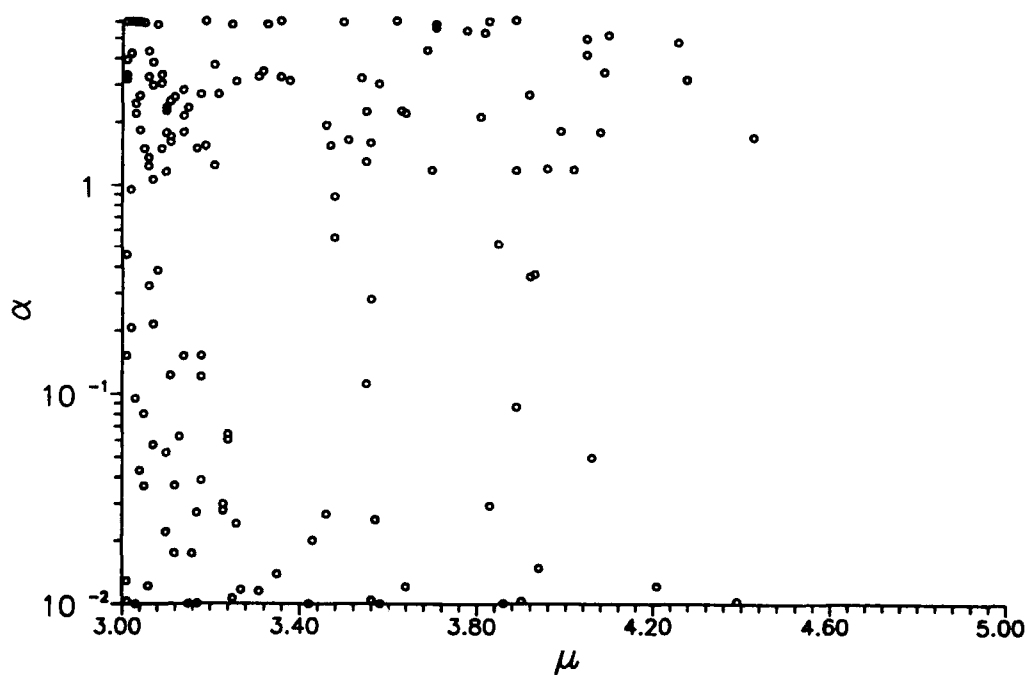


Figure 4. Plot of the backscatter α parameter against the power of the particle size distribution function μ .

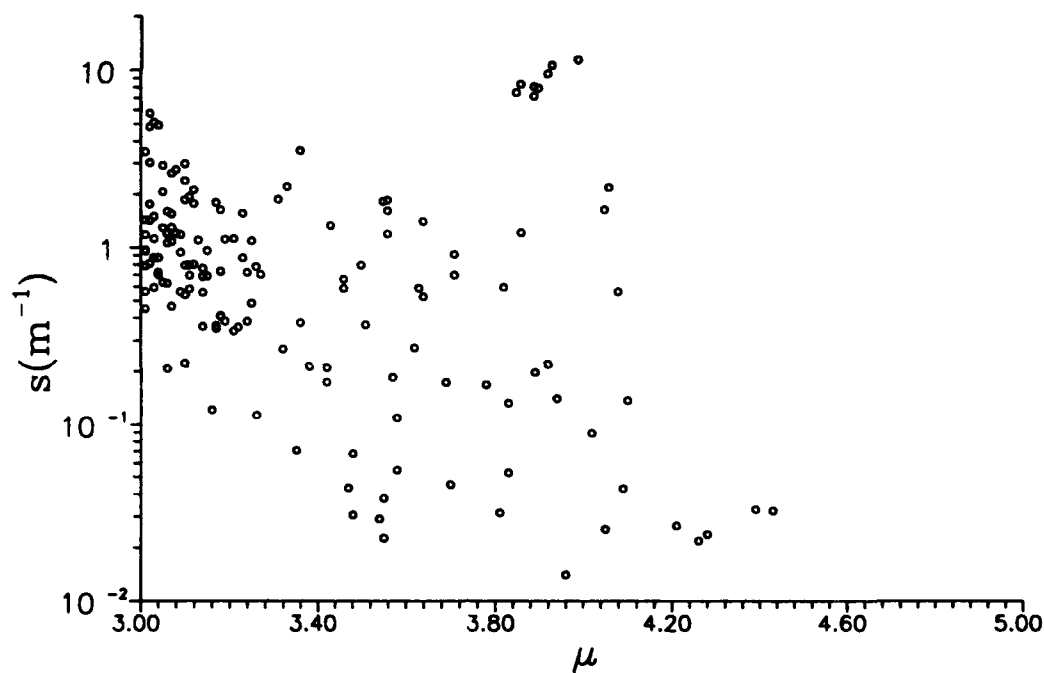


Figure 5. Plot of the total scattering coefficient against the power of the particle size distribution function μ .

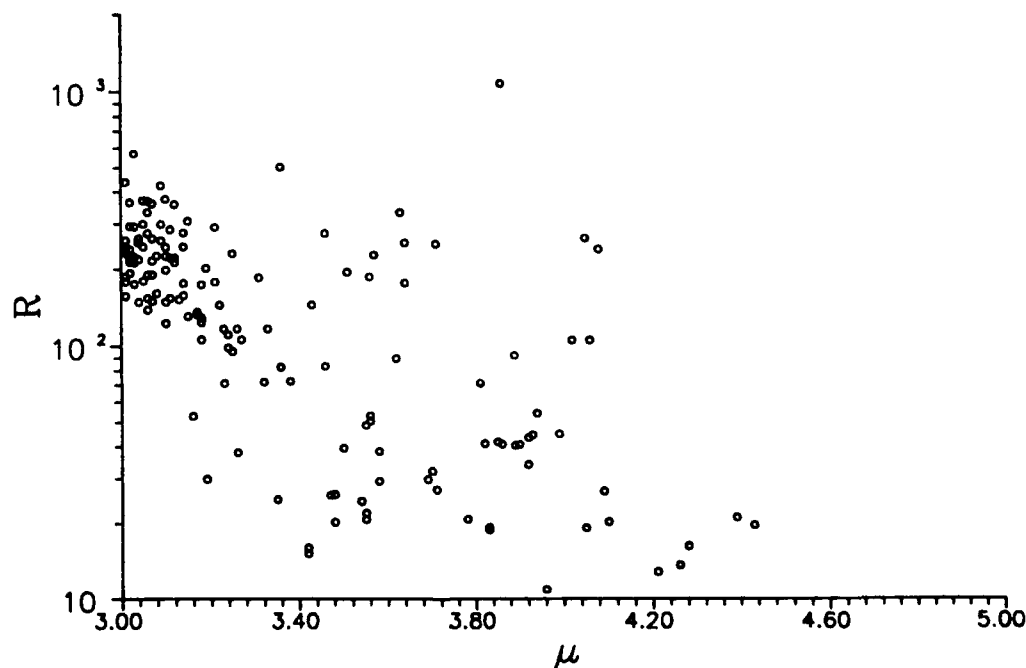


Figure 6. Plot of the ratio of forward to backward scattered light against the power of the particle size distribution function μ .

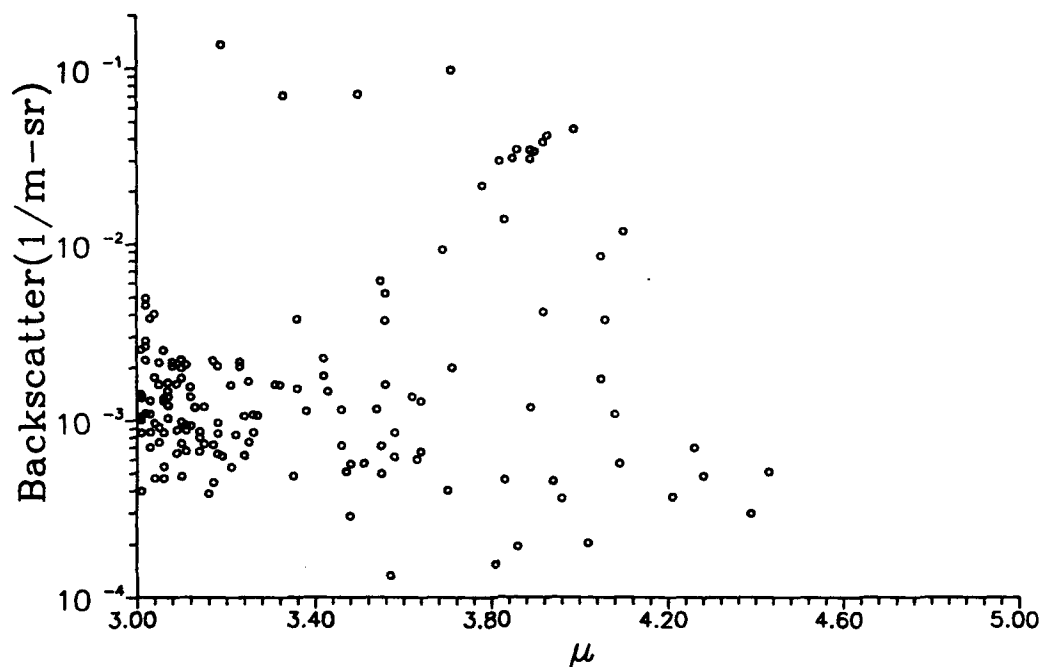


Figure 7. Plot of the backscatter coefficient against the power of the particle size distribution function μ .

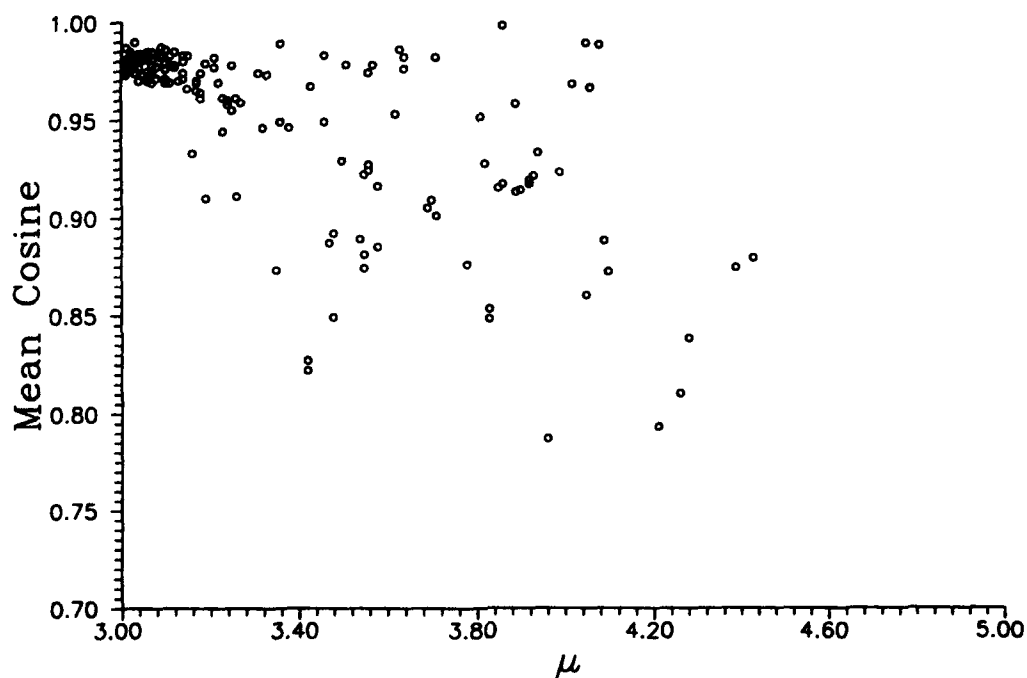


Figure 8. Plot of the mean cosine against the power of the particle size distribution function μ .

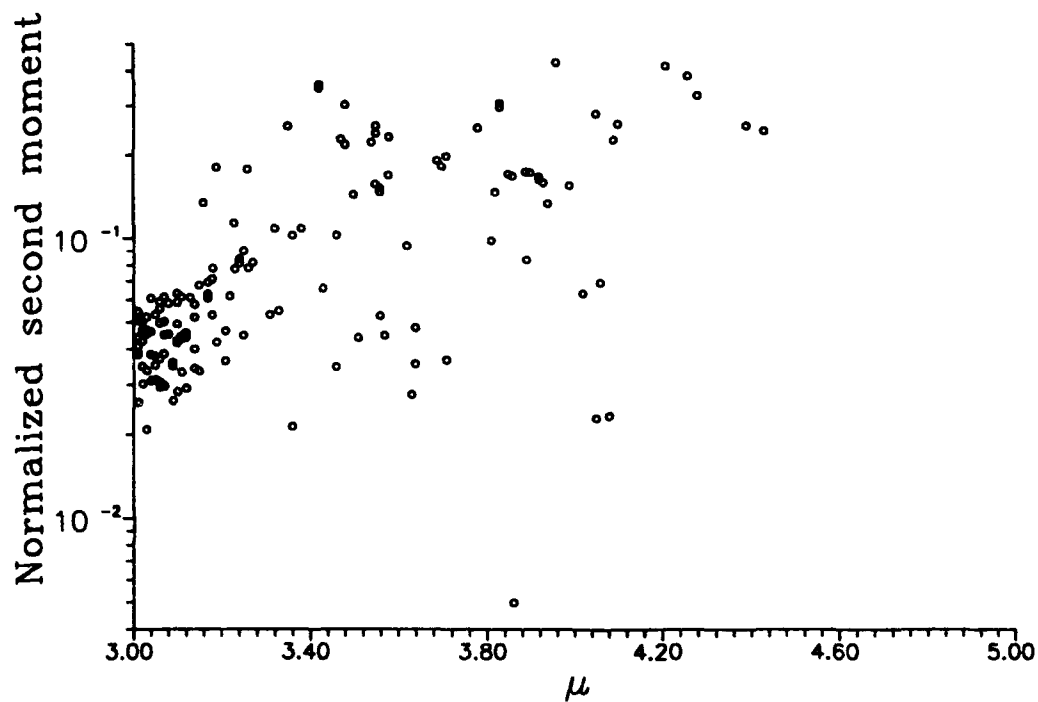


Figure 9. Plot of the normalized second moment against the power of the particle size distribution function μ .

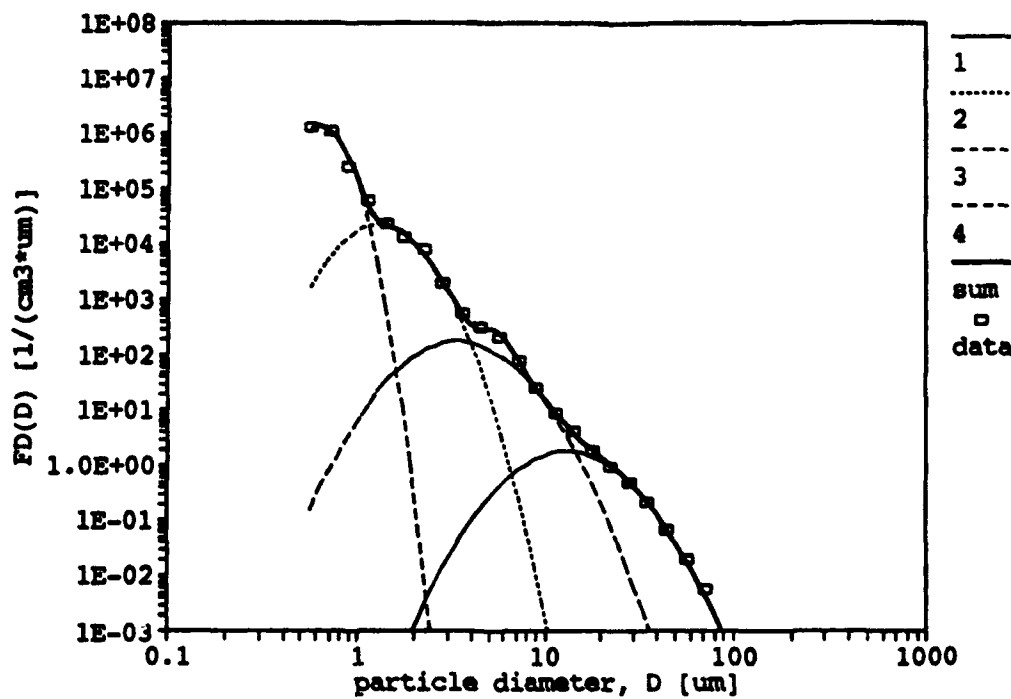


Figure 10. Particle size distribution represented by 4 log-normal components.

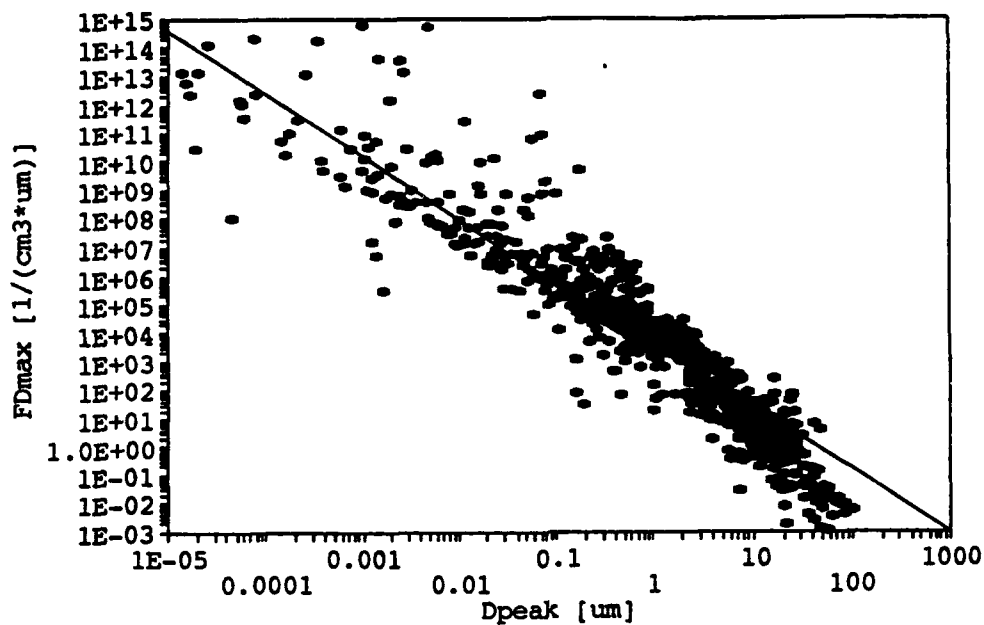


Figure 11. Relationship between the location and the amplitude of the peak of the distribution functions. The 904 log-normal components of the 412 experimental particle size distributions are plotted.

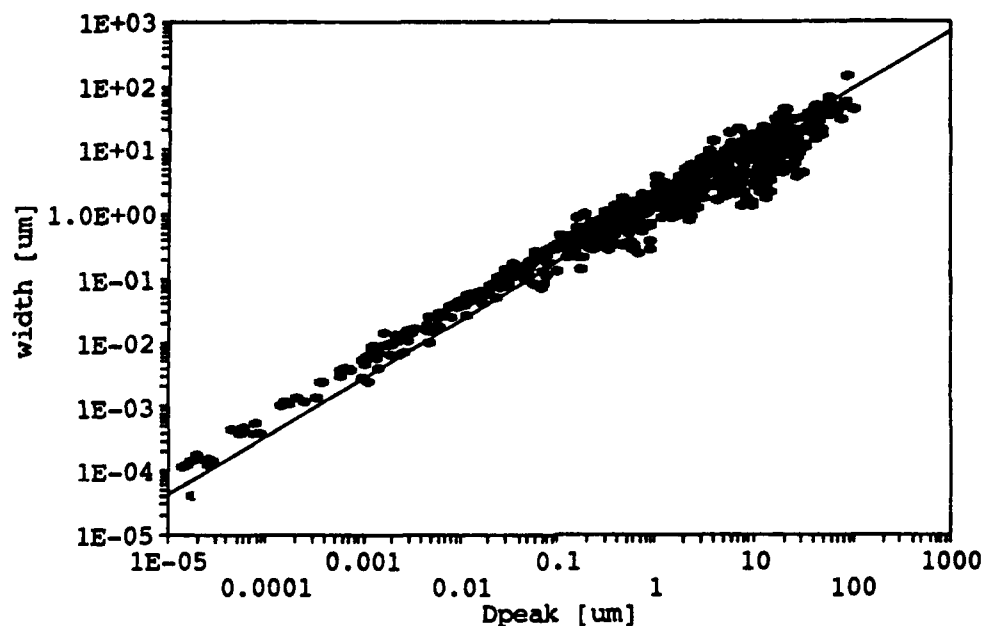


Figure 12. Relationship between the location of the peak of the distribution functions and their widths. The 904 log-normal components of the 412 experimental particle size distributions are plotted.

The theory of satellite observation of the sea bottom in coastal waters:
maximal sighting range and resolution

Lev S. Dolin

Institute of Applied Physics, Russian Academy of Science,
46, Uljanov Ul., Nizhny Novgorod, 603600

Iosif M. Levin

P.P.Shirshov Institute of Oceanology, St. Petersburg Branch,
Russian Academy of Sciences, 11, Tavricheskaja Ul.,
St. Petersburg, 193015

ABSTRACT

The paper deals with some aspects of the underwater imaging theory. The first effect discussed is the increasing of sighting range of sea bottom with an observer's altitude over the sea surface. Calculations show that the maximal sighting range from the space under the most favorable conditions does not exceed 500 meters. Secondly, the dependence of the sighting range and the resolution on size of target elements and target itself is considered. It is shown that the apparent contrast of target elements equal in size is higher for smaller targets. Computations prove the nonmonotone dependence of contrast on distance between the observer and the target. Finally, we consider the possibility of observation of the ocean bottom in coastal waters through clouds and show that large details of the bottom, such as sand spots against the seaweeds background, can be seen through continuous clouds with an optical thickness under 10.

1. INTRODUCTION

The theory of underwater imaging is now one of the most well studied parts of hydrooptics, represented in a number of monographs (e.g.¹⁻³) and in lots of papers. In the present paper, we do not pose any new problems of this theory. Rather, we shall discuss some of its traditional aspects which have to do with the paradoxes of abnormal sighting range (SR) or resolution in the sea water. It seems that the sources of these paradoxes lie in the long-existing desire to see in water as far as possible.

First, there is the well-known effect of increasing the SR by increasing the observer altitude over the sea surface. Pilots and cosmonauts sometimes reported about the visibility of the sea bottom relief even on the depth of about several kilometers. Such a SR evidently contradicts the underwater imaging theory. It seems that a reasonable explanation of the SR of several kilometers lies in the fact that a false image of the bottom relief might be formed by the water layers with increased turbidity, which rise on the several kilometers from the bottom and repeat the shape of the bottom relief^{4,5}. But the effect of a better visibility from an airplane or satellite compared with that from a ship, really exists. Here we shall discuss possible sources of this effect and find out the real maximal SR for the satellite observations.

We shall also discuss the effect of abnormal resolution in water discovered by Duntley⁶. We explain the cause of this effect and show the peculiarities of the

dependence of the SR and the spatial resolution on the size of the target.

Finally, we shall consider a possibility of viewing the sea bottom in coastal waters through clouds. The private information provided by cosmonaut Oleg Makarov, who have seen the river Volga from the satellite in conditions of total cloudiness, has given the impetus to this investigation.

2. THE DEPENDENCE OF VISIBILITY OF THE SEA BOTTOM ON THE OBSERVER'S ALTITUDE OVER THE SEA SURFACE

The apparent contrast of an underwater target C is related to its inherent contrast as

$$C = C_0 T(q, z, d) / [1 + L_{bs} / L_t], \quad (1)$$

where $T(q, z, d)$ is a function of the contrast transmitting, depending on spatial frequency of target details q , on the thickness of a water layer between the target and the observer z , and on the object size d ; L_{bs} and L_t are average apparent radiances of the backscattered light ("haze") and of the target, respectively. When a target is infinite, T is equal to the modulation transfer function MTF (q, z).

Neither L_{bs} nor L_t depend on the observer's altitude H over the sea surface (if not to take into account the atmosphere haze, which decreases the contrast and the SR). The main reason of increasing the SR of the sea bottom with H is that an observer begins to perceive the large-scale roughness of the bottom relief or the large-scale heterogeneity of its reflectance as a whole. In this case, the image of these details is transferred through a water layer without any loss of the contrast (due to their large sizes).

In order to clarify this assertion, let us consider a simplified model of the sea bottom in the form of a plane with irregular reflectivity, which consists of the infinite harmonics $\propto \cos ql$ with various spatial frequencies q . Instead of $q = 2\pi/l_0$ (l_0 is the length of "black-white" pair, or the period of the harmonic), the angular spatial frequency $\nu = zq/2\pi = z/l_0$ can be used. The image of the bottom will be the sum of harmonics with the same spatial frequencies q and the amplitudes, expressed by the MTF (q, z).

Using the refined small-angle diffusion approximation of the radiation transfer theory³ we obtain a simple expression for MTF:

$$\text{MTF}(\nu, bz) = \exp(-bz) + (1 - \exp(-bz)) \exp \left\{ - \frac{\pi^2 \langle \Theta_{45}^2 \rangle bz \nu^2}{3[1 - \exp(-bz)]} \right\}, \quad (2)$$

where b is the water scattering coefficient, $\langle \Theta_{45}^2 \rangle$ the variance of the scattering phase function calculated within an angle range $0 < \Theta < 45^\circ$. In the natural waters the value of $\langle \Theta_{45}^2 \rangle$ ranges from 0.03 to 0.08, its most typical value being 0.04³. It is evident from Eq.(2) that $\text{MTF} \rightarrow 1$ if $\nu \rightarrow 0$, and $\text{MTF} \rightarrow \exp(-bz)$ if $\nu \rightarrow \infty$. MTF for several bz with $\langle \Theta_{45}^2 \rangle = 0.04$ is presented in Fig.1. One can see that MTF is virtually equal to its asymptotic value $\exp(-bz)$ for $\nu = z/l_0 \approx 3 \text{ rad}^{-1}$.

Underwater imaging systems are usually used for viewing details which are smaller than one meter. So, for the usual z of tens of meters $\nu = z/l_0$ is always larger than 3 rad^{-1} , and the SR of these details (on the infinite target) does not depend on l_0 . Large details with $\nu < 3 \text{ rad}^{-1}$ can not go in a viewing field angle ψ of an underwater observer at all, if $1/\nu > \psi$, and thus he will not see them even if their apparent contrast is high. But if the observer is placed on the large altitude H above the sea surface such elements will easily fall in the viewing field.

To express this effect quantitatively, let us accept that the condition of the target visibility is that the viewing angle ψ must include not less than m periods l_0 . Then, for the observation from the altitude H , $m \propto \psi(H + z/n)/l_0$, where n is the water refractive index, or

$$\nu = \frac{z}{l_0} = \frac{zm}{\psi(H + z/n)}, \quad (3)$$

i.e. for fixed m and z , ν decreases with the increase of the altitude H .

The substitution of Eq.(3) to Eq.(2) gives an expression for contrast (MTF^*) of the harmonic, from which exactly m periods will go in observer's view on any altitude H . It is clear that a period of this harmonic l_0 will increase and, consequently, the angular frequency $\nu = z/l_0$ will decrease with H . The dependency of MTF^* on H calculated by Eqs.(2),(3) for $m = 4$, $z = 50 \text{ m}$, $b = 0.1 \text{ m}^{-1}$, $\psi = 30^\circ$, $\langle \theta_{45}^2 \rangle = 0.04$ is presented in Fig.2. For these conditions, MTF^* begins to increase from its asymptotical value $\exp(-bz)$ at $H \approx 100 \text{ m}$ and achieves an almost maximal value for $H \approx 1.5 \text{ km}$.

This effect becomes apparent, for example, when large sand banks are viewed against the background of dark bottom areas covered by seaweeds. The sand bank with uniform reflectance will not go in the viewing field and will turn out invisible if an observer is at a low altitude or under the sea surface. The small-scale inhomogeneities of bank reflectance may also be invisible because of the contrast attenuation in water $\exp(-bz)$. At the same time, the sand bank as a whole will be visible against the dark background when observed from a large altitude H , because the apparent contrast proves to be sufficiently high due to its large size.

An additional increase of the contrast in the this case is due to the spatial averaging of the fluctuations of bottom and surface images associated with the surface waves. However, the SR of underwater targets in daylight is mainly limited not by MTF, but by the backscattered light (L_{bs}). Let us find out, how far an observer really sees the sea bottom from the satellite under the most favorable conditions. Since we are interested in the largest possible sighting range, we shall ignore the light attenuation in the atmosphere and shall assume that $\text{MTF} = 1$, $C_0 = 1$, i.e. we shall consider very large light-colored targets against the dark background. In this case Eq.(1) for the apparent contrast has the following form

$$C = \left[1 + \frac{\rho + n^2(\rho_s + \rho_a)}{R \exp(-(1 + 1/\mu)az)} \right]^{-1}, \quad (4)$$

where ρ , ρ_s and ρ_a are the radiance coefficients of the water body, the sea surface and the atmosphere correspondingly, R the average reflectance of the target, μ the cosine of the sun ray refractive angle ($\mu^2 = 1 - \sin^2 \theta / n^2$, θ the solar zenith angle), and a the water absorption coefficient.

Let us further assume that $\theta = 40^\circ$ ($\mu = 0.88$), the typical values of $\rho_s = 0.04$ and $\rho = 0.02$ for the purest atmosphere and water, $\rho_a = 0.01$ for the wind velocity $v = 10$ m/s and nadir observation direction⁸. By putting these values in Eq (4), and by replacing C by the contrast threshold $C = 0.01$ and solving Eq.(4) with respect to z we obtain the maximal SR:

$$z_{\max} = 0.47(6.8 + \ln R) a^{-1}. \quad (5)$$

So the maximal SR is inversely proportional to the water absorption coefficient. Therefore, it is important to select the spectral region for viewing, which corresponds to the minimum water absorption in the place of observation. Let us choose for example, $R = 0.3$ and the absorption of the purest ocean water $a_{\min} = 0.005 \text{ m}^{-1}$ (wavelength $\lambda = 470 \text{ nm}$)⁹. Then Eq.(5) gives $L_{\max} \approx 530 \text{ m}$ which is slightly greater than reported by cosmonaut Sevast'anov¹⁰ $L_{\max} \approx 400 \text{ m}$. The value of $L_{\max} = 500 \text{ m}$ can apparently be considered as the maximal sighting range in natural waters.

It is interesting to compare this value with the SR under the same conditions, but for a small H (from a ship) and for a large $\nu > 3 \text{ rad}^{-1}$. In this case Eq.(4) can be written as:

$$C = \exp(-bz) \left[1 + \frac{\rho + n^2 \rho_s}{R \exp(-(1 + 1/\mu)az)} \right]^{-1}. \quad (6)$$

The solution of Eq.(6) with respect to z for the same values of C^* , R , ρ , μ , and a gives the maximal SR = 80 m for $b = 0.05 \text{ m}^{-1}$, SR = 260 m for $b = 0.01 \text{ m}^{-1}$, and SR = 40 m for $b = 0.1 \text{ m}^{-1}$.

3. THE SIGHTING RANGE AND SPATIAL RESOLUTION AS A FUNCTION OF TARGET SIZE

It is well known, that the SR of usual underwater targets in the daylighted sea or if the lamp is placed near an observer is about $bz = 2-5$ ⁶. If the target is self-luminous, or if the lamp is situated near the target, the backscattered radiance $L_{bs} \approx 0$, and the apparent contrast, as well as the SR, increase. In this case $C/C_0 = T(\nu, z, d)$ (see (Eq.1)). If the target is infinite, $T(\nu, z, d) = \text{MTF}(\nu, z)$ which takes the asymptotic value $\exp(-bz)$ for spatial frequency $\nu > 3 \text{ rad}^{-1}$. Therefore, if the scattering length $bz > 4.6$, the apparent contrast of an infinite target even for the maximal inherent contrast $C_0 = 1$ and without any haze (a self-luminous object) becomes less than the contrast threshold $C^* \approx 0.01$. Duntley⁶ photographed a small-sized underwater object (a dummy) with a lamp placed near the object and obtained a good image quality at the distance $bz = 7.2$. He treated this result as a "mystery". This phenomenon has in fact a simple explanation. For targets with the limited size d the contrast transmitting function is given by

$$T(q,z,d) = \text{MTF}(q,z) / F(\alpha,bz), \quad (7)$$

where F is the integral of the point spread function over the target area. It is a function of the target angular diameter $\alpha = d/z$ and the optical distance (bz) between the observer and the target.³ Using the refined small-angle diffusion approximation of the radiation transfer theory³, we obtain the following simple expression for F :

$$F(\alpha,bz) = 1 - (1 - \exp(-bz)) \exp \left[- \frac{3\alpha^2(1 - \exp(-bz))}{4\langle \theta_{45}^2 \rangle bz} \right]. \quad (8)$$

This function ranges from 1 for an infinitely large target to $\exp(-bz)$ for an infinitely small one. Thus for small targets, the value of T is much greater than the MTF, and the apparent contrast of details on the small self-luminous target may be greater than $\exp(-bz)$.

The dependencies of the function T which is the apparent contrast of details on the self-luminous target with the inherent contrast $C_0 = 1$, on a distance bz , for targets with various sizes $\alpha = d/z$ and $\nu > 3$ ($\text{MTF} = \exp(-bz)$) calculated by Eqs.(7),(8) are shown in Fig.3. Fig.4 represents dependency of the SR (bz_{max}) on the target angular size for the same targets. The SR has been found by solving the equation $T(bz) = \exp(-bz) / F(\alpha,bz) = C^* = 0.01$ with respect to bz . Note, that the dependency $T(bz)$ turned out to be nonmonotone with one minimum at $bz < 1$ and one maximum at $bz = 2-5$. The contrast increase occurs at the distances where a visible size of glow due to light scattering becomes greater than a visual target size.

Thus, the SR of elements with large spatial frequency on a small self-luminous object is always greater than that of the same elements on the large object. Consequently, the spatial resolution of object elements is greater for smaller objects at the given distance.

In the daylight observations the SR strongly depends on the value of the backscattered radiance L_{bs} . Since the average object radiance $L_t \propto L_t(\alpha = \infty) F(\alpha)$, one can see from Eqs.(1),(7), that if $L_{bs} \gg L_t$ then $C = C_0 \text{MTF } L_t(\alpha=\infty)/L_{bs}$, i.e. it does not depend on the object size.

So far we have considered a problem of "recognition" of the target, which presupposes that one may detect several elements on the object. Sometimes the goal of an observer is to detect the target as a whole, without distinguishing its elements. In this case the contrast of the target against the water background is greater for large objects with a larger apparent radiance. It is true for both illuminated and self-luminous targets.

4. VISIBILITY THROUGH CLOUDS

In order to estimate the possibility of viewing the sea bottom in coastal waters through a continuous cloud layer, let us use Eq.(1). In this case, the function T is a product of T_w and T_c for the water and the cloud respectively, L_{bs} and L_t are the radiances on the upper boundary of cloud layer. We shall again consider the large targets ($\text{MTF} = 1$ for water and clouds). Then Eq.(4) can be written as

$$C = C_0 \left[1 + \frac{R_c + t_c(\theta)t_c(0)(\rho + n^2(\rho_s + \rho_a))}{R \exp(-(1+1/\mu)az)t_c(\theta)t_c(0)} \right]^{-1} \quad (9)$$

where $t_c(\theta)$ is the transmittance of the cloud layer depending on the solar zenith angle θ , R_c the cloud reflectance. We have performed a Monte-Carlo simulation of R_c and $t_c(\theta)$ for the cloud optical thicknesses $\tau = 0-40$, the single scattering albedo $\omega_0 = 0.995-1.0$, $\theta = 0-60^\circ$ for Darmendjian cloud model C-1. Some results of the simulation are presented in Table 1.

Table 1
The transmittance t_c and the reflectance R_c of a continuous cloud layer

τ	$\omega_0 = 1$		$\omega_0 = 0.995$			
	$\theta = 0^\circ$	$\theta = 25^\circ$	$\theta = 0^\circ$		$\theta = 25^\circ$	
	t_c	t_c	t_c	R_c	t_c	R_c
2	0.909	0.891	0.899	0.088	0.879	0.106
4	0.809	0.783	0.788	0.182	0.760	0.207
5	0.726	0.687	0.694	0.257	0.654	0.293
7	0.655	0.614	0.613	0.319	0.572	0.355
10	0.596	0.553	0.545	0.366	0.501	0.405
20	0.408	0.369	0.317	0.498	0.282	0.533

Note: for $\omega_0 = 1$, $R_c = 1 - t_c$.

The result of calculation of C for clear water ($a = 0.01 \text{ m}^{-1}$) and for rather small depths $z = 25 \text{ m}$ and $z = 10 \text{ m}$ is presented in Fig.5 for $\omega_0 = 0.995$, $\theta = 25^\circ$ and various cloud optical thicknesses τ . The target is the large sand banks ($R_1 = 0.3$) against the seaweeds background ($R_2 = 0.1$). So the inherent contrast $C_0 = (R_1 - R_2)/(R_1 + R_2) = 0.5$, $R = 0.5(R_1 + R_2) = 0.2$. As above, we assume that $\rho = 0.02$, $\rho_s = 0.01$, and $\rho_a = 0.04$.

As follows from Fig.5, large details of the sea bottom can be seen through clouds with $\tau = 5-10$ if the contrast threshold is 4-10% (for viewing through inhomogeneous and fluctuating cloud layer the contrast threshold will be greater than 1%, as was taken for standard conditions).

The natural question arises: which object size is sufficient to take this object to be large enough, i.e. to put $\text{MTF} = 1$. We have computed the MTF of water and cloud layers (taking into account the distance between the sea surface and the cloud layer) by using

the small-angle approximation of the radiation transfer theory³. The computation has shown that for thin clouds ($\tau = 1-2$) the elements of 0.1-0.5 km can be taken as large, for more thick clouds ($\tau = 5-10$) only those of 1-5 km.

5. REFERENCES

1. R. W. Preisendorfer, *Hydrologic Optics*, US Dept. of Commerce, Hawaii, 1976.
2. E. P. Zege, A. P. Ivanov, and I. L. Katzev, *Image transfer through a scattering medium*, Springer-Verlag, Berlin, 1991.
3. L. S. Dolin, I. M. Levin, *Theory of underwater imaging (handbook)*, Gidrometeoizdat Publ., Leningrad, 1991 (in Russian).
4. J. A. Prochorenko and G. G. Neujmin, "Influence of deep bottom relief on the transparency of upper ocean layers", *Optical methods for investigations of the ocean and internal reservoirs*, AN of USSR, Tallinn, pp. 81-84, 1980 (in Russian).
5. V. L. Solomacha and L. N. Fedorov, "About the possibility of observation of the deep shape of bottom relief from the space", *Optics of sea and atmosphere*, Nauka Publ., Leningrad, pp. 248-249, 1984 (in Russian).
6. S. Q. Duntley, "Underwater visibility and photography", *Optical aspects of oceanography*, Acad. Press, London, pp. 135-149, 1974.
7. V. L. Veber and L. S. Dolin, "The image fluctuations for the observation through rough non-steady boundary", *Izv. AN SSSR, Fiz. Atm. Okeana*, Vol. 17, No. 11, pp. 1166-1177, 1983 (in Russian).
8. Y. A. R. Mullamaa, *Atlas of the rough sea surface optical properties*, Estonian Acad. of Sciences, Tartu, 1964 (in Russian).
9. O.V. Kopelevich and K. S. Shifrin, "Up-to-date conceptions of sea water optical properties", *Optics of ocean and atmosphere*, Nauka Publ., Moscow, pp. 4-55, 1981 (in Russian).
10. A. Lazarev and V. Sevast'yanov, "When face to face, the face is invisible", *Nauka i zhizn'*, No 9, pp. 27-32, 1987 (in Russian).

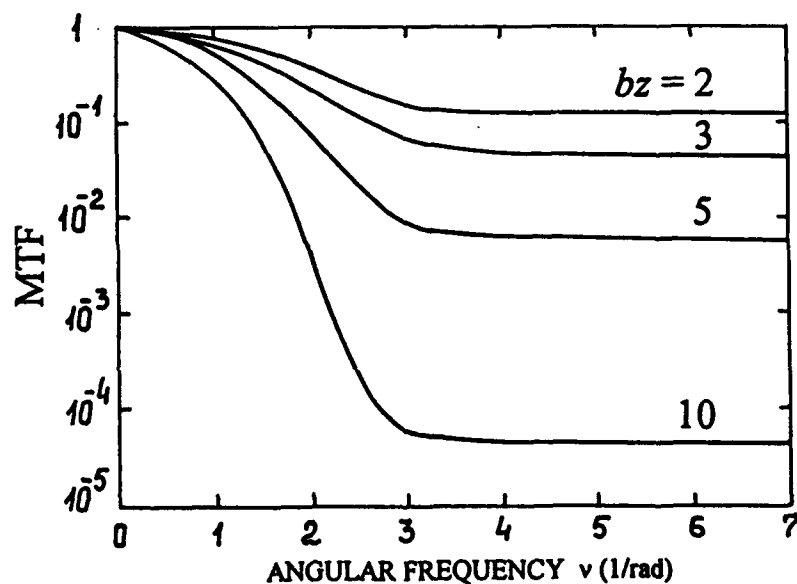


Fig.1 The MTF of a water layer for various scattering lengths bz .

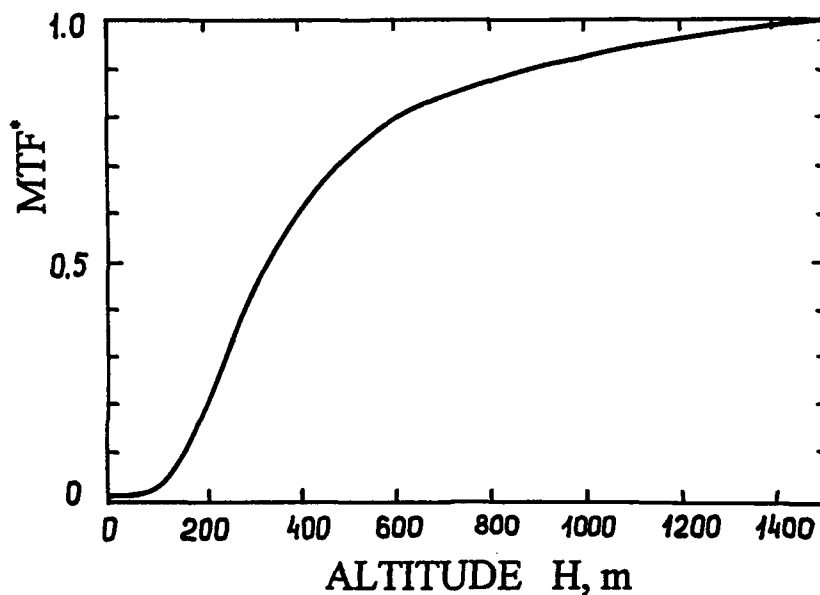


Fig.2 The MTF calculated for the fixed number $m = 4$ of elements on the sea bottom, going in the observer viewing field, as a function of the observer's altitude over the sea surface .

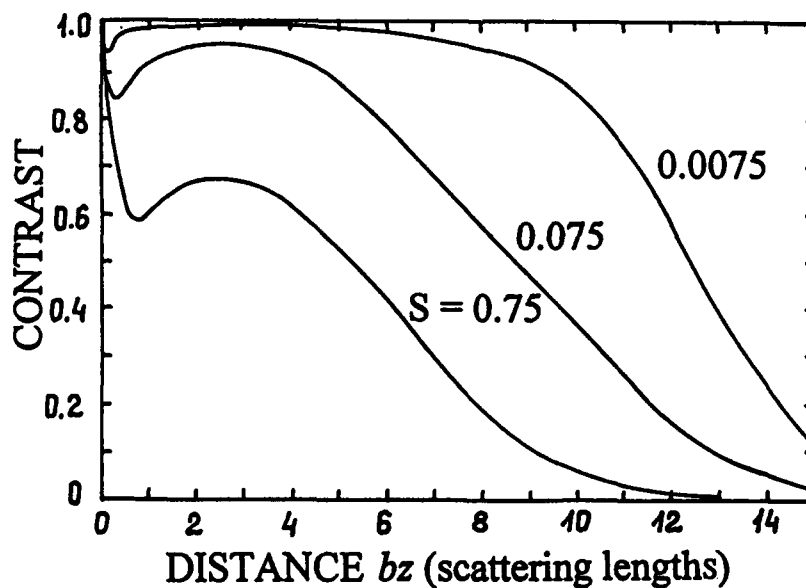


Fig.3 The contrast transmittance function T for small details of the self-luminous targets with various sizes d . The numbers near the curves are related to the dimensionless target area $S = 0.75b^2d^2/\langle\theta_{45}^2\rangle = 0.75, 0.075, \text{ and } 0.0075$ (for $b = 0.1 \text{ m}^{-1}$ and $\langle\theta_{45}^2\rangle = 0.04$ these values of S correspond to $d = 2\text{m}, 0.63\text{m}, \text{ and } 0.2\text{m}$).

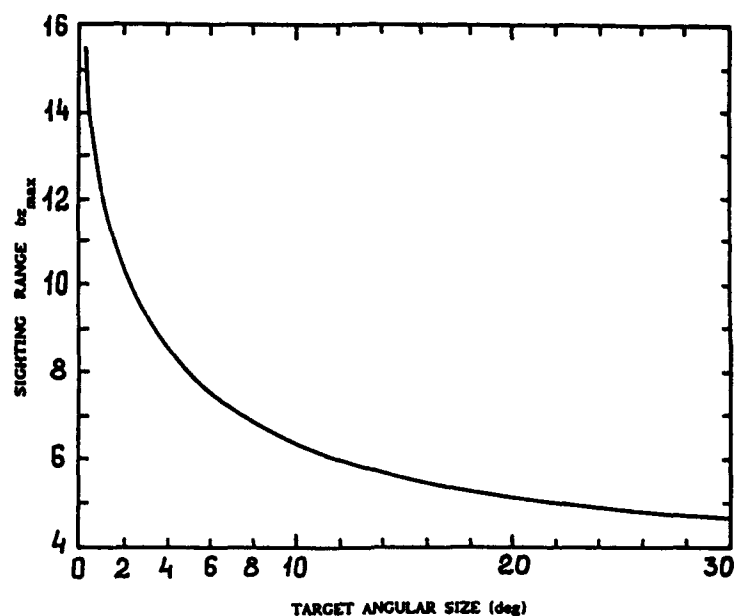


Fig.4 The maximal sighting range of small details as a function of the target angular size $\alpha = d/z$.

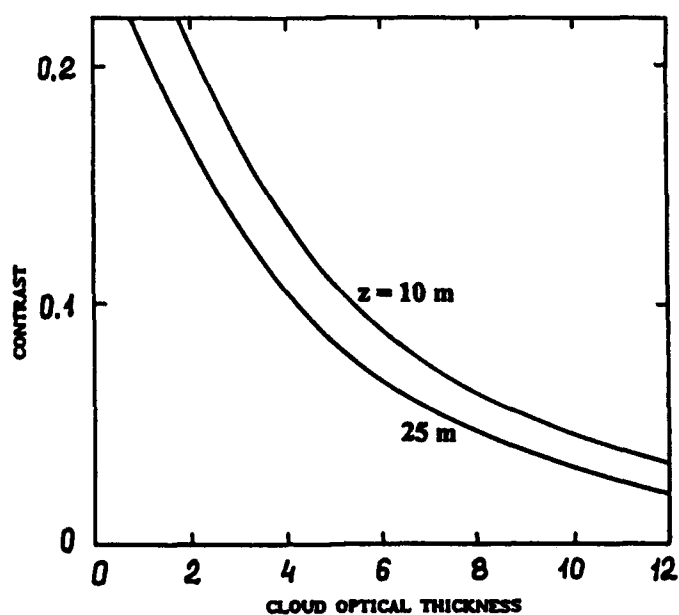


Fig.5 The apparent contrast of the sea bottom (large sand spots on the seaweeds background) in pure water (the absorption coefficient $a = 0.01 \text{ m}^{-1}$) as viewed through continuous clouds. Depths $z = 10 \text{ m}$ and 25 m .

Temperature dependence of the absorption coefficient of pure water in the visible portion of the spectrum

W. Scott Pegau and J. Ronald V. Zaneveld

College of Oceanographic and Atmospheric Sciences, Oregon State University
Ocean. Admin. Bldg. 104
Corvallis, OR 97331

ABSTRACT

We have studied temperature dependent changes of the absorption coefficient of pure water at several wavelength bands in the visible portion of the spectrum. A WET Labs Inc. nine wavelength absorption and attenuation meter (AC-9) was used to measure the absorption coefficient. We found the largest temperature dependence ($0.0034 \text{ m}^{-1}^{\circ}\text{C}^{-1}$) at the longest wavelength tested (715 nm). The temperature dependence at shorter wavelengths was less than a third of that observed at 715 nm. Because of the experimental arrangement we believe that the figures obtained represent the upper bound of possible values for the temperature dependence of the absorption coefficient.

1. INTRODUCTION

Absorption of light by water is a fundamental process of interest to many investigators who study light in hydrological environments. The absorption coefficient is the parameter used to provide a measure of the absorption in a length of water. The total absorption coefficient is the sum of the absorption coefficients of the individual components including the absorption coefficient of water. The total absorption coefficient is an input to the radiative transfer equation and is important for the study of remote sensing and to many biological studies.

There is good reason to suspect that environmental parameters may effect the value of the absorption coefficient of water at certain wavelengths. As early as 1925 the effect of temperature on the absorption coefficient in the infrared was studied¹. Collins shows that temperature is very important in determining the shape and magnitude of the absorption maxima associated with the overtones of the three O-H vibration frequencies for water. Since a water molecule is polar it tends to form loosely bonded clusters of molecules. The energy states of the clusters differ from those of individual molecules causing changes in the vibrational energy states and changes in the absorption coefficient. The bonds within these clusters are weak making the size and number of the clusters dependent on the temperature. Several works show that in the infrared portion of the spectrum the value of the absorption coefficient is highly dependent on temperature^{1,2,3}. The magnitude of the variation of $a(\lambda)$ with temperature is shown to decrease at shorter wavelengths. Temperature is not the only environmental parameter that changes the absorption coefficient of water in the infrared. Water molecule clusters also form around ions in solution. Variations in the absorption coefficient with ion type and concentration have been found. The magnitudes of these variations are smaller than the variations with temperature⁴.

The overtones of the O-H vibrational frequency continue into the visible portion of the spectrum (400 to 700 nm). Notably, the absorption shoulders at 515 and 605 nm are high order overtones. We then expect that the absorption coefficient in at least these regions of the spectrum depends on the environmental conditions. How the absorption coefficient varies with temperature at these overtones and whether other portions of the spectrum have temperature dependent absorption coefficients are questions that motivated this study.

Because of the low absorption in the visible part of the spectrum there have been relatively few studies of the absorption coefficient in this region. Some work has been done to determine the magnitude of $a(\lambda)$, but until recently little work has been done in trying to determine which environmental parameters might affect the absorption at visible wavelengths. Tam and Patel⁵ mention that the absorption shoulders at 515 nm and 605 nm have a temperature dependence. Højerslev and Trabjerg⁶ indicate that for the region of 400-600 nm there is an incremental change in $a(\lambda)$ with temperature of $\sim 3 \times 10^{-3} \text{ m}^{-1} \text{ }^{\circ}\text{C}^{-1}$ for the temperature range of 10 to 30 $^{\circ}\text{C}$. Pegau and Zaneveld⁷ show that the shape of the absorption maximum at 745 nm and the absorption shoulder at 605 nm change with temperature. Pegau and Zaneveld⁷ set the curves of the absorption coefficient equal at 685 nm to facilitate examination of changes in the shapes of the absorption coefficient curves. By normalizing all curves to the same value at 685 nm they were unable to study any possible systematic change in the absorption coefficient with temperature such as had been reported by Højerslev and Trabjerg⁶.

In this study we look at discrete wavelength bands from 412 to 715 nm using WET Labs Inc. AC-9 absorption and attenuation meters. We determine if there is a spectrally independent rise in the value of the absorption coefficient with temperature between approximately 10 and 35 $^{\circ}\text{C}$. We study the absorption shoulder at 515 nm to determine if there is an increased dependence on temperature at this O-H vibrational overtone.

2. METHODS

We used 25 cm pathlength WET Labs Inc. AC-9 combined absorption and attenuation meters to determine the absorption coefficient. Two separate instruments were used to ensure that the results were not dependent on the individual instrument. Two styles of detectors were used in one instrument for reasons explained below. In this study we only use the reflecting tube absorption meter⁸ portion of the AC-9. The spectral intervals studied were determined by the set of nine interference filters in each instrument. The interference filters had a 10 nm full width half max. bandpass. The filter sets of both instruments included 412, 440, 488, 650, 676, and 715 nm filters. The other three filters were different in each instrument with 520, 560, and 630 nm filters used in instrument 1 and 515, 532, and 550 nm filters in instrument 2.

The AC-9 was connected to a 350 l/day reverse osmosis water filter using 15 m of plastic tubing. Water flow temperature was varied by placing portions of the plastic tubing into hot or cold water baths. Water temperature was monitored at the discharge port of the absorption meter flow tube. Removing all of the coils from the baths allowed $a(\lambda)$ at a single temperature to be measured several times throughout an experiment to ensure that the water quality was constant.

Even though the electronics of the AC-9 are temperature compensated, we placed the instruments in a water bath to ensure constant instrument temperature throughout each experiment. We desired the extra temperature control on the instrumentation because the magnitude of the electronics temperature correction was often larger than the expected temperature dependence of the absorption coefficient of water. The water bath helped to prevent errors in the electronic temperature compensation from dominating our results. Placing the instruments in the water bath did not prevent possible localized variations in temperature especially at the detectors of the absorption meters. The detector of the absorption meters is potted to the diffuser window which is in contact with the water flow and the temperature of the detector may vary with the temperature of the sample water. This may allow some electronic errors associated with changes in the detector response with temperature to be included in our findings. Two styles of detectors were used to provide an indication of how the results depended on the detector response with temperature.

We measured the absorption coefficient for approximately 3.5 minutes to obtain 1000 samples at each temperature. The 1000 samples were then averaged to provide the data points used. We performed a linear regression between the measured absorption coefficients and the temperature measured at the absorption meter discharge (Figure 1). The slopes determined from the linear regressions are used as an indication of how the magnitude of the absorption coefficient depends on the water temperature.

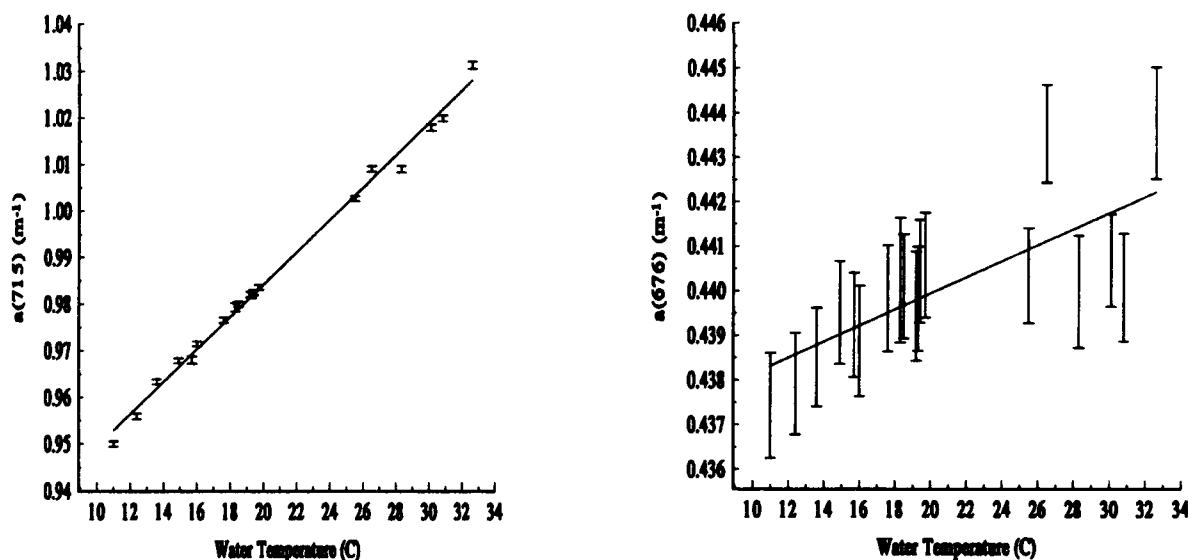


Figure 1. Linear regression fit to the absorption meter data from run 3. The data chosen represents the largest $[a(715)]$ and smallest $[a(676)]$ slopes. Data points are given with the 95% confidence interval. A constant has been added to the absorption coefficient data so that the absorption coefficient at 20°C is equal to the value of Smith and Baker⁹. Since we are only interested in the slope and not the intercept of the regression the addition of the constant does not change the results.

3. RESULTS AND DISCUSSION

Only at the 715 nm waveband was the temperature dependence of the absorption coefficient observed to be as high as $0.003 \text{ (m}^{-1} \text{ }^{\circ}\text{C}^{-1})$. The rest of the visible spectrum had much lower temperature dependencies (Figure 2). From the work that has been done in the infrared portion of the spectrum we would expect an increase in the temperature dependence in regions of the overtones of the O-H vibrational frequencies. This appears to be the case for the 715 nm absorption coefficient which is affected by the overtone at 745 nm. We did not sample at the 605 nm absorption shoulder but we did sample the 515 nm absorption shoulder. At 515 nm there is some hint that the overtone has a higher temperature dependence than the surrounding wavelengths, but the difference is small and not statistically significant. The value of $\Delta a(630)/\Delta T$ in this study was found to be the same as in the data included in Pegau and Zaneveld⁷. At 715 nm the value of $\Delta a/\Delta T$ was at the upper limit of the 95% confidence interval of our earlier work. The higher $\Delta a(715)/\Delta T$ found in the present study is probably due to the wide bandwidth of the interference filter used in the AC-9 allowing the longer wavelengths with higher temperature dependencies to contribute to the results.

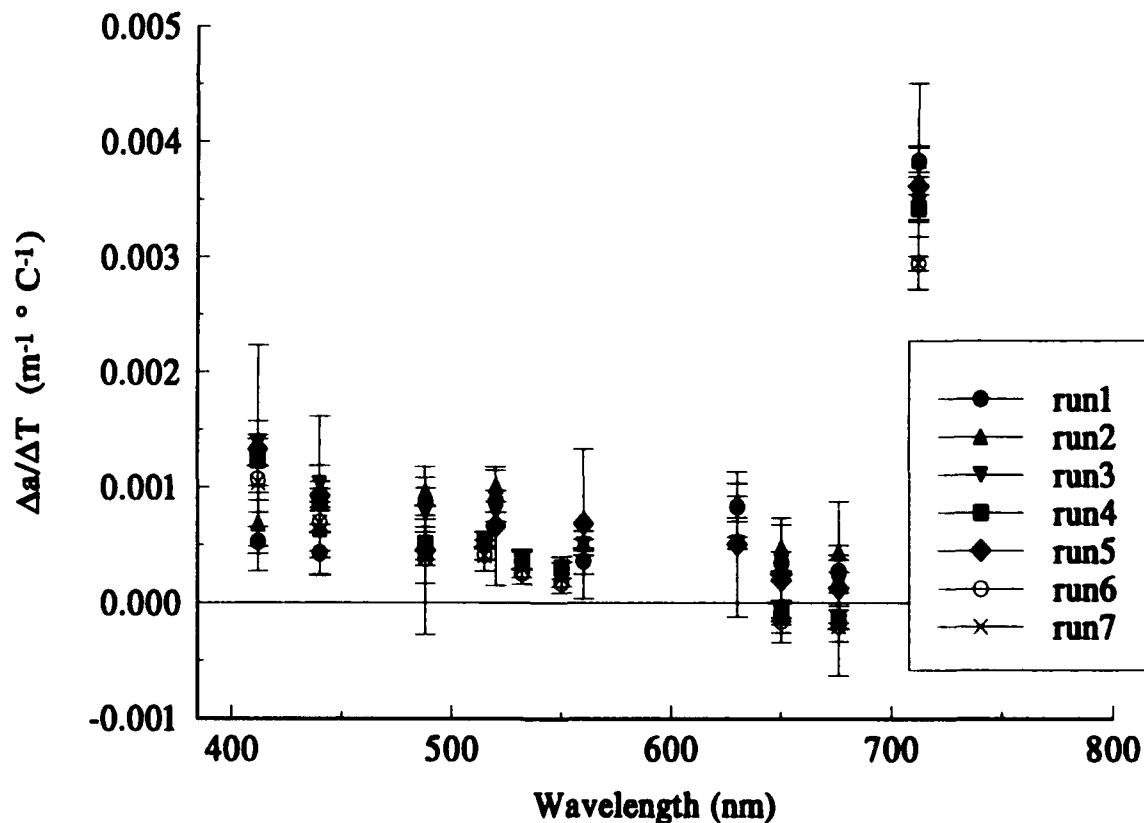


Figure 2. Slopes of the linear regressions with 95% confidence intervals for the seven runs.

Since we kept the instrument at a constant temperature of approximately 22° there is a possibility that the sample water either warmed up or cooled down during the time it was in the flow tube of the instrument. Since the temperature was monitored at the discharge port of the flow tube it is possible that the average temperature within the tube was different from that measured. Errors in determining the temperature may cause our estimates of the values of $\Delta a/\Delta T$ to be too large. We believe that our estimates of the temperature dependence represent the upper limit. The temperature range studied was approximately $\pm 10^\circ$ of the instrument temperature so that the thermal gradient between the instrument and sample water was kept small. Since the thermal gradient was small we do not expect large difference between the measured water temperature and the average temperature of the sample. In the instances where a much higher flow rate was used (runs 6 and 7) the slopes of the regression were smaller than those measured at a lower flow rate (run 4) (Figure 3). The only statistically significant difference was observed at 715 nm where the difference in slope was $5 \times 10^{-4} \text{ m}^{-1}^\circ\text{C}^{-1}$.

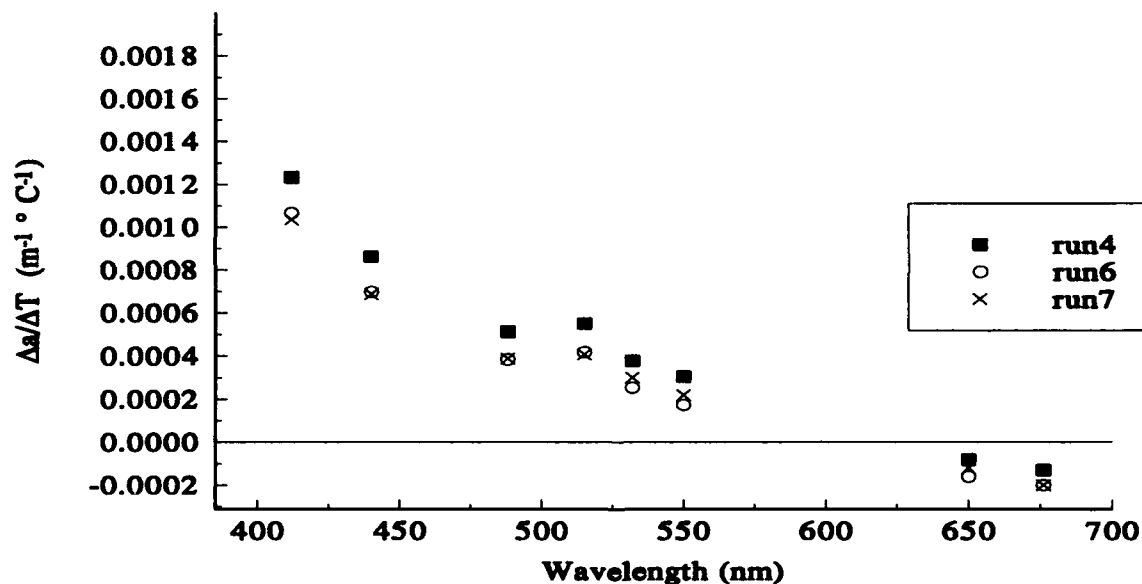


Figure 3. Slopes of the low flow (run 4) and high flow (runs 6, 7) experiments using instrument 2.

There is an apparent increase in the temperature dependence of the absorption coefficient at 412 and 440 nm (Figures 2 and 3) compared to wavelengths in the 500-600 nm range. From 488 nm to longer wavelengths there is no significant differences in the values of $\Delta a/\Delta T$ between the two types of detectors (Figure 4). When we used a different style of detector (runs 1 and 2) the increased temperature dependence was not observed. We believe that this result indicates that the apparent increase may be an instrumental error associated with the changes in the detector temperature.

There are small but consistent differences among the slopes of the two separate instruments used when the same flow rate and detector style are used. These differences are about $0.0003 \text{ m}^{-1}^\circ\text{C}^{-1}$ (Figure 5). We are uncertain why there would be a consistent difference between

instruments. Our best estimates of the temperature dependence of the absorption coefficient are given in Table 1. The estimates are based on the average of all measurements except at 412 and 440 nm where we use estimates based on results from detector style one only. The results at 515 and 520 nm were combined. The results from 550 and 560 nm were also combined.

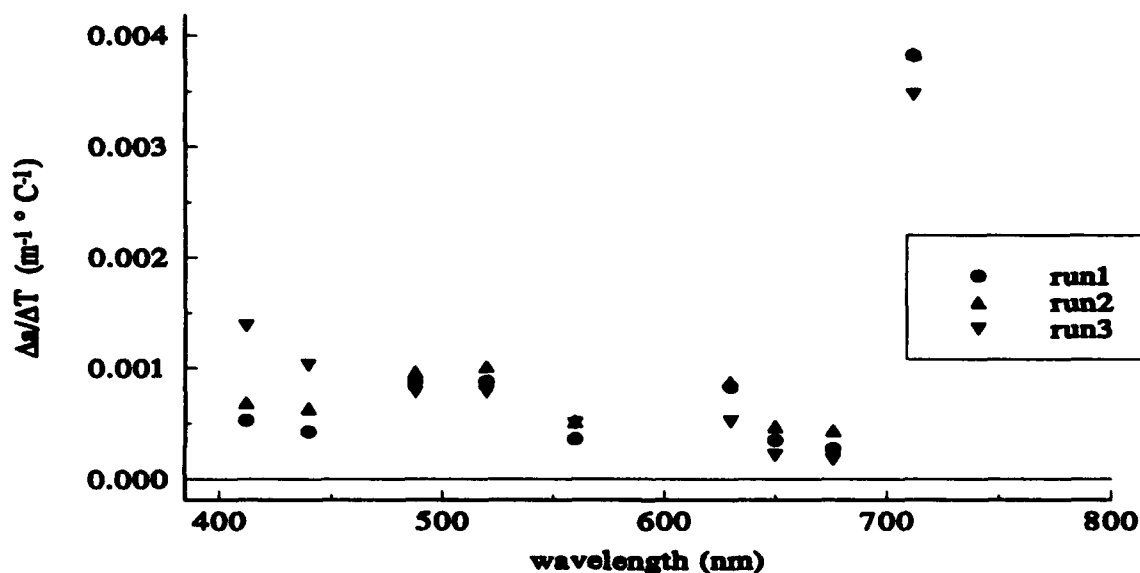


Figure 4. Runs made using the same instrument with different detectors. Runs 1 and 2 were made with detector 1 and run 3 was made with detector 2 using instrument 1 in all cases. The most significant differences between detectors occur at the shortest two wavelengths tested.

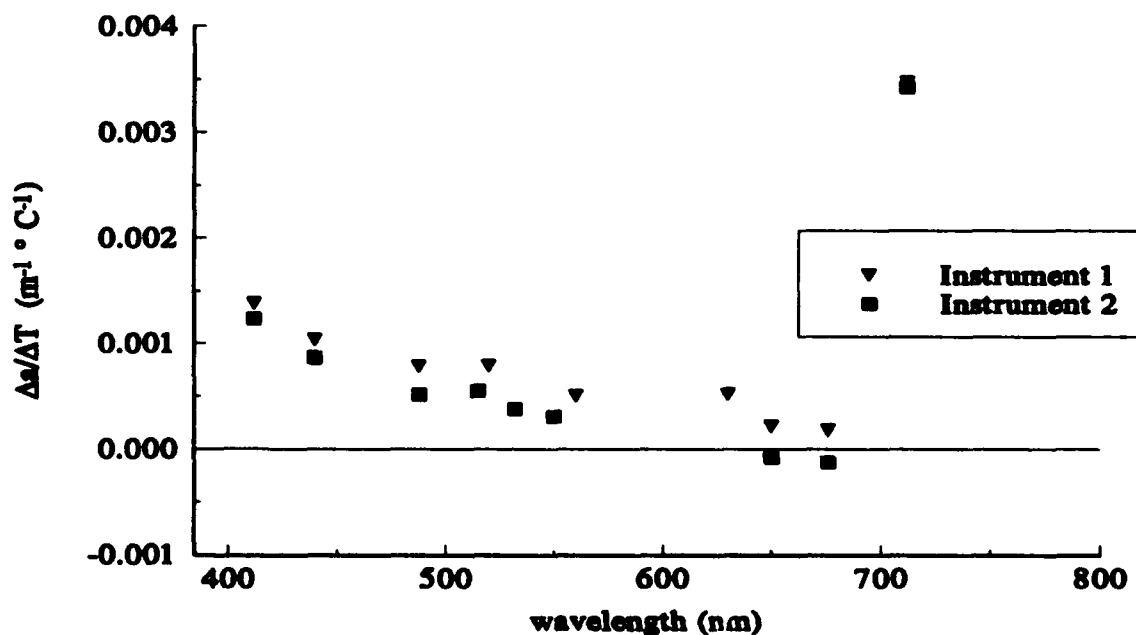


Figure 5. Results from the two instruments with the same detector and water flow configurations.

Table 1. Best estimates of $\Delta a/\Delta T$. The error in the slopes is estimated to be $\pm 3 \times 10^{-4} \text{ m}^{-1} \text{ }^{\circ}\text{C}^{-1}$.

wavelength	412	440	488	515-520	550-560	650	676	715
$\Delta a/\Delta T$	6×10^{-4}	5×10^{-4}	6×10^{-4}	7×10^{-4}	4×10^{-4}	1×10^{-4}	1×10^{-4}	3.4×10^{-3}

4. CONCLUSIONS

We found the largest temperature dependence ($0.0034 \text{ m}^{-1} \text{ }^{\circ}\text{C}^{-1}$) at 715 nm. This temperature dependence is strongly influenced by the O-H vibrational overtone at 745 nm. Outside the region of this overtone the temperature dependence of the absorption coefficient is smaller ($\sim 0.0005 \text{ m}^{-1} \text{ }^{\circ}\text{C}^{-1}$). Results from the 515 nm overtone hint of a slightly higher temperature dependence but there is no statistical difference between the temperature dependence at 515 nm and nearby wavelength bands. We were unable to reproduce the value of $3 \times 10^{-3} \text{ m}^{-1} \text{ }^{\circ}\text{C}^{-1}$ for $\Delta a/\Delta T$ from 400 to 600 nm reported by Højerslev and Trabjerg⁶.

Predicting light distributions in hydrological environments depends on understanding the absorption and scattering properties of the components contained within the environment. In all cases water will be a component that contributes to the total absorption coefficient. How the absorption coefficient of water changes with environmental parameters such as temperature and salinity is important in understanding the total absorption coefficient and parameters like the remotely sensed reflectance, that depend on the total absorption coefficient. Research on the effects of environmental parameters on the absorption coefficient is very limited and the different studies do not fully agree on the effects of temperature on the absorption coefficient of water in the visible portion of the spectrum. Changes to the absorption coefficient with temperature of the order of $1 \times 10^{-4} \text{ m}^{-1} \text{ }^{\circ}\text{C}^{-1}$ are important to know if we are to ever calibrate field instruments to measure the absorption coefficient to the third decimal place. In the near-infrared the possible errors in measurements due to uncorrected temperature changes is even larger. If the absorption coefficient of water is to be determined to 0.001 m^{-1} we will need to do further work to understand the importance of temperature and salinity in determining the magnitude of the absorption coefficient of natural waters.

5. ACKNOWLEDGMENTS

This work was supported by the Office of Naval research under grant number N00014-93-1-0649. We would like to thank Casey Moore of WET Labs Inc. for loaning us the AC-9s used in this work.

6. REFERENCES

1. J. R. Collins, "Change in the infra-red absorption spectrum of water with temperature", *Phys. Rev.*, vol. 25, pp. 771-779, 1925.
2. W. Luck, "Beitrag zur Assoziation des flüssigen Wassers. 1. Die Temperaturabhängigkeit der Ultrarotbanden des Wassers", *Ber. Bunsenges. Physik. Chem.*, vol. 67, pp. 186-189, 1963.

3. C. Jolicoeur, N. D. The, and A. Cabana, "Near Infrared Spectra of Water in Aqueous Solutions of Organic Salts. A Solvation Study of Bu_4NBr , $\phi_4\text{AsCl}$, and $\text{NaB}\phi_4$ ", *Can. J. Chem.*, vol. 49, pp. 2008-2013, 1971.
4. M. K. Phelan, C. H. Barlow, J. J. Kelly, T. M. Jinguji, and J. B. Callis, "Measurement of Caustic and Caustic Brine Solutions by Spectroscopic Detection of the Hydroxide Ion in the Near-Infrared Region, 700-1150 nm", *Anal. Chem.*, vol. 61, pp. 1419-1424, 1989.
5. A. C. Tam, and C. K. N. Patel, "Optical absorption of light and heavy water by laser optoacoustic spectroscopy", *Appl. Opt.*, vol. 18, pp. 3348-3357, 1979.
6. N. K. Højerslev and I. Trabjerg, "A new perspective for remote sensing measurements of plankton pigments and water quality", *Univ. Copenhagen Inst. Phys. Oceanogr. Rep.* 51, 1990.
7. W. S. Pegau and J. R. V. Zaneveld, "Temperature-dependent absorption of water in the red and near-infrared portions of the spectrum", *Limnol. Oceanogr.*, vol. 38, pp. 188-192, 1993.
8. C. Moore, J. R. V. Zaneveld, and J. C. Kitchen, "Preliminary results from an *in situ* spectral absorption meter" *Ocean Optics XI*, G. D. Gilbert, ed., Proc. Soc. Photo-Opt. Instrum. Eng., vol. 1750, pp. 330-337, 1992.
9. R. C. Smith and K. S. Baker, "Optical properties of the clearest natural waters (200-800 nm)", *Appl. Opt.*, vol. 20, pp. 177-184, 1981.

Method for detection of jump-like change points in optical data using approximations with distribution functions

Alexey K. Yasakov

Byelorussian University, Scientific Centre of Air and Spaceborn Diagnosis
of the Earth's Natural Resources, Minsk, BYELORUSSIA
Rokossovskogo Av., 4-4-100, Minsk, 220094, BYELORUSSIA

ABSTRACT

A method for detection and estimation the parameters of jump-like changes of the expectation of optical data for Ocean/ Sea investigations, based on changes approximations by cumulative distribution functions, is proposed. Algorithms and programs for the change-points detection and estimation of the expectation of a stochastic process, based on approximations of the changes by cumulative distribution functions, are constructed and tested.

2. INTRODUCTION

The change-points of characteristics of signals obtained, corresponding the changes of the structure and parameters of the media under investigation, are usually contained in the Ocean/Sea data. The changes of the mean intensity, for given delay, reflects, for example, the jumps of transparency coefficients (due to the presence of an object in the area investigated, like whale or fishes, etc.), or temperature/pressure, concentrations of chemicals in the areas concerned, etc.

Detection of the edges of the areas concerned is significant in different applications: fishing, detection of pollution or targets, detection of areas with jump like changes of pressure, temperature, concentrations, solving meteorology problems, etc. The nature of data available has usually stochastic nature, because of different noises, both in the media itself and in the receivers and multipliers used for reception. Hence, for evaluation the methods of detection the change points and estimation the parameters of the changes one must take into consideration the stochastic nature of data obtained.

Jump-like change points detection and parameters of the jumps' estimation is a problem of the statistical analysis of different data. The different approaches have been applied to solve the problem. The traditional approaches for detection of jump-like changes are sequential approaches. They use the cumulative sums algorithms (called CUSUM's algorithms) - applying the procedures like founded by E.C. Page must be processed for detection and parameters estimation of jump-like change points (in Ocean/Sea investigation data - jump-like changes of the mean of temperature or pressure, concentrations of chemicals etc. measurements) immediately.

3. MODELS OF JUMP-LIKE CHANGES IN OCEAN/SEA MEASUREMENTS

Due to Bugger's law for liquid media, the back scattered laser signal intensity, under jump-like changes of the mean and transparency coefficient (for example) may be written as

$$y(t) = \left\{ \Psi(t) + I(t-t^*) \cdot A \cdot e^{-\left\{ \alpha(t) \cdot (t-t^*) + G \cdot I(t-t_r) \right\}} \right\} \cdot S(t) + u(t), \quad (1)$$

where $y(t)$ - additive noise, $S(t)$ - known function of time t , A - unknown peak intensity, the quantity $\alpha(t)$ may be changed as a jump-like process

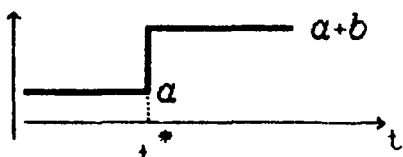
$$\alpha(t) = \begin{cases} a, & t < t_r, \\ a+b, & t \geq t_r, \end{cases} \quad I(t) = \begin{cases} 0, & t < 0, \\ 1, & t \geq 0, \end{cases} \quad \Psi(t) = \begin{cases} 0, & t < t^*, \\ C, & t \geq t^*. \end{cases} \quad (2)$$

The model is significant for description of the intensity of back scattered signals in Ocean/Sea experiments. The moment t^* corresponds meeting of laser pulse with the border "air - media1", the moment t_g corresponds meeting of laser pulse with the border "media1 - media2", the quantity a - the initial decrement in media1, b - the jump of decrement in media2, C - characterise the parameter of noise, G - characterises the gain of the signal due to the border, ...

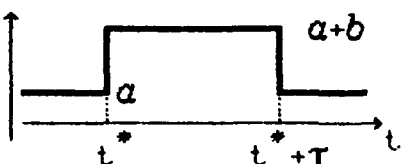
In the model like (1)-(2) the quantities A , α , b , G , t^* , t_g , C must be determined. The model is complicated enough and more simple models available for Ocean/Sea laser data, when, for example $C=0$, etc. Under similar conditions, when the logarithmic amplifiers are in use, the models for mean with jump like changes are possible. The technology of transforming the signals is not of interest here. Our goal is to detect jump-like changes and estimate its parameters.

Consider more simple models for jump like changes of the parameters under investigation.

Consider a stochastic process $x(t)$ (with bounded two first moments) with jump-like change points at t^* where process parameters are changing for example by models

$$E(x(t)) = \begin{cases} a, & t < t^*, \\ a + b, & t \geq t^*, \end{cases} \quad a, b \in \mathbb{R}^1, \quad (3)$$


- we call it "I" - type change-point, or

$$E(x(t)) = \begin{cases} a, & t < t^*, \\ a + b, & t \in [t^*, t^* + \tau], \\ a, & t > t^* + \tau, \end{cases} \quad a, b \in \mathbb{R}^1, \quad (4)$$


we call it "II" - type change-point, with unknown parameters α , b , t^* , τ . Note: the jumps may be positive and negative comparing with initial level a . The processes with the parameters corresponding models (3), (4) are usual in Ocean/Sea measurements. The problem is to determine t^* , τ , α , b when the observations

$$x_1, x_2, \dots, x_N$$

of the stochastic process $x(t)$ at $t=t_i$, $i=1,2,\dots,N$ are available.

4. DETECTION AND ESTIMATION OF PARAMETERS OF JUMP-LIKE CHANGES

Different procedures for change-points detection (cumulative sums (CUSUM) - like procedures) were applied to determine the t , t' and then to estimate parameters α , b . We propose another one.

4.1. Main Idea of the Approach proposed.

The main idea of the approach we propose lies in approximation of a change point in the data stored by distribution functions (cumulative distribution functions - c.d.f.) of random variables with several unknown parameters and estimation of the parameters of the approximation using the data obtained. It can be made as follows.

Consider a stochastic process $x(t)$ (with bounded two first moments) with jump-like change points at t^* , $t^* + \tau$. The process parameters, supposed, are changing by models (3), (4). Let $F(z, \Theta)$ be a distribution function (cumulative distribution functions -c.d.f.) of a random variable, with parameters Θ (Θ is like the scale parameters, position parameters are assumed to be zero). Then easy to write [1]:

$$E(x(t)) \cong a + b \cdot F(t - t^*, \Theta), \quad (5)$$

$$E(x(t)) \cong a + b \cdot F(t - t^*, \Theta) - b \cdot F(t - t^* - \tau, \Theta). \quad (6)$$

Using the approximations (5), (6) the problem of determining a , b , t , τ becomes the problem of estimation a , b , t^* , τ , which may be successfully solved by common procedures of the parameters estimation. When the data x_1, x_2, \dots, x_N are obtained, where $E(z)$ denotes the expectation of z . For solving the task we must find the nearest t close to t^* . Thus, it is necessary to approximate change-points and find t^* , τ , a , b as a solution (for example) of the tasks

$$\sum_{i=1}^N \left[x_i - a - b \cdot F(t_i - t^*, \Theta) \right]^2 \rightarrow \min_{a, b, t^*}, \quad (7)$$

$$\sum_{i=1}^N \left[x_i - a - b \cdot F(t_i - t^*, \Theta) + b \cdot F(t_i - t^* - \tau, \Theta) \right]^2 \rightarrow \min_{a, b, t^*, \tau} \quad (8)$$

Different distribution functions of random variables for similar approximations and the algorithm's construction can be used.

4.2. Detection and Estimation of Parameters of Jump - like Changes using Uniform Distribution c.d.f.

Denote sets:

$$N_1 = \{i \mid t_i \leq t^* - \Theta, \quad i=1, 2, \dots, N\},$$

$$N_2 = \{i \mid t_i \in (t^* - \Theta, t^* + \Theta), \quad i=1, 2, \dots, N\},$$

$$N_3 = \{i \mid t_i \geq t^* + \Theta, \quad i=1, 2, \dots, N\}.$$

The cumulative distribution function for uniform random variable at interval $(-\Theta, \Theta)$ - $F(t, \Theta)$, $t = ix\Delta$, (Δ - is the time interval between measurements) may be written as

$$F(i, \Theta) = \begin{cases} 0, & i \cdot \Delta \leq -\Theta, \\ (i \cdot \Delta + \Theta) / 2\Theta, & i \cdot \Delta \in (-\Theta, \Theta), \\ 1, & i \cdot \Delta \geq +\Theta. \end{cases}$$

Denoting $i^* = [t^* / \Delta]$, $t = t^*$, $i_0 = i^*$, the task for model (8) becomes

$$\sum_{i \in \mathbb{N}_1} [x_i - a]^2 + \sum_{i \in \mathbb{N}_2} \left[x_i - a - b \cdot \frac{t_i - t_0 + \Theta}{2 \cdot \Theta} \right]^2 + \sum_{i \in \mathbb{N}_3} [x_i - a - b]^2 \rightarrow \min_{a, b, t_0} \quad (9)$$

Then the system for the task, for estimation of a, b, i will be

$$\hat{b}(i_0) = \frac{\sum_{i=1}^N [x_i - a(i_0)]}{\|\mathbb{N}_3\| + \sum_{i \in \mathbb{N}_2} \left[\frac{t_i - t_0 + \Theta}{2 \cdot \Theta} \right]} \quad (10)$$

$$\hat{a}(i_0) = \frac{\sum_{i=1}^N x_i \cdot \left[\frac{\|\mathbb{N}_3\|}{\|\mathbb{N}_3\| + S_1(i_0)} + \frac{S_2(i_0)}{\|\mathbb{N}_3\| + S_1(i_0)} \right] - \sum_{i \in \mathbb{N}_3} x_i - \sum_{i \in \mathbb{N}_2} x_i \cdot \frac{t_i - t_0 + \Theta}{2\Theta}}{N \cdot \left[\frac{\|\mathbb{N}_3\|}{\|\mathbb{N}_3\| + S_1(i_0)} + \frac{S_2(i_0)}{\|\mathbb{N}_3\| + S_1(i_0)} \right] - \|\mathbb{N}_3\| - S_1(i_0)} \quad (11)$$

$$\begin{aligned} \sum_{i \in \mathbb{N}_1} [x_i - \hat{a}(i_0)]^2 + \sum_{i \in \mathbb{N}_2} \left[x_i - \hat{a}(i_0) - \hat{b}(i_0) \cdot \frac{t_i - t_0 + \Theta}{2 \cdot \Theta} \right]^2 + \\ + \sum_{i \in \mathbb{N}_3} [x_i - \hat{a}(i_0) - \hat{b}(i_0)]^2 \rightarrow \min_{i_0} \end{aligned} \quad (12)$$

$$S_1(i_o) = \sum_{i \in N_3} \left[\frac{t_i - t_o + \Theta}{2 \cdot \epsilon} \right],$$

where

$$S_2(i_o) = \sum_{i \in N_3} \left[\frac{t_i - t_o + \Theta}{2 \cdot \epsilon} \right]^2, \quad i_o = [t_o / \Delta].$$

Thus, the optimisation task for multi parameters becomes one parameter optimisation task. The equivalent expressions for (10), (11) are usable

$$\hat{a}(i_o) = \frac{\sum_{i=1}^N X_i}{N} - \frac{\hat{b}(i_o)}{N} \cdot (\|N_3\| + S_1(i_o)), \quad (13)$$

$$\hat{b}(i_o) = \frac{\sum_{i \in N_2} X_i \cdot \frac{t_i - t_o + \Theta}{2\Theta} - \frac{\sum_{i=1}^N X_i}{N} \cdot (\|N_3\| + S_1(i_o)) + \sum_{i \in N_3} X_i}{\|N_3\| + S_2(i_o) + (\|N_3\| + S_1(i_o)) \cdot \|N_2\| / N}. \quad (14)$$

The cases of special interest are:

1) $\Theta < \Delta$, when $\|N_2\| = 1$,

$$\sum_{i \in N_2} \left(\frac{t_i - t_o + \Theta}{2\Theta} \right) = 1/2, \quad \sum_{i \in N_2} \left(\frac{t_i - t_o + \Theta}{2\Theta} \right)^2 = 1/4;$$

2) $\Delta < \Theta < 2\Delta$, when $||N_2|| = 3$,

$$\sum_{i \in N_2} \left(\frac{t_i - t_o + \Theta}{2\Theta} \right) = 3/2, \quad \sum_{i \in N_2} \left(\frac{t_i - t_o + \Theta}{2\Theta} \right)^2 = (3 \cdot \Theta^2 + 2 \cdot \Delta^2) / (4 \cdot \Theta^2).$$

The number of necessary measurements N must be greater than $N > 0.5 \cdot (2\Theta/\Delta + 1) \cdot (\Theta/\Delta + 3)$, i.e. $N > 6$. The algorithm is clear to realize. The computational complexity depends on Θ . The greater the $||N_2|| > 3$, the less the accuracy of t estimation and the greater the computation complexity.

4.3. Detection and Estimation of Parameters of Jump like Changes using Gaussian distribution c.d.f.

For Gaussian c.d.f.

$$F(i, \Theta) = \frac{1}{2} \left[1 + \Phi \left(\frac{i}{2 \cdot \sigma} \right) \right],$$

where $F(z) = \text{ERF}(z)$:

$$\Phi(z) = \frac{2}{\sqrt{\pi}} \int_0^z \exp(-t^2) dt,$$

σ characterises the width of the jump. The system for the task, for estimation of a, b, i will be

$$\hat{a}(i_o) = \frac{\sum_{i=1}^N x_i}{N} - \sum_{i=1}^N \left[1 + \Phi \left(f(i, i_o) \right) \right] \cdot \frac{\hat{b}(i_o)}{2 \cdot N},$$

(15)

$$f(i, i_0) = (i - i_0) / (\sqrt{2} \cdot \sigma),$$

$$\hat{b}(i_0) = 2 \cdot \frac{\sum_{i=1}^N [1 + \Phi(f(i, i_0))] \cdot x_i - \sum_{i=1}^N [1 + \Phi(f(i, i_0))] \cdot \frac{\sum_{i=1}^N x_i}{N}}{\sum_{i=1}^N [1 + \Phi(f(i, i_0))] - \left(\sum_{i=1}^N [1 + \Phi(f(i, i_0))] \right)^2 / N}, \quad (16)$$

$$\sum_{i=1}^N [x_i - \hat{a}(i_0) - \hat{b}(i_0) \cdot [1 + \Phi(f(i, i_0))]] \cdot \exp(-f^2(i, i_0)) = 0. \quad (17)$$

The solving of this system is just identical to solving the system (10) - (12). It is useful to keep in memory (either in tables or in arrays) the quantities $F(f(i, i_0))$, $i=1, 2, \dots, N$, $i_0=2, 3, \dots, N-1$, solving the system (15) - (17) beforehand - it saves time for calculation.

5. SIMULATION OF DETECTION AND ESTIMATION

The algorithms and personal computer oriented programs for the change - points detection and estimation of the expectation of a stochastic process with bounded two first moments for models (3), (4) are constructed and tested. They are based on the approach proposed for jumps of the expectation approximations by cumulative distribution functions.

The algorithms and programs showed their good properties.

The approach is fully applicable for multiple change - points detection (for example for model (4)). Easy to apply similar approximations several times (double for model (4)) using of the model (3). It leads the similar equations that are easy to realize in computer. The algorithms were constructed and tested under different ratios of $|b|/\text{rms}(\text{noise})$ - it defines SNR (signal/noise ratio).

The detection and parameters of jumps estimation were robust enough even /when $|b|/\text{rms}(\text{noise}) > 0.75$ in computer simulations. The algorithms easy to apply for real data (experiments).

Another possibility for several jump like changes detection is in using the search algorithms (those like Fibonacci's "golden section" one). After the moment of one jump detected, easy to use model (3) and estimate

the parameters needed. The similar algorithms were developed and tested for different SNRs. for determining of "IT" type change - points with change points parameters estimation. The similar algorithms were developed and tested.

However some characteristics of random processes (the expectation, for example) changes not so quickly, are evolution (smooth enough) - because there are some trends in parameters of the processes and it is necessary to know the parameters of that trends, the moments of the trends arising. The method is useful for investigation (parameters estimation and classification) of so called evolution (smooth) trends of processes, evolution change points that are usual to arise in practice. This is productive enough because the estimation methods are well developed now.

6. SUMMARY

The method proposed needs hence no special data models for jump-like changes detection and estimation the parameters of the changes. The main significance of this approach is in its simplicity and usefulness for various tasks.

The programmes developed are easy to use for processing optical data with jump-like changes.

7. REFERENCES

1. Yasakov A.K. "A method of the expectation change point detection using approximations with distributions functions", *Sixth Int. Vilnius Conf. on Probability and Math. Stat. Abstr. comm.*, Vilnius, June 28 - July 3, 1993, vol.2, p.193-194.

Comparison of analytical calculations with experimental measurements for polarized light scattering by micro-organisms

Patricia G. Hull,* Felecia G. Shaw,* Mary S. Quinby-Hunt,** Daniel B. Shapiro,**
Arlon J. Hunt,** Terrence Leighton***

*Department of Physics, Tennessee State University, Nashville, TN 37209
Phone and FAX (615) 320-3797, OMNET = P.HULL

**Energy and Environment Division, Lawrence Berkeley Laboratory
Berkeley, CA 94720 Phone (510) 486-5645, FAX (510) 486-4260 OMNET = A.HUNT

***Division of Biochemistry and Molecular Biology, 401 Barker Hall
University of California Phone (510) 486-1620 Internet = leighton@bacillus.berkeley.edu

ABSTRACT

The consequences of light scattering from both spherical and non-spherical particles on the propagation of light in the ocean was investigated. The scattering from an ensemble of non-spherical micro-organisms is calculated using the coupled-dipole approximation with an orientational average over Euler angles using Gauss-Legendre integration. Mie calculations provide rigorous solutions for spherical particles and are considerably less computer intensive than the coupled-dipole approximation. Furthermore, they have been shown to accurately predict the scattering for marine organisms that are nearly spherical. Scattering matrix elements calculated using the coupled-dipole approximation were compared with those obtained using Mie calculations in the limit as an ellipsoidal object approaches a sphere in order to assess the limits of applicability of the Mie theory to ellipsoidal particles. Experimental measurements of the scattering matrix elements for spherical particles (latex spheres) and ellipsoidal particles (*Bacillus subtilis*) were used to test validity of our analytical approach.

1. INTRODUCTION

It is important to model the light scattering from larger irregularly-shaped particles in order to understand and adequately predict the scattering of polarized light in sea water, including coastal regions and the sea/air boundary layer. In coastal water containing large amounts of inorganic debris, relatively large and non-spherical particles may significantly effect the polarization state of scattered light. Using scattering predictions for spherical particles, which can vary considerably from that of most oceanic scatterers, could result in misinterpretation of scattering and visibility data, inaccurate irradiance computations, and errors in characterization of marine biomass. Since well-tested computer programs are in place for modeling spherical particles (Mie theory), considerable computational time can be saved in situations where Mie calculations can be used instead of a more computational-intensive method such as the coupled-dipole approximation. Thus, it is important to evaluate conditions for which Mie calculations produce an accurate description of the scattering of polarized light. Similarly, the Mie calculations can provide a means for establishing the limits for the coupled-dipole approach.

2. APPROACH

2.1 The Stokes Vector Formalism. The polarization states of the incident and scattered light are described by four-element Stokes vectors and the effect of a scattering medium on the beam is represented by a four by four Mueller or 'scattering' matrix. This formalism is described in texts by Bohren and Huffman,¹ van de Hulst² and Kerker.³ Precise definitions of the components of the Stokes vector in terms of the components of the electric field perpendicular (E_{\perp}) and parallel (E_{\parallel}) to the scattering plane are given by the relationships below. The

brackets indicate a time average. The angles in the physical interpretation of the element are measured relative to the scattering plane.

$$\begin{aligned}
 I_s &= \langle E_{//s} E_{//s}^* + E_{\perp s} E_{\perp s}^* \rangle && \text{(total intensity of scattered light)} \\
 Q_s &= \langle E_{//s} E_{//s}^* - E_{\perp s} E_{\perp s}^* \rangle && (\pm 90^\circ \text{ polarization}) \\
 U_s &= \langle E_{//s} E_{\perp s}^* + E_{\perp s} E_{//s}^* \rangle && (\pm 45^\circ \text{ polarization}) \\
 V_s &= i \langle E_{//s} E_{\perp s}^* - E_{\perp s} E_{//s}^* \rangle && \text{(circular polarization)}
 \end{aligned}$$

When similar expressions are written for the Stokes vector describing the incident beam, the Mueller or 'scattering' matrix, which transforms the incident light, is defined by the matrix equation;

$$\begin{bmatrix} I_s \\ Q_s \\ U_s \\ V_s \end{bmatrix} = \begin{bmatrix} S_{11} & S_{12} & S_{13} & S_{14} \\ S_{21} & S_{22} & S_{23} & S_{24} \\ S_{31} & S_{32} & S_{33} & S_{34} \\ S_{41} & S_{42} & S_{43} & S_{44} \end{bmatrix} \times \begin{bmatrix} I_i \\ Q_i \\ U_i \\ V_i \end{bmatrix}$$

The elements of the scattering matrix are functions of the scattering angle and depend on the size, structure, symmetry, orientation, complex refractive index, and ordering of the scatterers. In the general case of scattering from a randomly oriented collection of particles, there are only eight non-zero matrix elements. For a particle with spherical symmetry, $S_{22}=S_{11}$, $S_{12}=S_{21}$, $S_{33}=S_{44}$, $S_{34}=-S_{43}$, and all others are zero. An orientation average for a collection of particles has the same symmetry if the particle has a mirror plane of symmetry. Symmetry is a function of composition as well as shape. Thus, it is possible to have an optically active or linearly birefringent sphere that does not have spherical symmetry with respect to the incident light. As the particle deviates from spherical symmetry, the complexity of the scattering matrix and its angular dependence increase. Different elements of the Mueller scattering matrix are useful in describing various attributes of the scatterers, including symmetry, structure, chirality, optical properties, and orientation. In this paper, we will focus on the normalized matrix elements S_{11} , S_{12} and S_{34} in the interest of simplicity and availability of experimental data. All elements not written in italics will be normalized in the following way: S_{11} is normalized to 1.0 at a scattering angle of 0° . The elements S_{12} and S_{34} are normalized by the total intensity, S_{11} , and have values that range between 1 and -1. The experimental measurements of S_{12} and S_{34} are normalized by the total intensity in the instrumental set-up. A useful physical interpretation of each of these three elements of interest is as follows;

- S_{11} - measure of the total scattered intensity for unpolarized incident light;
gives general size information;
- S_{12} - measure of linear polarization parallel and perpendicular to the scattered plane;
- S_{34} - strongly dependent on size and complex refractive index of the particle;
is a measure of changing circularly-polarized light to linearly-polarized light that is $\pm 45^\circ$ to the scattering plane.

The size of the particle is best described by the size parameter, $x = 2\pi r/\lambda$, where r is the radius of a spherical particle and λ is the wavelength of the incident radiation in the medium. For non-spherical particles, r is taken to be the radius of a sphere of the same volume as the non-spherical particle. In the interest of simplicity, only two structures are considered here, spheres and ellipsoids. The effects of preferred orientation of the particles have been discussed by the authors previously.^{4,5} Only randomly oriented collections of particles of a single size are discussed in this paper.

2.2 Coupled-Dipole Approximation. The scattering from non-spherical micro-organisms is calculated using the coupled-dipole approximation. The coupled-dipole approximation was first proposed by Purcell and Pennypacker⁶ in 1973 and later applied by Singham *et al.*^{7,8} in 1986 and Draine⁹ in 1988. The theory can be used to calculate all 16 Mueller matrix elements for particles of any shape. In this model, an arbitrarily-shaped object is divided into a number of identical elements arranged on a cubic lattice. For isotropic materials, each element is treated as a spherical, dipolar oscillator with a scalar polarizability. For these cases, the Claussius-Mosotti relation as described in Bohren and Huffman¹ is used for calculating polarizability. Interactions between dipoles are included by determining the field at a particular dipole due to the incident field and the fields induced by the other dipole oscillators. The scattered field is then the sum of the fields due to each oscillator. The problem of determining the electric field at each dipole is the primary (and most difficult) task of the coupled-dipole method. A set of linear equations can be written in matrix form as $AE = B$, where E is a column matrix with $3N$ elements representing the (unknown) electric field components at dipole i , and B is a column matrix of $3N$ elements representing the incident radiation, $E_0 e^{ik \cdot r_i}$, at each dipole location. A is a $3N \times 3N$ matrix with complex elements representing the interactions between the individual dipoles. Its elements are functions of the dipole locations and the complex polarizability at each dipole location. A solution to this equation is written; $E = A^{-1}B$. Once the components of the scattered electric field are determined, the calculation of the elements of the Mueller matrix is straightforward.

A model for light scattering must include an effective method of representing a collection of organisms. A reasonable approach is to perform a numerical or analytical average over a set of orientations. Our approach is to fix the particle at one orientation and rotate the coordinate system as described by Singham *et al.*⁸ The computer-intensive calculation of the inverse of the interaction matrix, A , need be done only once in this model. The computer programs that we developed include a routine that rotates the coordinate system through the Euler angles, ϕ , θ , and ψ . Angle ϕ is a counterclockwise rotation about the z -axis, θ is a counterclockwise rotation about the new x -axis, and ψ is a counterclockwise rotation about the new z -axis.

We have achieved some success in modeling ensembles of irregularly shaped particles such as cylinders and helices (octopus sperm heads)^{10,11} using the coupled-dipole model with orientational averaging. However, due to practical limitations in memory of the CRAY computer, the maximum number of dipoles that can be used to model an organism at this time is on the order of 1200.

2.3 Experimental Measurements. The experimental determination of all sixteen Mueller matrix elements for a given scattering medium requires measurements of intensity of scattered light *vs.* scattering angle for various polarization states of incident and scattered light. Measurements were made on the polarization-modulated nephelometer developed by one of the authors.¹² Important components of the instrument include a photo-elastic modulator vibrating at 50 kHz and a matching two-phase lock-in amplifier. Scattering measurements were made at two wavelengths, 488 nm, and 633 nm for a suspension of *B. subtilis* spores in distilled water. The experimental measurements were transported into a software program for generating the graphs shown in the figures. The experimental data taken with the nephelometer for the latex spheres shown in Figure 2 has been published previously by Quinby-Hunt *et al.*¹³

3. RESULTS

3.1 Comparison of Coupled-dipole with Mie theory. In order to assess limits in the size of a micro-organism that might be successfully modeled with the coupled-dipole approximation method, the coupled-dipole calculations were compared to the Mie calculations for spheres. Figure 1 shows the normalized matrix elements S_{11} , S_{12} and S_{34} for light scattering from spheres calculated from both methods. The solid line shows the elements calculated using the coupled-dipole approximation and dashed line shows the Mie calculation. In figure 1(a) the size parameter is 4.46 and in Figure 1 (b) it is 8.92 if we consider a suspension of spheres in water. For incident light at a wavelength of 442 nm, size parameters of 4.46 and 8.92 correspond to spheres of radius .234 and .472 μm , respectively. Slight disagreement at larger scattering angles (greater than 130°) is apparent

at the smaller size parameter but the overall agreement is excellent. The agreement in structure (location of peaks) at the larger size parameter is reasonably good for scattering angles up to 120° .

3.2 Experimental Results and Coupled-dipole Predictions for Spheres. In the second set of graphs, shown in Figure 2, experimental measurements of the Mueller matrix elements, S_{11} , S_{12} and S_{34} are compared to those calculated from the coupled-dipole approximation for latex spheres with a size parameter of 4.46 (sphere radius of $.234 \mu\text{m}$ and incident light at 442 nm). The experimental data for S_{11} has been multiplied by the sine of the scattering angle to account for the the scattering volume seen by the detector. The overall agreement in the graphs is quite good. Although the magnitudes of the peaks differ slightly, the prominent features in the three graphs occur at corresponding angles. Excellent agreement between the experiment and Mie theory for these latex spheres and spherical marine micro-organisms has been obtained by Quinby-Hunt *et. al.*^{13,14} using a Gaussian distribution of homogeneous spheres centered at a diameter of 472 nm to represent the latex spheres. Although it would be helpful to be able to include a distribution of particle sizes in the coupled-dipole model, it is beyond the scope of the calculations at this time. It is important to note, however, that it is possible to achieve an acceptable model for spheres using a single size.

3.3 Experimental Results and Coupled-dipole Predictions for Ellipsoids. In Figures 3(a) and (b) and 4(a) and (b), experimental measurements of the Mueller matrix elements, S_{11} , S_{12} and S_{34} for a suspension of *B. subtilis* spores in distilled water are compared to those calculated from the coupled-dipole approximation for ellipsoids with a comparable size parameter. Comparisons were made at two wavelengths, 488 nm and 633 nm. Experimental data and coupled-dipole calculations show agreement in general features but display shifts in peak positions. The size parameters at both wavelengths ($x=5.66$ and $x=4.36$) are within the range where the predictions should be valid. The failure to achieve better agreement between the calculated values and the experimental values is probably due not to the large size of the spores, but to their complex structure. A photomicrograph of the spores shows that they are ellipsoidal in overall shape with a long axis about twice that of the short axis with an average length on the order of $1.4 \mu\text{m}$. We used homogeneous ellipsoids of these dimensions and an index of refraction of 1.48 in the coupled-dipole model. The choice of an index of refraction of 1.48 was somewhat arbitrary. It is within the range of values found in the literature for organic material and produced better results than numbers slightly larger or smaller. The spores as shown in the micrographs, however, appear to have a core with a much different index of refraction than the outer region. The core is roughly spherical and occupies about three fourths of the total volume. It seems that a more complex model with an appropriate index of refraction could be chosen to improve the agreement. The Mie theory for a coated sphere might also have potential for success in modeling the spores.

3.3 Dependence of Matrix Elements for Ellipsoids on Index of Refraction and Shape. In order to illustrate the influence of relative index of refraction on the scattering matrix elements, the left column, Figure 5(a), shows graphical results for an ellipsoid similar to the one used in Figures 3 and 4. Clearly, varying the relative index of refraction from 1.11 to 1.19 has a dramatic effect on the scattering. It is critical to have good values for the index of refraction of any particles being modeling. Finally, in the right-hand column, Figure 5(b), graphs generated for spherical particles using Mie theory are compared to coupled-dipole calculations of scattering from increasingly non-spherical particles. For ellipsoids, we define the aspect ratio, AR, to be the ratio of the major to the minor axis. The same figure shows the matrix elements for a sphere and ellipsoids with aspect ratios of 1.2, 1.4, and 1.6. Note that as AR increases, the scattering lobe becomes more intense the characteristics of the scattering become similar to that of a long cylinder. The most interesting result is in the element S_{12} . As the ellipsoid is elongated, the scattering features become broader, reducing characteristic spherical diffraction. S_{34} tends to broaden and exhibit less structure. In all three plots, the difference in the curves between successive increases in AR becomes smaller, indicating that we might be approaching limiting value. Calculations for aspect ratios of 1.8 and 2.0 confirm this trend, but to reduce the clutter, they were not shown in the figures.

4. CONCLUSIONS

The good agreement of the coupled-dipole calculations with both the Mie theory and the experimental data for light scattering from spheres at size parameters around five and possibly larger is promising. A size parameter of 6.0 translates into a particle size in the ocean of about 1.0 μm at visible light wavelengths. Many marine organisms and particulates of interest have sizes between 1 and 2 μm , including the *B. subtilis*, putting them within, or close, to the current modeling limits of the coupled-dipole method. Differences between coupled-dipole and Mie calculations at large scattering angles indicates that the coupled-dipole model should be used with caution for scattering of visible light from irregularly-shaped particles much larger than one micron. The model could be employed, however, to predict trends or prominent features in the scattering.

The results of the comparison between spheres and ellipsoids of various aspect ratios provide an understanding of the degree to which non-spherical particles in the scattering medium effect the polarization state of the scattered light. In addition to this understanding, the results can also serve as a guide for determining when Mie calculations are adequate to describe scattering from a collection of particles and when we must use a model that includes scattering from non-spherical particles.

5. ACKNOWLEDGMENTS

We wish to thank Steve Ackleson for his support and interest in this research. This work was supported by the Office of Naval Research under Contract N00014-92-J-1284 awarded to P.G.H. and N00014-94-F0043 awarded to M.S.Q.-H.

6. REFERENCES

1. C. Bohren, and D. Huffman, *Absorption and Scattering of Light by Small Particles*, Wiley, NY, NY, 1970.
2. H.C. van de Hulst, *Light Scattering by Small Particles*, Wiley, New York, 1957.
3. M. Kerker, *The Scattering of Light and Other Electromagnetic Radiation*. Academic Press, New York, 1969.
4. P. Hull, A. Hunt, M. Quinby-Hunt, and D. Shapiro, "Coupled-dipole approximation as an analytical model for predicting scattering from marine micro-organisms," American Geophysical Union 1990 Fall Meeting in San Francisco.
5. P. Hull, A. Hunt, M. Quinby-Hunt and D. Shapiro, "An analytical model for predicting light scattering from marine micro-organisms," Proc. SPIE, Vol. 1537, San Diego, July 1991.
6. E.M. Purcell and C.R. Pennypacker. "Scattering and absorption of light by nonspherical dielectric grains," *Astrophys. J.* Vol. 186, 705, 1973.
7. S. Singham and G. Salzman, "Evaluation of the scattering matrix using the coupled dipole approximation." *J. Chem. Phys.* 84 (5), 2658, 1986.
8. M. Singham, S. Singham and G. Salzman, "The scattering matrix for randomly oriented particles," *J. Chem. Phys.* 85, 3807, 1986.
9. B.T. Draine, "The discrete-dipole approximation and its application to interstellar grains," *The Astrophysical Journal*, 333, 848-892, 1988.
10. D. Shapiro, P. Hull, M. Quinby-Hunt, M. Maestre, J. Hearst, and A. Hunt, "Toward a working theory of polarized light scattering from helices," *J. Chem Phys.* 100 (1), 146-157, 1994.
11. D. Shapiro, A. Hunt, M. Quinby-Hunt, P. Hull, and M. Maestre, "Theoretical and experimental study of polarized light scattering on helices," *Ocean Optics XI* Proc. SPIE, Vol. 1750, San Diego, July, 1992.
12. A. Hunt and D. Huffman. "A new polarization-modulated light scattering instrument," *Rev. Sci. Instrum.* Vol. 44, 1753-1762, 1973.
13. M. Quinby-Hunt, A. Hunt, K. Lofftus, and D. Shapiro. "Polarized-Light Scattering Studies of Marine *Chlorella*," *Limnol. Oceanogr.*, 34, 1587-1600, 1989.
14. M. Quinby-Hunt and A. Hunt. "Effects of Structure on Scattering from Marine Organisms: Rayleigh-Debye and Mie Predictions," *Ocean Optics IX*. Proc. SPIE, 288-295, 1988.

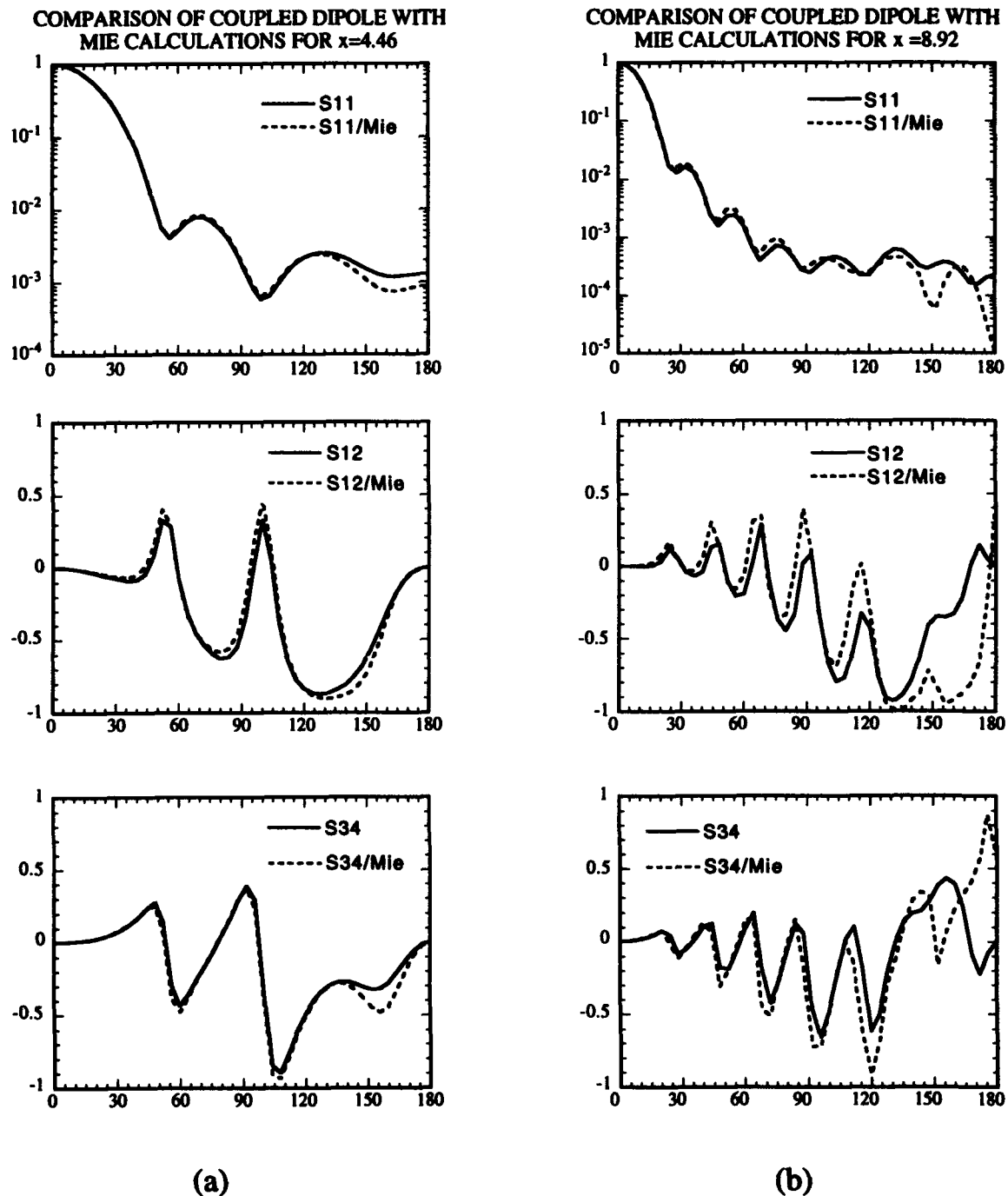
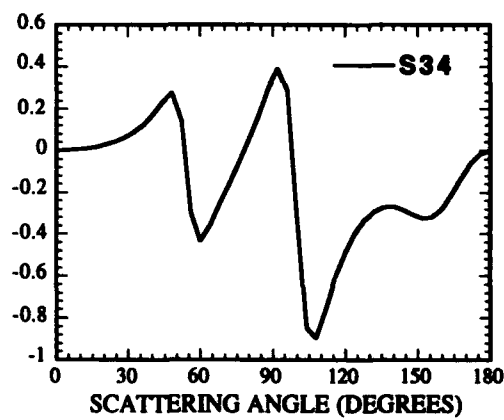
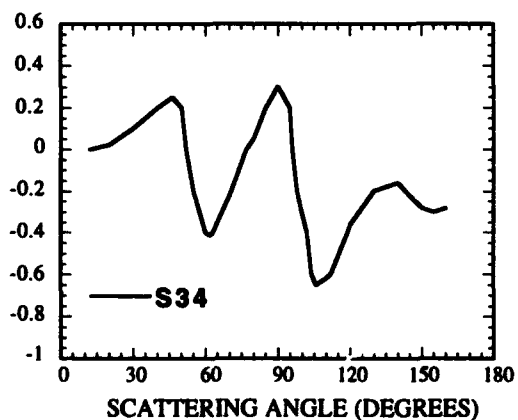
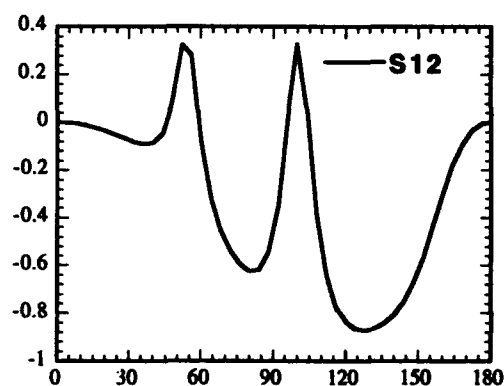
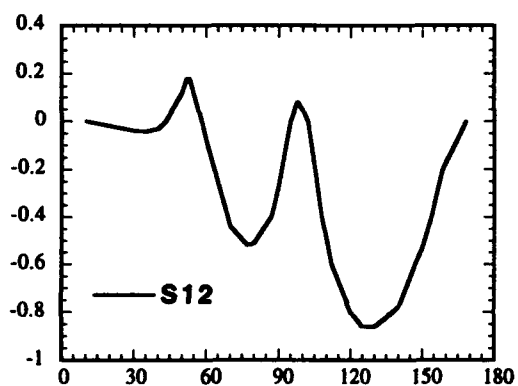
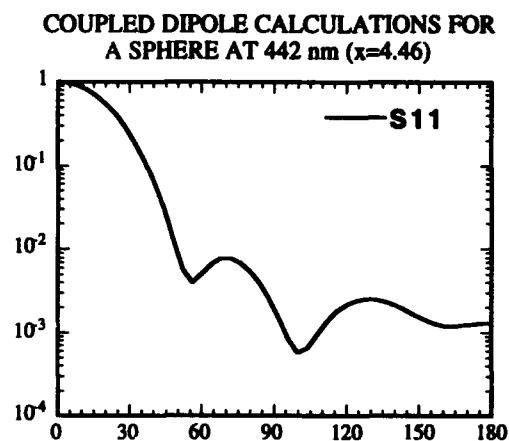
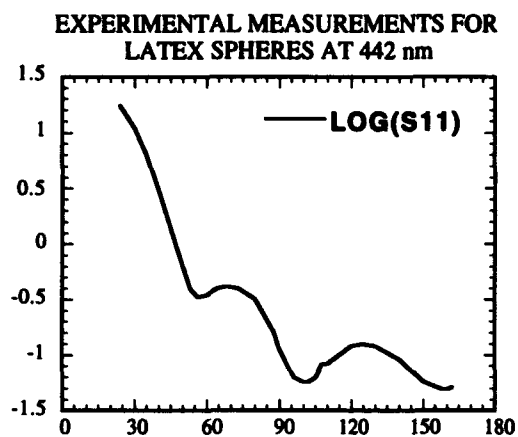


Figure 1. Comparison of the Mie calculations and the coupled-dipole approximation for spheres. The solid line represents coupled-dipole theory and dashed line represents Mie theory. Spheres with a size parameter of 4.46 are shown in column (a) and spheres with a size parameter of 8.92 are shown in column (b). In the coupled-dipole approximation, the sphere is modeled with 925 dipoles. In both calculations, the wavelength of incident light is 442 nm in air, the index of refraction of the medium (water) is 1.33, and the index of refraction of the sphere is 1.596.



(a)

(b)

Figure 2. (a) Experimental measurements of the Mueller matrix elements for latex spheres. (b) Coupled-dipole calculations of the corresponding matrix elements for spheres of equivalent size parameter. In the coupled-dipole calculation, the sphere is modeled with 925 dipoles. In both figure, the wavelength of the incident light is 442 nm in air. The index of refraction of the medium (water) is 1.33 and the index of refraction of the sphere is 1.596.

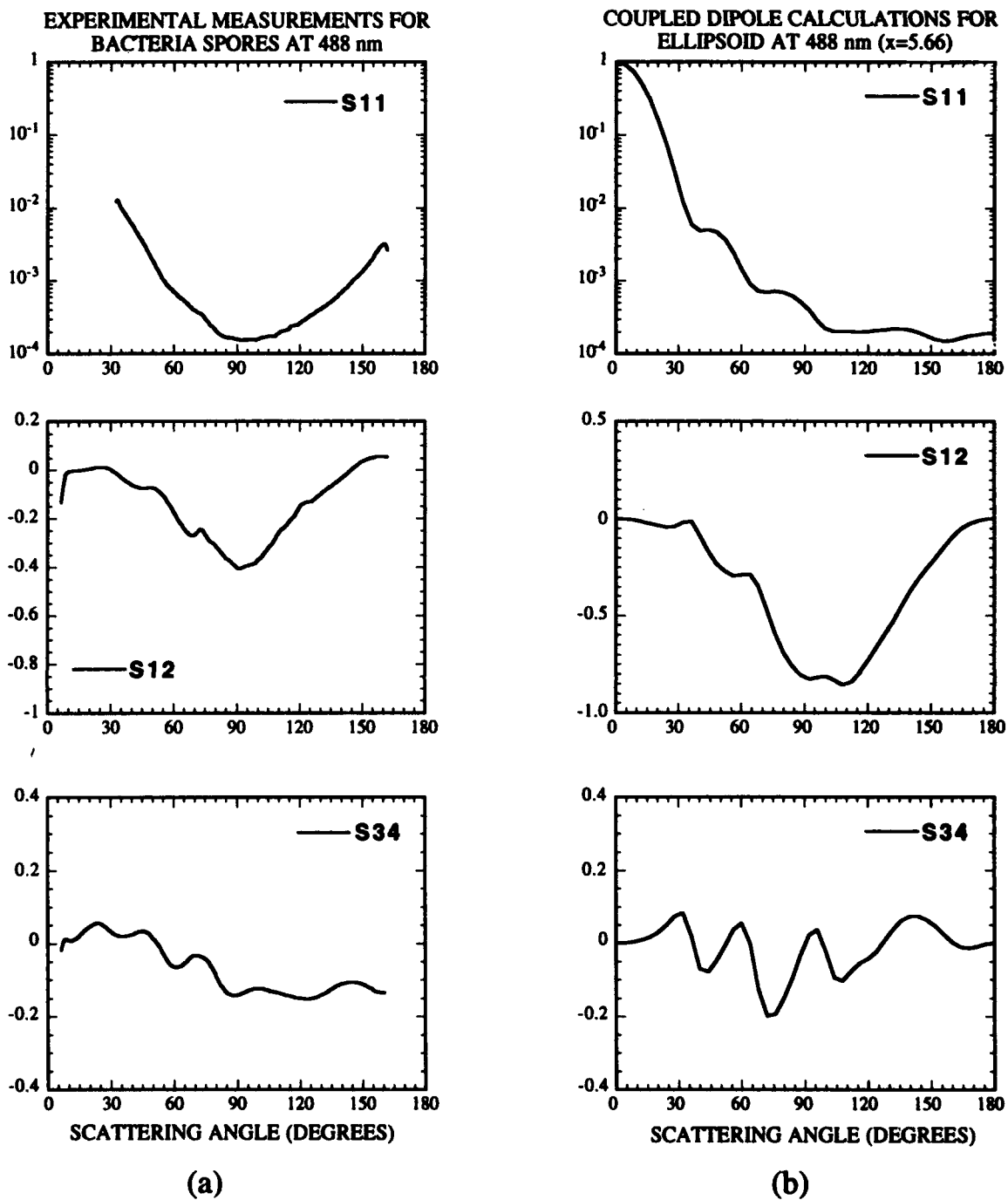
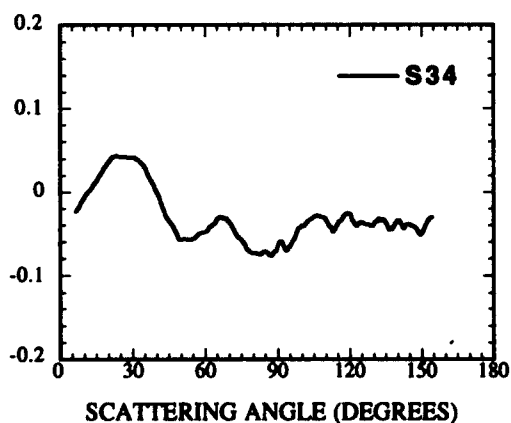
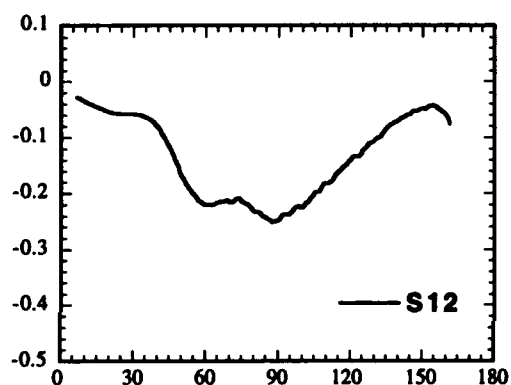
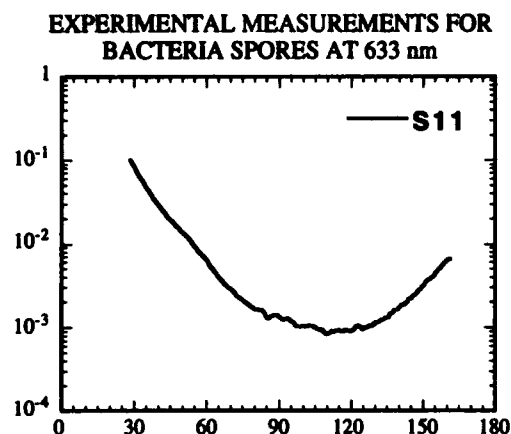
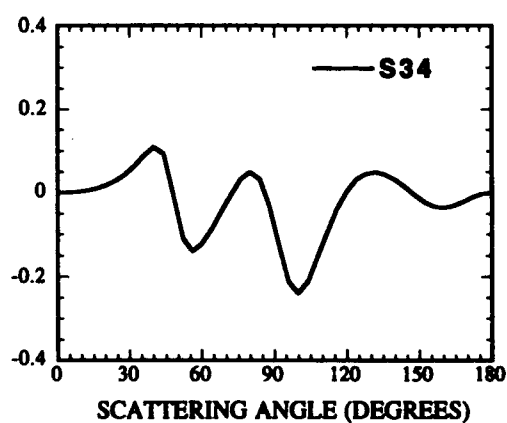
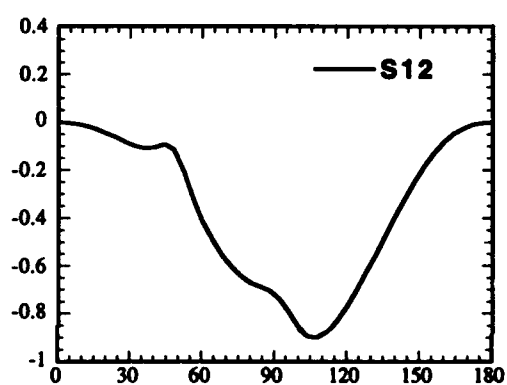
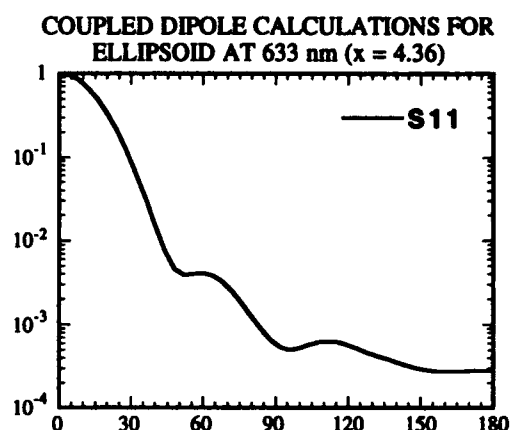


Figure 3. (a) Experimental measurements of the Mueller matrix elements for the *B. subtilis* spores. (b) Coupled-dipole calculations of the corresponding matrix elements for an ellipsoid. In the coupled-dipole calculations, the ellipsoid is modeled by 1032 dipoles and has a ratio of major to minor axis of 2.0. In both figures, the wavelength of incident light is 488 nm in air, the index of refraction of the medium (water) is 1.33 and the index of refraction of the ellipsoid is 1.48.

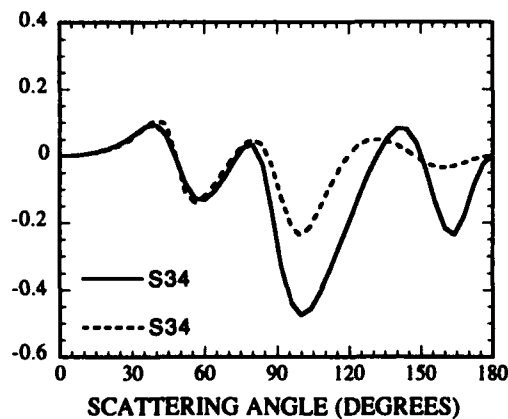
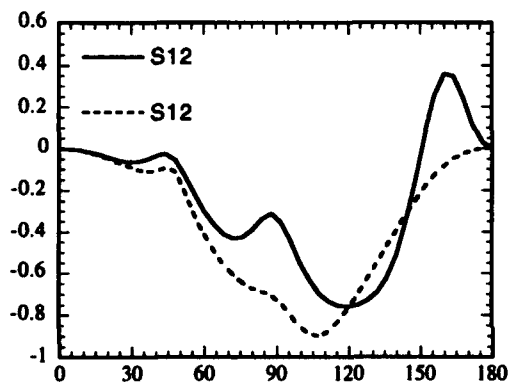
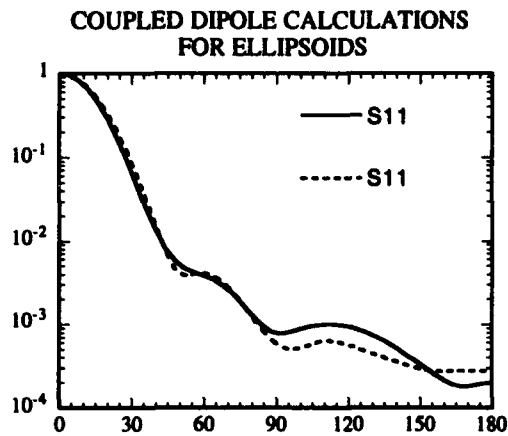


(a)

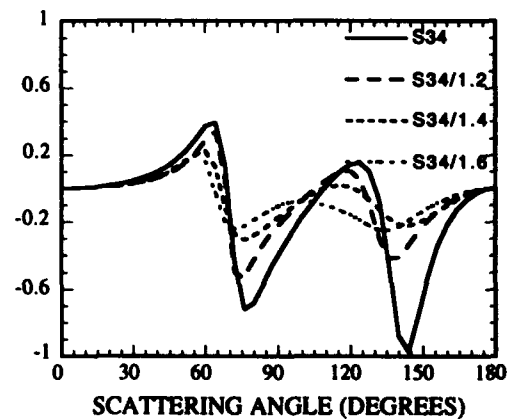
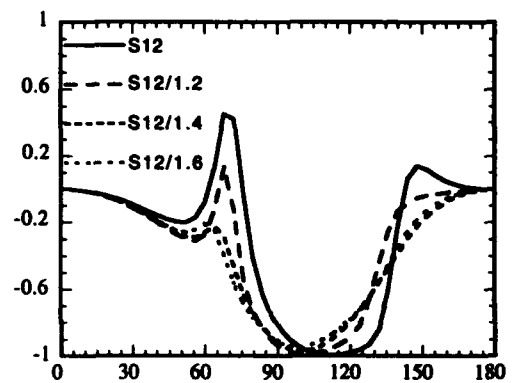
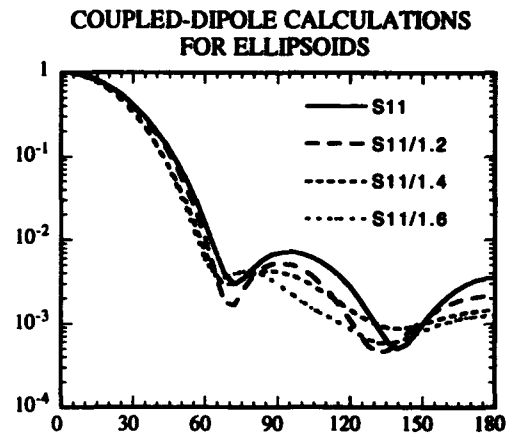


(b)

Figure 4. (a) Experimental measurements of the Mueller matrix elements for the *B. subtilis* spores. (b) Coupled-dipole calculations of the corresponding matrix elements for an ellipsoid. In the coupled-dipole calculations, the ellipsoid is modeled by 1032 dipoles and has a ratio of major to minor axis of 2.0. In both figures, the wavelength of incident light is 633 nm in air, the index of refraction of the medium (water) is 1.33 and the index of refraction of the ellipsoid is 1.48.



(a)



(b)

Figure 5. (a) Coupled-dipole calculations of the Mueller matrix elements for ellipsoids of two different values of the relative index of refraction. The solid line represents an ellipsoid with a relative index of refraction of 1.19 and the dashed line a relative index of refraction of 1.11. The size parameters are kept constant at 4.36 for both values of the relative index of refraction. (b) Mueller matrix elements for ellipsoids of varying ratios of major to minor axis. The solid line represents a sphere. Ratios of 1.2, 1.4 and 1.6 are labeled on each graph.

Assessment of sea water optical characteristics in the upper 200 m ocean by their subsurface values

Oleg V. Kopelevich and Olga V. Prokhorenko

P.P.Shirshov Institute of Oceanology, Laboratory of Ocean Optics,
Moscow, 117218 Russia

ABSTRACT

The specific goal of this work is to develop a model and algorithms of using the optical remote sensing or/and the Secchi disk depth data for an assessment of sea water optical characteristics up to 200 m taking into account the vertical stratification. Measurement data of the scattering coefficient $b(550)$ and of the volume scattering function at 1° , 6° , 45° angles at 550 nm as well of the absorption coefficient $a(390)$, $a(430)$ at 390 and 430 nm in the Atlantic, Pacific and Indian were grouped at five layers 0-10, 10-25, 25-50, 50-100, 100-200 m and were statistically analyzed. Relative standard errors of the $a(390)$, $a(430)$, $b(550)$ values being calculated for deeper layers by their values at 0-10 m layer are estimated as 12-35%. A model is also developed to estimate the values of the scattering coefficient in the upper 200 m through the Secchi disk depth; the values of the volume scattering function for different layers can be assessed by using the mean scattering phase functions calculated for clear and turbid waters. The spectral absorption coefficients in the upper 200 m can be evaluated in principle by values of the diffuse coefficient $K_D(490)$ at 0-10 m layer.

1. INTRODUCTION

Most of the available data on the optical characteristics of sea water falls in the subsurface layers. In particular, the World Ocean maps of the sea water optical characteristics constructed on the sea truth data are available only for the values of the Secchi depth¹, and of the diffuse attenuation coefficient $K_D(465)$ at the surface layer². Remote sensing observations, particularly from satellites, which especially perspective to obtain a global information about the ocean optical characteristics, are also limited by the subsurface layer. According to Gordon, McCluney³, its thickness Z_{pd} (penetration depth) is estimated to be $1/K_D$, so that doesn't exceed 20-30 m even for the clearest ocean waters. Obviously an assessment of the optical characteristics of the deeper layers by their subsurface values is very important. And not only of the optical characteristics but the biological ones. The latter is especially important for global assessment of the ocean primary production by using of the satellite data: it is necessary to relate the spectral upwelling radiances measured by satellite sensor with the primary production over the all euphotic layer. As noted above, the former is determined by the layer which thickness is $1/K_D$, whereas the latter has a thickness corresponding to the depth where the downwelling irradiance decreases to 1% value of the incident or even to 0.1%; hence this thickness is more than Z_{pd} by a factor of 4.6 or even 6.9.

In recent years some works devoted to the relation between the pigment concentrations at the subsurface and the all euphotic layer as well between the primary production and other characteristics of marine ecosystems were made⁴⁻⁶. In this work we consider the relation between only the optical characteristics. Previously Kopelevich⁷⁻⁸ examined the relation between the scattering and absorption coefficients at the 0-50 m layer and at the layers 50-100, 100-200, 200-1000 m and proposed a simple model for the calculation of these coefficients at the 50-100 and 100-200 m layers through their values at the 0-50 m layer. Here we examine the upper 0-200 m ocean in more detail and consider the models for the calculation of its optical characteristics by using various data available at the subsurface layer.

2. DATA

The statistical analysis was performed for the measurement data of the sea water scattering coefficient b and the values of the volume scattering function $\beta(1^\circ)$, $\beta(6^\circ)$, $\beta(45^\circ)$ at 550 nm as well as of the sea water absorption coefficients $a(390)$, $a(430)$. The contemporaneous data at other depths used to analyze the scattering characteristics were obtained from 38 ocean stations, and for the absorption coefficients analysis from 27 stations. The most part of the scattering data was obtained by laboratory measurements of the sea water samples by means of the spectrohydronephelometer "SGN"⁹ at the angle range $2.5^\circ - 145^\circ$ and by the small angle scattering meter "Strela"¹⁰ at the angle range $20' - 7^\circ$; the part of the scattering data was obtained by means of the submersible nephelometer "Neptun"¹¹ at the angle range $15^\circ - 165^\circ$ and the laboratory spectral

small angle scattering meter "Oreol"¹² at the angle range $15'-7^\circ$. All data on the absorption coefficients were obtained by means of the laboratory spectral absorption meter "Volna"¹⁰. A list of the expeditions, their dates, number of stations, apparatus used, the geographical regions covered, is given in Table 1.

The values of each of the characteristics for a given station were averaged over the layers 0-10, 10-25, 25-50, 50-100, 100-200 m. Total data sets both on the scattering and on the absorption characteristics were divided into two subsets: the values of b and $a(390)$ at 0-10 m layer were used as the criterion (see Table 2). For each of sets the mean values (\bar{y}_i), standard deviations (s_i), covariance (M_{ij}) and correlation (R_{ij}) matrices, their characteristic values and the eigenvectors, the regressions $y_i = B_i y_1 + A_i$ were calculated ($i = 1, 2, \dots, 5$ is the layer number). The mean values and standard deviations for the different layers for each of the sets are given in Table 2. The presented data display some features noted previously^{7, 8}. One of them is a distinction of the vertical structures of the scattering and absorption in the clear and turbid waters. For Set 1 the scattering values show a weak maximum at the 25-50 m (except $\beta(45)$ with maximum at 50-100 m), for Set 2 the ones are maximum at 0-10 m. The absorption values are maximum at 50-200 m for Set 1 and at 0-10 m for Set 2.

Table 1. Data base

Expedition	Dates	Stations	Region	Equipment
The scattering data				
DM-5*	Jan.-May 1971	4	Tropical Pacific	SGN, Strela
DM-10*	June-Oct. 1973	14	Tropical Indian	SGN, Strela
DM-14*	Feb.-May 1975	17	Southeast Pacific	SGN, Strela
DM-39*	May-July 1987	2	Philippine Sea	Neptun, Oreol
AK-49**	June-Sep. 1988	1	Northeast Atlantic	Neptun, Oreol
The absorption data				
DM-10*	June-Oct. 1973	10	Tropical Indian	Volna
DM-14*u	June-Oct. 1973	14	Tropical Indian	Volna

* - R/V "Dmitry Mendeleev" (a figure is the cruise number);

** - R/V "Akademik Kurchatov". Cruise 49.

For our purposes it is important that differences between the values of the characteristics, at least as concerns h , $\beta(1)$, $\beta(6)$ and $a(390)$ are projected into the deeper layers even if in smoothed form. The observed differences are not great, and it is hardly probable to expect a good accuracy of the estimation of the deep values by their subsurface ones but rough estimates are possible. Various versions of the calculation are discussed below.

3. REGRESSION BETWEEN THE VALUES AT 0 - 10 M AND AT THE DEEPER LAYERS

There is an usual situation in practice when the data at 0-10 m layer alone are available; for example the data of laboratory measurements of the sea water samples taken out from the surface layer during the ship route. The linear regressions were calculated

$$y_i = B_i y_1 + A_i, \quad i = 2, 3, 4, 5 \quad (1)$$

where y_i is the value of the characteristic at the i -layer; y_1 at 0-10 m layer; B_i , A_i are the regression coefficients.

Table 2. Statistical characteristics of the scattering and absorption coefficients

layer m	Set 1			Set 2			Total	
	range	mean value	standard deviation	range	mean value	standard deviation	mean value	standard deviation
b, m^{-1}								
0-10	0.060-0.154	0.112	0.023	0.170-1.21	0.415	0.362	0.192	0.225
10-25	0.069-0.160	0.111	0.024	0.172-0.96	0.377	0.295	0.181	0.190
25-50	0.066-0.220	0.117	0.031	0.169-0.74	0.290	0.184	0.163	0.122
50-100	0.065-0.172	0.111	0.027	0.054-0.28	0.162	0.058	0.124	0.044
100-200	0.042-0.134	0.082	0.023	0.054-0.145	0.108	0.034	0.089	0.028
$\beta(1^\circ), m^{-1} sr^{-1}$								
0-10	4.5-17.9	10.1	3.24	16.0-95.5	37.6	30.7	17.3	19.6
10-25	5-2-17.8	9.9	3.44	17.2-88.2	34.7	26.6	16.4	17.4
50-100	5.1-19.8	10.3	4.04	16.6-78.1	27.2	19.5	14.7	12.7
50-100	4.5-21.5	10.0	3.73	3.5-30.8	15.2	7.0	11.4	5.2
100-200	3.1-17.5	7.8	3.12	3.5-16.8	10.3	4.0	8.5	3.5
$\beta(6^\circ), m^{-1} sr^{-1}$								
0-10	0.18-0.58	0.344	0.098	0.48-5.7	1.59	1.65	0.672	0.988
10-25	0.16-0.59	0.344	0.097	0.49-4.6	1.43	1.33	0.630	0.820
25-50	0.20-0.78	0.362	0.125	0.52-2.5	1.04	0.70	0.542	0.471
50-100	0.20-0.57	0.339	0.099	0.16-0.95	0.55	0.22	0.395	0.166
100-200	0.11-0.52	0.221	0.089	0.13-0.54	0.34	0.15	0.251	0.120
$10^3 \beta(45^\circ), m^{-1} sr^{-1}$								
0-10	1.6-6.0	2.6	1.02	2.0-19.6	6.4	5.66	3.6	3.37
10-25	1.1-3.9	2.4	0.67	2.1-18.7	5.5	5.16	3.2	2.94
25-50	1.2-5.2	2.6	0.91	2.2-17.4	4.7	4.57	3.2	2.55
50-100	1.5-6.1	2.7	1.02	1.9-8.2	3.3	2.14	2.8	1.39
100-200	1.2-7.0	2.2	1.12	1.0-8.0	2.4	2.02	2.2	1.39
$a(390), m^{-1}$								
0-10	0.028-0.070	0.049	0.013	0.071-0.175	0.097	0.035	0.063	0.031
10-25	0.028-0.082	0.049	0.013	0.043-0.143	0.089	0.033	0.061	0.028
25-50	0.028-0.085	0.051	0.015	0.034-0.149	0.089	0.038	0.062	0.029
50-100	0.040-0.107	0.062	0.018	0.042-0.135	0.084	0.033	0.068	0.025
100-200	0.033-0.115	0.066	0.024	0.043-0.165	0.082	0.038	0.071	0.029
$a(430), m^{-1}$								
0-10	0.020-0.064	0.040	0.012	0.045-0.083	0.055	0.014	0.044	0.014
10-25	0.027-0.062	0.041	0.011	0.041-0.082	0.052	0.017	0.044	0.014
25-50	0.020-0.064	0.042	0.011	0.022-0.071	0.050	0.018	0.045	0.014
50-100	0.033-0.071	0.047	0.010	0.029-0.073	0.047	0.018	0.047	0.013
100-200	0.023-0.073	0.045	0.014	0.025-0.087	0.046	0.019	0.045	0.015

These coefficients with the squares of correlation coefficients and the regression errors calculated for the total sets are given in Table 3.

Table 3. Regression coefficients B_i , A_i ; correlation coefficient squares r^2_i ; regression errors S_i^2

layer	B_i	A_i	r^2_i	S_i^2	B_i	A_i	r^2_i	S_i^2
	b, m^{-1}				$\beta(1^\circ), m^{-1} sr^{-1}$			
2	0.836	0.020	0.986	0.022	0.879	1.22	0.986	2.05
3	0.480	0.071	0.779	0.058	0.593	4.46	0.845	5.00
4	0.109	0.103	0.318	0.036	0.166	8.48	0.390	4.08
5	0.068	0.076	0.294	0.023	0.086	6.98	0.233	3.06
	$\beta(6^\circ), m^{-1} sr^{-1}$				$\beta(45^\circ) 10^3, m^{-1} sr^{-1}$			
2	0.824	0.077	0.986	0.095	0.834	0.25	0.917	0.85
3	0.422	0.258	0.783	0.219	0.674	0.75	0.790	1.18
4	0.086	0.337	0.254	0.145	0.194	2.14	0.221	1.24
5	0.063	0.209	0.272	0.101	0.072	1.98	0.030	1.36
	$a(390), m^{-1}$				$a(430), m^{-1}$			
2	0.813	0.010	0.832	0.011	0.861	0.006	0.762	0.007
3	0.637	0.022	0.447	0.022	0.557	0.020	0.326	0.011
4	0.582	0.032	0.503	0.018	0.416	0.028	0.213	0.011
5	0.610	0.032	0.431	0.022	0.377	0.029	0.115	0.015

The square of correlation coefficient is equal to a part of the total dispersion accounted by the regression; the regression error is equal to $s_y \sqrt{1 - r^2}$, where s_y is a standard deviation of y , given in Table 2. As seen, the regressions allow to appreciably decrease uncertainties of the estimation for all the scattering characteristics at the 10-25 and 25-50 layers, and for the absorption coefficients at 10-25 m layer. They give practically no result for $\beta(45)$ and $a(430)$ at 100-200 m; in other cases the uncertainties are decreased by 10-30%.

The question can arise as to how the regressions derived from the total sets allow to approximate, even if with moderate accuracy, the vertical structures different for clear and turbid waters (subsets 1 and 2). To understand that, look at the coefficients B_i and A_i in Table 3 and compare their depth changes with the mean values changes in Table 2. As seen, B_i change similar to of the mean values for the sets 2, whereas A_i to the ones for the sets 1. Thus if the values y_i are small and an influence of A_i is key, the depth change of the values y_i will be similar to of the sets 1; if the values y_i are not small and an influence of B_i is essential, the depth change of y_i will be similar to of the sets 2. Figure 1 shows a comparison of the calculated by the regression (1) and measured values of the scattering coefficient b for the different layers. Figure 2 the same for the absorption coefficient $a(390)$. In Table 4 there are given the calculated by the regression (1) and measured values of all coefficients for two extreme cases corresponding to the lowest and the highest values of b and $a(390)$ at 0-10 m. Figures 1, 2 and Table 4 demonstrate an accuracy of the regression calculation, and allow to decide for each specific case if it is reasonable for the purpose in view or not. At least it is seen from Table 4, the calculated values display the distinctions between the clearest and most turbid waters at the deeper layers even if with moderate accuracy.

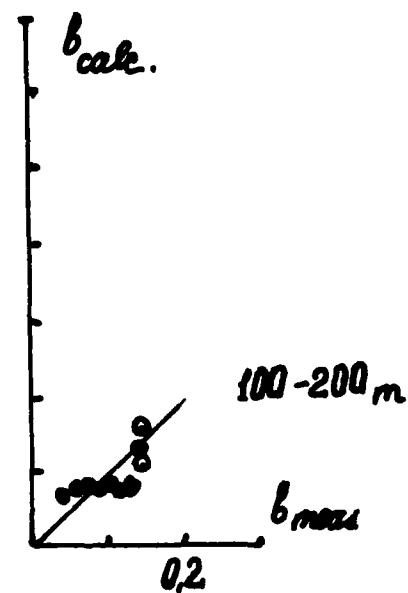
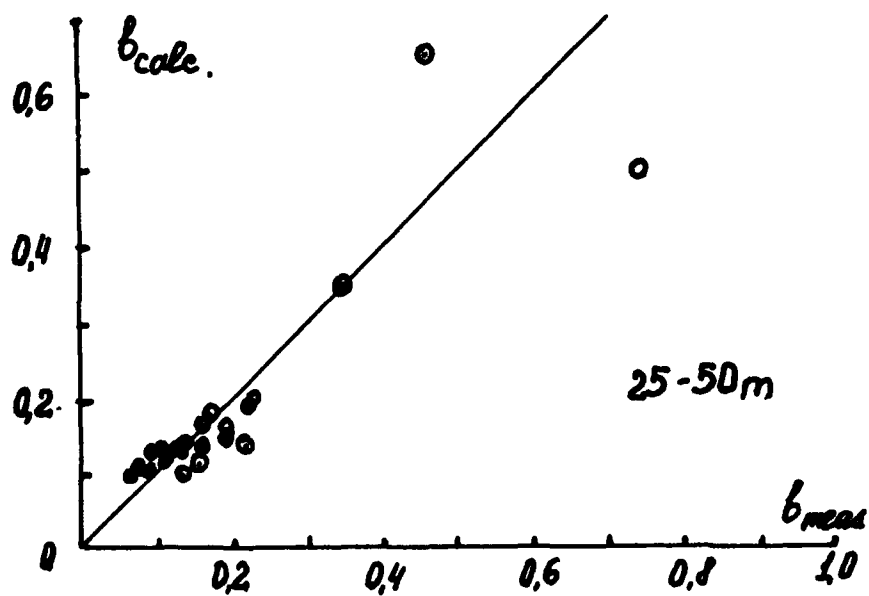
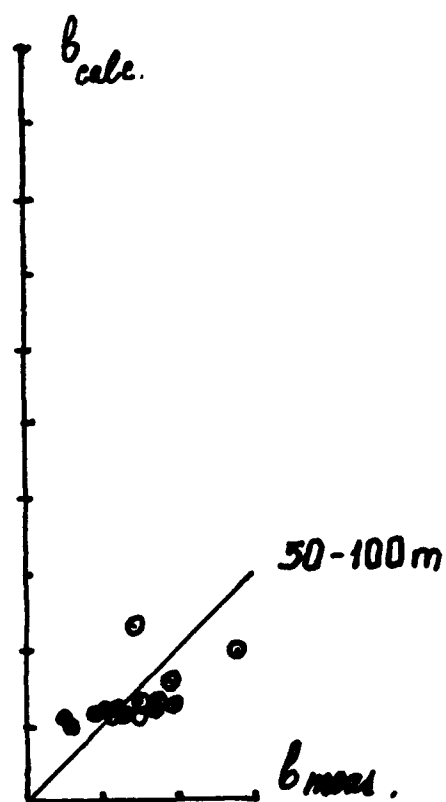
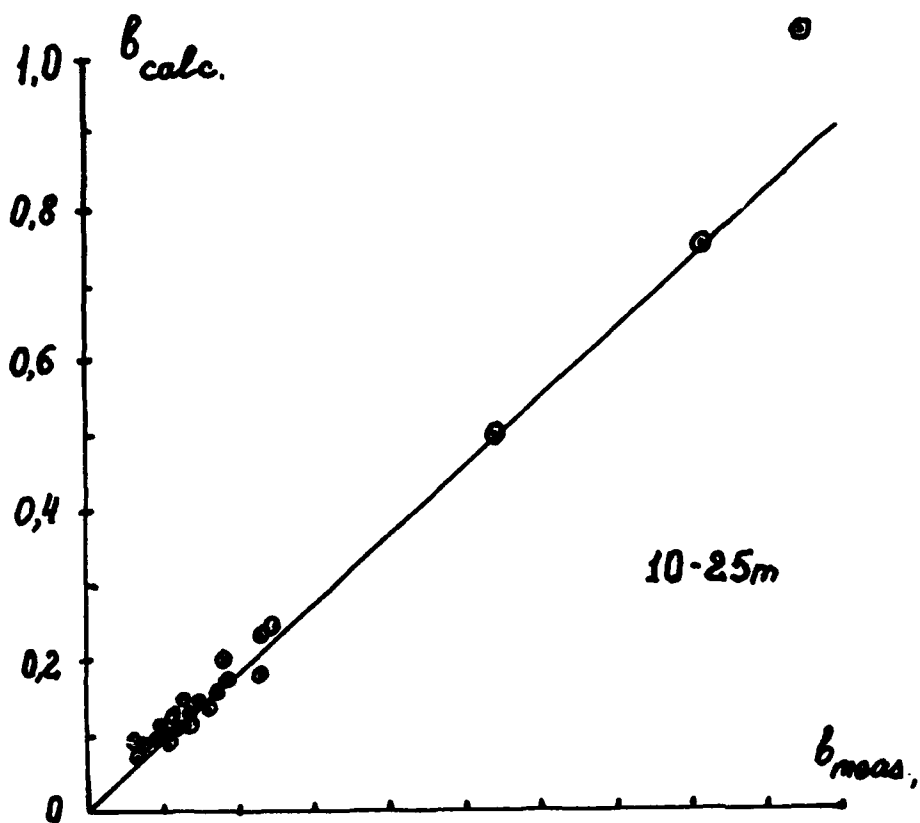


Fig.1 Comparison of the calculated (b_{calc}) and measured (b_{meas}) values of the scattering coefficient at the different layers.

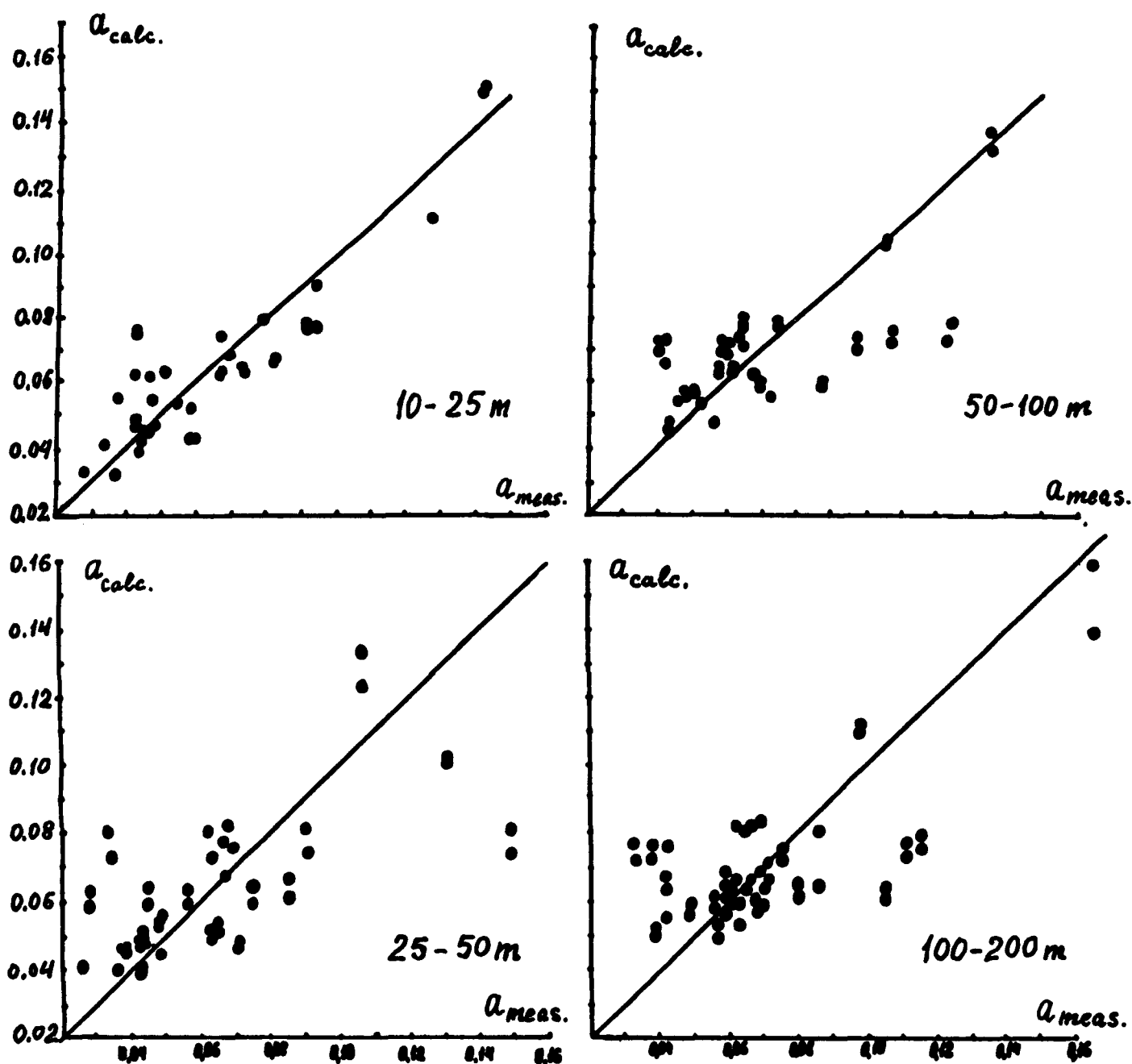


Fig.2 Comparison of the calculated ($a_{calc.}$) and measured ($a_{meas.}$) values of the absorption coefficient at 390nm at the different layers.

4. CALCULATION THROUGH VALUES OF THE SECCHI DEPTH AND OF THE DIFFUSE ATTENUATION COEFFICIENT

The values of the scattering coefficient b_i can be evaluated in principle through the Secchi depth D . The regression between the Secchi depth and the scattering coefficient b at 520-550 nm was calculated previously¹³

$$\ln b = 2.23 - 1.13 \ln D, \quad (2)$$

where b is the averaged over the layer D value of the scattering coefficient. The value of b found by means of (2) can be used then for the calculation of the values b_i ; the expansion by the eigenvectors of the covariance matrix $M_y = M[b, b]$ with the first term only is worth to apply

$$b_i = \bar{b}_i + e \Psi_i, \quad i=1,2,\dots,5 \quad (3)$$

where \bar{b}_i is the mean values b_i (see Table 2), Ψ_i is the first eigenvector value for the i -layer (Table 5)

Table 4. Calculated and measured values of the coefficients for the extreme cases

layer, m	lowest values		highest values					
	b, m^{-1}		$\beta(1^\circ), m^{-1} sr^{-1}$		b, m^{-1}		$\beta(1^\circ), m^{-1} sr^{-1}$	
	meas.	calc.	meas.	calc.	meas.	calc.	meas.	calc.
0-10	0.060	0.060	4.5	4.5	1.21	1.21	80	80
10-25	0.069	0.070	5.2	5.2	0.96	1.03	66	72
25-50	0.066	0.099	5.4	7.1	0.46	0.65	34	52
50-100	0.065	0.110	4.5	9.2	0.15	0.24	13	22
100-200	0.042	0.080	3.1	7.4	0.14	0.16	12	14

	$\beta(6^\circ), m^{-1} sr^{-1}$		$\beta(45^\circ), m^{-1} sr^{-1}$		$\beta(6^\circ), m^{-1} sr^{-1}$		$\beta(45^\circ), m^{-1} sr^{-1}$	
	meas.	calc.	meas.	calc.	meas.	calc.	meas.	calc.
0-10	0.19	0.19	0.0023	0.0023	5.7	5.7	0.013	0.013
10-25	0.22	0.23	0.0026	0.0022	4.6	4.8	0.0094	0.0111
25-50	0.20	0.34	0.0023	0.0023	2.0	2.7	0.0053	0.0095
50-100	0.20	0.35	0.0025	0.0026	0.52	0.82	0.0030	0.0047
100-200	0.13	0.22	0.0017	0.0022	0.46	0.57	0.0025	0.0029

	$a(390), m^{-1}$		$a(430), m^{-1}$		$a(390), m^{-1}$		$a(430), m^{-1}$	
	meas.	calc.	meas.	calc.	meas.	calc.	meas.	calc.
0-10	0.028	0.028	0.020	0.020	0.175	0.175	0.083	0.083
10-20	0.037	0.033	0.024	0.023	0.143	0.152	0.082	0.078
25-50	0.043	0.040	0.029	0.031	0.107	0.133	0.062	0.066
50-100	0.043	0.048	0.031	0.037	0.135	0.133	0.073	0.063
100-200	0.039	0.049	0.029	0.036	0.165	0.139	0.087	0.060

Table 5. The first eigenvector values for the different sets

i	layer, m	Set 1	Set 2	Total
1	0-10	0.388	0.727	0.708
2	10-25	0.468	0.597	0.600
3	25-50	0.633	0.330	0.359
4	50-100	0.452	0.060	0.087
5	100-200	0.160	0.043	0.050

The first characteristic value contributes 66.6% of the total dispersion for Set 1, 95.1% for Set 2, 95.7% for the Total. It is seen from Table 5, the depth changes are similar for Set 2 and for the Total: the values of Ψ_i decrease with the depth, and especially sharply the 3 - to - 4 layers; for Set 1 there is the maximum of Ψ at 25-50 m.

These distinctions do not exclude a possibility of using \bar{b}_i , Ψ_i of the Total Set for Set 1. The latter comprises samples with no high values of b_i , so for the most of them the values of the coefficient $e = (b_i - \bar{b}_i) / \Psi_i$ are negative; and the values of $b_i = \bar{b}_i + e \Psi_i$ are differences of two monotonically decreasing functions \bar{b}_i and Ψ_i that can result in a curve with maximum typical of Set 1. The efficiency of (2) was tested by means of finding the coefficients e from (2), and followed by calculation of the values b for each of the samples. The coefficient e was found as the averaged over one or two or three layers depending on the value of D . Table 6 presents the results of the testing.

Table 6. Standard errors of the calculation of b_i by means of (2) with \bar{b}_i , Ψ_i of the Total Set

i	layer, m	Set 1	Set 2	Total
1	0-10	0.021	0.011	0.012
2	10-25	0.010	0.037	0.018
3	25-50	0.014	0.104	0.051
4	50-100	0.024	0.054	0.032
5	100-200	0.022	0.026	0.023

As seen, the errors for the Total Set are even smaller than the ones in Table 3; it is attributable to the fact that the coefficients e in equation (2) were found with using not only b_1 but also b_2 and even b_3 for clear waters.

In order for the volume scattering function $\beta(\theta)$ to be found from b it is necessary to know the scattering phase function $P(\theta) = \beta(\theta)/b$. Our estimation showed it is possible to adopt two scattering functions $P_1(\theta)$ and $P_2(\theta)$; the former for all layers in the case of clear waters (Set 1) and for the layers 50-100 and 100-200 m for turbid (Set 2); the latter at the 0-50 m for turbid waters. These functions were computed on the available measurement data ($N_1=160$, $N_2=30$) and are given with their standard deviations in Table 7.

Table 7. The mean scattering functions $P_1(\theta)$, $P_2(\theta)$ and their standard deviations S_{P_1} and S_{P_2}

θ , degree	0.5	1	2	4	6	10	15	45	90	135
$P_1(\theta)$	245	88	32	8.4	3.0	0.92	0.40	0.023	0.0051	0.0054
S_{P_1}	93	21	5.0	1.4	0.65	0.26	0.10	0.009	0.0022	0.0022
$P_2(\theta)$	238	90	35	10.4	3.5	0.98	0.38	0.015	0.0025	0.0023
S_{P_2}	57	14	2.9	1.2	0.58	0.20	0.16	0.004	0.0008	0.0008

The function $P_1(\theta)$ is typical for the ocean waters with low bioproductivity, $P_2(\theta)$ for medium and high bioproductivity¹⁴; the values of the averaged cosine and of the asymmetry factor b_f/b_b (b_f and b_b are the forward and backscattering coefficients) are equal 0.908 and 29.8 correspondingly for $P_1(\theta)$, 0.950 and 69.7 for $P_2(\theta)$.

The results of comparison of the calculated and measured volume scattering functions at the 10-25, 25-50 and 50-100, 100-200 m layers for two extreme cases corresponding the lowest and highest scattering at 0-10 m layer are shown in Figures 3a and 3b. As seen, these results are in agreement with the findings above (See Tables 3, 4, 6, 7).

The diffuse attenuation coefficient $K_D(\lambda)$ can be used to assess the spectral absorption coefficient $a(\lambda)$, with an accuracy no worse than 20%¹⁵; the absorption coefficients of the deeper layers can be assessed then by using of the regression (1) between a_i and a_1 . That allows in principle to assess the values of the absorption coefficients in the upper 200 m ocean on the satellite data of the CZCS (Coastal Zone Color Scanner) and of the forthcoming SeaWiFS (Sea-viewing Wide Field-of-view Sensor), which include the diffuse attenuation coefficient $K_D(490)$ as a standard product. The scheme of the calculation can be as follows:

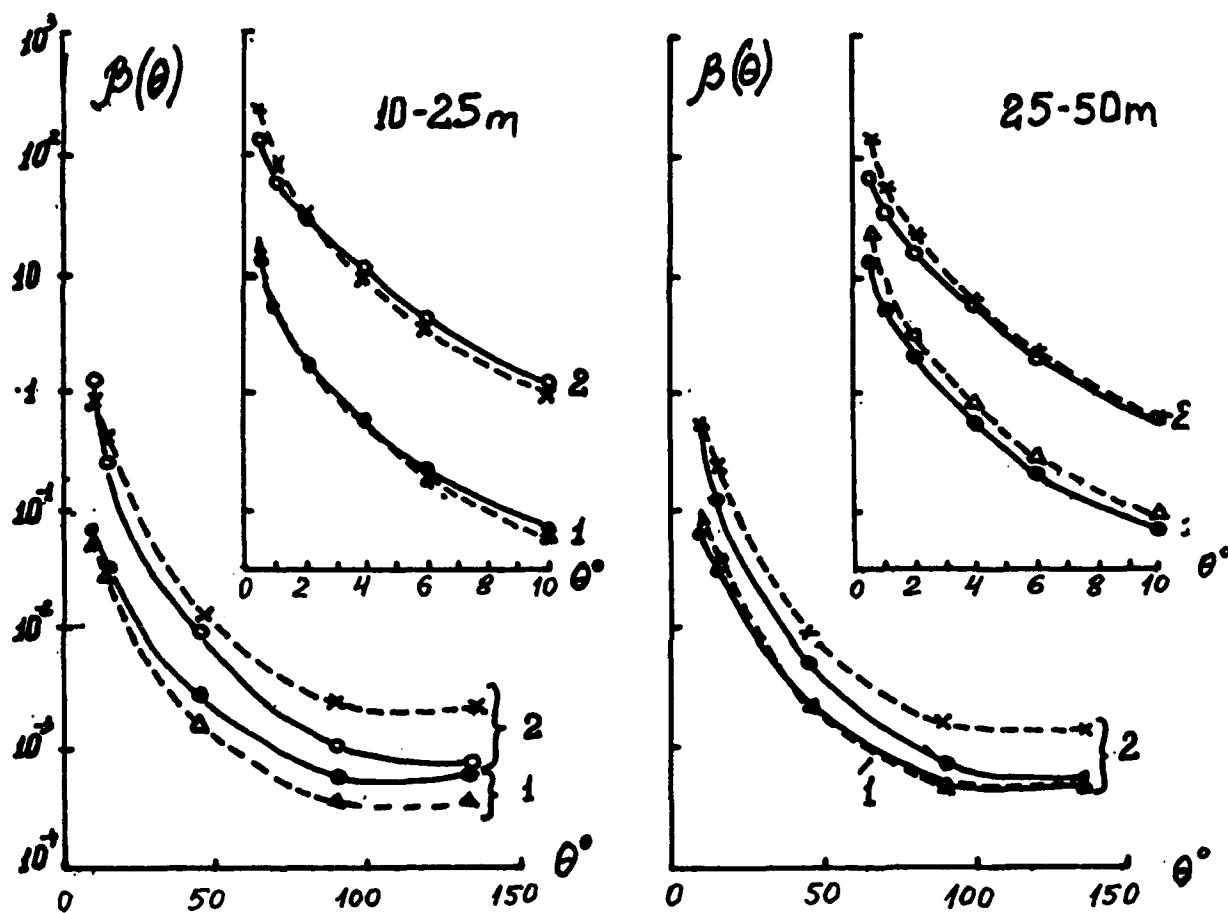


Fig.3a Comparison of the calculated(solid curves) and measured(dashed curves) volume scattering functions $\beta(\theta)$ at the 10-25 and 25-50m layers.

- 1 - Philippine Sea - the lowest scattering;
- 2 - Peruvian Shelf - the highest scattering.

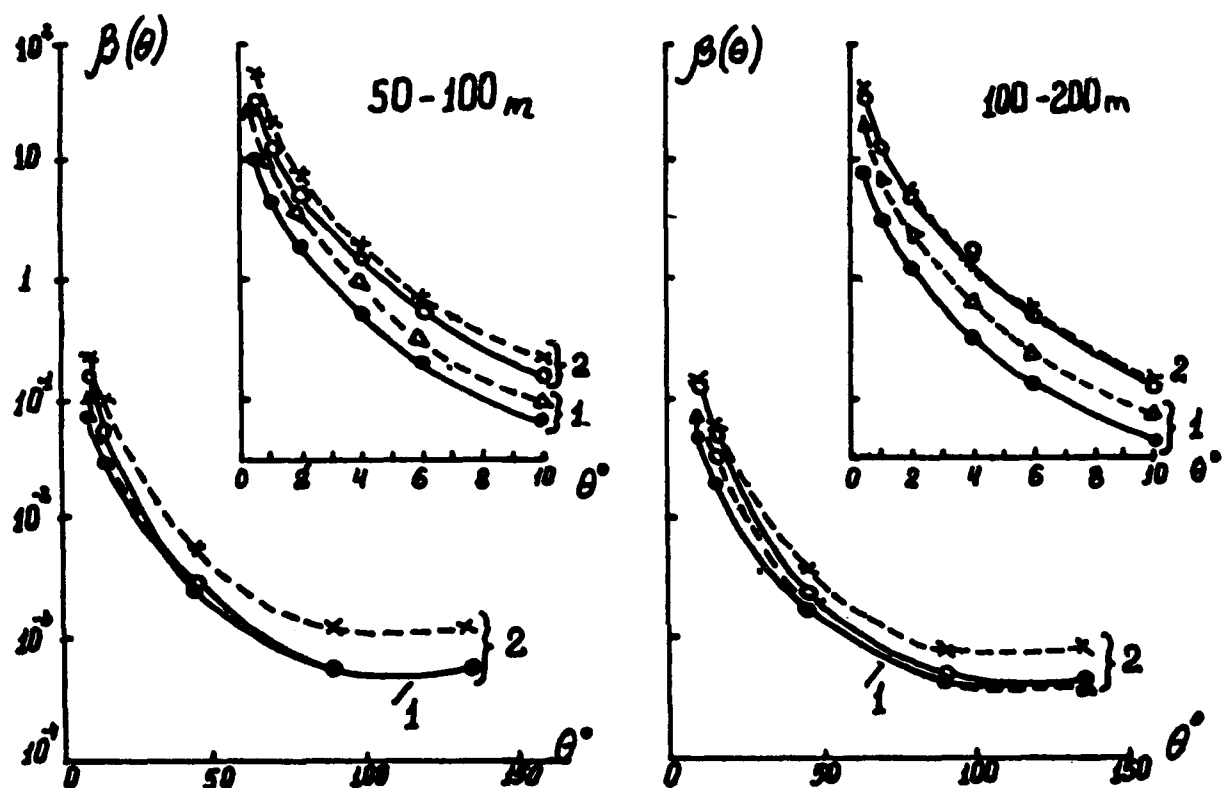


Fig.3b Comparison of the calculated (solid curves) and measured (dashed curves) volume scattering functions $\beta(\theta)$ at the 50-100 and 100-200m layers.
 1 - Philippine Sea - the lowest scattering,
 2 - Peruvian Shelf - the highest scattering.

1. the spectral values of $K_D(\lambda)$ are computed from $K_D(490)$ by using the spectral models AP or VS¹⁵;
2. the spectral values of $a(\lambda)$ are calculated from $K_D(\lambda)$ by means of a simple formula $a = 0.8 K_D$ ¹⁵;
3. if the penetration depth z_{pd} is less than 10-15 m, it is acceptable to use the regression (1) for assessment $a_i(390)$, $a_i(430)$ through the values of $a_i(390)$, $a_i(430)$; if z_{pd} is more than 15-20 m it is worth to use an approach similar to described above in relation to the calculation through the Secchi disk depth;
4. the spectral values of $a(\lambda)$ can be assessed through $a(390)$, $a(430)$ by means of the spectral model.

It is possible to use other schemes of the calculation. Among them the estimation of the K_D values at the deeper layer through the subsurface value just as Sud'bin, Volynsky estimated¹⁶, followed by the calculation of $a(\lambda)$ through K_D ¹⁵. Of course a practical development of the calculation algorithm and an assessment of its accuracy calls for special investigation.

5. REFERENCES

1. V.I.Voitov, "Relative Transparency", *Optica okeana*, ed. A.S.Monin, Vol. 2, pp. 21-26, Nauka, Moscow, 1983.
2. J.-Y.Simonot and H.Treut, "A climatological Field of mean optical properties of the World ocean", *J. Geophys. Res.*, Vol. c91, No. 5, pp. 6642-6646, 1986.
3. H.R. Gordon and W.R.McCluney, "Estimation of the depth of simlight penetration in the sea for remote sensing", *Appl. Opt.*, Vol. 14, No 2, pp. 413-416, 1975.
4. A. Morel and J.-F.Berthon, "Surface pigments, algal biomass profiles, and potential production of the euphotic layer: Relationships reinvestigated in vlew of remote-sensing applications", *Limn. Oceanogr.*, Vol. 34, No.8, pp. 1545-1562, 1989.
5. W. Balch, R.Evans, J.Brown, G.Feldman, Ch. McClain, W.Esaia, "The remote Sensing of Ocean Primary Productivity: Use of a New Data Complication to Test Satellite Algorithms. - *J. Geophys. Res.*, Vol. 97, No. C2, pp. 2279-2293, 1992.
6. M.E.Vinogradov, E.A.Shushkina, V.I.Vedernikov, V.N.Pelevin, "The ecological role of organic carbon flux in the waters of different productivity in the North Atlantic", *Russian Journal of Aquatic Ecology*, Vol.1, No.2, pp. 89-101, 1992.
7. O.V.Kopelevich "On the connection between the optical properties of surface and deep waters", *Okeanologia*, Vol.25, No.1, pp. 55-60, 1985.
8. O.V.Kopelevich, "Optical properties of ocean water", *Light Scattering and Absorption in natural and artificial dispersive media*, ed. A.P.Ivanov, pp. 289-309, Inst. Phys. Belorussian Acad. Sci., Minsk, 1991.
9. M.V.Kozlyaninov, "The manual on hydrooptical measurements in the sea", *Tr. Inst. Okeanol., Acad. Nauk S.S.S.R.*, Vol.47, pp. 37-79, 1961.
10. O.V.Kopelevich., Y.L.Mashtakov, S.Y.Rusanov, "Apparatus and methods of the measurements of the sea water optical properties", *Gydfropt. e Gydroopt. Issled. v Atlant. e Tykhom Okeanakh*, ed. A.S.Monin, K.S.Shifrin, pp. 97-107, Nauka, Moscow, 1974.
11. V.V.Rodionov, O.V.Kopelevich, Y.L.Mashtakov, "The submersible polarizational nephelometer "Neptun-M", *Optica morya e atmosfery*, ed. K.S.Shifrin, pp. 203-204, GOI, Leningrad, 1988.
12. O.V.Kopelevich, Y.L.Mashtakov, V.V.Rodionov, V.V.Volynsky, A.F.Kunin, M.Y.Puchkov, "Spectral measurements of the small angle scattering of sea water", *Teor. e Prikl. voprosy svetotekhniki r fotometry*, MEI, Moscow, 1986.
13. O.V.Kopelevich and V.E.Shemsura, "On the possibility of the evaluation of the scattering and absorption coefficients from the Secchi disk depth", *Okeanologia*, Vol. 28, No. 5, pp. 736-741, 1988.
14. O.V.Kopelevich, "On the distribution of the scattering function in the ocean waters", *Optica morya e atmosfery*, ed. F.Syd'ko, Vol. 1, pp. 110-111, Inst. Phys. 50 Acad. Sei. USSR, Krasnoyarsk, 1990.
15. O.V.Kopelevich, Y.V.Filippov, "Comparison between different spectral models of the diffuse attenuation and absorbtion coefficients of sea water", *Ocean Optics XII, Proceedings of SPIE*, 1994.
16. A.Sud'bin, V.Volynsky, "Vertical attenuation coefficient investigation in upper and deep layers", *SPIE Vol. 2048 Underwater Light Measurements (1993)*, pp. 73-79.

Statistical analysis of vertical profiles of beam attenuation coefficient and temperature in the North Atlantic

Vladimir I. Burenkov

P.P. Shirshov Institute of Oceanology
Moscow, 117218 Russia

ABSTRACT

Statistical analysis was applied for study of vertical profiles of beam attenuation coefficient $C(z)$ and temperature $T(z)$ measured in the North Atlantic in September 1988. Total set of data consisted of 60 profiles. Following statistical parameters were calculated: correlation and covariance matrices, eigenvalues and eigenvectors, factor loading. Correlation matrix for profiles of beam attenuation coefficient differs from temperature one. The later characterizes by high correlation at all depths (10-130 m). For profiles of beam attenuation coefficient correlation is high only at vertical separation less than 30-40 m. Eigenvector representation of observed profiles was carried out. Cumulative per cent of total variance explained by first few eigenvectors and corresponding standard errors of eigenvector representation of observed profiles were calculated. The first factor loading for beam attenuation coefficient is maximum at depths less than 30 m ($r=0.98$). The second factor loading is maximum at depth 50 m ($r=0.9$) where in many cases nepheloid layer is observed. Study of statistical connection between temperature and beam attenuation coefficient vertical profiles shows that correlation between the first principal components C and T is sufficiently high ($r=-0.89$). For the other principal components C and T correlation is close to zero.

1. INTRODUCTION

Representation of different variables by empirical orthogonal functions is widely used in meteorology and oceanography. Also this method has been applied for studies in different fields of hydrooptics¹⁻⁴. But it was not widely used for study of vertical profiles of sea water optical properties and was applied only for small areas of the ocean with approximately the same vertical structure^{5,6}.

In this paper empirical orthogonal expansion is applied for statistical analysis of vertical profiles of beam attenuation coefficient $C(z)$ and temperature $T(z)$ measured in spacious area of the North Atlantic. Main questions considered below are: what number of eigenvectors is needed for representation of observed profiles with desired accuracy? How much eigenvectors is needed for prediction of qualitative structure of profiles $C(z)$? How factor loadings change with depth? What is the statistical connection between beam attenuation coefficient and temperature?

2. EXPERIMENTAL DATA

Vertical profiles of beam attenuation coefficient $C(z)$ and temperature $T(z)$ were measured in September 1988 in the North Atlantic from 30° to 60° N. Measurements were carried out by transmissometer at the depth range 0-200 m. Accuracy of determination of beam attenuation coefficient is 0.02 m^{-1} , resolution - 0.003 m^{-1} . Measurements are carried out at wavelength 530 nm, half-width of the spectral range is 15 nm. Accuracy of depth and temperature sensors are 2 m and 0.1° respectively. Data set was mainly obtained at sections along 18° and 36° W and consisted of 60 profiles. Measurements were carried out in different climatic zones (from subtropic to subpolar) with various vertical structure of beam attenuation coefficient. Typical vertical profiles $C(z)$ are shown in Fig.1. In the northern part of the studied area near surface turbid layer was observed (curve 1).

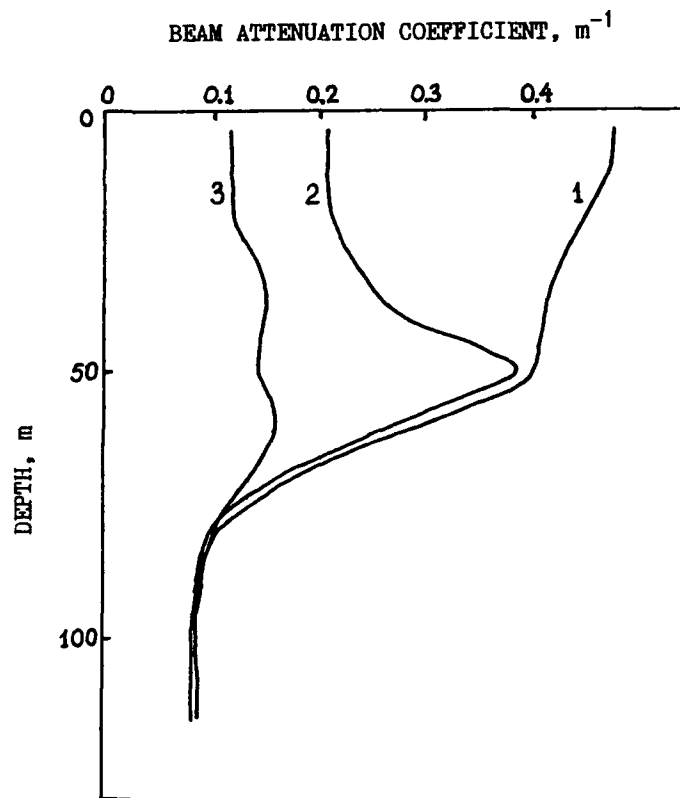


Fig.1. Typical vertical profiles of beam attenuation coefficient.

In the southern part and in the frontal zone between 40° and 50° N there was subsurface nepheloid layer (curves 2 and 3), which was of greater intensity in the frontal zone. Some profiles had more

complex structure.

Variations of near surface values of beam attenuation coefficient and temperature in the studied area were very great. Surface value of C increased from southern to northern regions from 0.1 to 0.72 m^{-1} and surface temperature decreased from 25° to 10° .

3. STATISTICAL ANALYSIS

The following set of statistical parameters were calculated: mean profiles $\bar{C}(z)$ and $\bar{T}(z)$, covariance and correlation matrices, eigenvalues and eigenvectors, factor loadings. Calculations were carried out in the depth range 10 – 130 m with step 10 m . This depth range was chosen because values of beam attenuation coefficient at smaller and greater depths were nearly the same as for $z=10 \text{ m}$ and $z=130 \text{ m}$ respectively.

Mean vertical profile $\bar{C}(z)$ and profile of normalized standard deviation $K(z) = \sigma_C(z)/\bar{C}(z)$ are shown in Fig.2. It can be seen in Fig.2 that $\bar{C}(z)$ and $K(z)$ decrease with depth. Value of standard deviation in surface layers is approximately 20 times greater than at depths $z > 100 \text{ m}$. This means that variations of beam attenuation

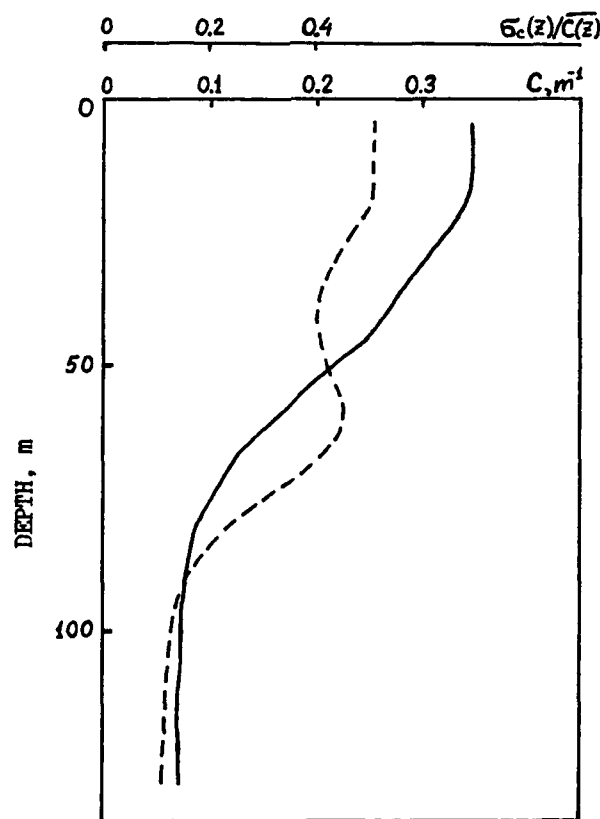


Fig.2. Mean vertical profile of beam attenuation coefficient (solid line) and vertical distribution of normalized standard deviation (dashed line).

coefficient are mainly concentrated in surface biologically productive layers.

Correlation matrix $r(C(z_i), C(z_j))$ is shown in Fig.3a. In surface layers and at depths $z > 100$ m high correlation between values of beam attenuation coefficient takes place at the depth range $\Delta z = z_i - z_j$ about 30-40 m. At intermediate depths 50-90 m depth range of high correlation is approximately two times less. This fact is explained by high variations in structure of vertical profiles $C(z)$ at this depths. It must be pointed out that correlation matrix for beam attenuation coefficient differs strongly from temperature one (Fig.3b). The later is characterized by high correlation at all depths.

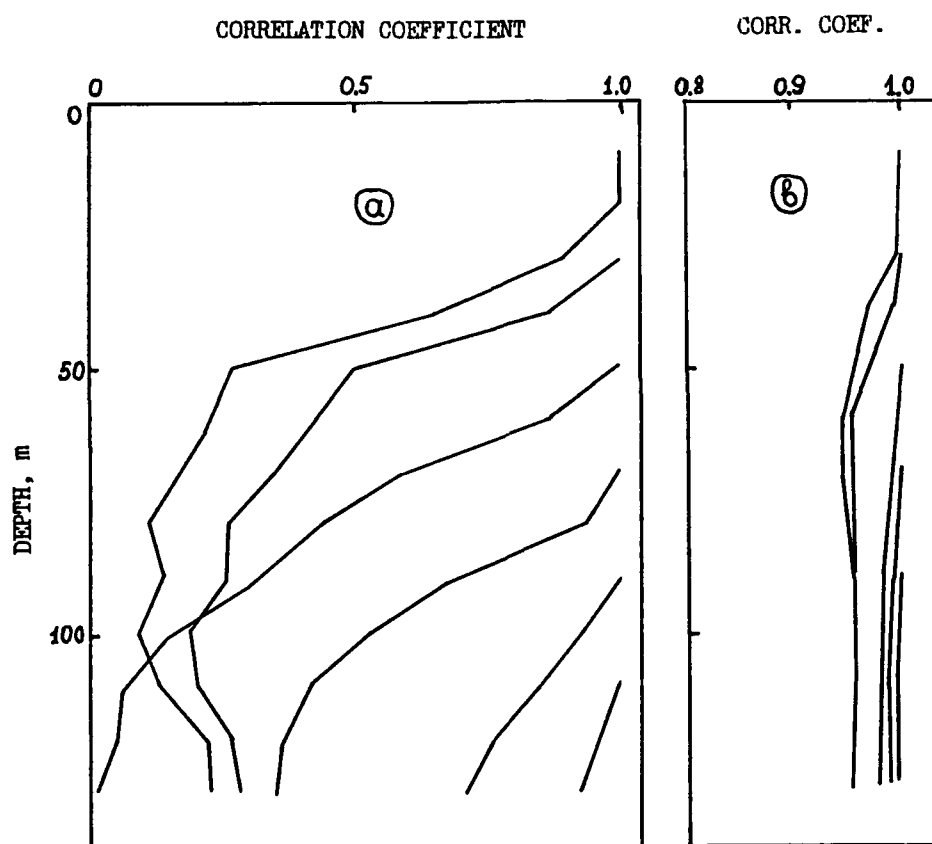


Fig.3. Correlation matrices of vertical profiles of beam attenuation coefficient (a) and temperature (b).

Following well known expansion has been used for representation of observed profiles $C(z)$ and $T(z)$:

$$C(z_j) = \overline{C(z_j)} + \sum_l H_l^C \Phi_l^C(z_j), \quad (1)$$

where Φ_l is l -th eigenvector of appropriate covariance matrix and

$H_i^0 = \sum_j (C(z_j) - \overline{C(z_j)}) \Phi_i^0(z_j)$ is i -th principal component. It's well known that the eigenvector representation is optimum in the sense that maximum variance may be accounted by choosing in order the eigenvectors associated with the largest eigenvalues of appropriate covariance matrix.

Calculations show that cumulative per cent of total variance V_i explained by the eigenvectors associated with the i largest eigenvalues of covariance matrix for beam attenuation coefficient are: $V_1 = 77\%$; $V_2 = 94\%$; $V_3 = 97\%$. Corresponding standard errors of representation of observed profiles $C(z)$ by i eigenvectors are: $\delta_1 = 0.046 \text{ m}^{-1}$; $\delta_2 = 0.024 \text{ m}^{-1}$; $\delta_3 = 0.017 \text{ m}^{-1}$. Thus first few eigenvectors explain main part of total variance and give high accuracy in representation of observed profiles $C(z)$.

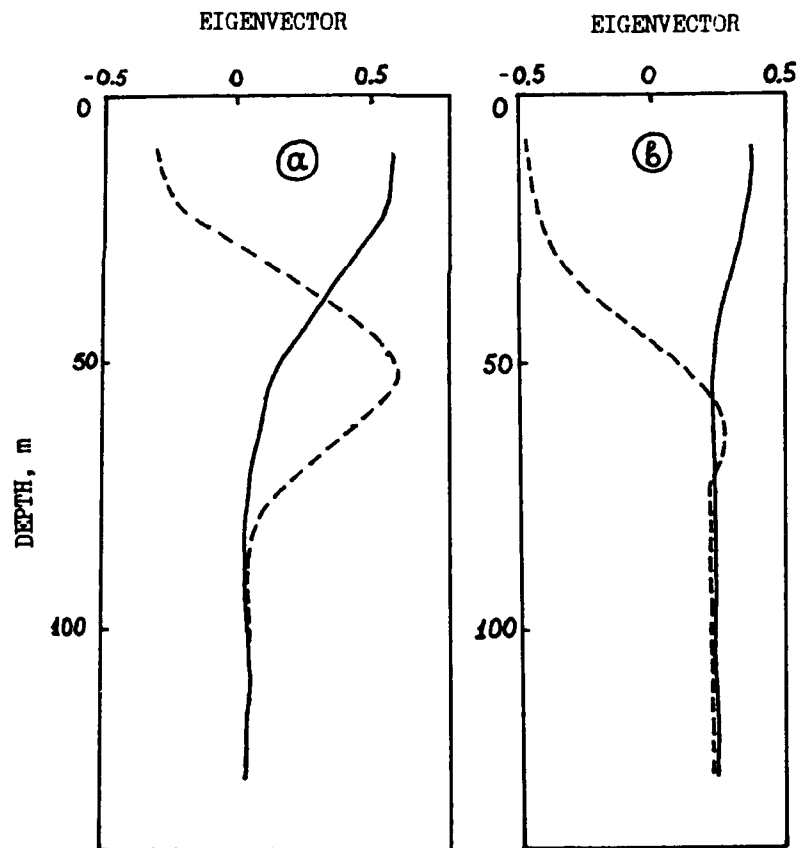


Fig.4. The first (solid line) and the second (dashed line) eigenvectors of beam attenuation coefficient (a) and temperature (b) covariance matrices.

Two eigenvectors associated with largest eigenvalues of covariance matrix for beam attenuation coefficient are shown in Fig.4a. The first eigenvector is maximum in surface layers and

decreases with depth. Its vertical distribution is nearly the same as for standard deviation $\sigma_c(z)$. The second eigenvector is maximum at depths 40-60 m and controls mainly the amplitude of nepheloid layer.

Eigenvectors of the temperature covariance matrix are qualitatively similar to described above (Fig.4b). For instance the first eigenvector decreases with depth but not so rapidly as for beam attenuation coefficient. This is connected with essentially less reduction of standard deviation with depth $\sigma_T(z)$ for temperature profiles. For example near the surface $\sigma_T = 4.1^\circ$ and at depth 100 m $\sigma_T = 2.7^\circ$.

Calculations of factor loadings for beam attenuation coefficient (Fig.5) show that the first factor loading is maximum at depths $z < 30$ m ($r=0.97-0.98$). The second factor loading passes through a maximum at depth 50 m ($r=0.9$). The third factor loading is maximum at depths $z > 100$ m but its value doesn't exceed 0.63. Thus without significant errors the first and the second principal components can be obtained from values of beam attenuation coefficient in surface layers and at depth 50 m respectively. For temperature profiles the first factor loading is great ($r=0.97-0.99$) at all depths.

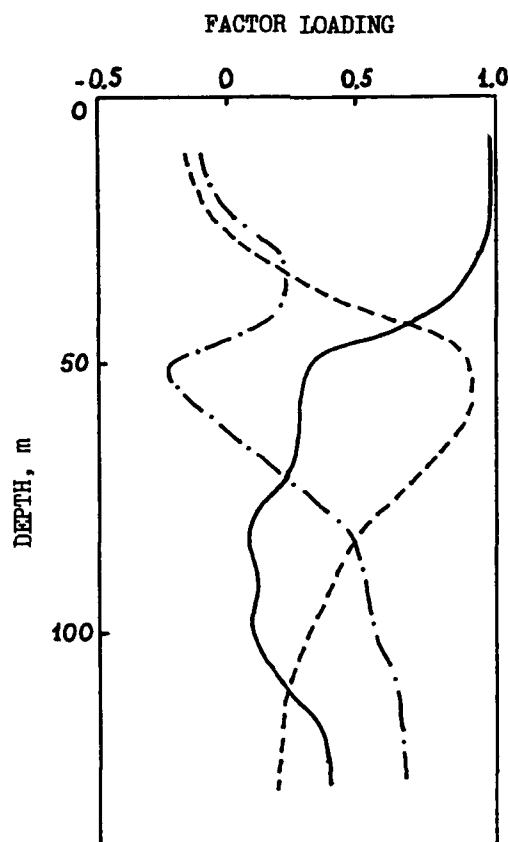


Fig.5. The first (solid line), the second (dashed line) and the third (dot-and-dash line) factor loading for profiles $C(z)$.

It must be pointed out that all statistical parameters calculated separately for the eastern and the western parts of the studied area are nearly the same as for the total set of data. This means that the total set of data can be used for statistical representation of observed profiles in different parts of the studied area.

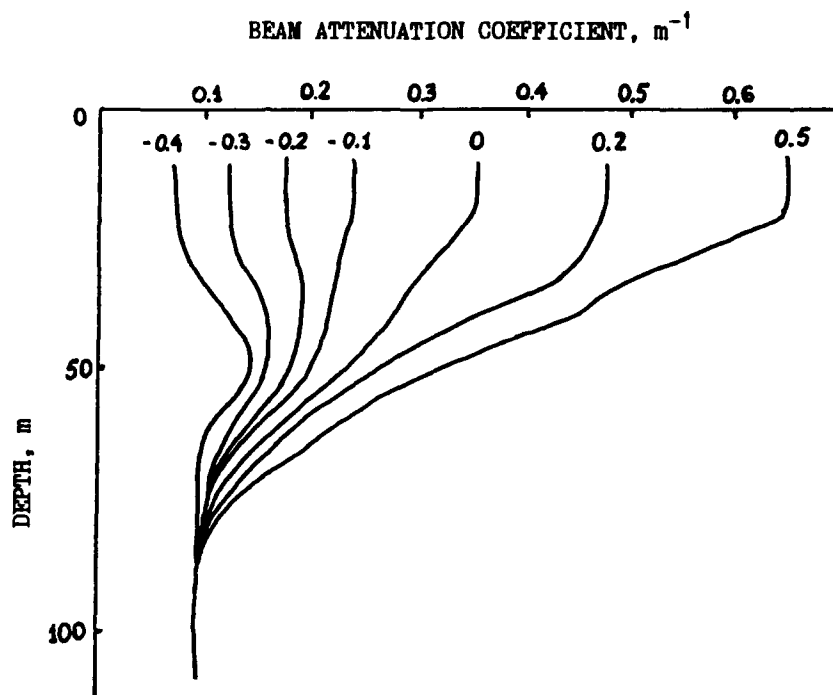


Fig.6. Transformation of vertical profile $C(z)$ in dependence of value of the first principal component.

Let's consider decomposition (1) in which only one eigenvector corresponding to the largest eigenvalue is used. For this case transformation of profile $C(z)$ in dependence of value of the first principal component H_1^0 is shown in Fig.6. It can be seen in Fig.6 that profiles with turbid near surface layer correspond to large positive values of H_1^0 . With reduction of H_1^0 values of beam attenuation coefficient in surface layers decrease and simultaneously thickness of turbid layer increases. From values of $H_1^0 = -0.2$ the nepheloid layer at depths 30-50 m forms. Such dependence allows to suppose that use of only first eigenvector in decomposition (1) gives possibility to predict the qualitative structure of profiles $C(z)$. We divided all profiles $C(z)$ into two types: 1 - profiles with maximum in surface layers and 2 - profiles with subsurface nepheloid layer. As the parameter dividing profiles $C(z)$ into two types value of $S = C_{\max} / C(z=10 \text{ m})$ was chosen. If value of S exceeded 1.2 profiles were attributed to the 2 type and others to 1 type (thus to the later type profiles with low amplitude nepheloid layer were attributed). Then

different number of terms in expansion (1) were used for representation of observed profile and obtained from expansion (1) value of S was compared with corresponding value for measured profile $C(z)$.

Calculations show that representation of observed profile by only first eigenvector in most cases (about 80%) allows to predict its type. Use of two eigenvectors in expansion (1) correctly predicts the type of observed profiles in 95% of cases.

One of the main goals of our study was statistical analysis of connection between different parameters of vertical profiles of beam attenuation coefficient and temperature. Existence of such correlation is very important in the sense of use of hydrological data for estimation of optical properties. For this purpose correlation between principal components and values of beam attenuation coefficient and temperature at different depths was considered.

Statistical analysis shows that temperature closely correlates with value of beam attenuation coefficient only in surface layer with thickness about 30 m ($r = -0.9$). At greater depths correlation sharply decreases. Existence of sufficiently high correlation is explained by increase of productivity in the northern part of the studied area. Corresponding linear equation which connects values of C and T at zero depth has the following form:

$$C = 1.05 - 0.041 T \quad (2)$$

Standard error in determination of C using this equation is 0.07 m^{-1} , relative error is 23%. Also high correlation between first principal components H_1^C and H_1^T takes place ($r = -0.89$) Corresponding linear equation has the following form:

$$H_1^C = -0.025 H_1^T \quad (3)$$

Correlation coefficient between other principal components C and T is close to zero.

It was shown above that use of only one eigenvector in expansion (1) allowed to predict the type of vertical profile $C(z)$. Because of close correlation between the first principal components of C and T it is possible to predict the type of profile $C(z)$ using value of H_1^T . For analysis of this possibility value of H_1^C was obtained from equation (3) and then profile $C(z)$ was determined using only first term in expansion (1). Calculations carried out for the total set of data showed that in 80% of cases type of profile $C(z)$ was predicted correctly. Examples of representation of vertical profiles $C(z)$ in this way are shown in Fig.7. Because the first factor loading for temperature profiles is great at all depths it is possible to

BEAM ATTENUATION COEFFICIENT, m^{-1}

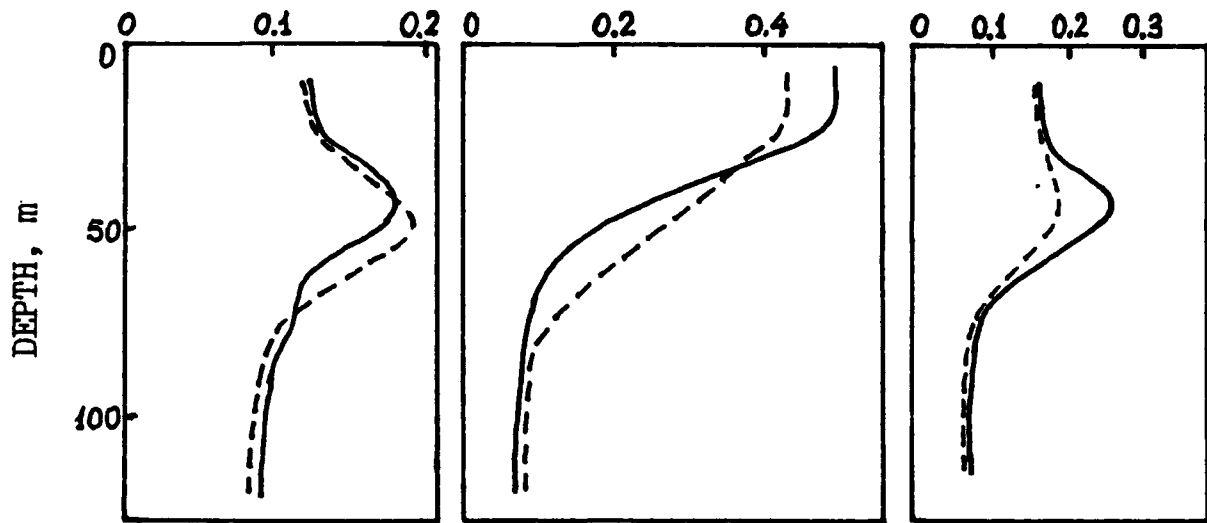


Fig.7. Examples of representation of observed profiles $C(z)$ from the value of the first principal component H_1^T . Observed profiles - solid line, computed - dashed line.

obtain value of the first principal component H_1^T from value of temperature at one depth (for instance from surface temperature). Analysis shows that value of surface temperature $T = 18^\circ$ in most cases can be treated as the boundary value separating areas with different types of profiles $C(z)$.

It's well known that temperature doesn't influence directly on sea water optical properties. Correlation considered above appears to be the consequence of dynamical processes which influence in the proper way on hydrological and optical structure.

Strictly speaking results of statistical analysis can be applied only to experimental data obtained in the studied area of the North Atlantic in corresponding season. But preliminary analysis shows that in many cases statistical characteristics obtained in our study are applicable to profiles measured in other regions of the Atlantic ocean. In future we plan to carry out analogous statistical analysis for the greater set of experimental data obtained in different regions of the World ocean.

4. REFERENCES

1. V.I.Burenkov, A.P.Vasilkov, "Statistical analysis of the spectral reflectance of ocean waters", *Izvestiya USSR Academy of Science, Atmos. and Oceanic physics*, Vol.27, No.11, 1256-1261, 1991.
2. O.V.Kopelevich, V.I.Burenkov, "On the connection between spectral values of absorption coefficient, phytoplankton pigments, yellow substance", *Oceanology*, Vol.17, No.3, 427-433, 1977.
3. O.V.Kopelevich, V.I.Burenkov, O.A.Gushin, Yu.L.Mashtakov, M.A.Shmatko, "Universal system of functions for representation of

- sea water volume scattering function", Izvestiya USSR Academy of Science, Atmos. and Oceanic physics, Vol.11, No.7, 770-773, 1975.
4. J.L.Muller, "Ocean color spectra measured off the Oregon coast: characteristic vectors", Appl.Opt., Vol.15, No.2, 394-402, 1976.
5. A.A.Kumeisha, "On parametrization of the transparency field in the central part of the tropical zone of the Pacific Ocean", Oceanology, Vol.32, No.1, 22-28, 1992.
6. V.I.Burenkov, "Statistical analysis of vertical profiles of beam attenuation coefficient in the north-west Pacific", Optics of sea and atmosphere, Leningrad, 1988, 112.

Optical properties of the Northwest African upwelling region

Vladimir I. Burenkov, Oleg V. Kopelevich, Anatoly I. Sud'bin

P.P. Shirshov Institute of Oceanology
Moscow, 117218 Russia

ABSTRACT

In July-August 1988 optical measurements in the Northwest African upwelling region (21° - $22^{\circ}20'$ N, $17^{\circ}20'$ - 18° W) were carried out. Measurements of vertical profiles of beam attenuation coefficient $C(z)$, diffuse attenuation coefficient K_d , temperature and salinity were made at 39 stations during 9 days. In addition continuous measurements of chlorophyll fluorescence and surface temperature were carried out between stations. Observations showed very high spatial variability of optical properties in the study area. For instance surface value of beam attenuation coefficient at wavelength 530 nm varied from 0.15 m^{-1} to 2.6 m^{-1} . In the central part of the study area the filament of relatively cold (temperature about 18°) and transparent (value of beam attenuation coefficient less than 0.6 m^{-1}) was observed. This filament was oriented perpendicularly to the coast line, its width was 30-35 km near the shore and 10-15 km at 18° W. The filament was separated from surrounding waters by frontal zones where value of optical properties increased sharply. Most turbid waters were observed in the south-western corner of the study area and most transparent - in the north-eastern corner.

1. INTRODUCTION

Many years coastal upwelling regions are objects of intense study. Mainly this is connected with high productivity of these regions caused by upwelling of cold, nutrient-rich waters. Upwelling occurs when there is a divergence in the surface current at the coastal boundary, because of offshore Ekman transport induced by alongshore winds. Upwelling of nutrient-rich waters leads to phytoplankton growth in surface layers.

Intensive hydrophysical studies of coastal upwelling have been carried out in last years. Optical observations of coastal upwelling are not so numerous¹⁻⁶. Measurements in these studies have been carried out mainly at separate transects oriented perpendicularly to the coast line. Such measurements can give adequate description of upwelling region only if distribution of hydrophysical parameters appears to be two dimensional (in other words there is no dependence on alongshore coordinate). But because of different reasons, in many cases distribution of various parameters is more complex and there is a necessity for

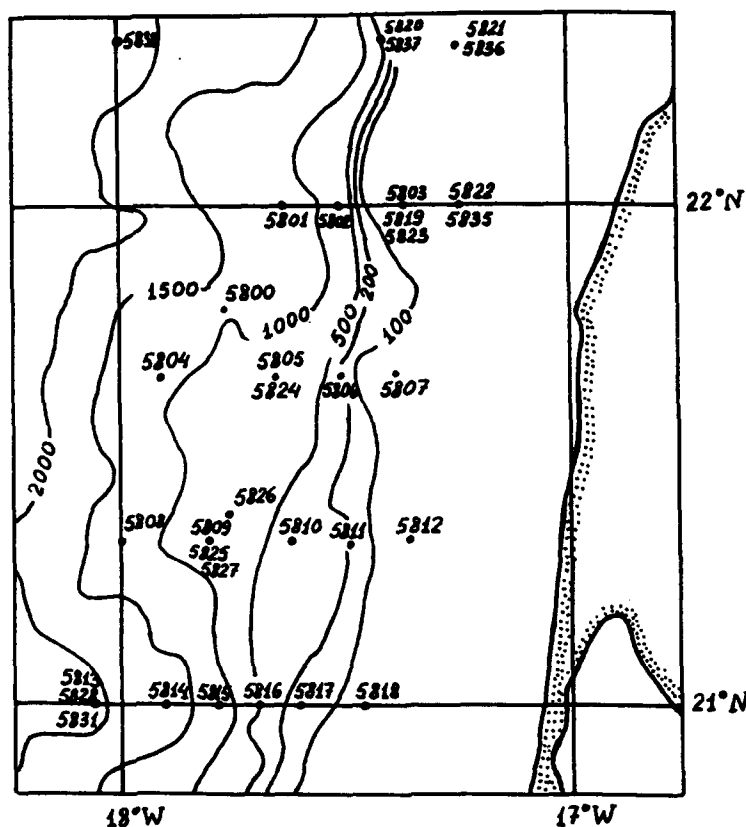


Fig.1 Location of stations in the study area.

carrying out measurements at few transects.

2.STUDY AREA.

Observations in the Northwest African upwelling region were carried out during 9 days from July 26 to August 3, 1988. Size of the main study area was 80×40 nautical miles (21°- 22°20'N, 17°20'- 18° N). In addition transect along 21° N (from 18° to 20° W) was made. Location of stations in the study area is shown in Fig.1. Depths in the study area varied from 2000 to 60 m. Minimum distance from the shore was 20 km.

Basic data (19 stations) were obtained at the first stage of observations during three days (July 27 - July 29). Later on measurements were carried out in different parts of the study area and observations at few stations were repeated. At the last stage of observations few transects were made for estimation of temporal variability of observed distributions. In the shelf waters diurnal station 5823 was carried out.

3.METHODS

Following set of optical measurements were carried out: vertical profile of beam attenuation coefficient $C(z)$ (at wavelength $\lambda = 530$ nm), vertical profile of diffuse attenuation

coefficient $K_d(z)$ ($\lambda = 534$ nm), vertical profiles of volume scattering function at different angles $\sigma(\gamma, z)$ ($\lambda = 633$ nm). Between stations continuous measurements of surface chlorophyll fluorescence I_{chl} and temperature T were carried out. Because of complex structure of distribution of hydrophysical and hydrooptical parameters continuous measurement were very useful for adequate description of upwelling region.

Optical observations were accompanied by measurements of temperature and salinity vertical profiles. Also concentrations of chlorophyll and suspended particulate matter (using Coulter counter) were determined in water samples taken from different depths.

4. WIND CONDITIONS

It's well known that Ekman transport strongly depends on wind speed and direction. During our measurements wind conditions were changeable. At the beginning of observations (on July 27) there were strong north trade winds (favorable for upwelling) with speed 12-15 m/s. During July 28 wind speed diminished to 5-6 m/s. During next days wind direction changed to westward and wind speed still more diminished. These changes led to relaxation of upwelling. Twice local intensification of north trade winds were observed (on July 30 and August 2).

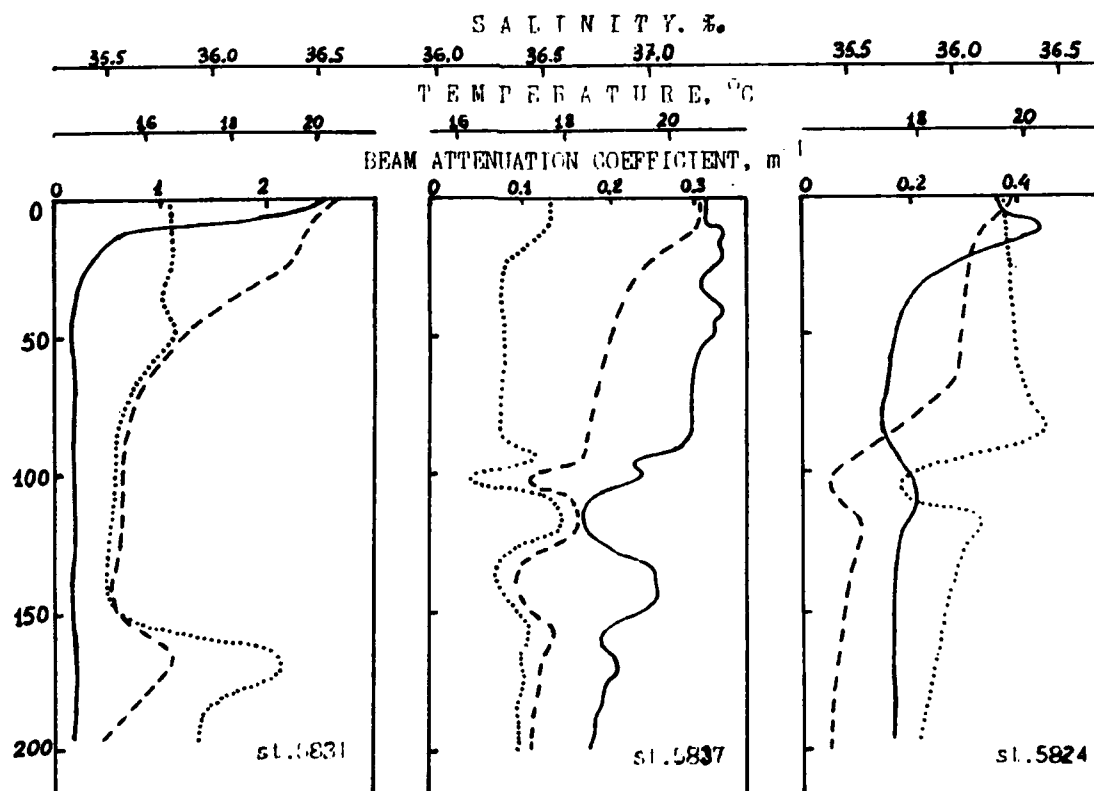


Fig.2. Typical vertical profiles of beam attenuation coefficient (solid line), temperature (dashed line), salinity (dotted line).

5. VERTICAL DISTRIBUTION OF OPTICAL PROPERTIES.

Vertical profiles of beam attenuation coefficient in the study area were typical for upwelling regions (Fig.2.). They are characterized by surface turbid layer and decreasing of beam attenuation coefficient with depth. In many cases variations of C with depth were very high. For instance at st.5831 beam attenuation coefficient varied from 2.6 m^{-1} near the surface to 0.12 m^{-1} at depth 200 m. In surface layer vertical gradient dC/dz exceeded $0.2 \text{ m}^{-1}/\text{m}$. Vertical profiles of other optical properties were nearly the same as for beam attenuation coefficient.

Thickness of surface turbid layer varied from 10 to 60 m and usually coincided with thickness of mixed layer. Maximum thickness of turbid layer was observed in the northern part of the study area. Minimum thickness of surface turbid layer was observed in frontal zones and regions of intensive upwelling where mixed layer practically was absent.

In many cases at depth greater than 100 m there were local nepheloid layers coinciding with analogous layers in vertical profiles of temperature and salinity. Formation of such layers is connected with intrusions.

6. DISTRIBUTION OF OPTICAL PROPERTIES.

The most notable feature of optical properties distribution in surface layers of the study area is very high spatial variability. Value of beam attenuation coefficient varies more than 10 times - from 0.15 m^{-1} (st.5838) to 2.6 m^{-1} (st.5831). It is interesting that most turbid waters were observed far from the coast, in the south-western corner of the study area. At the same time transparent waters (with value of C about 0.2 m^{-1}) were situated in shelf zone, in the north-eastern corner of the study area. Analogous variations are inherent to other optical properties. Great range of variations was also observed for concentrations of chlorophyll ($0.1 - 8.9 \text{ mg/m}^3$) and suspended particulate matter ($0.32 - 5.8 \text{ mm}^3/\text{l}$).

Distributions of surface values of beam attenuation coefficient and temperature at the first stage of measurements (July 27 - July 29) are shown in Fig.3,4. For mapping of these distributions, measurements at stations and continuous measurements between stations were used. Statistical analysis showed that beam attenuation coefficient closely correlated with chlorophyll fluorescence (correlation coefficient 0.94). Thus results of chlorophyll fluorescence measurements could be used for mapping of beam attenuation coefficient distribution.

Later on we will consider only distribution of beam attenuation coefficient because distributions of other optical properties and concentrations of chlorophyll and suspended particulate matter are nearly the same.

Most notable feature of temperature and beam attenuation

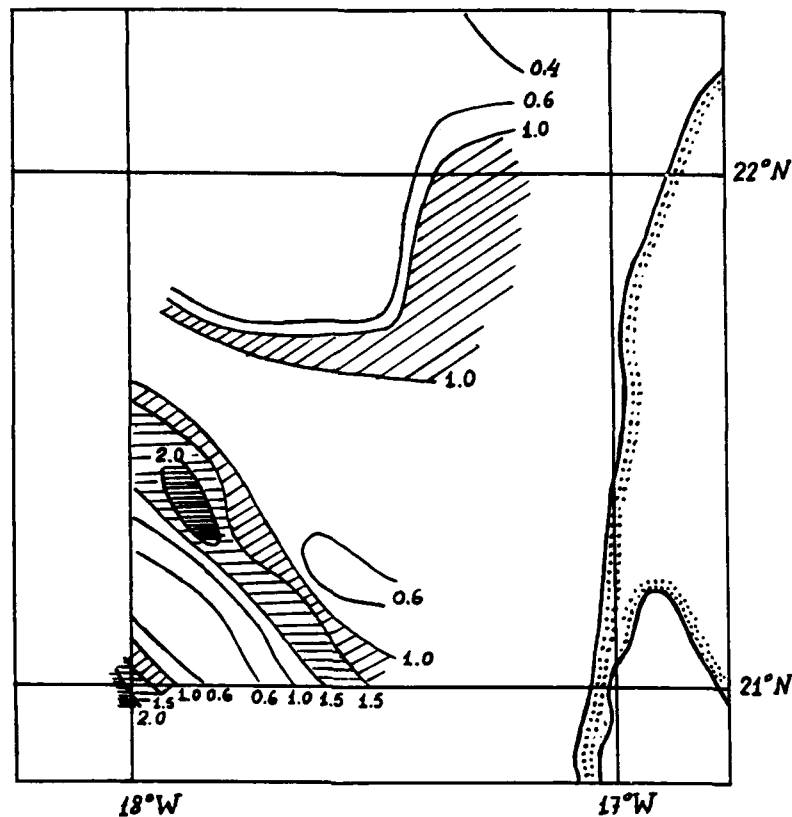


Fig.3. Isolines of surface values of beam attenuation coefficient. Areas of most turbid waters are shaded.

coefficient distributions consists in existence of the filament with relatively cold (temperature about 18°) and transparent (value of beam attenuation coefficient less than 0.6 m^{-1}) waters in the central part of the study area. This filament is oriented nearly perpendicularly to the coast line. Its width is about 30-35 km near the coast and decreases to 10-15 km at 18° W. Value of beam attenuation coefficient inside the cold filament is less than in surrounding waters and increases only near its boundary. Thus areas of turbid waters are extended along the cold filament.

Distributions of surface chlorophyll fluorescence and temperature at transect crossing the cold filament (Fig.5) show that frontal zones bound the cold filament and from its southern side frontal zone is more intensive. Chlorophyll fluorescence increases at these frontal zones and at south-western boundary of the cold filament, waters are more turbid than at opposite boundary.

Combination of relatively low temperature with low values of beam attenuation coefficient and low concentrations of chlorophyll and suspended particulate matter in the filament allows to suppose that this filament is caused by upwelling. This assumption is confirmed by vertical temperature sections crossing the cold filament (Fig.6). Sharp displacement of isotherms (about 100 m)

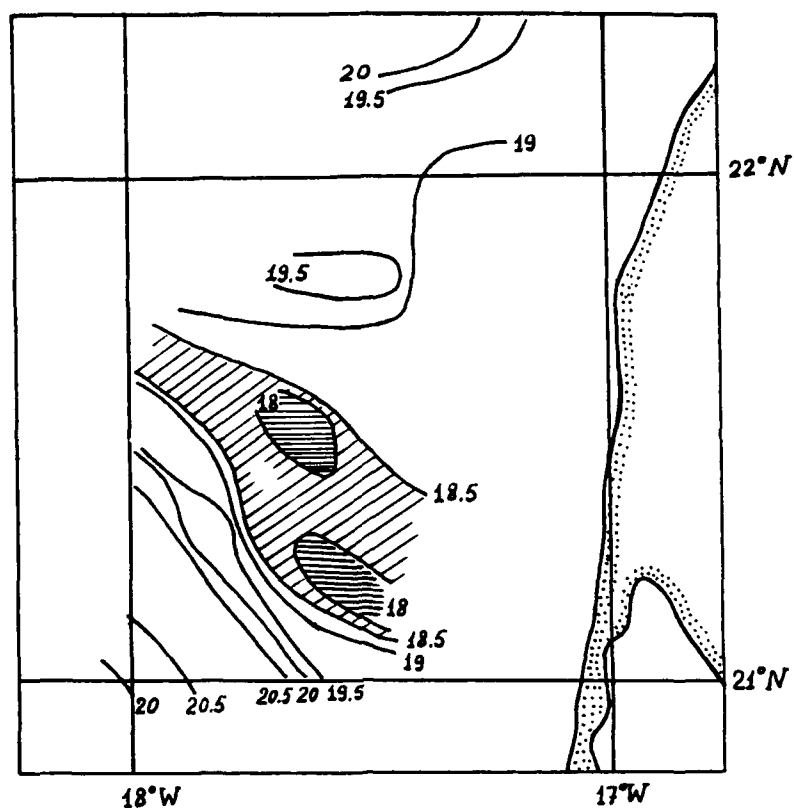


Fig.4. Isolines of surface temperature. Areas of cold waters are shaded.

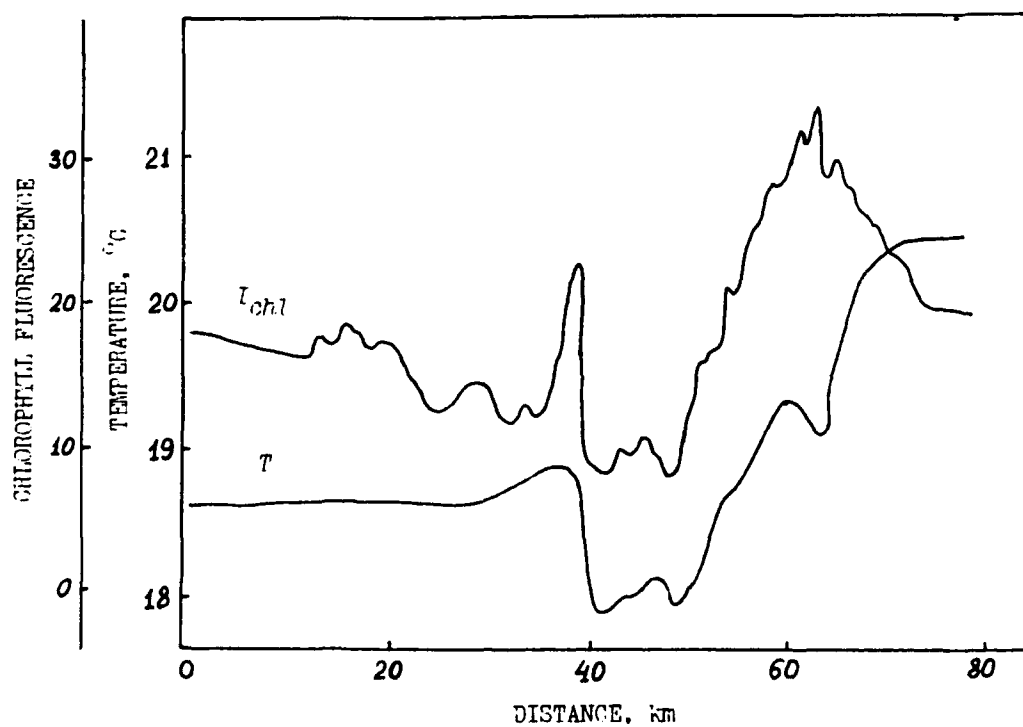


Fig.5. Example of distribution of surface chlorophyll fluorescence and temperature at transect crossing the cold filament.

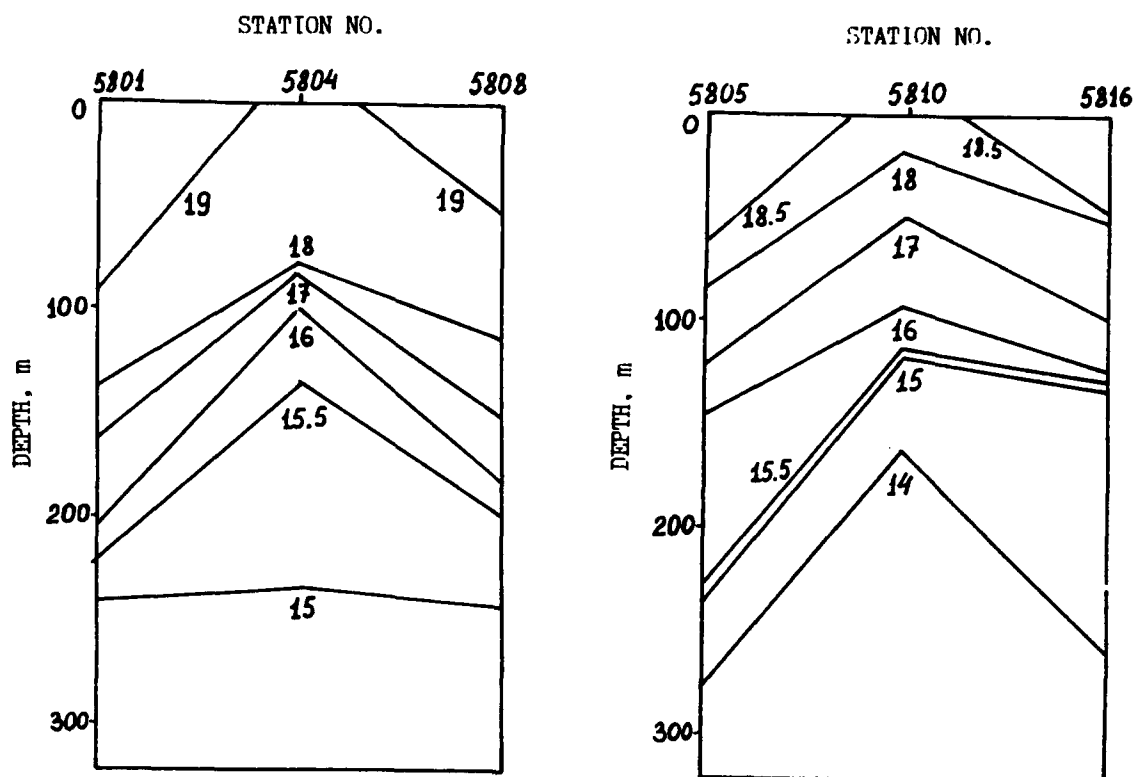


Fig.6. Vertical temperature sections crossing the cold filament. Stations 5804 and 5810 are located inside the cold filament.

inside the cold filament is the evidence of intensive upwelling. Relatively low productivity of waters inside the cold filament can be explained by horizontal spread of upwelled waters due to which, phytoplankton growth occurs only near the boundary of the filament.

At the end of our measurements, width of the cold filament decreased and its temperature increased, areas of turbid waters near its boundary narrowed. This can be explained by the change of wind conditions which led to relaxation of upwelling.

Similar cold filaments in coastal upwelling regions with with approximately same parameters were observed from satellites⁷. Also there were optical observations of cold filaments from "Nimbus-7" by CZCS⁸. Unlike our case these data showed that in cold filaments high concentrations of chlorophyll were observed. This discrepancy can be connected with different stages of upwelling events.

Another interesting features of beam attenuation coefficient distribution are the existence of transparent waters near the shore, in the north-eastern corner and turbid waters far from the shore, in the south-western corner of the study area.

Measurements in the north-eastern corner were carried out twice: at the beginning of our experiment, when waters with value

of beam attenuation coefficient about 0.2 m^{-1} were observed, and after few days when there were essentially more turbid waters in this area. Hydrological data showed the existence of upwelling in the north-eastern corner. Low productivity of these waters indicated that there was initial stage of upwelling event when phytoplankton growth didn't begin. Only after few days phytoplankton growth led to increasing of optical properties and concentration of chlorophyll.

Vigorous upwelling led to low water transparency was observed in the south-western corner of the study area. Depth of isotherm $T = 16^{\circ}$ here (71 m) was minimum for the study area (maximum depth of this isotherm was 227 m). Upwelling velocity estimated by displacement of isopycnals during 1 day was about 10^{-2} cm/s . During all our observations in this area value of beam attenuation coefficient increased. Value of $C = 2.6 \text{ m}^{-1}$ at st.5831 was maximum for the study area. Vertical profile of beam attenuation coefficient at this station (Fig.2) was typical for intensive upwelling, with absence of mixed layer.

Observed distributions appears to be very complex and not two dimensional. Isolines are oriented nearly perpendicularly to the coast line. Comparison of temperature and beam attenuation coefficient distributions in surface layers of the study area shows similarity in isolines structure. Isohalines and isopycnals are oriented nearly the same as isotherms but unlike temperature, salinity and density monotonously increase in north-eastern direction.

Values of beam attenuation coefficient at depths 100-200 m were essentially less than in surface layers. In spite of high turbidity of surface waters, typical for open ocean values of C about 0.1 m^{-1} were observed at this depths. Distribution of beam attenuation coefficient at depth 100 m (Fig.7) was more homogeneous than in surface layers (range of variations of C was $0.085 - 0.2 \text{ m}^{-1}$). Isolines of beam attenuation coefficient at depth 100 m are oriented nearly the same as in surface layers. Most transparent waters are located in south-western and north-eastern parts of the study area. Relatively turbid waters are observed in its central and south-eastern parts.

Measurements at st.5823 located at continental shelf, showed high diurnal variability of optical properties. During 10 hours value of beam attenuation coefficient decreased from 1.3 m^{-1} to 0.6 m^{-1} . Similar variations were observed for diffuse attenuation coefficient and concentrations of chlorophyll and suspended particulate matter. At the end of diurnal st.5823 values of optical properties increased to approximately the same values as at the beginning of measurements. Also changes in vertical structure of optical properties were observed. In particular during first 10 hours nepheloid layer at depths 15-25 m was formed. Variations of optical properties were closely correlated with temperature variations. Also they were accompanied by changes in current speed and velocity.

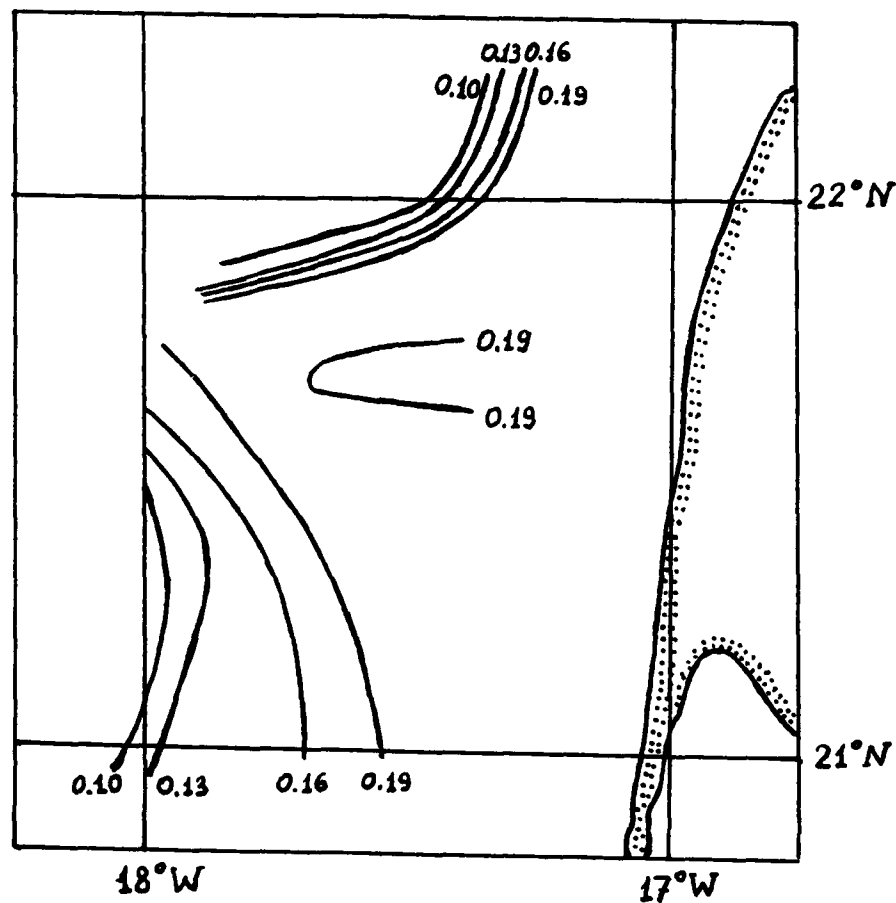


Fig.7. Isolines of beam attenuation coefficient at depth 100 m.

Measurements at transect along 21° N (from 18° W to 20° W) showed high spatial variability of chlorophyll fluorescence and temperature in its initial parts. Surface value of beam attenuation coefficient at the end of this transect (0.43 m^{-1}) was few times greater than typical for open ocean at this latitudes. This means that coastal upwelling influences on water productivity very far from the shore.

7. REFERENCES

1. J.C.Kitchen, J.R.V.Zaneveld, H.Pak "The vertical structure and size distribution of suspended particles off Oregon during the upwelling season", Deep-Sea Res., v.25, No.7, 402-409, 1978.
2. H.Pak, L.A.Godispoti, J.R.V.Zaneveld "On the intermediate particle maxima associated with oxygen-poor water off Western South America", Deep-Sea Res., v.27, No.10, 783-797, 1980.
3. V.N.Pelevin, V.M.Grinberg, Yu.L.Mashtakov, M.A.Shmatko "Optical characteristics of the waters in the Pacific Equatorial and Peruvian upwellings", Transactions of the P.P.Shirshov Institute of Oceanology, v.102, Moscow, Nauka, 56-60, 1975.
4. O.V.Kopelevich, V.I.Burenkov, Yu.L.Mashtakov, N.M.Nosenko,

S.Yu.Rusanov "Optical properties of sea water factors determining them in some areas of the Pacific ", Oceanological studies, v.29, Moscow, Nauka, 55-82, 1976.

5. H.S.Karabashev "Peculiarities in distribution of fluorescence and scattering at intensive vertical mixing and upwelling", Oceanology, v.18, No.2, 312-318, 1977.

6. V.M.Pavlov "On the optical properties of the Peruvian upwelling region", Variability of transparency and scattering of the ocean waters, Moscow, Inst. Oceanology Press, p.6-11, 1981.

7. K.N.Fedorov, A.I.Ginsburg "The Subsurface Layer of the Ocean", Leningrad, Hydrometeoizdat, 304, 1988.

8. L.Nykjaer, L.Van Camp, P.Schlittenhardt "The structure and variability of a filament in the northwest African upwelling area as observed from AVHRR and CZCS images", Proceedings of IGARSS'88 Symposium, Edinburg, Scotland, 13-16 Sept.1988, 1097-1100.

Errors in the reporting of solar spectral irradiance using moderate bandwidth radiometers: an experimental investigation

C. R. Booth, T. Mestechkina, and J. H. Morrow

Biospherical Instruments Inc.
5340 Riley Street
San Diego, California 92110, USA
VOX: (619) 686-1888, FAX: (619) 686-1887
Internet: booth@biospherical.com

1. ABSTRACT

Moderate bandwidth (defined here to be between 1 and 12 nm) radiometers, used frequently in remote sensing studies, are routinely calibrated by exposure to optical standards composed of incandescent lamps. These radiometers are subsequently used to measure solar irradiances having significantly different spectral distributions from the standard lamps. When working in regions of the solar spectrum with large variations in intensity as a function of wavelength, significant errors can be introduced from the difference between the lamp spectrum and the solar spectrum. Under these conditions, a "perfect" radiometer can grossly over- or under-estimate the solar irradiance, while several otherwise identical radiometers with center bandwidths ranging over ± 2 nm can report significantly different irradiances. A direct instrument intercomparison experiment was conducted in San Diego using 15 five-channel filter radiometers. The instruments were operated for approximately one week alongside a 0.7 nm bandwidth scanning spectroradiometer under a variety of solar conditions. All of these instruments had been calibrated with lamp standards traceable to NIST.

There are fundamental disparities between the spectrum of sunlight incident on the earth's surface and that normally used for calibration sources. At certain parts of the spectrum between 350 and 700 nm *sunlight changes in intensity by as much as 89% per nm wavelength* while calibration sources change by no more than 2.5% per nm. This rapid rate of change in some parts of the spectrum makes 1% solar irradiance measurements potentially unachievable. In an effort to reduce the uncertainties of transferring calibrations made with standard lamps to filter-based radiometers, we previously¹ suggested that "source-specific" calibration constants, referenced to both lamps and reference solar spectra, be used. This investigation explores how well this procedure can work, and contrasts this result with intercomparison- and regression-based calibrations.

2. BACKGROUND

PUV and GUV series UV Radiometers (Biospherical Instruments Inc., San Diego, CA, USA) are filter radiometers which have four nominal 10 nm bandwidth channels in the UV at 305, 320, 340, and 380 nm and a single broadband PAR (Photosynthetically Active Radiation) sensor (Figure 1)¹. These systems were designed to fill the need for a simple radiometer to detect UV irradiance and its relationship to changes in atmospheric ozone concentration.

The absolute spectral responsivity of each channel in these radiometers can be described by a function $R(\lambda)$, where λ is wavelength. The determination of $R(\lambda)$ can be done by direct measurement, but requires a wavelength tunable light source whose output is accurately known and which can illuminate the instrument's irradiance collector in the same manner as sunlight (i.e. can fully illuminate the detector). Such instrumentation should also have a bandwidth which is small relative to the bandwidth of the sensor, particularly when used in the UV-B spectral region.

An alternate approach to the determination of $R(\lambda)$ is to compute the spectral product of the response of the detector, $R_{\text{det}}(\lambda)$, the spectral transmission of all filter components, $T_{\text{filt}}(\lambda)$, and the diffuser, $T_{\text{diff}}(\lambda)$, as follows:

$$R(\lambda) = R_{\text{det}}(\lambda) T_{\text{filt}}(\lambda) T_{\text{diff}}(\lambda) C_r \quad (1.)$$

In practice, $R_{\text{det}}(\lambda)$ is only known in a relative fashion because flux from the diffuser overfills the detector. An additional source of uncertainty is introduced because the filter transmissions are usually measured in a spectrophotometer, and the geometry (i.e.,

angle of incidence and field of view) of the spectrophotometer does not match that of the assembled instrument. To account for these uncertainties, a constant C_r is introduced in Equation 1. Conceptually, the response function of this sensor may be modeled using these spectra and Equation 1.

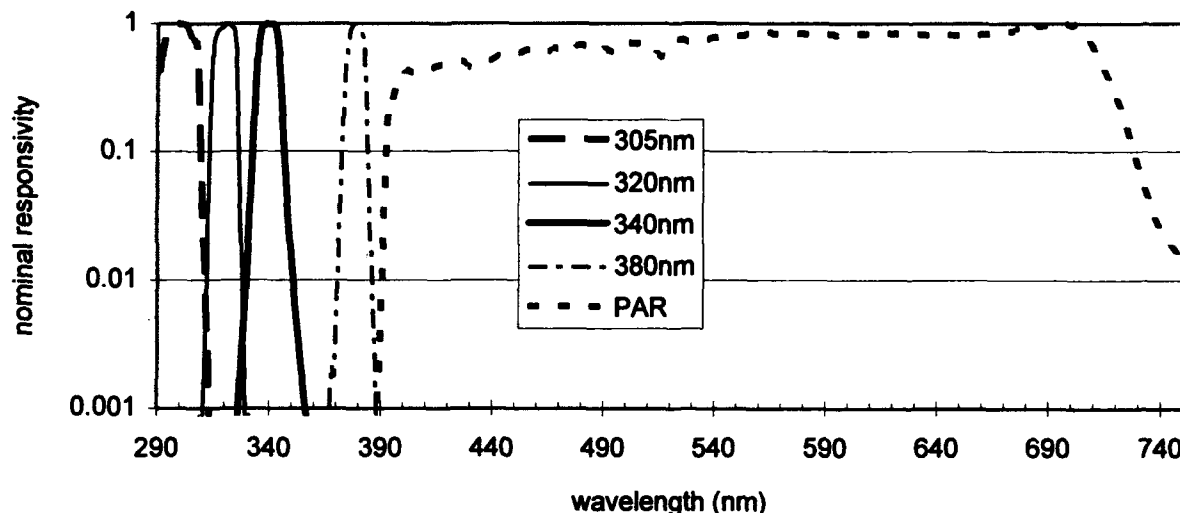


Figure 1. Nominal spectral response of the GUV/PUV-500 series filter radiometers. Each channel has been normalized to 1 at the peak.

Determination of the "absolute" calibration of a radiometer (such as the one whose response is shown in Figure 1) is frequently conducted by placing the device in front of a Standard of Spectral Irradiance (typically a 1000 watt type FEL lamp) under conditions specified by the National Institute of Standards and Technology². The output voltage may be related to irradiance through a nominal calibration constant, C_n :

$$C_n = \frac{V_n}{E_I(\lambda_n)} \quad (2.)$$

Using data from such a lamp-based calibration and the individual optical properties of the sensor constituents, we can then calculate the responsivity constant, C_r , where V_n is the output voltage generated by the calibration irradiance, $E_I(\lambda_n)$, at the nominal center wavelength of the device, λ_n :

$$C_r = \frac{V_n}{\int_{\lambda=0}^{\infty} E_I(\lambda) R_{det}(\lambda) T_{filt}(\lambda) T_{diff}(\lambda) d\lambda} \quad (3.)$$

By knowing C_r and assuming a specific source stability, an absolute responsivity can be calculated.

In an attempt to remove the effects of the different shapes of the lamp and solar spectra, a source-specific calibration constant can be devised that is normalized to a reference solar spectra, $E_{in}(\lambda)$, assumed to be more like the unknown source spectrum. In this case, we have chosen a reference spectrum generated by Lowtran³.

$$C_s = \frac{\int_{\lambda_1}^{\lambda_2} R(\lambda) E_{in}(\lambda) d\lambda}{E_{in}(\lambda)} \quad (4.)$$

Unless the relative spectral irradiance of the unknown source matches $E_l(\lambda_n)$, errors in the irradiance estimate will occur. *Thus, even with the source-specific calibration, inherent errors exist in the measurements of all radiometers or spectroradiometers with finite bandwidths that are calibrated with lamp standards and applied to measurements where the spectral distributions are different.*

An additional method of "calibration," by comparison with an instrument believed to be accurate, may also be used. In this procedure, a large number of near-simultaneous observations are made using both a filter radiometer and a high-resolution scanning spectroradiometer⁴, and statistical techniques are used to derive a calibration constant which we will term C_j , for intercomparison-based calibration. Such calibrations are, of course, only as good as the reference instrument. To investigate the ability of this calibration method to yield "correct" measurements, some of the results of just such an intercomparison will be examined.

3. PROCEDURE:

An intercomparison of instruments was made on the roof of the facility at Biospherical Instruments in San Diego. The scanning spectroradiometer used was a Biospherical Instruments SUV-100 Spectroradiometer which is permanently mounted on the facility roof, free of obstructions. This instrument is a part of the NSF-sponsored UV Monitoring Network⁴. It was calibrated in place using a 200 watt Standard of Spectral Irradiance calibrated by Optronics Laboratories (Orlando, FL) to the specifications of Biospherical Instruments.

During the calibration, data scans were conducted every half hour. Scans were made at increments of 0.2 nm (280-315 nm), 0.5 nm (280-380 nm) and 1.0 nm (280-620 nm). The time and date recorded in the resulting data files were corrected once per day by comparison with the Universal time and date (UT) transmitted by GPS (Global Positioning System). The GUV and PUV filter radiometers recorded data at two minute intervals, representing a two minute average. A database paired filter radiometer observations with sequences of spectral irradiance measurements.

The filter radiometers were calibrated in the calibration facility of Biospherical Instruments using a 1000 watt FEL-type working Standard of Spectral Irradiance generated at Biospherical Instruments by comparison with a NIST issued FEL Standard of Spectral Irradiance. Therefore, both the filter radiometer and the scanning spectroradiometer had independent calibration paths joining at NIST.

The regression analysis was performed by taking the full dataset of between 120 and 160 daytime observations taken at San Diego, CA between 7/23/93 20:41 and 8/1/93 19:09. During that period, solar angles ranged from 13.6 to 89.4°, and the sky conditions ranged between clear and overcast.

4. SOURCE-SPECIFIC AND INTERCOMPARISON-BASED CALIBRATIONS AT 305 NM

Various approaches to calibrating moderate bandwidth radiometers were examined in the intercomparison at Biospherical Instruments. Table 1 shows the results of measurements taken on 8/2/93 at 20:38 hrs (UT). The GUV-511 SN 9228 reported an irradiance of $1.57 \mu\text{W}/\text{cm}^2/\text{nm}$ when referenced to the traditional lamp calibration (Equation 2). This differed from the SUV spectroradiometer irradiance by -74%. When the calibration approach described by Equation 4 (i.e., the "source-specific" calibration with the reference source using a Lowtran generated spectrum) was used then this "error" was reduced to -43%. A much better regression-based calibration constant (see Figure 3) was obtained by comparison against the SUV-100. It was found that most of the outliers in the regression were traceable to conditions where cloud cover caused changes in the light field within the ± 1 minute registered sample windows.

There are several factors that may have contributed to this poor agreement between calibration results. First, the spectral response of the GUV-511 is imperfectly known. It is well-known that interference filters "detune" or shift their spectral response toward shorter wavelengths when the transmitted light differs from normal incidence. In the case of the GUV-511, the flux passing through the filters to the detector is contained in a larger solid angle than when measured in the spectrophotometer, thus some shift to shorter wavelengths can be expected. When $R(\lambda)$ was simply shifted down by 2nm, this "error" was reduced to -27%. Shifting $R(\lambda)$ by -4nm practically eliminated the "error" (-1%).

A second factor that contributed to the apparently poor agreement of the source-specific calibration constant was that the reference Lowtran spectrum and the SUV-100 measured spectrum exhibited relatively poor agreement in this spectral region. Figure 4 shows details of these two spectra. When a solar spectrum measured by the SUV-100 spectroradiometer four days earlier was substituted for the Lowtran reference, the error dropped to -31%. When $R(\lambda)$ was downshifted by -1.4 nm, a reasonable estimate for filter detuning, then "errors" disappeared. By using this analytic technique at 305 nm, the accuracy in the determination of $R(\lambda)$ as a function of λ was estimated to be accurate to 0.03 nm to yield agreement at the 1% level. It is beyond the scope of this document to analyze the causes of these differences, but it should be pointed out that causes included atmospheric gas concentrations used in Lowtran, the bandwidth of both the reference and observed spectra, and geometric measurement differences.

Regression- or comparison-based calibration factors are only as good as the instrument against which they are compared. When instruments of different bandwidths are compared, it is important to examine the residuals of the regression against air mass to determine if there would be a bias introduced due to changes in ozone or other atmospheric gases. Figure 5 examines the residuals from a comparison of the GUV data against three different wavelengths measured by the SUV-100. Analysis suggests that at low sun angles the measured spectra were experiencing a shift toward a slightly longer wavelength.

Table 1. Contrast of calibration methods at 305 nm.

Irradiance Measure Source	$\mu\text{watts}/\text{cm}^2/\text{nm}$	Relative to SUV-100
SUV-100 (scanning spectroradiometer)	6.034*	
GUV with lamp based calibration	1.575	- 74%
GUV with lamp based/source specific cal.	3.430	- 43%**
GUV Irradiance based on regression with SUV-100	6.029	0.1%

* SUV-100 scan on 8/2/93 scan at 20:38

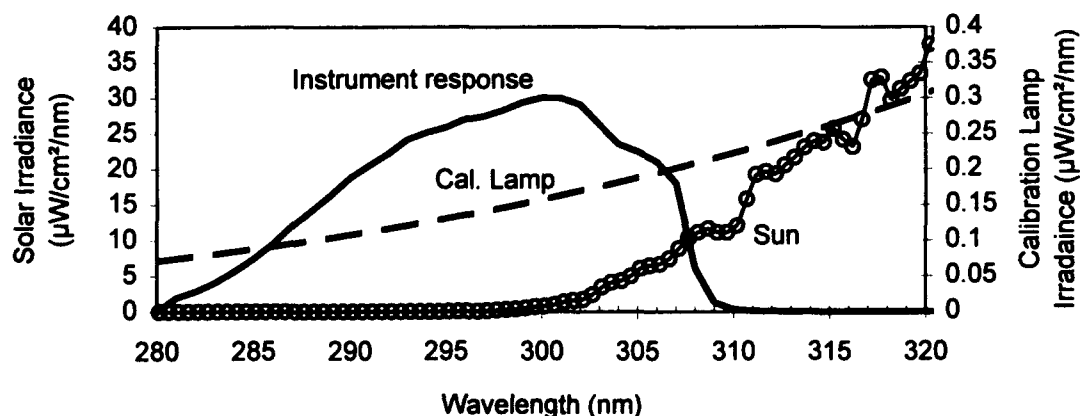


Figure 2. Comparison of target solar spectrum (referenced to left axis), calibration lamp spectral irradiance (smooth increasing curve referenced to right axis), and instrument response in the UV-B region. The instrument response is relative.

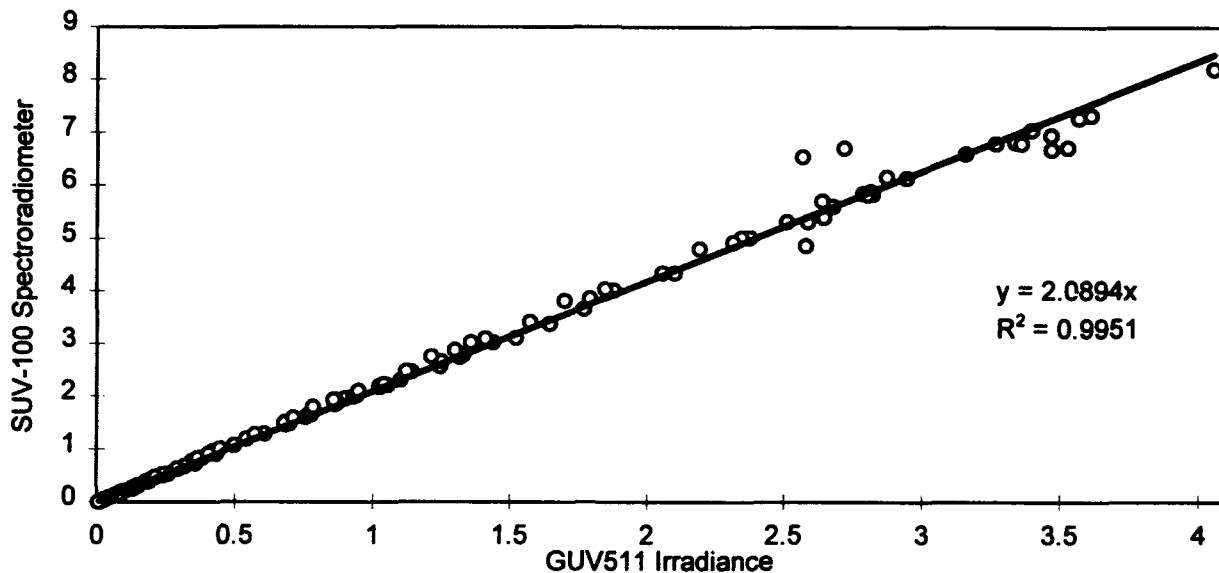


Figure 3. Correlation of Scanning Spectroradiometer measured irradiance at 305 nm with the 305 nm GU511 Irradiance given a lamp-based calibration. Both values are in microwatts/cm²/nm. The regression equation and statistic are also shown.

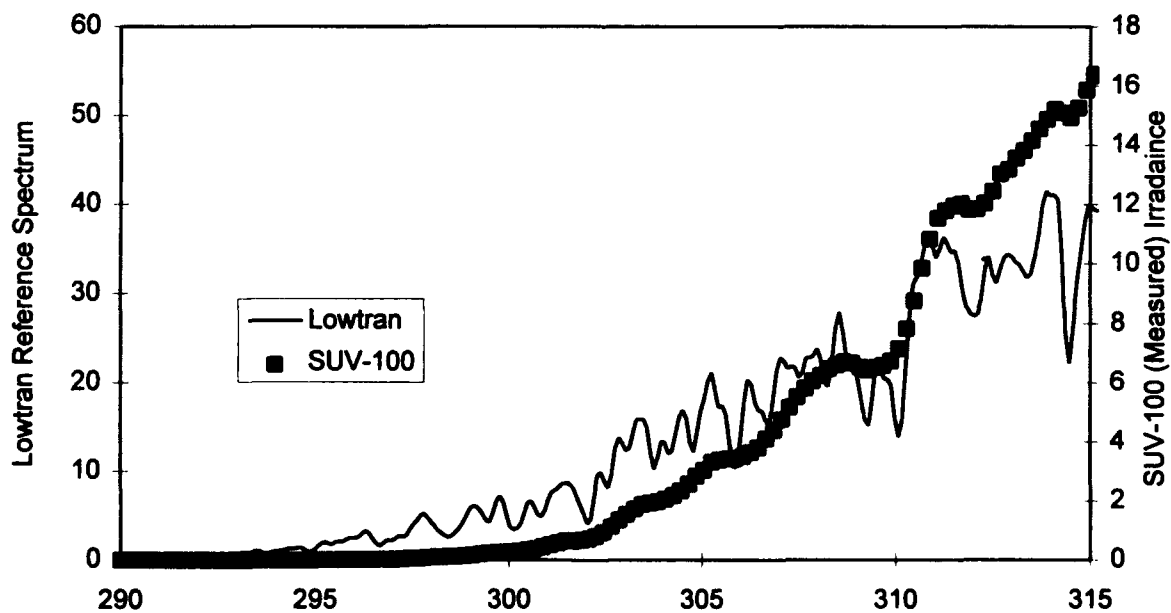


Figure 4. Comparison of Lowtran reference spectrum and SUV-100 measured spectral irradiance (microwatts/cm²/nm) whose results are displayed in Table 1.

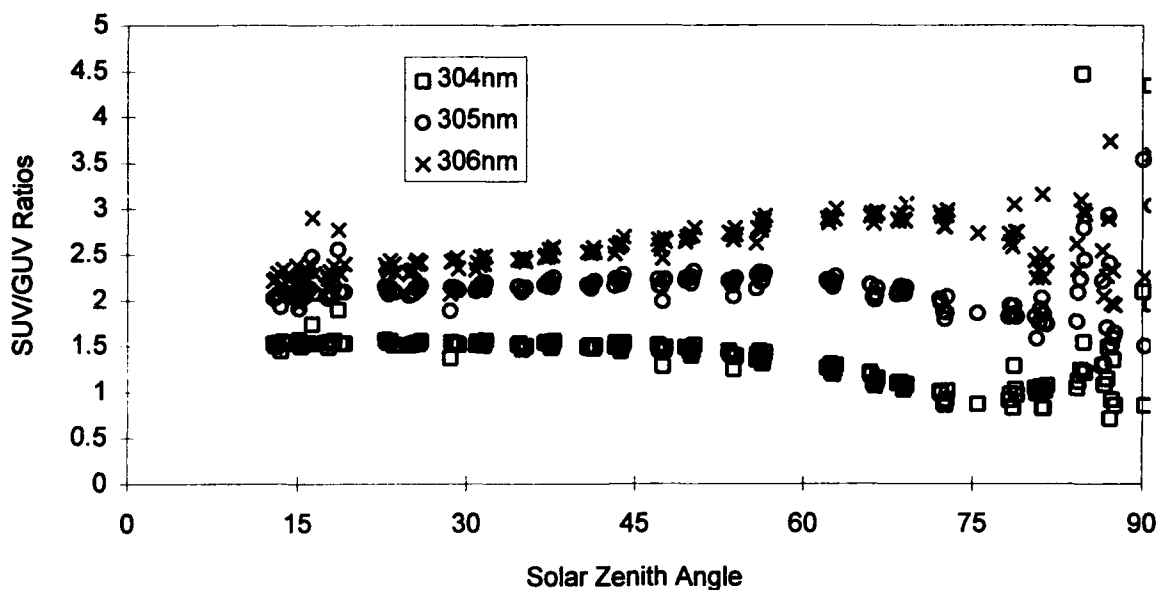


Figure 5. Residuals of the correlation of Scanning Spectroradiometer measured irradiance at 304, 305, and 306 nm with the 305 nm channel of the GUV filter radiometer. This is displayed against solar zenith angle to illustrate the impact of differing air mass and consequently differing ozone absorption.

5. SOURCE-SPECIFIC AND INTERCOMPARISON-BASED CALIBRATIONS AT 380 NM

In a fashion similar to that used with the 305 nm channel, an analysis was conducted at 380 nm. Details of this spectral region are shown in Figure 6. The intercomparison-based calibration regression is displayed in Figure 7, and the residuals are displayed in Figure 8. In this case the source-specific calibration constant worked quite well, but great care had to be used in extracting the wavelengths at 380 nm, a region where measured intensity changed by more than 10% per nm. Table 2 summarizes the results.

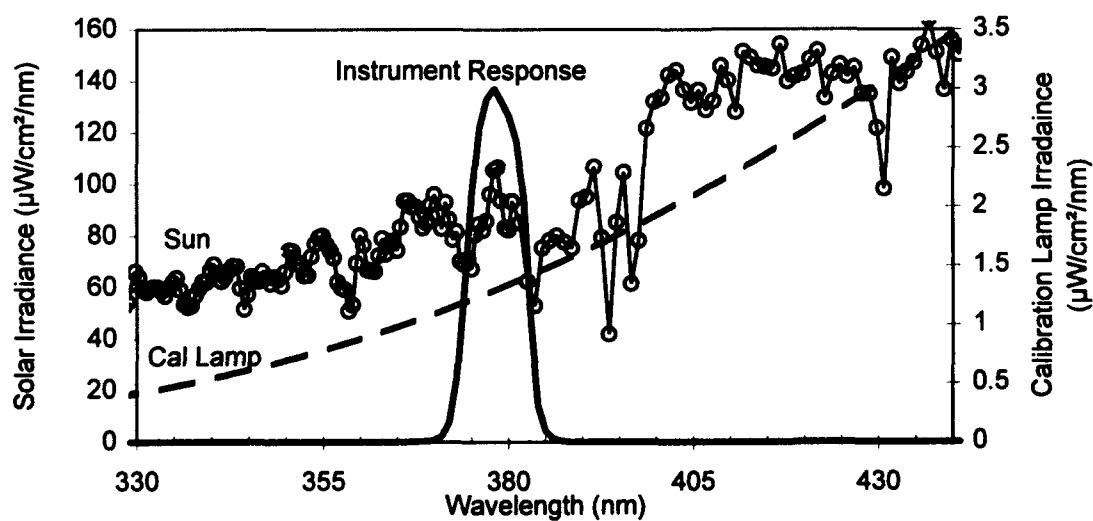


Figure 6. Comparison of target solar spectrum, calibration lamp spectral irradiance, and instrument response in the UV-A and blue regions.

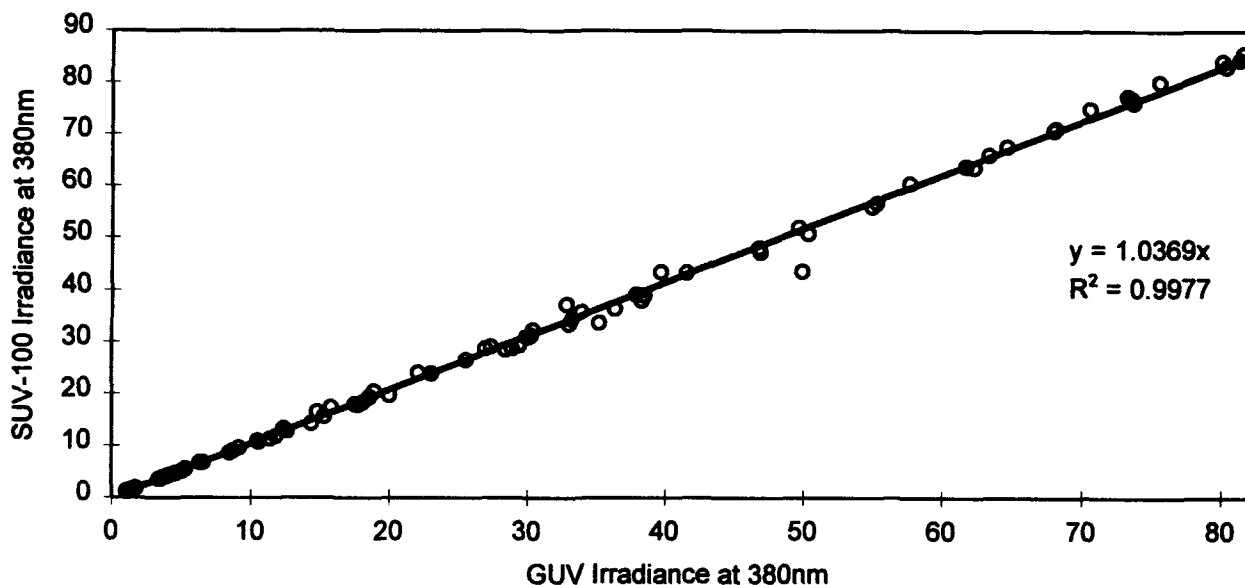


Figure 7. 130 daytime observations taken at San Diego, CA between 7/23/93 20:41 and 8/1/93 19:09. Used to derive the intercomparison or regression-based calibration constant. Regression equation and statistic are shown. Solar angles ranged from 13.6 to 89.4°.

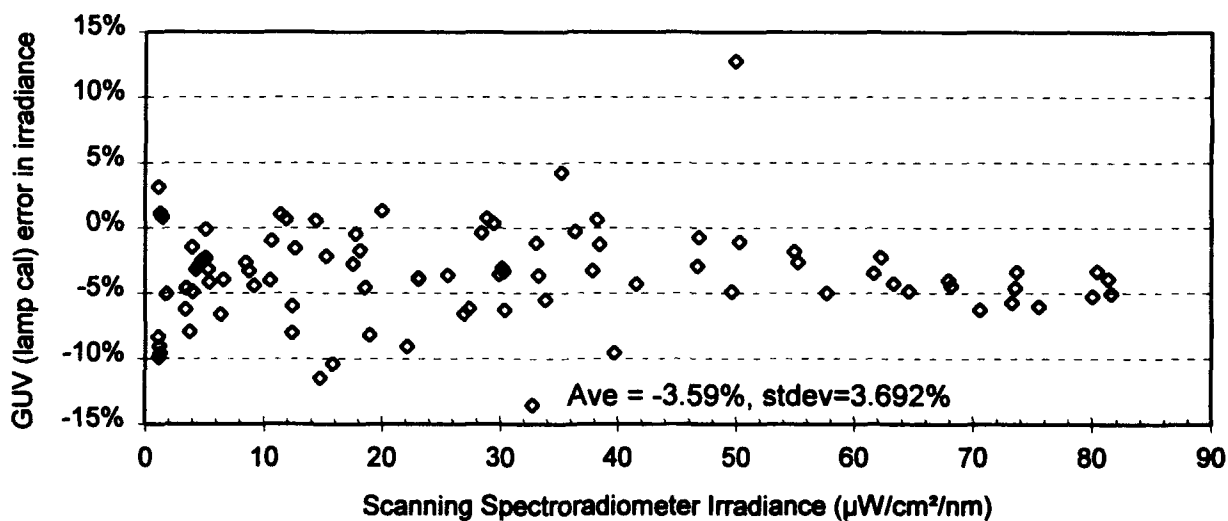


Figure 8. Errors in the irradiance measurements at 380 nm when using the lamp-based calibration constant.

Table 2. Contrast of calibration methods at 380 nm.

Irradiance Measure Source	$\mu\text{watts/cm}^2/\text{nm}$	Relative to SUV-100
SUV-100 (scanning spectroradiometer)	88.215	
GUV with lamp based calibration	91.331	4%
GUV with lamp based/source specific cal.	89.356	1%
GUV Irradiance based on regression with SUV-100	87.851	0%

6. UV Instrument Intercomparison - 305nm

When PUV/GUV instruments have returned to Biospherical Instruments for recalibration they have been run in parallel with the SUV-100A high-resolution system for purposes of intercomparison. Table 3 shows the results of this effort. It is divided into groups according to the filter revision used in the 305 nm channel. As expected, the ratio of the lamp-based calibrations to the spectroradiometer regression-based calibrations is different from unity. The final column expresses the difference of individual instrument in a group to the average of the group. The first group was composed of instruments using the earliest design filters employed, and shows an effective wavelength between 307 and 309 nm. The instrument designs were subsequently revised to employ a new filter technology, and the redesigned filter shows a statistical matching much closer to 305 nm. This is evident in the second and third groups. The difference of the significant wavelengths of 305 nm and 304 nm in these groups corresponds to the individually measured filter characteristics.

There are significant differences between instruments compared in this study. The results shown in Table 3, though clustered into groups, still show differences in both the "significant" wavelength, and in the ratio of the lamp to intercomparison-based calibrations. The reason for this difference is that the interference filters used in each instrument, although within specifications, are in fact not exactly identical. Figure 9 shows the solar convolution responses for two instruments representing the extremes in filter differences. From this figure it is apparent that to improve upon the $\pm 10\%$ spread in the ratios between lamp- and solar-based calibrations, it is necessary to conduct an intercomparison such as described here.

Table 3: Comparison of lamp-based calibration with solar-based calibrations.

Model	SN	Regress. Ctr WL	Lamp/Reg Cal Ratio	In-Group Contrast
Early Production and prototype models				
PUV500	9200	309	2.92	-2.5%
PUV510	9201	308	2.97	-0.8%
PUV500	9202	308	3.19	6.6%
PUV510	9203	307	2.90	-3.3%
Revision A Instruments - 1992 Filter Batches				
PUV500	9206	305	2.52	-3.8%
PUV510	9207	305	2.77	5.9%
PUV510	9209	305	2.79	6.6%
GUV511	9210	305	2.73	4.2%
PUV510	9216	305	2.57	-2.0%
GUV511	9222	305	2.34	-10.8%
Revision A Instruments - 1993 Filter Batches				
PUV500	9224	304	2.16	-8.1%
PUV510	9225	304	2.54	8.4%
GUV511	9226	304	2.44	3.9%
PUV500	9227	304	2.45	4.5%
PUV510	9228	304	2.14	-8.7%

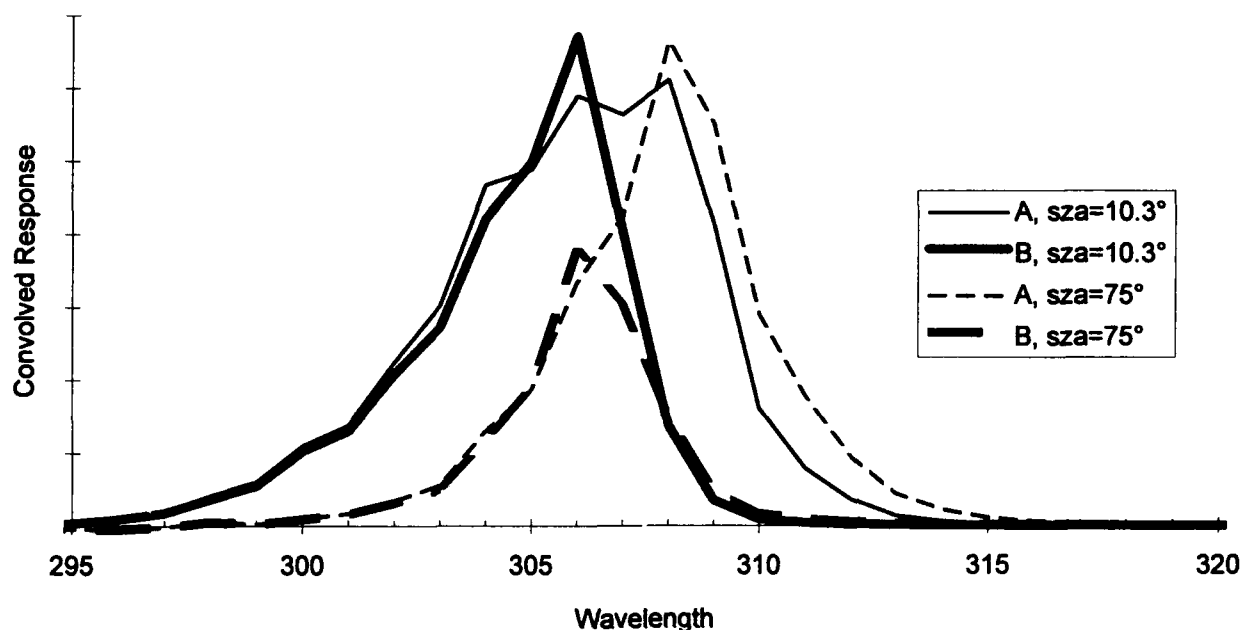


Figure 9. Convolution of the spectral response of two different GUV radiometers representing extremes ("A" and "B") of filters that may be used in GUV and PUV radiometers now being produced. Each of these is convolved with two different solar spectra, one at 10° and the other at 75° solar zenith angles (but with closely matching ozone concentrations).

7. CONCLUSIONS

Calibration of radiometers with bandwidths greater than 1 nm using lamp standards can yield significant errors when measuring solar irradiance, particularly in the UV. The use of a source-specific calibration constant, referenced to the solar spectrum, may reduce this error, but the procedure requires accurate knowledge (better than 0.1 nm in the wavelength domain) of the spectral response of the radiometer. A further limitation is that the Lowtran spectrum used as the specific source may not agree with spectra measured other ways. The performance of the source-specific calibration (referenced to Lowtran) is relatively good at 380 nm, but relatively poor in the UV-B where there are considerable differences in the solar spectrum due to atmospheric constituents (e.g. ozone). Finally, in highly complex parts of the spectrum the reference spectrum may deviate considerably from spectral irradiance determined using a scanning spectroradiometer due to bandwidth differences.

Hence, accuracy in the measurement of solar global spectral irradiance with narrow bandwidth spectroradiometers is extremely challenging and the best results are accurate to a few percent. Measurements using moderate bandwidth radiometers at the 1% accuracy level will remain challenging for some time to come. Research on the spectral response of such moderate bandwidth radiometers is an ongoing internal research program at Biospherical Instruments, Inc.

8. ACKNOWLEDGMENTS

Partial development of the PUV and GUV ultraviolet radiometers was funded under contract number N00014-88-C-0752 from the Office of Naval Research, under the Department of Defense Small Business Innovative Research program. Antarctic UV Irradiance spectra were made using the National Science Foundation, Division of Polar Programs, UV Monitoring Network operated by Biospherical Instruments. For details about the availability of these data consult C. R. Booth, Biospherical Instruments Inc. San Diego, CA.

9. REFERENCES

1. Booth, C. R., J. H. Morrow and D. A. Neuschuler. "A New Profiling Spectroradiometer Optimized for use in the Ultraviolet". SPIE Vol. 1750, Ocean Optics XI, pp. 354-365, 1992.
2. Walker, J. H., R. D. Saunders, J. K. Jackson, and D. A. McSparron. "Spectral Irradiance Calibrations". NBS Special Publication 250-20. U.S. Department of Commerce, 1987.
3. Lowtran. US Air Force Geophysics Laboratory, Hanscom AFB, Mass 01731-5000.
4. Booth, C. R., T. B. Lucas, and J. H. Morrow. "The United States National Science Foundation's Polar Network for Monitoring Ultraviolet Radiation". In Ultraviolet Radiation in Antarctica: Measurements and Biological Effects. Antarctic Research Series, AGU, V. 62, pp. 17-37, 1994.

SPATIAL DISTRIBUTION OF RADIATION NEAR THE SEA LINE IN THE MID-INFRARED REGION

Matsunaga Matsui, Shigeyoshi Tamashige*
and Shizuko Matsui**

Fukuyama University, Faculty of Engineering, Fukuyama, 729-02 JAPAN

* Okayama Polytechnic College, Kurashiki, 710-02 JAPAN

** Nara Saho-Jogakuin Junior College, Nara, 630 JAPAN

ABSTRACT

An accurate knowledge about the spatial distribution of infrared radiation near the sea line, is very important as the background when designing remote sensing or marine traffic surveillance system with infrared radiation for the use from the shore or ships. For this purpose, the distribution of infrared radiation from the sky and the sea surface near the sea line was measured by radiometer and scanner. Further, spatial distribution characteristics of infrared radiation were studied on meteorological models. As a result, it was confirmed that there was a high radiance zone of mid infrared region ($8 \sim 13 \mu\text{m}$) near the sea line. This was also confirmed by a simulation that was conducted at the same time using meteorological models. It was also confirmed that in the middle latitudes, because the width of that high radiance zone was broadening in summer, the marine traffic surveillance system which used the mid-infrared region provided poor images with very low contrast between islands, ships and the background so the images even disappeared.

1. INTRODUCTION

In passive infrared detection and surveillance systems, all the background radiation such as the radiation from sky, sea surface, ground surface other than the target brings about the lowering of the S/N ratio of the systems or the lowering of contrast in output images.

In the case of considering infrared remote sensing or marine traffic surveillance systems toward the direction of sea, generally the background in field of view is sky and sea surface having horizon at the center. This report is the summary of the results of observation in the last several years about the spatial distribution of infrared radiation in the vicinity of the horizon like this.

In middle infrared region ($8 \sim 13 \mu\text{m}$), the zone of high radiance exists in the vicinity of sea line, and in summer, this zone of high radiance extends consequently, the contrast of islands, ships and others to the background lowers in this wavelength region, and it was confirmed also that sometimes their discernment became impossible. Moreover, as to the zone of high radiance like this, it was supported also by the simulation using a weather model¹.

Beside, for the observation of infrared radiation distribution, infrared imager [(A) for $8 \sim 13 \mu\text{m}$ band, liquid nitrogen-cooled HgCdTe sensor, (B) for $3 \sim 5 \mu\text{m}$ band, electronically cooled HgCdTe sensor, angle of field of view is both $25^\circ \times 25^\circ$] and a filter type infrared spectro radiometer (interference filter: $3.3 \sim 4.7 \mu\text{m}$, $7.6 \sim 12.2 \mu\text{m}$, detector: pyroelectric type) were used.

2. INFRARED RADIATION DISTRIBUTION IN THE VICINITY OF SEA LINE

In Fig. 1, a part of the results of observation is shown. Fig.1(a) shows the example in winter, and Fig. 1(b) shows that in summer. It is indicated clearly according to the images in middle infrared region and the distribution of radiance at left end that at horizon, the radiance became the maximum. This phenomenon was particularly

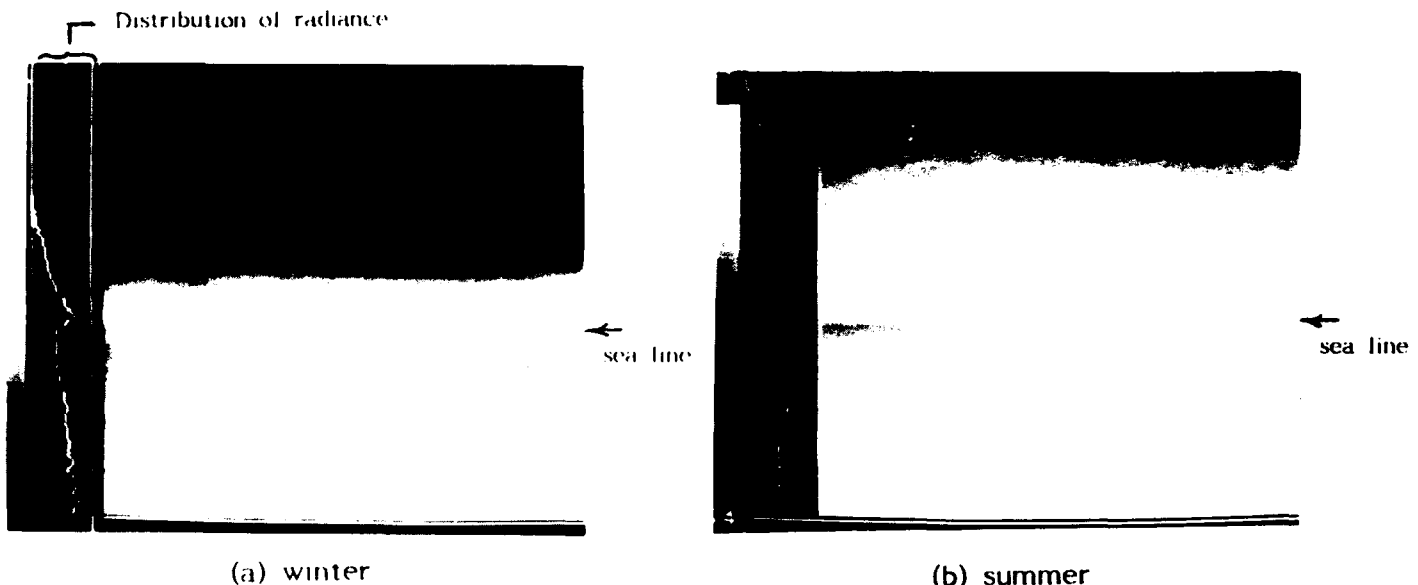


Fig. 1 Spatial distribution of radiation near the sea line
(Clear sky, $8\sim13\ \mu\text{m}$ band)

conspicuous in $8\sim13\ \mu\text{m}$ band, but in other wavelength region, it was not clear. For comparison's sake, in Fig. 3, an example of the results of measurement by using a filter type radiometer is shown.

According to the result of observation obtained so far, in western Japan, namely in the sea area of medium latitude, it was confirmed that there are summer type and winter type in the distribution forms of radiation in the vicinity of horizon. The feature of the radiance distribution in the vicinity of horizon in summer was, as shown in Fig. 1, that the zone of high radiance just above horizon was very wide as compared with that in winter. This fact means that the lowering of the contrast of the object of detection near normal temperature at the distance more than $2\sim3\ \text{km}$ to the background is remarkable, or it vanishes completely. Fig. 2 shows its one example, and Tashima and Yokoshima (both in the middle part of Seto Inland Sea) at the distance of $3\sim10\ \text{km}$ on the middle left side of the picture have become difficult to be discerned by the infrared images in summer as compared with in winter.

The cause of the lowering of contrast or vanishment like this mainly originated in the increase of the sky radiation at low elevation in the vicinity of horizon [N.(Z) in Equation (1) and (2) in Chapter 3, the infrared radiation from the atmosphere]. In winter, generally atmospheric temperature is lower than water temperature and ground temperature, and absolute humidity is low, therefore, it is considered that the transmissivity of the atmosphere which is the optical path becomes high, the atmospheric radiation increases rapidly in the narrow range which is very close to horizon, and the extent of the zone of high radiance also becomes narrow to less than 1° ($10\sim15\ \text{m rad}$). To the contrary, in summer generally atmospheric temperature becomes higher than water

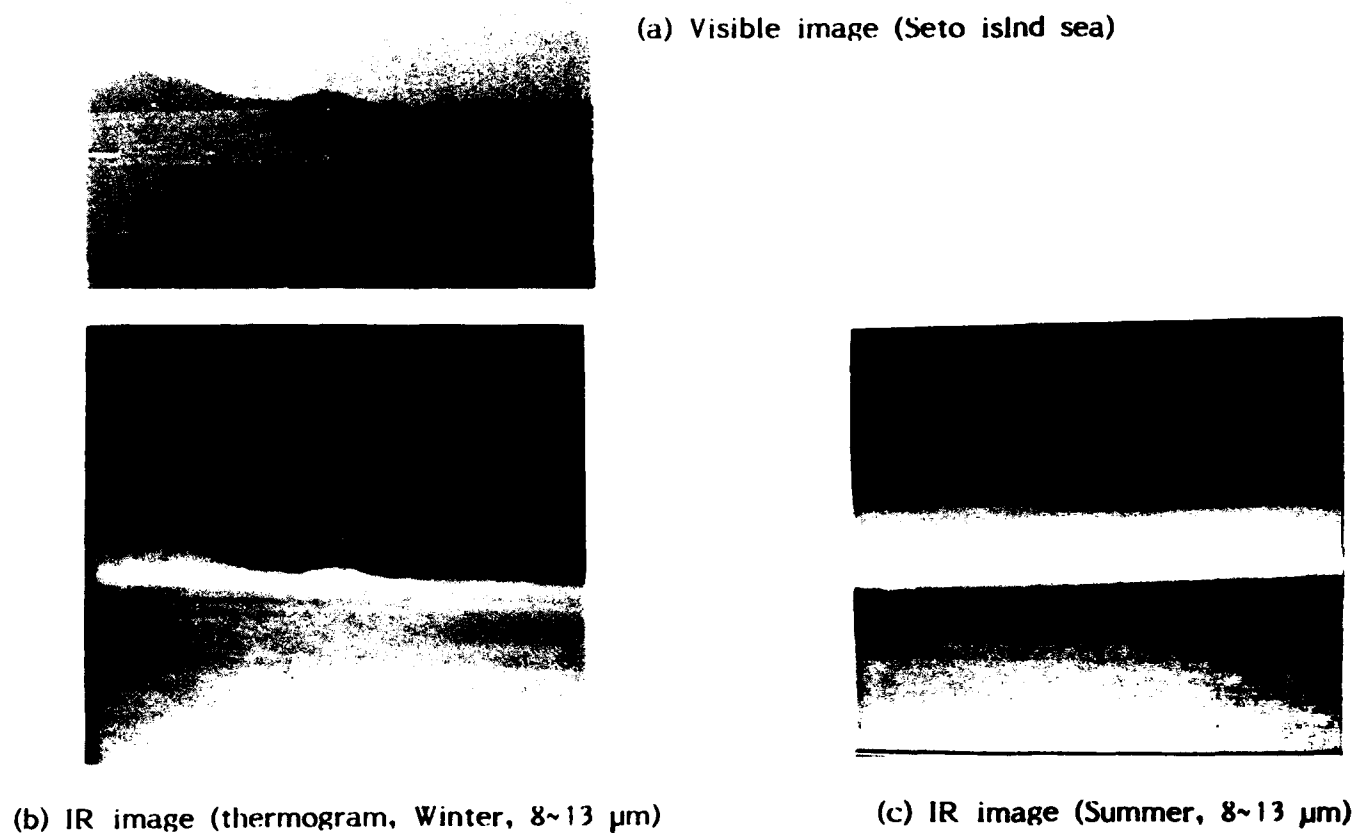


Fig. 2 The image of islands is disappeared in summer

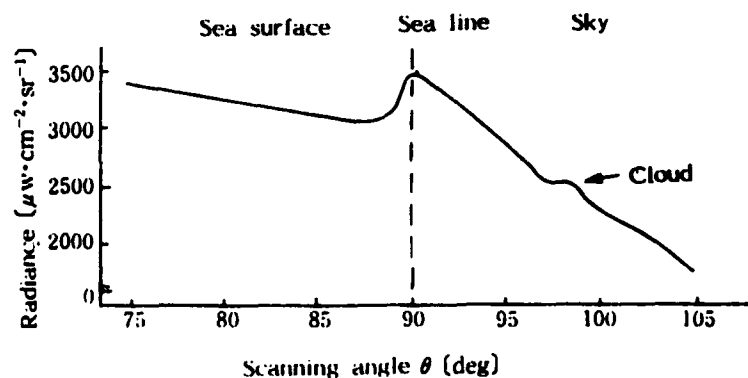


Fig. 3 The angular dependency of radiation from sea surface and sky
(Filter type radio meter, Summer, 8~12 μm band)

temperature and ground temperature, absolute humidity increases, and sky radiance is to exceed sea surface radiance. Namely, it is considered that as this zone of high radiance extends, the images of the objects of detection vanish, or the lowering of contrast is brought about. The width of the zone of high radiance in summer reached 3 ~ 4 times (3 ~ 4°, 50 ~ 70 m rad) as wide as that in winter, consequently, also island were to have been masked, not to mention ships.

3. INVESTIGATION OF RADIATION DISTRIBUTION BY USING METEOROLOGICAL MODEL

The radiance of the background $N_{b,z}$ in the vicinity of horizon as seen from the low position such as on seashore or on a ship as shown in Fig. 4 is expressed as follows in the range below horizon (the direction of sea surface).²

$$N_{b,z}(\theta) = N_w(\theta) \\ = \tau_a(\theta) \{ \epsilon_w(\theta) \cdot N_b(T_w) + \rho_w(\theta) \cdot N_s(Z) \} + N_a(\theta) \quad (1)$$

where τ_a : transmissivity of the atmosphere between sea surface and radiometer,
 ϵ_w : emissivity of water surface,
 N_b : radiance of black body equal to water surface temperature T_w ,
 ρ_w : reflectivity of water surface,
 N_s : radiance of sky,
 N_a : radiance of the atmosphere between sea surface and radiometer,
 $Z(=\theta)$: zenith angle
 T_w : water surface temperature.

Moreover, in the range above horizon (the direction of sky), since there is sky radiation itself, $N_{b,z}$ becomes

$$N_{b,z}(\theta) = N_s(Z) \quad (2)$$

Fig. 5(a) and (b) show the results of calculation determined by substituting the weather conditions in Table 1 into the above two equations, and when these distribution curves were compared with the results of observation in Fig. 1, both agreed qualitatively.

In this case, the factor that exerts largely the influence to the lowering of contrast and the vanishment is the distribution form of sky radiation (atmospheric radiation) $N_s(z)$, and in winter, it is

$$N_s(z) \approx N_b(T_a) \{ 1 - \exp(-\alpha_s \sec^{1/2} Z) \} \quad (3)$$

but in summer, atmospheric temperature becomes higher than water temperature, and humidity increases, accordingly, the second term in the above equation becomes nearly $\exp(-\alpha_s \sec^{2/3} Z)$. In Fig. 6, the zenith angle dependence of sky radiation is shown.

Besides, it is considered that the difference in the distribution forms of the measured values (Fig. 1) and the calculated values (Fig. 5) in the range of scanning angle of 80 ~ 90° (the part just before horizon) is due to the assumption of the sea surface with wind and waves as the mirror surface of reflectivity ≈ 1 .

4. VARIOUS CHARACTERISTICS OF THE ZONE OF HIGH RADIANCE

Based on the data of the observation carried out several times so far, investigation was performed from various angle on the mechanism of the occurrence of the zone of high radiance. The results are summarised as follows.

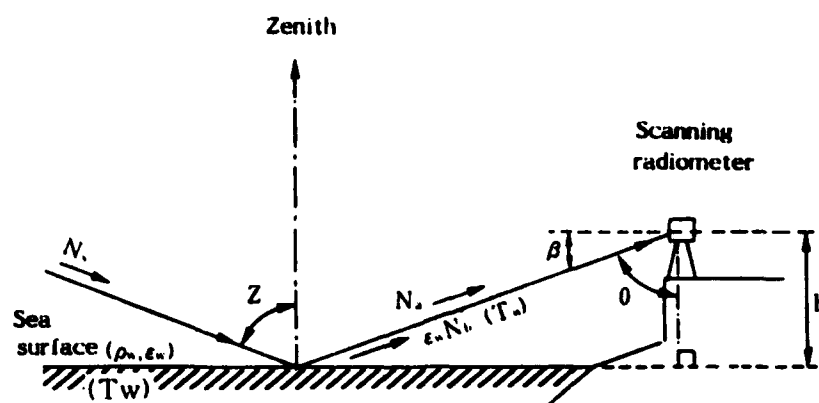
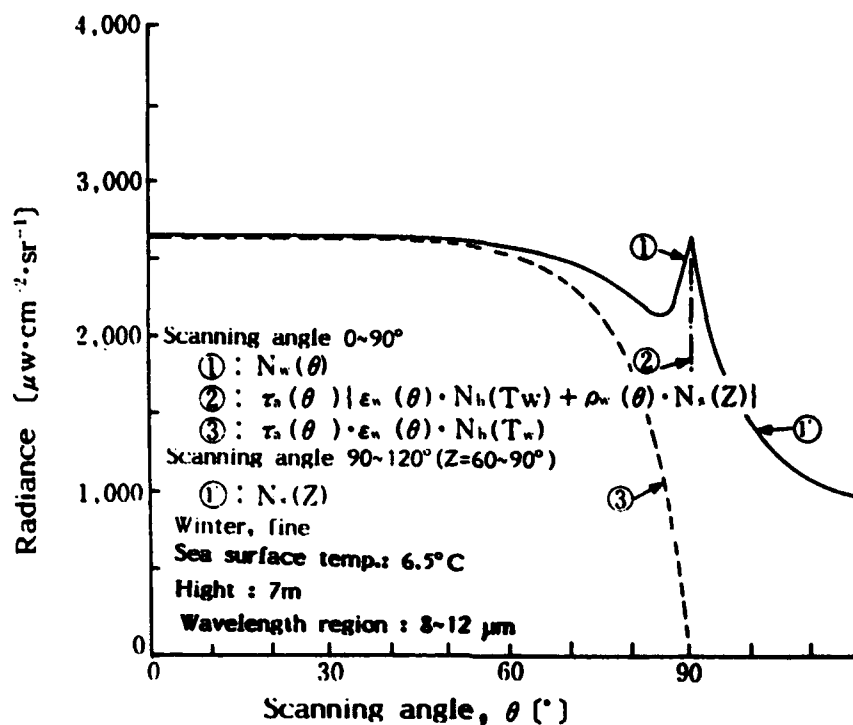


Fig. 4 The relation between incident radiation and radiometer

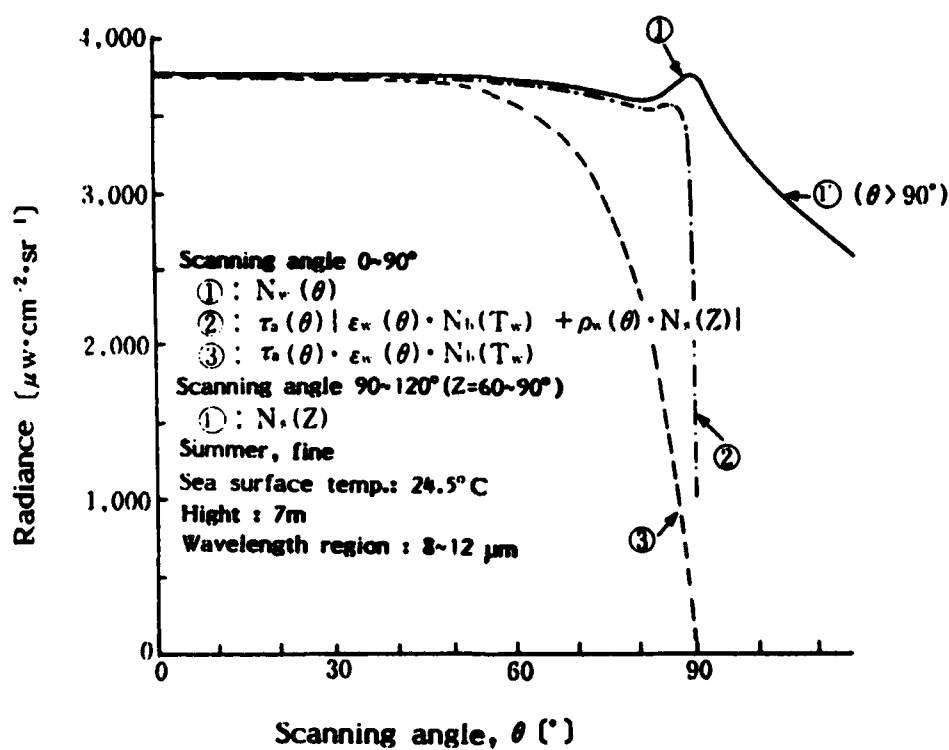
Table 1 Meteorological model

	Winter	Summer
Sea surface temp. [°C]	8.0	24.5
Air temp. [°C]	6.5	26.0
Relative humidity [%]	64.0	58.0
Weather	Fine	Fine

- (1) The zone of high radiance is the phenomenon peculiar to low positions, and with the increase of altitude, the peak of radiation became small. As its cause, whereas the reflection component of sky radiation at low elevation is dominant at low positions, in the case of high altitude, it is considered because it depends largely on the atmospheric radiation at relatively low temperature between sea surface and the points of observation.
- (2) In summer, the zone of high radiance in the vicinity of horizon extended, and its width reached 3 ~ 4 times as wide as that in winter (seasonal change).
- (3) The zone of high radiance in the vicinity of horizon is the phenomenon peculiar to the wavelength region of 8 ~ 13 μm .
- (4) In the distribution forms of the zone of high radiance in the vicinity of horizon in summer, there was some difference according to sea areas, but all were the distribution form of summer type with wide width.
- (5) In the period when atmospheric temperature and water temperature became equal, sometimes the zone of high radiance vanished. (It is presumed as late spring and early autumn in the sea areas at medium latitude.)



(a) Winter



(b) Summer

Fig. 5 The results of calculation determined by substituting the meteorological models

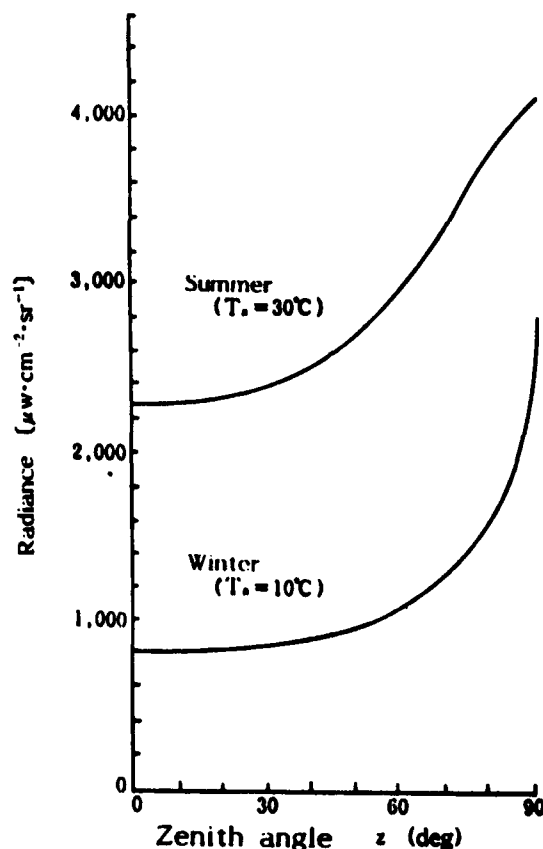


Fig. 6 The zenith angle dependency of clear skyradiation (8~12 μm band)

5. CONCLUSION

Sea surface radiation changes largely according to the positions of observation. In the case of looking down from sky, the radiance was nearly constant in the range of 45° from vertically downward, but in more than 45° , the reflectivity became high, and the effect of sky radiation became large. In the case of the points of observation being low positions, horizon (the angle of reflection $\approx 90^\circ$) becomes the center of visual field, therefore, the value becomes close to 1, and in the vicinity of horizon, the zone of high radiance was formed due to the sky radiation close to black body radiation level (= atmospheric radiation). The distribution form in vertical direction of this zone of high radiance was narrow width and pointed in winter, and trapezoid of wide width in summer. In summer, due to this zone of high radiance peculiar to mid infrared region, it is not rare that the distant view at more than 2 ~ 3 km is completely concealed. It was pointed out that this peculiar atmospheric effect becomes the large hindrance to the infrared detection and surveillance systems for sea surface.

REFERENCES

1. M. Matsui, et al., "On spatial distribution of infrared radiation near the sea line" Joint Convention Record of Chugoku Branch of Electrical Engineering Institutes, No.100616, 1984; No.020606, 1985; No.040621, 1986.
2. M. Matsui, "Angular dependency of sea surface radiation in the middle infrared", J. Illum. Engng. Inst. Jap. Vol. 59, pp. 468~471, 1975.

Remote sensing investigations of dissolved organic matter and chlorophyll fluorescence fields

Vladimir I. Repin, Eduard G. Goncharov, Olga I. Repina

S.I. Vavilov State Optical Institute
St.-Petersburg, Russia

ABSTRACT

Simultaneous studies of dissolved organic matter and chlorophyll "a" fluorescence intensity horizontal distributions were carried out by the method of a remote-acting laser fluorometry in the eastern part of the Black Sea. Investigations of upwelling radiation spectra from the subsurface layer of a sea water in a passive mode were carried out also. A computer program for graphic representation of the data statistical processing results was created. Correlation functions of the distributions were studied. Some results of experimental data processing are represented as isolines at electronic maps of sea areas under consideration. The existence of spatial nonuniformities with a different scale in the fluorescence fields was found to take place. Multipurpose applications of the multi-channel analyzer of spectra are discussed.

1. INTRODUCTION

Some results of data processing of experimental investigations carried out in 1989-1993 in the Black Sea are presented in this paper. Besides we present here some results of our early studies, which were taken with water samples at a laboratory setup in 1986, to compare with last works. Data as regards 1989-1991 were collected by a three-channel remote-acting laser spectrometer and data as for 1993 were acquired from a multi-channel fluorometric lidar. As a whole, our investigations were devoted to study spatial inhomogeneities in the horizontal distributions of water fluorescent constituents such as dissolved organic matter (DOM) and chlorophyll "a" of phytoplankton. The field sea studies of DOM and phytoplankton chlorophyll "a" fluorescence were carried out by a remote sensing technique aboard research ship (RS), specially designed and equipped for hydrological investigating, in coastal waters off the Crimea and the Caucasus.

2. EXPERIMENTAL SETUP

In our experiments measurements were produced through a trunk designed in the hull of RS to except surface wind waves and specular sun-glints influence and also to decrease to a considerable extent influence of ship's rolling and pitching oscillations as the trunk was almost in the central part of the ship near its axial line. The trunk was situated in a laboratory compartment and presented itself a hole through the hull of the ship, having a square cross section 1m x 1m, a distance apart the top of the trunk and the sea surface being about 3.5 m.

At the three-channel laser spectrometer measurements were accomplished in one of two modes: either in the mode of time series, when DOM and chlorophyll "a" fluorescence intensity dependences vs time were recorded simultaneously (so named "time selection" mode), or in the mode of wavelength scanning, when spectra of radiation were recorded by turning of a diffraction grating (so named "spectral survey" mode).

At the multichannel fluorometric lidar an integral spectrum of radiation was recorded by accumulating signals simultaneously in 256 channels. Next spectra processing gives an opportunity to derive dependences of radiation intensities vs time in each of 256 spectral channels with time averaging 1 up to 128 sec, that corresponds to number of storage cycles 1 up to 128 (at 1-Hz repetition rate). An excitation of a secondary radiation was induced by a pulsed frequency-doubled Nd:YAG-laser with output at 532 nm at both installations. It should be noted, that in the multichannel equipment the collinear, i.e. wholly coincident, arrangement of the receiver and the laser optical paths

was employed, and also a small-sized polychromator having a considerable light-grasp, was applied. The employment of this design gave an opportunity to diminish losses at recording useful signals. The polychromator designed and produced in State Optical Institute presents itself a spectrograph with a plane field (of the exit window), the relative aperture 1:3, the wavelength range from 380 to 800 nm. The main unit of the polychromator is a concave unclassic diffraction grating ($N = 450 \text{ mm}^{-1}$) having a radius of curvature 100 mm. The plane of exit window of the polychromator is made to coincide with the plane of entrance (cathode) fiber plate (FP) of an image-intensifier tube, and the plane of its exit FP (at the side of a luminescent screen) is made to coincide with the plane of entrance window of a linear charge-coupled device (CCD) having 1024 elements, but each four sequential elements are coupled together by an electronic way, therefore at recording photosignals there were 256 spectral channels with the wavelength width less 1 nm. In the rest this installation seems to be similar to that described in the paper of D. K. Bunin et al.¹ The first remote-acting apparatus from those mentioned above presented itself a program-controlled complex with a laser excitation of fluorescence and a three-channel receiving system. The excitation was produced by a pulsed YAG:Nd - laser at 532-nm wavelength and 10-Hz repetition rate. The duration of pulses was approximately equal 15 ns, the pulse energy was about 300 kW. The large turning mirror was employed to direct the laser beam towards the sea surface at the angle about 1° off nadir. Secondary radiation intensities were recorded by three photomultipliers (PMTs) simultaneously in three wavelength regions, corresponding to maxima of DOM fluorescence intensity (560 nm), phytoplankton chlorophyll "a" fluorescence intensity (685 nm) and water Raman scattering (651 nm). In our investigations we employed the water Raman scattering calibration (so named "method of internal bench mark")². It was used to compare studies results carried out by us during some years and by other authors also. Integrated signals of fluorescence intensity from an upper layer of the sea (from the surface to the maximum depth of a remote-sensing operation) were recorded by the receiving system. Measurements were realized adrift and on the move (with the average velocity 6 knots). The duration of one record was 5 minutes, that accorded 300 points of measurements at 10-Hz laser pulses repetition rate and the averaging among 10 pulses). A computer program was created to process data massives, characterizing DOM and chlorophyll "a" fluorescence intensities (and represented as time series with constant discreteness). This computer program produced a calculation and graphic representation of statistical characteristics of initial realization simultaneously for series of experimental records ("time selections"), corresponding a time interval near 1 hour. Results of data processing were represented as graphics of averages and dispersions of DOM and chlorophyll "a" fluorescence intensities (for different scales) and also autocorrelation functions, spectral density and cross-correlation functions for DOM and chlorophyll "a" distributions. Mapping DOM and chlorophyll "a" fluorescence fields was carried out for the limited area of studies (10x10 miles). Wavelength studies of backscatter signals were carried out along with the time studies. A spectra record was realized by diffraction grating scanning. The data received for DOM fluorescence band were in a consent with values of the fluorescent parameter Φ_0 calculated³ for the surface layer, that confirms a high stability of wavelength characteristics of DOM fluorescence in the area under consideration. All cycles of studies were accompanied by measurements of hydrology parameters.

3. DIRECTIVITY AND PROBLEMS OF SEA FIELD STUDIES

At carrying out sea field studies a principal attention was given to searching for nonuniformities over the microscale ($10^0 - 10^2 \text{ m}$) and near meso-scale ($10^2 - 10^4 \text{ m}$) ranges in distributions of DOM and phytoplankton chlorophyll "a" fluorescence fields, that represented an interest both for ecologic problems (in particularly, to detect the source of pollutions of sea and other basins) and more thorough understanding of sea organisms species functioning (feeding on plankton) with the aim of increasing fishery efficiency. It is known, that in the open ocean mass abundances of algae and sea organisms are often occurred nearly temperature fronts or frontal interfaces. Over and above, it is found to be an occurrence of fronts connected with vortical motions of waters or diverse disturbances of fields of hydrophysical characteristics, including on those in meso-scale range ($10^2 - 10^4 \text{ m}$). However, inhomogeneities in micro-scale range of phytoplankton and DOM distributions

near similar disturbances have been studied far worse as yet. Our early investigations carried out at a laboratory setup with water samples (gathered by a bathometer) in April, 1986 demonstrated a presence of considerable inhomogeneities in horizontal and vertical distributions of DOM fluorescence field near the estuary of river Bzyb in the south-eastern part of the Black Sea (Fig. 1). This work was devoted, in particular, to study river flows and coastal currents influence on forming horizontal distributions of phytoplankton and DOM in coastal areas of the Black Sea.

4. FACTORS, INFLUENCING ON FORMING DOM AND PHYTOPLANKTON DISTRIBUTIONS

Forming DOM and phytoplankton natural distributions results from joint effect of many factors, the main ones of which are irradiance, availability of nutrient medium (in a general significance), temperature etc. Besides, forming and variability of natural distributions are influenced on currents, convectional motions of waters, wind actions, "activity" of objects to be dealt with (i.e. their ability to oppose against variation of external conditions), et al. As the result of integral influence of these factors (in particular, upwelling due to convection) relocations of phytoplankton and DOM can be the case in the sea surface layer. In the sea area in question (near cape Pitzunda) DOM and phytoplankton distributions are formed by a combined effect of some key factors. In particular, river Bzyb influences considerably on a character of these distributions, as its cold waters along with sea waters make layeringous structure in the surface layer (with exchangable layers of warm sea and cold river waters). Influence of river Bzyb was measurable at a distance up to 15 - 20 miles from estuary offshore. Another important factor is a great surface current along coastline, direction of which is changed during a day.

The vertical distributions of hydrology parameters T, S, P have a strictly expressed stratification. In summer and in the beginning of autumn a season thermocline is on depth 15 - 30 m, an upper layer is quasihomogenous, well-exchangable (in steady-state zones), a lower layer has temperature about 7° C. To the end of autumn the layer depth (of thermocline) increases to 35 - 40 m and its slowly continuous "smearing" along depth takes place.

On the whole, one can say, that (in conjunction with irradiance and biogenous elements, to influence on the pattern of the distributions) in the region to be studied DOM and chlorophyll fluorescence fields distributions are formed also as the result of interaction of some additional factors (currents, river cold waters aiming-off, internal waves, et al.) leading, in particular, to convectional motions, which, in turn, can give rise to relocations of phytoplankton and DOM in the sea surface layer. It should be remarked, that at carrying out point-detection measurements it was experimentally found a layeringous structure (along a vertical) having a speckled pattern of horizontal distributions. They had a quasi-symmetric structure (along a horizontal) with axis, direction of which had a slight displacement (on current velocity field) in relation to aiming-off direction of the river Bzyb waters.

5. RESULTS OF EXPERIMENTAL STUDIES

The results of data processing of experimental studies are represented in Figures. These data were collected when the vessel moved along intended route, the spatial resolution being about 30 m (averaging among 100 laser pulses). There are plots of DOM (channel 1) and chlorophyll "a" (channel 2) fluorescence intensity vs time in Fig. 2.

These dependences have a quasi-periodic pattern with periods about 30 and 50 sec., that corresponds to distances about 90 and 150 m along the route of the move of the vessel, variations of signals being 20% for DOM and 5% for chlorophyll respectively. This periodicity seems to result from the internal waves influence on horizontal distributions of DOM and phytoplankton.

A complicated pattern of the time dependences of fluorescence signals and related with that hardships of an identical interpretation of experimental data stimulated a search for some derived parameters of fluorescent fields, which could be used to characterize inhomogeneities of those and could be compared in an order of the value both for DOM and chlorophyll "a". As a such parameter of

fluorescent field we selected a ratio of the dispersion to the average of fluorescence intensity. A value of this parameter was found to be in the order of a value of the fluorescent parameter Φ_0 .

In Fig. 3 the values of this parameter D/M are plotted vs time for channels of DOM and chlorophyll "a" based on experimental data of fluorescence intensity, represented in Fig. 2. We notice here, that a pattern of variations of the parameter D/M distinguishes from that of time series of fluorescence intensity. Such as, maximum of fluorescence field inhomogeneity, being characterized by maximum of parameter D/M , is related to PROF38 ($t = 15.27$) both for DOM and for chlorophyll "a", whereas maximum of DOM fluorescence intensity is remarked for PROF19 ($t=11.58$), and maximum of chlorophyll "a" fluorescence intensity - for PROF16 ($t = 11.30$). As distinct from that it is found to be almost a complete analogy between pattern of changing of integral (when averaging among 3000 laser pulses) values of "inhomogeneity" parameter D/M for DOM and chlorophyll "a", with, may be, a slight time lag of the beginning of parameter D/M variation for chlorophyll as compared with that for DOM.

Figs 4 and 5 are illustrated results of experimental data processing collected in coastal zone the last of September, 1991. There are shown isolines of DOM and chlorophyll "a" phytoplankton fluorescence intensity in Fig. 4. Isolines of parameter D/M are added in Fig. 5 for the same cycle of measurements.

In Figs 1a, 1b, 1c isolines of fluorescent parameter F for DOM are showed, that represent the results of experimental data processing, acquired in April, 1986 near the same area. They result from 20 marine stations data processing. There are plots for horizontal distributions of DOM at three depths 5, 10 and 20 m respectively here. They are apparently demonstrated an influence of a river flow on forming spatial distributions of DOM (in particularly, it is noticed what there is a quasi-symmetry of distributions as relative to the direction of the river flow if it is took in account the offset due to an effect of considerable sea coastal currents.

Our last cycle of works was carried out at the sea area not far from Feodosia gulf in October, 1993. There upwelling radiation spectra were acquired in a passive operating mode of the fluorometric lidar complex. The lidar receiver permitted to record radiation spectra over the wavelength range from 490 to 710 nm with a spectral resolution about 1 nm. In these measurements a width of entrance slit of the polychromator was 0.25 mm, that corresponded a wavelength resolution 4-5 nm. Upwelling radiation spectra were acquired in day and in evening. Representative spectra presented themselves wide bands with two maximums (at 504 and 533 nm) and a slight trough between them ("twohump-shaped" band) having a long-wavelength limit near 600 nm. In evening (just after sunset) "red-wavelength" limit tended to displacement towards more short wavelengths up to 5-6 nm, and in the rest a shape of the band was quite similar that as it was in day.

6. CONCLUSIONS

1. In region of the Black sea in question DOM and chlorophyll "a" phytoplankton fluorescence fields have dynamic character.
2. Principal factors, influencing on forming DOM and phytoplankton distributions, are current along coastline, that changes its direction during a day, and aiming-offs of river Bzyb, resulting in convectional motions of sea waters in a zone of mixing (intensive water-exchange) with river waters.
3. For characterizing a degree of the inhomogeneity of fluorescence fields (micro- and meso-scale ranges) in zones with complicated hydrologic situation parameter D/M (ratio of dispersion to average of fluorescence intensity) is suggested to use.

7. REFERENCES

1. D. K. Bunin, M. Yu. Gorbunov, D. V. Zilimov, Ya. V. Uvenkov, V. V. Fadeev, A. M. Chekalyuk, A. V. Chechendaev, "Laser remote sensing of phytoplankton and organic admixtures in the Black sea coastal zone", *Physics of Atmosphere and Ocean*, Vol. 29, N. 1, pp. 131-139, 1993.

2. D. N. Klyshko, V. V. Fadeev, "Remote determination of admixtures concentration in water by laser spectroscopy technique by using the water Raman scattering calibration", Reports Academy of Sciences, Vol. 238, N. 2, pp. 320-323, 1978.

3. E. I. Krasovsky, V. I. Repin, V. M. Sidorenko, E.V. Baulin, "A semiempirical method of impurities quantitative definition in a sea water by fluorimetric lidars", Oceanology, Vol. 30, iss. 6, pp. 1027-1030, 1990.

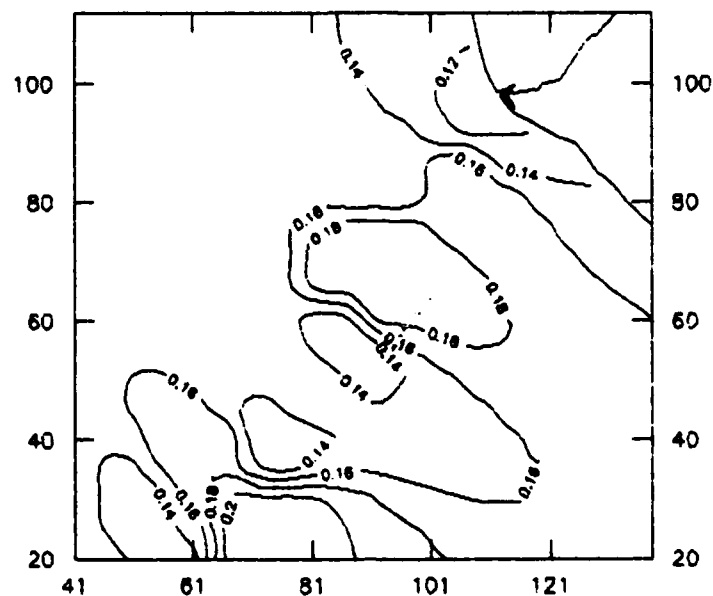


Fig.1a The isolines of fluorescence parameter ($h=5m$).

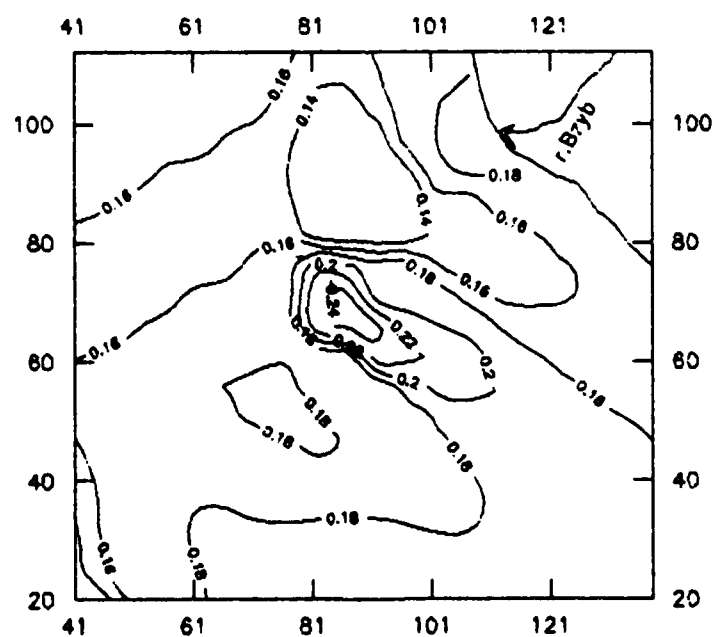


Fig.1b The isolines of fluorescence parameter ($h=10m$).

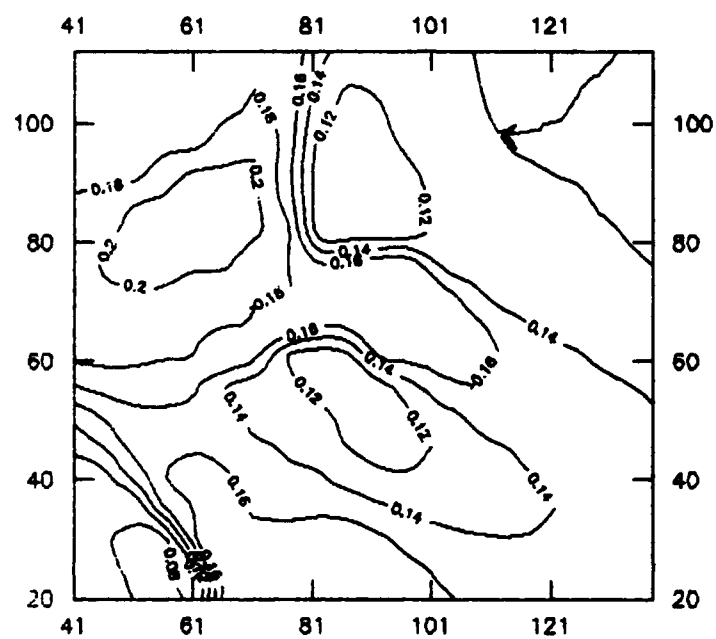


Fig.1c.The isolines of fluorescence parameter ($h=20\text{m}$).

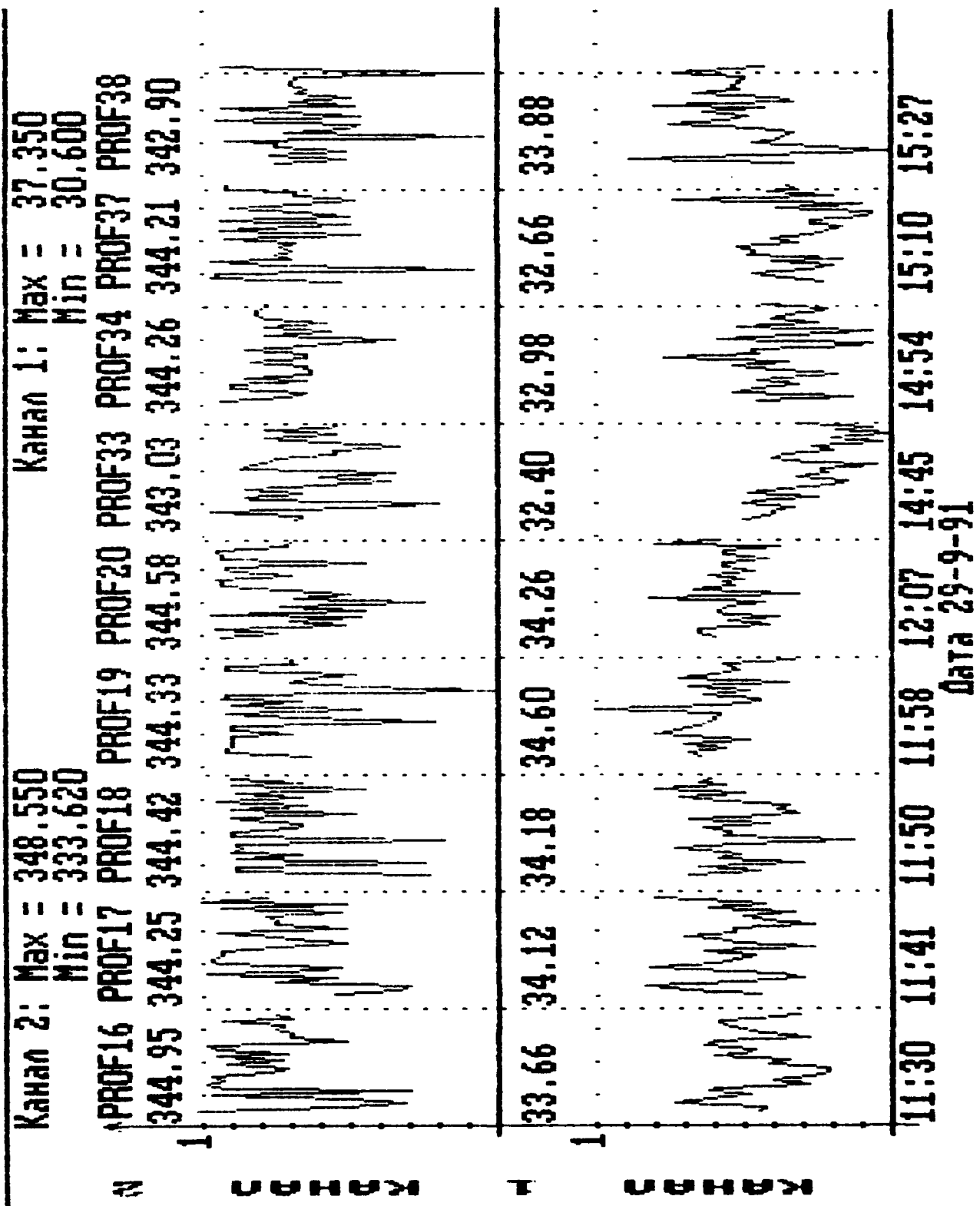


Fig.2. Left plot - chlorophyll, right plot - DOM.

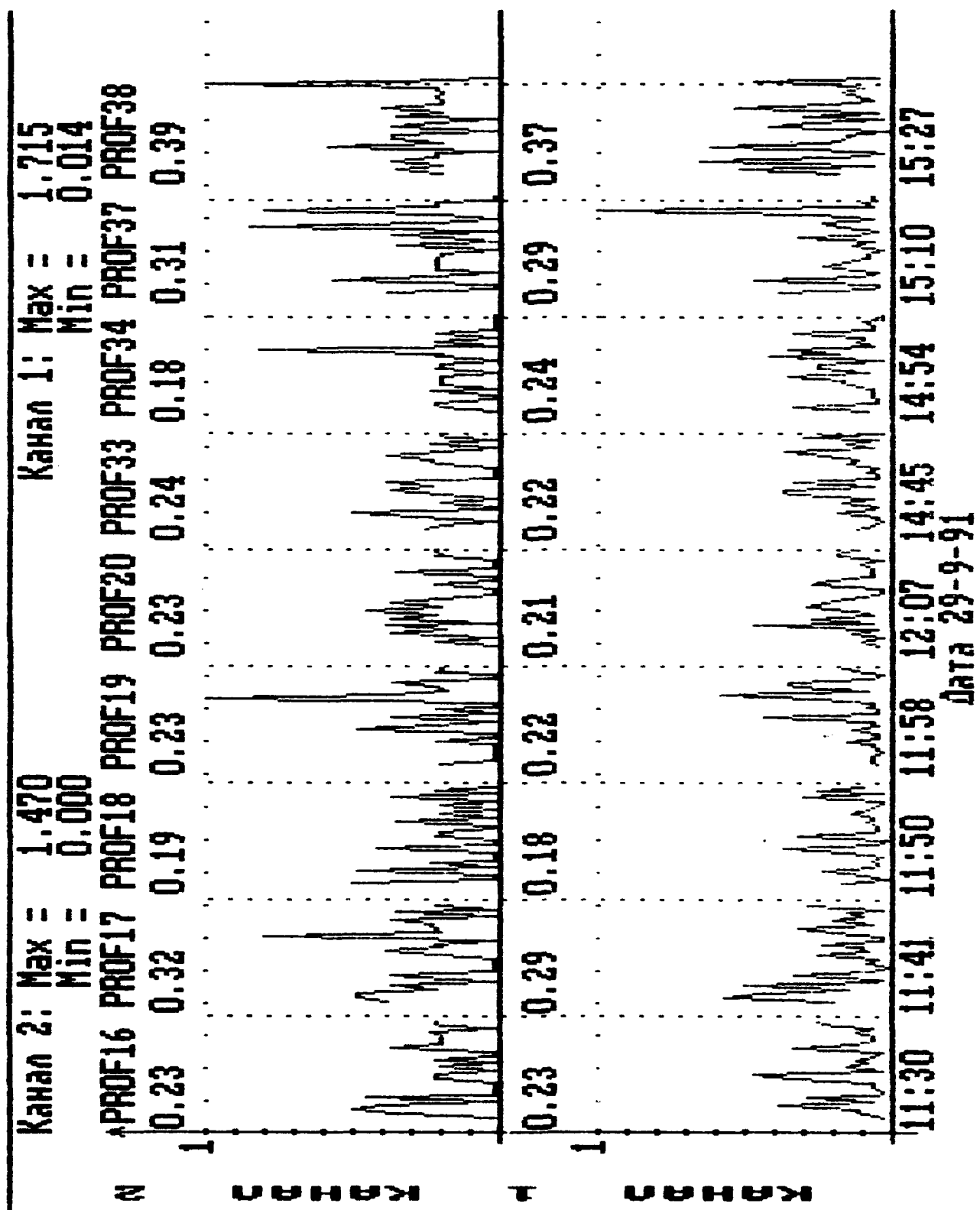


Fig.3. Plots of D/M (left - chlorophyll, right - DOM).

Fig.4. Isolines of fluorescence intensity (DOM).

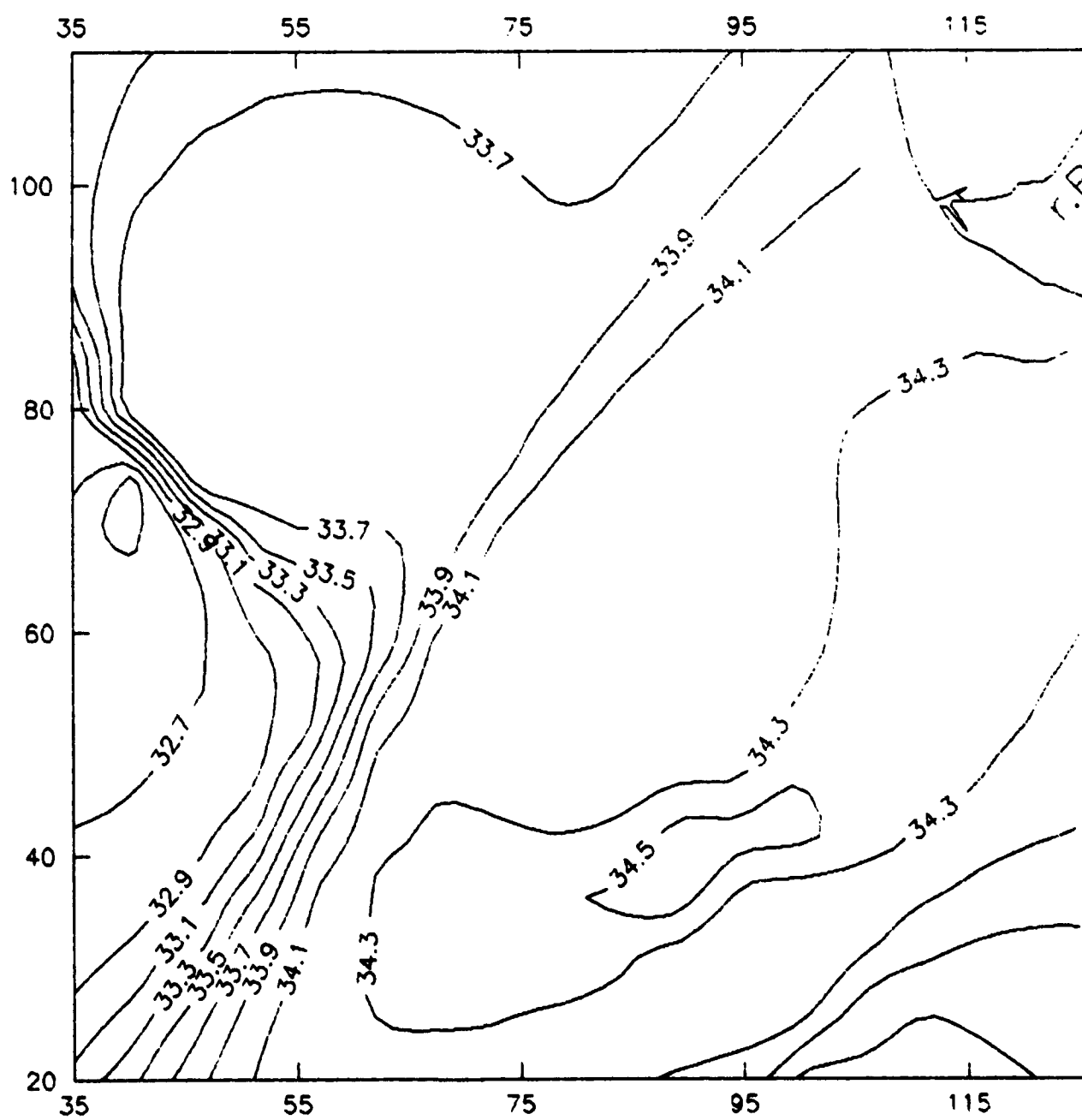
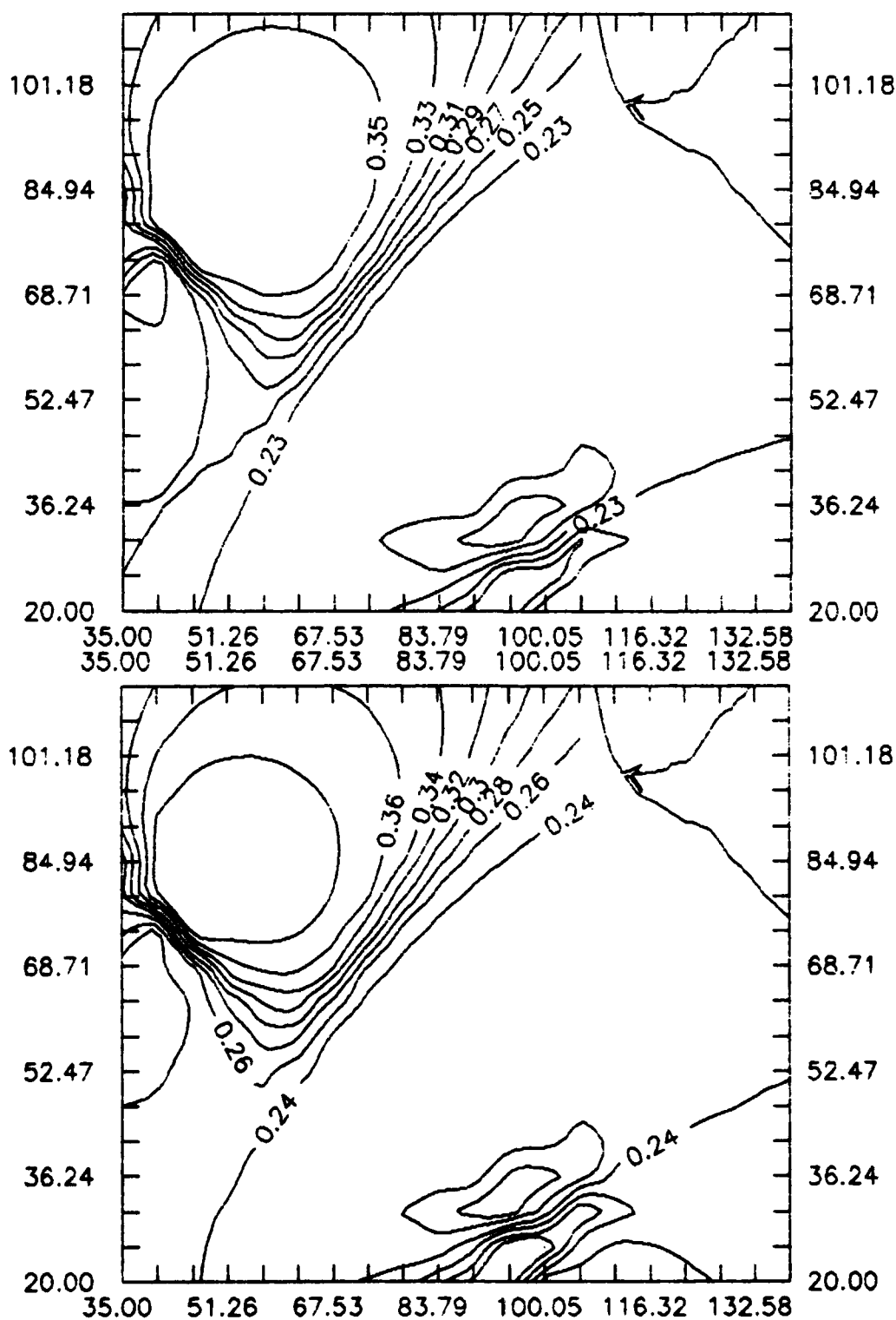


Fig.5. Isolines of D/M (top-DOM, bottom-chlorophyll).



Photometry of optical fields of the upper layers of seawaters

I.V. Aleshin, E.A. Tsvetkov

S.I. Vavilov State Optical Institute
Department of Hydrooptics & Thermovision
3 Pochtamskay st., St-Petersburg, Russia 190000

V.N. Ryabova

St.-Petersburg University, Biological Institute
7/9, University embankment, Russia, St.-Petersburg, 199053

ABSTRACT

The problems of sea ecological monitoring are discussed. It's established that identical operative estimations of situation in coastal regions can be made with the aid of in situ measuring of total (integral) ecological parameters. The examples of such estimations are given. Peculiarities of remote sensing applications in colored and turbid waters are examined.

2. INTRODUCTION

Ecological monitoring of humic loaded waters can be carried out in two stages.¹ The first in situ (operative) stage includes:

- the operative estimation of the general ecological situation,
- the discovery of humic anomalies and the study their dynamics,
- the determination of integral ecological parameters (IEP).

Usually, on this stage remote and contact sensors from quick carriers are used.

The second (sanitary) stage includes:

- the identification of pollutions in discovered anomalies,
- the determination of specific pollution contents. Traditionally, on this stage the analytical laboratory techniques are used to investigate water samples.

Described two-stages ecological monitoring makes it possible to cut down time measuring and expenditures.

3. METHODS

The advantages of multispectral optical sensors compared with any other integral ecological ones are in possibility of the adaptation for specific pollutions. The modern laboratory analytical technique provides measuring all of water ingredients and admixtures. But in situ one has occasion to use IEP of water, for example:

- temperature,
- electroconductivity,
- pH,
- dissolved oxygen concentration,
- Secchi disc visibility,
- color index, spectral transparency,
- fluorescence of phytoplankton pigments (PPP) and dissolved organic materials (DOM) and others.

It should be mentioned that integral parameters of water quality are defined by combined influence of all ecological components of environment (contents of PPP, DOM, total suspended material (TSM) etc.). For example, the content of PPP characterizes the total level of humic loading. The gradients of temperature, contents of dissolved oxygen, DOM, TSM indicate humic anomalies.¹

The ecological study of colored and turbid coastal waters has some peculiarities. The structure of optical fields in upper levels of such waters are defined by joint influence of some ecological components. The use of remote sensing data to estimate PPP concentration, as well as water transparency² in shallow estuaries is not sufficiently correct.³ For example, average depths in the east parts of the Gulf of Finland are congruent with Secchi disc visibility and the problem of bottom reflections is arisen.

4. RESULTS

During last years our multispectral optical ship equipment (ECOTEST) has been used for calibrations of remote sensors and operative ecological control of colored and turbid coastal waters in the Mediterranean Sea, the Black Sea and the Baltic Sea. ECOTEST consists of:

- in water spectroradiometers,
- spectrotransmissometer,
- fluorometer,
- STD - probe.³ The technical characteristics correspond to SeaWiFS standards.

Electronic maps of temperature and spectral optical density of the coastal region with gutters of industrial object (1), river (2) and town water-cleaning systems (3) are shown in Fig. 1-4.³ There are the definite gradients of optical density in UV-spectral region near sites (1), (2) and (3) (Fig. 2). The main sources of light attenuation in this spectral region are DOM and TSM. In the blue spectral region the summary picture of optical density is determined by PPP, DOM and TSM (Fig. 3). Contributions of DOM and TSM influence on the total optical density at 560 nm etc. The reconstruction of specific concentrations of DOM, PPP and TSM is carried out with simple algorithms^{3,4} from in situ multispectral photometry. For example, spectral absorption coefficients $a(\lambda)$ can be expressed by the approximate formulas³:

$$a_{\text{DOM}}(360) \approx [c(360) - c_w(360)] - [c(712) - c_w(712)] (712/360)^n \quad (1)$$

$$a_{\text{DOM}}(450) + a_{\text{PPP}}(450) \approx [c(450) - c_w(450)] - [c(712) - c_w(712)] (712/450)^n \text{ etc.} \quad (2)$$

where

$c(360)$, $c(450)$, $c(712)$ - are the total beam attenuation coefficients;

$c_w(360)$, $c_w(450)$ and $c_w(712)$ - are contributions of pure water;

n is 0,7 ÷ 1,0 for different sea regions.³ Results for the same region after the storm are shown in Fig. 4. Redistributions of optical density are caused by the intensive water-exchange. The reconstruction of some IEP contents can be realized with the help of specific spectral absorption coefficients $a_c(\lambda)$:

$$a(\lambda) = a_c(\lambda) C \quad (3)$$

where C is concentration of the component (PPP, DOM or TSM).

The accuracy of such reconstruction is about 25-30%.

5. CONCLUSIONS

Considered application of multispectral ship equipment makes it possible to detect humic anomalies almost in the real time regime and to investigate their dynamics. Ecological situations in humic loaded regions can be described by integral ecological parameters of water quality.

6. ACKNOWLEDGMENTS

The authors would like to thank I.N. Kagakina, A.V. Nikitin, O.A. Trofimov for their support for optical measuring. This work was supported by Hydrooptical Program at S.I. Vavilov State Optical Institute and Hydrobiological Program at St.-Petersburg University.

7. REFERENCES

1. I.V. Aleshin, G.D. Andreev, E.E. Markov, V.N. Ryabova, "Remote and contact sensing of coastal water", 1 International Congress "ECOLOGY OF RUSSIA", Moscow, Materials of Congress, p.10, 1993
2. J.L. Mueller, C.C. Trees, R.A. Arnone, "Evaluation of coastal zone color scanner diffuse attenuation coefficient algorithms for application to coastal waters", SPIE, Vol. 1302 Ocean Optics X, p.72-78, 1990.
3. I.V. Aleshin, V.G. Lyskov, V.N. Pisarev, E.A. Tzvetkov, "Photometry of optical fields of the sea surface layers", Soviet Journal of Optical Technology, N12, p.31-39, 1993
4. A. Morel, A. Bricaud, L. Prier, "Absorption by dissolved organic matter of sea in UV and visible domains", Oceanogr., v.26, N1, p.43-53, 1981

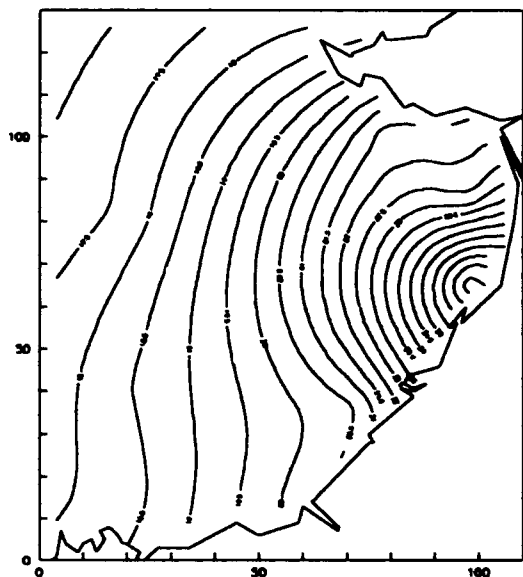


Fig.1.

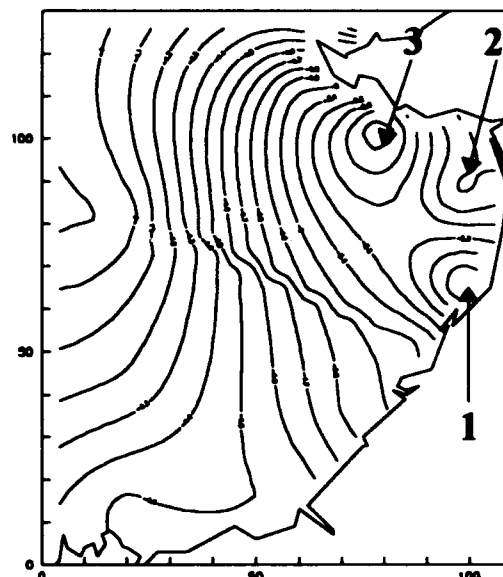


Fig.2.

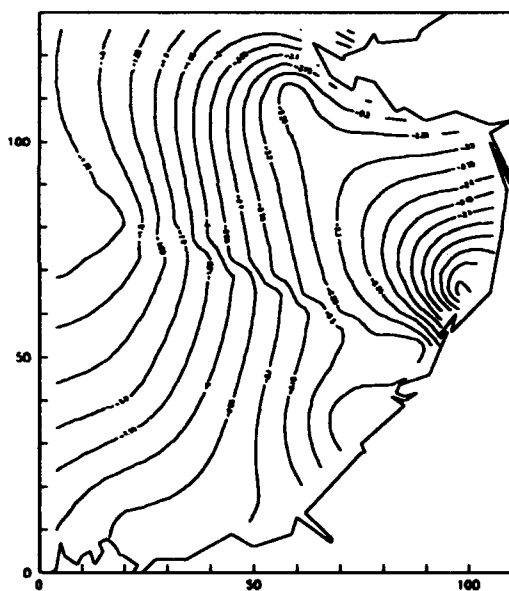


Fig.3.

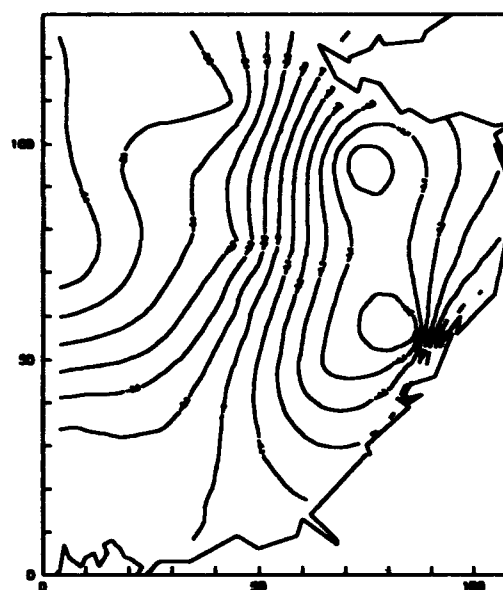


Fig.4.

Distributions of: temperature (Fig.1), optical density at 360 nm (Fig.2), at 443 nm (Fig.3), at 360nm after the storm (Fig.4).

A numerical model for prediction of sublittoral optical visibility

Jon S. Schoonmaker
Naval Command Control and Surveillance Center
San Diego, CA 92152

Robert R. Hammond and Alan L. Heath
Science Applications International Corporation
San Diego, CA 92121

Joan S. Cleveland
Center for Hydro-Optics and Remote Sensing
San Diego State University
San Diego, CA 92182

ABSTRACT

A model for prediction of visibility in nearshore waters must estimate inherent optical properties directly from spatially and temporally varying concentrations of optically important organic and inorganic materials. Models which describe these concentrations utilize both theoretical and empirical relationships. The estimation of coastal underwater visibility is based on Mie scattering calculations combined with laboratory measurements to obtain a set of calibration constants used to calculate the inherent optical properties from concentrations of generic water column constituents. These constituents are presently limited to sediments, phytoplankton and colored dissolved organic materials.

Number concentrations of cells and sediment particles, normally provided by water constituent source models, were measured in the laboratory. These measurements were taken over a range of sediment and phytoplankton concentrations. Modeled scattering and absorption estimates are compared with laboratory data and data from one coastal station.

The optical modeling procedures provide acceptable estimates over the range of available data, but begin to deviate as the proportion of large particles increases in very turbid waters. These results indicate that useful predictions of episodic coastal visibility variations are feasible. However, comprehensive model validation, testing and calibration over the full range of coastal particle distributions is required.

1. INTRODUCTION

Coastal water clarity modeling has the objective of predicting the inherent underwater optical properties required for interpreting the performance of optical systems in the complicated shallow coastal region. It is not expected that predictions for these high sediment (Morel "case II", 1977) coastal regions will be as accurate as those achievable for extensively studied open ocean waters (case I). The initial goal of the Predictive Visibility Model (PVM) is the prediction of relative and episodic changes in the optical environment. Improvements in absolute accuracy will be sought only after feasibility has been established and the dominant driving mechanisms identified. The computer architecture for the PVM is sub-divided into modules related to: 1) the sources of water column constituents critically affecting optical propagation; 2) the mixing and advection of these constituent concentrations in the dynamic coastal environment; and 3) the optical scattering and absorption which converts these concentrations into the required properties.

The sources of optical variability are presently limited to sediments, biology, and colored dissolved organic materials (CDOM). Others may be added in a specific location if they are determined to be significant. The source modules numerically estimate the concentration of these constituents based on geospecific bathymetry/topography and water characteristics, quasi-empirical inputs from contemporary remote-sensing data and weather forecasts. These estimations are made through a sequence of time steps on the order of fractions of the tidal cycle (2 hrs). The hydrodynamic mixing and advection module estimates the spatial distributions on a nominal 100 meter grid. The optical scattering and absorption module digests these inputs to estimate spatially and temporally varying optical properties. These mean

value predictions are for the stated spatial and temporal scales. Responses for higher frequency phenomenon are not included.

The integrated response of optical properties to principal drivers such as tidal currents, ocean swell, plankton growth and episodic changes in storm related land runoff are believed to be within our modeling capability. It is essential that all inputs be adequately defined and parametrically investigated to determine their relative effects on optical property estimates. A simplified approach to the PVM utilized the most obvious controlling factors first. Our goal was to develop a multi-tiered framework for testing interactions and alternative approaches. This provides a continually improving model in an evolving state of sophistication. This paper briefly describes the optical scattering and absorption modeling assumptions and a series of laboratory experiments undertaken to provide model calibrations for an initial generic classification of water constituents applicable for the very nearshore area (0-100 meters). Predictions are compared with limited *in situ* optical measurements. An example of PVM generated spatial variations in optical properties is presented.

2. OPTICS MODULE DEVELOPMENT

A high discrimination technique must be used to account for the space and time dependence of optical properties on constituents in the coastal water column. It has been hypothesized, but not conclusively demonstrated, that optical properties of individual ingredients can be linearly combined to estimate the optical properties of varied mixtures of biology and sediment. This separation is important due to the necessity to model the generation of each source concentration separately. The input parameters are particle number concentrations of organic and inorganic materials respectively, and a single absorption at 440 nm for the yellow substance. These concentrations are characterized in terms of variable size distributions and indices of refraction for similar particle groupings. Using these input parameters, absorption and scattering coefficients for the composite medium are determined along with the angular scattering dependence at a reference wavelength of 530 nm. This is done through the use of the Mie theory of light scattering by small particles (van de Hulst, 1981).

In order to apply Mie theory to particles of all sizes it will be necessary to assume that the majority of the particles are either spherical in shape or that their effect on light can be described using an "equivalent spherical radius". Burt (1952) suggests that this assumption does not lead to serious error. This assumption has been used extensively in the literature and has been supported by experimental verification of Mie theory with a number of different types of solid crystalline materials in suspension. With this in mind, the particles in suspension here will be considered as a dispersoid of equivalent spheres of varying sizes with a single complex index of refraction adjusted to produce angular volume scattering compatible with measured data. Another restriction is that the number concentration of particles must be low enough to justify use of a single scattering model; this assumption can be tested by evaluating linearity as concentrations increase in the laboratory. While descriptions of these procedures abound in the literature (Brown & Gordon, 1974; Morel, 1975; Kitchen & Zaneveld, 1992), the single scattering assumption could be restrictive in the turbid coastal regime. These assumptions allow for an exact solution for absorption and scattering cross sections which includes scattering angle-dependence using only a few input parameters.

Due to the absence of concurrent particle size, optical absorption and scattering measurements for documented sediment and plankton constituents, laboratory measurements and a limited coastal data set were used together with Scripps Visibility Laboratory data (Petzold, 1972) as the data for the parametric tradeoffs presented here. The data were used to test the modeling on inherent optical properties from constituents.

In the laboratory, water samples consisting of various mixtures of phytoplankton, sediment and filtered seawater were prepared. The concentrations of phytoplankton and sediment are characteristic of nearshore coastal waters. For each sample the number of suspended particles and their size distribution was measured along with its inherent optical properties. Using the measured particle data and the known

concentrations of phytoplankton and sediment as inputs to the optical model, the inherent optical properties were calculated and compared with the measured values.

The sediment solution used in the test was made from sediment samples taken off of the coast of San Diego in 20 meters of water. Just the surface of the sediment bed was taken and then sieved to pass only particles smaller than 90 μm . The sediments were further processed to remove any particles which did not remain in suspension for 10 seconds. The concentration of the resulting suspension was determined by centrifuging a portion for 60 minutes and letting the weight difference between the centrifuged and raw solution be the weight of the suspended solids. This process yielded a sediment concentration of 89.8 grams per liter. The dilution water was collected at the same location and was filtered (0.2 μm effective diameter) to remove most of the particles. The level of dissolved organic material in this mix water will be discussed below.

The phytoplankton, *Dunaliella tertiolecta*, was grown in a unialgal culture in nutrient-enriched, sterile-filtered seawater growth medium (IMR medium; Eppley et al., 1967). The aerated culture was under 24 hour illumination by cool-white fluorescent lamps at 22°C in a polycarbonate carboy. The concentration of chlorophyll was determined roughly from *in vivo* fluorescence during the experiments then followed by more accurate measurements on acetone extracts. Mixtures were made using chlorophyll concentration of 0, 2.34, 7.25, and 26.49 $\mu\text{g/l}$ and sediment concentrations of 0, 22.4, 44.9, 89.8 and 124.7 mg/l . For measurements of chlorophyll, pigments were extracted from the filters in 5ml of 90% acetone for 24 hours in the freezer in the dark. Extinction of acetone extracts was measured in a Perkin-Elmer Lambda 3B dual beam spectrophotometer in 1-cm quartz cuvettes. Concentrations of chlorophylls a, b, and c were calculated according to Jeffrey and Humphrey (1975).

Particle size distributions were measured using a Hach particle counter. The Hach instrument uses a 400 μm diameter flow tube insuring that one particle at a time passes a laser diode. The amount and time of light extinction along with the flow rate determine the particle size. The sizes are sorted into size bins of >2 μm , >5 μm , >10 μm , and >20 μm diameters. The sediment particle size distributions are assumed to fit a hyperbolic distribution and thus can be completely described with a number concentration parameter and a slope parameter. This distribution will be discussed later.

Spectral absorption and attenuation were also measured for each sample using a WetLabs a/c-9 absorption/attenuation meter. This instrument uses an incandescent source and a 9 band filter wheel to transmit narrow band light through a reflecting tube onto a diffuser for the absorption measurement and a non-reflecting tube for the transmission measurement. The path length is 25 cm. The center wavelengths of the 10 nm optical bands are shown in Table 3. It should be noted that no significant sediment-phytoplankton interaction is found in the particle number concentrations or the optical properties of the mixed samples. That is, it appears that the optical properties as well as the particle number concentrations of the constituent turbidity sources can be combined linearly.

For measurement of particulate absorption, particles were concentrated by filtering subsamples (100 to 500 ml) of the experimental mixtures through Whatman GF/F glass fiber filters (effective pore size 0.7 μm). Filters were immediately frozen in liquid nitrogen. Optical density spectra of particles on the filters were measured from 380 to 760 nm at 2 nm resolution in a Hewlett-Packard Photodiode Array Spectrophotometer equipped with an integrating sphere. A wet filter was used as a blank. Corrections for pathlength amplification were made as in Cleveland and Weidemann (1993) with an adjustment 1.29 (unpub.) for the diffuse light of the integrated sphere. Pigments in the concentrated particles were extracted with hot methanol (Kishino et al., 1985) and optical density spectra were measured on the residual particles. Absorption by residual particles, a_{sed} , was calculated as described for total particulates. In these experiments the residual particles consist of the sediments and associated particulate materials added to the mixtures. Phytoplankton absorption was calculated as the difference between total particulate and residual absorption.

Absorption by colored dissolved organic matter, a_{CDOM} , was measured on the filtrate collected from the particulate filtration. These filtrates were stored in amber bottles in the freezer for 2 months. Optical density spectra were measured from 200 to 800 nm at 2 nm resolution in 10 cm quartz cuvettes in a Hewlett-Packard Photodiode Array Spectrophotometer. Water purified by reverse osmosis was used as a blank. The mean of optical density between 630 and 640 nm was subtracted as a baseline correction and optical densities values were converted to a_{CDOM} .

Total absorption in the experimental mixtures includes absorption by water, dissolved matter, and particles. Absorption spectra of dissolved matter and particles were directly measured, as described above. The total absorption is now given by equation 1, where the values for the absorption of clear natural seawaters, a_{water} , were estimated by Smith and Baker (1981) and the values of $a_{particle}$ and a_{CDOM} were as determined above. The absorption at 10 nm resolution was calculated (equation 1) and used to determine the absorption calibration factors, A_{sed} and A_{bio} . (Table 3).

$$a(\lambda) = a_{water}(\lambda) + a_{particle}(\lambda) + a_{CDOM}(\lambda) \quad (1)$$

Throughout this paper the scattering and absorption contributions for pure ocean water (Smith & Baker, 1981) have been removed to simplify absorption data comparison. These values, shown in Table 3, are included to provide complete optical coefficient estimates.

3. PARTICLE SIZE DISTRIBUTION

The particles which occur in natural waters have a continuous size distribution which is roughly hyperbolic; the number of particles being defined in terms of the number N_l with diameter greater than $d > 1$ as shown in (2), (Junge, 1963; Bader, 1970). The exponent, γ , being constant for a particular body of water but varying between 0.7 to 6.0 for different water bodies (Kirk, 1983). Morel (1975) suggests a value of >3 and Apel (1987) an average of 2.5 for offshore ocean areas. Different values are expected near the coastline due to the variety and increasing size of particulate sources.

$$N = N_l d^{-\gamma}, \quad \gamma = 0.7 \text{ to } 6.0 \quad (2)$$

Although a hyperbolic distribution predicts many more smaller particles than large ones, their interaction cross sections are much smaller. Large particles have larger interaction cross sections but these smaller numbers result in a smaller contribution. Thus particles with diameters between 1 μm and 5 μm , which can dominate the scattering process (Jerlov, 1976 and Morel, 1975). While the slope, γ , and proportionality constant, N_l , defining the total number of measurable particles are the parameters to be supplied by the source models, they must be experimentally determined for optical model calibration. A value of $\gamma = 2.1$ was derived by fitting the scattering model described below to Petzold's volume scattering function measurements (1972). This value appears appropriate for a wide range of offshore coastal waters. Indeed most measurements for near coastal waters produce values over 2.0. Further offshore, higher values are expected where number concentrations are dominated by sub-micron particulate and phytoplankton in the low to sub-micron size range. Open ocean optical properties are primarily responsive to the plankton, detrital fragments and particles from terrestrial runoff small enough to remain suspended over long periods.

As shoreline particulate source areas are approached the number concentration is expected to shift toward larger sediment particles as shown in Figure 1. Bottom resuspension creates a continuous source of sediments as the near-bottom components of surface wave orbital velocity exceed the "Shields" entrainment criterion (Dyer, 1986) which is dependent on grain size and the density. This is labeled the Null Point in Figure 1. The largest inorganic particles quickly fall out and are absent further off shore because of their higher settling rates (Sverdrup, et. al., 1942). Bottom resuspension of particles reduces γ while increasing N_l . In locations where rivers and coastal runoff sources are present, a continuous sequence of point and surf-energy modulated sources exist along the surf zone; surf break line in Figure 1.

In fetch limited waters like quiescent bays these trends may reverse in favor of smaller sediments due to decreased resuspension and diffusivity.

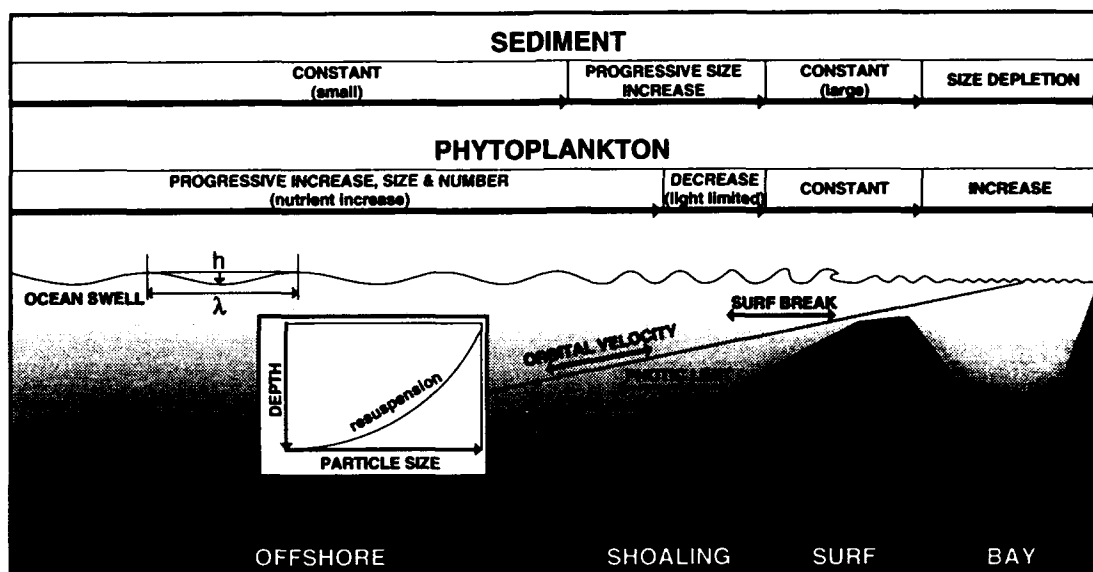


Figure 1. Hypothetical sublittoral particle size distribution trends

Simultaneously the relative abundance of nutrients increases the size of the organic constituents as the coastline is approached (Gregg and Walsh, 1992), but this increase can be reversed at the photic limit in Figure 1 as subsurface photosynthetically available irradiance dwindles due to the increased particulate attenuation. This increase would also reduce γ while increasing N_I .

Table 1. Laboratory measured particle number concentration for sediment and plankton samples.

Plankton Concentration	Sediment Concentration				
	0.0 mg/l	22.4 mg/l	44.9 mg/l	89.8 mg/l	124.7 mg/l
0.0 $\mu\text{g/l}$	$N_0=344$	$N_0=3721$	$N_0=6214$	$N_0=11195$	$N_0=15410$
	$N_w=344$	$N_s=3327$	$N_s=5870$	$N_s=10851$	$N_s=15066$
	$N_I=344$	$N_I=3721$	$N_I=6214$	$N_I=11195$	$N_I=15410$
2.34 $\mu\text{g/l}$	$N_0=878$	$N_0=3944$	$N_0=6410$	$N_0=11427$	$N_0=15768$
	$N_b=534$	$N_I=4255$	$N_I=6748$	$N_I=11729$	$N_I=15944$
	$N_I=878$	$N_I/N_0=1.08$	$N_I/N_0=1.05$	$N_I/N_0=1.03$	$N_I/N_0=1.01$
	bio fract=0.60	bio fract=0.13	bio fract=0.08	bio fract=0.05	bio fract=0.03
7.25 $\mu\text{g/l}$	$N_0=2189$	$N_0=5253$	$N_0=7759$	$N_0=12618$	$N_0=16944$
	$N_b=1845$	$N_I=5566$	$N_I=8059$	$N_I=13040$	$N_I=17255$
	$N_I=2189$	$N_I/N_0=1.06$	$N_I/N_0=1.04$	$N_I/N_0=1.03$	$N_I/N_0=1.02$
	bio fract=0.84	bio fract=0.33	bio fract=0.23	bio fract=0.14	bio fract=0.11
26.49 $\mu\text{g/l}$	$N_0=5681$	$N_0=7934$	$N_0=11359$	$N_0=15081$	
	$N_b=5337$	$N_I=9058$	$N_I=11557$	$N_I=16532$	
	$N_I=5681$	$N_I/N_0=1.14$	$N_I/N_0=1.02$	$N_I/N_0=1.10$	
	bio fract=0.94	bio fract=0.59	bio fract=0.46	bio fract=0.32	

Table 1 displays the particle number concentrations for a series of laboratory experiments performed to evaluate the effects of combined sediment-plankton solutions. Sediment and plankton were combined in concentrations covering expected coastal values. The sediment particulate concentration, N_s , and the

phytoplankton cell concentration, N_b , were separately calculated as the difference between measured and blank water, N_w , in the zero sediment and plankton row and column respectively. The total particulate numbers, N_0 , were measured after combination of sediment and phytoplankton. The mathematical total ($N_I = N_w + N_s + N_b$) consistently averaged only slightly more (5%) than the observed number, N_0 . This may be due to unknown effects like agglomeration (Rashid, 1972) or flocculation (Krone, 1978). Flocculation is salinity dependent and occurs primarily at lower salinities when river meets saline ocean water. Approximately 77% of particle diameter increase occurs between salinities of 3-7ppt followed by a much slower increase out to 33ppt (Aijaz and Jenkins, in press). This result is critical for linear addition of modeled optical properties. The measured number concentrations used for computational comparisons are included in Table 1 along with their ratio and the fraction of plankton cell numbers.

4. OPTICAL PROPERTY ESTIMATION PROCEDURES

The calculation of optical properties splits naturally into scattering and absorption calculations for sediment and phytoplankton designated by the customary interaction coefficients: b_{sed} , b_{bio} , a_{sed} and a_{bio} . The method used to calculate these parameters employs Mie scattering calculations for suspended particles and calibration coefficients. The calibration coefficients B_{sed} , B_{bio} , and A_{sed} , A_{bio} are applied to the modeled coefficients to obtain the scattering coefficients b_{sed} and b_{bio} and the absorption coefficients a_{sed} and a_{bio} for sediment and biological water constituents respectively. b_{sed} and b_{bio} are summed to give the total scattering coefficient, b , and a_{sed} and a_{bio} are added to provide the particulate absorption, $a_{particle}$, used to calculate the total absorption coefficient, a , in equation (1).

The process requires laboratory and coastal measurements to determine the calibration coefficients for generic types or assemblages of optically significant constituents so that they can be applied for predictions in "similar" coastal regions. Five geologically similar classifications of sediment constituents, j , are envisioned for the PVM along with a yet to be determined number of biological classifications, i . Initial calibrations for just one sediment category ($j=1$) and one biological category ($i=1$) are provided here.

4.1 Particulate scattering

Petzold (1972) provides the most comprehensive and most quoted angular scattering ($\beta(\theta)$) data available in the literature. Figure 2 shows Petzold's data for eight locations normalized by dividing by the scattering coefficient, b , to produce a non-dimensional curve independent of particulate concentration. At most, these curves deviate by a factor of ± 2.5 , predominantly in small solid angles about the forward and backscatter directions in response to changes in the slope of the particle size distribution. This agreement seems somewhat amazing since the data cover extreme differences in water types from a shallow enclosed bay to clear deep ocean water. Figure 4 shows the mean and standard deviation of five of these scattering curves selected for near coastal water characterization along with the calculated Mie scattering approximation.

Mie theory provides the solution for the scattering matrix of homogenous spheres in the form of two complex amplitude functions, $S_1(\theta)$ and $S_2(\theta)$, of an axially symmetric scattering angle, θ , (Hansen and Travis, 1974). These functions involve spherical Bessel functions which are computed using recursion relationships (van de Hulst, 1957). The functions, $S_1(\theta)$ and $S_2(\theta)$, provided by the Mie code are in turn used to calculate the directional scattering function $\beta(\theta)$ and the spectral absorption and scattering coefficients, a and b , in terms of a non-dimensional parameter, $k = r/\lambda$, where r is the equivalent spherical radius and λ the optical wavelength. The factor of 2π , often included in k in the literature has not been included in the size parameter used here to facilitate comparisons. The scattering model integrates bulk particles over three decades of k covering particle sizes from 0.1λ to 100λ , roughly 0.05 to 50 μm , using a hyperbolic particle size distribution. Phytoplankton cell scattering and absorption are treated independently.

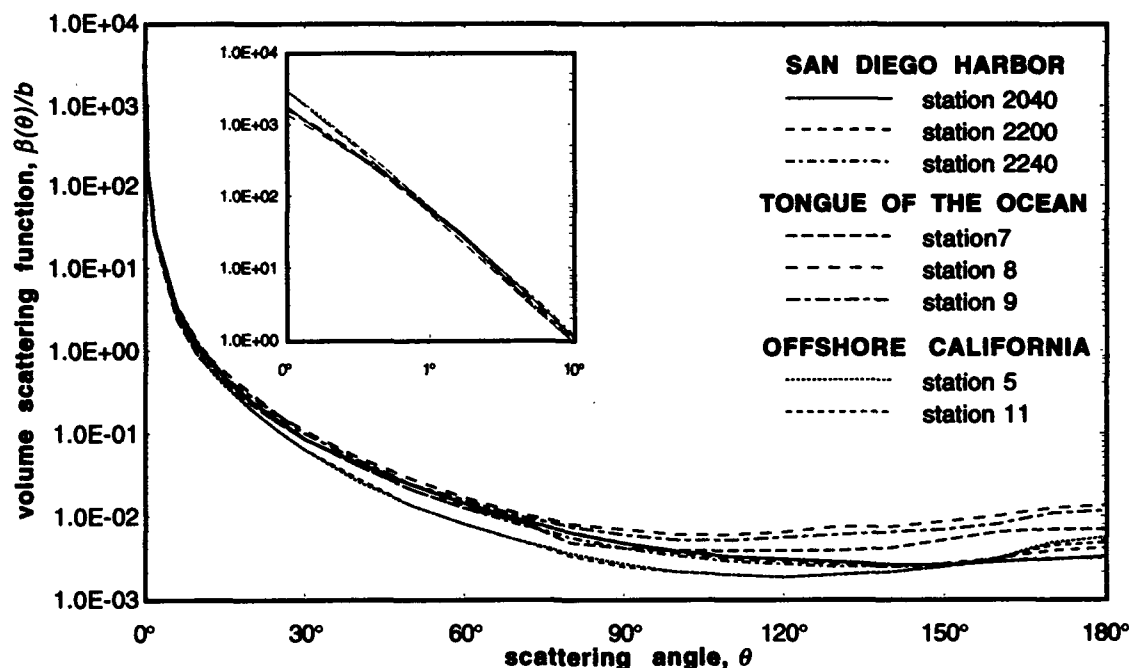


Figure 2. Concentration independent volume scattering functions normalize to b for various waters.

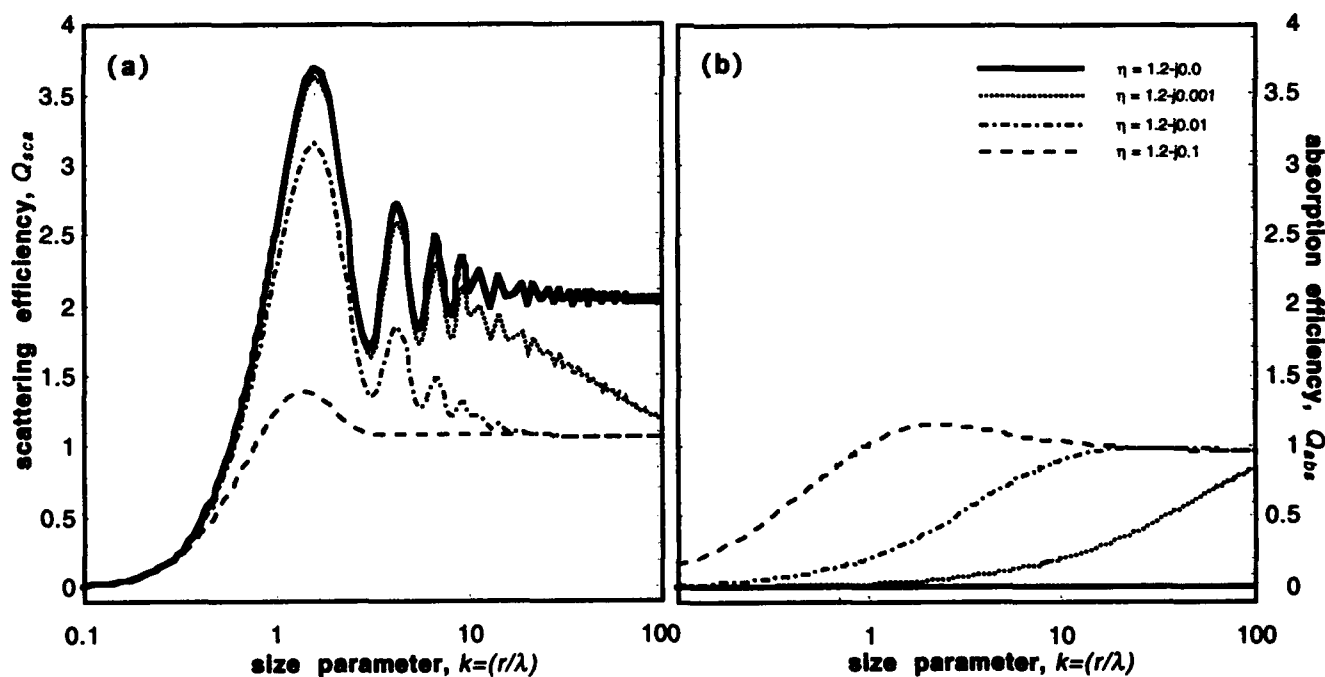


Figure 3. Efficiencies vs. particle size for a) scattering; b) absorption

Scattering efficiency, Q_{sca} , and absorption efficiency, Q_{abs} , for dielectric spherical particles as a function of k are shown in Figure 3 varying the imaginary part of the index of refraction, η'' . Scattering efficiency is multiplied by geometric cross section, πr^2 , to obtain interaction cross section. For the transparent sphere case, with the imaginary part of the index of refraction equal to zero, the scattering efficiency oscillates above $k = 1$ due to interference between the diffracted and transmitted light, and

approach a value of two as k increases. As the absolute value of the imaginary coefficient increases, the oscillation is damped and the value tends to one as particle size increases. This is because the imaginary part corresponds to the internal absorption, a_{int} , of the particle substance as given by $\eta'' = a_{int}\lambda/4\pi$ (van de Hulst, 1957) which, when totally absorbing, leaves only the diffractive interaction contribution to the cross section. The real parts of indices of refraction reported in the literature for the water to quartz interface are $1.15 < \eta' < 1.2$, and values of η'' vary between 1.005 and 1.03 for the water to chloroplast interface. The imaginary indices are expected to vary with outer shell thickness, and the location and amount of chlorophyll in the cell. Since these terms vary with cell size, (Beardsley et al., 1970), species, and ambient light, variable imaginary parts were tested using homogenous spheres, both with and without concentric shells, to achieve agreement with absorption measurements.

Efforts to fit the Mie Scattering model output to the shape of Petzold's volume scattering data for shallow waters (Figure 2) using plausible values for the particle distribution parameters and the refractive index followed the approach of Morel (1975) and Brown and Gordon (1974). This effort involves only three variables since the concentration (number of particles) simply moves the scattering curve up and down without altering its shape and has been normalized in Figure 2. The parameters which control the shape of the function are the slope, γ , of the size distribution discussed above and the real and imaginary coefficients of the refractive index, $\eta = \eta' - j\eta''$. These parameters were investigated over the range of values quoted in the literature. The best fit to the most detailed volume scattering data available for the very nearshore area, actually inside San Diego Bay (Petzold, 1972), is shown in Figure 4. Petzold's measurements were all made at 530 nm.

This fit was achieved using $\gamma = 2.1$ and $\eta = 1.2 - j0.015$. The large imaginary index required to fit the data gives rise to an unrealistically high particulate absorption. If a smaller imaginary index of refraction is used, forward scattering can be modeled but the backscatter displays the rainbowing effect which results from the use of perfect spherical shapes. The large imaginary index results in a reduced slope which supports forward scattering by increasing the percent of larger particles. A slope of 3 for the size distribution (Morel, 1975) may be closer to physical measurements and give a better fit in the forward

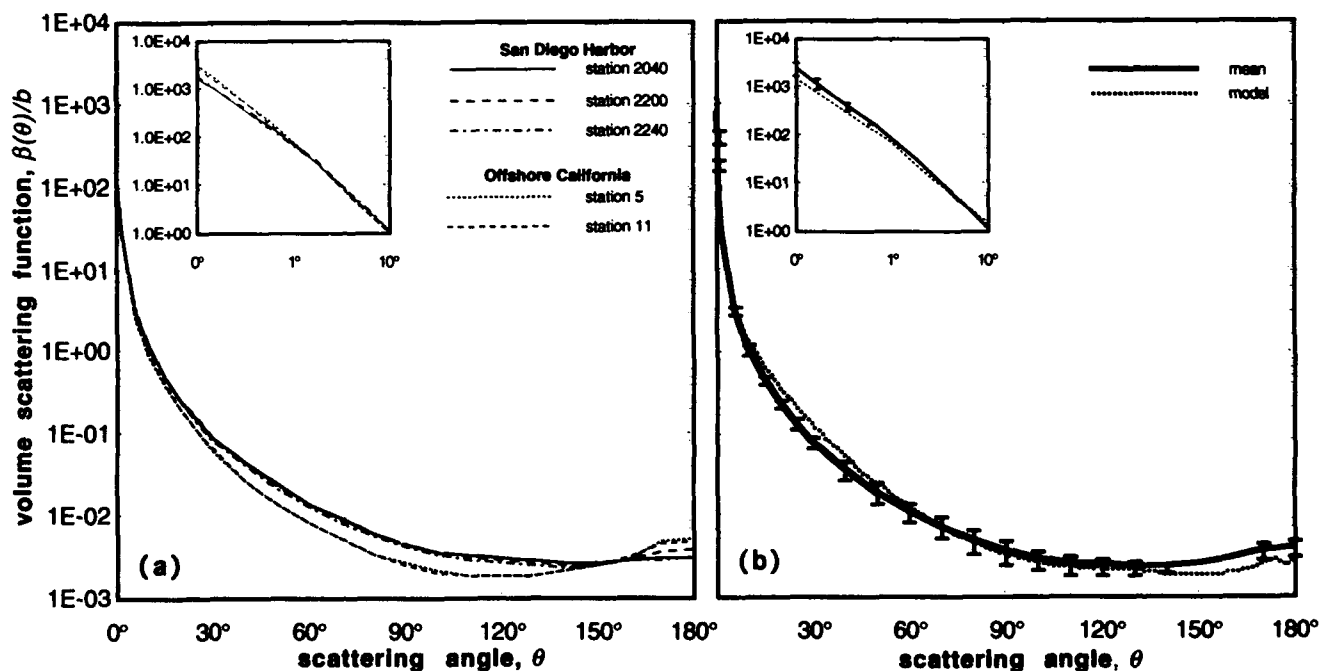


Figure 4. Concentration independent volume scattering functions for offshore California and San Diego bay and the optical model; a) measurements; b) statistical fit

scattering area if rainbowing is neglected, ($\eta'' = 0.0$). Since available volume scattering data indicate that seawater suspended materials do not strongly display the rainbow effect, we suggest that spherical particulate shapes are not important constituents of seawater. This appears true for the open ocean, coastal and bay waters which all fit closely using identical parameters.

Correction for this artificially high sediment absorption, required to achieve agreement between the spherical calculations and the angular scattering observations, was accomplished and added to measured spectral absorptions for generic phytoplankton categories, detrital materials and CDOM. These corrections must be based on measured data since the Mie code does not account for pigments or dissolved substances. This will be discussed later. It should be noted that even though particle concentration values are not available for Petzold's scattering measurements, calculated concentrations agree with recent San Diego Bay particle measurements (Schoonmaker, 1993). Model estimates of particulate concentrations for Petzold's scattering data are shown in Table 2.

Due to the many uncertainties involved and the absence of data covering the many possible variables, a single index of refraction was selected for use on all materials. As shown by the statistical curve in Figure 4b, a satisfactory fit was obtained using $\eta = \eta' - \eta'' = 1.2 - j1.015$ even though biological materials were clearly present. Different index coefficients would probably be selected if volume scattering function data were available at wavelengths other than 530 nm. A satisfactory procedure for spectral compensation of the scattering model coefficient, b_{model} , derived relative to 530 nm is given by equations (3) and (4).

Table 2. Estimated particle concentrations and scattering coefficients for Petzold's data

Offshore California		San Diego Bay		Tongue of the Ocean	
N_i	$b(m^{-1})$	N_i	$b(m^{-1})$	N_i	$b(m^{-1})$
1627	0.275	10800	1.824	692	0.117
1296	0.219	9368	1.583	254	0.043
		7131	1.205	219	0.037

$$B_{sed}(\lambda) = \left(\frac{\lambda}{530} \right)^2 \quad (3)$$

$$b_{sed}(j, \lambda) = B_{sed}(\lambda) b_{model}(j, \lambda) \quad (4)$$

Values of $B_{sed}(\lambda)$ vary by the square of the wavelength (van de Hulst, 1957) and are included in Table 3 for selected wavelengths. The j in equation (4) refers to the sediment category. The concentrations shown in Table 1, together with the $\gamma = 2.1$ and the above index of refraction, combine to produce both accurate values at 530nm and accurate spectral values when b_{model} is corrected using (3) and (4). This is shown in Figure 5 for combined sediment and phytoplankton laboratory samples.

Biological particulate scattering requires a unique calibration coefficient for each local water column community when it displays significantly different optical properties. Mean cell size and shape may affect this coefficient so that the procedure is posed in terms of multiple constituents even though only one phytoplankton species is presently included. For each biological constituent, i , the biological particulate scattering scaling factor B_{bio} is given in terms of the mean laboratory measured spectral scattering coefficient $b_{meas}(i, \lambda)$,

$$B_{bio}(i, \lambda) = \left\{ \frac{b_{meas}(i, \lambda)}{b_{model}(i, \lambda)} \right\} \text{weighted average} \quad (5)$$

and the combined biological scattering coefficient in terms of the weighted number concentration $N_b = \sum N_i$ is

$$b_{bio}(\lambda) = \frac{\sum_i N_i B_{bio}(i, \lambda) b_{model}(i, \lambda)}{\sum_i N_i} \quad (6)$$

Figure 5 illustrates these results and the reduced scattering near 676 nm where the chlorophyll absorption peak reduces the scattering interaction cross section ($Q_{sca} = Q_{att} - Q_{abs}$). Similar reductions in scattering at pigment absorption peaks were seen in laboratory measurement of phytoplankton scattering (Bricaud, et al., 1983).

4.2 Particulate absorption

The scattering model was run with the above parameters to produce values for both scattering and absorption coefficients. For the sediments, the absorption value includes the artifact discussed above to correct for the mathematical convenience of using spherical particles. Since the sediment samples tested in the laboratory were composed of real coastal sediment materials, they contained an unknown fraction of biological material which is evidenced by a small chlorophyll or pheopigment absorption increase at 676 nm. In addition, the coastal mix water contained dissolved organics. This makes it difficult to determine the relative contributions to the total absorption.

To circumvent determining these fractions the optical model was calibrated to adjust the sediment absorption coefficient to yield the laboratory measured value as a function of optical wavelength, λ , and sediment concentration, N_s . It must be emphasized that these calibration coefficients are for a single classification of sediment; nearshore southern California. The number of sediment classifications required to model a wide variety of sublittoral visibility conditions must be determined by sensitivity comparisons for samples covering the range of optic constituents. As suggested later, it would be advisable to include the slope of the particle concentration as a variable in future constituent calibrations. Dilution with mix water changed the concentration but the relative number of particles of each size remained constant. It was determined that N_s did not appreciably affect the sediment absorption scaling constant, A_{sed} , which has been evaluated constant γ . For each optical constituent, j , the sediment absorption scaling coefficient is given by;

$$A_{sed}(j, \lambda) = \left\{ \frac{a_{meas}(j, \lambda)}{a_{model}(j, \lambda)} \right\} \text{weighted average} \quad (7)$$

Table 3. Laboratory derived corrections parameters

$\lambda(nm)$	Seawater (Smith&Baker, 1981)		NRaD Lab Measurement Calibration/Corrections			
	$b(m^{-1})$	$a(m^{-1})$	B_{sed}	B_{bio}	A_{sed}	A_{bio}
412	0.00666	0.01602	0.6043	2.4902	0.1529	12.8205
440	0.00490	0.01450	0.6892	2.5543	0.1317	14.5447
488	0.00316	0.01920	0.8478	2.6327	0.1006	12.0498
515	0.00250	0.04170	0.9442	2.7058	0.0831	5.5483
532	0.00218	0.05172	1.0076	2.7142	0.0752	3.0719
550	0.00190	0.06380	1.0769	2.7065	0.0673	2.6708
650	0.00100	0.34900	1.5041	2.6253	0.0384	7.5583
676	0.00074	0.44200	1.6268	2.1460	0.0355	11.2663
715	0.00065	1.00400	1.8200	2.7852	0.0159	0.4989

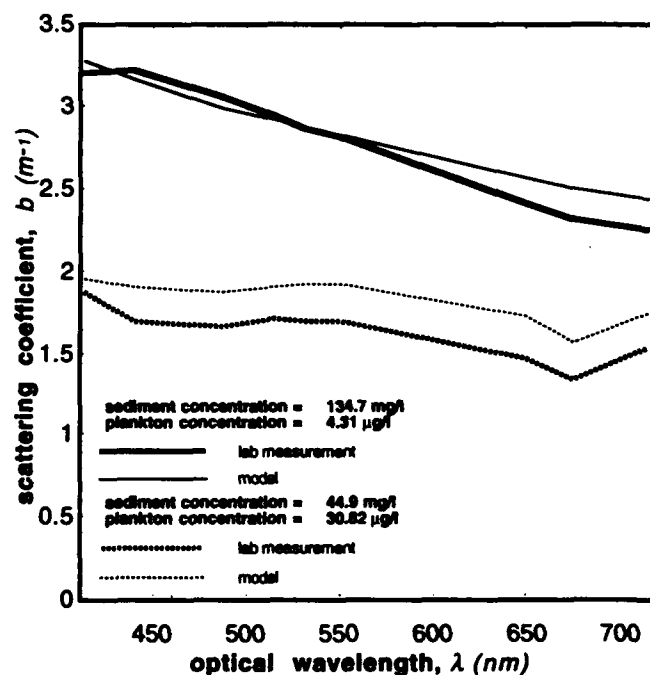


Figure 5 Comparison of model calculations with laboratory estimates for selected particulate concentrations.

Note that a_{model} for sediment is calculated using the same index of refraction, η and slope, γ , as used in the calculation of b_{model} . The weighted optical constituent for sediment absorption is;

$$a_{sed}(\lambda) = \frac{\sum_j N_j A_{sed}(j, \lambda) a_{model}(j, \lambda)}{\sum_j N_j} \quad (8)$$

where N_j is the number concentration of optical absorption constituent, j .

For biological absorption the matter is approached differently due to the unique spectral absorption properties of many materials. Since modeling of detailed spatial variations demands treatment of particle dynamics, it is assumed that absorption can be estimated as the product of biological constituent particle concentration and a mean absorption per particle. A biological community would be treated as a single biological classification, or evaluated as a combination of independent constituents, depending on the accuracy required for a specific application.

For the phytoplankton, *Dunaliella tertiolecta*, data used in this paper as a preliminary biological constituent we make the assumptions (cell = particle):

1. spectral absorption is proportional to chlorophyll present
2. chlorophyll per ml is proportional to (cells per ml) x (chlorophyll per cell)
3. the absorption per unit chlorophyll concentration, A_{bio} (m^{-1} per $\mu g/ml$), is given by the slope of the laboratory measured spectral absorption as a function of chlorophyll concentration.

Laboratory measured values are shown in Table 3 for category $i=1$ (*Dunaliella tertiolecta*).

Using the laboratory determined value for the chlorophyll per cell ($C_{cell} = 4.96 \times 10^{-6} \mu g/cell$) with the number of cells per ml determined, either by measurement or modeling, gives the spectral absorption coefficient, so that;

$$a_{bio}(i, \lambda) = N_i C_{cell}(i) A_{bio}(i, \lambda) \quad (9)$$

The laboratory measurements of a_{bio} are compared with the modeled values in Figure 6.

Combining the sediment and biological scattering and absorption terms given by equations (4), (6), (8) and (9) with equation (1) provides the required estimates of total absorption and scattering coefficients. This assumes that a separate estimate procedure for a_{CDOM} is available for the location in question. A technique for unfolding this from measured data is included in the next section.

$$a_{particle}(\lambda) = a_{sed}(j, \lambda) + a_{bio}(i, \lambda) \quad (10)$$

$$b(\lambda) = b_{sed}(j, \lambda) + b_{bio}(i, \lambda) \quad (11)$$

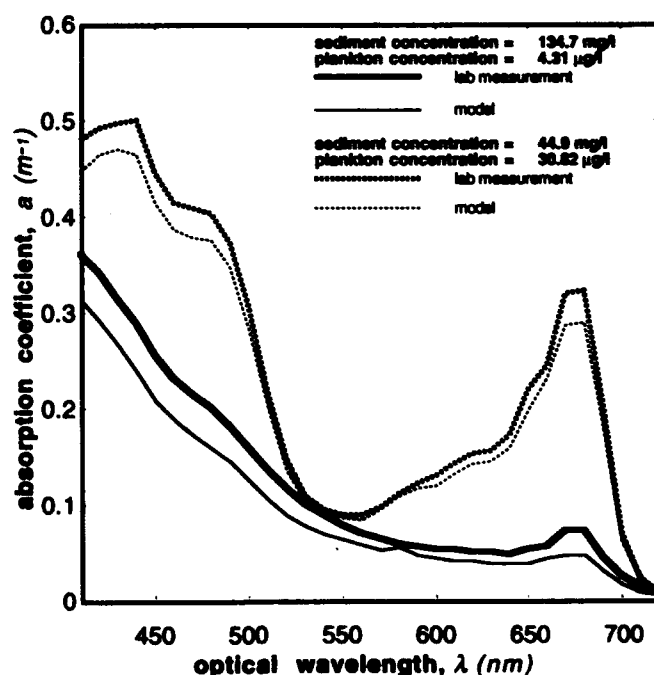


Figure 6. Comparison of modeled absorption with laboratory measurements.

5. OCEANSIDE NEARSHORE EXAMPLE

The optics model presented here has yet to be evaluated due to the absence of nearshore data, however two nearshore samples were available to support preliminary order-of-magnitude comparisons and search out problem areas. For these measurements the winds were calm but there was a long (12-14 sec) swell of approximately 1 meter height stimulating abundant bottom resuspension and a well developed Bottom Turbid Layer (BTL).

Water samples were collected at three equally spaced positions in nominally 20 meter deep water approximately one half mile north of the breakwater at Oceanside California. The sediment samples that were used for determining optical property corrections came from a similar coastal site and depth approximately 20 miles south of this location. Water samples were taken for subsequent laboratory size distribution determination. *In situ* absorption and total attenuation measurements were made using the WetLabs absorption/attenuation meter used in the laboratory. Figure 7 compares preliminary, two component, modeled with measured values of spectral absorption and scattering coefficients for the surface and mid depth. Optical data in close proximity to the bottom was also measured, but with total attenuation coefficients around ten ($c_{532} \approx 10$), these data have not been processed.

Unlike the PVM source models, which estimate N_s and N_b separately, the ocean measurements are presently limited to total particles, N_T . This confronts us with the need to split N_T into phytoplankton and sediment particles in order to reconcile the data and model predictions. This was done using an approximation provided by Zaneveld (personal communication, 1994) wherein the observed absorption at 676 nm above the line connecting 650 nm and 715 nm in the data is attributed to chlorophyll a. The contribution of dissolved organics at 676 nm is assumed to be negligible. The chlorophyll absorption determined in this way corresponds to a specific N_b in the laboratory calibrated model. Subtracting N_b from the measured total particulate gives N_s . Table 4 shows the measured N_T , and calculated N_s and N_b for the surface (2.5 meters) and 10 meters. The calculated N_s and N_b together with the laboratory calibration coefficients were used in equations (8) and (9) for the sediment and phytoplankton absorption calculations shown in Figure 7. An estimate of the spectral absorption of CDOM, a_{CDOM} , is calculated using the remaining absorption at 412 nm after the sediment and biological contributions have been subtracted from the measured values. This procedure gave $a_{CDOM}(440)$ values of approximately 0.07 for both depths. We assumed the biology particle cell diameter was the same 7.6 μm as the mean Gamma distribution in the laboratory since we were unable to separate the biology size distribution from the total distribution. This diameter along with the calculated N_b is used to estimate the biological scattering in equation 6.

A final step is required to adjust the slope of the particle size distribution (fraction of large particles) so that the spectral sediment scattering curves fit the data. This step was unanticipated because γ derived from Petzold's volume scattering data fit all of the observed water types reasonably well with a single value of 2.1. In the nearshore region, the sediment size distribution appears to be significantly modified by the addition of large particles resuspended from the bottom. For the hyperbolic distribution in equation (2), a doubling of the number of particles in the 1 to 10 μm band will decrease γ from 2.1 to 1.8. The PVM sediment source models calculate this variation as input to the optics module.

This nearshore increase in large particles results in a shift towards forward scattering as shown in Figure 8. Recalling that we have defined $k = d/2\lambda$ so that in the center of the visible spectrum (0.5 μm), k is approximately equal to the particle diameter. The Mie scattering solution in Figure 8 shows the contribution of particle sizes, grouped in three decades, to angular scattering. The smaller particles in the Rayleigh scattering decade compose 99+% of total particle number but contribute little to $\beta(\theta)$ in the forward direction due to their small optical cross-sections. Inversely the largest particles, while only a very small percentage of total, dominate forward scattering and point spread functions and make very little contribution to backscatter.

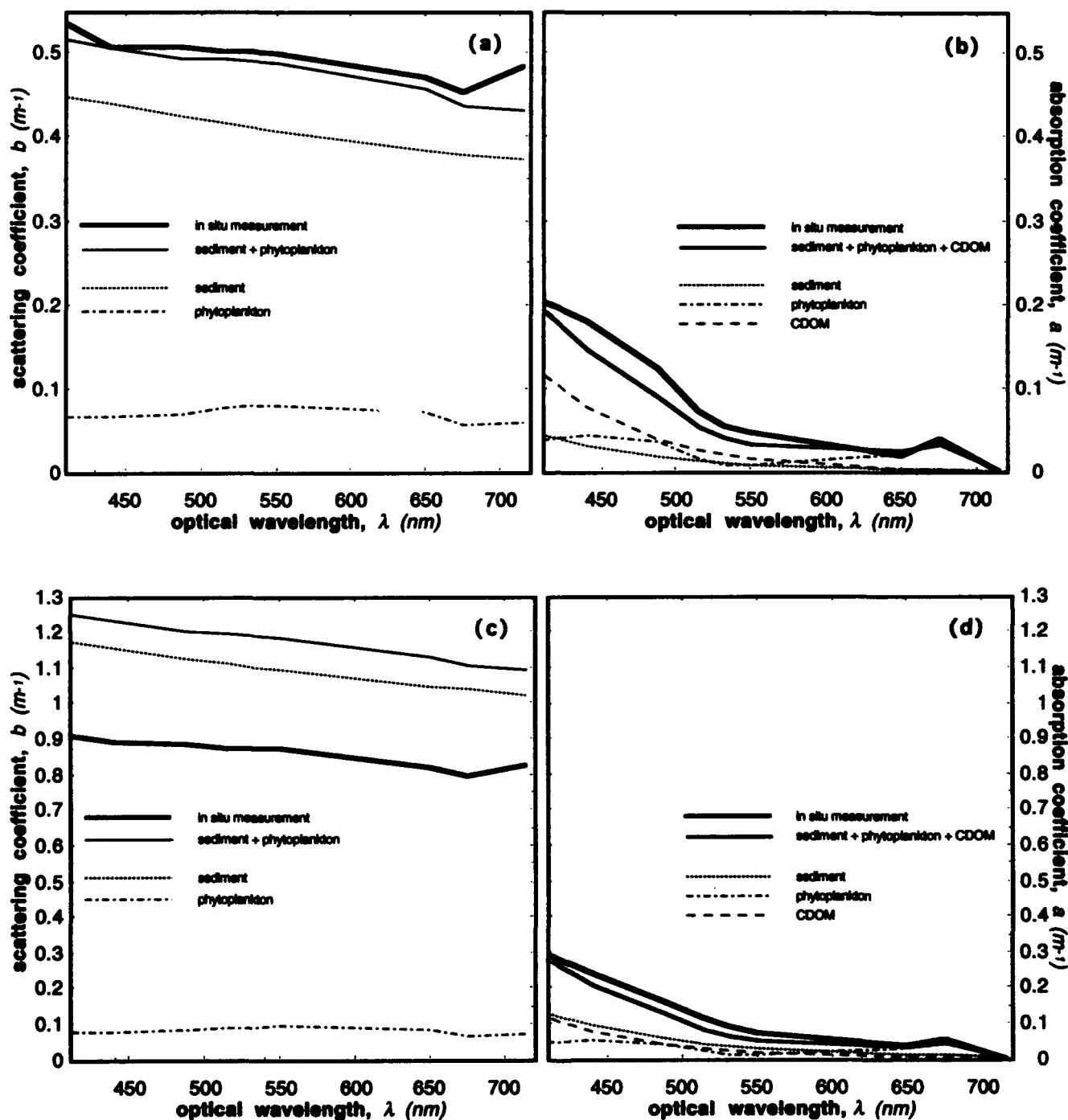


Figure 7. Oceanside scattering and absorption comparison of measurements vs. modeled: a) surface layer scattering; b) surface layer absorption; c) mid depth scattering; d) mid depth absorption

Table 5 summarizes Mie scattering estimates of particulate scattering as a function of changing size distribution slope, γ , with a constant number of particles greater than $1\ \mu\text{m}$. Decreases in γ increase the relative number of large particles (Table 4). The effects of this relative increase in large particles are clearly evident as an increase in the front-to-back scatter ratio, b_{fwd}/b_{bck} , and an increase in the contribution of large particles to total scatter (Table 5). This suggests that the larger difference between modeled and measured scattering at mid-depth is due to the presence of larger particles. Clearly, there is a need for laboratory measurements which calculate the sediment absorption correction factor as a function of both N_s and γ to describe the optical properties near the bottom for shallow coastal areas subject to bottom sediment resuspension. The estimated scattering of phytoplankton cells is very small compared to the total particles and could probably be neglected in many nearshore regions (Figure 7).

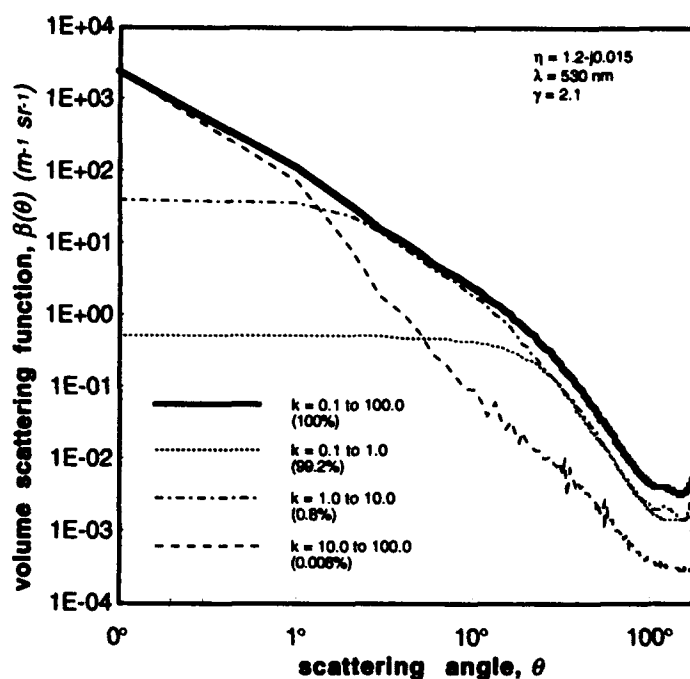


Figure 8. Three decade volume scattering function.

Table 4. Particle parameters for Oceanside water

depth (m)	slope γ	particle number > $1\ \mu\text{m}$		
		N_l	N_s	N_b
2.5	1.9	2930	2422	508
10.0	1.7	7143	6572	571
Bottom	1.3	16190	—	—

Table 5. Scattering fraction variations with slope

slope γ	b_{decade}/b_{total}			$b_{fwd}b_{bck}$ 0.1-100 μm
	0.1-1 μm	1-10 μm	10-100 μm	
1.5	5.40%	40.83%	53.77%	96.6995
1.8	10.99%	52.79%	36.22%	81.2036
2.1	19.07%	59.74%	21.19%	64.9435
2.4	28.84%	60.17%	10.98%	50.3499
2.7	39.34%	55.49%	5.18%	37.9628

Visibility distance can be characterized by the total beam attenuation coefficient, c , which is shown in Figure 9a for the Oceanside surface layer. The measured spectral values for the shallow water sample follow the modeled values very closely. However identical treatment for the mid-depth sample produces an offset of approximately 25%. The mid-depth sample shows a 70% increase in scattering coefficient because it is closer to the sediment resuspension source. The 25% spread between measured and modeled may result from the change in the size distribution close to shore discussed above. More data will be needed to resolve the problems associated with the large particle cases.

Figure 9b compares a generic chlorophyte spectral absorption curve (Cleveland and Perry, 1994) with modeled biological absorption for the Oceanside surface and mid-depth samples. The curves have been normalized at 676 nm. The normalized modeled absorption spectrum (based on one phytoplankton species) generally resembles the normalized chlorophyll spectrum. Differences in spectral peak ratios are probably due to different ratios of chlorophyll b to chlorophyll a in the model assumptions compared to the generic chlorophyte. Nearshore data includes absorption by other phytoplankton pigments, organic detritus, and inorganic particles. These particles give rise to differences between modeled and "generic" absorption. All of the phytoplankton absorption values are small relative to the scattering coefficients and could almost be neglected without seriously impacting total attenuation in this Oceanside case.

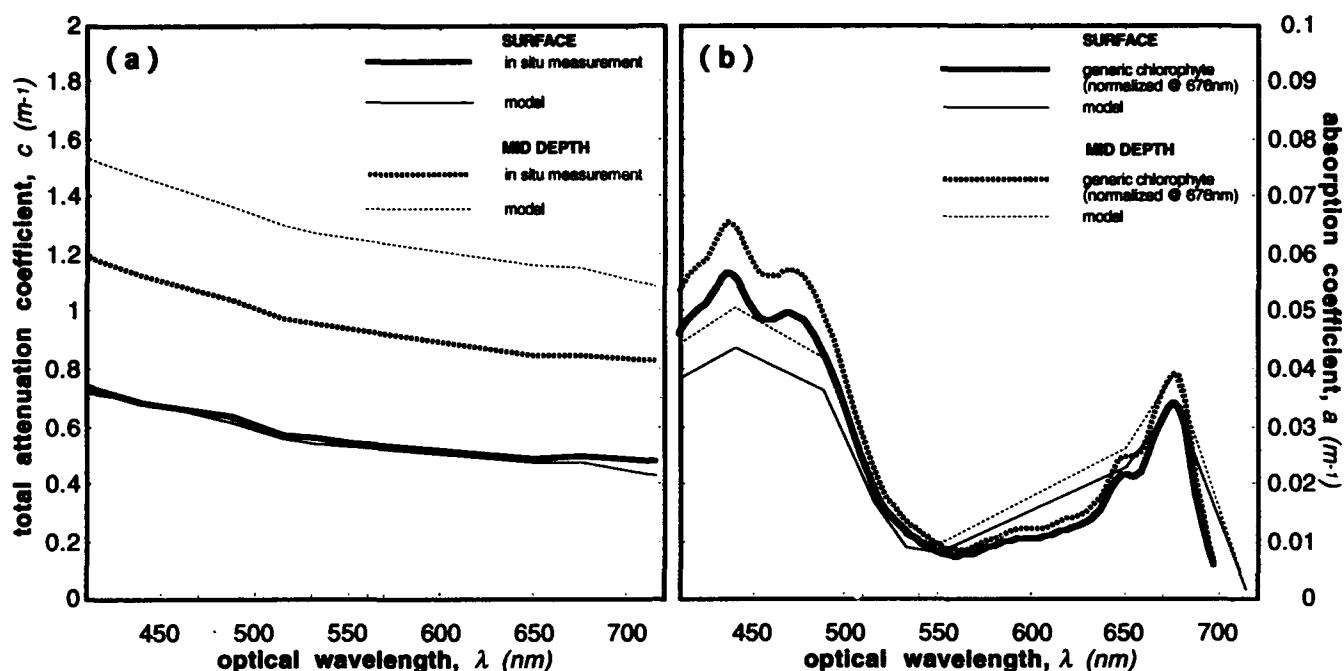


Figure 9. Oceanside nearshore data comparison: a) total attenuation; b) biological absorption

6. CONCLUSIONS AND RECOMMENDATIONS

Laboratory measurements have demonstrated small decreases (Table 1) in the combined sum of particle numbers as sediment and/or plankton concentrations are increased. This decrease may be due to unknown effects like agglomeration or flocculation. The absence of significant changes in particle number is critical for optical modeling which independently combines the absorption and scattering contributions of particulate concentrations. The optical model calibration constants presently used in the optical calculations were established using a single sediment sample (size-number distribution) and mix water (salinity). Slope variations and possible salinity effects require further investigation when data becomes available.

The results of the Bohren-Huffman based Mie scattering code calculations agree remarkably well with the laboratory measurements (Figure 5) and one nearshore surface water sample (Figure 6). The internal absorption coefficients, introduced to fit Petzold's angular scattering data and compensate for the mathematical convenience of spherical particles, also provide tractable representations for the laboratory sediment data and the nearshore surface water example. Thus far we have not succeeded in separating the artifact caused by assumptions of spherical particles from true internal absorption.

Disagreement between modeled and measured scattering coefficients for the mid-depth sample (Figure 7c) is thought to be due to a change in particle size distribution slope caused by bottom resuspension of larger particles. The absorption correction coefficients were determined from a single sediment size distribution but the size distribution is significantly altered when wave action doubles the relative concentration of larger particles. Sediment samples including these large particles need to be measured in the laboratory to obtain sufficient data to include the slope variable as a parameter in both the scattering and absorption calculations. Slope variations are a routine output of the PVM sediment source models.

The modeled sediment plus phytoplankton absorption compare favorably to the measured *in situ* absorption for both depths in the coastal example (figure 7b, 7d). The modeled phytoplankton spectral

shape resembled the spectral shape for generic chlorophyte (Figure 9b). This spectral shape is entirely fixed by the reference water corrections. The generic chlorophyte curve appears reasonably close for the Oceanside case but the number of biological reference water classifications required to cover the range of desired coastal conditions depends on biological community variations and the optical accuracy required. Modeled attenuation, which is the sum of the absorption and scattering also agreed with measured *in situ* attenuation for surface waters (Figure 9a).

The steep gradient in optical properties near the bottom can be expected to complicate passive remote sensing algorithms. Above the surface passive sensors will respond to the surface layer. Algorithms for simultaneous extraction of sediment, phytoplankton and CDOM need to be rigorously tested and verified *in situ*. SeaWiFS will include new spectral bands designed expressly for this purpose, although it will be spatially constrained to waters further offshore with resolution too crude for resolving kilometer scale coastal eddy structures.

In the bottom turbid layer, prediction of optical properties will require separate algorithms responsive to the larger particles which strongly affect the front-to-back scatter ratio and hence extinction length and diffuse attenuation in different ways. In the BTL it may be expedient to neglect biological effects entirely since the absorption term may be overwhelmed by scattering by sediments. This suggestion is based on very limited data and more laboratory and *in situ* measurements will be required to validate this approach. The primary optical measurement are extinction in the BTL and perhaps diffuse attenuation coefficient, K_d , of the upper waters which reduce the light available for passive visibility.

Figure 10 demonstrates a preliminary example of predicted visibility distance (three extinction lengths) in centimeters for 23 January 1993 for the surface layer near Oceanside with bottom resuspension, surf and active river sources contributing. This is the type of integrated inherent optical property prediction that our measurements and optical modeling efforts are intended to support in the future. Hyperspectral remote sensing is rapidly advancing in its ability to extract terrestrial data from the 3-D "data cube", two space and one spectral dimension. For the ocean this paper has suggested complications in extracting data on a fourth dimension, depth. To this we must hasten to add the critical fifth dimension of time which is essential in the dynamic nearshore environment and which is treated by the PVM. When one considers this five dimensional data space the ocean truth data collection problem becomes insurmountable without a model framework in which to conduct the sensitivity analysis which identifies and prioritizes the dominant parameters for the planning and execution of algorithm validation experiments. The optical algorithms presented above are intended to develop into a ubiquitous predictive capability as more sediment and biological descriptive categories are added.

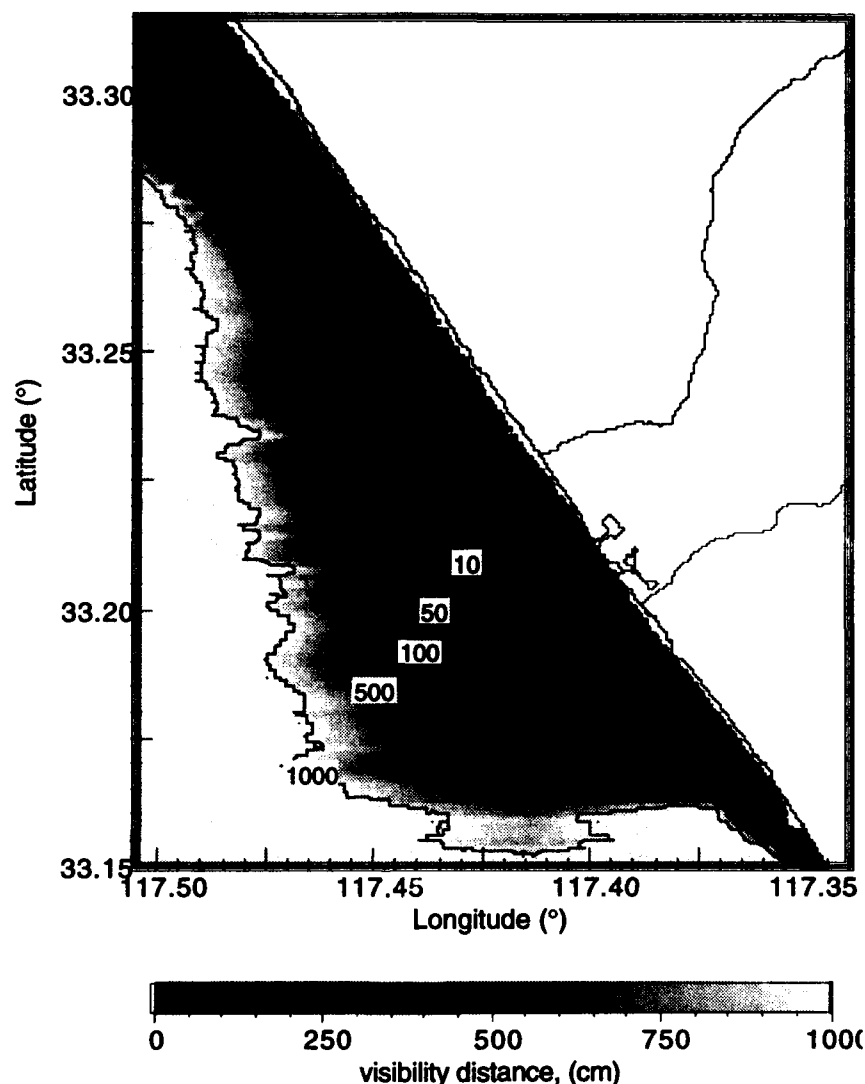


Figure 10. PVM example of visibility distance prediction for Oceanside (cm)

7.0 ACKNOWLEDGMENTS

Funding of the experimental measurements and data reconciliation reported here was provided to the NRaD division of the NCCOSC by the Naval Coastal Systems Station. Funding of the optical model was supported by the Office of Naval Research (Contract No. N00014-93-C-0140) as part of their coastal water clarity program which is developing the Predictive Visibility Model (PVM).

8.0 REFERENCES

- Ackleson, S. G. and R. W. Spinrad: 1988, Size and refraction index of individual marine particulates: a flow cytometric approach, *Applied Optics*, Vol. 27, No. 7.
- Aijaz, S. and S.A. Jenkins: in press, On the Electrokinetics of Shear Stress Behavior in Fluid-Mud Suspensions, *J. Geophys. Res.*, pp20.
- Apel, J. R.: 1987, *Principles of Ocean Physics*, Academic Press, p. 511-605.
- Bader, H.: 1970, The Hyperbolic Distribution of Particle Sizes, *J. Geophys. Res.*, Vol. 75, p.2822-2830.
- Bohren, C. F. and D. R. Huffman: 1983, *Absorption and Scattering of Light by Small Particles*, John Wiley & Sons, pp.477.
- Bricaud, A, A Morel and L. Prieur: 1983, Optical efficiency factors of some phytoplankters, *Limnol. Oceanogr* 28, 816-832.

- Brown, O. B. and H. R. Gordon: 1974, Size-Refractive Index Distribution of Clear Coastal Water Particulates from Light Scattering, *Applied Optics*, Vol. 13, No. 12.
- Burt, W. V.: 1952, Scattering of Light in Turbid Water, University of California, Los Angeles graduate dissertation.
- Carder, K. L., Tomlinson, R.D. and G. F. Beardsley, Jr.: 1972, A Technique for the Estimation of Indices of Refraction of Marine Phytoplankters, *Limnol. Oceanogr.*, Vol. 17, No. 6.
- Cleveland, J.S. and A.D. Weidemann: 1993., Quantifying absorption by aquatic particles: A multiple scattering correction for glass-fiber filters. *Limnol. Oceanogr.* 38, 1321-1327.
- Cleveland, J. S. and M. J. Perry: 1994, A plankton model for partitioning particulate absorption into planktonic and detrital components, *Deep-Sea Res.*, vol. 41, no. 1, pp. 197-221.
- Dyer, K. R.: 1986, *Coastal and Estuarine Sediment Dynamics*, Wiley & Sons, New York, pp.342
- Eppley, R.W., R.W. Holmes and J.D.H. Strickland: 1967, Sinking rates of marine phytoplankton measured with a fluorometer. *J. Exp. Mar. Biol. Ecol.* 1, 191-208.
- Hansen, J. E., and L. D. Travis: 1974, Light Scattering in Planetary Atmospheres, submitted to *Space Science Reviews*.
- Jeffrey, S.W. and G.F. Humphrey : 1975, New spectrophotometric equations for determining chlorophylls a, b, c1 and c2 in higher plants, algae, and natural phytoplankton. *Biochem. Physiol. Pflanzen* 167: 191-194.
- Jerlov, N. G.: 1976, *Marine Optics*, Amsterdam: Elsevier.
- Junge, C.E.: 1963, *Air Chemistry and Radioactivity*, Academic Press, New York, p.382.
- Kirk, J. T.: 1983, Light and photosynthesis in aquatic ecosystems, Cambridge University Press, New York, pp. 72.
- Kishino, M., M. Takahashi, N. Okami, and S. Ichimura: 1985, Estimation of the spectral absorption coefficients of phytoplankton in the sea. *Bulletin of Mar. Sci.* 37, 634-642.
- Kitchen, J. C. and J. R. V. Zaneveld: 1992, A three-layer sphere model of the optical properties of phytoplankton, *Limnol. Oceanogr.*, Vol. 37, No. 8, 1680-1690.
- Krone, R.B. :1978, Aggregation of Suspended Particles in an Estuary, In: *Estuarine Transport Process*, B. Kjerfve, (ed.), Univ. of So. Carolina Press, Columbia, SC, pp177-190.
- Lee, Z., Carder K. L., Hawes, S. K., Steward, R. G., Peacock, T. G. and C. O. Davis: 1994, *J. Appl Optics* (in press).
- Morel, A.: 1975, The scattering of light by seawater; Experimental results and theoretical approach., NATO Advisory Group for Aerospace Research and Development, AGARD Lecture Series No. 61, "Optics of the Sea, Interface and in-water transmission and imaging."
- Morel, A. and L. Prieur: 1977, Analysis of variations in ocean color., *Limnol. Oceanogr.* vol. 22, pp 709-722.
- Petzold, T. J., 1972, Volume Scattering Functions for Selected Ocean Waters, Scripps Institution of Oceanography, SIO Ref. 72-78.
- Rashid, M. A., Muckley, D. E. and K. R. Robertson: 1972, Interactions of a marine humic acid with clay minerals and a natural sediment, *Geoderma*, vol. 8, p.11-27.
- Schoonmaker, J. S.: 1993., San Diego Bay Particle Size Data, unpublished data.
- Schoonmaker, J. S.: 1994, Oceanside nearshore Particle Size and Optical Measurements, unpublished data.
- Smith, R.C. and K.S. Baker: 1981, Optical properties of the clearest natural waters (200- 800 nm). *Appl. Opt.* 20, 177-184.
- Sverdrup, H. U., Johnson, M. W. and R. H. Fleming.: 1942, *The Oceans*, Prentice-Hall, Englewood Cliffs, N. J. , pp 1087.
- Tassan, S.: 1988, The effect of dissolved 'yellow substance' on the quantitative retrieval of chlorophyll and total suspended sediment concentrations from remote measurements of water colour, *International Journal of Remote Sensing*, vol. 9, no. 4, pp. 787-797.
- van de Hulst, H. C.: 1957, *Light Scattering by Small Particles*, John Wiley & Sons, New York, pp.857.

SESSION 9

General

Gas microbubbles: An assessment of their significance to light scattering in quiescent seas

Dariusz Stramski

Department of Biological Sciences
University of Southern California
Los Angeles, California 90089-0371

ABSTRACT

A review of the oceanographic literature reveals a paucity of information about the possible influences of gas microbubbles on light scattering within oceanic water. Previous in situ acoustic and holographic measurements indicate that large and persistent populations of bubbles ($> 20 \mu\text{m}$ in diameter) are a common feature of the near-surface ocean, even in the absence of whitecapping waves. In this study the main features of the light scattering by an air bubble in water are summarized using Mie scattering calculations. The possible contribution of persistent populations of microbubbles to total scattering and backscattering coefficients of sea water in quiescent seas is evaluated. This assessment is made assuming various concentrations and size distributions of bubbles larger than $20 \mu\text{m}$ in diameter, which are representative of surface waters during nearly calm sea conditions. It appears that the contribution of these bubbles to the total scattering and backscattering coefficients cannot be neglected in some oceanic situations. This contribution varies between a fraction of 1% to several percent, and might possibly be as high as a dozen or so percent. The major uncertainty in these calculations is the lack of simultaneous measurements of bubbles and light scattering. In addition, because no in situ data about bubbles less than $20 \mu\text{m}$ in size are available, these small bubbles are not taken into account in the present assessment. There is, however, circumstantial evidence that smaller bubbles with sizes down to a submicrometer range may exist in natural sea water due to stabilization by surface-active molecules and adsorbed particles. Therefore, the estimates of the influence of persistent bubble populations on light scattering in quiescent seas in the present study should be considered as preliminary and conservative.

1. INTRODUCTION

Gas bubbles in the surface layer of the ocean are important in a variety of subjects that include underwater sound propagation, air-sea gas exchange, aerosol formation, sea surface chemistry, fractionation of organic and inorganic materials and cavitation.¹⁻⁶ However, a review of the literature reveal a paucity of information about the possible influences of bubbles on oceanic optics, especially in quiescent seas. Bubbles can efficiently scatter light in water because their refractive index is considerably less than that of the surrounding media. It is therefore conceivable that bubbles, if present in sufficient numbers, can make a sizeable contribution to light scattering in sea water.

Marine bubble populations have been extensively investigated in the past using various optical and acoustical techniques.⁷⁻¹² The available information is limited to bubbles larger than $20 \mu\text{m}$ in diameter, and indicates that concentration of such bubbles may vary by several orders of magnitude under different oceanic conditions.¹³ Although at higher sea states wave injection is a major source of bubbles that make a considerable contribution to light scattering in the near-surface ocean, it is also well-documented that significant background bubble populations occur in quiescent seas in the absence of breaking waves. Recent observations using laser holography indicated that the concentration of bubbles with diameters between 20 and $30 \mu\text{m}$ can be as high as 15 bubbles per cm^3 in calm seas in the near-surface layer.¹² These data seem to support the relatively large numbers of bubbles obtained by acoustic measurements.⁹⁻¹¹ The bubbles in the background population may exist for several reasons, for example because of biological activity (e.g. photosynthesis), droplet impact, sediment outgassing and the decay of earlier whitecapping events.¹⁴ Stabilization of bubbles by surfactant films and adsorbed particles appears to be an important factor for the persistence of background populations.¹⁵⁻¹⁷

This study has been largely motivated by the need to have preliminary estimates of the contribution of the background bubble population to the scattering and backscattering coefficients in the near-surface waters under calm sea conditions.

Using Mie scattering calculations I first summarize the patterns of scattering and backscattering efficiencies for bubbles of different size suspended in sea water. I then estimate the bulk scattering and backscattering coefficients associated with typical populations of bubbles larger than 20 μm in diameter, and compare these values with the scattering and backscattering coefficients of sea water.

2. SCATTERING AND BACKSCATTERING EFFICIENCIES

Mie scattering calculations for an air bubble suspended in sea water with a real part of refractive index of 1.34 were made using an algorithm for homogeneous spheres.¹⁸ Specifically, the scattering efficiency factor, Q_b , and the backscattering efficiency factor, Q_{bb} , were calculated at a light wavelength of 550 nm for bubbles ranging in diameter D from 0.01 to 300 μm . The increment in these calculations was 0.001 μm between 0.01 and 0.1 μm , 0.01 μm between 0.1 and 1 μm , 0.1 μm between 1 and 10 μm , and 1 μm between 10 and 300 μm . While the scattering efficiency represents the total scattered light, the backscattering efficiency represents the integral of light scattered at angles between 90° and 180° . For comparison similar calculations were made for non-absorbing particles with a comparatively low refractive index relative to water (1.05) and a high refractive index (1.15).

The results of these calculations are shown in Figures 1 and 2. The initial increase of the scattering efficiency with increasing diameter is steeper for bubbles than for particles. The Q_b values at 550 nm for bubbles are higher than those of high-index particles in the submicrometer range. In comparison to low-index particles, the bubbles have higher scattering efficiency for $D < 3 \mu\text{m}$. The first maximum of Q_b for bubbles is reached at approximately 1.1 μm , but its magnitude is significantly lower than that for particles. The second maximum for bubbles (which is at $D = 2.8 \mu\text{m}$) is relatively well pronounced and its magnitude is in fact slightly higher than that of the first maximum. In contrast, such a feature is absent in the patterns representing particles. With increasing diameter Q_b approaches 2 and its oscillations are reduced which is a well-known characteristic of large scattering objects.

The backscattering efficiency, Q_{bb} , of bubbles at 550 nm is significantly higher, generally by more than an order of magnitude, than that of low-index particles over the entire size range examined. If compared with high-index particles, Q_{bb} of bubbles is higher or similar in the submicrometer range but lower for larger diameters. The maximum value of Q_{bb} for bubbles is 0.041 and occurs at a diameter of 0.23 μm . For bubbles $> 1 \mu\text{m}$ there is very little variation in Q_{bb} which is generally between 0.02 and 0.025.

3. BULK SCATTERING AND BACKSCATTERING BY BUBBLE POPULATIONS

The bulk scattering and backscattering coefficients at 550 nm associated with a given population of bubbles present in sea water were calculated from:

$$b(\text{bubbles}) = \int_{D_{\min}}^{D_{\max}} Q_b(D) (\pi D^2/4) F(D) dD \quad (1)$$

$$b_b(\text{bubbles}) = \int_{D_{\min}}^{D_{\max}} Q_{bb}(D) (\pi D^2/4) F(D) dD \quad (2)$$

where $F(D)$ is the density function of size distribution of bubbles such that $F(D) dD$ is the concentration of bubbles with diameters in the range $(D, D + dD)$, D_{\min} and D_{\max} delimit the size range of the bubble population, and $\pi D^2/4$ is the projected area of the bubble with a diameter D .

At present there is no in situ data about microbubbles less than 20 μm in diameter; therefore it is not yet possible to determine the size distribution $F(D)$ of bubbles over all diameters. Most data from acoustical and optical determinations of bubbles at sea cover the diameter range from about 20 μm to several hundred of micrometers.¹³ In addition, there is often a significant discrepancy between acoustical and optical determinations which result from inherent inaccuracies associated with these techniques and the fact that these techniques may count, to some extent, different objects.¹⁹ Recent measurements at sea by O'Hern et al.¹² using laser holography seem to support fairly high concentrations of bubbles usually derived by acoustic measurements⁹⁻¹¹ during nearly calm sea conditions. The concentration of bubbles ranging in diameter from 20 to 30 μm determined by O'Hern and his co-workers varied between $6 \cdot 10^5 \text{ m}^{-3}$ and $1.5 \cdot 10^7 \text{ m}^{-3}$ in the top 30 meters of the ocean off southern California near Santa Catalina Island in calm sea conditions (sea state was 0 to 1, with

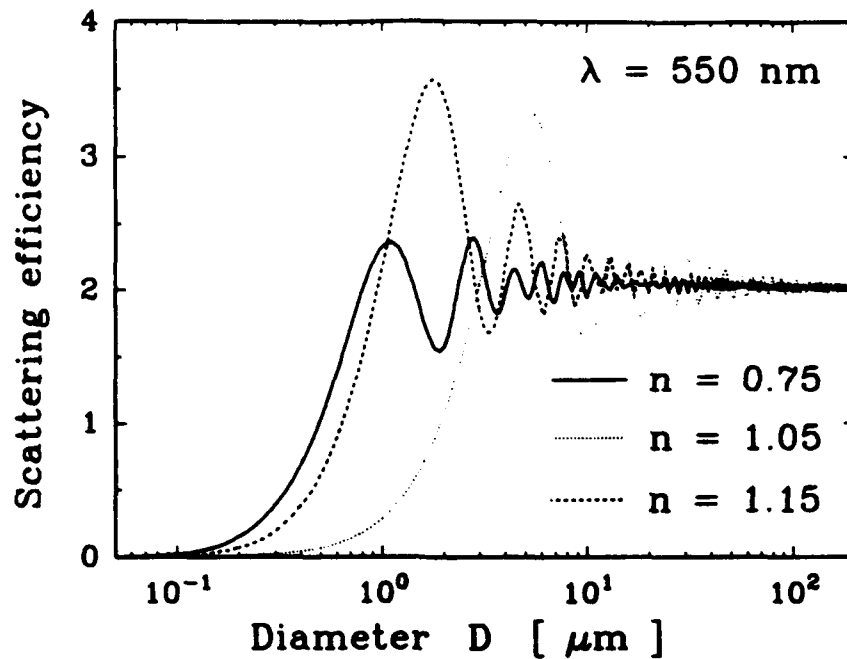


Fig. 1. The scattering efficiency factor at 550 nm for air bubbles suspended in sea water as a function of bubble diameter (solid line). The approximate value of the real part of refractive index of a bubble relative to sea water ($n = 0.75$) is indicated. For comparison, similar curves are plotted for particles with relatively low ($n = 1.05$) and high ($n = 1.15$) refractive index as indicated.

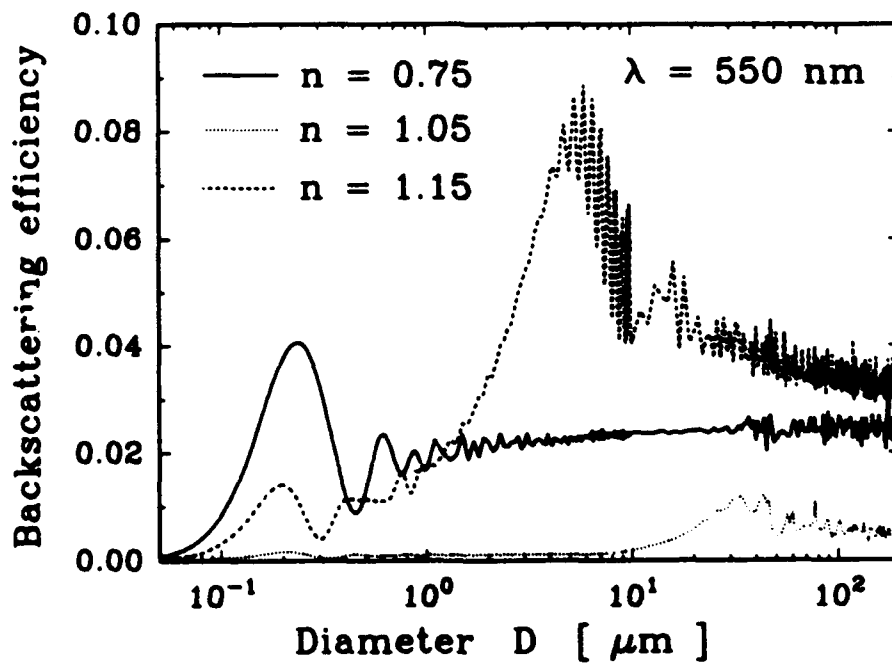


Fig. 2. As Figure 1 but for backscattering efficiency.

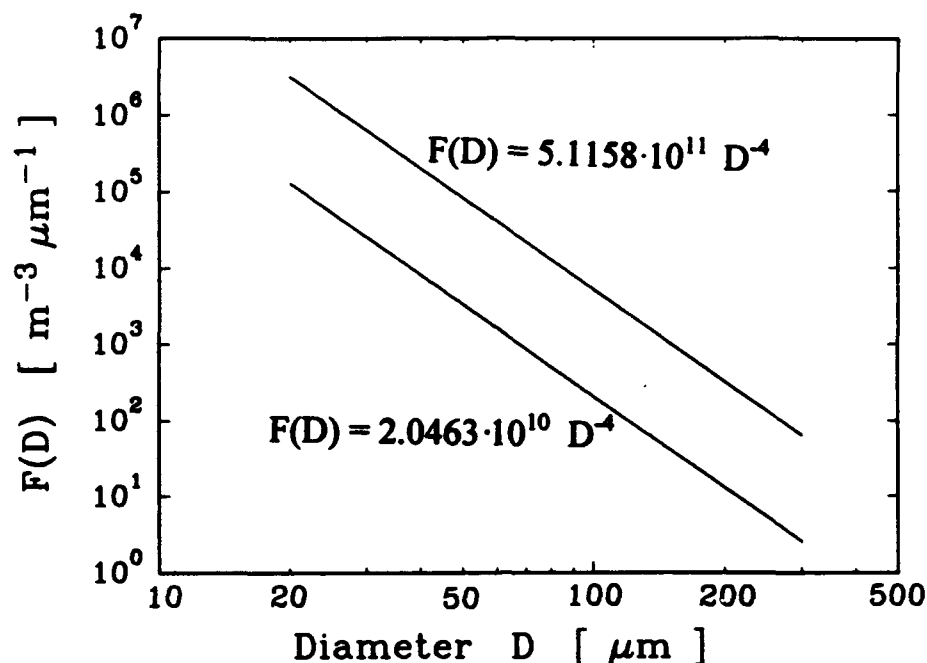


Fig. 3. The density functions of size distribution of bubbles which represent low and high concentration of bubbles in the diameter range between 20 and 300 μm in the near-surface ocean in calm conditions. The equations describing these distributions are given.

less than 0.3 m swell and no wind). For the purpose of this study, I use two size distribution functions, $F(D)$, such that their integral between $D = 20 \mu\text{m}$ and $D = 300 \mu\text{m}$ corresponds to the two values of bubble concentration mentioned above (Fig.3). These two cases will be referred to as low and high bubble concentration. In addition, it is assumed that $F(D)$ has a diameter dependence D^{-4} over the entire range considered between $D_{\min} = 20 \mu\text{m}$ and $D_{\max} = 300 \mu\text{m}$. This dependence is generally consistent with acoustic measurements of bubble populations at sea although most data suggest that the slope of the $F(D)$ function is less steep for diameters $> 120 \mu\text{m}$.⁹⁻¹¹ I have chosen to keep the slope of -4 over the entire diameter range to assure that the estimates of bubble concentration and the associated scattering coefficients are more conservative. The total bubble concentration between $D_{\min} = 20 \mu\text{m}$ and $D_{\max} = 300 \mu\text{m}$ is approximately $9.179 \cdot 10^5 \text{ m}^{-3}$ and $2.295 \cdot 10^7 \text{ m}^{-3}$ for the case of low and high concentration respectively.

The scattering coefficient, $b(\text{bubbles})$, calculated from equation (1) is $1.514 \cdot 10^{-3} \text{ m}^{-1}$ for the low bubble concentration and $3.785 \cdot 10^{-2} \text{ m}^{-1}$ for the high bubble concentration. Similarly, the calculations of the backscattering coefficient according to equation (2) yield $b_b(\text{bubbles})$ of $1.810 \cdot 10^{-5} \text{ m}^{-1}$ and $4.525 \cdot 10^{-4} \text{ m}^{-1}$ for the low and high bubble concentration respectively. It is of interest to compare these values with typical scattering and backscattering coefficients which occur in the near-surface ocean. Using a large database from simultaneous measurements of total scattering coefficient at 550 nm, $b(550)$, and pigment concentration C (chlorophyll a plus phaeophytin a) Gordon and Morel²⁰ proposed a relationship for Case 1 surface waters:

$$b(550) = 0.3 C^{0.62} \quad (3)$$

In fact, most data in such waters are confined to the band between two curves described by similar equation with the exception that the factor 0.3 is replaced by 0.15 for the lower limit and 0.45 for the upper limit (see also Morel²¹). Figure 4 shows such a band representing typical range of $b(550)$ values as a function of pigment concentration in Case 1 surface waters. The range of $b(\text{bubble})$ delimited by the values corresponding to the low and high bubble concentration and the scattering coefficient of pure sea water, $b_w(550) = 0.0019 \text{ m}^{-1}$, are also shown. This figure suggests that bubbles may have a sizeable and non-negligible contribution to the total scattering coefficient of sea water in certain oceanic situations,

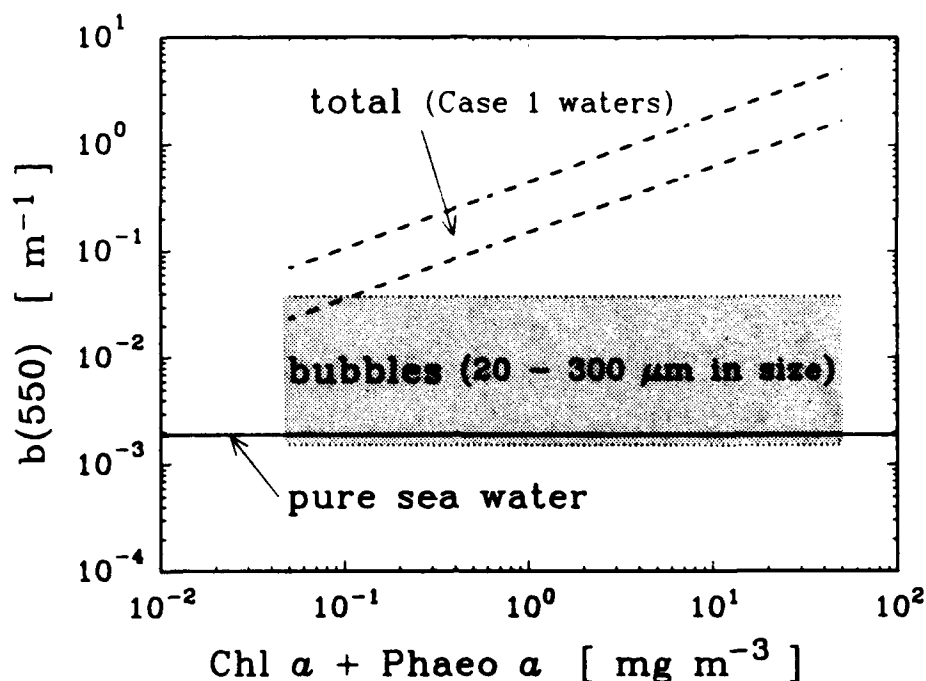


Fig. 4. Typical range of the total scattering coefficient at 550 nm in Case 1 surface waters as a function of pigment concentration (dashed lines) after Morel.²¹ The range of the scattering coefficient associated with the bubble populations is indicated in the shaded area. The lower and upper limits of this range correspond to the lower and upper size distributions of bubbles presented in Fig. 3. For comparison, the scattering coefficient of pure sea water at 550 nm is also shown (solid line).

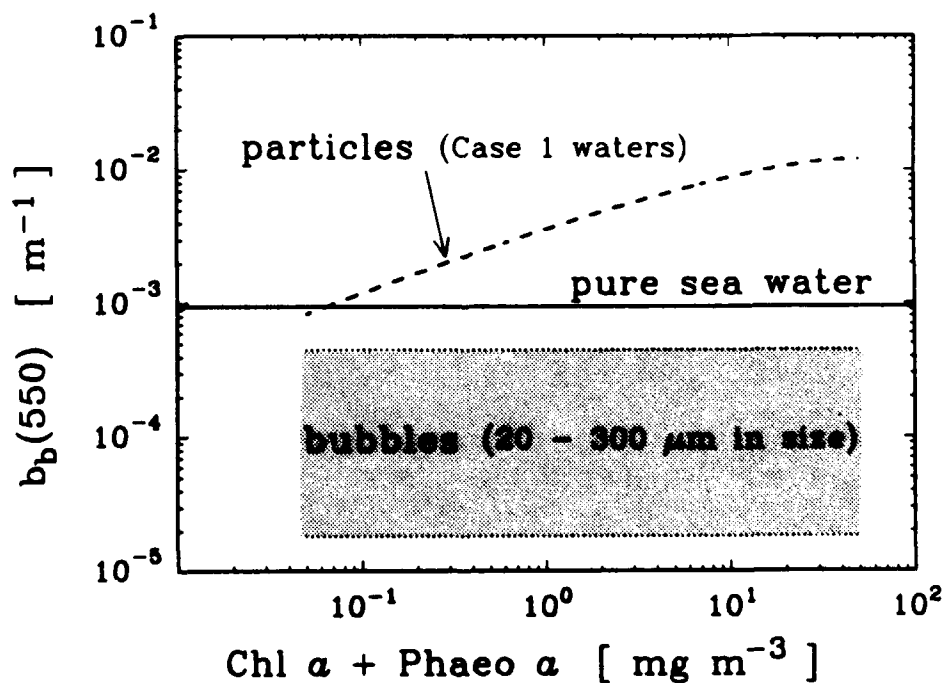


Fig. 5. The backscattering coefficient of marine particles at 550 nm as a function of pigment concentration in surface oceanic waters (dashed line) after Morel.²² The range of the backscattering coefficient of bubbles corresponding to different bubble concentrations as presented in Fig. 3 is shown in the shaded area. For comparison, the backscattering coefficient of pure sea water at 550 nm is also shown (solid line).

under calm windless conditions. As an example, at pigment concentration of 0.5 mg m^{-3} , $b(\text{bubbles})$ is 0.8% and 19% of $b(550)$ determined from equation (3) for the low and high bubble concentration respectively. In addition, the light scattering at 550 nm associated with bubbles is expected to be usually higher than that of pure sea water; $b(\text{bubbles})$ is lower than $b_w(550)$ by about 20% for the low bubble concentration but higher by a factor of approximately 20 at high bubble concentration.

No in situ data on the total backscattering coefficient of sea water are available; therefore I here use the relationship proposed by Morel²² for the backscattering of particles, b_{bp} , as a function of pigment concentration C , which was derived through theoretical considerations with some support from experimental data:

$$b_{bp}(550) = [0.3 C^{0.62} - b_w(550)] [0.002 + 0.02 (0.5 - 0.25 \log C)] \quad (4)$$

In contrast to the original formulation by Morel, the first term in equation (4) is corrected by subtracting the contribution of pure sea water $b_w(550)$. Figure 5 shows $b_{bp}(550)$ along with the backscattering coefficient of pure seawater, $b_{bw}(550) = 0.00095 \text{ m}^{-1}$, and the range of $b_b(\text{bubbles})$ delimited by values corresponding to the low and high bubble concentration. The estimates of $b_b(\text{bubbles})$ are lower than the backscattering associated with pure sea water; the values of $b_b(\text{bubbles})$ are 1.9 to 47.6% of $b_{bw}(550)$. Nevertheless, similarly to the total scattering, bubbles may have sizeable and non-negligible contribution to the backscattering coefficient of sea water. At the pigment concentration $C = 0.5 \text{ mg m}^{-3}$, $b_b(\text{bubbles})$ is 0.7% and 17.3% of particulate backscattering $b_{bp}(550)$ for the low and high bubble concentration respectively. These percent values decrease to 0.5% and 12.7% if $b_b(\text{bubbles})$ is compared to the sum of $b_{bw}(550)$ and $b_{bp}(550)$.

4. CONCLUSIONS

While it is well-known that gas bubbles may dominate light scattering in the near-surface water in rough seas due to injection by breaking waves, the question of what effect the persistent bubble populations might have on ocean optics in quiescent seas has not received, to my knowledge, any significant attention in the past. In this study, I obtained preliminary estimates of the magnitude of scattering and backscattering coefficients associated with typical populations of bubbles ($> 20 \mu\text{m}$ in diameter) present in the near-surface layer in calm sea conditions. This assessment has been largely prompted by recent holographic measurements of bubbles at sea¹² which appear to provide reliable estimates of bubble concentration and resolve, at least partly, the apparent conflict between acoustical and optical results.^{11,19} The present calculations suggest that bubbles may have a sizeable and non-negligible contribution, occasionally perhaps even as high as dozen or so percent, to the scattering and backscattering coefficients of sea water in calm sea conditions. Although this result is preliminary, the estimated contribution is high enough to indicate a need for further research to clarify the influences of microbubbles on oceanic optics.

It is important to emphasize that this assessment should only be considered as a starting point for continuing study because it is based on relatively simple assumptions and necessarily omits some phenomena which are presently difficult to consider in quantitative terms. For example, it has been here assumed that only free bubbles in the diameter range from 20 to $300 \mu\text{m}$ are present although very small bubbles, even in the submicrometer range, may persist in sea water.¹⁶⁻¹⁷ Unfortunately, no in situ data for bubble diameters $< 20 \mu\text{m}$ are now available. Small bubbles, once formed, may persist for an extended period of time because of surfactant coating or attachment to particles.²³ However, the scattering properties of such objects in marine environments may be very difficult to quantify accurately, and simple Mie calculations for homogeneous spheres will likely be inadequate in this case. In addition, there is circumstantial evidence that microbubbles, similar to gas vacuoles in the blue-green algae, are associated with various species of marine phytoplankton.²⁴ Finally, it is possible that bubbles will have significantly different effect on light scattering at various light wavelengths which has not been addressed in the present study.

5. ACKNOWLEDGEMENTS

This work was supported by the Oceanic Optics Program of the U.S. Office of Naval Research (grant N00014-93-1-0134), and NASA Ocean Biogeochemistry Program (grant NAGW-3574). My interest in the subject was provoked by discussions with A. Shalapyonok, and this work also benefited from discussions with D.A. Kiefer.

6. REFERENCES

1. M. Shulkin, "Surface-coupled losses in surface sound channel propagation. II.", *J. Acoust. Soc. Am.*, 45, pp. 1054-1055, 1969.
2. S. A. Thorpe, "On the clouds of bubbles formed by breaking wind-waves in deep water, and their role in air-sea gas transfer", *Phil Trans. R. Soc. Lond.*, A 304, pp. 155-210, 1982.
3. D. C. Blanchard and A. H. Woodcock, "Bubble formation and modification in the sea and its meteorological significance", *Tellus*, 9, pp. 145-158, 1957.
4. W. H. Sutcliffe, Jr., E. R. Baylor and D.W. Menzel, "Sea surface chemistry and Langmuir circulation", *Deep-Sea Res.*, 10, pp. 233-243, 1963.
5. G.T. Wallace, Jr., and R. A. Duce, "Concentration of particulate trace metals and particulate organic carbon in marine surface waters by a bubble flotation mechanism", *Mar. Chem.*, 3, pp. 157-181, 1975.
6. F.E. Fox and K. F. Herzfeld, "Gas bubbles with organic skin as cavitation nuclei", *J. Acoust. Soc.*, 26, pp. 984-989, 1954.
7. P. A. Kolovayev, "Investigation of the concentration and the statistical size distribution of wind-produced bubbles in the near-surface ocean layer", *Oceanology*, 15, pp. 659-661, 1976.
8. B. D. Johnson and R. C. Cooke, "Bubble populations and spectra in coastal water: A photographic approach", *J. Geophys. Res.*, 84, pp. 3761-3766, 1979.
9. H. Medwin, "In situ acoustic measurements of bubble populations in coastal ocean waters", *J. Geophys. Res.*, 75, pp. 599-611, 1970.
10. H. Medwin, "In situ acoustic measurements of microbubbles at sea", *J. Geophys. Res.*, 82, pp. 971-976, 1977.
11. H. Medwin and N. D. Breitz, "Ambient and transient bubble spectral densities in quiescent seas and under spilling breakers", *J. Geophys. Res.*, 94 (C9), pp. 12751-12759, 1989.
12. T. J. O'Hern, L. d'Agostino, and A. J. Acosta, "Comparison of holographic and Coulter counter measurements of cavitation nuclei in the ocean", *Transactions of the ASME, J. Fluids Eng.*, 110, pp. 200-207, 1988.
13. V. Akulichev and V. Bulanov, "The study of sound backscattering from micro-inhomogeneities in seawater", In: H. M. Merklinger [ed.], *Progress in Underwater Acoustics*, pp. 250-268, Plenum, New York, 1987.
14. B. D. Johnson, "Bubble populations: Background and breaking waves", In: E. C. Monahan and G. Mac Niocaill [eds.], *Oceanic Whitecaps and Their Role in Air-Sea Exchange Processes*, pp. 69-73, D. Reidel Publishing Co., Dordrecht, 1986.
15. D. E. Yount, "Skins of varying permeability: A stabilization mechanism for gas cavitation nuclei", *J. Acoust. Soc. Am.*, 65, pp. 1429-1439, 1979.
16. B. D. Johnson and R. C. Cooke, "Generation of stabilized microbubbles in seawater", *Science*, 213, pp. 209-211, 1981.
17. B. D. Johnson and P. J. Wangersky, "Microbubbles: Stabilization by monolayers of adsorbed particles", *J. Geophys. Res.*, 92 (C13), pp. 14641-14647, 1987.
18. C. F. Bohren and D. R. Huffman, *Absorption and Scattering of Light by Small Particles*, John Wiley & Sons, New York, 1983.
19. F. MacIntyre, "On reconciling optical and acoustical bubble spectra in the mixed layer", In: E. C. Monahan and G. Mac Niocaill [eds.], *Oceanic Whitecaps and Their Role in Air-Sea Exchange Processes*, pp. 75-94, D. Reidel Publishing Co., Dordrecht, 1986.
20. H. R. Gordon and A. Y. Morel, "Remote assessment of ocean color for interpretation of satellite visible imagery, a review", In: R. T. Barber, M. J. Bowman, C. N. K. Mooers and B. Zeitzschel [eds.], *Lecture Notes on Coastal and Estuarine Studies*, Springer-Verlag, New York, 1983.
21. A. Morel, "Chlorophyll-specific scattering coefficient of phytoplankton. A simplified theoretical approach", *Deep-Sea Res.*, 34, pp. 1093-1105, 1987.
22. A. Morel, "Optical modeling of the upper ocean in relation to its biogeochemical matter content (case I waters)", *J. Geophys. Res.*, 93(C9), pp. 10749-10768, 1988.
23. P. J. Mulhearn, "Distribution of microbubbles in coastal waters", *J. Geophys. Res.*, 86 (C7), pp. 6429-6434, 1981.
24. B. M. Sandler, D. A. Selivanovsky, P. A. Stunzha, and D. K. Krupatkina, "Gas vacuoles in marine phytoplankton: Ultrasonic resonance measurements", *Oceanology*, 32, pp. 60-65, 1992.

Ocean source estimation using irradiance measurements at only one depth

N.J. McCormick

University of Washington, Department of Mechanical Engineering
Seattle, Washington 98195 USA

ABSTRACT

A preliminary investigation is made of a method to estimate the spatial distribution of an optical source at a single wavelength in a spatially-uniform seawater of known absorption and scattering properties. The source at the wavelength of interest could be inelastic scattering, fluorescence, or bioluminescence, for example. An algorithm is developed with which to estimate two coefficients that describe the source from only downward and upward irradiance measurements at two depths that can be far apart, or four coefficients if the downward and upward scalar irradiances also are measured. For the special case of a spatially-uniform, semi-infinite seawater then measurements at one depth are sufficient but the number of coefficients that can be estimated is reduced by a factor of two. The algorithm is derived assuming that the radiance is in the asymptotic regime, which means results will be less accurate if measurements are made too near the sea surface.

Keywords: ocean optics, radiative transfer, inverse problem, inelastic scattering, fluorescence, bioluminescence

1. INTRODUCTION

Procedures have been developed earlier for the estimation of sources in seawater using *in situ* measurements of the downward and upward components of the (vector) irradiance and scalar irradiance.¹⁻⁴ Such procedures offer the possibility of estimating the sources in waters for which the optical properties, such as the absorption coefficient, are not known; a further advantage is that the layers of water need not be of uniform optical properties since depth-profiling measurements are made. In these earlier "small-step" procedures, optical measurements at two depths separated by at most a few meters were used to estimate the source and other properties between the two depths.

The objective here, however, is to develop a "large-step" algorithm to estimate a spatially-dependent source (such as inelastic scattering, fluorescence, or bioluminescence) between two measurement positions far apart. As a consequence of the more limited number of measurements, however, it must be assumed that all the optical properties are known for seawater that is spatially-uniform between the two measurement positions. Even if such conditions are not precisely met, however, the algorithm can be used with depth-dependent profiling measurements whenever the inherent optical properties are approximately uniform with depth.

An important feature of the algorithm is that if the seawater of uniform optical properties is so deep that it can be considered as a semi-infinite medium, then there is no need

for the measurements at the deeper depth. The large-step algorithm then becomes a "one-depth" procedure.

It is worth mentioning that the new, large-step algorithm can be used in certain situations (such as a slowly-changing source with depth) to check the accuracy of the small-step algorithm of Ref. 2 for which the optical properties are assumed known.

Earlier work on the large-step source estimation problem is presented in Refs. 5-7. Larsen⁵ considered a semi-infinite medium and developed a closed-form equation with which to determine a spatially-dependent isotropic source from an inverse Laplace transform of an integral of the inward and outward radiance data at the boundary. Li and Özişik⁶ solved for an isotropic source distribution in a spatially-uniform layer using an iterative method that relied on radiance measurements and P_N radiative transfer calculations of the radiance. Siewert⁷ developed an explicit solution generalizing the earlier work that also relied on radiance measurements. Since almost all ocean optics optical measurements are of downward and upward irradiances which are sometimes supplemented by downward and upward scalar irradiance measurements, our principal interest here is to derive an algorithm that requires only irradiance and scalar measurements and not radiance measurements.

After establishing some notation in Sec. 2, the general ideas behind the development of the algorithm are presented in Sec. 3 for cases when the measurements are made at two depths deep enough that the radiance is in the asymptotic regime. Several simple numerical tests of the algorithm are presented in Sec. 4 which lead to some tentative conclusions about the algorithm that are given in Sec. 5.

2. NOTATION

The analysis is based on the linear, integrodifferential radiative transfer equation for a time-independent, azimuthally-integrated radiance $L(z, \mu)$, where μ is the cosine of the nadir angle with respect to depth z at an implicit wavelength for the source and detector. The equation is

$$\mu \frac{\partial}{\partial z} L(z, \mu) + cL(z, \mu) = \frac{b}{2} \sum_{n=0}^N (2n+1) f_n P_n(\mu) \int_{-1}^1 P_n(\mu') L(z, \mu') d\mu' + \frac{c}{2} S(z). \quad (1)$$

Here $cS(z)/2$ is the rate per unit volume at which photons are isotropically emitted by inelastic scattering, fluorescence, or bioluminescence. The absorption coefficient a and the scattering coefficient b are the probability per unit distance of travel that a photon will be absorbed and scattered, respectively; $c = a + b$ is the beam attenuation coefficient. The scattering phase function has been expanded in terms of Legendre polynomials $P_n(\mu)$, with the expansion coefficients f_n normalized so that $f_0 = 1$.

Since the optical properties of the layer are assumed known, we can use the dimensionless variable $cz = \tau + \tau_r$ for the depth. Here τ_r is a reference depth for the shallowest boundary of the layer, and $0 \leq \tau \leq \tau_o$ where τ_o is the optical thickness of the layer of interest.

The general, analytical solution of the direct radiative transfer problem can be expressed using the complete set of eigenfunctions $\phi_\nu(\mu)$ of the homogeneous radiative transfer equation.⁸⁻¹⁰ The eigenfunction expansion for the layer can be written as

$$L(\tau, \mu; \tau_r) = \sum_{j=1}^J [A(\nu_j) \phi_{\nu_j}(\mu) \exp(-\tau/\nu_j) + A(-\nu_j) \phi_{-\nu_j}(\mu) \exp(\tau/\nu_j)] \\ + \int_{-1}^1 A(\nu) \phi_\nu(\mu) \exp(-\tau/\nu) d\mu + L_p(\tau, \mu; \tau_r), \quad 0 \leq \tau \leq \tau_o. \quad (2)$$

The expansion coefficients $A(\pm\nu_j)$ and $A(\nu)$ are determined from the boundary conditions when solving a direct radiative transfer problem using Eq. (1) but, since we wish to solve an inverse problem without solving a direct problem, the coefficients must be eliminated when we develop a source estimation algorithm. The eigenvalues of the homogeneous radiative transfer equation are $\pm\nu_j$ for $j = 1$ to J , with $1 < |\nu_j| < \infty$. The eigenvalues are dimensionless, inherent optical properties that depend only on other optical properties such as the single-scattering albedo $\omega = b/c$ and the expansion coefficients f_n . The eigenvalues will be ordered so that $\nu_1 > \nu_2 > \dots \geq 1$; the value of c/ν_1 is just the asymptotic diffuse attenuation coefficient (often denoted as K_∞). For a weakly absorbing wavelength, up to 13 eigenvalues have been reported,¹¹ but fewer occur as ω decreases.

The eigenvalues ν_j can be calculated as the roots of the transcendental equation⁸⁻¹⁰

$$1 - \frac{\omega x}{2} \int_{-1}^1 \frac{g(\mu, \mu)}{x - \mu} d\mu = 0$$

for $x \notin (-1, 1)$. Here

$$g(\nu, \mu) = \sum_{n=0}^N (2n+1) f_n g_n(\nu) P_n(\mu), \quad (3)$$

where the $g_n(\nu)$ are polynomials of degree n , even or odd depending on whether n is even or odd, that satisfy the recursion relation

$$(n+1)g_{n+1}(\nu) - (2n+1)(1 - \omega f_n)\nu g_n(\nu) + n g_{n-1}(\nu) = 0, \quad n \geq 0.$$

The $g_n(\nu)$ are defined by

$$g_n(\nu) = \int_{-1}^1 P_n(\mu) \phi_\nu(\mu) d\mu, \quad (4)$$

with a normalization of the eigenfunctions given by $g_0(\nu) = 1$, and with $g_{-1}(\nu) = 0$. The eigenfunctions satisfy the equation⁸⁻¹⁰

$$(\nu - \mu) \phi_\nu(\mu) = \frac{\omega}{2} \nu g(\nu, \mu). \quad (5)$$

The particular solution $L_p(\tau, \mu; \tau_r)$ in Eq. (2) is a function of the source and must be computed by assuming a source profile within the layer $0 \leq \tau \leq \tau_o$ and evaluating $L_p(\tau, \mu; \tau_r)$ as any solution of the radiative transfer (i.e., it need not necessarily match the boundary conditions). For example, for an isotropic source that is assumed to spatially vary as

$$S(\tau; \tau_r) = \sum_{k=0}^K \hat{Q}_k \tau^k, \quad (6a)$$

the constants \hat{Q}_k must be estimated. The particular solution for such a source is¹²

$$L_p(\tau, \mu; \tau_r) = \frac{1}{2h_0} \sum_{k=0}^K \hat{Q}_k \sum_{\ell=0}^k (2\ell + 1) T_\ell^k(\tau) P_\ell(\mu), \quad (6b)$$

where $h_\ell = (2\ell + 1)(1 - \omega_{f\ell})$ and, for $K \leq 3$, the polynomials $T_\ell^k(\tau)$ of degree $k - \ell$ are listed in Table 1. Particular solutions for other spatially-distributed sources, such as $S(\tau) = \hat{Q}_0 \exp(-\tau/\hat{\alpha})$ for a constant $\hat{\alpha} > 0$, also are available.^{12,13}

Table 1. Some coefficients $T_\ell^k(\tau)$ for the particular solution expansions of Eqs. (6b) and (8).

ℓ	$k=0$	$k=1$	$k=2$	$k=3$
0	1	τ	$\frac{2}{h_0 h_1} + \tau^2$	$\frac{6}{h_0 h_1} \tau + \tau^3$
1		$-\frac{1}{h_1}$	$-\frac{2}{h_1} \tau$	$-6 \left(\frac{4h_0 + h_2}{h_0 h_1^2 h_2} \right) - \frac{3}{h_1} \tau^2$
2			$\frac{4}{h_1 h_2}$	$\frac{12}{h_1 h_2} \tau$
3				$-\frac{36}{h_1 h_2 h_3}$

In ocean optics investigations, hemispherically-integrated moments of the downward (+) and upward (-) radiance are often measured,

$$\begin{aligned} E_{n+}(\tau; \tau_r) &= \int_0^1 P_n(\mu) L(\tau, \mu; \tau_r) d\mu, \\ E_{n-}(\tau; \tau_r) &= \int_{-1}^0 P_n(\mu) L(\tau, \mu; \tau_r) d\mu. \end{aligned} \quad (7)$$

(The moments $\pm E_{1\pm}(\tau; \tau_r)$, for example, are the downward/upward irradiances.) Similar definitions for hemispherical angular moments of the particular solution give two equations (one for the top sign and the other for the bottom sign) for the particular solution of Eq. (6b),

$$E_{pn\pm}(\tau; \tau_r) = \frac{1}{2h_0} \sum_{k=0}^K \hat{Q}_k \sum_{\ell=0}^k (\pm 1)^{n+\ell} (2\ell + 1) \gamma_{\ell n} T_\ell^k(\tau), \quad (8\pm)$$

where the values of $\gamma_{\ell n} = \int_0^1 P_\ell(\mu)P_n(\mu)d\mu$ are given in Table 2.

Table 2. Some coefficients $\gamma_{\ell n} = \gamma_{n\ell}$ for the particular solution expansions of Eq. (8).

ℓ	$n=0$	$n=1$	$n=2$	$n=3$
0	1	1/2	0	-1/8
1		1/3	1/8	0
2			1/5	1/8
3				1/7

It is convenient to also define the downward and upward moments of the eigenfunctions,

$$g_{n+}(\nu) = \int_0^1 P_n(\mu)\phi_\nu(\mu)d\mu, \quad (9a)$$

$$g_{n-}(\nu) = \int_{-1}^0 P_n(\mu)\phi_\nu(\mu)d\mu, \quad (9b)$$

where we immediately see that $g_{n+}(\nu) + g_{n-}(\nu) = g_n(\nu)$. Because of the property

$$g_{n-}(\pm\nu) = (-1)^n g_{n+}(\mp\nu), \quad (9c\pm)$$

it follows that only two values, say $g_{n\pm}(\nu)$ for positive ν , need be computed using Eqs. (9a,b). With the preceding definitions it follows, after integrating Eq. (2) and using Eq. (9c), that

$$E_{n\pm}(\tau; \tau_r) - E_{pn\pm}(\tau; \tau_r) = \sum_{j=1}^J [A(\nu_j)g_{n\pm}(\nu_j) \exp(-\tau/\nu_j) + (-1)^n A(-\nu_j)g_{n\mp}(\nu_j) \exp(\tau/\nu_j)] \\ + \int_{-1}^1 A(\nu)g_{n\pm}(\nu) \exp(-\tau/\nu)d\nu, \quad 0 \leq \tau \leq \tau_o. \quad (10\pm)$$

3. THE ALGORITHM

The eigenfunction expansion of Eq. (2) is an especially convenient way to represent an asymptotic light field. Because $\nu_j \geq 1$ and $\nu < 1$, the integral (i.e., "transient") terms disappear most rapidly as τ increases, and for a sufficiently large depth the terms with the larger ν_j values (ν_2, ν_3 , etc.) also can be neglected. The hemispherical angular moments of the asymptotic light field thus can be described by the two equations

$$E_{n\pm}(\tau; \tau_r) - E_{pn\pm}(\tau; \tau_r) = A(\nu_1)g_{n\pm}(\nu_1) \exp(-\tau/\nu_1) + (-1)^n A(-\nu_1)g_{n\mp}(\nu_1) \exp(\tau/\nu_1). \quad (11\pm)$$

Once the asymptotic approximation is made, however, the value of n should be restricted to either 0 or 1 because there is a degeneracy with higher-order angular moments of the radiance; see Ref. 4, for example.

To derive the algorithm we need to eliminate the expansion coefficients $A(\pm\nu_1)$ that depend on the boundary conditions for $\tau = 0$ and $\tau = \tau_o$. We first multiply Eq. (11) by $g_{n\pm}(\nu_1)$ to find

$$g_{n\pm}(\nu_1)[E_{n\pm}(\tau; \tau_r) - E_{pn\pm}(\tau; \tau_r)] \\ = A(\nu_1)g_{n\pm}^2(\nu_1)\exp(-\tau/\nu_1) + (-1)^n A(-\nu_1)g_{n\pm}(\nu_1)g_{n\mp}(\nu_1)\exp(\tau/\nu_1), \quad n = 0, 1,$$

and then subtract one of these equations from the other to obtain

$$g_{n+}(\nu_1)[E_{n+}(\tau; \tau_r) - E_{pn+}(\tau; \tau_r)] - g_{n-}(\nu_1)[E_{n-}(\tau; \tau_r) - E_{pn-}(\tau; \tau_r)] \\ = A(\nu_1)[g_{n+}^2(\nu_1) - g_{n-}^2(\nu_1)]\exp(-\tau/\nu_1), \quad n = 0, 1.$$

After setting $\tau = 0$ and $\tau = \tau_o$ in the last equation, two equations for the unknown $A(\nu_1)[g_{n+}^2(\nu_1) - g_{n-}^2(\nu_1)]$ are obtained that can be equated. After algebraic rearrangement we finally obtain (for the equation with the top sign)

$$[E_{n+}(0; \tau_r) - \exp(\pm\tau_o/\nu_1)E_{n+}(\tau_o; \tau_r)] - \beta_n^{\mp 1}[E_{n-}(0; \tau_r) - \exp(\pm\tau_o/\nu_1)E_{n-}(\tau_o; \tau_r)] \\ = [E_{pn+}(0; \tau_r) - \exp(\pm\tau_o/\nu_1)E_{pn+}(\tau_o; \tau_r)] \\ - \beta_n^{\mp 1}[E_{pn-}(0; \tau_r) - \exp(\pm\tau_o/\nu_1)E_{pn-}(\tau_o; \tau_r)], \quad n = 0, 1, \quad (12\pm)$$

where β_n is defined by

$$\beta_n = \frac{g_{n+}(\nu_1)}{g_{n-}(\nu_1)} \quad (13)$$

and can be computed from Eqs. (9a,b). (Equation (12-) follows by first multiplying Eq. (11) by $g_{n\mp}(\nu_1)$ and then following the same procedure as above to obtain two equations for the unknown $(-1)^n A(-\nu_1)[g_{n+}^2(\nu_1) - g_{n-}^2(\nu_1)]$ that can be equated.)

We first consider the case when the spatially-uniform layer between the two measurement positions is of finite thickness. Equations (12) then are a set of four equations in which measured downward and upward irradiances and scalar irradiances at the two boundaries $cz = \tau_r$ and $cz = \tau_o + \tau_r$ can be inserted on the left-hand side and assumed source distributions containing unknown parameters are put in the right-hand side. The combination of Eqs. (8) and (12), for example, gives a means of estimating the unknown coefficients \hat{Q}_k , $k = 0$ to 3, from the downward and upward irradiances $\pm E_{1\pm}(0; \tau_r)$ and $\pm E_{1\pm}(\tau_o; \tau_r)$ and the downward and upward scalar irradiances $E_{0\pm}(0; \tau_r)$ and $E_{0\pm}(\tau_o; \tau_r)$ at the two boundaries. If a source with only the unknown parameters \hat{Q}_0 and \hat{Q}_1 were to be estimated, then only the two equations for $n = 1$ involving the downward and upward irradiances at $\tau = 0$ and $\tau = \tau_o$ would be needed, for example.

We next consider the case when the spatially-uniform layer between the two measurement positions is semi-infinite in extent. Then $\tau_o \rightarrow \infty$ and the two equations for Eq. (12+) cannot be used, while those for Eq. (12-) simplify to

$$E_{n+}(0; \tau_r) - \beta_n E_{n-}(0; \tau_r) = E_{pn+}(0; \tau_r) - \beta_n E_{pn-}(0; \tau_r), \quad n = 0, 1. \quad (14)$$

These two equations would enable \hat{Q}_0 and \hat{Q}_1 to be estimated from the downward and upward irradiances and scalar irradiances at the single depth $\tau = 0$. Using Eqs. (8) and Tables 1 and 2 we find, for example,

$$E_{p0\pm}(\tau; \tau_r) = \frac{1}{2h_0} \left(\hat{Q}_0 + \hat{Q}_1\tau \mp \frac{3\hat{Q}_1}{2h_1} \right), \quad (15a\pm)$$

$$E_{p1\pm}(\tau; \tau_r) = \frac{1}{4h_0} \left[\pm(\hat{Q}_0 + \hat{Q}_1\tau) - \frac{2\hat{Q}_1}{h_1} \right]. \quad (15b\pm)$$

From Eqs. (14) and (15) it then follows for the special case where the measurements are taken just beneath the surface ($\tau_r = 0$) and at night (so that there is no surface illumination and $E_{0+}(0;0) = E_{1+}(0;0) = 0$) that

$$\hat{Q}_0 = 4h_0\Delta^{-1}[2\beta_0(1 - \beta_1)E_{0-}(0;0) - 3\beta_1(1 + \beta_0)E_{1-}(0;0)], \quad (16a)$$

$$\hat{Q}_1 = 4h_0h_1\Delta^{-1}[\beta_0(1 + \beta_1)E_{0-}(0;0) - 2\beta_1(1 - \beta_0)E_{1-}(0;0)], \quad (16b)$$

where

$$\Delta = 3(1 + \beta_0)(1 + \beta_1) - 4(1 - \beta_0)(1 - \beta_1).$$

Another possible use of Eqs. (14) is to make the (rather drastic!) assumption that the source is spatially-constant throughout the spatially-uniform seawater below the depth τ_r so that $\hat{Q}_1 = 0$. Then \hat{Q}_0 could be estimated from just the downward and upward irradiances or the corresponding scalar irradiances. For example, from Eqs. (14) and (15) it follows that either of the following equations could be used,

$$\hat{Q}_0 = \frac{2h_0}{1 - \beta_0}[E_{0+}(0; \tau_r) - \beta_0 E_{0-}(0; \tau_r)], \quad (17a)$$

$$= \frac{4h_0}{1 + \beta_1}[E_{1+}(0; \tau_r) - \beta_1 E_{1-}(0; \tau_r)]. \quad (17b)$$

A summary of the use of the preceding equations is given in Table 3.

Table 3. Summary of the different applications of the asymptotic inverse source estimation algorithm.

Eq. no.	τ_o	Measurements required	No. of \hat{Q}_i estimated
12	$< \infty$	$E_{n\pm}(0; \tau_r)$ and $E_{n\pm}(\tau_o; \tau_r)$ for $n = 0, 1$	4
12	$< \infty$	$E_{0\pm}(0; \tau_r)$ and $E_{0\pm}(\tau_o; \tau_r)$	2
12	$< \infty$	$E_{1\pm}(0; \tau_r)$ and $E_{1\pm}(\tau_o; \tau_r)$	2
14	$\rightarrow \infty$	$E_{0\pm}(0; \tau_r)$ and $E_{1\pm}(0; \tau_r)$	2
17	$\rightarrow \infty$	$E_{0\pm}(0; \tau_r)$ or $E_{1\pm}(0; \tau_r)$	1

A strong caution is warranted concerning the preceding equations, however. If Eqs. (12), (14), or (17) are applied for measurements just beneath the sea surface where τ_r is

small, then the estimated parameters may not be very good. This is because these equations are based on the assumption that the radiance is in an asymptotic distribution at all depths; only under very special circumstances does this occur.¹⁰ Thus Eqs. (12), (14), and (17) are better used at depths τ_r below which the radiance can be assumed to be nearly asymptotic.

Admittedly the asymptotic algorithm of Eqs. (12) has limited utility in situations where the source profile $S(\tau; \tau_r)$ changes with depth in a manner requiring more than the four coefficients that can be determined by using Eqs. (12). In those instances a more complicated algorithm is needed that requires the measurement of the radiance at each boundary. A straight-forward application of the above procedure to Eqs. (10) does not eliminate the coefficients $A(\pm\nu_j)$ and $A(\nu)$, however, so a different approach is currently under investigation.

4. SOME NUMERICAL TESTS OF THE ONE-LEVEL ALGORITHM

For a set of simple, extreme tests of the errors from the algorithm as given in Eqs. (16) and (17), we consider a semi-infinite, homogeneous medium and attempt to estimate the coefficient \hat{Q}_0 using one detector just beneath the sea surface (which serves as the reference position so $\tau = \tau_r = 0$). With this extreme test, we will be applying the asymptotic algorithm outside of its normal range of validity, but in this way we can examine the errors analytically. We will assume the experiment would be done when there is no surface illumination, so that $E_{0+}(0;0) = E_{1+}(0;0) = 0$, and that the source is actually given by $S(\tau) = Q_0 + Q_1\tau$. Since we assume that the scattering is at most linearly anisotropic, the upward scalar irradiance and irradiance can be conveniently expressed in closed form in terms of the moments $\alpha_n = \int_0^1 \mu^n H(\mu) d\mu$, $n = 0, 1$, of Chandrasekhar's H -function.¹⁴ After some tedious manipulations these "measured" irradiances can be shown to satisfy

$$E_{0-}(0;0) = \frac{1}{2 - \omega\alpha_0} \left[\alpha_0 Q_0 + \left(\frac{3}{h_0 h_1} \right)^{1/2} \alpha_1 Q_1 \right], \quad (18a)$$

$$E_{1-}(0;0) = -\frac{1}{2 - \omega\alpha_0} \left[\alpha_1 Q_0 - \frac{3\alpha_2 Q_1}{h_1} + \frac{(2 - \omega\alpha_0) Q_1}{h_0 h_1} \right]. \quad (18b)$$

In deriving Eq. (18a), for example, the following identities have been used (Ref. 14, Sec. 46.2):

$$2 - \omega\alpha_0 = 3\omega f_1 h_0 \alpha_2 + 2 \left(\frac{h_0 h_1}{3} \right)^{1/2}, \quad (19a)$$

$$4\alpha_0 - 4 = \omega\alpha_0^2 + 3\omega f_1 h_0 \alpha_1^2. \quad (19b)$$

With the substitution of $E_{n+}(0;0) = 0$ and Eqs. (15) and (18) into Eqs. (17) it follows that

$$\frac{\hat{Q}_0}{Q_0} = -\frac{2h_0\alpha_0}{(2 - \omega\alpha_0)(1 - \beta_0)} \left[1 + \left(\frac{3}{h_0 h_1} \right)^{1/2} \frac{\alpha_1}{\alpha_0} \frac{Q_1}{Q_0} \right] \quad \text{using } E_{0-}(0;0), \quad (20a)$$

$$= \frac{4h_0\alpha_1}{(2 - \omega\alpha_0)(1 + \beta_1)} \left[1 - \frac{1}{\alpha_1} \left(\frac{3\alpha_2}{h_1} - \frac{2 - \omega\alpha_0}{h_0 h_1} \right) \frac{Q_1}{Q_0} \right] \quad \text{using } E_{1-}(0;0). \quad (20b)$$

The values of β_0 and β_1 can be computed from Eq. (13) and the equations

$$g_{0\pm}(\nu_1) = (\omega\nu_1/2)[\mp(1 + 3f_1h_0\nu_1^2)\ln(1 \mp \nu_1^{-1}) - 3f_1h_0\nu_1], \quad (21a)$$

$$g_{1\pm}(\nu_1) = \nu_1g_{0\pm}(\nu_1) - (\omega\nu_1/2)(1 \pm 3f_1h_0\nu_1/2). \quad (21b)$$

As can be seen from Eqs. (20), the ratio \hat{Q}_0/Q_0 of the estimated source to the actual source magnitude depends on the inherent optical properties and Q_1/Q_0 , the relative rate of change with depth of the actual source.

In the simplest case of isotropic scattering, $2 - \omega\alpha_0 = 2h_0^{1/2}$ from Eq. (19a) and $3h_0^{1/2}\alpha_2 = (1 - 3\omega\alpha_1^2/4)$ from Ref. 14, Sec. 38. Then Eqs. (20) can be simplified even further to

$$\frac{\hat{Q}_0}{Q_0} = -\alpha_0h_0^{1/2} \frac{\beta_0}{1 - \beta_0} \left[1 + \frac{\alpha_1}{h_0^{1/2}\alpha_0} \frac{Q_1}{Q_0} \right], \quad (22a)$$

$$= 2\alpha_1h_0^{1/2} \frac{\beta_1}{1 + \beta_1} \left[1 + \frac{1 + 3\omega\alpha_1^2/4}{3h_0^{1/2}\alpha_1} \frac{Q_1}{Q_0} \right]. \quad (22b)$$

The results in Table 4 are for the first numerical test of Eqs. (20) when it is assumed that $Q_1 = 0$ and the scattering is isotropic; values of α_1 were obtained from Ref. 15. The accuracy of the algorithm using the irradiance detectors is very good but using the scalar irradiance detectors is very poor. It appears that the results from Eq. (22a) are too small by a factor of $h_0^{1/2}$, but the cause for this discrepancy has not yet been determined. Table 5 gives the coefficients of the terms proportional to Q_1/Q_0 in Eqs. (22) and demonstrates that if one assumes that the source is spatially uniform when it is not, then major errors will arise when estimating \hat{Q}_0 unless Q_1/Q_0 is small.

Table 4. The ratio of the estimated spatially-constant source to the actual spatially-constant source (i.e., $Q_1 = 0$) when the scattering is isotropic.

ω	\hat{Q}_0/Q_0 from Eq. (22a)	\hat{Q}_0/Q_0 from Eq. (22b)	ω	\hat{Q}_0/Q_0 from Eq. (22a)	\hat{Q}_0/Q_0 from Eq. (22b)
0.995	0.07	1.00 ⁻	0.7	0.53	0.98
0.99	0.10	0.99	0.6	0.61	0.98
0.95	0.22	0.99	0.5	0.68	0.98
0.9	0.30	0.98	0.4	0.75	0.98
0.85	0.37	0.98	0.3	0.82	0.98
0.8	0.43	0.98	0.05	1.00 ⁻	1.00 ⁻

Table 5. The factors $K_0 = \alpha_1/(h^{1/2}\alpha_0)$ and $K_1 = (1 + 3\omega\alpha_1^2/4)/(3h_0^{1/2}\alpha_1)$ of the terms in Eqs. (22) that contain Q_1/Q_0 .

ω	K_0 in Eq. (22a)	K_1 in Eq. (22b)	ω	K_0 in Eq. (22a)	K_1 in Eq. (22b)
0.995	8.04	8.17	0.7	0.96	1.11
0.99	5.65	5.79	0.6	0.82	0.98
0.95	2.47	2.61	0.5	0.73	0.89
0.9	1.72	1.86	0.4	0.66	0.82
0.85	1.39	1.54	0.3	0.61	0.77
0.8	0.96	1.11	0.05	0.51	0.68

We now check to see if anisotropic scattering significantly affects the results obtained from Eq. (22b) for isotropic scattering. The results in Table 6 again are when $Q_1 = 0$ except that the scattering is now linearly anisotropic with $f_1 = 1/3$, which is the largest possible f_1 for which the volume scattering function will everywhere remain positive in a linearly anisotropic model. (The values of α_0 and α_1 for this case were obtained from Ref. 14, Sec. 47.) We can conclude that the accuracy of the algorithm that relies on the irradiance is relatively insensitive to scattering anisotropy.

Table 6. The ratio of the estimated spatially-constant source to the actual spatially-constant source (i.e., $Q_1 = 0$) when the scattering is linearly anisotropic with $f_1 = 1/3$, as obtained from Eq. (22b).

ω	\hat{Q}_0/Q_0	ω	\hat{Q}_0/Q_0	ω	\hat{Q}_0/Q_0
0.975	0.99	0.8	0.98	0.4	0.98
0.95	0.98	0.7	0.98	0.3	0.98
0.925	0.98	0.6	0.98	0.2	0.99
0.9	0.98	0.5	0.98		

As the final set of tests, we examine the numerical results in Table 7 from the algorithm of Eqs. (16) in which both \hat{Q}_0/Q_0 and \hat{Q}_1/Q_0 are estimated using measurements of $E_{0-}(0; 0)$

Table 7. The ratios \hat{Q}_0/Q_0 and \hat{Q}_1/Q_0 of the estimated spatially-constant source to the actual spatially-constant source (i.e., $Q_1 = 0$) when the scattering is isotropic, as obtained from Eqs. (16).

ω	\hat{Q}_0/Q_0	\hat{Q}_1/Q_0	ω	\hat{Q}_0/Q_0	\hat{Q}_1/Q_0
0.995	0.07	0.11	0.7	0.40	0.54
0.99	0.09	0.13	0.6	0.45	0.55
0.95	0.19	0.31	0.5	0.50	0.55
0.9	0.25	0.40	0.4	0.56	0.52
0.85	0.30	0.45	0.3	0.63	0.47
0.8	0.33	0.49	0.05	0.90	0.14

and $E_{1-}(0;0)$ for the special case of $Q_1 = 0$ and isotropic scattering. The equations are

$$\hat{Q}_0/Q_0 = \frac{2h_0^{1/2}}{\Delta} \left[\frac{4(1 - h^{1/2})\beta_0(1 - \beta_1)}{\omega} + 3\beta_1(1 + \beta_0)\alpha_1 \right], \quad (23a)$$

$$\hat{Q}_1/Q_0 = \frac{12h_0^{1/2}}{\Delta} \left[\frac{(1 - h_0^{1/2})}{\omega} + \beta_1(1 - \beta_0)\alpha_1 \right]. \quad (23b)$$

In Table 7 \hat{Q}_1/Q_0 should vanish since $Q_1 = 0$, but this does not occur. Furthermore, the results for \hat{Q}_0/Q_0 are poorer than they were when we assumed *a priori* that $Q_1 = 0$ and used the algorithm of Eq. (17) to achieve the good results of Table 4 from an upward irradiance measurement. Finally, to assess the impact of not setting $Q_1 = 0$ in Eq. (16), for isotropic scattering we examine in Table 8 the factor κ_0 in the equation

$$\frac{\hat{Q}_0}{Q_0} = \frac{\hat{Q}_0}{Q_0} \bigg|_{Q_1=0} + \kappa_0 \frac{Q_1}{Q_0}, \quad (24)$$

where the first term on the right hand side is given in Eq. (23a), and where

$$\kappa_0 = (2/\Delta)[2\beta_0(1 - \beta_1)\alpha_1 + (1 + 3\omega\alpha_1^2/4)\beta_1(1 + \beta_0)]$$

and Δ is given in Eq. (16).

Table 8. The factor κ_0 of the term containing Q_1/Q_0 in Eq. (24).

ω	κ_0	ω	κ_0	ω	κ_0
0.995	0.53	0.85	0.39	0.5	0.27
0.99	0.52	0.8	0.37	0.4	0.24
0.95	0.46	0.7	0.34	0.3	0.20
0.9	0.42	0.6	0.30	0.05	0.05

As the single scattering albedo becomes small, when estimating \hat{Q}_0 it is less important to incorporate the complications of Eq. (16) instead of using one of the simpler Eqs. (22).

5. SUMMARY

An algorithm has been developed for estimating a few coefficients describing the spatial distribution of an isotropic source from irradiance measurements and/or scalar irradiance measurements. The advantage of the algorithm compared to earlier source estimation algorithms is that the measurements can be made at widely spaced locations in waters with spatially-uniform inherent optical properties, but the disadvantage is that those optical properties must be known. The algorithm is based on the assumption that the radiance is in the asymptotic regime. Tests for an extreme case when the numerically-simulated radiance is not asymptotic showed that the accuracy of the algorithm using only irradiance detectors is

very good for estimating a spatially uniform source, for example, but the accuracy is very poor using scalar irradiance detectors.

Numerical tests will be done for more realistic waters and source conditions.

ACKNOWLEDGMENTS

This work was supported by an Office of Naval Research contract. I thank Lydia Holl and Richard Sanchez for help.

REFERENCES

1. N. J. McCormick, R. Sanchez, and H.C. Yi, "Marine bioluminescence estimation algorithms for in situ irradiance measurements," in *Ocean Optics X* (R.W. Spinrad, ed.), SPIE Proceedings, Vol. 1302, 38-44 (1990).
2. H. C. Yi, N. J. McCormick, and R. Sanchez, Bioluminescence estimation from ocean *in situ* irradiances," *Appl. Opt.* **31**, 822-830 (1992).
3. Z. Tao and N. J. McCormick, Bioluminescence estimation using explicit and implicit algorithms, in *Ocean Optics XI* (G. Gilbert, ed.), SPIE Proceedings, Vol. 1750, 126-137 (1992).
4. Z. Tao, N. J. McCormick, and R. Sanchez, "Ocean source and optical property estimation using explicit and implicit algorithms," *Appl. Opt.* **33**, 3265-3275 (1994).
5. E. W. Larsen, "The inverse source problem in radiative transfer," *J. Quant. Spectrosc. Rad. Transfer* **15**, 1-5, (1975).
6. H. Y. Li and M. N. Özişik, "Estimation of the radiation source term with a conjugate-gradient method of inverse analysis," *J. Quant. Spectrosc. Rad. Transfer* **48**, 237-244 (1992).
7. C. E. Siewert, "An inverse source problem in radiative transfer," *J. Quant. Spectrosc. Rad. Transfer* **50**, 603-609 (1993).
8. K. M. Case and P. F. Zweifel, *Linear Transport Theory*, Addison-Wesley, Reading, MA (1967).
9. I. Kuščer and N. J. McCormick, "Some analytical results for radiative transfer in thick atmospheres," *Transport Th. Statist. Phys.* **20**, 351-381 (1991).
10. N. J. McCormick, "Asymptotic optical attenuation," *Limnol. Ocean.* **37**, 1570-1578 (1992).
11. P. W. Francisco and N. J. McCormick, "Chlorophyll concentration effects on asymptotic optical attenuation," *Limnol. Ocean.* **39**, in press.
12. C. E. Siewert and F. O. Oruma, "Particular solutions of the equation of transfer," *J. Quant. Spectrosc. Rad. Transfer* **26**, 223-227 (1981).
13. N. J. McCormick and C. E. Siewert, "Particular solutions for the radiative transfer equation," *Transport Theory Stat. Phys.* **46**, 519-522 (1991).
14. S. Chandrasekhar, *Radiative Transfer*, Dover, New York (1960).
15. D. W. N. Stibbs and R. E. Weir, "On the H -functions for isotropic scattering," *Mon. Not. Roy. Astron. Soc.* **119**, 512-525 (1959).

Pose estimation and representation of cylinders from single two-dimensional images in modeling ROV environments

Rune Volden

Department of Engineering Cybernetics
The Norwegian Institute of Technology
N-7034 Trondheim
Norway
Email: rv@itk.unit.no

ABSTRACT

In this paper a method is proposed on how to extract cylinders from single two-dimensional images. The operator restricts the search area for the image ellipse from the projected cylinder, and a least-square ellipse is obtained and verified by the operator. By knowing the radius and length of the cylinder, an algorithm using projective geometry back projects the image ellipse to a circle in three-space. The center and normal vector to this circle are obtained. If both cylinder tangents are visible, a better estimate of cylinder axis is obtained. From this a synthetic cylinder is computed and projected onto the original image. If the synthetic cylinder is a good fit, it is transferred to a CAD model of the environment, which is updated. The operator receives an updated version of the environment, which either includes a new cylinder or a better pose estimate of one of the previous identified cylinders.

1 INTRODUCTION

Object recognition is useful for maneuvering a vehicle in an unknown environment. A three-dimensional map of the environment can, with the help of an operator, be made from a set of monocular images. In an environment of tubes and pipeline structures, it is advantageous of being able to map cylinders. A major advantage for an ROV (Remotely Operated Vehicle) operator is to have a view of the environment he is working in. The environment for an ROV operator working on oil-installations will consist of man-made objects, which can be modeled as objects with planar surfaces and cylinders. A method of obtaining the pose and shape of planar objects (cubes, polyhedra, tetrahedra etc.) was presented in¹⁴ as part of the MOBATEL (Model Based TELEoperation of an underwater vehicle over a narrow band communication link) program.²

In this paper a method of obtaining the pose of a cylinder is presented, where the length and radius of the cylinder are assumed to be known. By using a single camera and "seeing" the top or bottom profile of a cylinder, the pose can be uniquely determined. If also the cylinder tangents are visible, a better pose estimate can be obtained. The method is described in figure 1. The projected top or bottom of the cylinder is an ellipse in the image plane. This ellipse is obtained by sampling all pixels in the relevant area which have a large pixel gradient magnitude. These pixels represent the image ellipse and by computing the least-squares ellipse from these points, our synthetic

ellipse is obtained. The synthetic ellipse is projected onto the original image and verified by the operator. If the operator accepts it as a good fit, a method of back projection an ellipse in 2D to a circle in 3D⁴ is used to obtain the position and orientation of the cylinder.

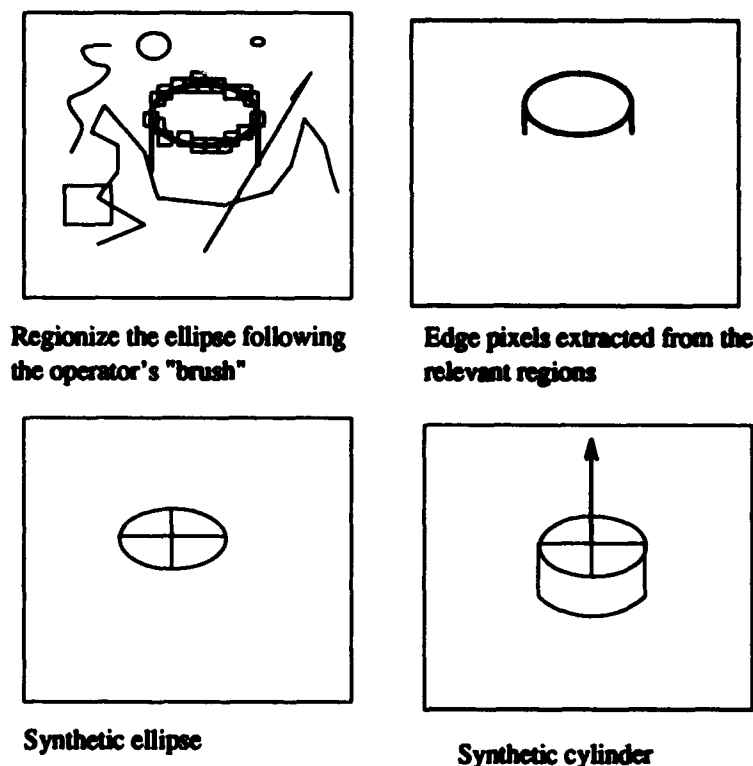


Figure 1: The process of finding cylinders

2 OBTAINING IMAGE ELLIPSE

An ellipse in a real Euclidean plane can be described as a plane cutting a conic. The ellipse equation for the plane $z=1$ is

$$\bar{a}x^2 + \bar{b}xy + \bar{c}y^2 + \bar{d}x + \bar{e}y + \bar{f} = 0 \quad (1)$$

There are various ways of obtaining the image ellipse. A commonly used method is the Generalized Hough Transform^{16,6}. The method has in spite of efficient algorithms large computational complexity. Since we have an operator available, he can fast obtain regions of interest and thus save unnecessary computations.

2.1 Ellipse through five points

A fast way is to let the operator mark 5 points on the ellipse. This provides a solution, but it is highly dependent on the operator's accuracy. From projective geometry we have Pascal's theorem³:

THEOREM 1. *If a hexagon is inscribed in a conic, the three pairs of opposite sides meet in collinear points. This theorem enables us to draw a conic through 5 given points in the real Euclidean plane, no four of which are collinear.⁹ The 5 points uniquely define a conic in the projective space P^{210} page 369. See¹⁵ for details.*

2.2 Least squares ellipse

If we obtain a number $N > 5$ of points on the image ellipse, we can find the least-squares ellipse. The operator can either mark out a number of points which are on the ellipse or mark out regions of interest for which an edge operator can obtain the points on the ellipse. Given equation 1, we divide by \tilde{f} and say that we obtain a series of points which each has an error ϵ . We can write the ellipse equation as:

$$ax^2 + bxy + cy^2 + dx + ey + 1 = \epsilon \quad (2)$$

To find the least squares estimate of the ellipse, we simply minimize the quadratic error by differentiating $\epsilon\epsilon^t$ by each variable.

$$\frac{\partial(\epsilon\epsilon^t)}{\partial a} = \frac{\partial(\epsilon\epsilon^t)}{\partial b} = \frac{\partial(\epsilon\epsilon^t)}{\partial c} = \frac{\partial(\epsilon\epsilon^t)}{\partial d} = \frac{\partial(\epsilon\epsilon^t)}{\partial e} = 0 \quad (3)$$

From this a set of linear equations for n points in the neighborhood of the ellipse is obtained.

$$\begin{bmatrix} \langle x_i^4 \rangle & \langle x_i^3 y_i \rangle & \langle x_i^2 y_i^2 \rangle & \langle x_i^3 \rangle & \langle x_i^2 y_i \rangle \\ \langle x_i^3 y_i \rangle & \langle x_i^2 y_i^2 \rangle & \langle x_i y_i^3 \rangle & \langle x_i^2 y_i \rangle & \langle x_i y_i^2 \rangle \\ \langle x_i^2 y_i^2 \rangle & \langle x_i y_i^3 \rangle & \langle y_i^4 \rangle & \langle x_i y_i^2 \rangle & \langle y_i^3 \rangle \\ \langle x_i^3 \rangle & \langle x_i^2 y_i \rangle & \langle x_i y_i^2 \rangle & \langle x_i^2 \rangle & \langle x_i y_i \rangle \\ \langle x_i^2 y_i \rangle & \langle x_i y_i^2 \rangle & \langle y_i^3 \rangle & \langle x_i y_i \rangle & \langle y_i^2 \rangle \end{bmatrix} \begin{bmatrix} a \\ b \\ c \\ d \\ e \end{bmatrix} = \begin{bmatrix} -\langle x_i^2 \rangle \\ -\langle x_i y_i \rangle \\ -\langle y_i^2 \rangle \\ -\langle x_i \rangle \\ -\langle y_i \rangle \end{bmatrix} \quad (4)$$

where $\langle x_i^4 \rangle = \frac{1}{N} \sum_{i=1}^N x_i^4$ etc. The notation is similar to⁸ chapter 12.

This can be represented as:

$$y = \Phi \theta \quad (5)$$

Provided Φ is invertible, the estimated parameters are obtained.

3 ELLIPSE PRESENTATION

When the ellipse parameters are found, the synthetic ellipse is reprojected onto the original image. The operator can either accept or reject the synthetic ellipse based on the fit. The transformations: Size, shape, rotation and translation are obtained using the following methods.

The ellipse equation in matrix form is:

$$x^t A x + K x + f = 0 \quad (6)$$

By applying Principle Axes Theorem,¹ given in Appendix A, eigenvector matrix P and eigenvalues λ_1, λ_2 are obtained and we get:

$$\lambda_1 \hat{x}^2 + \lambda_2 \hat{y}^2 + d\hat{x} + e\hat{y} + f = 0 \quad (7)$$

P can also be obtained directly as in⁵:

$$P = \begin{bmatrix} \cos(\theta) & -\sin(\theta) \\ \sin(\theta) & \cos(\theta) \end{bmatrix} \quad (8)$$

where

$$\theta = \frac{1}{2} \tan^{-1} \left(\frac{b}{a-c} \right) \quad (9)$$

From equation 7 we complete the squares to obtain:

$$\lambda_1 \tilde{x}^2 + \lambda_2 \tilde{y}^2 = r \quad (10)$$

Now since the ellipse in \mathbb{R}^2 can be written as

$$\frac{x^2}{a^2} + \frac{y^2}{b^2} = 1 \quad (11)$$

we can compare the equations 10 and 11 to find the size, shape, rotation and translation of the ellipse.

$$r = \frac{d^2}{4\lambda_1} + \frac{e^2}{4\lambda_2} - f \quad (12)$$

$$\tilde{x} = \hat{x} + c_x \quad (13)$$

$$\tilde{y} = \hat{y} + c_y \quad (14)$$

3.1 Ellipse Transformation

The ellipse on a quadratic form in \mathbb{R}^3 :

$$\mathbf{x}^t \mathbf{A} \mathbf{x} = \begin{bmatrix} x \\ y \\ z \end{bmatrix} \mathbf{A} \begin{bmatrix} x & y & z \end{bmatrix} = 0 \quad (15)$$

Starting with the circle centered at the origin, we get $\mathbf{A} = \begin{bmatrix} 1 & 0 & 0 \\ 0 & 1 & 0 \\ 0 & 0 & -1 \end{bmatrix} = \mathbf{S}$.

\mathbf{S} represents the quadratic form of a circle and $\mathbf{A} = \mathbf{N}^t \mathbf{S} \mathbf{N}$ transforms the circle into an ellipse.

The size and shape are determined by altering a_{11} and a_{22} in \mathbf{A} , where

$$\mathbf{L} = \begin{bmatrix} \sqrt{\frac{r}{\lambda_1}} & 0 & 0 \\ 0 & \sqrt{\frac{r}{\lambda_2}} & 0 \\ 0 & 0 & 1 \end{bmatrix} \quad (16)$$

A 3 by 3 matrix \mathbf{E} is defined based on the eigenvector matrix \mathbf{P} in equation 8, which corresponds to the rotation around z-axis of the image plane.

$$\mathbf{E} = \begin{bmatrix} P_{11} & P_{21} & 0 \\ P_{12} & P_{22} & 0 \\ 0 & 0 & 1 \end{bmatrix} \quad (17)$$

A translation matrix can be defined as

$$T = \begin{bmatrix} 1 & 0 & 0 \\ 0 & 1 & 0 \\ \frac{d}{2\lambda_1} & \frac{e}{2\lambda_2} & 1 \end{bmatrix} \quad (18)$$

A general transformation will be a concatenation of the mentioned matrices, and we get the quadratic equation:

$$X^t E^t L^t S L^t E^t X = X^t N^t S N^t X = 0 \quad (19)$$

The concatenated matrix $N = \begin{bmatrix} n_{11} & n_{12} & 0 \\ n_{21} & n_{22} & 0 \\ n_{31} & n_{32} & 1 \end{bmatrix}$

When N is found the parameterization of the ellipse is just:

$$\begin{bmatrix} x & y & z \end{bmatrix} = \begin{bmatrix} \cos(t) & \sin(t) & 1 \end{bmatrix} \begin{bmatrix} n_{11} & n_{12} & 0 \\ n_{21} & n_{22} & 0 \\ n_{31} & n_{32} & 1 \end{bmatrix} \quad (20)$$

where $t \in [0..2\pi]$. A similar derivation can be found in¹⁰ chapter 7.1.

4 BACK PROJECTION OF AN ELLIPSE IN A PLANE TO A CIRCLE IN THREE-SPACE

If we have our own position and orientation from a model, we can by knowing the circle's radius, find its center and normal vector from only one image^{413,7}. There are 2 solutions for inverting the perspective projection for an ellipse, which is known coming from a circle. One of them can easily be rejected when it is back projected on the image plane. Following Ferri's approach of using Projective Geometry, we describe the conic with the origin as vertex:

$$\Phi = ax^2 + bxy + cxz + dy^2 + eyz + fz^2 = 0 \quad (21)$$

This can be represented in matrix form as $XM X^T$, where

$$M = \begin{bmatrix} a & \frac{b}{2} & \frac{c}{2} \\ \frac{b}{2} & d & \frac{e}{2} \\ \frac{c}{2} & \frac{e}{2} & f \end{bmatrix} \quad (22)$$

The absolute circle is

$$\Theta = x^2 + y^2 + z^2 \quad (23)$$

Consider all conics that intersects the conic at infinity and the absolute circle. The solution is:

$$\Phi - k\Theta = 0 \quad (24)$$

for a suitable $k \in \mathbb{R}$. This gives at most two planes which can be coincident. k represents one of the maximum three roots of

$$|M - kI_3| = 0$$

We compute

$$|M - kI_3 - \lambda I_3| = -\lambda^3 + b_2\lambda^2 + b_1\lambda + b_0$$

The k satisfying $b_0 = 0$ and $b_1 > 0$ is the correct value in equation 24. The solution of equation 24 is a quadratic form, which can be decomposed into two linear forms representing the two possible normal vectors of the circle.

$$v_1 w_2 = a - k$$

$$v_2 w_2 = d - k$$

$$v_3 w_3 = f - k$$

$$v_1 w_2 + v_2 w_1 = b/2$$

$$v_1 w_3 + v_3 w_1 = c/2$$

$$v_2 w_3 + v_3 w_2 = e/2$$

These 6 nonlinear equations can be solved by the equations:

$$(d - k)w_1^2 + (a - k)w_2^2 - \frac{b}{2}w_1 w_2 = 0 \quad (25)$$

$$(f - k)w_1^2 + (a - k)w_3^2 - \frac{c}{2}w_1 w_3 = 0 \quad (26)$$

$$(f - k)w_2^2 + (d - k)w_3^2 - \frac{e}{2}w_2 w_3 = 0 \quad (27)$$

From equation 25 we get $w_2 = A_1 w_1$ or $w_2 = A_2 w_1$ and for the other two equations we get $w_1 = B_1 w_3$ or $w_1 = B_2 w_3$, and $w_3 = C_1 w_2$ or $w_3 = C_2 w_2$, leaving us with 8 possible solutions. Since $w_2 = A w_1 = A B w_3 = A B C w_2$

$$A B C = 1 \quad (28)$$

must be satisfied. This eliminates 6 out of the 8 solutions. The two we are left with will give the same vectors. By letting $w_3 = 1$, we can solve for w_1 and w_2 . We substitute into the original equations to obtain $[v_1, v_2, v_3]$.

v and w represent the normal vectors to the circle in three-space. Only one of the vectors give the true solution. We now want to find the circle center in 3D. Let E be the orthogonal matrix with respect to the normalized v or w . The matrix is composed of either v or w in the third row. The other two rows are vectors found from the null-space of v or w . In the new reference frame \hat{S} where the circle is pointing towards the z -axis, $\hat{M} = E M E^T$. In \hat{S} , let (X_s, Y_s, Z_s) be the center of the circle Ω , where the plane where Ω lies on has the equation $z_s = Z_s$. The equation of the cone is generally for $Z > 0$

$$X^2 + Y^2 - R^2 Z^2 = 0 \quad (29)$$

Z coincides with z_s and

$$X = \begin{vmatrix} Y_s & Z_s \\ y_s & z_s \end{vmatrix}$$

$$Y = \begin{vmatrix} X_s & Z_s \\ x_s & z_s \end{vmatrix}$$

By substituting into equation 29 we obtain

$$x_s^2 + y_s^2 - 2 \frac{Y_s}{Z_s} y_s z_s - 2 \frac{X_s}{Z_s} x_s z_s + \frac{X_s^2 + Y_s^2 - R^2}{Z_s^2} z_s^2 = 0 \quad (30)$$

We can from this obtain the associated \dot{M} .

$$\dot{M} = \begin{bmatrix} 1 & 0 & -\frac{X_s}{Z_s} \\ 0 & 1 & -\frac{Y_s}{Z_s} \\ -\frac{X_s}{Z_s} & -\frac{Y_s}{Z_s} & \frac{X_s^2 + Y_s^2 - R^2}{Z_s^2} \end{bmatrix} \quad (31)$$

therefore

$$Z_s = \frac{|\dot{m}_{11}|R}{\sqrt{\dot{m}_{13}^2 + \dot{m}_{23}^2 - \dot{m}_{11}\dot{m}_{33}}} \quad (32)$$

Also

$$X_s = -Z_s \frac{\dot{m}_{13}}{\dot{m}_{11}}$$

$$Y_s = -Z_s \frac{\dot{m}_{23}}{\dot{m}_{11}}$$

If this is substituted from \dot{S} into the original reference frame, the circle center is obtained:

$$\begin{bmatrix} X_c & Y_c & Z_c \end{bmatrix} = \frac{-\text{sign}(\dot{m}_{11})R}{\sqrt{\dot{m}_{13}^2 + \dot{m}_{23}^2 - \dot{m}_{11}\dot{m}_{33}}} \begin{bmatrix} -\dot{m}_{13} & -\dot{m}_{23} & \dot{m}_{11} \end{bmatrix} E \quad (33)$$

5 FINDING THE CYLINDER POSE

For a cylinder in space, we define 8 parameters: Length, radius, cylinder axis (x_1, y_1, z_1) and basepoint (X_1, Y_1, Z_1) . If the image contains an end of the cylinder, this can give us both the cylinder axis and basepoint using the technique in the previous section. The remaining unknowns R and L can be found from a model when the operator recognizes what kind of cylinder it is. We continue using both vector solutions, and by projecting them onto the original image, one of them can easily be rejected, and if the projected synthetic cylinder match the original image, the pose determination are assumed to be successful.

5.1 Obtaining the synthetic cylinder

From the solutions of the back projection, two normal vectors and centers of the circle are obtained. The respective cylinders are developed along the negative normal vectors with length L . The rotations of the cylinders with respect to the viewer is for rotation ϕ around the x-axis:

$$\phi_1 = \tan^{-1} \left(\frac{v_2}{v_3} \right)$$

$$\phi_2 = \tan^{-1} \left(\frac{w_2}{w_3} \right)$$

and for θ around the y-axis:

$$\theta_1 = \tan^{-1} \left(\frac{v_1}{v_3} \right)$$

$$\theta_2 = \tan^{-1} \left(\frac{w_1}{w_3} \right)$$



Figure 2: Edge pixels

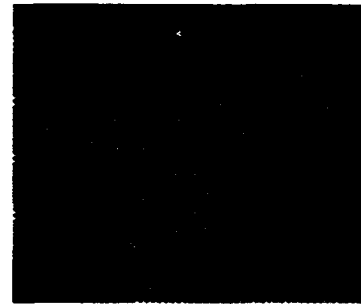


Figure 3: Synthetic ellipse

5.2 Cylinder tangents

Ferri⁴ described a method on how to extract the cylinder axis from its tangents in the image plane. If the lines describing the tangents are represented by the normalized vectors n_1 and n_2 , the cylinder vector as described in the previous section: u or $v = n_1 + n_2$. If both tangents are available in the image, this can most often tell whether the u or v vector represent the true solution.

6 PROGRAM AND OPERATOR INTERACTION

The operator receives an image, and he decides what sort of object he is looking for. In this case it is a cylinder. The threshold level of the pixel gradient is set by the operator, so only the edge pixels are considered. To sample the ellipse data, the cursor works like a "brush". First the path following the operator's cursor is traced. Then the path is divided into squares of overlapping regions, 8x8 or 16x16 pixels, which will contain the path. The region size is set by the operator.

For all pixels in all regions selected, the pixel gradients are computed. The pixels with gradient level greater than the threshold are entering a list of ellipse edge candidates. Now since the regions are quite small, the amount of ellipse edge pixels in each region is very few. If one region has many pixels with high pixel gradient, only the pixels with highest pixel gradient will be considered as ellipse edge pixels. A test is also made to avoid edge pixels of occurring twice. See figure 2.

From ellipse edge pixels, the least-squares ellipse is produced, using methods mentioned in 2.2. The 5 parameters are then used to obtain the matrix M in equation 20 from methods described in section 3. The synthetic ellipse is displayed onto the image as in figure 3, and the operator decides if it is a good fit or not. He can either start a new trace with new parameters or continue.

From ellipse parameters, the position and orientation are determined for the circle in three-space with two solutions based on the method in section 4. The cylinders are developed using the method in section 5, and the operator can in most cases reject one of the solutions as in figure 4 and figure 5. The solutions will coincide when the circle normal is orthogonal to the image plane.

If the operator is satisfied with the projection of the synthetic cylinder onto the image, he exports the 8 parameters to the model database. The pilot can use these data either to update his environmental model with the new cylinder, or make an update of one of the previous defined cylinders.



Figure 4: Two possible solutions

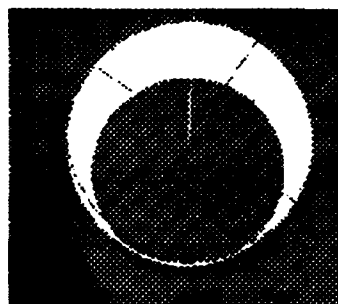


Figure 5: The solution

7 EXPERIMENT AND RESULTS

The vision system was implemented using a Silicon Graphics Indigo workstation. Software was written in C and C++. Our camera is a Pulnix TM-765 with a 12.5 mm lens. We tried the algorithms on 3 objects, each with different radius and length. See figure 6.

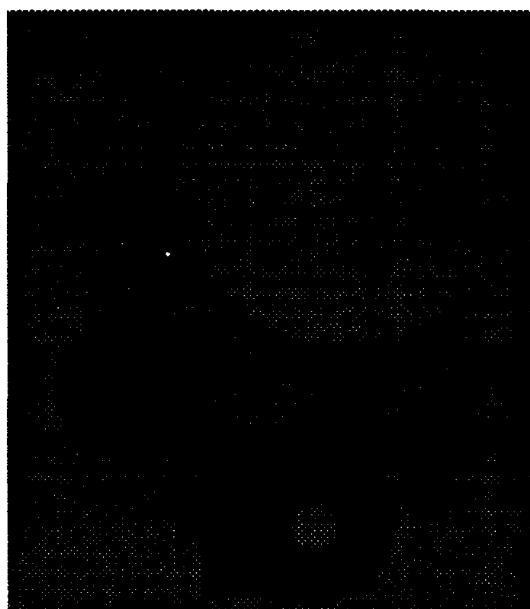


Figure 6: Experiment setup

Object 1 was a polystyrene cylinder with $R = 7.5$ cm and $L = 27.0$ cm. Object 2 was a tape roll with $R = 5.1$ cm and $L = 5.2$ cm. Object 3 was a cup with $R = 4.0$ cm and $L = 9.2$ cm. The distance from the common ground to the camera was 120 cm. Since the object and camera position was calibrated, we could calculate the error between the measured (m) and estimated cylinder axis direction (est) with respect to the camera. Given the estimated depth to the top of a cylinder, the depth to the ground from the camera was calculated and compared with the measured distance. The results are shown in table 1 to 3.

The results are satisfactory with respect to depth, but the error in the cylinder axis can be improved either by using other ellipse finders^{11,12} or make use of the tangents to the cylinder, when they are visible. Object 1 was partially occluded when the depth was at 100 cm, and thus the error in cylinder axis was large.

<i>Object 1</i>	<i>Position and angles with respect to camera</i>				
<i>Depth_m (cm)</i>	<i>Depth_{est} (cm)</i>	<i>φ_m (deg)</i>	<i>φ_{est} (deg)</i>	<i>θ_m (deg)</i>	<i>θ_{est} (deg)</i>
120	116.5	5.7	-3.8	7.7	1.4
120	119	5.7	1.8	7.7	1.6
120	118	5.7	6.8	7.7	6.5
100	101	9.2	-10.5	6.9	0.5
100	98	9.2	-7.9	6.9	-2.9
100	102	9.2	-9.5	6.9	0.9

Table 1: Object 1

<i>Object 2</i>	<i>Position and angles with respect to camera</i>				
<i>Depth_m (cm)</i>	<i>Depth_{est} (cm)</i>	<i>φ_m (deg)</i>	<i>φ_{est} (deg)</i>	<i>θ_m (deg)</i>	<i>θ_{est} (deg)</i>
120	122	-2.1	1.8	4.9	4.2
120	121	-2.1	1.7	4.9	0.2
120	122	-2.1	-0.9	4.9	2.3
100	98	-2.5	5.3	5.9	-2.9
100	101	-2.5	2.2	5.9	0.4
100	100	-2.5	-1.1	5.9	8.7
80	80	-3.2	3.5	7.3	0.1
80	77	-3.2	7.1	7.3	-3.0
80	80	-3.2	2.6	7.3	-1.0

Table 2: Object 2

<i>Object 3</i>	<i>Position and angles with respect to camera</i>				
<i>Depth_m (cm)</i>	<i>Depth_{est} (cm)</i>	<i>φ_m (deg)</i>	<i>φ_{est} (deg)</i>	<i>θ_m (deg)</i>	<i>θ_{est} (deg)</i>
120	124	1.4	-4.1	-4.5	-3.1
120	122	1.4	2.8	-4.5	4.7
120	119	1.4	-4.4	-4.5	3.4
100	103	1.7	-0.1	-5.5	1.1
100	103	1.7	-4.1	-5.5	-1.9
100	101	1.7	0.1	-5.5	2.1
80	81	2.1	-0.9	-6.8	3.0
80	82	2.1	-0.1	-6.8	-1.8
80	81	2.1	-0.2	-6.8	0.2

Table 3: Object 3

8 CONCLUSION AND FURTHER RESEARCH

From one image knowing the radius and length of the cylinder, the orientation and position of the cylinder is found with respect to camera position. By having an operator who can compare the synthetic projections to the real images, we are able to use CAD-based tools for mapping and refining the pose of the cylinders in the ROV environment. A limitation is that we have to see one of the end sides of the cylinder. If the cylinder tangents are visible, there is an improvement in the accuracy of the estimated cylinder axis. However a possibility of using a laser plane to extract radius and elliptic features from the cylinder is considered for future research.

9 REFERENCES

- [1] H. Anton. *Elementary Linear Algebra*. John Wiley, 1987.
- [2] J.G. Balchen and T.I. Fossen. Model based teleoperation of an underwater vehicle over a narrow band communication link - mobatel. In *International Advanced Robotics Programme 4th Workshop on Underwater Robotics*, Genova, Nov 1992. IARP.
- [3] H.S.M. Coxeter. *Projective Geometry*. Springer-Verlag, second edition, 1987.
- [4] M. Ferri, F. Mangili, and G. Viano. Projective pose estimation of linear and quadratic primitives in monocular computer vision. *Computer Vision, Graphics, and Image Processing*, 58(1):66-84, July 1993.
- [5] R.M. Haralick and L.G. Shapiro. *Computer and Robot Vision*, volume I of 0-201-56949-4. Addison Wesley, 1993. Appendix A.3.
- [6] J. Illingworth and J. Kittler. A survey of the hough transform. *Computer Vision, Graphics, and Image Processing*, 44(1):87-116, October 1988.
- [7] S. Masciangelo. 3-d cues from a single view: detection of elliptical arcs and model-based perspective back-projection. In *BMVC90 Proceedings of the British Machine Vision Conference*, pages 223-228, Oxford, 1990.
- [8] J.L. Mundy and A. Zisserman. *Geometric Invariance in Computer Vision*. MIT Press, 1992.
- [9] D. Pedoe. *Geometry, a comprehensive course*. Dover books on advanced mathematics. Dover Publications Inc., second edition, 1988.
- [10] M.A. Penna and R.R. Patterson. *Projective Geometry and its application to Computer Graphics*. Prentice-Hall, first edition, 1986.
- [11] J. Porill. Fitting ellipses and predicting confidence envelopes using a biased corrected kalman filter. *Image and vision computing*, 8(1):37-41, February 1990.
- [12] D.D. Sheu and A.H. Bond. A generalized method for 3d object location from 2d images. *Pattern Recognition Society*, 25(8):771-786, August 1992.
- [13] Y.C. Shiu and S. Ahmad. Viewpoint determination of cylinders and spheres from a single view. In *IEEE Int. Conf. on Systems Engineering*, pages 566-569, 1990.
- [14] R. Volden and J.G. Balchen. Determining 3-d object coordinates from a sequence of 2-d images in modelling rov environments. In *Eighth Int. Symposium on Unmanned Untethered Submersible Technology*, pages 359-369, University of New Hampshire, September, 27-29 1993.
- [15] Rune Volden. *Navigation and object pose determination from images in modeling ROV environments*. PhD thesis, Norwegian Institute of Technology, to appear in 1994.

- [16] H.K. Yuen, J. Illingworth, and J. Kittler. Detecting partially occluded ellipses using the hough transform. In *Fourth Alvey Computer Vision Conference*, volume 7, pages 31-37, Manchester, UK, February 1989.

A Principle Axes Theorem for \mathbb{R}^2

Let

$$ax^2 + 2bxy + cy^2 + dx + ey + f = 0$$

be the equation of the conic C, and let

$$\mathbf{x}^t \mathbf{A} \mathbf{x} = ax^2 + 2bxy + cy^2$$

be the associated quadratic form. Then the coordinate axes can be rotated so that the equation C in the new $\hat{x}\hat{y}$ -coordinate system has the form

$$\lambda_1 \hat{x}^2 + \lambda_2 \hat{y}^2 + \hat{d}\hat{x} + \hat{e}\hat{y} + f = 0$$

where λ_1 and λ_2 are the eigenvalues of A. The rotation can be accomplished by the substitution

$$\mathbf{x} = \mathbf{P}\hat{\mathbf{x}}$$

where \mathbf{P} orthogonally diagonalizes $\mathbf{x}^t \mathbf{A} \mathbf{x}$ and $\det(\mathbf{P}) = 1$.

Predicting Polarization Properties of Marine Aerosols
Mary S. Quinby-Hunt,* Patricia G. Hull§ and Arlon J. Hunt*

*Energy and Environment Division, Lawrence Berkeley Laboratory, University of California, 1 Cyclotron Rd., Berkeley, CA 94720; (510) 486-5645, FAX (510) 486-4260; OMNET = a.hunt;

§Department of Physics, Tennessee State University, Nashville, TN 37209; Telephone and FAX: (615) 320-3797; OMNET = p.hull

ABSTRACT

Knowledge of the intensity and polarization of light scattered from marine aerosols can aid in understanding (1) visibility and propagation of light in the marine boundary layer (MBL), (2) composition and variability of marine aerosols, and (3) formation and disappearance of marine aerosols. This paper investigates the variation in the polarization properties of light scattered by aerosols in the MBL arising from various aerosol sources and environmental conditions. Mie scattering models of Gaussian and log normal distributions of spheres and combinations thereof were used to calculate the polarization properties of light scattered from various models and from experimentally determined distributions of aerosols in the marine boundary layer. The results of the models were verified by comparison to scattering from $(\text{NH}_4)_2\text{SO}_4$ particles, a component of aerosols in the MBL that is nearly spherical and readily generated in the laboratory. The modelling experiments will be used to explore the variability of the polarization light propagating in the MBL. Calculations indicate that scattering by aerosols is distinctly not Rayleigh-like. The polarization properties of light scattered in the MBL vary with size, refractive index, and number distributions of particles in the MBL. These differences should be instrumentally detectable and could be important for visibility.

1. INTRODUCTION

Particles in the MBL affect visibility, cloud formation, radiative transfer, and the heating and cooling of the earth. Dense MBL hazes modify the propagation of sunlight affecting both the intensity and polarization of light reaching the sea surface. Both these quantities must be included in radiant transfer calculations at the surface of and within the ocean.^{1,2} Aerosols in the MBL affect visibility because the scattered light reduces the contrast between the viewed scene and the background. Near-forward scattered light is the most effective in reducing contrast of a naturally lighted scene and thus is dominated by the large particles in the aerosol. If the scene is illuminated by a source near the detector, backscattered light is most important in reducing contrast. Conversely, sunlight or moonlight scattered into the detector from along the target-detector path also reduces contrast. Since this scattering can occur at any angle, it can be caused by particles of nearly any size. Thus, depending on the situation, aerosol particles of all sizes are important in determining visibility.

The angular dependence of the linear and circular polarization of light scattered by the MBL provides the most complete information regarding the aerosol characteristics obtainable by remote sensing. Measurements of the polarization properties of aerosols can be used to infer effective size distribution and refractive index of marine aerosols, without the problems of collection devices. The limited research on the scattering properties of atmospheric aerosols has been primarily with terrestrial aerosols.³ Few studies have investigated the polarization properties of scattered light in marine aerosols^{4,5} and even fewer using the fullest description of the polarization as embodied by the Mueller scattering matrix formalism.^{6,7}

This formalism represents all the available polarization information of the scattered light as a function of angle.

Past measurements of the polarization properties of atmospheric aerosols have been very limited and most of those involved monostatic lidar measurements that do not treat angle dependence. Hansen and Evans⁸ presented angle-dependent measurements of four elements of the Mueller matrix. These measurements were taken on urban aerosols drawn into a laboratory nephelometer and presented without normalization or phase information.

Factors important in formation of aerosols in the MBL include the physical, chemical and biological conditions of the underlying ocean, meteorological processes (temperature, humidity, wind and cloud conditions) and terrestrial (both natural and anthropogenic) inputs. Marine sources include condensation of water vapor and gases from biological ocean sources, aqueous salt aerosols from the wind-sea interface, and settling from the troposphere. Under normal conditions, the main constituents of aerosols over the ocean include water, sea salt, non-sea-salt (nss) sulfate, mineral dust, a small fraction of nitrates,^{4,5} and organic matter.⁹ The sea salt component is believed to make up the coarser fraction of the aerosols ($r > 0.3 \mu\text{m}$), while non-sea-salt sulfates, continental aerosols, and organic matter contribute to the smaller fractions. The size distribution of the smaller, nss marine aerosols in the MBL has been described as bimodal with the smallest particles ($r_{\text{mode}} \approx 0.03 \mu\text{m}$) made up of gas-phase reaction products such as H_2SO_4 , or $(\text{NH}_4)_2\text{SO}_4$ probably derived from marine-generated dimethyl sulfide,¹⁰ H_2S or continentally-derived aerosols.¹¹ The term r_{mode} refers to the radius of the particles whose number density is greatest in a log normal distribution.

In the coastal zone, particles of varying optical properties are introduced into the MBL by various sources including anthropogenic sources of pollution and smoke (from ships, fires, coastal industries, *etc.*), natural continental dusts, volcanic emissions, and virtually any terrestrial source, in addition to the aerosols normally observed over blue ocean regions. The influence of coastal aerosols extends for great distances to sea depending on prevailing winds and weather conditions. A major factor in determining the polarization properties of aerosols in the MBL involves the relative importance of terrestrial sources.

The particles resulting from all sources may be homogenous or inhomogeneous and of varying size, composition, real and imaginary refractive index, and shape. Each component of an MBL aerosol has different optical properties, causing varied polarization effects from the resulting aerosol.

This paper presents calculations of scattering in terms of normalized Mueller matrix elements based on aerosol characteristics derived primarily from measurements that did not involve light scattering. The calculations, which predict the light scattering behavior in the MBL, permit determination of the most important polarization characteristics and their effect on light propagation and visibility. These predictions can be used to understand the probable scattering behavior, but they should be verified with field measurements. The calculations may also be used to identify critical polarization phenomena of interest to determine visibility in the MBL.

1.1 Model of Aerosols in the MBL. A number of models have been developed to describe the size and composition of marine aerosols. Some are relatively simple, such as those of Diermendingian,⁷ involving a gamma distribution of a single component.

A commonly employed model is that developed by Shettle and Fenn.¹¹ For marine aerosols the model sums log normal distributions of two components. The actual size distribution of each component varies depending on the source and relative humidity (RH). The smaller of the two components is a log normal distribution of a rural, terrestrially-derived aerosol mixture of soluble and insoluble matter - both with $r_{\text{mode}} \approx 0.03 \mu\text{m}$. Approximately 70% of the mixture is water soluble [$(\text{NH}_4)_2\text{SO}_4$, CaSO_4 and organic matter] and 30% is dust-like aerosols. The second component is primarily a sea-salt mixture - $r_{\text{mode}} \approx 0.3 \mu\text{m}$ at 80% RH. The size of the particles making up each component varies with RH, based on Hänel's formulation.¹² The refractive index for water was based on the survey by Hale and Querry.¹³ For the refractive index of sea salt, Shettle and Fenn reference the work by Volz¹⁴ and Dorsey,¹⁵ which at 0% RH is

slightly less than that reported for $(\text{NH}_4)_2\text{SO}_4$ by Perry *et al.*⁶ At higher RH, the refractive index is a weighted average of the refractive indices of water and sea salt. Each component is treated as a log normal distribution of single spherical scatterers. Table 1 presents the size, standard deviation, and refractive index for a marine aerosol based on this model at a wavelength of 514 nm. Although there is an imaginary part of the refractive index for the maritime component, the value is so small as to be unimportant in the Mie calculations (*i.e.* $<10^{-7}$). The Shettle-Fenn model weights the smaller component as 0.999875 and the larger component 0.000125.

Table 1. Input parameters for the Shettle-Fenn¹¹ model for marine aerosols. These were used to calculate the effect of humidity on the polarization of light scattered in the MBL.

	r_{mode}	r_{min}	r_{max}	σ	n
Component 1: Small Aerosol Component					
50% RH	0.028 μm	0.003 μm	0.2 μm	0.35	1.52-0.006i
80% RH	0.033 μm	0.005 μm	0.2 μm	0.35	1.44-0.004i
99% RH	0.053 μm	0.007 μm	0.4 μm	0.35	1.36-0.001i
Component 2: Maritime Component					
50% RH	0.18 μm	0.016 μm	1.0 μm	0.4	1.470-0i
80% RH	0.33 μm	0.04 μm	2.5 μm	0.4	1.355-0i
98% RH	0.74 μm	0.07 μm	5.5 μm	0.4	1.337-0i

A more recent "Navy Oceanic Vertical Aerosol Model" developed by Gathman and Davidson uses a four component system, which is a sum of four log normal distributions.¹⁶ While this model introduces a greater complexity to modelling aerosols in the MBL, preliminary calculations focussed on the Shettle-Fenn model, as it is commonly used, and models derived from experimental observations reported in the literature (see below).

1.2 Experimental Measurements of Particle Distributions in the MBL. A number of researchers (see the review article by Fitzgerald⁹) have examined the particle size distributions in the MBL with various sampling and collection devices - both at sea (for example, Hoppel *et al.*⁴) and in the coastal zone.⁹ Most report the predominance of the small component(s) with $r_{\text{mode}} \sim 0.03 \mu\text{m}$ in agreement with the Shettle-Fenn¹¹ and Gathman-Davidson¹⁶ models and a second component with somewhat larger r_{mode} , generally in the range of 0.09-0.15 μm , which is somewhat smaller than that used in the Shettle-Fenn¹¹ and Navy¹⁶ models. The size distributions vary considerably based on humidity, wind speed, and proximity to land.⁴

1.3 Polarization and Light Scattering. The polarization properties of light are described by the 4-element Stokes vector defined in terms of the complex electric fields E_i and E_r parallel and perpendicular to the scattering plane:^{17,18}

$$\begin{aligned}
 I &= \text{total intensity of light, } \langle E_i E_i^* + E_r E_r^* \rangle \\
 Q &= \pm 90^\circ \text{ polarization, } \langle E_i E_i^* - E_r E_r^* \rangle \\
 U &= \pm 45^\circ \text{ polarization, } \langle E_i E_r^* + E_r E_i^* \rangle \\
 V &= \text{circular polarization, } \langle i(E_i E_r^* - E_r E_i^*) \rangle
 \end{aligned}$$

The angular brackets indicate time averages and the asterisks denote complex conjugates. The scattering of light is described by a transformation of the Stokes vector by a 4×4 Mueller matrix. The Mueller matrix associated with a particular suspension of marine aerosol particles can be used to describe and quantify the effects that the suspension will have on scattered light in the MBL. Various elements of the Mueller scattering matrix are useful to describe attributes of the scatterers, including symmetry, structure, chirality, optical properties, and orientation. In general, eight of the elements of the Mueller matrix are non-zero for aerosols (normalized by the total intensity; designated as $S_{xy}/S_{11} = S_{xy}$) these are S_{11} , $S_{12} = S_{21}$, S_{22} , S_{33} , S_{44} , and $S_{34} = -S_{43}$.

While terrestrial atmospheric aerosols are generally inhomogeneous, and some of their components irregularly-shaped, scattering from them has been approximated as originating from distribution of spheres. Measurements and calculations using Mie theory have shown that an important component of the two smaller-sized fractions of marine aerosols, $(\text{NH}_4)_2\text{SO}_4$, is well approximated as an ensemble of spheres.⁶

The polarization properties of the larger marine aerosols ($r > 0.25 \mu\text{m}$) can be predicted using Mie theory as long as they are nearly spherical. The sphericity of these particles depends upon RH and composition. Whereas many sulfates appear to form spherical particles, dry NaCl aerosols are cubical, and the scattering from ensembles of NaCl crystals, roughly the size of the sea salt component deviates significantly from that predicted for spheres.⁶ It is probable, however, that sea salt crystals formed under more humid conditions would be roughly spherical.

Although it is expected that a majority of marine aerosols can be approximated as ensembles of spheres, deviation from sphericity can provide important information regarding the properties of non-spherical marine aerosols. If the particles have spherical symmetry, then the matrix element S_{22} normalized by S_{11} is unity. A deviation of S_{22} from unity has been observed for laboratory aerosols and marine particles.^{6,19-22} Quinby-Hunt *et al.*²⁰ have shown that it is possible to use the measured values of S_{22} to quantify and separate the non-spherical contributions to scattering on S_{11} and S_{12} .

2. CALCULATIONS AND MODEL VERIFICATION

Mie scattering models²⁰ were used to calculate the polarization properties of light scattered from a variety ensembles of spheres and coated spheres. The LBL model predicts the polarization properties of light scattered from sums of multiple components of Gaussian, and log normal distributions of spheres and coated spheres. The model was verified using the experimental results of Perry *et al.*⁶ and unpublished results (courtesy of D. Huffman) for $(\text{NH}_4)_2\text{SO}_4$ and NaCl. At both 325 and 633 nm, the LBL model agreed with both the $(\text{NH}_4)_2\text{SO}_4$ data and the earlier calculations.

3. RESULTS AND DISCUSSION

The models were used to predict the polarization properties of light scattered from various distributions of particles in the MBL representing a variety of components observed in the MBL.

3.1 Deviations of MBL scattering from the Rayleigh Approximation and Variations with Humidity. To determine whether the scattering predicted by a commonly used model (Shettle-Fenn¹¹) for the aerosols in the MBL deviates from the Rayleigh approximation and varies with humidity, scattering predicted for a typical marine aerosol was calculated using the data in Table 1 at 50%, 80% and 99% RH. The relative number concentrations were as in Shettle-Fenn, the smaller component - 0.999875, the larger 0.000125. The results are displayed in Figure 1. S_{11} is plotted by dividing the sums of the single particle calculations by the sine of the scattering angle to facilitate comparison with experimental data (the sine factor corrects for the scattering volume). Figure 1 shows the deviation of the polarization from that which would be expected for Rayleigh scatterers in all elements.

As Figure 1 shows, varying the humidity has a small impact on the polarization properties at angles $> 150^\circ$. S_{11} increases with size indicating that the size effect is greater than the decreasing polarizability caused by the increased RH which dilutes the concentration of solute in the particles lowering index of refraction.

If the relative number of sea salt particles is increased (Figure 2), the polarization of scattered light deviates further from the Rayleigh approximation. Figure 2 compares the scattering expected for the marine aerosol by the Shettle-Fenn model¹¹ at 50% RH and that predicted when the sea salt component is increased ten-fold to simulate a more constant mass or Jungian distribution. Under these conditions, S_{12} changes from + to - at roughly 150° , indicating a change from horizontal to vertical polarization. This increase in numbers of sea-salt particles in lower MBL could result from increased wind and wave action.

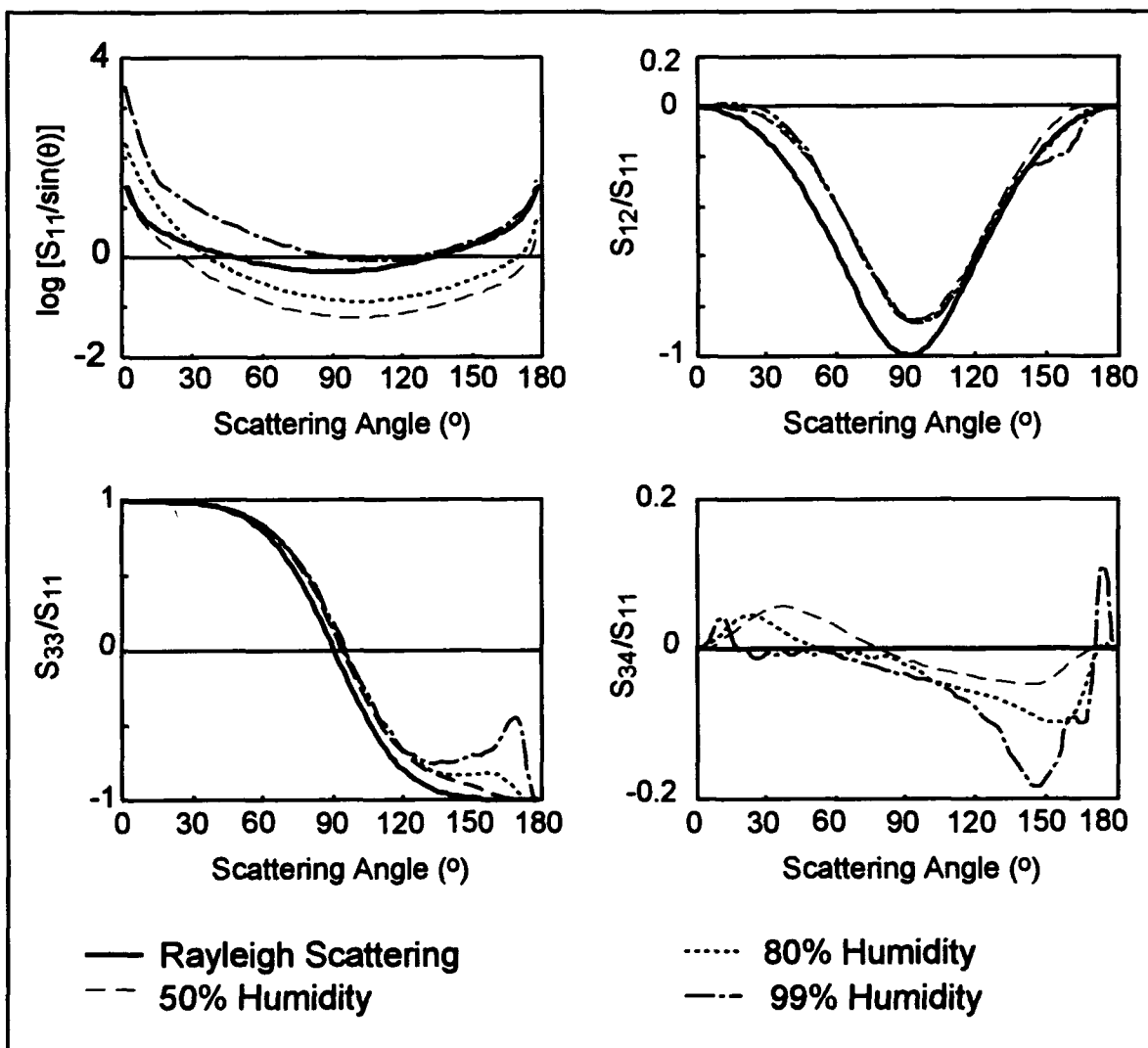


Figure 1. Comparison of scattering predicted for a marine aerosol as described in the Shettle-Fenn model¹¹ for marine aerosols at various humidities with scattering calculated with the Rayleigh approximation. Details of the Shettle-Fenn model is described in the text and Table 1 (S_{34} is zero in the Rayleigh approximation).

3.2 Models of the Component with $r_{\text{mode}} \sim 0.03 \mu\text{m}$. The above calculations demonstrated that the polarization properties of aerosols in the MBL are dependent on the composition of the aerosol. Several questions remained. One question was the veracity of the approximation of the smaller particles ($r_{\text{mode}} \sim 0.03 \mu\text{m}$) as solid spheres. Presumably for the water soluble component, the approximation is valid. However, dusts are not necessarily soluble and therefore several other models are possible. The dust may form a nucleus around which a shell of sea water forms; the dust may remain undissolved; or the small component may be well-described by the 30%/70% insoluble/soluble approximation of Shettle-Fenn.¹¹ Calculations show that all the above descriptions would be indistinguishable given current instrumentation. S_{12} , and S_{33} for all these possible models is well-described by the Rayleigh approximation. S_{11} and S_{34} show some deviation from Rayleigh scattering even though the particles are 1/20th the wavelength of light. S_{34} deviates from zero, and the results of the various approximations vary, but is in all cases less than 1%.

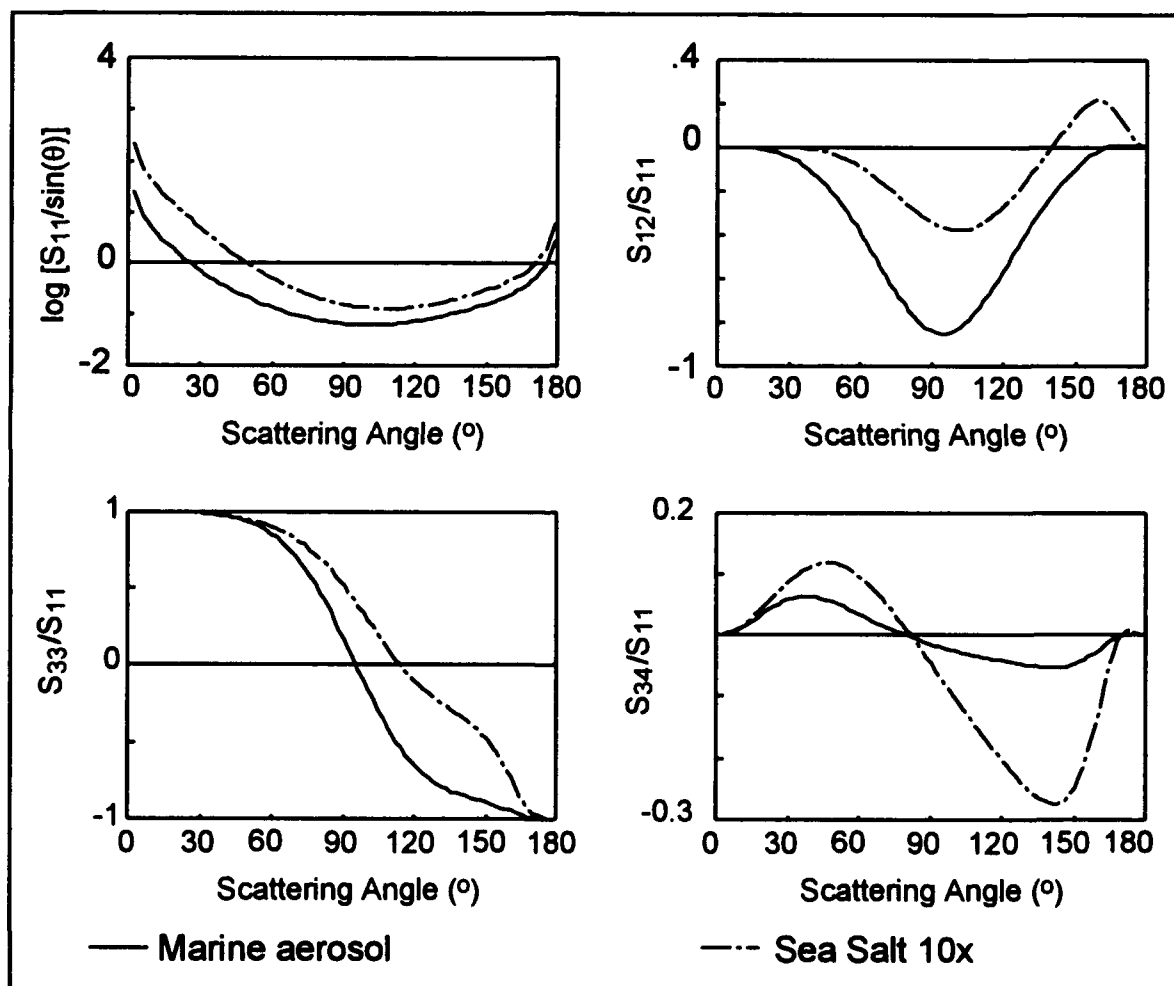


Figure 2. Comparison of the scattering predicted by the Shettle-Fenn¹¹ marine aerosol at 50% RH with an aerosol in which the sea salt number distribution is increased ten-fold.

3.3 Comparisons of the Shettle-Fenn Model with Experimentally-Determined Distributions. As noted above, measurements of number distributions of particles in the MBL show a component larger than the Rayleigh-like component ($r_{\text{mode}} \sim 0.03 \mu\text{m}$) and smaller than the sea salt (maritime) component of Shettle and Fenn.^{4,5,11} The

measurements of the small components by Hoppel *et al.* indicated a component with $r_{\text{mode}} \approx 0.1 \mu\text{m}$ in addition to a smaller component with $r_{\text{mode}} \approx 0.02 \mu\text{m}$.⁴ The exact r_{mode} and relative contributions of each of these components varies with RH, wind speed and distance from land. For the purpose of comparison to the Shettle-Fenn model, we calculated the scattering of an aerosol composed of two components which represent the average of observations typical of conditions with no continental influence (Hoppel *et al.*⁴) plus a marine, primarily sea salt, component as described by Shettle and Fenn. The refractive index for the two smaller components was that of $(\text{NH}_4)_2\text{SO}_4$ at 80% relative humidity (smallest component, $r_{\text{mode}} \approx 0.016 \mu\text{m}$; middle component, $r_{\text{mode}} \approx 0.095 \mu\text{m}$; in proportions of about 3/2, number distribution). The scattering predicted using the Hoppel *et al.* components differs significantly from that of the Shettle-Fenn model (Figure 3). The degree of linear polarization (S_{12}) decreases significantly at 90° and that the peak polarization is shifted to higher angle. The absolute value of S_{34} is much larger.

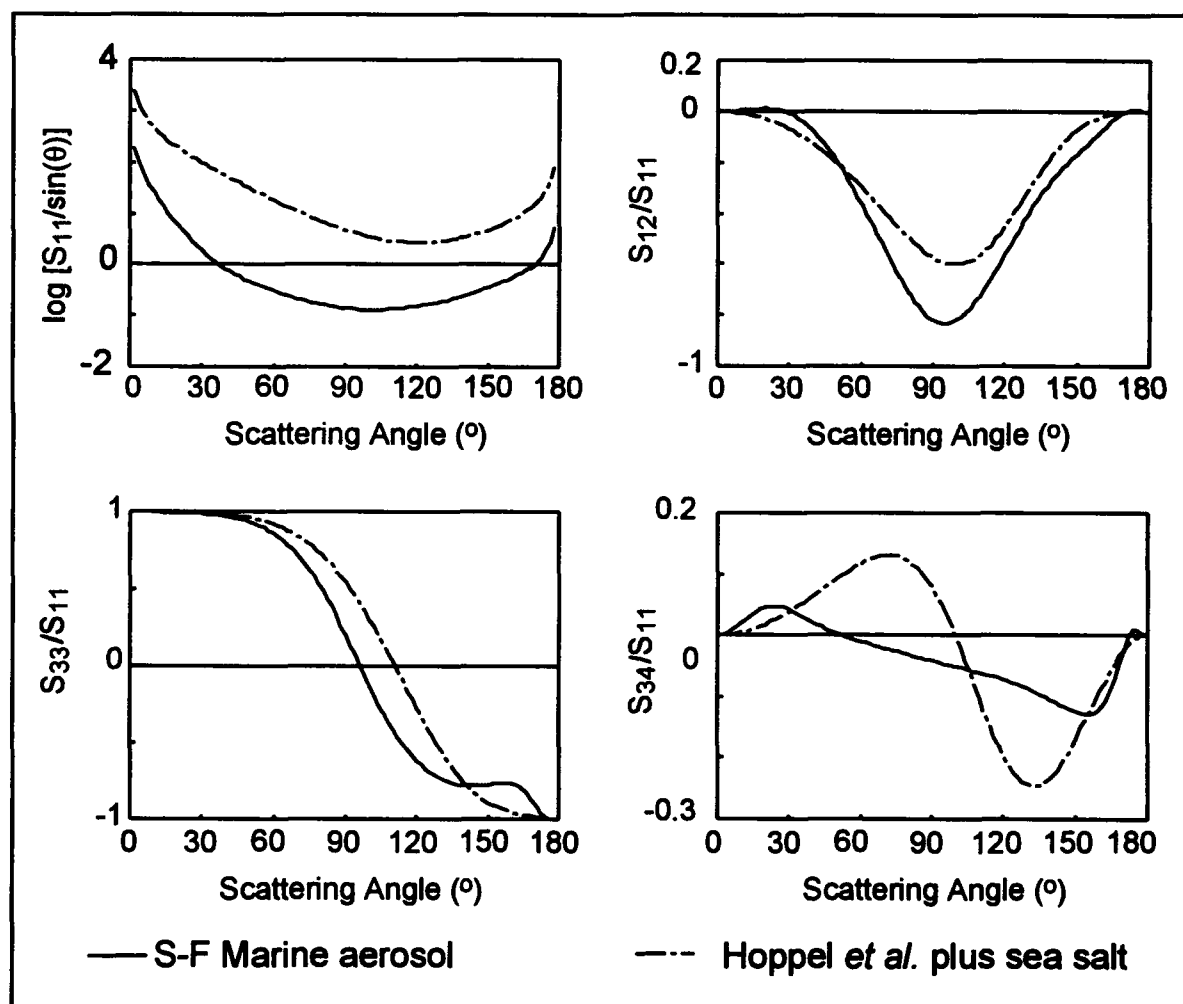


Figure 3. Comparison of the Shettle-Fenn¹¹ marine aerosol with an aerosol made up of the $\sim 0.02 \mu\text{m}$ and $\sim 0.1 \mu\text{m}$ components observed by Hoppel *et al.*⁴ plus a sea salt component.

Sea salt is present in the MBL in varying quantities. Wind speed, sea state and RH determine the size, shape, distribution, and refractive index of the aerosol. The variations are infinite. At extremely low humidities, the aerosol might well assume the cubic configuration of its primary component, NaCl. In this case the scattering might become similar to that observed by Perry *et al.*⁶, when none of the four matrix elements, S_{11} , S_{12} , S_{33} , and S_{34} can be reasonably described by a Mie calculation.⁶ However, the conditions for formation of the cubes measured by Perry *et al.*⁴ are unlikely in the MBL (it required the Tucson desert and a furnace to achieve the neat cubes observed by Perry *et al.*).

A calculation of the scattering of the Shettle Fenn¹¹ sea salt component at 80% RH shows (Figure 4) the linear polarization S_{12} is positive (horizontal) and close to zero until 120° when the polarization becomes vertically polarized and more intense reaching a maximum at about 150°. At higher angles, the polarization returns to horizontal polarization.

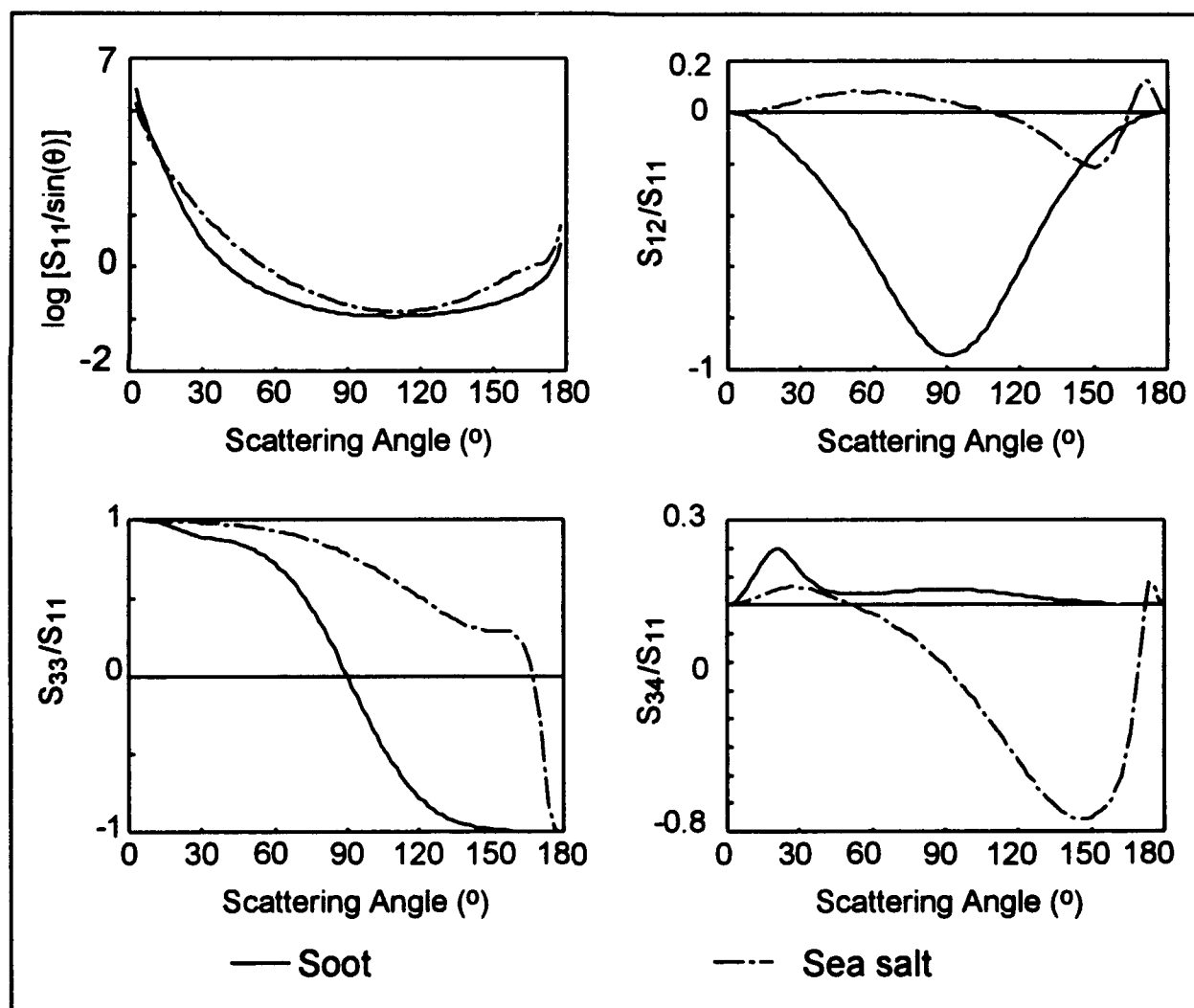


Figure 4. Scattering of soot as described by the Shettle-Fenn¹¹ model compared with the scattering predicted for the sea salt component.

3.4 Effect of Soot on Scattering in the MBL. To explore the presence of a widely occurring and highly absorptive component in the MBL, scattering from carbon soot was calculated. In coastal areas and near shipping lanes soot can be an important component of marine aerosols. This component tends to have an important effect on the scattering because the real and imaginary parts of the refractive index are large. To further complicate matters, the values for the refractive index varies considerably with source of data, which may indicate real variation among soots depending on source. This is probably due to non-fully dense agglomerations of carbon particles or the presence of homogeneous low- to non- absorptive products in the aerosol. Sampling and quantifying the amounts and density of carbon present presents difficulties. Table 2 summarizes some of the data available from particle measurements and pure carbon. Diesel combustion products tend to be in the size range of the small component of the Shettle-Fenn¹¹ values. The refractive indices of pure carbon are closest to those given by Arakawa *et al.*²³

Table 2. Various descriptions of soot used for investigating the effect of varying refractive indices and distributions on scattering in the MBL. NOTE: for the first 4 models, the reference refers to the refractive index; the number distribution is based on the Shettle-Fenn model. For the Kuwaiti soot, the distribution was from the literature, and the refractive index was from Shettle-Fenn.

Model	r_{mode}	r_{min}	r_{max}	σ	n
Shettle Fenn ¹¹ small component large component	0.025 μm 0.43 μm	0.0035 μm 0.04 μm	0.2 μm 3.5 μm	0.35 0.4	1.75-0.45i 1.75-0.45i
Arakawa <i>et al.</i> ²³ Soot	as for the two components of Shettle Fenn				2.29-0.87i
Dalzell and Sarofim ²⁴ Soot	as for the two components of Shettle Fenn				1.7-0.8i
Batten ²⁵ Soot	as for the two components of Shettle Fenn				1.4-0.13i
Kuwaiti ²⁶ Soot	0.2 μm	0.005 μm	10 μm	1	1.75-0.45i

The first four models listed in Table 2 varied only in the refractive index (the ratio of small to large component was 0.999875 to 0.000125). The Shettle-Fenn refractive index is a composite of a number of observations¹¹; that of Arakawa *et al.*²³ is from arc evaporated carbon films; Dalzell and Sarofim²⁴ measured soot from acetylene; and Batten²⁵ measured soot from kerosene. The Dalzell and Sarofim²⁴ description was confirmed by Pluchino *et al.*²⁷ who measured the angular distribution of the intensity of light scattered from a isolated carbon particle ($r = 3.06 \mu m$) determined by electron microscope to be spherical. Their Mie calculations of the scattering are in excellent agreement with the observations.

The last soot description is a model based on the size distribution observed by Parungo *et al.*²⁶ of the soots derived from the oil fires in Kuwait. Observations at various distances from Kuwait were taken at 1-6 km altitude, considerably above the MBL, but of practical interest as they were collected in the field. Parungo *et al.* report a broad distribution of particle sizes which were approximated here as a broad log normal distribution adjusted to roughly fit the number distribution reported which was at 3.7 km altitude and 160 km from Kuwait.

The results of scattering calculations for the various soots in Table 2 are given in Figure 5. The form of the scattering is generally similar with the largest differences arising from the broad distribution of particles (including very large

ones) in the Kuwaiti soot. Although the calculation shown here used the average to low refractive index reported by Shettle and Fenn¹¹ for soot - $1.75-0.45i$, using another refractive index does not change the qualitative conclusions that can be drawn from an examination of Figure 5. If the soot has the broad distribution of sizes reported in the Kuwaiti soot, the linear polarization is dramatically reduced. S_{34} actually changes sign at angles $> 60^\circ$.

One last comparison is of interest - that of the contribution to the polarization of scattering from soot and sea salt. To make this comparison, the scattering predicted from the "maritime component" of Shettle-Fenn¹¹ at 80% RH was compared with the scattering predicted by the same researchers for the large soot component. The size distribution for the soot component was that which Shettle and Fenn suggest for 0% RH, because soot is not particularly soluble. The shape of the angular distributions of the total intensities (S_{11}) of these components do not differ considerably (Figure 4). The polarizations do differ significantly (Figure 4). The implications with respect to the linear polarization is dramatic. As noted above, the scattering predicted for the sea salt is largely horizontal (+), and not particularly intense. When the soot is present, scattered light will be primarily vertically polarized, particularly near 90° .

4. CONCLUSIONS

In this preliminary study of the polarized scattering predicted for the MBL, the scattering significantly varies from the Rayleigh-like. The results are sensitive to the details of the size and number distributions and therefore may be used to discriminate various aerosols. Knowledge of the predominate character may be used to choose polarimetric sensing methods that discriminate against scattered ambient light in the MBL. The effects of the size, number density, real and imaginary indices of refraction and particle shape all have significant effects on the polarization characterization of the scattered light and potentially on visibility.

5. ACKNOWLEDGMENTS

We wish to thank Steve Ackleson for his support and interest in this research. This work was supported by the Office of Naval Research under Contract N00014-94-F0043 through the U.S. Department of Energy under Contract DE-AC03-76SF00098 awarded to M.S.Q.-H and N00014-92-J-1284 awarded to P.G.H.

6. REFERENCES

1. G.N. Plass, T.J. Humphreys, and G.W. Kattawar. "Ocean-atmosphere interface: its influence on radiation," *Appl. Opt.*, 20, 917-930, 1981.
2. G.W. Kattawar and C.N. Adams. "Stokes Vector Calculations of the Submarine Light Field in an Atmosphere-Ocean with Scattering According to a Rayleigh Phase Matrix: Effect of Interface Refractive Index on Radiance and Polarization," *Limnol. Oceanogr.*, 34, 1453-1472, 1989.
3. P. Koepke and M. Hess. "Scattering functions of tropospheric aerosols: the effects of non-spherical particles," *Appl. Opt.*, 27, 2422-2430, 1988.
4. W.A. Hoppel, J.W. Fitzgerald, G.M. Frick, R.E. Larson, and E.J. Mack. "Aerosol size distributions and optical properties found in the marine boundary layer over the Atlantic Ocean," *J. Geophys. Res.-Atmospheres*, 95D, 3659-3686, 1990.
5. J.W. Fitzgerald. "Marine aerosols - A review," *Atmospheric Environment Part A-General Topics*, 25, 533-545, 1991.

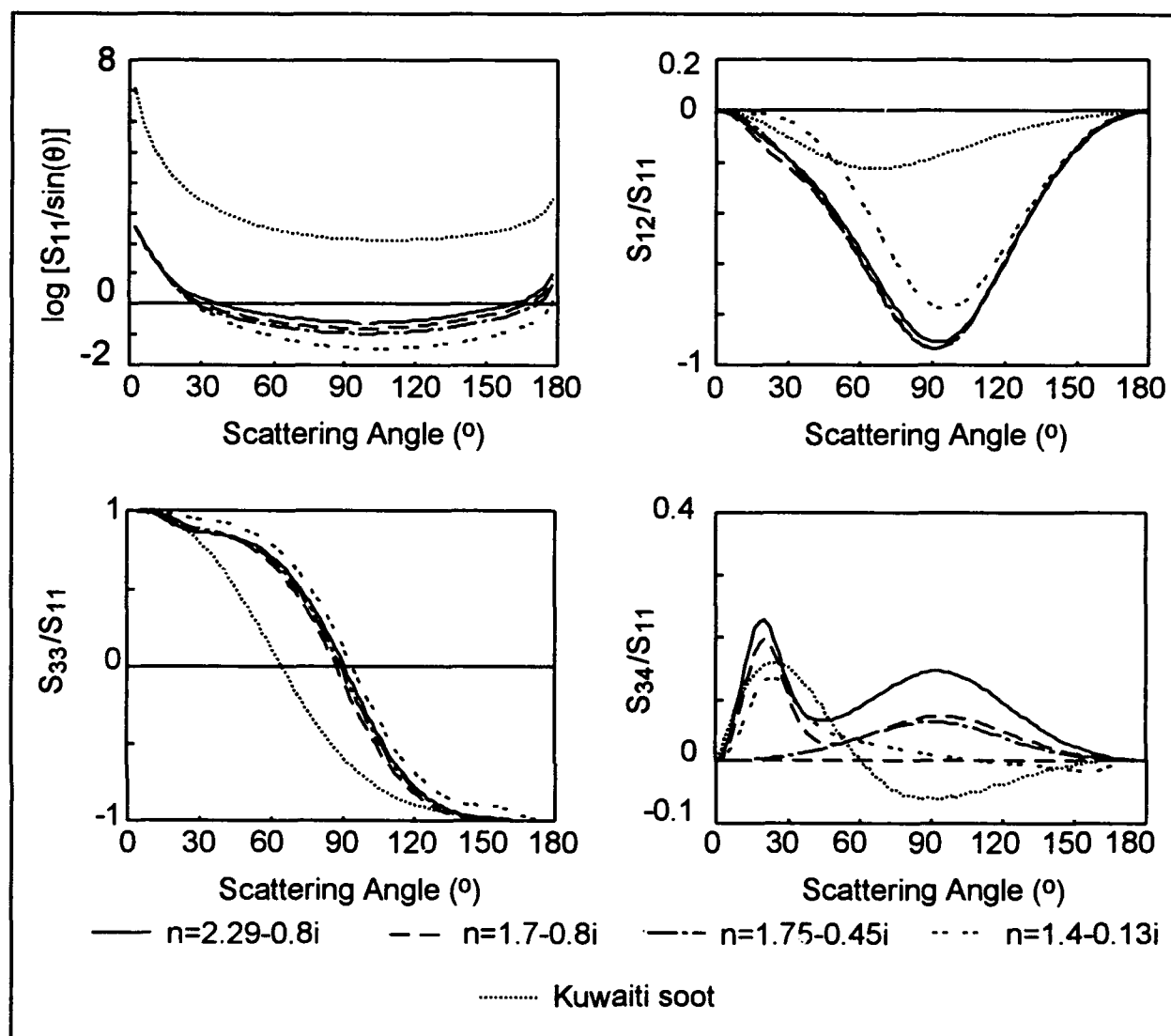


Figure 5. Scattering predicted for soots of various refractive indices and size distributions. Details of the models are found in Table 2.

6. R.J. Perry, A.J. Hunt, and D.R. Huffman. "Experimental determinations of Mueller scattering matrices for nonspherical particles," *Appl. Opt.*, 17, 2700-2710, 1978.
7. D. Diarmidjian. *Electromagnetic Scattering on Spherical Polydispersions*, American Elsevier Publishing Company, New York, 290 pp, 1969.
8. M.Z. Hansen and W.H. Evans. "Polar nephelometer for atmospheric particulate studies," *Appl. Opt.*, 19, 3389-3395.
9. T. Novakov and J.E. Penner. "The effect of anthropogenic sulfate aerosols on marine cloud droplet concentrations," *Nature*, 365, 823-826, 1992.

10. R.J. Charlson, J.E. Lovelock, M.O. Andreae, and S.G. Warren. "Oceanic phytoplankton, atmospheric sulphur, cloud albedo and climate," *Nature*, 326, 655-661, 1987. M.O. Andreae. "The ocean as a source of atmospheric sulfur compounds," in: *The Role of Air-Sea Exchange in Geochemical Cycling*. P. Buat-Menard, ed., Reidel, Dordrecht, pp.331-362, 1986.
11. E.P. Shettle and R.W. Fenn. *Models for the Aerosols of the Lower Atmosphere and the Effects of Humidity Variations on Their Optical Properties*. Report No. AFGL-TR-79-0214, Air Force Geophysics Laboratory, Project 7670, Hanscomb AFB, MA. 94 pp, 1979.
12. G. Hänel. "The properties of atmospheric aerosol particles as functions of the relative humidity at thermodynamic equilibrium with the surrounding moist air," in: *Advances in Geophysics*, H.E. Landsberg and J. van Mieghem, eds., Academic Press, New York, 19, 73-188, 1976.
13. G.M. Hale and M.R. Querry. "Optical constants of water in the 200-nm to 200- μ m wavelength region," *Appl. Opt.*, 12, 555-563, 1973.
14. F.E. Volz. "Infrared refractive index of atmospheric aerosol substance." *Appl. Opt.*, 11, 755-759, 1972.
15. N.E. Dorsey. *Properties of Ordinary Water-Substance in all its Phases: Water Vapor, Water and All the Ices.*, Am. Chem. Soc. Monograph Series, Reinhold, New York, pp. 332-338, 1940.
16. S.G. Gathman and K.L. Davidson. *The Navy Oceanic Vertical Aerosol Model*. Technical Report 1634, Naval Command, Control and Ocean Surveillance Center, San Diego, CA, 107 pp., 1993.
17. C.F. Bohren and D.R. Huffman, *Absorption and Scattering of Light by Small Particles*. Wiley, New York, 1983.
18. H.C. van de Hulst. *Light Scattering by Small Particles*, Wiley, New York, 1957.
19. A.C. Holland and G. Gagne. "The Scattering of Polarized Light by Polydisperse Systems of Irregular Particles" *Appl. Opt.*, 9, 1113-1121, 1970.
20. M.S. Quinby-Hunt, A.J. Hunt, K. Lofftus, and D.B. Shapiro. "Polarized-Light Scattering Studies of Marine *Chlorella*," *Limnol. Oceanogr.*, 34, 1587-1600, 1989.
21. K.J. Voss and E.S. Fry. "Measurement of the Mueller matrix for ocean water," *Appl. Opt.*, 23, 4427-4439, 1984.
22. K.J. Voss and E.S. Fry. "Measurement of the Mueller matrix for phytoplankton," *Limnol. Oceanogr.*, 30, 1322-1326, 1985.
23. E.T. Arakawa, M.W. Williams, and T. Inagaki, "Optical properties of arc-evaporated carbon films between 0.6 and 3.8 eV," *J. Appl. Phys.*, 48, 3176-77, 1977.
24. W.H. Dalzell and A.F. Sarofim. "Optical constants of soot and their application to heat-flux calculations," *J. of Heat Transfer*, 91, 100-104, 1969.
25. C.E. Batten. "Spectral optical constants of soots from polarized angular reflectance measurements," *Appl. Opt.*, 24, 1193-1199, 1985.
26. F. Parungo, B. Kopcewicz, C. Nagamoto, R. Schnell, P. Sheridan, C. Zhu, and J. Harris. "Aerosol particles in the Kuwait oil fire plumes: Their morphology, size distribution, chemical composition, transport, and potential effect on climate," *J. Geophys. Res.*, 97, 15867-15882, 1992.
27. A.B. Pluchino, S.S. Goldberg, J.M. Dowling, and C.M. Randall. "Refractive-index measurements of single micron-sized carbon particles," *Appl. Opt.*, 19, 3370-3372, 1980.

Remote sensing and measurement of the thickness of oil films
on the sea surface using the reflectivity contrast

V.U.Osadchy
P.P.Shirshov Institute of Oceanology (Russia)
K.S.Shifrin
Oregon State University
I.Y.Gurevich
P.P.Shirsov Institute of Oceanology (Russia)

ABSTRACT

Contrast in the reflectivity between pure and contaminated sea surfaces is the result of two effects, namely (a) differing reflectivities of pure sea water and oil on water and (b) damping effect of the oil film on the sea waves. The problem is to estimate their separate contributions to total contrast so that the substance effect can be isolated. Its magnitude provides assessment of the oil film thickness which can be obtained for sufficiently large averaging scales. The spectral behavior and film thickness dependence of contrast have been calculated for an undisturbed sea surface. The estimate of the damping effect has been made using the Cox-Munk distributions for pure and contaminated surfaces. The method chosen has been verified during a series of tests conducted in situ from an aircraft carrying a CO₂ laser sensor operating at 10.6 μ m.

1. INTRODUCTION

A significant part of optical methods for remote sensing of oil films on the sea surface is based on the difference between reflectivities of contaminated and pure areas of the surface. The measure of this difference is the contrast between mean radiances of the areas. Contrast is the result of two effects, namely (a) differing reflectivities of pure sea water and oil on water¹, the so-called "substance effect", and (b) damping effect of the oil film on sea waves, causing a change in surface roughness.

The main problem in interpretation of the optical remote sensing results is estimation of separate contributions of the two effects to total contrast so that the substance effect can be isolated. Its magnitude provides assessment of the oil film thickness which can be obtained for sufficiently large averaging scales when the sea slopes distribution function is available and the term "mean radiance" can thus be explained. It is essential that in all calculations and experiments we deal with mean radiances.

The aim of this work is to make calculated estimates of contrasts between oil slicks and pure sea surface, to perform real sea measurements of contrasts and to estimate the possibility to measure the oil film thickness by means of a remote active optical technique.

2. THE CALM SEA MODEL

2.1. Calculation formulas

For investigation of the substance effect we shall confine ourselves to the simplest case - normal incidence of light on a flat film lying on calm

water. Our aim is to investigate the dependence of the contrast K on the oil physical properties and to reveal the spectral intervals of high contrast. The contrast may be written as

$$K(l, \lambda) = \frac{R_{23}(l, \lambda) - R_{13}(\lambda)}{R_{23}(l, \lambda)} \quad (1)$$

where the subscripts 1, 2, 3 correspond to water, oil and air; R_{23} is the energy reflectance coefficient at the oil-air boundary and R_{13} is that for the air-water boundary. The reflection coefficient is found as:

$$V_{23}(l, \lambda) = \frac{(Z_1 + Z_2)(Z_2 - Z_3)e^{i\alpha_2 l} + (Z_1 - Z_2)(Z_2 + Z_3)e^{-i\alpha_2 l}}{(Z_1 + Z_2)(Z_2 + Z_3)e^{i\alpha_2 l} + (Z_1 - Z_2)(Z_2 - Z_3)e^{-i\alpha_2 l}} \quad (2)$$

where l is the oil film thickness; $\alpha_2 = \frac{2\pi}{\lambda} n_2 \cos \theta_2$; λ is the wavelength in vacuum; θ is the angle of incidence in the corresponding medium (θ_2 is for oil); and Z_i are impedances of the corresponding media. They are expressed through a complex refractive index by

$$Z^{(s)} = \frac{1}{n \cos \theta}; \quad Z^{(p)} = \frac{\cos \theta}{n}$$

for the s- and p-waves, respectively; n is a complex refractive index of the medium; $n = n - i\kappa$; n and κ are refraction and absorption indices.

For the case of normal incidence

$$\theta = 0, \quad Z^{(s)} = Z^{(p)} = \frac{1}{n}$$

Taking into account the fact that $n_3 = 1$ (air) and designating $l/\lambda = x$, we have for V :

$$\begin{aligned} V_{23} &= V_{23}' + iV_{23}'' = \\ &= \frac{(n_2 + n_1)(1 - n_2) + (n_2 - n_1)(1 + n_2)e^{-i4\pi x n_2}}{(n_2 + n_1)(1 + n_2) + (n_2 - n_1)(1 - n_2)e^{-i4\pi x n_2}} \end{aligned} \quad (3)$$

The reflection coefficient for intensity is:

$$R_{23} = |V_{23}|^2 \quad (4)$$

2.2. Optical constants of sea water and oil

We used optical constants n and κ for the ultra-violet (UV), visible (VIS) and infrared (IR) regions obtained for 16 oil samples from different oil fields and wells and for one diesel fuel sample². It is worthwhile to emphasize some peculiarities of the typical spectral behavior of n and κ . In the UV, absorption of almost all samples is very high. In the VIS, κ becomes very low (the order of magnitude of κ is 10^{-3}). The refraction index does not change strongly: from 1.57-1.67 in the UV to 1.48-1.52 in the VIS. In the IR there are three rather strong absorption bands: near 3.3-3.6 μm , 6.7-7.1 μm and 11.1-16.7 μm . It is significant that the first two bands are near the absorption bands of water ($\sim 3.2 \mu\text{m}$ and 6.1 μm). The important matter is dispersion of n and κ of oils causing an additional variability of contrasts. According to some publications³, in the VIS, n and κ increase with growing oil density ρ ; κ grows by two orders of magnitude while ρ changes from 0.7936 to 0.8973 and the growth of $(n - 1)$ is equal only to 10-15 %.

2.3. Reflection by thick layers of oil and water. Contrast

For this simplest case the reflection coefficients have been calculated using the Fresnel formulas. The results are given in Fig. 1. As one can see, within nearly all of the spectral range considered the oil is brighter than the water. Contrast is strongly influenced by spectral behavior of the reflection coefficient R_w of sea water because R_{oil} of oil changes slightly in a wide spectral range, whereas R_w of water changes significantly. Thus, in the 8-12 μm -interval where R_w of water is minimum the contrast is maximum and reaches about 80%. In the VIS and near the IR-region, contrast is high enough - 30-40 % and in the vicinity of $\lambda = 3.30-3.40 \mu\text{m}$ it is almost equal to zero!

2.4. Reflection by the thin oil film

Formulas (3) and (4) have been used to calculate dependence of the reflection coefficient for intensity on the oil film thickness⁴. The calculations have been performed for 20 wavelengths within the spectral range (0.3-15 μm) considered. The n and κ of oils were the same as in calculations for thick layers of oil. The results can be seen in Fig. 2. Two extreme cases have been chosen to illustrate variability of the results. For $\lambda = 0.60 \mu\text{m}$, the absorption index $\kappa = 0.0029$ is minimum and for $\lambda = 3.40 \mu\text{m}$ $\kappa = 0.11$ it is maximum. The difference in κ causes a difference in fading of the oscillations. For $\lambda = 3.4 \mu\text{m}$ and $x = 4$ ($x = 1/\lambda$ is relative thickness of the film), the film may be considered as optically thick and for $\lambda = 0.60 \mu\text{m}$ and $x = 4$ it is still optically thin, so that reflectance depends strongly on the interference oscillations.

2.5. Reflection by films of variable thickness. Distribution of the oil film thickness

In real sea conditions, the oil film thickness becomes randomly distributed within a contaminated area. Real optical sensors have a finite view field and averaging time and so their response is the result of light interaction with the oil film, with the thickness randomly distributed within the sensor view field. This response can be calculated provided the distribution law is known. Unfortunately, we have not found direct experimental data on such distributions.

In order to be able to obtain some estimates of impact of the oil film thickness distribution on the remote sensor response, we had to make some plausible assumptions about the distribution law⁶. First, the law must be valid for positive values of thickness (contrary to the Gaussian law permitting a negative thickness); second, it must be similar to the normal law. The simplest law with such properties is the log-normal one describing normally distributed $\ln l$ (l is thickness). It has been shown⁶ that the log-normal law may be approximated by gamma-distribution which in many cases is more convenient for calculations retaining the right description of the phenomenon investigated. This is why we have used this distribution in the calculations.

The normalized gamma-distribution may be written as

$$f(l) = \frac{\beta^{\mu+1}}{\Gamma(\mu+1)} l^{\mu} e^{-\beta l}, \int_0^{\infty} f(l) dl = 1 \quad (5)$$

Here l is oil film thickness, μ and β are the distribution parameters.

$$l_m = \frac{\mu}{\beta}, \quad l = \frac{\mu+1}{\beta} = l_m \frac{\mu+1}{\mu} \quad (6)$$

For the description of the distribution shape it is well to introduce a relative width of the distribution

$$\Delta\varepsilon = \frac{l_2 - l_1}{l_m} = \frac{\Delta l}{l_m} \quad (7)$$

where the distribution width Δl is an interval between the points l_2 and l_1 , for which $f(l_{1/2}) = 1/2f(l_m)$. It has been shown that the relative width is equal to

$$\Delta\varepsilon = \frac{2.48...}{\sqrt{\mu}} \quad (8)$$

It can be seen from this formula that $\Delta\varepsilon$ defines the distribution parameter μ and both parameters β and μ can be expressed through l_m and $\Delta\varepsilon$:

$$\mu = \frac{6.15 \dots}{(\Delta \varepsilon)^2} ; \beta = \frac{6.15 \dots}{(\Delta \varepsilon)^2} \frac{1}{l_m} \quad (9)$$

Let us introduce $f^*(x)$ for the relative film thickness $x=l/\lambda$; $f^*(x)$ is connected with $f(l)$ by the relation $f(l)dl=f^*(x)dx$ and so

$$f^*(x) = f(l) \frac{dl}{dx} = f(l, \lambda) = \left[\frac{\mu+1}{x} \right]^{\mu+1} \frac{1}{\Gamma(\mu+1)} x^{\mu} \exp \left[-\frac{\mu+1}{x} x \right] \quad (10)$$

where $\bar{x} = l/\lambda$. Designating the constant factor as C_{μ} , we have

$$f^*(x) = C_{\mu} x^{\mu} \exp \left[-\frac{\mu+1}{x} x \right] \quad (11)$$

Response of the monochromatic light receiver is defined (to an accuracy of the calibration factor) by the formula:

$$W_{\mu}(\bar{x}) = \int_0^{\infty} R(x) f^*(x) dx. \quad (12)$$

Here $R(x)$ is reflection coefficient of a flat film with relative thickness \bar{x} . dependencies of W on the mean relative film thickness \bar{x} have been calculated for 10 values of parameter $\mu = \infty, 24, 18, 12, 6, 4, 2, 1, 0$, corresponding to dispersion changing from zero to the maximum possible magnitude for this distribution law. The calculations have been made for 4 wavelengths corresponding to emission of the known lasers: $\lambda = 0.63 \mu m$ (He-Ne laser); $\lambda = 3.40 \mu m$ (Ne laser); $\lambda = 5.40 \mu m$ (Ne laser); $\lambda = 10.6 \mu m$ (CO_2 laser).

Qualitatively, results of the calculations for different wavelengths are quite similar, so we show here only the dependence of W on \bar{x} for $\lambda = 10.6 \mu m$ (with different μ) (Fig. 3). Figure 4 presents the dependence of W on \bar{x} for different wavelengths but with fixed $\Delta \varepsilon = 1.24$, ($\mu = 4$). As one can see, for all wavelengths, W shows a series of fading oscillations. The intensity of fading increases with growing distribution width (with a decrease of μ). For a maximum distribution width (in our case for $\mu = 1, 2, 3, 4$), only the first maximum W of oscillations remains retained (see Fig.4). The position of maximum is equal to that for a monodispersed film. The magnitude of W_m can be obtained from investigation into the dependence $W_m = f[R(\alpha, \lambda)]$. For wide distributions (which is likely to be met in practice)

$$W_m = 33.2 R^2$$

This formula provides an accuracy ~ 10 % which appears to be enough for estimates. Summarizing the results of this section we must emphasize that the strong impact of distribution of the oil film thickness on the remote sensor response severely limits the possibility of remote measurement of the oil film thickness (using, for example, the multifrequency technique).

3. WAVY SEA MODEL. LIDAR CROSS-SECTION

For calculations of reflection from a wavy sea we have used a well-known model of the wavy surface presented as an aggregate of statistically distributed facets, each reflecting light according to the laws of geometrical optics. The distribution of facet orientations has been taken from Cox and Munk⁷. The geometrical features of reflection including relations between all angles which determine light interaction with sea surface have been obtained in⁸. In general, for any geometry of reflection chosen the properties of the reflected beam are given by the Stokes vector-parameter.

Here, we are interested only in the lidar version of the problem, which is urgent for active remote sensing. For backward reflection the polarization state of light does not change and thus we shall consider only radiance B_1 , the first Stokes parameter. For this case

$$B_1 = \frac{1}{4} \pi \varepsilon^2 \sec^2 \theta P(\theta_n, \varphi_n) R B_0 \quad (13)$$

Here, ε is angular radius of the light source (in radians); $P(\theta_n, \varphi_n)$ is the Cox and Munk function in polar coordinates; R is the Fresnel coefficient; θ is the zenith angle of incident and reflected beams. The incident light radiance is $B_0 = E_0 / \omega_s$, where E_0 is irradiance of the area normal to the incident beam, and ω_s is a solid angle of the light source ($\omega_s = \pi \varepsilon^2$). Thus, $B_0 = E_0 / \pi \varepsilon^2$ and (13) becomes

$$B_1 = \frac{1}{4} \sec^2 \theta P(\theta_n, \varphi_n) R E_0 \quad (14)$$

The lidar cross-section B is defined as the ratio between radiance of light reflected in the direction of the source and that of an ideal scatter put in similar illumination conditions. So, B is a radiance coefficient for backward reflection. The ideal scatter radiance is $B_{sc} = E_0 / \pi$. Thus,

$$B = \frac{B_1}{B_{sc}} = \frac{\pi}{4} \sec^2 \theta P(\theta_n, \varphi_n) R \quad (15)$$

Results of the calculations of B for different θ for pure and oiled surfaces are presented in Fig. 5. It was considered that dispersion σ^2 of the distribution $P(\theta_n, \varphi_n)$ for an oiled surface is smaller than σ^2 for a pure surface by about a factor of three⁷. It follows from Fig. 5 that for direction

of sensing at nadir ($\theta = 0^\circ$) radiance of an oiled surface is always greater than that of a pure surface, i.e. contrast is positive. For the cases when $\theta \neq 0^\circ$, contrast may be positive and negative, which is essential for use of scanning systems.

4. EXPERIMENTAL RESULTS IN ACTIVE REMOTE SENSING OF OIL FILMS ON THE SEA SURFACE

4.1. Choice of the experimental technique

Results reported in previous sections appear to be suitable for interpretation of the experimental data obtained using either active or passive optical remote sensors. But it is obvious that the active technique is preferable for remote sensing of oil films being less dependent on external conditions of the experiment. We have designed and manufactured an air-borne prototype of the lidar with a view of obtaining experimental data on contributions of the two above-mentioned effects to total contrast.

Choice of the wavelength of sounding emission was of critical significance. Actual wavelength $\lambda = 10.6 \mu\text{m}$ has been taken from the following considerations: (1) for this wavelength, contrast between oil and sea water (i.e. the substance effect) is maximum in all of the spectral range from the UV to the far IR; (2) the period of the oscillating dependence of contrast on the oil film thickness is long enough (this is significant for the possibility of measuring the oil film thickness); (3) $10.6 \mu\text{m}$ emission does not penetrate in the water body because of the large water absorption coefficient making unnecessary consideration of scattering by the hydrosols; (4) low absorption in the atmosphere making it possible to neglect absorption for suitable aircraft altitudes of flight. (5) existence of a suitable CO_2 laser as the source of sounding emission.

For the wavelength chosen, principal technical parameters of the lidar have been calculated. The actual lidar parameters were as follows: (1) continuous-wave CO_2 laser emission power, not smaller than 4 watts; (2) diameter of the telescope mirror, 400 mm; (3) threshold sensitivity of the piro-electrical receiver of $10.6 \mu\text{m}$ emission, 10^{-8} watts; (4) frequency of the emission modulation, 300 Hz; (5) averaging time of recording the lidar response signal, 0.5 or 1 s. These parameters provided recording the lidar response at flight altitudes to 500 m above sea surface. The optico-mechanical unit was mounted in the photo hatch of an IL-14 air plane having a flight speed of 70-100 m/s during the experiment. In order to obtain more obvious estimates of the contributions to contrast made by the effects of substance and damping waves, it will be more appropriate to use the ratio $R_r = \bar{F}_{oil} / \bar{F}_w$ as a measure of contrast rather than the conventional formula (1). Here, \bar{F}_{oil} and \bar{F}_w are mean fluxes (in the sense of section 1) of the IR-laser emission reflected by oiled and pure surfaces, respectively.

To an accuracy of the constant factor

$$R_{\text{rel}} = \frac{\overline{R}_{\text{oil}}}{R_w} \cdot \frac{\int_{\Omega} P_{\text{oil}} d\omega}{\int_{\Omega} P_w d\omega} \quad (16)$$

Here, $\overline{R}_{\text{oil}}/R_w$ is the ratio of reflection coefficients of the oil film and pure water giving a measure of the substance effect and $\overline{P}_{\text{oil}}/\overline{P}_w = \int_{\Omega} P_{\text{oil}} d\omega / \int_{\Omega} P_w d\omega$ gives a measure of the effect of damping waves; P_{oil} is the sea slope distribution function for a contaminated surface and P_w is that for a pure sea surface; $d\omega$ is an element of the solid angle. Integration limits Ω are determined by angular width of the laser beam, view field of the receiving optical system and the direction of sensing.

4.2. Experimental cases

The major part of experimental data have been obtained in flights over oil fields on the Caspian Sea not far from the city of Baku. Airplane courses were chosen so as to obtain records of the lidar response from a pure sea surface and then after crossing the oil slick boundary, from a contaminated surface. There were many cases with vast oil slicks providing the duration of records to tens of seconds and even longer. In order to illustrate the experiments, we have chosen results obtained in two undoubtedly clear cases: (1) sensing of a vast obviously optically thick film and (2) sensing of a film formed by oil oozing out of an isolated underwater source. For an optically thick film, data have been obtained in a series of flights during one day from different altitudes of the plane (from 50 to 200 meters) over one and the same oil slick⁹. The wind speed was about 10 m/s. Sensing direction was at nadir. In all flights, the ratio measured $\overline{F}_{\text{oil}}/\overline{F}_w$ was equal to ~ 35 . Since

$\overline{R}_{\text{oil}}/R_w = 5$ for the 10- μm wavelength, $\overline{P}_{\text{oil}}/\overline{P}_w = 7$. This value is significantly greater than the estimate made using the Cox and Munk data. This fact can be explained on the assumption of a change in the shape of the sea slope distribution law for a contaminated sea surface area.

The flights over an isolated underwater source of oil (derelict underwater bore-hole) have been performed in moderate wind-wave conditions (wind speed was equal to 2-3 m/s) making the picture of oil spreading rather simple¹⁰. A survey of the oil slick is represented in the lower part of Fig. 8. In the upper part of the figure, a copy of a record of lidar response is shown demonstrating the dependence of $\overline{F}_{\text{oil}}$ on distance L from the source S along the direction of flights. In the first 600 m of the path AA' marked by the asterisked braces the law of oil thickness change can be approximated by $1/L$.

The law of change of \overline{F}_{oil} appeared to be quite similar: $\overline{F}_{oil} \sim 1/L$ demonstrating good correlation between \overline{F}_{oil} and $1/L$. The range of oil thicknesses along the first 600 m of the path AA' can be estimated as $(2 \pm 0.1) \mu\text{m}$; these thicknesses are quite usual for vast tails of large oil slicks in warm sea water.

5. ACKNOWLEDGEMENTS

The authors wish to thank their colleague, Dr. Iosif M. Levin, for fruitful discussions and help in the work. Thanks are also due to Mr. Ernie V. Popov for creative assistance in the preparation of the manuscript.

6. REFERENCES

1. I.Ya. Gurevich and K.S. Shifrin, "Physical fundamentals of optical remote techniques for sensing oil contaminations at the sea surface", *Trudy GOIN*, Vyp.166, pp.107-123, 1981 (in Russian).
2. L.I. Alperovich, A.I. Komarova, B.P. Narzyiev and V.N. Pushkarev, "Optical constants of oil in the region of $0.25-0.25 \mu\text{m}$ ", *Zhurnal prikladnoy spektroskopii*, Vol.28, No.4, pp.719-723, 1978 (in Russian).
3. V.S. Zolotarev, I.A. Kitushina and S.M. Sutovsky, "Optical constants of oil in the region of $0.4-15 \mu\text{m}$ ", *Okeanologiya*, Vol.7, No.6, pp.1113-1117, 1977 (in Russian).
4. I.Ya. Gurevich and K.S. Shifrin, "Reflection of visual and infrared radiation by oil films on the sea", *Optical methods used in the study of oceans and internal reservoirs*, Nauka Publ., Novosibirsk, pp.166-183, 1979 (in Russian).
5. I.Ya. Gurevich, A.M. Kokorin and K.S. Shifrin, "Reflection of optical emission by oil films of variable thickness", *Okeanologiya*, Vol.22, No.4, pp.573-579, 1982 (in Russian).
6. L.M. Levin, "On functions for size distribution of the cloud drops. Optical density of the cloud", *Izv. Akad. Nauk SSSR, Ser. Geophys.*, No.10, pp.1211-1217, 1958 (in Russian).
7. C. Cox and W.H. Munk, "Slopes of the sea surface deduced from photographs of sun glitter", *Scripps. Inst. of Oceanogr. Bull.*, Vol. 6, No. 9, pp. 401-479, 1956.
8. Yu.A.R. Mullamaa, *Atlas of rough sea surface optical properties*, Estonian Acad. of Sciences, Tartu, 1964 (in Russian).
9. K.S. Shifrin, V.Yu. Osadchy, G.N. Belyakov et al., "Sensing of oil films at the sea surface using the CO_2 lidar", In: *Tezisy vsesoyuznogo simpoziuma po lazernomu zondirovaniyu atmosfery*, pp.155-159, Tomsk, 1978 (in Russian).
10. V.Yu. Osadchy, G.N. Belyakov and K.S. Shifrin, "Lidar measurements of oil films on the sea", In: *Oceanic and Atmospheric Optics*, pp. 241-242, Leningrad, 1984 (in Russian).

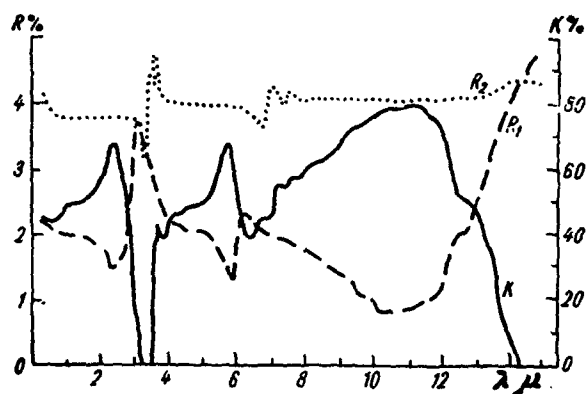


Fig.1

Fig.1. Spectral variability of the reflection coefficient and contrast for normal incidence on a thick oil layer and sea water. R_1 is the reflection coefficient of sea water; R_2 is reflection coefficient of oil; K is contrast for oil on water.

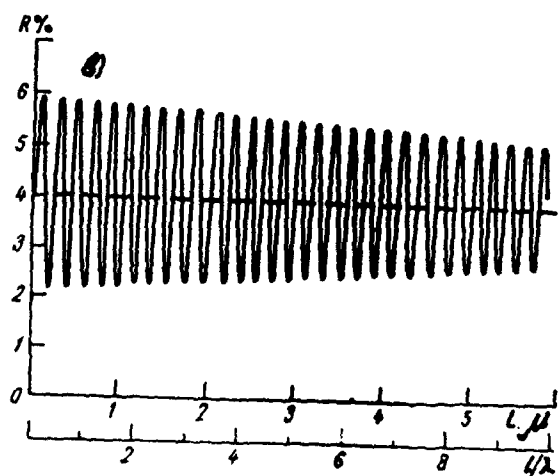
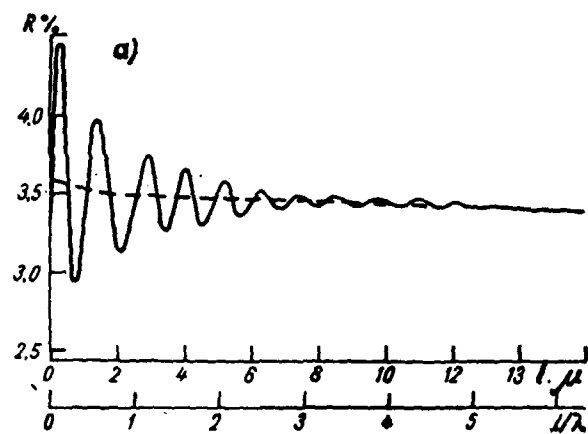


Fig.2

Fig.2. Dependence of the reflection coefficient on film thickness. a is the region of strong absorption, $\lambda = 3.4 \mu\text{m}$; b is the region of weak absorption, $\lambda = 0.6 \mu\text{m}$.

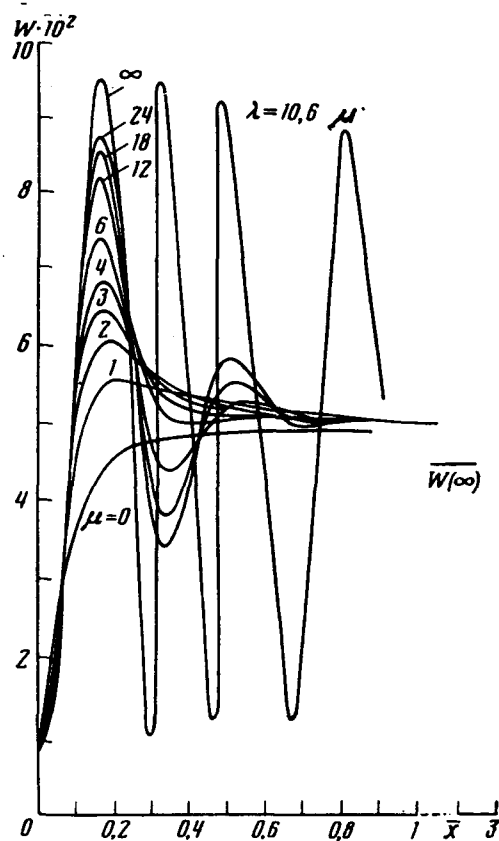


Fig.3

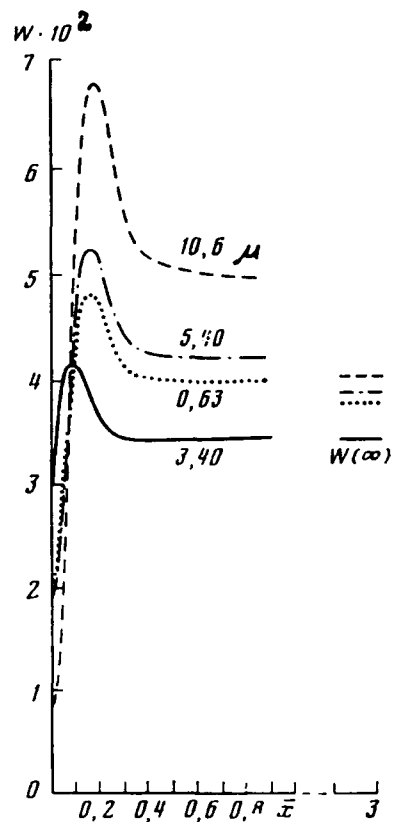


Fig.4

Fig.3. Dependence of the reflection coefficient on mean oil film thickness for different widths of distribution of the oil film thickness for $\lambda = 10.6 \mu\text{m}$.

Fig.4. Dependencies of the reflection coefficient on mean oil film thickness for different wavelengths of emission for width of distribution of the oil film thickness $\Delta\epsilon = 1.24$, ($\mu = 4$).

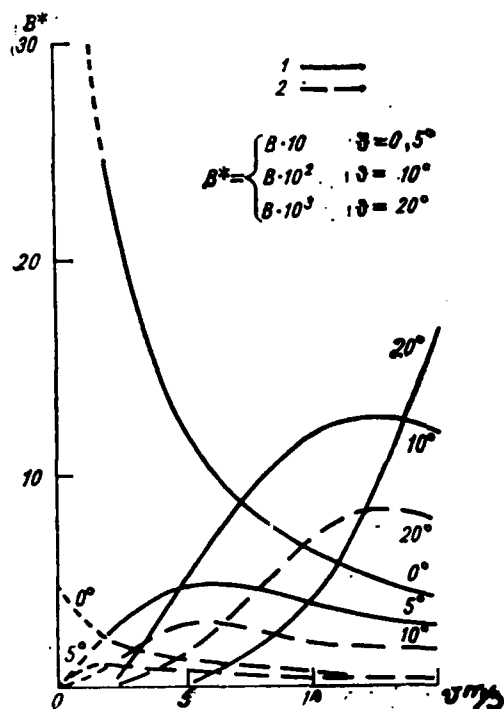


Fig.5

Fig.5. Dependence of the magnitude of lidar cross-section on the wind speed for a pure and oiled sea surface for different sensing directions $\theta = 0.5, 10, 20^\circ$. 1 is oil; 2 is water.

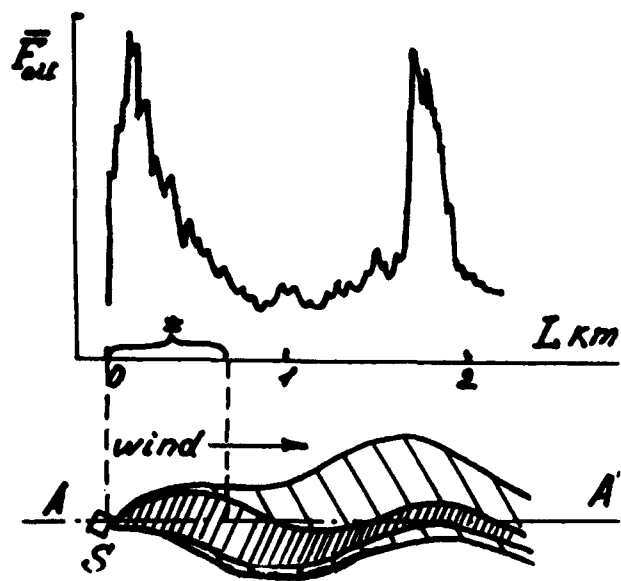


Fig.6

Fig.6. Schematic representation of flights over an isolated oil source and a copy of a lidar response record.

Spectral contrast of oil films on the sea surface:
influence of water type, wind velocity, and solar altitude

Iosif M. Levin

P.P. Shirshov Institute of Oceanology, St. Petersburg Branch,
Russian Academy of Sciences, 11, Tavricheskaja Ul.
St. Petersburg, 193015

ABSTRACT

Contrast of oil film against the rough sea surface background was estimated for the wavelength range from 300 to 800 nm in various observation conditions. Morel and Prieur's experimental data on water reflectance in the visible spectrum were used as the basis for computations. Extrapolations of these data to the UV and IR regions are based on the well-known low-parametric models for water properties. The computations show that the contrast magnitude varies depending on the water type, wavelength, wind velocity and solar altitude from -90% to +60% (plus relates to the case when oil is brighter than water, minus relates to the opposite case). To avoid small or zero contrasts, observations apparently should be fulfilled in several spectral channels. Calculation method was verified during a flight over the Black Sea when predicted oil-water contrast was obtained with two airborne TV-cameras operating in the visible and UV spectral regions.

1. INTRODUCTION

For observations of oil films against the rough sea surface background, it is important to know what spectral sensitivity of the receiver provides the maximal image contrast. In 1989 we observed oil spills in the Black Sea near Odessa from the airplane. We used two TV-cameras, one sensitive in the visual spectrum, and the other, in the ultraviolet one. The weather was cloudy. In the UV the image contrast turned to be rather high (about 50%) and distinctly higher than in the visual spectrum. We carried out the calculations of contrast for this sea region and cloudy weather. The basis of these calculations was water optical properties, namely absorption (a) and backscattering (b_b) coefficients measured previously in the same sea region. We used formulae obtained before and relating the water radiance coefficient to a and b_b . The calculated contrast values agree closely with measurement results. However, it is clear that the UV spectral channel need not be optimal for other regions of the World Ocean and for other observation conditions. It should be pointed out that dependency of contrast on observation conditions in daylight is more complicated than for the lidar case. For the lidar directed to nadir the well-known effect of wave damping by oil films² always leads to increasing oil radiance because in an oil slick more wave slopes are perpendicular to the light beam than at uncontaminated sea surface. Accordingly, the contrast for the lidar case is always positive (oil is brighter than water). For daylight, the damping of waves by oil may either increase or decrease the film radiance depending on wind velocity and solar altitude. Hence, the contrast may be either positive or negative.

Our goal is to compute the oil-water contrast for various water types and observation conditions for the wavelength range from 300 to 800 nm. The data on spectral water reflectance R (under the sea surface) from classical Morel and Prieur's article³ were used

as the basis for these computations. Only the case of observation from a low altitude (without regard for the atmospheric effects) in the nadir direction was considered.

2. COMPUTATION MODEL

Contrast of the oil film against the water background is

$$C = (I^{(f)} - I^{(s)} - I^{(w)}) / I^{(f)} = (\rho^{(f)} - \rho^{(s)} - \rho^{(w)}) / \rho^{(f)}, \quad (1)$$

where

$$I^{(f)} = I_d^{(f)} + I_{dif}^{(f)}, \quad I^{(s)} = I_d^{(s)} + I_{dif}^{(s)}, \quad I^{(w)} = I_d^{(w)} + I_{dif}^{(w)} \quad (2)$$

are radiances of the oil film, rough sea surface and water body (the latter is due to light backscattered in the sea). Each of these radiances is the sum of two components. The first one is determined by direct sunlight (subscript "d"), and the second, by diffusive light of the sky (subscript "dif"). Instead of radiances, the associated radiance coefficients may be used:

$$\rho^{(f,s,w)} = \pi I_0^{(f,s,w)} / E_0, \quad (3)$$

where $E_0 = E_d + E_{dif}$ is the sea surface irradiance.

The radiance coefficients for each component are

$$\rho_d^{(f,s,w)} = \pi I_d^{(f,s,w)} / E_d, \quad \rho_{dif}^{(f,s,w)} = \pi I_{dif}^{(f,s,w)} / E_{dif}, \quad (4)$$

or

$$\rho^{(f,s,w)} = y \rho_d^{(f,s,w)} + (1-y) \rho_{dif}^{(f,s,w)}, \quad (5)$$

where $y = E_d / E_0$ is the contribution of direct sunlight to the total surface irradiance.

The data on y for the wavelength range $\lambda = 400-700$ nm have been presented by Austin⁴. To evaluate y in the whole region from 300 to 800 nm, we used the equations

$$E_d(\lambda) = E_0(\lambda) \exp [-\tau(\lambda) / \cos \theta], \quad (6)$$

$$E_{dif}(\lambda) = E_0(\lambda) f(\theta) \tau(\lambda), \quad (7)$$

where $\tau(\lambda) = \tau_R(\lambda) + \tau_a(\lambda)$ is the atmosphere optical thickness which is the sum of Rayleigh ($\tau_R(\lambda)$) and aerosol ($\tau_a(\lambda)$) optical thicknesses, and $f(\theta)$ is a function which depends only on the solar zenith angle θ . From these equations, $y(\lambda)$ can be easily expressed through $y(\lambda_0)$:

$$y(\theta, \lambda) = \left[1 + \frac{1 - y(\theta, \lambda_0)}{y(\theta, \lambda_0)} A \right]^{-1}, \quad (8)$$

$$A = \frac{\tau(\lambda) \exp[-\tau(\lambda_0)/\cos\theta]}{\tau(\lambda_0) \exp[-\tau(\lambda)/\cos\theta]}. \quad (9)$$

For the standard atmosphere and $\lambda_0 = 550$ nm, $\tau_R(\lambda_0) = 0.0952$, $\tau(\lambda_0) = \tau_R(\lambda_0) + \tau_a(\lambda_0) = 0.3$.

Optical thickness $\tau(\lambda)$ is computed from

$$\tau(\lambda) = \tau_R(\lambda_0) (\lambda_0/\lambda)^4 + \tau_a(\lambda_0)(\lambda_0/\lambda). \quad (10)$$

Using the Austin⁴ data on $y(\theta, \lambda_0)$ (for example, $y(20^\circ, 550 \text{ nm}) = 0.84$), we have found the values of $y(\theta, \lambda)$ for the wavelength range from 300 to 800 nm by Eqs. (8)-(10). They agree closely with the Austin experimental data. Selected values of y are presented in Table.1.

Table 1

Contribution of direct sunlight to the total surface irradiance (y)

λ (nm)	300	400	500	550	600	700	800
$\theta = 20^\circ$	0.26	0.65	0.80	0.84	0.87	0.90	0.92
$\theta = 45^\circ$	0.23	0.62	0.78	0.82	0.85	0.89	0.91

Let us now consider the technique used for calculations of the radiance coefficients for surface, oil film and water.

2.1. Sea surface radiance coefficients

The magnitude of $\rho_d^{(s)}$ depends on wind velocity v , solar zenith angle θ , and wind azimuth ϕ with respect to the solar vertical. In a spectral region of 300 to 800 nm it weakly depends on the wavelength. For several values of v , θ and ϕ the radiance coefficients have been calculated by Mullamaa⁵ on the basis of the Cox-Munk surface slope distribution⁶. Using the same calculation technique we have computed the surface radiance coefficients for a wide range of v , θ and ϕ without regard for polarization. Some of them are shown in Table 2.

Table 2

The values of sea surface radiance coefficients $\rho_d^{(s)}$ (averaged over azimuth ϕ) for direct sunlight in the nadir observation direction

Solar zenith angle θ°	Wind velocity v (m/s)				
	2	5	10	15	20
0	0.42	0.20	0.10	0.072	0.054
20	0.036	0.064	0.061	0.051	0.043
45	0.0001	0.0016	0.008	0.014	0.018

For a uniform sky and nadir observation direction, when light from low sky areas virtually does not fall within the observer's view (there are no large slopes in the Cox-Munk distribution), the radiance coefficient

$$\rho_{dif}^{(s)} \approx 0.02 \quad (11)$$

and does not, in practice, depend on wind velocity⁵.

2.2. Oil film radiance coefficients

Fresnel reflectivity of the thick oil film in the spectral region considered does not depend on the wavelength with an accuracy of about 10% and its average value is about 0.04,² whereas that of water Fresnel reflectivity in the same spectral region is about 0.02.

It is known that the oil film damps the surface roughness. As Cox and Munk have shown, the contaminated sea surface may be considered as a random surface with the same Cox-Munk slope distribution, but the variance of this distribution is approximately three times smaller than that of the slope distribution of the uncontaminated sea surface. This corresponds to a threefold decrease of wind velocity⁶. Therefore, it may be assumed that

$$\rho_d^{(r)}(\theta, v) \approx 2 \rho_d^{(s)}(\theta, v/3), \quad (12)$$

$$\rho_{dif}^{(r)} \approx 2 \rho_{dif}^{(s)} \approx 0.04. \quad (13)$$

2.3. Water radiance coefficients

Water radiance coefficients $\rho^{(w)}$ ($\rho_d^{(w)}$ or $\rho_{dif}^{(w)}$) measured above the sea surface are

related to the undersurface radiance coefficients $r^{(w)}$ ($r_d^{(w)}$ or $r_{dif}^{(w)}$) by the equation:

$$\rho^{(w)} = T_1 T_2 r^{(w)} / n^2 \approx 0.54 r^{(w)}, \quad (14)$$

where $T_1 \approx T_2 \approx 0.98$ are transmittances of the surface for upward and downward radiation, $n \approx 1.34$ is the refractive index of water.

It follows from our Monte-Carlo simulations¹ that

$$r_d^{(w)} = \frac{1}{2(1+\mu)} X, \quad \rho_{dif}^{(w)} \approx 0.27 X, \quad (15)$$

where $X = b_b / (a + b_b) \approx b_b / a$,

$$\mu = \cos \theta' = (1 - \sin^2 \theta / n^2)^{0.5}, \quad (16)$$

θ' is the sun ray refraction angle.

We must relate the radiance coefficients $\rho^{(w)}$ to water reflectance R which has been measured and computed by Morel and Prieur.³ There they used the formula

$$R = 0.33 X = 0.33 b_b / a. \quad (17)$$

Therefore, we calculated $\rho^{(w)}$ from the equations which follows from Eqs. (14), (15), (17):

$$\rho_d^{(w)} = 0.82 R / (1 + \mu), \quad \rho_{dif}^{(w)} = 0.44 R. \quad (18)$$

3. MODEL USED FOR EXTRAPOLATIONS OF WATER REFLECTIVITY IN THE VISIBLE SPECTRUM TO THE UV AND IR

To extrapolate Morel and Prieur's experimental values of R to the UV and IR, we used Kopelevich's model⁷ of the water optical properties. This model is based on the assumption that absorption is due to pure sea water, yellow substance and chlorophyll, whereas scattering is due to pure sea water and suspended non-chlorophyllous particles:

$$a(\lambda) = a_w(\lambda) + a_y(\lambda) + a_c(\lambda), \quad (19)$$

$$b_b(\lambda) = 0.5 b_w(\lambda) + b_{bp}(\lambda). \quad (20)$$

Here a_w , a_y and a_c (m^{-1}) are the absorption coefficients for water, yellow substance and chlorophyll, correspondingly; b_w (m^{-1}) is the scattering coefficient of pure sea water, and b_{bp} (m^{-1}), the backscattering coefficient of particles. Data on $a_w(\lambda)$ and $b_w(\lambda)$ are presented by Smith and Baker⁸, the rest of the parameters involved in Eqs.(19), (20) were computed from the formulae^{3,7,9,10}

$$a_y(\lambda) = a_y(\lambda_0) \exp [-0.014 (\lambda - \lambda_0)], \quad (21)$$

$$a_c(\lambda_0) = a_c(440 \text{ nm}) a_c^*(\lambda_0), \quad (22)$$

$$a_c(440) = \begin{cases} 0.07 C, & \text{if } C < 1 \text{ mg m}^{-3}, \\ 0.018 C, & \text{if } C > 1 \text{ mg m}^{-3}, \end{cases} \quad (23)$$

$$b_{bp}(\lambda) = b_{bp}(\lambda_0) \lambda_0 / \lambda, \quad (24)$$

where C is the chlorophyll concentration (mg m^{-3}); the dimensionless specific absorption coefficients a_c for $\lambda = 400\text{--}700$ nm are presented in the table¹⁰, $\lambda_0 = 400$ nm for extrapolation to the UV and $\lambda_0 = 700$ nm for that to the IR.

For green waters (Cases 1 and 2 in Morel's classification), extrapolation to the UV was performed according to the following algorithm. We took experimental values³ of $R(400 \text{ nm})$, C and $a(400 \text{ nm})$ for various stations; we assumed⁷ that $a_c(300 < \lambda < 400) = a_c(400)$; using the tables for $a_w(\lambda)$ and $b_w(\lambda)$ ⁸ and for $a_c^*(\lambda)$ ¹⁰, we found $R(300 < \lambda < 400)$ from Eqs.(17), (19)–(24). For blue waters this algorithm is simplified because we supposed that $a_y = a_c = 0$.

Extrapolation to the IR for all water types was realized by the same algorithm with the same assumption ($a_y = a_c = 0$), and the value of $\lambda_0 = 400$ nm was replaced by $\lambda_0 = 700$ nm.

4. SOME RESULTS OF COMPUTATIONS

Computations of the oil-water contrasts were performed by Eqs. (1)–(13), (16), (18), $\rho_d^{(s)}$ being taken from Table 2, and R , from the Morel and Prieur experimental data for blue and green (Case 1, station 15, 98, and 71, Case 2, stations 16 and 57) waters, with extrapolation of R to the UV and IR according to Eqs. (19)–(24).

Some of computation results are shown in Fig.1. The positive contrasts belong to the case when oil is brighter than water, the negative ones belong to the opposite case.

5. DISCUSSION

It can be seen from Fig.1 that the spectral contrast strongly depends on wind velocity, solar zenith angle, and water type. For diffuse illumination, it does not depend on wind velocity, and the damping effect does not act. In this case, the contrast mainly is due to radiation backscattered by the sea ($\rho_w^{(w)}$). In the spectral region where R and $\rho_w^{(w)}$ are rather large (about 400 nm in blue and about 550 nm in green waters) the contrast decreases. In the general case (sun and sky) several factors affect the contrast. As one can see from Table 2, if the sun is in zenith, surface radiance $\rho_d^{(s)}$ increases sharply with decreasing wind velocity v . For the solar zenith angle $\theta = 20^\circ$, $\rho_d^{(s)}$ weakly depends on v , and for $\theta = 45^\circ$ it decreases sharply with decreasing v . So, for the sun in zenith the

damping effect leads to increase of contrast, and for $\theta = 45^\circ$, to its decrease. Therefore, for $\theta = 45^\circ$ the contrast is nearly always negative. In the shortwave spectral region, where the sky contribution to total irradiance is greater (see Table 1), the contrast for $\theta = 45^\circ$ increases because the damping effect is partially compensated. For $\theta = 20^\circ$ in green waters the contrast depends mainly on the ratio between oil and water Fresnel reflectivity and so depends weakly on the wavelength. For low wind velocity ($v=6$ m/s) in both cases ($\theta = 45^\circ$ and 20°) in the longwave region the contrast is small because the damping effect leads to a decrease in radiance of the contaminated surface (see Table 2), and water radiance in the red and IR spectral region is small in relation to the surface one.

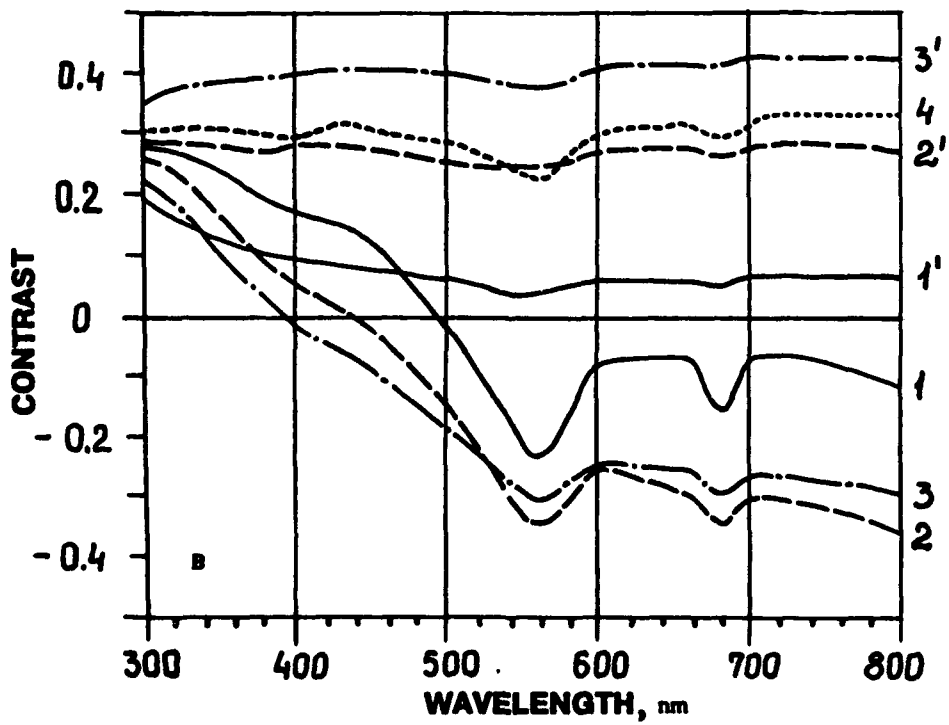
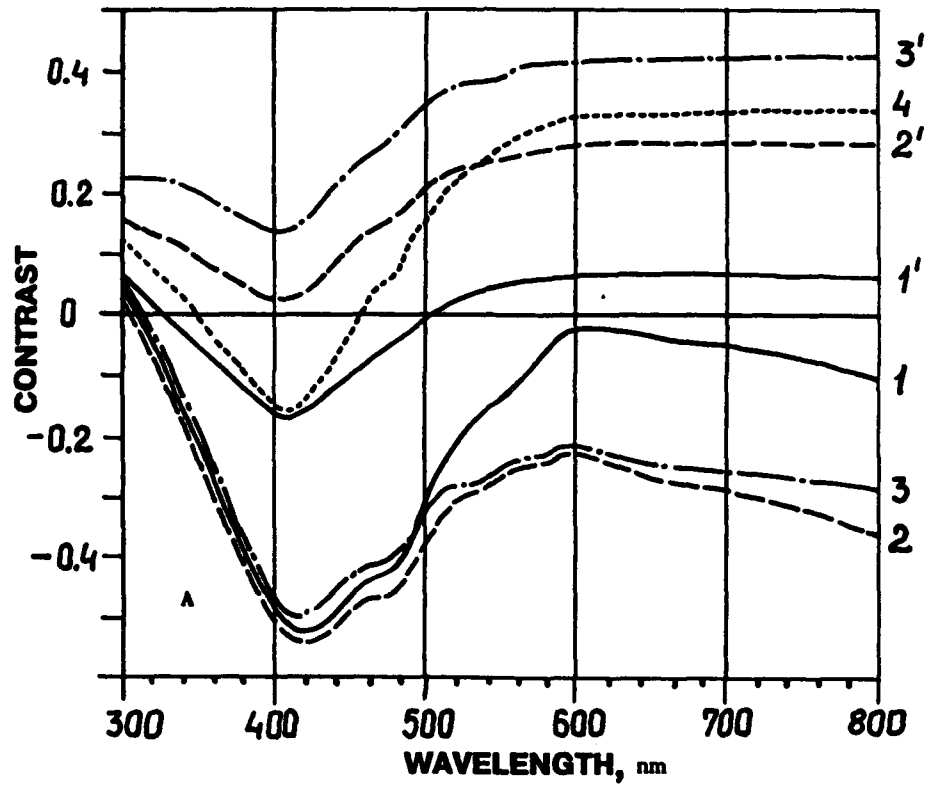
When the solar zenith angle varies from 20° to 45° , the contrast at a given wavelength changes from positive to negative, so for some θ it must be zero. It is obvious that one spectral channel which would be optimal for all observation conditions can hardly be chosen. It appears that it is worth having two or more spectral channels, so that the optimal channel can be chosen depending on observation conditions.

6. ACKNOWLEDGEMENTS

The author wishes to thank for fruitful discussions his colleagues Dr. Vladimir Osadchy and Dr. Irina Gurevich, who for many years have investigated the problem "Oil on the water" under the leadership of Prof. Kusieli S. Shifrin. Thanks are also due to Tamara Radomysl'skaya and Elizaveta Levina for assistance in the computations, and to the TV-engineer Vulf Perlov, who performed airborne TV-observations.

7. REFERENCES

1. B. M. Golubitskiy and I. M. Levin, "Transmission and reflection in a layer of a medium with strongly anisotropic scattering", *Izv. Atmos. Ocean. Phys.*, Vol. 16, No. 10, pp. 775-780, 1980.
2. I. Y. Gurevich and K. S. Shifrin, "Reflection of visual and infrared radiation by oil films on the sea", *Optical methods for studying oceans and internal reservoirs*, Nauka Publ., Novosibirsk, pp.166-183, 1979 (in Russian).
3. A. Morel and L. Prieur, "Analysis of variations in ocean color", *Limnol. Oceanogr.*, Vol. 22, No. 4, pp. 709-722, 1977.
4. R. W. Austin, "Coastal zone color scanner radiometry", *Proc. SPIE*, Vol. 208, Ocean Optics VI, pp. 170-177, 1979.
5. Y. A. R. Mullamaa, *Atlas of rough sea surface optical properties*, Estonian Acad. of Sciences, Tartu, 1964 (in Russian).
6. C. Cox and W. H. Munk, "Slopes of the sea surface deduced from photographs of sun glitter", *Scripps. Inst. of Oceanogr. Bull.*, Vol. 6, No. 9, pp. 401-479, 1956.
7. O. V. Kopelevich, "Low-parametric model of sea water optical properties", *Ocean Optics*, Vol. 1, Nauka Publ., Moscow, pp. 208-236, 1983 (in Russian).
8. R. C. Smith and K. S. Baker, "Optical properties of the clearest natural waters (200-800 nm)", *Appl. Opt.*, Vol. 20, No.2, pp. 177-184, 1981.
9. S. Sathyendranath, L. Prieur and A. Morel, "A three-component model of ocean colour and its application to remote sensing of phytoplankton pigments in coastal waters", *Int. J. Remote Sensing*, Vol. 10, No. 8, pp. 1373-1394, 1989.
10. L. Prieur and S. Sathyendranath, "An optical classification of coastal and oceanic waters based on the specific spectral absorption of phytoplankton pigments, dissolved organic matter and other particulate materials", *Limnol. and Oceanogr.*, 26, No. 4, pp.671-689, 1981.



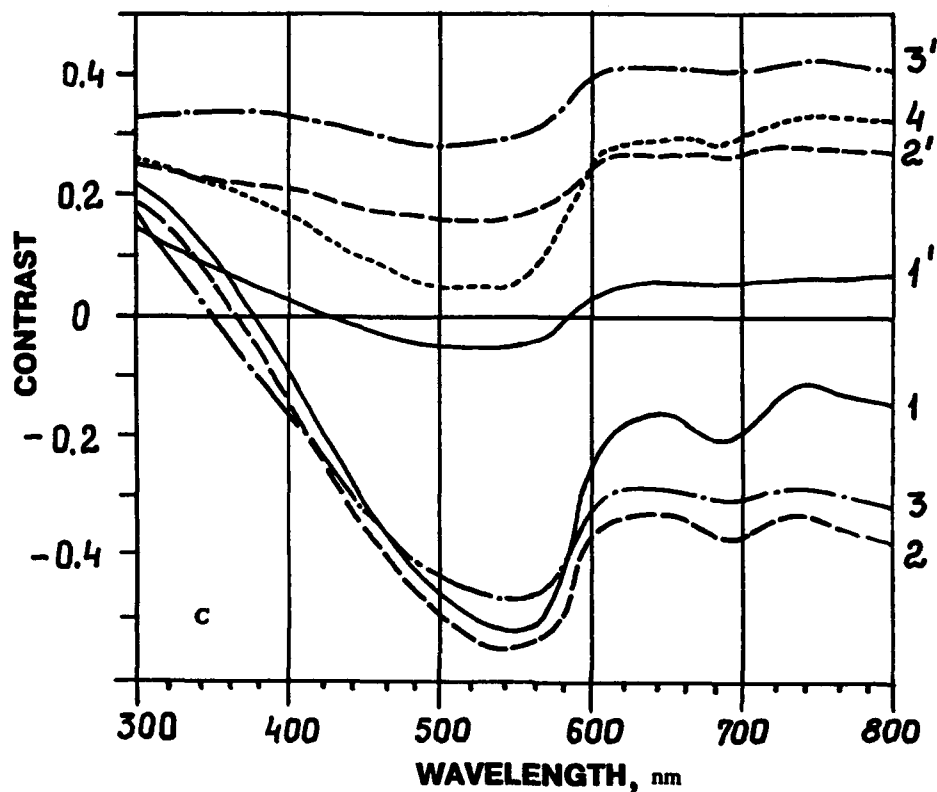


Figure 1 A-C. Spectral oil-water contrast for various wind velocity (v) and solar zenith angle (θ).

A: Blue waters.

B: Green waters, Case 1 (station 71).

C: Green waters, Case 2 (station 57).

- | | |
|---|--|
| 1. $v = 6 \text{ m/s}$, $\theta = 45^\circ$. | 1'. $v = 6 \text{ m/s}$, $\theta = 20^\circ$. |
| 2. $v = 10 \text{ m/s}$, $\theta = 45^\circ$. | 2'. $v = 10 \text{ m/s}$, $\theta = 20^\circ$. |
| 3. $v = 20 \text{ m/s}$, $\theta = 45^\circ$. | 3'. $v = 20 \text{ m/s}$, $\theta = 20^\circ$. |
| 4. Sky without the sun | |

Some Effects of the Sensitivity Threshold and Spatial Resolution of a Particle Imaging System on the Shape of the Measured Particle Size Distribution

D. K. Costello,* W. Hou,* and K. L. Carder*

**Department of Marine Science, University of South Florida, 140 7th Avenue South, St. Petersburg,
FL 33701, U.S.A.*

ABSTRACT

Numerous scientific research efforts require knowledge of the particle volume concentration. For many studies, this information is required as a function of particle size. These particle volume spectra are often inferred from optically measured particle areal size distributions after the areal size distributions have been transformed into equivalent spherical diameter (ESD) distributions. Resolution and sensitivity differences between imaging systems will result in different shapes for the measured particle size distribution. Artifacts will be introduced at the small-particle end of the distribution by the finite spatial resolution of an imaging system while, on the large particle end, artifacts due to under-sampling (a direct corollary of finite spatial resolution) become probable. Additionally, the sensitivity threshold of the imaging system is not only fundamental to the determination of the particle edge but also determines the optical density (reflectivity) level below which material will not be imaged. All this affects the measured size of a particle. Finally, if non-spherical and/or porous particles are present, the measured size distributions, when particle sizes are presented in equivalent spherical diameter (ESD), are no longer necessarily representative of the original 1-dimensional geometric projections of the particles, an important consideration for some applications.

This contribution utilizes laboratory data and unique, synchronous, ocean field data collected by three coincident imaging systems to evaluate these effects in the study of large marine particles. Also, for applications which require a measure of the geometric spread of a particle (e.g. perimeter/area ratio) and/or applications involving partially translucent particles, an algorithm rooted in the theory of moment invariants is presented which avoids the distortions to the particle size distributions when the size of non-spherical and/or porous particles are presented as ESD.

1. INTRODUCTION

Electronic imaging is one of society's most rapidly advancing technologies. The evolution is being driven by the desire to provide greater quantities of higher-quality information at an increasingly faster rate. The fields of entertainment, banking, medicine, communications, among many others are benefitting and expanding. This expansion tends to drive down the cost of the necessary equipment, which allows more researchers to enter the arena with new applications, again accelerating the expansion.

An important subset of electronic imaging is digital image processing (DIP). DIP is in widespread industrial use in applications including communications, process and quality control, employee identification, signature verification, etc. One of these applications, in both the industrial and the scientific arena, is object counting and sizing, the measurement of the particle size distribution in an environment. Although the imaging environment and the nature of the particles can vary widely (e.g. tablets, droplets, bubbles, cells, bacteria, aggregates, dust), processing an image in the digital domain is strictly governed by rules inherent to the process.

This contribution focuses on a specific application, the use of DIP technology to describe the *in situ* size distribution of marine particles. Laboratory and theoretical work are presented which show how the perceived size distributions can vary depending on the resolution and sensitivity of the system. Additionally, problems which arise when the size of non-spherical and/or porous particles are presented as equivalent spherical diameter (ESD) are discussed and illustrated. It should be noted here that the "porosity" of a particle can be an artifact of the finite sensitivity of the imaging system employed; that is, the "holes" may be filled with a material which can not be visualized by a particular imaging system but would be visualized by a system of higher sensitivity. An alternate approach to describing the functional "size" of a non-spherical and/or porous particle is presented and compared to the ESD representation. We propose that this approach has utility in applications such as particle settling which require a measurement which is representative of the geometric spread (e.g. 1/compactness) or extent of the particle and also more accurately describes the size (and, by inference, mass) of aggregated particles. These can often be formed upon a matrix of transparent exopolymers (TEP)^{1,2}. Finally, field imagery acquired by three coincident, synchronous CCD video systems is presented which shows the effects of variable resolution on size distributions acquired *in situ* as well as on the images of individual particles.

2. IMAGE RESOLUTION

A great potential pitfall inherent in digital image processing, spurious resolution, is illustrated in the following hypothetical example. A researcher involved in a land-use study acquires high-resolution, photographic imagery from an aircraft at an altitude which yields a horizontal field-of-view (FOV) of 1.28 km. At the laboratory, an image analysis workstation automatically transfers the photographic images to VHS video tape. The video images are then digitized at 1,280H x 960V pixel resolution. The image analysis workstation software package, then, yields voluminous data with one-square-meter accuracy. The actual resolution, however, is a function of the lowest resolution component in the data acquisition/processing system and the VHS video tape recorder has only a horizontal resolution, for example, of about 240 lines. Pixel resolution in this example overestimates actual resolution by at least a factor of 6, and, if the Nyquist sampling frequency theorem is considered, by at least a factor of 12. When errors attributable to spurious vertical resolution are also considered, the actual areal resolution could be overestimated by two orders of magnitude.

2.1 The Video Signal

In order to understand digital image processing the conversion of the analog video signal to digital data needs to be considered. Image frame grabbers perform this conversion in real-time, utilizing flash analog-to-digital converters (ADCs). "Real-time" for NTSC video is 30 frames per second (25 for the PAL standard), and the conversion most often follows the convention shown in Figure 1 (the PAL standard differs slightly). The 1 volt (V) video signal is divided into 140 IRE units with a baseline (0 IRE units) corresponding to 0.286 V. In the A/D conversion, some additional voltage (usually 0.054 V) above the baseline is used as a reference black level. The voltage range above this level (0.66 V) is converted by an 8-bit flash ADC to 255 gray scales (GS). Numerous tests in our laboratory with several different frame grabbers confirm that the conversion is, in fact, linear. There are several variables involved in the reproduction of the A/D conversion convention shown in Figure 1., however, and, as variables, they can be changed.

Equation 1 describes the volts to gray scale conversion utilized to process images with a Data Translation Inc. Integrated Image Processor and Precision Frame Grabber (DT-2867).

$$V = (2048 - ZO) * 3.272 * 10^{-4} + 2.311 * 10^{-4} * (ADR * GS) / (GN * 255) \quad (1)$$

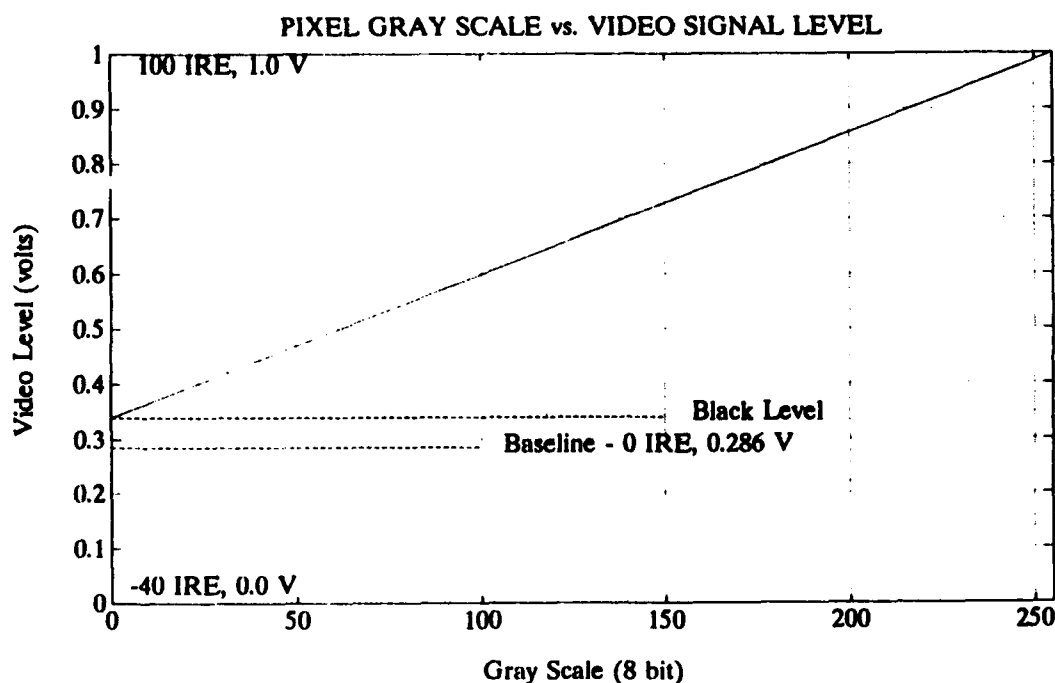


Figure 1. The relationship of pixel gray scale to video signal level (see text for discussion).

Note that, generally, in the conversion from video-signal voltage level (V) to digitized gray scale (GS), the zero offset (ZO), the gain level (GN), and the A/D reference (ADR) can all be changed in the frame grabber control software and/or through hardware adjustments. It is relevant here that changing the V to GS conversion variables will confound any algorithm which utilizes GS thresholds for particle edge detection. Also, at higher voltage levels, it takes relatively longer for video circuitry to return to black level (electronic overshoot). This results in brighter targets measuring longer in the horizontal dimension than similarly sized targets of lower gray scale (illustrated below). The amount of this elongation is a function of the programmed black level. A consequence of the above is also that even identical imaging systems will produce differing measurements of a particle suite when different ADC variables are utilized.

2.2 Laboratory Measurements

To investigate the effects of video format resolution and system radiometric sensitivity on the shape of a measured size distribution, a diffusely backlit, 1951 USAF test target negative was imaged using an interline-transfer CCD camera (Sony XC-75). The camera specifications include a S/N ratio of 56 dB and horizontal resolution of 570 TV lines (HTVL). The images were recorded at each of two aperture settings (f/8 and f/16) in both VHS (240 HTVL) and S-VHS (400 HTVL) formats and were also grabbed directly at full resolution by the DT-2867. The light source was current- and voltage-regulated to $\pm 1.0\%$.

Target groups (-2, 1 to 6), (-1, 1 to 6), and (0, 1 to 6) were utilized. The 1951 USAF test pattern displays three vertical and three horizontal bars in each sub-group and decrease in linear dimension and spacing from sub-group to sub-group by a factor of $2^{-1/6}$ ($2^{-1/3}$ in area). The line spacing of the smallest target sub-group processed, (-1,6), is $280 \mu\text{m}$ and, with the imaging configuration and digitization (640H x 480V pixels) utilized, was slightly less than 2 pixels (one pixel representing a $150 \times 150 \mu\text{m}$ square).

The images acquired were processed with our Image Control and Examination (ICE) system. ICE was developed in our laboratory and provides for unattended, frame-by-frame, image digitization, processing, and

target detection. The target detection algorithm is written in the C language and allows for adaptive, target-intensity and variable thresholds and closing tolerance (search area for the connection of pixels above threshold, the utility of an adaptive closing tolerance is under evaluation). It also adjusts for bright-pixel recovery delays (pixel overshoot) in the horizontal dimension due to electronic circuitry.

For the purposes of this exercise, comparing the DIP response at different intensity values for different resolution with off-the-shelf systems, we did not utilize available ICE hardware: an infinite-window time-base corrector (Nova 900S Super TBC), a Umatic-SP 3/4" industrial video tape recorder (Sony), or a programmable-resolution frame grabber (Epix Video MUX). Tests with this more sophisticated but often unavailable hardware will be considered in a future report. The ADC convention follows that shown in Figure 1 and the ICE system variables were severely constrained. That is, the target detection closing tolerance and the horizontal overshoot-compensation values were set to zero. The result at GS threshold 1, for example, is that any video voltage above 0.34 V is interpreted as target area. Processing the images at GS threshold levels 0 through 30 in 5-GS-unit increments, then, acts as a surrogate for imaging sensitivity and allows the quantification of measurement artifacts due to both system sensitivity and resolution.

Figure 2 shows the computed particle size distributions for, respectively, the SVHS and VHS formats at f/8 and at f/16. Results from the directly grabbed images did not differ substantially from the SVHS results.

Since each sub-group contains 6 targets (3 each, horizontal and vertical), a perfectly measured size distribution would be a horizontal line at a value of 6 (shown by the dotted line in each plot) for all bins except the last two "overflow" bins which would be zero in a perfect measurement. The overflow bins were used because targets which are not resolved will be lumped together and placed in a larger size group, perhaps even larger than the largest real target. A comparison of Figures 2a and 2b (the SVHS and VHS formats at F/8) shows that the higher-resolution SVHS format did, in fact, resolve more targets than the VHS format and that resolution for both formats apparently improved as the processing threshold was increased. A comparison of Figures 2c and 2d (the two formats at f/16) is not as straightforward with both formats performing better than at f/8.

Another way to analyze these results is to sum the targets detected, since there are 108 individual targets in the 16 subgroups utilized, and adjacent targets which are not resolved would be lumped together into a single, larger target. Figure 3 shows total targets detected for Figures 2a through 2d at the different GS threshold levels. The highest number of detected targets was 103 with SVHS at f/16 and a GS threshold of 15. The best performance for both formats was at f/16 and GS thresholds of 20 or less. At higher GS threshold levels, both formats "lost" targets at f/16. Conversely, at f/8, SVHS again outperformed VHS, but both formats performed better at increasing GS thresholds.

Since an increasing GS threshold effectively reduces the blur surrounding even a perfectly focused target due to edge diffraction or imperfect alignment of a target image with a pixel edge (in the horizontal and the vertical) and the blur to the right of a target (in the horizontal) caused by electronic overshoot, linear measurements were taken in order to estimate the relative errors due to the above phenomena. The vertical measurement errors for all cases were minimal except for the smallest targets at f/8 where the imperfect alignment of a target image on the pixel matrix could introduce a proportionately significant error. The errors in the horizontal dimension were, however, much more substantial and are shown in Figure 4 for f/8 and Figure 5 for f/16. Also shown are the computed errors after corrections for the horizontal electronic overshoot for both "high" and the "low" signal cases. For the high-signal case (f/8), the target GS values were about 200 counts (corresponding to 0.86 V) and it was assumed that the overshoot was simply a function of system resolution. Therefore, three pixels of the original horizontal measurements for VHS (640 pixels/240 HTVL = 3 when rounded up) and two pixels of the original horizontal measurements for SVHS (640 pixels/400 HTVL = 2 when rounded up) were attributed to overshoot. The errors for both formats after this correction were reduced to within about 5% across the size spectrum for the high-signal case. For the low signal case (f/16) shown in Figure

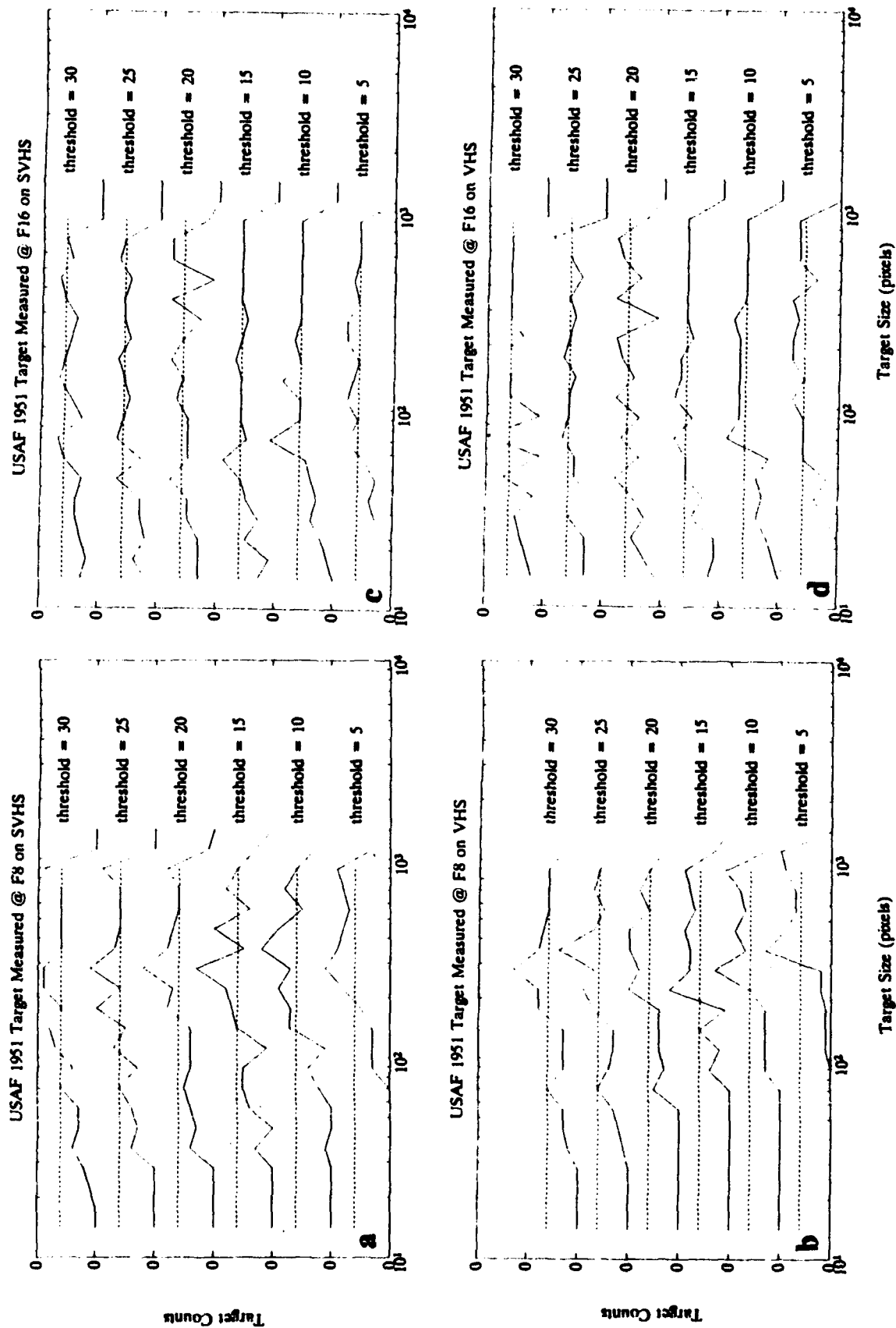


Figure 2. See text for discussion.

5, the target GS values were about 50 counts (corresponding to 0.47 V) and it was assumed that the overshoot was minimal, not a function of resolution, and that both formats would return to black level in one horizontal pixel. The measurement errors after this correction were also confined to about 5%.

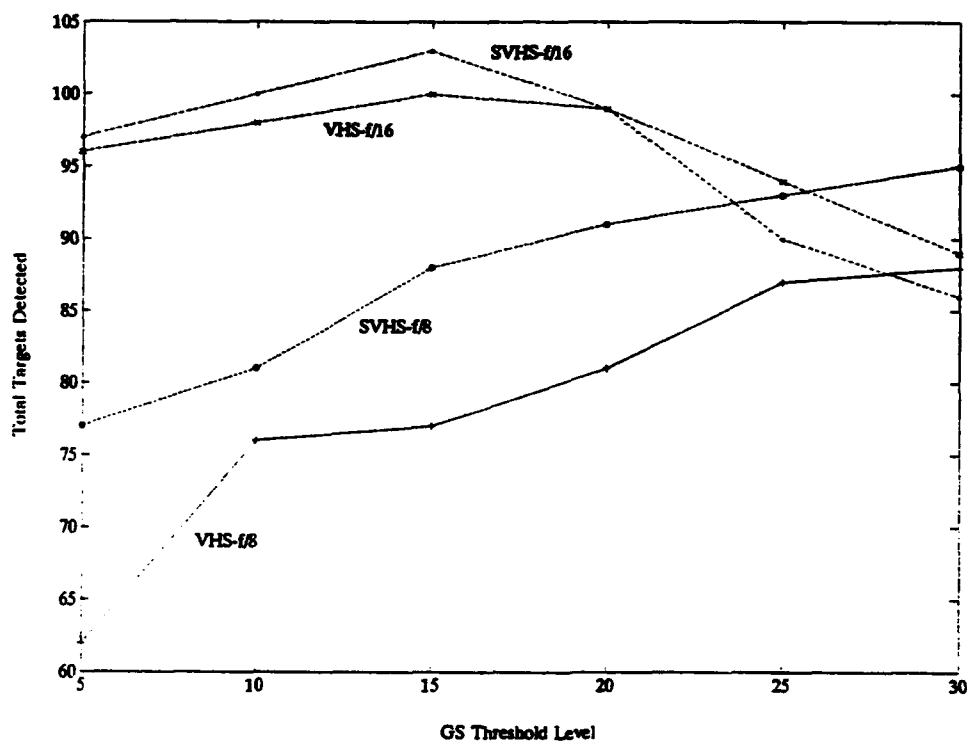


Figure 3. Total targets detected using the SVHS and the VHS format at f/8 and f/16 (see text for discussion).

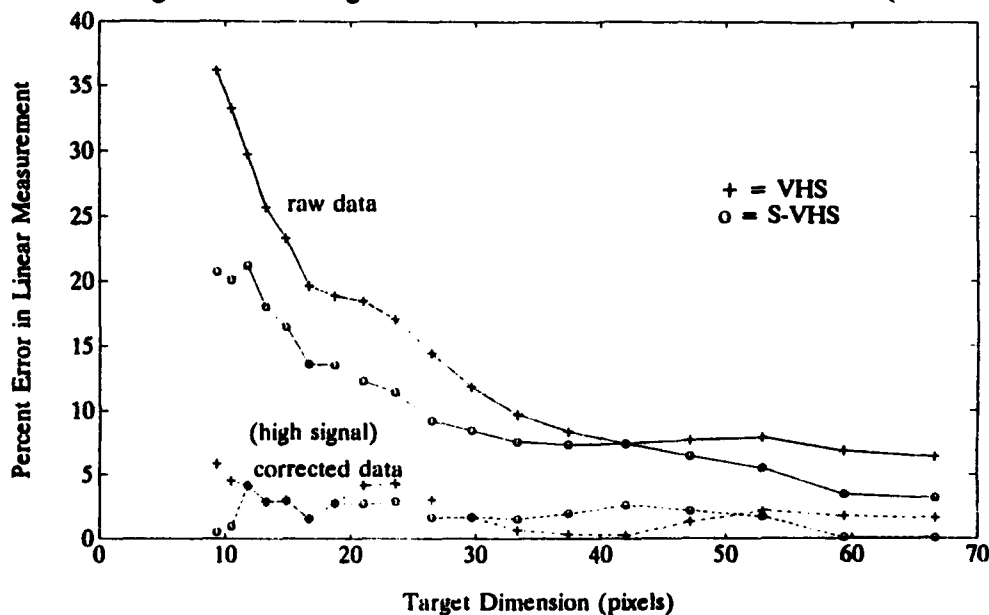


Figure 4. Horizontal measurement error after overshoot correction at f/8 (see text for discussion).

The goal of this work is to develop an algorithmic correction for electronic overshoot which adapts to target brightness and resolution. The motivation is from field imagery where the brightness of the images of a copepod and a diatom aggregate, for example, can easily differ by an order of magnitude (see Section 4.1).

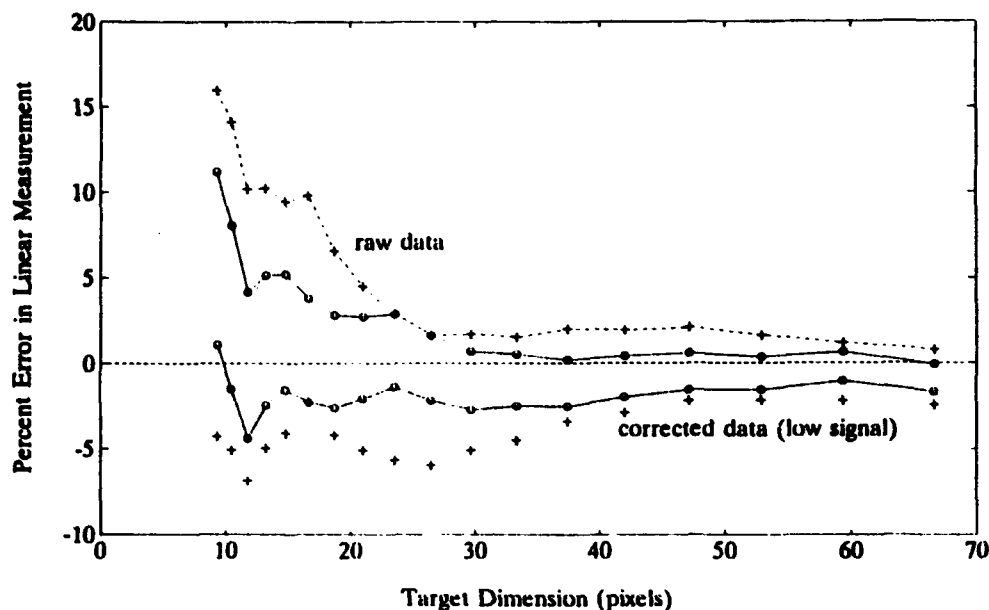


Figure 5. Horizontal measurement error after overshoot correction at $f/16$ (see text for discussion).

3. THE PARTICLE SIZE DISTRIBUTION

For certain modelling or classification studies, particle counts need to be separated into size bins. A particle size distribution spectrum is obtained by dividing the counts in a bin by the width of the bin. These spectra are often described by the hyperbolic (Junge-type) power law distribution:

$$\frac{dN}{dD} = kD^{-B} \quad (2)$$

where dN is particle counts of size D , dD is a diameter interval (i.e. $D_2 - D_1$), k is a concentration constant which normalizes the distribution, and B is the negative slope of the distribution in log-log coordinate space. The utility of this form is that, since it describes a spectrum with known normalization, intercomparison can be made between measurements with different sample volumes and (with the assumption of a continuous distribution) with measurements spanning different ranges of the size spectrum.

Equation 2 can be used to calculate the number of particles within a size range of interest, particle area, volume, or mass (when an average density is assumed). The integration for particle volume is shown below.

$$dV = \frac{\pi}{6} D^3 dN = \frac{\pi}{6} k D^{3-B} dD \quad (3)$$

$$V = \int_{D_1}^{D_2} \frac{\pi}{6} k D^{3-B} dD \quad (4)$$

$$V = \frac{\pi k}{6(4-B)} (D_2^{4-B} - D_1^{4-B}), B \neq 4 \quad (5)$$

$$= \frac{\pi k}{6} \ln\left(\frac{D_2}{D_1}\right), B = 4 \quad (6)$$

When the measured particles are solid spheres and the imaging system accurately records their sizes, equations 3 through 6 are exact. If, however, the particles are not spherical and/or have "holes", the equations are approximations. For aggregated particles built on a matrix of TEP, for example, utilizing a size distribution (Eq. 1) where the diameter is ESD, would lead to significant errors in a volume determination (Eq. 5 or 6).

3.1 Effects of the Conversion to Equivalent Spherical Diameter

Because physical forces often arrange small, individual particles in spherical form (e.g. water droplets), the equivalent spherical diameter is widely used as a particle size descriptor. By definition, ESD is an exact dimensional descriptor for spherical particles. It also provides for exact conversion back to measured particle cross-sectional area with the caveat that the area measurement retrieved is only the area represented in the original measurement; that is, only the measurable area above some image intensity threshold and not necessarily the cross-sectional area of the particle as imaged by another system. Particles that are, indeed, spherical but have areas within their image which fall below sensitivity threshold of an imaging system, (e.g. bubbles, cells, spherical aggregates formed around a semi-translucent matrix, etc.) will be misrepresented by an ESD description. For example, consider a young versus an older Larvacean house. The Larvacean is a barely-macroscopic marine animal which creates translucent filtering structures or nets which gradually accumulate marine material. When the amount of accumulated material reduces filtering efficiency, the houses are discarded by the animal. In the conversion of measured optical area to ESD, a new Larvacean house would be quantified much differently than a remnant house, even if both had the same geometrical cross-section, since more of the house would be visualized because of the accumulated debris.

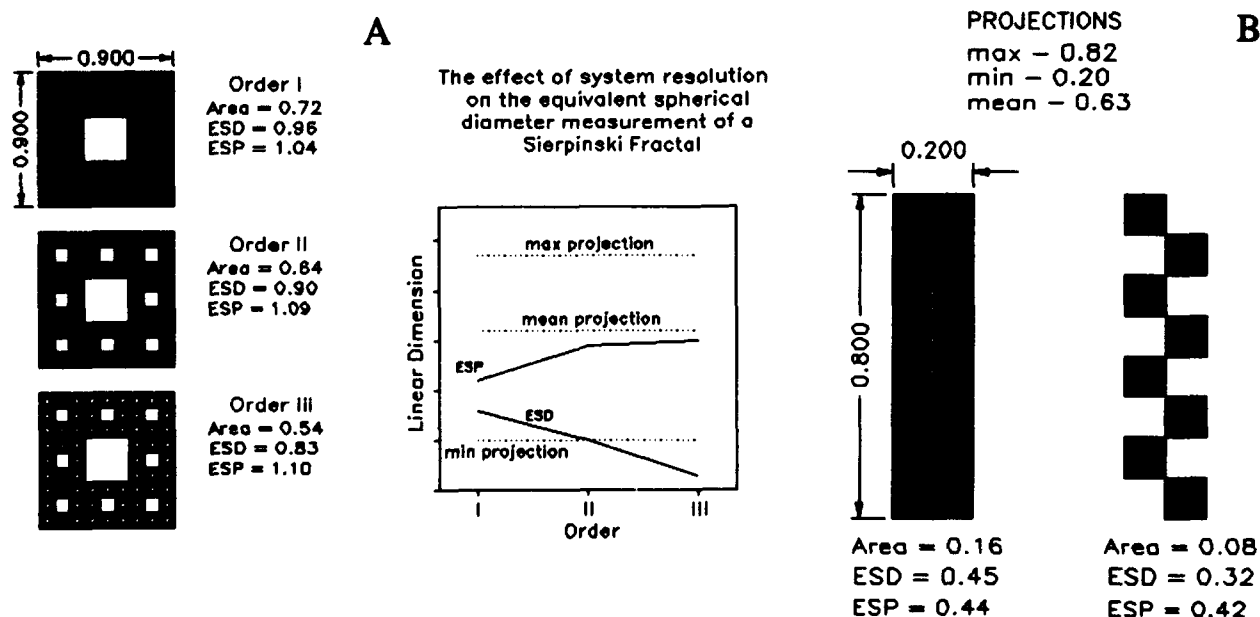


Figure 6. ESD of a fractal object and of a particle with a complicated edge (see text for discussion).

To illustrate, consider Figure 6a which depicts different measurement strategies applied to a 2-dimensional fractal object, the "Sierpinski Carpet". The fractal scheme of the object is apparent upon inspection. Fractal Orders I, II, and III are illustrated and are analogous to the same object viewed by three imaging systems of normalized magnification of 1X, 3X and 9X.

The graph in the lower right of the figure shows how the ESD measurement would change as a function of system resolution (or object distance, depending on the scenario). Also plotted are horizontal lines for the maximum (in this case, the diagonal), the minimum (in this case, dx or dy in pixel space), the mean (defined as the average of all projections obtained by rotating the object through 360 degrees in 1 degree increments) geometric projections of the object, and the "equivalent spherical projection" (ESP), which is discussed below. Even in the Order I object, the ESD is significantly less than the mean or maximum geometrical projection and, at order III, is significantly less than even the minimum geometric projection. Again, for applications where the geometric projection is important or where there is a question whether apparent holes or particle edge features are real or merely below imaging resolution or sensitivity threshold, the ESD representation is deficient. For these types of applications, an alternative to the ESD representation is required.

3.2 Equivalent Spherical Projection (ESP), An Alternative to ESD

To summarize the above, the ESD representation of particle size is deficient when: 1) the application requires a measure of the geometric projections of particles for dynamical considerations (i.e. differential settling and impact probabilities); 2) for some mass flux considerations (i.e. when particles with organic components which are not imaged at the image system maximum sensitivity level), and; 3) in efforts which require the inter-calibration of imaging systems of different resolution. What is required in these circumstances is a methodology which emphasizes the geometrical spread of the intensity image of a particle instead of the collapsed sum of the image intensity. One method to accomplish this follows.

The method of moment invariants can be used to describe the distribution of radiance from a particle within an $x - y$ field (i.e. a digitized particle image). The method was first proposed by Hu³ and utilized in alphabetic character recognition. The method was expanded by Teague⁴ and by Dudani et al.⁵, applying it to automatic identification of aircraft. The expanded method was tested on computer-generated objects and proposed for application for automatic identification of individual and aggregated marine particles by Costello et al.⁶. Carder and Costello⁷ tested the expanded method on images of marine particles acquired by an *in situ* holographic imaging system⁸. They reported that the method successfully identified (separated in classification-space) the images of several different types of particles.

The technique is generated as follows. The two-dimensional $(i + j)$ th order moments of a reflectance density distribution function $\rho(x,y)$, the image, are defined in terms of Riemann integrals (proper, bounded) as²³

$$m_{ij} = \int_{-\infty}^{\infty} \int_{-\infty}^{\infty} x^i y^j \rho(x,y) dx dy \quad i, j = 1, 2, 3 \dots \quad (7)$$

For the purposes of this section, a description of particle size, $\rho(x,y)$ is treated as a binary distribution (equal to 1 if the processing threshold is exceeded and otherwise equal to 0) and only moments to second order are required. The higher-order moments are utilized in pattern recognition strategies^{3,4,5,6,7} and are not constrained to binary computations. The low-order ordinary moments are especially useful to the extent that m_{10}/m_{00} , m_{01}/m_{00} locate the (x, y) coordinate position for the centroid of the image intensity distribution which, in this application of the technique, is the centroid of the binary particle.

For this approach to be useful for automated image analysis, however, the sample-space vectors generated must be invariant with object position and/or orientation within the image field. Translational invariance can be achieved by the determination of object centroid (from the first and zero order ordinary moments) and recalculation of the ordinary moments relative to image centroid of the object. This first step toward both translational and rotational invariance, however, can be achieved (and computational time minimized) by transforming the ordinary moments (m_{ij}) into central moments (μ_{ij}), moments relative to the centroid of the object image. Using the notation of Hu³:

$$\mu_{00} = m_{00} = \mu \quad (8)$$

$$\mu_{10} = \mu_{01} = 0 \quad (9)$$

$$\mu_{20} = m_{20} - \mu \bar{x}^2 \quad (10)$$

$$\mu_{11} = m_{11} - \mu \bar{x} \bar{y} \quad (11)$$

$$\mu_{02} = m_{02} - \mu \bar{y}^2 \quad (12)$$

$$\text{where } \bar{x} = m_{10}/m_{00}, \quad \bar{y} = m_{01}/m_{00}.$$

Note that the first-order central moments μ_{10} , μ_{01} are equal to zero under this transformation. This follows intuitively since the first order "spread" of an object relative to any axis of a coordinate system drawn through its centroid would center about the origin.

These central moments can then be utilized to produce moment functions which possess the desired invariance with rotation and translation. Seven such functions were first formulated in the pioneering work by Hu³. Two of these functions are relevant here and are presented following the form of Dudani et al.⁵:

$$M_1 = (\mu_{20} + \mu_{02}) \quad (13)$$

$$M_2 = (\mu_{20} - \mu_{02})^2 + 4\mu_{11}^2 \quad (14)$$

which correspond to the classification factors, X and Y, utilized by Hu³. Four additional, moment-generated, elliptical classification (measurement) factors, originally developed by Teague⁴, are relevant here.

$$\alpha = ((\mu_{20} + \mu_{02} + ((\mu_{20} - \mu_{02})^2 + 4\mu_{11}^2)^{1/2})/2\mu_{00})^{1/2} \quad (15)$$

$$\zeta = ((\mu_{20} + \mu_{02} - ((\mu_{20} - \mu_{02})^2 + 4\mu_{11}^2)^{1/2})/2\mu_{00})^{1/2} \quad (16)$$

$$\Gamma = (1/2)\tan^{-1}(2\mu_{11}(\mu_{20} - \mu_{02})^{-1}) \quad (17)$$

$$F = \mu_{00}/\pi\alpha\zeta \quad (18)$$

These factors characterize any image as a constant intensity ellipse with intensity F inside and zero outside, defined by the semimajor axis α , semiminor axis ζ , and angular orientation Γ within the 2-dimensional coordinate field. The method is also computationally attractive since it requires the computation of moments to only second order. Additionally, since α , ζ , and F can be expressed in terms of μ_{00} (an invariant quantity) and the Moment Invariant Functions, M_1 and M_2 (Eq. 13 and 14), the results are invariant to object rotation and/or translation. The factor Γ , on the other hand, contains object orientation information and, hence, is not an invariant function. (Note that equations 15 and 16 presented here differ from equations for α and ζ shown in Carder and Costello⁷,

their's containing a typographical error.)

In order to provide insight into the mathematics employed, consider Equations 15 and 16 as applied to the image of an ideal sphere. In this case, $\mu_{11} = 0$, $\mu_{20} = \mu_{02}$ and the equations are equivalent, consisting of a linear dimension normalized by a factor of two in the numerator and by the square root of the image power in the denominator. The square root of the image power, however, also is embedded in the numerator, a result of the inclusion of image power as a factor in the original moment-generating function (Eq. 7). The linear dimension, then, is directly equivalent to the radius of the sphere and exactly equal to $ESD/2$. Therefore, $2\alpha = 2\zeta = ESP = ESD$. For non-spherical particles, the area of the ellipse, $\pi\alpha\zeta$, can be transformed to the ESP dimension by $ESP = 2(\alpha\zeta)^{1/2}$.

For the Sierpinski Carpet shown in Figure 6a, for example, the increased interior porosity between Orders I and III changed the calculated ESD by 15% while the ESP changed only 4%. Figure 6b demonstrates the consequences of using ESD for two particles similar in maximum and minimum dimensions but with one having an intricate edge. (This could also demonstrate the same particle, with the edge intricacy resolved in one system but not resolved in another.) Here, the ESPs for the two objects differ by 5% while the ESDs differ by 40%.

3.3 Relationship Between the ESD and the ESP Representation of Length

The relationship between the ESD and the ESP representation of object length is not readily apparent. A simple observation which sheds light on the relationship is that, for a common, naturally occurring particle shape, an ideal sphere, the ESD and ESP are equivalent. For particles with holes or otherwise not conforming to this ideal shape, the ESD describes the diameter of the collapsed area of an object while the ESP describes the diameter of the geometric spread of the object. A higher level of understanding of the relationship can be realized through the observation that μ_{00} is the measured area of a binary object (the sum of all pixels above threshold, regardless of position). Then following the definition of ESD, $ESD = [(4/\pi)\mu_{00}]^{1/2}$, and from the previous section $ESP = [(4/\pi)\pi\alpha\zeta]^{1/2} = 2(\alpha\zeta)^{1/2}$. This is the diameter of the spherical equivalent of the moment-generated ellipse (or sphere, in the case of X-Y symmetry). The relationship between ESD and ESP is perhaps most readily illustrated by their ratio, ESD/ESP which can be expressed as $[(4/\pi)\mu_{00}]^{1/2}/[2(\alpha\zeta)^{1/2}]$ and reduced to $(\mu_{00})^{1/2}/(\pi\alpha\zeta)^{1/2}$. Now recalling Eq. 18, $F = (\mu_{00})/(\pi\alpha\zeta)$, which describes the measured object area over the computed area of the geometric spread of the object, and is directly related to the object "porosity". When porosity is defined as the percentage of the area of the geometric spread of the object which is not filled by the object, $F = (1 - \text{porosity})$ and, hence, could be termed the "fill-factor". Therefore, the ratio, $ESD/ESP = (F)^{1/2}$, the square root of the object fill-factor, a potentially valuable analytical measurement. Additionally, through the functions involved in the ESP computation, information regarding object shape and orientation are also available and, when higher-order moments are considered, automated image pattern recognition is possible.

4.0 Field Measurements

In situ particle imagery was obtained in 40 deployments of the Marine Aggregated Particle Profiling and Enumerating Rover (MAPPER), an instrument system developed during the ONR Accelerated Research Initiative Significant Interactions Governing Marine Aggregation (SIGMA). The MAPPER system and the type of data acquired are described by Costello et al.^{9 (this volume)} and elsewhere^{6,10,11}. Succinctly, MAPPER is a free-fall, vertical profiling system which utilizes structured, visible diode laser illumination to produce a thin sheet of light at the image planes of three, synchronized CCD video cameras of differing magnifications. This unique, synchronous imagery from the three independent cameras allows the investigation of imaging artifacts which would not be noticed nor quantifiable in a system with a single camera.

4.1 Individual particles

Figure 7 shows the ESD and ESP measurements of a circa 15 mm diameter organism ("jellyfish") imaged by the MAPPER "medium field" (MF) camera. Much of the organism is transparent at the sensitivity level of this imaging system, that is, the sensor did not collect enough photons from those areas to raise the output voltage above 0.34 volts. With higher system sensitivity or higher illumination, and/or by manipulating the variables in Equation 1, the transparent areas would be visualized and the ESD measurement would change considerably more substantially than the ESP measurement as is illustrated in the graph at the lower right.

Figure 8 is a mosaic of the three images of a single particle simultaneously acquired by all three MAPPER cameras. It shows the effects of size-measurement artifacts introduced by the spatial resolution (here a function of magnification) of an imaging system combined with electronic overshoot. The images were digitized at 640 x 480 pixels from the three time-coded S-VHS video tapes which are recorded *in situ* during a MAPPER deployment. During this series of deployments (April 1994, East Sound, San Juan Islands, WA), the pixel resolution for the three MAPPER imaging systems were 285 μm , 85 μm , and 17.5 μm , respectively, for the large-field (LF), medium-field (MF), and small-field (SF) cameras. The three images at the bottom of the figure are normalized to the SF magnification.

Figure 9 plots the measurements of the particle from the three systems at GS threshold values 3 through 24. The ESD measurements at the three different magnifications differ considerably while the ESP measurements generally agree. Processing at higher GS thresholds, on the other hand, did not affect any of the measurements substantially with the exception of the SF ESP measurement which fell appreciably at $\text{GS} = 9$, apparently when one or both of the organism's antenna becoming "disconnected" at that GS threshold level.

4.2 Size Distributions

Figure 10 shows size distribution spectra (expressed as ESD) for the entire water column for a MAPPER deployment during the East Sound experiment. The data were generated by analysis of the images of 60,130 individual particles. Curves for each of the three systems are plotted as is the interpolated curve for all three systems (solid line). Since the three systems do not have the same field-of-view (FOV), small-scale particle patchiness could affect inter-curve agreement, but we feel that much of the disagreement is due to differences in resolution. This hypothesis is supported by Figure 11 which presents the data for the 60,130 particles using the ESP expression of particle length. Here, the three fields agree more closely in magnitude and in slope.

Finally, Figure 12 shows the interpolated curves from Figures 10 and 11. The curve obtained using the ESP calculation for diameter shows a smoother, more linear slope ($B = 3.57$ vs 3.49) than that obtained using the ESD because of the better agreement between the different fields. This is consistent with assumption of continuity which is intrinsic to the Junge-type description of the size distribution (Eq. 2).

5.0 Summary

This work originated from analysis of the data generated by MAPPER, a unique, *in situ* instrument which utilizes three synchronized, co-incident imaging systems. Analysis of some of the size distribution spectra from multiple systems showed distinct "bumps" which were indicative of a discrete population. The population, however, was sized differently by the different systems. In the MAPPER system, however, the target range is fixed by the structure-light sheet, the FOV is known, and conventional target sizing is not ambiguous. This work is part of the effort to understand sizing discrepancies between systems.

This contribution demonstrates the following:



Figure 7. The ESP and ESD representations of the size of a marine organism (see text for discussion).

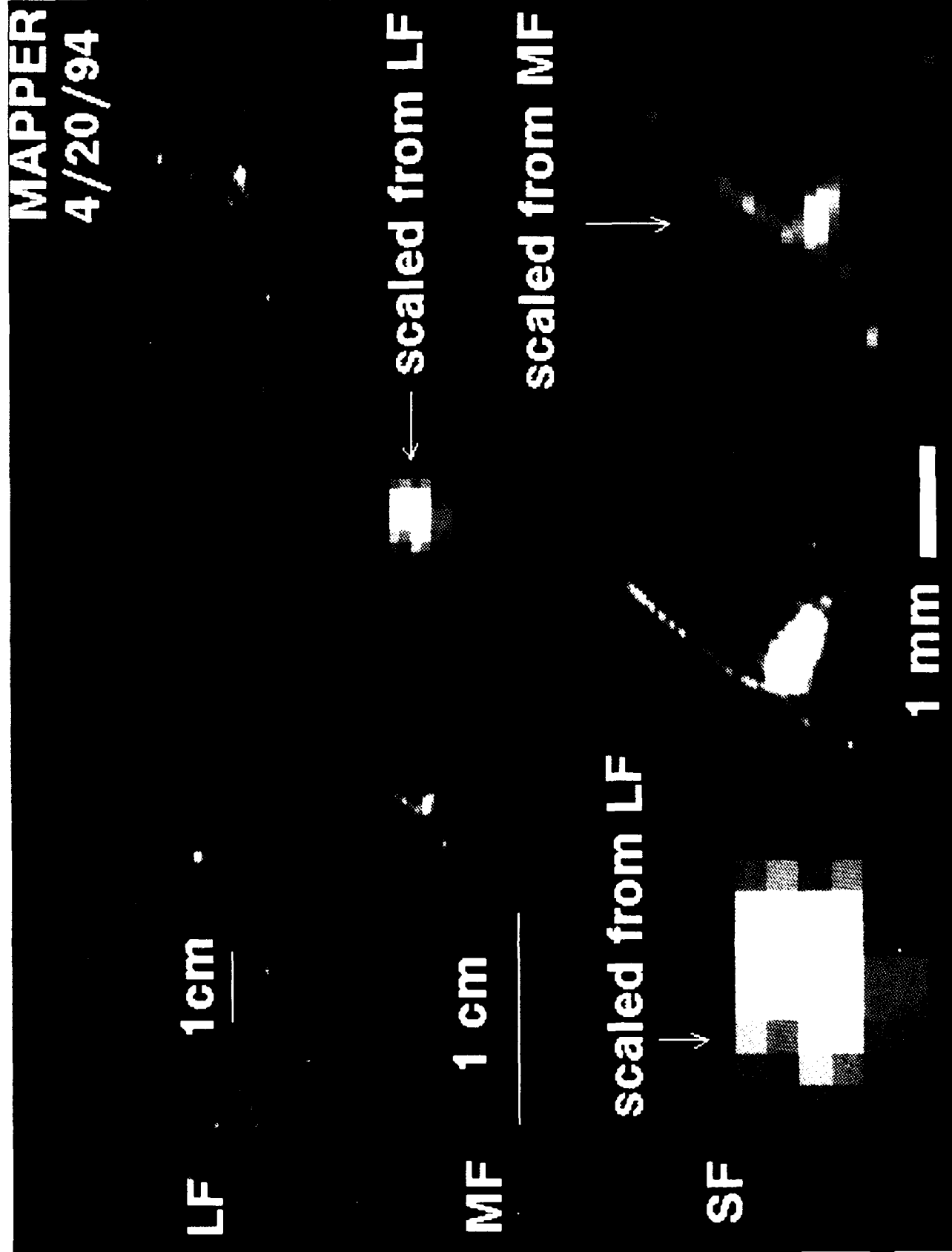


Figure 8. Three simultaneous images of a copepod at three different magnifications. (see text for discussion).

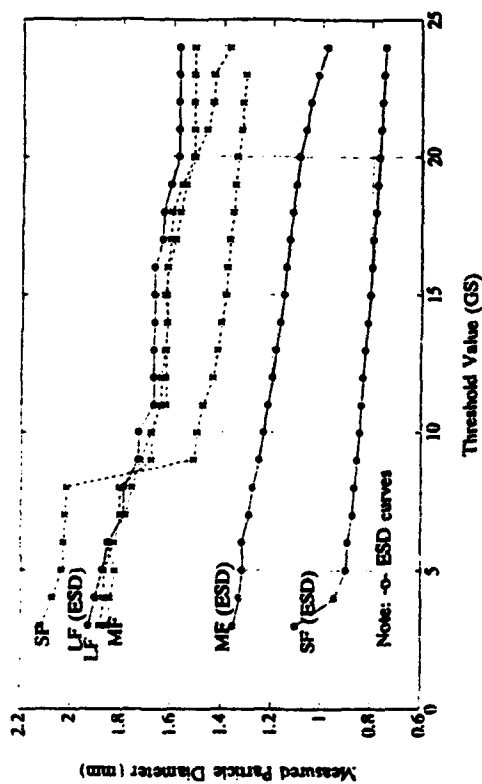


Figure 9. Particle diameter expressed as ESD and ESP.

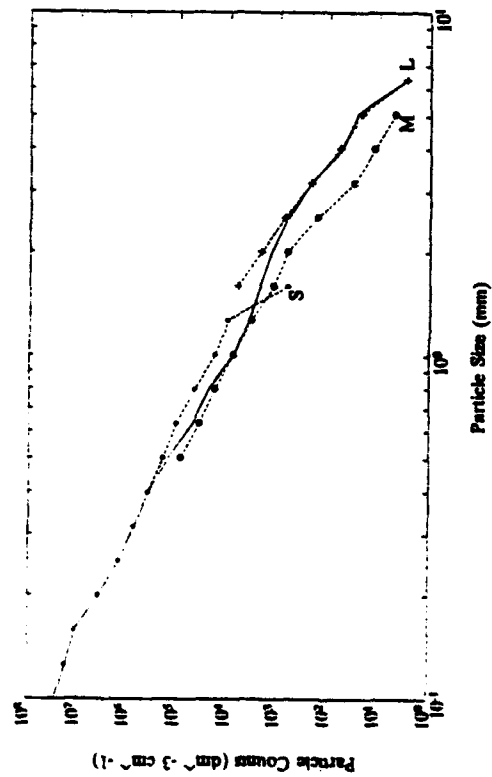


Figure 11. ESP particle size distribution.

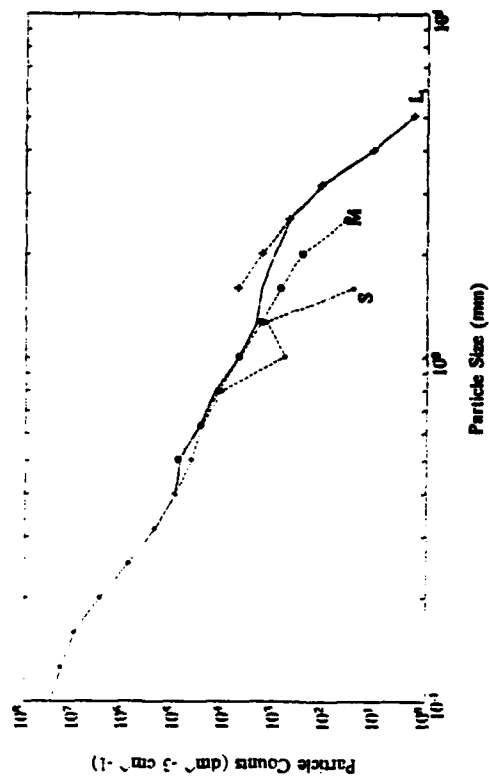


Figure 10. ESD particle size distribution.

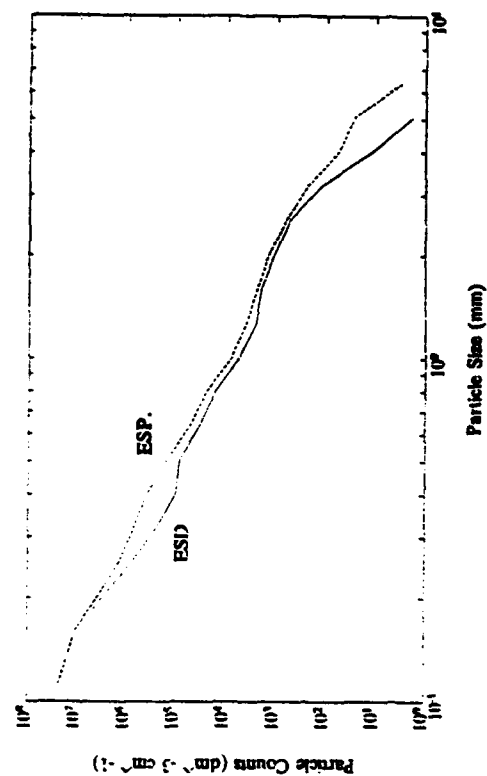


Figure 12. ESD and ESP interpolated size distributions.

1) System response to bright targets is a function of target contrast, sensor sensitivity, threshold setting, and image resolution. Its effect on particle size can be interpreted and corrected.

2) Image resolution affects derived particle size spectra. Errors depend on particle contrast, threshold setting, resolution, and particle compactness. A modified size descriptor ESP, which is $ESD/(F)^{1/2}$, has a much lower sensitivity than ESD to variations in resolution. This allows more accurate intercalibration of imaging systems of differing resolution and radiometric sensitivity.

3) For high-resolution systems, ESD/ESP provides a measure of the compactness of the particles and the method utilized to generate the ESP also provides particle shape and orientation information, prerequisites for automated pattern recognition.

In summary, through the use of Digital Image Processing, researchers are now able to rapidly identify, enumerate, size, and classify targets within an image. An automated DIP system, moreover, allows for unattended processing of a virtually unlimited number of images. Great care needs to be taken, however, to insure that the artifacts introduced by the finite spatial resolution and radiometric sensitivity of the system are understood and accounted for in the data produced. We hope this work makes a contribution toward a greater understanding of the strengths and limitations of DIP technology in *in situ* applications where the optical properties of potential targets are often not well known and, by definition, not controlled.

Acknowledgements

Financial support was provided by the Office of Naval Research to the University of South Florida through Grant N00014-88-J-1017 and by the National Oceanic and Atmospheric Administration through Grant NA360A0292.

References

1. Alldredge, A.L., U. Passow, and B.E. Logan (1993) The abundance and significance of a class of large, transparent organic particles in the ocean, Deep-Sea Res. 40: 1131-1140.
2. Passow, U., A.L. Alldredge and B.E. Logan, In press. The role of particulate carbohydrate exudates in the flocculation of diatom blooms, Deep-Sea Res.
3. Hu, M. (1962) Visual Pattern Recognition by Moment Invariants. IRE Trans. Inf. Theory, IT-8, 179.
4. Teague, M.R. (1980) Image analysis via the the general theory of moments. J. Opt. Soc. Am., v. 70, n. 8.
5. Dudani, S.A., K.A. Breeding, and R.B. McGee. (1977) Aircraft identification by moment invariants. IEEE Trans. Comput. C-26, 39-45.
6. Costello, D.K., K.L. Carder and R.G. Steward. (1991) Development of the Marine Aggregated Particle Profiling and Enumerating Rover (MAPPER). Underwater Imaging, Photography, and Visibility, Richard W. Spinrad, Editor, Proc. SPIE 1537, 161-172.
7. Carder, K. L. and D. K. Costello (1994) Optical effects of Large Particles. Ocean Optics. R.W. Spinrad, K.L. Carder, and M.J. Perry, and R.W. Spinrad, editors, Oxford University Press, New York, N.Y.
8. Costello, D.K., K.L. Carder, P.R. Betzer, and R.W. Young. 1989. In-situ holographic imaging of settling particles: Applications for Individual Particle Dynamics and Oceanic Flux Measurements. Deep-Sea Research, 36, 10, 1989.
9. Costello, D.K., W. Hou and K.L. Carder (1994) Some effects of the sensitivity threshold and spatial resolution of a particle imaging system on the shape of the measured particle size distribution. Ocean Optics XII, Bergen, Norway.
10. Costello, D.K., K.L. Carder and W. Hou (1992) Structured visible diode laser illumination for quantitative underwater imaging. Ocean Optics XI. Gary D. Gilbert, Editor, Proc. SPIE 1750, 95-103.
11. Hou, W., D.K. Costello, K.L. Carder and R.G. Steward (1994) High-resolution Marine Particle data from MAPPER, a new, in situ optical ocean instrument. EOS AGU/ASLO (75), 3, 21.

Scattering by cylindrically symmetric particles

Anri Perelman

Forestry Academy, Department of Mathematics
St. Petersburg 194018, Russia

ABSTRACT

Two kinds of potentials to solve the scattering from a radially inhomogeneous cylinder are presented. The models of the refraction indices for which these potentials are effective have been considered. The methods developed allow the solution of the scattering problem for any angle of incidence of the plane wave to be evaluated.

1. MAXWELL'S EQUATIONS

A nonmagnetic cylindrically symmetric medium, where electric charge density vanishes, immersed in the homogeneous nonconducting outer medium $r > a$ (r =radial distance from the axis of the cylinder), is completely described by its refraction index $m=m(\rho)$,

$$m(\rho) = \begin{cases} (\epsilon(\rho) - 4\pi\omega^{-1}\delta(\rho)i)^{1/2}, & 0 \leq \rho < k_0 a, \\ m_a > 0 \quad (m_a = \text{const}), & \rho > a k_0, \end{cases} \quad (1)$$

in which

$$\rho = k_0 r, \quad k_0 = 2\pi\lambda^{-1}. \quad (2)$$

Here, ρ =wave distance, k_0 =wavenumber, λ =wavelength in a vacuum, $\epsilon(\rho)$ =permittivity, $\delta(\rho)$ =specific conductivity, ω =circular frequency. The electric vector \mathbf{E} and the magnetic vector \mathbf{H} in their time free form (with time factor $e^{i\omega t}$) satisfy Maxwell's equations 1,2

$$\begin{cases} \text{curl} \mathbf{H} = i k_0 m^2(\rho) \mathbf{E}, \\ \text{curl} \mathbf{E} = -i k_0 \mathbf{H}. \end{cases} \quad (3)$$

The problem is stated as follows. Let the refraction index (1) and the sources of perturbation be given. The field vectors \mathbf{E} and \mathbf{H} within the external region $r > a$ of the obstacle described by its cylindrical coordinates

$$r \ (0 < r < a), \quad \varphi \ (0 < \varphi < 2\pi), \quad z \ (-\infty < z < +\infty) \quad (4)$$

are to be determined. We shall designate the quantities related to the cylindrical and Cartesian coordinates by some subscripts and superscripts, respectively. For any vector \mathbf{A} , we thus have

$$\mathbf{A} = \sum_i^3 A_k \mathbf{i}_k = \sum_i^3 A^k \mathbf{i}^k, \quad (5)$$

in which the corresponding unit vectors have been introduced. In the dimensionless cylindrical coordinates $x_1 = \rho$, $x_2 = \varphi$, $x_3 = \zeta$, where $\zeta = k_0 z$,

we get

$$\frac{1}{k_0} \text{curl} \mathbf{A} = \left(\frac{1}{\rho} \frac{\partial A_3}{\partial \varphi} - \frac{\partial A_2}{\partial \zeta} \right) \mathbf{i}_1 + \left(\frac{\partial A_1}{\partial \zeta} - \frac{\partial A_3}{\partial \rho} \right) \mathbf{i}_2 + \frac{1}{\rho} \left(\frac{\partial (\rho A_2)}{\partial \rho} - \frac{\partial A_1}{\partial \varphi} \right) \mathbf{i}_3 \quad (7)$$

In this paper we confine ourselves to the case of the plane wave \mathbf{V} as the only source of perturbation. We suppose (see Fig.1)

$$(\mathbf{V}, \mathbf{x}^1) = \alpha, \quad (\mathbf{V}, \mathbf{x}^2) = \pi/2 \quad (8)$$

and set

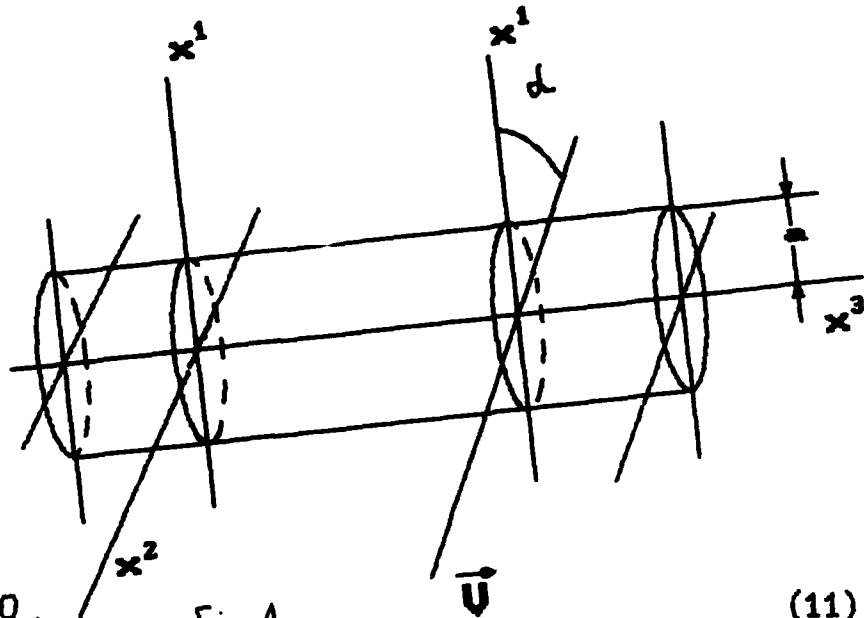
$$f = m \sin \alpha, \quad g = m \cos \alpha, \quad e = \exp(-i f \zeta) \quad (9)$$

Let us find the solution of (3) in the form³

$$\mathbf{A} = \sum_i^3 A_k \mathbf{i}_k, \quad A_k = e \sum_i^3 a_{kn} \exp(in\varphi), \quad a_{kn} = a_{kn}(\rho) \quad (10)$$

where $A_k = E_k$ or H_k . Having used the fact of the linear independen-

oe of the functions $\exp(in\varphi)$, it is easy to verify the equivalence of the system (3) to the system of the form



$$\left\{ \begin{array}{l} \rho m^2 e_1 - f \rho h_2 - n h_3 = 0, \\ f h_1 + m^2 e_2 - i h_3' - \zeta f' h_3 = 0, \\ n h_1 + i (\rho h_2)' + \rho \zeta f' h_2 + \rho m^2 e_3 = 0, \\ \rho h_1 + f \rho e_2 + n e_3 = 0, \\ f e_1 - h_2 - i e_3' - \zeta f' e_3 = 0, \\ n e_1 + i (\rho e_2)' + \rho \zeta f' e_2 - \rho h_3 = 0. \end{array} \right. \quad \begin{array}{l} \text{Fig. 1} \\ (11) \\ (12) \\ (13) \\ (14) \\ (15) \\ (16) \end{array}$$

We have dropped the subscript n which can be equal to any integer, and the prime denotes the differentiation with respect to ρ .

2. POTENTIALS OF THE FIRST AND SECOND KIND

Being solved the equations (12), (14) and (11), (15), we get the representations

$$\left\{ \begin{array}{l} e_1 = (n/\rho\mu) h_3 - (if/\mu) e_3' - (ff'\zeta/\mu) e_3, \\ h_1 = -(nm^2/\rho\mu) e_3 - (if/\mu) h_3' - (ff'\zeta/\mu) h_3, \\ e_2 = (i/\mu) h_3' + (fn/\rho\mu) e_3 + (f'\zeta/\mu) h_3, \\ h_2 = -(im^2/\mu) e_3' + (fn/\rho\mu) h_3 - (m^2 f'\zeta/\mu) e_3 \end{array} \right. \quad (17)$$

in terms of the functions e_3 and h_3 which will be called the potentials of the first kind.

Here, we have put

$$\mu = m^2 - f^2. \quad (18)$$

Next, by (13) and (16), we obtain the system of the following ordinary differential equation to determine the potentials of the first kind:

$$\begin{cases} \rho^2 e_3'' + (1 - f^2 R) \rho e_3' + \tau e_3 - i(R_1 e_3)' - 4R_1 e_3 - n(ifR + R_2)h_3 = 0, \end{cases} \quad (19)$$

$$\begin{cases} \rho^2 h_3'' + (1 - m^2 R) \rho h_3' + \tau h_3 + i(R_1 h_3)' + 4R_1 h_3 + nm^2(ifR - R_2)e_3 = 0, \end{cases} \quad (20)$$

in which

$$\tau = \mu \rho^2 - n^2 \quad (21)$$

and

$$R = 2pm' / \mu m, \quad R_1 = pm^2 f' / 4\mu^{-1}, \quad R_2 = ff' / 4\mu^{-1}. \quad (22)$$

From (19) and (20) it follows that $e_3 = 0$ implies $h_3 = 0$ and $h_3 = 0$ implies $e_3 = 0$, respectively.

Let us consider

Model 1. $m = \text{const}$, $f > 0$.

In this case $\mu = \text{const}$, too, and we get the known results (cf. (A4))

$$\begin{cases} e_1 = (n/\rho)Z - ifZ', \\ h_1 = -(nm^2/\rho)Z - ifZ', \\ e_2 = iZ' + (fn/\rho)Z, \\ h_2 = -im^2Z' + (fn/\rho)Z, \\ e_3 = \mu Z, \\ h_3 = \mu Z, \end{cases} \quad (23)$$

where

$$Z = Z_n(\sqrt{\mu\rho}), \quad Z = Z_n(\sqrt{\mu\rho}) \quad (24)$$

are any cylindrical functions.

In turn, being solved (11), (16) and (13), (14), we get the representations

$$\begin{cases} e_1 = (in/v)e' + (fp/v)\eta - (nf'\zeta/v)e, \\ h_1 = (in/v)\eta' - (fpm^2/v)e - (nf'\zeta/v)\eta, \\ e_2 = (1/\rho)e, \\ h_2 = (1/\rho)\eta, \\ e_3 = -(ip/v)\eta' + (fn/v)e - (pf'\zeta/v)\eta, \\ h_3 = (ipm^2/v)e' + (fn/v)\eta - (f'\zeta/v)e \end{cases} \quad (25)$$

in terms of the functions e and η which will be called the potentials of the second kind. Here, we have put

$$v = \rho^2 m^2 - n^2. \quad (26)$$

Next, by (12) and (15), we obtain the system of following ordinary differential equations to determine the potentials of the second kind:

$$\begin{cases} \rho^2 e'' + (1 + 2m'\rho/m - v'\zeta/\rho)pe' + \tau e + ifn(\rho v'\zeta/m^2 v)\eta = 0, \end{cases} \quad (27)$$

$$\begin{cases} \rho^2 \eta'' + (1 - v'\zeta/\rho)\rho\eta' + \tau\eta - ifn(\rho v'\zeta/v)e = 0. \end{cases} \quad (28)$$

From (27) and (28), it follows that $e=0$ implies $\eta=0$ and $\eta=0$ implies $e=0$, respectively.

Let us consider

Model 2. $m(\rho) = M\rho^{-1}$ ($M = \text{const}$), $f > 0$.

In this case

$$v = M^2 - n^2 \quad (29)$$

is a constant. By the use of (A1) and (A3), we get from (27) and (28)

$$\begin{cases} e_1 = in(\rho z)' + fpz, \\ h_1 = inz' - (fM^2/\rho)z, \\ e_2 = vZ, \\ h_2 = (v/\rho)z, \\ e_3 = -ipz' + fnpz, \\ h_3 = (iM^2/\rho)(\rho z)' + fnz, \end{cases} \quad (30)$$

where

$$z = Z\sqrt{1-\nu}(if\rho), \quad \gamma = Z\sqrt{-\nu}(if\rho). \quad (31)$$

Model 3. $m(\rho) = M\rho^{-1}$ ($M = \text{const}$), $f = 0$.

By the use of (A2) and (A4), we get from (27) and (28)

$$\begin{cases} e_1 = in(\rho Q)', \\ h_1 = inq', \\ e_2 = \nu Q, \\ h_2 = (\nu/\rho)q, \\ e_3 = -ipq', \\ h_3 = (iM^2/\rho)(\rho Q)', \end{cases} \quad (32)$$

where

$$Q = Q\sqrt{1-\nu}(\rho), \quad q = Q\sqrt{-\nu}(\rho) \quad (33)$$

and (29) have been used.

3. INCIDENT PLANE WAVE

For any fixed angle of incidence α , the plane wave

$$\begin{cases} E = e(-E_1^0 \sin \alpha i^1 + E_2^0 i^2 + E_1^0 \cos \alpha i^3), \\ H = m_0 e(-E_2^0 \sin \alpha i^1 - E_1^0 i^2 + E_2^0 \cos \alpha i^3), \end{cases} \quad (34)$$

where E_1^0 and E_2^0 are arbitrary constants and

$$e = \exp(-im_0 k_0 (x_1 \cos \alpha + x_3 \sin \alpha)) \quad (35)$$

satisfy the Maxwell equations (3) within the region $r > k_0 a$ (see (1) and Fig.1). It can be directly verified without difficulty.

With the help of transition formula

$$\begin{cases} [A_1, A_2, A_3]^T = C[A^1, A^2, A^3], \\ C = \begin{bmatrix} \cos\varphi & \sin\varphi & 0 \\ -\sin\varphi & \cos\varphi & 0 \\ 0 & 0 & 1 \end{bmatrix}, \end{cases} \quad (36)$$

we find the corresponding cylindrical components of (34):

$$\begin{cases} E_r = -e(E_1^0 \sin\alpha \cos\varphi + E_2^0 \sin\varphi), \\ E_\varphi = e(E_1^0 \sin\alpha \sin\varphi + E_2^0 \cos\varphi), \\ E_z = eE_1^0 \cos\alpha \end{cases} \quad (37)$$

and

$$\begin{cases} H_r = m_0 e (-E_2^0 \sin\alpha \cos\varphi - E_1^0 \sin\varphi), \\ H_\varphi = m_0 e (E_2^0 \sin\alpha \sin\varphi - E_1^0 \cos\varphi), \\ H_z = m_0 e E_2^0 \cos\alpha. \end{cases} \quad (38)$$

Using (A.5)-(A.7), we are able to write these components in the form (10), namely,

$$\begin{cases} E_r = e \sum_{n=0}^{\infty} (-iE_1^0 \sin\alpha J_n'(gp) + E_2^0 \ln(gp) (-i)^n \exp(in\varphi), \\ E_\varphi = e \sum_{n=0}^{\infty} (E_1^0 \sin\alpha \ln(gp) + iE_2^0 J_n'(gp) (-i)^n \exp(in\varphi), \\ E_z = eE_1^0 \cos\alpha \sum_{n=0}^{\infty} J_n(gp) (-i)^n \exp(in\varphi) \end{cases} \quad (39)$$

and

$$\begin{cases} H_r = m_0 e \sum_{n=0}^{\infty} (-iE_2^0 \sin\alpha J_n'(gp) - E_1^0 \ln(gp) (-i)^n \exp(in\varphi), \\ H_\varphi = m_0 e \sum_{n=0}^{\infty} (E_2^0 \sin\alpha \ln(gp) - E_1^0 J_n'(gp) (-i)^n \exp(in\varphi), \\ H_z = m_0 e E_2^0 \cos\alpha \sum_{n=0}^{\infty} J_n(gp) (-i)^n \exp(in\varphi). \end{cases} \quad (40)$$

We have used (9) with $m=m_0$ and (A8).

4. STANDARD MODEL OF APPROXIMATION

The particle under consideration can be treated as k -layer cylindrical shell ($k=1,2,\dots$). Similar construction was used earlier⁴ in the case of a sphere. Standard model of approximation is

termed as one described by the refraction index

$$m(\rho) = \begin{cases} M(x_0), & 0 \leq \rho < k_0 a_0 \\ x_i M(x_i) \rho^{-1}, & k_0 a_{i-1} < \rho < k_0 a_i \quad (i = 1, \dots, k) \\ m_a, & \rho > k_0 a_k, \end{cases} \quad (41)$$

where

$$x_i = 0.5 k_0 (a_{i-1} + a_i), \quad a_{-1} = 0 \quad (42)$$

The rigorous solution due to the standard model can be found in terms of the above reasoning. Indeed, we are able to write the boundary conditions for the field vectors E and H on the basis of the expansions of the type (10) for the waves involved and, then, taking advantage of the linear independence of $\exp(in\varphi)$, we obtain the linear system of algebraic equations in the unknown coefficients $e_{kn} = e_{kn}(\rho)$ and $h_{kn} = h_{kn}(\rho)$ ($k = 1, 2, 3$; $n = \text{any integer}$).

APPENDIX. SOME AUXILIARY FORMULAS

Let us denote

$$\begin{cases} Z_\nu(x) = A J_\nu(x) + B Y_\nu(x) \end{cases} \quad (A1)$$

$$\begin{cases} Q_\nu(x) = A x^\nu + B x^{-\nu} \end{cases} \quad (A2)$$

where A and B are arbitrary constants. It is known that

$$\begin{cases} x^2 y'' + a x y' + (b x^{2d} + b) y = 0 & (\alpha \beta \neq 0), \quad \text{then} \\ y = x^{(1-a)/2} Z_\nu(\sqrt{\beta} x^d / \alpha), & \nu = 1/2 \alpha \sqrt{(1-a)^2 - 4b} \end{cases} \quad (A3)$$

and

$$\begin{cases} x^2 y'' + a x y' + b y = 0, & \text{then} \\ y = x^{(1-a)/2} Q_\nu(x), & \nu = 1/2 \sqrt{(1-a)^2 - 4b} \end{cases} \quad (A4)$$

In turn, we have

$$\begin{cases} \exp(-ig\rho \cos\varphi) = \sum_{n=-\infty}^{\infty} (-i)^n J_n(g\rho) \exp(in\varphi) \end{cases} \quad (A5)$$

$$\begin{cases} \exp(-ig\rho \cos\varphi) \cos\varphi = \sum_{n=-\infty}^{\infty} i (-i)^n J_n'(g\rho) \exp(in\varphi) \end{cases} \quad (A6)$$

$$\begin{cases} \exp(-ig\rho \cos\varphi) \sin\varphi = \sum_{n=-\infty}^{\infty} (-i)^n i_n(g\rho) \exp(in\varphi) \end{cases} \quad (A7)$$

where

$$t_n(x) = nx^{-1} J_n(x) \quad (A8)$$

Formula (A5) follows from the expansion

$$\exp(iz \sin \phi) = \sum_{n=-\infty}^{\infty} J_n(z) \exp(in\phi)$$

while the proof of (A6) and (A7) is based on the relations:

$$\begin{cases} J_{n-1}(x) - J_{n+1}(x) = 2J'_n(x) \\ J_{n-1}(x) + J_{n+1}(x) = 2t'_n(x) \end{cases}$$

5. REFERENCES

1. M. Born and E. Wolf, *Principles of Optics*, Pergamon Press, New York, 1964.
2. H.C. van de Hulst, *Light Scattering by Small Particles*, Wiley, New York, 1957.
3. C.F. Bohren and D.R. Huffman, *Absorption and Scattering of Light by Small Particles*, Wiley, New York, 1983.
4. A.Y. Perelman, "Scattering in spherically symmetric media", *Appl. Opt.* 18, pp2307 - 2314, July 1979.

Intensity of the water fluorescence variation caused by organic matter
transition from suspended state into the solution

Vladimir M. Sidorenko
Sulo A. Pakkonen

S.I. Vavilov State Optical Institute
3 Pochtamtskaya st., St.-Petersburg, 190000 Russia.

ABSTRACT

In the context of notions earlier developed for absorption spectra the correlation between the suspended matter fluorescence intensity and solution one is obtained. A model with help of which the relation has been obtained involved a new method of consideration of exciting radiation absorption and reabsorption of the fluorescence emission by a suspended matter particle. The form of the suspended matter particle was approximated by a sphere. The quantity estimating this effect value by the example of phytoplankton in the water is considered. Experimental result of the sea water fluorescence intensity changing caused by organic matter transition from phytoplankton cells into the solution are discussed.

1. INTRODUCTION

Determination a connection between spectra's intensities of particulate and dissolved matter is important for optical investigation the ocean. Correlation between absorption spectra suspended matter and solution studied for a long time. Analytical connection was received between absorption coefficients of solution and homogeneous particles in continuous medium containing an equal amount of the same absorbing substance¹:

$$a = Q_a(\rho_v) \cdot \frac{N \cdot S}{V}, \quad (1)$$

where: $Q_a(\rho_v)$ - dimensionless efficiency factor for absorption, that is defined as the ratio of energy absorbed within the particle to the energy impinging on its geometrical cross-section S . Equation for $Q_a(\rho_v)$ was given for spherical particle with refractive index $n = n' - i n''$, where n' is close to surrounding medium one and imaginary part n'' remains small. N - number of uniform size particles in a volume V of suspension; $\rho = K/l$, where: K - absorption coefficient of the particle, l - diameter of the sphere. It was shown, that the most difference between suspended state and solution intensities is when the parameter ρ_v value is great. Relationship received was used for investigation phytoplankton absorption spectra in the sea water. The problem of connection between fluorescent spectra of suspended state and solution one is not solved correctly at the present time. The influence reabsorption effect on fluorescence spectra phytoplankton chloroplasts was investigated and equation for calculation was offered². But it was assumed that consideration of the effect for spherical particle may be done separately for exciting light and emitted light. Arguments for confirmation this assumption are absent. That is why the connection between fluorescence intensities of particulate matter and its solution must be determined.

2. THEORY

Let us consider a connection between fluorescence intensity of suspended state and solution on the basis of fluorescence phenomenon as a combination processes of absorption and emission by molecular with frequencies accordingly ν and ν' . We shall consider only influence difference of light absorption efficiencies with frequencies ν and ν' by suspended state and solution on its fluorescence intensity. We do not consider influence of other factors that transition organic matter from particulate state into solution accompany on quantum efficiency its fluorescence (such as fluorescence quenching, variation own molecular characteristics et.al). Dimensionless factor of particle fluorescence efficiency Q_f can be determined as a product of dividing quanta number of fluorescence emission by exciting emission one that falls on its geometrical cross-section with considering quantum fluorescence efficiency of

molecular $\sigma = 1$. Equations for fluorescence powers of suspended matter W_p and solution W_s , that equal amounts of fluorescence matter contain are:

$$W_p = Q_f \cdot \sigma \cdot \frac{N \cdot S}{V} \cdot L \cdot W_0 \cdot \frac{V}{v}, \quad (2)$$

$$W_s = K_v \cdot \sigma \cdot \frac{N \cdot v}{V} \cdot L \cdot W_0 \cdot \frac{V}{v}, \quad (3)$$

where: W_0 - excitation light power, K_v - absorption coefficient for absorbing substance of particle at excitation frequency, v - volume of particle, L - optical layer thickness. Thus, connection between fluorescence intensity of particulate matter I_p and solution I_s is given by equation:

$$I_p = Q_f \cdot \frac{S}{v \cdot K_v} \cdot I_s = Q_f^* \cdot I_s. \quad (4)$$

To compute Q_f value, consider the spherical particle with radius R . The beginning of Cartesian coordinates is put in center of homogeneous particle. The exciting light flux with density of quanta P_v is parallel "X" axis and registration of fluorescent emission is in axis "Y" direction in the little solid angle. Accordingly with earlier works we consider conditions, when particle refractive index is near that of surrounding medium, such that the rays are not bent during their passage through the particle. The number of fluorescent emission quanta from the elementary volume $dx \, dy \, dz$ that reaches the surface of the sphere is proportional the number of exciting quanta absorbed by layer $dx = P_v \cdot K_v \cdot dx \, dy \, dz$, multiplied by functions $\exp\left[-K_v \cdot \left(\sqrt{R^2 - z^2 - y^2} - x\right)\right]$ and $\exp\left[-K_v \cdot \left(\sqrt{R^2 - z^2 - x^2} - y\right)\right]$. These functions take into consideration the light flux absorption in the sphere with frequencies v and v' . The number of fluorescent quanta emitted by particle per time unit can be determined after integrating over the volume of sphere. After dividing result of integrating by quanta number of exciting light that falls on particle's geometrical cross-section per time unit - $P_v \cdot \pi R^2$, equation for Q_f value is given by:

$$Q_f = \frac{2}{\pi \cdot R^2} \cdot \int_0^R dz \cdot \int_{-\sqrt{R^2 - z^2}}^{\sqrt{R^2 - z^2}} dx \cdot \int_{-\sqrt{R^2 - z^2 - x^2}}^{\sqrt{R^2 - z^2 - x^2}} dy \cdot \exp\left[-K_v \left(\sqrt{R^2 - z^2 - y^2} - x\right)\right] \times \\ \times \exp\left[-K_v \left(\sqrt{R^2 - z^2 - x^2} - y\right)\right] \cdot K_v dy. \quad (5)$$

Equation (5) for Q_f differs from corresponding equation that was presented earlier, because it is not a product of multiplication factors of absorbency efficiencies at frequencies v and v' .

Let us estimate Q_f value with help of equation (5) for various optical densities of particles. Equation (5) was solved with help of numerical method. Sphere volume was presented as a sum of cubes with side dimension $2R/N'$, where N' was 10. The error of estimation sphere volume was less then 2 %. Result of numerical analysis equation (5) shows Q_f value dependence on parameters $\rho_v = 2R \cdot K_v$ and $\rho_{v'} = 2R \cdot K_{v'}$ only. With help of equations (4), (5) connection between Q_f and Q_f^* for spherical particles can be obtained:

$$Q_f^* = \frac{3 \cdot Q_f}{2 \cdot \rho_v}. \quad (6)$$

3. RESULTS

Results of calculation Q_f values for different ρ_v and ρ_{v^*} are presented in figure 1. The range of ρ_v and ρ_{v^*} variation was chosen on the base of phytoplankton size variation limit and absorbency properties of the cell material. These particles in the water satisfy conditions that were made for refractive index value. It is necessary to notice that $Q_a(\rho_v)$ dependencies for absorption and $Q_f(\rho_v)$ one with ρ_{v^*} constant (see figure 1) are similar. Really, it is growth Q_f value with ρ_v increasing. Functions $Q_f^*(\rho_v)$ for fixed ρ_{v^*} are presented in figure 1. Results of analysis show the more significant influence the considered effect on fluorescent spectra intensity then on absorption one. This is result of "two quanta" nature of the fluorescence phenomenon that is a product of absorption and emission light by molecular.

Q_f, Q_f^*

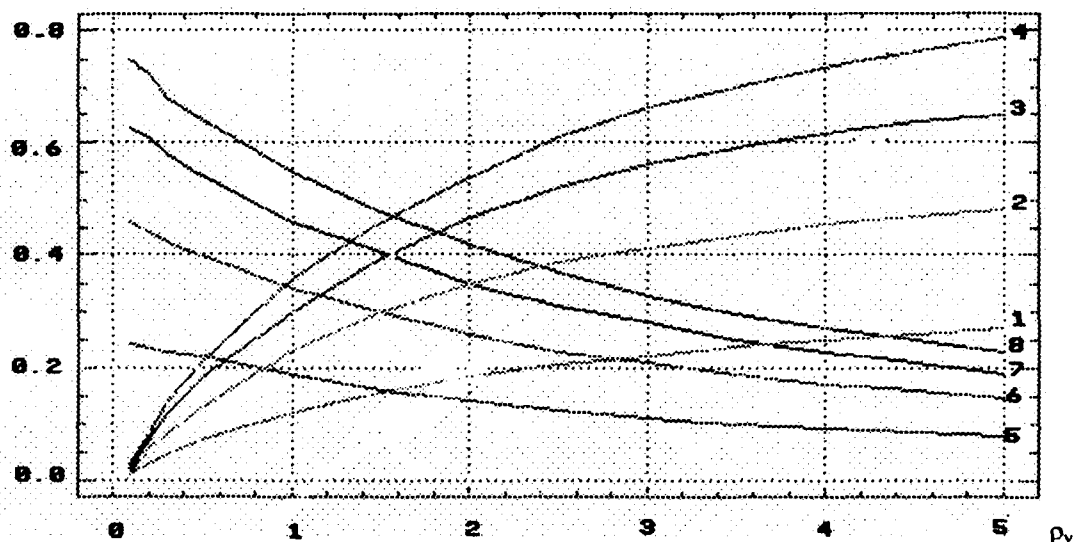


Figure 1. Functions $Q_f(\rho_v)$ and $Q_f^*(\rho_v)$

Function $Q_f(\rho_v)$	
1	$\rho_{v^*}=5$
2	$\rho_{v^*}=2$
3	$\rho_{v^*}=1$
4	$\rho_{v^*}=0.5$

Function $Q_f^*(\rho_v)$	
5	$\rho_{v^*}=5$
6	$\rho_{v^*}=2$
7	$\rho_{v^*}=1$
8	$\rho_{v^*}=0.5$

One of the most important problems of the sea water fluorometry is determination chlorophyll concentration. Calibration of fluorometers usually fulfills with help of chlorophyll solutions, but natural sea water contains chlorophyll as chloroplasts in phytoplankton cells. It is necessary to take into consideration this circumstance for quantitative investigations. Let us compare results of using above-mentioned theory, early suggested theory and data of laboratory investigations of chlorophyll concentration in the sea water that phytoplankton cells with different diameters contain. Experimental fluorescence intensities P^3 , results of calculation Q_f^* values with help of equations (4), (5), (6) and on the basis of early theory ^{2,4} are presented in relative scale in table 1. for different types of phytoplankton. Calculations were made with using parameters $K_v = 2 \cdot 10^{-5} \text{ m}^{-1}$ and $\rho_v = 0.43 \rho_v$.

Table 1. Influence the transition from the phytoplankton to the solution on chlorophyll fluorescence intensity for different phytoplankton types.

Phytoplankton type	l [mkm]	ρ_v	Q_r^* (from eq.4-6)	$Q_r^{*2,4}$	P^3
Nanoplankton	2	0.4	13.1	16.3	12.0
Monochrysis sp.	6	1.2	9.0	11.1	5.0
D.tertiolecta	6	1.2	9.0	11.1	4.0
Fragillaria sp.	10	2.0	6.4	7.9	5.0
Phaeodactylum tricornutum	15	3.0	4.8	5.3	4.2
G.splendens	35	7.0	1.6	1.6	2.0
G.nelsoni	48	9.6	1.0	1.0	1.0

It is clear, that using theory allows to decrease an error of determination chlorophyll concentration caused by variation phytoplankton size. Moreover, it describes fluorescence intensity dependence from phytoplankton size better than method earlier suggested.

4. CONCLUSION

The present results can be used for quantitative estimation of fluorescence intensity variation caused by organic matter transition from the particles into the solution. An example of determination chlorophyll concentration in sea water shows an error of such estimation in laboratory conditions. This error is caused by assumptions, that were done in theory and by other reasons. Some of these reasons in natural conditions are unhomogeneous of phytoplankton composition and effects of photoadaptation. These reasons must be considered during sea water investigations with help of fluorometers.

5. ACKNOWLEDGEMENTS

We would like to thank Dmitry V. Ivanov for his assistance with the preparation of this manuscript.

6. REFERENCES

1. A. Morel, A. Bricaud, "Theoretical results concerning light absorption in a discrete medium and application to specific absorption of phytoplankton", *Deep-Sea Res.*, Vol. 28, pp. 1375-1393, November 1981.
2. D. I. Collins, et. al., "The role of reabsorption in the spectral distribution of phytoplankton fluorescence emission", *Deep-Sea Res.*, Vol. 32, pp. 983-1003, August 1985.
3. M. E. Loftus, D. V. Subba Rao, H. H. Seliger, "Growth and dissipation of phytoplankton in Chesapeake Bay. I. Response to a large pulse of rainfall", *Chesapeake Science*, Vol. 13, pp. 282-299, 1972.
4. B. G. Mitchell, D. A. Kiefer, "Chlorophyll a specific absorption and fluorescence excitation spectra for light-limited phytoplankton", *Deep-Sea Res.*, Vol. 35, pp. 639-663, May 1988.

Investigation of the oil spreading in the deep sea and search for method of discover the oil pollution under sea surface

Vadim K. Goncharov

A.N. Krylov Shipbuilding Research Institute
44 Moskovskoye shosse, St. Petersburg, 196158, Russia.

Vladimir G. Lyskov

S.I. Vavilov State Optical Institute
3 Pochtamtskaya st., St. Petersburg, 190000, Russia.

ABSTRACT

This report is dealing with the problem of estimation the damages to environment caused by the crude oil (or oil products) spills from the underwater sources. The peculiarities of the oil movement caused by flotation and turbulence in the deep sea were considered on the basis of assumption that the oil dispersed on the separate drops. It is showed that the oil which coming to the surface is divided into separate clusters in accordance with sizes of drops. The mathematical expressions were obtained that permitted to evaluate the sizes of oil drops and clusters as well as oil concentration depending on time. The analysis of experimental data confirmed the theoretical results while using the diesel oil. Its drops had sizes from 0.10 to 1.34 mm. The diesel oil concentration in clusters corresponds to theoretical predictions.

1. EXPERIMENTAL DATA.

No considering some problems caused by processes of oil obtaining or crash situation during its transportation, we are concentrating on the problem of creating effective method for revealing of underwater throwing out the oil products (OP), which may be stimulated by the throwing out from ships (oily ballast, bilge water) and sewerage, or streams of oil products from bottom drill holes and pipelines. When OP spills of the sea surface where studied and possibilities of their obtaining evaluated, at the same time the underwater throwing was investigated less carefully especially its transfer and interaction¹.

Conventionally, one of the effective method of obtaining OP in the sea is using an aviation, which permits to perform monitoring sea surface with velocity 50...500 sq.km/hour and space resolution from 10 to 100 m accordingly. But in this case there is need for theoretical and experimental consideration of optical characteristics of OP dispersed in sea layers, their distribution in time and space and transfer under influence natural processes as well as quantitative characteristics of throwing out. This demand may be fulfilled in condition of metrological calibration of apparatus. There is a need valid methods for estimating results obtained by aviation optical measurements. Optical properties of emulsion and solution, contained oil products and sea water, depend not only on concentration or composition, but also on temperature of water, sea and weather conditions, flows and others. Some researchers stress the additional dependence upon time of spill existence, structure and particle size which are dispersion system^{2,7,8}. Many researchers consider possibilities of applying optical methods for obtaining OP in sea, such as scattering and absorption light or fluorescence. The results of their works on comparison of sensitivity different methods demonstrate that no one of them have some advantages while obtaining little concentration oil in water³. The values for obtain of extreme concentration for organic substances is attracted from³. Table 1 demonstrated the extreme values of organic concentration.

Table 1.

Optical method	Extreme concentration mg/l
Liquid chromatography	0.001...1
Absorption molecular spectroscopy inclusively colorimetry (UV and VD)	0.001...1
Fluorescent molecular spectroscopy	0.0001...01.

The most effective method revealing organic substances is a fluorescent one. It allows to discover the smallest portions of oil and identify sorts (kinds, types) of OP by exit light and fluorescent emission in some conditions. Optical characteristics of oil and its derivatives were defined in laboratory by means of chromatography with application of specific dissolvents and activators. Results of laser spectrofluorimetry of oil (N-laser, 337 nm) are showing, that the maxima of fluorescent emission lies in interval 450...550 nm and band of emission is equal to 150 nm for majority of samples. The oil extracted from various places has various bands. The derivatives of oil has many additions, which influence on emission light, for example, time of fluorescent emission is 1...8 ns for oil, and from 3...4 to 35...37 ns for oil products. The application of fluorescent method in sea research has two variations. The apparatus using this method may be installed on ship board or underwater tug (contact methods). Also it can be assembled on board of airplane or other carrier (non-contact methods). Using non-contact measurements it is necessary to know the distribution of OP by depth and its concentration as well as its optical characteristics. The report consist of experimental data which were obtained by studying the regularity of OP spreading in sea using the contact fluorimeter. This fluorimeter was specially designed as submerged apparatus for installation on towed carrier or for installation on ship board and sonding to depth no more 80 m. The on-board part of fluorimeter contained of control and registration currents. The submerged part of fluorimeter included in itself an optical scheme. There were two channel: one of them was intended for measurements and the other was intended for controlling the stimulating light. Their electronic schemes were identical. The volume of fluorescent substances was 20 cub.sm. Analogous systems of submersible fluorimeter is described in ⁴.

Source of excitation radiation is an impulse lamp with energy 0.25 J. Frequency of impulses 50 Hz, time of light impulse 1.5...2 mks. The lamp radiates in region 320...600 nm, with maxima 400...500 nm ⁵. Our modernisation of typical scheme lamp included some investigations to extend time of service and stability of radiation. Exiting radiation in apparatus was 405 nm and band of radiation was 45 nm. The receivers of radiation were a photomultipliers with band of signal registration from 0 to 5 Hz. The signals are measured in band 50 dB. Spectral band of measurements channel 40 nm with maxima 550 nm. The fluorimeter's sensitivity limit was defined by unstable brightness of impulse lamp radiation, which is more than noise of receiver and amplifier. That is an essential feature of apparatus: coefficients of signal variance were from 0.01 to 0.05 with errors from 0.001 to 0.005 for 5 Hz bands. Afterwards the special research was carried out and a new type 9 of impulse lamp was worked out (cappillary, with an exit of light from tip end). In laboratory the sensitivity of fluorimeter was fulfilled on traditional method by means of OP solution in CCl₄ with concentration 50 mg/l. Graded graph was received in laboratory by solution of sample. It allowed to estimated a minimal concentration of OP, which may be detected (to 0.1 mg/l).

The presence of fluorescent substances in sea water such as a dissolved organic matter (DOM) or chlorophyll pigments (phytoplankton) is a source for disturbances, because the optical bands of optical bands of this substances are coincide. For details related to this phenomenon see ⁴. Then the first stage of sea research was devoted to a study of fluorescent field in planned aquatorium. Two or three or more soundings were made to each series of experiments. The average value of natural fluorescence was calculated using the data of sounding for each concrete depth. The full cycle of experiments consist of 15 realization. The variance of mean data (i.e. ratio of dispersion to the mean of signals) and gradients of signals by depth are demonstrated by drawing 1. It may be seen, that fluorescent field was very heterogeneous. The fluctuation of apparatus signals on constant depth in long duration regime may be described by abnormal statistical law. The principal disturbance, which we could register in regime of hanging, was a fluctuation of signal because of ship shake. This permitted us to make a conclusion: the sensibility of contact method is determined by noise of environment. The real sensibility of apparatus was 18...60 mg/l in undersea depth to 15 m, and 0.3...0.5 mg/l on depth more 30...40 m.

The difficulties of carrying out of the sea research with oil products throw out are connected with precise placing ship and retaining apparatus in confined region (not speaking about ecological restrictions). The method of submersible throwing in our experiments was analogous to one 6 detailed described in ⁶. The submersible arrangement for throwing moved with velocity 2 m/s on depth 50 m. The mixture of diesel oil and sea water (75 l of OP, 1:3, density about 0.865) was prepared and located in special tank. This mixture thrown out during more 10 min, that is less 0.125 l/s oil. Research vessel drifted with mean velocity 0.2 m/s. The apparatus was positioned on constants depth or it may be sounding in interval from 5 to 55 m. An alteration of signal was connected with appearance of OP in scanning space. During observation and result processing this event was identified with other independent data. The conditions of experiment is showed in Table 2.

Table 2.

Character	Value
Depth of transition zone of fluorescence:	
- upper boundary	5 m at beginning of experiment,
- lower boundary	10 m at end of experiment,
	24 m at beginning,
	29 m at end.
Maxima gradient of fluorescence in transition zone:	0,058...0.056 conditional units/m. ³
Gradient on positioning depth (12 m):	0.012...0.022 conditional units/m. ³
Wind	120 grade, 7-8 m/s.
The sea-way ³	2-3 ball
The conditions of sonding :	
- depth,	5...55 m,
mean velocity of sonding -	0.15 m/s,
diameter of windows	0.03 m,
response time	0.06 s.

During the first experiment it was registered a signal fluctuation in background condition (constant depth) with following characteristics :

maxima attitude of means	- 1.6 conditional units,
coefficient of variance	- 0.22...0.25.
The maxima signals in region of throwing	- more then 25 conditional units.

Drawing 2 demonstrates a copy of signal's tape recording after throwing out the OP. An experiment started at 11h43min with duration of measuring more than 120 min (time constant of recording was 12 s). During research four experiments were fulfilled, but only two from four was resultative. Along with a registration of signals on constant depth (12 m) it was periodical sounding from a horizon of throwing (50 m) to the surface (plot 7 and 10 on drawing 2). It is possible to emphasis one or several layers by tape record, where it is mark an increasing level of fluorescence. It is

identify as a OP layers (see scheme on drawing 1). The upper boundary of the most fluorescent layers was on depth 10 m and thickness of layer was 18..25 m at the end of observing. During the second experiment analogous results was received but after 180 min. The evaluation of drops velocity coming to the sea surface give that data: 0.0074 m/s for "easy" fraction (upper boundary) and 0.0028 m/s for "heavy" one (lower boundary). The processing of the same soundings signals, but registered on magnetic tape (time of meaning less 0.5 s), allowed to see that a signal consist of short time impulses with a much more amplitude (drawing 3, respective to plot 7 on drawing 2). On this recording it is possible to emphasis 3 layers, which consist of impulses be noted for amplitude and frequency. Impulse nature of registered signals in sounding regime and in longitudinal observation on constant depth 12 m, just alternation layers of clear water with OP, give a reason to consider that a underwater throwing is dispersed (in process of rise to the surface) on the accumulations of close size drops (clusters). Each accumulation rise to the surface with distinguish velocity of propagation. The peculiarity of apparatus allowed to evaluate the size of drops or thickness of layers. The minimal sizes of this drops and layers are restricted equal to a diameter of apparatus windows (or his part). The results of treatment of distribution relative size of fluorescent layers are presented on drawing 4. It may be seen, that the cloud of OP consist of a layers of fluorescent substances, which are nonuniform in size. The minimal size of drops (layers) is about 0.8...1 cm, the maximal one is about 20 cm according to experimental data (drawing 4). The concentration of OP in this regions is varied from 0.6 to 4 mg/l on depth about 30 m (on results of laboratory graded graph).

2. TEORETICAL RESULTS

With the purpose of estimating the drop size according to its velocity of coming to the 10 surface it is possible to use the published experimental data for the oil drops in water¹⁰. On base the approximation of these data by nonlinear regression there are received the empirical formulas:

for $w_p < 6.2$ cm/s :

$$d_p = 4.82 * [\delta\gamma/\gamma_s * g]^{-0.60} * v_s^{0.4} * w_p \quad (1)$$

and for $w_p > 6.2$ cm/s :

$$d_p = 0.672 * [\delta\gamma/\gamma * g]^{-1} * w_p \quad (2)$$

In these formulas:

d_p - drop diameter, m,

w_p - velocity of coming to the surface, m/c,

γ_s - specific weight of sea water, kg/m³,

$\gamma_s - \gamma_p$ - difference of oil and sea water specific weights, kg/m³,

v_s - kinematic viscosity of sea water, m²/c,

g - gravity constant.

With the help of these formulas on the basis of the fluorimeter signal tape record showed on drawing 2 it is possible to estimate the oil drops sizes which are going across the test section of fluorimeter in the constant depth measurement regime. Take into consideration the fluorimeter signal amplitude and duration it is possible to estimate the oil drops number or the oil drops concentration. Then on the basis of these data it is possible to obtain the drop size distribution in the deep sea oil spill. The drop size distribution for 40 minute after the oil spill which was obtained by aforesaid method is shown on drawing 5.

On the basis of these data and with use the methods of the oil spreading description and the concentration calculation caused by oil spill from the underwater sources elaborated by it may be computed the proposed variation of the fluorimeter signal in sounding measurement regime and carried the comparison with real fluorimeter signals obtained in the sea experiments. The quantity Q of oil spilled on some depth it is possible to present as limited number oil drops, which sizes locate in the range contained N subranges, that is

$$\sum_{i=1}^N n_i d_{pi3} = 6/\pi * Q/\gamma_s \quad (3)$$

where n is number of oil drops with diameter d_p in the i -subrange or in the I -fraction. Then the oil drops concentration C_n in some point of deep sea space is received by summing up the every portion C_n of oil drop size I -fraction:

$$C_n = \frac{1}{8\pi^{1.5} K_1 K_{z0.5} t^{1.5}} \sum_{i \in N} n_i \exp \left[-\frac{r^2}{4 K_1 t} - \frac{(z - w_{pi} t)^2}{4 K_z t} \right] * \left\{ 1 - \exp \left[-\frac{(h - z) h}{K_z t} \right] \right\}. \quad (4)$$

In this formula:

- r, z - polar coordinates with origin in the point of oil spill,
- t - time,
- K_1, K_z - turbulent diffusivity coefficients in horizontal and vertical directions,
- h - depth of oil spill.

The analysis of solution (4) carried out by ⁷ showed that the oil drop accumulations consisted of the drops from every individual drop size fraction came to the sea surface with the velocity corresponding to velocity of oil drop from ones size fraction and the sea turbulent diffusion resulted in horizontal and vertical expansion of drop accumulations. Moreover in the process of coming to the sea surface as result of difference in the velocities it is took place the vertical separation of the oil drops accumulations in accordance with oil drops velocities. On this cause the initial drop size separation in the point of oil spill lead to drop depth separation which increase in the course of time. These theoretical predictions are confirmed by the data of sea experiments. With use of the formula (4) and on the basis of the drop size distribution in drawing 5 it was computed the vertical distribution of the oil drop concentration for time $t=5000s$ after the oil spill, when the fluorimeter sounding was carried out (plot 7 on drawing 2). It needs take into consideration what in this moment in the sea water it was estimated only the oil drops which were coming to the sea surface with velocity that was less then 1 cm/s and with diameter that was less then 0.45mm. For computation it was selected $K_z=0.1 \cdot K_1=0.01 \text{ m}^2/\text{s}$, $h=50\text{m}$, $r=0$ and z was varied from 0 to 45m. w_{pi} for every D_{pi} was calculated according to formulas (1) and (2) which were transformed for this purpose.

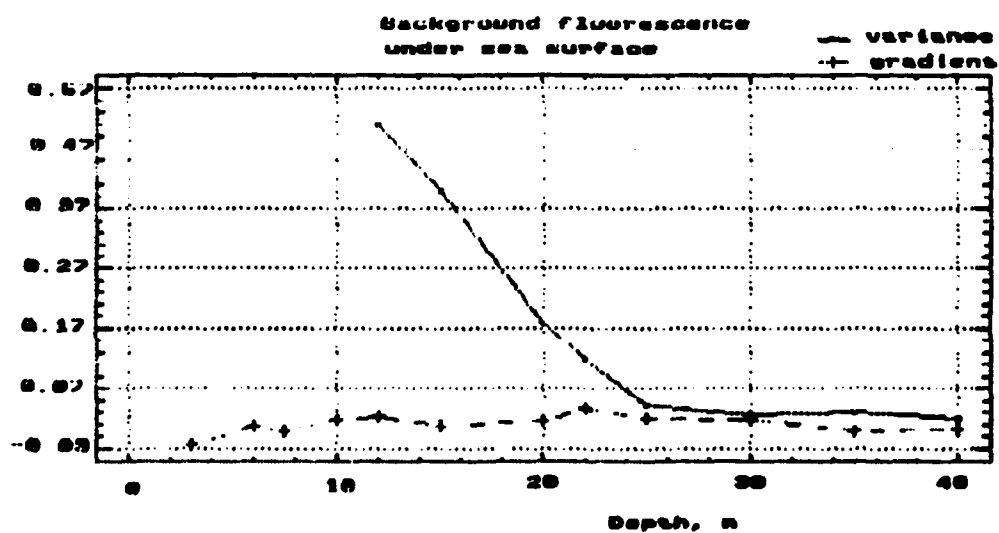
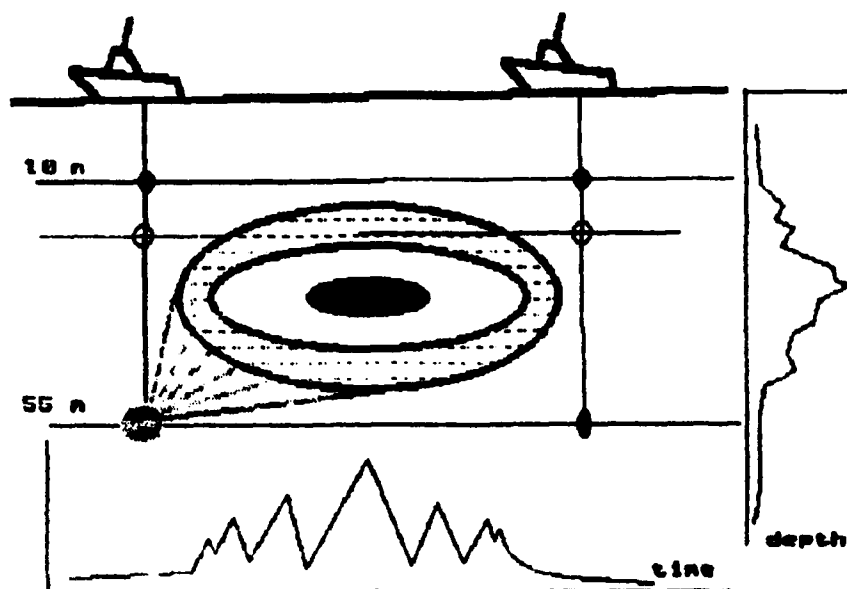
The comparison of the computed results and the experimental data permitted to make the conclusion about the sufficient conformity of ones, and as result to make conclusion about the reliability of the theoretical description of oil spreading in the deep sea and about the efficiency of the experimental method used for investigation of this process.

During the experiments it is not marked visually outlet of oil pollution on the sea surface. This fact confirm the actuality on researching and working out of optical method for discover and monitoring of undersea oil pollution. The experimental dates, which discussed above, were obtained by "contact" method. This results is recommended not only for evaluations of undersea oil spills structure but for evaluation conditions of reveals oil spills by lidar fluorimetric system, which may be possible to describe the structure, to reveal and to classify surface and undersurface OP spills.

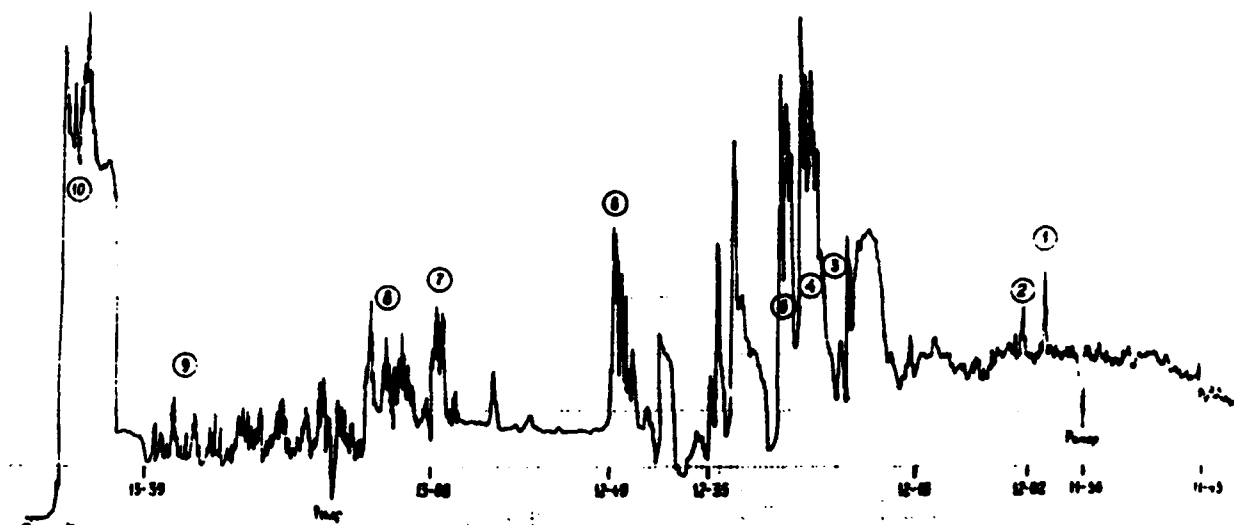
REFERENCES

1. A.Nelson-Smith. "The problem of the oil pollution of the sea ". Advances in marine biology, v.8. Academic Press, London & New York. 1970.
2. Стонь М., Шифрин К.С. "Определение структуры эмульсии "нефть-морская вода" по данным ее прозрачности". Оптика моря и атмосферы. Тезисы докладов на 11 Пленуме рабочей группы по оптике океана АН СССР, ч.1, с.156.
3. "Спектроскопические методы определения следов элементов". Под редакцией Дж.Вайнфорднера."Мир", М., 1979.
4. Карабашев Г.С. "Флуоресценция в океане" Гидрометеиздат, Л, 1987.
5. "Импульсные источники света". Под ред. И.С. Маршака. "Энергия", М., 1978.
6. Озмидов Р.В. "Диффузия примесей в океане". Гидрометеиздат, Л., 1986.
7. Гончаров В.К., Лысков В.Г. "Исследование особенностей распространения нефти в морской среде и условий ее всплытия на поверхность". Океанология, N 6, 1993, с.856-862.
8. J. Williams. Introduction to marin pollution control. A Willey Interscience Publication. New York.

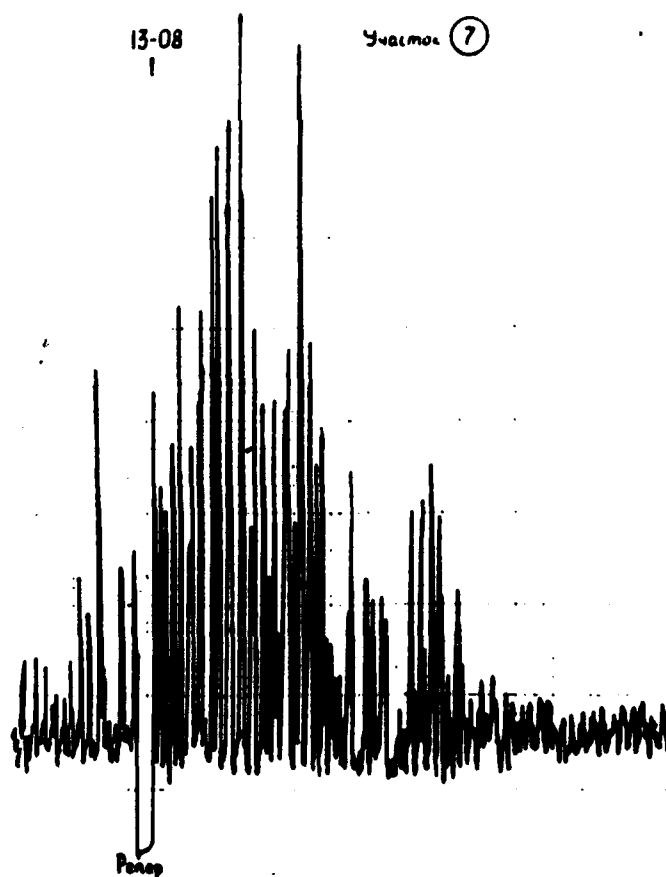
9. Волкова Г.А., Лысков В.Г., Храпунович И.А. "Стабильность яркости капиллярных импульсных ламп" Приборы и техника эксперимента, М., N 1, 1987 с.206-208.
10. Кутателадзе С.С. "Анализ подобия в теплофизике". С.О. АН СССР, Наука, 1982.



Drawing 1.

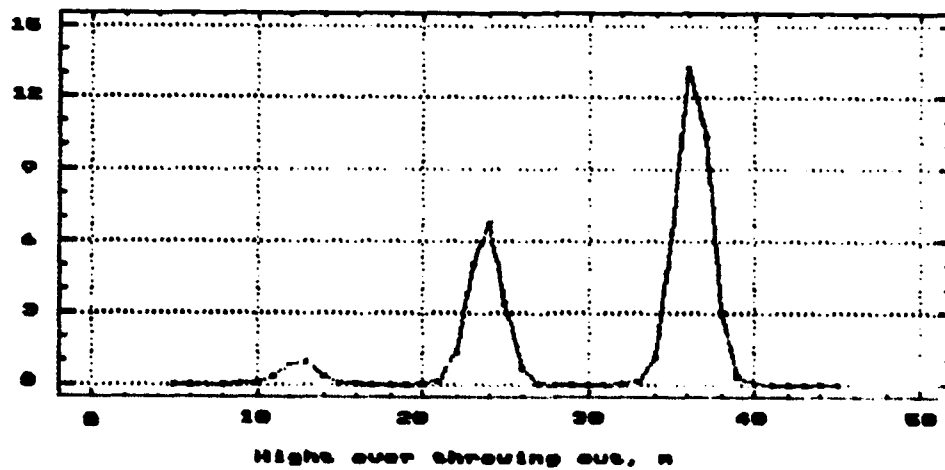


Drawing 2.



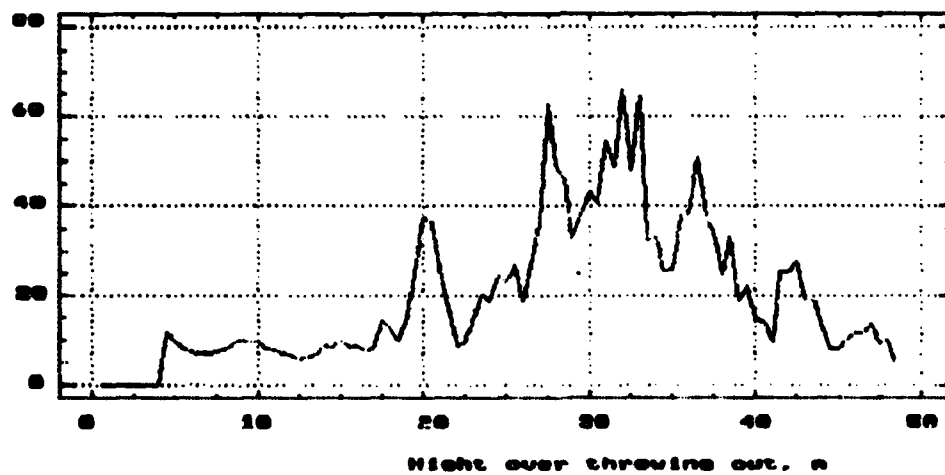
Drawing 3.

Conditional size of drops on depth
(theoretical)



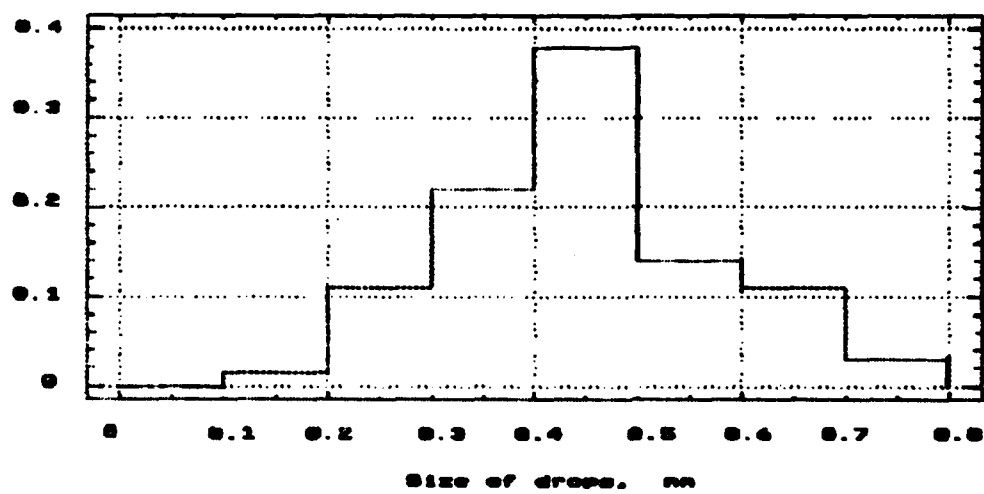
Drawing 4a.

Conditional concentration of drops in layers



Drawing 4b.

Frequency, n/N



Drawing 5.

Vertical stratification of the fluorescence
intensity dissolved in the sea water organic matter

Vladimir M. Sidorenko
Sulo A. Pakkonen

S.I. Vavilov State Optical Institute
3 Pochtamtskaya st., St.-Petersburg, 190000 Russia.

ABSTRACT

A model of formation the sea water fluorescence intensity of dissolved organic matter vertical stratification $I(z)$ is proposed. It allows to explain the increasing I with z depth on the horizons situated below photic zone. The influence of different hydrophysical characteristics on the $I(z)$ dependence and comparison with experimental data are considered.

1. INTRODUCTION

At the present time it is well known that sea water fluorescence intensity I in a spectral region 350–600 nm grows with depth z on horizons situated below photic zone. Fluorescence properties of the water in this spectral region are connected with presence dissolved organic matter (DOM), the sources of which are sinking dead phytoplankton cells. Meanwhile the generally accepted point of view on cause of increasing I with a depth z is absent. But some hypotheses are present¹, one of which explains I growth with z by the biological activity. Experiments show the correlation between $I(z)$ and ammonium and phosphate concentrations. But this hypothesis is not examined and it is based only on the fact of this correlation. In other hypothesis it is supposed that fluorescent matter of the sea water is sublimated on the surface of mineral particulate matter, that includes metals which can quench fluorescence. Fluorescent matter dissolves in the water during sedimentation these particles and it causes I growth. But quantitative calculations that an estimate a role of these processes in $I(z)$ growth are absent and experimental results do not confirm assumptions that were made. The third hypothesis explains I growth with depth by vertical diffusion of fluorescent components from sediments. But this effect can be significant only near the bottom. Kalle hypothesis also exists³. It explains dissolved fluorescence substance formation by Mayar reaction between dissolved aminoacides and hydrocarbons after its transition from sinking dead phytoplankton cells into the water. But results of calculations show that reaction velocity is very slow because of low DOM concentration. Moreover manners of $I(z)$ interpretation have qualitative nature and can not give quantitative description of hydrological characters influence on $I(z)$. Accompanying these reasons it is actual to give a new solution of the problem.

2. THEORETICAL MODEL

Our model is based on an assumption, that fluorescent matter forms generally in dead phytoplankton cells. The forming of new fluorescent matter may be caused by Mayar reaction as an example. The velocity of this reaction must be greater inside cells, than in surrounding water because of high reaction component's concentration. Thus the model proposed considers processes of accumulation fluorescent matter inside sinking particles of dead phytoplankton cells and dissolving organized fluorescent matter from particles into surrounding water.

Let us determine vertical distribution I caused by these reasons. Fluorescent intensity I can be expressed as a sum of two terms:

$$I(z) = I_d(z) + I_p(z) \quad (1)$$

where: I_p - fluorescent intensity of particulate matter
 I_d - fluorescent intensity of DOM

Absorption of exciting light and reabsorption of fluorescent emission by particle and their influence on fluorescence intensity were considered earlier^{2,5}. It was shown that fluorescence intensity I_p may be considerably lower, than I_d of equal fluorescent matter concentration. This effect was taken into account with help of Q^* factor. It presents in correlation between I_p and particulate fluorescent matter concentration. Its value depends on absorption coefficient and size of particle. A spectrum of optical density for detrital diatom cell was measured by microphotometric method⁴. It shows, that Q^* factor value may be considerably less than one. In assumption, that I_p and I_d are proportional corresponding concentrations, next expression can be written:

$$I_p(z) = \gamma Q^* C_p(z) I_0, \quad (2)$$

$$I_d(z) = \gamma C_d(z) I_0, \quad (3)$$

where: γ - proportionality coefficient
 C_p - fluorescent organic matter concentration inside particles
 C_d - fluorescent DOM concentration
 I_0 - exciting light intensity

Let us define the initial organic matter amount in the particle that is a source of forming fluorescent matter as q_0 . In assumption that fluorescent matter forming process can be described by the first order kinetic equation, we have:

$$\frac{dq_{fp}}{dt} = -(\lambda_1 + \lambda_2) \cdot q_{fp} + \lambda_1 \cdot F \cdot q_0, \quad (4)$$

where: q_p - amount of fluorescent matter in the particle
 λ_1 - constant of reaction velocity
 $\lambda_2 = u/V$, where: u - velocity of decreasing fluorescent matter in the particle
 V - volume of particle
 F - ratio of reaction coefficients

Equation for q_p after integration (4) is:

$$q_{fp} = \frac{\lambda_1 \cdot F \cdot q_0}{\lambda_1 + \lambda_2} \cdot \left(1 - e^{-(\lambda_1 + \lambda_2) \cdot t}\right). \quad (5)$$

Expression $\exp \{ -(\lambda_1 + \lambda_2) t \}$ describes a time dependency the initial organic matter concentration. Expression for particulate organic matter concentration in a water can be determined as $C_p(z) = q_p(t) N(z)$, where: $N(z)$ - particles number in the unit of water value on horizon with z depth. After transition from t to z parameter in equation (5) equation for C_p can be written:

$$C_{fp} = \frac{\lambda_1 \cdot F}{\lambda_1 + \lambda_2} \cdot \left(C_0(z) - C_p(z)\right). \quad (6)$$

We have for $I(z)$ from equations (1-3),(6):

$$I(z) = \gamma \cdot \left[\frac{\lambda_1 \cdot F \cdot Q^*}{\lambda_1 + \lambda_2} \cdot \left(C_0(z) - C_p(z)\right) + C_{fp}(z) \right] \cdot I_0. \quad (7)$$

Turbulent diffusion stationary equations for $C_0(z)$ and $C_p(z)$ are:

$$\frac{d}{dz} \left(K \cdot \frac{dC_0(z)}{dz} \right) - (v + w) \cdot \frac{dC_0(z)}{dz} = 0, \quad (8)$$

$$\frac{d}{dz} \left(K \cdot \frac{dC_p(z)}{dz} \right) - (v + w) \cdot \frac{dC_p(z)}{dz} - \lambda \cdot C_p(z) = 0, \quad (9)$$

where: K - vertical turbulent diffusion coefficient,
 v - sinking velocity of particles,
 w - vertical component of stream velocity,
 $\lambda = \lambda_1 + \lambda_2$

Vertical stratification $C_{fd}(z)$ can be determined from equation (10) that takes into account transition of fluorescent matter from the particle into solution and its destruction:

$$\frac{d}{dz} \left(K \cdot \frac{dC_{fd}(z)}{dz} \right) - w \cdot \frac{dC_{fd}(z)}{dz} + \lambda_2 \cdot C_{fp}(z) - \lambda_3 \cdot C_{fd}(z) = 0, \quad (10)$$

where: λ_3 - parameter inversely proportioned the time of fluorescent DOM mineralizing.
 With help of equations (7-10) numerical values $I(z)$ can be received in spite of arbitrary hydrophysical characteristics distribution.

3. RESULTS

As an example of using the new model let us consider $I(z)$ dependence on hydrophysical characters, when homogeneous distribution water density with depth z and $w = 0$ are present. We have made assumption that general contribution in I value is caused by I_d and I_p role is small. This condition is true for rather big particles of dead phytoplankton. Equation (8) has analytical decision and gives $C_0 = \text{Const}$. Decisions of equations (9),(10) were found with help of numerical method. Calculations were done for depths 0-1000 meters with 10 m discreteness and for boundary conditions: $C_p = C_0$; $C_{fp} = 0$, when $z = 0$ and $C_p = 0$; $dC_p/dz = 0$ when $z \rightarrow 1000$. Maximum parameter λ_3 value was chosen 10^{-6} c^{-1} , $\lambda_1 = \lambda_2$, $\lambda = \lambda_3$. Value of w was considered zero. Calculated profiles $I(z)$ in relative scale are presented on figure 2. It is clear, that this model of vertical stratification forming $I(z)$ with using reasonable initial parameters allows to describe character and value intensity of sea water fluorescence variation with depth, that experimentally observed (see figure 1). Data that are presented on figure 2, show more rapid growth I with depth on high horizons than in deep, when increases. Opposite influence on $I(z)$ function is founded when v and K increases.

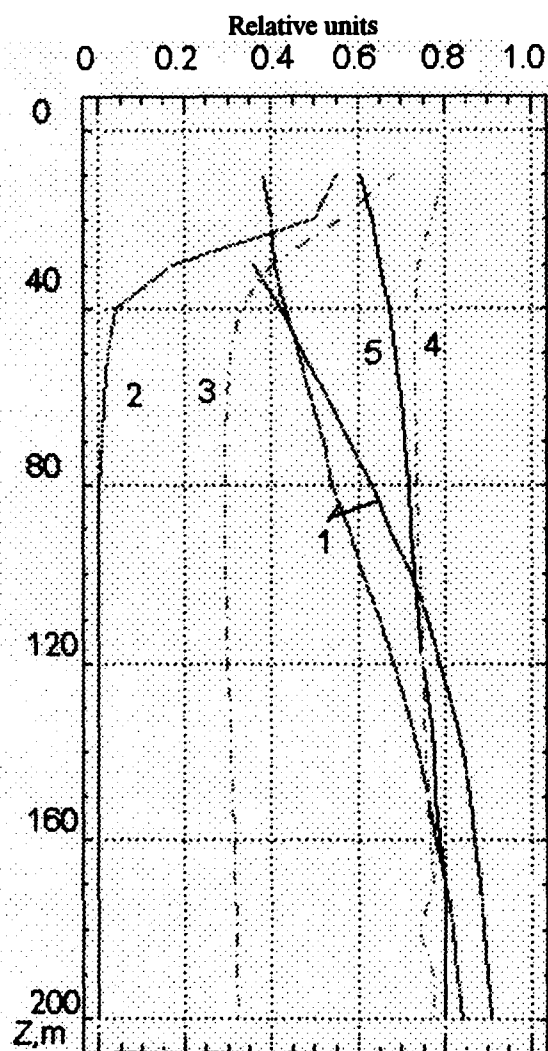


Figure 1. Experimental distributions $I(z)$ and some other characters of water in the Black Sea

- 1 - $I(z)$
- 2 - Chlorophyll fluorescence intensity $I_{ch}(z)$
- 3 - temperature $T(z)$
- 4 - electroconductivity $\xi(z)$
- 5 - density $\rho(z)$

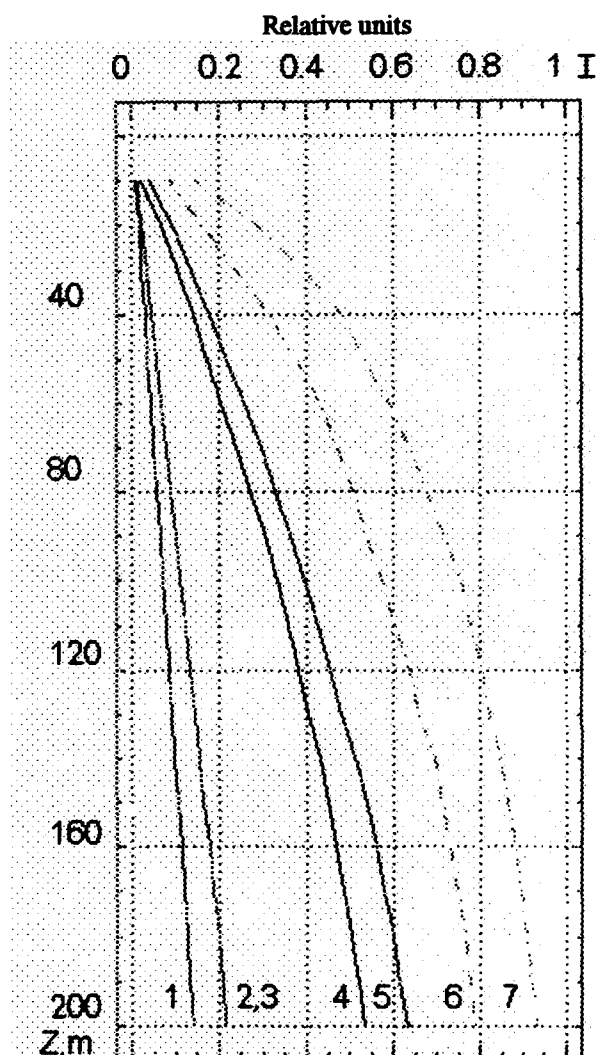


Figure 2. Theoretical distribution $I(z)$ for $w = 0$ and for different values K, λ, v .

- 1. $\text{cm}^2\text{c}^{-1}, \lambda = 10^{-8} \text{ c}^{-1}, v = 10 \text{ cm c}^{-1}$,
- 2. $K = 100 \text{ cm}^2\text{c}^{-1}, \lambda = 10^{-7} \text{ c}^{-1}, v = 10 \text{ cm c}^{-1}$
- 3. $K = 10 \text{ cm}^2\text{c}^{-1}, \lambda = 10^{-7} \text{ c}^{-1}, v = 10 \text{ cm c}^{-1}$
- 4. $K = 10 \text{ cm}^2\text{c}^{-1}, \lambda = 10^{-7} \text{ c}^{-1}, v = 10 \text{ cm c}^{-1}$
- 5. $K = 10 \text{ cm}^2\text{c}^{-1}, \lambda = 10^{-7} \text{ c}^{-1}, v = 10 \text{ cm c}^{-1}$,
- 6. $K = 0,1 \text{ cm}^2\text{c}^{-1}, \lambda = 10^{-7} \text{ c}^{-1}, v = 10 \text{ cm c}^{-1}$,
- 7. $K = 0,1 \text{ cm}^2\text{c}^{-1}, \lambda = 10^{-7} \text{ c}^{-1}, v = 10 \text{ cm c}^{-1}$,

4. CONCLUSION

The present results are somewhat preliminary. A detailed comparison of described model predictions with experimental results in different controlled hydrological conditions would be useful. It is necessary to notice, that considered process of $I(z)$ forming takes a predominant role on horizons, that deeps lower then photic zone is situated. Satisfactory conformity between theory and experiment in photic zone may be obtained only after additional factors

consideration. Some of these factors are photochemical degradation of fluorescent matter and presence of fluorescent components in vital phytoplankton cells.

5. ACKNOWLEDGEMENTS

We would like to thank Dmitry V. Ivanov for his assistance with the preparation of this manuscript.

6. REFERENCES

1. P.G.Coble ,et.al., "Vertical distribution of dissolved and particulate fluorescence in the Black Sea", *Deep-Sea Res.*, Vol.38, suppl. 2., pp.986-1001, 1991.
2. D.I.Collins,et.al., "The role of reabsorption in the spectral distribution of phytoplankton fluorescence emission", *Deep-Sea Res.*, Vol.32, pp.983-1003, August 1985.
3. K.Kalle, "Über das Verhalten und die Herkunft in der Gewässern und in der Atmosphäre Vorhandenen himmelblauen". *Fluoreszenz-Dt. Hydrogr. Zc.*, Bd. 16, N 4, 1963.
4. B.G.Mitchell, D.A.Kiefer, "Variability in pigment specific particulate fluorescence and absorption spectra in the northeastern Pacific Ocean" *Deep-Sea Res.*, Vol.35, pp.665-689, May 1988.
5. V.M.Sidorenko, S.A.Pakkonen, "Intensity of water fluorescence variation caused by organic matter transition from suspended state into the solution", *Proceeding SPIE*, V.2258, *Ocean Optic XII*, 1994.
6. A.I.Agatova, B.B.Saposchnikov, N.I.Torgunova, "New results in biohydrochemistry of the Black Sea organic matter". *Doklady Akad.Nauk SSSR*, Vol.309, pp.706-709, March 1989.

Problem of ocean hydrophysical parameters
evaluation from multispectral optical sensing data

A.G.Zhurenkov, V.A.Yakovlev

Vavilov State Optical Institute
Department of Hydrooptics & Termovision
3 Pochtamtskay st., St.Petersburg, Russia, 190000

ABSTRACT

The problem of multispectral remote measurements of ocean hydrophysical characteristics by means of optical methods is discussed. The algorithm and method of such measurements are proposed.

1. INTRODUCTION

The object of this work is to solve the problem of the ocean hydrophysical and ecological parameters reconstruction from the multispectral optical sensing data. We are carrying out the analysis of that problem in several ways:

- we are solving the inverse problem of the radiation transfer theory, real parameters of the medium under investigation being taken into account;
- we are elaborating the realistic models of the sea so as to provide a possibility of both reducing the reconstruction errors to a minimum and regularizing the solution of the corresponding inverse problem;
- we are elaborating the corrective methods for the remote sensing data received through a disturbed water surface, both the subsurface multispectral optical sensing data and the analysis of a sky radiation being exploited.

2. MODEL DESCRIPTION

In the analysis we make such admissions as:

- the optical properties of the sea water (OPSW) are described by the linear model;
- there is a variability of OPSW due to a finite set of dashes and dissolved matters being in the sea water;
- the vertical stratification of OPSW is approximated by a piece-linear function of depth (in particular: linear or piece-constant);
- solving the problem we make use of the two-stream approach of the radiation transfer theory;
- factors distorting the multispectral optical sensing data (conditions of atmosphere and sea surface, device factors, etc.) are constant everywhere over the region under investigation during the research;
- the contact sensing of the sea medium is made by registering upward and downward irradiance streams as functions of depth;
- the spectral widths in use is sufficiently small ($\Delta\lambda/2 \approx 10$ nm).

In which case the optical parameters of the sea water can be written as:

$$\alpha(\lambda, z) = \alpha_0(\lambda) + \sum_{k=1}^K \alpha_k(\lambda) C_k(z), \quad \sigma(\lambda, z) = \sigma_0(\lambda) + \sum_{k=1}^K \sigma_k(\lambda) C_k(z), \quad (1)$$

where

$\kappa(\lambda, z)$, $\sigma(\lambda, z)$ are absorption and scattering coefficients respectively (λ is a wavelength and z is a depth),

$\kappa_0(\lambda)$, $\sigma_0(\lambda)$ are the same parameters of the clear sea water,

$C_k(z)$ is a concentration of the k -dash,

$\kappa_k(\lambda)$, $\sigma_k(\lambda)$ are k -dash additions to the respective parameters, the concentration of this dash being equal to unit,

K is the overall number of the dashes in the model.

The model of the vertical distribution has the form

$$C_k(z) = t_{ki}(z - z_{i-1}) + y_{ki}, z \in [z_{i-1}, z_i], \quad (2)$$

$$i = 1, M+1, z_0 = 0, z_{M+1} < \infty, \text{ where}$$

$M+1$ is the number of layers in the model,

z_i is the down bound depth of the i -layer,

y_{ki} is the k -dash concentration at $z = z_{i-1}$,

t_{ki} is the k -dash concentration gradient within the i -layer.

3. DERIVED EXPRESSIONS

For these admissions, for the ocean albedo $R(\lambda)$ (without regard for a surface reflection) we obtain
a) for $t_{ki}=0$ ($\forall k, \forall i$)

$$R(\lambda) = 0.5 \left[B_1(\lambda) A_1^{-1}(\lambda) + \sum_{i=1}^M \left\{ [B_{i+1}(\lambda) A_{i+1}^{-1}(\lambda) - B_i(\lambda) A_i^{-1}(\lambda)] \exp \left[-2 \sum_{m=0}^{i-1} (A_{m+1}(\lambda) (z_{m+1} - z_m)) \right] \right\} \right] \quad (3a)$$

b) for $M=0$

$$R(\lambda) = b/(2a) + \sqrt{\pi/(4a)} (B - bA/a) \operatorname{erfc}(x) \exp(x^2), \quad (3b)$$

$$x = A_1(\lambda) [a_1(\lambda)]^{1/2}, A = A_1(\lambda), B = B_1(\lambda), a = a_1(\lambda), b = b_1(\lambda).$$

Where

$$A_i(\lambda) = \mu^{-1} \left(\kappa_0(\lambda) + \phi_0 \sigma_0(\lambda) + \sum_{k=1}^K [\kappa_k(\lambda) + \phi_k \sigma_k(\lambda)] y_{ki} \right), \quad (4)$$

$$a_i(\lambda) = \mu^{-1} \sum_{k=1}^K [\kappa_k(\lambda) + \phi_k \sigma_k(\lambda)] t_{ki},$$

$$B_i(\lambda) = \mu^{-1} \left(\Phi_0 \sigma_0(\lambda) + \sum_{k=1}^K \Phi_k \sigma_k(\lambda) y_{ki} \right), \quad b_i(\lambda) = \mu^{-1} \sum_{k=1}^K \Phi_k \sigma_k(\lambda) t_{ki},$$

μ, Φ_k ($k = 0, K$) are the parameters of the two-stream approach^{1,2}.

It is assumed that $\alpha_0(\lambda), \alpha_k(\lambda), \sigma_0(\lambda), \sigma_k(\lambda)$ are known and y_{ki}, t_{ki}, z_i are values will be found.

4. EXPERIMENTAL PROCEDURE

We assume L to be the total number of spectral bands of the our device. With the proviso that $L \geq 2K(M+1)+M$, the equations (3) and (4) are solved by usual methods for the parameters t_{ki}, y_{ki} and z_i . Below we will be describing the experimental procedure making use of the presented expressions.

At any point (with the coordinate r_0) on the region under investigation the parameters $\alpha(\lambda, z)$ and $\sigma(\lambda, z)$ are measured by the contact method on wavelengths of λ_j ($j=1, L$). In order for this work to be done, upward ($E_{\uparrow}(\lambda, z)$) and downward ($E_{\downarrow}(\lambda, z)$) irradiance streams as functions of depth need to be measured.

In that case

$$\phi\sigma(\lambda, z) = \mu \frac{E_{\uparrow}(\lambda, z) \frac{dE_{\downarrow}(\lambda, z)}{dz} + E_{\downarrow}(\lambda, z) \frac{dE_{\uparrow}(\lambda, z)}{dz}}{E_{\uparrow}^2(\lambda, z) - E_{\downarrow}^2(\lambda, z)}, \quad (5)$$

$$\alpha(\lambda, z) = \mu (E_{\downarrow}(\lambda, z) - E_{\uparrow}(\lambda, z)) \frac{\frac{dE_{\downarrow}(\lambda, z)}{dz} - \frac{dE_{\uparrow}(\lambda, z)}{dz}}{E_{\uparrow}^2(\lambda, z) - E_{\downarrow}^2(\lambda, z)}, \text{ where}$$

(This is true for the two-parameter-two-stream approach only.)

When $E_{\uparrow}^2(\lambda, z) \ll E_{\downarrow}^2(\lambda, z)$ and $\left| E_{\uparrow}(\lambda, z) \frac{dE_{\uparrow}(\lambda, z)}{dz} \right| \ll \left| E_{\downarrow}(\lambda, z) \frac{dE_{\downarrow}(\lambda, z)}{dz} \right|$, then

$$\phi\sigma(\lambda, z) \cong -\frac{\mu}{E_{\downarrow}(\lambda, z)} \left[\frac{dE_{\uparrow}(\lambda, z)}{dz} + \frac{E_{\uparrow}(\lambda, z)}{E_{\downarrow}(\lambda, z)} \frac{dE_{\downarrow}(\lambda, z)}{dz} \right], \quad (5')$$

$$\alpha(\lambda, z) \cong - \left[\frac{\mu}{E_{\downarrow}(\lambda, z)} \frac{dE_{\downarrow}(\lambda, z)}{dz} + \phi\sigma(\lambda, z) \right].$$

The last admission permits the vertical distribution in deriving the expressions (3) to take into account.

In what follows we find the parameters M (for the model) and y_M, t_M, z_i ($i=1, M+1, k=1, K$) (in this point) so as the expressions (1) and (2) to be best approximation of the measured functions. At the same time the values of a sea surface brightness $I_T^*(\lambda_j, r)$ are measured by the remote sensing everywhere over the region with the resolution as better as possibly. The symbol * indicates that these values distorted by factors not connected with the subject under investigation. The "normalized" downward irradiance stream on the region is to be found as

$$I_d^*(\lambda_j) = I_T^*(\lambda_j, r_s) / R(\lambda_j, r_s), \quad (6)$$

where

$R(\lambda_j, r_s)$ is albedo at the point r_s calculated by the formulas (3).

Then

$$R^*(\lambda_j, r) = I_T^*(\lambda_j, r) / I_d^*(\lambda_j) \quad (7)$$

is the "corrected" albedo at a some point r on the region. The influence of distorting factors on $R^*(\lambda_j, r)$ is expect to be reduced.

5. CONCLUSION

The presented procedure enables the temporal characteristics of the vertical and horizontal distributions of the sea water ecological parameters everywhere over the region under investigation with the resolution defined by parameters of the devices in use to reconstruct. This procedure makes use of both the sea surface optical remote sensing data measured everywhere over the region and the vertical distribution of the sea water optical properties received in a limited number of points on that region. Also the signal treatment algorithm is elaborated. It allows the addition of the radiation reflected by the sea surface to exclude.

6. REFERENCES

1. Zege E.P., Ivanov A.P., Katzev I.L. *Perenos izobrazheniya v rasseivayuschaey srede*. (Image transfer in scattering medium). Minsk.: Nauka i tehnika, 1985. 327 p.
2. Van de Hulst H.C. *Multiple Light Scattering. Tables, Formulas and Applications*. V.1 and 2. New York: Academic Press, 1980 739 p.

IN SITU EVALUATION OF A SHIP'S SHADOW

Christian T. Weir¹, D.A. Siegel¹, A.F. Michaels² and D.W. Menzies¹

1-Center for Remote Sensing and Environmental Optics and Department of Geography, University of California at Santa Barbara, Santa Barbara, CA 93106, USA

2-Bermuda Biological Station for Research, Ferry Reach, GE 01, Bermuda

ABSTRACT

In situ measurements of optical properties made from a ship can be biased by the ship's shadow. In an effort to evaluate the ship shadow perturbation created by the *R/V Weatherbird II*, profiles of downwelling irradiance, $E_d(z, \lambda)$, upwelling radiance, $L_u(z, \lambda)$, as well as derived apparent optical properties (AOPs) were obtained at distances of 1, 3, 6 and ≥ 20 m off the ship's stern. Two statistical analyses are explored here. The first compares the mean difference between simultaneously obtained fluxes and AOPs sampled at distances greater than 20 m from the ship to those taken 1 and 6 m off the stern. The second analysis compares derived AOPs taken at each of the four distances throughout the length of the experiment. Only rarely are significant differences found for data beyond three meters off the ship's stern; however at 1 m off the stern significant discrepancies are intermittently observed. This work illustrates that the inherent sources of noise in determining fluxes and AOPs in the upper ocean are generally greater than the effects incurred by the ship's own shadow under optimal conditions.

INTRODUCTION

Accurate measurements of apparent optical properties (AOPs) are required in order to develop a detailed understanding of processes regulating bio-optical property distributions and their relationship to remotely sensed signals. Instrumentation designed to measure properties of the underwater radiation field deployed at relatively close distances to a ship may encounter perturbations caused by the ship's shadow (e.g., Poole, 1936; Strickland, 1958; Gordon 1985; Voss *et al.*, 1986; Waters *et al.*, 1990; Helliwell *et al.*, 1990). This source of error is of obvious importance and must be accurately assessed. Poole (1936) estimated that the ship shadow error under diffuse skylight is about 10% at 5 m depth when the radiometer is deployed ~2 m off the stern and it decreases with depth. The Monte-Carlo simulations by Gordon (1985) indicate that the error in downwelling irradiance rarely exceeds 2% as long as skies are clear and the sun is within 45 degrees of the stern. However at low solar elevations, these errors can increase to about 10%. Gordon (1985) also shows that the errors are reduced as the instrument is moved horizontally away from the ship although errors during diffuse light conditions may remain as high as 30%. Voss *et al.* (1986) conducted an experiment with an extendible sea-going crane which showed that values of upwelling radiance, $L_u(z, \lambda)$, decrease by 10 to 20% unless the instrument is deployed more than 5 m from the ship.

Ship shadow perturbations are likely to be the greatest near the sea surface. This is critical for the development of ocean color algorithms as the maximum accuracy must be insured for parameters, such as the remote sensing reflectance, $R_{rs}(\lambda)$. Several studies have attempted to avoid the ship's shadow completely by floating optical instrumentation a considerable distance from ship (Gordon and Clark, 1980; Clark, 1981; Waters *et al.*, 1990). However, these deployment strategies are difficult to conduct operationally, particularly in rough seas, and place severe limits on the amount of data that can be collected, its linking to other oceanographic observations, and the time-scales resolved (e.g., Dickey and Siegel, 1993).

In order to completely avoid the ship's shadow when making measurements of downwelling irradiance, $E_d(z, \lambda)$, the SeaWiFS Ocean Optics Protocols (Mueller and Austin 1992) suggest that the deployment of optical instrumentation should be at a distance, ζ_d , in order to avoid the ship's shadow. Mueller and Austin (1992) define ζ_d using

$$\zeta_d = \frac{\sin(48.4^\circ)}{K_d(\lambda)} \quad (1a)$$

where $K_d(\lambda)$ is the diffuse attenuation coefficient for downwelling irradiance. Typical values for $K_d(\lambda)$ off Bermuda range from 0.02 to 0.08 m^{-1} (Siegel *et al.*, 1994) which result in recommended deployment distances of 9 to 40 meters from ship's stern. Similarly, recommendations for deployment distances for $E_u(z, \lambda)$ and $L_u(z, \lambda)$ (ζ_u and ζ_L , respectively) are given by Mueller and Austin (1992) as

$$\zeta_u = \frac{3}{K_u(\lambda)} \quad (1b)$$

$$\zeta_L = \frac{1.5}{K_L(\lambda)} \quad (1c)$$

where $K_u(\lambda)$ and $K_L(\lambda)$ are the diffuse attenuation coefficients for upwelled irradiance and radiance, respectively. Values of $K_u(\lambda)$ and $K_L(\lambda)$ are roughly equal to values of $K_d(\lambda)$. Typical values of ζ_u and ζ_L are greater than 30 m, which is nearly the length of the ship used in this study (the *R/V Weatherbird II*; length 35.05 m). The distances recommended by these relations are based only on geometric relations and are independent of ship size, sky and sea condition, deployment method and orientation of the ship with respect to the solar beam.

Here, we examine the effects of ship shadows upon data collected from the *R/V Weatherbird II* (length 35.05 m, beam 8.53 m, draft 2.60 m). The *R/V Weatherbird II* is used by the Bermuda Bio-Optics Project (BBOP) to make routine spectroradiometer casts in conjunction with the Joint Global Ocean Flux Study (JGOFS) Bermuda Atlantic Time-series Study (BATS). Spectroradiometer profiles were made using the BBOP package with an extendible boom which allowed profiles to be made from up to 6 m off the stern of the *R/V Weatherbird II*. These data are compared with data collected using the optical free-falling instrument (OFFI; Waters et al., 1990). The OFFI data provide a "control" from which we can search statistically for the effects of the ship's shadow. The measurements used were made under optimal conditions (i.e., clear skies, ship oriented with stern to sun, near-constant illumination, etc.) and hence, provide the basis for evaluating the role of the ship shadows in developing ocean color remote sensing algorithms using the BBOP data set.

DATA AND METHODS

The present observations were made from the *R/V Weatherbird II* off Bermuda on July 7, 9 and 10, 1992. Two underwater spectroradiometers, the BBOP and OFFI, were lowered simultaneously from the *R/V Weatherbird II* to about 50 m (fig. 1). The BBOP package consisted of a MER-2040 underwater spectroradiometer, (Biospherical Instruments, San Diego, CA) interfaced with a SeaTech transmissometer, chlorophyll fluorometer and SeaBird conductivity, temperature and pressure sensors (Siegel et al., 1994a). The OFFI is a modification of a MER-2020 underwater unit with a case outfitted with buoyant fins to give stability and control in its descent rate (Waters et al., 1990). The BBOP was lowered at three distances off the stern (1, 3 and 6 m) using an extended boom. The OFFI was "fished out" to at least 20 m from the ship before descent. Profiles were made simultaneously so that instantaneous fluxes from the two instruments could be compared. Both instruments were deployed with the sun off the stern so that the ship's shadow trailed away and behind, which is part of the normal BBOP sampling procedure. Both instruments sampled downwelling irradiance, $E_d(z, \lambda)$, and upwelling radiance $L_u(z, \lambda)$, in spectral wavebands centered at 410, 441, 488, 520 and 565 nm.

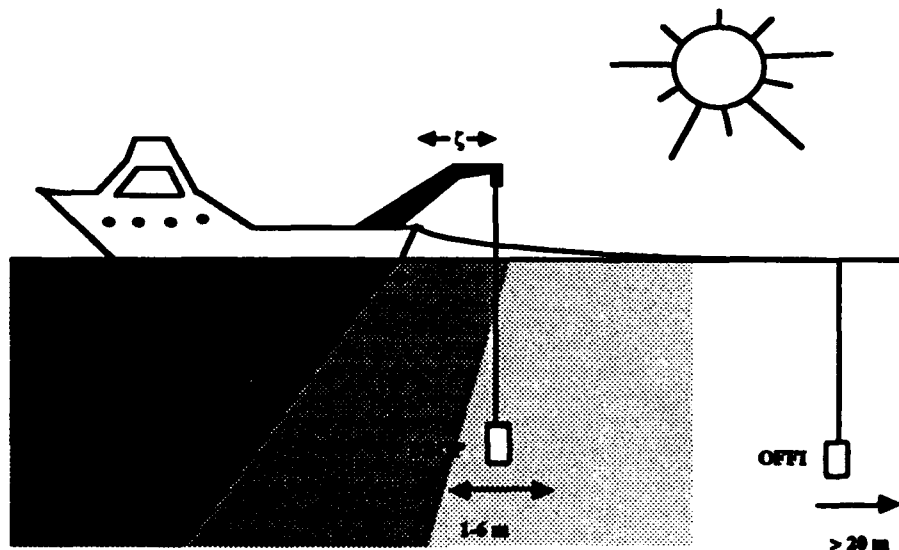


Figure 1: Diagram of the BBOP ship shadow evaluation experimental design.

Radiometric calibrations were performed on both instruments two weeks prior to the cruise and two months after using calibration facilities at the University of California at Santa Barbara. The same calibration lamp (UCSB lamp F-303) was used for both calibrations. The calibration coefficients for the BBOP instrument varied by less than 0.5% for irradiance and less than 3% for radiance between both calibration dates. The OFFI calibration coefficients differed by 1 to 4% for

both the irradiance and radiance channels. Calibration coefficients from the pre-cruise determinations were used for the present analysis.

The two individual bio-optical data sets were processed using the BBOP data processing system (Sorensen *et al.*, 1994, this volume). The BBOP data processing system is used to eliminate radiation values below a specified threshold, identify time segments where cloud perturbations were minimal, smooth and despiked specified channels of data (although not $E_d(z, \lambda)$ or $L_u(z, \lambda)$), and bin the data into 1 m vertical depth bins. Derived apparent optical properties (AOPs), such as the remote sensed reflectance, $R_{rs}(z, \lambda)$, and the diffuse attenuation coefficient for downwelling irradiance, $K_d(z, \lambda)$, are also calculated. In addition, the downwelling irradiance and upwelling radiance spectra just beneath the sea surface, $E_d(0, \lambda)$ and $L_u(0, \lambda)$, are determined by fitting profile data from the upper 20 m to the Beer-Lambert relation. Sorensen *et al.*, (1994, this volume) gives a complete description of BBOP data processing system and data handling procedures used by BBOP.

ANALYSIS AND RESULTS

Two distinct statistical analyses are performed to evaluate the effects of the *R/V Weatherbird II's* shadow. The first analysis compares the statistical differences between simultaneously sampled BBOP and OFFI data as the BBOP radiometer is deployed at various distances off the ship's stern. Here, differences between the two data sets are interpreted to indicate the effects of the ship shadow after accounting for a constant calibration error and the occurrence of random errors (i.e., noise). This analysis will be referred to as the simultaneous comparison. The second analysis compares mean values of derived AOPs at each of the four distances (1, 3, 6 and > 20 m) throughout the experiment and is referred to as the multi-distance comparison. The object of this comparison is to address whether any significant differences can be found among the determinations of apparent optical properties.

Simultaneous Comparison.

The simultaneous comparison evaluates the statistical difference between fluxes and AOPs measured by the BBOP profiler obtained at two distances off the ship's stern and identical parameters determined using the OFFI profiler. The BBOP casts with $\zeta = 1$ m are referred to as the CLOSE casts and the BBOP casts with $\zeta = 6$ m are denoted as FAR. A total of 15 paired OFFI-BBOP casts (7 FAR and 8 CLOSE casts) are used in this analysis. Data from the two instruments are estimated to be collected "simultaneously" to within 5 seconds. The statistical difference between OFFI and BBOP measurements of downwelling irradiance, upwelling radiance, and derived AOPs are compared. A positive difference means that the BBOP measurements underestimate the OFFI values which may indicate a ship shadow. Throughout, the error bars shown correspond to 90% confidence intervals for the mean estimates.

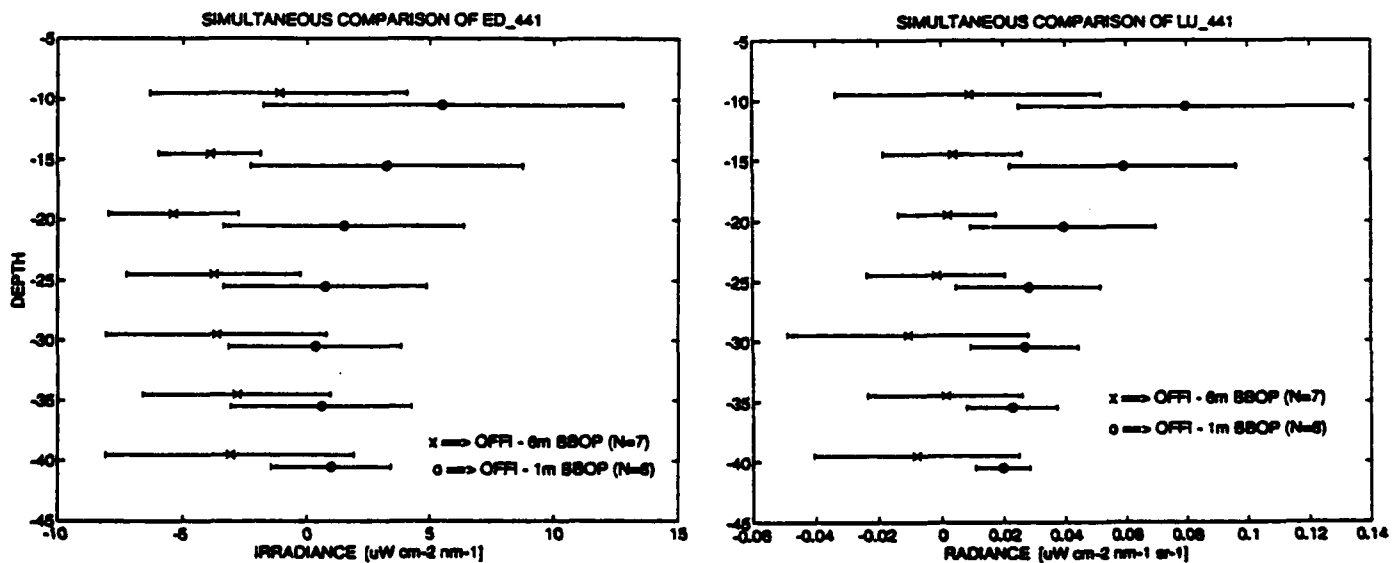


Figure 2: Mean differences (with 90% c.i.) of simultaneous determinations of a) downwelling irradiance at 441 nm and b) upwelling radiance at 441 nm between OFFI casts and CLOSE ('o'; 1 m off stern) and FAR ('x'; 6 m off stern) casts.

For the determination of downwelling irradiance at 441 nm, there are no statistically significant differences (at the 90% confidence level) between the OFFI casts and either the CLOSE or the FAR casts (fig. 2a). However, the CLOSE mean differences are consistently positive suggesting that the CLOSE casts may be affected by the ship's shadow although not in a statistically significant manner. The CLOSE-OFFI difference increases as the sea surface is approached which also suggests the signature of a ship shadow. The vertical profile of the FAR-OFFI differences does not give any indication of a ship shadow influence. The other matching λ 's (410, 488, 520 and 565 nm) for $E_d(z, \lambda)$ show similar results (not shown). The difference between the CLOSE and OFFI upwelled radiance data at 441 nm, $L_u(z, 441)$, are significantly different from zero and show a "ship shadow pattern" with depth as the mean difference increases significantly towards the sea surface (fig. 2b). This difference is particularly apparent over the top 20 m as these differences decrease with depth. The FAR-OFFI mean difference for $L_u(z, 441)$ shows no statistically significant pattern with depth. This reduction in ship shadow effects with distance from the ship is consistent with previous studies.

In terms of the derived AOPs ($K_d(z, \lambda)$ and $R_{rs}(z, \lambda)$), there are no significant differences found between either the CLOSE or FAR BBOP casts and the OFFI data (figs. 3). In particular, there are no consistent variations in these differences with depth that may be simply attributed to a ship shadow. This is true even for the mean $R_{rs}(z, \lambda)$ differences (fig. 3b) where the OFFI-CLOSE $L_u(z, \lambda)$ observations showed some deviations attributed to the ship's shadow. This lack of a signature in $R_{rs}(z, \lambda)$ may be due to the fact that both the OFFI-CLOSE $L_u(z, \lambda)$ and $E_d(z, \lambda)$ determinations are affected by the ship shadow. The decrease in both of the signals ratio to derive $R_{rs}(z, \lambda)$ may actually cancel the effects of the ship shadow.

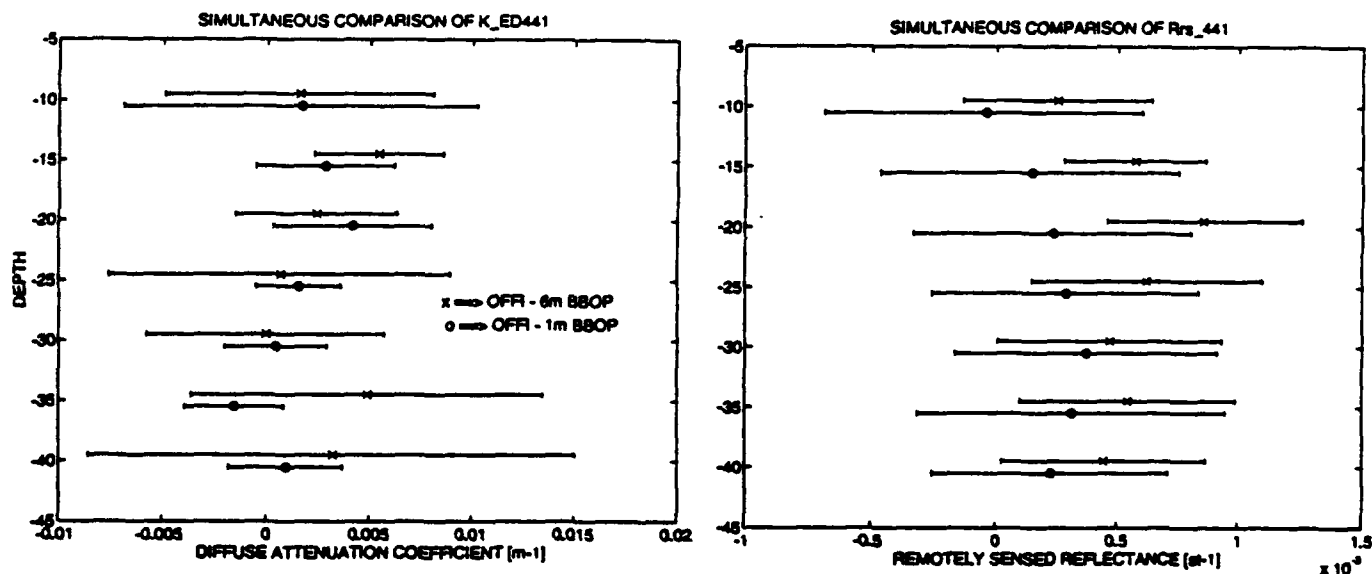


Figure 3: Mean differences (with 90% c.i.) of simultaneous determinations of a) the diffuse attenuation coefficient for downwelling irradiance, $K_d(z, 441)$, and b) the remotely sensed reflectance, $R_{rs}(z, 441)$, between OFFI casts and CLOSE ('o'; 1 m off stern) and FAR ('x'; 6 m off stern) casts.

The accurate determination of the upwelling and downwelling light streams just beneath the sea surface is critical for the development of algorithms for estimating bio-optical properties from space-borne sensors. The differences between the OFFI and BBOP estimates of $E_d(0, \lambda)$ and $L_u(0, \lambda)$ for both the CLOSE and FAR distances off the stern are shown in figure 4. The mean $E_d(0, \lambda)$ differences show no significant differences from zero or between the two deployment distances (fig. 4a). However, significant differences are found for the mean $L_u(0, \lambda)$ differences for all wavelengths except for 565 nm. Significant differences are also found for some of the wavelengths in the FAR-OFFI difference although it is unclear how large of a calibration difference remains between the two instruments. In particular, the size of the disparity in the mean differences between the two BBOP deployment distances increases as λ is decreased. These spectral observations are consistent with numerical results which indicate that the ship shadow effects scale as $c(\lambda) \zeta$ where $c(\lambda)$ is the beam attenuation coefficient and ζ is the distance from the ship (Gordon, 1985). The value of $c(\lambda)$ at 565 nm is likely to be larger than its value at 441 nm. Further, these results show that the influence of the ship's shadow is more critical for the upwelling light stream rather than downwelling light as is expected (cf., Mueller and Austin, 1992).

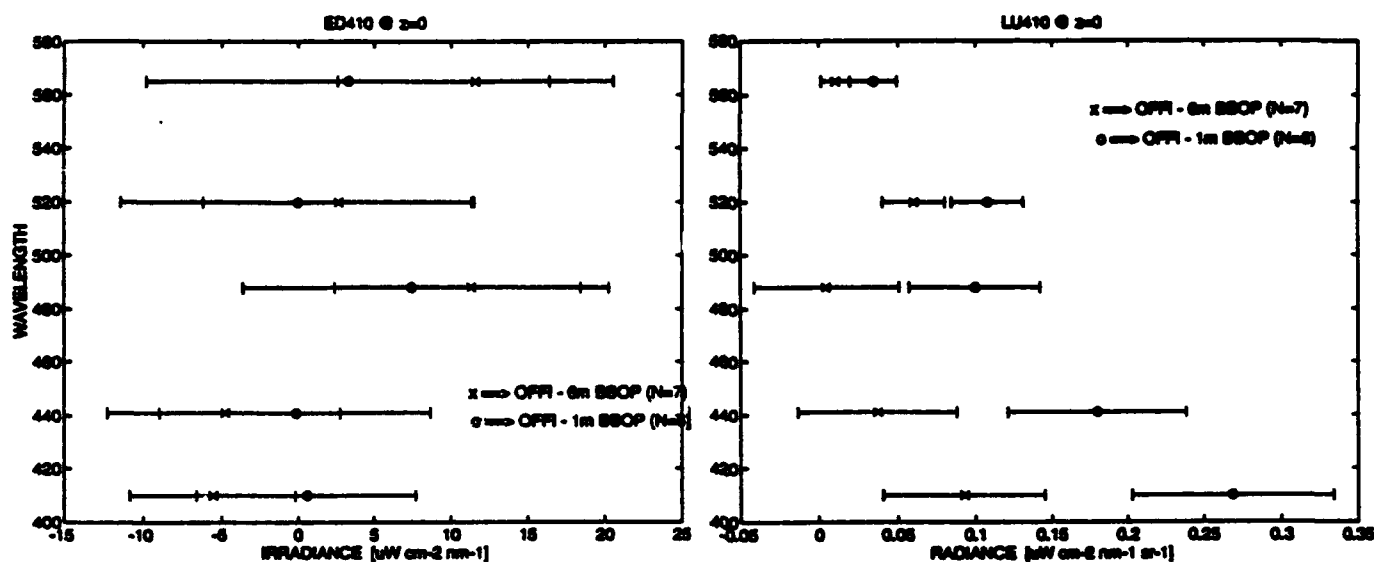


Figure 4: Mean differences (with 90% c.i.) of simultaneous determinations of a) the downwelling irradiance spectrum just beneath the sea surface, $E_d(0^-, \lambda)$, and b) the upwelling radiance spectrum just beneath the sea surface, $L_u(0^-, \lambda)$, between OFFI casts and CLOSE ('o'; 1 m off stern) and FAR ('x'; 6 m off stern) casts.

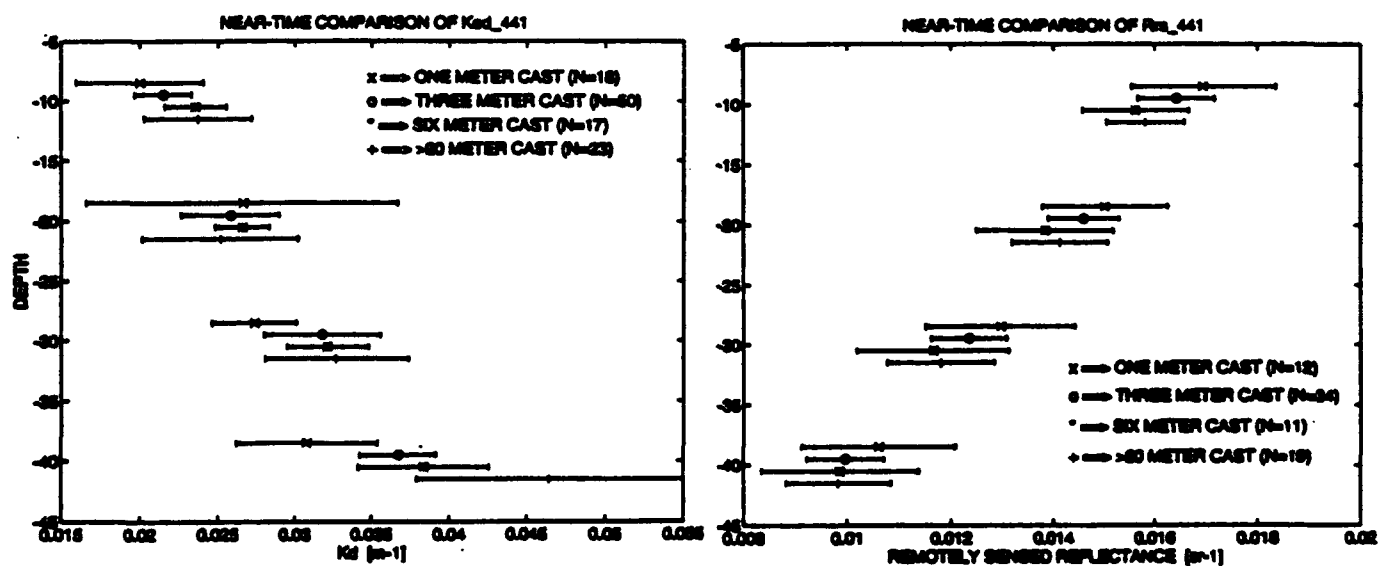


Figure 5: Mean (with 90% c.i.) determinations of a) the diffuse attenuation coefficient for downwelling irradiance, $K_d(z, 441)$, and b) the remotely sensed reflectance, $R_{rs}(z, 441)$, as a function of depth for four different deployment distances (1, 3, 6 and > 20 m).

Multi-Distance Comparison

The second analysis compares mean values of derived apparent optical properties (AOPs) at each of the four distances (1, 3, 6 and >20m) throughout the experiment. All available casts are used for this analysis and the determinations of AOPs are classified by their distance from the stern of the *R/V Weatherbird II*. Distances of 1, 3, 6 and >20 m are used here. The variations in the diffuse attenuation coefficient and remote sensed reflectance at 441 nm with depth and deployment distance are shown in figures 5. Only rarely are there statistically significant differences (i.e., non-overlapping error bars) for the four deployment distances; although trends with distance are apparent. Similar results are found with the other wavelengths sampled (not shown).

Spectral differences in the remote sensed reflectance just beneath the sea surface, $R_{rs}(0^-, \lambda)$, can be used to surmise the spectral structure of the ship's shadow (fig. 6). Again, no significant differences are found for any of the wavelengths. This again suggests that the effects of the ship shadow on the upwelled light field may be effectively "canceled out" when normalized by the downwelling irradiance.

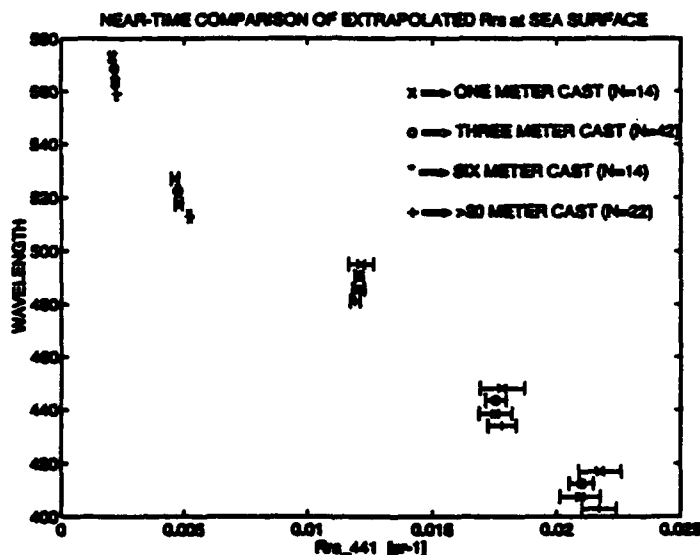


Figure 6: Spectral structure of the remote sensed reflectance just beneath the sea surface, $R_{rs}(0^-, \lambda)$, evaluated at 4 different deployment distances (1, 3, 6 and > 20 m).

DISCUSSION AND CONCLUSIONS

In order to correctly interpret the present results, one must recognize that the observed mean differences are a composite of one or more signals: the actual ship shadow perturbation, a constant calibration difference between the OFFI and BBOP and random errors due to the poor sampling of short time-scale noise (i.e., wave glint, small clouds, ship roll, etc.). Much of the noise can be reduced by averaging over many individual casts; however, the sample size for the simultaneous comparison is relatively small ($N=7$ or so). Differences between the pre- and post-cruise calibrations indicate that only small differences in calibrations occur. Thus, the mean difference observed is primarily composed of the ship shadow perturbation as modulated by an incompletely sampled random noise field. It is this elucidation of the ship shadow perturbation above this random noise element which is the present goal.

The results of the simultaneous comparison shows that there are no significant differences between the comparison of OFFI $E_d(z, \lambda)$ values and either FAR or CLOSE irradiance determinations (fig. 2a). This is consistent with the irradiance direct beam "cone" remaining off the stern (see also Gordon 1985 and Voss et al., 1986). However, the determination of upwelled radiance shows the effects of the ship shadow clearly for the CLOSE comparison, but not for the FAR (fig. 2b). A strong difference is also observed between the CLOSE and FAR mean differences of $L_u(0^-, \lambda)$ (fig. 4b). At all wavelengths CLOSE mean differences were consistently larger than those calculated from FAR data, with the OFFI value being predictably and significantly greater than its simultaneous BBOP measurement. These results show clearly that BBOP data must be taken more than 1 m off the stern of the *R/V Weatherbird II*, but not beyond 6 m, in order to avoid the ship's shadow perturbation.

The results of the multi-distance comparison provides additional information for fine tuning of the distance criteria for the *R/V Weatherbird II*. The derived AOP profiles showed little variability among the four different deployment distances. The multi-distance comparisons supports the notion that the effects of the ship's shadow may be effectively masked by the random errors associated with the many sources of geophysical and sampling noise. Voss et al., (1986) found very little differences (less than 6%) in values of $K_d(z, \lambda)$ and $R_{rs}(z, \lambda)$ taken at 0 and 9 m from the ship (0-3% and 1-6% respectively in the upper 20 m). Moreover below twenty meters, they find that the effects of the ship shadow have altogether disappeared, as is shown here.

In conclusion, little variability in downwelling irradiance is observed for any of the deployment distances off the *R/V Weatherbird II*. However, significant variations are found for upwelling radiance with deployment distances less than 3 m. Our findings suggest that the ship's shadow exerts its greatest influence in the upper twenty meters with the largest perturbation at the sea surface. Measurements of optical properties from the *R/V Weatherbird II* during clear skies with the stern pointed into the sun can be made as long as the deployment distance off the stern is 3 m or greater. It is stressed that this analysis holds only under clear sky conditions and for deployments made off the stern of the *R/V Weatherbird II*. The effects of variable sea state, sun glint, diffuse sky have not been evaluated and additional experiments are necessary.

ACKNOWLEDGMENTS

This work is supported by NSF (OCE 91-16372 and OCE 90-16990), NASA (NAGW-3145) and the SeaWiFS Project Office. Computational support from Digital Equipment Corporation's flagship research project, Sequoia 2000, is also gratefully acknowledged.

REFERENCES

- Clark, D.K., 1981: Phytoplankton pigment algorithms for the Nimbus-7 CZCS. In: *Oceanography from Space*. J.F.R. Gower, ed., Plenum, New York, 227-237.
- Dickey, T.D., and D.A. Siegel, (eds.), 1993: Bio-Optics in U.S. JGOFS. Report of the Bio-Optics Workshop, U. S. JGOFS Planning and Coordination Office, Woods Hole, MA, p 180.
- Gordon, H.R., 1985: Ship perturbation of irradiance measurements at sea. 1: Monte Carlo simulations. *Appl. Opt.*, 24, 4172-4182.
- Gordon, H.R., and D.K. Clark, 1980: Atmospheric effects in the remote sensing of phytoplankton pigments. *Boundary Layer Meteorol.*, 18, 299-313.
- Helliwell, W.S., Sullivan, G.N., Macdonald, B., Voss, K.J., 1990: Ship shadowing: model and data comparisons. *Society of Photo-Optical Instrumentation Engineers. Ocean Optics X*, 1302, 55-71.
- Mueller, J.L. and R.W. Austin, 1992: Ocean Optics Protocols. *NASA Tech Memo. 104566, Vol. 5*, S.B. Hooker and E.R. Firestone, Eds. 45 pp.
- Poole, H. H., 1936: The photo-electric measurement of submarine illumination in offshore waters. *Rapp. Proc-Verb. Conseil Expl. Mar.*, 101(2): 9
- Siegel, D.A., A.F. Michaels, J. Sorensen, M. Hammer, and M.C. O'Brien, 1994: Seasonal variability of light availability and its utilization in the Sargasso Sea. Submitted to *Journal of Geophysical Research*.
- Sorensen, J.C., M. O'Brien, D. Konoff, D.A. Siegel, 1994: The BBOP data processing system. This volume.
- Strickland, J.D.H., 1958: Solar radiation penetrating the ocean, A review of requirements, data and methods of measurement, with particular reference to photosynthetic productivity. *J. Fish. Res. Bd. Canada*, 15, 453-493.
- Voss, K.J., J.W. Noltén and G.D. Edwards, 1986: Ship shadow effects on apparent optical properties. *Proceedings of The Society of Photo-Optical Instrumentation Engineers. Ocean Optics VIII*, 637, 186-190.
- Waters, K.J., Smith, R.C., Lewis, M.R., 1990: Avoiding ship induced light-field perturbation in the determination of oceanic optical properties. *Oceanography*, November 1990, 18-21.

DIAGNOSTICS OF SEA-WATER TURBULENCE BY SMALL - ANGLE LIGHT SCATTERING

Yu.I.Kopilevich, N.V.Aleksejev, B.V.Kurasov, and V.A.Yakovlev

S.I.Vavilov State Optical Institute,
Department of Hydrooptics & Thermovision
3 Pochtamtskaja st., St.Petersburg, Russia 190000

ABSTRACT

The results to be presented are related to a series of investigations carried out at the Department of Hydrooptics of SOI during a number of years with the aim of development, design and practical employment of optical instruments for measuring the statistical characteristics of turbulent inhomogeneities in the sea water. The values of magnitude and characteristic scales of refractive index fluctuations caused by turbulent convection in the sea water with temperature and salinity stratification, as well as the presence of suspended hydrosol particles, stipulate the choice of devices based on photo-electrical registration of small-angle scattering of light beam propagating through the volume of analyzed medium. The developed modifications of phase-contrast methods (shadow methods) make it possible to detect the variations of light beam angle-of-arrival at the level of $0.03'' - 0.05''$; the instrument may be mounted on remotely controlled underwater carrier towed by research vessel with the velocity 4 - 12 knots at the desired depth in the range from 0 to 300 m. The interpretation of registered signals from photo-electrical output of the optical instrument is based on the connection between the signal correlation function or spectrum and the energetic spectrum of refractive index fluctuations. The corresponded relations are obtained with the help of the theory of light propagation in random media, namely, the closed equations for light field statistical moments in parabolic approximation. The results of theoretical analysis allows the optimization of optical scheme to meet the requirements of linearity of the signal relation to the analyzed fluctuations magnitude, high spatial resolution and low sensitivity threshold, as well as sufficient resistance to vibrations and changes in pressure and temperature. A measurement of optical fluctuations spectrum in turbulent flow behind a heated grating in hydrodynamic tube are shown to demonstrate the designed instruments abilities. Some results of in-situ experiments made in calm waters and in turbulized layer near thermocline are presented.

2. INTRODUCTION

Various types of mechanical motions of ocean waters in most cases are of turbulent character. While the turbulence in the ocean has a multi-scale structure, the principle role in energy transport along the spectrum belongs to external scale of intensive energy influx, and internal scale, corresponding to energy dissipation. The main sources of turbulent energy supply are internal and surface ocean waves, and therefore measurements in the spectral region of external scale are performed with standard oceanographic methods (see, e.g.,¹). For dissipation scale range, optical methods seem to be the most reliable and metrologically secured².

From optics' point of view, the sea water may be characterized by the field of dielectric permittivity, ϵ , in the form

$$\epsilon(\mathbf{r}, t) = \epsilon_0 + \epsilon_T(\mathbf{r}, t) + \epsilon_D(\mathbf{r}, t) \quad (1)$$

$$\epsilon_D(\mathbf{r}, t) = \sum_j [\epsilon_j - \epsilon_0 - \epsilon_T(\mathbf{r}, t)] \Psi_j(\mathbf{r} - \mathbf{r}_j(t), t),$$

where ϵ_0 is the dielectric permittivity of unperturbed media, function ϵ_T , continuous both in spatial coordinates, r , and time, t , describes the "refractive turbulence", while ϵ_D corresponds to suspended particles in the water. In the series in j r_j is the radius-vector and ϵ_j is the dielectric permittivity of j -th particle; Ψ_j characterizes the effect of form, orientation and internal structure of the particle.

In the frames of the model ³ used throughout the paper, function ϵ is assumed to be real-valued, and equal to the medium refractive index squared.

The random field $\epsilon(r, t)$ is characterized by a set of statistical moments obtained by an averaging over an ensemble of realizations of the random medium ⁴; we denote the averaging by angled parentheses, $\langle \cdot \rangle$. If the turbulent fluctuations ϵ_T and suspended particles distribution are statistically independent, and the both components of the field $\epsilon(r, t)$ may be considered as homogeneous and stationary in a given spatial\temporal region, the mean value, $\langle \epsilon(r, t) \rangle$, shall be included in ϵ_0 [see (1)] and thus one can assume

$$\langle \epsilon_T(r, t) \rangle = 0, \quad \langle \epsilon(r, t) \rangle = \epsilon_0 + \langle \epsilon_D(r, t) \rangle.$$

Taking into account that the volume of suspended particles is relatively small, and the turbulent fluctuations are weak compared with optical contrast of the particles, for the second moment of the fluctuations $\epsilon'(r, t) = \epsilon(r, t) - \langle \epsilon \rangle$ the following expression may be shown to be accurate enough ³:

$$B_\epsilon(r_1 - r_2) \equiv \langle \epsilon'(r_1, t) \epsilon'(r_2, t) \rangle = B_T(r_1 - r_2) + B_D(r_1 - r_2), \quad (2)$$

where B_T is the (spatial) correlation function of turbulent component,

$$B_T(r_1 - r_2) = \langle \epsilon_T(r_1, t) \epsilon_T(r_2, t) \rangle, \quad (3)$$

and B_D is the analogous independent characteristic of discrete scatterers contribution. In just the same way, the 3-D Fourier transform $\Phi_T(\eta)$ of the correlation function (2) is the sum

$$\Phi_\epsilon(\eta) = \Phi_T(\eta) + \Phi_D(\eta)$$

of refractive turbulence energy spectrum ⁴

$$\Phi_\epsilon(\eta) = \frac{1}{(2\pi)^3} \int e^{i\eta r} B_\epsilon(r) d^3r \quad (4)$$

and the term Φ_D corresponds to suspended particles. It is well known that continuous component of dielectric permittivity of ocean water is determined by its temperature and salinity ⁵. The quantities may be regarded as passive admixtures when small-scale variations are considered and the effect of Archimedian forces is negligible; it is correct ⁴ for turbulent scales

$l = \frac{2\pi}{\eta} < 10^1 + 10^2$ m to be discussed here. With the use of water medium state equation and Lorentz-Lorenz formula some estimates may be obtained for internal scale, l_T , and variation, or MSV, $\sigma_T = B_T^{1/2}(0)$, of random field $\epsilon_T(r, t)$ in (1). For typical ocean conditions ⁵,

$$l_T \sim 10^{-4} + 10^{-2} \text{ m}; \quad \sigma_T \sim 10^{-7} + 10^{-5}. \quad (5)$$

For hydrosol particles concentration, n , characteristic size, d and $\sigma_D = B_D^{1/2}(0)$ one has ^{5,6}

$$n \sim 10^{-4} + 10^{-4} \text{ m}^{-3}; \quad d \sim 10^{-4} + 10^{-4} \mu\text{m}; \quad \sigma_D \sim 10^{-4} + 2 \cdot 10^{-1} \quad (6)$$

The values demonstrate the severe restrictions to be met by optical methods for refractive turbulence diagnostics in the spectral region corresponding to internal scale. It is obvious that the interaction of a visible light beam with the turbulent inhomogeneities in question results in small-angle light scattering, the characteristic angles being measured by the ratio of light wavelength, λ , to the scale, l_T :

$$\lambda/l_T \sim 10^{-3} + 10^{-5} \text{ radian}.$$

3. GENERAL THEORY

According to what has been said in previous Section, it seems reasonable to consider, for feasible optical-turbulence-meters, the class of instruments with photo-electrical registration analyzing the light field passing through investigated layer of the medium (see, e.g., ⁸⁻¹¹). The general layout of the devices being under consideration is given in the Figure 1. A partially coherent monochromatic beam from the light source 1 travels the layer of the medium under investigation of thickness L between planes 2 and 3 and is incident upon the input to the optical system 4. When the light beam is transformed by the system, it falls on the photocell 6 through its aperture situated in the plane 5. The class of examined systems includes the optical arrangements for which the relation of the optical field $\tilde{u}(\mathbf{x}, t)$, $\mathbf{x} = \{x, y\}$ at the exit plane 5 to the field $u(\mathbf{p}, t)$, $\mathbf{p} = \{x, y\}$ at the entrance plane 3 for any moment of the time t has the form

$$\tilde{u}(\mathbf{x}, t) = \int A(\mathbf{p}, \mathbf{x}) u(\mathbf{p}, t) d^2 \mathbf{p}, \quad (7)$$

where $A(\mathbf{p}, \mathbf{x})$ is the transmission function of the system. Thus, we are not examining systems, the transmission function of which are time-dependent (modulation), or systems with reference beams (interferometric).

It is assumed that the instrument moves relatively to the medium with controlled velocity v , directed perpendicularly to the light beam axis inside the analyzed volume. The velocity is high enough to secure the "frozen inhomogeneities" hypothesis ¹² to be valid, that is

$$\langle \varepsilon'(\mathbf{r}_1, t + \tau) \varepsilon'(\mathbf{r}_2, t) \rangle = \langle \varepsilon'(\mathbf{r}_1 - \mathbf{v}t, t) \varepsilon'(\mathbf{r}_2, t) \rangle \quad (8)$$

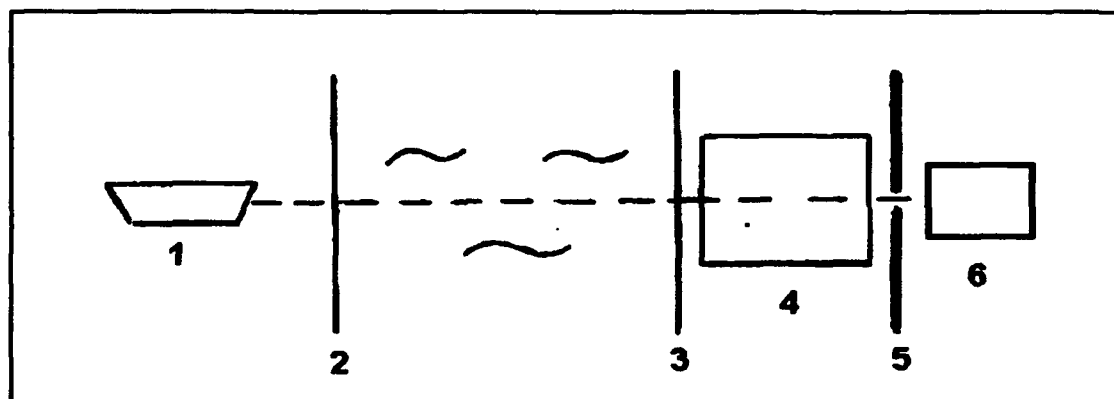


Figure 1. General layout of considered instruments. 1 - light source; 2,3 - windows; 4 - optical system; 5 - diaphragm; 6 - photodetector.

By virtue of Eq. (7), the "instant" signal value, or the total intensity of the light incident on the photodetector at the moment of time t is defined by the expression

$$I(t) = \iint R(\rho_1, \rho_2) \overline{u(\rho_1, t) u^*(\rho_2, t)} d^2\rho_1 d^2\rho_2, \quad (9)$$

where

$$R(\rho_1, \rho_2) = \int \Sigma(\mathbf{a}) A(\rho_1, \mathbf{a}) A^*(\rho_2, \mathbf{a}) d^2\mathbf{a}, \quad (10)$$

$\Sigma(\mathbf{a})$ is the intensity transmission function of the photodetector aperture; the asterisk denotes the complex conjugation, while the horizontal bar denotes a time average performed by the photocell. The registered quantities are the signal mean value

$$\langle I(t) \rangle = \iint R(\rho_1, \rho_2) \Gamma_2(L | \rho_1, t; \rho_2, t) d^2\rho_1 d^2\rho_2, \quad (11)$$

and correlation function of signal fluctuations

$$B_I(t_1 - t_2) \equiv \langle [I(t_1) - \langle I(t_1) \rangle] [I(t_2) - \langle I(t_2) \rangle] \rangle = \iiint R(\rho_1, \rho_2) R(\rho_3, \rho_4) \cdot \\ \cdot [\Gamma_4(L | \rho_1, t_1; \rho_2, t_1; \rho_3, t_2; \rho_4, t_2) - \Gamma_2(L | \rho_1, t_1; \rho_2, t_1) \Gamma_2(L | \rho_3, t_2; \rho_4, t_2)] d^2\rho_1 d^2\rho_2 d^2\rho_3 d^2\rho_4, \quad (12)$$

or spectrum

$$S(\omega) = \frac{1}{2\pi} \int B_I(\tau) \exp(i\omega\tau) d\tau.$$

In Eq. (11) and (12)

$$\Gamma_{2n}(L | \rho_1, t_1; \rho'_1, t_1; \dots; \rho_n, t_n; \rho'_n, t_n) = \overline{u(\rho_1, t_1) u^*(\rho'_1, t_1) \dots u(\rho_n, t_n) u^*(\rho'_n, t_n)} \quad (13)$$

are the corresponding moments, for $n = 1, 2$, of the light field $u(\rho, t)$ in the entrance plane 3 for the optical system 4 (see Figure 1).

The next step is establishing the connection between the light field moments in the right-hand sides of Eqs. (11) and (12) and statistical characteristics of turbulent inhomogeneities in the medium. It is very important to investigate the conditions for validity of the results leading to a linear relation between the statistical moments (11), (12) of the signal and the energy spectrum (4) of the turbulence and enable us to solve the problem of the turbulence spectrum reconstruction from the data of optical measurements.

First of all, we have to find out when the Born approximation¹² can be applied to the problem of the light beam scattering in the analyzed volume, that is the conditions for the following equality to be valid:

$$u(\rho, t) = u_0(r) - k^2 \int \int \int_{z=0}^{z=L} u_0(r') \epsilon'(r', t) G(r, r') d^3r', \quad (14)$$

where $r = \{x, \rho\}$, $\rho = \{x, y\}$ are the Cartesian coordinates, z axis coincides with the axis of propagation of light, $z = 0$ corresponds to plane 2 and $z = L$ to plane 3 (see Figure 1); u_0 is the incident light field in the volume;

$$k = \frac{2\pi}{\lambda} \sqrt{\epsilon}$$

is the wave number of the light in the medium;

$$G(\mathbf{r}, \mathbf{r}') = - \frac{\exp(i k |\mathbf{r} - \mathbf{r}'|)}{4\pi |\mathbf{r} - \mathbf{r}'|}$$

is the Green function for the wave equation. With the use of Eq. (14), the terms containing ε' in the third and higher degrees must be omitted in the expressions obtained for the light field moments in the right-hand sides of Eqs. (11) and (12) to yield, with the account for Eqs. (2), (4), (8), (11), and (12),

$$\langle I(t) \rangle = I_0 + \int N(\eta) [\Phi_T(\eta) + \Phi_D(\eta)] d^3\eta ; \quad (15)$$

$$B_f(\tau) = \int M(\eta) [\Phi_T(\eta) + \Phi_D(\eta)] \exp(-i \eta \nu \tau) d^3\eta ; \quad (16)$$

$$S(\omega) = \int M(\eta) [\Phi_T(\eta) + \Phi_D(\eta)] \delta(\omega - \eta \nu) d^3\eta ,$$

where $N(\eta)$, $M(\eta)$ may be called the instrumental functions of the device, and I_0 depends on $\langle \varepsilon_D \rangle$ via effective mean dielectric permittivity of the medium.

It may be shown (see ¹¹) that the condition of applicability of Eqs. (15) depends on the optical system 4 (Figure 1) and the shape of incident light beam; mathematically it is determined by the symmetry properties of the function

$$T(\rho_1, \rho_2) \equiv R(\rho_1, \rho_2) \Gamma_2^0(L | \rho_1, t; \rho_2, t)$$

where Γ_2^0 is the second moment [see Eq. (13)] of the incident light beam at the entrance of the optical system (see Figure 1), and R is defined by Eq. (10). Symmetric part of the function T

$$T^+(\rho_1, \rho_2) \equiv \frac{1}{2} [T(\rho_1, \rho_2) + T(\rho_2, \rho_1)]$$

is found to respond for the instrument sensitivity to phase fluctuations of the analyzed random light field, while anti-symmetric part of T

$$T^-(\rho_1, \rho_2) \equiv \frac{1}{2} [T(\rho_1, \rho_2) - T(\rho_2, \rho_1)]$$

corresponds to contribution to the signal variations caused by amplitude fluctuations of the field ¹¹. In the case of "phase" device, for which $|T^-| \gg |T^+|$, the restrictions turn out to be less stringent than for "amplitude" ones: usual "energetic" condition for applicability of single scattering approximation ¹¹

$$L k^2 l_T \sigma_T^2 \ll 1 \quad (17)$$

is just sufficient if it is complemented with additional relation for light scattering by particles ^{13,14}:

$$L k^2 l_T \sigma_D^2 \langle d^4 \rangle \ll 1 \quad (18)$$

where $\langle d^4 \rangle$ is the mean value of particle size, d , in the power of 4; averaging over different hydrosol types (mineral and organic) gives the estimate

$$\sigma_D^2 n \sim 10^{-14} + 10^{-15} \text{ m}^{-1}$$

According to the estimate and (5),(6), the inequalities (17) and (18) hold in the wide enough range of situations for short-base instruments,

$$L \leq 10^{-1} + 1 \text{ m.}$$

Now the equalities (16) may be used⁸ for determining the total spectrum $\Phi_T + \Phi_D$ in the case of statistically isotropic inhomogeneities^{4,12}, when the both spectra depends only on the module of the spatial frequency vector,

$$\Phi_{T,D}(\eta) \equiv \Phi_{T,D}(\eta). \quad (19)$$

To evaluate the spectrum F of refractive turbulence in the medium, one has to extract the contribution by discrete scatterers. In general case it can not be done. For example, the following estimate may be given for the ratio of "discrete" and "turbulent" terms in B_I from (16) for "phase" devices:

$$\frac{B_I^{(D)}(0)}{B_I^{(T)}(0)} \geq \frac{n \sigma_D^2 \langle d^6 \rangle}{\sigma_T^2 l_T^3} (1 + l_T^2 \eta_{\max}^2) - (3 \cdot 10^{-1} + 10^{-7}) (1 + l_T^2 \eta_{\max}^2),$$

where

$$B_I^{(D,T)}(0) = \int M(\eta) \Phi_{D,T}(\eta) d^3 \eta,$$

and η_{\max} characterize the instrument filtering:

$$M(\eta) = 0, \quad \eta \geq \eta_{\max}.$$

It is important that in the considered spectral range (i.e. for $\eta \sim l_T^{-1}$) the spectrum Φ_D is practically constant because $l_T \gg d_{\max}$, and thus does not affect the shape of the spectrum to be reconstructed. However the statement may be invalid for very large and relatively rare particles (like zooplankton, etc.).

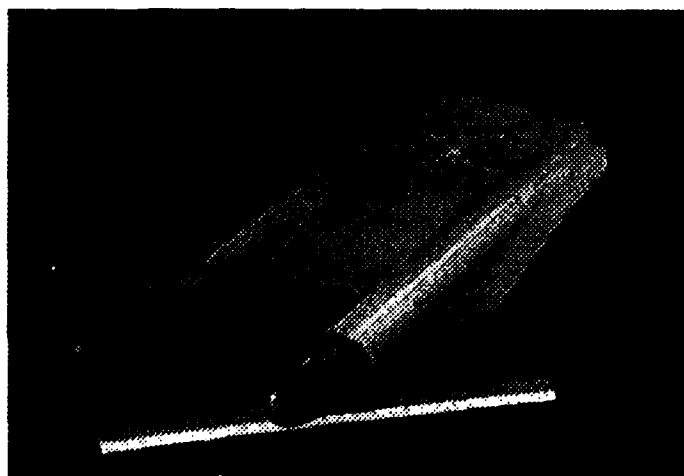


Figure 2. General view of the photoelectric schlieren device.

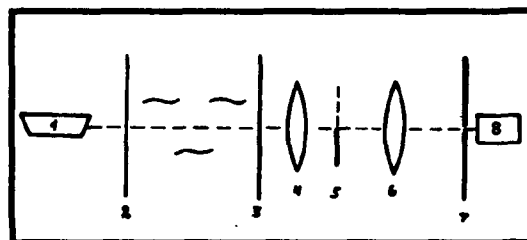


Figure 3. Schematic diagram of the photoelectric schlieren device. 1 - light source; 2,3 - windows; 4,6 - objectives; 5 - "shadow diaphragm" - the Foucault knife-edge; 7 - filtering diaphragm; 8 - photodetector.

4. EXPERIMENTAL

According to the theoretical background presented in the previous Section a photoelectric schlieren device scheme is chosen for practical realization of optical-turbulence-meter¹⁵. The general view of the instrument is shown in Figure 2, and its schematic diagram is depicted in Figure 3. The transforming optical system (cf. Figure 1) is the consistent spatial-frequency filter formed by the objectives 4 and 6, and the "shadow diaphragm" at the Fourier plane 5 - the Foucault knife-edge perpendicular to the velocity v of ordered motion of the device (scanning). The exit plane 7 of the system is optically conjugated with its entrance plane 3.

Let x axis of the Cartesian coordinates $\{x, y\}$ in a plane perpendicular to the light beam coincide with the direction of v . It is convenient to introduce also the coordinates $\mathbf{x} = \{x_x, x_y\}$ in the plane 7 differing from the "physical" coordinates $\{x, y\}$ by the scale factor equal to the system magnification. Then the effective intensity transmittance function $\Sigma(\mathbf{x})$ of the filtering diaphragm at the plane 7 may be written as

$$\Sigma(x_x, x_y) = \left[\text{rect}\left(\frac{x_x}{b}\right) - \frac{b}{c} \text{rect}\left(\frac{x_x}{c}\right) \right] \text{rect}\left(\frac{x_y}{c}\right), \quad (20)$$

where $b < c$, and the subtraction is realized with the use of a matrix photodetector and corresponding electronic arrangement. The cross-section of the collimated light beam formed by the illuminator 1 is large enough for its image to cover the diaphragm (20). The angle θ_x of the beam divergence in the x direction is large enough to determine the light spot size in the Fourier plane 5; the parameter is of principle importance for the instrument protection against vibrations.

The spectrum $S(\omega)$ of the registered signal in the case of isotropic inhomogeneities (19) is expressed by the formula [cf. Eq. (16)]:

$$S(\omega) = \iiint M(\eta_x, \eta_y, \eta_z) \delta(\omega - \eta_x v) \Phi(\sqrt{\eta_x^2 + \eta_y^2 + \eta_z^2}) d\eta_x d\eta_y d\eta_z \quad (21)$$

with the instrumental function of the form

$$M(\eta_x, \eta_y, \eta_z) = \frac{4 L^2 Q^2}{b^2} \sin^2\left(\eta_x \frac{b}{2}\right) \sin^2\left(\eta_y \frac{c}{2}\right) \sin^2\left(\eta_z \frac{L}{2}\right) F(\eta_x) \left[1 - \frac{\sin^2\left(\eta_x \frac{c}{2}\right)}{\sin^2\left(\eta_x \frac{b}{2}\right)} \right]^2 + S_N(\omega) + S_D(\omega),$$

where Q is the instrument sensitivity (in Volts per radian) for beam deflection in the x direction (obtained with the use of an appropriate optical wedge), and

$$F(h) = \begin{cases} 1, & \left| \frac{2 \eta_x}{k \theta_x} \right| \leq 1 \\ \frac{k \theta_x}{2 \eta_x}, & \left| \frac{2 \eta_x}{k \theta_x} \right| > 1 \end{cases};$$

at last, the components S_N and S_D are caused by electronic noise of the registration channel and suspended particles in the medium, correspondingly. The spectrum S_D is approximately constant in the spectral range of interest. According to the note at the end of previous Section, the pulses from large particles are filtered out by a special electronic device. In the frequency range bounded by the inequalities

$$\left(\frac{2\pi}{b}\right)^2 < \left(\frac{\omega}{v}\right)^2 \ll \left(\frac{2\pi}{L}\right)^2 + \left(\frac{2\pi}{c}\right)^2 \quad (22)$$

the Eq. (21) may be simplified to yield the approximate equality

$$S(\omega) \approx \frac{16 \pi^2 Q^2 L}{v b^2 c} \sin^2\left(\omega \frac{b}{2v}\right) F\left(\frac{\omega}{v}\right) \left[1 - \frac{\text{sinc}\left(\omega \frac{c}{2v}\right)}{\text{sinc}\left(\omega \frac{b}{2v}\right)} \right]^2 \Phi_T\left(\frac{\omega}{v}\right) + S_N(\omega) + S_D(\omega), \quad (23)$$

which may be used for determining the shape of turbulence spectrum Φ_T in the indicated interval. According to (22) the spatial resolution of the instrument, i.e. is the minimal scale l_{\min} of registered inhomogeneities, is determined by the dimension b of the filtering diaphragm (20): $l_{\min} \geq b$.

The described instrument had been tested during a set of field experiments carried out at the Black Sea. The optical-turbulence-meter was mounted on remotely controlled underwater carrier (shown in Figure 4) towed by research vessel with the velocity 4.5 - 6 knots at the depth up to 200 m. The typical examples of the reconstruction of refractive turbulence spectrum shape from the registered data are depicted in Figure 5. Note the different background level for the spectrum corresponding to the undisturbed water (curve 1) and the spectra of intensive turbulence near the horizon of jump in the water density (curves 2 and 3). The effect is likely caused by the variations in suspended particles concentration at the separated horizons and thus is due to the difference in the values of S_D term in (23).

5. CONCLUSIONS

The optical shadow instruments with photoelectric registration appear to be effective tools for investigating the refractive turbulence in the sea water. The problem of turbulence spectrum reconstruction from optical measurements is shown to be solved correctly in the spectral range including the dissipation scale. The high spatial resolution and sensitivity achieved by the optical method significantly exceed the potential means provided by the "point" detectors measuring the fluctuations in temperature, velocity, and electric conductivity of the sea water.

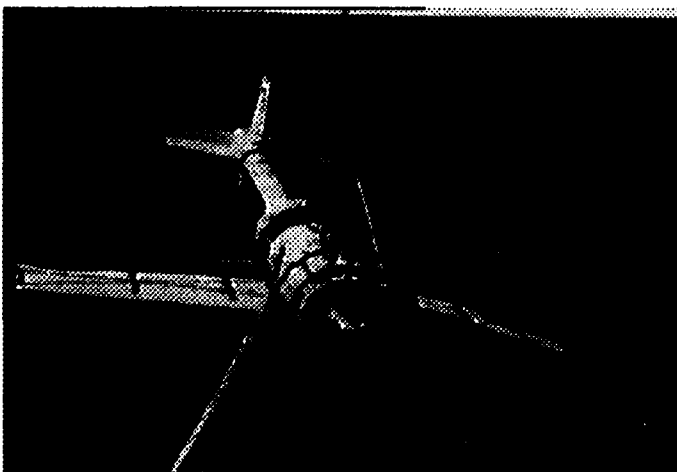


Figure 4. Remotely Controlled Underwater Carrier over-board of R/V "Hydroptic".

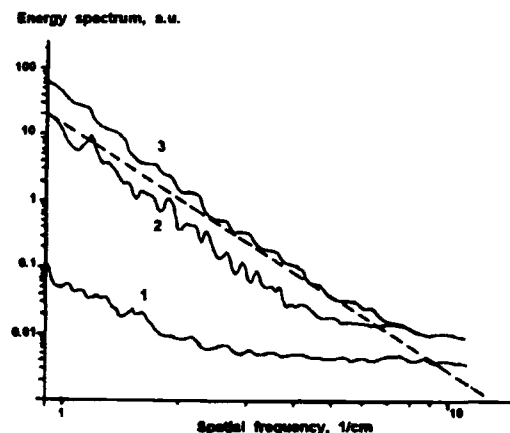


Figure 5. Examples of reconstructed turbulence spectra (dashed line corresponds to the Kolmogorov "11/3" spectrum). 1 - weak turbulence spectrum in undisturbed sea water below the density jump; 2, 3 - spectra of turbulence in the vicinity of the jump.

6. REFERENCES

1. J.O.Hinze, *Turbulence*, McGraw-Hill, New-York - Toronto - London, 1959.
2. M.A.Bramson, E.I.Krasovskij, and B.V.Naumov, *Marine Refractometry*, Gidrometeoizdat, Leningrad, 1986 (in Russian).
3. V.A.Yakovlev, "On the Spatial Spectrum of the Random Field of Dielectric Permittivity of Ocean Medium", *Izv. Akad. Nauk USSR: Atmos. and Ocean Phys.*, v. 21, n. 6, pp. 669-671, 1985 (in Russian).
4. A.S.Monin and A.M.Yaglom, *Statistical Hydrodynamics*, Part I, Part II, Nauka, Moscow, 1965, 1967 (in Russian).
5. K.N.Fedorov, *Fine Thermohalin Structure of the Ocean*, Nauka, Moskow, 1978 (in Russian).
6. N.G.Erlov, *Marine Optics*, Elsevier, Amsterdam - Oxford - New-York, 1976.
7. A.Ivanoff, *Introduction À L'océanographis*, Tome I, II, Librairie Vulbert, Paris, 1972, 1975.
8. Yu.I.Kopilevich, G.B.Sochilin, "Reconstruction of Turbulence Spectrum from Optical Measurements", *Opt. Spectrosc.*, v. 41, pp. 136-142, July 1976.
9. Yu.I.Kopilevich, A.S.Tibilov, and V.A.Yakovlev, "Determining the Spectrum of Local Isotropic Turbulence from Optical Measurements", *Opt.Spectrosc.*, v. 44, pp. 366-369, February 1978.
10. Yu.I.Kopilevich, "Instrumental Functions of Photoelectric Schlieren Devices for Investigating Randomly Inhomogeneous Media", *Opt.Spectrosc.*, v. 50, pp. 770-777, April 1981.
11. Yu.I.Kopilevich, A.S.Tibilov, and V.A.Yakovlev, "Linear Approximations in Calculating the Statistical Characteristics of Optical-turbulence-meter signals", *Opt.Spectrosc.*, v. 51, pp. 915-923, November 1981.
12. V.I.Tatarski, *Wave Propagation in a Turbulent Atmosphere*, Dover, New-York, 1961.
13. V.K.Kachurin and V.A.Yakovlev, "Born Approximation for the Problem of Light Scattering by an Ensemble of Rigid Particles", *Opt. Spectrosc.*, v. 62, pp. 1170-1172, May 1987.
14. V.K.Kachurin and V.A.Yakovlev, "On the Opportunity for Determining the Characteristics of Turbulent Fluctuations of Dielectric Permittivity of a Medium by Optical Methods in the Presence of Suspension", *Opt.Spectrosc.*, v. 65, pp. 388-392, February 1988.
15. N.V.Alekseev, Yu.V.Borodich, and B.V.Kurasov, "Some Feasibilities of Photoelectric Shadow Instruments with Spatial Filtering of Shadow Image in Application for Investigation of Turbulence", *Opt. Spectrosc.*, v. 56, pp. 531-536, March 1984.

A moored optical particle flux instrument

Enson Chang, Randall J. Patton and Robert L. Gran

Dynamics Technology, Inc.
21311 Hawthorne Boulevard, Suite 300, Torrance, California 90503

ABSTRACT

A prototype instrument has been developed to measure the settling velocity of marine particulates using optical techniques in an in-situ settling chamber. Particles from 100 μm to several mm are imaged by a shadowgraph system, which has a 30 cm depth of field. Particles in the 10 to 100 μm range are monitored by a laser diffraction system. Flow management considerations have been incorporated into the instrument to ensure minimal disruption of the aggregates and their settling rates. We present the results of laboratory tests in which the settling rates of polystyrene spheres and natural marine particulates have been measured using the component systems. Design considerations for the self-contained moored version are also specified.

1. INTRODUCTION

In recent years, there has been an increasing interest in the greenhouse effect and the eventual fate of carbon, a significant portion of which is embodied in marine snow aggregates and smaller organic particulates. In order to understand the complicated processes controlling the flux of particles and their constituents from the atmosphere and upper ocean to the ocean floor, there is the need to employ long term vertical flux measurements in the ocean. Traditionally this is done with the aid of sediment traps. It is recognized, however, that sediment traps tend to suffer from sample integrity, trapping inefficiencies and lack of temporal resolution, which casts doubt on the vertical particle flux derived from these measurements¹.

The instrument described in this document is designed to alleviate problems associated with sediment traps. The moored optical particle flux measurement system (MOPAR) incorporates a horizontally oriented flow-through chamber (Figure 1), which efficiently captures a volume of water and creates a quiescent settling volume without disrupting the fragile aggregates or creating large secondary flows which would affect settling rate measurements. Two types of optical techniques are utilized to monitor in real-time the settling rate of particles over the range from 10 μm to several millimeters in size. The weathervaning design continually aligns the sample chamber with the ambient flow, thus avoiding trapping efficiency problems. Other design considerations include improved anti-biofouling characteristics and low power consumption for long term moored applications.

A ship-deployable prototype system has been constructed and tested in the lab (Figure 2). In addition to the mechanical and optical systems developed for the self-contained moored version, the prototype has two "ground-truth" video cameras to record the behavior of the particles from the side and the bottom of the chamber. A two axis current meter and compass monitor the effectiveness of the weathervane design. The prototype system is affixed to a tethered buoy near the test vessel with an umbilical cord linking the instrument to on-board power supply and recording devices.

The prototype system is scheduled to be tested off the Southern California coast (Catalina Island) during the writing of this paper. The results of the deployment will be published in the near future. This paper describes various components of the system and laboratory test results.

2. PROTOTYPE SYSTEM DESCRIPTION

The following is a brief description of the prototype system and its components. Detailed descriptions of the main optical components and results of laboratory testing are presented in Sections 3 and 4.

The MOPAR instrument obtains optical measurements of particle flux in the settling chamber. The weathervane tail aligns the settling chamber with the horizontal ambient flow (the chamber is upstream from the mooring line to avoid wakes); the leading edges of the chamber are rounded to minimize disturbances to the incoming flow. The front and back doors of the chamber are streamlined louvers and which should only generate minimal (small scale) turbulence.

At the beginning of a measurement cycle, the back (or downstream) louvers of the chamber are quickly closed (duration ~ 1 second) to uniformly decelerate the flow. This technique avoids the generation of secondary circulations and turbulence (as confirmed by laboratory dye visualization tests), which could affect subsequent settling rate measurements or disrupt the fragile particulate flocs. Turbulence associated with the boundary layers along the sides of the chamber (which may become unstable during the deceleration) is confined to within a few millimeters of the walls and does not significantly affect the interior fluid. The front louvers are then slowly closed (duration ~ 5 seconds) to seal off the chamber from the exterior flow and to provide a light-tight environment. Particle size and settling rate measurements are begun immediately after the rear doors are closed.

The settling rates of particles in the chamber are monitored by two optical modules. Large aggregates, from 100 μm up to several millimeters in size are imaged by a CCD camera as part of the shadowgraph system (Figure 2) and recorded on video tape (giving the prototype system a nominal resolution of 300 lines/frame). The images are post-processed to obtain particle settling velocity and vertical and horizontal dimensions using an algorithm that detects the passage of specific particles through three (non-contiguous) horizontal rows of the CCD array. This approach emulates the measurement technique to be implemented in the self-contained version which will utilize three horizontally-oriented, linear CCD arrays (to minimize data processing and power requirements for moored deployments; see Section 5). The column of water above the optical beam constitutes the sample volume, which is 30 cm wide, 50 cm high and 3 cm thick (4.5 liters).

Particles between 10 and 100 μm in size are monitored by a laser diffraction system (known as the Near Forward Scatter or NFS system). Mathematical inversion of the near-forward scattered intensity distribution is used to obtain the particle size distribution. Samples of the 2-D scattering distribution are obtained using a CID camera (charge injected detector; similar to a CCD) periodically during the measurement cycle to obtain a time series ("snapshots") of the particle size distribution. The collimated beam through which the particles pass is located near the top of the chamber. Since the particles settle at different rates depending on the size, the depletion of the faster (larger) particles results in a changing particle size distribution from which settling rates can be inferred. Because of the very slow settling rates of the smaller particles, the samples are taken at intervals of several minutes over a period of time that can extend to hours.

To provide additional information on the particle environment and to verify system performance during the ocean test, two video-based ground-truth systems have been integrated into the prototype design (Figure 2). The bottom viewing ground-truth system (BVGT) views a clear acrylic plate at the bottom of the chamber using a macro lens and CCD (Pulnix). This system records the accumulation of particles on the plate, allowing the estimation of size vs. settling rate. This technique emulates one described in Ref. 2 which was used to obtain settling rates of ocean aggregates using a film-based imaging system. A second macro-lens and CCD are used to view the interior of the chamber from the side (side viewing ground-truth or SVGT system). This system is mainly intended to give an overall view of what is going on inside the chamber, such as residual circulations, overall particle concentration, etc. during deployment. The lens for this system thus has a very high f-number to provide a large depth-of-field (ca. 5 cm for $f/32$). This system requires a bright light (100W; Deep Sea Power and Light) which is mounted on the side of the chamber opposite the SVGT and also serves to illuminate the bottom panel viewed by the BVGT.

3. COMPONENT SYSTEM DESCRIPTION

3.1 Shadowgraph (SG) System

The shadowgraph (SG) system (Figure 3) was developed to image particles in the range from 100 μm to several millimeters. Based on a shadow imaging technique, it makes use of multiple lenses and a pinhole in the receiver optics to provide an extremely large depth-of-field (DOF) which greatly expands the volume being sampled. The system described below can extend the usable depth-of-field from a few millimeters to over 3 cm with very little loss of resolution or contrast. This allows more simple and robust algorithms based on a single threshold to be used to identify and measure particle shape.

The DOF for an imaging system depends on how much its aperture restricts the angles of the rays collected by the receiving optics. This is illustrated in Figure 4, where the standard practice of limiting the aperture *at the lens* reduces the blurring of objects as they move longitudinally away from the point of best focus (i.e., object plane). Placing a pinhole in the focal or Fourier transform plane of the 1st receiving lens also restricts the angles that are allowed to pass through the system to be imaged without restricting the real aperture of the system, as shown in Figure 5. This method also minimizes the dependence of the DOF on the imaged particle's position away (radially) from the optical axis. It is this alternative method of extending the DOF along with the back lighting of the particles that forms the basis for this new technique. This pinhole arrangement is known as a telecentric

configuration and is used in applications where parallax is to be avoided since only rays that are nearly parallel to the optic axis are imaged³.

The size of the pinhole improves the DOF of the system but it can also degrade the resolution through diffraction. A very small pinhole will give a very large DOF but can distort the particle image by diffraction of the imaged rays as they pass through the pinhole. The varying contrast thus created would make the thresholding of the imagery for particle size and shape analysis more difficult. It was found that a pinhole diameter of 400 μm provides a greatly increased DOF without significantly degrading the resolution of the particle images, as shown in Figure 6.

The configuration of the launch optics for the shadowgraph system is also simpler than similar systems where particles are back illuminated. In a system described in Ref. 4, the DOF is determined by the small divergence of rays due to diffraction rather than the aperture of the receiving optics (higher divergence gives shorter DOF). This divergence, which can be characterized by the angular spread of the Airy disk (given by $\theta = 0.61\lambda/D$ where D = particle diameter), depends on the particle size. In the system of Ref. 4, the collimation of the illuminating beam can become the limiting factor in the divergence of the rays for the largest particles (ca. $D = 500 \mu\text{m}$). This system thus requires a carefully collimated beam. Since the depth of field is controlled by the pinhole in the focal plane of the receiving optics in the MOPAR system, the effects of diffraction and/or beam divergence are not important and the launch optics can be made much simpler and less expensive.

3.2 Near-Forward Scattering (NFS) System

A schematic of the NFS system is shown in Figure 7. It utilizes standard laser diffraction techniques^{5,6} to monitor the small particle size distribution in the sample volume as a function of time. The output from a 2.5 mW, 670 nm diode is spatially filtered and expanded into a collimated beam, approximately 2 cm in diameter. The collimation is achieved with a 10.7 cm, $f/2.7$ achromatic, aspheric lens. The beam path through the sample is 30 cm long and located 5 cm (measured from the beam center) below the top of the chamber. The near-forward scattered light is collected by a 6.29 cm, $f/1.2$ plano-convex lens (lens aperture = 2.0 inches). The largest scattering angle measured by this lens is 4.8 degrees.

The detector system is a CID camera, the imaging array of which is placed in the focal plane of the collector lens. With the CID camera, an extra dynamic range of 30 or so can be achieved by controlling the integration time. Furthermore, the image does not "bleed" when a pixel saturates, allowing simple azimuthal averaging to reduce noise. These features make the CID camera an attractive tool for prototyping purposes. The moored version will make use of spatially and energywise more economical linear CCD arrays^{6,7}.

Near the transmitter end of the system, part of the laser output is deflected by a beam splitter and monitored by a reference photodiode. On the collector side, a similar detector monitors the transmitted beam, part of which is deflected into the photodiode by an ND 2.0 filter. A 200 μm pinhole in front of the photodiode restricts the acceptance angle to about 0.1° . The ratio of the two photodetector outputs provides an accurate measure of the sample's transmissivity, corrected for laser power fluctuations and contaminated only minimally by the small amount of highly near-forward scattered light.

Due to the Fourier transforming property of the collector lens, radial distances in its focal plane correspond to scattering angles. Therefore, the intensity distribution measured by the CID array (positioned in the focal plane of the lens) is directly related to the volume scattering function of the sample in the near-forward direction. This function can be inverted to obtain the sample's particle size distribution, $n(D)$, where D is the diameter of the particle, and $n(D)$ is the number of particles per unit volume in the size range between D and $D + dD$. The inverse calculation is known to be ill-conditioned and requires special care^{5,6}. We use here the inverse method described in Ref. 6, which employs a nonnegative least squares scheme with logarithmic size and angular intervals.

To infer particle settling rate and density distribution from the laser diffraction measurements, we make the simplifying assumption that the volume of particles sampled is rectangular in shape and extends from the top of the chamber to the bottom of the laser beam. Since the decrease in the number of particles in a certain size class is due to the depletion of particles in this rectangular volume as they settle out, the rate of decrease is a direct measurement of the settling velocity and the density distribution of the particles in this size class. According to Stokes law⁸, the settling velocity of a spherical particle is related to its size and density by

$$v = \frac{D^2 g}{18\nu} (s-1) \quad (1)$$

where s is the specific gravity of the particle, and ν is the kinematic viscosity, which is about $0.01 \text{ cm}^2/\text{sec}$.

Based on Equation (1), it is straightforward to show that

$$\frac{\partial n(D, t)}{\partial t} = - \frac{18 h \nu}{D^2 g t^2} f(s, D) \quad (2)$$

where $f(s, D)$ is the joint size and density distribution for particles of diameter D , h is the distance from the top of the chamber to the bottom of the beam, and the rate of decrease, dn/dt , can be derived from differencing the data in time. The parameter s_t is given

$$s_t = \frac{18 h \nu}{t D^2 g} + 1 \quad (3)$$

The vertical mass flux is then given by

$$\Phi_m = \iint f(s, D) \rho_o s \frac{\pi D^3}{6} \nu ds dD \quad (4)$$

where ρ_o is the density of water.

3.3 Flow Management System

Fluid currents and turbulence can affect the measurements obtained by MOPAR in two ways, a) by disrupting aggregates, and b) by affecting the settling rate measurements of particles (by virtue of residual currents remaining after the aft and front louvers are closed).

Previous estimates indicate that one common type of marine aggregate, "marine snow," is ruptured when the fluid dynamic strain rate exceeds approximately $1\text{-}2 \text{ sec}^{-1}$ ^{9,10}. This strain rate corresponds to a Newtonian shear stress of approximately 0.02 dynes/cm^2 or to a turbulent energy dissipation rate of about $0.1 \text{ cm}^2/\text{sec}^3$, which is well above that due to ambient turbulence levels in the ocean. (Ambient dissipation rate is typically 0.001 to $0.01 \text{ cm}^2/\text{sec}^3$ in the ocean's mixed layer / seasonal thermocline¹¹.)

In the MOPAR settling chamber, fluid strain occurs in the boundary layer on the interior walls and the wake behind each front door louver. In the open-flow condition (doors open), the fluid dynamic boundary layer on the interior walls will remain laminar if the through-flow speed is less than $R_T \nu / L$, where L is the length of the chamber and R_T is the transition Reynolds number ($\sim 10^5$). Given the length of the settling chamber (50 cm), the chamber wall boundary layer flow should remain laminar for speeds less than 20 cm/sec . The laminar boundary layer thickness, δ , can be estimated from the Blasius solution¹², which gives

$$\frac{\delta}{L} = \frac{6}{\sqrt{uL/\nu}} \quad (5)$$

where u is the flow speed. With the 50 cm chamber length and a flow speed of 20 cm/sec , the boundary layer thickness is estimated to be 0.9 cm at the chamber exit. Thus, only a few percent of the flow within the chamber is subjected to a high strain rate due to the wall boundary layer.

The wake behind each louver can also disrupt the aggregates. The wake half width, δ_w , is given by¹³

$$\delta_w = \frac{2L}{\sqrt{uL/\nu}} \quad (6)$$

For the MOPAR chamber, the wake half width is approximately 0.3 cm at the chamber exit. Therefore, the volume fraction occupied by the wakes from all six front louvers is less than 7% of the total chamber volume.

The closing action of the louvers can introduce some turbulence in the chamber interior, increasing with the rapidity with which they are closed. The time it takes to stop the flow and enclose the chamber is an important parameter, since measurements of the faster sinking particles must be initiated quickly (within several seconds). A tow-tank experiment was carried out to visualize the behavior of dye streaks passing into and through the chamber. The results of this experiment suggest that there is a negligible amount of turbulence generated by the louver closing action, even at a flow speed of 20 cm/sec. The interested reader is referred to Ref. 7.

4. LABORATORY TEST RESULTS

A series of laboratory tests were conducted to test the optical components of the system, the results of which are reported below.

4.1 Shadowgraph System

The performance of the SG system was tested in a quiescent settling environment (clear acrylic tank), using both polystyrene spheres and marine aggregates. Polystyrene spheres of two different diameters, $100 \pm 2.0 \mu\text{m}$ and $202 \pm 4.0 \mu\text{m}$ (from Duke Scientific), were used in the calibration tests. A digitized SG image of the $100 \mu\text{m}$ particles, without background subtraction, is shown in Figure 8a. The dark region near the top of the image is the shadow of a plastic tube used to guide the particles from the water surface down to a position near the SG beam. Although the $100 \mu\text{m}$ particles are barely discernable in the gray scale image near the plastic tube, they are readily identifiable when the intensity cross sections are examined. One typical cross section, with background subtraction, is shown in Figure 9. A digitized SG image of the $200 \mu\text{m}$ particles is shown in Figure 8b. While the particle circled in the figure appears somewhat larger than the other particles, closer examination reveals that it is actually a cluster of two $200 \mu\text{m}$ polystyrenes.

A sequence of about 10 seconds of SG recordings of $200 \mu\text{m}$ spheres were digitized and processed by the numerical technique described in the Appendix. Figure 10 shows the resultant size distribution (for 64 particles), which has a mean diameter of $259 \mu\text{m}$ and a standard deviation of $54 \mu\text{m}$. This spread in particles sizes is due to the clustering of the spheres, as verified by visual inspection of the background subtracted images.

Sea water collected from the energetic tidal zone near Whites Point in San Pedro, California was used for the natural aggregate test. The salinity of the water in the tank was adjusted to match that of the sample. The sample bottle was also immersed in the tank for approximately two hours prior to the test in order to compensate for any temperature difference. The bottle was then carefully inverted and opened so that the aggregates would fall through the measurement volume. Figure 11 shows a typical background-subtracted shadowgraph image of these aggregates.

Since the sample originated from a near shore location next to a storm drain, there is an artificially high concentration of large particles, some of which are highly compacted and quite dense. A recording of more than 300 particles was processed, the resulting size distribution is shown in Figure 12. The peak number of particles occur in the 300 to $400 \mu\text{m}$ range. There also appears to be an increasing number of smaller particles with decreasing size, down to the resolution limit of the SG system.

The settling velocity distribution for several size classes is shown in Figure 13. The smaller particles tend to have a larger settling velocity spread, indicative of different material constituents. The $100 - 150 \mu\text{m}$ particles, for instance, have settling velocities ranging from 1 to 35 mm/sec. Assuming a mean particle size of $125 \mu\text{m}$, Stokes law predicts the specific gravity of these particles to be in the range from 1.1 to 5.1, which suggests a wide range of material constituents, anywhere from organic materials to metallic debris. The more consistent velocity of the larger particles (Figures 13b and c) is probably the result of a better averaging of the subparticle material properties.

The mean settling velocity of the size classes in general decreases with particle size. Based on the mean settling velocity and Stokes law, we compute the mean density of each size class. These values are shown in Figure 14 as a function of mean particle size. The average density decreases from about 1.9 for $125 \mu\text{m}$ particles down to 1.01 for $675 \mu\text{m}$ particles. This trend suggests higher porosity and possibly higher fraction of organic constituents in the larger aggregates. It also confirms the intuitive hypothesis that the energetic tidal zone from which these samples were collected is able to suspend small particles of high density.

4.2 NFS System

A sample of water collected from the tidal zone near Whites Point was used in the NFS system test. The particles were first suspended in the test tank by stirring and then allowing them to settle. Eight intensity images were recorded over a time span of two and a half hours. A ninth reading was taken after 19 hours from the initial measurement to verify the stability of the system and also to serve as a background reading. The intensity images were azimuthally averaged and then inverted to obtain particle size distributions. Since the residual turbulence from the initial stirring will keep the particles suspended for a certain time, the settling rate measured in this experiment represents a lower bound of the actual, undisturbed value.

According to Ref. 5 and 6, stable inverse calculations might be achieved if the size and angular intervals grow geometrically, i.e., the ratio between two consecutive intervals is a fixed constant. Twelve size and angular intervals are used in the calculations presented in this paper. The angular intervals span the range from 0.4° to 3.3° . The size classes span the range from 1 to 100 μm .

The inverted particle size distributions at three different times are shown in Figure 16. The relatively rapid depletion of large particles from the sample volume is evident. (The apparent high concentration of very small particles, about 1 μm in size, has been hypothesized to be an artifact from using the diffraction approximation of the Mie theory⁶.) The concentration of certain size classes, however, does not always decrease uniformly. This is especially noticeable when we examine the full concentration history (including the data from all eight sample times) of a size class. Figure 17a shows the concentration history of the size class centered at 8.4 μm . The fluctuation seen in the figure is due to the instability inherent to the inverse calculation. Since there are not enough data points taken at the early times to warrant a statistically significant result, we will not attempt to smooth the data and calculate the density distribution from Equation 2. The average density of the 8.4 μm particles, however, can be estimated from the time that its concentration drops to half of the maximum value (72 min. after the initial time). Based on the known distance (5 cm) from the top of the sample to the bottom of the laser beam, the settling velocity and hence the average particle density can be estimated from Equation 1. The resultant specific gravity for these particles is 1.30, which suggests a mostly organic makeup with a smaller but significant fraction of inorganic constituents.

5. SELF-CONTAINED MOORED VERSION

In this section we summarize the main differences between the self-contained moored version and the prototype system. The moored version will be significantly more compact due to the absence of the ground-truth systems and the use of more compact components. (The NFS receiver housing in the prototype needs to have a 9 in. I.D. in order to envelop the CID camera body, which is a 9 x 8 x 1 in. box.)

The SG and NFS detector cameras in the prototype will be replaced by linear CCD arrays to save space, power, and to reduce processing rates and data storage. The SG receiver will consist of three linear arrays, as described in Appendix A. The NFS detector will consist of a single linear CCD array. Past experiments^{6,7} have shown that data derived from a linear CCD array can be successfully inverted to obtain particle size distribution.

Biofouling of the optical surfaces in the moored version will be minimized by slowly releasing silver and copper ions into the settling chamber¹⁴. The metal ions inhibit the growth of a bacterial layer on the optical surfaces. Since larger organisms tend not to accumulate in the absence of the bacterial layer, this method should effectively minimize biofouling. The efficiency of this sterilizing operation is further enhanced by the fact that the sample chamber should be enclosed most of the time.

The power consumption of the moored version will also be greatly reduced. The CID camera requires 1.5 amps at 12 volts; the lamp for the ground-truth systems requires more than 5 amps at 12 volts. These power hungry components will not be present in the moored version. The estimated power requirement of the moored version, including operating the microcontroller, the A/D converter, and the detector electronics, is between 10 and 20 watts. If we assume 4 SG and 4 NFS samples a day, the system will need to be on for a total of about one hour per day. Assuming the system will stay deployed for six months, the total weight of lithium batteries (rated at 200 watt-hour per kg) required is approximately 12 kg, which is not excessive for a moored instrument.

6. ACKNOWLEDGEMENT

This research was supported by Department of Energy SBIR Phase II Contract DE-FG03-91ER81117. The authors wish to thank Derek Manov of USC and Don Wiggins and Victor Jordan at the USC Natural Sciences Machine Shop for their help and considerable expertise in developing the MOPAR prototype.

APPENDIX A: SHADOWGRAPH PROCESSING SYSTEM

In order to capture the faster sinking marine aggregates (a few mm/sec), the SG system must operate in the 30 - 60 Hz range. With the present video based system, a prohibitive amount of data is generated for storage in a long-term deployment. To overcome this problem, we developed a near real-time processor that detects particles' shadows and reduces the information down to a few simple statistics for storage. The processing cycle consists of about a minute's worth of data acquisition phase and a 10 second processing and storage phase. This cycle is then repeated indefinitely.

In the data acquisition phase, the video camera and the frame grabber (Matrox PIP-512 board) both run at a 30 Hz frame rate. During the "dead period" between the end of the A/D conversion and the beginning of the next frame, there is ample time to process three of the 512 rows of data. This emulates the operation of using three linear CCD arrays in the moored version of the instrument. (Since a fast falling particle may skip a horizontal row entirely, three linear arrays are used to increase the chance of catching all of the particle shadows.) The simple processing at this stage consists of reading a row of data, subtracting away the background, and recording the location and extent of darkened segments with pixel intensities falling below a certain threshold. Since the edge of a particle shadow is never perfectly sharp, the level of this threshold determines the recorded size of the shadow and serves as a calibration parameter.

After the data acquisition phase, a routine searches through the collection of dark segments for each linear array and groups contiguous and overlapping segments into particle shadows. The following characteristics of each particle are then computed: horizontal centroid, centroid in time, total darkened pixels, maximum horizontal extent, and maximum time extent. Particles seen by two arrays are then matched according to these characteristics. When two particles from two arrays are found to have characteristics falling within a certain range of each other, they are identified as the same particle and its velocity components computed, based on the time its centroid crosses the two arrays. The particle dimensions and velocity components are the only data items to be permanently stored on disk and retrieved at the end of a long deployment period.

Computing the vertical velocity of particles by determining the time it takes a particle to fall *between* the horizontal arrays is a more accurate method than simply timing how long it takes a particle to fall *through* an array. In this latter method, vertical velocity is inferred based on the assumed vertical dimension of the particle, which is usually taken to be the same as the width (which is measured directly as the particle falls through the array). If the vertical dimension is not the same as the horizontal dimension, which is generally the case for amorphous aggregates, the error in velocity will be in proportion to the discrepancy. Conversely, using multiple arrays to determine vertical velocity will also allow the vertical dimension to be deduced, based on the time it takes the particle shadow to traverse the array.

7. REFERENCES

1. Sediment Trap Technology and Sampling, U.S. GOFS Planning Report Number 10, August 1989.
2. V. L. Asper, "Measuring the Flux and Sinking Speed of Marine Snow Aggregates," *Deep Sea Res.*, Vol. 34, No. 1, pp. 1-17, 1987.
3. A.C. Hardy and F.H. Perrin, *The Principles of Optics*, pp. 74-75 1st ed. McGraw-Hill Book Company, New York, 1932.
4. R.T. Knollenberg, "The Optical Array: An Alternative to Scattering or Extinction for Airborne Particle Size Determination," *J. App. Met.*, Vol. 9, No. 1, pp. 86-103, 1970.
5. E. D. Hirleman, "Optimal scaling of the inverse Fraunhofer diffraction particle sizing problem: the linear system produced by quadrature," *Particle Charact.*, 4, pp. 128-133, 1987.

6. Y.C. Agrawal and H.C. Pottsmith, "Laser Diffraction Particle Sizing in Stres," in press, to be published in Continental Shelf Research.
7. E. Chang and R. J. Patton, Moored Optical Particle Flux Sensor (MOPAR). SBIR Phase II Interim Report, Dynamics Technology Report, DTW-9138-93006, June 1993.
8. G. K. Batchelor, Introduction to Fluid Dynamics, pp. 230-235, Cambridge University Press, Cambridge, 1967.
9. R.L. Gran and A. Huang, The Marine Snow Void, Dynamics Technology Report, DT-8727-02, 1988, (Secret).
10. A. L. Alldredge, T. C. Granata, C. C. Gotschalk and T. D. Dickey, "The Physical Strength of Marine Snow and Its Implications for Particle Disaggregation in the Ocean," Limnol. Oceanogr., Vol. 35, No. 7, pp. 1415-1428.
11. H. Peters and M.C. Gregg, "Equatorial Turbulence: Mixed Layer and Thermocline," in Dynamics of the Oceanic Surface Mixed Layer, P. Muller and D. Henderson, eds., Proc. 'Aha Hulikoa' Workshop at Manoa, Hawaii, 1987.
12. N. Curle, The Laminar Boundary Layer Equations, Oxford Press, Oxford, 1962.
13. G. Birkhoff and E. H. Zarantonello, Jets, Wakes and Cavities, Academic Press, New York, 1957.
14. D. Kiefer, personal communication.

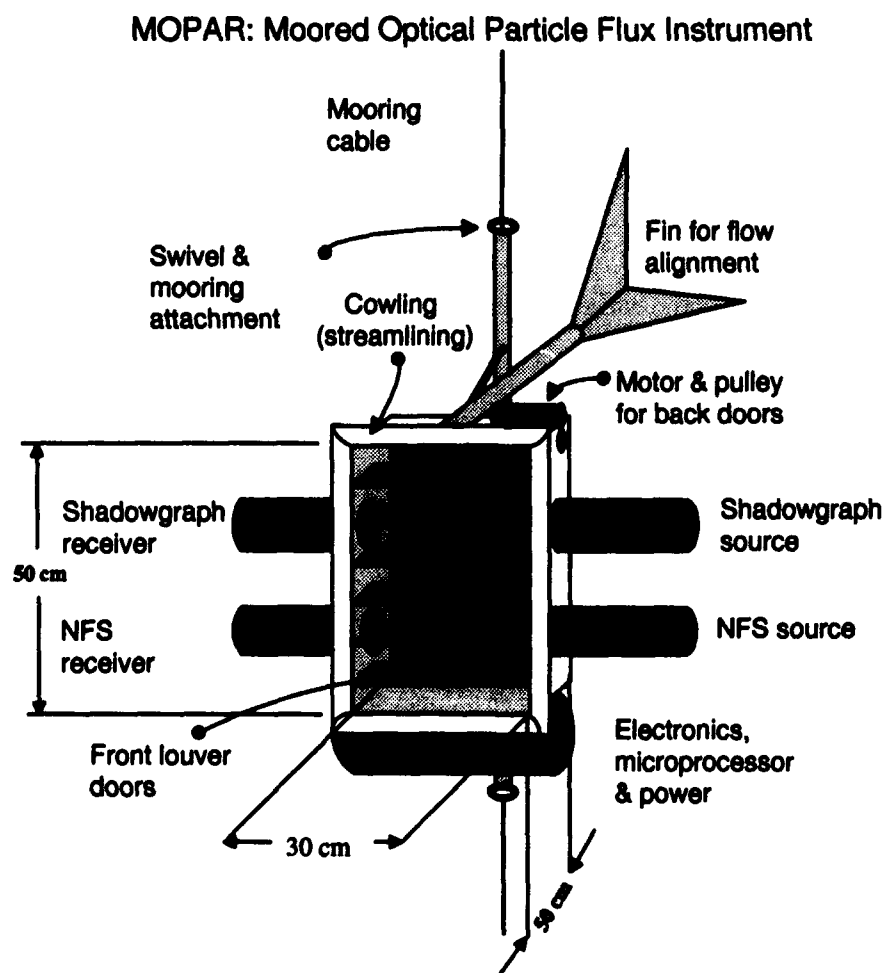


Figure 1. A schematic of the moored optical particle flux measurement instrument (MOPAR).

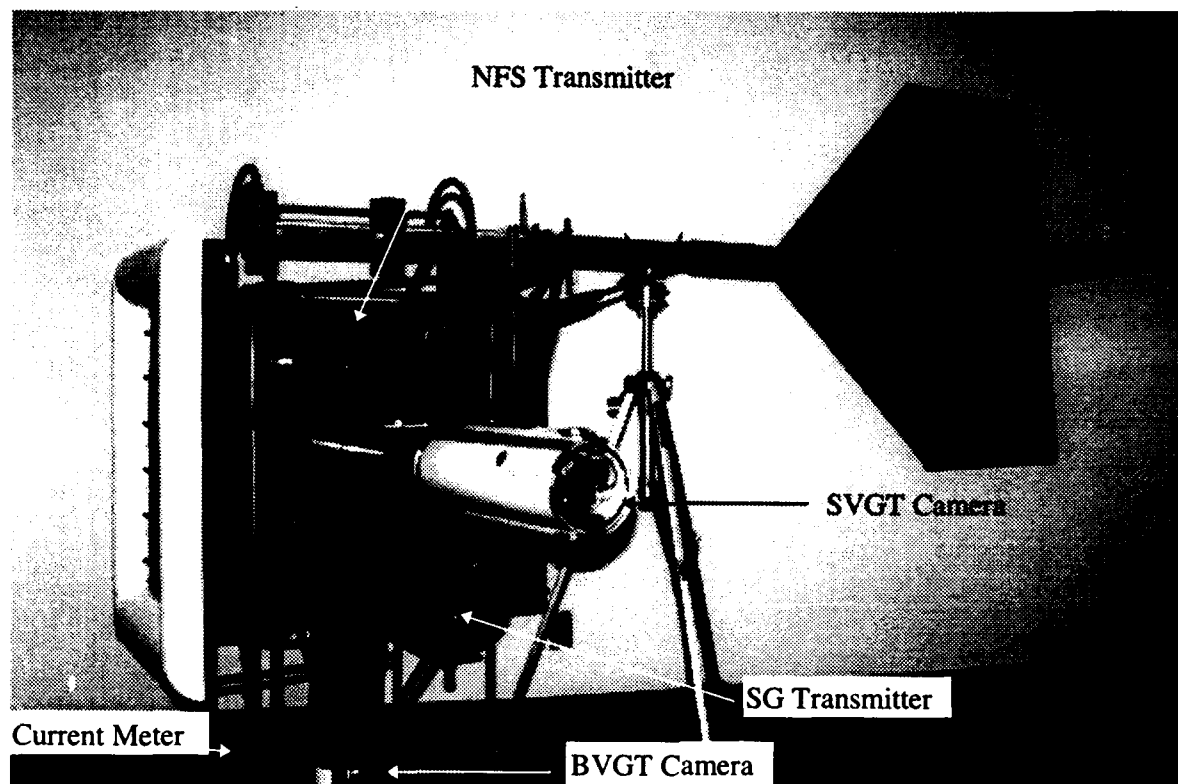


Figure 2. A photograph of the prototype instrument.

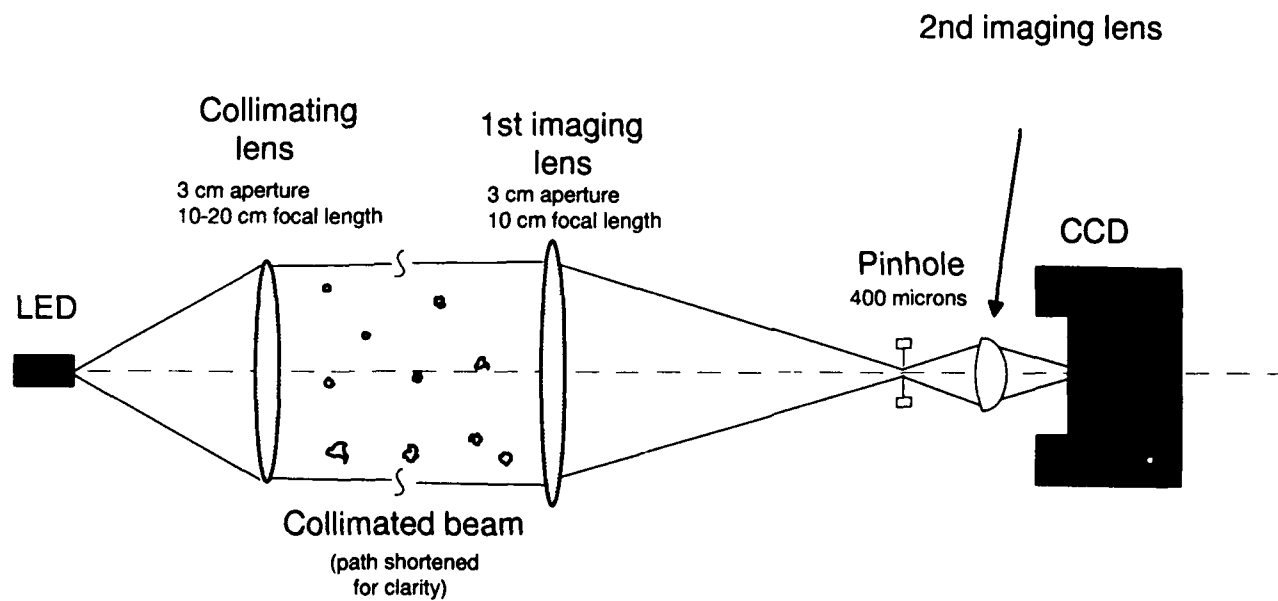


Figure 3. Schematic of the shadowgraph imaging system .

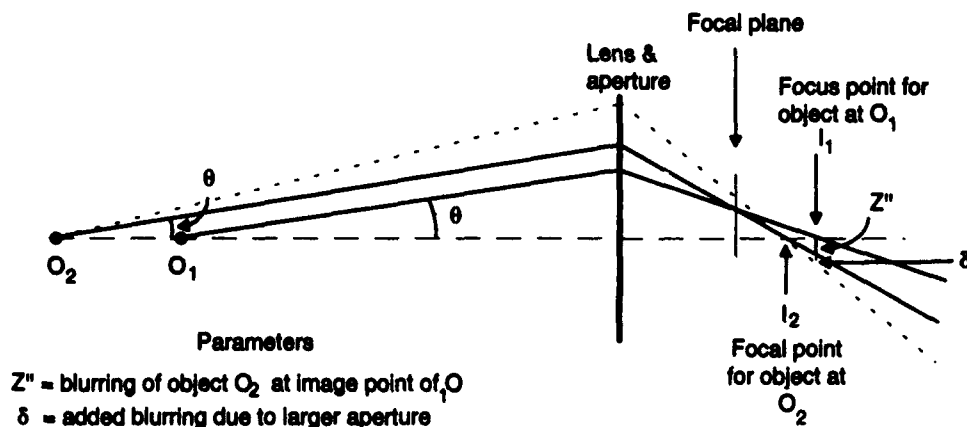


Figure 4. A particle at O_1 is focused at I_1 and a particle at O_2 is focused at I_2 . If the detector for the imaging system is placed at I_1 then only the particle at O_1 will be in focus, the particle at O_2 having a blur spot of extent Z'' . How far the particle can move away from the object plane at O_1 and still be in focus depends on how fast Z'' grows. A larger aperture subtends a larger angle and creates a larger blur spot at I_2 , as depicted by the dashed line in the above figure.

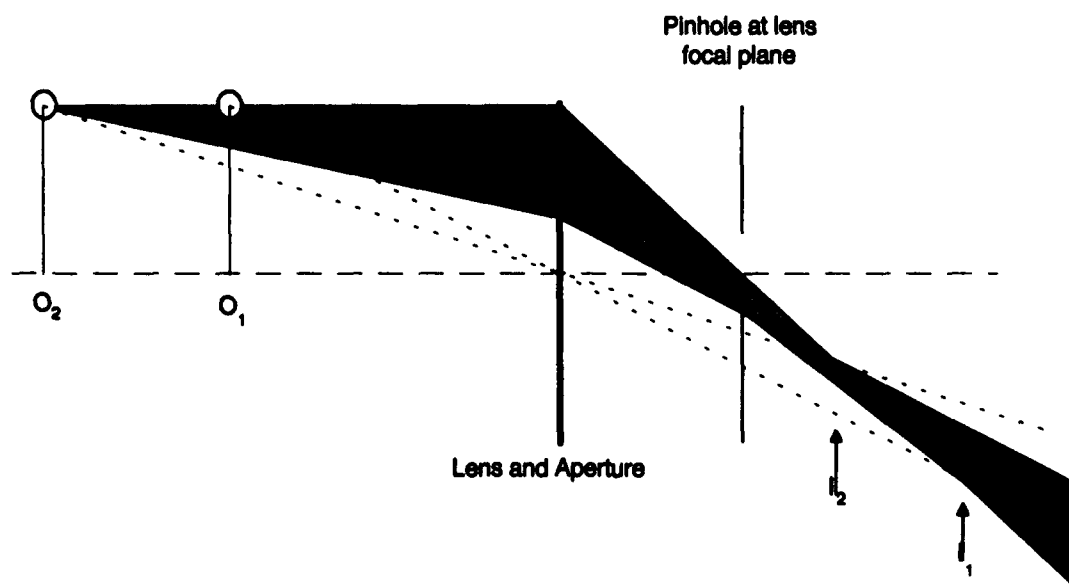


Figure 5. Placing a pinhole in the focal plane of the lens also restricts the angles of the rays imaged by the system. In this case, the angles subtended by the effective aperture of the system are independent of the location of the particles in the object space.

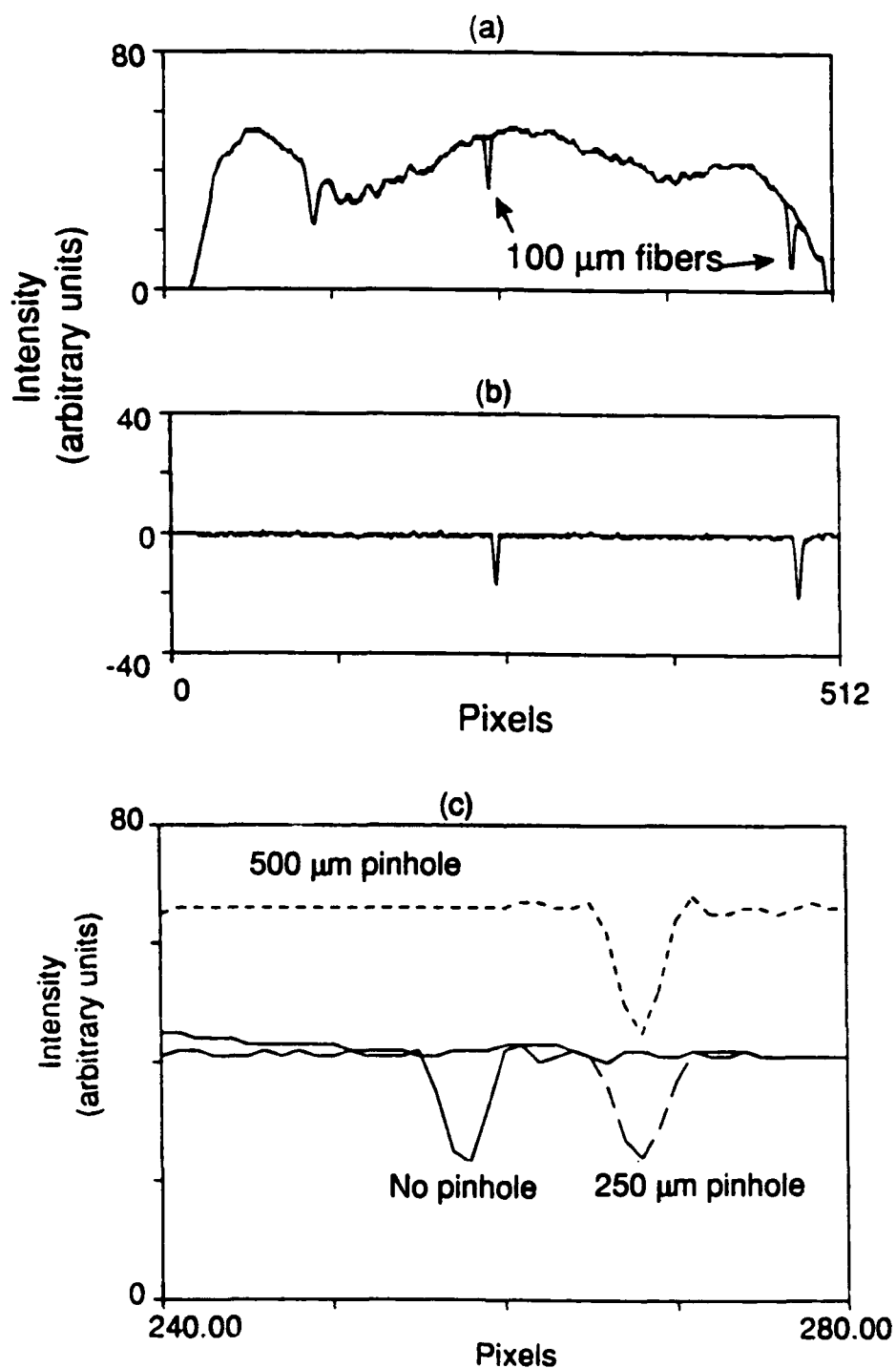


Figure 6. Cross-sections of shadowgraph images of 100 μm optical fibers. The top two plots (a & b) show cross-sections through the fiber shadows with and without background subtraction. The bottom plot, (c), shows cross-sections of a 100 μm fiber using pinholes of different sizes in the receiving optics, compared with the best focused image with no pinhole.

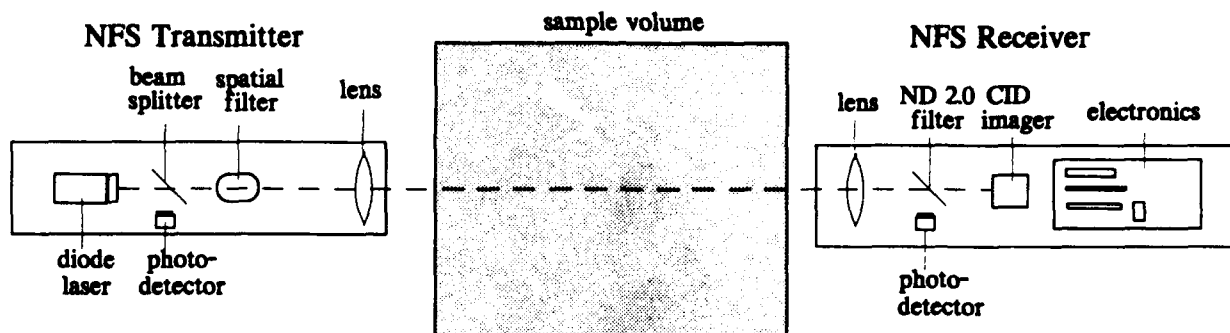


Figure 7. A schematic of the NFS system.

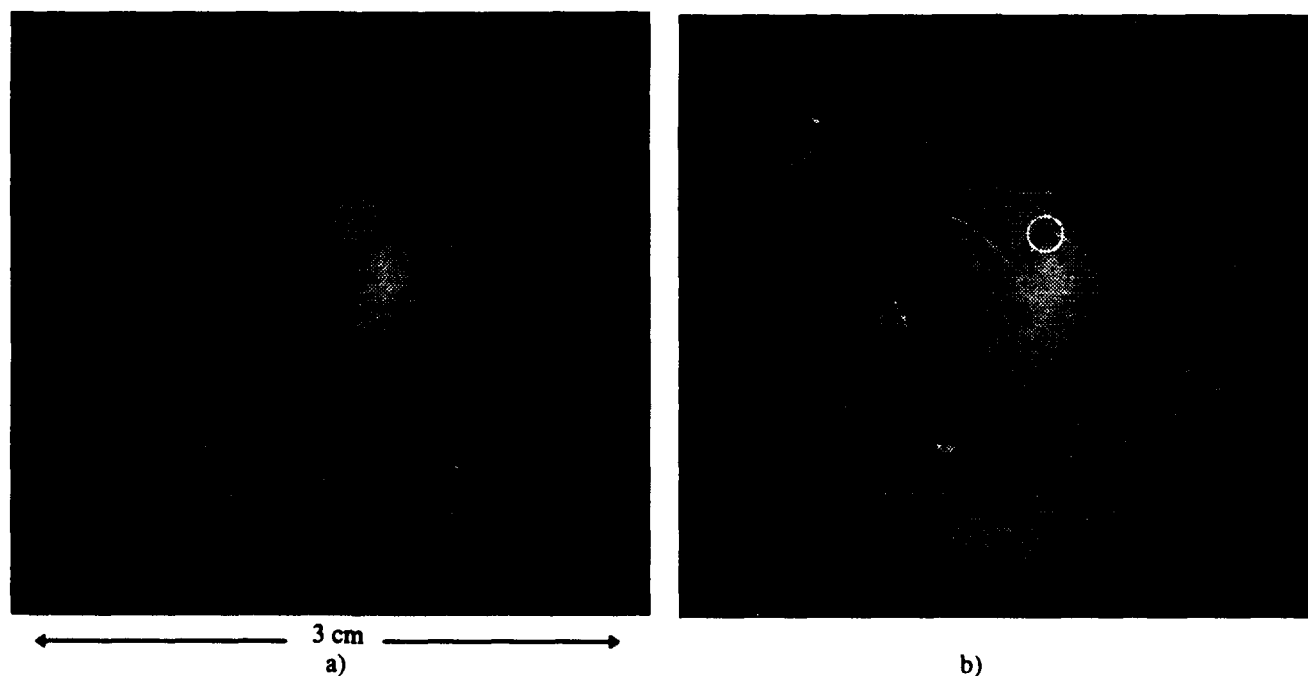


Figure 8. Shadowgraph images of polystyrene spheres, a) 100 μm spheres, and b) 200 μm spheres. The particle circled in a) is a cluster of two 200 μm spheres and appears larger than the other single particles in the same image.

Single Row of SG Data

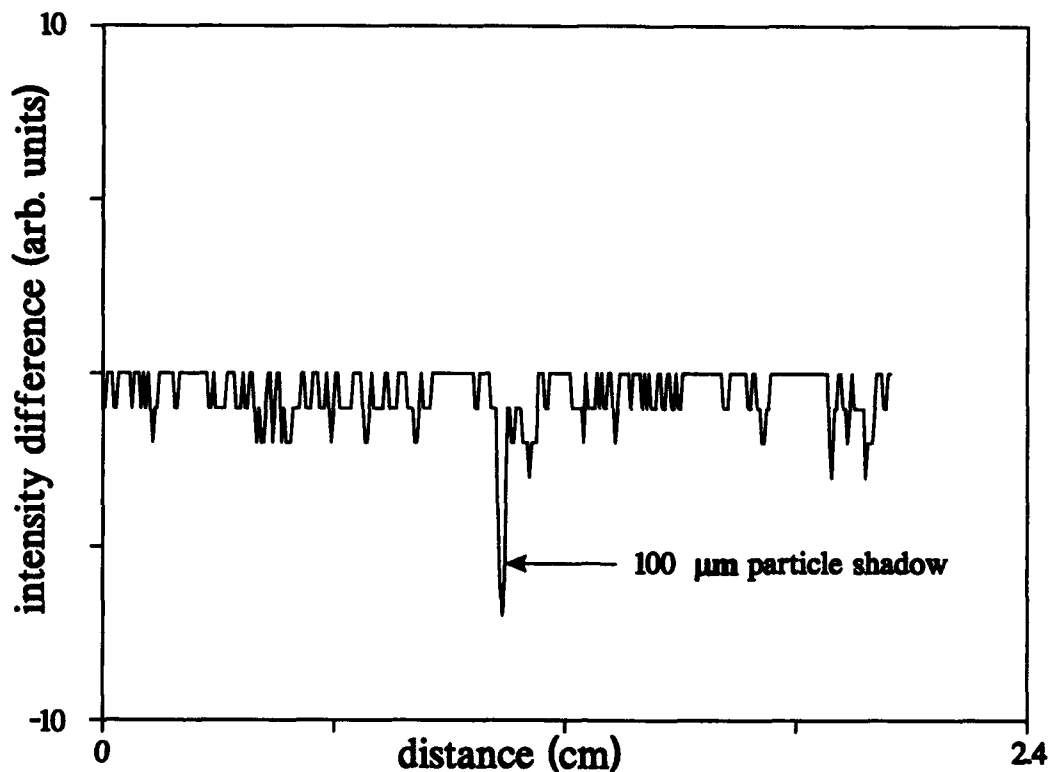


Figure 9. A linear (horizontal) cut of the intensity image in Figure 8a through a 100 μm particle. The background intensity has been subtracted from the image. The particle's shadow is clearly discernable from the background noise.

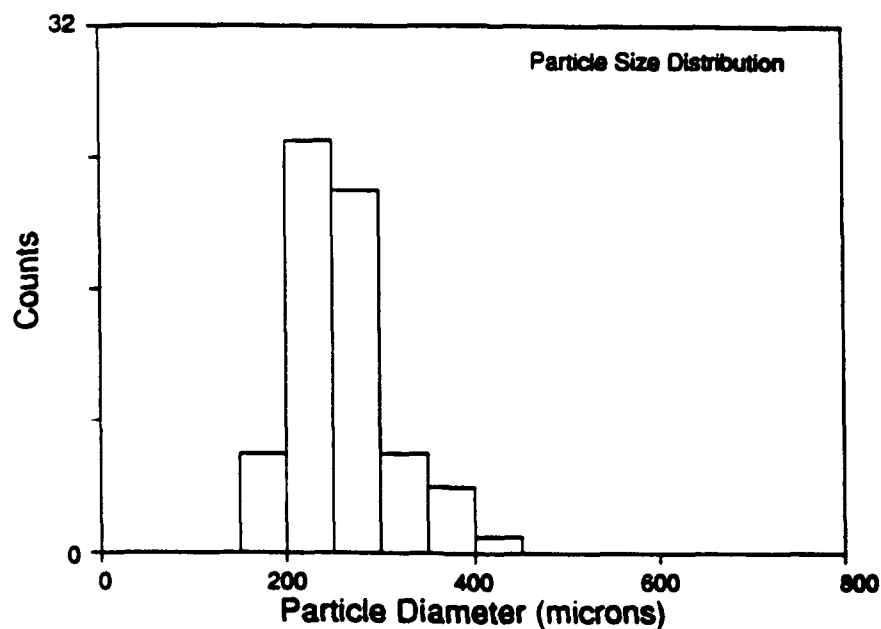


Figure 10. Shadowgraph size distribution for the sample of 200 μm polyspheres.

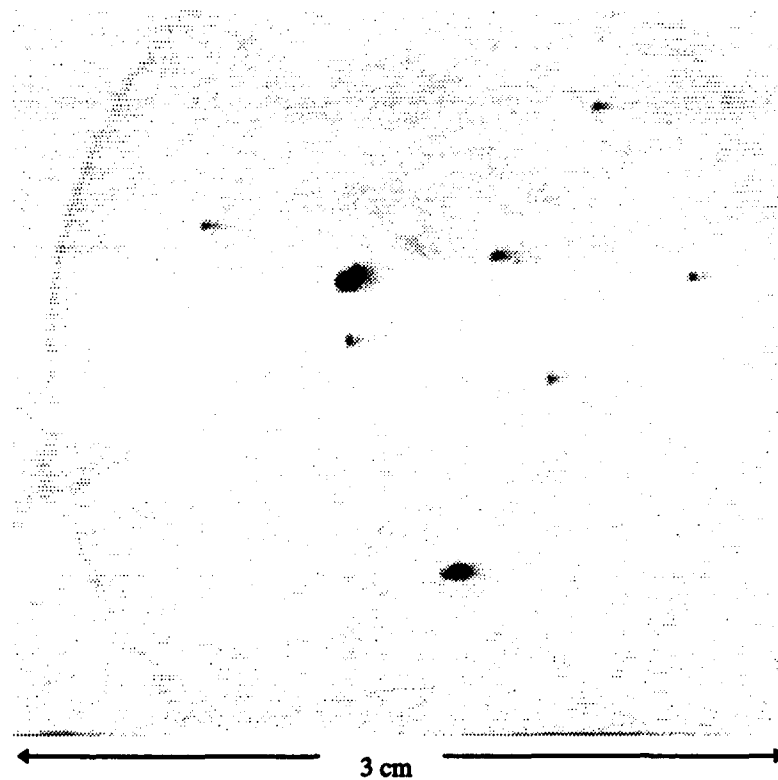


Figure 11. A background-subtracted shadowgraph image of the natural aggregate sample. The smaller particles seen in the image are about 200 to 300 μm in size.

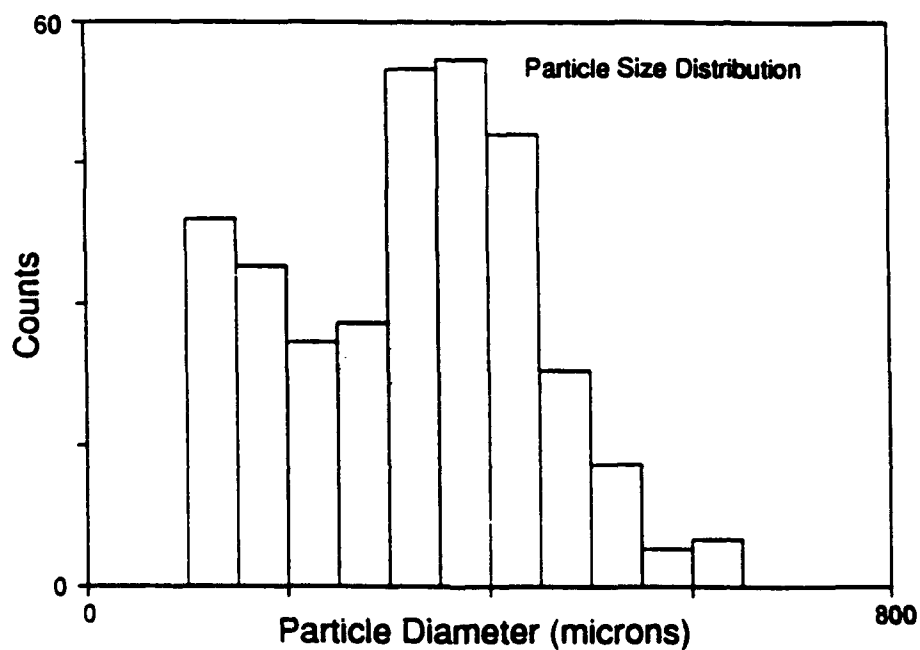


Figure 12. Aggregate size distribution of the sea water sample.

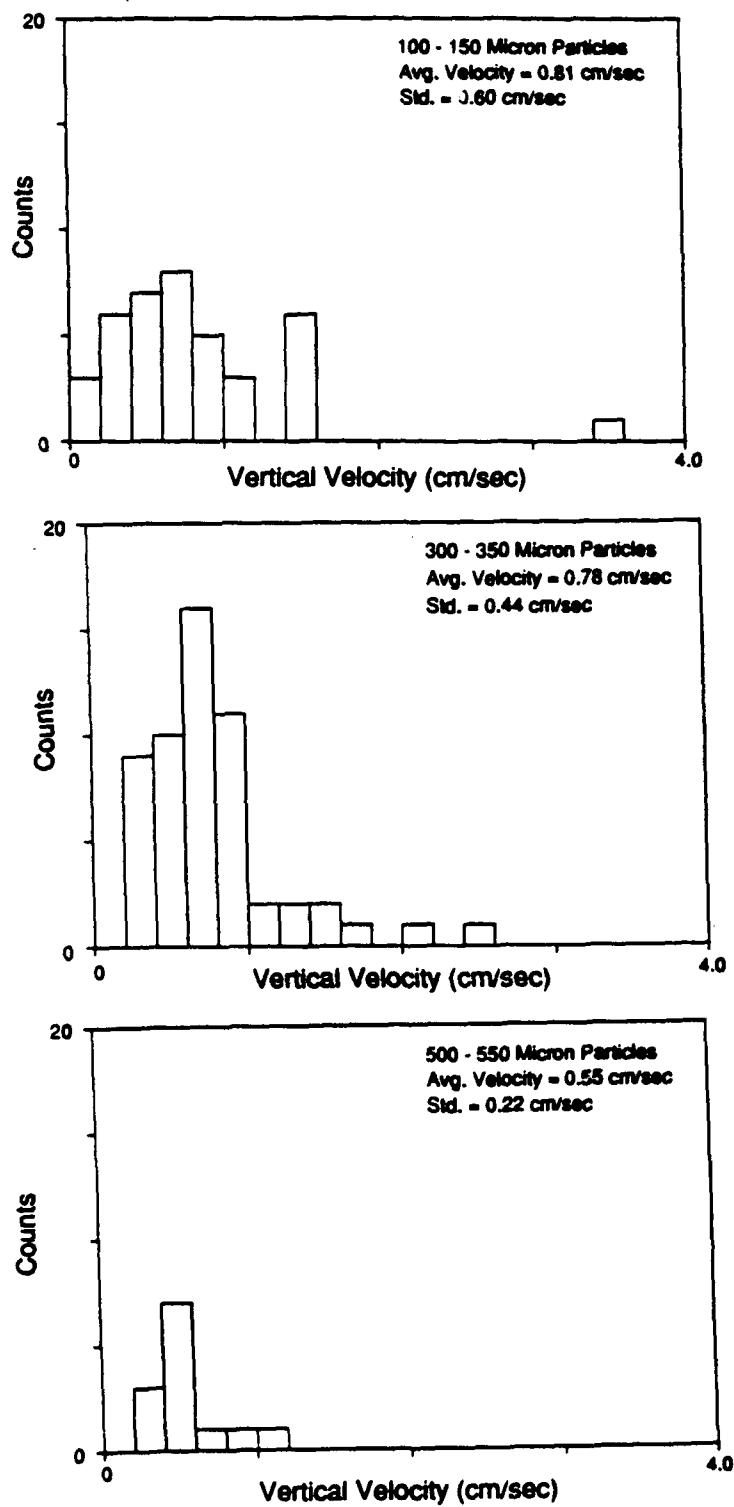


Figure 13. The velocity distribution of three particle size classes, a) 100-150 μm , b) 300-350 μm and c) 500-550 μm particles.

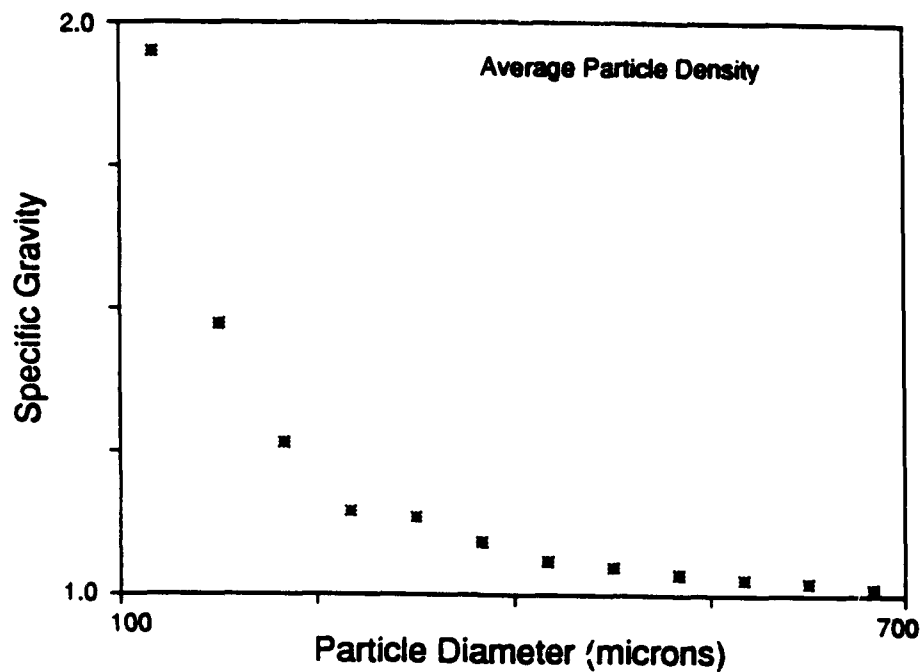


Figure 14. Mean density of aggregates as a function of the aggregate size, derived from Stokes law.

Intensity Profiles

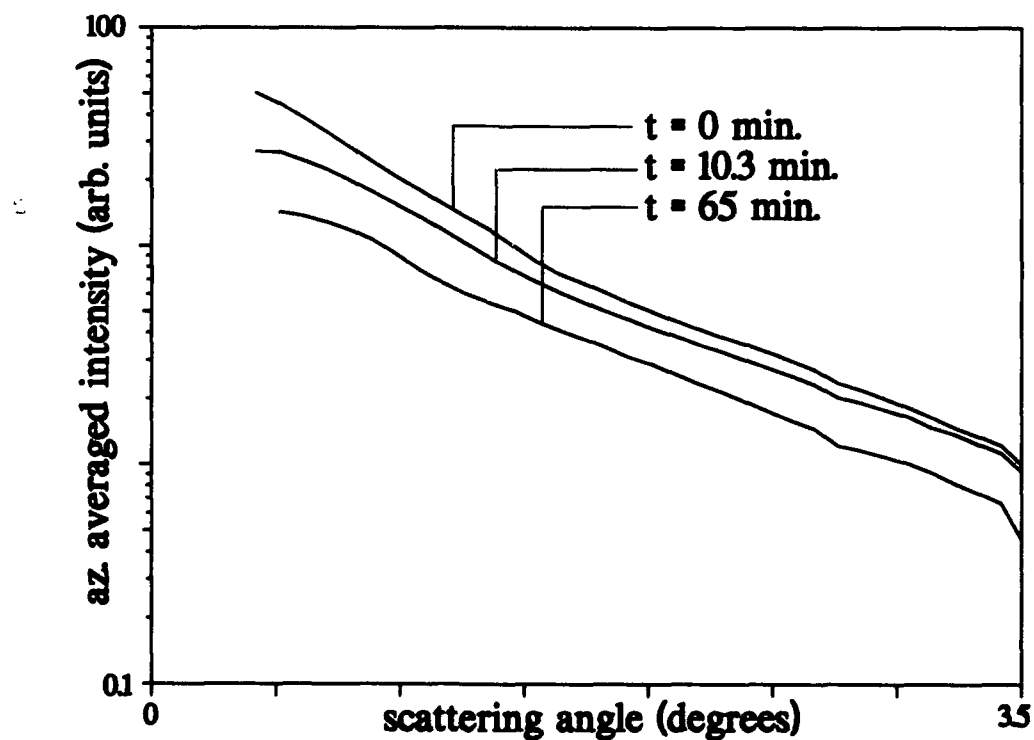


Figure 15. Azimuthally averaged intensity distribution at three different times, after the stirring has stopped.

Particle Size Distribution

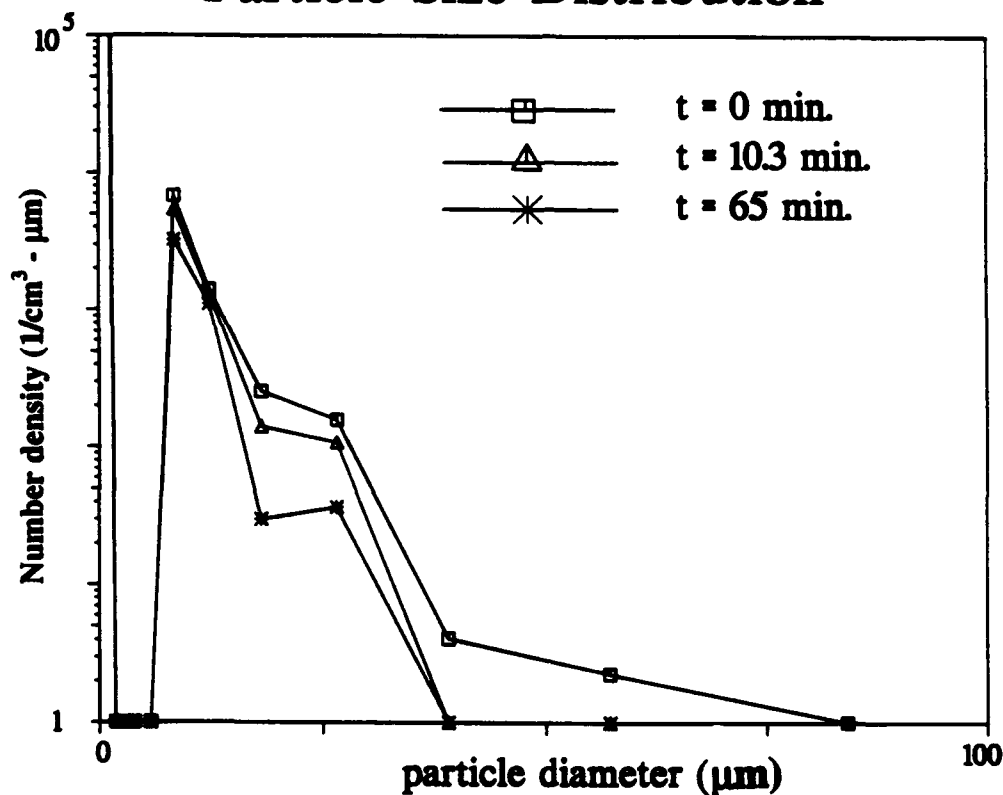


Figure 16. The particle size distribution at three different time late, derived from the inverse calculation.

Concentration History

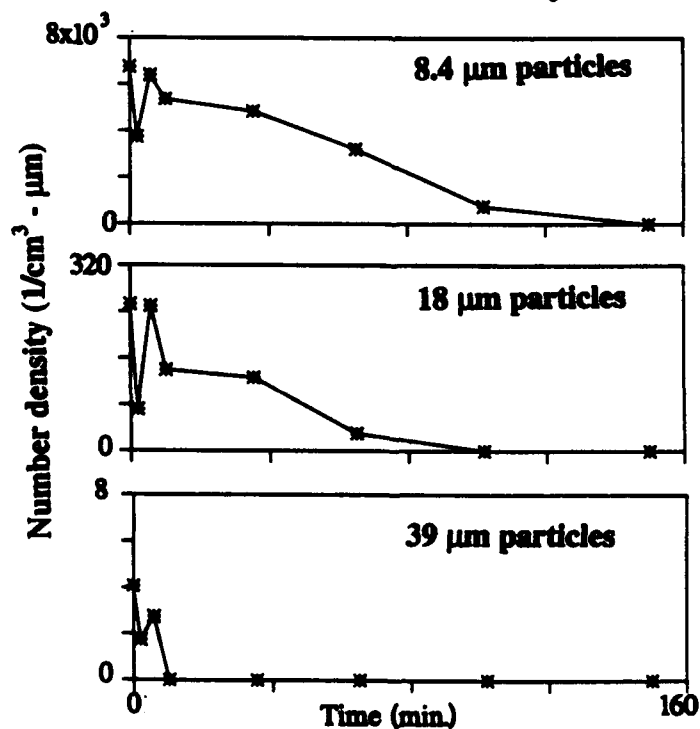


Figure 17. The time dependence of the particle concentration for three different size classes.

SESSION 10

Remote Sensing and Algorithm Development

Scalar irradiance estimation from downward and upward irradiance measurements

Zheng Tao and N.J. McCormick

University of Washington, Department of Mechanical Engineering
Seattle, Washington 98195 USA

ABSTRACT

An inverse problem of ocean optics is solved for estimating the scalar irradiance and a source, such as fluorescence, bioluminescence, or Raman scattering, or an optical property such as the absorption coefficient. The solution requires *in situ* measurements of the downward and upward irradiances and *a priori* estimation of the angular shape of the volume scattering function. The iterative inversion procedure is developed from asymptotic two-stream radiative transfer equations and the conjugate gradient method.

Preliminary numerical tests show that the algorithm is quite accurate in the region away from the surface but gives appreciable errors close to the surface where the asymptotic two-stream equations are a poor approximation.

Keywords: ocean optics, radiative transfer, inverse problem, scalar irradiance, fluorescence, bioluminescence

1. INTRODUCTION

The Gershun¹ equation of ocean optics is the conservation principle of radiative transfer for source-free waters. The equation can be viewed as an algorithm for estimating the absorption coefficient for the water between two closely-spaced positions where measurements of the net irradiance and scalar irradiance are made. A straight-forward extension of this algorithm exists for estimating a source, such as fluorescence, bioluminescence, or Raman scattering, provided the absorption coefficient is known or can be approximately estimated.^{2,3}

More recently an algorithm to simultaneously estimate three parameters, such as the absorption and scattering coefficients and a source, has been formulated and numerically tested.⁴ The algorithm, which requires measurements of the downward and upward components of the irradiance and scalar irradiance, was developed from new asymptotic, two-stream radiative transfer equations. To use this algorithm it must be assumed that the anisotropic angular scattering behavior is known, which is not a bad approximation since Petzold⁵ has shown that the angular shape of the scattering function is reasonably similar for different open ocean waters.

The objective of this investigation is to use the asymptotic two-stream radiative transfer equations to develop an implicit (i.e., iterative) method for estimating the scalar irradiance and a second parameter. One possibility for the second parameter is a source, in which case it must be assumed that the absorption and scattering coefficients and the phase function

are known. Another possibility for the second quantity is that the absorption coefficient be estimated. On the other hand, a pigment concentration such as chlorophyll *a* can be estimated if a model exists that correlates the absorption and scattering coefficients to the concentration. The new feature of this analysis is that no measurements of the scalar irradiance are needed since that quantity also will be estimated using the downward and upward irradiance measurements.

The estimation of the scalar irradiance from the downward and upward irradiances is a worthy objective even if a second parameter such as a source or absorption coefficient is not desired. Jerome *et al.*⁶ and Bannister,⁷ for example, have performed Monte Carlo calculations in order to develop correlations between irradiances and scalar irradiances for specific waters; such correlations can improve the estimation of photosynthetic active radiation (PAR).

2. THE ASYMPTOTIC TWO-STREAM EQUATIONS

It is assumed that the seawater is stratified in plane layers for which the radiance at an implied wavelength is $L(z, \mu, \phi)$ and where z is the depth measured from the surface, μ is the cosine of the polar angle defined with respect to the nadir direction, and ϕ is the azimuthal angle. If the azimuthally-integrated radiance

$$L(z, \mu) = \int_0^{2\pi} L(z, \mu, \phi) d\phi \quad (1)$$

is measured, then the radiance $L(z, \mu)$ for an isotropic source $Q(z)$ satisfies the radiative transfer equation

$$\begin{aligned} \mu \frac{\partial}{\partial z} L(z, \mu) + c(z) L(z, \mu) &= b(z) \int_{-1}^1 \beta(\mu, \mu') L(z, \mu') d\mu' + \frac{Q(z)}{2}, \\ &= \frac{b(z)}{2} \sum_{n=0}^N (2n+1) f_n P_n(\mu) E_n(z) + \frac{Q(z)}{2}. \end{aligned} \quad (2)$$

The $P_n(\mu)$ are Legendre polynomials and the radiance moments

$$E_n(z) = \int_{-1}^1 P_n(\mu) L(z, \mu) d\mu \quad (3)$$

for $n = 0$ and 1 are the scalar irradiance and the difference of the downward and upward irradiances, respectively. Also, $c(z) = a(z) + b(z)$ is the attenuation coefficient and the azimuthally-integrated volume scattering function is normalized such that $f_0 = 1$.

For simplicity we will assume that the source varies in a piecewise constant manner between any two measurement depths so that $dQ(z)/dz = 0$, although this approximation

could be relaxed as was done when deriving three equations for a new, asymptotic two-stream model.⁴ For this special case of the model, two of the equations are

$$\frac{dE_1(z)}{dz} + aE_0(z) = Q(z), \quad (4a)$$

$$\nu_0^2(1 - \omega) \frac{dE_0(z)}{dz} + cE_1(z) \approx 0, \quad (4b)$$

where $\omega = b/c$ is the single scattering albedo. The first equation is merely Gershun's equation with a source, as obtained by integrating Eq. (2) over μ ; the second equation was derived by multiplying Eq. (2) by μ and integrating over μ to find

$$d[2E_2(z) + E_0(z)]/dz + 3c(1 - \omega f_1)E_1(z) = 0,$$

and then assuming the "higher-order" $E_2(z)$ could be approximated by

$$E_2(z) \approx g_2(\nu_0)[E_0(z) - Q(z)/a],$$

which corresponds to $L(z, \mu)$ being in the asymptotic regime.

Here ν_0 , the largest eigenvalue of the homogeneous radiative transfer equation, is the largest positive root of

$$\frac{x}{2} \sum_{n=0}^N (2n+1)f_n \int_{-1}^1 \frac{g_n(\mu)P_n(\mu)}{x-\mu} d\mu = 1, \quad (5)$$

while the $g_n(\mu)$ are the Chandrasekhar polynomials⁸ of degree n , even or odd depending on whether n is even or odd, that satisfy the recursion relation

$$(n+1)g_{n+1}(\mu) - (2n+1)(1 - \omega f_n)\mu g_n(\mu) + ng_{n-1}(\mu) = 0, \quad n \geq 0, \quad (6)$$

with $g_{-1}(\mu) = 0$ and $g_0(\mu) = 1$.

Equations (4) can be numerically solved by dividing the depth range into N intervals, denoted by Δz_i , $i = 1$ to N , and averaging the equations over spatial region $z_i \leq z \leq z_{i+1}$, $i = 0$ to $(N-1)$. We define $\Delta z_i = z_{i+1} - z_i$, $\bar{z}_i = (z_{i+1} + z_i)/2$, and

$$\bar{E}_{ni} = [E_n(z_{i+1}) + E_n(z_i)]/2, \quad (7a)$$

$$\Delta E_{ni} = E_n(z_{i+1}) - E_n(z_i), \quad (7b)$$

$$\int_{z_i}^{z_{i+1}} E_n(z) dz \approx \Delta z_i \bar{E}_{ni}. \quad (7c)$$

The resulting equations are

$$\frac{\Delta E_{1i}}{\Delta z_i} + \bar{a}_i \bar{E}_{0i} = \bar{Q}_i, \quad (8a)$$

$$\bar{\nu}_{0i}^2(1 - \bar{\omega}_i) \frac{\Delta E_{0i}}{\Delta z_i} + \bar{c}_i \bar{E}_{1i} \approx 0, \quad (8b)$$

where \bar{a}_i denotes the average value of a in region $z_i \leq z \leq z_{i+1}$ and $\bar{\omega}_i = 1 - \bar{a}_i/\bar{c}_i$. Also, $\bar{\nu}_{0i}$ is the largest eigenvalue for spatial region i .

3. ESTIMATION OF THE SCALAR IRRADIANCE AND A SOURCE

To solve this problem we must assume that \bar{a}_i and $\bar{c}_i = \bar{a}_i/(1 - \bar{w}_i)$ are known. We then use Eq. (7a) in (8a) and (7b) in (8b) to obtain

$$\begin{aligned} E_{0,i+1} + E_{0i} &\approx \frac{2\bar{Q}_i}{\bar{a}_i} - \frac{2\Delta E_{1i}}{\bar{a}_i\Delta z_i}, \\ E_{0,i+1} - E_{0i} &\approx -\frac{\bar{a}_i\bar{E}_{1i}\Delta z_i}{\bar{\nu}_{0i}^2(1 - \bar{w}_i)^2}. \end{aligned}$$

Subtraction of the two equations leads to the result

$$E_{0i} = \frac{\bar{Q}_i}{\bar{a}_i} - \frac{\Delta E_{1i}}{\bar{a}_i\Delta z_i} + \frac{\bar{a}_i\bar{E}_{1i}\Delta z_i}{2\bar{\nu}_{0i}^2(1 - \bar{w}_i)^2}, \quad i = 0 \text{ to } (N - 1). \quad (9)$$

With this set of equations we first use an assumed source distribution, as denoted by \bar{Q}_i^a , to estimate the scalar irradiances E_{0i} . To close the set of equations, at least three approximations are possible. One can use the asymptotic distribution $E_0(z) \sim \exp(-cz/\nu_0)$ at deep depths to assume that $dE_0(z)/dz \approx -(\bar{c}/\bar{\nu}_0)E_0(z)$ for the deepest region z_{N-1} to z_N ; then a first-order finite difference approximation leads to

$$E_{0N} \approx E_{0,N-1} \left[1 - \frac{\bar{c}_{N-1}\Delta z_{N-1}}{\bar{\nu}_{0,N-1}} \right]. \quad (10a)$$

Another equation for E_{0N} , developed by assuming a linear relationship for the scalar irradiance between the last three positions, is

$$E_{0N} \approx 2E_{0,N-1} - E_{0,N-2}. \quad (10b)$$

If ratios of the scalar irradiances at the deepest positions are the same, then a third approximation for estimating the scalar irradiance at the deepest node is

$$E_{0N} \approx E_{0,N-1}^2 / E_{0,N-2}. \quad (10c)$$

To estimate E_{0i} and \bar{Q}_i as a function of depth, a source distribution \bar{Q}_i^a is assumed so that the estimated values of the scalar irradiances can be computed from Eq. (9) and one of the Eqs. (10). The estimated values then are used in Eq. (8a) to compute a source distribution \bar{Q}_i^c . The difference between the calculated and assumed sources is minimized by using the conjugate gradient method^{9,10} and the functional

$$J = \sum_{i=0}^{N-1} [\bar{Q}_i^c - \bar{Q}_i^a]^2. \quad (11)$$

Once J has been minimized to a sufficiently small value the final estimates of \bar{Q}_i^c are used to obtain E_{0i} for $i = 1$ to N from Eqs. (9) and (10).

To test the algorithm it was first necessary to assume a model for the dependence of the optical properties; we selected a model used by Gordon *et al.*¹¹ and Mobley *et al.*^{12,13} that depends on pigment concentration. This model is for a mixture of pure water (labeled with subscript w) and particles (labeled with subscript p) in which it is assumed that the wavelength and pigment concentration for the particles can be factored as

$$a_p(\lambda, C) = 0.06 \frac{a_p(\lambda)}{a_p(440)} C^{0.602}, \quad (12)$$

where C is the concentration in mg m^{-3} and $C \leq 10 \text{ mg m}^{-3}$. For the scattering coefficient, an approximate, special case of the model was selected,

$$b_p(\lambda, C) = 0.3 \frac{550}{\lambda} C^{0.62}. \quad (13)$$

The mixing of the particles and pure water to get the albedo of single scattering for the mixture was done using the equation

$$\omega = \frac{\omega_p(c_p/c_w) + \omega_w}{(c_p/c_w) + 1}, \quad (14)$$

where $c_p = a_p + b_p$, for example.

Numerical tests on the algorithm of Eqs. (9) and (10c) were done for three cases of a deep body of water of uniform optical properties. Case A, for a wavelength of 570 nm, had no source and a pigment concentration of 6 mg m^{-3} . The optical properties were $a_w = 0.0799 \text{ m}^{-1}$, $b_w = 0.0017 \text{ m}^{-1}$, $a = 0.1286 \text{ m}^{-1}$, and $b = 0.8808 \text{ m}^{-1}$; the expansion coefficients f_n for the phase function were computed in the manner of Francisco and McCormick.¹⁴ The computed downward and upward irradiances to be used as simulated measurements at every meter of depth are shown in Fig. 1, Case A. Case B of Fig. 1 illustrates the irradiances computed with no source and a wavelength of 500 nm, $C = 10 \text{ mg/m}^3$, $a_w = 0.0257 \text{ m}^{-1}$, $b_w = 0.0029 \text{ m}^{-1}$, $a = 0.1860 \text{ m}^{-1}$, and $b = 1.3786 \text{ m}^{-1}$. For Cases A–C the boundary conditions were $L(0, \mu) = 10 \delta(\mu - 0.866)$, $0 \leq \mu \leq 1$, and $L(z, \mu) \rightarrow 0$ for large z .

For Case C we took a bioluminescence profile of Greenblatt *et al.*¹⁵ (California station, 33.46 degrees N, 119.36 degrees W, 0055, July 20, 1982). The calculation was done for a wavelength of 670 nm for which the pure water properties are $a_w = 0.4300 \text{ m}^{-1}$ and $b_w = 0.6421 \text{ m}^{-1}$. The pigment concentration was assumed to be 10 mg m^{-3} which resulted in water-particle properties of $a = 1.6002 \text{ m}^{-1}$ and $b = 0.6421 \text{ m}^{-1}$. The simulated downward and upward irradiance measurements versus depth are shown in Fig. 1, Case C.

Figure 2 shows the estimated scalar irradiance compared to the simulated scalar irradiance, and Fig. 3 shows the estimated source that should have been zero everywhere. It is seen that there are significant errors, until one gets below 6–8 m, that arise from the fact that the asymptotic two-stream algorithm is a poor approximation near the surface; errors also occur at deeper depths when the value of $E_0(z)$ becomes so small that numerical inaccuracies become significant. Similar results are seen in Figs. 4 and 5 for Case B except that the estimates are good at depths as small as 4 m because the asymptotic distribution is reached at a shallower location than for Case A.

Figure 6 shows the estimated scalar irradiance compared to the scalar irradiance for Case C and Fig. 7 shows the corresponding comparison for the estimated source and the source measured by Greenblatt *et al.*¹⁵ The estimated source is most accurate in the mid-depth region where the asymptotic assumption is a good approximation and the scalar irradiance is not too small.

4. ESTIMATION OF THE SCALAR IRRADIANCE AND A DIFFERENT QUANTITY

The procedures for solving two other inverse problems using the asymptotic two-stream equations of Eq. (8) can be briefly mentioned. Both require that there be no source so $\bar{Q}_i = 0$.

4.1 Estimation of the Scalar Irradiance and the Absorption Coefficient.

In this application it is necessary to assume that the scattering coefficient $b(z)$ is known as a function of depth. An assumed value of the absorption coefficient \bar{a}_i^a is used to compute $\bar{\omega}_i = \bar{b}_i / (\bar{a}_i + \bar{b}_i)$ and then the eigenvalue $\bar{\nu}_0$ can be determined from Eq. (5). The source-less form of Eq. (9) plus one form of Eq. (10) then is used to compute E_{0i} , and a computed absorption coefficient \bar{a}_i^c is obtained from the source-less form of Eq. (8a). Then the conjugate gradient method is used to minimize the functional

$$J = \sum_{i=0}^{N-1} [\bar{a}_i^c - \bar{a}_i^a]^2. \quad (15)$$

Once J has been minimized the final estimates of E_{0i} and \bar{a}_i can be obtained.

4.2. Estimation of the Scalar Irradiance and the Pigment Concentration.

In this more realistic problem where neither the absorption nor scattering coefficient need be known, a correlation of the two coefficients to pigment concentration is required, such as the model of Eqs. (12) to (14). The iterative solution is done by first assuming a pigment concentration \bar{C}_i^a and then computing $\bar{\omega}_i$ from Eqs. (12) to (14). The eigenvalue $\bar{\nu}_0$ then can be determined from Eq. (5) and the value of E_{0i} then is computed from the source-less form of Eq. (9) plus one form of Eq. (10). After \bar{a}_i is estimated from the source-less form Eq. (8a) the pigment concentration \bar{C}_i^c can be computed from Eq. (12). The conjugate gradient method is then used to minimize the functional

$$J = \sum_{i=0}^{N-1} [\bar{C}_i^c - \bar{C}_i^a]^2. \quad (16)$$

Once J has been minimized the final estimates of E_{0i} and \bar{C}_i can be obtained.

5. CONCLUSIONS

A new algorithm is proposed for estimating the scalar irradiance and a second quantity such as a spatially-varying source, the absorption coefficient, or the pigment concentration. The method requires only the measurement of the downward and upward irradiances

and appropriate information about the optical properties. Because asymptotic two-stream equations are used for the algorithm the results are poorest for depths near the surface.

ACKNOWLEDGMENTS

This work was supported by an Office of Naval Research contract and by a grant from the San Diego Supercomputer Center. We appreciate the help of Paul Francisco in computing the optical properties used in the numerical tests.

REFERENCES

1. A.A. Gershun, "The light field," J. Math. & Phys. **18**, 51-151 (1939).
2. N.J. McCormick, R. Sanchez, and H.C. Yi, "Marine bioluminescent estimation algorithms for *in situ* irradiance measurements," in Ocean Optics X, R.W. Spinrad, ed., (Society of Photo-Optical Instrumentation Engineers, 1990), Vol. 1302, pp. 38-48.
3. H.C. Yi, R. Sanchez, and N.J. McCormick, "Bioluminescence estimation from ocean *in situ* irradiances," Appl. Opt. **31**, 822-830 (1992).
4. Z. Tao, N.J. McCormick, and R. Sanchez, "Ocean optical property estimation using explicit and implicit algorithms," Appl. Opt. **33**, 3265-3275 (1994).
5. T.J. Petzold, "Volume scattering functions for selected ocean waters," Scripps Inst. Ocean. Publ. 72-78 (1972), pp. 1-78.
6. J.H. Jerome, R.P. Bukata, and J.E. Bruton, "Utilizing the components of vector irradiance to estimate the scalar irradiance in natural waters," Appl. Opt. **27**, 4012-4018 (1988).
7. T.T. Bannister, "Model of the mean cosine of underwater radiance and estimation of underwater scalar irradiance," Limnol. Oceanogr. **37**, 773-780 (1992).
8. S. Chandrasekhar, Radiative Transfer, (Dover, New York), Sec. 48.3 (1960).
9. M. Hestenes, Conjugate Direction Methods in Optimization, (Springer-Verlag, New York) (1980).
10. W.H. Press, B.P. Flannery, S.A. Teukolsky, and W.T. Vetterling, Numerical Recipes, The Art of Scientific Computing, (Cambridge Univ. Press, Cambridge), Secs. 10.5-10.7 (1986).
11. H.R. Gordon, K. Ding, and W. Gong, "Radiative transfer in the ocean: computations relating to the asymptotic and near-asymptotic daylight field," Appl. Opt. **32**, 1606-1619 (1993).
12. C.D. Mobley, Light and Water: Radiative Transfer in Natural Waters, Academic Press (in press).
13. C.D. Mobley, B. Gentili, H.R. Gordon, Z. Jin, G.W. Kattawar, A. Morel, P. Reinersman, K. Stamnes, and R.H. Stavn, "Comparison of numerical models for computing underwater light fields," Appl. Opt. **32**, 7484-7504 (1992).
14. P.W. Francisco and N.J. McCormick, "Chlorophyll concentration effects on asymptotic optical attenuation," Limnol. Oceanogr. (to be published).
15. P.R. Greenblatt, D.F. Feng, A. Zirino, and J.R. Losee, "Observations of planktonic bioluminescence in the euphotic zone of the California Current," Mar. Biol. **84**, 75-82 (1984).

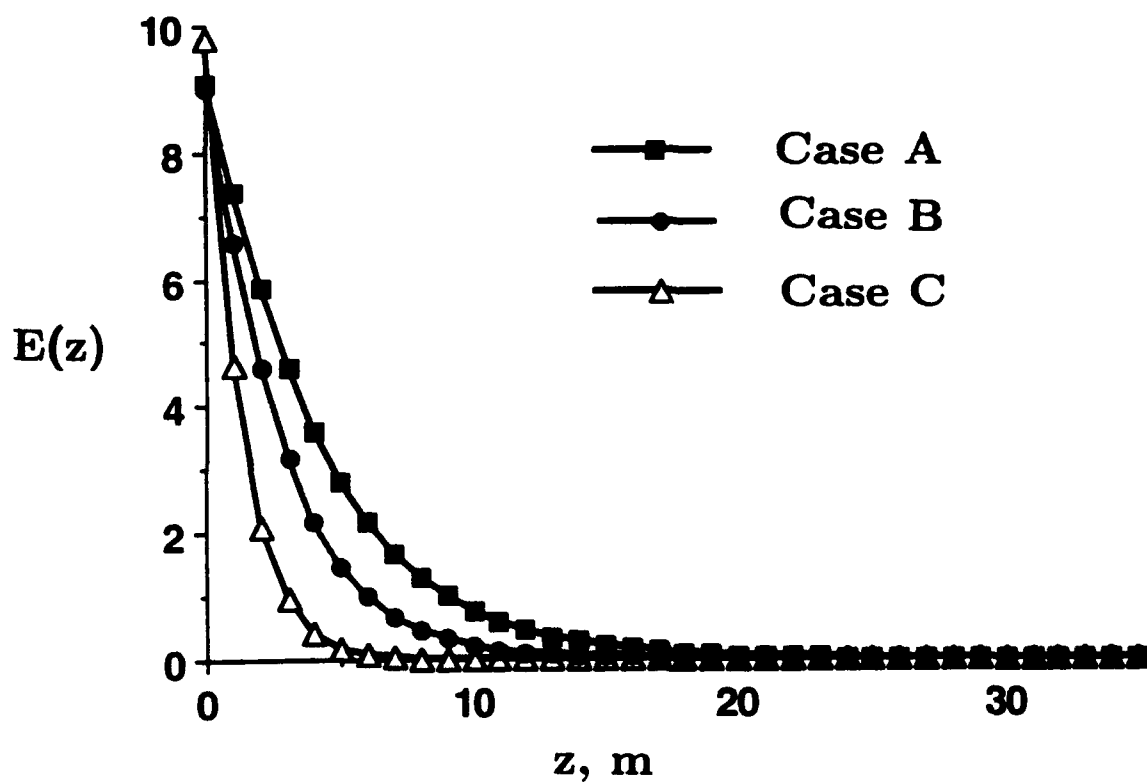


Fig. 1. Simulated measurement data for the irradiance for Case A, no source at 570 nm for a pigment concentration of 6 mg m^{-3} ; Case B, no source at 500 nm for a pigment concentration of 10 mg m^{-3} ; and Case C, the Greenblatt et al.¹⁵ source at 670 nm for a pigment concentration of 10 mg m^{-3} .

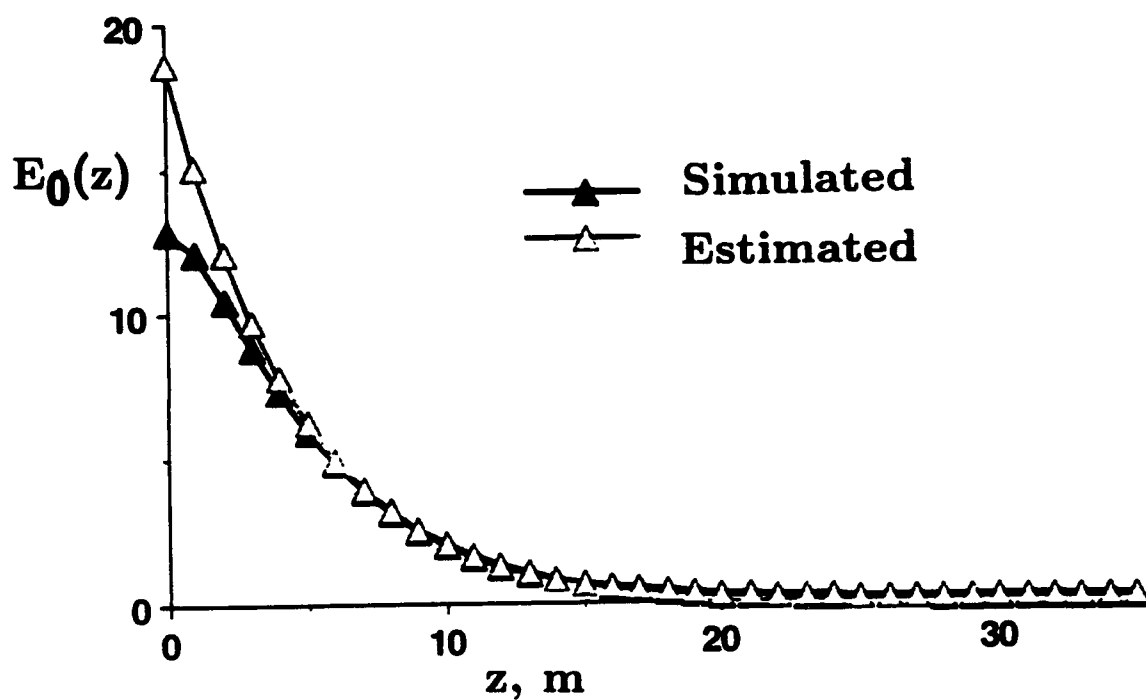


Fig. 2. Case A simulated scalar irradiance vs. depth and values estimated from the simulated measurements of Fig. 1.

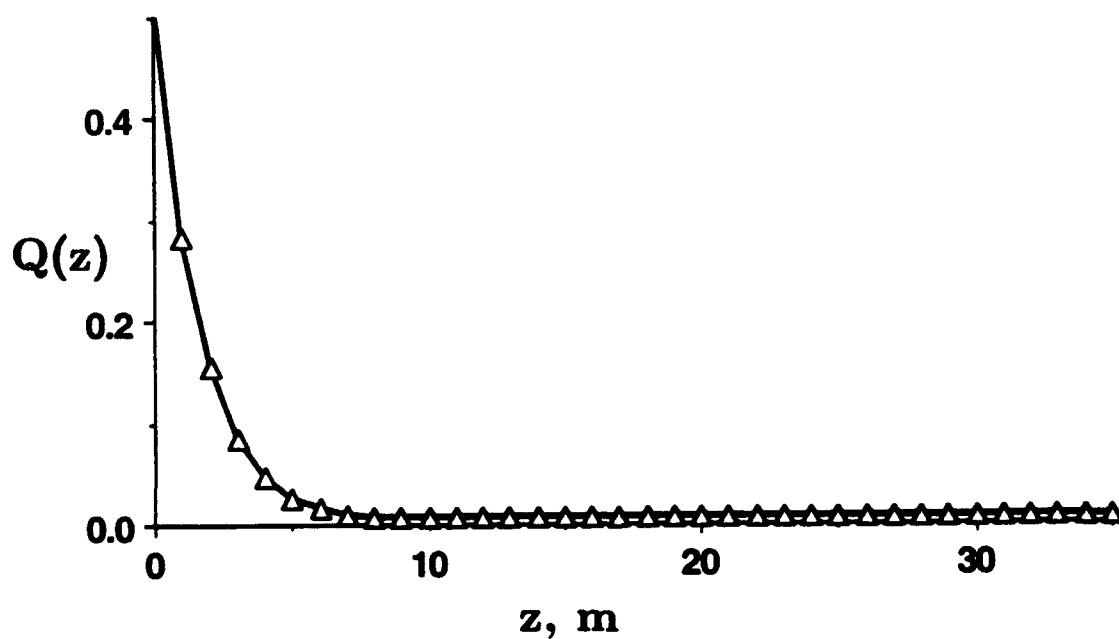


Fig. 3. Case A source vs. depth estimated from the simulated measurements of Fig. 1.

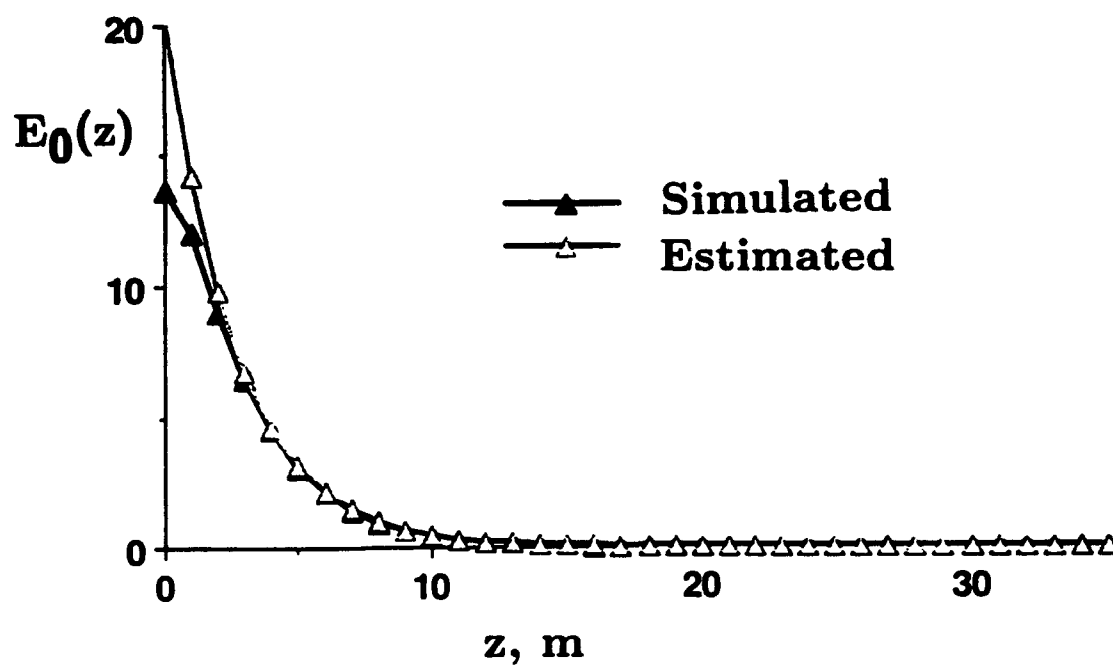


Fig. 4. Case B simulated scalar irradiance vs. depth and values estimated from the simulated measurements of Fig. 1.

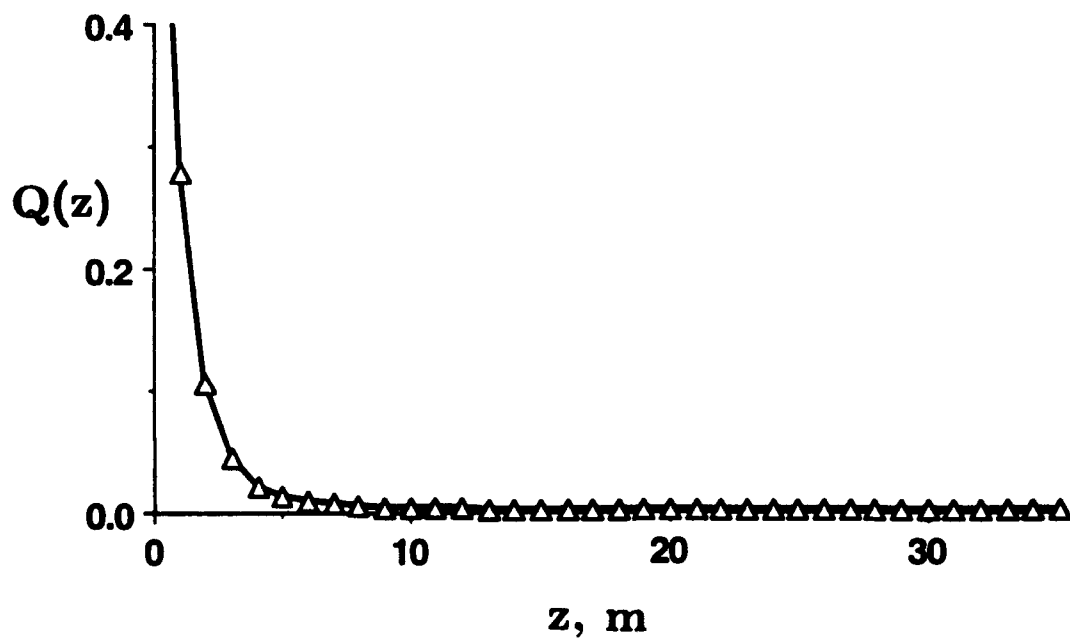


Fig. 5. Case B source vs. depth estimated from the simulated measurements of Fig. 1.

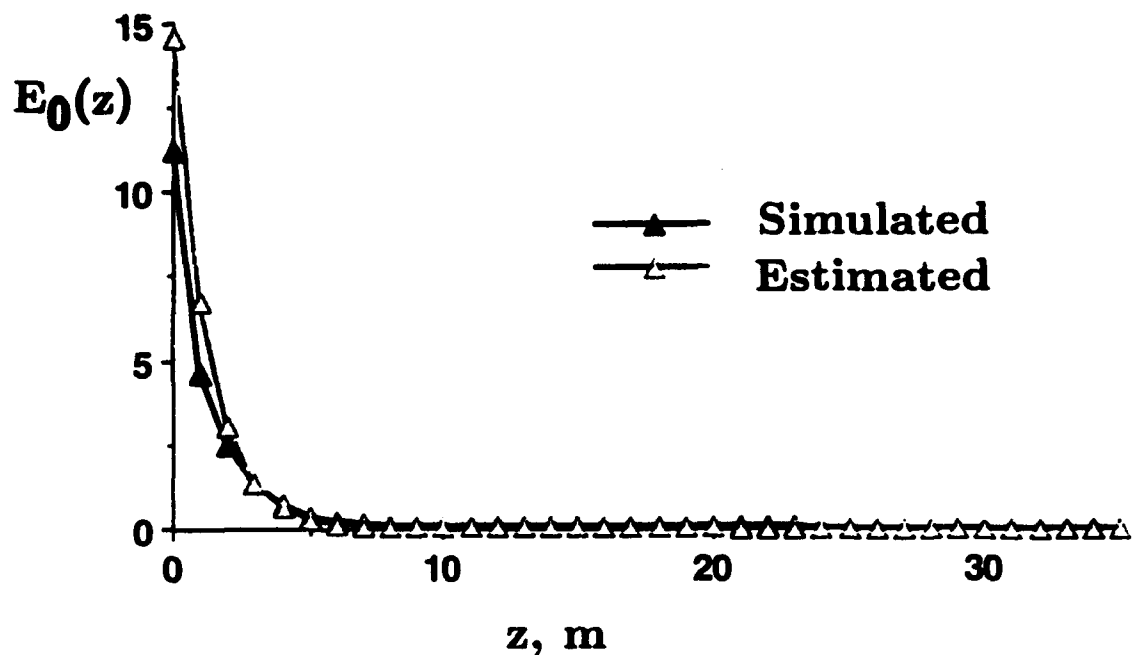


Fig. 6. Case C simulated scalar irradiance vs. depth and values estimated from the simulated measurements of Fig. 1.

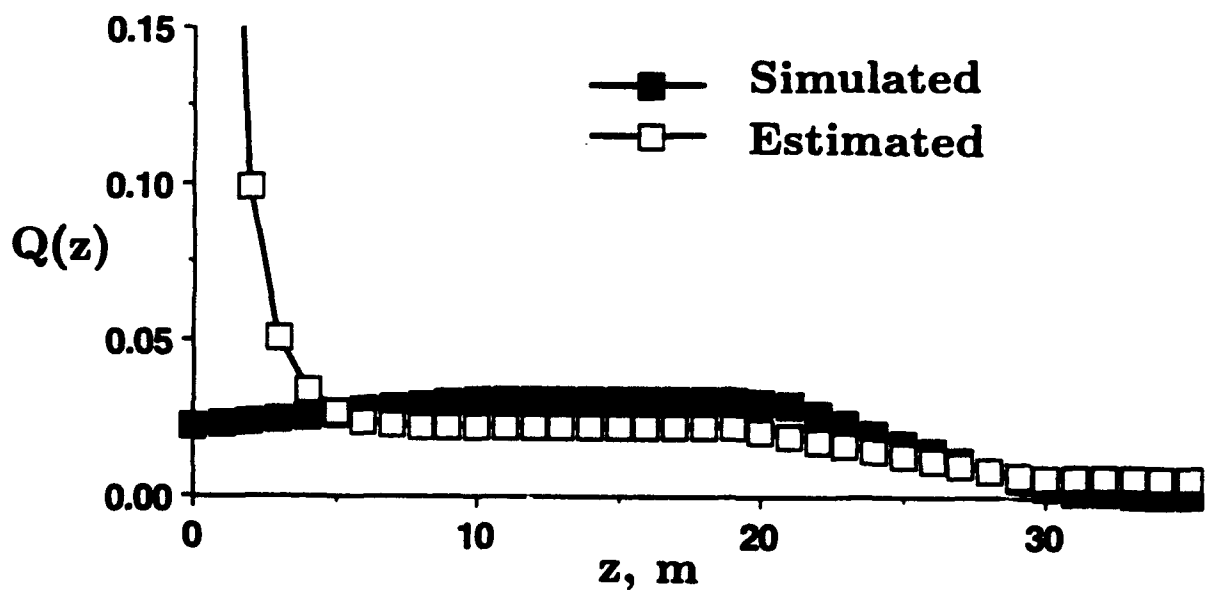


Fig. 7. Case C source vs. depth estimated from the simulated measurements of Fig. 1.

Method of experimental design for optical remote sensing
of chlorophyll concentration in ocean waters

Iosif M. Levin and Igor V. Zolotukhin

P.P. Shirshov Institute of Oceanology, St. Petersburg Branch,
Russian Academy of Sciences, 11, Tavricheskaja Ul.,
St. Petersburg, 193015

In memory of Victor P. Kozlov, an outstanding
physicist and mathematician. Without his
fundamental results, this paper could not have
been written.

ABSTRACT

In order to increase the accuracy of measuring the chlorophyll concentration from shipboard or satellite and to find out maximum potentials of remote sensing, the method of mathematical design of experiment is recommended. It is shown that the optimum design includes not more than two wide composite spectral channels. A recurrent algorithm for selection of the optimal spectral channel is suggested. In order to use this algorithm, one must know statistical characteristics of the system "water-leaving radiance spectrum - chlorophyll concentration in surface waters". They were simulated on the basis of well-known low-parametric models for water optical properties because of lack of experimental data on these characteristics. Optimal spectral channels have been computed and an example of chlorophyll concentration retrieval is shown. They may be considered as preliminary results demonstrating possibilities of the experimental design method.

1. INTRODUCTION

Optimal remote sensing is one of the most effective methods of studying the ocean properties. Well-known and widely used methods of estimating the chlorophyll concentration C in sea waters are based on upwelling water radiance measurements in several wavelengths and subsequent retrieval of C using regression dependencies between C and some functionals of measured spectra. Usually, the color index (ratio of radiances in two wavelengths) is used as such a functional¹. Recently, the principal component analysis has been used for this problem. Here, the weighting factors and expansions of radiance spectra with respect to eigenvectors of the correlation matrix are used as such a functional². Complexity of retrieval the C is due to many interference factors, especially for satellite observations when atmospheric radiance is 5-10 times the "useful" ocean radiance. The accuracy of the retrieval is still rather low. We think that the most promising way to increase it is application of the theory of experimental design³. This theory provides the maximal possible accuracy of the retrieval.

The problem of experimental design in our case is to find the optimal spectral channels for measurements of the water-leaving radiance and to retrieve the chlorophyll concentration by measurements in these channels. In the visual spectrum both the dark-current receiver noise, with the variance independent of the useful signal level, and

the shot noise, the variance of which is directly proportional to the signal level, are present. It is this feature that makes our formulation of the problem different from that known before⁴⁻⁶. Our goal is to develop a convergent iterative algorithm for searching the optimal spectral channels in visual spectrum. We used this algorithm for computation of the optimal spectral channels in the case of shipboard measurements (without account of the atmosphere). The computations are based on the simulated radiance spectra.

2. THE METHOD

The following measurement model is accepted⁶. Let $u(\lambda)$ be the measured radiation spectrum, namely the average number of "effective" photons (primary electrons for electronic detectors) at the receiver input per unit wavelength and per unit time. Let $x(\lambda)$ be the spectral filter transmittance (the spectral channel). Then, the number of the "effective" photons registered in the time period t will obey the Poisson distribution with the conditional mathematical expectation

$$Ey = t \left(\int u(\lambda)x(\lambda)d\lambda + \nu \right), \quad (1)$$

where ν is the dark current at detector measured in units of the number of electrons per second. The integrals here and everywhere in this paper are taken over the entire spectral region used in the measurements. The aim of the experimenter is to estimate a certain state parameter of the underlying surface θ which is statistically associated with the spectrum $u(\lambda)$, by means of measurements in several spectral channels. It is supposed that the first two moments of joint distribution $(u(\lambda), \theta)$ are known quantities. They are: $\langle \theta \rangle$, mean value of θ ; σ^2 , variance of θ ; $f(\lambda)$, mean value of $u(\lambda)$; $K(\lambda, \lambda')$, covariance function of $u(\lambda)$; and $q(\lambda)$, covariance between $u(\lambda)$ and θ .

In our case, the parameter θ is the chlorophyll concentration C . It is assumed that the measurements can be performed during the time interval t . The set of channels $x_i(\lambda)$ and the time periods for signal accumulations in them t_i , $i=1 \dots r$ which satisfy natural limitations $0 \leq x_i(\lambda) \leq 1$, $\sum t_i = t$, will be named the experimental design ξ for θ estimation.

We shall search for an optimal design ξ only for linear estimates of θ from results of the measurements $y_1 \dots y_r$ in spectral channels $x_1(\lambda) \dots x_r(\lambda)$. Hence, it is natural to consider the variance $h(\xi)$ of the best linear estimate $\hat{\theta}$ of the parameter θ as the criterion of the design ξ optimality.

We introduce the following notation :

$$f_i = \int f(\lambda)x_i(\lambda)d\lambda, \quad (2)$$

$$q_i = \int q(\lambda)x_i(\lambda)d\lambda, \quad (3)$$

$$k_i(\lambda) = \int K(\lambda, \lambda') x_i(\lambda') d\lambda', \quad (4)$$

$$K_{ij} = \iint K(\lambda, \lambda') x_i(\lambda) x_j(\lambda') d\lambda d\lambda', \quad (5)$$

$$q = (q_1 \dots q_r)^T, \quad k(\lambda) = (k_1(\lambda) \dots k_r(\lambda))^T, \quad y = (y_1 \dots y_r)^T, \quad (6)$$

$$K = \left\| K_{ij} \right\|_{i,j=1}^r, \quad T = \text{diag}(t_i), \quad \Phi = \text{diag}(f_i + \nu), \quad (7)$$

$$D = K + \Phi T^{-1}, \quad (8)$$

$$F(x(\lambda)) = \int f(\lambda) x(\lambda) d\lambda, \quad (9)$$

$$\phi(\lambda, \xi) = q(\lambda) - k^T(\lambda) D^{-1} q, \quad (10)$$

$$d(x(\lambda), \xi) = (F(x(\lambda)) + \nu)^{-1/2} \int \phi(\lambda, \xi) x(\lambda) d\lambda. \quad (11)$$

The function $x(\lambda)$ in Eqs. (9), (11) is an arbitrary spectral channel optionally included in design ξ . The values of estimate $\hat{\theta}$ and variance $h(\xi)$ are easily derived to be

$$\hat{\theta} = \langle \theta \rangle + q^T D^{-1} T^{-1} y, \quad (12)$$

$$h(\xi) = \sigma^2 - q^T D^{-1} q. \quad (13)$$

The authors have found the following properties of the optimum design⁷:

1. If design ξ is optimal, then for any channel $x(\lambda)$

$$d^2(x(\lambda), \xi) \leq \sum_i (t_i / t) d^2(x_i(\lambda), \xi), \quad (14)$$

otherwise, if design ξ is not optimal, then there exists channel $x(\lambda)$ such that

$$d^2(x(\lambda), \xi) > \sum_i (t_i / t) d^2(x_i(\lambda), \xi). \quad (15)$$

2. Let ξ be the arbitrary design. Then, the following inequality estimates the approximation of this design to optimal design ξ^* :

$$|h(\xi^*) - h(\xi)| / t \leq \max_{0 \leq x(\lambda) \leq 1} d^2(x, \xi) - (t_i / t) d^2(x_i, \xi). \quad (16)$$

3. With a certain additional condition, the optimum design includes not more than two spectral channels $x_+(\lambda)$ and $x_-(\lambda)$ taking only values of 0 or 1.

The optimum design structure thus determined makes it possible to suggest a convergent algorithm for optimum spectral channel selection which follows.

0. As an initial approximation we choose indicators of intervals of increasing and decreasing function $q(\lambda)$ and designate them as $x_+(\lambda)$ and $x_-(\lambda)$, respectively. If $q(\lambda)$ is monotonic, there will be only one channel.

1. Let us find the optimum time periods t_+ , t_- which minimize the variance $h(\xi)$ for channels $x_+(\lambda)$, $x_-(\lambda)$ already selected. Because of $x_+(\lambda)$, $x_-(\lambda)$, $t_+ + t_- = t$ is fixed, $h(\xi)$ is a function of only one variable (with a single minimum, as proved⁷), and we will find the minimum, e.g. by the golden section method.

2. Let us find the "extreme" channel $x_+^*(\lambda)$ that makes it possible to achieve $\max d(x(\lambda), \xi)$. It has been proved⁷ that a constant c_+ exists, such that this channel is equal to 1 for points λ where $\phi(\lambda, \xi) > c_+ f(\lambda)$, and is equal to 0 for points λ where $\phi(\lambda, \xi) < c_+ f(\lambda)$, i.e. the value $d(x_+^*(\lambda), \xi)$ is uniquely defined by the constant c_+ . It has been proved⁷ that there is a single maximum of the function $d(c_+)$, which should be located by the golden section method.

3. Acting similarly we find the extreme functional $x_-^*(\lambda)$ for which $\min d(x(\lambda), \xi)$ is reached.

4. Having prescribing the value of ϵ , i.e. the difference between variance $h(\xi)$ reached and variance of optimal design $h(\xi^*)$, let us calculate

$$t \max(d^2(x_+^*(\lambda), \xi), d^2(x_-^*(\lambda), \xi)) - t_+ d^2(x_+(\lambda), \xi) - t_- d^2(x_-(\lambda), \xi). \quad (17)$$

If this quantity is smaller than ϵ , the algorithm stops functioning. Otherwise, we pass over to Point 5.

5. Let us select the following new channels

$$x_+^\alpha(\lambda) = (1 - \alpha)x_+(\lambda) + \alpha x_+^*(\lambda), \quad x_-^\alpha(\lambda) = (1 - \alpha)x_-(\lambda) + \alpha x_-^*(\lambda). \quad (18)$$

Then we shall obtain the design: $\xi(\alpha) = (x_+^\alpha, x_-^\alpha; t_+, t_-)$, depending on one parameter α , $0 \leq \alpha \leq 1$. Optimal value of weight $\alpha = \alpha^*$ corresponding to a minimum of $h(\xi(\alpha))$ should be located by the golden section method, too.

6. Let us go to point 1 with a new design: $(x_+^\alpha, x_-^\alpha; t_+, t_-)$.

The authors have realized this algorithm as a program for a personal computer in the TURBO-PASCAL computer language.

3. SIMULATION

The input data of algorithm developed are the statistical characteristics of the system "water-leaving radiation spectrum - chlorophyll concentration in surface waters", namely, $\langle \theta \rangle$, σ^2 , $f(\lambda)$, $K(\lambda, \lambda')$ and $q(\lambda)$. However, statistics of this system known to the authors from available literature is highly insufficient. So, we performed the statistical simulation of this system for shipboard observations.

Spectrum $u(\lambda)$ is given by

$$u(\lambda) = E(\lambda) (\rho(\lambda) + \rho_s(\lambda)) A \gamma^2 \eta(\lambda) / e, \quad (19)$$

where $E(\lambda)$ is the spectral density of solar irradiance on the sea surface; $\rho(\lambda)$ and $\rho_s(\lambda)$ are the radiance coefficients of water body and rough sea surface, respectively; A is the receiving aperture (area of the receiver entrance pupil); 2γ is the receiving angle, $\eta(\lambda)$ the spectral sensitivity of the detector's photocathode, e the elementary charge. The coefficients $\rho_s(\lambda)$ have been computed in accordance with the Cox and Munk distribution^{8,9} for various wind velocities V , azimuth Ψ and solar zenith angle Θ . The coefficients $\rho(\lambda)$ were calculated as:

$$\rho(\lambda) = 0.54[z(\lambda)\rho'_d(\lambda) + (1 - z(\lambda))\rho'_{dif}(\lambda)], \quad (20)$$

where $z(\lambda)$ is the ratio of direct sunlight to the total irradiance of sea surface; $\rho'_d(\lambda)$ and $\rho'_{dif}(\lambda)$ are the undersurface radiance coefficients for direct sunlight and diffusive light of the sky, which were computed by¹⁰

$$\rho'_d(\lambda) = 0.5(1 + \mu)^{-1} b_b(\lambda) / [a(\lambda) + b_b(\lambda)], \quad (21)$$

$$\rho'_{dif}(\lambda) = 0.27b_b(\lambda) / [a(\lambda) + b_b(\lambda)], \quad (22)$$

where a and b_b are the total absorption and backscattering coefficients, μ is the cosine of the sun ray refraction angle.

Values of z have been taken from the Austin experimental data¹¹, a and b_b were defined in accordance with model²:

$$a(\lambda) = a_w(\lambda) + X a_x^*(\lambda) + C a_c^*(\lambda) + Y a_y^*(\lambda), \quad (23)$$

$$b_b(\lambda) = 0.5 b_w(\lambda) + 0.015 b_x(\lambda) + 0.005 b_c(\lambda), \quad (24)$$

$$b_c(\lambda) = 0.12 C^{0.63} a_c^*(550) / a_c^*(\lambda), \quad (25)$$

$$b_x(\lambda) = X (550 / \lambda), \quad (26)$$

where $a_w(\lambda)$ and $b_w(\lambda)$ are the absorption and scattering coefficients of pure sea water; $a_x^*(\lambda)$, $a_c^*(\lambda)$, $a_y^*(\lambda)$ are the specific absorption coefficients of non-chlorophyllous

particles, chlorophyll and yellow substance, respectively; b_c and b_x are the scattering coefficients of chlorophyll and particles; C is the chlorophyll concentration, X the concentration of particles in terms of scattering coefficient $b_x(550)$, and Y the concentration of yellow substance in terms of absorption coefficient $a_y(440)$.

The values of $a_w(\lambda)$ and $b_w(\lambda)$ have been taken from tables¹²; the values of $a_x^*(\lambda)$, $a_c^*(\lambda)$, $a_y^*(\lambda)$ from tables¹³. The values of C , X , Y as well as of V , ψ , θ , have been simulated by the pseudo random number transducer.

Computations of radiation spectra in accordance with this model have been performed in spectral interval 400-700 nm with a scale step of 5 nm. We have employed an array consisting of 200 spectra for estimating statistical characteristics of our system. We assumed that: C varies from 10^{-2} to 10^2 mg m⁻³, X from 10^{-2} to 10 m⁻¹, and Y from 10^{-2} to 1 m⁻¹. We supposed that the velocity of wind have Rayleigh distribution with an expectation of 10 m/sec; the zenith angle of the sun is distributed uniformly in a range of 40° to 60°. The full number of the electrons received, if input is completely opened, was taken 10^{11} . This corresponds, for example, to values $A = 10$ cm², $\gamma = 4^\circ$, $t = 0.01$ s. If the input is completely closed (only dark-current electrons are received), then this number was assumed to be 10^7 .

4. PRELIMINARY RESULTS

The optimal design has appeared to consist of two composite channels, "positive" and "negative" (x_+ and x_-). The results of computations are presented in Table 1 and Fig. 1. Fig. 1 shows four simulated spectra of radiance coefficients and both the optimal channels found. Table 1 represents the values of parameters for which these spectra have been simulated. The chlorophyll concentration has been retrieved from "measured" signals y_+ and y_- according to Eq.(12):

$$\log C = A_0 + A_1 y_+ - A_2 y_-, \quad (27)$$

where $A_0 = 0.03$, $A_1 = 1.39$, $A_2 = 2.31$, if the signals y_+ and y_- are measured in picocoulombs. The time periods t of measurements in two optimal channels are $t_+/t = 0.39$, $t_-/t = 0.61$. The computed coefficients in Eq.(27) correspond to the device parameters pointed above only. In the common case one must use Eq.(12) for the computation of these coefficients. For comparison, Table 1 includes also the estimate C_1 based on the "color index" for the pair of wavelength 520 and 550 nm. The regression coefficients were computed for our array of simulated spectra by the least square method. Since there are many spectra corresponding to the large values of C in our simulated array, this pair of wavelengths gives higher accuracy of C retrieval than pair of 440 and 550 nm. The standard deviations of $\log C$ are 0.10 for our estimate by Eq.(27), and 0.28 for the "color index" estimate. The accuracy of the retrieval of C by the color index might be too low because of rather exotic values of concentrations C , X and Y chosen for this examples. However, our estimate has turned out to be satisfactory in this case.

Table 1. The values of the concentrations of chlorophyll (C , mg m^{-3}), sediment (X , m^{-1}), and yellow substance (Y , m^{-1}), and the estimates of C by the optimal design (\hat{C}) and by the color index (C_1)

Curve No.	1	2	3	4
X	1.0	5.0	0.01	1.0
Y	0.3	0.3	0.01	0.3
real C	20.0	2.0	2.0	0.01
\hat{C}	16.8	2.3	2.0	0.0135
C_1	44.0	0.51	0.44	0.08

5. DISCUSSION

We do not recommend the above described design for practical application since it was computed by using rather rough models (in particular, the fluorescence was not taken into account). So, this design is to be considered as an example of application of the optimal design theory for the problem in question. In future we hope to get experimental data on the "water-leaving radiance - chlorophyll concentration" system in a sufficient amount. Then, the design calculated in accordance with the above described algorithm will be optimal, indeed. We are also going to compute the optimal experimental design for satellite measurements.

We do not consider here the problem of physical realization of the optimal design found. An ideal device realizing this design must sum signals in several spectral bands and besides, switch from one set of these bands ("positive") to the other ("negative") once during the measurement time period.

One can suggest several single-band receivers (seven for our design), one for each band of both spectral channels, which operate simultaneously during entire time period t . It is easy to show that variance $h(\xi)$ of estimate $\hat{\theta}$ for such a set of receivers will not be higher than for an ideal one, i.e. this set of real devices will replace the ideal one, the coefficients of linear estimate for θ being only different.

If our detector is a set of many simultaneously operated detectors, for example, the mosaic from photo diodes, when the entrance pupil of the receiver is large, then the number of these detectors must be divided between two channels in ratio t_+/t_- .

6. REFERENCES

1. H. R. Gordon, D. K. Clark, J. W. Brown, O. B. Brown, R. H. Evans and W. W. Broenkow, "Phytoplankton pigment concentrations in the Middle Atlantic Bight: comparison of ship determinations and CZCS estimates", *Applied Optics*, Vol. 22, pp. 20-36, 1983.
2. S. Sathyendranath, L. Prieur and A. Morel, "A three-component model of ocean color and its application to remote sensing of phytoplankton pigments in coastal waters", *Int.*

J. Remote Sensing, Vol. 10, No. 8, pp. 1373-1394, 1989.

3. V. P. Kozlov, "Problem of the experimental design with range in functional space", *Mathematical theory of experimental design*, S. M. Ermakov (Ed.), Nauka Publ., Novosibirsk, pp. 189-208, 1981 (in Russian).

4. V. P. Kozlov, "Perspective methods of experimental design and analysis for investigations of random fields and processes", *Proc. First All-Union Conference*, Part 1, Nauka Publ., Moscow, pp. 192-193, 1982 (in Russian).

5. V. P. Kozlov, "Perspective methods of experimental design and analysis for investigations of random fields and processes", *Proc. Second All-Union Conference*, Part 2, Nauka Publ., Moscow, pp. 15-17, 1985 (in Russian).

6. V. P. Kozlov, I. M. Levin and I. V. Zolotukhin, "Optimum selection of spectral channels in the problem of remote sensing of phytoplankton concentration in ocean water.", *Proc. Pacific Ocean Remote Sensing Conf. (PORSEC-92)*, pp.1073-1075, Convention Center, Okinawa, 1992.

7. V. P. Kozlov and I. V. Zolotukhin, "Computer methods of experimental design and multifactor system optimization", *Trans. Higher Educational Institutions*, Novosibirsk, pp. 51-58, 1988 (in Russian).

8. C. Cox and W. H. Munk, "Slopes of the sea surface deduced from photographs of sun glitter", *Scripps. Inst. of Oceanogr. Bull.*, Vol. 6, No. 9, pp. 401-479, 1956.

9. Y. A. R. Mullamaa, *Atlas of rough sea surface optical properties*, Estonian Acad. of Sciences, Tartu, 1964 (in Russian).

10. B. M. Golubitskiy and I. M. Levin, "Transmission and reflection in a layer of a medium with strongly anisotropic scattering", *Izv. Atmos. Ocean. Phys.*, Vol. 16, No. 10, pp. 775-780, 1980.

11. R. W. Austin, "Coastal zone color scanner radiometry", *Proc. SPIE*, Vol. 208, Ocean Optics VI, pp. 170-177, 1979.

12. R. C. Smith and K. S. Baker, "Optical properties of the clearest natural waters (200-800 nm)", *Appl. Opt.*, Vol. 20, No.2, pp. 177-184, 1981.

13. L. Prieur and S. Sathyendranath, "An optical classification of coastal and oceanic waters based on the specific spectral absorption of phytoplankton pigments, dissolved organic matter and other particulate materials", *Limnol. and Oceanogr.*, 26, No. 4, pp. 671-689, 1981.

Accounting for the marine reflectance bidirectionality when processing remotely sensed ocean colour data.

Cathrine Myrmehl^{1,2} and André Morel¹

¹Laboratoire de Physique et Chimie Marines, BP. 8,
06230 VILLEFRANCHE-SUR-MER, France
and

²Nansen Environmental and Remote Sensing Center, Edv. Griegsvei 3a,
5037 SOLHEIMSVIKEN, Norway.

ABSTRACT

In this study, the bidirectional character of the ocean reflectance has been taken into account in the processing of Coastal Zone Color Scanner (CZCS) imagery, taken as an example. This effect is represented by a factor Q , which relates a given upwelling radiance to the upwelling irradiance, and depends on wavelength, the zenith Sun angle, the viewing angle of the sensor, the azimuth difference between the vertical planes of the Sun and the satellite, the chlorophyll concentration, the visibility and the wind speed. For a perfect Lambertian reflector, this factor takes the value of π . In the previous processing of CZCS imagery, the Q factor was generally given a constant value of 4.5, whatever the wavelength. In this study, the Q factor has been calculated for many cases, using Monte Carlo simulations and a lookup table for Q has been produced for the wavelengths corresponding to the CZCS channels. The $Q(\lambda)$ values computed for a chlorophyll concentration of 0.3 mg/m^3 , (based on the average value in the oceans), are used for a first iteration in the pixel-by-pixel processing method developed for CZCS data. The chlorophyll concentration obtained at the issue of this first loop is used to adjust the Q factor and the chlorophyll concentration is again computed. These iterative calculations are repeated until the convergence in the chlorophyll values is reached. The final results generally show higher values in chlorophyll than those obtained with $Q = 4.5$, by 20-80%. In these preliminary tests, the atmospheric visibility and the wind speed were kept constant, (23 km and 5 m/s, respectively), when computing the Q factor; this limitation can be relaxed thereafter. These tests show that convergence is rapidly obtained and that two iterations suffice to obtain stable values of chlorophyll concentration.

1. INTRODUCTION

This work is a contribution to the development of future algorithms to be used for processing ocean colour data, expected from the new generation of instruments, such as SeaWiFS, POLDER, MERIS, OCTS, etc. To better exploit their improved radiometric sensibility, it becomes necessary to take into account phenomena which have been neglected so far (e.g., when dealing with the Coastal Zone Color Scanner, CZCS). The anisotropy of the ocean reflectance is one of the phenomena which have to be considered. The bidirectional character of the backscattered radiation by the upper ocean was examined through Monte Carlo simulations (Morel and Gentili^{1,2}); the results of this theoretical study were recently compared to field data (Morel et al.³) and this comparison quantitatively confirms the importance of this anisotropy effect.

The geometrical dimensionless quantity Q (as sr) relates the in-water upwelling radiance, L_u , to the in-water upwelling irradiance, E_u , at the same depth (pratically just beneath the surface, denoted 0^-).

$$L_u(0^-) = \frac{E_u(0^-)}{Q} \quad (1a)$$

If the ocean were a perfect Lambertian diffuse reflector, the Q factor would be exactly π . If the anisotropic structure of the upward radiant field, as well as its dependence upon the illumination condition above the surface are accounted for, the above expression becomes

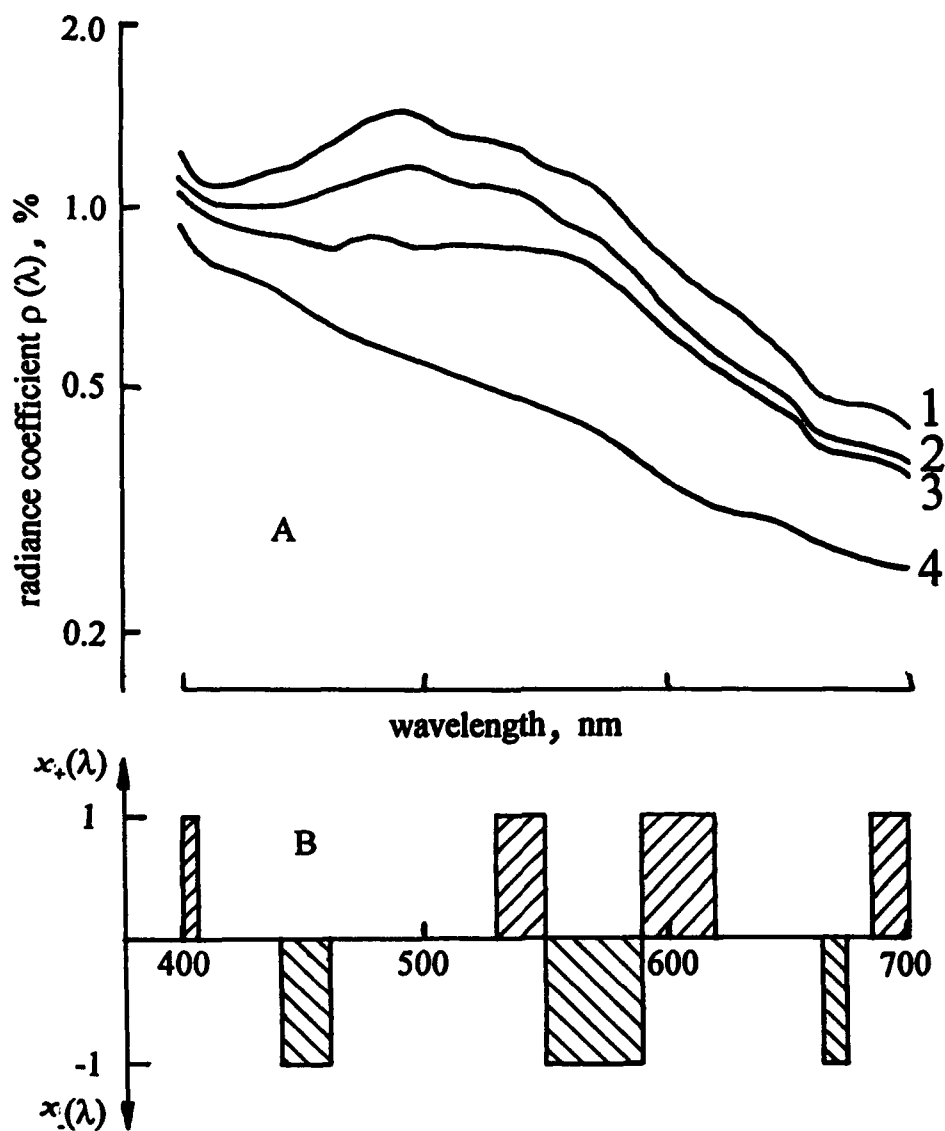


Fig. 1. A: Simulated spectra of radiance coefficients for various concentrations of chlorophyll (C), sediment (X), and yellow substance (Y). Values of C, X, and Y are presented in Table 1.

B: Two optimal spectral channels $x_+(\lambda)$ and $x_-(\lambda)$.

$$L_u(0^-, \theta_0, \theta', \Delta\phi) = \frac{E_u(0^-)}{Q(\theta_0, \theta', \Delta\phi)} \quad (1b)$$

where θ_0 is the zenithal Sun angle; θ' is the nadir angle corresponding to the in-water radiance directed toward the sensor after having crossed the interface, so that

$$\theta' = \sin^{-1}\left(\frac{\sin\theta_v}{n}\right) \quad (2)$$

θ_v is the viewing angle of the sensor and $\Delta\phi$ is the azimuth difference between the vertical planes of the Sun and the satellite (see Fig. 1); n is the refractive index of water. The anisotropy of the ocean reflectance is conveniently expressed by the bidirectional function $Q(\theta_0, \theta', \Delta\phi)$.

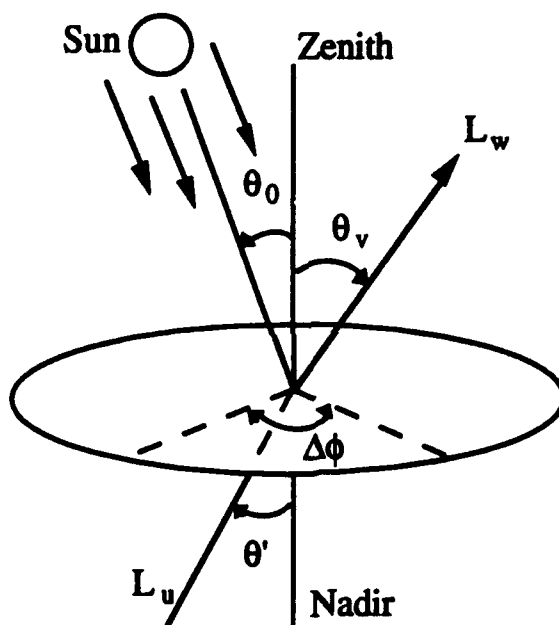


Figure 1. Schematic geometry and symbols.

In methods previously developed to process ocean colour data (acquired by the CZCS), Q was given a constant value of 4.5 (an experimental value, adopted from Austin⁴), regardless of the wavelength. In the basic equations giving water-leaving radiance, L_w , as described by Gordon and Morel⁵, and Gordon *et al.*⁶, the reflectance ratio, defined by

$$R(0^-) = \frac{E_u(0^-)}{E_d(0^-)} \quad (3)$$

is also involved (E_d and E_u are downward and upward irradiances at null depth). This ratio can also be related to the inherent optical properties (Preisendorfer⁷); namely to a , the absorption coefficient, and to b_b , the backscattering coefficient of the water body, through a functional expression involving their ratio

$$R = f \frac{b_b}{a} \quad (4)$$

where f is not a constant number, but depends on the Sun zenith angle, θ_0 , and on the optical parameters of the water, namely ω , the single-scattering albedo and η , the ratio of molecular scattering to total scattering (Morel and Gentili²). In this equation, the Q factor can be introduced

$$\frac{R}{Q} = \left(\frac{f}{Q}\right) \left(\frac{b_b}{a}\right) \quad (5)$$

This expression is found when relating the upwelling water-leaving radiance to the reflectance or to the "normalized" water-leaving radiances and Q ^{5,6}. The f factors are implicitly involved when discrimination between case 1 waters and turbid case 2 waters (Bricaud and Morel⁸) and more generally when forming the ratio of two marine signals, received at two wavelengths, to the extent that f and Q cannot be considered as spectrally constant.

Remotely sensed ocean colour has nevertheless been successfully processed and interpreted, despite the ignorance of the Q and f variations. The reason lies in a favourable conjunction of their approximately parallel evolutions. As was pointed out by Gordon⁹, the similar trends of f and Q with solar elevation result in an approximate stability in their ratio. The question is however, more complex, since the Q factor cannot be straightforwardly averaged and its zonal and azimuthal dependencies cannot be ignored.

Morel and Gentili¹ saw a need for including a variable Q factor in the processing of ocean colour imagery. The Q factor, separately considered is more variable than the f/Q ratio. It depends on wavelength, λ , on θ_0 , on θ_v and $\Delta\phi$, and also on the visibility and the wind speed, and finally on the chlorophyll concentration to which the optical properties of the water can be related for Case 1 waters. The Q factor has been calculated using Monte Carlo simulations (Morel and Gentili²; see the next section). When processing ocean colour data by using the atmospheric pixel-by-pixel correction algorithm, developed at Laboratoire de Physique et Chimie Marines (Bricaud and Morel⁸, and André and Morel¹⁰), the algorithm selects the appropriate Q factor in a look-up table.

In the following sections, it will be briefly described how and for which cases the Q factors have been calculated. Then the way of changing the ocean colour processing code (for CZCS) to include the variations of the Q factor is described. The last section includes an interpretation of the results and the conclusions of this preliminary work, together with some recommendations for future works.

2. MONTE CARLO SIMULATIONS

The calculation of the Q factor is based on Monte Carlo simulations as thoroughly described in Morel and Gentili^{1,2} and in Mobley *et al.*¹¹. Briefly, photons travelling upward from the water column are collected when they reach the surface in 480 contiguous submarine detectors, corresponding to 20 polar directions (0.05 increments in $\cos\theta'$, from nadir to horizon) and 24 azimuthal directions (7.5° increments in $\Delta\phi$, from 0 to 180°). The upwelling irradiance $E_u(0^-)$ is straightforwardly determined by integration. Then, using Eq. [1b] with the L_u values resulting from the simulations, the bidirectional $Q(\theta_0, \theta', \Delta\phi)$ values can be derived.

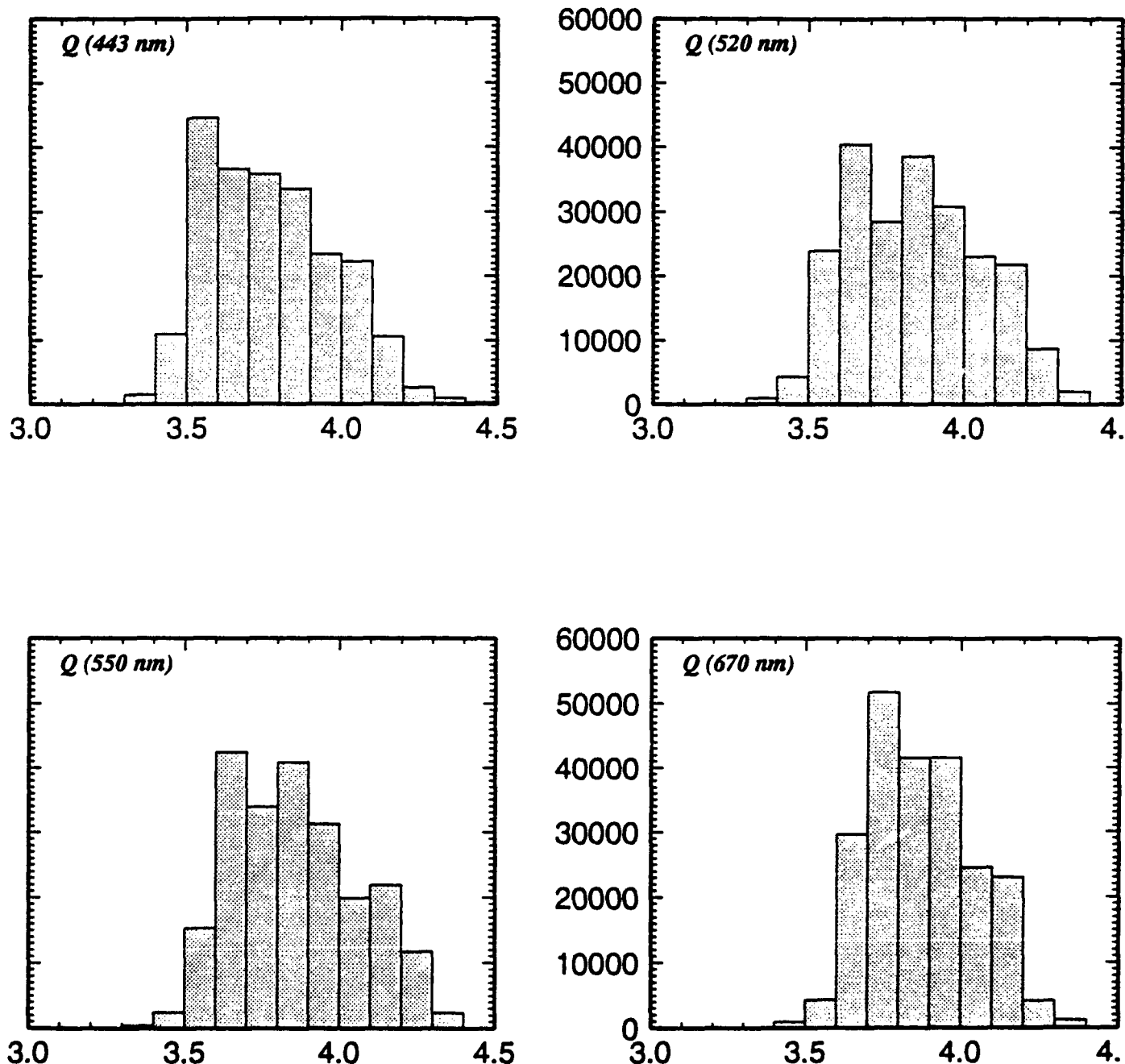
These simulations have been performed for the wavelengths, corresponding to the first four bands of the CZCS, in the visible part of the electromagnetic spectrum, 443, 520, 550 and 670 nm. The chlorophyll concentrations considered are 0.03, 0.1, 0.3, 1.0, 3.0 and 10.0 mg/m³. The zenith Sun angles are 0, 20, 40, 60 and 70°, and the Sun disc is given an angular diameter of 0.5°. The photons are generated from the Sun and travel through fifty 1 km-thick atmospheric layers, with specified values for Rayleigh and aerosol scattering and for ozone absorption as in Elterman¹². The aerosol phase function is that of a maritime aerosol. The visibility is 23 km. A wind-roughened interface is modeled using the Cox and Munk¹³ surface slope distribution for a wind speed of 5 m/s.

3. RESULTS AND DISCUSSION

To assess in a practical way the impact of the Q variations, three CZCS images from the Mediterranean Sea have been studied. The first one was acquired December 7, 1979, i.e., near the winter solstice in order to examine a situation with a low solar elevation (θ_0 was on average 60° over this scene); the second one (June 24, 1980) is close to the summer solstice and θ_0 is on average 20°. In both these images, the chlorophyll concentrations were rather low. Therefore another scene with higher pigment concentration in blooming conditions (May 6, 1981; $\theta_0 \approx 30^\circ$) has also been selected. For the sake of comparison, these three scenes have also been processed according to the "normal" procedure with a constant Q factor (= 4.5 for all channels).

Fig. 2 provides an example of the Q values used for the last loop in the iterative procedure and depending on the geometrical conditions and chlorophyll content for each pixel of a given scene (May 6, 1981). The number of pixels to which a given Q value applies is plotted vs. Q .

- CZCS - 060581 -



The calculations of Q are very time-demanding, so it has been chosen to produce and use a look-up table. The varying Q factor has been introduced in the algorithm of atmospheric correction developed for CZCS by Bricaud and Morel⁸ and by André and Morel¹⁰; the modified algorithm accounting for the Q variations, through an iterative scheme, is as follows.

In the first step of the iterative scheme, the Q factor is only varying with the wavelength and not with geometry. The Q values for each wavelength are those corresponding to a chlorophyll concentration of 0.3 mg/m^3 , when $\theta_0 = 30^\circ$, $\theta_v = 0^\circ$ and $\Delta\phi = 135^\circ$ (note that other choices are equally possible). The results are $Q(443) = 3.47$, $Q(520) = 3.48$, $Q(550) = 3.51$ and $Q(670) = 3.59$.

The processing, initialized with this set of $Q(\lambda)$ values, produce chlorophyll concentrations varying throughout the scene. In the second step of the iterative process, these computed concentrations are used to select in the look up table the appropriate Q values, now depending on the geometry (see Fig. 2). A new set of chlorophyll values is obtained and these iterations are done until a convergence is reached in terms of chlorophyll concentration.

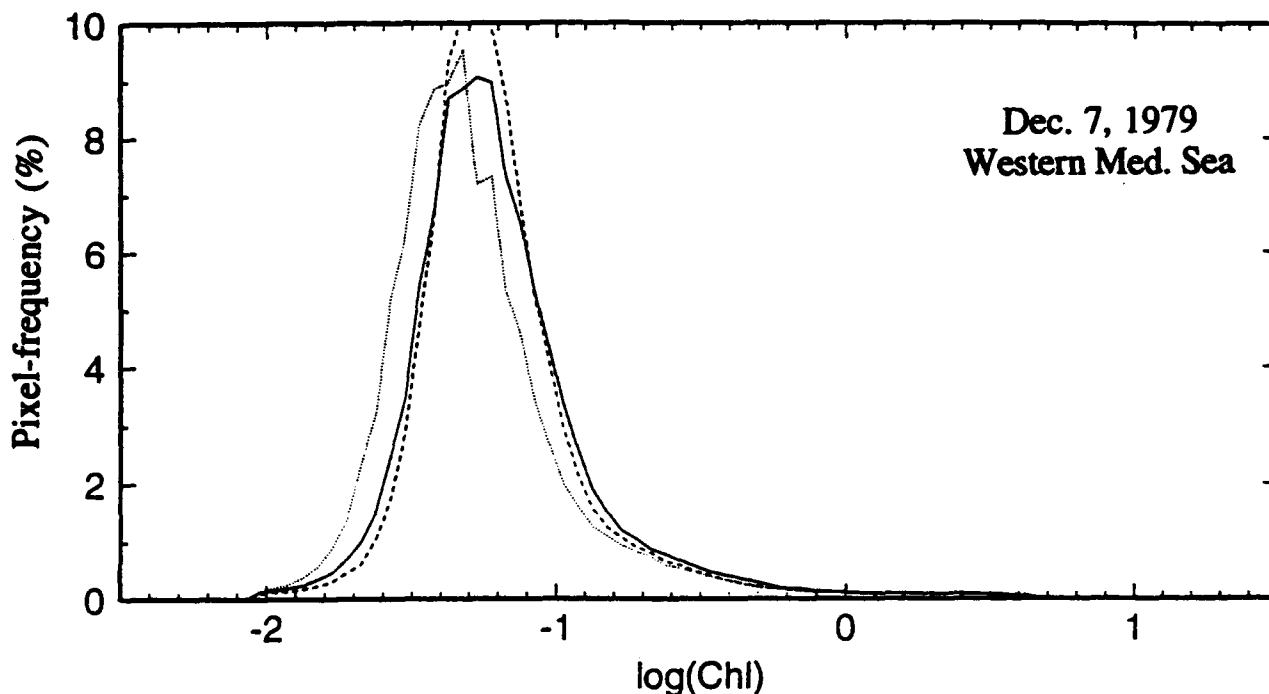


Figure 3. Histogram of the chlorophyll concentrations of a CZCS scene, December 7, 1979. The dotted curve indicates processing of an image with a constant Q factor ($= 4.5$), the dashed curve presents the results at the first step with a set of constant $Q(\lambda)$ values corresponding to a chlorophyll concentration $= 0.3 \text{ mg/m}^3$, $\theta_v = 0^\circ$, $\theta_0 = 30^\circ$, and $\Delta\phi = 135^\circ$. The solid curve represents the results after two iterations.

The convergence is considered as achieved when 90% of the pixels in a scanline are within $\pm 4\%$ of the previous calculated chlorophyll values. When using the ratio of CZCS channels 1 and 3, the convergence actually is obtained after two iterations. This was also the case when using the ratio of channels 2 and 3, but not necessarily when combining the two ratios, as described later, and the results of the three studied scenes are shown in Figs. 3 - 5. The convergence can be seen in Fig. 6.

The results of the iterative method show clearly a shift towards higher chlorophyll concentrations, in all three cases, except when the concentrations are very high (over 5 mg/m^3 , as in the scene of May 6, 1981). However, at this end of the scale, the results are questionable anyway. As Morel and Gentili² mentioned, reservations have to be made about the validity of the Q values, because of the adoption of a unique volume scattering function (VSF) for suspended particles, leading to a unique value for the backscattering probability for these particles. Secondly, when dealing with relatively high chlorophyll concentrations, the ratio of channels 2/3 ($R(520)/R(550)$) should be used, as stated by Gordon and Morel⁵. This will be done later.

It is clear that the iterations with varying Q factor in the processing of satellite images are time-demanding. The processing time is doubled, or even tripled, and that is the reason for examining the results obtained after the first loop using only constant $Q(\lambda)$ values. In all three cases, the results at the issue of the first loop are markedly differing from those obtained with $Q = 4.5$ at all λ and are not far from the final ones. This is particularly clear in the scene from May 6, 1981 (Fig. 5); the reason may lie in a favourably chosen chlorophyll concentration (0.3 mg/m^3) as input when selecting the initial $Q(\lambda)$ values. The histogram of the chlorophyll content for this scene is precisely concentrated around this value.

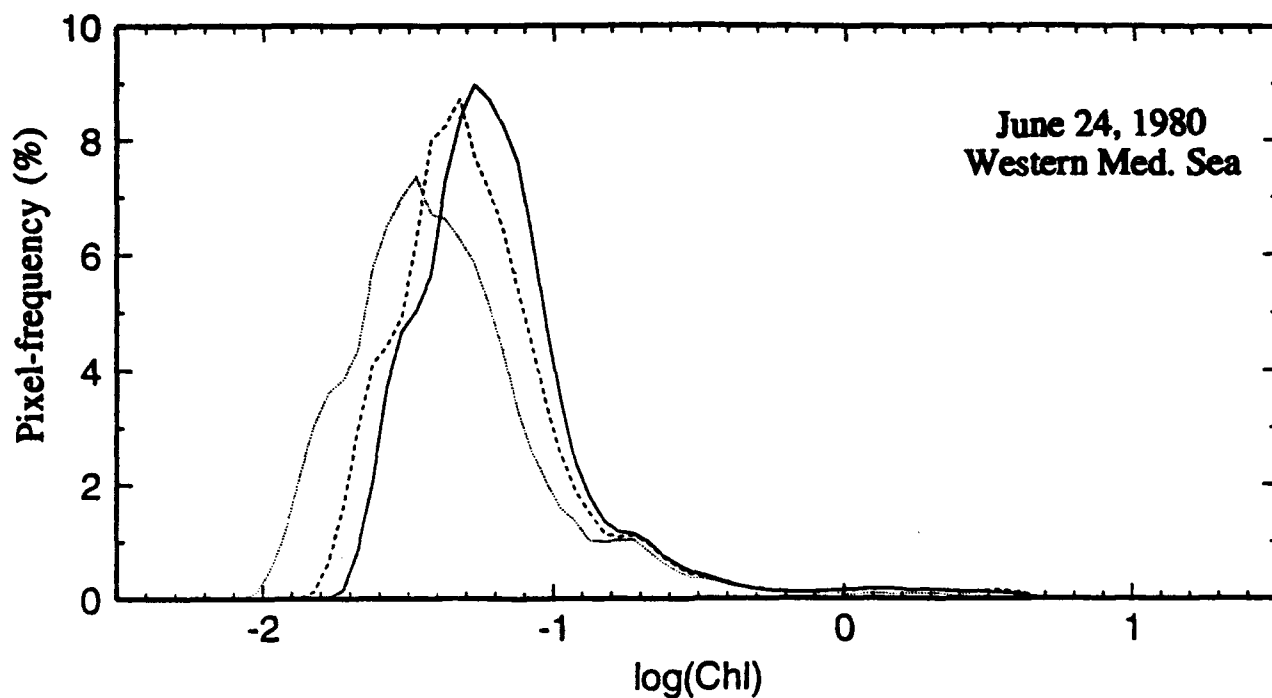


Figure 4. As Fig. 3, but for the CZCS scene of June 24, 1980.

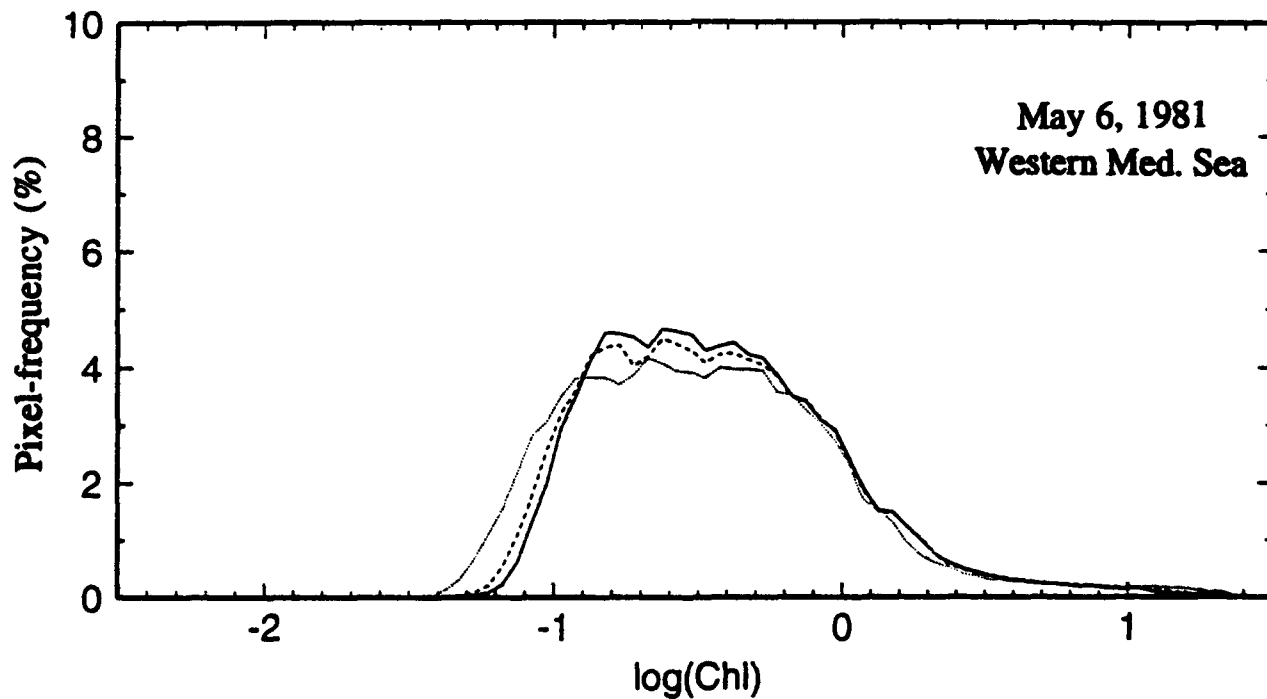


Figure 5. As Fig. 3, but for the CZCS scene of May 6, 1981.

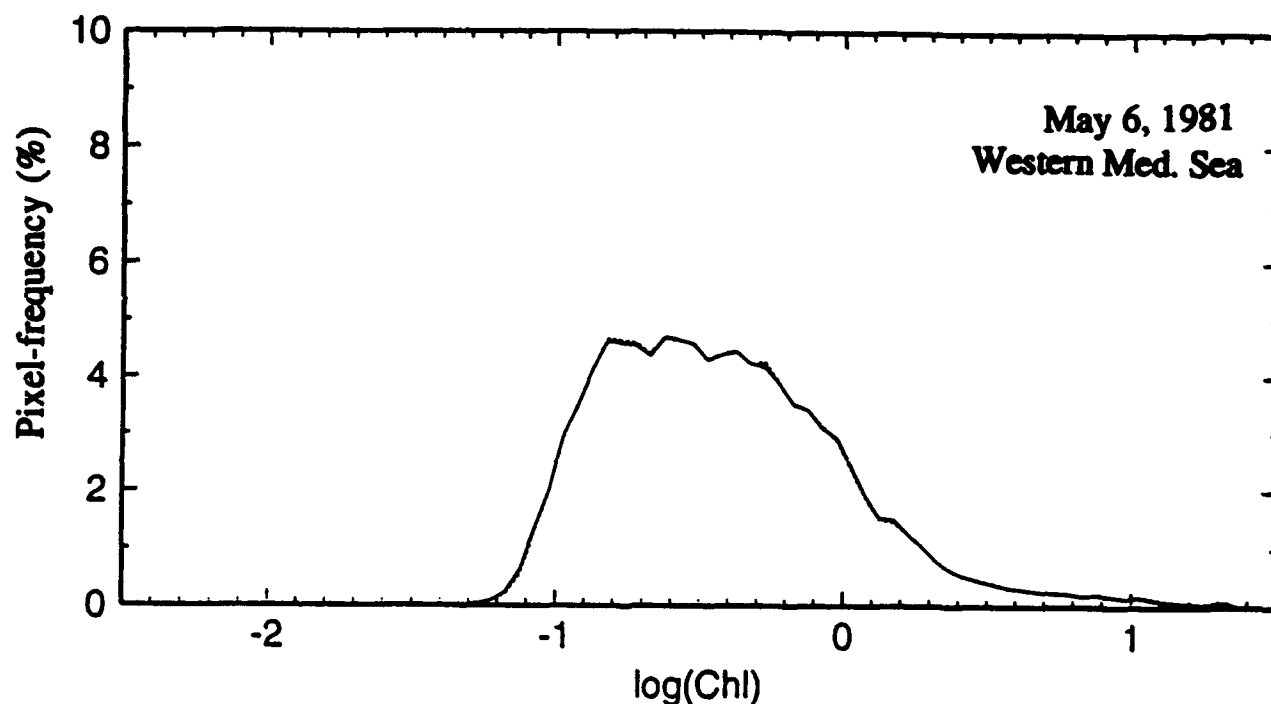


Figure 6. Convergence in the chlorophyll concentrations. The dashed histogram indicates the results after two iterations and the solid one represents the results after the third one. These are the results from May 6, 1981, calculated using only the ratio 1/3.

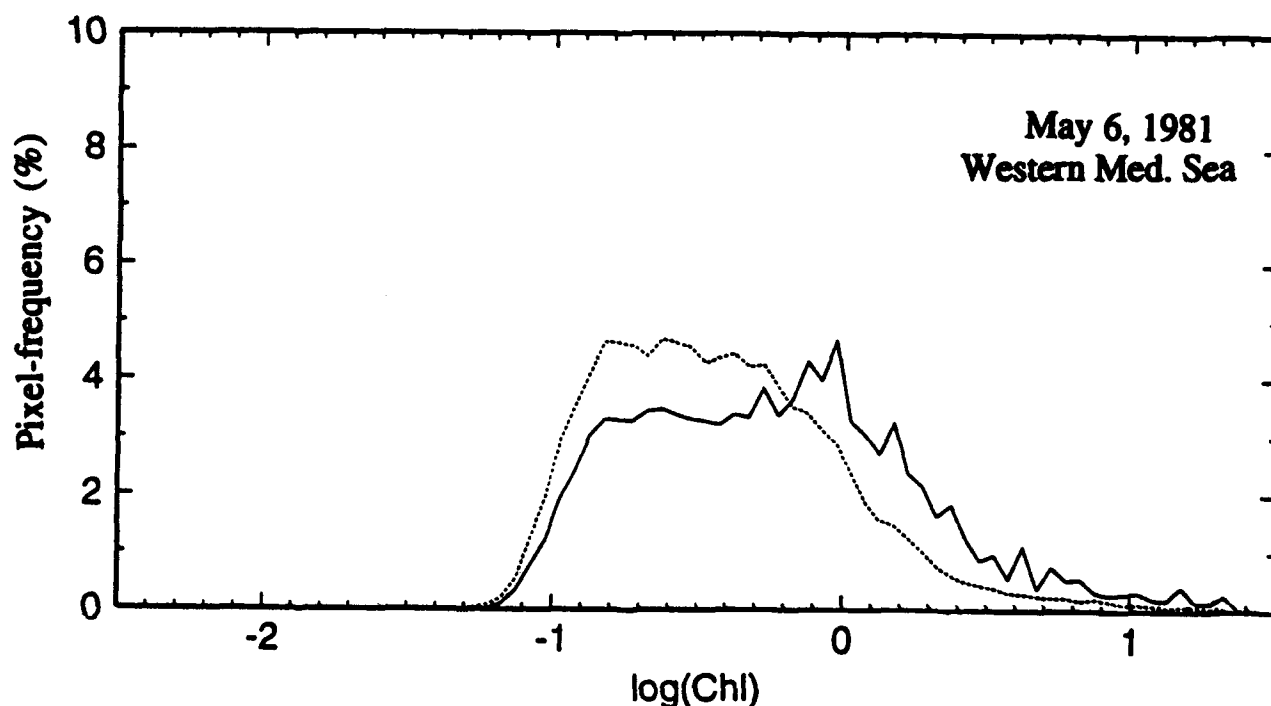


Figure 7. Histogram of the chlorophyll concentrations from the CZCS scene of May 6, 1981. The dashed curve is the calculation using only the ratio of CZCS channels 1 and 3 (the solid curve in Fig. 5). The solid curve represents the results, when convergence is reached, for the chlorophyll concentration calculated with the ratio 1/3 for pixels with values less than or equal to 3 mg/m^3 and 2/3 for values higher than 3 mg/m^3 .

For the two other scenes with low chlorophyll, the results after the first computation are approximately at midway between the results with $Q = 4.5$ and those at the end of the iterative process. It can be concluded that the iterations are necessary. Obviously, if the constant $Q(\lambda)$ values, adopted in the first step, were more "adapted" to the chlorophyll concentration within the scene, the results would have been more acceptable without iteration (for instance, by selecting as input the $Q(\lambda)$ values for $\text{Chl} = 0.05 \text{ mg/m}^3$, the results for the June 24 scene without iteration are better than those shown in Fig. 4).

With respect to the standard method making use of $Q = 4.5$ for all wavelengths, the iterative method leads to chlorophyll values increased by a factor of about 1.8 when $\text{Chl} < 0.05 \text{ mg/m}^3$; this factor progressively approaches 1 for chlorophyll concentration exceeding 1 mg/m^3 . Therefore, for most oceanic waters with rather low chlorophyll concentration, the effect is considerable and cannot be ignored.

Another study was made to examine how the iterative process can cope with the blue-green-to-green ratio to be used in alternance with the blue-to-green ratio when the chlorophyll concentrations exceed $1 - 2 \text{ mg/m}^3$ (André and Morel¹⁰). Note that this need is typical of the CZCS instrument and likely will be less crucial for future sensors. In this study the hinge point for switching from 1/3 to 2/3 algorithm was set to 3 mg/m^3 . The algorithm is initialized with the $Q(\lambda)$ values for a chlorophyll content of 0.3 mg/m^3 , using only the 1/3 ratio. In the next iteration, the algorithm makes use, on a pixel-by-pixel basis, of the 1/3 or 2/3 ratio, depending on the concentration. This iteration is repeated until a convergence is reached. In this approach, more iterations are required before convergence than in the previous approach, particularly, in the vicinity of the threshold. In the scene from May 6, 1981, the convergence was, however, reached after two iterations. The differences between the two histograms, shown in Fig. 7, are not well explained and this switching procedure combined with the Q -iterative process requires future work.

4. CONCLUSION

The impact of the bidirectional effects of marine reflectance on the processing of ocean colour data has been examined and three CZCS scenes of the Mediterranean Sea have been studied. The first two scenes represent low chlorophyll concentrations, contrary to the third one. In every case, three different algorithms have been used to process the images, the first one with a constant $Q = 4.5$, the second one with a Q factor varying only with wavelength, and the third one with a Q factor depending on the three angles involved, on the wavelength and iteratively on the chlorophyll concentration.

The results show that a Q factor of 4.5 is clearly overestimated, resulting in too low chlorophyll concentrations. This is no longer the case when the concentration is higher than 5 mg/m^3 , when the 4.5 constant value is not far from the actual values.

Using Q factors (only dependent on the wavelength and the chlorophyll concentration) is sometimes a reasonably good first approximation. This procedure does not add extra time in the processing of CZCS images, as does the iterative procedure. It requires, however, that an *a priori* knowledge of the chlorophyll concentration within the scene to be processed already exists and also that this concentration is not too much varying throughout the scene. The adoption of an average solar angle for the whole image is also needed.

The iterative procedure is efficient as apparently, an acceptable convergence is quickly reached; the computational time, however, is at least doubled.

It must be noted that the final increase in the chlorophyll concentration, as found when reprocessing the CZCS scenes is a general trend. This trend will hold true for any sensor as it originates from the spectrally dependent Q values in the visible part of the spectrum. The amplitude of the shift in chlorophyll as found here (up to 80%), however, cannot be generalized because it depends (and this dependency is typical of the CZCS) on the way of partitioning the signal received at 670 nm between the aerosol and marine contributions; therefore the Q factor at 670 nm is also involved in the iterations. For the next generation of ocean colour sensors, it is envisaged that the estimate of the aerosol contribution will be based on independent information (within near-infrared), so that the coupling between the atmospheric correction and the retrieval of the marine signal will disappear. According to preliminary studies (not reported here), a shift towards higher chlorophyll concentrations of about 30 - 40% is still to be expected (when $\text{Chl} < 0.5 \text{ mg/m}^3$) from the due consideration of the Q effect.

All effects have not been accounted for; Q , in principle, is also weakly dependent on the diffuseness of the illumination conditions (the ratio of the diffuse sky radiation to the direct solar radiation) and on the sea state. The Q factor could be assessed and used more accurately, taking into consideration the visibility and the wind speed as additional variables. The visibility can be derived from the atmospheric correction itself, whereas the wind speed requires external information. Further studies about the importance of these parameters are still necessary, particularly for a meaningful use of the future data.

5. ACKNOWLEDGEMENTS

We would like to thank Bernard Gentili for the calculation of the Q factor, using Monte Carlo simulations. This work is in partial fulfilment of the Diplôme d'Etudes Supérieures Spécialisées, Université Pierre et Marie Curie, Paris-6 and GDTA, Toulouse of C. Myrmehl. She would like to thank Annick Bricaud for giving her this opportunity to work at Laboratoire de Physique et Chimie Marines, and she appreciates the time and effort spent by David Antoine, helping her with the atmospheric correction algorithm.

6. REFERENCES

- [1] Morel, A. and B. Gentili, "Diffuse reflectance of oceanic waters: its dependence on Sun angle as influenced by the molecular scattering contribution", *Applied Optics*, 30(30), pp. 4427-4438, 1991.
- [2] Morel, A. and B. Gentili, "Diffuse reflectance of oceanic waters: II. Bidirectional aspects", *Applied Optics*, 32(33), pp. 6864-6879, 1993.
- [3] Morel, A., K. J. Voss and B. Gentili, "Bidirectional reflectance of oceanic waters: A comparison of model and experimental results". Submitted to *J. Geophys. Res.*, Special issue on ocean optics, 1994.
- [4] Austin, R. W., "Coastal Zone Color Scanner radiometry", in *Ocean Optics VI*, S. Q. Duntley, ed., *Proc. Soc. Photo. Opt. Instrum. Eng.*, 208, pp. 170-177, 1979.
- [5] Gordon, H. R. and A. Morel, *Remote assessment of ocean color for interpretation of satellite visible imagery: A review*, (Springer Verlag, New York), p. 114, 1983.
- [6] Gordon, H. R., O. B. Brown, R. H. Evans, J. W. Brown, R. C. Smith, K. S. Baker and D. K. Clark, "A semianalytic radiance model of ocean color", *J. Geophys. Res.*, 93, pp. 10909-10924, 1988.
- [7] Preisendorfer, R. W., "Application of radiative transfer theory to light measurements in the sea", *Monogr. Int. Union Geod. Geophysics Paris*, 10, pp. 11-30, 1961.
- [8] Bricaud, A. and A. Morel, "Atmospheric corrections and interpretation of marine radiances in CZCS imagery: use of a reflectance model", *Oceanologica Acta*, SP, pp. 33-50, 1987.
- [9] Gordon, H. R., "Dependence of the diffuse reflectance of natural waters on the sun angle", *Limnol. Oceanogr.*, 34, pp. 1484-1489, 1989.
- [10] André, J.-M. and A. Morel, "Atmospheric corrections and interpretation of marine radiances in CZCS imagery: revisited", *Oceanologica Acta*, 14(1), pp. 3-22, 1991.
- [11] Mobley, C. D., B. Gentili, H. R. Gordon, J. Zhonghai, G. W. Kattawar, A. Morel, P. Reinersman, K. Stamnes and R. H. Stavn, "Comparison of numerical models for computing underwater light fields", *Applied Optics*, 32, pp. 7484-7504, 1993.
- [12] Elterman, L., "UV, visible, and IR attenuation for altitudes to 50 km", Rep AFCRL-68-0153 (US Air Force Cambridge Research Laboratory, Bedford, Mass.), 1968.
- [13] Cox, C. and W. Munk, "Some problems in optical oceanography", *J. Mar. Res.*, 14, pp. 63-78, 1955.

Design and Evaluation of a Cosine Collector for a SeaWiFS-compatible Marine Reflectance Radiometer

John H. Morrow, Michael S. Duhig, and Charles R. Booth

Biospherical Instruments Inc.

5340 Riley St., San Diego, CA 92110-2621, USA

VOX: (619) 686-1888 FAX: (619) 686-1887

Internet: morrow@biospherical.com

ABSTRACT

The impending launch of a number of remote sensing platforms such as the NASA SeaWiFS (Sea-viewing Wide Field-of-view Sensor) has generated renewed interest in instrumentation for measuring ocean color *in situ*. The increased number of spectral bands desired and the large dynamic range of the measurements place special challenges on the design of these instruments. Of particular interest in measurements of spectral irradiance and in the calculation of irradiance reflectance are errors introduced by the departure of the instrument response from a true cosine at increasing angles of incident irradiance. Using field data as well as a modelled radiance distribution, this paper presents an evaluation of a commercial cosine collector for measurements of spectral irradiance. Preliminary results from a new program sampling the variability in immersion coefficient are also presented.

1. INTRODUCTION

The impending launch of a number of remote sensing platforms such as the NASA SeaWiFS (Sea-viewing Wide Field-of-view Sensor) has generated renewed interest in instrumentation for measuring ocean color *in situ*. Both the increased number of spectral bands desired and the large dynamic range of the measurements place special challenges on the design of these instruments. In order to accurately quantify light under a wide variety of conditions, vector irradiance has been measured using instruments whose responses follow the cosine law of illumination. The cosine law is most easily illustrated with a collimated beam projected onto a flat surface. In the ideal case, the irradiance, E , on that surface will be given by equation 1^{1,2}:

$$E = E_0 \cos \theta \quad (1)$$

where θ is the angle of incidence and E_0 is the irradiance on the surface for $\theta=0$. A collector constructed such that its response is proportional to the cosine of the angle of incidence is known as a "cosine corrected collector." Of particular interest in measurements of spectral irradiance and in the calculation of irradiance reflectance are errors introduced by the departure of the instrument response from a true cosine at increasing angles of incident irradiance.

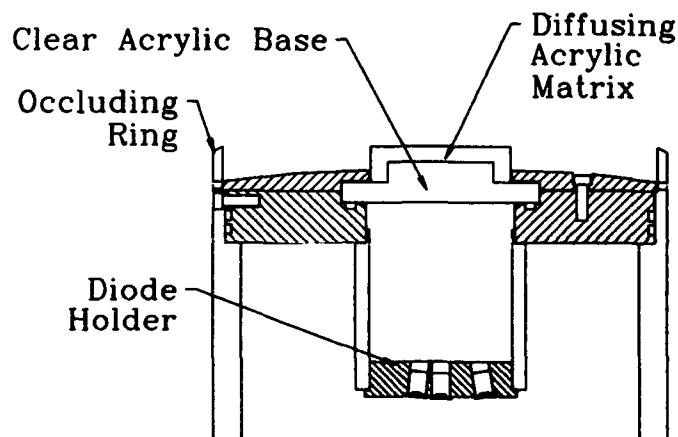


Figure 1. Modified Vislab cosine collector design commonly employed on the Biospherical Multiwavelength Environmental Radiometer (MER) series spectroradiometers.

The theoretical ideal cosine collector is an aperture which collects all transversing photons. To work in the ocean, diffusers are often used to approximate this ideal collector. At large zenith angles (large angles of incidence relative to the normal of the plate), reflection of light off even the best diffusing materials causes a significant decrease in the flux reaching the photodetector. A wide variety of submersible cosine collector designs have been used, including flat plate¹, raised plate² and variously curved collectors. Largely because of their ease of manufacture, the plate-type collector (Figure 1) is one of the most commonly found in submersible spectroradiometers. The cosine response of the popular raised plate design patterned after the Scripps Spectroradiometer and tested by the Visibility Laboratory (Vislab), Scripps Institution of Oceanography is documented². The anticipated launch and validation of satellites for monitoring ocean color has increased awareness by the ocean optics community on the impact of cosine collector design³. A number of factors may contribute to departures from a true cosine response. These include transmission characteristics of the diffusing material at different wavelengths, reflection off the surface at differing angles of incidence, and asymmetric placement of detectors when multiple diodes view a common collector.

Determination of the absolute radiometric calibration of a radiometer such as the PRR-600 is typically conducted by placing the device in front of a Standard of Spectral Irradiance (typically a 1000 watt type FEL lamp) under conditions specified by the National Institute of Standards and Technology. The output voltage may be related to irradiance through a nominal calibration constant, C_n :

$$C_n = \frac{V_n}{E_l(\lambda_n)} \quad (2)$$

where V_n is the output voltage caused by the calibration irradiance, $E_l(\lambda_n)$, at the nominal center wavelength of the device, λ_n . An unknown irradiance may be determined by rearrangement of Equation 2 and the voltage output during the measurement. It has been shown^{2,3,4,5} that changes in the index of refraction of the surrounding media (e.g. submerging the instrument) causes a change in calibration, known as the "immersion effect." In addition to determining the required immersion coefficient of a given design, the range of unit-to-unit variation in the immersion coefficient should be established to determine if individual instruments must be characterized routinely in the calibration process.

2. METHODS

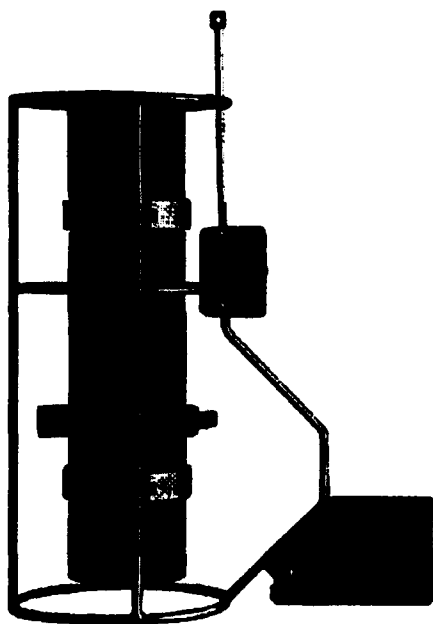


Figure 2. Profiling Reflectance Radiometer.

The PRR-600 (Figure 2) is a small (10 cm diameter by 40 cm long), battery powered multiwavelength spectroradiometer designed primarily for SeaWiFS ocean color research. Using two analog to digital converters and two independent microprocessors, the instrument synchronously measures seven channels of downwelling irradiance, $E_d(\lambda)$, seven channels of upwelling radiance, $L_u(\lambda)$, and a number of additional variables including pressure, water temperature, and two axis platform orientation. Wavelengths for the PRR typically follow the SeaWiFS recommendations at 412, 443, 490, 510, 555, 665, and 683 nm. The specific PRR-600 used in this analysis was fitted with a 560 nm rather than a 555 nm detector. The PRR-610 surface reference may be fitted with a detector in the near infrared at 780 nm.

The cosine collector for the PRR-600 (Figure 3) was specifically designed to try to meet the specifications of the SeaWiFS Ocean Optics Protocols³ in an economical and robust design. The irradiance diffuser consists of a raised trapezoidal quartz or acrylic piece covered with a thin sheet of vacuum-formed Teflon[®], which acts as a diffuser. Photodiodes are arranged in a circular array at the base of the assembly, such that all view the same area of the

bottom of the diffuser. As with all diffusers, the upper Teflon surface reflects light at large angles of incidence, significantly underreporting the flux. To mitigate this problem, the sides of the trapezoid were raised to provide a surface with a reduced angle of incidence, thereby increasing the response from larger zenith angles. A cosine collector should not transmit light from angles greater than 90° ; an outer rim raised to the level of the top of the diffuser acts as an occluding ring. In the optimization process, the dimensions of the trapezoid, diffuser retainer, and occluding rings were varied systematically to achieve better cosine response over the spectrum.

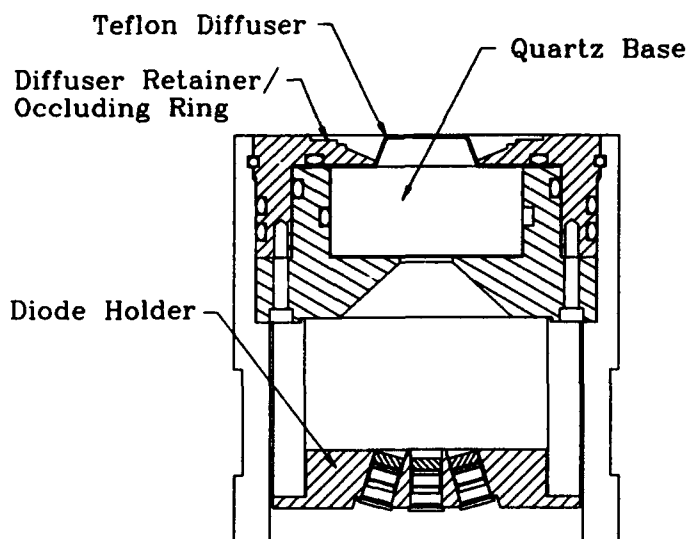


Figure 3. Cosine collector for PRR-600.

To test its cosine response, the PRR-600 was placed on a automated rotating arm in a water-tight test tank equipped with nonreflecting sides (Figure 4). A collimated beam was positioned to fill the collector at the precise center of rotation of the assembly. Under computer control, the instrument is rotated in 5° increments from $+90^\circ$ to -90° "zenith" angle and the response from each channel was recorded relative to the source. In order to test for geometric asymmetries in the response due to the arrangement of the photodiodes, the instrument was turned axially at 10° increments and the cosine response retested.

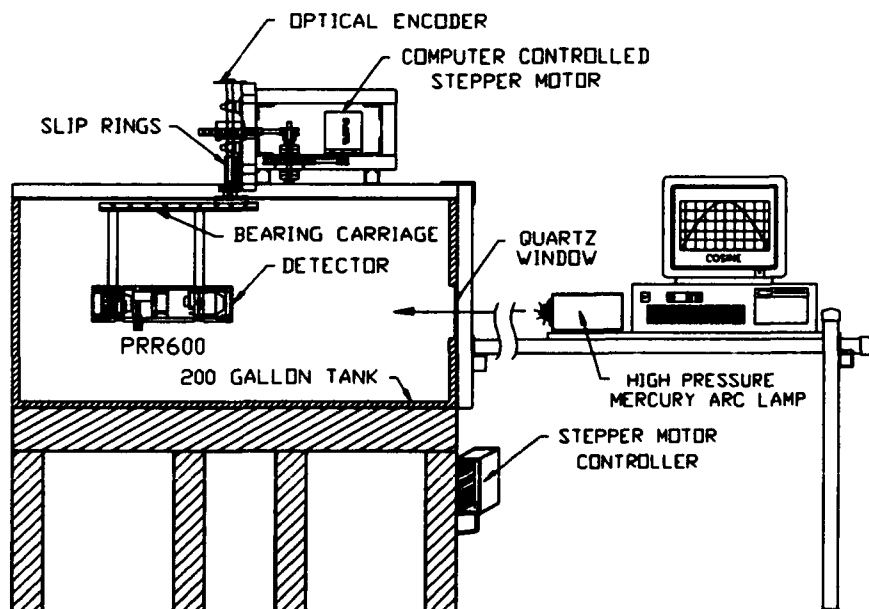


Figure 4. Computer controlled test apparatus and tank for measuring cosine response of PRR-600.

The immersion coefficient was determined experimentally from irradiance measurements made in air and under water (Figure 5). The instrument was carefully positioned in the test tank beneath a calibration lamp fixture. Readings were recorded in air and at 5 cm depth increments both during filling and emptying the tank.

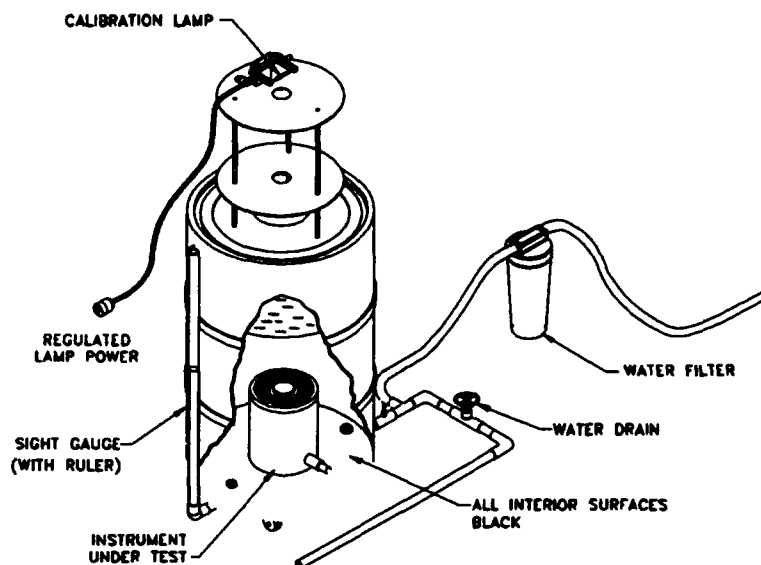


Figure 5. Immersion coefficient test tank.

A complete discussion of the theory behind the immersion coefficient is beyond the scope of this paper. However, Mueller and Austin³ provide an excellent overview of computation of the immersion coefficient, as derived in Petzold and Austin⁴. In brief, the flux from the calibration source are attenuated both by losses due to the air-water interface as well as by the water when submerged. Further, it also is necessary to account for the change in the solid angle of the flux caused by the air-water interface. Following Mueller and Austin³, Data from the test tank are used to measure the attenuation coefficient for the water used in the test and to solve for the immersion coefficient at each wavelength.

3. RESULTS

Results of cosine testing may be presented in a number of ways. Figure 6 shows one typical cosine plot for the PRR-600 and a collimated beam. A less marketable but perhaps more useful analysis in evaluating collector design examines the percent difference between a true cosine function and the actual response of the instrument (Figure 7) at different wavelengths. This example tends to emphasize deviations at higher zenith angles because the surface reflectance and Teflon transmittance are increasing, while the signal to noise ratio is decreasing. Both analyses indicate that the final PRR-600 design exhibits good cosine response in the range $+65^\circ$ to -65° , with increasing deviation from true cosine in the red. In the region from 412 to 560 nm, the bias is within $\pm 3\%$ over the range $+70^\circ$ to -70° zenith angle and within $\pm 10^\circ$ beyond that range. In the red (683 nm), the response typically underestimates the flux of a collimated beam within -10% over the range $+70^\circ$ to -70° .

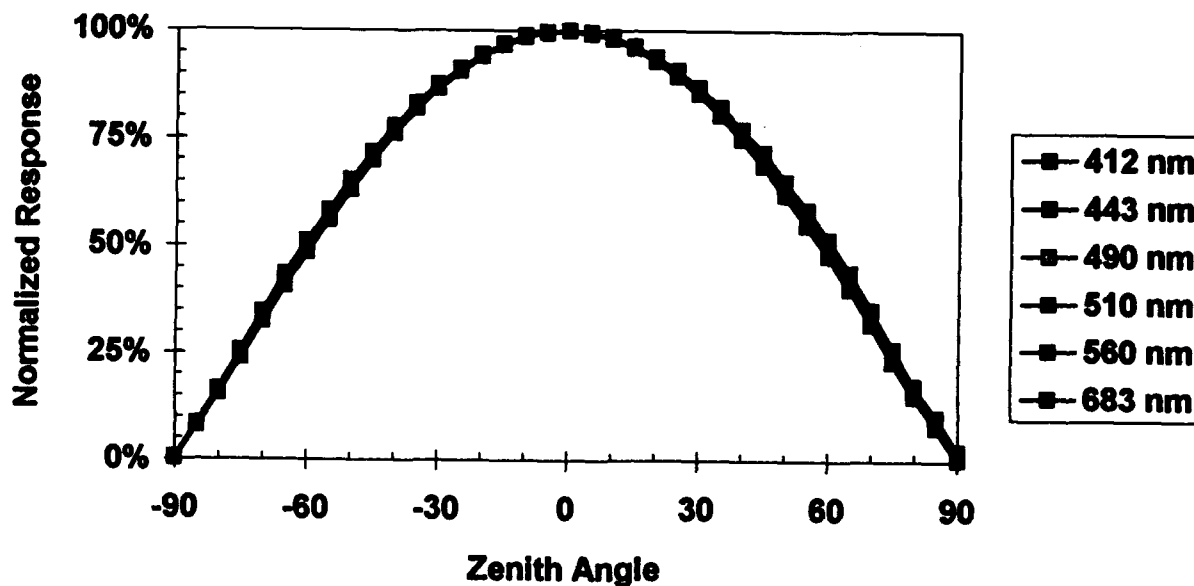


Figure 6. Typical results from cosine collector test of PRR-600 in water normalized to the response at $\theta=0^\circ$.

In order to detect potential asymmetries resulting from the position of the individual detectors, the PRR is turned on its axis at 10° intervals and the cosine response recorded. The result is a matrix of responses to a collimated beam covering $\pm 90^\circ$ in zenith angle and $\pm 90^\circ$ in axial rotation (azimuth) for each spectral channel. Figure 7 shows a contour plot of percent deviation from cosine response at 443 nm for the PRR-600 in water. Although there is some evidence of asymmetry, the impact of this asymmetry is not significant on the measurement at any wavelength.

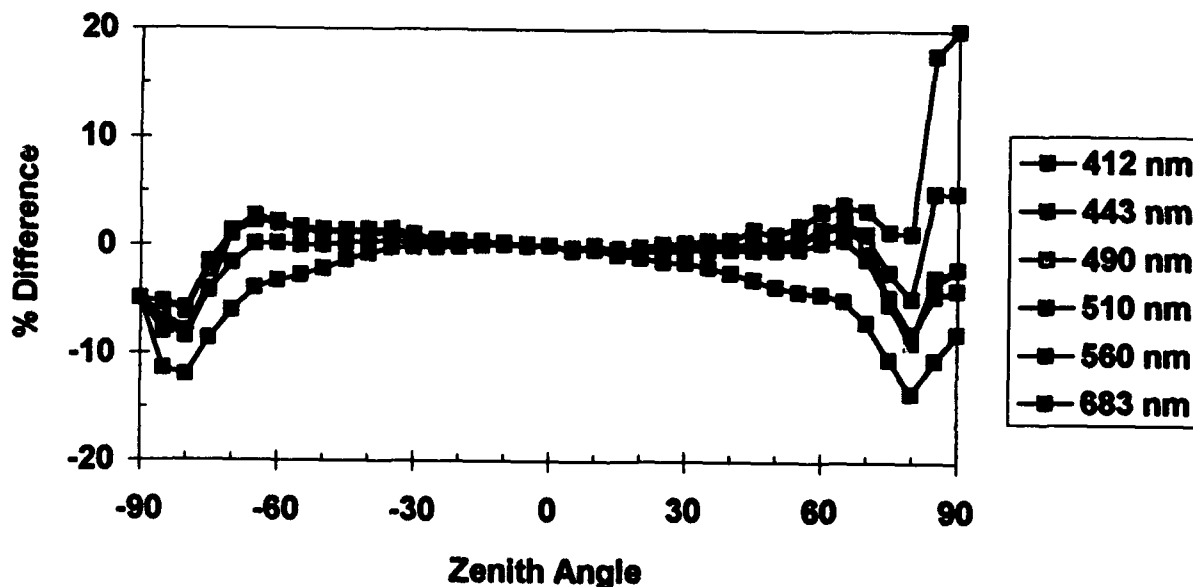


Figure 7. Typical percent difference from ideal cosine function for PRR-600 in water.

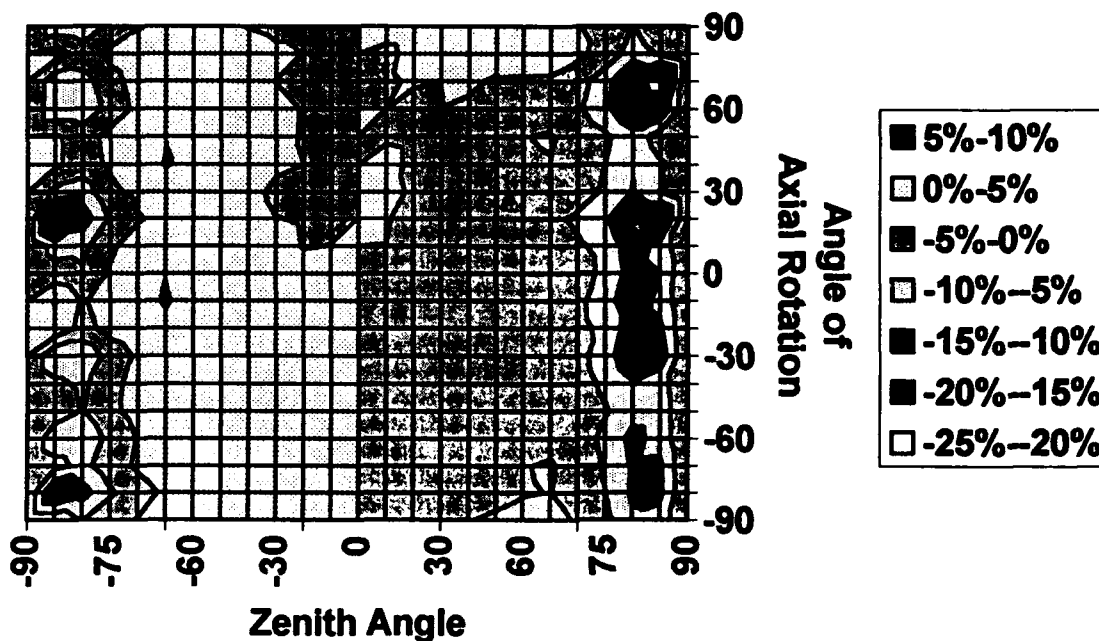


Figure 8. Percentage deviation from true cosine for a collimated beam for the PRR-600 at 443 nm in water.

For contrast, the PRR-600 collector was analyzed identically, but without submersing the instrument. Figure 9 displays the results for 443 nm in air. As in Figure 8, the collector continues to show a moderate asymmetric response resulting from photodiode placement, but the irradiance response is consistently in the range 0% to +10% from -60° to $+60^\circ$ zenith angles.

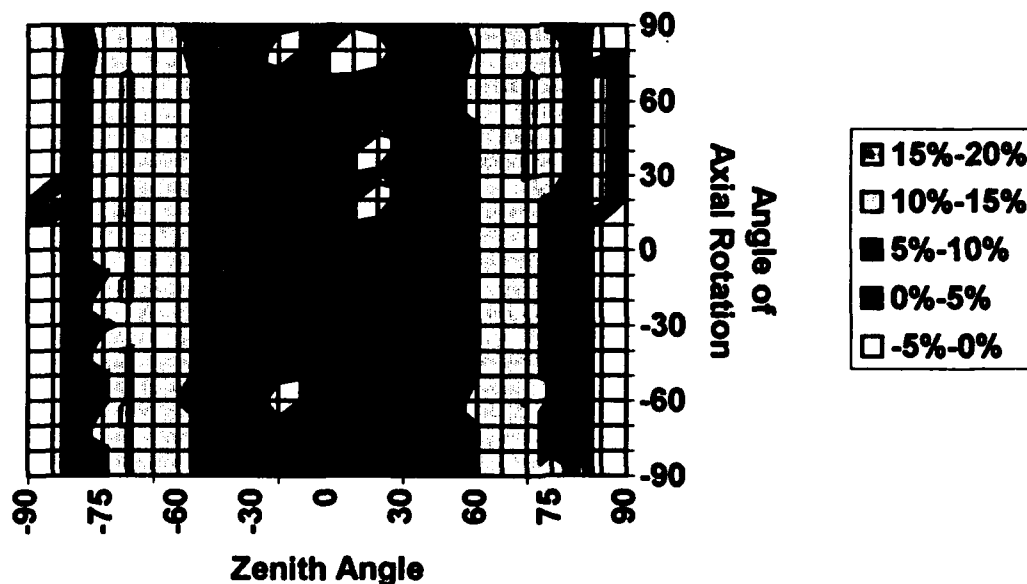


Figure 9. Percentage deviation from true cosine for a collimated beam for the PRR-600 at 443 nm in air.

The above analysis tends to emphasize systematic biases in the measurement of irradiance caused by departure from a true cosine response because the analysis was performed with a collimated beam. In actual practice, downwelling irradiance measurements are made in a light field that is not collimated. The angles of incidence are more generally near normal to the plane of the collector, and biases due to cosine errors are small. To determine the impact of cosine errors in the field, the measured biases are weighted by the cosine of the radiance distribution. Integrating over all zenith (θ) and azimuthal (ϕ) angles, the net percent bias in the geometric cosine response for any irradiance light field $E(\theta, \phi, \lambda)$ may be calculated for each wavelength:

$$\%bias(\lambda) = \frac{100}{2\pi} \int_0^{2\pi} \int_0^{\pi/2} [R_n(\theta, \phi, \lambda) - \cos(\theta)] E(\theta, \phi, \lambda) d\theta d\phi \quad (3)$$

$R_n(\theta, \phi, \lambda)$ is the normalized response of the detector to the lamp, $R_{max}(\lambda)$ is the response with the source positioned normal to the plane of the collector, and R_{dark} is the response in the dark:

$$R_n(\theta, \phi, \lambda) = \frac{R(\theta, \phi, \lambda) - R_{dark}(\lambda)}{R_{max}(\lambda) - R_{dark}(\lambda)} \quad (4)$$

Table 1 shows the results of such an analysis for the PRR-600 applied in both a light field with a modelled, uniform radiance distribution and in a light field off San Diego, California at 25 m as measured by an electro-optic radiance distribution camera system (RADS data provided courtesy of K. Voss⁶). The uniform radiance distribution is equivalent to a totally diffuse light field, which represents the "worst-case" systematic bias that the collector design would apply to the measurement.

Table 1. Integrated cosine bias for PRR-600 irradiance collector in modelled uniform and RADS measured light fields.

Light Field	412 nm	443 nm	490 nm	510 nm	560 nm	683 nm
Uniform	1.3%	0.8%	0.3%	0.3%	-0.4%	-3.7%
Marine	0.5%	0.4%	0.2%	0.2%	-0.2%	-2.1%

Although a systematic analysis of variability in immersion coefficient for different classes of spectroradiometers is still underway, Table 2 presents results from testing of two PRR-600's produced from the same lot in early 1993 and one produced a year later. Although the sample size is small, the range of instrument-to-instrument variability in immersion coefficients over all wavelengths is low: $\pm 2\%$ (Table 3).

Table 2. Immersion coefficients for three PRR-600 irradiance collectors.

Serial Number	412 nm	443 nm	490 nm	510 nm	555 nm	683 nm
9604	0.694	0.700	0.704	0.706	0.710	0.735
9605	0.677	0.695	0.694	0.698	0.706	0.730
9617	0.678	0.677	0.693	0.693	0.703	—
Mean	0.683	0.691	0.697	0.699	0.706	0.733

Table 3. Variation in immersion coefficients for PRR-600 irradiance collectors.

% Variation	412 nm	443 nm	490 nm	510 nm	555 nm	683 nm
9604	1.6%	1.4%	1.0%	1.0%	0.5%	0.3%
9605	-0.9%	0.6%	-0.4%	-0.1%	0.0%	-0.3%
9617	-0.7%	-2.0%	-0.6%	-0.9%	-0.05%	—
Mean	1.07%	1.32%	0.67%	0.67%	0.35%	0.34%

4. SUMMARY

Although cosine collector testing is easily automated, our experience suggests that cosine collector design is not. The evolution of the PRR-600 underwater collector involved optimizing a large number of design variables with occasionally confounding results. Testing has shown repeatedly that a collector optimized for use underwater is not appropriate for SeaWiFS in air. An added problem for commercial instruments are the requirements for economic manufacturing, reproducibility, and stability over time. Our results indicate that good adherence to the cosine law can be achieved in a robust design that can be commercially made. Finally, as instruments are returned to Biospherical for calibration, the database covering variability in immersion coefficients will increase, and we will be able to more carefully evaluate if this additional calibration procedure should be performed on individual marine radiometers routinely.

5. REFERENCES

1. Boyd, R.A., "The development of prismatic glass block and the daylighting Laboratory," Engineering Research Bulletin No. 32, University of Michigan, Ann Arbor. 1951.
2. Smith, R.C., "An underwater spectral irradiance collector," Journal of Marine Research 27(1):341-351. 1969.
3. Mueller, J.L. and R.W. Austin, "Volume 5, Ocean Optics Protocols for SeaWiFS Validation," NASA Technical Memorandum 104566, Vol. 5., NASA SeaWiFS Technical Report Series, S.B. Hooker, Ed. 1992
4. Petzold, T.J. and R.W. Austin, "Characterization of MER-1032," Scripps Inst. of Oceanography Technical Memorandum EV-001-88t. 1988.
5. Aas, E., "On submarine irradiance measurements," Kobenhavns Universitet, Institut for Fysisk Oceanografi Report No. 6, 1969.
6. Voss, K.J. "Use of the radiance distribution to measure the optical absorption coefficient in the ocean," Limnol. Oceanogr. 34(8):1614-1622. 1989.

**Inverse modeling for retrieval of ocean color parameters
in case II coastal waters
- An analysis of the minimum error -**

Roland Doerffer & Helmut Schiller

GKSS Forschungszentrum
21502 Geesthacht, F.R. Germany

Abstract

In turbid waters of coastal zones (Case II water) the retrieval of the concentration of chlorophyll from remotely sensed spectral radiances becomes difficult because of the influence of gelbstoff and suspended matter on the radiance spectrum. For the Coastal Zone Color Scanner (CZCS) an inverse modeling method was developed to derive the concentrations of gelbstoff, suspended matter and chlorophyll and the aerosol path radiance. The minimum error we have to expect for this system is analyzed by modeling the concentration change which is necessary to cause a change in the radiance corresponding to 1 digital count. The determination of the minimum error in the retrieval procedure is based on the evaluation of the Hesse Matrix of the chi square function. It turns out that for case II water the channel most sensitive to changes to all three groups of water constituents is CZCS 4 at 670 nm. The retrieval of the concentration is most difficult for chlorophyll, while the error for suspended matter and gelbstoff and for the aerosol path radiance is much smaller.

1. Introduction

The retrieval of chlorophyll concentrations from CZCS radiances, but also other sensors, in so called Case II waters causes problems, since other substances such as other suspended particles (mineralic and organic detritus) and dissolved organic matter (which is summarized as gelbstoff) influences also the spectral composition of the upward directed radiances. It has been demonstrated that the inverse modeling technique can be used to separate the influence of different groups of substances on the radiance spectra and to calculate their concentrations. For radiances measured from a ship or aircraft this method was firstly used by Jain & Miller¹ and by Fischer². For the retrieval of substances from CZCS data a further problem is atmospheric correction over turbid waters, since the channel CZCS 4 (670 nm) which is used for determining the aerosol path radiance over clear oceanic waters³ is also effected by suspended matter in turbid coastal waters. Fischer & Doerffer⁴ and Doerffer & Fischer⁵, Doerffer et al.⁶ have shown that it is possible to derive 4 parameters from CZCS images of the North Sea: suspended matter, gelbstoff, chlorophyll and aerosol path radiance. Comparison between statistical parameters such as mean, standard deviation and frequency distribution values of ship and CZCS data show a good agreement with a deviation which is less than the typical error of water samples. One example of CZCS evaluation by inverse modeling is given in Fig. 1. It shows the distribution of gelbstoff in the North Sea (German Bight) caused by the river Elbe plume.

A particular problem in case II water is the determination of the errors which occur in the analysis. In general one can imagine a high number of variables which are not described by the model in a proper way for a particular pixel, such as the unknown vertical distribution, deviation of the optical properties of the substances and the aerosol considered from those used in the model, other substances, such as different phytoplankton populations which are not considered in the model etc. Despite these unknown sources of errors, which of course cause problems for any algorithm, one can also look for the minimum error one has to face. The minimum error as defined here is the error introduced by the measurement system including the evaluation procedure assuming that the model used for the interpretation including all its parameters corresponds to the actual situation of that pixel. This will be the main topic of this paper. It will be demonstrated for inverse modeling of a CZCS scene.

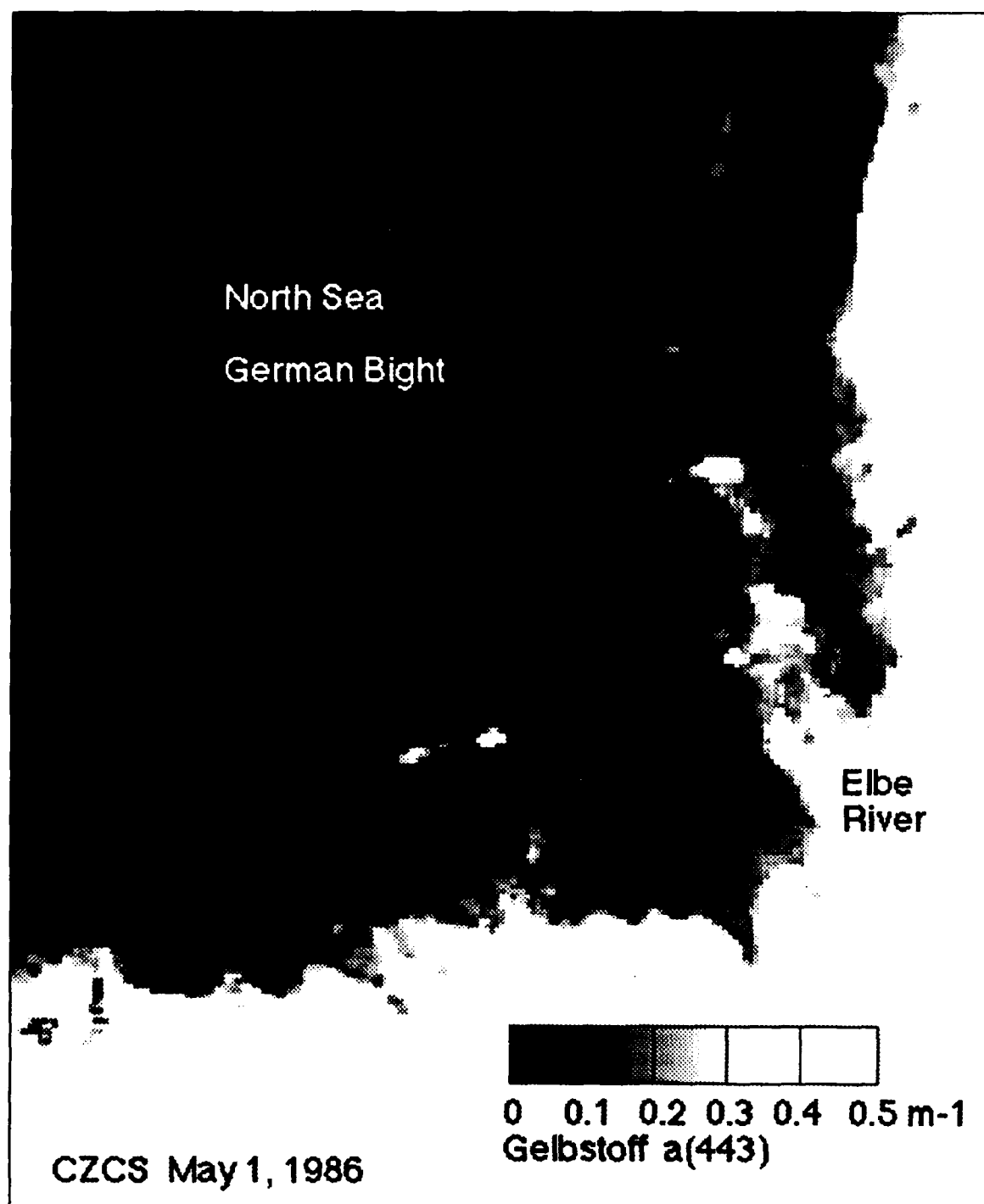


Fig. 1 Gelbstoff plume of the river Elbe as derived from a CZCS image by inverse modeling.

2. Method and Data

The radiative transfer model used in the inverse algorithm and for the simulation is a single scattering model for the atmosphere which includes absorption due to atmospheric gases, reflection of sunlight at a rough sea surface and reflection of skylight at the sea surface. The underwater radiative transfer is described by a two-flow model. It is based on formulations of Andre & Morel⁷, Joseph⁸, Sturm⁹ and is summarized in Doerffer¹⁰. For inverse modeling the Simplex-Algorithm of Nelder & Meads¹¹ was modified by introducing constraints adapted to the chi_square criteria. The principles of inverse modeling for CZCS data is given in Fig. 2. The optical properties of water constituents are taken from Prieur & Sathyendranath¹² and Doerffer¹³. The parameters of the atmosphere were taken from Iqbal¹⁴. The correction scheme for the sensitivity loss of CZCS is from Sturm¹⁵. For the simulation for the sensitivity analysis a gain setting of 1 and no sensitivity loss was assumed. Each of the 4 CZCS bands is represented by a single wavelength only. The concentration range as used in the CZCS simulation is typical for North Sea water as found in the German Bight. The CZCS scene used is of the North Sea (May, 1st, 1986). For demonstration of the minimum error analysis only one pixel is used here showing typical concentrations of the coastal North Sea.

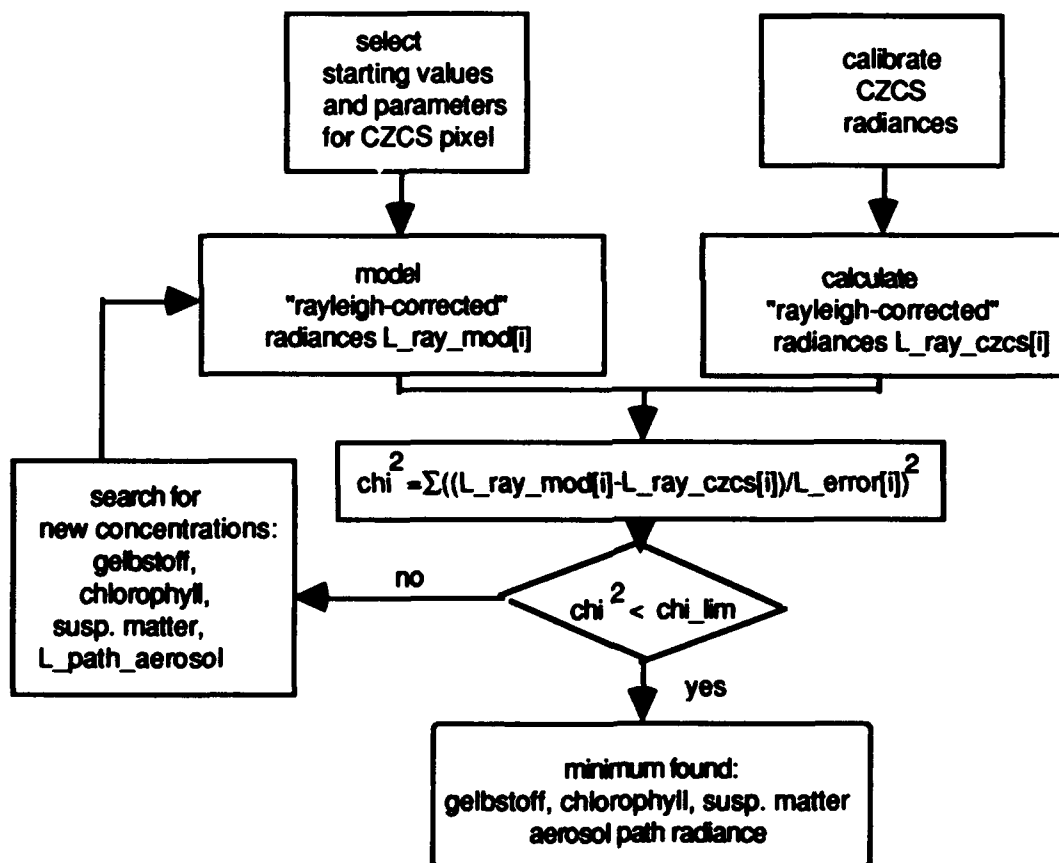


Fig. 2 CZCS Inverse modelling

The method for error analysis when fitting data to a model is based on a procedure described in Thacker¹⁶. It analyses the Hesse Matrix, which is the matrix of the second partial derivatives of the cost function, which is the chi square function formulated as

$$\chi^2 = \sum_{i=1}^{nch} \left(\frac{L_{ray_czcs[i]} - L_{ray_mod[i]}}{L_{error[i]}} \right)^2$$

with L_{error} as the error being the radiance corresponding to of 1 digital count which is assumed the minimum error. The inverse of the Hessian is the unweighted covariance matrix. Since the cost function is chi_square from two times the unweighted covariance matrix the errors for each of the parameters, i.e. the concentration of gelbstoff, suspended matter and chlorophyll as well as of the aerosol path radiance, can be derived as the squareroots of the diagonal and the correlation matrix by dividing the elements of the covariance matrix by the squareroots of the corresponding products of the variances.

3. Results

The minimum error occurring in the retrieval of the concentration of water constituents from radiance measurements is determined by the quantization of the analog signal and is ± 1 digital count. For the CZCS we carried out a simulation of the radiances as seen by the sensor and ask the question, which change in concentration of a water substance is necessary in order to produce a change of 1 digital count for each of the 4 CZCS channels assuming a gainsetting of 1 and no sensitivity loss, a sun zenith angle of 20 deg and a nadir looking sensor. A standard atmosphere was assumed with a visibility of 20 km, no wind. The result for Case I water with chlorophyll as the only water constituent is shown in Fig. 3a.

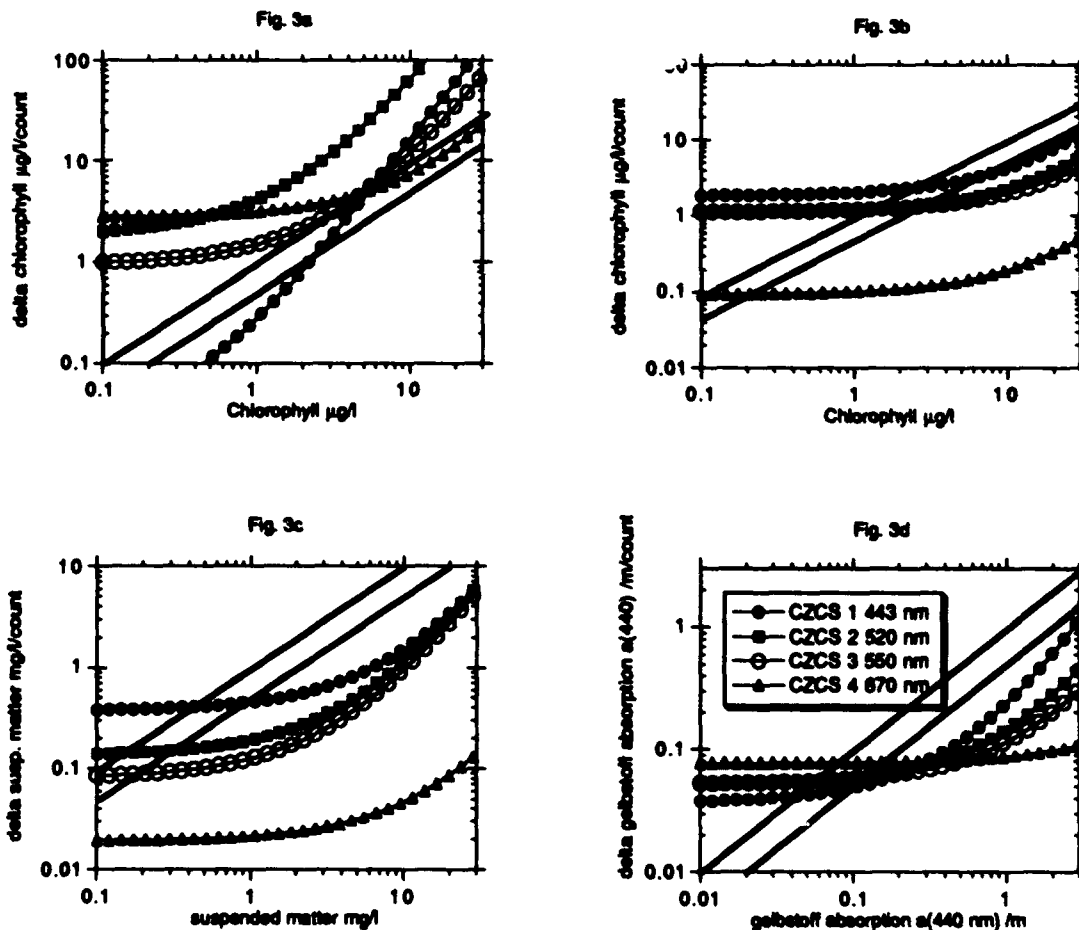


Fig 3 Results of minimum error analysis for CZCS radiances. (a) for case I water, f(-d) for case II with $5\mu\text{g/l}$ chlorophyll, 5 mg/l suspended matter and gelbstoff absorption of $0.5/\text{m}$ at 440 nm . The x-axis shows the concentration, the y-axis the change of concentration which is necessary to cause a radiance change of 1 digital count. The diagonal lines indicate the area in which more than a 100% change or more than a 50% change is necessary.

From this graph it can be clearly seen that the most sensitive channel is - as expected - CZCS channel 1 (443 nm). A

CZCS channel	centre wavelength [nm]	L_ray_sat	L_ray_mod	delta L	delta digital count	Dev. %
1	443	12.75	12.70	0.05	0.11	0.4
2	520	15.71	15.47	0.24	0.77	1.5
3	550	17.34	17.11	0.23	0.93	1.3
4	670	7.99	8.42	0.43	3.8	5.2
5	750	7.28	5.61			

Table 1: Comparison between the "rayleigh-corrected" radiances of CZCS and model at the end of the inverse modeling loop for 1 pixel of a typical Case II water section of the North Sea. CZCS channel 5 was not used for the optimization. Radiances are in $W m^{-2} sr^{-1} \mu m^{-1}$

sufficient accuracy with a 50% error limit can only be achieved in the concentration range up to 3 $\mu g/l$. Above 5 $\mu g/l$ the most sensitive channel becomes CZCS channel 4 (670 nm), while the channels 2 and 3 (520 and 550 nm) never passes under the 100% line.

For case II water we have assumed a concentration of chlorophyll of 5 $\mu g/l$, of suspended matter of 5 mg/l and a gelbstoff absorption of 1/m at 380 nm with a spectral absorption slope exponent of 0.0135. These values are typical for coastal North Sea water as found e.g. in the German Bight. Now we modify each of these 3 water constituents while the other two remain constant. Fig. 3 b shows the result for a changing chlorophyll. Channel 4 is now the most sensitive channel over the whole range and stays below the 50% limit while channel 1 is the last sensitive which never subpasses the 50% line. This behaviour is caused by the suspended matter concentration which is at this concentration most sensitive in the red part of the spectrum to changes of its own concentration and to that of any absorbing material. This can also be seen in Fig.3 c, where the concentration of suspended matter was varied. The sensitivity increases (minimum error decreases) with increasing wavelength. A varying gelbstoff concentration (Fig. 3d) shows a different behaviour. In the range of low concentrations the blue channel is most sensitive to changes while in the concentration range such as found in the coastal waters of the southern North Sea again the red channel 4 has the lowest minimum error.

In the minimum error analysis of the pixel of the CZCS image we have used here for demonstration a corresponding result appears. Table 1 shows the differences between the modeled and measured "Rayleigh-corrected" radiances at the end of the optimization loop, i.e. the radiances at the top of atmosphere after subtracting the contribution by the air molecular scattering including reflections at the sea surface. While CZCS channels 1-3 are below 1 digital count difference, channel 4 shows a deviation of 3 digital counts. So the modeling of channel 4 in this range of concentrations still has to be improved.

The errors for the four concentration parameters as derived from the inverse of the Hesse matrix of the chi_square function are listed in Table 2. They are asymmetrically because the logarithms of the concentrations were used in the optimization loop (search space of the simplex). The order of increasing error corresponds to that we have found in the simple analysis as shown above: aerosol path radiance, gelbstoff, suspended matter and chlorophyll. Due to the small correlations of the parameters the ordering of errors can be assessed from the diagonal of the Hess matrix, which elements are the second derivatives by the parameters. However, it has to be pointed out that this analysis is valid only for this particular pixel, although it is typical for case II water, in the clearer parts of the North Sea with Case I like water results are different.

4. Conclusion

The errors of remotely sensed concentrations of water constituents depends on many influences such as the vertical

Parameter	2nd derivative	Fit value	Range of one Std. Deviation	Unit
Chlorophyll	1.4	0.45	0.08 - 2.6	µg/l
Suspended Matter	137	1.9	1.1 - 3.3	mg/l
Gelbstoff absorption	242	0.35	0.30 - 0.40	m-1 (440 nm)
Aerosol path radiance	1400	5.7	5.4 - 6.1	Wm-2sr-1µm-1
Table 2: Errors of the retrieved concentrations of the same pixel of Table 1 as derived from the Hesse matrix of the chi square function of the inverse modeling procedure				

distribution and the specific inherent optical properties, of which most are unknown for the actual situation as represented by the radiances of a pixel. Thus, we have analyzed only the minimum error which is caused by the sensor and the algorithm applied, in our case the inverse modeling procedure.

The following conclusions can be drawn from the results:

- In Case II water all 4 channels of the CZCS, that means the whole range of the visible spectrum is influenced by all 3 groups of water constituents: suspended matter, gelbstoff and phytoplankton pigments. There is no channel where one of the substances can be neglected. Only evaluation procedures, such as inverse modeling which consider all spectral channels and the influence of all parameters, i.e. suspended matter, gelbstoff, pigments and aerosol path radiance simultaneously can be used to derive the concentration of one of these substances. Simple color ratio algorithm can work only in the case of a high covariance between these substances.
- In turbid water, the most sensitive channel with the smallest minimum error is CZCS channel 4 (670 nm) with respect to all 3 groups of water constituents.
- The most critical parameter with the largest error in turbid Case II water is chlorophyll.
- Although the CZCS radiometer is not very accurate due to its sensor performance and although the derived concentrations are very sensitive to small changes in digital counts, the whole measurement system of CZCS inverse modeling despite different errors has been proven to lead to results being in accordance with the knowledge from other sources.

Future sensors which will be dedicated also to Case II waters (as it was the original purpose of the Coastal Zone Color Scanner) have to include more channels in the red part of the spectrum for allowing a pigment determination in different waters with varying concentrations of suspended matter and gelbstoff.

5. Acknowledgement

This analysis was supported by the project KUSTOS of the Federal Minister of Research and Technology (BMFT) of Germany and by the project OCEAN of the Joint Research Centre of the European Union and the European Space Agency ESA.

6. References

- [1] S. C. Jain and J. R. Miller, "Subsurface water parameters: optimization approach to their determination from remotely sensed water color data," *Applied Optics*, vol. 15, pp. 886-890, 1976.
- [2] J. Fischer, "Remote Sensing of Suspended Matter, phytoplankton and yellow substances over coastal waters, 1, aircraft measurements," *Mitt. Geol. Palaeontol.Inst. Univ. Hamburg*, vol. 55, p. 85 pp., 1984.

- [3] H. R. Gordon and A. Morel, "Remote assessment of ocean color for interpretation of satellite visible imagery. A review". *Lecture notes on coastal and estuarine studies*. New York, Berlin: Springer Verlag, 1983.
- [4] J. Fischer and R. Doerffer, "An inverse technique for remote detection of suspended matter, phytoplankton and yellow substances from CZCS measurements," *Adv. Space Res.*, vol. 7, pp. 21-26, 1987.
- [5] R. Doerffer and J. Fischer, "Concentrations of chlorophyll, suspended matter, and gelbstoff in case II waters derived from satellite coastal zone color scanner data with inverse modeling methods," *Journal Geophysical Research*, vol. 99, pp. 7457-7466, 1994.
- [6] R. Doerffer, W. Puls, D. Pan, Hans-H. Essen, K.-W. Gurgel, K. Hessner, T. Pohlmann, F. Schirmer, and T. Schlick, "Evaluation of the North Sea joining in situ and remotely sensed data with model results," in *Circulation and Contaminant Fluxes in the North Sea*, 1st ed., J. Sündermann, Ed. Berlin: Springer-Verlag, 1994, ch. 4.1, pp. 434-457.
- [7] J. M. André and A. Morel, "Simulated effects of barometric pressure and ozone content upon the estimate of marine phytoplankton from space," *Journal Geophysical Research*, vol. 94, pp. 1029-1037, 1989.
- [8] J. Joseph, "Untersuchungen über Ober- und Unterlichtmessungen im Meere und über ihren Zusammenhang mit Durchsichtigkeitsmessungen," *Dtsch. Hydrogr. Z.*, vol. 3, pp. 324-335, 1950.
- [9] B. Sturm, "The atmospheric corrections of remotely sensed data and the qualitative determination of suspended matter in marine water surface layers," in *Remote Sensing in Meteorology, Oceanography and Hydrology*, A. P. Cracknell, Ed. Chichester: Ellis Horwood, 1980, pp. 163-197.
- [10] R. Doerffer, "Imaging spectroscopy for detection of chlorophyll and suspended matter," in *Imaging spectroscopy: fundamentals and prospective applications*, F. Toselli and J. Bodechtel, Eds. Brussels and Luxembourg: ECSC, EEC, EAEC (Kluwer), 1992, pp. 215-257.
- [11] J. A. Nelder and R. Mead, "A simplex method for function minimization," *Comput. J.*, vol. 7, pp. 308-313, 1965.
- [12] L. Prieur and S. Sathyendranath, "An optical classification of coastal and oceanic water based on the specific spectral absorption curves of phytoplankton pigments, dissolved organic matter, and other particulate materials," *Limnol. Oceanogr.*, vol. 26, pp. 671-689, 1981.
- [13] R. Doerffer, "Untersuchungen über die Verteilung oberflächennaher Substanzen im Elbe-Aestuar mit Hilfe von Fernmeßverfahren," *Arch. Hydrobiol.*, vol. Suppl. 43 Elbe-Aestuar 4 2/3, pp. 119-224, 1979.
- [14] M. Iqbal, *An Introduction to Solar Radiation*. Toronto, New York, London: Academic Press, 1983.
- [15] B. Sturm, "Updated sensitivity compensation factors for CZCS", unpublished document, May 30, 1987, JRC Research Centre, Ispra, Italy.
- [16] W. C. Thacker, "The Role of the Hessian Matrix in Fitting Models to Measurements," *Journal Geophysical Research*, vol. 94, pp. 6177-6196, 1989.

The variation of optical properties in the Baltic Sea and algorithms for the application of remote sensing data

Herbert Siegel, Monika Gerth, Marko Beckert

**Baltic Sea Research Institute Warnemuende
at the University of Rostock
Seestrasse 15
D- 18119 Rostock
Germany**

ABSTRACT

The variation of optical properties of the water was studied in the open Baltic Sea and in coastal waters of the Pomeranian Bight for more than ten years. The optical properties in the open Baltic Sea are strongly influenced by plankton blooms with typical phytoplankton compositions. This led to significant seasonal variations in spectral reflectances. In coastal waters of the Pomeranian Bight, the origin of the water masses and the dwell period of the river water in different lagoon-like areas and bays determine the composition of the water constituents and their optical properties. Strong temporal and spatial variations in spectral reflectance, the spectral absorption of phytoplankton pigments, detritus and yellow substances were found within an area of 50 km².

The data set was used to develop ground truth algorithms to determine water constituents of Baltic Sea water from from satellite data using CZCS, SeaWiFS and MERIS.

2. INTRODUCTION

The spectral reflectances of the sea water are dominated and modified by its absorbing and scattering properties and the dissolved and suspended matter it contains. Therefore, seasonal and regional differences in reflectance result from the compositions and concentrations of that matter and from their inherent optical properties.

The Baltic Sea is a marginal sea with a limited water exchange to the North Sea and oceans. The freshwater from rivers transports high concentrations of nutrients, organic and inorganic suspended material and dissolved organic substances into the Baltic. In the southern part of the Baltic, the water transport takes place via shallow lagoon-like regions where plankton production starts. The river water also contains high concentration of terrigenous yellow substances draining from swampy areas. In the central part of the Baltic Sea, the Baltic proper, the concentrations of the water constituents are strongly influenced by plankton blooms, the species composition of which varies according to season.

The application of satellite data of ocean colour for the investigation of temporal and spatial distribution of the concentrations of water constituents requires ground truth algorithms on the basis of reflectances or specific optical properties.

This paper discusses temporal and spatial variations in optical properties caused by different concentrations and compositions of various water constituents and presents ground truth algorithms based on reflectance ratios. The algorithms are already being used in the procedure of the OCEAN project to calculate concentrations of water constituents from CZCS data for the Baltic Sea for oceanological applications in the Baltic Sea Research Institute.

3. METHODS AND AREAS OF INVESTIGATION

The spectral reflectances were measured for more than ten years in various areas and seasons in order to study regional and seasonal variations and the influence of different water constituents. The total internal reflectances were calculated from measurements of the upward radiance just beneath the sea surface (L_u) and of the downward irradiance (E_d) above the sea surface using the equation

$$R = \pi L_u / E_d, \quad (1)$$

which is applicable on the assumption of completely diffused upwelling light.

The measurements were carried out with a radiometric calibrated BAS-W¹ spectrometer at 25 wavelength in the spectral interval between 400 and 735 nm with a spectral resolution of $\Delta\lambda = 10$ nm.

Spectral absorption was measured with a Lambda 2 spectral photometer (PERKIN ELMER). The absorption of yellow substances was determined from filtered samples, and the filter method² was used for particulate matter (phytoplankton, detritus).

The volume scattering function was measured at a wavelength of 633 nm and angles between 5° and 165° by means of a laboratory light scattering photometer to calculate the scattering coefficients.³

To characterize the transmission properties of the water column and the depth of the productive euphotic zone were determined its depth from quantum irradiance measurements (LICOR).

The water constituents taken into account were the chlorophyll and phaeopigment concentrations⁴, suspended matter and, in some cases, the phytoplankton composition.

The station map in Fig. 1 shows the positions at which measurements were taken during selected cruises in the Baltic Sea. The measurements were carried out along a transect through the central Baltic as well as in special grids in the Gotland Sea and Pomeranian Bight.

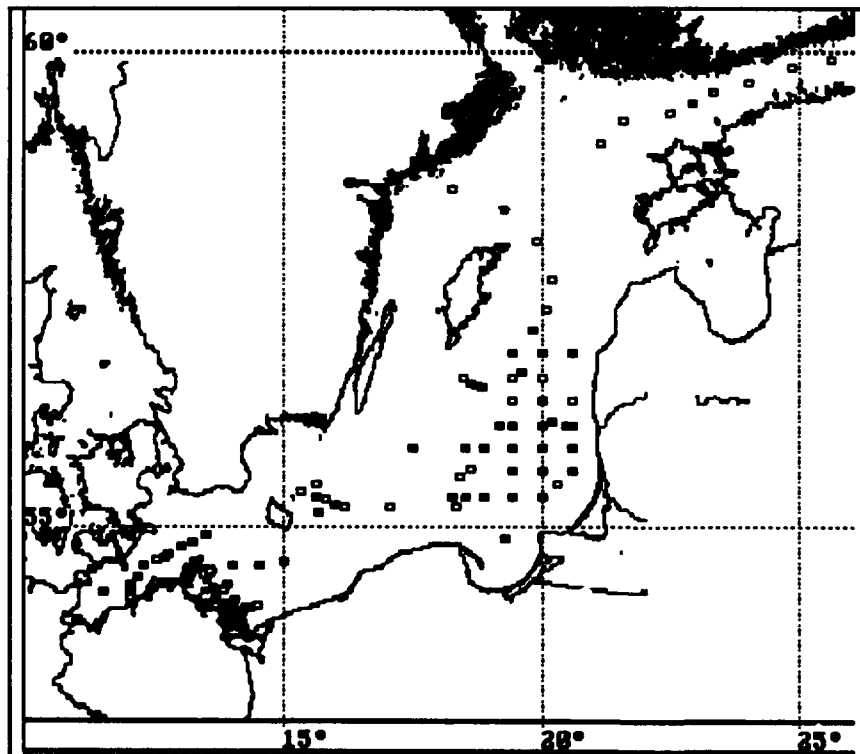


Figure 1: Station map of selected cruises in the Baltic Sea

4. VARIATIONS IN THE SPECTRAL REFLECTANCE

The total internal reflectance R can be approximated by the reflectance of the water, R_w , if the sea bottom has no influence on the radiation field below the sea surface. In this case, $R = R_w$ is determined by the optical properties of the sea water and the materials dissolved and suspended in it. The spectral reflectance of the water, R_w , is proportional to the ratio between the backscattering b_b and absorption coefficients a ($R_w = 0.33 b_b / a$ is a practically used formula for case 1 water)⁵. The backscattering coefficient, b_b , can be calculated from measurements of the volume scattering function $B(\gamma)$

$$b_b = 2\pi \int_0^\pi B(\gamma) \sin \gamma d\gamma \quad (2)$$

where γ is the scattering angle. The total absorption, a , and backscattering coefficients, b_b , consist of the following components:

$$a = a_w + a_{ph} + a_y + a_s + a_d + a_x, \quad b_b = b_{bw} + b_{bp} \quad (3)$$

The index w denotes pure seawater, ph phytoplankton, y yellow substances, s suspended matter, d detritus, p particulate matter, and x other constituents. The actual absorption coefficient in a specific area can be calculated as the product of the specific coefficient of the material concerned and its concentration. The spectral shape of the reflectance is modified mainly by the spectral absorptions of the water, the yellow substances and phytoplankton.⁶

4.1. Reflectances of different water areas

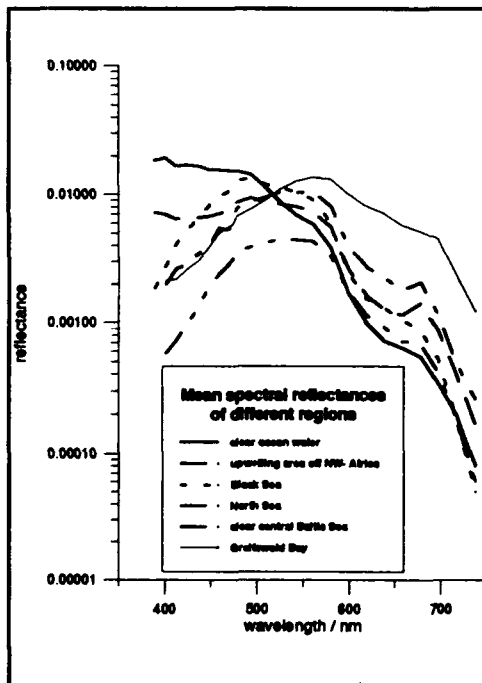


Figure 2: Mean spectral reflectances in different regions

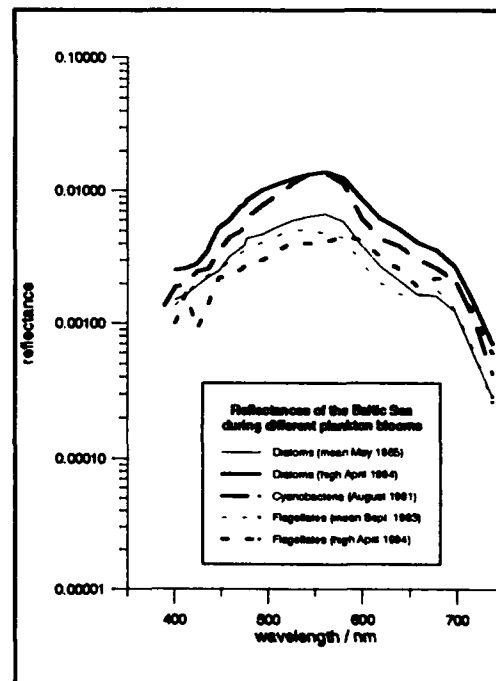


Figure 3: Reflectances of the Baltic during blooms of diatoms, cyanobacteria, flagellates and dinoflagellates

The mean reflectances measured in different areas are shown in Fig. 2 to illustrate the spectral shape and the variations in reflectance encountered in the Baltic Sea.⁷ The clear oceanic water of the Atlantic is characterized by the highest values being in the short and the lowest in the long wavelength range because it is influenced only by the absorption and scattering of pure sea water.

In upwelling areas, the higher chlorophyll concentrations and their absorption properties lead to a reduction in the short wavelength interval, and scattering due to the particulate phytoplankton leads to an increase at the long wavelengths. In the North Sea and in Black Sea, the yellow substances reduce the reflectance in the blue region owing to their exponentially increasing absorption as the wavelength decreases. The high concentrations of yellow substances reduce the curves for Baltic Sea water up to 580 nm. In the bay Greifswalder Bodden, high concentrations of suspended matter increase the whole spectrum, and the steeper slope in the short wave range is caused by the yellow substances. In some areas as the upwelling area and the North Sea a maximum occurs in the reflectance near 685 nm due to the natural fluorescence of chlorophyll a.

4.2. Variations in the reflectance of the Baltic

Variations in the spectral reflectance of the Baltic are caused by seasonal and regional differences in the compositions and concentrations of optically active water constituents. Seasonal variations are produced by the development of plankton blooms in which specific algae are dominant. The spring bloom consists mostly of diatoms, whereas cyanobacteria are dominant in summer and flagellates in September.

Regional differences are caused by temporal differences in the bloom development which starts in March in the western part and reaches the northern part in May. In coastal areas the river transports high concentrations of phytoplankton, yellow substances and suspended inorganic matter into the Baltic Sea.

4.2.1 Seasonal differences

Mean reflectances measured during various plankton blooms in the Baltic proper are presented in Fig. 3 and completed by selected curves from measurement in April 1994. The mean curve of the diatom bloom in 1985 show nearly the same shape as that measured in April 1994 but the magnitude was higher this year due to the diatom concentration. The reflectance from the cyanobacteria bloom differ only slightly from this. Owing to the different fluorescence chlorophyll ratio of the dominant algal groups, the natural fluorescence maximum in the spectral reflectance near 685 nm is found in all measurements during a bloom of flagellates and dinoflagellates, but never during diatom and cyanobacteria bloom.

Diatoms and cyanobacteria are characterized by a low fluorescence chlorophyll ratios in contrary to flagellates and dinoflagellates.

4.2.2 Regional variability

The influence of river water on the compositions and concentrations of various water constituents, their inherent optical properties and the spectral reflectance was studied during three different cruises in the Pomeranian Bight⁸ in comparison with those of the open Baltic Sea water in the Arkona Basin. Fig. 4 contains all reflectance measurements taken during the cruise in May 1991.

These measurements yielded reflectance curves with three different shapes corresponding to water from the river Oder, mixed bay water and clear water from the open Baltic Sea (Fig. 5).

During north-easterly winds, the core of the plume from the river Oder was observed a distance of 6 km from the coast, where it was 10 km wide. The plume could still be detected up to 25 km from the estuary. Vertically, it is restricted to the top 5 m. The river water plume was bounded by a mixed bay water, and clear Baltic Sea water was found farther north in the Arkona Sea.

The spectral reflectances at the sea surface also indicated these different water bodies. Unlike the reflectances of the Baltic proper, the differences occur in the whole spectral range as a result of the higher particle concentrations in the Pomeranian Bight. The river water is characterized by a greater decrease towards short

wavelengths caused by absorption by yellow substances. The maximum in the reflectance changes from 520 nm in Baltic water to 580 nm in water from the river Oder. The reflectance of the river water has a secondary maximum near 700 nm due to the high backscattering caused by suspended matter and the high absorption of the phytoplankton pigments in the spectral interval up to that wavelength.

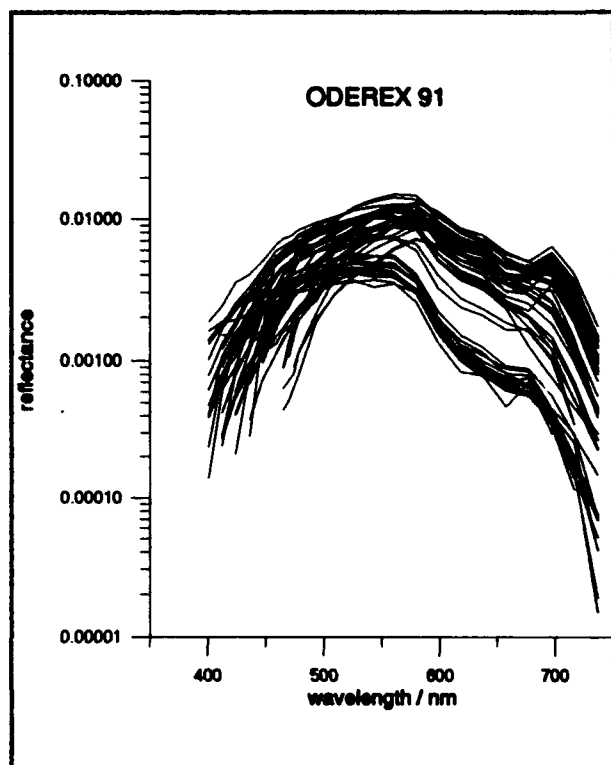


Fig. 4: Spectral reflectances of the Baltic Sea water, Pomeranian Bight and the Oder river plume

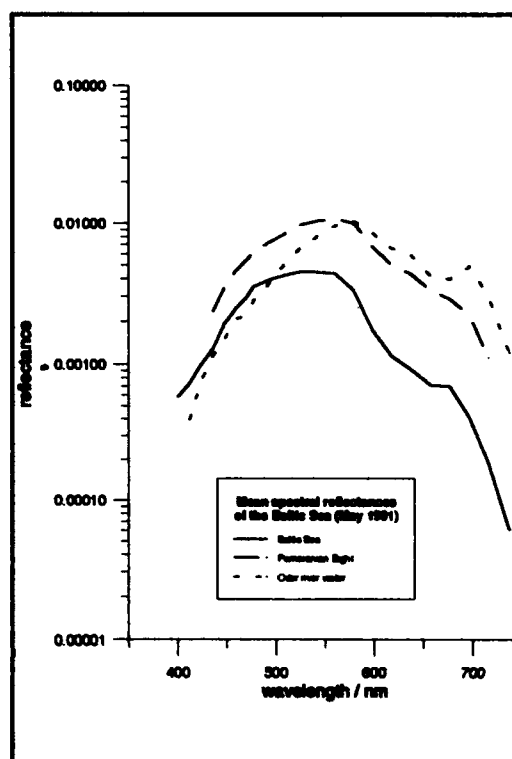


Fig. 5: Mean spectral reflectances of the Baltic, the Pomeranian Bight and the Oder river

Table 1 summarizes the differences between the river water, the surrounding bight water and the Baltic proper in salinity, chlorophyll-a and phaeopigment concentrations, seston and yellow substances as well as in the optical parameters transparency (Secchi-depth), depth of the euphotic zone and wavelength of the maximum in the spectral reflectance during May 1991.

Table 1: Comparison between different water constituents of the river Oder, the Pomeranian Bight and the Baltic Sea (Arkona Sea)

	Oder river	Bight	Baltic
Salinity / PSU	3 - 6.5	7 - 8	7 - 9
Seston / $\text{mg} \cdot \text{dm}^{-3}$	8 - 10	4 - 5	2 - 4
chl.a+phae / $\text{mg} \cdot \text{m}^{-3}$	10 - 30	2 - 5	1 - 3
Gelbstoff / $\text{mg} \cdot \text{dm}^{-3}$	4 - 6	2 - 3	1 - 2
Secchi depth / m	1.0 - 3.5	4 - 7	8 - 11
Euphotic depth / m	3 - 7	10 - 14	12 - 22
Lamda Rmax / nm	580	540 - 560	520 - 550

The river water is characterized by lower salinity, higher oxygen concentration, higher concentrations of water constituents such as chlorophyll-a and phaeopigments and total suspended solids. Due to the large differences in the concentration of water constituents, the depth of the euphotic zone changes from 10 m in the bight water to less than 5 m in the river water.

5. OPTICAL PROPERTIES

The specific optical properties of the water and its dissolved and suspended constituents are basic variables for the development of methods for the determining water constituents by means of satellite data. The main optically active substances in the Baltic are phytoplankton, suspended sediments and yellow substances. In the following selected results concerning the variability of optical properties are presented.

5.1. Absorption of yellow substances

The spectral absorption of filtered samples (yellow substances, a_y) was measured during different cruises in order to investigate the distribution patterns and the exponential dependence on the wavelength. In Fig. 7, the exponent s is related to the absorption of 440 nm. Its value varies between $s = 0.009$ in very turbid and $s = 0.040$ in the clearest water and shows a good correlation to the absorption at 440 nm. At most of the stations absorption coefficients between 0.3 and 0.7 m^{-1} were measured at 440 nm. For this range the value of the exponent s was between 0.010 and 0.017. This confirms the common mean value of 0.014.

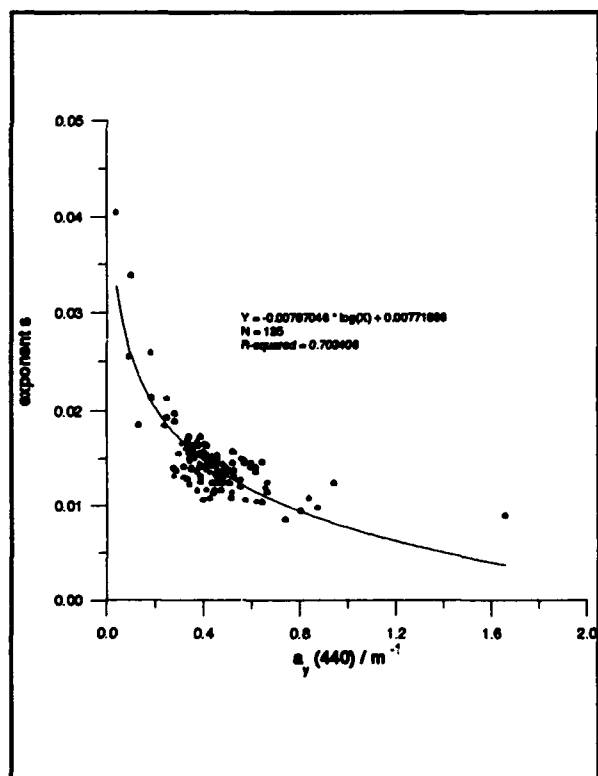


Figure 7: Variation of the exponent s of wavelength dependence of the absorption of yellow substances versus absorption coefficient at 440 nm

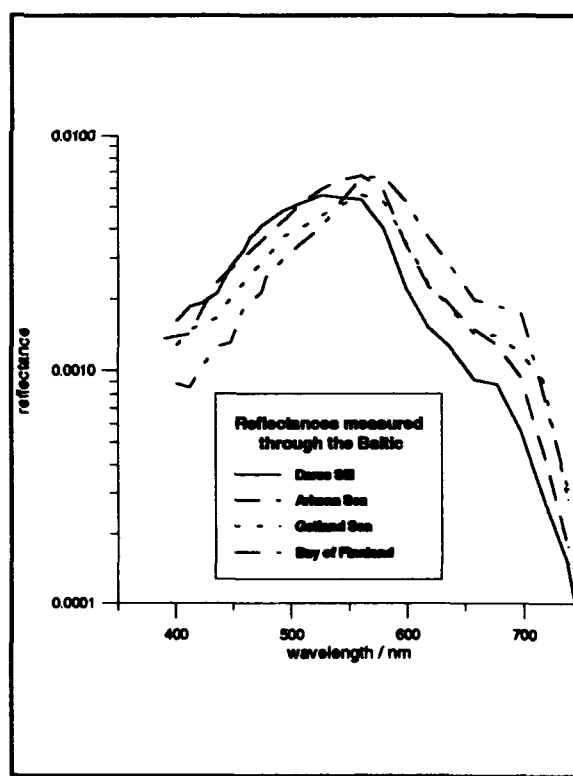


Figure 8: Differences in reflectance from the western Baltic to the Gulf of Finland

The differences in the spectral reflectance due to yellow substances are not restricted to the coastal area. Their concentrations also decrease from north to south. In the northern part of the Baltic, and especially in the Baltic countries, the land is covered by a large number of swampy areas which drain via rivers into the Baltic Sea. Depending on the salinity, yellow substances change to some extent from dissolved into colloidal solution and thus cause this gradient.

The selected reflectances in the western Baltic, Arkona Sea, Gotland Sea and Gulf of Finland shown in Fig.8 illustrate the variation of the slope in the short wavelength range caused by the absorption of yellow substances.

5.2. The backscattering coefficient

The backscattering coefficient is a basic parameter for ocean colour remote sensing problems and radiative transfer computation using two-flow models, but it is difficult to measure directly. Besides the absorption coefficients of sea water and its constituents, it strongly influences the colour of the ocean and is used in different approaches.

Because of the difficulties in measuring the backscattering coefficient, approximations based on simply determined quantities are useful. Mie computations were carried out and compared with measurements from various areas to investigate the relationship between the backscattering coefficient and the scattering intensity S at various scattering angles. The best correlations were found with $S(120^\circ)$.⁹ Fig. 9 shows how the backscattering coefficient varies with the scattering intensity $S(120^\circ)$ for measurements with surface samples from 112 different stations. The measurements were made during the three cruises in the Pomeranian Bight where the suspended matter consists mainly of phytoplankton and its derivative by-products.

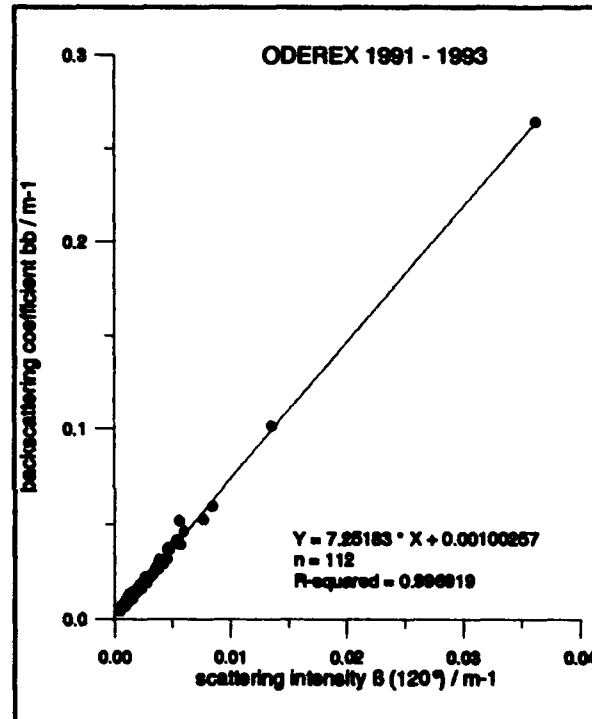


Figure 9: Relationship between the backscattering coefficient and volume scattering intensity $S(120^\circ)$

5.3. Absorption of suspended particles

The absorption of suspended material was measured by the filter method during a cruise in the southern Baltic in 1993. The water samples were filtered through Whatman GF/C glass fibre filters and their absorbance measured against wet filters. For quantitative estimation of the absorption of suspended particles by this method, the measured signal had to be compensated for the amplification caused by the scattering of light within the filter. Consequently, we computed the absorption coefficients for particulate matter, separated the absorption coefficients of phytoplankton and detritus and calculated specific absorption coefficients for the phytoplankton. Selected results are presented in fig. 10.

The highest absorption coefficients for suspended matter were found in water from the river Oder, for detritus and, owing to the high chlorophyll concentrations, for phytoplankton. The specific absorption coefficients (per unit chlorophyll) reflect variations in pigment composition, cell size and intracellular Chla concentrations depending on the dominant algal groups. The samples were distinguished by amount of

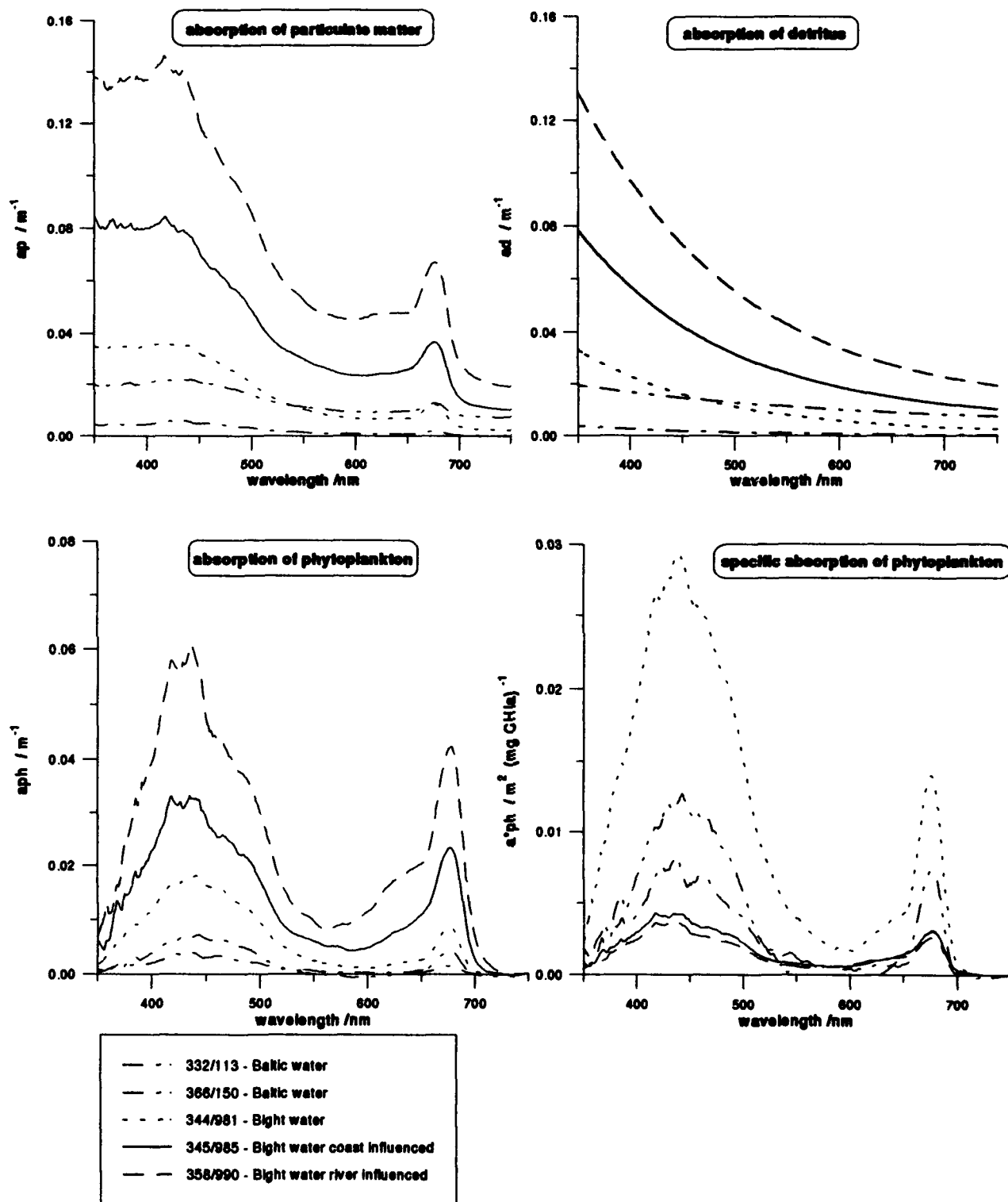


Figure 10 : Absorption coefficient of particulate matter , detritus, phytoplankton and specific absorption coefficient of phytoplankton of different water types

accessory pigments such as carotenoids. At stations with high specific absorption coefficients were observed higher ratios between carotenoids and chlorophyll a, which may explain their more effective light utilization. The highest values measured at stations in the open Baltic were caused by the activity of the young growing phytoplankton.

6. GROUND TRUTH ALGORITHMS

The application of remote sensing data in the visible spectral range to the estimation of biologically relevant quantities such as chlorophyll-a requires relationships between concentration of chlorophyll-a and optical parameters in addition to the corrections for atmospheric and water surface effects. Various methods have been used for this purpose, including empirical colour ratio algorithms and inverse techniques based on specific optical properties.

CZCS data suitable for use in Baltic Sea research have been received from the Ocean Colour European Archive Network (OCEAN) Application Programme of the ESA and EC. Colour ratio algorithms for estimating chlorophyll are included in the standard procedure. Our aim was to adapt this procedure to conditions in the Baltic Sea and to determine additional variables such as yellow substance concentrations and the depth of the euphotic zone. To verify the results of this procedure a comparison to the inverse modelling technique based on specific optical properties¹⁰ was carried out. The investigations were necessary to permit the utilization of future satellite sensors (SeaWiFS, MERIS). The selected algorithms presented in the following all have the general form

$$G = A * X^B \quad (4)$$

where G is a parameter standing for a concentration of chlorophyll, suspended matter, yellow substances, and A and B are constants obtained by regression analysis of measured values. X represents reflectance ratios at two different wavelengths λ_1 and λ_2 . The channels of the satellite sensors CZCS, SeaWiFS, MERIS were chosen as the wavelengths λ_1 and λ_2 in order to identify those channels that are suitable for a variety of different variables and for the area of investigation.

Regression analysis for different regions¹¹ has shown that the optimal wavelength changes. For oceanic case 1 (waters of the upwelling area off NW-Africa) the most suitable wavelengths for chlorophyll algorithms were $\lambda_1 = 440$ nm and $\lambda_2 = 550-520$ nm. In case 2 waters with high concentrations of yellow substances, chlorophyll absorption near 440 nm is strongly influenced by the absorption of yellow substances, and this shifts the optimal channel to longer wavelengths.

In view of the spatial and seasonal variations in the optical properties of the water masses, we did not expect to find a universal chlorophyll algorithm for all regions and seasons.

Ch, Ph, Ch+Ph, Seston, yellow substances and the depth of the euphotic zone were included in the regression analysis, and curvature as well as colour index algorithms were tested. The best correlations were found for the colour ratio algorithms. The optimal wavelengths for CZCS, SeaWiFS and MERIS are summarized in Table 2.

Table 2: Optimal channel- ratios for estimating different variables and sensors

$$Y = a * X^b, \quad X = R(\lambda_1) / R(\lambda_2)$$

(5)

Variable	Sensor	Lambda 1	Lambda 2	R
Ch + Ph	CZCS	520, 550	670	>0.9
	SeaWiFS	510, 550, 490	670	>0.9
	MERIS	520, 565, 445	710, 677	>0.93
C_T	CZCS	443, 520	670	>0.6
	SeaWiFS	443, 412	670	>0.65
	MERIS	565, 445	670	>0.7
1% depth	CZCS	520, 550	670	>0.9
	SeaWiFS	510, 490, 443	670	>0.9
	MERIS	445, 490, 520	710, 665	>0.93
Seston	CZCS	520, 550	670	>0.7
	SeaWiFS	490, 510, 550	670	>0.7
	MERIS	665, 620, 677	710	>0.8

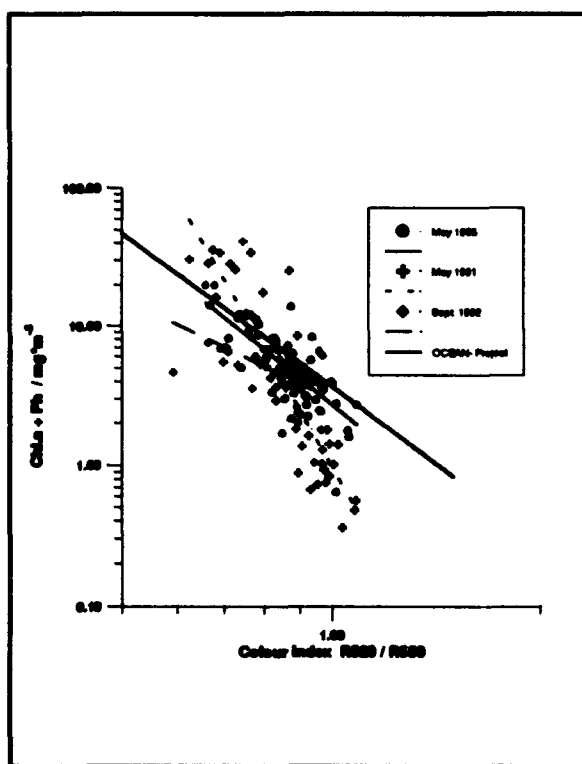


Figure 11: Chlorophyll + Phaeopigment concentration versus colour index $R(520)/R(550)$ for CZCS applications

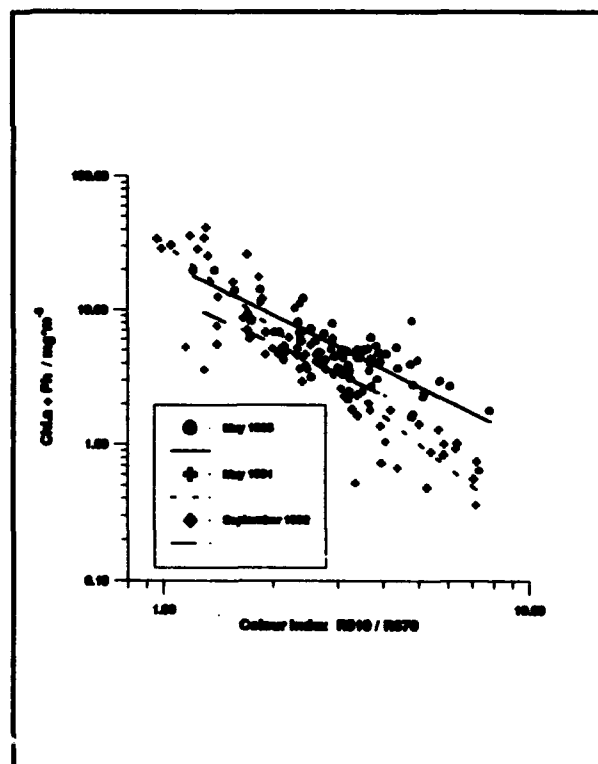


Figure 12: Chlorophyll + Phaeopigment concentration versus colour index $R(510)/R(670)$ for SeaWiFS

The optimal channels for use in the Baltic are to be found at longer wavelengths than those for oceanic waters. When determining chlorophyll from CZCS data by means of the OCEAN procedure, channel 4 is needed for the correction for atmospheric effects. Therefore, the ratio between channels 2 and 3 must be used. The results obtained with these algorithms on three different cruises and the best fits for SeaWiFS channels are shown in Fig. 11 and 12. Table 3 presents selected algorithms for estimating chlorophyll + phaeopigment, yellow substances, the depth of the euphotic zone and suspended matter for CZCS, SeaWiFS and MERIS.

Table 3: Selected algorithms for using CZCS, SeaWiFS and MERIS data in the Baltic Sea.

<u>Chl.a + Ph</u>	RCor	Sigma	A-Parameter	B-Parameter	n	X-Wert
CZCS	-0.926	7.18252	48.17178 ±19%	-2.31542 ±7%	41	520/670
	-0.747	10.96059	1.13478 ±23%	-7.13817 ±14%	41	520/550
SeaWiFS	-0.924	9.20880	31.04893 ±17%	-2.11508 ±7%	40	510/670
MERIS	-0.938	12.17239	46.40576 ±18%	-1.46670 ±6%	39	520/710
<u>Seston</u>						
CZCS	-0.717	1.37586	9.92936 ±7%	-0.36995 ±16%	41	520/670
	-0.580	1.71958	5.45282 ±6%	-1.14333 ±22%	41	520/550
SeaWiFS	-0.734	3.29307	8.22045 ±5%	-0.29065 ±15%	40	490/670
MERIS	-0.823	3.44537	9.89068 ±6%	-0.63301 ±11%	38	665/710
<u>Gelbstoff</u>						
CZCS	-0.640	0.70078	1.98429 ±5%	-0.40314 ±21%	36	443/670
	-0.534	0.77042	1.20477 ±19%	-0.43403 ±27%	36	443/550
SeaWiFS	-0.640	0.70078	1.98429 ±5%	-0.40314 ±21%	36	443/670
MERIS	-0.719	0.64605	9.69194 ±22%	-0.79451 ±15%	42	565/710
	-0.693	0.66383	2.63131 ±4%	-0.37688 ±18%	36	445/710
<u>Euphotic depth</u>						
CZCS	0.942	1.15718	2.06604 ±6%	0.78950 ±6%	40	520/670
	0.791	1.67780	7.55864 ±7%	2.52542 ±13%	40	520/550
SeaWiFS	0.933	5.57770	4.54223 ±6%	0.74062 ±6%	39	510/670
MERIS	0.947	5.83532	7.56812 ±4%	0.41946 ±7%	29	445/710

7. CONCLUSIONS

In the Baltic Sea, concentrations and compositions of water constituents and their optical properties are subject to seasonal and regional variations.

The spectral reflectance of the water is influenced by the backscattering and absorption properties of the water and its constituents and therefore contains information that can be used for remote sensing.

Regional differences in the spectral reflectance of the Baltic are caused by temporal differences in the development of plankton blooms in the various regions, the north - south gradient in the concentration of yellow substances and, in coastal regions, by freshwater input. In river plumes, high concentrations of chlorophyll, suspended matter and yellow substances have a strong impact on inherent optical properties, spectral reflectance and depth of the euphotic zone.

Seasonal variations are caused by plankton blooms in which different plankton groups such as diatoms, cyanobacteria, flagellates and dinoflagellates predominate.

The variability in the composition of the water constituents leads to a variation in specific optical properties. This is taken into account when these specific properties are used to conclude from satellite data to the concentration of water constituents (inverse modelling technique).

The regression analysis for the derivation of algorithms for the determination of chlorophyll and other water constituents from satellite data on the basis of reflectance measurements shows the relationships with the best correlations and the optimal wavelength for CZCS, SeaWiFS and MERIS.

Selected algorithm for the estimating chlorophyll, seston and yellow substance concentrations as well as the depth of the euphotic zone from CZCS, SeaWiFS and MERIS- data are presented. The algorithms are already being used to analyze CZCS data from the OCEAN project.

8. ACKNOWLEDGEMENT

This work was partly sponsored by projects of the Deutsche Forschungsgemeinschaft (DFG) and the Deutsche Agentur für Raumfahrtangelegenheiten (DARA).

9. REFERENCES

1. SIEGEL, H. und U. LEITERER, "Die Wasservariante des Spektralfotometers BAS (BAS-W)". *Feingerätetechnik*, 35, 279-281, 1986
2. BRICAUD, A., and D. STRAMSKI, "Spectral absorption coefficients of living phytoplankton and nonalgal biogenous matter: A comparison between the Peru upwelling area and the Sargasso Sea". *Limnol. Oceanogr.*, 35(3), 562-582, 1990
3. PRANDKE, H., "Konstruktion eines Laborstreulichtphotometers für den Einsatz in der Meeresforschung", *Beitr. Meeresk.*, 43, 109-122, 1980
4. LORENZEN, C.J. and S.W. JEFFREY, "Determination of chlorophyll in seawater", *UNESCO Technical Papers in Marine Science*, 35, 20 p, 1980
5. MOREL, A. and L.PRIEUR, "Analysis of variations in ocean color", *Limnol. Oceanogr.* 22, 709-722, 1977
6. SIEGEL, H., "On the relationship between the spectral reflectance and inherent optical properties of oceanic water", *Beitr. Meeresk.*, 56, 73-80, 1987
7. SIEGEL, H. and H.-J. BROSIN, "Regional differences in the spectral reflectance of seawater", *Beitr. z. Meereskunde*, 55, 71-77, 1986
8. SIEGEL, H., M. GERTH and T. SCHMIDT, "Riverplume in the Pomeranian Bight investigated by satellite and shipborne measurements", 18 Conference of the Baltic Oceanographers, Nov. 1992
9. OISHI, T., "Significant relationship between the backscattering coefficient of sea water and the scatterance at 120°", *Applied Optics*, Vol. 29, No.31, 4658-4665, 1990
10. DOERFFER, R., "Imaging spectroscopy for detection of chlorophyll and suspended matter", 215-257 in Toselli/Bodechtel(Eds.) "Imaging spectroscopy: Fundamentals and Prospective Applications", Kluwer Academic Press, Dordrecht, Netherlands, 1992
11. SIEGEL, H., "Empirical algorithms for the determination of chlorophyll by remote sensing methods" *Beitr. Meereskd.*, 62, 69-78, 1991

SESSION 11

Sea Ice

Polarization Dependent Measurements of Light Scattering in Sea Ice

D. Miller, M. S. Quinby-Hunt and A. J. Hunt

**Energy and Environment Division, Lawrence Berkeley Laboratory
1 Cyclotron Rd., Berkeley, CA 94720**

Abstract

We have developed a bistatic, polarization-modulated nephelometer for making *in situ* measurements of angle- and polarization- dependent light scattering in sea ice. The instrument sits directly and non-invasively on the surface of the sea ice, and can also be used for studying scattering in sea water. A visible laser beam is directed into the medium and the scattered light is detected by the analyzer optics. Both laser and detector angles can be varied. The technique of ac polarimetry is used to accurately obtain phase function and polarization information of the scattered light. This instrument was tested by scattering from monodisperse polystyrene (latex) spheres in the laboratory. Results of Mie calculations are in good qualitative agreement with scattering measured in the laboratory. This instrument was used to measure the angle- and polarization- dependent scattering in sea ice at Pt. Barrow, Alaska, May 1994. Preliminary findings indicate a large polarization signal associated with the orientational ordering of the sea ice crystallites.

1. Introduction

The optical properties of sea ice at visible wavelengths are dominated by scattering. A complete description of the angle- and polarization- dependent scattering properties of sea ice does not exist in the literature, yet is believed to be an essential ingredient of realistic radiative transfer models.^{1, 2} Most radiance calculations in an atmosphere-ocean system have been performed using a scalar theory approach where polarization effects are neglected. This approach is incomplete and, in the presence of significant polarization-dependent scattering, will be in error.^{1, 2}

Nephelometry is the study of light scattering; a scanning polar nephelometer is capable of measuring angle- and polarization- dependent light scattering. The most complete description of the polarization properties of a scattering system is provided by the Mueller matrix

formalism.^{3, 4} The polarization state of any beam of partially polarized radiation can be characterized by a four element Stokes vector. The four-by-four matrix representing the linear transformation of the Stokes vector is referred to as the Mueller matrix. The sixteen elements of the Mueller matrix are each functions of the scattering angle θ and depend on the properties of the scatterer. The polarization properties of light can be determined by using light of known polarization state, or equivalently known Stokes vector, to probe the scattering system. The Stokes vector of the scattered light is analyzed using combinations of polarizers and retarders and is detected with a photomultiplier tube (PMT). By knowing the incident and scattered Stokes vectors one can determine the respective Mueller matrix elements of the unknown scattering system.⁵

Sea ice is a complex, heterogeneous material. Sea water begins to freeze from liquid brine at $T = -1.8^\circ \text{C}$, at which temperature crystals of pure water ice form, increasing the salinity of the remaining brine.⁶ Sea ice contains pockets of pure water ice, brine, and air bubbles which form as the brine drains from the ice lattice under the influence of gravity. The morphology of the sea ice depends not only on initial growth conditions but also on its age, temperature, and gas content. Under certain growth conditions the crystallites, which are optically birefringent, can show considerable alignment.⁶ The optical properties of the sea ice arise from the scattering that occurs at the geometrical discontinuities between the pure ice ($n = 1.31$),⁷ brine ($n \geq 1.34$)⁸ and air pockets ($n = 1.00$). The different types of sea ice have different optical properties.

We have developed a bistatic nephelometer for making *in situ* measurements of angle and polarization dependent light scattering in sea ice. The instrument measures polarization-dependent light-scattering signatures presented by sea ice and its connection to ice morphology. In addition, the results will be used to evaluate the efficacy of polarimetry in optical remote sensing studies of sea ice. Such data can be used to predict radiant transfer in sea ice and to evaluate effects of incident sunlight on climate change and on biological processes under the ice pack. The instrument was designed to measure the Mueller matrix elements which describe the scattering of sunlight from sea ice. The bistatic nephelometer was deployed to Pt. Barrow, Alaska in May 1994 under the auspices of the Office of Naval Research (ONR) sponsored Electromagnetic Properties of Sea Ice (EMPOSI) initiative. This paper describes instrument development, initial verification of the technique using scattering from latex spheres, and preliminary results of the Pt. Barrow measurements.

2. Experimental Approach

2.1 Instrument Description

The bistatic nephelometer is shown schematically in Fig. 1 (a) and in cross section in Fig. 1 (b). The light source is a three stage cw laser with a frequency doubled YAG output at 532 nm (green). The single mode output power is 50 mW. Collimated light from the laser passes through a linear polarizer and photoelastic modulator (PEM). The PEM modulates the polarization state of the laser beam at 50 kHz. The beam is incident on and deflected by two

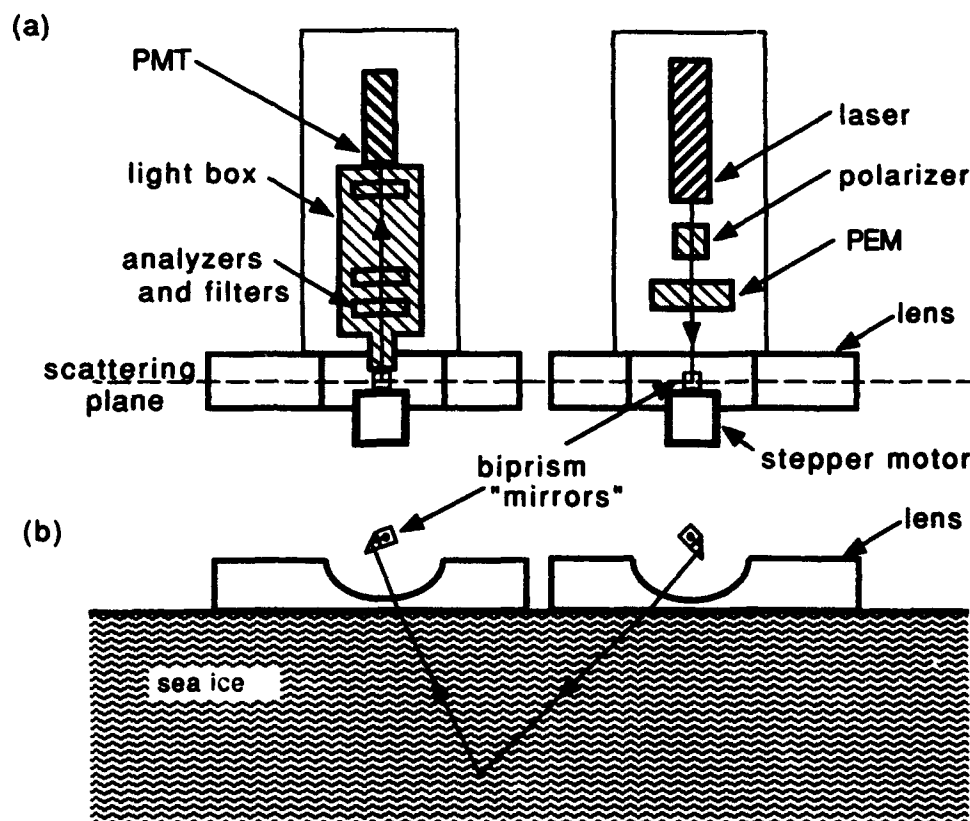


Figure 1. (a) Schematic view of the bistatic nephelometer. The length of the lenses is 50 cm and is determined by the critical angle at the Plexiglas-ice interface. The lenses are slightly asymmetric because of the presence of the biprism "mirrors". (b) Cross section of the instrument in the scattering plane, for arbitrary laser and detector "mirror" angles.

back-to-back right angle prisms, described below, in such a way that the light re-emerges from this biprism "mirror" in the plane defined by the initial beam direction. The dotted line in Fig. 1 (a) lies in the scattering plane. The biprism "mirror" is attached to a stepper motor to vary the angle of the deflected beam. The beam enters a cylindrical plano-concave Plexiglas lens before entering the sea ice, where it propagates and is scattered. The scattered light is collected by a second cylindrical plano-concave Plexiglas lens and then passes through a second biprism "mirror" and analyzing filters before being detected at the PMT. To reduce stray background light the light train is enclosed in a light tight box after the second biprism "mirror". The

measured signal is due to scattered light originating in the common volume between the viewing optics and the sea ice illuminated by the laser. This shared volume is called the scattering volume. Both the angle of the laser and detector biprism "mirrors" can be varied to study various scattering geometries. Fig. 1 (b) is a cross section of the instrument in the scattering plane, for arbitrary laser and detector "mirror" angles. The choice of laser and detector "mirror" angles and spacing determines scattering angle and depth of the scattering volume. A given scattering angle can be obtained for a variety of laser and detector "mirror" angles. In this approach the ice pack is probed by the laser light in the same fashion as the ice pack is probed by sunlight in satellite observations.

It is necessary to use mirrors to deflect the laser and detector beams in order to vary the scattering geometry. The polarization state of the laser light should not be modified at these mirrors because this will lead to spurious signals. Conventional mirrors modify the polarization state of the reflected light as a function of reflected angle. This effect is avoided by using two stacked right-angle prisms in place of a mirror. The prisms are aligned so that they share a common square face, with the remaining two square faces at right angles to each other. Light incident on the first square face undergoes two total internal reflections and exits the second square face at a right angle to the incident beam. Due to the symmetry of the prisms the amplitude of the exiting beam has been multiplied by $(r_{\perp} r_{\parallel})$ where r_{\perp} (r_{\parallel}) is the complex reflection coefficient for polarization perpendicular (parallel) to the plane of incidence. Because the product of the two total internal reflections is commutative, the polarization state of the exiting light is unaltered, apart from an arbitrary phase shift. If the prisms are rotated about the axis defined by the incident beam then the two prisms act as a mirror. This is schematically indicated in Fig. 1 (b).

Introducing the laser beam directly into the sea ice is complicated by surface scattering and by refraction at the air-ice interface. Detecting the scattered light is affected in the same way. The range of angles of light that can be introduced into or detected at the ice-air interface is limited by total internal reflection. By using negative plano-cylindrical lenses made of Plexiglas at the air-ice interfaces ($n_{\text{Plexiglas}} \sim 1.48$ at $0.53 \mu\text{m}$) we can reduce and control these effects. The axis of rotation of the laser and detector "mirrors" lie at the center of curvature of the respective lens surface, with the planar surface of the lens in contact with the ice. In this geometry the effect of total internal reflection of the scattered light is avoided. The length of the lenses is determined by the critical angle at the Plexiglas-ice interface. The lenses are slightly asymmetric because of the presence of the biprism "mirrors". In practice, a shallow trench was dug into the ice and filled with water. The lens was frozen into place. This significantly reduced surface scattering and acted like an artificial melt pond. Because the focal length of the interface lenses is negative, the incident and scattered beams would be defocused. A positive focal length lens elsewhere in the wave-train compensates for this effect. The detector optics have a 2.4° half-width field of view in the scattering plane.

The PEM produces polarization-modulated light at 50 and 100 kHz. The signal incident on the PMT is detected synchronously with a lock-in amplifier. The dc component of the scattered light is measured separately. By choosing the proper combination of (1) initial linear polarizer orientation and PEM position, (2) final polarizing filter and (3) first or second harmonic

of the PEM or dc detection, measurements can be made which will allow determination of all 16 components of the Mueller matrix.

For all ac measurements it is desirable to operate the detection system in such a way that the dc signal from the PMT is held constant as the angular scan proceeds. As shown below, this enables direct measurement of normalized Mueller matrices. The PMT output signal is $S_{dc}(V) = I_{dc}g(V)$, $S_{ac}(V) = I_{ac}g(V)$, where I is the dc or ac light intensity, respectively, incident at the PMT (Watts), $g(V)$ is the PMT gain (Volts/Watt), and V is the PMT supply voltage. As the scattering angle θ varies, V is continuously adjusted so that $S_{dc}(V) = S_0$, a constant. Under these conditions $S_{ac}(V) = S_0(I_{ac} / I_{dc})$. Therefore, by adjusting V so that the dc signal from the PMT remains at a constant level, the ac signal is automatically normalized.

There are several advantage of this automatic normalization procedure. First, changes in scattering volume, or in distance of scattering volume to the detector, which occur as a function of θ are corrected for automatically. Second, changes in the intensity of the laser will not affect the measured ac signal. Third, since $S_0 = I_{dc}g(V)$ is kept constant, then by knowing $g(V)$ we can determine I_{dc} . Therefore, in the ac detection scheme where V is dynamically adjusted, both the dc and the ac component of the Mueller matrix are determined simultaneously. Scattering matrix elements that can only be measured using the dc detection procedure where V is not dynamically adjusted must still be corrected for changes in the scattering volume. The scattering volume depends on the distance and angle to the detector as well as on the beam spread function,⁹ which is a measure of the divergence of the beam.

The detector optics collects light scattered within the ice. Scattered sunlight contributes an unwanted component to the detected dc signal which can lead to significant errors in the automatic normalization procedure described above. The effect of the background sunlight can be compensated for as follows: The PMT output signal is $S_{dc}(V) = (I_{sun} + I_{dc})g(V)$. This is the same equation as before but now modified by the presence of the background light intensity due to the sun, I_{sun} . We can measure the dc PMT signal as a function of V and the detector angle with the laser turned off. This is equivalent to measuring the quantity $I_{sung}(V)$. With the laser turned on the measured signal is $(I_{sun} + I_{dc})g(V)$. If the PMT voltage V is adjusted so that $[(I_{sun} + I_{dc})g(V)]_{measured} - [I_{sung}(V)]_{measured} = S_0$, a constant then the effects of the scattered sunlight are removed from the detection scheme. Because $I_{sung}(V)$ varies with V , the above equation must be solved iteratively. The 'feedback' system described here is implemented with a computer. Note that if $I_{sun} \gg I_{dc}$ then the accuracy of the subtraction is reduced and our technique is compromised. In the field experiment I_{sun} was minimized by shielding the detection optics from direct sunlight and by laying absorbing black polyethylene directly on the sea ice for a radius of approximately 6 meters surrounding our measurement. This technique sufficiently reduced the ambient light so that $I_{sun} \ll I_{dc}$ and the correction technique was able to compensate for the remaining background. Operating without ambient light was not possible during the time of year of the Pt. Barrow experiment.

2.2 Instrument Discussion

In a conventional nephelometer,^{5, 10, 11} a stationary sample is illuminated by a laser and the scattered light is detected by a PMT which rotates around the sample. Light scattered as a function of scattering angle θ originates within the finite sample volume. The distance between the scattering volume and the detector is fixed. The scattering volume varies as $\sin(\theta)$. In the bistatic nephelometer, the half-space of the undisturbed ice pack acts as the sample. Light scattered as a function of θ may originate at different locations in the ice, depending on the choice of laser and detector "mirror" angles and spacing. The distance between the scattering volume and the detector depends on the scanning strategy used. The scattering volume depends on the scanning strategy used as well as on the beam spread function.

Because both the laser and detector angles can be varied, there are many scanning strategies that can be used. The most simple case is to scan either the laser or detector "mirror" angle while leaving the other fixed (fixed-detector or fixed-laser scan). An advantage of this scanning strategy is that, in the absence of multiple scattering, the scattering volume changes simply with θ . Another scanning strategy is to adjust the laser and detector "mirror" angles so that the optical path length traversed by the light within the ice is kept constant (constant chord scan). The locus of scattering volumes then follows a pseudo-elliptical trajectory. The trajectory is not precisely elliptical since the foci change with changing "mirror" angles. An advantage of this scanning strategy is that the total optical path length traversed by the light is independent of θ . In this scanning strategy the minimum θ occurs when the scattering volume is located directly in between the laser and detector "mirrors." Scanning on either side of this position will be symmetric in θ .

A problem associated with the Plexiglas-ice interface is that light which is obliquely incident to this interface will be depolarized, that is, $(T_r - T_l)/(T_r + T_l)$ deviates from zero. T is the transmissivity corresponding to the polarization perpendicular (r) or parallel (l) to the plane of incidence. This deviation from zero may mimic an S_{12} or an S_{13} signal at some angles.

The bistatic nephelometer measures the first row of the Mueller matrix elements (S_{11} , S_{12} , S_{13} and S_{14}). S_{11} , also called the phase function, describes the total scattered light intensity. S_{12} and S_{13} describe the conversion between linearly-polarized light and unpolarized light in a coordinate system either defined by the scattering plane (S_{12}) or at 45° to the scattering plane (S_{13}). A non-vanishing S_{13} indicates orientation in the scattering system. S_{14} describes the conversion between circularly-polarized light and unpolarized light. There are two reasons for limiting our study to these elements: (A) The first column of the Mueller matrix of sea ice (S_{11} , S_{21} , S_{31} and S_{41}) describes the process of scattering unpolarized sunlight from sea ice and is therefore of interest. It is difficult to directly measure the first column using the ac detection technique. Because of the symmetry of the Mueller matrix, measuring the first column is essentially equivalent to measuring the first row. (B) The presence of stress-induced birefringence in the Plexiglas lenses will tend to modify the phase angle of the scattered radiation. However, the first row (or column) of Mueller matrix elements depend on the conversion between polarized and unpolarized light but not on the phase angle of the scattered light, and so will not be affected by the Plexiglas lenses.

2.3 Measurements on Latex spheres

The bistatic nephelometer was tested by scattering from latex spheres in the laboratory. Previous measurements of scattering from latex spheres using a conventional nephelometer^{5, 10, 11} showed good agreement with Mie calculations.¹² A large trough (12 cm W × 50 cm D × 125 cm L) was used to hold a suspension of 0.482 μm latex spheres in a 1 mmolar solution of NaCl to prevent flocculation.¹³ The walls of the trough were painted black to reduce stray scattered light. Scattering from the walls is difficult to eliminate, but by operating the nephelometer so that the laser angle is fixed and scanning the detector, a large range of scattering angles can be studied without changing the distribution of scattered light. The measured phase function S_{11} is shown in Fig. 2 (a) and the measured S_{12}/S_{11} is shown in Fig. 2 (b) versus scattering angle θ (solid lines). Also shown are Mie calculations at a wavelength of 532 nm assuming a suspension of spheres with diameter of 0.482 μm (dotted lines), and a narrow gaussian distribution of spheres with a mean diameter of 0.482 μm diameter (dashed lines). The calculated curves for S_{11} (a) have been divided by $\sin(\theta)$ to correct for scattering volume.

There is generally good agreement between the measured S_{11} and the zero-free-parameter model calculation for S_{11} . The agreement between the measured and calculated S_{12}/S_{11} is less good, however the overall features reproduce qualitatively. In particular, the peaks seen in the measured quantity are shifted down in scattering angle by approximately 15 degrees from the calculated quantity. The agreement is especially poor in the forward scattering region, where the measured S_{12}/S_{11} crosses zero. We have not ruled out the possibility of systematic errors in this measurement, especially from the possibility of stray scattered light and are continuing our investigation of the instrument. In addition, the character of the trough and the large amount of water used precluded the use of very particle free water, so significant Rayleigh and contaminant scattering was present. The addition of latex spheres increased the scattering at $\sim 90^\circ$ by a factor of five above the background.

2.4 Sites Studied at Pt. Barrow, Alaska

Two sites were chosen for the study of the sea ice. The first site (I) was to the West of Point Barrow (in the Chukchi Sea); the second site (II), to the East of Point Barrow (in the Beaufort Sea). Both sites consisted of shore fast ice approximately 1.2 m (1.5 m) thick at Site I (II), with an ocean depth of 7 m. The ice at Site I was roughly three months old; the ice at Site II was slightly older. From the point the shore runs NE to SW (NW to SE) at Site I (II). Both sites consisted of congelation ice for the top ~ 10 cm below which the sea ice was highly aligned, with the c axis parallel to the shore. Sea ice forms platelet type crystallites, whose c axis is perpendicular to the platelets. The platelets will often align due to the presence of currents, whose direction is defined by the shoreline. In all of our measurements the bistatic

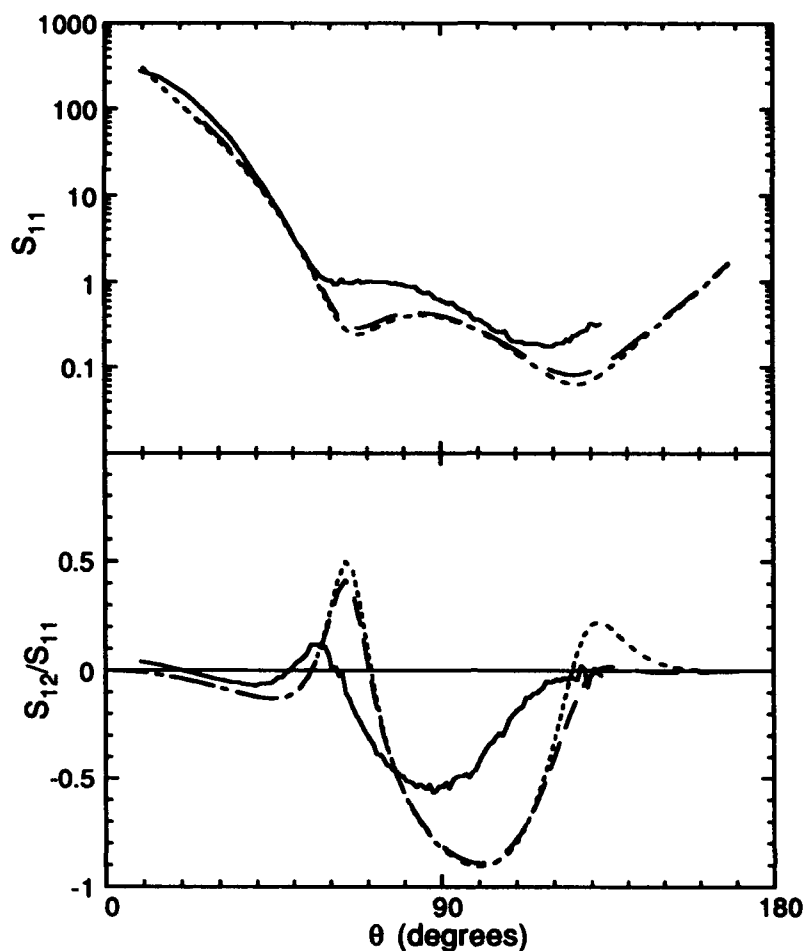


Figure 2. (a) The phase function $\text{Log}[S_{11}]$ and (b) S_{12}/S_{11} versus scattering angle θ for 0.482 μm diameter latex spheres measured in the laboratory (solid lines). Mie calculations assuming a light wavelength of 532 nm and 0.482 μm diameter spheres (dotted lines) and a narrow Gaussian distribution of sphere sizes with mean diameter of 0.482 μm (dashed lines). The calculated curves for S_{11} (a) have been divided by $\sin(\theta)$ to correct for changes in scattering volume.

nephelometer was aligned either with the scattering plane parallel or perpendicular to the platelets.

3. Experimental Results

Figure 3 represents some preliminary results of our measurements at Pt. Barrow. The quantity S_{13}/S_{11} for sea ice is plotted in Fig. 3 versus θ at Site II for scans where (a) the detector

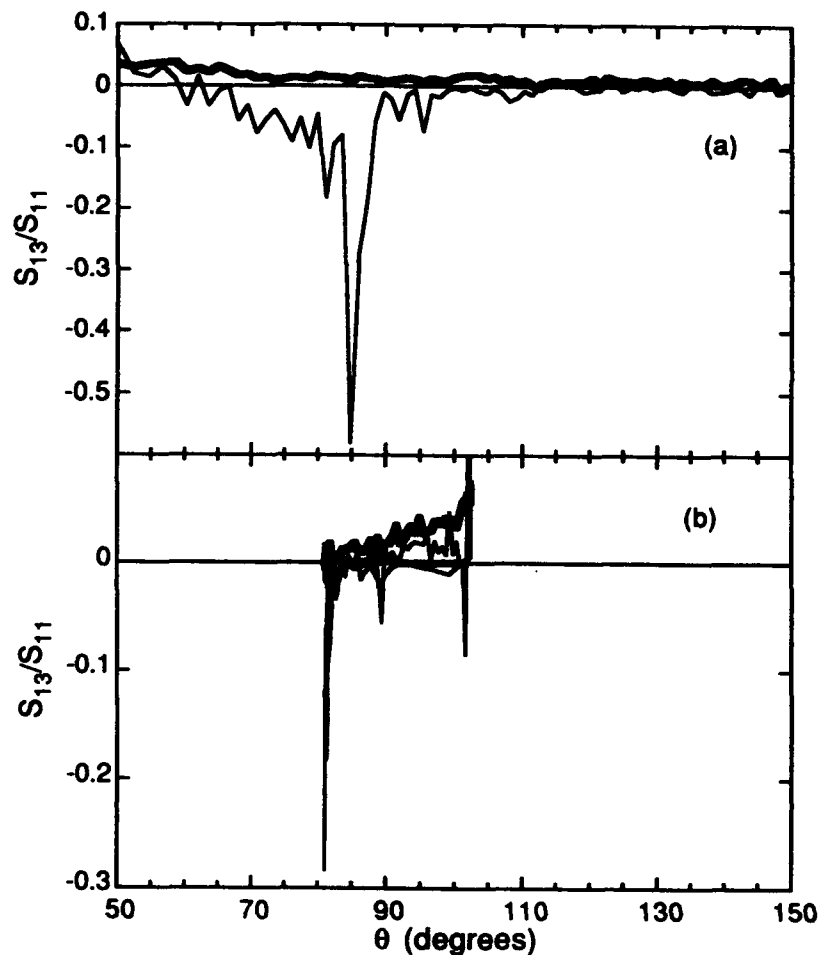


Figure 3. S_{13}/S_{11} of sea ice versus scattering angle θ for scans of the bistatic nephelometer where (a) the detector is held fixed and the laser is moved (fixed detector scan) and (b) the optical path length traversed by the light is held constant (constant chord scan). The thin (thick) lines correspond to scans where the scattering plane is parallel (perpendicular) to the ice platelets.

is held fixed and the laser is moved (fixed detector scan) and (b) the optical path length traversed by the light is held constant (constant chord scan). The thin (thick) lines correspond to scans where the scattering plane is parallel (perpendicular) to the ice platelets. In Fig. 3 (a) there is a large feature at $\theta \sim 85^\circ$ for the parallel scan. The scan in the perpendicular orientation is featureless. In Fig. 3 (b) there is also a large reproducible feature near $\theta \sim 80^\circ$ for the parallel scan. The scan in the perpendicular orientation in Fig. 3 (b) shows little structure near $\theta \sim 80^\circ$ and increases with increasing θ for one half of the scan, showing little symmetry in the other half of the scan.

4. Discussion

When the nephelometer scattering plane is perpendicular to the platelets light passes through and is scattered by the platelets while when the scattering plane is parallel to the platelets light can pass through channels in between the platelets. Therefore we expect less scattering and therefore less depolarization when the scattering plane is parallel to the platelets. This is consistent with our observations, where the feature observed in S_{13}/S_{11} is present only when the scattering plane is parallel to the platelets. The peak occurs both for the fixed detector and for the constant chord scans at approximately the same value of θ . The Mueller matrix S_{13} has been associated with orientation within the scattering system. The feature we observe at $\theta \sim 80^\circ$ may arise from the ordering of the ice platelets in the sea ice.

The asymmetry in the constant chord scans may result from inhomogeneities in the sea ice. Recall that in the constant chord scan the two values of S_{13}/S_{11} for a given scattering angle θ correspond to scattering volumes at different locations in the ice. The upturn in S_{13}/S_{11} in Fig. 3 (b) occurs for light obliquely incident to the Plexiglas-ice interface and may systematically result from the change in transmissivity at the Plexiglas-ice interface as discussed in Section 2.2.

5. Conclusions

We have developed a novel bistatic nephelometer for making *in situ* measurements of the angle- and polarization- dependent scattering in sea ice. Scattering measured using this instrument agrees with that calculated for latex spheres. This instrument was used in Pt. Barrow, Alaska in May 1994 to measure scattering in sea ice. The sea ice crystallites at the sites studied were highly aligned. Preliminary results of these measurements show a large ($>30\%$) signal in S_{13}/S_{11} occurring near a scattering angle of $\theta \sim 80^\circ$ when the scattering plane was parallel to the ice platelets. This feature occurs at both sites studied (Sites I and II) and was not present when the scattering plane was perpendicular to the ice platelets. Our observations are consistent with the expectation that light will be scattered more and hence be more highly depolarized when the scattering plane is perpendicular to the ice platelets. A non-vanishing S_{13}/S_{11} is consistent with the presence of orientation in the sea ice. Measurements of the phase function S_{11} (total intensity), S_{12} and S_{14} show repeatable signals. However, further analysis is necessary to rule out the possibility of systematic error.

The presence of a non-vanishing Mueller matrix in sea ice has significant implications for radiative transfer modeling, as ignoring polarization-dependent scattering has been shown to cause significant errors.^{1, 2} Additionally, the presence of a large signature in S_{13}/S_{11} could potentially facilitate remote observations of the orientation of sea ice.

6. Acknowledgments

We gratefully acknowledge support from the Office of Naval Research (ONR), especially from R. W. Spinrad, G. D. Gilbert and S. G. Ackleson. We would also like to give special thanks to P. C. Stevens for helping in the design, building and logistical support and to D. B. Shapiro for helpful discussions. This work was supported by the Office of Naval Research under grant No. DE-AC-03-76SF00098 through the U. S. Department of Energy under contract No. N00014-92-J-1284 (AJH).

7. References

1. C. N. Adams and G. W. Kattawar, "Effect of volume-scattering function on the errors induced when polarization is neglected in radiance calculations in an atmosphere-ocean system," *Appl. Optics* **32**, 4610 - 4617 (1993)
2. G. W. Kattawar and C. N. Adams, "Errors in radiance calculations induced by using scalar rather than Stokes vector theory in a realistic atmosphere-ocean system," *SPIE Ocean Optics X 1302*, 2 - 12 (1990)
3. D. S. Kliger, J. W. Lewis and C. E. Randall, *"Polarized Light in Optics and Spectroscopy,"* (Academic, New York, 1990)
4. C. F. Bohren and D. R. Huffman, *"Absorption and Scattering of Light,"* (John Wiley, New York, 1983)
5. A. J. Hunt and D. R. Huffman, "A new polarization-modulated light scattering instrument," *Rev. Sci. Instrum.* **44**, 1753 - 1762 (1973)
6. W. F. Weeks and S. F. Ackley, "The growth, structure, and properties of sea ice," in *The Geophysics of Sea Ice*, N. Untersteiner, Ed. (Plenum, New York, 1986)
7. J. A. Richter-Menge and D. K. Perovich, "An overview of sea ice physical properties and their variability," *SPIE Ocean Optics XI 1750*, 486 - 497 (1992)
8. H. V. Sverdrup, M. W. Johnson and R. H. Fleming, *"The Oceans: Their physics, chemistry and general biology,"* (Prentice-Hall, Englewood Cliffs, NJ, 1942)
9. G. D. Gilbert and J. Schoonmaker, "Measurements of beam spread in new sea ice," *SPIE Ocean Optics X 1302*, 545 - 555 (1990)
10. K. J. Voss and E. S. Fry, "Measurement of the Mueller matrix for ocean waters," *Appl. Optics* **23**, 4427 - 4439 (1984)
11. K. J. Voss and E. S. Fry, "Measurement of the Mueller matrix for phytoplankton," *Limnol. Oceanogr.* **30**, 1322 - 1326 (1985)
12. M. S. Q. Hunt, A. J. Hunt, K. Lofftus and D. B. Shapiro, "Polarized-light scattering studies of marine *chlorella*," *Limnol. Oceanogr.* **34**, 1587-1600 (1989)
13. *The latex spheres come from Ted Pella Inc., P.O. Box 510, Tustin, CA 92680*

FLUOROMETRIC CHARACTERIZATION OF DISSOLVED AND PARTICULATE MATTER IN ARCTIC SEA ICE.

R.Iturriaga*, Naval Research Laboratory, Stennis Space Center, CODE
7240, MS 39529-5004.

Collin S.Roesler+, College of Oceanic and Atmospheric Sciences, Oregon
State University, Oregon 97331-550.

ABSTRACT

Fluorescence spectroscopy has been used to characterize and assess the vertical distribution of dissolved (DOM) and particulate matter (POM) entrapped in sea ice. Fluorescence excitation-emission of bulk particulates, performed on first-year ice and multi-year flow ice, indicated that microalgae present in different layers of the first year ice resembled typical water column phytoplankton spectra, where those in the multi-year ice samples resembled detrital spectra. Fluorescence analysis also indicated that DOM present in sea ice can be characterized by their excitation-emission in unconcentrated samples. Maximal values for DOM fluorescence were observed at shorter excitation wavelengths (250nm-300nm), with an emission centered between 390-425nm.

1. INTRODUCTION

Recent investigations have indicated that particulate matter present in sea ice can significantly affect the optical variability and light field within the ice, as well as the underlying water column^{1,2,3,4,5,6}. It has also been reported that algal growth in sea ice is highly dependent upon the *in situ* light field⁷. However, the contribution of dissolved organic matter upon optical properties of sea ice is virtually unknown. A recent investigation of optical properties of blue and green icebergs in Antarctic waters revealed that the observed shifts in the spectral absorption were a consequence of DOM (Gelbstoff), in concentrations capable of altering their reflectance properties of the icebergs⁸.

Present Address: *Department of Biological Sciences, University of
Southern California, Los Angeles, CA 90089-0371.

+Department of Marine Sciences, University of
Connecticut, Groton, CT 06340-60997.

The study of particulate and dissolved organic matter in the ocean, and other aquatic environments has been largely facilitated by the introduction of fluorometric analysis. This technique has been used to characterize phytoplankton groups using the spectral signatures of their pigments^{9,10,11,12}.

Furthermore, during the last decade, high-sensitivity and spectral resolution spectrofluorometers have permitted the identification of the bulk part of dissolved organic substances in marine and freshwater environments by direct analysis^{13,14,15,16}. New information suggests that dissolved fluorescing matter in the ocean can be associated with two major groups of organic compounds, one that is related to an aromatic amino acids-protein type of fluorescence, and one that is a more refractive type of organic compounds related to humic-acids¹⁷.

The need to understand and improve our knowledge in terms of the composition of dissolved and particulate organic matter present in sea ice, which can strongly affect the transfer of energy through the ice layer, has largely motivated this study. Results of preliminary investigations attempting to characterize the bulk part of dissolved and particulate matter entrapped in sea ice by fluorescence spectroscopy are reported.

2. METHODS

Samples were collected from different types of ice in the vicinity of Point Barrow, Alaska, during mid May, 1993. First-year and multi-year ice samples were collected from the Elson Lagoon and from the seaward side of Point Barrow (Chukchi Sea). Ice cores were collected with a stainless steel ice coring system provided by the Polar Ice Coring Office (Fairbanks). Ice cores were cut into 20-30cm length sections and placed into polyethylene bags and kept sealed. Extra precautions were taken with the handling of the cores to avoid contamination of the ice samples with organic substances or exposure to direct sunlight. Once at the laboratory, samples were slowly melted and processed for further analysis. No significant effect of the plastic bags on fluorescence measurements was found in preliminary tests.

2.1. Fluorescence properties of POM: Samples were processed as described by Bower and Iturriaga (1992)¹⁸. Depending on particle concentration, a volume of 30 to 50ml was concentrated onto an Anopore 0.2um pore size filter under low vacuum pressure. The filter was then placed face-up over a gelatin-coated microscope slide. After placing one or two drops (approx. 50ul) of a gelatin solution over the filter, this was covered with a microscope coverslip. The slides were kept frozen (-20 °C) until analysis at the laboratory.

Fluorescence excitation and emission spectra of the particulates

concentrated on the filters were performed by front-face illumination. An Anopore filter mounted in the same fashion was used as a Blank. Fluorescence spectra were determined on a SPEX Industries (New Jersey, USA) Fluorolog 2, Model F1-112 fluorometer. A double monochromator on the emission side, reduces stray light contamination to a minimum. A 450W Xenon (Ozone producing) lamp, and a water cooled PMT provided sufficient excitation energy within the UV region, as well as the sensitivity required for the measurements.

2.2. Fluorescence properties of DOM: Small volumes (approx. 10ml) were filtered through pre-combusted glass fiber filters (Whatman G/FF), placed in pre-cleaned vials (Teflon lined caps), and kept frozen until fluorometric analysis. Small aliquots of the sample were used to rinse the filtration device and vials to minimize the effect of contaminants. Fluorescence emission scans were performed at following excitations: 200nm, 250nm, 300nm, 350nm, 400nm, and 450nm. Data were collected every 2 nanometers with an integration time of 0.5 seconds. A blank consisting of distilled water (Quartz distilled daily) was subtracted from the samples to correct for water Raman scattering. The Raman scattering peak, measured in each sample at the respective excitation, was then used to normalize the corresponding emission spectra.

3. RESULTS AND DISCUSSION

3.1. Fluorescence properties of in-ice bulk particulate matter.

Front-face fluorescence excitation (Emission: 683nm) performed on bulk particulates, suggest that microalgae entrapped throughout the different layers of first-year ice resembled typical spectra commonly observed in healthy phytoplankton cells. At the Elson Lagoon, higher values were found at the bottom of the core (total length of this ice core was 95cm from top to bottom). At the seaward side of Point Barrow (Chukchi Sea), higher values also corresponded to the deeper part of the core (total length of this core was 140cm). Similar spectra were observed by microphotometric analysis in individual cells³⁰, indicating that most micro algae present in first-year ice were well preserved not only in shape, but also in optical properties as well (Fig.1). In multi-year ice no algal photosynthetic pigments or degradation products were detectable in any sections of the core.

Fluorescence emission, as a function of different excitation wavelengths, suggested that detrital matter constituted the main component of the particulates present in the ice samples. For an excitation at 370nm, distinctive emission maxima were observed between 400-425nm and 450-500nm regions of the spectrum. At this excitation, and at 430nm (chlorophyll maximum absorption), only a small

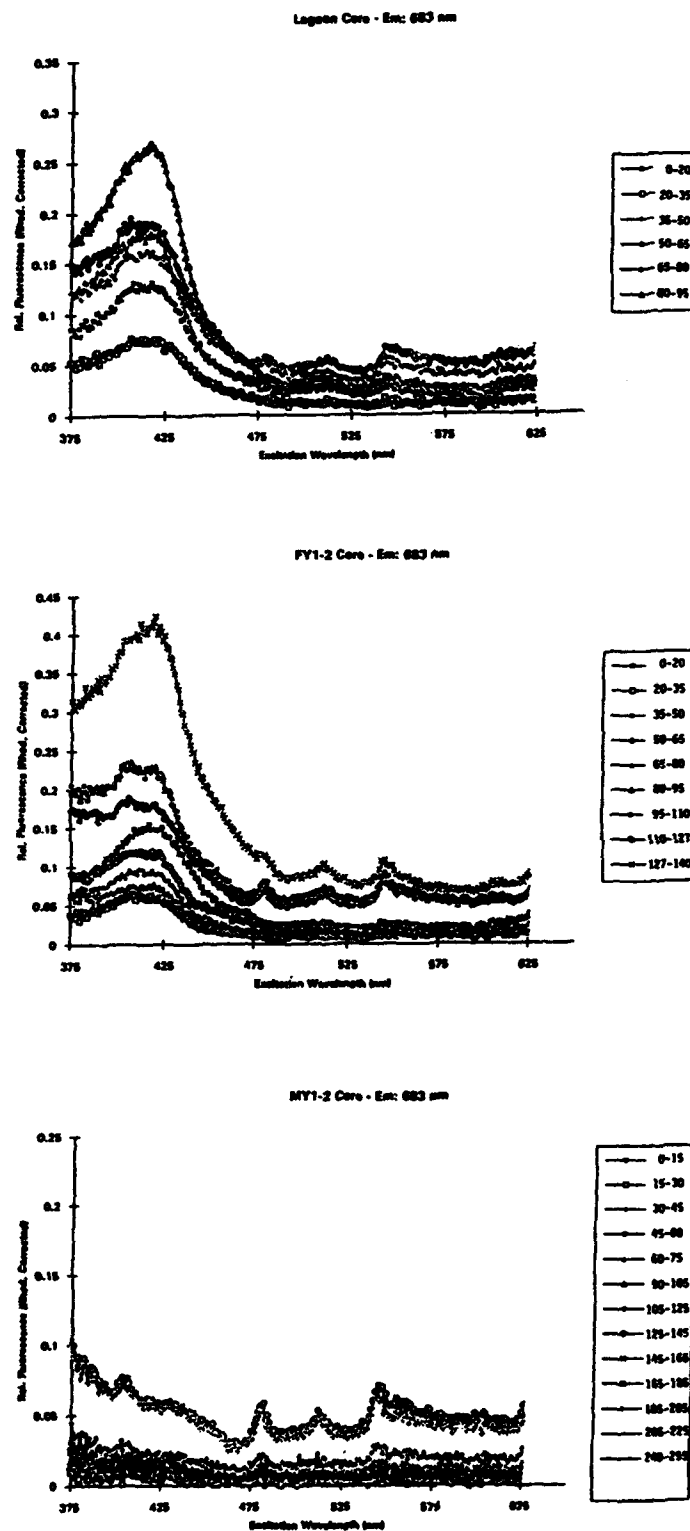


Figure 1. Fluorescence excitation spectra (Em 683nm) of particulate matter in first-year ice; Elson Lagoon (top), Chukchi Sea (middle), and multi-year ice (bottom).

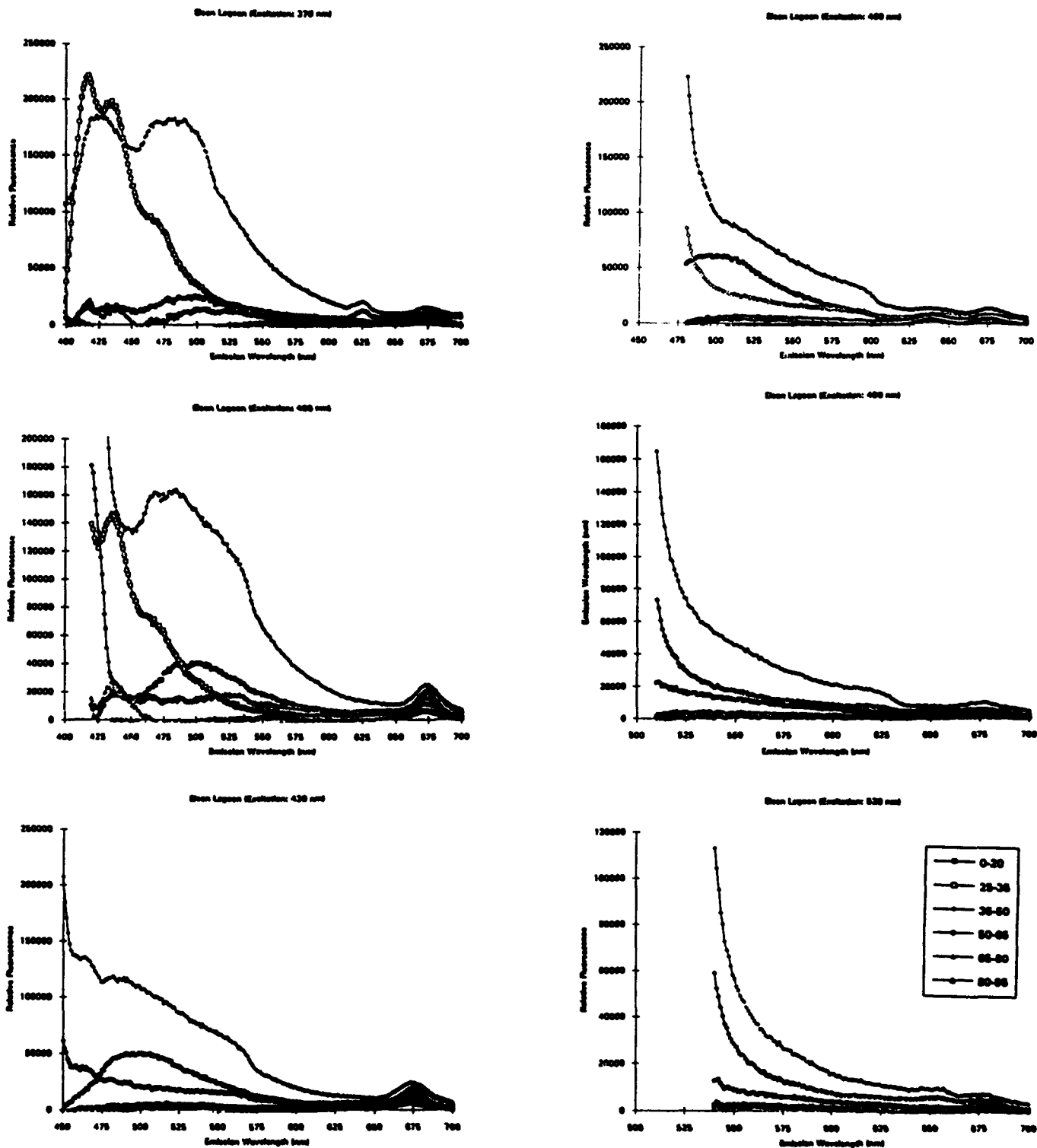


Figure 2. Fluorescence emission of particulate matter of first-year ice (Elson Lagoon), as a function of different excitation wavelengths.

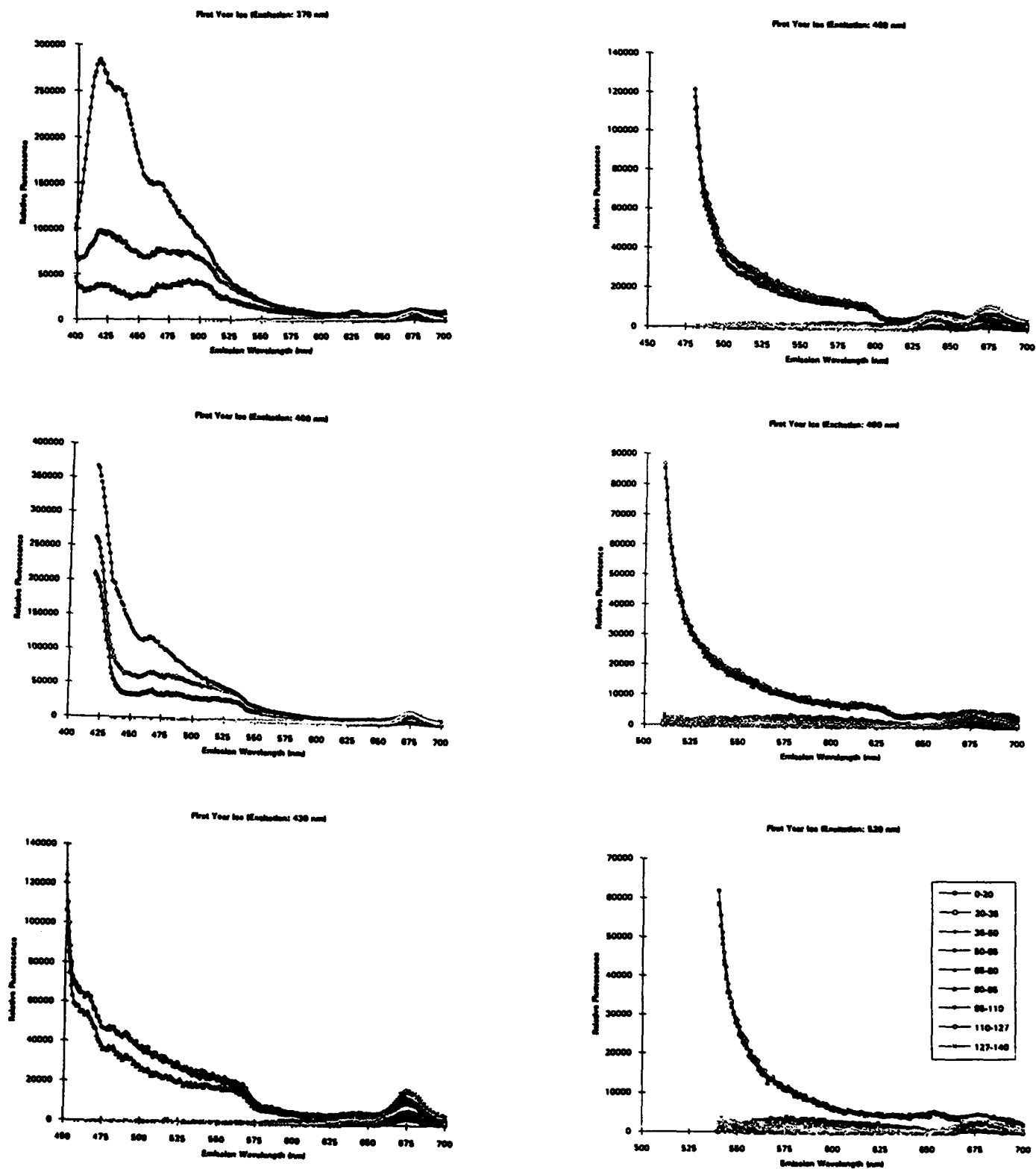


Figure 3. Fluorescence emission of particulate first-year ice (Chukchi Sea), as a function of different excitation wavelengths.

fraction of the spectral emission can be attributed to chlorophyll (emission maxima between 675-680nm when excited between 400-430nm). Spectral emission with such properties was only observed in the first-year ice samples (Figs.2,3). Multi-year ice emission values were low in comparison to the first-year samples, and all spectra resembled detrital matter. Similar detrital fluorescence emission spectra (maximal values centered between 400-420 and 450-500nm, for a 370nm excitation), has been observed by microphotometry in individual marine detrital particulates¹⁹.

3.2. Fluorescence properties of in-ice dissolved organic matter.

Fluorescence has long been used for the characterization of dissolved organic matter in sea water. This technique was first reported by Kalle (1937, 1949)^{20,21}, who measured the fluorescence intensity for a fixed excitation and emission wavelength. Similar determinations were performed by several other investigators^{22,23,24}. A more recent approach has been to measure whole fluorescence emission as a function of different excitations. Such a measurement has been possible due to the high sensitivity and spectral resolution of commercial spectrofluorometers developed during the last decade^{25,26,27}.

Analyses of different types of sea water samples using excitation-emission spectroscopy have indicated that it is possible to discriminate the nature and sources of dissolved organic matter by fluorescence analysis^{13,14,15,16,17,25,26}. Such studies suggest that in the ocean two distinctive organic compounds can be discriminated by their fluorescence properties. One type is related to amino acid-protein fluorescence, as a product of recent biological activity. This type has an emission maxima between 300-350nm, when excitation is set between 220-275nm. The other type of compound has been associated with humic substances with an emission maxima between 420-450nm, for an excitation between 320-350nm^{15,16,17}.

The characterization of DOM present in the ice was determined by recording the fluorescence emission as a function of the following excitations: 200nm, 250nm, 300nm, 350nm, 400nm, and 450nm. Measurements were performed in different sections of the multi-year ice core from 30cm depth to 255cm, in an ice column of 600cm total length. Concentrations of dissolved fluorescing substances were very low in most of the core sections analyzed. However, relatively higher values were found in the 240-255cm depth section, indicating that either an accumulation of dissolved products may have occurred, or an ice layer of different origin may have been encountered at that depth. Discontinuity between ice layers is characteristic of multi-year ice. Maximal fluorescence emission values were found between 400nm-450nm, for an excitation at 250nm. Lower emission values were observed at longer excitations wavelengths (Fig.4).

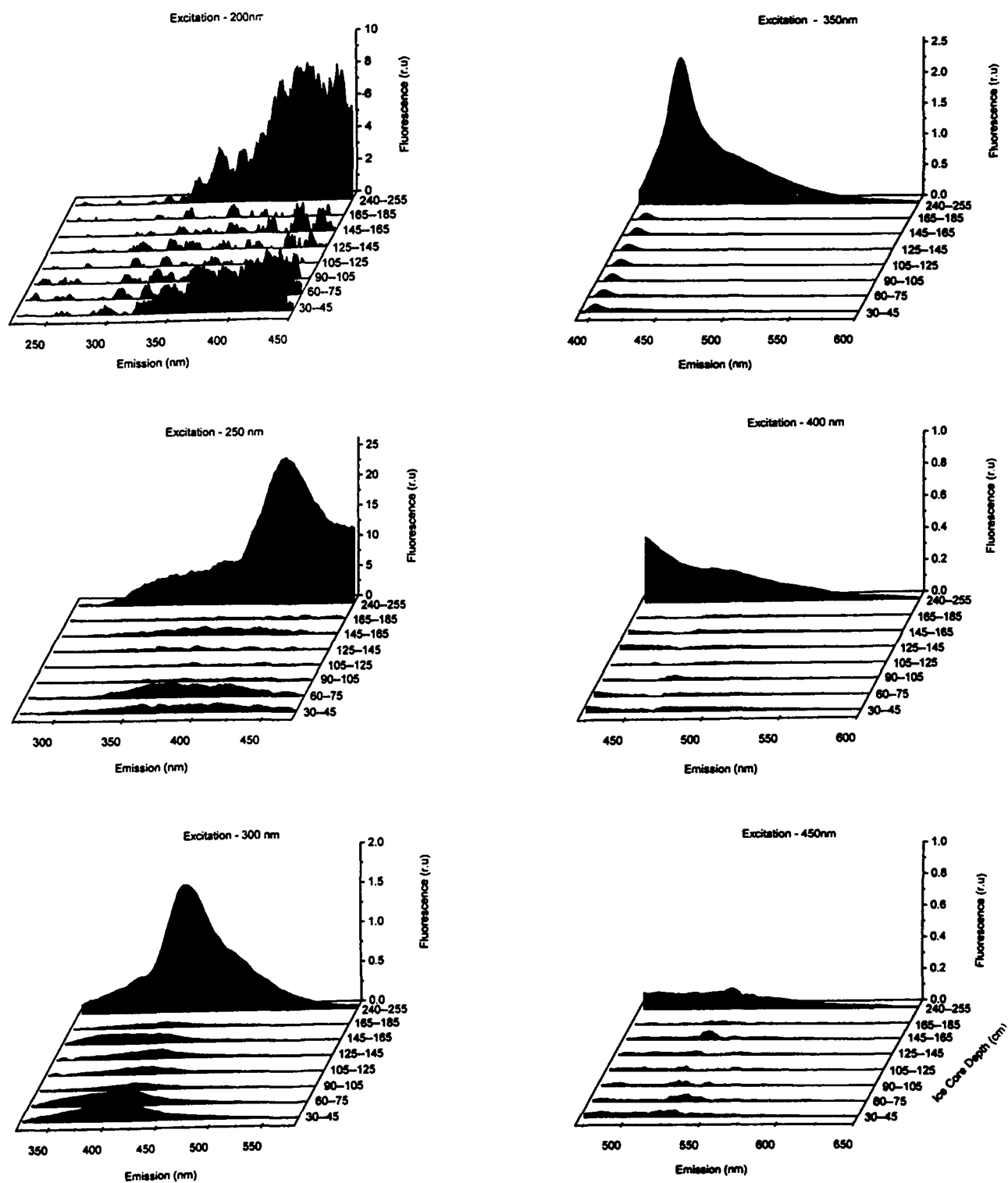


Figure 4. Fluorescence emission of DOM (multi-year ice), as a function of different excitation wavelengths.

Emission spectra (excitation: 250nm) were used to determine differences in concentration and type of DOM between the multi-year ice sections, the Elson Lagoon bottom core, and a Chukchi sea water sample (Fig. 5, top). The total ice depth of the multi-year ice was approximately 6 meters, of which nearly half of that depth was analyzed. Multi-year ice undergoes many morphological changes, which may explain the large difference between the upper layers and the one at 240-255cm depth. On the other hand, it is possible to assume that lower concentration of dissolved organic compounds in the upper layers may occur as a result of brine drainage throughout the ice column. Salinity measurements performed through the multi-year ice indicated an increased from 0.05(o/oo) to 3.6(o/oo) from surface to 265cm depth. An increase in fluorescence is observed when plotted against salinity (Fig 5, bottom). Such an effect on fluorescence has been previously reported. Other factors should not be excluded, particularly in multi-year ice, where the layers are constituted by different types of ice. Further interpretation of such differences would be speculative at this time.

In a recent study Mopper and Schultz¹⁷ reported that the protein-type fluorescence (Ex 220-270nm-Em 300-350nm) was dominant in the upper water column for the Atlantic and Pacific Ocean samples. Deeper water samples showed two distinctive excitation-emission regions one at 230nm with an emission maximum at 430nm, and other at 310nm with an emission maximum at 430nm, which has been commonly associated with humic substances²⁶. Strong fluorescence signals have also been detected at <260nm/435nm in the Black Sea¹⁵ and in aquatic fulvic substances¹⁴. The Ex 230nm-Em 430nm fluorescence has been found to be the dominant feature for humic-rich freshwater and marine sediment pore water^{17,26}. For the sea ice samples examined, a common characteristic was a maximal emission at approximately 400nm, when the excitation maxima was 250nm, which appears to be close to the fluorescence characteristics reported for the humic rather than the protein-type substances. However, the protein-type, as detected by spectral fluorescence analysis, is restricted to the presence of fluorescent aromatic amino acids, such as tryptophan, phenylalanine, tyrosine, or proteins containing such amino acids²⁷. Spectral absorption spectra indicated a distinctive shoulder at 280nm in many of the ice samples, which is commonly associated with protein absorption. Therefore the presence of protein can not be excluded. According to these observations, the effects of dissolved organic matter upon attenuation of incident irradiance will be more relevant within the UV region (350nm-200nm) of the spectrum. However, their fluorescence emission may affect the light field within the visible region.

Depending on their concentration, the presence of particulate and dissolved organic matter in the congelation ice layers will affect not only the physical structural properties of the ice, but also the quantity and spectral composition of the solar irradiance throughout the ice column^{1,28}. During bloom conditions, large concentrations of

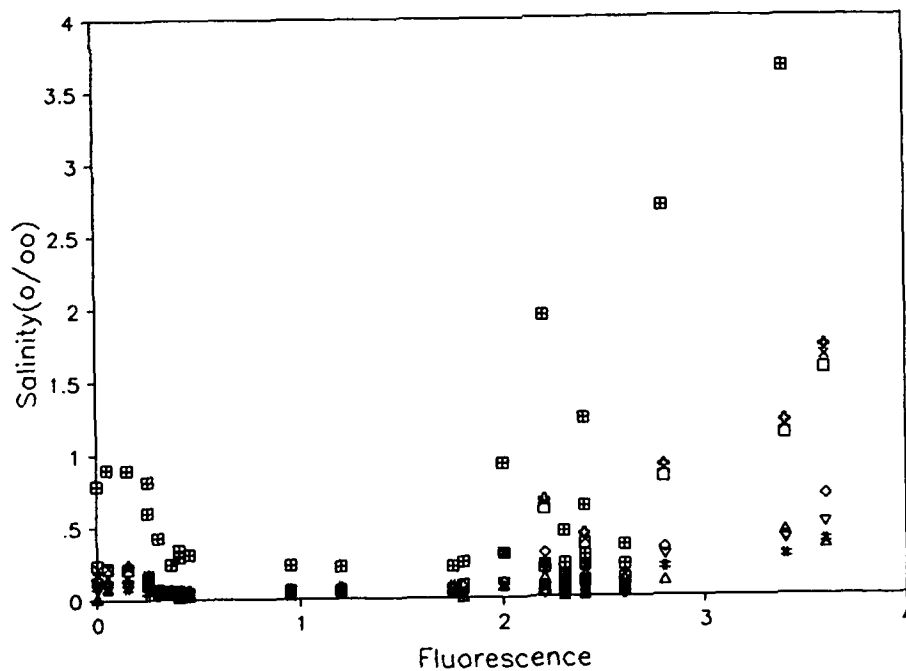
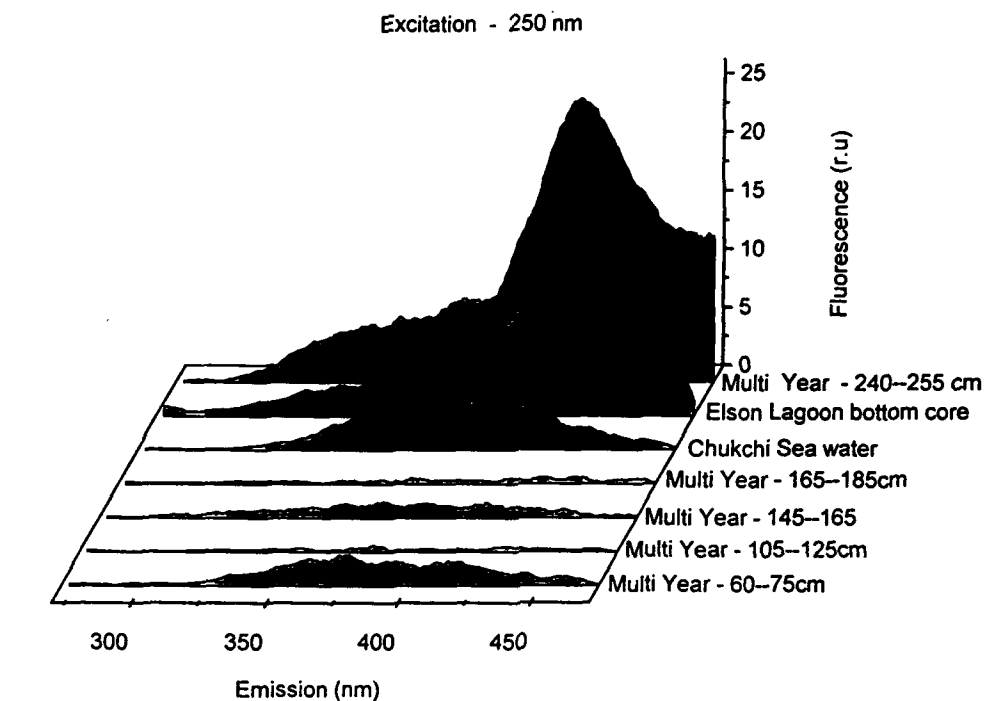


Figure 5. Fluorescence emission characteristics of different DOM samples (top), and effect of salinity on the fluorescence signal (bottom).

microalgae can be found within the bottom of the congelation ice and the underlaying platelet ice layer. It is also expected that such large concentrations will also contribute significant amounts of dissolved organic extracellular products.

The transfer of electromagnetic radiation through the ice is dependent not only on the inherent optical properties of the ice and covering snow, but also on the amount of dissolved and particulate matter present. Previous radiative transfer models for sea ice assumed structural homogeneity and composition simplicity^{20,21,22}. More recently, other models have incorporated the effect of particulate matter in sea ice, and have included absorption and scattering^{3,29}. Both models indicate that absorption and scattering properties of sea ice microalgae can significantly affect the propagation of spectral irradiances within the visible spectrum. However, more information is required before the effects of dissolved organic matter and the fluorescence parameter can be included in radiative transfer models of sea ice.

4. SUMMARY

This preliminary study suggest that fluorescence spectroscopy represents a useful technique for assessing differences between particulate matter entrapped in sea-ice, such as photosynthetic pigments an their degradation products. A characterization of dissolved organic compounds by direct analysis using fluorescence excitation-emission can also be performed without concentration of the sample. This analysis suggests that DOM entrapped in the ice may fall within the marine humic-acid type of fluorescence. However, this does not include any other type of organic compounds not detected by fluorescence, such as non fluorescing amino acids, proteins, or other organic products.

5. ACKNOWLEDGMENTS

This research was supported by the Ocean Optics Program of the Office of Naval Research, grants # N00014-93-I0169 (R.I) and # N00014-93-I0149 (C.R.). We also thanks Jesse Collins, Robert Maffione, Scott Pegau and Richard Glenn for field assistance, Susan Bower for help with data processing, and Denise Gineris for helpful comments.

6. REFERENCES

1. J. B. Soohoo, A. C. Palmisano, S. T. Kottmeier, M. P. Lizotte, S. L. Soohoo, and C. W. Sullivan, "Spectral light absorption and quantum yield of photosynthesis in sea ice microalgae and a bloom of *Phaeocystis pouchettii* from MacMurdo Sound Antarctica", *Mar.Ecol.Progr.Ser.*, 35:153-164, 1987.
2. R. Iturriaga, C.W. Sullivan, "Spectral light absorption characteristics of individual sea ice microalgae from McMurdo Sound, Antarctica", *Antarc.J.U.S.*, 24:188-190, 1989.
3. K. R. Arrigo, C. W. Sullivan, and J. Kremer, "A biological model of Antarctic sea ice", *J.Geophys.Res.*, 96:10581-10592, 1991.
4. B. Gulliksen, O. J. Loenne, "Sea ice microfauna in the Antarctic and Arctic", *J.Mar.Sys.*, 2:53-61, 1991.
5. C. H. Fritzen, R. Iturriaga, C. W. Sullivan, "Influence of particulate matter on spectral irradiance fields and energy transfer in the Easter Arctic Ocean", *SPIE vol.1750 Ocean Optics XI*, 527-541, 1992.
6. G. F. Cota, L. Legendre, M. Gosselin, and R.G. Ingram, "Ecology of bottom ice algae: I. Environmental controls and variability", *J.Mar.Sys.*, 2:257-277, 1991.
7. G. F. Cota, and R. E. Smith, "Ecology of bottom ice algae: II. Dynamics, distribution and productivity", *J.Mar.Sys.*, 2:279-295, 1991.
8. S. G. Warren, C. S. Roesler, V. I. Morgan, R. E. Brandt, I. D. Goodwin, and I. Allison, "Green Icebergs formed by freezing of organic-rich seawater to the base of Antarctic ice shelves", *Jour.Geophys.Res.*, 98:6921-6928, 1993.
9. C. S. Yentsch, and C. M. Yentsch, "Fluorescence spectral signatures: the characterization of phytoplankton populations by the use of excitation and emission spectra", *J. Mar.Res.*, 37:
10. C. S. Yentsch, and D. A. Phiney, "Spectral fluorescence: an a taxonomic tool for studying the structure of phytoplankton populations", *J.Plank.Res.*, 7:617-632, 1985.
11. J. Hilton, E. Rigg, and G. Jaworski, "Algal identification using in vivo fluorescence spectra", *J.Plank.Res.* 11:65-74, 1989.
12. R. Iturriaga, and S. Bower, "Microphotometric analysis of the spectral absorption and fluorescence of individual phytoplankton cells and detrital matter", In: Current Methods in Aquatic Microbial Ecology, P. Kemp, J. Cole, B. Sherr, and E. Sherr, Lewis Pub., Miami, 1993.
13. S. E. Cabanis, and M. S. Schuman, "Synchronous fluorescence spectra of natural waters: Tracing sources of dissolved organic matter", *Mar.Chem.*, 21:37-50, 1987.
14. O. F. Donard, M. Lamotte, C. Belin, and M. Bewald, "High-sensitivity fluorescence spectroscopy of a Mediterranean waters using a conventional or a pulsed laser excitation source", *Mar.Chem.*, 27:117-136, 1989.
15. P. G. Coble, S. A. Green, N. W. Blough, and R. B. Gagosian, "Characterization of dissolved organic matter in the Black Sea by fluorescence spectroscopy", *Nature*, 348:432-435, 1990.

16. P. G. Coble, C. A. Schultz, K. Mopper, "Fluorescence contouring analysis of DOC intercalibration experiment samples: A comparison of techniques", *Mar.Chem.*, 41:173-178, 1993.
17. K. Mopper, and C. A. Schultz, "Fluorescence as a possible tool for studying the nature and water column distribution of DOC components. *Mar Chem.*, 41:229-238, 1993.
18. S. L. Bower, and R. Iturriaga, "Preparation of natural phytoplankton communities to preserve spectral fluorescence properties", *SPIE Vol.*, 1750, *Ocean Optics XI*, 224-232, 1992.
19. R. Iturriaga, "Effect of bacterial colonization on the absorption and fluorescence properties of detrital particulates", *SPIE Vol.*, 1750, *Ocean Optics XI*, 202-211, 1992.
20. K. Kalle, "Nahrstoff Untersuchungen als Hydrographisches Hilfsmittel zur Unterscheidung von Wasserkörpern", *Ann.Hydrogr.*, Berlin, 65:276-282, 1937.
21. K. Kalle, "Fluoreszenz und Gelbstoff im Bottnischen und Finnischen Meerbussen", *Dt.Hydrog.Z.*, 2:117-124, 1949.
22. E.K. Duursma, and J.W. Rommets, "Interpretation mathématique de la de la fluorescence des eaux douces, saumâtres et marine", *Neth.J.Sea Res.*, 1:391-405, 1961.
23. N.K. Hojerslev, "On the origin of yellow substances in the marine environment. The role of solar ultraviolet radiation in marine ecosystems", *NATO-ARI Workshop*, Woods Hole, MA, pp:39-56, 1983.
24. K. Hayase, M. Yamamoto, I. Nakazana, and H. Tsubota, "Behavior of natural fluorescence in Sagami Bay and Tokyo Bay, Japan-vertical and lateral distributions", *Mar.Chem.*, 20:265-267, 1987.
25. E.D. Traganza, "Fluorescence excitation and emission spectra of dissolved organic matter in sea water", *Bull.Mar. Sci.*, 19:897-904, 1969.
26. R.F. Chen, and J.L. Bada, "Seawater and porewater fluorescence in the Santa Barbara Basin", *Geophys. Res. Lett.*, 16:687-690, 1989.
27. O.S. Wolfbeis, "The fluorescence of organic natural products", In: Molecular Luminescence spectroscopy. Part I: pp. 167-370. S.G. Schulman, ed. Wiley-Interscience. New York, 1985.
28. G.A. Maykut, and T.C. Greenfell, "The spectral distribution of light beneath first-year sea ice in the Arctic Ocean", *Limnol.Oceanogr.*, 20:554-563, 1975.
29. T.C. Greenfell, "A multi-layer radiative transfer model for sea ice with vertical structure variations", *J.Geophys.Res.*, 96:16,991-17,001, 1991.
30. C.S. Roesler, and R.Iturriaga, "Absorption properties of marine-derived material in Arctic sea ice," *Ocean Optics*, This issue.

Absorption properties of marine-derived material in Arctic sea ice

Collin S. Roesler

College of Oceanic and Atmospheric Sciences
Oregon State University, Corvallis, Oregon 97331

and Rodolfo Iturriaga

Department of Biological Sciences
University of Southern California, Los Angeles, California 90089

ABSTRACT

The distribution and concentration of particulate and dissolved material was determined for first year and multiyear sea ice collected from the fast ice off Barrow, Alaska. The particles were identified as intact algal cells, bacteria, organic aggregates colonized by bacteria and detrital particles. The largest concentrations of particles occurred in the zones of fine grain or in zones of concentrated brine drainage features. The absorption efficiencies of these particles in combination with measured particle concentrations was shown to provide a reasonable estimate of the bulk particulate spectral absorption coefficients in the case of a first year ice sample. The sum of the absorption coefficients of the particulate and dissolved fractions were up to an order of magnitude greater than the absorption coefficients of pure ice. The enhanced absorption of visible radiation by the entrapped material was estimated to cause increases in sea ice temperature of up to 3 °C per day in the absence of snow cover. The marine-derived particulate and dissolved materials are not negligible contributors to the optical and thermal characteristics of sea ice.

1. INTRODUCTION

The presence of significant amounts of marine-derived organic material in the skeletal layer of sea ice has been observed in both the Arctic and the Antarctic. Bottom ice algal communities accumulate to large concentrations ($>100 \text{ mg chl m}^{-3}$) and are some of the most productive communities in the polar regions^{1,2}. Material entrapped within the ice column is most commonly found in the brine drainage system between ice crystals³. The remaining entrapped material which is not directly associated with drainage features, the so-called *diffuse* interior community of ice biota, has been poorly studied^{2,4}. Interior algal communities are found in much lower concentrations ($<10 \text{ mg chl m}^{-3}$) and consist of those cells both entrapped during the freezing season and those accumulated due to local growth within the ice. Along with the incorporation of algae into the ice column is evidence for the entrapment and survival of larger organisms⁵ and dissolved organic material⁶. The diffuse algal communities have been found only in Antarctic sea ice to date⁷, they may account for a significant fraction of the algal concentration and production in regions of persistent ice cover and perhaps should not be overlooked with respect to relatively ephemeral bottom ice communities.

While the presence of particulate organic material within or at the base of the ice column affect the optical properties significantly^{4,9,10}, the contribution of dissolved organic material to the optical properties of sea ice is virtually unknown². The first report of the effect of dissolved organic material on the optical properties of marine ice was observed in Antarctic icebergs originating from basal freezing of seawater to the undersides of ice shelves⁶. The concentrations of this material were sufficient to alter the spectral reflectance by enhanced absorption of blue photons over that by pure ice. These observations suggest that all constituents found in seawater are potentially incorporated into sea ice during the freezing process and that the strong absorption coefficients may contribute to the optical properties of the sea ice, particularly with respect to the attenuation coefficients⁹.

Pure ice has relatively low absorption coefficients at short wavelengths (400 - 550 nm)¹¹, resulting in a large portion of the incident solar energy being transmitted through the ice⁸ and backscattered out the surface¹². However, the presence of absorbing components in the ice may significantly increase the amount of radiation trapped in the ice and thus alter not only the spectral composition of the transmitted and backscattered radiation, but also the temperature distribution due to heat trapping. Because brine pocket formation is extremely sensitive to small changes in temperature¹³, the entrapped organic material may also have an effect on the sea ice structure.

The purpose of this investigation was to determine the concentrations, distributions, and absorption properties of marine-derived particulate and dissolved material entrapped in first and multiyear Arctic sea ice with the goal to estimate the effect of this absorbing material on the sea ice heating rates.

2. METHODS

First and multiyear sea ice cores were collected from fast ice west of Barrow, Alaska, in the Chukchi Sea. A first year sea ice core was also collected from Elson Lagoon southeast of Pt. Barrow. Cores were subsampled at 10 to 20 cm intervals on site and melted for salinity, chemical, particle, and optical analyses. Replicate cores were collected for thin sections and petrographic analyses.

Chlorophyll *a* concentrations were determined fluorometrically on filtered samples (combusted Whatman GF/F filters) which were extracted in 90% acetone for 48 h. Particle size distributions were measured with the Galai CIS100 Particle Analyzer for diameters 0.5 to 150 μm . The Galai determines particle diameters from the time of transit of a rotating laser as it intersects the midpoint of a particle. The shape of the voltage trace of the laser across the particle is used to reject off center interactions and chord diameters. An LED light source and CCD camera provides video display of the particles in suspension and allowed identification of the particles associated with each size class.

Spectral absorption efficiency factors of individual algal cells, $Q_{\text{sp}}(\lambda)$, and detrital particles, $Q_{\text{sd}}(\lambda)$ were measured microphotometrically¹⁴. Bulk particle absorption spectra, $a_p(\lambda)$, were determined spectrophotometrically on filtered samples (combusted Whatman GF/F filters)¹⁵. Bulk dissolved absorption spectra, $a_d(\lambda)$, were measured spectrophotometrically on the filtrate in 10 cm cuvettes¹⁶.

3. RESULTS

*3.1 Relation between chlorophyll *a* concentrations and sea ice crystal structure*

Chlorophyll concentrations (chl) for the three ice types are shown in Fig. 1. The largest concentrations were found in the first year Chukchi Sea ice core with concentrations ranging from 0.6 to 10 mg chl m^{-3} , comparable to productive ocean waters. The chl concentrations in the Elson Lagoon sea ice core ranged from 0.03 to 0.4 mg m^{-3} . In these first year ice cores maximal concentrations of chl were associated with visible bands of brine drainage structures and fine grain ice. Minimal concentrations occurred in regions dominated by coarse grain congelation ice.

Only 250 cm of the more than 600 cm ice column was retrieved from the multiyear ice site. The chl concentrations were one to three orders of magnitude less than those for the first year ice (0.001 to 0.05 mg m^{-3}). The maxima in chl concentration at the surface, 60 cm, 155 cm, and 245 cm coincided with patches of oriented fine grained ice in the midst of unoriented or medium grained ice.

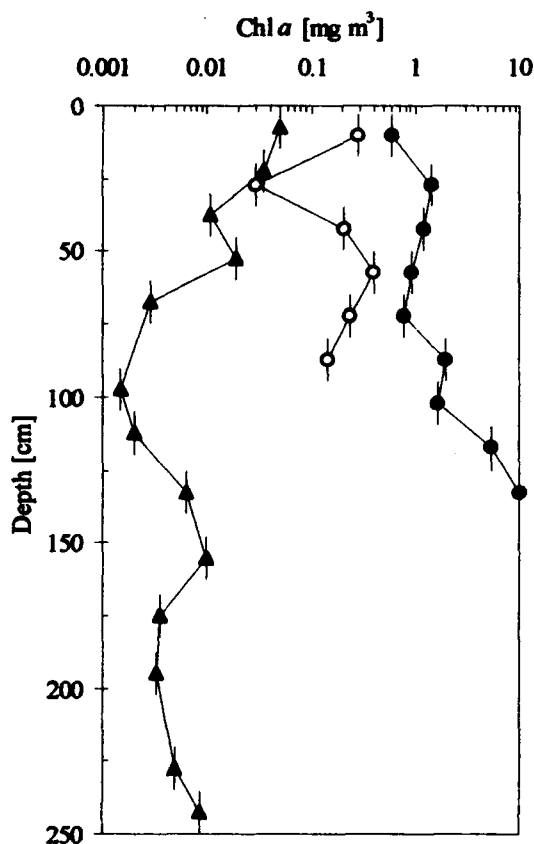


Fig. 1. Chlorophyll *a* concentrations for the multiyear (triangles) and first year ice from the Chukchi Sea (solid circles) and Elson Lagoon (open circles). Vertical bars indicate the depth range of the core samples.

3.2 Particle distributions and optical properties

Particle size distributions (PSDs) are presented in term of total particle volume in each size class as a function of depth in the ice core (Fig. 2). The population of particles associated with the peak at 4 μm was identified as a pennate diatom (*Nitzschia ssp.*). The populations associated with the peaks at 10 - 30 μm diameters were identified as large organic flocs colonized by bacteria.

The absorption efficiency spectra for individual algal cells indicate that the dominant pigments are chl *a* and *c*, consistent with a diatom dominated population (Fig. 3a). The absorption by the carotenoid accessory pigments was minimal in these cells as can be seen by the lack of a significant absorption peak or shoulder between 450 to 550 nm. The absorption efficiency spectra for individual detrital particles decreased from blue to red with a slight shoulder at 510 nm (Fig. 3b).

A histogram of particle diameters was constructed from the microscopic analysis of particles concentrated on a filter. This histogram was compared to a normalized particle size distribution determined using the Galai CIS100 (Fig. 4). Because the Galai randomly samples particle diameters, the probability of intersecting a rectangle along the minor axes is greater than that along the major axis. Thus the microscope-based histogram was scaled to the probability of axis encounter. For example, a particle with a minor axis (width) of 4 μm and a major axis (length) of 12 μm was divided into 1- μm intervals such that a total of 16 possible intersections were obtained (4 length wise, 12 widthwise). The probability histogram would be 75% at 4 μm and 25% at 12 μm . The reconstructed histogram agreed well with the measured histogram. It

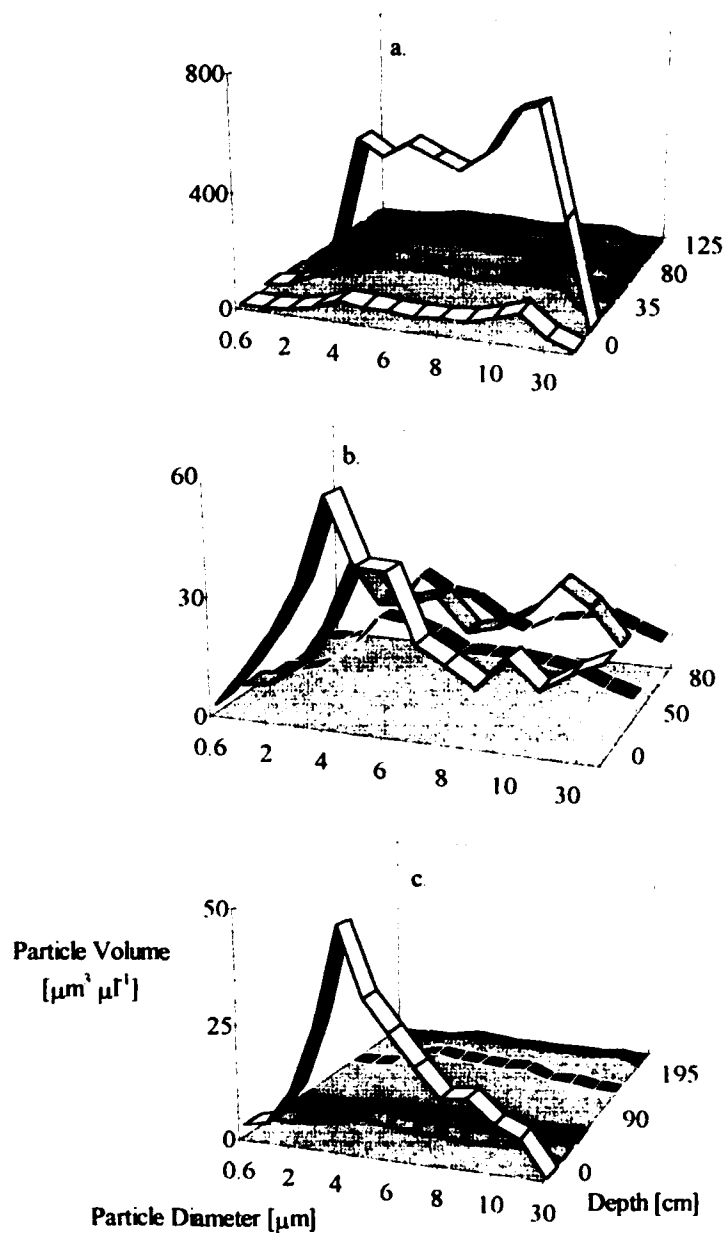


Fig. 2. Particle volume distributions for (a) the first year ice from the Chukchi Sea, (b) the first year ice from Elson Lagoon, and (c) multiyear ice from the Chukchi Sea. Note the different scales. Particle volumes were determined from measurements of particle diameters assuming spherical particles. The peak at $4\text{ }\mu\text{m}$ was identified as a pennate diatom with minor axis length of $4\text{ }\mu\text{m}$ and major axis length of $8\text{ to }12\text{ }\mu\text{m}$. The particles responsible for peaks occurring from $10\text{ to }30\text{ }\mu\text{m}$ were identified as large aggregates of organic material (flocs) colonized by bacteria. The particles of diameters $<4\text{ }\mu\text{m}$ were identified as spherical bacteria and detrital particles.

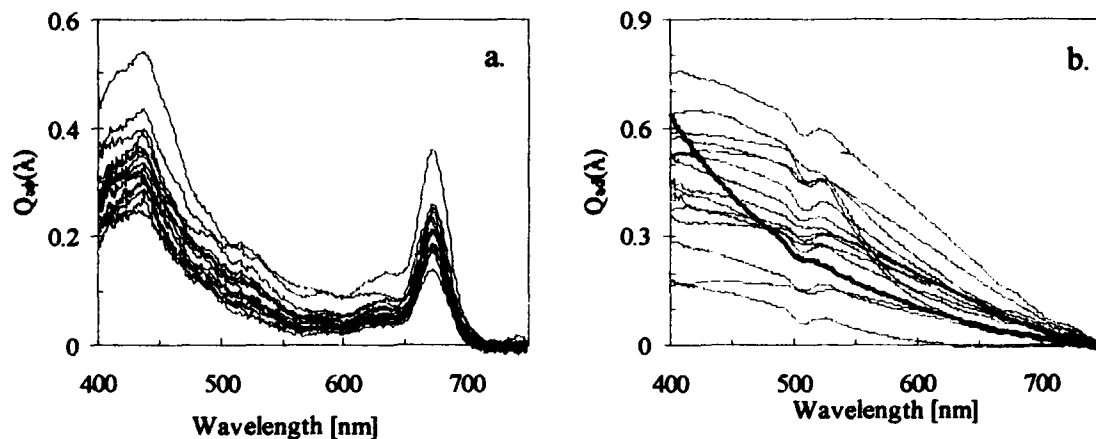


Fig. 3. Absorption efficiency spectra for (a) intact algal cells and (b) detrital particles for the 0 - 15 cm section of the Chukchi first year ice core. The bold spectrum in (b) is used in the modeled bulk absorption spectrum in Fig. 5.

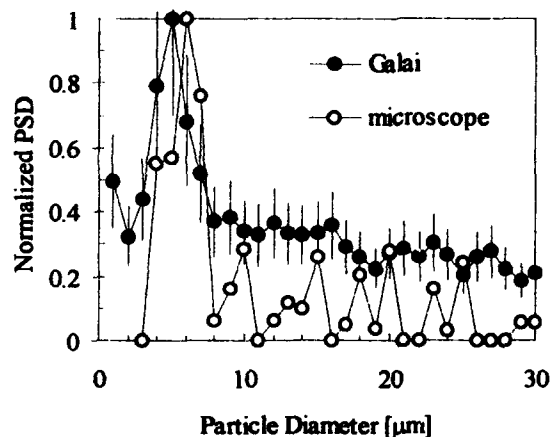


Fig. 4. Normalized particle size distributions measured microscopically (open circles) and with the Galai CIS100 Particle size Analyzer (solid circles) on the 0-15 cm section of the Chukchi first year ice core. The error bars represent ± 1 standard deviation for triplicate measurements.

should be noted that only 32 particles were identified microscopically while the Galai measured over 30,000 particle diameters. This likely accounts for the underestimation of the larger sized particles by microscopy.

Using the particle size distribution measured by the Galai and the absorption efficiency factors for individual particles in the appropriate size class, bulk absorption coefficients were determined from Mie theory¹⁷:

$$a [m^{-1}] = \sum Q_{\alpha} G_i N_i \quad (1)$$

where the summation $i = 4$ to $30 \mu m$ (the largest observed particle diameter), Q_{α} is the particle absorption efficiency, G_i is particle cross sectional area, and N_i is the particle concentration of particles in size class i . The reconstructed absorption spectrum was compared to the bulk absorption spectrum (Fig. 5). The magnitude of the reconstructed spectrum overestimated the measured bulk absorption spectrum by approximately 25%. The shape of the reconstructed spectrum is dominated by absorption features associated with algal pigments (absorption peaks at 440 and 675 nm), while the bulk absorption spectrum appears more detrital with a much smaller absorption peak at 675 nm and no apparent peak at 440 nm.

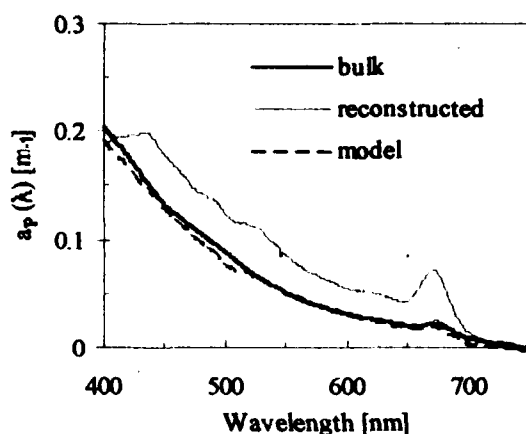


Fig. 5. Measured bulk particulate absorption spectrum (bold) for the 0-15 cm section of Chukchi Sea first year ice. The reconstructed absorption spectrum (solid) is given by equation (1) with particle size distributions measured by the Galai (Fig. 4 un-normalized) and absorption efficiency spectra in Fig. 3 assigned to the appropriate particle size interval. The modeled reconstructed absorption spectrum (dashed) assigned a detrital to algal particle ratio of 15:1 and the detrital efficiency spectrum shown as the bold line in Fig. 3b.

A model based upon modification of the reconstruction was developed to better estimate the bulk absorption spectrum. The PSD measured by the Galai indicated that there was considerable concentrations of particles with diameters less than 4 μm , the minimal diameter recorded by microscopy. These particles were identified as bacteria which have absorption spectra similar to an exponentially-decaying detrital absorption spectrum (bold spectrum in Fig. 3b). By increasing the proportion of detrital to phytoplankton absorption efficiencies to 15:1 and assigning the bacterial absorption spectrum to the detrital fraction, the reconstructed bulk absorption spectrum more accurately predicts the magnitude and spectral shape of the measured spectrum (Fig. 5).

3.3 Absorption properties of particles and dissolved material

The bulk absorption spectra observed for all three ice types varied from purely detrital in appearance (decaying exponential¹⁶) to those with strong red absorption peaks due to chl (Fig. 6a). The range in the bulk particulate absorption coefficients was approximately 25% in the Elson Lagoon first year ice, 4-fold in the multiyear ice, and over an order of magnitude in the Chukchi first year ice. The absorption spectra for the dissolved fraction was approximately the same magnitude as that for the particulate fraction. The largest coefficients were observed in the Chukchi first year ice. However the ratio of the contributions of dissolved to particulate absorption coefficients was greater in the Elson Lagoon first year ice than in the Chukchi first year ice or multiyear ice (1:1 vs. 1:4 and 2:3, respectively, at 400 nm).

The ultraviolet absorption coefficients for the dissolved fraction were approximately two orders of magnitude greater than the absorption coefficients in the visible (Fig. 6c). The absorption coefficient at 200 nm was strongly correlated with the bulk salinity (Fig. 6d).

The distribution of total absorption coefficients due to the marine-derived particulate and dissolved material within the ice column was approximately the same as that of chl although the range was not as large (Fig. 7a). These absorption coefficients represent a significant increase over the absorption coefficients due to pure crystalline ice¹¹. In the presence of incident solar irradiance a greater portion of the short wave radiation will be trapped in the ice column. The increased absorbed radiation will cause localized heating and increased temperatures in the ice column. The depth dependent change in temperature in the ice column, $\Delta T(z)$, due to the additional absorption by the particulate and dissolved material over that of pure ice, $\Delta a(z)$, was calculated from:

$$\Delta T(z) = \frac{\Delta a(z) E(z) t}{\rho C_{\text{ice}}} \quad (2)$$

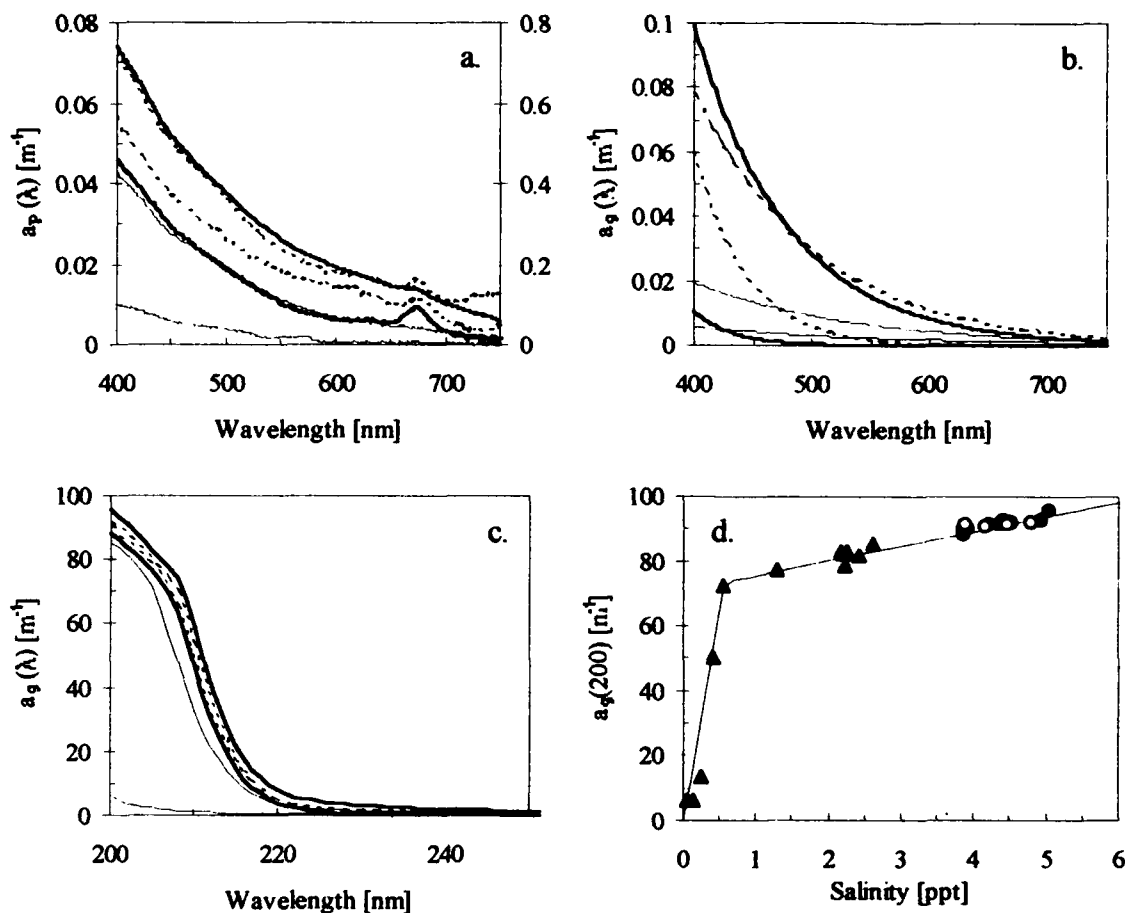


Fig. 6. Range of spectral absorption coefficients for the (a) particulate, $a_p(\lambda)$, and (b and c) dissolved, $a_d(\lambda)$, fractions in Chukchi Sea first year ice (bold), Elson Lagoon first year ice (dashed), and multiyear ice (solid). (d) Absorption coefficient for the dissolved fraction at 200 nm vs. bulk salinity. Symbols as in Fig. 1, lines are best fit by eye.

where $E(z)$ is the depth dependent irradiance calculated from a surface irradiance value of 500 Wm^{-2} over the wavelength range 400 to 750 nm^{12} and the irradiance attenuation for ice thickness given by Maykut and Grenfell⁸ for sea ice with no snow covering (from their Fig. 7). t is the time period of solar heating (10 h), ρ is the density of sea ice (taken to be 90% of the density of sea water), and C_{si} is the specific heat of sea ice¹⁸. The ΔT calculated in this manner range from 0.01 to 3°C , with the largest predicted heating occurring in the first year ice.

4. CONCLUSIONS

Algal biomass was found throughout the ice profiles of all three ice types. Maximal concentrations occurred in association with brine drainage features or with fine grain ice structures. Minimal concentrations were observed in the congelation ice zones. These results are consistent with observations in Antarctic sea ice where enhanced concentrations of chlorophyll¹⁹ and viable foraminifera⁵ have been found in the frazil ice. Laboratory experiments confirm that algae and other particles are accumulated into sea ice by concentration in the frazil ice^{20, 21}.

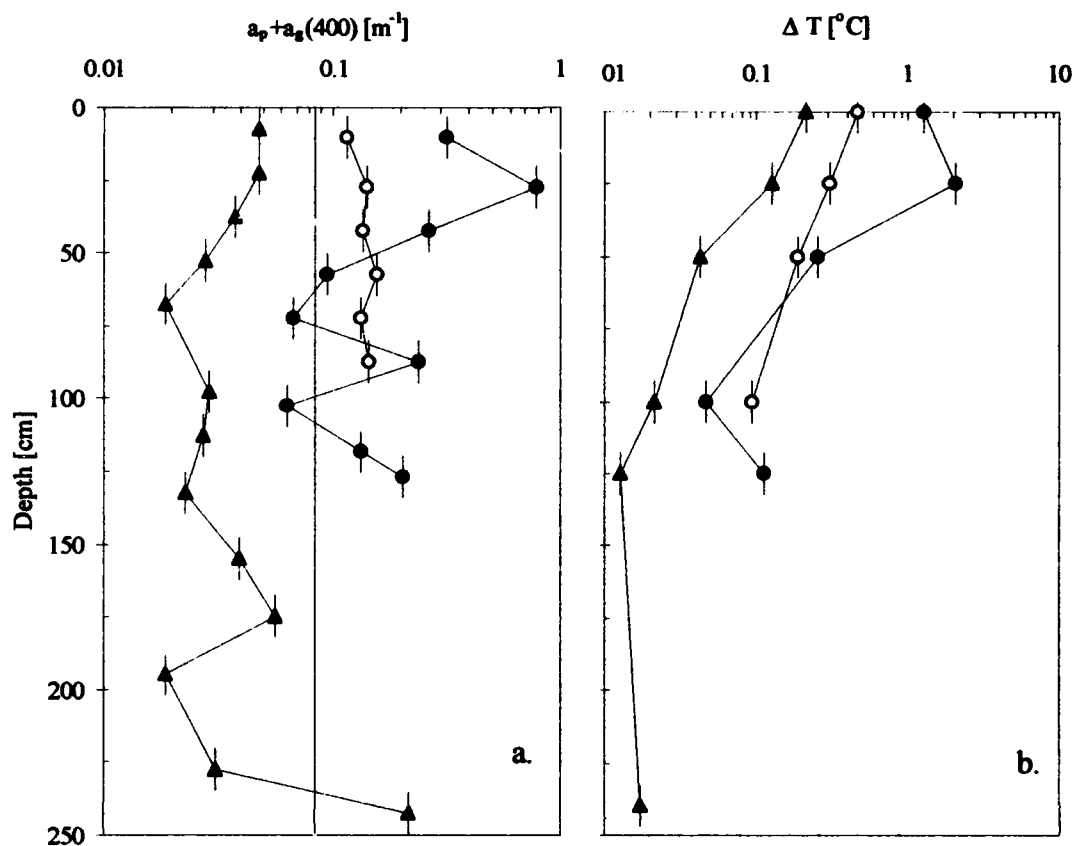


Fig. 7. (a) Absorption coefficient of the particulate and dissolved fractions at 400 nm for the three ice types. Vertical line indicates the absorption coefficient of pure ice⁹ at 400 nm. (b) Change in bulk ice temperature over a solar day as calculated with equation (2) due to enhanced absorption by the entrapped particulate and dissolved material. Symbols and error bars as in Fig. 1.

Interior algal communities in the Antarctic have been shown to exhibit local growth⁷. The algal populations observed in the first year ice in this study appear viable in as much as chl was not degraded to pheopigments and the absorption spectra for the individual cells were characteristic of relatively healthy cells, albeit depleted in carotenoid pigments. Fluorescence excitation spectra measured on the individual algal cells (R. Iturriaga, unpub. data) suggest that the photosystems are intact and thus the cells may be actively growing. Productivity measurements of these populations are needed to assess their contribution to total primary production in sea ice.

The absorption efficiency spectra for the detrital particles differed spectrally from measured bulk detrital absorption spectra¹⁶. The detrital particles measured were large aggregates $>5 \mu\text{m}$ in diameter (the majority were 10 to 30 μm in diameter). The feature in $Q_{ad}(\lambda)$ at approximately 500 nm may have been due to minerals caught in the aggregates⁹ or due to cytochromes in the colonizing bacteria²².

Bulk absorption coefficients have previously been deconvolved into the phytoplankton and detrital components of absorption efficiency²³ which suggested that merging scales of optical measurements from bulk to individual particles was possible. In this study, the inverse approach was taken, to reconstruct the bulk absorption from the sum of the individual parts. The utility of this approach is to understand how

variability in the individual absorption efficiencies is translated into variability in bulk coefficients. The reconstruction of the bulk particle absorption coefficient from the individual particle absorption efficiency spectra for a first year ice sample was within 25% of the magnitude of the measured spectrum. However, the spectral composition of the reconstructed spectrum indicated that the algal component was overestimated relative to that in the bulk absorption spectrum. The particles below microscopic detection ($<4\ \mu\text{m}$) were observed to be unattached bacteria and detrital particles. If that fraction was included in the reconstruction, and was defined to be characterized by the exponentially decaying absorption efficiency spectrum, the reconstructed absorption was more similar in magnitude and spectral composition to the measured bulk absorption spectrum. This indicates that the small particles ($<4\ \mu\text{m}$) contribute significantly to the particulate absorption coefficients in sea ice.

The particulate absorption spectra observed in these samples were approximately the same magnitude as those observed in multiyear and refrozen lead ice in the Eastern Arctic⁹, which were found to have significant effects on the magnitude and spectral composition of the irradiance field in the ice. The absorption coefficients of the dissolved material was found to be 25 to 100% of the particulate absorption coefficients (400-750 nm range) in all ice types. The contribution of this fraction should therefore not be neglected in optical modeling. The absorption coefficients of the dissolved fraction in the ultraviolet part of the spectrum were found to be comparable with the absorption coefficients measured on pure ice (0.2 to 1.4 m^{-1} at 250 nm compared with 0.7 m^{-1} for pure ice²⁴ and 6 to 98 m^{-1} at 200 nm compared with 10 to 100 m^{-1} for pure ice²⁵). The increase in the absorption of ultraviolet light due to the presence of particulate and dissolved organic material minimizes the amount of damaging ultraviolet light that will penetrate the ice column and potentially damage the bottom algal populations²⁶.

The relationship between the dissolved absorption coefficient and salinity is intriguing as it is not merely a dilution of a salt or some component that covaries with salinity. That the change in slope occurs within the multiyear ice core also indicates that the relationship is not ice-type dependent. The slope that occurs at salinities greater than 0.5 ppt gives no indication of asymptotic behavior as would be expected if Beer's Law were being violated in the spectrophotometric measurement. The component responsible for the absorption needs to be identified. If, perhaps, a particular ion is responsible, and some fractionation of that ion occurs in the drainage of multiyear ice²⁷, the relationship in Fig. 6d could be explained and the ultraviolet absorption coefficient might be another tool for determining the chemical composition of sea ice.

The absorption coefficients of the particulate and dissolved material entrapped in sea are non-negligible with respect to absorption by pure ice. While it has been previously shown that the presence of particles (algal or detrital) changes the spectral distribution of irradiance in sea ice^{8,10}, the effect of this absorbed radiation has not been quantified in terms of heating rates. For the absorption coefficients measured in this study, the estimated temperature changes were maximal at the surface of the ice where irradiance is highest but were still significant 1 to 2 m downcore. These estimates were for snow free ice and thus they provide an upper range for temperature changes over a 10 h solar day. A 10 cm layer of snow would decrease the $\Delta T(z)$ values by approximately 30%; still significant changes in temperature. Thus, the presence of particles in sea ice might stimulate the springtime melting rates of entire sea ice column, with maximal rates occurring at maximal concentrations of particulate and dissolved material. The absorption coefficients measured in this study were bulk coefficients and thus the calculated $\Delta T(z)$ values represent bulk heating. If however, the particulate and dissolved material was isolated in brine pockets or in limited spaces between ice grains, then the effective absorption would be occurring on much smaller spatial scales as would the effective $\Delta T(z)$ values. Thus, the changes in temperature would have a much greater impact on the ice structure in the region of enhanced absorption.

5. ACKNOWLEDGMENTS

This work was funded by the Ocean Optics Program of the Office of Naval Research grants #N00014-93-I0149 (Roesler) and #N00014-93-I0169 (Iturriaga) in support of the Electromagnetic Properties of Sea Ice ARI. The authors wish to thank Richard Glenn for salinity measurements and petrographic analysis, Jesse Collins, Scott Pegau, and Robert Maffione for field assistance, Susan Bower for laboratory assistance, and Rebecca Hansing for assistance with data analysis.

6. REFERENCES

1. K. R. Arrigo, G. S. Dieckmann, M. Gosselin, and C. W. Sullivan, "Studies on the nutrient status in sea ice and underlying platelet layer," *Antarct. J. US*, 25, 185-188, 1990.
2. G. F. Cota and R. E. H. Smith, "Ecology of bottom algae: II. Dynamics, distributions and productivity," *J. Mar. Sys.*, 2, 279-295, 1991.
3. S. F. Ackley, K. R. Buck, and S. Taguchi, "Standing crop of algae in the sea ice of the Weddell Sea region," *Deep-Sea Res.*, 26A, 269-281, 1979.
4. R. Horner, S. F. Ackley, G. S. Dieckmann, B. Gulliksen, T. Hoshiai, L. Legendre, I. A. Melnikov, W. S. Reeburgh, M. Spindler, and C. W. Sullivan, "Ecology of sea ice biota 1. Habitat, terminology, and methodology," *Polar Biol.*, 12, 417-427, 1992.
5. G. Dieckmann, M. Spindler, M. A. Lange, S. F. Ackley, and H. Eicken, "Sea Ice, a habitat for the Foraminifer *Neogloboquadrina pachyderma*?", In *Proceedings of the W. F. Weeks Sea Ice Symposium on Sea Ice Properties and Processes*, S. F. Ackley and W. F. Weeks [eds.], USA CRREL Monograph 90-1, 86-92, 1990.
6. S. G. Warren, C. S. Roesler, V. Morgan, R. Brandt, I. Goodwin, and I. Allison, "Green icebergs formed by freezing of organic-rich seawater to the base of Antarctic ice shelves," *J. Geophys. Res.*, 98(C4), 6921-6928, 1993.
7. L. Legendre, S. F. Ackley, G. S. Dieckmann, B. Gulliksen, R. Horner, T. Hoshiai, I. A. Melnikov, W. S. Reeburgh, M. Spindler, and C. W. Sullivan, "Ecology of sea ice biota 2. Global significance," *Polar Biol.*, 12, 429-444, 1992.
8. G. A. Maykut and T. C. Grenfell, "The spectral distribution of light beneath first-year sea ice in the Arctic Ocean," *Limnol. Oceanogr.*, 20, 554-563, 1975.
9. C. H. Fritsen, R. Iturriaga, and C. W. Sullivan, "Influence of particulate matter on spectral irradiance fields and energy transfer in the Eastern Arctic Ocean," *SPIE Ocean Optics XI*, 1750, 527-541, 1992.
10. G. F. Cota, "Arctic sea ice bio-optics," *EOS Transactions AGU*, 75, 229, 1994.
11. T. C. Grenfell and D. K. Perovich, "Radiation absorption coefficients of polycrystalline ice from 400-1400 nm," *J. Geophys. Res.*, 86, 7447-7450, 1981.
12. T. C. Grenfell and D. K. Perovich, "Spectral albedos of sea ice and incident solar irradiance in the Southern Beauford Sea," *J. Geophys. Res.*, 89, 3573-3580, 1984.
13. G. F. N. Cox and W. F. Weeks, "Changes in salinity and porosity of sea ice samples during shipping and storage," *J. Glaciol.*, 32, 371-375, 1986.
14. R. Iturriaga and D. Siegel, "Microphotometric characterization of phytoplankton and detrital absorption properties in the Sargasso Sea," *Limnol. Oceanogr.* 34, 1706-1726, 1989.
15. C. S. Roesler, "The determination of in situ phytoplankton spectral absorption coefficients: direct measurements, modeled estimates, and applications to bio-optical modeling," *Ph. D. thesis*, Univ. of Washington, 1992.
16. C. S. Roesler, M. J. Perry, and K. L. Carder, "Modeling in situ phytoplankton absorption from total absorption spectra in productive inland waters," *Limnol. Oceanogr.* 34, 1510-1523, 1989.
17. A. Bricaud and A. Morel, "Light attenuation and scattering by phytoplanktonic cells: a theoretical modeling," *Appl. Opt.*, 25, 571-580, 1986.
18. G. A. Maykut, T. C. Grenfell, and W. F. Weeks, "On estimating the spatial and temporal variations in the properties of ice in the polar oceans," *J. Mar. Sys.*, 3, 41-72, 1992.

19. G. S. Dieckmann, M. A. Lange, S. F. Ackley, and J. C. Jennings, Jr., "The nutrient status in sea ice of the Weddell Sea during winter: effects of sea ice texture and algae," *Polar Biol.*, 11, 449-456, 1991.
20. D. L. Garrison, A. R. Close, and E. Reimnitz, "Microorganisms concentrated by frazil ice, evidence from laboratory experiments and field measurements," In *Proceedings of the W. F. Weeks Sea Ice Symposium on Sea Ice Properties and Processes*, S. F. Ackley and W. F. Weeks [eds.], USA CRREL Monograph 90-1, 92-96, 1990.
21. E. Reimnitz, E. W. Kempema, W. S. Wever, J. R. Clayton, and J. R. Payne, "Suspended-matter scavenging by rising frazil ice," In *Proceedings of the W. F. Weeks Sea Ice Symposium on Sea Ice Properties and Processes*, S. F. Ackley and W. F. Weeks [eds.], USA CRREL Monograph 90-1, 97-100, 1990.
22. R. Iturriaga, "Effects of bacterial colonization on the absorption and fluorescence properties of detrital particulates," *SPIE Ocean Optics XI*, 1750, 201-211, 1992.
23. R. Iturriaga, A. Morel, C. Roesler, and D. Stramski, "Individual and bulk analyses of the optical properties of marine particulates: examples of merging these two scales of analysis," In: S. Demers [ed.], *Particle Analysis in Oceanography*, NATO ASI Series, Vol. G27, 339-347.
24. D. K. Perovich and J. W. Govoni, "Absorption coefficients of ice from 250 to 400 nm," *Geophys. Res. Letters*, 18, 1233-1235, 1991.
25. A. P. Minton, "The far ultraviolet spectrum of ice," *J. Phys. Chem.*, 75, 1162-1164, 1971.
26. J. J. Cullen, P. J. Neale, R. F. Davis, and D. R. S. Lean, "Ultraviolet radiation, vertical mixing, and primary productivity in the Antarctic," *EOS Transactions, AGU*, 75, 200, 1994.
27. D. A. Meese, "The chemical and structural properties of sea ice in the Southern Beauford Sea," In *Proceedings of the W. F. Weeks Sea Ice Symposium on Sea Ice Properties and Processes*, S. F. Ackley and W. F. Weeks [eds.], USA CRREL Monograph 90-1, 32-5, 1990.

In-situ measurements of optical scattering from the water-ice interface of sea ice

Jacob R. Longacre and Mark A. Landry

**Electro-optic Systems Branch
Submarine Electromagnetic Systems Department
Detachment New London
Naval Undersea Warfare Center
Code 3422, New London, CT 06320
Phone (203) 440-5105, Fax (203) 440-6725**

ABSTRACT

An apparatus has been developed to measure the optical scattering of laser light from the water-ice interface of sea ice. To avoid changes that occur in the optical characteristics of inhomogeneous natural sea ice when removed from its environment, this apparatus operates in situ. Testing with this apparatus was conducted on shore-fast ice at Resolute Bay in Canada. We investigated the capabilities of this apparatus to measure in situ scattering profiles from the underside of the ice (the water-ice interface) as a function of detector angle. Testing was conducted on ice containing biological material in the bottom layer and on ice cleared of 0.5 cm of this bottom layer. Results were compared to characterize the optical effects of the biological material layer.

1. INTRODUCTION

Knowledge of the optical properties of sea ice is critical for optical remote sensing analysis, under-ice bio-optical measurements, and polar energy balance research. However, optical propagation in sea ice is not well characterized. The optical properties of sea ice are affected by many variables, including ice thickness, surface conditions¹, dissolved and particulate components², air bubble content³, brine volume⁴, and growth history⁵. Inherent optical properties of ice are difficult to measure in situ, but these properties change when the ice is removed from its environment.

The goal of this research is to determine the optical characteristics of the water-ice interface as a function of its morphological/physical properties. The optical properties of the water-ice interface strongly influence the under-ice light field⁶, and the capabilities of optical remote sensors employed under the ice. In order to measure the optical characteristics of the water-ice interface, an optical apparatus was constructed to direct a pulsed, frequency doubled Nd:YAG laser beam (emitting at 532 nm) upward onto a selected spot on the water-ice interface, and measure the profile of the backscattered light.

2. TECHNICAL APPROACH

Two optical test units were constructed for this research. Both of these test units were designed to be deployed from the surface. The first test unit was designed to measure the effects of diver operations on the water-ice interface by monitoring the under-ice ambient light field. This test unit contained a detector that was deployed under the ice to measure ambient light (figure 1). The under-ice detector was mounted on a 125 cm arm to minimize the optical effect of the deployment hole on the measurements. The detector arm folded for deployment and retrieval of the detector.

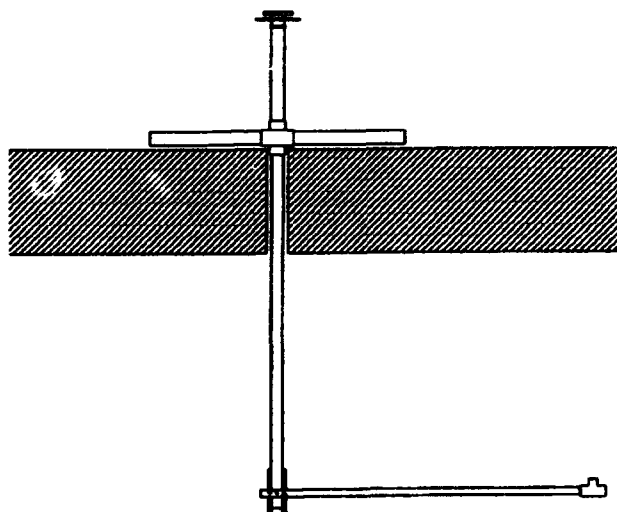


Fig. 1. Under-ice ambient light monitor diagram.

The second test unit was designed to measure backscatter profiles from the water-ice interface. This test unit contained a detector carriage mounted on a two meter horizontal underwater track that was deployed under the ice (figure 2). A frequency doubled Nd:YAG laser

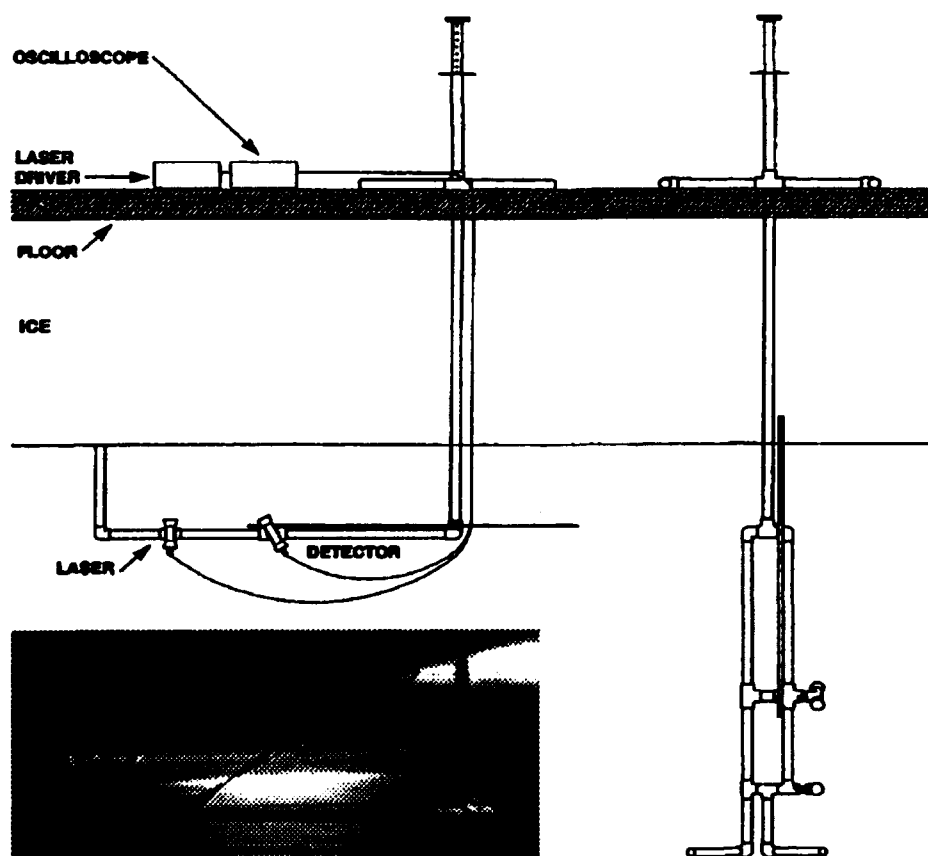


Fig. 2. Under-ice beam profile apparatus diagram and photograph (insert).

was mounted at the far end of the track. The detector carriage could be moved to any position along the track. The detector carriage contained an avalanche photodiode (APD) that was used to map spatial profiles of the light backscattered from the laser beam. This detector had a field of view of approximately 2° . An interference filter was mounted in front of the APD detector to minimize ambient light noise. The APD detector mount was adjustable so that spatial profiles of the reflected laser light could be measured as a function of detector look angle. However, the detector look angles could not be adjusted from the surface. Therefore, divers were used to set the detector look angle.

3. EXPERIMENTAL PROCEDURE

Testing was conducted on shore-fast ice at Resolute Bay in Canada in May of 1993. Ice in the test area was approximately 1.65 meters thick. Monitoring of the under-ice ambient light field began on 8 May. For these tests, an undisturbed site was chosen. After an access hole was drilled, the ambient light monitor was deployed under the ice. Ambient light measurements were taken as a function of position and time to determine the effects of diver activity on the water-ice interface (figure 3).

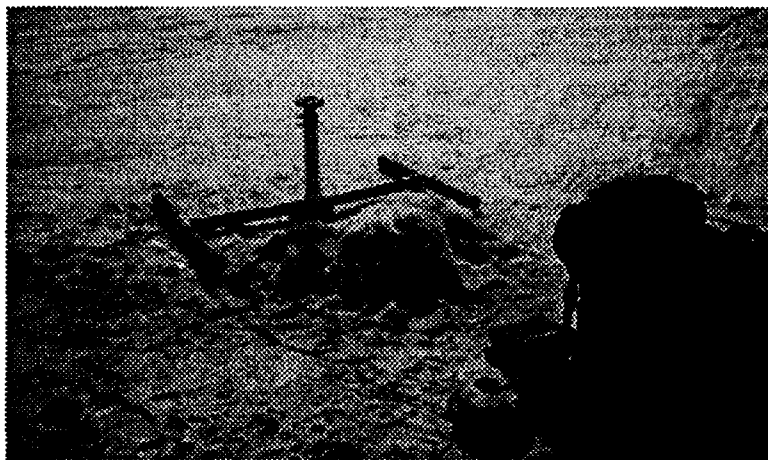


Fig. 3. Monitoring the under-ice ambient light field on 8 May 1993.

Preliminary testing of the beam profile apparatus was also conducted on 8 May. A 1.5 m^2 hole was cut in the ice for diver access. The apparatus was initially deployed through this hole to allow observation from the surface, streamline communication with divers, and simplify deployment during shakedown. The apparatus was deployed vertically through the access hole. The under-ice track was positively buoyant. One end of the track was attached to the vertical column with an elbow joint to allow the track to rotate into position. Weights attached to the free end of the under-ice track via cable were used to submerge the track and maintain it in a vertical position. When the track was submerged below the water-ice interface, the weights were raised, allowing the track to float upward, rotating at the joint until the legs at the free end of the track came into contact with the ice. The track was then levelled by adjusting the depth of the joint to compensate for depth variations of the water-ice interface. The laser was aligned to transmit upward, perpendicular to the track. Backscatter measurements were then taken as a function of position by moving the detector carriage along the track. The detector carriage could be positioned along the track by divers (figure 4) or by an operator on the surface. When the detector look angle was changed, the detector carriage was positioned next to the joint so that a diver could set the detector angle without disturbing the test site.

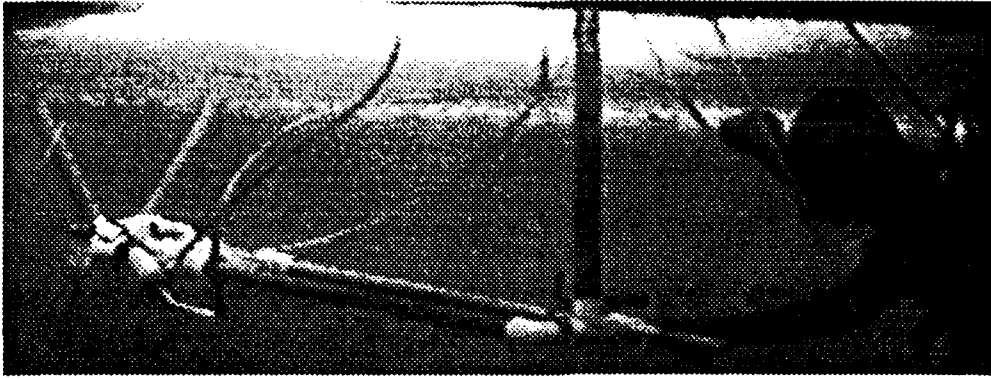


Fig. 4. Diver positioning the detector carriage for backscatter profile measurements.

On 9 May the beam profile apparatus was deployed at an undisturbed site where the water-ice interface contained a layer of biological material. Backscatter profiles from the water-ice interface were measured for detector look angles of 0° , 15° , 30° , 45° , and 60° , where 0° represents the detector positioned vertically looking directly up at the ice. Once this series of measurements was completed, divers removed a layer approximately 0.5 cm thick from the underside of the ice over an area of approximately 0.2 m^2 centered where the laser spot was incident on the water-ice interface (figure 5). Backscatter profile measurements as a function of detector look angle were then repeated for this section of ice. A lambertian scatterer was then placed against the ice and backscatter measurements were taken for comparison.

Testing was suspended on 10 May due to blizzard conditions. On 11 May, the laser was removed from the apparatus and mounted above the ice propagating downward. The apparatus was deployed under the ice and used to measure profiles of the laser beam transmitted through the ice. Transmission profiles were taken for ice thicknesses of 1.65 m, 1.26 m, and 0.85 m, and for detector look angles of 0° , 15° , 30° , and 45° . Different thicknesses were achieved by drilling down into the ice to a set depth, then transmitting the laser through the remaining ice thickness. Before making transmission measurements, the ice surface at the bottom of the drilled hole was smoothed and a small amount of seawater was applied to minimize surface effects. After these measurements were completed, divers again removed a layer approximately 0.5 cm thick from the underside of the ice, and another series of transmission profiles was taken.

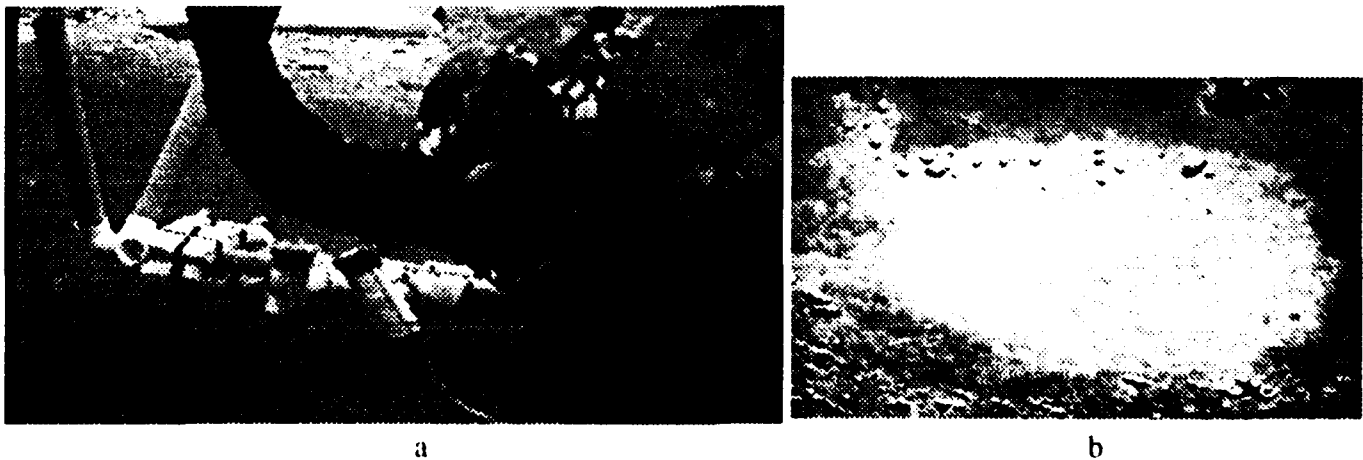


Fig. 5. Photographs of (a) a diver removing 0.5 cm layer from the underside of the ice above the laser, and (b) the underside of the ice after the layer was removed.

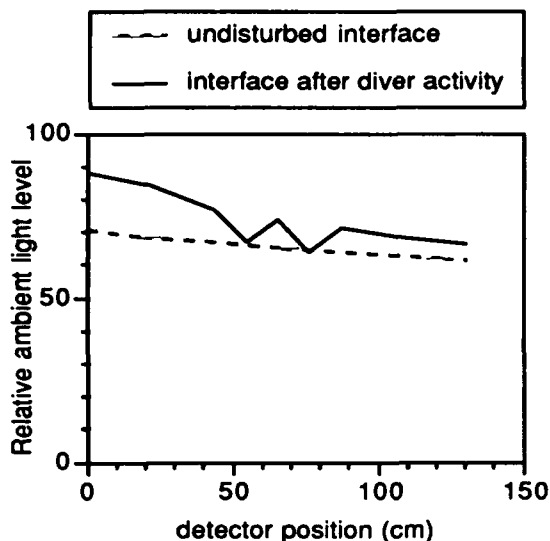


Fig. 6. Under-ice ambient light data.



Fig. 7. Trapped air bubble causing refraction of scattered laser light.

After transmission measurements were completed, the laser was mounted on the apparatus, and the apparatus was moved to an undisturbed site. Backscatter profiles from the water-ice interface were measured for detector look angles of 0° , 15° , 30° , 45° , and 60° .

4. RESULTS

Data from the under-ice ambient light monitor (figure 6) and diver observations (figure 5) demonstrated that diver operations affected the optical properties of the water-ice interface. Bubbles trapped under the ice affected optical propagation directly by creating an interface that produced refractive effects (figure 7). Over a matter of hours, trapped bubbles also caused depletion of the biological material and some melting of the ice surface above them. Therefore, procedures were followed to keep divers from disturbing the test sites.

Water transmission was measured on 9 May and 11 May. The attenuation coefficient for the water was 0.11 m^{-1} on 9 May and 0.12 m^{-1} on 11 May. Both of these values were constant to a depth of 10 meters.

Backscatter profiles from the water-ice interface were measured as a function of detector look angle before and after divers removed a 0.5 cm layer from the underside of the ice in the region of laser incidence. Results of these tests were compared to determine the optical effects of the biological material. From figure 8, it is evident that the presence of the biological material significantly reduced the received laser light. The normalized backscatter profiles show that the biological material also reduced the detectable beams spread. A comparison of the backscatter from the ice at 30° with and without the 0.5 cm layer to that of the lambertian scatterer at 30° is shown in figure 9. Backscatter measurements were also made on 11 May. Backscatter results from 9 May and 11 May are compared in figure 10. Significant differences were observed in the backscatter profiles from different locations.

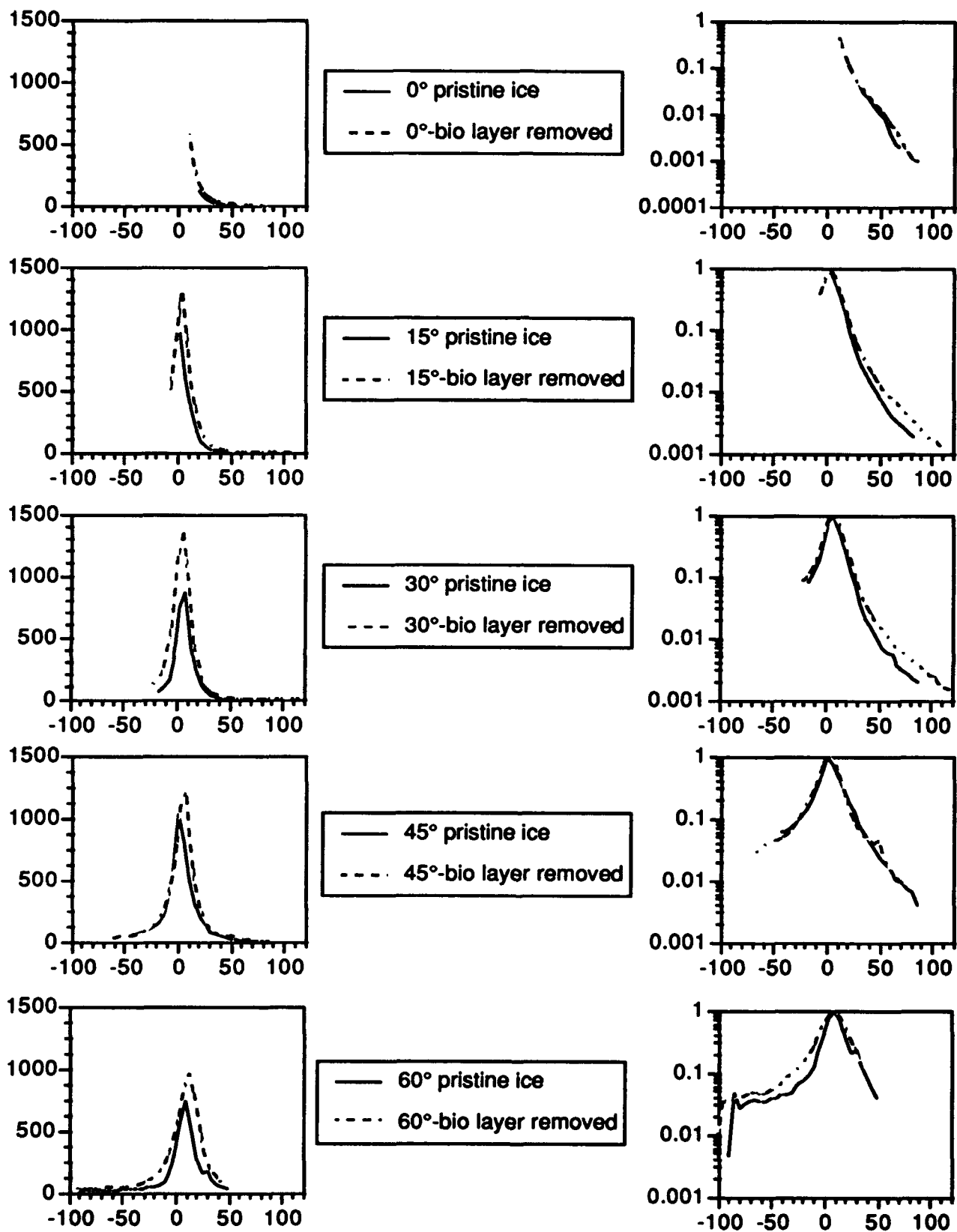


Fig. 8. Comparison of ice backscatter profiles taken before and after a 0.5 cm layer was removed from the bottom of the ice: received signal (mV) and normalized signal versus displacement (cm).

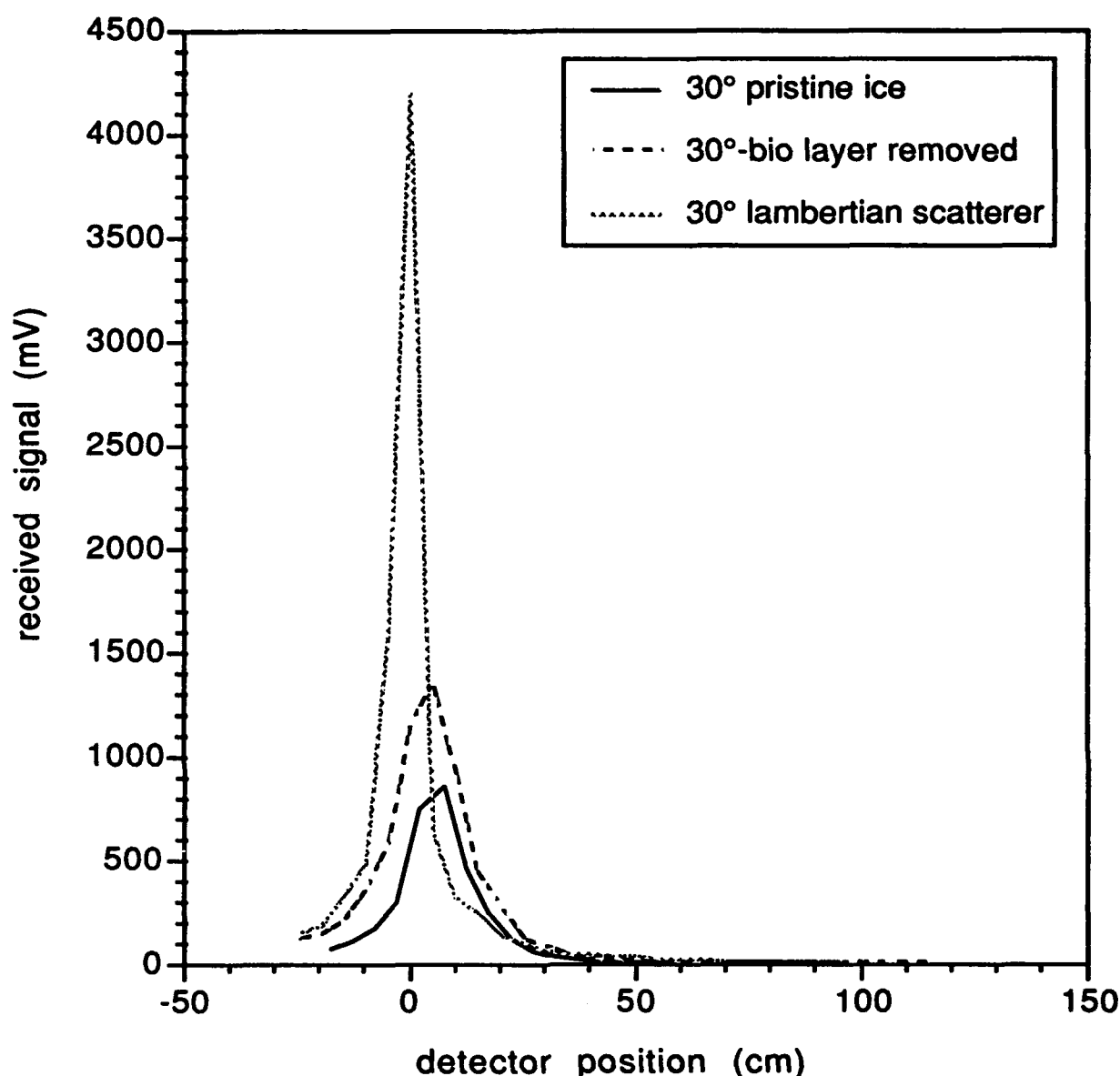


Fig. 9. Comparison of 30° backscatter profile from the ice with and without the 0.5 cm layer to that of a lambertian scatterer at 30°.

Transmission profiles are presented in figure 11. These profiles show that, for the detector look angles investigated, the intensity of the transmitted beam was nearly independent of detector look angle. Beamwidths were calculated for each ice thickness tested. The average value for beamwidth at full width, half maximum (FWHM) was approximately 1.08 m after transmission through 1.65 m of ice, 0.75 m after transmission through 1.26 m of ice, and 0.62 m after transmission through 0.85 m of ice. Beam attenuation coefficients were calculated for different layers of ice. The average attenuation coefficients were 3.55 m⁻¹ for the upper 39 cm of ice, 0.65 m⁻¹ for the central portion of the ice, and 10.9 m⁻¹ for the 0.5 cm layer of ice containing biological material.

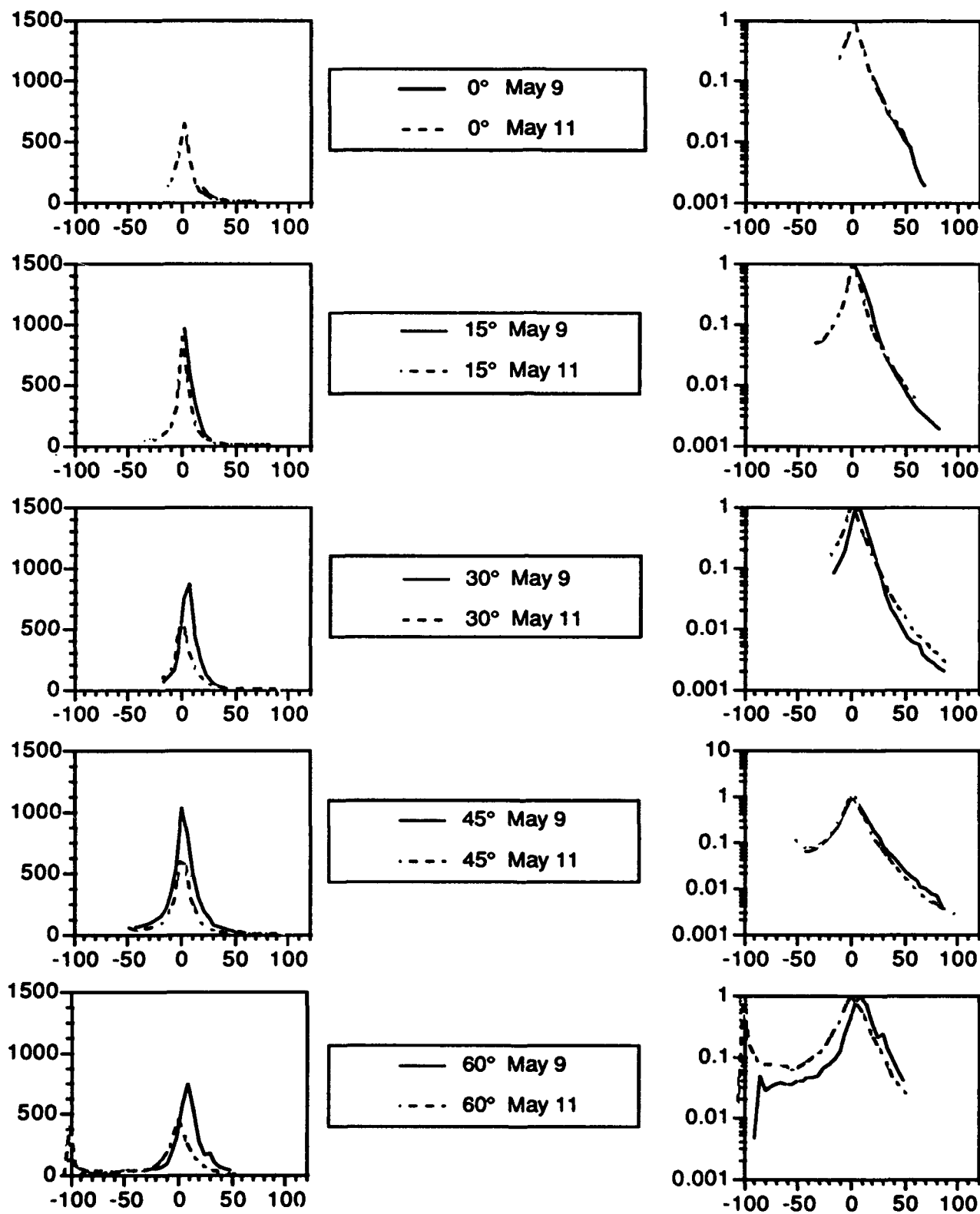


Fig. 10. Comparison of ice backscatter profiles taken on 9 May with those taken on 11 May at a different location: received signal (mV) and normalized signal versus displacement (cm).

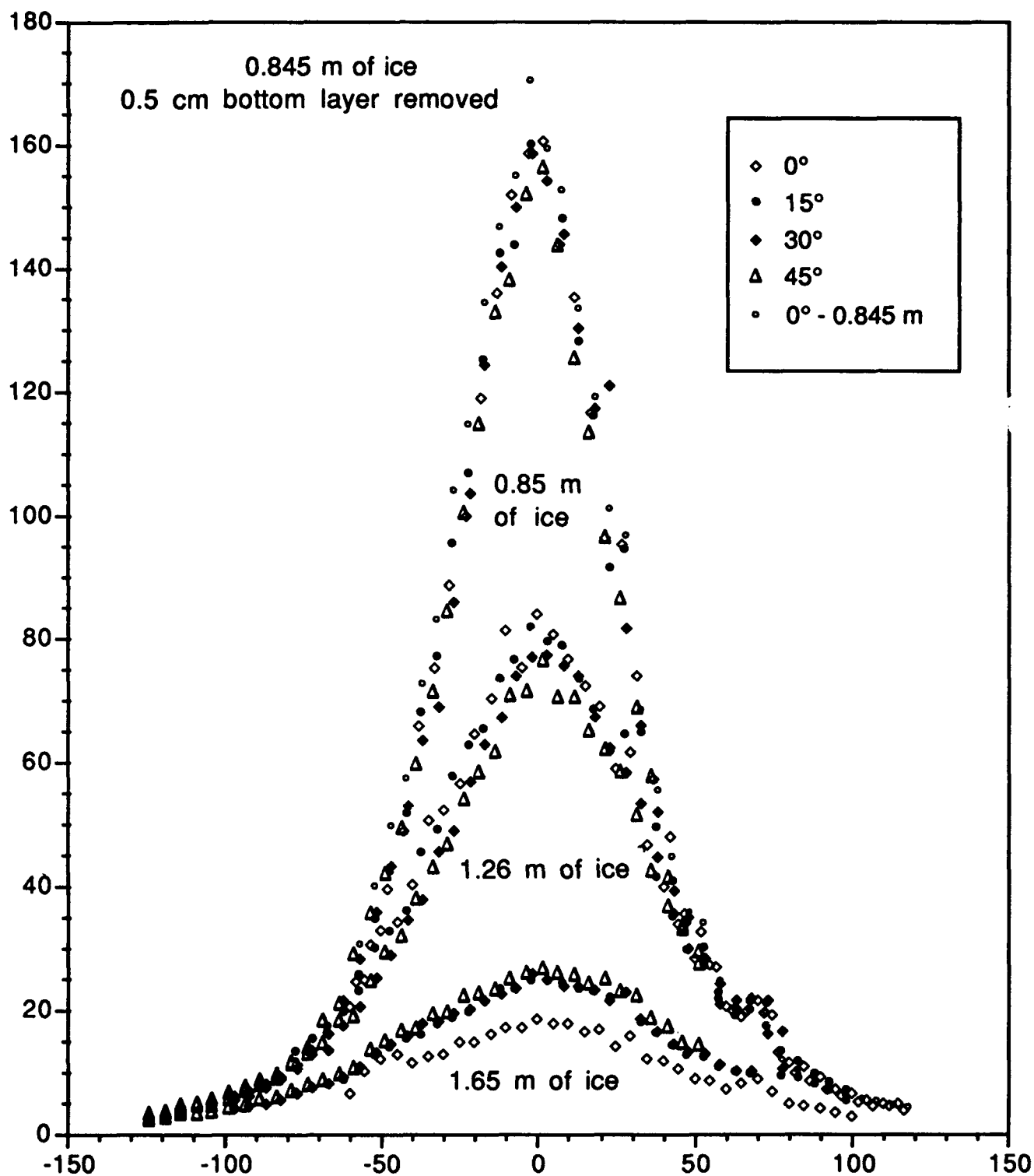


Fig. 11. Transmission profiles as a function of detector look angle for ice thicknesses of 1.65 meters, 1.26 meters, 0.85 meters, and 0.845 meters (0.5 cm of the bottom layer removed).

An attenuation coefficient was also calculated for the biological material using the backscatter data. For this calculation, we assumed that the backscatter from the biological material was small relative to that of the ice and that large-angle multiple scattering was negligible. We also assumed that the majority of the backscattered laser light propagated completely through the 0.5 cm layer, was scattered, then propagated back through the 0.5 cm layer at the angle it was detected. With these assumptions, we obtained attenuation coefficient values of 17.5 m^{-1} at 60° , 13.3 m^{-1} at 45° , and 38.5 m^{-1} at 30° . These correspond fairly well with the attenuation coefficient calculated from the transmission data, and with the values obtained by G.F. Cota⁷. Sources of the differences in attenuation values include the surface roughness and variability of the water-ice interface, surface effects caused by removal of the bottom layer of the ice, variations in the thickness of the removed layer, and changes in the biological material concentration.

5. CONCLUSION

The under-ice beam profile apparatus was used to measure the backscatter profile from the underside of the ice as a function of detector look angle. The backscatter measurements showed that a significant amount of light (greater than 10% of the lambertian return for the detector look angles tested) is backscattered from the underside of the ice. However, the backscattered signal was strongly influenced by location and by the amount of biological material present in the bottom layer of the ice.

6. ACKNOWLEDGEMENTS

This research was supported by the Office of Naval Research and by the NUWC Independent Research Office. The authors would like to thank the NUWC scientific dive team for their invaluable help in this research, and G.F. Cota for his assistance in the field testing at Resolute.

7. REFERENCES

1. T.C. Grenfell and G.A. Maykut, "The optical of ice and snow in the Arctic Basin," *J. Glaciol.*, 18(80), pp. 445-463, 1977.
2. C. H. Fritsen and R.H. Iturriaga, "Influence of particulate matter on spectral irradiance fields and energy transfer in the Eastern Arctic Ocean.", SPIE Vol.1750, Ocean Optics XI, pp. 527-541, 1992.
3. D.K. Perovich, G.A. Maykut, and T.C. Grenfell, "Optical properties of ice and snow in the polar oceans. I: observations," SPIE Vol. 637 Ocean Optics VII, pp. 232-241, 1986.
4. D.K. Perovich and T.C. Grenfell, "Laboratory studies of the optical properties of young sea ice," *J. Glaciol.*, 27(96), pp. 331-346, 1981.
5. J.A. Richter-Menge and D.K. Perovich, "An overview of sea ice physical properties and their variability," SPIE Vol.1750, Ocean Optics XI, pp. 486-497, 1992.
6. R.E.H. Smith, J. Anning, P. Clement, and G.F. Cota, "Abundance and production of ice algae in Resolute Passage, Canadian Arctic," *Mar. Ecol. Prog. Ser.*, Vol. 48, pp. 251-263, 1988.
7. G.F. Cota, "Arctic sea ice bio-optics," *EOS Journal*, Vol. 75, p. 229, 1994.

**Transport of photosynthetically active radiation
in sea ice and ocean**

Zhonghai Jin, Knut Stamnes, and W. F. Weeks

**Geophysical Institute, University of Alaska
Fairbanks, AK 99775-7320**

ABSTRACT

A recently developed radiative transfer model is applied to study the transport of photosynthetically active radiation (PAR) in the whole coupled atmosphere, sea ice and ocean system. This model rigorously accounts for the multiple scattering and absorption by the atmospheric molecules, clouds, snow and sea water, as well as the brine pockets and air bubbles trapped in sea ice. Both the spectral distribution and the seasonal variation of PAR at various levels in the ice and ocean have been investigated for different conditions. Results show that clouds, snow and ice algae all have important effects on the PAR availability to the microbial community under ice. For example, 10 cm of new snow can reduce the total PAR entering the ocean under a 1.0 m of ice by a factor of 10. The algae in the ice also significantly alters the spectral distribution of PAR transmitted to the ocean. Compared with the effects of clouds, snow and ice algae, the effect of changes in the amount of ozone in the atmosphere, the main absorptive gas in the PAR spectrum, on the amount of PAR entering the ice and ocean is negligible. The total PAR transmitted to the ocean is also sensitive to the ice thickness, especially when the ice is thin and the solar elevation is high. Clouds not only reduce the total PAR entering the ocean, but also reduce the sensitivity of this PAR variation to the variation in ice thickness.

1. INTRODUCTION

In the polar oceans, light transmission through the atmosphere and sea ice is essential to the growth of plankton and algae.¹⁻³ Understanding the physical conditions that affect the growth of plankton and algae is not only of interest in its own right, but as this material represents primary production upon which the food chains of the polar oceans are based, it is a requisite to understanding the behavior of the complete marine ecosystem in such regions. The atmosphere is almost transparent to photosynthetically active radiation (PAR). Within the spectral region of PAR (400 nm--700 nm), ozone is the only absorptive gas of significance present in the atmosphere. Even clouds and sea ice have a relatively weak absorption in this part of the spectrum. In addition, nearly 40% of the extra-terrestrial solar radiation lies within this narrow spectral region and much more than 40% of the total solar radiation incident on the ice surface is within the PAR range, depending on the atmospheric conditions. Therefore, PAR constitutes the main light resource for the primary productivity in the ice-covered oceans. PAR also experiences much greater seasonal variability and rapid temporal variations at high latitudes. Clouds and snow as well as the amount and distribution of algae within the ice also have a significant impact on the light availability under sea ice. To quantify the light transport in the atmosphere, snow, sea ice and ocean, we have developed a radiative transfer model for this coupled system. Our purpose here is to study the transfer of PAR in this system, and to quantify the effects of clouds, snow and algae as well as ozone in the atmosphere on the available light for photosynthesis both within the ice and in the ocean below.

2. MODEL DESCRIPTION

The discrete ordinate method has been used to solve the radiative transfer equation in the coupled atmosphere, sea ice and ocean system. The theoretical treatment is described by Jin and Stamnes.⁴ For convenience, we give a brief description here. The main difference in solving the radiative transfer equation consistently in such a coupled system from a solution that treats only the atmosphere is caused by the changes in refractive index across the air-ice or air-water interface. The reflection and refraction occurring at these interfaces give rise to different source terms in the transfer equation, and therefore to different solutions. In addition, they complicate the continuity conditions across the interface. To take into account the refraction and reflection automatically and solve the transfer equation consistently in the whole system, different and appropriate quadrature directions (streams) and weights have been applied in the atmosphere, sea ice and ocean. The same number of streams is used in the atmosphere and the refractive region of the ice and ocean that communicate directly with the atmosphere. In addition, separate streams are adopted to take into account the total reflection region in the ice and ocean. The choice of stream numbers is flexible and may be tailored to satisfy competing requirements of computational accuracy and speed. The atmosphere, ice and ocean each can be divided into a sufficient number of layers to adequately resolve the optical properties. The computational speed is proportional to the number of layers in the model, but entirely independent of the optical depth of individual layers (and thus of the total optical depth).

Within the atmosphere, we consider the absorption and scattering by atmospheric gases, clouds and aerosols. The optical properties of clouds are parameterized in terms of the equivalent droplet radius and the liquid water content of clouds,^{5,6} an approach which has been proven to produce satisfactory results.

The optical properties of snow including possible soot contamination are obtained through Mie computations, which require the refractive index of ice/soot and the mean radius of snow grains and soot particles as input.⁶ We have adopted the model of Wiscombe and Warren⁷, whose results for computed snow albedo agree well with available field measurements.

In sea ice, the processes considered include absorption by pure ice, as well as scattering and absorption by brine pockets and air bubbles trapped within the ice as described by Grenfell⁸. To obtain the optical properties for the bulk ice, the relative amounts of each component in a given volume in the sea ice have to be determined. Based on the work by Cox and Weeks,⁹ certain relations exist among the brine volume fraction, air volume fraction, salinity (S), temperature (T), bulk density (ρ), and pure ice density (ρ_i) due to the phase equilibrium constraints. Therefore, the brine volume fraction (V_{br}) and the air volume fraction (V_{bu}) can be determined by

$$V_{br} = \rho S / F_1(T) \quad (1)$$

$$V_{bu} = 1 - \frac{\rho}{\rho_i} + \rho S F_2(T) / F_1(T) \quad (2)$$

where $F_1(T)$, $F_2(T)$, $C(T)$ and ρ_i are parameterized functions of temperature.

The optical properties of the brine pockets and air bubbles are obtained from Mie calculations⁸. The absorption coefficient for pure ice is based on the data sets reported by Grenfell and Perovich¹⁰ and by Warren.¹¹ The chlorophyll a specific absorption coefficient for sea ice microalgae was kindly provided to us by Arrigo.¹² Therefore, the attenuation in the sea ice is related to the ice temperature, density and salinity as well as to the ice algae concentration, which may vary from layer to layer.

In the ocean, scattering and absorption coefficients of the sea water are taken from Smith and Baker.¹³ Only pure sea water is considered in this work. We have neglected the refraction at the ice-ocean interface, because the refractive indices of water and ice are very similar within the spectral region of PAR.

3. RESULTS AND DISCUSSION

In the following computations, we adopt the McClatchey atmosphere model for the subarctic summer¹⁴ and the atmosphere is divided into 25 layers. In the spectral region of PAR, atmospheric

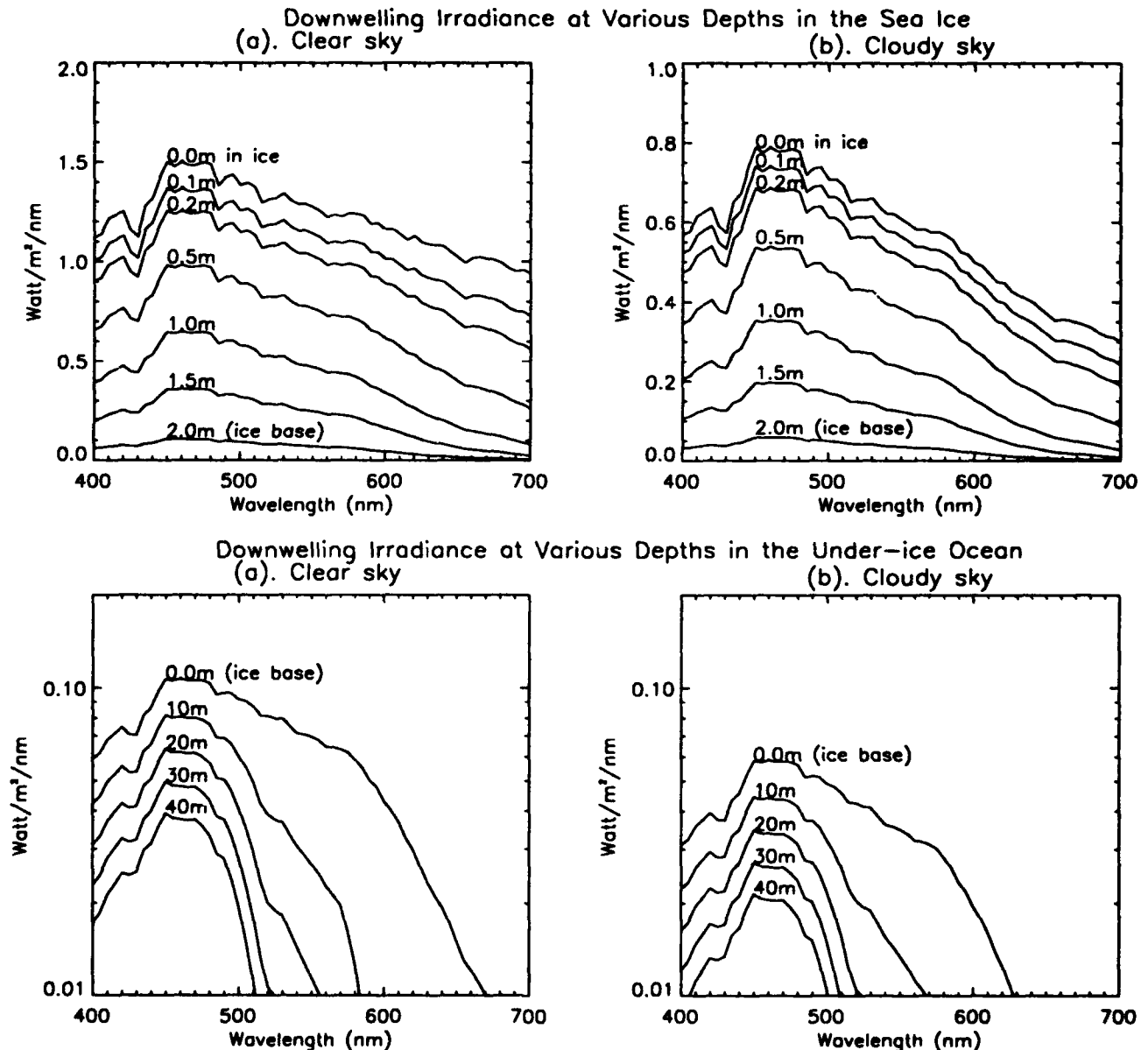


Figure 1: The spectral distribution of downwelling irradiance at various depths in the sea ice and ocean for clear skies and cloudy skies respectively. Ice thickness is specified to be 2.0 m, salinity 8‰, density 0.9 Mg/m³ and solar elevation 30°.

absorption is mainly by ozone. The ozone profile is also taken from the McClatchey atmosphere while the absorption cross section of ozone and the scattering cross section by air molecules are taken from a compilation by WMO.¹⁵ For sea ice, we assume a constant salinity of 8‰ and a constant density of 0.90 Mg/m^3 . We will also assume that there is a linear temperature profile with the bottom temperature of the ice fixed at -1.8°C . The ice is divided into 4 layers. In the ocean, we will neglect vertical variations in the properties of sea water and consider it as one homogeneous layer. Also, we will apply 16 streams in the atmosphere and 28 streams in the ice and ocean in most of the following computations, which provides a computational accuracy better than 1%.

Using the atmosphere, sea ice and ocean models described above, We show Figure 1 the spectral distribution of PAR at different levels in the ice and in the ocean respectively. The ice is assumed to have a thickness of 2.0 m and surface temperature of -15°C . The spectral distribution of PAR incident at the top of atmosphere is from Nicolet¹⁶ and the solar elevation is specified to be 30° .

In the right panels of Figure 1, we have included a layer of low-level stratiform cloud in the atmosphere, a condition which is known to be persistent and extensive in the summer Arctic.^{17,18} The cloud is specified to have an equivalent droplet radius of $7 \mu\text{m}$ and a water content of 0.3 g/m^3 , with a thickness of 400 m and cloud base at 600 m, values typical for the Arctic summer stratus.

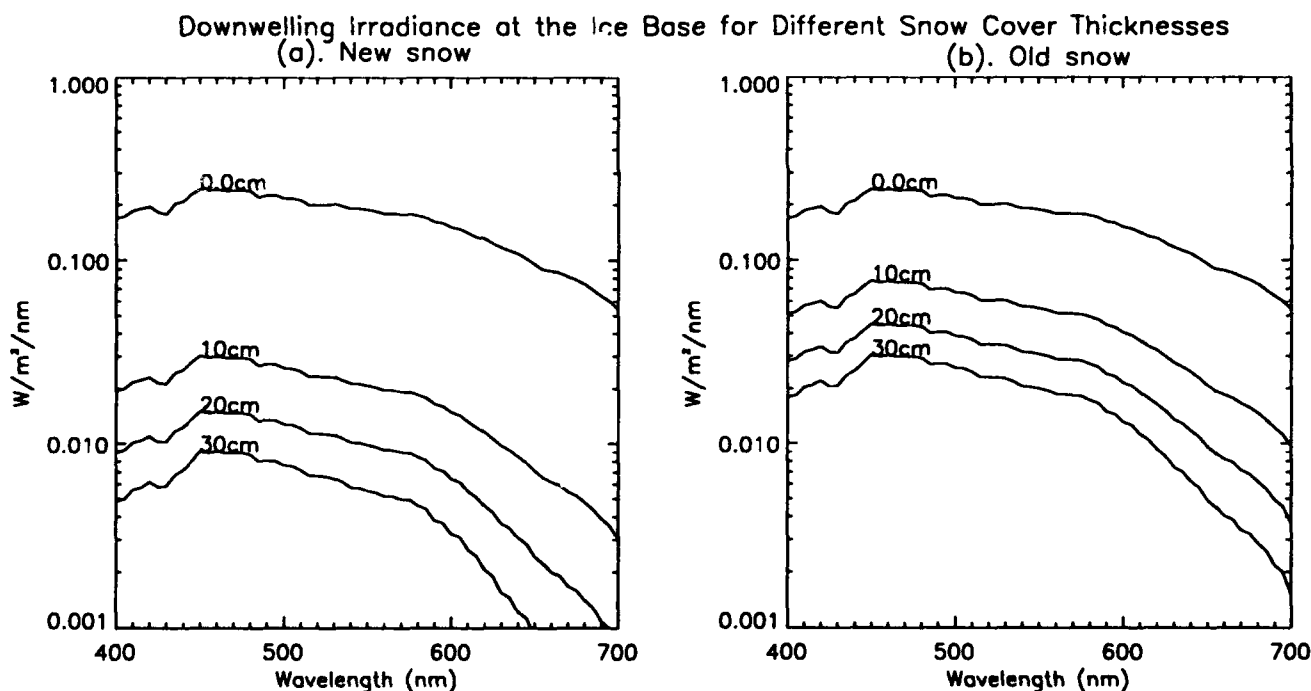


Figure 2: The spectral distribution of downwelling irradiance at the ice base as affected by the thickness and type of snow cover on the surface. The same atmosphere, sea ice and ocean models are used as in Figure 1. The ice thickness is taken to be 1.0 m and the skies are assumed to be clear. The values on each line denote the snow thickness.

Snow cover is another prevalent feature in the high latitude oceans. Based on field observations, new snow has a smaller grain size and a lesser density than melting old snow. We specify a mean grain radius of $100 \mu\text{m}$ and density of 0.2 Mg/m^3 as representative of new snow, and a grain radius of 1000

μm and density of 0.45 Mg/m^3 as representative of melting old snow. The simulated downwelling irradiance at the ice base for different snow thicknesses is shown in Figure 2. The same atmosphere, sea ice and ocean models as above are used here, but the ice thickness is specified as 1.0 m. Figure 2 shows that the snow significantly reduces the light availability under the ice, especially for the new snow. Only 10 cm of new snow can reduce the irradiance at the ice base by a factor of 10. Because of the small grain size, new snow efficiently scatters light back to the atmosphere.

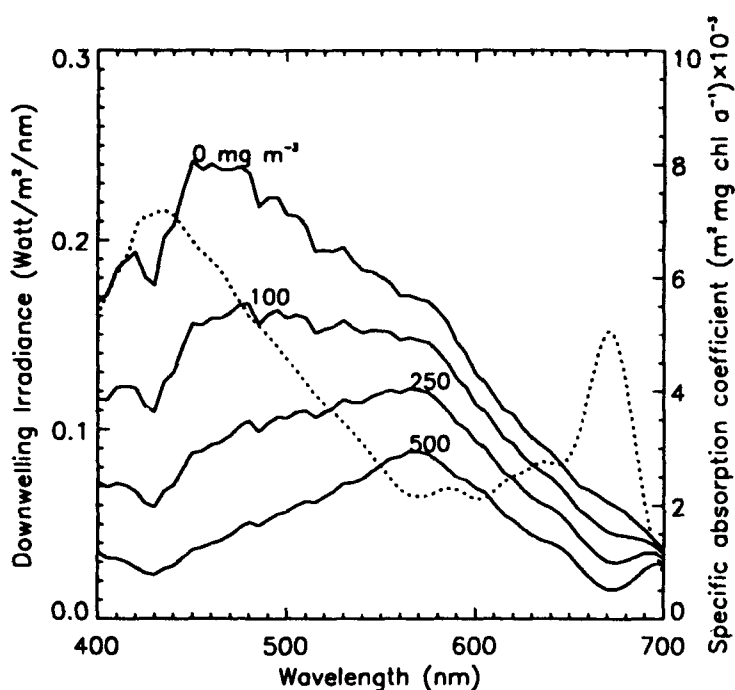


Figure 3: The downwelling irradiance entering the ocean under a 1.0 m thick sea ice sheet for various ice algae concentrations. The algae is assumed to occur in the lowest 40 cm of the ice. The values on each line represent the chl *a* concentration (mg/m^3). The dotted line represents the chl *a* specific absorption coefficient for sea ice microalgae.

variation of the total PAR as calculated at 78°N at local noon under a clear sky and a cloudy sky respectively. The same atmosphere, cloud, sea ice and ocean models as above have been adopted and the surface is assumed to be snow-free. The right panels demonstrate the corresponding decrease of total PAR relative to the clear sky conditions at three levels due to the presence of the cloud. The results show that a decrease in PAR over 50% can occur for the typical Arctic cloud used here. Although the absolute decreases at every level show a maximum at the summer solstice, the relative changes show a minimum at this time. This is caused by different solar elevations at noon on different days.

Similarly, Figure 5 shows the downwelling PAR at the same 1.0 m ice base at 78°N at local noon for clear skies and four different snow and ice conditions: (i) without snow on the ice surface or algae in the ice, conditions which represent an upper limit; (ii) snow-free but with a layer of algae with a

The ice algae has been shown to have a important impact on light transmission into the ocean.^{1,19} Including a layer of algae in the lowest 40 cm of ice, we show in Figure 3 the downwelling irradiance at the ice base for four different chlorophyll *a* concentrations (0, 100, 250 and 500 mg/m^3). The results indicate that the presence of algae not only reduces the light transmission, but it also significantly changes the spectral distribution of PAR entering the ocean. The spectral alteration of the transmitted light is well correlated to the spectrum of the chl *a* absorption coefficient for sea ice microalgae, which exhibits two big absorption peaks in the PAR spectrum (the dotted curve in Figure 3).

Although the daily solar radiation at high latitudes experiences a greater seasonal variability than at lower latitudes, the pattern of temporal change of daily PAR is similar to the pattern of noon value evolution. Figure 4 shows the temporal

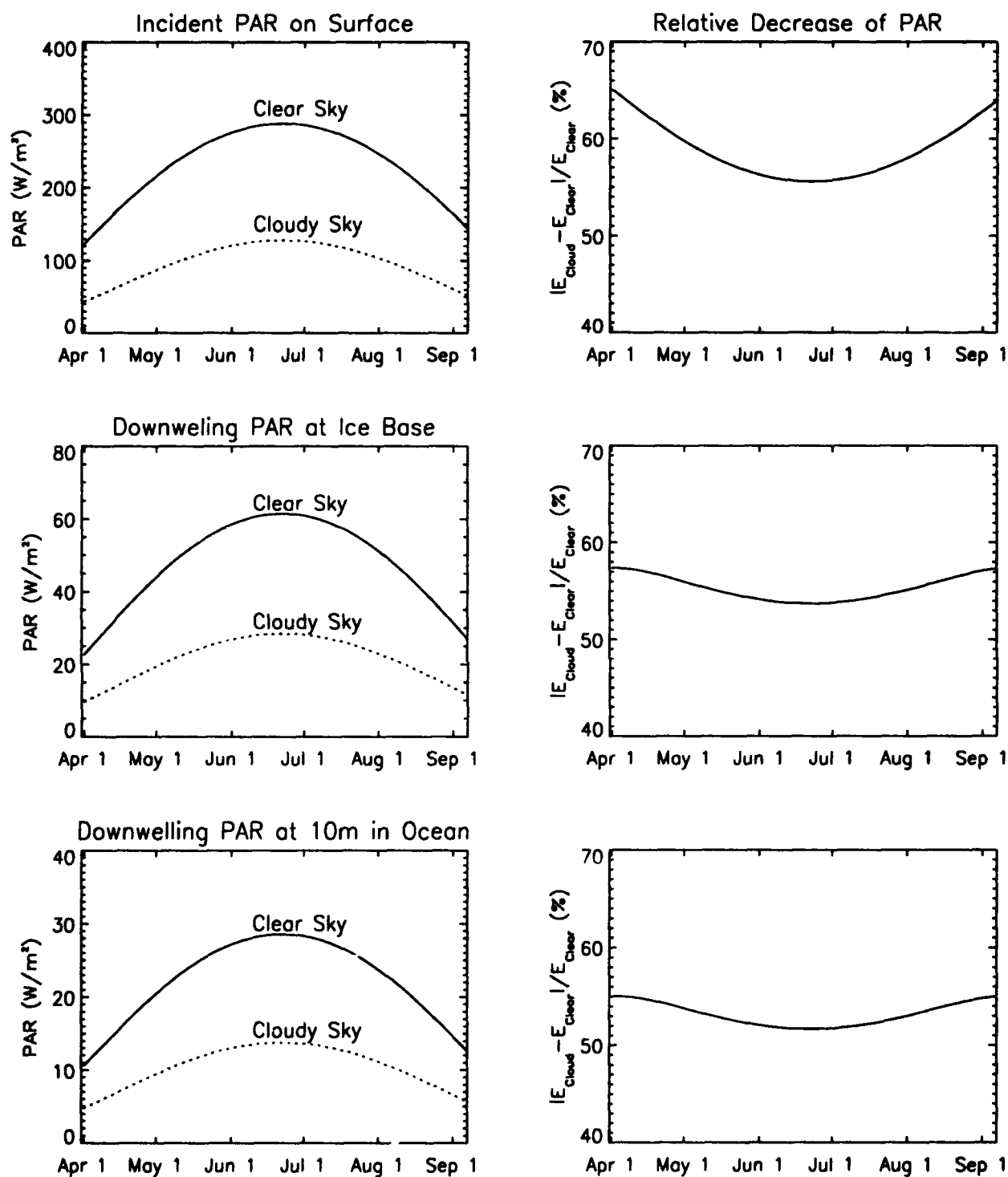


Figure 4: Seasonal variation of total PAR at the surface, at the base of a 1.0 m thick ice sheet and at 10 m depth in the ocean under clear skies and cloudy skies respectively. The right panels demonstrate the corresponding relative decrease due to the presence of cloud. The same atmosphere, cloud, sea ice and ocean model as above are adopted. Values are derived at latitude 78°N at local noon.

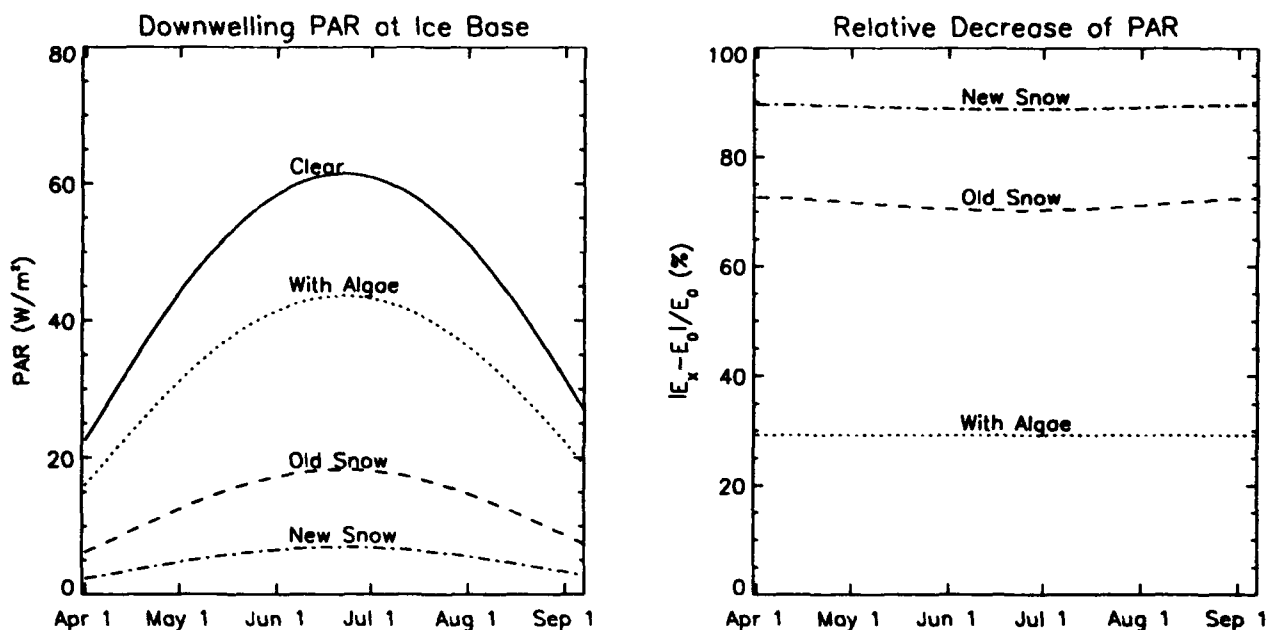


Figure 5: Total downwelling PAR entering the ocean under a 1.0 m of ice for four different conditions: (i) clear sky without snow on surface and algae in ice, hence represents an upper limit; (ii) including a layer of algae with chl *a* concentration of 100 mg/m^3 ; (iii) with a 10 cm layer of melting old snow and (iv) with 10 cm of new snow. The right panel shows the corresponding decrease of PAR relative to the "clear" case.

chl *a* concentration of 100 mg/m^3 in the lowest 40 cm of ice; (iii) with a 10 cm layer of melting old snow and (iv) with a 10 cm of new snow. The algae and snow models are the same as discussed earlier. The results show that 10 cm of new snow can reduce the PAR available at the ice base by 90%. The independence of the relative change caused by algae to the day number or the solar elevation is due to the fact that only the absorption is considered for the ice algae and the direct component of the solar radiation is negligible in the algae layer.

Acting as the only significant absorptive gas affecting the transfer of PAR in the atmosphere, ozone is another factor affecting the availability of PAR to the marine microbial communities existing under sea ice covers. Here we take the total column ozone abundance of 350 DU as normal. Figure 6 shows the seasonal variation of PAR at three different levels and three different ozone depletion scenarios. The right panels show the corresponding increases of PAR for the ozone depletion scenarios of 250 DU (30% less than normal) and 175 DU (50% less than normal). Depending on the solar elevation, a 50% ozone depletion yields an increase in total PAR at the ice base as well as at 10 m depth in the ocean less than 4%, a minor change compared with the impacts of clouds, snow and algae as shown above.

Figure 7 shows the downwelling PAR at the ice base as a function of the ice thickness for different solar elevations under a clear sky and a cloudy sky respectively. Obviously, ice thickness has a significant effect on the light transmission into the ocean, especially when the ice is thin. Higher solar elevations enhance this ice thickness dependence. Not only do clouds drastically reduce the PAR entering the ocean, but they also reduce the sensitivity of the variation of the under-ice PAR to the

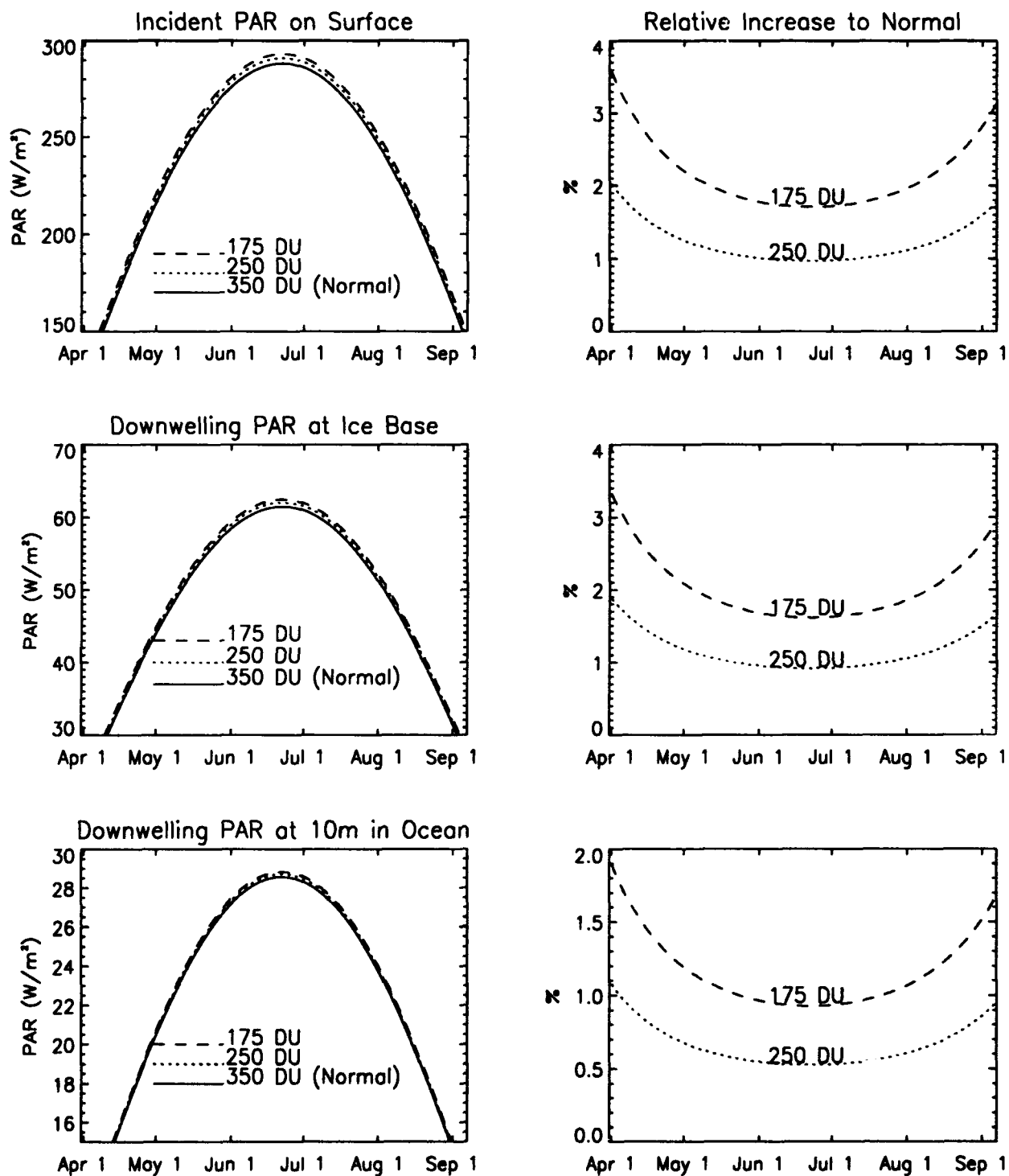


Figure 6: Similar to Figure 4, but showing the ozone effect under clear skies. The total column ozone abundance of 350 DU is taken as normal. The increases of total PAR relative to normal values are shown in the right figures for two ozone depletion scenarios (250 DU, 30% less than normal and 175 DU, 50% less than normal).

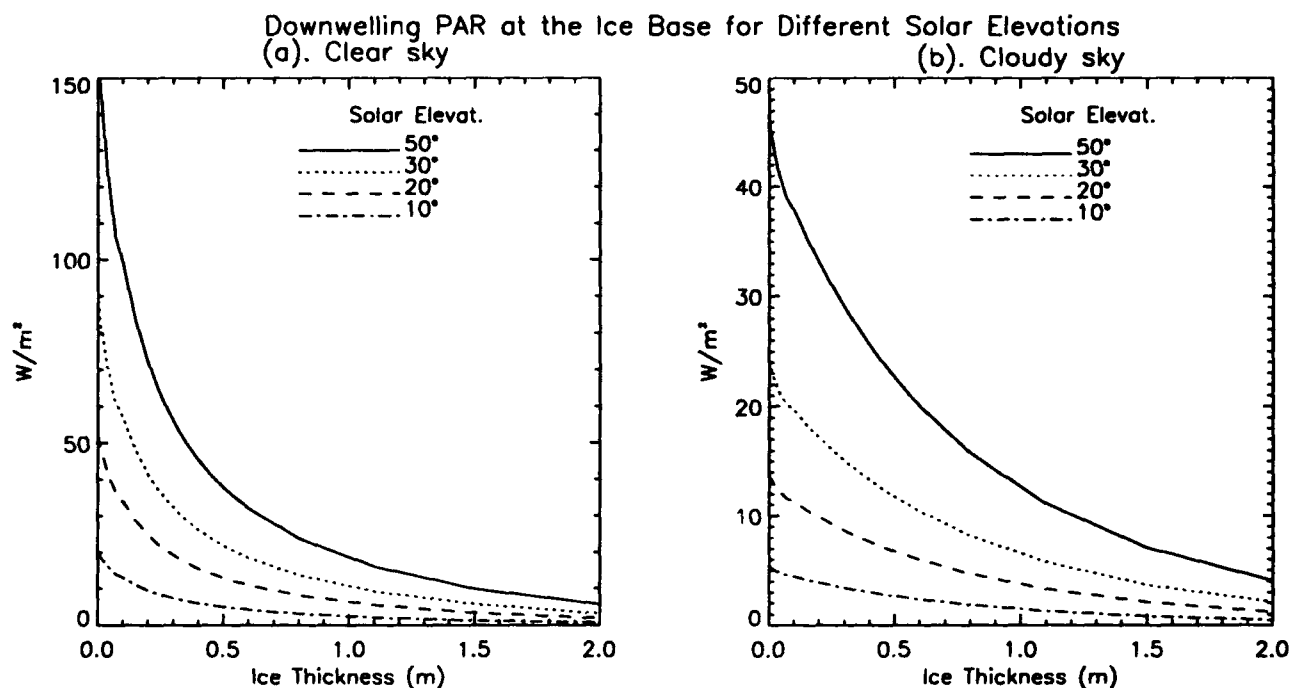


Figure 7: Total downwelling PAR entering the ocean as a function of ice thickness for various solar elevations.

ice thickness. This is due to the relative increase in the diffuse irradiance (as compared to the direct component) for cloudy conditions.

4. CONCLUSION

The transport of the photosynthetically active radiation in the atmosphere, snow, ice and ocean column has been studied by implementing a newly developed radiative transfer model for the coupled atmosphere, ice and ocean system. This model solves the radiative transfer equation in the whole system consistently and automatically takes into account the refraction and reflection at the air-ice interface. The atmosphere, sea ice and ocean are divided into a sufficient number of layers to adequately resolve the variations in their optical properties. Cloud effects have been incorporated by parameterizing their optical properties in terms of liquid water content and cloud droplet equivalent radius. The optical properties of brine pockets and air bubbles trapped in the ice are obtained through Mie calculations, which are based on the fraction volume of each component which, in turn, is derived from the temperature, density and salinity of the sea ice. The model rigorously accounts for multiple scattering. The number of streams depends on the refractive index and can be specified based on ones accuracy requirements.

The modeling results show that clouds, snow and ice algae all have significant effects on the transport of PAR in the sea ice and ocean. A 10 cm layer of new snow is sufficient to reduce by 90% the total PAR available to the marine biological communities under ice. The ice algae also drastically changes the spectral distribution of PAR transmitted through the ice. Although it is acting as the main absorptive gas in the spectral region of PAR, the ozone in the atmosphere has a negligible effect on the light available to the biosphere under the ice when compared with the effects of clouds, snow and

algae. A 50% ozone depletion would increase the total PAR by less than 4% at any level in the ice and ocean. The total PAR transmitted through the ice is sensitive to ice thickness, especially when the ice is thin and the solar elevation is high. Clouds not only reduce the PAR amount in the ocean, but also reduce the sensitivity of the available PAR under the ice to variations in ice thickness.

5. ACKNOWLEDGMENTS

This work is supported by DOE grant 091574-A-Q1 and NSF grant DPP92-00747 to the university of alaska.

6. REFERENCES

1. J. B. Soo Hoo, A. C. Palmisano, S. T. Kottmeier, M. P. Lizotte, S. L. Soo Hoo, and C. W. Sullivan, "Spectral light absorption and quantum yield of photosynthesis in sea ice microalgae and bloom of *Phaeocystis Pouchetii* from McMurdo Sound, Antarctic," *Mar. Ecol. Prog. Ser.*, 39, 175-189, 1987.
2. O. Holm-Hansen, S. Z. El-Sayed, G. A. Franceschini, and R. L. Cuhel, "Primary production and the factors controlling phytoplankton growth in the Southern Ocean," in *Adaptations within Antarctic ecosystems*, G. A. Llano, editor, p. 11-50, Smithsonian Institute, Washington, D. C., 1977.
3. K. R. Arrigo, J. N. Kremer and C. W. Sullivan, "A simulated Antarctic fast ice ecosystem," *J. Geophys. Res.*, 98, 6929-6946, 1993.
4. Z. Jin and K. Stamnes, "Radiative transfer in nonuniformly refracting layered media: atmosphere-ocean system," *Appl. Opt.*, 33, 431-442, 1994.
5. A. Slingo and H. M. Schrecker, "On the shortwave radiative properties of stratiform water clouds," *Quart. J. Roy. Meteor. Soc.*, 108, 427-426, 1982.
6. S. C. Tsay, K. Stamnes and K. Jayaweera, "Radiative energy budget in the cloudy and hazy Arctic," *J. Atmos. Sci.*, 46, 1002-1018, 1989.
7. W. J. Wiscombe and S. G. Warren, "A model for the spectral albedos of snow, 1, Pure snow," *J. Atmos. Sci.*, 37, 2712-2733, 1980.
8. T. C. Grenfell, "A radiative transfer model for sea ice with vertical structure variations," *J. Geophys. Res.*, 96, 16,991-17,001, 1991.
9. G. F. N. Cox and W. F. Weeks, "Equations for determining the gas and brine volumes in sea ice samples," *J. Glaciol.*, 29, 306-316, 1983.
10. T. C. Grenfell and D. K. Perovich, "Radiation absorption coefficients of polycrystalline ice from 400-1400nm," *J. Geophys. Res.*, 86, 7447-7450, 1981.
11. S. G. Warren, "Optical constants of ice from the ultraviolet to the microwave," *Appl. Opt.*, 23, 1206-1225, 1984.
12. K. R. Arrigo, Personal communication, 1993.
13. R. C. Smith and Baker, K. S., "Optical properties of the clearest natural waters," *Appl. Opt.*, 20, 177-184, 1981.

14. R. A. McClatchey, R. W. Fenn, J. E. A. Selby, F. E. Volz, and J. S. Garing, Rep. AFCRL-72-0497, (Air Force Cambridge Research Laboratories, Bedford, Mass., 1972).
15. World Meteorological Organization, "Global ozone research and monitoring project: Atmospheric ozone 1985," *World Meteorological Organization Rep. No. 16*, Volume 1, 1985.
16. M. Nicolet, "Solar spectral irradiances with their diversity between 120 and 900 nm," *Planet Space Sci.* 37, 1249-1289, 1989.
17. G. F. Herman and R. M. Goody, "Formation and persistence of summertime Arctic stratus clouds," *J. Atmos. Sci.*, 33, 1537-1553, 1976.
18. S. C. Tsay and K. Jayaweera, "Physical characteristics of arctic stratus clouds," *J. Climate Appl. Meteor.*, 23, 584-596, 1984.
19. K. R. Arrigo, C. W. Sullivan and J. N. Kremer, "A bio-optical model of Antarctic sea ice," *J. Geophys. Res.*, 96, 10,581-10,592, 1991.

USE OF BEAM SPREADING MEASUREMENTS TO ESTIMATE VOLUME SCATTERING PROPERTIES IN SEA ICE

Fred J. Tanis
Center for Earth Sciences
Environmental Research Institute of Michigan
Ann Arbor, Michigan 48107
tel: 313-994-1200
fax: 313-994-5824
e-mail: TANIS@vaxa.crim.org

ABSTRACT

Beam spread measurements have been made on sea ice samples and used to develop estimates of the volume scattering function at small scattering angles. In this technique Gaussian-like modelled beam spread functions (BSF) are used to derive the modulation transfer function (MTF) and Well's theory is applied to estimate the volume scattering function for the sea ice medium. A Monte Carlo model for beam propagation through homogeneous sea ice layers was used to estimate beam spreading and the surface distributions of irradiance and radiance. Light scattering was assumed to occur from the presence of spherical bubbles trapped within the ice. Volume scattering functions used in the model were calculated with Mie theory or derived from measured BSF's. The BSF's generated by the model, using estimated optical properties, were found to be comparable to those derived from the transforms over a range of ice thicknesses. The scattering transform technique was applied to beam spread data collected during Arctic and laboratory experiments for samples of young, first year, and multiyear ice to derive estimated MTF values. Requirements and limitations for applying this technique to sea ice are discussed.

1. INTRODUCTION

In sea ice, optical scattering properties are highly dependent on the intricate structure of air bubbles, brine channels, and internal platelet boundaries and considered important to the estimation of the visible radiative transfer through the Arctic sea ice cover. Variability in optical properties results from changes in the size and shape of these structural features induced by seasonal morphological changes to the ice sheet. Phytoplankton and detrital particles can also be present in large quantities to both absorb and scatter light. Measurement of the BSF may be the most direct means to characterize scattering for such a complex and highly variable medium. Volume scattering measurements have been previously made on sea ice samples over large angles in the laboratory but have not been made for small angle forward scattering angles¹. Extensive field measurements of beam spread will improve knowledge of light scattering phenomena in sea ice and its relationship to observed physical properties. These physical properties impact the optical albedo and transmission of the ice sheet and snow cover which are essential to understanding seasonal short and long wave radiation exchanges. For sea ice, frequently the greatest concentration of discrete scatterers is found in the upper portion of the ice sheet as associated with desalination processes in first year ice and formation of a bubbly low density ice (LDI) layers in multiyear meltponds and hummocks. Physical measurement of these bubbles in multiyear ice samples (0.1 - 5mm dia.) can be made from microscopic analysis of ice core thin sections. Analysis of optical beam scattering is directly related

to these ice characterizations.

Beam spread measurement techniques have been applied by several investigators to samples of Arctic sea ice and laboratory growth saline ice^{2,3}. In the present work, the beam spread measurements are first used to derive the modulation transfer function (MTF) using a Fourier-Bessel transform. The MTF was then used to estimate the volume scattering function, $\sigma(\theta)$, for small angles. For thin snow and many sea ice samples, the beam spread functions frequently displayed a Gaussian shape. Transmission was measured for snow and sea ice samples as the loss along the beam axis made as a function of sample thickness. These measurements provide an estimate of beam extinction. The scattering coefficient (σ) can be estimated as the difference between absorption (a) and beam extinction (c , $c = a + \sigma$). An estimate of the MTF for the entire ice sheet can be obtained as the product of individual layers which can have large variability in optical properties.

2. BEAM SPREAD FUNCTIONS

A collimated light beam through sea ice will produce a blur distribution or beam spread function BSF, $f(x,r)$, which is dependent on the off-axis distance, x , and the sample thickness, r . The corresponding MTF, $F(\psi,r)$, is a function of the spatial frequency, ψ (cyc./cm), and r . The medium MTF describes how spatial frequencies are attenuated with thickness. The BSF spread function can be expressed in units of flux per unit solid angle at an angle θ off axis per unit of flux transmitted⁴. Alternatively, one can express the blur function as irradiance with units of watts per m² at radius R from the source for a detector of area⁵.

Reference to an azimuthal angle can be dropped because the BSF is assumed to be circularly symmetric which is consistent also with field observations. The Fourier transform of the BSF in this case becomes the Fourier-Bessel transform and defines the optical transfer function (OTF) with modulus MTF and phase PTF(=0). The small angle approximation is used implicitly in this theory since $\sin(x)$ is replaced by x in the Bessel integral.

$$F(\psi, r) = 2\pi \int_0^\infty J_0(2\pi x\psi) f(x, r) x dx \quad (1)$$

The Well's transform can be used to derive an estimate of the small angle volume scattering function, $\sigma(\theta)$, from the MTF⁴. This theory incorporates all orders of multiple scattering. The irradiance, $E(\theta,r)$, associated with beam spread is used to derive the volume scattering function. The Fourier-Bessel transform to the radiative transfer equation is written as⁶:

$$\frac{dF(\psi, r)}{dr} = -cF(\psi, r) + H(\psi) F(\psi, r) \quad (2)$$

where $H(\psi)$ is the Fourier-Bessel of $\sigma(\theta)$ and the transform of the source term is eliminated. Solution to this linear differential equation is:

$$F(\psi, r) = F(\psi, 0) e^{-(c-H(\psi))r} \quad (3)$$

In the above equation, $F(0,\psi)$ is effectively the MTF for the narrow beam incident on the ice

sample. The MTF for ice layer, $F^*(r, \psi)$ is then given as:

$$F^*(\psi, r) = \frac{F(\psi, r)}{F(\psi, 0)} \quad (4)$$

Thus, to resolve the MTF for an ice layer one needs simply two slabs of different thickness preferably measured, *in situ*, using layer stripping techniques. It is assumed that the ice intrinsic optical properties are the same for both samples. The ratio of the MTF's, as obtained by equation (4) from the measurement data, will yield an estimate of MTF for sea ice with thickness equal to the difference in the two sample slabs. The MTF can then be inverted using equation (3) to derive $H(\psi)$ followed by the transform of equation (1) to estimate the small angle forward volume scattering function. This theory was developed for a homogeneous medium. Sea ice is a very inhomogeneous medium so stability and validity of these transforms may be very important to any small angle scattering estimates.

3. MEASUREMENTS

Optical transmission and beam spreading data were gathered during the April 1992 LEADDEX (Leads Experiment) conducted in the Beaufort Sea to study atmospheric, ice, and ocean interactions². Thin slabs with parallel faces (1-20cm thick) of lead, first year, and multiyear ice types were taken from cores and placed in a 2cm diameter collimated laser beam. The resulting diffuse beam spread pattern due to scattering in the ice sample was recorded using an array detection system. Measurements were also made by placing a laser (Nd:YAG 532nm) source, *in situ*, beneath the ice with the beam directed upward and the resulting beam spread pattern was measured by sliding an irradiance detector along the ice surface. The beam had an approximate diameter of 2cm and divergence of 12mrad. The signal was chopped to separate it from background illumination resulting in a possible measurement signal to noise ratio of 70 dB. The sample slabs were all maintained below the eutectic point so that brine pockets were optically stabilized.

4. MODEL STUDIES

Beam spreading model calculations were made by directing photons from a laser beam upward through a composite set of sea ice and snow layers to a linear detector array position on the surface and centered on the beam. A Monte Carlo model was constructed to simulate the associated multiple scattering processes. Simulation models have several advantages over analytical models since the divergence of the laser beam, multiple scattering effects, and Mie scattering can be included. However, they are limited by the statistics of counting individual photon events and the accuracy of physical models. In the present model specification of the location of inclusions, such as bubbles and brine channels, was not included and the ice layers were assumed to be horizontally and vertically homogeneous. The ocean-ice, ice-snow, and snow-air boundaries were all assumed to be flat in the present case, but statistically rough surfaces will be added to future versions. In its present form, the model simulates a photon randomly walking through a uniform scattering medium with straight segments followed by directional changes caused by either by volumetric scattering or surface reflection (ice-air interface only). A uniform random number generator selects the lengths for each segment and angles of scattering from an appropriate cumulative probability distribution. A truncated distribution forces scattering within the restricted volume and improves model efficiency.

The next scattering event determines the direction of the next photon segment. The angular distribution of scattering was assumed to be azimuthally symmetric and the azimuthal angle was selected from a uniform distribution. The Mie scattering was calculated at every 0.001 degree from 0 to 0.1 degrees, at every 0.01 degree from 0.1 to 1 degree, at every 0.1 degrees from 1 to 10 degrees, and at 1 degree intervals elsewhere. The cpd values were calculated and assembled into a look-up table. Sample scattering angles were found by using a uniform random number generator to select a cpd value, searching this table to find the closest value, and interpolating between values to determine the exact scattering angle. All photons are forced to stay within the scattering medium until the cumulative weight reaches a preset minimum or the photon is scattered to the detector. Only a very small error is introduced by photons scattered out of the medium and subsequently scatter back into the medium and eventually to the detector. The photon probability for returning to the receiver is calculated at each scattering and reflective event.

$$P_d(x) = W_p P(x_0) e^{-cR_d(x)} (4\pi R(x)^2)^{-1} \quad (5)$$

where $P_d(x)$ is the probability of detection at position x on the detector array, W_p is photon weight, $R_d(x)$ is the distance to position x within the scattering medium and $R(x)$ is the distance to the detector, and c is the attenuation coefficient. Forward and backward scattering probabilities were determined directly by integrating the forward and backward hemispheres respectively of the volume scattering phase function.

The numerical Fourier-Bessel transform was used to calculate the MTF from the measured beam spread data and to estimate the small angle volume scattering function from the MTF using the method described previously. In this inverse operation, stability of the numerical transform is more difficult to maintain. The scattering angle spacing needs to be adjusted in the forward peak to get satisfactory estimates. For this reason, an adaptive Labatto quadrature technique was implemented. The adaptive quadrature makes adjustments to the angle spacing automatically. In this technique the integration intervals are bisected repeatedly and differences examined after each iteration until convergence is achieved. Thus, in this procedure the integrand is evaluated over a fine mesh of points where it is rapidly varying and otherwise over a coarse mesh. Characteristically, if the beam spread data are Gaussian then the MTF will be Gaussian and also the scattering function.

5. RESULTS

Individual beam spread scan measurements were found frequently to have a highly variable profile due to the presence of individual volumetric and surface scatterers as illustrated by the example in Figure 1. Multiple profile from the same set of ice samples was used to estimate an average beam spread profile which has Gaussian shape. Examples of the beam spread functions were developed from the measurements made during LEADDEX on lead, first year, and multiyear ice, to calculate the MTF's as shown in Figure 2. The MTF's were then used with estimates of beam extinction to derive corresponding estimates of the small angle volume scattering function. These estimates are shown in Figure 3 for the three example ice types. The oscillations in the scattering function at 1 mrad are thought to be Gibbs artifacts due to the finite width of the numerical transform. Work is continuing to remove these artifacts from the numerical transform. One

approach is to assume the beam spread functions are Gaussian and force the products at each step to a Gaussian fit.

The Monte Carlo model was used to simulate beam spreading through selected thicknesses of lead ice by directing the Gaussian shaped laser beam upward perpendicular through the ice sample. The index of refraction was assumed constant for sea ice and ocean water. The detector array was placed in contact with the ice surface and centered on the beam. Scattering properties were assumed to be uniform within the sample slab and the estimated volume scattering function for lead ice with the artifact oscillation removed was used to calculate the cumulative distribution probabilities. A single scattering albedo value of 0.99 was used in this analysis. The model generated beam spreading patterns are shown in Figure 4 for 3cm, 10cm, and 40cm thick slabs. Simulations were also made for 1cm, and 16cm ice thicknesses. The 3cm and 50cm pattern, have been rescaled horizontally (4X,0.5X) to facilitate comparison. The numerical Fourier Bessel transform was applied to the spread data from the 3cm thick slab simulation to produce the MTF transfer function shown in Figure 5 which compares favorably to the data derived MTF. The consistency between the simulated beam spread data with that implied by transform relationships was examined in the following comparison. The MTF generated by the 3cm sample was used with equation (4) to estimate the MTF at other ice thicknesses. These estimates were converted to beam spread functions. The simulated and transform derived beam spread pattern radiuses are compared at the one-half peak amplitudes as shown in Figure 6. The average slope of these curves provides an estimate of characteristic beam spreading for the ice scattering medium. For the simulated data, this estimate is 8.5 mm/cm of sample thickness and for the transform data is 10.4mm/cm. The field measurements made at LEADDEX gave beam spreading characteristics in the range of 7-11 mm/cm for lead ice samples.

6. DISCUSSION AND CONCLUSIONS

Small angle volume scattering properties of sea ice have been derived from measured beam spread data. Application of this approach recognizes the need for such information to more fully understand the range of optical scattering in sea ice and to support multilayer radiative transfer models. There are several issues surrounding both the measurement and analysis techniques which need to be addressed. The numerical transforms were found to be very sensitive to fine scale variability and possibly noise in the input functions. Smoothing of the input data improves stability but may also reduce accuracy. Variability of the scattering phase function in sea ice is unknown, but since most discrete scatterers have physical dimensions much larger than a wavelength (i.e. scattering efficiency $Q=2$). The indexes of refraction for ice and air bubbles is constant. Under these circumstances the small angle forward portion of the phase function should have nearly constant shape as suggested by the results shown in Figure 3. Additional investigation is needed to define the shape of the phase function for the forward scattering peak and to test similarity over major ice types including those with biological particles. Large angle measurements are also needed to define the volume scattering function. The useful optical thickness limits need to be established for application of the scattering transform. As applied here the transform is not expected to work in the diffusion regime. In addition to retrieval of scattering properties, beam spread measurements are considered valuable, in their own right, to the optical characterization of sea ice.

ACKNOWLEDGEMENTS

This work was supported in part by the Office of Naval Research (ONR) contract N00014-90-C-0148. The technical monitor was Steve Ackleson. This work was also supported in part by ERIM internal research projects.

REFERENCES

1. T.C. Grenfell, and D. Hedrick, Scattering of Visible and Near Infrared Radiation by NaCL Ice and Glacier Ice, Cold Regions Science and Technology, n.8 1983
2. F.J. Tanis, R.Shuchman, and R. Onstott, Optical Properties for Sea Ice Measured During LEADEx '92, IGARSS '93, Tokyo, Japan, August 1993
3. J.S. Schoonmaker, K.J. Voss, G.D. Gilbert, Laboratory Measurements of Optical Beam in Young Sea Ice, Limnology and oceanography, vol.34 no. 8, December 1989
4. W.H. Wells, Loss of Resolution in Water as a Result of Multiple Small Angle Scatering, J. Opt. Soc Am. vol. 59, p.686, June 1969
5. L.E. Mertens and F.S. Reploge jr. Use of Point Spread and Beam Spread Functions for the Analysis of Imaging Systems in Water, J. opt Soc. Am, Vol. 67 pp. 1105-1117, 1977
6. D. Arnush, Underwater Light-Beam Propagation in the Small Angle Scattering Approximation J. Opt. Soc. Am. vol.62 no. 9, September 1972

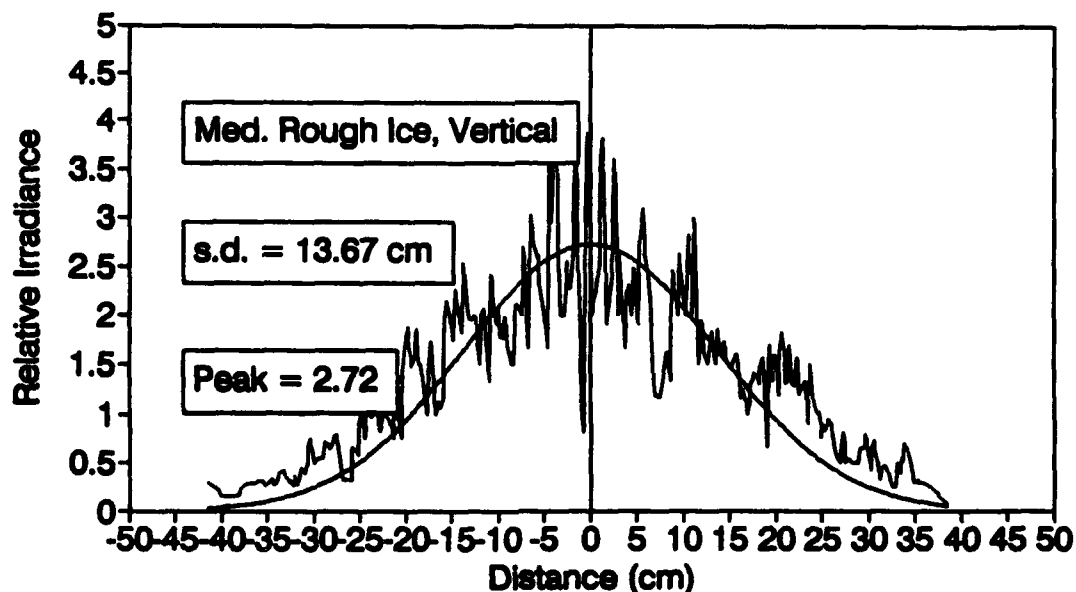


Figure 1. Measured Beam Spread for CRREL Saline Ice (20cm)

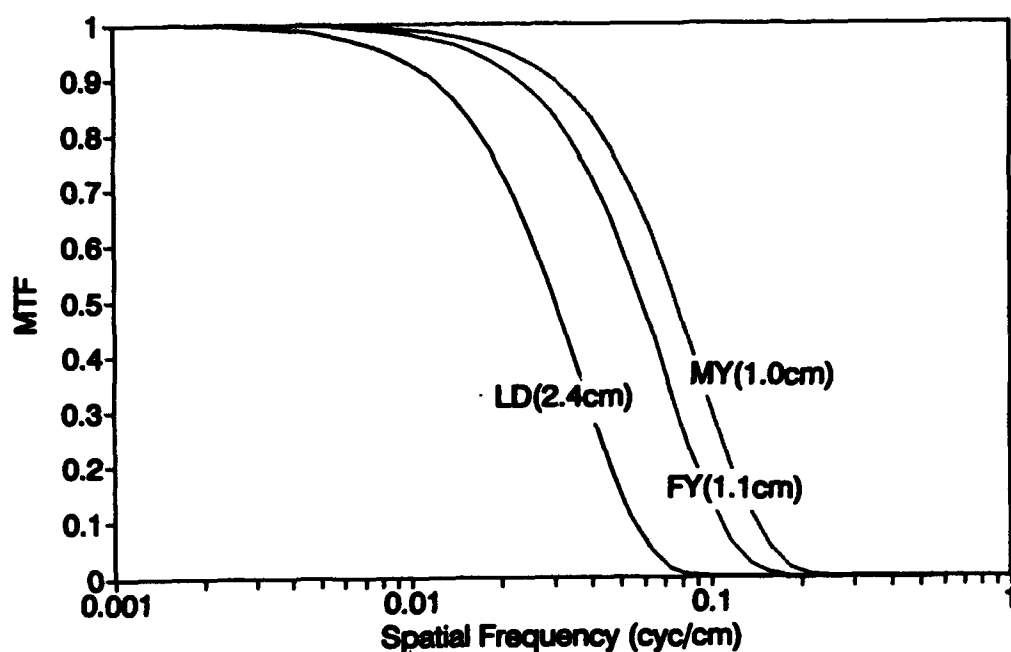


Figure 2. Derived Modulation Transfer Functions for First Year Ice and Multiyear Hummock Ice Samples

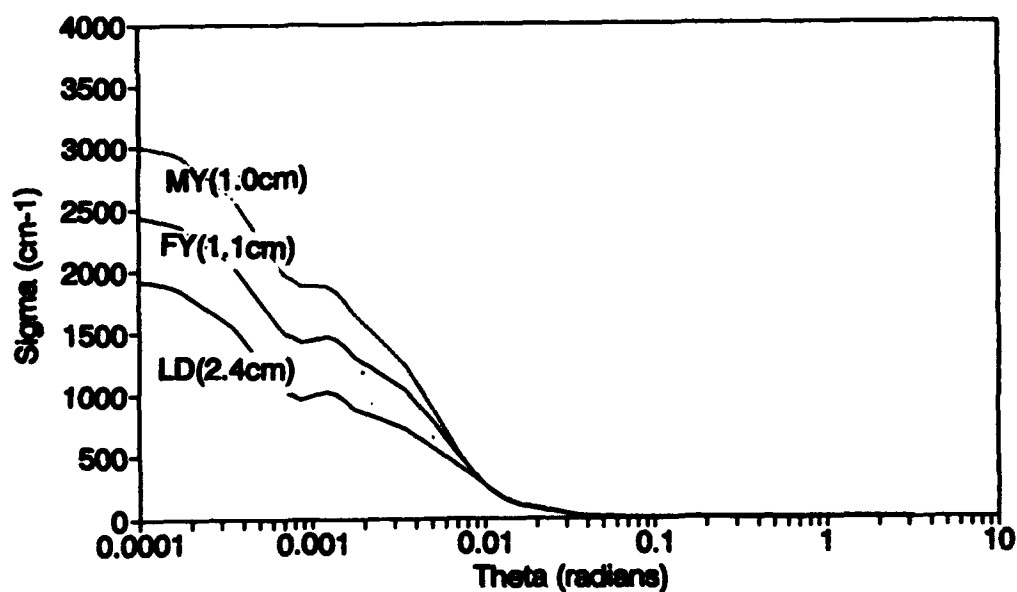


Figure 3. Derived Volumetric Scattering Functions for First Year and Multiyear Ice Core Samples

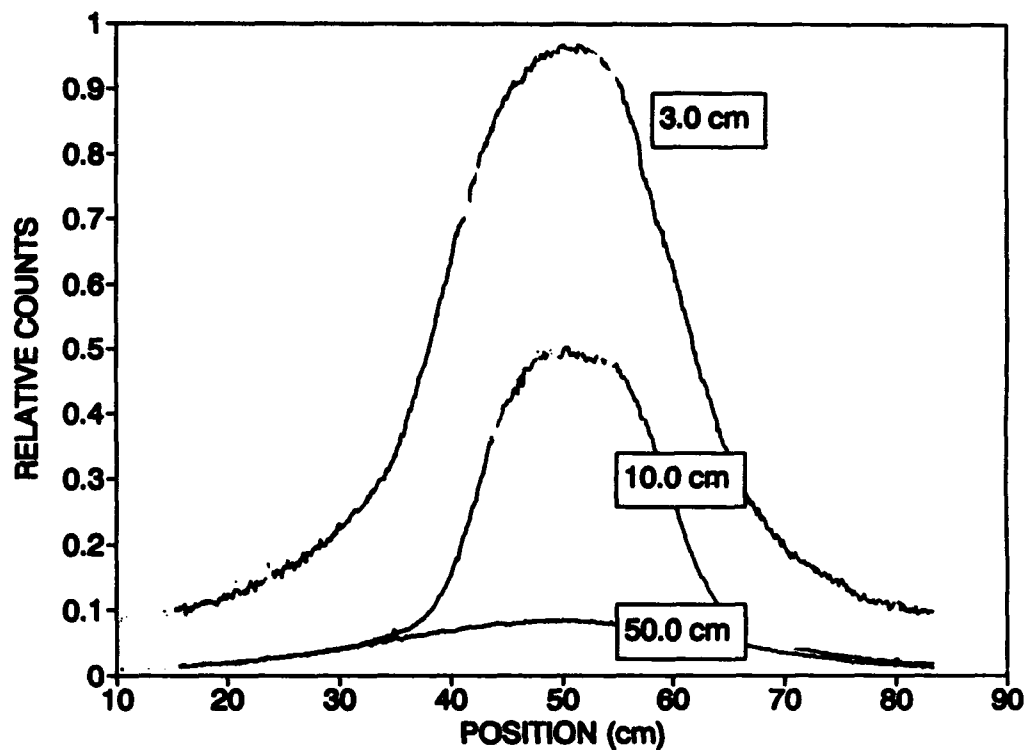


Figure 4. Simulated Beam Spread Patterns

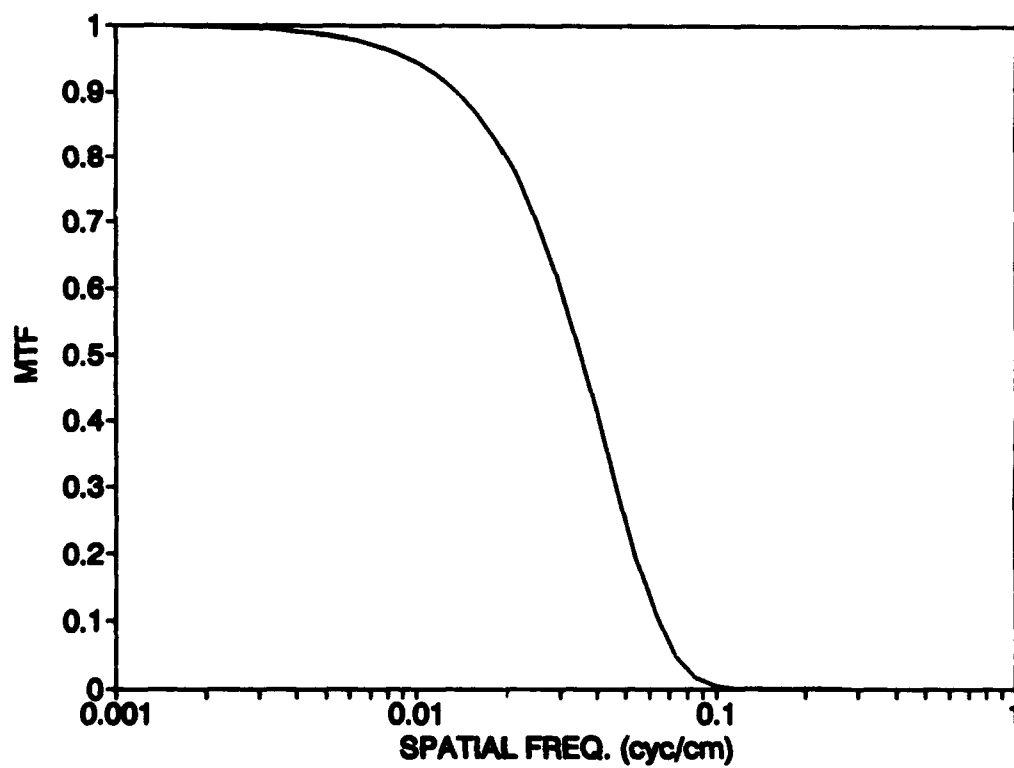


Figure 5. Derived Modulation Transfer Function for Simulated Beam Spread Pattern for 3cm Thick Ice

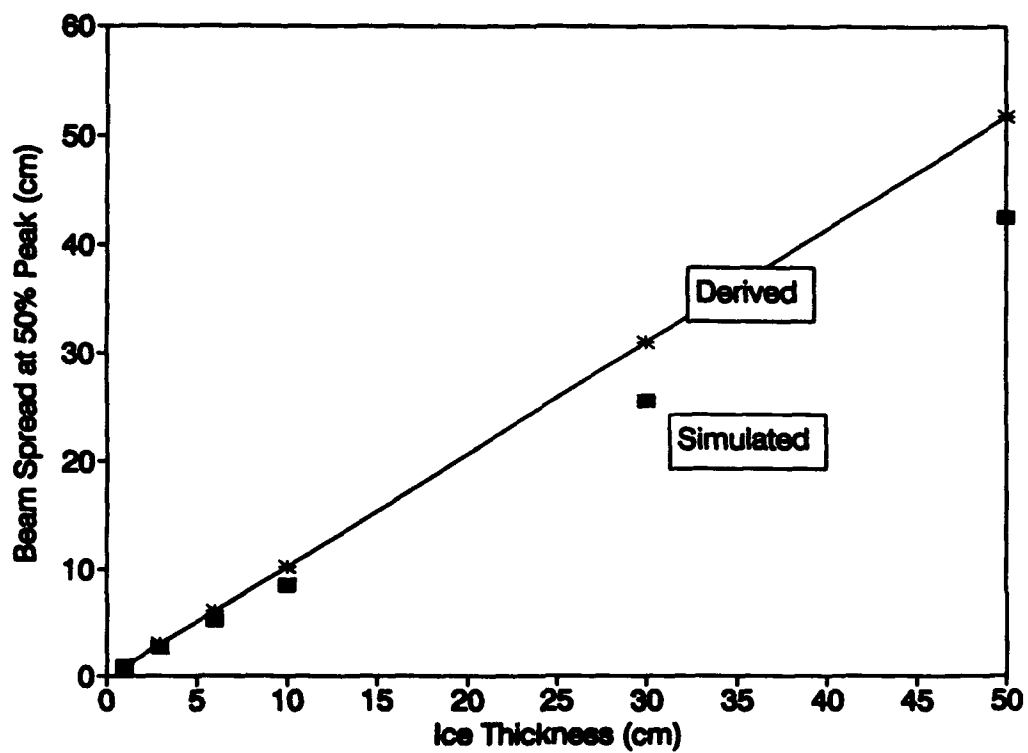


Figure 6. Comparison of Simulated Beam Spread at 50% of Peak with Transform Derived Estimates

SESSION 12

Additional Papers

International Conference on OCEAN OPTICS XII
13 - 15 June 1994
Bergen, Norway

On the Relationship Between Spectral Reflected Irradiance at the Sea Surface and Optical Properties of Marine Phytoplankton

**Bogdan Wozniak ¹⁾, Witold von Smekot-Wensierksi ²⁾, Roland Doerffer ³⁾, Hartmut
Graßl ²⁾**

**1) Institute of Oceanology of the Polish Academy of Sciences
Powstancow Warszawy 55, 81-712 Sopot/Poland**

**2) Max-Planck-Institute for Meteorology,
Bundesstrasse 55, 20146 Hamburg, Germany**

**3) GKSS Research Center, Institute of Physics
Max-Planck-Strasse, 21502 Geesthacht, Germany**

Abstract

Two models of relative spectral reflectances (semi-empirical and theoretical) as a function of chlorophyll-like pigment concentrations in the upper layer of oceanic waters and thus absorption and scattering properties of phytoplankton are described. These models are developed on the basis of statistical relationships between measured spectral diffuse attenuation coefficients and chlorophyll density in various oceanic waters (from oligotrophic to eutrophic).

The **semi-empirical model** includes new spectral irradiance measurements in different waters. The strongly nonlinear regression equation (reflectance versus chlorophyll concentration) is compared with direct measurements giving a negligible systematic error and a standard deviation of only 15% and of 20%, if applied to other spectra.

The **theoretical model** is based on the principle of invariance of the emergent radiation for a semi-infinite plane-parallel medium, the delta function approximation for the forward scattering peak, the approximate solution of the radiative transfer equation as well as Cox and Munk's statistics of the roughness of the sea surface. It recovers formulae derived by others with more complicated models.

Both models convert reflectances or reflected radiances reliably into inherent optical phytoplankton properties for different open ocean waters indicating no need for a regional algorithm.

Introduction

The remote measurement of water colour is the most promising way to monitor the biological activity on a global scale, since the optical properties of phytoplankton are responsible for part of the water colour changes. Therefore, the evaluation of measured spectra of reflected relative irradiance at the sea surface, R_λ , is a basic tool for the monitoring of marine ecosystems (Gordon et al., 1975; Morel and Prieur, 1984; Kondratyev and Pozdnyakov, 1984). The reflectance R_λ just below the sea surface as well as the reflected spectral radiance ρ_λ depend on the inherent optical properties of water bodies, mainly from, the backscattering coefficient $b_{b\lambda}$ and the absorption coefficient a_λ . In case I waters (most open sea waters belong to this category) these coefficients are dominated by phytoplankton and its detritus. It is possible to take the spectra dominating pigment concentration (chlorophyll-a + pheophytin-a) as a measure of phytoplankton concentration. Sometimes even primary productivity is derived with some further assumptions.

Many scientists have attempted to classify the optical properties of sea water bodies through the determination of the statistical dependence between the in-situ measured spectral diffuse irradiance attenuation coefficient $K_{d\lambda}$ and chlorophyll-a density C_a (see Smith and Baker, 1978; Prieur and Sathyendranath, 1981; Morel, 1988; Wozniak and Pelevin, 1991; Wozniak et al., 1992a, b).

In the present paper we try to improve the formulae for the relation between measured spectral reflected relative irradiance R_λ or reflected relative radiance ρ_λ and chlorophyll-a density C_a , in order to establish a more reliable (remote sensing) algorithm.

Our two approaches

As a basis for this general algorithm we take firstly the bio-optical classification of natural waters by Wozniak et al. (1992b), i.e. the analytical relationship between $K_{d\lambda}$ and C_a (see Figure 1 and Table 1), derived from about 1200 spectra of K_d measured in many different water bodies with chlorophyll-a densities ranging from very oligotrophic 0.03 to hyperthrophic 60 mg m^{-3} . The relative accuracy of this relation is depending on the wavelengths chosen and on the trophic type of the water body, it is as high as 28% but may also be as low as 9% in some cases (for the definition of errors see Appendix 2).

Table 1: Trophicity types and the chlorophyll-a-like pigment density C_a for different sea-water bodies

Trophicity Type	C_a Range mg/m^3	C_a Average mg/m^3
0 - 1	< 0.05	0.035
0 - 2	0.05 - 0.10	0.07
0 - 3	0.10 - 0.20	0.15
M	0.20 - 0.50	0.35
P	0.50 - 1.00	0.7
E - 1	1.00 - 2.00	1.5

Table 1: Trophicity types and the chlorophyll-a-like pigment density C_a for different sea-water bodies

Trophicity Type	C_a Range mg/m^3	C_a Average mg/m^3
E - 2	2.00 - 5.00	3.5
E - 3	5.00 - 10.0	7.0
E - 4	10.0 - 20.0	15

O = oligotrophic waters
 M = mesotrophic waters
 P = intermediate waters
 E = eutrophic waters divided into 4-sub-types

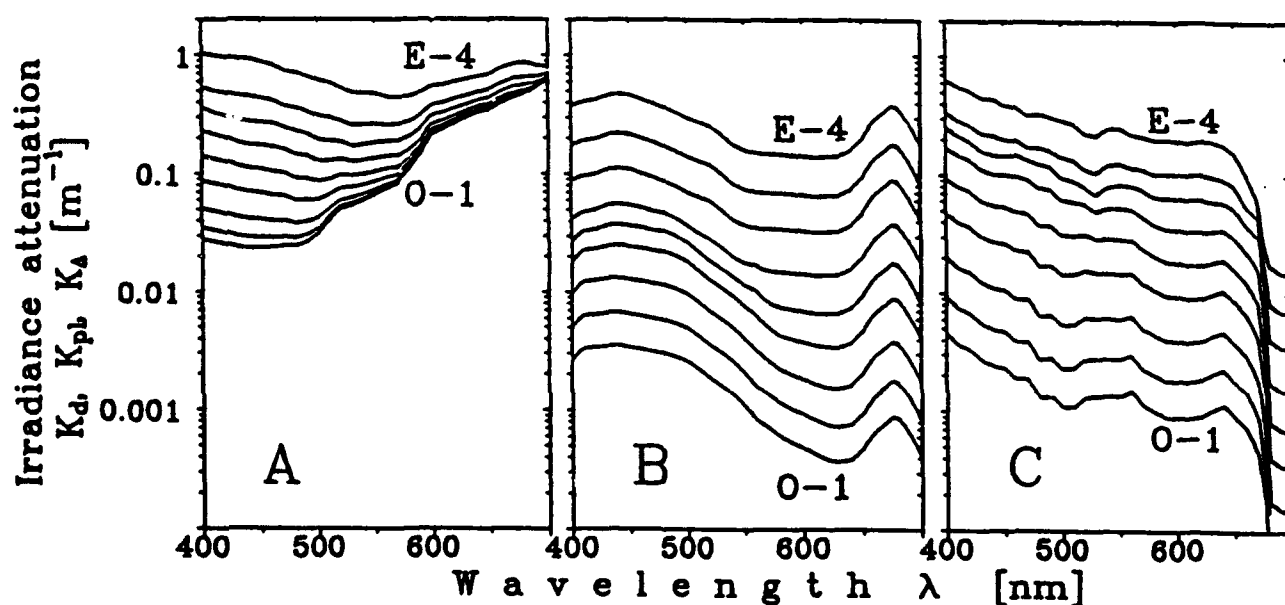


Fig. 1: Spectra of diffuse attenuation coefficients in case 1 water according to Wozniak's bio-optical classification: a) total diffuse attenuation K_d ; b) attenuation by phytoplankton $K_{pl, \lambda}$; c) attenuation of other optically active substances $K_{\Delta, \lambda}$. Chlorophyll-a-like pigment densities for trophicity types O-1 to E-4 are given in Table 1.

Secondly, we take two approaches for the relation between $K_{d, \lambda}$ or C_a and R_λ . The first is called semi-empirical approach because we just combine the analytical relation between $K_{d, \lambda}$ and C_a as shown in Figure 1 and measured spectra of Pelevin (1980) relating R_λ and $K_{d, \lambda}$ (see Figure 2). The second one applies the principle of invariance for radiation emerging from a semi-infinite plane parallel medium if layers of arbitrary thickness are added or subtracted (Ambarzumyan et al., 1952; Chandrasekhar, 1960) and the delta function approximation for forward scattering of light (see e.g. Potter, 1970) to the equation of radiative transfer (Chandrasekhar, 1960). We call this approach the theoretical model. It relates R_λ to C_a if the

zenith angle of the Sun, sea surface roughness (windspeed) and atmospheric turbidity are known.

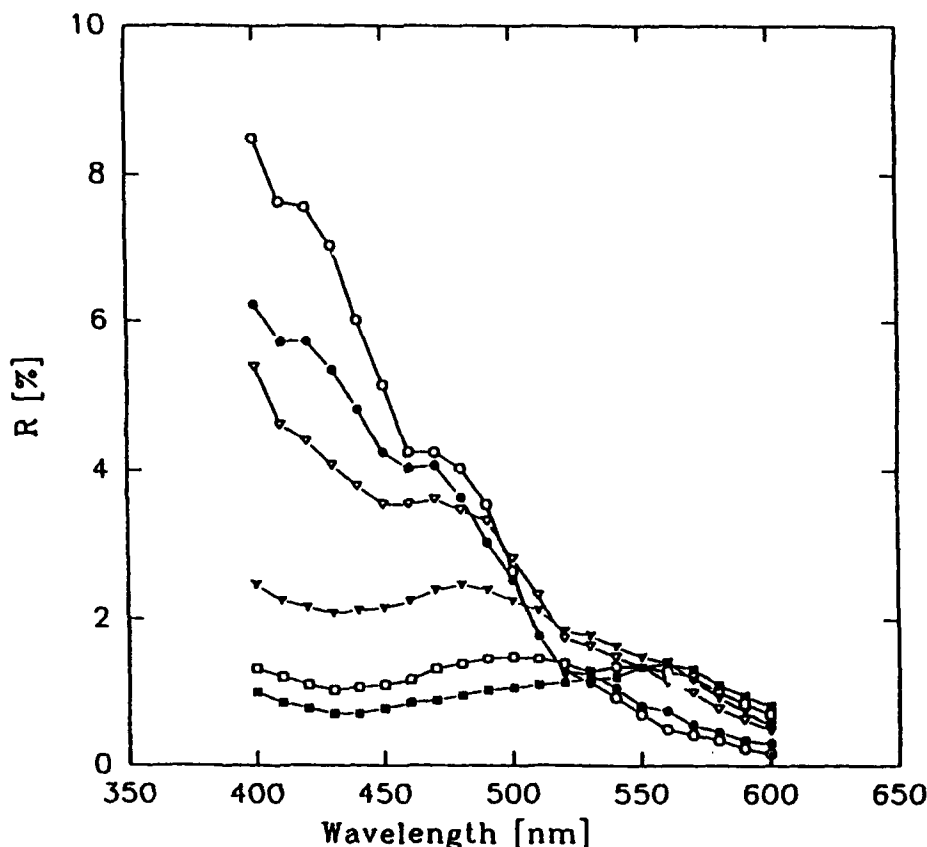


Fig. 2: Measured averaged spectra of relative reflected irradiance R for varying water bodies. Mean chlorophyll- a density C_a for curves 1 to 6 is 0.013, 0.079, 0.25, 0.52, 1.87 and 4.5 mg/m^3 (see text); from Pelevin, 1980.

The semi-empirical approach

This approach is based on two large data sets and their statistical evaluation as already displayed in Figures 1 and 2. In order to relate and compare $K_{d,\lambda}$ as function of C_a (Wozniak et al., 1992b) with R_λ as a function of C_a (Pelevin, 1980) we have taken

$$R_\lambda = 0.32 (b_{b,\lambda} / a_\lambda) / \mu_o \quad (1)$$

from Jerome et al. (1987) derived from Monte Carlo simulations and valid for $0 \leq b_b/a \leq 0.25$ as normally found in sea water. μ_o is the average cosine of downwelling radiance. For the relative radiance reflected, ρ_λ , Pelevin and Solomaha (1989) have proposed

$$\rho_{\lambda} = 0.21 b_b / (a + b_b) \quad (2)$$

which is accurate to better than 10% for $0.007 \leq \rho_{\lambda} \leq 0.07$. Since μ_o is rather constant at 0.86 equation (1) is reduced (see Prieur and Sathyendranath, 1981; Jerome et al., 1987) to

$$R_{\lambda} = 0.37 (b_{b,\lambda} / a_{\lambda}) \quad (3)$$

Relating absorption and diffuse attenuation by

$$a_{\lambda} \approx \mu_o K_{d,\lambda} \approx 0.86 K_{d,\lambda} \quad (4)$$

now allows to simply relate R_{λ} and $b_{b,\lambda}$:

$$b_{b,\lambda} \approx 2.3 K_{d,\lambda} \cdot R_{\lambda} \quad (5)$$

The connection to C_a is found via a separation of $b_{b,\lambda}$ into the Rayleigh backscattering part $b_{b,w}$ and $b_{b,p}$ for phytoplankton.

We get for the phytoplankton backscattering

$$b_{b,p,\lambda} = b_{b,\lambda} - 0.00065 \text{ m}^{-1} \cdot (550 \text{ nm} / \lambda)^4 \quad (6)$$

$$2.3 K_{d,\lambda} \cdot R_{\lambda} - 0.00065 \text{ m}^{-1} \cdot (550 \text{ nm} / \lambda)^4$$

The average spectra of $b_{b,p}$ for the average chlorophyll-a densities of Figure 2 can now be calculated from R_{λ} . Using the known values C_a we further get a relation between C_a and $b_{b,p}$

$$b_{b,\lambda}(C_a) = 0.00065 \text{ m}^{-1} (550 \text{ nm} / \lambda)^{4.3} + \\ + 0.00289 \cdot C_a^{0.48} \cdot (550 \text{ nm} / \lambda)^p(C_a) \quad (7)$$

where the exponent $p(C_a) = 4.3 \cdot \exp(-1.882 \text{ m}^3 \text{ mg}^{-1} \cdot C_a)$ accounts not only for the wavelength dependence of phytoplankton backscattering but also its change with pigment density C_a due to a change in size distribution. Equation (7) has been derived by a non-linear regression analysis. The results of the semi-empirical approach are displayed in Figure 3 for the different types of trophicity of sea-water. A comparison to the measurements of Pelvin (1988) shows only a marginal bias for R_λ of + 0.6% at a standard deviation of 13.7% (see also Table 2 for definition of errors see Appendix 2) and thus demonstrates the robustness of equations (7) and (3) if used to calculate near surface pigment densities from reflectance spectra just below the sea surface. If $R_\lambda/R_{550 \text{ nm}}$ and $\rho_\lambda/\rho_{550 \text{ nm}}$ ratios are plotted as in Figure 4 one easily discovers the well-known strong dependency of the ratio $\rho_\lambda/\rho_{550 \text{ nm}}$ or $R_\lambda/R_{550 \text{ nm}}$ on C_a for wavelengths $\lambda < 490 \text{ nm}$ often used for chlorophyll-a mapping.

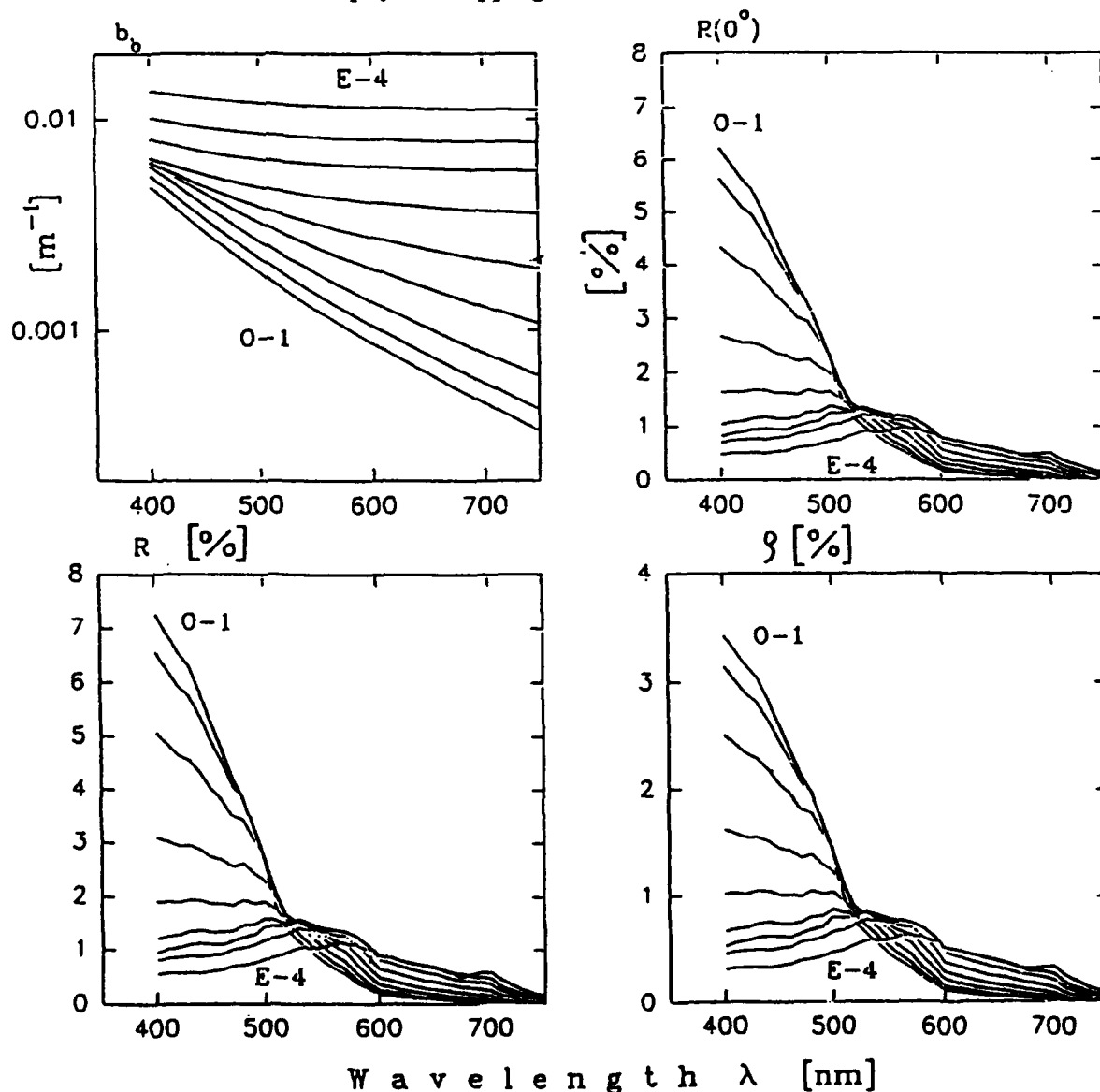


Fig. 3: Results of the semi-empirical model for all trophicity types: Spectra of b_b (see Eq. (7)), relative reflected irradiance R for a zenith angle of 0° , relative reflected irradiance R (see Eq. (3)) and relative reflected radiance ρ (see Eq. (2)) for varying water bodies; trophicity types 0-1 to E-4 see Table 1.

Table 2: Semi-empirical model: Formulae and error estimates.

<p>1. Formulae</p> $R_{\lambda}(C_a) = 0.37 [b_{b,\lambda}(C_a) / a_{\lambda}(C_a)]$ $\rho_{\lambda}(C_a) = 0.21 b_{b,\lambda}(C_a) / [a_{\lambda}(C_a) + b_{b,\lambda}(C_a)]$
$b_{b,\lambda}(C_a) = 0.00065 (550\text{nm}/\lambda)^{4.3} + 0.00289 C_a^{0.48} (550\text{nm}/\lambda)^{p(C_a)}$ <p>with</p> $p(C_a) = 4.3 \exp(-1.882 \text{ mg}^{-1} \text{ m}^3 C_a)$ $a_{\lambda}(C_a) \approx 0.86 K_{d,\lambda}(C_a)$
<p>2. Error estimates (see also Appendix 2) if formulae are applied to the generating data set</p> $\langle \epsilon \rangle = +0.6\%, \quad \sigma_{\epsilon} = \pm 13.7\%$ $\langle \epsilon \rangle_g = -0.34\%, \quad \epsilon_{\min} = -8.9\%, \quad \epsilon_{\max} = +8.3\%$

Also the scatter diagram of pigment density C_a in Figure 5 as well as the related histogram of the pigment density ratio $C_a(\text{model}) / C_a(\text{obs})$ show the applicability of equations (3) and (7) for 60 strongly different water bodies.

The retrieval of C_a from R_{λ} values at different wavelengths, if based on equations in Table 2 and using a simple reflectance ratio $R_{\lambda_1}/R_{\lambda_2}$ algorithm as given in Table 3, shows rather low errors for $\lambda_1 = 440$ and $\lambda_2 = 550$ nm.

Table 3: Algorithm and errors of estimation of chlorophyll density C_a from reflectances R or radiances ρ using the semi-empirical model of table 2 for an independent data set.

1. Alorithm $\log_{10} C_a [mgm^{-3}] = a_0 + a_1 \log_{10} x + a_2 \log_{10} x^2 + a_3 \log_{10} x^3$ <p>with</p> $x = R(\lambda_1) / R(\lambda_2) \text{ or } x = \rho(\lambda_1) / \rho(\lambda_2)$			
2. Coefficients a_i for different $x = R(\lambda_1)/R(550nm)$			
	$\lambda_1 = 400 \text{ nm}$	$\lambda_1 = 440 \text{ nm}$	$\lambda_1 = 490 \text{ nm}$
a_0	0.1028	0.183	0.324
a_1	- 2.343	- 2.636	- 4.831
a_2	3.969	4.333	13.983
a_3	- 3.502	- 4.228	- 18.673
$x = \rho(\lambda_1) / \rho(550 \text{ nm})$			
a_0	0.0997	0.184	0.319
a_1	- 2.397	- 2.707	- 4.966
a_2	4.236	4.531	14.38
a_3	- 4.097	- 4.781	- 20.00
3. Relative errors Reflectances: $\langle \epsilon \rangle = - 3\%$, $\sigma_\epsilon = 20\%$ Radiances: $\langle \epsilon \rangle = + 3\%$, $\sigma_\epsilon = 28\%$ For definitions see Appendix 2.			

A simpler theoretical model

This approach uses the principle of invariance for semi-infinite media and applies it to marine optics. Additionally, we assume that the scattering function can be approximated by replacing the forward scattering peak by Dirac's delta function and that the remaining volume scattering function is isotropic. Therefore, the scattering coefficient of phytoplankton b_p is reduced to (Monin, 1983)

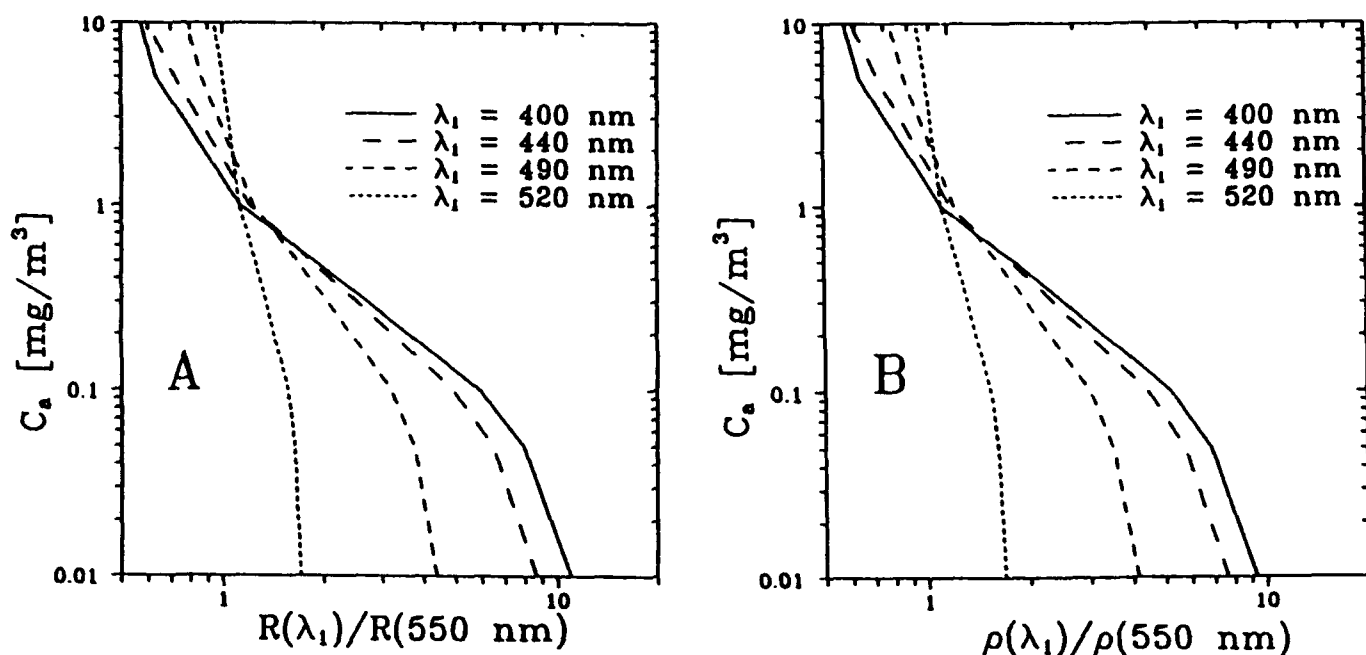


Fig. 4: Calculated relationship between chlorophyll-a density C_a and ratio of reflected irradiances $R_\lambda/R_{550 \text{ nm}}$ (A) or the ratios of reflected radiances $\rho_\lambda/\rho_{550 \text{ nm}}$ (B) for some wavelengths λ_1 and $\lambda_2 = 550 \text{ nm}$.

$$b'_p = b_p (1 - \overline{\cos \gamma_p}) \quad (8)$$

with $\overline{\cos \gamma_p}$ = average cosine of the particle volume scattering function leading to a changed single scattering albedo ω_0 as well as optical depth τ

$$b' = b'_p + b_w ; \quad \omega'_o = b' / (a + b') ; \quad \tau' = \int_0^z (a + b') dz \quad (9)$$

The principle of invariance (Ambarzumyan et al., 1952) allows to calculate the upwelling radiance $L_u(\mu)$ just below the surface in direction $\mu = \cos \Theta$ simply from incoming solar irradiance $E_{o,s}(z)$ just below the surface ($z = 0$) and ω'_o via

$$L_u(\mu) = \frac{\omega'_o}{4\pi} E_{o,s}(0) \mu_o \frac{H(\mu) H(\mu_o)}{\mu + \mu_o} \quad (10)$$

where the H-function can only be derived from an integral equation

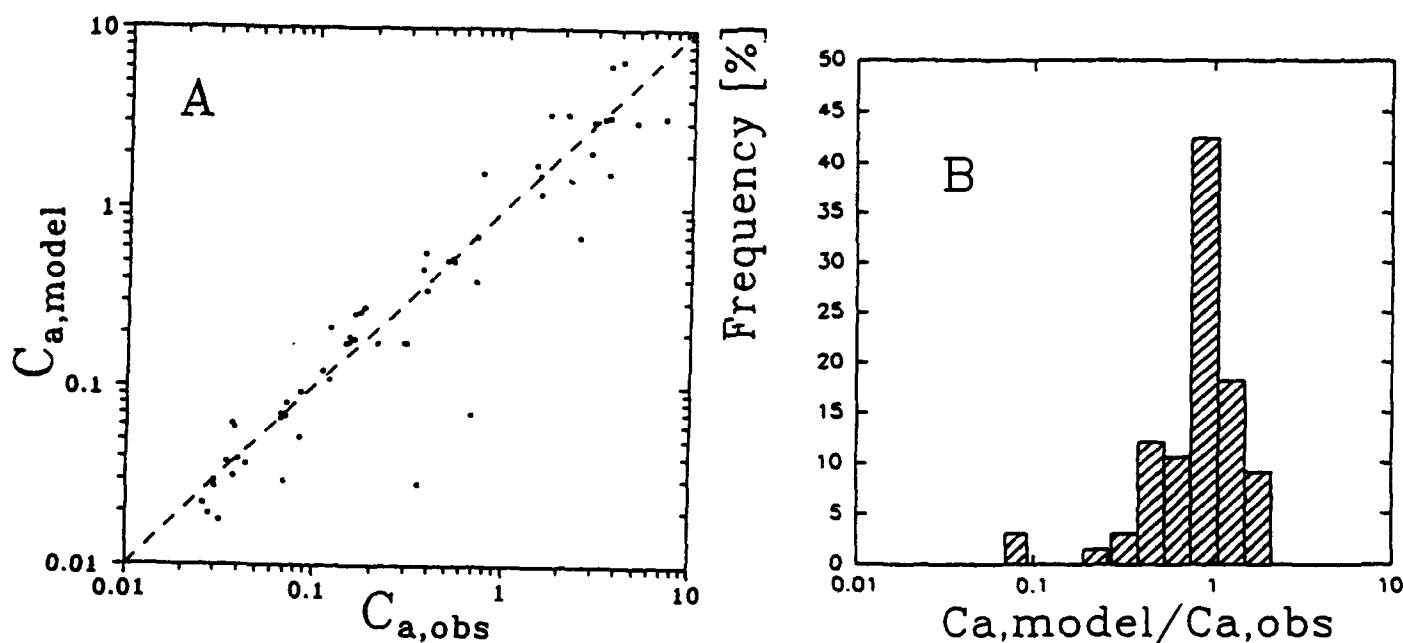


Fig. 5: Relations between calculated and observed near surface chlorophyll-a density C_a , (A) and the histogram of the ratio C_a (model)/ C_a (obs).

$$H(\mu) = 1 + \frac{\omega'_o}{2} \mu_o H(\mu) \int_0^1 \frac{H(\mu')}{\mu + \mu'} d\mu' \quad (11)$$

by iteration. However, the average value of H is simply

$$H = \int_0^1 H(\mu) d\mu = \frac{2}{\omega'_o} (1 - \sqrt{1 - \omega'_o}) \quad (12)$$

From equation (10) the upwelling irradiance $E_u(0)$ just below the surface can be calculated

$$E_u(0) = \mu_o E_{o,s}(0) (1 - H(\mu_o) \sqrt{1 - \omega'_o}) \quad (13)$$

Accordingly, the downwelling irradiance E_d at $z=0$ just below the surface is given by

$$E_d(0) = \mu_o \cdot E_{o,s}(0) \quad (14)$$

leading to a very simple relation for the relative reflected irradiance

$$R = 1 - H(\mu_o) \sqrt{1 - \omega'_o} . \quad (15)$$

Even this formula can be further simplified for sea-water because $\omega'_o \leq 0.4$ and $H(\mu, \omega'_o)$ is rather constant for $\omega'_o < 0.4$ and $H(\mu_o)$ in equation (15) may be replaced by \bar{H} of equation (12). Then R of marine waters is only depending on ω'_o .

$$R = \frac{2}{\omega'_o} (1 - \sqrt{1 - \omega'_o}) - 1 . \quad (16)$$

Until now the above given assumption of isotropy for the truncated scattering function has still not been used. Using it now gives $b_b = b'/2$, leading to

$$\omega'_o = \frac{2(b_b/a)}{1 + 2(b_b/a)} . \quad (17)$$

For equation (16) this results in an equation which has been derived earlier by others who started with different assumptions:

$$R = \frac{1 + (b_b/a) - \sqrt{1 + 2b_b/a}}{b_b/a} \quad (18)$$

Equation (18) is identical to results of Duntley (1942), Joseph (1950) and Kozlyaninov and Pelevin (1965), who all assumed a two-stream radiative transfer equation. If we neglect the simplification which led to equation (16) but use equation (18) in equation (15) we nearly find Gordon's formula which was derived from Monte Carlo simulations (see also Figure 6).

$$\text{This paper: } R = 1 - H(\mu_o) \sqrt{\frac{1}{1 + 2(b_b/a)}} \quad (19a)$$

$$\text{Gordon, 1991: } R = m(D_o - 1) \cdot R^* + R^* \quad (19b)$$

$$\text{with } R^* \approx 0.3244 (b_b/a) / (1 + b_b/a)$$

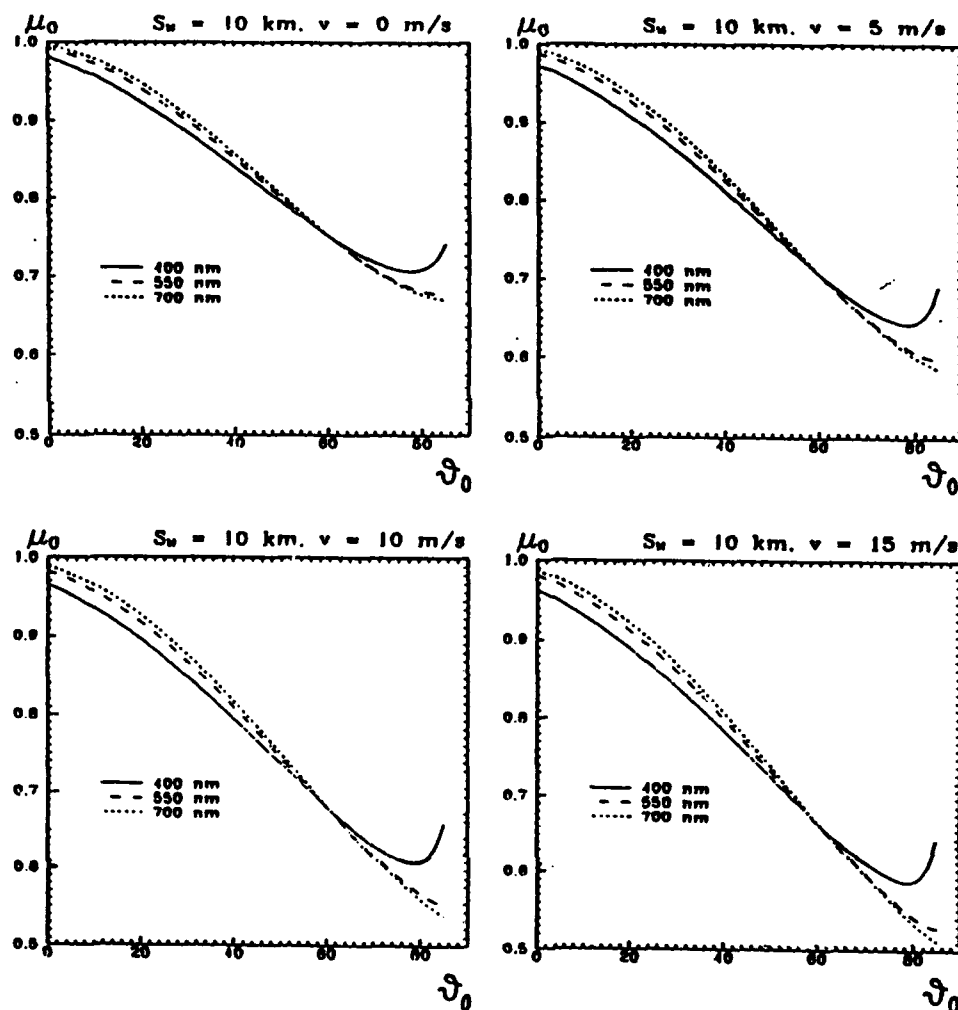


Fig. 6: Relative reflected irradiance R as a function of μ_0 for different ratios b_0/a . A = this paper, G = computed from Eq. (19b) using $m = 0.465$ (Gordon et al., 1975; Gordon, 1991).

Although the above derivation of equation (18) uses rather stringent assumptions (simplifications) it regains well established formulae, it shows that $R(\mu_0, b_0/a)$ is not depending on a complicated treatment of the scattering function, allowing a delta function truncation and isotropicity for the rest.

The average cosine of downwelling irradiance μ_0 just below sea surface is depending on solar zenith distance, atmospheric aerosol optical depth and surface roughness (wind speed). We have calculated μ_0 for various parameter combinations and some are displayed in Figure 7. μ_0 varies only from 0.96 to 0.995 if the Sun is in the zenith, decreases to values of 0.75 to 0.65 mainly as a function of zenith distances of the Sun and also is influenced by the surface roughness, which lowers μ_0 generally. However, these variations do not impact strongly on the result of the theoretical model as shown by the step from equation (15) to (16).

Since in many cases b_0 or a are not available but K_d is, we also derived its relation to b_0/a under the above assumptions. The result also agrees with Joseph (1950) as well as Kozlyanihov and Pelevin (1965) and also Preisendorfer (1976).

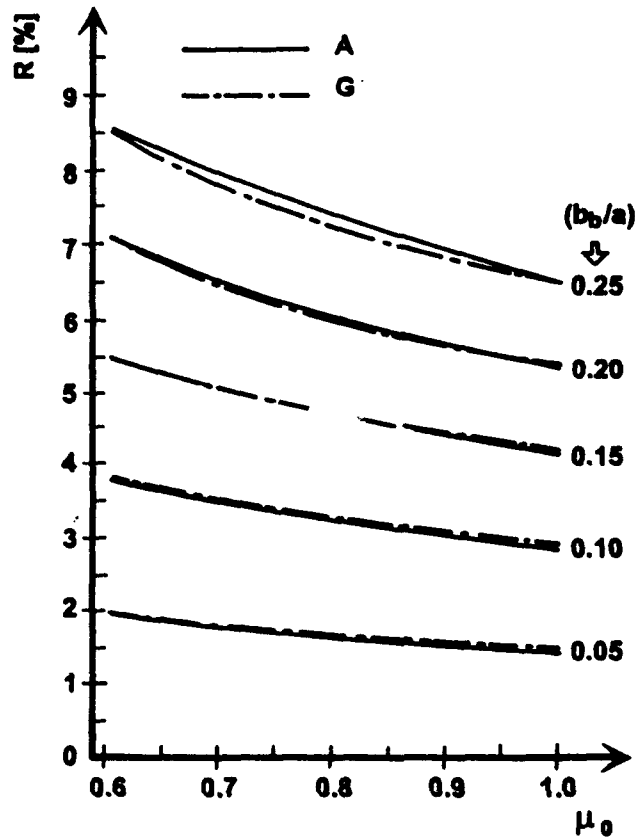


Fig. 7: The computed average cosine of downwelling radiance μ_0 just below the sea surface for three wavelengths $\lambda = 400, 550$ and 700 nm and for four different surface roughnesses due to wind speeds $v = 0, 5, 10$ and 15 m/s as a function of solar zenith angle at a horizontal visibility $S_M = 10$ km.

$$K'_d(z = 0) = \frac{1}{\mu_o} \left(1 - \frac{\omega'_o}{2} H(\mu_o) \right) \quad (20)$$

$$\text{with } K'_d = K_d / (a + b') .$$

If we use again $H(\mu_o) \approx \bar{H}$ equation (20) takes the very simple form also found by the mentioned authors

$$K'_d(z = 0) = \frac{1}{\mu_o} \sqrt{a(a + 2b_b)} \quad (21)$$

Conclusion

We have introduced new large sets of observations of upwelling radiances or irradiances at known pigment concentration into earlier semi-empirical relations between phytoplankton pigment concentration and radiation characteristics of sun-lit open ocean waters. Applying the revised semi-empirical approach of table 2 to other data (65 stations in the Atlantic from the Sargasso Sea to Europe for oligotrophic to eutrophic conditions) we get a systematic error of only -3% in pigment concentration for reflectance and +3% for reflected radiance measurements at standard deviations of 20 and 28%, respectively. There seems to be no need for regionalized algorithms since variations at a distinct site are as large as those between distant sites.

In order to get a simple but reliable theoretical expression for reflectance R as a function of inherent optical properties we have recovered from the invariance principle of semi-infinite optical media together with a rough scattering function approximation (delta function for forward scattering and isotropic scattering for the rest) a very simple but rather accurate relation (Figure 6) between the diffuse attenuation coefficient, the absorption to backscattering ratio a/b_b and reflectances R . For the relation of a/b_b to pigment density C_a , however, we still need the empirical relations in table 2.

For remote sensing the correction of the atmospheric masking will introduce additional errors making the above tolerable inaccuracy possibly unacceptable.

References

- Ambarzumyan, V.A., E.R. Mustel, A.B. Severnyi, V.V. Sobolev (1952): *Teoreticheskaya astrophysika*. Gos. Izd. Techn.-Teoret. Lit., Moscva (in Russian).
- Bukata, R.P., J.H. Jerome, K.Ya. Kondratyev, D.V. Posdnyakov (1991a): Estimation of organic and inorganic matter in inland waters: optical cross sections of lakes Ontario and Ladoga. *J. Great Lakes Res.*, 17 (4), 461-469.
- Bukata, R.P., J.H. Jerome, K.Ya. Kondratyev, D.V. Posdnyakov (1991b): Satellite monitoring of optically-active components of inland waters: an essential input to regional climate change impact studies. *J. Great Lakes Res.*, 17(4), 470-471.
- Chandrasekhar, S. (1960): *Radiative transfer*. Dover Publications, Inc. New York, 393 pp.
- Cox, C., W.H. Munk (1956): Slopes of the sea surface deduced from photograph of sun glitter. *Scripps Inst. of Oceanogr., Bul.* 6, 1956, No. 9.
- Dera, J. (1992): *Marine physics*. Elsevier Sci. Publ. Comp., Amsterdam-Oxford-New York-Tokyo.
- Doerffer, R. (1979): Untersuchungen über die Verteilung oberflächennaher Substanzen im Elbe-Ästuar mit Hilfe von Fernmeßverfahren. *Arch. Hydrobiol., Suppl.* 43, (2/3), 119-224.
- Duntley, S.Q. (1942): Optical properties of diffusing materials. *J. Opt. Soc. Am.*, 32, 61-70.
- Gordon, H.R., O.B. Brown, M.M. Jacobs (1975): Computed relationships between the inherent and apparent optical properties of a flat homogeneous ocean. *Appl. Opt.*, Vol. 14, No. 2, 417-442.
- Gordon, H.R., A. Morel (1983): Remote assessment of ocean color for interpretation of satellite visible imagery. in: R.T. Barber et al. (Eds.): *A Review in Lecture Notes on Coastal and Estuarine Studies*. Springer-Verlag, New York.
- Gordon, H.R. (1991): Absorption and scattering estimates from irradiance measurements. Monte Carlo simulations. *Limnol. Oceanogr.*, 36 (4), 769-777.

- Jerlov, N.G. (1976): *Marine Optics*. Elsevier Amsterdam-Oxford-New York, 231 pp.
- Jerome, J.H., R.P. Bukata, J.E. Bruton (1987): Monte Carlo determinations of volume reflectance for natural waters. Burlington (Ontario), 10 p, (NWRI Rep. IV 87-149).
- Joseph, J. (1950): Untersuchungen über Ober- und Unterlichtmessungen im Meere und über den Zusammenhang mit Durchsichtigkeitsmessungen. Dtsch. Hydrograph. Zeitschrift, Bd. 3, 324-335.
- Kirk, J.T.O. (1981): Monte Carlo study of the nature of the underwater light field in and relationships between optical properties of turbid yellow waters. Austral. J. Mar. Freshwater Res., Vol. 32, 517-532.
- Kirk, J.T.O. (1983): *Light and photosynthesis in aquatic ecosystems*. Cambridge University Press, New York.
- Kirk, J.T.O. (1984): Dependence of relationship between inherent and apparent optical properties of water on solar altitude. Limnol. Oceanogr., Vol. 29, 350-356.
- Koslyaninov, M.V., V.N. Pelevin (1966): On the application of a one-dimensional approximation in the investigation of the propagation of optical radiation in the sea. U.S. Dep. Comm. Jount Publ. Res. Ser., Rep. 36, 54-63.
- Kondratyev, K.Ya., D.V. Pozdnyakov (1984): Kachesvo prirodnkh vod i opredelyaynshchiye yevo komponenty. AN SSSR, Izd. Nauka, Leningrad, 54 pp.
- Kondratyev, K.Ya., D.V. Pozdnyakov, V.Yu. Isakov (1990): Radiacionno - Gidroopticheskiye eksperimenty na ozerakh. AN SSSR, Izd. Nauka, Leningrad, 115 pp (in Russian).
- Monin, A.S. (Ed.) (1983): *Optika okeana*, Vol. 1, Izd. Nauka, Moskwa, 371 pp.
- Morel, A., L. Prieur (1975): Analyse spectrale des coefficients d'attenuation diffuse, de reflexion diffuse, d'absorption et de retrodiffusion pour diverses regions marines. Lab. Oceanogr. Phys. Villefranche-sur-Mer, Rapp., 17, 157 pp.
- Morel, A., L. Prieur (1984): Analysis of variation in ocean color. Limnol. Oceanogr., Vol. 29, 340-349.
- Morel, A. (1988): Optical modeling of the upper ocean in relation to its biogenous matter content (Case I Water). J. of Geophys. Res., vol. 93, Nr. C9, 10749-10768.
- Morel, A. (1991): Light and marine photosynthesis: A spectral model with geochemical and climatological implications. Prog. Oceanogr., Vol. 26, 263-306.
- Mullamaa, Yu.A.R. (1964): Atlas opticheskikh kharakteristik vzvdnovannoy poverkhnosti monja. Tartu, 494 pp (in Russian).
- Pelevin, V.N. (1980): On the spectral characteristics of the solar radiation field in the sea and above the latter's surface. in: Pelevin V.N., M.V. Kozlyaninov(Eds.): *Light Fields in the Ocean*. USSR Academy of Science, P.P. Shirshov Institute of Oceanology, Moscow, 16-25.
- Pelevin, V.N., V.L. Solomaha (1989): O vosstanovlenii koncentraciyi primesei v eftrofirovannykh vodakh Baltiiskogo morya po spektru voskhodyashchevo izlucheniya. Issledovaniye Zemli iz Kosmosa 1, 27-33 (in Russian).
- Potter, J.F. (1970): The delta function approximation in radiative transfer theory. J. Atmos. Sci., Vol. 27, No. 6, 676-687.
- Preisendorfer, W.W. (1976): *Hydrologic optics*. Vol. 5, Pac. Mar. Environ. Lab., Natl. Oceanic and Atmos. Admin., Seattle, Washington.
- Prieur, L. (1976): Transfert radiatif dans les eaux de mer. D. Sci. Thesis., Université. Pierre et Marie Curie, Paris, 243 pp.
- Prieur, L., S. Sathyendranath (1981): An optical classification of coastal and oceanic waters based on the specific observation curves of phytoplankton pigments, dissolved organic matter and other particulate materials. Limnol. Oceanogr., Vol. 26, 671-689.
- Smekot-Wensierski, W., B. Wozniak, H. Grassl, R. Doerffer (1992): Die Absorptionseigenschaften des marinen Phytoplanktons. GKSS 92/E/105, 104 pp.

- Smekot-Wensierksi, W., B. Wozniak, H. Graßl, R. Doerffer, (1994): Modeling of irradiance reflectance of the sea in relation to chlorophyll concentration (case 1 Waters). Max-Planck-Institut für Meteorologie, Hamburg (in preparation).
- Smith, R.C., K.S. Baker (1978): Optical classification of natural waters. *Limnol. Oceanogr.*, 23 (2), 260-267.
- Shifrin, K.S., I.N. Salganik (1973): *Tablicy po svetorasseyaniyu*. AN SSSR, Gidrometeorizdat, Leningrad, Vol. 5, 218 pp.
- Sobolev, V.V. (1972): *Rasseyaniye sveta v atmosferakh planet*. Izd. Nauka, Moscow, 335 pp.
- Vertucci, F.A., G.E. Likens (1989): Spectral reflectance and water quality of Adirondack mountain region lakes. *Limnol. Oceanogr.*, 34, 1656-1672.
- Wozniak, B., V.N. Pelevin (1991): Optical classifications of the seas in relation to phytoplankton characteristics. *Oceanologia*, 31, 25-55.
- Wozniak, B., J. Dera, O.J. Koblentz-Mishke (1992a): Modeling the relationship between primary production, optical properties, and nutrients in the sea. in: *Ocean Optics XI, Proceedings SPIE*, Vol. 1750, 244-295.
- Wozniak, B., J. Dera, O.J. Koblentz-Mishke (1992b): Bio-optical relationships for estimating primary production in the ocean. *Oceanologia*, 33, 5-38.

Appendix 1

List of symbols

a	Absorption coefficient; m^{-1}
b	Scattering coefficient; m^{-1}
b_b	Backscattering coefficient; m^{-1}
b_{bp}	Backscattering coefficient of phytoplankton; m^{-1}
b_p	Particle scattering coefficient; m^{-1}
b_w	Scattering coefficient of water; m^{-1}
$\beta(\gamma)$	Volume scattering function; $m^{-1} sr^{-1}$
$\beta_p(\gamma)$	Particle volume scattering function; $m^{-1} sr^{-1}$
γ	Scattering angle
C_a	Chlorophyll-a-like pigment density; $mg m^{-3}$
$\overline{\cos\gamma}$	Average cosine of $\beta(\gamma)$
$\overline{\cos\gamma_p}$	Average cosine of $\beta_p(\gamma)$
$E_d(z)$	Downwelling irradiance at depth z ; $W m^{-2}$
$E_u(z)$	Upwelling irradiance at depth z ; $W m^{-2}$
$E_{od}(z)$	Downwelling scalar irradiance at depth z ; $W m^{-2}$
E_{os}	Solar constant; $W m^{-2}$
$E_{os}(0)$	Solar constant after propagation through the atmosphere and refraction at the sea surface; $W m^{-2}$
$K_d(z)$	Diffuse attenuation coefficient derived from $E_d(z)$ at depth z ; m^{-1} $K_d(z) = -d \ln E_d(z)/dz$
$L(\Theta, \varphi, z)$	Radiance in direction (Θ, φ) at depth z ; $W m^{-2} sr^{-1}$
L_d, L_u	Downwelling and upwelling radiance; $W m^{-2} sr^{-1}$
λ	Wavelength; nm
$\mu = \cos \Theta$	$L(\Theta, \varphi) \equiv L(\mu, \varphi)$
$\mu_0(z)$	Average cosine of downwelling radiance at depth z ; $\mu_0 = E_d/E_{od}$
$\mu_0(z=0)$	Average cosine of downwelling radiance just below the surface
$R(z)$	Relative irradiance reflected at depth z ; $R(z) = E_u(z)/E_d(z)$
$R(z=0)$	Relative reflected irradiance just below the sea surface
$\rho(\Theta, \varphi)$	Relative reflected radiance just below the surface $\rho(\Theta, \varphi) = \pi \cdot L_w(z=0, \Theta, \varphi) / E_d(z=0)$
$\rho = \rho(\Theta=180^\circ)$	Relative reflected radiance into zenith-direction
S_m	Horizontal visibility in air just above the sea surface
τ	Optical depth; $\tau = \int (a + b) dz$
τ^a	Optical depth of the atmosphere
τ^{acr}	Aerosol optical depth
τ^{mol}	Rayleigh optical depth of the atmosphere
ϑ_0	Solar zenith angle
ω_0	Single scattering albedo; $\omega_0 = b/(a + b)$
v	Wind speed; $m s^{-1}$
z	Depth; m

Appendix 2

Definition of errors applied in the present study.

F = the physical parameter F_{obs} = the observed parameter F_{mod} = the modelled parameter				
Arithmetic statistics		Logarithmic statistics		
bias	standard deviation	bias	Range of variability	
$\langle \epsilon \rangle$	σ_{ϵ}	$\langle \epsilon \rangle_g$	ϵ_{\min}	ϵ_{\max}
<p>N = number of observations</p> <p>ϵ_i = relative error = $(F_{\text{imod}} - F_{\text{iobs}})/F_{\text{iobs}}$, $i = 1, \dots, N$</p> <p>$\epsilon_{li} = \log (F_{\text{iobs}}/F_{\text{imod}})$, $\epsilon_l = \sum \epsilon_{li} / N$</p> <p>$\langle \epsilon \rangle = \sum \epsilon_i / N$ = mean of errors ϵ_i</p> <p>$\sigma_{\epsilon} = \{ [\sum (\epsilon_i - \langle \epsilon \rangle)^2] / N \}^{1/2}$ = standard deviation</p> <p>$\langle \epsilon \rangle_g = 10^{\epsilon_l} - 1$ = geometric mean of errors</p> <p>$\sigma_l = \{ [\sum (\epsilon_{li} - \epsilon_l)^2] / N \}^{1/2}$</p> <p>$\epsilon_{\min} = 10^{(\epsilon_l - \sigma_l)} - 1$</p> <p>$\epsilon_{\max} = 10^{(\epsilon_l + \sigma_l)} - 1$</p>				

**Remote sensing of natural water quality parameters:
retrieval algorithm development and optimisation analysis**

K. Ya. Kondratyev * , D.V. Pozdnyakov ** , and L. H. Pettersson ***

* Scientific Research Centre for Ecological Safety, Korpousnaya Str. 18, 197042 St. Petersburg, Russia,

** Nansen International Environmental and Remote Sensing Center, Korpousnaya Str. 18,
197042, St. Petersburg, Russia,

*** Nansen Environmental and Remote Sensing Centre, Edv. Griegsv. 3A, N-5037 Solheimsviken, Norway.

ABSTRACT

Development of water quality retrieval algorithms is discussed in terms of causal dependence of the upwelling spectral radiance upon the water composition. Unlike clean marine/oceanic waters for which linear regression retrieval relationships are valid, inland and coastal zone water masses with high degree of optical complexity necessitate the development of non parametric retrieval approaches. At the basis of these techniques are models considering the optical competitiveness of several co-existing aquatic components. Such models for Lakes Ladoga and Ontario are described and compared.

Monte Carlo simulations have been performed to analyse the spectral and angular variations of the upwelling radiance scattered by the water column out into the atmosphere. Analysis of optimal conditions for running remote sounding of natural waters of various optical complexity is carried out. Relevant recommendations are formulated.

1. INTRODUCTION

The topicality of the water quality problem is mostly due nowadays to a continuously declining ecological state of inland water basins as well as coastal zones of seas and oceanic gulfs¹. One of the major mainsprings of the phenomenon resides in the unprecedented intensification of eutrophication processes in the above categories of water bodies: their natural "ageing" turns out to be immensely accelerated because of extensive anthropogenic admissions of nutrients (phosphorous and nitrogen in the first place). Fairly often these processes find themselves further promoted by virtue of water temperature increase as entailed by either thermal industrial inflows or anthropogenically provoked basin shallowing (as a result of enhanced run-off and river discharge). A substantial increase in water turbidity caused by increased concentrations in suspended and dissolved matter is liable to contribute to the water temperature increase. All these factors acting concurrently lead to a rapid transition of the water body up to a higher tropic level. This transition, in its turn, entails algae bloom events, anoxia, and eventually, a drastic deterioration of water quality parameters².

It is noteworthy that the above outlined causal sequence does not cease at this level. The primary production growth in such water bodies tells on carbon and sulphur cycles thus influencing atmospheric processes directly related to local and global climate changes³.

The first investigations on the application of remote sensing in the visible to studying natural water quality go back to 60s and 70s, and were primarily intended to infer algae chlorophyll concentrations in clear and optically simple marine and oceanic waters (i.e. waters assigned, according to the Morel's classification⁴, to case - I waters).

2. SPECTRAL FEATURES OF THE UPWELLING RADIANCE RELEVANT TO NON CASE - I WATERS: IMPLICATIONS FOR DEVELOPING REMOTELY SENSED DATA RETRIEVAL TECHNIQUES

Model calculations of the upwelling radiance B_λ coming out from below the water surface conducted by Bukata et al.⁵ have simulated the spectral variations of B_λ in dependence of naturally occurring combinations of optically active components indigenous to non case-I waters. These extensive simulations revealed the existence of two spectral regions centred at λ_i and λ_j , where B_λ appears to be, respectively, predominantly controlled by and almost insensitive to the presence of phytoplankton provided the concentrations of suspended minerals (C_{sm}) and dissolved organic matter (C_{dom}) are only marginal. Under these conditions the value of B at $\lambda_i = 430-450$ nm (the so called "chlorophyll dip") decreases continuously but not linearly with increasing phytoplankton concentration due to the enhancement of light absorption by chlorophyll (CHL) molecules. At the same time the value of B at $\lambda_j = 505$ nm (C_{sm}, C_{dom} are zero) or at $\lambda_j = 570 - 610$ nm ($C_{dom} = 0; 0.1 < C_{sm} < 0.5$ g/m³) rests invariable, i.e. $(\partial B / \partial C_{chl})_{\lambda = \lambda_j} = 0$. This finding obviously explains the feasibility of various regression relationships relating the upwelling radiance B (or its derivatives) at one or several wavelengths to a respective CHL concentration in case - I waters.

Nevertheless as soon as the water column turns out to be enriched with SM and/or DOM, the spectral distribution of the radiance B_λ undergoes dramatic changes. First the wavelength λ_j at which $(\partial B_{\lambda_j} / \partial C_{chl}) = 0$ no longer exists, and, second, as a result of the DOM absorption in the short portion of the visible, the depth of the CHL dip can no more be related unambiguously to the CHL loading. The same conclusion can be drawn from the chromaticity analysis also carried out by Bukata et al.⁵: with increasing C_{sm} (C_{dom} was assumed to be 2.0 gC/m³), the dependence of the chromaticity co-ordinates X, Y, and Z on C_{chl} becomes much less pronounced (as compared to case - I waters), and when $C_{sm} > 5.0$ g/m³, all the three chromaticity co-ordinates are practically insensitive to changes in C_{chl} . In addition, even at low C_{sm} values, the sensitivity of chromaticity co-ordinates to C_{chl} variations weakens when $C_{chl} > 8-10$ µg/m³. The inefficiency of the chromaticity approach in terms of remote sensing of non case - I waters becomes particularly evident when $C_{dom} > 5$ gC/m³: the practical use of colorimetric retrieval algorithms is simply inappropriate in view of their extremely low accuracy. These findings convincingly show that for reliable remote sensing of inland and coastal zone waters (which are regularly non case - I waters) it is not worthwhile trying to adjust the regression algorithms to the multitude of naturally occurring variations in the optical properties of water bodies in question as far as the conditions of existence of a "pivotal" point $(\partial B / \partial C_{chl})_{\lambda = \lambda_j} = 0$ in the upwelling radiance spectral distribution could no longer be met. The inappropriateness of applying oceanic CHL-retrieval algorithms to inland waters was illustrated for Lake Ladoga⁶.

For the solution of this problem at list two approaches could be employed: either a multivariate optimisation technique or regularization technique (known as the Levenberg - Marquardt and Tikhonov - Arsonin techniques respectively).

The Levenberg-Marquardt (L - M) finite difference algorithm as described by Bukata et al.⁷ systematically determines for each wavelength of a measured subsurface irradiance reflectance spectrum $\{S_i\}$ a local minimum of $f(\vec{C})$ if a suitable initial value of the starting concentration vector \vec{C}_0 is given. Here $f(\vec{C}) = \sum_i g^2_i(C) = \sum_i [S_i - R(0, a_i, Bb_i, \vec{C})]^2 / R^2(0, a_i, Bb_i, \vec{C})$, where $\vec{C} = (1, C_{chl}, C_{sm}, C_{dom})$, R is the value of the theoretical reflectance (calculated through any pertinent parametrization), and a and Bb are bulk water inherent optical properties (absorption and backscattering respectively).

Since bulk water inherent optical properties display additive properties, which depend upon the presence of all scattering and absorption centers within the water column, it may be written for a four-component optical system (pure water (W), CHL, SM, and DOM):

$$\begin{aligned} a(\lambda) &= a_w + C_{chl} \cdot a_{chl}^*(\lambda) + C_{sm} \cdot a_{sm}^*(\lambda) + C_{dom} \cdot a_{dom}^*(\lambda) \\ b(\lambda) &= b_w + C_{chl} \cdot b_{chl}^*(\lambda) + C_{sm} \cdot b_{sm}(\lambda), \end{aligned} \quad (1)$$

where a_i^* and b_i^* are absorption and scattering coefficients for a unit concentration of an i -th component (the so-called cross sections) ($i = 1-4$: H₂O, CHL, SM, DOM). Analogous equations can be drawn up for the other inherent optical characteristics.

Since this value of $f(\vec{C})$ may not, however, be the smallest achievable over the valid range of \vec{C} , numerous starting concentration vectors \vec{C}_{0j} could be chosen to permit the L-M algorithm determining the corresponding minima $f_j(\vec{C})$. The \vec{C} associated with the minimum $f_j(\vec{C})$ of this set is then selected as the appropriate solution. Nevertheless, even pursuing this procedure there is no guarantee that any particular starting point \vec{C}_{0j} will result in the algorithm successfully finding any minimum for $f(\vec{C})$, since the algorithm may diverge. In addition, a \vec{C} found through the minimisation of $f(\vec{C})$, can prove to be physically meaningless (e.g. negative concentrations). To obviate such difficulties some constraints should be placed on \vec{C} such that $C_{i \min} < C_i < C_{i \max}$ and transformation from the constrained \vec{C} space to an unconstrained W space ($-\infty < W_i < +\infty$) must be effected using the error function relationship:

$$C_i = C_{i \min} + (C_{i \max} - C_{i \min}) (1 + \operatorname{erf}(W_i)) / 2. \quad (2)$$

The Tikhonov and Arsonin (T-A) approach as described by Kondratyev et al.⁸ assumes that the irradiance reflectance;

$$R_\lambda = A\vec{C}_i + \xi_\lambda, \quad (3)$$

where A is some operator, \vec{C}_i is the concentration vector (as before, a set of concentrations of optically active components forming the value of R_λ), ξ_λ the error in R_λ measurements. It is shown that the solution of the above equation could be found in the following way:

$$\Delta\vec{C} = (A^t \Sigma^{-1} A + D^{-1})^{-1} A^t \Sigma^{-1} \Delta R, \quad (4)$$

where $\Delta R = R - R_0$, $\Delta\vec{C} = \vec{C} - \vec{C}_0$, where \vec{C}_0 is some a - priori given value of the concentration vector accounting for the optically active components which determine the value of R_λ ; R_0 the value of irradiance reflectance at $\vec{C} = \vec{C}_0$; R the actually measured value of irradiance reflectance, Σ^{-1} the R_λ dispersion matrix; D^{-1} an a - priori \vec{C}_i dispersion matrix. Sign t means that the matrix is a transposed one, sign -1 stands for denoting an inverse matrix. The solution for \vec{C} can be found making use of the iteration procedure:

$$\vec{C}_{i+1} = \vec{C}_0 + (A_i \Sigma^{-1} A_i + D^{-1})^{-1} A_i^t \Sigma^{-1} (S(0, 1) - R_i(0, 1) + A_i(\vec{C}_i - \vec{C}_0)), \quad (5)$$

where, according to the previously adopted notations, \vec{C}_0 is the initial value of the concentration vector \vec{C} ; \vec{C}_i the value of vector \vec{C} at an i -th iteration step calculated with the application of a chosen parametrization for R_λ ; A_i the variational derivatives $(\partial R / \partial \vec{C}_i)$ matrix; Σ the $R(0, \lambda)$ dispersion matrix; D the a - priori \vec{C}_i dispersion matrix.

Consequently this approach consists in minimisation in the course of iteration of the standard deviation:

$$\delta = 1/n \sum_\lambda [R(0, \lambda)^2 - (S(0, \lambda))^2], \quad (6)$$

which eventually plays the role of criterion of the vector \vec{C} retrieval precision.

The employment of both retrieval algorithms imply the availability of an adequate optical model, i.e. a set of cross sections of major optically active components of waters liable to remote sounding. The first model with the required self-sufficiency has been elaborated by Bukata et al.⁷ for Lake Ontario making use of direct in situ measurements of $R(0, \lambda)$ and \vec{C} and applying the same L-M algorithm. But this time the least-squares solution was found through minimising over vector \vec{X} the function

$$f(\vec{X}) = \sum g_j^2(\vec{X}), \quad (7)$$

where $\vec{X} = (a_w, a_{chl}^*, a_{sm}^*, a_{dom}^*, Bb_w, Bb_{chl}^*, Bb_{sm}^*, 0)$. As before, the appropriate constraints were imposed on \vec{X} :

$$X_i \min < X_i < X_i \max, \quad (8)$$

and the algorithm was permitted to operate in W space according to the error function transformation:

$$X_i = X_i \min + (X_i \max - X_i \min)(1 + \operatorname{erf}(W_i))/2. \quad (9)$$

The resulting least-squares solution for \vec{X} is, of course, applicable only to the specific wavelength of the S_j used, and the same procedure must be repeated substituting the S_j corresponding to each wavelength at which \vec{X} is desired. In this way it is possible to determine the entire cross section spectrum $\vec{X}(\lambda)$.

Fig. 1⁸ illustrates cross section spectra for CHL, SM and DOM as experimentally determined for Lakes Ladoga and Ontario making use of the M - L multivariate optimisation technique, and concurrent in situ measurements of subsurface volume reflectance spectra and concentrations of CHL, SM, and DOM. These spectra constitute optical water quality models for both lakes assuming that at any instant of time a natural water mass may be defined as a homogeneous combination of pure water, unique suspended organic material (represented by the CHL-a concentration), unique suspended inorganic material (represented by the SM concentration), and dissolved organic material (represented by DOM concentration). Obviously, the definitive model should consider the cross sections of every distinct aquatic component present in natural water masses, as well as any temporally-varying characteristics of these components. Such a model is clearly unattainable. Moreover, since the water mass is assumed here homogeneous, the current model does not include layering effects. Also, no provision is incorporated for chemical impurities. Nevertheless, the actual feasibility of the model in question depends on the relative significance of optical effects caused by the water mass properties overlooked by the model. The degree of adequacy of the optical model (which in general seems to be explicitly time and location dependant) can be assessed through extensive field retrieval experiments involving shipborne subsurface volume reflectance spectra measurements supplemented by the collection of water samples to determine concentrations of CHL, SM and DOM for validation purposes.

Applying the above described L - M and T - A techniques to the measured subsurface volume reflectance spectra, and using the appropriate optical model in the form of cross sections, it is possible to infer the sought for concentration vector C , and then to compare it with its directly (in situ) measured counterpart.

The results of these retrieval and validation studies performed in Lake Ladoga are shown in Fig. 2⁸. It can be clearly seen that there is quite a gratifying conformity between the retrieved and measured values of C_{chl} , C_{sm} , and C_{dom} . Since these retrieval and validation studies have been reiterated in midsummer time during three consecutive years invariably giving good results, the elaborated optical model seems fairly adequate, though, of course, it is open to further improvements.

3. MODELLING OF RADIATIVE AND OPTICAL CHARACTERISTICS OF THE WATER BODY - ATMOSPHERE SYSTEM AS A WAY TO OPTIMISE OF THE VISIBLE REMOTE SENSING OF NATURAL BASINS

Extensive numerical experiments have been carried out using the Monte-Carlo (M-C) technique described elsewhere⁸. When running M-C simulations, the following processes were taken into account: photon interactions with wind -roughened water surface, absorption, and scattering of light on molecules of atmospheric gases and on aerosols, as well as on water molecules and hydrosols. Simulations were performed by way of designing a homogeneous Markov chain of photon collisions and employing a local estimation technique⁹. A cloudless atmosphere was designed using scattering and absorption coefficients suggested by McClatchey et al.¹⁰. Models of rural, tropospheric and background stratospheric aerosols were related, respectively, to layers 0 - 2, 2 - 10 and 10 - 30 km. The vertically integrated optical depth of such an atmosphere proved to be 0.8, 0.5, 0.48, 0.45, 0.39, 0.29 at wavelengths 400, 500, 520, 550, 600, and 800 nm respectively. The optical depths of the first (from the earth surface) 10 - km layer of the

atmosphere at $\lambda = 400, 600$ and 800 nm were, respectively, 0.201, 0.129, 0.129, 0.102. For the layers mentioned the aerosol phase functions were calculated with Mie formulae using the aerosol size distribution given in McClatchey et al. ¹⁰. The estimates of refraction indices for aerosol particles as well as the limits of variations of both particle sizes and their refraction indices were also taken from the above publication.

The water basin was assumed 60 m deep. It was supposed that its hydrooptical properties were determined by pure water, phytoplankton (CHL), SM and DOM. The water column was subdivided into several layers characterised by certain vertical profiles of CHL concentrations. Loading in SM and DOM were taken vertically invariable. Calculations were based on the spectral cross sections of absorption and scattering of the major optically active components (H_2O , CHL, SM, DOM) obtained by us for Lake Ladoga (see above). The hydrosol phase functions were calculated with Mie formulae using the particle size distribution parametrization derived as the best fit to the available experimental data on Lake Ladoga ⁸:

$$f(r) = 3.09 \cdot 10^8 r^{-3.575} \quad (0.01 < r < 2 \text{ nm}). \quad (10)$$

The optical depth of the modelled water basin, depending on the concentrations of CHL, SM and DOM representative of Lake Ladoga, lay within the ranges $180 < \tau_{400} < 630$; $36 < \tau_{600} < 486$; $30 < \tau_{800} < 360$. The bottom albedo was assumed to be zero. The water-atmosphere interface was designed as an array of elementary facets whose normals were distributed following a "truncated" Cox-Munk parametrization with the exponential part assumed to be unity. Therefore the elevations of facets in this model were taken to be zero, and the effect of foam formations was left out of account.

The following notations were introduced: B_λ is the spectral radiance scattered by water column out in the atmosphere; I_λ the spectral radiance upwelling from the water surface (this entity comprises the Fresnel reflection component, B_λ , and the contribution of the intervening atmospheric layer).

When analysing the sensitivity of B_λ and I_λ to the vertical distribution of CHL concentration in the water body, several options of CHL profiles have been tried, whereas concentrations of SM and DOM were kept vertically invariant. Results of numerical experiments (calculations refer to the situation characterised by the solar zenith angle $\theta_0 = 30^\circ$, viewing angle $\theta = 0^\circ$, azimuthal viewing angle $\phi = 0^\circ$, the altitude of observations - 1 km, zero wind speed; the spectral region $400 < \lambda < 700$ nm) suggest the following conclusions. Changes of radiance B_λ due to the C_{chl} vertical inhomogeneity do not exceed 10 - 15 % (the error of simulations is estimated at 5 - 10 %), if C_{chl} varies substantially in the upper and middle layers of the water column. The presence or the absence of the C_{chl} maximum in the lower layers affects still less B_λ . The effect of the C_{chl} profile shape on I_λ does not exceed several per cent.

In view of this result and all the uncertainties inevitably accompanying field measurements of hydrooptical parameters and characteristics of the radiation field, it appears only reasonable (at least for typical conditions occurring in Lakes Ladoga and Onega) to only consider the cases with homogeneous vertical profiles of C_{chl} , C_{sm} and C_{dom} , when simulating the radiance field in the water basin - atmosphere system. Therefore, the sensitivity of B_λ and I_λ to concentrations of principal optically active components has been studied for the above stated conditions.

An increase in C_{sm} from zero to 5 mg/l results in a sharp increase in B_λ and in a marked growth of I_λ . However, a further enhancement of C_{chl} (up to 10 - 15 $\mu\text{g/l}$), results in B_λ and I_λ growth rate slowing down, so that at some stage neither B_λ nor I_λ sensibly response to further loading in C_{sm} .

To reveal the optimal conditions for remote sensing of water basins in the visible, the characteristics of the radiance field were calculated with varying viewing angles (θ), sun zenith angles (θ_0) and wind speeds near the water surface. It was equally assumed that the concentrations of CHL, SM and DOM were respectively: 10 $\mu\text{g/l}$, 10 mg/l and 2 mgC/l.

According to Fisher and Grasse¹¹, the radiance B_λ of the light emerging from beneath the water surface exhibits but a very weak azimuthal dependence in case of clean oceanic waters. Our simulation experiments indicate that this quasi-isotropy is no longer valid in inland waters heavily laden with CHL, SM and DOM: the value of B is maximum in the sun direction and proves to be dependant on the viewing angle ϑ unless $\vartheta < 30^\circ$ and $\varphi > 90^\circ$. Relevant experimental data obtained by us in Lake Ladoga waters seem to substantiate the simulation results.

Spectral variations of radiance B in meso- and eutrophic inland waters under calm weather conditions (i.e. $V = 0$ m/s) is shown in Fig. 3 for $\lambda = 410, 500, 660$ nm, and varying both sun zenithal and nadir viewing angles (ϑ_0, ϑ), whereas the azimuthal viewing angle φ is taken to be zero. The graphs offer a further confirmation to the earlier findings pointing to a very substantial decrease in B in the short wavelength portion of the visible spectrum. This effect proves to be even more pronounced at low values of ϑ_0 and slant viewing directions.

The ratio $P_\lambda = (B_\lambda / I_\lambda) \times 100\%$ was taken as a criterion of the information content inferable from low-level remote sensing data, since it gives an idea about the share of the radiance B contribution to the net radiance signal captured by the remote sensor. Fig. 4 shows the graphs of variability of P ($\lambda = 600$ nm) as a function of ϑ and ϑ_0 at a fixed values of the azimuthal angle ($\varphi = 0^\circ$), the altitude of the "observer" (0.2 km) and wind speed (5 m/s). It could be seen that the curves have a distinct maximum, whose value and position (on the axis of sun zenith angles) reveal a stable trend to, respectively, a decrease and a shift to small viewing angles ϑ with an increase of ϑ and the elevation of the "observer" over the sea level (the effect of the latter parameter is not shown in Fig. 4). It can be seen that in nadir viewing, optimal conditions for remote sounding could be reached at $\vartheta_0 = 35^\circ$. The variations of the ratio P_λ depending on varying azimuthal angle φ were also simulated. From the viewpoint of remote sensing, the range $80 - 180^\circ$ seems to be the most favourable range of azimuthal angles. In fact, this range is sufficiently isotropic (which appears very essential in terms of routine remote sensing, when it is practically impossible, for several reasons, to strictly maintain the needed azimuthal angle) and is characterised by maximum possible energetics of the remotely recorded response signal (which implies the maximum signal to noise ratio).

The spectral variations of the ratio P (Fig. 5) faithfully comply with the run of the B_λ curve (Fig. 3) progressively growing with λ . But very much unlike B_λ , the ratio P_λ , while increasing with the wavelength, sensibly diminishes at slant viewing directions and grows with declining sun elevations over the horizon.

Analysis of the wind effect on the ratio P_λ shows that the increase in the wind speed V inevitably entails a decrease of the ratio P . With growing V , the optimal conditions of sounding could be reached at small viewing angles and high sun elevations over the horizon.

The above results of M - C numerical simulations are strictly speaking only pertinent to Lakes Ladoga and Onega hydrooptical conditions. Nevertheless they are believed to be applicable to a more wide variety of moderately eutrophic inland waters of temperate latitudes. These results clearly indicate, that, when sounding waters laden with CHL, SM and DOM, the highest signal -to-noise ratio can be reached at $\lambda = 550$ nm. The inter comparison of graphs in Fig. 3 and Fig. 5 implicitly indicate that the optimal conditions (in terms of reasonable levels of upwelling energy and the highest signal-to-noise ratios) for running remote sensing of non case - I waters could be achieved at mean sun zenith angles (about $35 - 40^\circ$) and near vertical viewing angles, whereas the preferential zone of azimuthal viewing angles lies in the range $80 - 280^\circ$.

4. CONCLUSIONS

The analysis of the present state of the issue concerning the optical remote sensing of natural water bodies points to a necessity of deriving more flexible and versatile approaches to the solution of this problem. These approaches are liable to be responsive to specific hydrooptical properties of target basins. Rigid regression relationships relating the concentration of a sought for constituent to the ratio of water surface radiances at two or more wavelengths prove to be reliable if applied to clean off-shore oceanic/marine waters (Case - I waters). Hydrooptically more complex waters of coastal zones as well as inland water bodies necessitate the application of non-parametric techniques capable of a more adaptable solution of inverse problems. The realisation of such approaches implies the existence of hydrooptical models of target basins in the form of tabulated spectral values of absorption and backscattering cross sections for a set of principal optically active components of natural waters. Such models are already successfully elaborated for North American and European Great Lakes. The optical water models currently in use in both lake regions assume that at any instant of time a natural water mass may be defined as a homogeneous combination of pure water, unique suspended organic material (represented by the chlorophyll -a concentration), unique suspended inorganic material (represented by the suspended mineral concentration), and dissolved organic carbon concentration. Obviously, the definite model should consider the cross sections of every distinct aquatic component present in natural water masses as well as any temporally-varying characteristics of these components. Such a model is clearly unattainable. However, an extension to a reasonable number of additional components would certainly appear to be possible.

Mathematical modelling clearly indicate that both the spectral region and the sun illumination and viewing geometries are of paramount importance for a successful remote monitoring. Since these parameters are dependent on the composition of natural waters (i.e. state of eutrophication and general pollution), the performance of airborne monitoring should be invariably preceded by a thorough analysis of actual hydrooptical situation in the water body to be surveyed.

5. REFERENCES

- 1 NASA, Coastal zone imagery for selected coastal regions. Level II. Photographic Product. The Walter A. Bohan Company, Park Ridge, IL., 1990.
- 2 B. Henderson-Sellers and H.R. Markland, Decaying lakes., John Willey & Sons Publ., Chister e.a., 1987.
- 3 K.Ya. Kondratyev, Global Climate, Nauka Publ., St. Petersburg, 1992.
- 4 A. Morel and L. Prieur, "Analysis of variations in ocean color", *Limnol. Oceanogr.*, Vol.22, pp. 709 - 722, 1977.
- 5 R.P. Bukata, J.E. Bruton and J.H. Jerome, "Use of chromaticity in remote measurements of water quality" *Remote Sens. Environ.*, Vol.3, No.2, pp.161 - 177, 1983.
- 6 R.P. Bukata, J.H. Jerome, K.Ya. Kondratyev and D.V. Pozdnyakov, "Estimation of organic and inorganic matter in inland waters: optical cross sections of Lakes Ladoga and Ontario", *J. Great Lakes Res.*, Vol. 17, No.4, pp.461 - 469, 1991.
- 7 R.P. Bukata, J.E. Bruton and J.H. Jerome, Application of direct measurements of optical parameters to the estimation of lake water quality indicators. CCTW Publ., Burlington (Ontario), 1985.
- 8 K.Ya. Kondratyev, D.V. Pozdnyakov D.V. and Isakov V.Yu., Radiative and hydrooptical experiments in lakes. Nauka Publ., Leningrad, 1990.
- 9 B.A. Kargin, On a statistical modelling of optical radiation interaction with a wind - roughened sea surface. Nauka Publ., Novosibirsk, 1983.
- 10 R.A. McClatchey, H.-J. Bolle and K.Ya. Kondratyev, Report of the IAMAP RCWG on a Standart Radiation Atmosphere. WMO/IAMAP, Et. Collins .Co., USA, Preprint, 1982.
- 11 J. Fisher and H. Grassl, "Radiative transfer in an atmosphere - ocean system: an azimuthally dependent matrix-operator approach", *Appl. Opt*, Vol.23, No.7, pp.1032 - 1039, 1984.

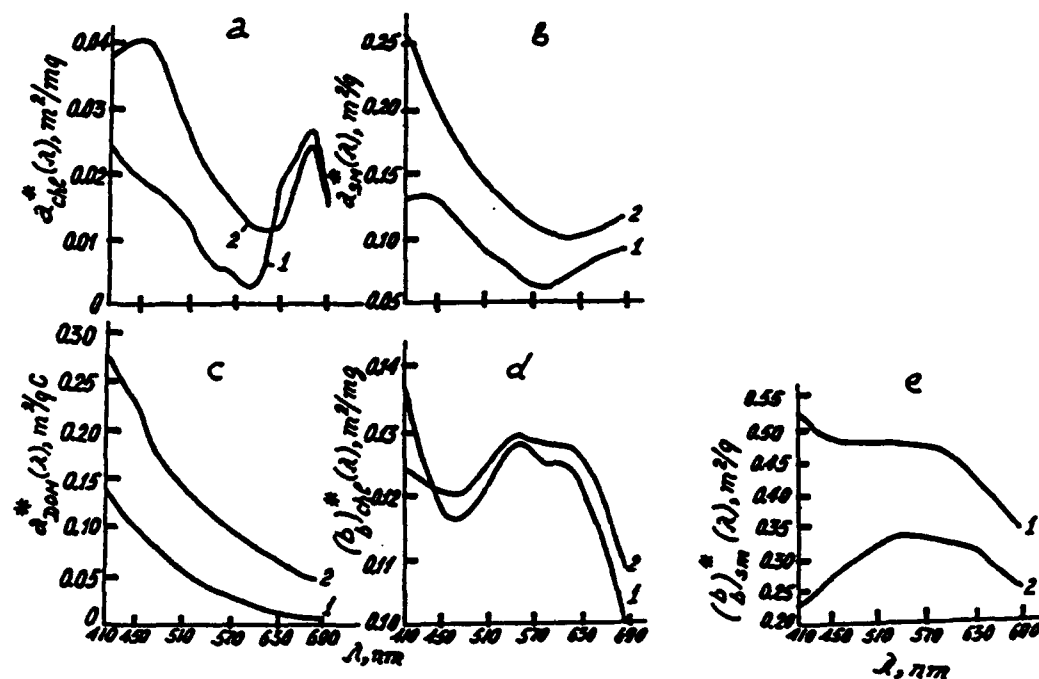


Figure 1. Graphical comparison of hydrooptical models suggested for Lakes Ladoga (1) and Ontario (2):
a, b, c -retrieved absorption cross sections respectively for CHL- a, SM , and DOM
d, e -retrieved backscattering cross sections respectively for CHL and SM.

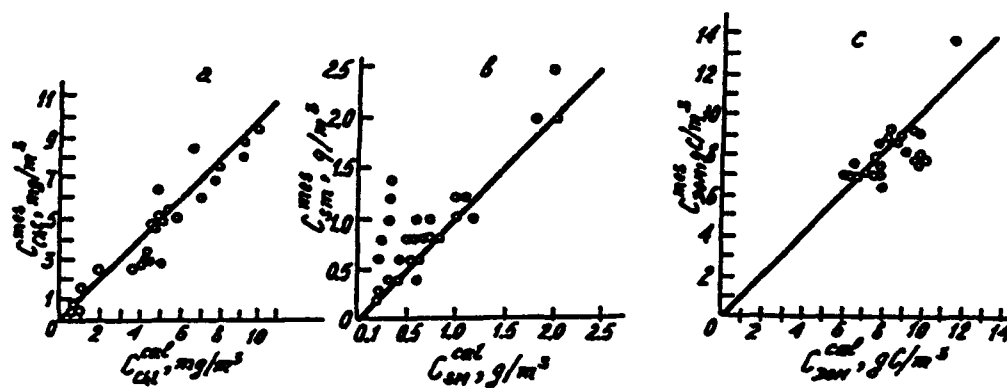


Figure 2. Directly sampled and predicted by the use of the optical water quality model concentrations of CHL (a), SM (b), and DOM (c) in Lake Ladoga.

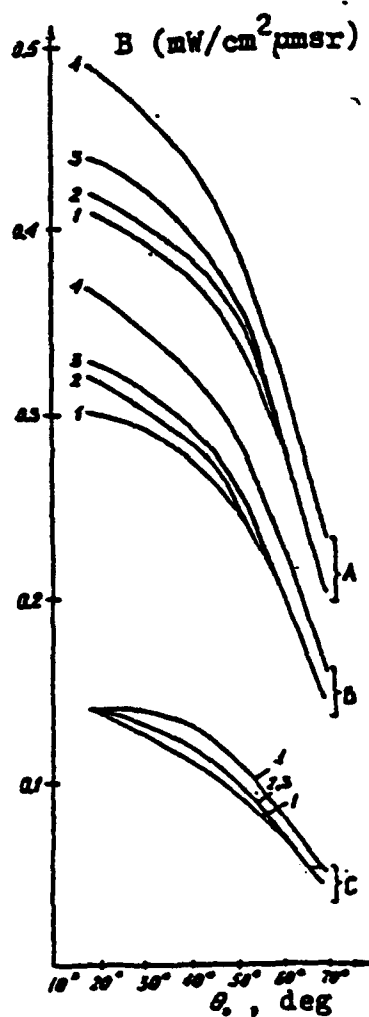


Figure 3. Variations of radiance B against the solar zenith angle θ_0 when viewing angles are 0° (1), 18° (2), 32° (3) and 60° (4), and the azimuthal angle ϕ is equal to 90° .

A - $\lambda = 560$ nm, B - $\lambda = 500$ nm, C - $\lambda = 410$ nm.

The water surface is assumed perfectly calm ($V = 0$ m/s).

$C_{chl} = 5.6 \mu\text{g/l}$, $C_{sm} = 1$ mg/l, $C_{dom} = 8.5$ mgC/l.

The curves for $\lambda = 610$ nm almost coincide with curves labelled B, and therefore are left out of the picture.

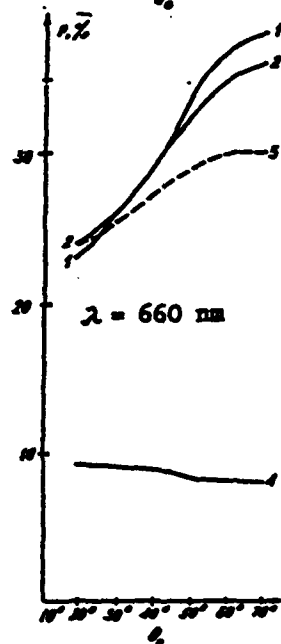
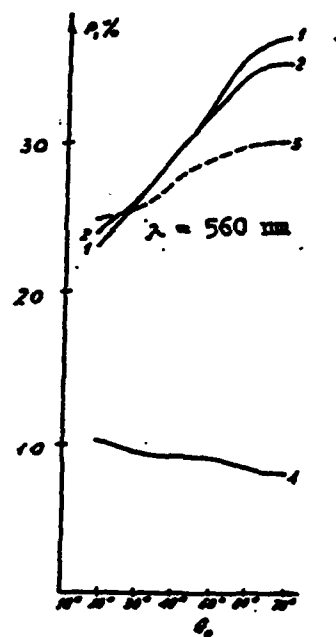
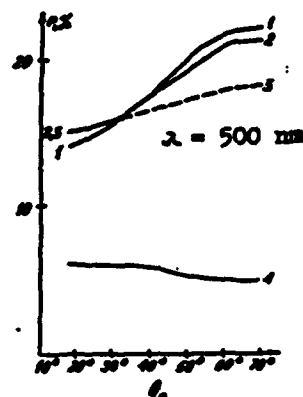
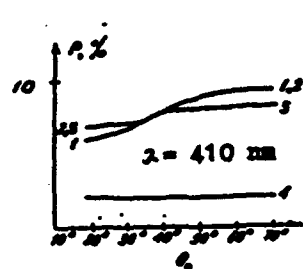


Figure 4. Sensitivity of the ratio P ($\lambda = 600$ nm), in %, to variations of the sun zenith angle θ_0 with viewing angles θ equal to 0° (1), 10° (2), 20° (3), 40° (4), 60° (5) and $\varphi = 0^\circ$; $V = 5$ m/s. The height of the remote sensor over the water surface $H = 0.2$ km; $C_{\text{chl}} = 10$ $\mu\text{g/l}$; $C_{\text{sm}} = 10$ mg/l ; $C_{\text{dom}} = 2$ mgC/l .

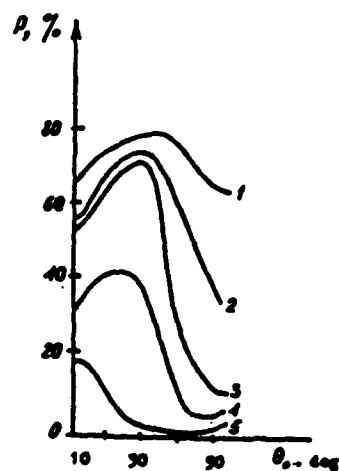


Figure 5. Angular variations of the ratio P at $\lambda = 410$, 500, 560, and 660 nm and nadir viewing angles 0° (1), 18° (2), 32° (3), 60° (4). The azimuthal viewing angle was taken to be 90° . The state of the water surface and the composition of the water column are assumed the same as in Figure 3.

Addendum

The following papers were announced for publication in this proceedings but have been withdrawn or are unavailable.

- [2258-03] **New variable path-length beam transmissometer**
R. A. Maffione, J. M. Voss, D. R. Dana, SRI International; G. D. Gilbert, Naval Command, Control and Ocean Surveillance Ctr.
- [2258-15] **Effect of solar UV radiation on light absorption and fluorescence of seawater**
I. A. Samokhina, A. S. Tibilov, S.I. Vavilov State Optical Institute (Russia)
- [2258-32] **High-resolution profiles of inherent optical properties from the Saragasso Sea**
D. A. Siegel, Univ. of California/Santa Barbara; A. F. Michaels, E. Caporelli, Bermuda Biological Station for Research; C. C. Moore, Western Environmental Technology Labs. Inc.
- [2258-42] **Remote sensing of vertical distribution of seawater scattering coefficient by means of airborne polarization lidar**
A. P. Vasilkov, Y. A. Goldin, B. A. Gureev, P.P. Shirshov Institute of Oceanology (Russia)
- [2258-44] **Multifrequency laser system of optical inhomogeneities in upper hydrosphere**
S. I. Chubarov, I. A. Malevich, Byelorussian Univ.
- [2258-45] **Laser system for analysis of profiles of optical characteristics of atmosphere-hydrosphere medias**
I. A. Malevich, M. M. Kugeiko, S. I. Chubarov, Byelorussian Univ.
- [2258-47] **Pulse propagation in the ocean: WKB solution for the time-dependent radiance distribution**
J. A. Tessendorf, D. Wasson, Arete Associates
- [2258-53] **Models and algorithms for processing remote sensing data of inhomogeneous scattering sea media under a priori unknown reference or calibration values of the optical characteristics**
D. M. Onoshko, Byelorussian Univ.
- [2258-54] **Reference-free methods of measuring the optical characteristics of water medias**
M. M. Kugeiko, I. A. Malevich, Byelorussian Univ.
- [2258-55] **Lidar biomonitoring in the sea: the problems and new solutions**
A. M. Chekalyuk, M. Y. Gorbunov, Moscow State Univ. (Russia)
- [2258-58] **Calibration and characterization of a nine wavelength in-situ attenuation and absorption meter (ac-9)**
C. C. Moore, Western Environmental Technology Labs. Inc.; J. V. Zaneveld, J. C. Kitchen, Oregon State Univ.

- [2258-63] **Fiber optic thermosensor based on shape memory effect**
M. I. Bessarabov, P. A. Shirokikh, Y. A. Bykovsky, A. V. Shelyakov, Moscow Engineering Physics Institute (Russia)

- [2258-64] **Complex of IR instruments for airborne measurements of sea surface temperature field**
V. I. Solovyev, M. M. Miroshnikov, V. N. Minyeev, V. I. Povarkov, V. M. Samkov, S.I. Vavilov State Optical Institute (Russia)

- [2258-65] **Bio-optical profiles with a remotely operated submersible during a bloom in Monterey Bay**
R. A. Maffione, SRI International

- [2258-74] **Remarkable vertical structure of seawater optical characteristics in the western Mediterranean Sea**
O. V. Kopelevich, V. I. Burenkov, P. P. Shirshov Institute of Oceanology (Russia)

- [2258-76] **Optical structure of subpolar front in northern Atlantic**
V. I. Burenkov, P. P. Shirshov Institute of Oceanology (Russia)

- [2258-91] **Irradiance calculation on large depths**
A. I. Sud'bin, V. A. Volynsky, V. I. Burenkov, P. P. Shirshov Institute of Oceanology (Russia)

- [2258-92] **Calculation of absorption and backscattering coefficients using vertical attenuation coefficient and irradiance index**
A. I. Sud'bin, V. A. Volynsky, P. P. Shirshov Institute of Oceanology (Russia)

- [2258-93] **Evaluation of the marine suspension microstructure of the polydisperse intensity**
A. Y. Perelman, St. Petersburg Forestry Academy (Russia); K. S. Shifrin, Oregon State Univ.

- [2258-102] **Retrieval of the ocean chlorophyll concentration from spectral radiance during high-altitude airborne experiment**
S. V. Efimov, T. V. Kondranin, Moscow Institute of Physics and Technology (Russia); A. P. Vasilkov, P.P. Shirshov Institute of Oceanology (Russia); A. G. Zhestkov, C. V. Gazzarov, N. A. Askerov, NPO VNIIFTRI (Russia)

- [2258-109] **In-situ profiling system for the measurement of optical properties of sea ice**
W. S. Pegau, Oregon State Univ.; R. A. Maffione, SRI International;
J. R. V. Zaneveld, Oregon State Univ.

- [2258-117] **Light extinction and absorption by layered ellipsoids**
A. A. Kokhanovsky, Institute of Physics (Belarus)

Author Index

- Aas, Eyvind, 332
 Aiken, James, 90
 Alekseyev, N. V., 822
 Aleshin, Igor V., 682
 Allwood, Robert L., 547
 Amone, Robert A., 322, 342
 Askerov, Nizami A., Addendum
 Asper, Vernon L., 33
 Atkinson, Charles A., 163
 Balch, William M., 512
 Beckert, Marko, 894
 Beeker, A. E. R., 77
 Bessarabov, Mikhail I., Addendum
 Bidigare, Robert R., 152
 Bogucki, Darek, 247
 Bonnier, Denis, 413
 Booth, Charles R., 654, 879
 Braescu, Cora, 366
 Brophy, M. Michele, 377
 Bruce, Elizabeth J., 12
 Buiteveld, Hendrik, 174
 Burca, Mihai, 366
 Burenkov, Vladimir I., Addendum, 634, 644
 Bykovsky, Yuri A., Addendum
 Caporelli, Elizabeth, Addendum
 Carder, Kendall L., 21, 768
 Cariou, Jack, 438
 Chang, Enson, 831
 Chekalyuk, Alexander M., Addendum, 140
 Chen, Wei-biao, 556
 Chubarov, S. I., Addendum
 Ciotti, Aurea M., 105
 Cleveland, Joan S., 685
 Coble, Paula G., 377
 Costello, David K., 21, 768
 Cullen, John J., 105
 Culver, Mary E., 123
 D'Sa, Eurico J., 33
 Dalløkken, Runar, 266
 Dana, David R., Addendum
 Davis, Richard F., 123
 Diaconu, Vasile, 366
 Dickey, Tom D., 247
 Dörffer, Roland, 887, 976
 Dolin, Lev S., 522, 588
 Domaradzki, Andrzej, 247
 Donze, M., 174
 Duhig, Michael S., 879
 Efimov, Sergei V., Addendum
 Feigels, Victor I., 449, 458
 Filippov, Yury V., 210
 Forand, J. L., 194, 413
 Fournier, Georges R., 194, 413, 576
 Gazzarov, Christophor V., Addendum
 Ge, Yuntao, 512
 Gerth, Monika, 894
 Gilbert, Gary D., Addendum, 472
 Goldin, Yuri A., Addendum
 Goncharov, Eduard G., 671
 Goncharov, Vladimir K., 797
 Gorbunov, M. Yu., Addendum, 140
 Gould, Richard W., 322, 342
 Gran, Robert L., 831
 Graßl, Hartmut, 976
 Guenther, Gary C., 422
 Gureev, Boris A., Addendum
 Gurevich, Irina Y., 747
 Hakvoort, J. H. M., 77, 174, 529
 Hammond, Robert R., 685
 Handley, Philip L., 12
 Hapter, Ryszard, 277
 He, Ming-xia, 556
 Heath, Alan L., 685
 Højerslev, Niels Kristian, 357
 Holl, Lydia J., 2
 Hou, Weilin, 768
 Huang, Xiao-Sheng, 556, 560
 Hull, Patricia G., 613, 735
 Hunt, Arlon J., 613, 735, 908
 Iturriaga, Rodolfo H., 568, 920, 933
 Jaffe, Jules S., 56
 Jin, Zhonghai, 954
 Joelson, Brad D., 234
 Jonasz, Miroslaw, 576
 Kakui, Yoshimi, 67
 Karlsson, Ulf C., 392
 Kattawar, George W., 222, 234
 Keeler, Roger N., 480
 Kiefer, Dale A., 163
 Kilpatrick, Katherine A., 512
 Kitchen, James C., Addendum, 44
 Kokhanovsky, Alexander A., Addendum
 Kondranin, Timofey V., Addendum
 Kondratyev, K. Ya., 994
 Konnoff, Daniel, 539
 Kopelevich, Oleg V., Addendum, 210, 623, 644
 Kopilevich, Yuri I., 449, 458, 822
 Koppari, Kurt R., 392
 Krijgsman, J., 77
 Król, Tadeusz, 134
 Kugeiko, Michail M., Addendum
 Kurasov, B. V., 822
 LaRocque, Paul E., 422
 Landry, Mark A., 944
 Leighton, Terrence, 613
 Levin, Iosif M., 522, 588, 759, 861
 Lewis, Marlon R., 105
 Lillycrop, W. Jeff, 422

- Liu, Hai, 564
 Liu, Yagang, 568
 Liu, Zhi-Shen, 556, 560
 Lohrenz, Steven E., 33
 Longacre, Jacob R., 944
 Łotocka, Maria, 134
 Lotrian, Jean, 438
 Lyskov, Vladimir G., 797
 Maffione, Robert A., Addendum, 256
 Malevich, Igor A., Addendum
 Marra, John, 152
 Matsui, Matsunaga, 664
 Matsui, Shizuko, 664
 McCormick, Norman J., 2, 711, 850
 Menzies, Dave W., 815
 Mestechkina, T., 654
 Michaels, Anthony F., Addendum, 815
 Miller, David, 908
 Minyeev, V. N., Addendum
 Miroshnikov, Mikhail M., Addendum
 Mobley, Curtis D., 184
 Moore, Casey C., Addendum, 44
 Moore, G. F., 90
 Morel, André, 870
 Morris, Michael J., 33
 Morrow, John H., 654, 879
 Myrmehl, Cathrine, 870
 Nanjo, M., 67
 Necsoiu, Marius, 366
 Nishimoto, Akio, 67
 North, Mark H., 472
 O'Brien, M. C., 539
 Ondercin, Dan, 163
 Onoshko, Dmitry M., Addendum
 Opreacu, Nicolaie, 366
 Oriol, Ramon A., 322
 Osadchy, V. U., 747
 Pakkonen, Sulo A., 793, 806
 Palowitch, Andrew W., 56
 Patton, Randall J., 831
 Pegau, W. Scott, Addendum, 597
 Perehrian, Anri Y., Addendum, 784
 Perennou, André, 438
 Perry, Mary Jane, 123
 Pettersson, Lasse H., 994
 Piskozub, Jacek, 300
 Povarkov, V. I., Addendum
 Pozdnyakov, Dmitry V., 994
 Prokhorenko, Olga V., 623
 Quinby-Hunt, Mary S., 613, 735, 908
 Radomysl'skaya, Tamara M., 522
 Rathbun, Catherine, 33
 Repin, Vladimir I., 671
 Repina, Olga I., 671
 Robinson, I. S., 90
 Roesler, Collin S., 309, 920, 933
 Ryabova, V. N., 682
 Saito, Toshiyuki, 67
 Sakshaug, Egil, 266
 Samkov, V. M., Addendum
 Samokhina, Irene A., Addendum
 Sandvik, Roar, 266
 Schiller, Helmut, 887
 Schoonmaker, Jon S., 685
 Semovski, Sergey V., 277
 Shapiro, Daniel B., 613
 Shaw, Felecia G., 613
 Shelyakov, Alexander V., Addendum
 Shifrin, Kusiel S., Addendum, 431, 747
 Shirokikh, P. A., Addendum
 Sidorenko, Vladimir M., 793, 806
 Siegel, David A., Addendum, 539, 815
 Siegel, Herbert, 894
 Smart, Jeffrey H., 116, 502
 Smith, Raymond C., 12
 Solovyev, Valentine I., Addendum
 Sonek, Gregory J., 568
 Sorensen, Jens C., 539
 Sørensen, Kai, 332
 Stamnes, Knut H., 954
 Stavn, Robert Hans, 202
 Steinvall, Ove K., 392
 Stramski, Dariusz, 184, 704
 Sud'bin, Anatoly I., Addendum, 644
 Tamashige, Shigeyoshi, 664
 Tanis, Fred J., 965
 Tao, Zheng, 850
 Terrie, Gregory E., 322
 Tessendorf, Jerry A., Addendum
 Tetlow, Steve, 547
 Tibilov, Alexander S., Addendum
 Tsuda, Ryohei, 67
 Tsvetkov, E. A., 682
 Ulich, Bobby L., 480
 van de Hulst, Hendrik C., 234
 Vasilkov, Alexander P., Addendum, 288
 Volden, Rune, 723
 Volynsky, Vladimir A., Addendum
 von Smekot-Wensierksi, Witold, 976
 Voss, Jeffrey M., Addendum, 116
 Voss, Kenneth J., 256, 512
 Walters, Roy A., 33
 Wan, Zhengming, 12
 Wasson, David, Addendum
 Weeks, Alison R., 90
 Weeks, W. F., 954
 Weidemann, Alan Dean, 202
 Weir, Christian T., 815
 Wouts, Remco R., 529
 Woźniak, Bogdan, 277, 976
 Xu, Xin, 222
 Yakovlev, V. A., 811, 822
 Yasakov, Alexey K., 605
 Zaneveld, J. Ronald V., Addendum, 44, 247, 309, 597
 Zhang, Jin-Long, 556
 Zhang, Ting-Lu, 556, 560, 564
 Zhestkov, Anatoly G., Addendum
 Zhurenkov, A. G., 811
 Zolotov, Ilja G., 431
 Zolotukhin, Igor V., 861